

Springer Proceedings in Energy

Mohan Lal Kolhe

S. B. Jaju

P. M. Diagavane *Editors*

Smart Technologies for Energy, Environment and Sustainable Development, Vol 1

Select Proceedings of ICSTEESD 2020

 Springer

Springer Proceedings in Energy

The series Springer Proceedings in Energy covers a broad range of multidisciplinary subjects in those research fields closely related to present and future forms of energy as a resource for human societies. Typically based on material presented at conferences, workshops and similar scientific meetings, volumes published in this series will constitute comprehensive state-of-the-art references on energy-related science and technology studies. The subjects of these conferences will fall typically within these broad categories:

- Energy Efficiency
- Fossil Fuels
- Nuclear Energy
- Policy, Economics, Management & Transport
- Renewable and Green Energy
- Systems, Storage and Harvesting
- Materials for Energy

eBook Volumes in the Springer Proceedings in Energy will be available online in the world's most extensive eBook collection, as part of the Springer Energy eBook Collection. To submit a proposal or for further inquiries, please contact the Springer Editor in your region:

Kamiya Khatter (India)

Email: kamiya.khatter@springer.com

Loyola D'Silva (All other countries)

Email: loyola.dsilva@springer.com

More information about this series at <https://link.springer.com/bookseries/13370>

Mohan Lal Kolhe · S. B. Jaju · P. M. Diagavane
Editors

Smart Technologies for Energy, Environment and Sustainable Development, Vol 1

Select Proceedings of ICSTEESD 2020

 Springer

Editors

Mohan Lal Kolhe
Faculty of Engineering and Science
University of Agder
Kristiansand, Norway

S. B. Jaju
Department of Mechanical Engineering
G. H. Raisoni College of Engineering
Nagpur, Maharashtra, India

P. M. Diagavane
Department of Electrical Engineering
G. H. Raisoni College of Engineering
Nagpur, Maharashtra, India

ISSN 2352-2534

ISSN 2352-2542 (electronic)

Springer Proceedings in Energy

ISBN 978-981-16-6874-6

ISBN 978-981-16-6875-3 (eBook)

<https://doi.org/10.1007/978-981-16-6875-3>

© The Editor(s) (if applicable) and The Author(s), under exclusive license to Springer Nature Singapore Pte Ltd. 2022

This work is subject to copyright. All rights are solely and exclusively licensed by the Publisher, whether the whole or part of the material is concerned, specifically the rights of translation, reprinting, reuse of illustrations, recitation, broadcasting, reproduction on microfilms or in any other physical way, and transmission or information storage and retrieval, electronic adaptation, computer software, or by similar or dissimilar methodology now known or hereafter developed.

The use of general descriptive names, registered names, trademarks, service marks, etc. in this publication does not imply, even in the absence of a specific statement, that such names are exempt from the relevant protective laws and regulations and therefore free for general use.

The publisher, the authors and the editors are safe to assume that the advice and information in this book are believed to be true and accurate at the date of publication. Neither the publisher nor the authors or the editors give a warranty, expressed or implied, with respect to the material contained herein or for any errors or omissions that may have been made. The publisher remains neutral with regard to jurisdictional claims in published maps and institutional affiliations.

This Springer imprint is published by the registered company Springer Nature Singapore Pte Ltd.

The registered company address is: 152 Beach Road, #21-01/04 Gateway East, Singapore 189721, Singapore

Preface

Substantial amounts of smart technologies are going to be integrated in the near future for development of environmental-friendly infrastructure. They will be important part of the electricity, heat, gas, transport, building sectors, etc. However, energy security, greenhouse gas emissions, sustainable buildings, cleaner transportation, and resilience are key challenges, and they need to be solved for a low-carbon economy through focused and integrated efforts with the use of smart technologies.

Smart grid performs an important role in the ‘Energy Transition’ to integrate environmental-friendly energy systems within the distributed network infrastructure (e.g., electricity, heat, gas, transport, etc.) for the sustainable development. The necessity for ‘Energy Transition’ is broadly understood and shared, as the world starts to embrace a transition towards sustainable energy systems by shifting from fossil fuel-based energy production to decentralized renewable energy and energy efficient systems.

As the editors of the Select Proceeding of ICSTEESD-2020, ‘Smart Technologies for Energy, Environment and Sustainable Development’, Special Volume of Springer Proceedings in Energy (ISSN: 2352-2534), we wish to express sincere gratitude to the authors for diligent research dissemination as well as to the reviewers for providing constructive and critical comments in improving the quality of the selected articles. The objective of this special volume is to present advancements in smart technologies for environmental-friendly energy systems and their management, policies for making an energy transition towards sustainable societies. The selected peer-reviewed articles are classified in the categories of (i) Sustainable Electrical Energy Systems, (ii) Environmental Management and (iii) Industrial Engineering with focus on sustainable development. ICSTEESD-2020 is a major multidisciplinary sustainable engineering conference organized with the objective of bringing together academia, industry practitioners and engineering graduates to analyze scientific studies focusing on both clean energy technologies, environmental sustainability and smart network concepts to integrate the relationship among them. ICSTEESD-2020 is envisioned to analyze the increasing penetration of environmental-friendly technologies with energy efficiency and management as central topics with effective participation from the academicians, industry practitioners, governmental policy

makers, as well as of community service providers. ICSTEESD-2020 has been organized at G. H. Raisoni College of Engineering (GHRCE), Nagpur, India, on December 4–5, 2020.

As editor(s) of this special issue of Springer's proceeding of ICSTEESD-2020, we want to tribute deep sense of appreciations to the international academic partners (e.g., University of Agder, Norway; University of Ruhuna, Sri Lanka; Kyushu Sangyo University, Japan; University of Dundee, UK; Mie University, Japan) for academically assisting ICSTEESD-2020. We wish to express our sincere appreciation to the authors, plenary speakers, presenters, participants, supporters, reviewers, technical committee members as well as the entire team of G. H. Raisoni College of Engineering, Nagpur (India). We are very grateful to Shri Sunil Raisoni, Chairperson of the Raisoni Group of Institutions; Dr. Sachin Untawale, Director, GHRCE, Nagpur; Dr. Rupesh Shelke, Dr. Bhalchandra Khode and ICSTEESD-2020 organizing committee members for contributing effectively in making the Springer's ICSTEESD-2020 and publication of the special volume successful.

We strongly believe that ICSTEESD-2020 has provided an effective platform to integrate academia, industry practitioners and engineering graduates to share their research and innovations for the sustainable development of the society.

Kristiansand, Norway
Nagpur, Maharashtra, India
Nagpur, Maharashtra, India
December 2020

Prof. Dr. Mohan Lal Kolhe
Prof. S. B. Jaju
Prof. P. M. Diagavane

Contents

Seismic Analysis of 3D Printed Structures	1
Poojith Prakash and G. M. Basavangowda	
Efficiency of Linear Univariate Programming Method in Estimating the Parameters Reflecting the Behavior of R.C.C Beam Along the Span	13
R. Rakesh and Puttaraju	
Geopolymer a Sustainable Material: A Review	29
Priyanka Salunkhe, Prathamesh Balip, Tejas Deshmukh, Siddesh Gadge, and Prasad Vhanmane	
Effect of Creep and Shrinkage on Construction Sequence Analysis of High-Rise Building	43
Leroy M. Tuscano and Priyanka Jadhav	
Experimental Investigation of Concrete Used in Spent Fuel Pools of Nuclear Power Plants Subjected to Boiling Water Exposure	65
Priyanka Jadhav, Keshav Sangle, Apurv Vaidya, Ankit Dhoot, and Siddhant Biyani	
Experimental and Analytical Study of Shape Memory Alloy in Civil Structures—A Review	81
Priyanka Salunkhe, Prajakta Agawane, Durita Chaudhari, and Sakshi Patil	
Effect of Aspect Ratio on Fatigue Behaviour of Steel Shear Wall	91
R. K. Chethan Gowda, K. Ashwini, and H. M. Rajashekaraswamy	
An Overview—The Effect of Radon on the Existing Building	99
Anil Pawade and Shrikant Charhate	
Extreme Rainfall Analysis Using Extreme Value (EV-I) Distribution Based on L-Moment Approach	107
Sanjay Kumar, L. N. Thakural, J. P. Patra, and Sunil Gurrapu	

Application of Machine Learning for Accuracy Improvement of Projected Precipitation of Climate Change Data with Observed Data	117
Lakhwinder Singh, Deepak Khare, and Nitin Mishra	
Statistical Downscaling of Climate Change Scenarios of Rainfall in Haridwar District of Uttarakhand, India	131
Gaurav Singh, Nitin Mishra, L. N. Thakural, and Sanjeev Kumar	
Land Use/Land Cover Change Detection of Bina River Basin, Madhya Pradesh	143
Gaurav Singh, Nitin Mishra, L. N. Thakural, and Amit Kumar Shrama	
Biocomposites and Their Applications in Civil Engineering—An Overview	151
Manish S. Dharek, Jagadish Vengala, Prashant Sunagar, K. S. Sreekeasha, Pramod Kilabanur, and Poornachandra Thejaswi	
Analysis and Design of Pipe Rack Structures: A Review	167
Jamaluddin Maghrabi, Prerana Landge, and Riya Kotian	
Removal of Methylene Blue Using Activated Carbon Prepared from Waste Fruit (Orange) Peels	177
Shantini A. Bokil and Niraj S. Topare	
Effect of Elevated Temperatures on Conventional Concrete	189
Vinayak Vaidya, Valsson Varghese, and Preeti K. Morey	
Extracted Sand from Overburden of WCL Mines as Sustainable Sand Solution	199
B. V. Bahoria and Ashwini Badhiye	
Domestic Greywater Treatment by Hybrid Electrocoagulation and Filtration Method in Continuous Mode	211
Sanket Devikar, Khalid Ansari, Charuta Wagmare, and Mangesh Bhokar	
Computing the Compressive Strength of Fly Ash Concrete by Using Machine Learning	219
Lomesh S. Mahajan and S. R. Bhagat	
Water Budget Allocation for Curing of Residential Bungalow and Self-curing Concrete as a Smart Material for Construction	225
Mahesh Navnath Patil and Shailendrakumar Dubey	
Applications of Engineering Mathematics in Real Life Civil Engineering: Practical Examples	241
Mahesh Navnath Patil, Vinay Ashok Rangari, Aakash Suresh Pawar, and Shailendrakumar Dubey	

Shear Strength Improvement of Black Cotton Soil Reinforced with Waste Plastic Bottle Strips 261
 Nilesh Shirpurkar, Dhanraj Saste, Vaibhav Varpe, and Bhaskar Wabhitkar

A Study on Behaviour of Pedestrians to Improve the Riding Quality and Comfortability Through Metro Rail System: A Review 273
 Vamsi Kommanamanchi, Jyoti Prakash Giri, and Koorma Rajendra Babu

Improvement in Liquid and Plastic Limit for Black Cotton Soil by Addition of RBI Grade 81 293
 Prashant Khedkar, Shraddha Shinde, Sakshi Wayal, and Bhaskar Wabhitkar

Effect of Infill Wall on Reinforced Concrete Frame 299
 Swati D. Ambadkar and Vinayak S. Dakre

Development of Eco-Friendly Pervious Concrete Utilizing Granite Cutting Sludge Waste 309
 Yash Agrawal, Manish Varma, Trilok Gupta, and Ravi K. Sharma

Strength and Durability of Nano-silica Added Cement Composites—A Way Forward 321
 Babalu Rajput and S. S. Pimplikar

Controller for the Power Injection from a Grid-Interfaced Energy Storage within an AC Micro Grid 337
 D. J. K. Dassanayake, H. M. A. P. Ruwanthi, K. K. D. I. Karunanayaka, K. M. S. Y. Konara, P. D. C. Perera, and Mohan Lal Kolhe

Economic Load Dispatch in Power System by Using Elephant Herding Optimization Technique 357
 Leena Daniel, Krishna Teerth Chaturvedi, and Mohan Lal Kolhe

Role of Subsidies for PV Solar Installations in India: A Cost–Benefit Analysis 369
 Pooja Sharma, Mohan Lal Kolhe, Stina Torjesen, and Arvind Sharma

An Efficient Ensemble-Based Protection Technique for Transmission Line Protection 381
 Murli Manohar, Prema Diagavane, and Sunil Kumar Shukla

Electric Vehicle (EV) Powertrain Modeling and Optimization 391
 Vinay Pawar and Shridhar Rakhonde

Static 2D-Finite Element Analysis of Eccentricity Fault in Induction Motor 409
 E. Fantin Irudaya Raj and M. Appadurai

The Saturated Core Fault Current Limiter in Modern Power Systems—A Laboratory Model Test Results	423
Vittesh Naphade, Kiran Naphade, and Vilas Ghate	
Double Stage Voltage Lift Switched Capacitor Converter for High-Voltage Applications in DC Microgrids	433
Md. Samiullah, Imtiaz Ashraf, and Atif Iqbal	
Impact Analysis of Different Gap on CIGS Photovoltaic Device with MoSe₂ as Tunnel Layer	443
R. Akter, R. A. Anonto, K. Nahreen, A. A. Badhon, T. Mahubb, M. J. Alam, and S. S. Mahtab	
A Review on Architecture of Hybrid Electrical Vehicle and Multiple Energy Storage Devices	459
Kiran H. Raut and Asha Shendge	
Comprehensive Topological Analysis of Solar Integrated Multilevel Inverter for Power Filters	475
Bipasa Patra and Pragya Nema	
Implementation of Scalable Low Cost Industrial IoT GATEWAY for Uninterrupted Monitoring and Data Acquisition of Industrial Machines	487
Suraj Satyawandan Dudhe, Amit Khawse, Pankaj Ramtekkar, and Ankur Gupta	
Verification of Microprocessor Using Universal Verification Methodology	495
Sarabjeet Singh Tieth and P. M. Menghal	
Optimal Operation Strategy for A. A. Energy Ltd. 10 MW Cogeneration Power Plants, Wadsa	503
Sachin Shedmake, Ramchandra Adware, and Dhanraj Rajurkar	
Analysis of Ferroresonance in a Transformer with B-H Loop Having Variable Core Loss	511
Rajat Shubhra Pal	
A Brief Review of Cathode Materials for Li-ion Batteries	521
D. Saritha	
A Review of Electric Vehicle Components	531
Mali Rohini and Shendge Asha	
Contribution Generation of Electricity from Treadmill Using Piezoelectric Transducers	559
L. Divakar, Dheeraj Mohan, Dimpa Moni Kalita, and P. V. Abhishek	

Influence of Pyrolysis Technologies on Biofuel Production and Its Physicochemical Properties: A Review 569
 Ashish Pawar and N. L. Panwar

Bayesian Regularization Neural Network-Based Fault Detection System in HVDC Transmission System 601
 Aditya S. Londhe, Aashutosh S. Ingale, and Chetan B. Khadse

Revisited the Design Technique of Hybrid Dielectric Resonator Antenna 609
 Dipali Soren and Nilesh Tamboli

A Review on Different Technology Used in Battery Management System of Electric Vehicle 621
 Madina S. Tamboli and Asha Shendge

Power Quality Analysis of Grid Connected Solar Farm with FC-TCR and UPFC 633
 Abhishek Kumar Sinha, Sachin Mishra, and Javed Dhillon

Five-Phase Induction Motor Modeling and Its Analysis Using MATLAB/Simulink 645
 Sandip A. Gaikwad and S. M. Shinde

Air Writing-Based Automated Room 655
 Sagnik Ghosh and Aniruddha Mitra

Reliability Assessment of Smart Grid with Renewable Energy Sources, Storage Devices, and Cyber Intrusion 669
 Lalit Tak, Atul Kumar Yadav, Neeraj Kumar Singh, and Vasundhara Mahajan

Development of Unstructured Kinetic Model for Bioethanol Production by *Saccharomyces cerevisiae* MTCC 171 from Sorghum Grain Waste 687
 Sheetal Deshmukh and Dheeraj Deshmukh

Experimental Investigation on RCCI Engine Operated with Dairy Scum Oil Methyl Ester and Producer Gas 695
 V. S. Yaliwal, P. A. Harari, and N. R. Banapurmath

A Study on Women Police Bullet-Proof Jacket Considering Anthropometry Data, Comfort and Safety in Pune, India 707
 Chinmayanand Prakash Jagtap, Shilpi Bora, Pranjal Arun Patil, Abhijeet Malge, and Mahesh Goudar

Scrap Reduction and Proper Utilization of Raw Materials During Cutting Operations in SMEs 725
 Arpita R. Shukla, A. M. Khalatkar, and Inayat Ullah

Fuel-Purpose Bioethanol from Agricultural Waste: A Step Towards Sustainable Environment and Energy Security	739
Debasmita Dash and Bhabani Prasanna Pattanaik	
Bio-Dielectric as an Alternative Degradable and Sustainable Fluid in EDM: A Review	751
Tapas Chakraborty and Amitava Mandal	
Laboratory Investigation of Composite Made of Alumina Dispersed Aluminum Prepared by UTM Pressed Powder Metallurgy Method	761
M. K. Manik, Mani Bhushan Shing, and Vishal Vhagat	
Numerical Investigation on Can-Combustor's Performance for Different Alternative Fuels Using CFD	783
P. Shankara Narayanan, Padma Ganesan, R. Arul Prakash, R. Vijayanandh, and M. Ramesh	
Modal Analysis of Special Type of Flexure Bearing for Space Application	799
Suraj Bhojar, Virendra Bhojwani, Ganesh Khutwad, Gaurav Sawant, Jay Lad, and Stephen Sebastian	
Numerical Simulation of a Finned-Surface Prismatic Lithium-Ion Battery Thermal Management System	811
Pranjali Tete, Puneet Kedar, Mahendra Gupta, and Sandeep Joshi	
A Review on Performance and Evaluation of Modified Regenerator's Material in Stirling-Type Pulse Tube CryoCooler	821
Raj A. Aasole, Kaustub Ambarwele, Harshad Vaidya, Shubham Joshi, and Ashish Raut	
Real-Time Problem of Knob Assembly in Automobile Manufacturing Industries	831
Prabinkumar R. Jachak, Abhay Khalatkar, and Nilesh M. Narkhede	
Effect of Various Parameters on Aerodynamic Performance of Savonius VAWT: A Review	837
Shivaji Suryabhan Aher and Netra Pal Singh	
Finite Time Thermodynamic Investigation of a Solar-Boosted Irreversible OTEC	849
Aravind Ramachandran, U. B. Arun Shal, and Siddharth Ramachandran	
Process Parameter Optimization of Fused Deposition Modeling Using Taguchi's Design of Experiment	861
Pankaj B. Ranade, Shivam H. Dandgavhal, Apurva K. Dhokane, and Apoorva R. Kale	

Optimization of Process Parameters to Analyze Wear Behavior of an Uncoated Tool on AL-MMC 883
 Seema V. Yerigeri and Shantisagar K. Biradar

Estimation of Natural Frequencies of Gear Meshing System Using Modal Analysis 893
 Rahul A. Jibhakate, Prafull S. Thakare, Chetan J. Choudhari, and Piyush Patil

An Arrangement and Robust Design of Automated Grass Cutter Gadget Using Computer-Aided Design 903
 Kanchan D. Ganvir and Akshay D. Anjekar

Performance Evaluation of Adhesive Bonded Tools Using Design of Experiments 913
 Shrikant Jachak, Ashvin Amale, and Sachin Mahakalkar

Analyzing the Mutual Interaction Among the Barriers of Additive Manufacturing: An Interpretive Structural Modelling Approach 923
 Reetika Pandey and Ubaid Ahmad Khan

Addressing the Agile Manufacturing Drivers Using Interpretive Structural Modeling 935
 Rohit Sharma and Ubaid Ahmad Khan

Minimization of Surface Roughness of WEDM’ed H13 Tool Steel Using Taguchi Method 945
 Lakhan Rathod, Bonde Assefa, Duba Chena Dero, and Ramesh Rudrapati

Brief Overview on Study of Various Parameters Affecting the Productivity of Cotton Yarn 955
 Kedar M. Kulkarni and Anil R. Sahu

Experimental Investigation of Hybrid Nanofluids Characteristics in Ti6Al4V Drilling Using Minimum Quantity Lubrication Technique 965
 P. A. Dalke, B. N. Tripathi, and G. P. Deshmukh

Simple Automatic Temperature Controller for Chemical Batch Reactor 977
 Gogullan Amirthakulasingham, Rohan Edirisooriya Patabendige, Sumith Baduge, and Buddhika Annasiwaththa

Editors and Contributors

About the Editors

Prof. Dr. Mohan Lal Kolhe is a full professor in smart grid and renewable energy at the Faculty of Engineering and Science of the University of Agder (Norway). He is a leading renewable energy technologist with three decades of academic experience at the international level and previously held academic positions at the world's prestigious universities, e.g., University College London (UK/Australia), University of Dundee (UK); University of Jyväskylä (Finland); Hydrogen Research Institute, QC (Canada); etc. In addition, he was a member of the Government of South Australia's first Renewable Energy Board (2009–2011) and worked on developing renewable energy policies. Due to his enormous academic contributions to sustainable energy systems, he has been offered the posts of Vice-Chancellor of Homi Bhabha State University Mumbai (Cluster University of Maharashtra Government, India), full professorship(s)/chair(s) in 'sustainable engineering technologies/systems' and 'smart grid' from the Teesside University (UK) and Norwegian University of Science and Technology (NTNU) respectively. He is Series Editor of Springer Proceedings in Energy. His research works in energy systems have been recognized within the top 2% of scientists globally by Stanford University's 2020, 2021 matrix. He is an internationally recognized pioneer in energy field, whose top 10 published works have an average of over 175 citations each.

Prof. Dr. S. B. Jaju obtained his master's degree in Industrial Engineering from VRCE (Now known to be VNIT), Nagpur, and received Ph.D. from Rashtrasant Tukadoji Maharaj Nagpur University. He has completed Master of Business Administration from IGNOU, New Delhi. He is presently working as Dean (Research & Development) and Professor in the Department of Mechanical Engineering of G. H. Raisoni College of Engineering. He has more than 23 years of teaching experience. He has to his credit more than 100 research papers published in national and international journals and conferences, one book and six book chapters. He has attended more than 50 symposiums, short-term courses, training, and workshops. He has delivered more

than 50 expert lectures in short-term training programmes and workshops. He served as convener of series of All India Seminar Quality Progress, general chair of International conference on advances in mechanical engineering, and program chair in IEEE International Conference on Emerging Trends in Engineering & Technology. He is serving as member on editorial board, reviewer of international journal, chaired number of technical sessions in conferences. He is associated with many prestigious professional societies like Institution of Engineers (India); ISTE New Delhi; Indian Institution of Industrial Engineering, Mumbai; Indian Society of Mechanical Engineers (ISME), New Delhi; IEEE-Robotics and Automation Society and ASME. He is a certified Lead Auditor of ISO 9001: 2008 QMS by IRCA UK. He has guided more than 20 PG dissertations, five Ph.Ds. awarded, one Ph.D. student have submitted thesis. He has filed six patents, one copyright, completed research project of AICTE. He has visited National University of Singapore; Multimedia University, Malaysia; University of Technology, Mauritius; and various universities in Dubai. He received Best Teacher Award given by G. H. Raisoni College of Engineering for the year 2003–2004. He has also received Best Case Study Award (non-traditional area) in the form of Silver Medal by National Council of Indian Institution of Industrial Engineering, Navi Mumbai, for the year 2004–2005. He has received 07 Best Paper Awards. His research area includes quality cost, total quality management, supply chain management, service quality, lean manufacturing, productivity improvement techniques and industrial engineering areas.

Prof. Dr. P. M. Diagavane is currently professor at the Department of Electrical Engineering, G. H. Raisoni College of Engineering, Nagpur. She obtained her B.E. (Electrical) from Government college of Engineering Amravati and M.S. (Electronics and Control) from BITS Pilani and Ph.D. from Rashtrasant Tukadoji Maharaj Nagpur University, Nagpur. Her major areas of research interests include control engineering, soft computing tools, optimization techniques, renewable energy in electrical engineering. She has more than 30 years of teaching experience. He has to her credit more than 65 research papers published in national and international journals and conferences, two book chapters. She has attended more than 50 symposiums, short-term courses, training, and workshops. She received Best Teacher Award given by G. H. Raisoni College of Engineering for the year 2014–2015. She had organized and was general chair of International conference published by IEEE and Springer. She is serving as reviewer of international journal and chaired number of technical sessions in conferences. She is associated to many prestigious professional societies like Institution of Engineers (India), ISTE New Delhi and IEEE.

Contributors

Raj A. Aasole G. H. Raisoni College of Engineering, Nagpur, India

P. V. Abhishek Ramaiah University of Applied Sciences, Bangalore, Karnataka, India

Ramchandra Adware Department of Electrical Engineering, G. H. Rasoni College of Engineering, Nagpur, India

Prajakta Agawane Department of Civil Engineering, Terna Engineering College, Nerul, Navi Mumbai, India

Yash Agrawal Department of Civil Engineering, College of Technology and Engineering, MPUAT, Udaipur, Rajasthan, India

Shivaji Suryabhan Aher Research Scholar, Department of Mechanical Engineering, Oriental University, Indore, MP, India

R. Akter Department of EEE, Mymensingh Engineering College, Mymensingh, Bangladesh

M. J. Alam Department of EEE, Feni University, Feni, Bangladesh

Ashvin Amale Department of Mechanical Engineering, Yeshwantrao Chavan College of Engineering, Nagpur, Maharashtra, India

Swati D. Ambadkar Department of Civil Engineering, G. H. Rasoni University, Amravati, India

Kaustub Ambarwele G. H. Rasoni College of Engineering, Nagpur, India

Gogullan Amirthakulasingam Department of Mechanical and Manufacturing Engineering, Faculty of Engineering, University of Ruhuna, Galle, Sri Lanka

Akshay D. Anjekar Department of Mechanical Engineering, Priyadarshini Bhagwati College of Engineering, Nagpur, Maharashtra, India

Buddhika Annasiwaththa Department of Mechanical and Manufacturing Engineering, Faculty of Engineering, University of Ruhuna, Galle, Sri Lanka

R. A. Anonto Department of EEE, American International University Bangladesh, Dhaka, Bangladesh

Khalid Ansari Department of Civil Engineering, Yeshwantrao Chavan College of Engineering, Nagpur, India

M. Appadurai Department of Mechanical Engineering, Dr. Sivanthi Aditanar College of Engineering, Tiruchendur, India

R. Arul Prakash Department of Aeronautical Engineering, Kumaraguru College of Technology, Coimbatore, Tamil Nadu, India

U. B. Arun Shal Government Engineering College, Kozhikode, Kerala, India

Shendge Asha GHRIT, Electrical Department, Savitribai Phule University, Wagholi, Pune, India

Imtiaz Ashraf Aligarh Muslim University, Aligarh, India

K. Ashwini M. S. Ramaiah University of Applied Sciences, Bengaluru, India

Bonde Assefa Department Industrial Engineering, Bule Hora University, Bule Hora, Ethiopia

Ashwini Badhiye Rajiv Gandhi College of Engineering and Research, Nagpur, India

A. A. Badhon Department of ECE, Khulna University of Engineering and Technology, Khulna, Bangladesh

Sumith Baduge Department of Mechanical and Manufacturing Engineering, Faculty of Engineering, University of Ruhuna, Galle, Sri Lanka

B. V. Bahoria Yeshwantrao Chavan College of Engineering, Nagpur, India

Prathamesh Balip Department of Civil Engineering, Terna Engineering College, Nerul, Navi Mumbai, India

N. R. Banapurmath Department of Mechanical Engineering, BVB College of Engineering and Technology, Hubballi, Karnataka, India

G. M. Basavangowda Ramaiah Institute of Technology, Bangalore, Karnataka, India

S. R. Bhagat Department of Civil Engineering, Dr. Babasaheb Ambedkar Technological University, Maharashtra, India

Virendra Bhojwani Department of Mechanical Engineering, MIT-ADT University, Pune, India

Mangesh Bhokar Department of Civil Engineering, G. H. Raison College of Engineering, Nagpur, India

Suraj Bhojar Department of Mechanical Engineering, MIT-ADT University, Pune, India

Shantisagar K. Biradar M.S.S. College of Engineering and Technology, Jalna, India

Siddhant Biyani VJTI, Mumbai, Maharashtra, India

Shantini A. Bokil School of Civil Engineering, Dr. Vishwanath Karad MIT World Peace University, Pune, India

Shilpi Bora School of Design, MIT, Academy of Engineering (MITAOE), Pune, Maharashtra, India

Tapas Chakraborty Department of Mechanical Engineering, Saroj Mohan Institute of Technology, Hooghly, West Bengal, India

Shrikant Charhate Amity School of Engineering and Technology, Amity University, Mumbai, India

Krishna Teerth Chaturvedi UIT, RGPV, Bhopal, M.P., India

Durita Chaudhari Department of Civil Engineering, Terna Engineering College, Nerul, Navi Mumbai, India

R. K. Chethan Gowda M. S. Ramaiah University of Applied Sciences, Bengaluru, India

Chetan J. Choudhari Julelal Institute of Technology, Nagpur, India

Prema Diagavane G. H. Raisonni College of Engineering, Nagpur, MH, India

Vinayak S. Dakre Department of Mechanical Engineering, G. H. Raisonni University, Amravati, India

P. A. Dalke Department of Mechanical Engineering, Chhatrapati Shivaji Maharaj University, Panvel Navi Mumbai, India

Shivam H. Dandgavhal Department of Mechanical Engineering, KKWIEER, Nashik, Maharashtra, India

Leena Daniel UIT, RGPV, Bhopal, M.P., India

Debasmita Dash Department of Chemistry, KMBB College of Engineering and Technology, Khordha Bhubaneswar, Odisha, India

D. J. K. Dassanayake Faculty of Engineering, Department of Electrical and Information Engineering, University of Ruhuna, Galle, Sri Lanka

Duba Chena Dero College of Engineering and Technology, Bule Hora University, Bule Hora, Ethiopia

Dheeraj Deshmukh Department of Mechanical Engineering, G. H. Raisonni College of Engineering, Nagpur, Maharashtra, India

G. P. Deshmukh Department of Mechanical Engineering, A C Patil College of Engineering, Navi Mumbai, India

Sheetal Deshmukh Department of Food Technology, L.I.T., RTMNU, Nagpur, MS, India

Tejas Deshmukh Department of Civil Engineering, Terna Engineering College, Nerul, Navi Mumbai, India

Sanket Devikar Department of Civil Engineering, Yeshwantrao Chavan College of Engineering, Nagpur, India

Manish S. Dharek Department of Civil Engineering, BMS College of Engineering (Affiliated to VTU, Belagavi), Bengaluru, India

Javed Dhillon School of Electronics and Electrical Engineering, Lovely Professional University, Phagwara, Punjab, India

Apurva K. Dhokane Department of Mechanical Engineering, KKWIEER, Nashik, Maharashtra, India

Ankit Dhoot VJTI, Mumbai, Maharashtra, India

L. Divakar Ramaiah University of Applied Sciences, Bangalore, Karnataka, India

Shailendrakumar Dubey Professor and Head of Civil Engineering Department, SSVPS BSD College of Engineering, Dhule, India

Suraj Satyawar Dudhe G. H. Rasoni College of Engineering, Nagpur, India

E. Fantin Irudaya Raj Department of Electrical and Electronics Engineering, Dr. Sivanthi Aditanar College of Engineering, Tiruchendur, India

Siddesh Gadge Department of Civil Engineering, Terna Engineering College, Nerul, Navi Mumbai, India

Sandip A. Gaikwad Electrical Engineering Department, Government College of Engineering, Aurangabad, Maharashtra, India

Padma Ganesan Department of Aeronautical Engineering, Kumaraguru College of Technology, Coimbatore, Tamil Nadu, India

Kanchan D. Ganvir Department of Mechanical Engineering, Priyadarshini Bhagwati College of Engineering, Nagpur, Maharashtra, India

Vilas Ghate Department of Electrical Engineering, Government College of Engineering, Amravati, Maharashtra, India

Sagnik Ghosh St.Thomas College of Engineering and Technology, Kolkata, India

Mahesh Goudar School of Mechanical Engineering, Academy of Engineering (MITAOE), Pune, Maharashtra, India

Ankur Gupta G. H. Rasoni College of Engineering, Nagpur, India

Mahendra Gupta Department of Mechanical Engineering, Shri Ramdeobaba College of Engineering and Management, Nagpur, India

Trilok Gupta Department of Civil Engineering, College of Technology and Engineering, MPUAT, Udaipur, Rajasthan, India

Sunil Gurrapu Surface Water Hydrology Division, NIH Roorkee, Roorkee, India

P. A. Harari Department of Mechanical Engineering, SDM College of Engineering and Technology, Dharwad, Karnataka, India

Aashutosh S. Ingale MIT World Peace University, Pune, Maharashtra, India

Atif Iqbal Qatar University, Doha, Qatar

Prabinkumar R. Jachak G. H. Raisoni College of Engineering, Nagpur, India

Shrikant Jachak Department of Mechanical Engineering, Yeshwantrao Chavan College of Engineering, Nagpur, Maharashtra, India

Priyanka Jadhav Department of Civil Engineering, Terna Engineering College, Nerul Navi-Mumbai, Maharashtra, India

Chinmayanand Prakash Jagtap School of Mechanical Engineering, Academy of Engineering (MITAOE), Pune, Maharashtra, India

Rahul A. Jibhakate G. H. Raisoni College of Engineering, Nagpur, India

Sandeep Joshi Department of Mechanical Engineering, Shri Ramdeobaba College of Engineering and Management, Nagpur, India

Shubham Joshi G. H. Raisoni College of Engineering, Nagpur, India

Apoorva R. Kale Department of Mechanical Engineering, KKWIEER, Nashik, Maharashtra, India

Dimpa Moni Kalita The Assam Royal Global University, Assam, India

K. K. D. I. Karunanayaka Faculty of Engineering, Department of Electrical and Information Engineering, University of Ruhuna, Galle, Sri Lanka

Puneet Kedar Department of Mechanical Engineering, Shri Ramdeobaba College of Engineering and Management, Nagpur, India

Chetan B. Khadse MIT World Peace University, Pune, Maharashtra, India

A. M. Khalatkar Department of Mechanical Engineering, G. H. Raisoni College of Engineering, Nagpur, Maharashtra, India

Abhay Khalatkar G. H. Raisoni College of Engineering, Nagpur, India

Ubaid Ahmad Khan Department of Mechanical Engineering, Shambhunath Institute of Engineering and Technology, Prayagraj, U.P., India

Deepak Khare Department of Water Resources Development and Management, Indian Institute of Technology Roorkee, Roorkee, India

Amit Khawse Kapilansh Dhatu Udyog Pvt Ltd., Nagpur, India

Prashant Khedkar Department of Civil Engineering, MIT Academy of Engineering, Pune, India

Ganesh Khutwad Department of Mechanical Engineering, MIT-ADT University, Pune, India

Pramod Kilabanur Ionidea Private Limited, Bengaluru, India

Mohan Lal Kolhe Faculty of Engineering and Science, University of Agder, Kristiansand, Norway

Vamsi Kommanamanchi Department of Civil Engineering, GMR Institute of Technology, Rajam, India

K. M. S. Y. Konara Faculty of Engineering, Department of Electrical and Information Engineering, University of Ruhuna, Galle, Sri Lanka;
Faculty of Engineering and Science, University of Agder, Kristiansand, Norway

Riya Kotian Department of Civil Engineering, Terna Engineering College, Nerul, Navi Mumbai, India

Kedar M. Kulkarni Department of Mechanical Engineering, G. H. Rasoni College of Engineering and Management, Pune, Wagholi, India

Sanjay Kumar Surface Water Hydrology Division, NIH Roorkee, Roorkee, India

Sanjeev Kumar Department of Civil Engineering, Graphic Era Deemed to be University, Dehradun, India

Jay Lad Department of Mechanical Engineering, MIT-ADT University, Pune, India

Prerana Landge Department of Civil Engineering, Terna Engineering College, Nerul, Navi Mumbai, India

Aditya S. Londhe MIT World Peace University, Pune, Maharashtra, India

Jamaluddin Maghrabi Department of Civil Engineering, Terna Engineering College, Nerul, Navi Mumbai, India

Lomesh S. Mahajan Department of Civil Engineering, Dr. Babasaheb Ambedkar Technological University, Maharashtra, India

Vasundhara Mahajan SVNIT, Surat, Gujarat, India

Sachin Mahakalkar Department of Mechanical Engineering, Rajiv Gandhi College of Engineering and Research, Nagpur, Maharashtra, India

T. Mahbub Department of EEE, Independent University Bangladesh, Dhaka, Bangladesh

S. S. Mahtab Department of EEE, Feni University, Feni, Bangladesh

Abhijeet Malge School of Design, MIT, Academy of Engineering (MITAOE), Pune, Maharashtra, India

Amitava Mandal Department of Mechanical Engineering, Indian Institute of Technology (Indian School of Mines), Dhanbad, Jharkhand, India

M. K. Manik Department of Mechanical Engineering, LDC Institute of Technical Studies, Soraon Prayagraj, India

Murli Manohar National Institute of Technology, Raipur, Raipur, CG, India

P. M. Menghal Faculty of Electronics, Military College of Electronics and Mechanical Engineering, Secunderabad, Telangana, India

Nitin Mishra Department of Civil Engineering, Graphic Era Deemed to be University, Dehradun, India

Sachin Mishra School of Electronics and Electrical Engineering, Lovely Professional University, Phagwara, Punjab, India

Aniruddha Mitra St.Thomas College of Engineering and Technology, Kolkata, India

Dheeraj Mohan Ramaiah University of Applied Sciences, Bangalore, Karnataka, India

Preeti K. Morey Department of Civil Engineering, Suryodaya College of Engineering and Technology, Nagpur, India

K. Nahreen Department of EEE, Mymensingh Engineering College, Mymensingh, Bangladesh

Kiran Naphade Department of Electrical Engineering, LOGMIEER, Nashik, Maharashtra, India

Vitresh Naphade Department of Electrical Engineering, R. H. Sapat College of Engineering, Nashik, Maharashtra, India

Nilesh M. Narkhede Mahindra and Mahindra Limited, Nagpur, India

Pragya Nema Oriental University, Indore, Madhya Pradesh, India

Rajat Shubhra Pal Institute of Engineering & Management, Kolkata, India

Reetika Pandey Department of Mechanical Engineering, Shambhunath Institute of Engineering & Technology, Prayagraj, U.P., India

N. L. Panwar Department of Renewable Energy Engineering, College of Technology and Engineering, Maharana Pratap University of Agriculture and Technology, Udaipur, Rajasthan, India

Rohan Edirisooriya Patabendige Department of Mechanical and Manufacturing Engineering, Faculty of Engineering, University of Ruhuna, Galle, Sri Lanka

Mahesh Navnath Patil Research Scholar, KBC NMU, Jalgaon, Maharashtra, India;

Department of Civil Engineering, RCPIT, Shirpur, Maharashtra, India

Piyush Patil Suryodaya College Raisoni College of Engineering, Nagpur, India

Pranjal Arun Patil School of Mechanical Engineering, Academy of Engineering (MITAOE), Pune, Maharashtra, India

Sakshi Patil Department of Civil Engineering, Terna Engineering College, Nerul, Navi Mumbai, India

Bipasa Patra Oriental University, Indore, Madhya Pradesh, India

- J. P. Patra** Surface Water Hydrology Division, NIH Roorkee, Roorkee, India
- Bhabani Prasanna Pattanaik** Department of Mechanical Engineering, KMBB College of Engineering and Technology, Khordha, Bhubaneswar, Odisha, India
- Anil Pawade** Amity University, Mumbai, India
- Aakash Suresh Pawar** Department of Civil Engineering, RCPIT, Shirpur, Maharashtra, India
- Ashish Pawar** Department of Renewable Energy Engineering, College of Technology and Engineering, Maharana Pratap University of Agriculture and Technology, Udaipur, Rajasthan, India
- Vinay Pawar** Bhiwarabai Sawant College of Engineering and Research, Pune, India
- P. D. C. Perera** Faculty of Engineering, Department of Electrical and Information Engineering, University of Ruhuna, Galle, Sri Lanka
- S. S. Pimplikar** Research Guide, SPPU and Program Head, Dr. Vishwanath Karad MIT World Peace University, Pune, Maharashtra, India
- Jyoti Prakash Giri** Department of Civil Engineering, GMR Institute of Technology, Rajam, India
- Poojith Prakash** Ramaiah Institute of Technology, Bangalore, Karnataka, India
- Puttaraju** SJB Institute of Technology, Kengeri, Bengaluru, Karnataka, India
- H. M. Rajashekaraswamy** M. S. Ramaiah University of Applied Sciences, Bengaluru, India
- Koorma Rajendra Babu** Department of Civil Engineering, GMR Institute of Technology, Rajam, India
- Babalu Rajput** Research Scholar, Department of Technology, Savitribai Phule Pune University, Pune, Maharashtra, India
- Dhanraj Rajurkar** A. A. Energy Pvt. Limited, Wadsa, Gadchiroli, India
- R. Rakesh** SJB Institute of Technology, Kengeri, Bengaluru, Karnataka, India
- Shridhar Rakhonde** Vidyapratishthans Kamal Nayan Bajaj Institute of Engineering, Baramati, India
- Aravind Ramachandran** Government Engineering College, Kozhikode, Kerala, India
- Siddharth Ramachandran** Indian Institute of Information Technology, Design and Manufacturing, Kanchipuram, Chennai, Tamil Nadu, India
- M. Ramesh** Department of Aeronautical Engineering, Kumaraguru College of Technology, Coimbatore, Tamil Nadu, India
- Pankaj Ramtekkar** G. H. Raisonni College of Engineering, Nagpur, India

Pankaj B. Ranade Department of Mechanical Engineering, KKWIEER, Nashik, Maharashtra, India

Vinay Ashok Rangari Department of Civil Engineering, Sree Vidyanikethan Engineering College, Tirupati, India

Lakhan Rathod Department of Mechanical Engineering, JSPM's BSIOTR, Wagholi, Pune, India

Ashish Raut G. H. Raisoni College of Engineering, Nagpur, India

Kiran H. Raut Electrical Engineering Department, G. H. Raisoni University, Amravati, India

Mali Rohini GHRIT, Electrical Department, Savitribai Phule University, Wagholi, Pune, India

Ramesh Rudrapati Department Industrial Engineering, Bule Hora University, Bule Hora, Ethiopia

H. M. A. P. Ruwanthi Faculty of Engineering, Department of Electrical and Information Engineering, University of Ruhuna, Galle, Sri Lanka

Anil R. Sahu Department of Mechanical Engineering, G. H. Raisoni College of Engineering and Management, Pune, Wagholi, India

Priyanka Salunkhe Department of Civil Engineering, Terna Engineering College, Nerul, Navi Mumbai, India

Md. Samiullah Aligarh Muslim University, Aligarh, India

Keshav Sangle VJTI, Mumbai, Maharashtra, India

D. Saritha Department of Chemistry, Chaitanya Bharathi Institute of Technology, Hyderabad, India

Dhanraj Saste Department of Civil Engineering, MIT Academy of Engineering, Pune, India

Gaurav Sawant Department of Mechanical Engineering, MIT-ADT University, Pune, India

Stephen Sebastian Department of Mechanical Engineering, MIT-ADT University, Pune, India

P. Shankara Narayanan Department of Aeronautical Engineering, Kumaraguru College of Technology, Coimbatore, Tamil Nadu, India

Arvind Sharma Faculty of Engineering and Science, University of Agder, Kristiansand, Norway

Pooja Sharma Faculty of Department of Economics, Daulat Ram College, University of Delhi, New Delhi, India

Ravi K. Sharma Department of Civil Engineering, College of Technology and Engineering, MPUAT, Udaipur, Rajasthan, India

Rohit Sharma Department of Mechanical Engineering, Shambhunath Institute of Engineering and Technology, Prayagraj, U.P., India

Sachin Shedmake Department of Electrical Engineering, G. H. Rasoni College of Engineering, Nagpur, India

Asha Shendge Department of Electrical Engineering, G. H. Rasoni Institute of Engineering and Technology, Wagholi, Pune, India

S. M. Shinde Electrical Engineering Department, Government College of Engineering, Aurangabad, Maharashtra, India

Shraddha Shinde Department of Civil Engineering, MIT Academy of Engineering, Pune, India

Mani Bhushan Shing Department of Mechanical Engineering, LDC Institute of Technical Studies, Soraon Prayagraj, India

Nilesh Shirpurkar Department of Civil Engineering, MIT Academy of Engineering, Pune, India

Amit Kumar Shrama Department of Civil Engineering, Graphic Era Deemed to be University, Dehradun, India

Arpita R. Shukla Department of Mechanical Engineering, G. H. Rasoni College of Engineering, Nagpur, Maharashtra, India

Sunil Kumar Shukla Nirma University, Ahmedabad, Gujarat, India

Gaurav Singh Department of Civil Engineering, Graphic Era Deemed to be University, Dehradun, India

Lakhwinder Singh Department of Water Resources Development and Management, Indian Institute of Technology Roorkee, Roorkee, India

Neeraj Kumar Singh SVNIT, Surat, Gujarat, India

Netra Pal Singh Research Scholar, Department of Mechanical Engineering, Oriental University, Indore, MP, India

Abhishek Kumar Sinha School of Electronics and Electrical Engineering, Lovely Professional University, Phagwara, Punjab, India

Dipali Soren ETCE Department, Christian College of Engineering Technology, Bhilai, Chhattisgarh, India

K. S. Sreekeasha Department of Civil Engineering, Jyothy Institute of Technology (Affiliated to VTU, Belagavi), Bengaluru, India

Prashant Sunagar Department of Civil Engineering, Ramaiah Institute of Technology (Affiliated to VTU, Belagavi), Bengaluru, India

Lalit Tak SVNIT, Surat, Gujarat, India

Madina S. Tamboli Department of Electrical Engineering, G. H. Rasoni Institute of Engineering and Technology, Wagholi, Pune, India

Nilesh Tamboli ETCE Department, Lakhmi Chand Institute of Technology, Bilaspur, Chhattisgarh, India

Pranjali Tete Department of Mechanical Engineering, Shri Ramdeobaba College of Engineering and Management, Nagpur, India

Prafull S. Thakare MSS College of Engineering and Technology, Jalna, India

L. N. Thakural Water Resources Division, National Institute of Hydrology, Roorkee, India;

Surface Water Hydrology Division, National Institute of Hydrology, Roorkee, India

Poornachandra Thejaswi Department of Civil Engineering, Bangalore Institute of Technology (Affiliated to VTU, Belagavi), Bengaluru, India

Sarabjeet Singh Tieth Faculty of Electronics, Military College of Electronics and Mechanical Engineering, Secunderabad, Telangana, India

Niraj S. Topare School of Chemical Engineering, Dr. Vishwanath Karad MIT World Peace University, Pune, India

Stina Torjesen School of Business and Law, University of Agder, Kristiansand, Norway

B. N. Tripathi Department of Mechanical Engineering, Chhatrapati Shivaji Maharaj University, Panvel Navi Mumbai, India

Leroy M. Tuscano Technip Energies, Mumbai, Maharashtra, India

Inayat Ullah Department of Mechanical Engineering, G. H. Rasoni College of Engineering, Nagpur, Maharashtra, India

Apurv Vaidya K. K. Wagh Institute of Engineering Education and Research, Nashik, Maharashtra, India

Harshad Vaidya G. H. Rasoni College of Engineering, Nagpur, India

Vinayak Vaidya Department of Civil Engineering, K.D.K. College of Engineering, Nagpur, India

Valsson Varghese Department of Civil Engineering, K.D.K. College of Engineering, Nagpur, India

Manish Varma Department of Civil Engineering, Geetanjali Institute of Technical Studies, Udaipur, Rajasthan, India

Vaibhav Varpe Department of Civil Engineering, MIT Academy of Engineering, Pune, India

Jagadish Vengala Department of Civil Engineering, Prasad V. Potluri Siddhartha Institute of Technology, Vijayawada, Andhra Pradesh, India

Vishal Vhagat CCET, Bhilai, Chhattisgarh, India

Prasad Vhanmane Department of Civil Engineering, Terna Engineering College, Nerul, Navi Mumbai, India

R. Vijayanandh Department of Aeronautical Engineering, Kumaraguru College of Technology, Coimbatore, Tamil Nadu, India

Bhaskar Wabhitkar Department of Civil Engineering, MIT Academy of Engineering, Pune, India

Charuta Waghmare Department of Civil Engineering, Yeshwantrao Chavan College of Engineering, Nagpur, India

Sakshi Wayal Department of Civil Engineering, MIT Academy of Engineering, Pune, India

Atul Kumar Yadav SVNIT, Surat, Gujarat, India

V. S. Yaliwal Department of Mechanical Engineering, SDM College of Engineering and Technology, Dharwad, Karnataka, India

Seema V. Yerigeri Department Mechanical Engineering, M.B.E. Society's College of Engineering, Ambajogai, Beed, India;
Department of Mechanical Engineering, G. S. Mandal's, Maharashtra Institute of Technology, Aurangabad, India

Seismic Analysis of 3D Printed Structures



Poojith Prakash  and G. M. Basavangowda 

Abstract Conventional construction of structures takes more time and labor, and hence, there is a need for rapid and fast construction in today's world. Complex designs are expensive or rather not possible to construct due to the complexity in the design. A small structure can be 3D printed in approximately 24 h. The time required to complete the construction of the structure is also reduced in 3D printing several times. This plays a major role during a disaster where it is important to provide shelter as quickly as possible. It is also important that these structures should be stable to external forces such as wind and earthquake forces. In this study, an effort is made to prepare geometrically scaled-down models of 3D printed structures and is analyzed for Bhuj and Uttarkashi earthquake motions using 1-D Shake Table, and the prototype is modeled and analyzed in software. The models are 3D printed to a scale of 1:30 using the free flow method for cement and a Creality Ender 3 for polylactic acid (PLA). The accelerations in each floor of these models are recorded, and the maximum acceleration is obtained. The results are then compared to identify the factor of difference between geometrically scaled models and the analytical method. The study is further extended to model a beam in SOLIDWORKS, finite element analysis software for replicated 3D printed fiber-reinforced concrete and polylactic acid (PLA) models. The results of the same are discussed in the study.

Keywords 3D printing · Bhuj · Uttarkashi · Earthquake · Finite element analysis · Polylactic acid (PLA) · Seismic analysis

1 Introduction

In today's world, there is a need to manufacture in the quickest way possible. There are two methods of manufacturing, additive manufacturing and subtractive manufacturing. One such process is 3D printing which is the process involving making of 3D

P. Prakash (✉) · G. M. Basavangowda
Ramaiah Institute of Technology, Bangalore, Karnataka 560054, India

© The Author(s), under exclusive license to Springer Nature Singapore Pte Ltd. 2022
M. L. Kolhe et al. (eds.), *Smart Technologies for Energy, Environment and Sustainable Development, Vol 1*, Springer Proceedings in Energy,
https://doi.org/10.1007/978-981-16-6875-3_1

elements using a design file. 3D printing is one of the additive manufacturing techniques (AM). AM technology was first developed in 1980s and is being successfully applied to various industries [1].

This technology of AM was first introduced in the year 1984 by Charles Hull. He was instrumental in the manufacture and design of the first 3D printer that we have heard. He also introduced. STL format into the world of 3D printing. STL stands for stereolithography which is the only format that the 3D slicing software recognizes. The first known 3D print from a STL file is said to be printer by Hideo Kodama [Nayoga Municipal Industrial Research Institute] [2].

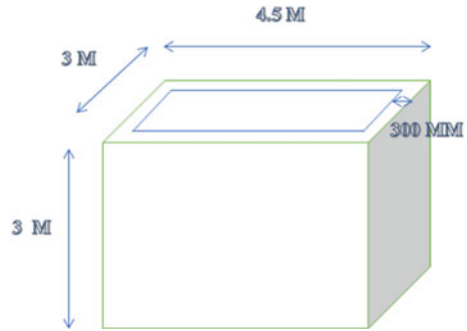
3D printing has a huge advantage in reducing cost of construction compared to conventional construction processes, and hence, there is a need to understand more in order to successfully implement in construction industry. According to Marchment et al. [3] some of the applications are (1) Decreasing cost by eliminating or reducing expensive formwork. (2) Decreased injury rates, as machine is doing tough jobs. (3) Increase in jobs. (4) Reduction of construction in-situ time. (5) Reducing mistakes by highly accurate formation of materials. (6) Giving freedom to architects to design extraordinary structures with sophisticated designs. (7) Reduce, reuse and recycle is followed for a sustainable construction.

2 Scope of Investigation

1. To analyze 3D printed, single and multi-storey buildings and formulate them for further analysis [4].
2. To create geometrically scaled models of 3D printed structures, single and multi-storey geometrically scaled-down structures from a 3D printer (Creality Ender 3) using polylactic acid (PLA) widely used 3D printing material.
3. To investigate seismic parameters of these 3D printed structures and compare the results of both PLA and cement printed structures in terms of deflection and floor acceleration due to earthquake.
4. To conduct finite element analysis of 3D printed element.
5. To compare its result with actual structure.

A scaling factor is to be adopted in order to create models to be tested in lab. For the same Purpose, two literatures are referred firstly, Krodell [5] created megastructures in the scale of 1:30 in order to verify the design concept that the authors have come up in the literature. These megastructures were tested with different numbers of resonators. Secondly, Ghaemmaghami and Ghaemian [6] studied the effect of an earthquake on a dam. The earthquake caused a crack in the dam which resulted in a severe leak. In this study, a model of empty dam with construction joints is created to a scale of 1:30 and tested on shake table to understand the behavior of model to cracking that is caused dynamically when tested with high frequency. From the above two literatures, it is evident that a 1:30 scale model can be used for lab-based

Fig. 1 Dimensions of the prototype model—fabricated at lab



shake table analysis as it fits the shake table perfectly and also helps to compare it with the actual site conditions.

The dimensions of the structure being considered in this study are as shown in Fig. 1.

The scaling factor of 1:30 leads to a geometrically scaled-down model of

$$3 \text{ m} = 3/30 = 0.1 \text{ m} = 10 \text{ cm} \quad (1)$$

$$4.5 \text{ m} = 4/30 = 0.15 \text{ m} = 15 \text{ cm} \quad (2)$$

$$300 \text{ mm} = 300/30 = 10 \text{ mm} = 1 \text{ cm} \quad (3)$$

The above dimensions are considered for seismic analysis.

Dimensions of 3D printed frame.

$$\text{Beam} = 210 \text{ mm} \times 210 \text{ mm} = 210/30 = 0.7 \text{ cm} \times 0.7 \text{ cm} \quad (4)$$

$$\text{Roof Dimension} = 4.5 \text{ m} \times 3 \text{ m} = 4.5/30 \times 3/30 = 15 \text{ cm} \times 10 \text{ cm} \quad (5)$$

3 Methodology

3.1 Free Flow Cement Models

The measurements of the geometrically scaled-down models are $10 \text{ cm} \times 15 \text{ cm} \times 10 \text{ cm}$ height and a thickness of 1 cm as discussed in the section above.

Fig. 2 Geometrically scaled-down cement model

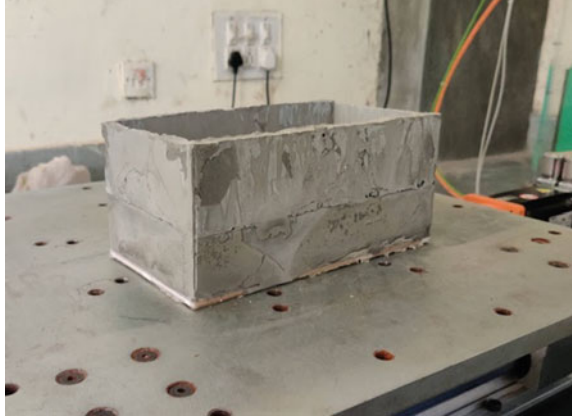
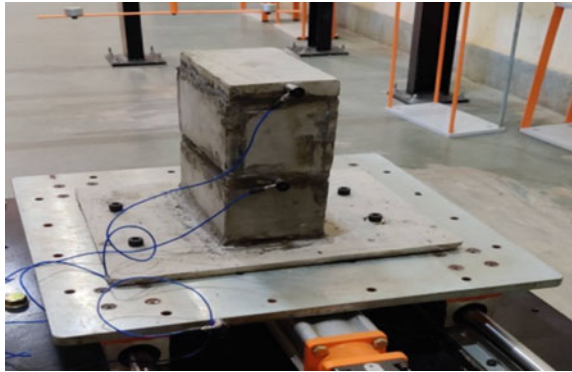


Fig. 3 Geometrically scaled-down cement model (G + 1)



1. The cement models of single floor (G) and two floors (G + 1) shown in Figs. 2 and 3, which are geometrically scaled down, are analyzed for Bhuj and Uttarkashi earthquake motions using shake table.
2. The maximum accelerations at each floor are recorded.

3.2 3D Printed Models

A commercially available 3D printer—Creality Ender 3—is used to print geometrically scaled-down models of structures.

1. The PLA model (G + 2) is 3D printed (Fig. 4).
2. The model is subjected to Bhuj earthquake and Uttarkashi earthquake using shake table.
3. The maximum acceleration of each floor is recorded and compared.

Fig. 4 Geometrically scaled-down PLA model (G + 2)

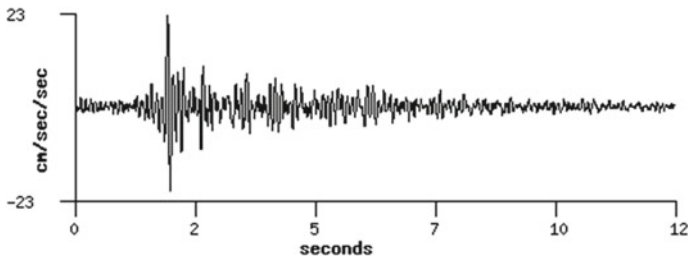
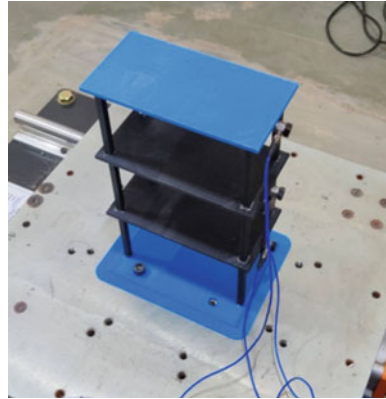


Fig. 5 Bhuj earthquake data plot

3.3 Bhuj Earthquake

Bhuj earthquake happened on January 26 in the year 2020 at 8:46 a.m. The earthquake has a magnitude of 7.7 and recorded the intensity of X on MMI scale. The peak input acceleration of recorded Bhuj earthquake is 1.038 g (Fig. 5).

3.4 Uttarkashi Earthquake

The earthquake in Uttarkashi occurred in the year 1991, and this earthquake is also called as Garhwal earthquake. The magnitude of the earthquake is 6.8 and an intensity of IX on the MMI (Modified Mercalli) scale. The peak input acceleration of recorded Uttarkashi earthquake is 0.988 g (Fig. 6).

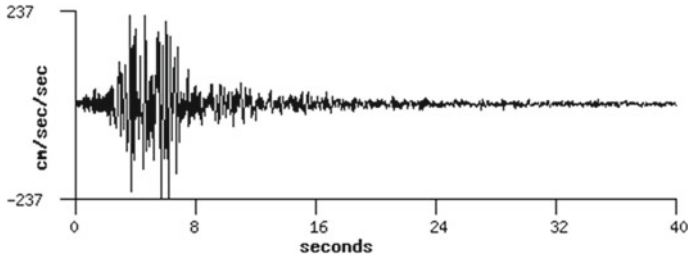
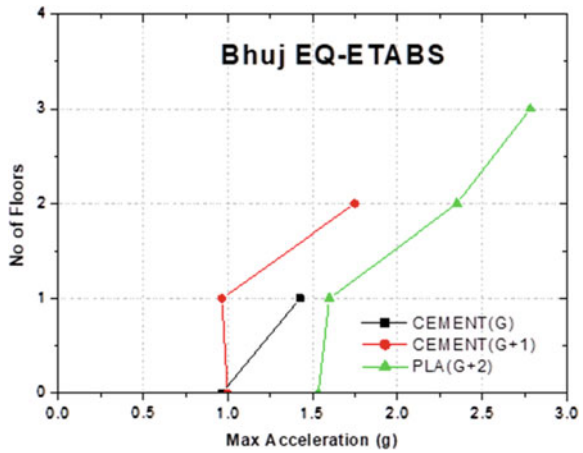


Fig. 6 Uttarkashi earthquake data plot

Fig. 7 Number of floors versus maximum acceleration values—Bhuj EQ ETABS



4 Results and Discussions

4.1 Seismic Analysis

See Figs. 7, 8, 9 and 10 and Tables 1, 2, 3 and 4.

4.2 Finite Element Analysis

Finite element analysis [FEA] is carried out in order to associate for the difference in material between lab analysis and field. For the results obtained from shake table analysis to be valid, we have to account for the difference in material, which is obtained from this analysis. The package used for FEA in this research work is SOLIDWORKS. As the entire structure could not be modeled, a beam is considered for analysis. A beam was modeled in SOLIDWORKS for PLA and FRC. The models were analyzed separately for maximum normal displacement for both materials,

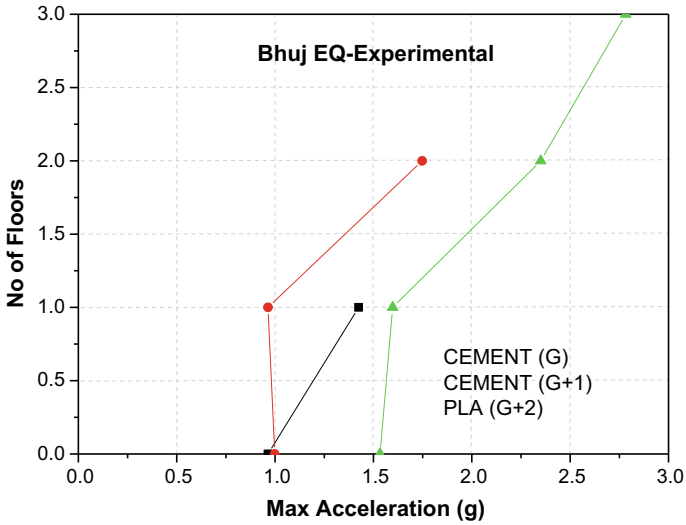
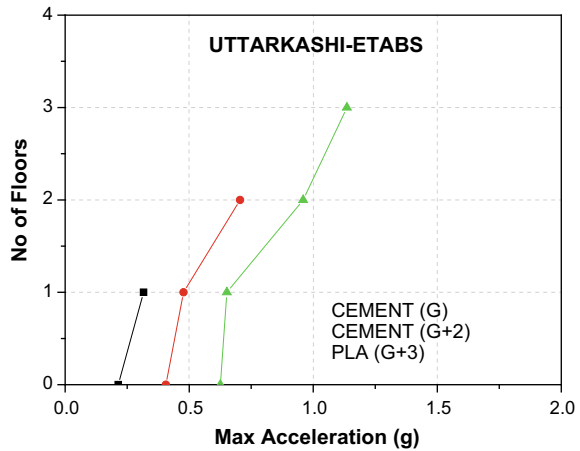


Fig. 8 Number of floors versus maximum acceleration values—Bhuj EQ experimental

Fig. 9 Number of floors versus maximum acceleration values—Uttarkashi EQ ETABS



firstly, polylactic acid and secondly fiber-reinforced concrete. A tetrahedral mesh was created with a mesh size of 25 mm as seen in the results above. The beam was loaded with a UDL of 3 kN/m for its length of 4.5 m. The size of beam taken into consideration was 210 × 210 mm as per calculations in Sect. 2.

The FRC beam showed a displacement of 0.8502 mm, and the polylactic acid model showed a displacement of 6.909 mm as PLA is ductile. The difference between the two models gives a factor of 8.12 which is also the difference factor between the elasticity (*E*) of FRC and PLA. Hence, from finite element analysis, it is clear that

Fig. 10 Number of floors versus maximum acceleration values—Uttarkashi EQ experimental

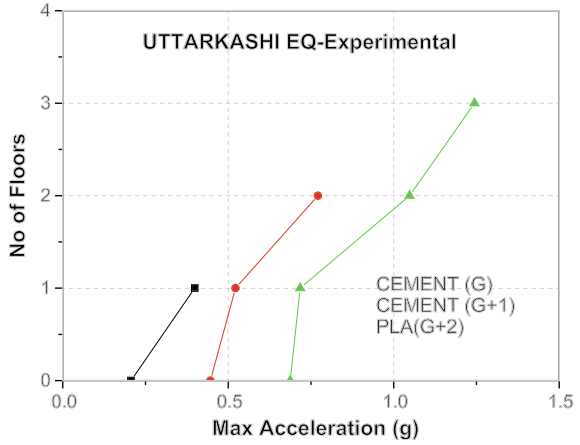


Table 1 Acceleration values for three models—analytical—Bhuj EQ

Model	G	G + 1	PLA
Floors	Maximum acceleration (g)		
0	0.964	0.998	1.533
1	1.425	0.964	1.598
2	0	1.748	2.351
3	0	0	2.783

Table 2 Acceleration values for three models—experimental—Bhuj EQ

Model	G	G + 1	PLA
Floors	Maximum acceleration (g)		
0	0.964	0.998	1.533
1	1.425	0.964	1.598
2	0	1.748	2.351
3	0	0	2.783

Table 3 Acceleration values for three models—analytical—Uttarkashi EQ

Model	G	G + 1	PLA
Floors	Maximum acceleration (g)		
0	0.214	0.406	0.6257
1	0.316	0.477	0.6522
2	0	0.705	0.9595
3	0	0	1.1359

Table 4 Acceleration values for three models—experimental—Uttarkashi EQ

Model	G	G + 1	PLA
Floors	Maximum acceleration (g)		
0	0.206	0.446	0.6873
1	0.399	0.522	0.7174
2	0	0.771	1.048
3	0	0	1.244

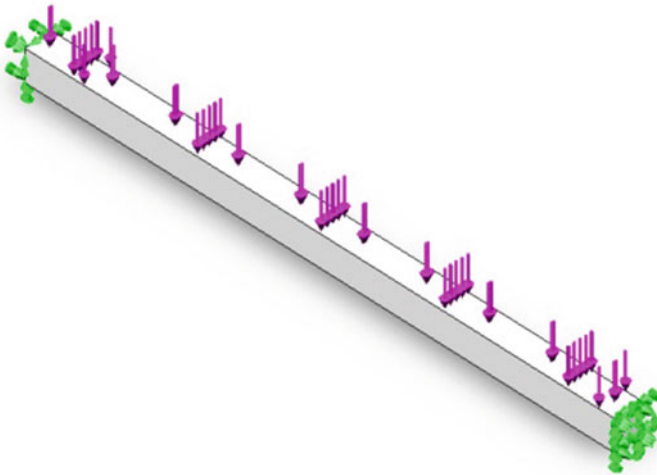


Fig. 11 Beam model representing loading and support condition in FEA—SOLIDWORKS

the displacement of the PLA model can be directly co-related to that of the FRC model on field by considering the factor of 8.12 (Figs. 11, 12 and 13).

5 Conclusion

In this work, the 3D printed models were prepared and were analyzed for seismic loads for previously recorded earthquake.

1. For the input maximum peak acceleration of 1.038 g (Bhuj earthquake) and 0.988 g (Uttarkashi earthquake), the difference in results between experimental analysis and analytical analysis is as seen in Tables 5 and 6.

The average difference between the experimental and the analytical is found to be 9.39% for Bhuj earthquake and 8.25% for Uttarkashi earthquake.

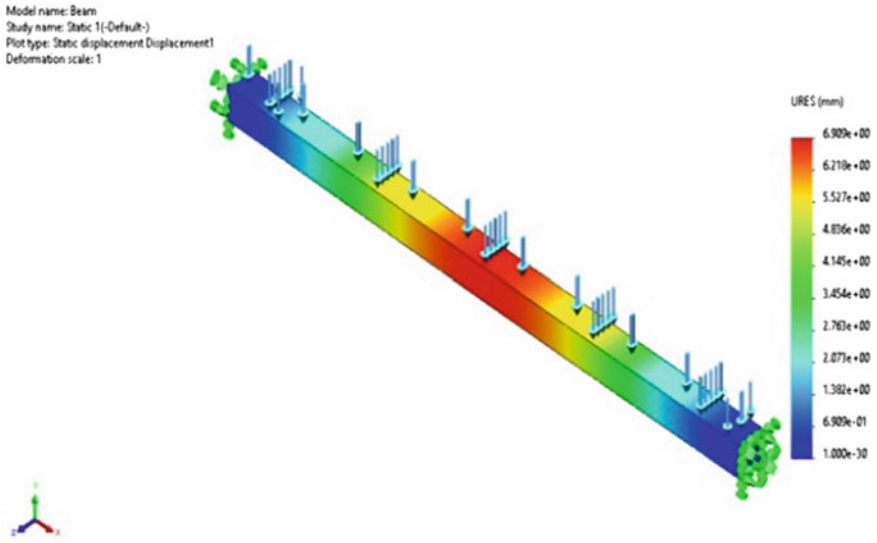


Fig. 12 Beam model showing maximum displacement PLA—SOLIDWORKS

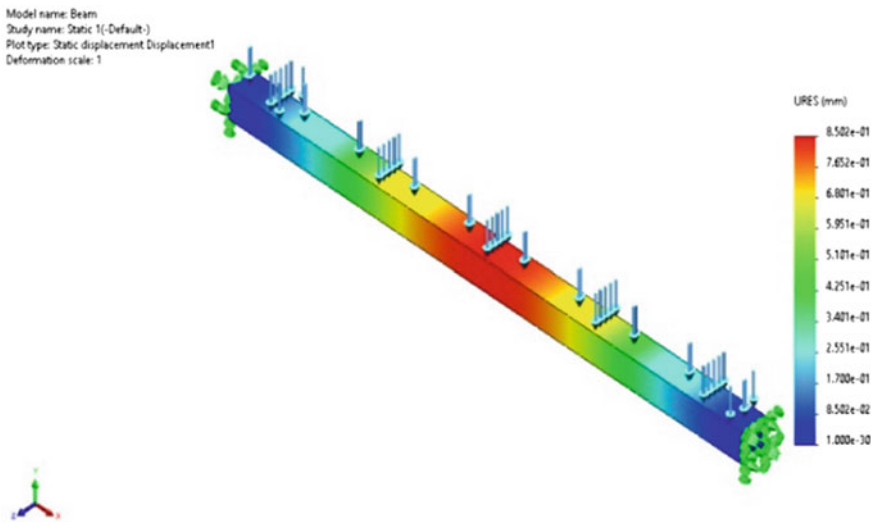


Fig. 13 Beam model showing maximum displacement FRC—SOLIDWORKS

2. The multiplication factor of 1.09 was found for the difference between the results obtained experimentally and analytically, i.e., the analytical results are 1.09 times that of experimental analysis.
3. The difference in the experimentally obtained values can be considered to be caused due to internal damping in the models.

Table 5 Difference B/W experimental and analytical results (Bhuj earthquake)

Floors	G	G + 1	PLA
	Diff %	Diff %	Diff %
Base	9.43	9.09	8.92
1	13.85	9.43	8.04
2	NA	8.37	8.56
3	NA	NA	8.85

Table 6 Difference B/W experimental and analytical results (Uttarkashi earthquake)

Floors	G	G + 1	PLA
	Diff %	Diff %	Diff %
Base	4.76	8.88	8.69
1	20.00	7.69	0.72
2	NA	7.79	8.57
3	NA	NA	8.06

- From FEA, the maximum displacement of PLA and FRC beams was found to be 6.909 and 0.8502 for the considered elasticity of 2910 N/mm² (PLA) and 23,760 N/mm² for 0.6% of fibers by percentage of cement [7]. The ratio of displacement obtained between PLA and FRC is 8.13.
- The ratio of displacement obtained from FEA is inversely proportional to the ratio of elasticity of PLA to that of FRC, i.e., 1/Er where Er = elasticity ratio, i.e., 23,760/2910 = 8.16. The difference of 0.03 may be accounted as error.

References

- T. Wholers, T. Caffrey, *Wholers Report 2014-3D Printing and Additive Manufacturing State of the Industry* (Wholers Associates, 2014)
- R. Bogue, 3D printing: the dawn of a new era in manufacturing? *Assem. Autom.* (2013)
- T. Marchment, J.G. Sanjayan, B. Nematollahi, M. Xia, Interlayer strength of 3D printed concrete: influencing factors and method of enhancing, in *3D Concrete Printing Technology* (Butterworth-Heinemann, 2019), pp. 241–264
- J.G. Sanjayan, B. Nematollahi, 3D concrete printing for construction applications, in *3D Concrete Printing Technology* (Butterworth-Heinemann, 2019), pp. 1–11
- S. Krödel, N. Thomé, C. Daraió, Wide band-gap seismic metastructures. *Extreme Mech. Lett.* **4**, 111–117 (2015). <https://doi.org/10.1016/j.eml.2015.05.004>
- A.R. Ghaemmaghami, M. Ghaemian, Experimental seismic investigation of Sefid-rud concrete buttress dam model on shaking table. *Earthq. Eng. Struct. Dyn.* **37**(5), 809–823 (2008). <https://doi.org/10.1002/eqe.791>
- M. Sakin, Y.C. Kiroglu, 3D printing of buildings: construction of the sustainable houses of the future by BIM. *Energy Procedia* **134**, 702–711 (2017)

Efficiency of Linear Univariate Programming Method in Estimating the Parameters Reflecting the Behavior of R.C.C Beam Along the Span



R. Rakesh  and Puttaraju

Abstract In this paper, the parameters which influence the behavior of the beam are studied using univariate linear optimization. Concrete being a heterogeneous and also a multiphase material, determining all the properties is an expensive and time consuming task. To overcome these mathematical optimizers are used by programming equation to reflect the behaviors of a beam from the experimental data by assigning each property a parameter and estimating it by subjecting it to different constraints and boundary conditions and giving this data as input, inverse analysis is carried out to find how efficiently dual simplex method is able to estimate the parameters. The results obtained showed no deviation from the experimentally obtained results.

Keywords Univariate · Dual simplex · R.C.C beam · Inverse analysis · Parameters

1 Introduction

Optimization methods were in use since the days of Sir Isaac Newton (25th of December 1642–20th of March 1726/27), Joseph-Louis Lagrange (25th of January 1736–10th of April 1813), and Augustin-Louis Cauchy (21st of August 1789–23rd of May 1857) around seventeenth century. Mathematical optimization is a numerical method where “optimal” means “best”, selection of best result out of the available alternatives with some selection criteria is a mathematical programming problem and can be represented as

Function $f: A \rightarrow \mathbb{R}$ from set A to real numbers.

Linear programming to be chosen above others is its ability to handle large problems and to give results very fast with less cost. Mathematics having the widest spectrum of application. Polynkin et al. [9, 10] in their paper explain the use of linear

R. Rakesh (✉) · Puttaraju
SJB Institute of Technology, Kengeri, Bengaluru, Karnataka 560060, India

Puttaraju
e-mail: principal@sjbit.edu

regression for large scale optimization problems in finding tuning parameters and Matiz and Barner [8] conducts conformal prediction for face and object image classification by the method of least squares. MacBain and Spillers [6] using incremental equations and sequential linear programming as a general solver achieves structural optimization for design problems. With fast growing pace of developing countries, Larrea-Gallegos and Vázquez-Rowe [5] take a case to explain the environmental performance of food diets in Peru region which is a developing nation with an objective of linking life cycle Assessment results with their dietary pattern by optimizing the linear programming and life cycle methods. Nature being the largest source of resources to mankind with reusable energy which is often not adequately utilized like solar, biomass, and wind resources as inputs for polygeneration system. Ray and De [13] use linear optimization as a decider for fixing the size of the components to achieve cost optimization. Water also being a natural resource that is at risk of shortage. Wang et al. [15, 16] develops a bi level multi-objective linear programming to optimize the water utilization structure based on risk of water shortage. Matlab one of the widely used software these days in the field of optimization. Majeed et al. [7] explains the application optimization in high voltage distribution systems by improving performance by reducing loss by 29.5% compared to low voltage distribution system by linear optimization method. Shawki et al. [13] introduced a model for deciding the minimum weight for a heavy and high reinforced concrete slab shuttering system assessing the design, bearing and steadiness constraints.

Advantages and limitations of the experimental and inverse analysis methods have been derived by Baby et al. [1] on ultrahigh performance fiber reinforced concrete (UHPFRC) under four-point loading test results. Wang et al. [14] uses probabilistic inverse analysis of braced excavations which is based on the maximum likelihood formulation to analyze assessing potential damage due to excavation of land next to a building. Gajewski and Garbowski [3] utilize advanced digital image correlation and backward investigation in calibration of results obtained of concrete parameters. Fracture parameters of C40/50 and C50/60 concrete was determined by experimental investigation and various non-linear numerical simulation via back analysis was carried out by Zimmermann and Lehký [18] and recommended stochastic non-linear FE analyses to be giving better results. Planas et al. [9] conducted a 3-point bending test and fracture behavior at prior and around the peak load was found using linear inverse analysis. Jepsen et al. [4] in their paper determine the relation between direct tensile strength and Young's modulus of cementitious materials using multi-linear inverse analysis from the data obtained from three-point bending experiment and the results thus obtained were very accurate fit.

Linear Programming Problem: Leonid Kantorovich, an economist during the 1930s, while developing optimal allocation of resources by reducing cost and by increasing efficiency during World War II was the earliest to introduce linear programming by Eiselt and Sandblom [2]. Linear programming is the type of optimization program method to obtain the best outcome with minimum cost. The mathematical programming problem is called a linear programming (LP) problem if the objective function and all the constraints in Eq. (1) are linear functions of the design variables. A linear programming problem is stated in the following standard form:

$$\text{Minimize } f(x_1, x_2, \dots, x_n) = c_1x_1 + c_2x_2 + \dots + c_nx_n \quad (1)$$

subject to,

$$\begin{aligned} a_{11}x_1 + a_{12}x_2 + \dots + a_{1n}x_n &= b_1 \\ a_{21}x_1 + a_{22}x_2 + \dots + a_{2n}x_n &= b_2 \\ &\vdots \\ a_{m1}x_1 + a_{m2}x_2 + \dots + a_{mn}x_n &= b_m \\ x_1 &\geq 0 \\ x_2 &\geq 0 \\ &\vdots \\ x_n &\geq 0 \end{aligned}$$

where c_j , b_j and a_{ij} ($i = 1, 2, \dots, m; j = 1, 2, \dots, n$) are known constants and x_j are the decision variables.

A special form of problem where optimality is maintained in all iterations. These two problems possess very interesting and closely related properties. On the off chance that the ideal answer for anyone is known, the optimal solution for the other can promptly be acquired. Indeed, it is irrelevant which issue is assigned the primal since the dual of a dual is primal.

2 Experimental Details

2.1 Concrete Specimen

Concrete mix was designed for M25 grade and four types of specimen were cast. Controlled specimen of reinforced concrete beam (RB), 0.3% steel fiber reinforced concrete beam (SFRB), 1% glass fiber reinforced concrete beam (GFRB), and 0.2% steel fiber and 0.5% glass fiber reinforced concrete hybrid beam (HFRB). After 28 days of curing compression and static Young's modulus elasticity of concrete specimen was tested for $150 \times 150 \times 150$ mm cubes and cylinder of 300 mm depth with 150 mm diameter results are as in Table 1.

2.2 Beam Specimen

Beam specimen of $200 \text{ mm} \times 200 \text{ mm} \times 2500 \text{ mm}$ cast at minimum dimension according to IS 13920:2016 clause 6 was maintained to be square with span/depth

Table 1 Average compressive strength and modulus of elasticity of concrete specimens

Specimen	Compressive strength (MPa)	Static modulus of elasticity (MPa)
RB	31.3	26,775
GFRB	36.34	29,195
SFRB	40.78	31,395
HFRB	39.73	30,579

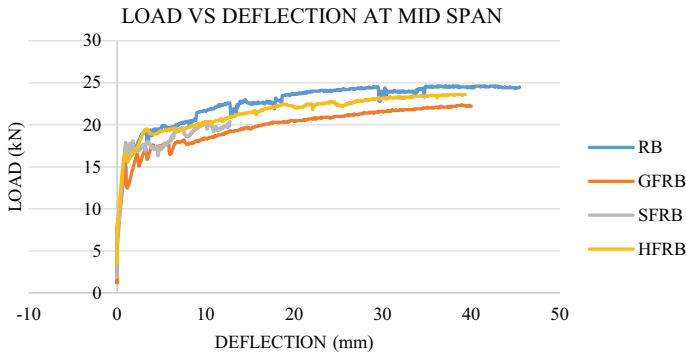


Fig. 1 Load versus deflection data of the all the beams

ratio = 12.5. Designed according to IS 456:2000 with reinforcement of #10 mm diameter bar of 2no's as top hanger bar and #12 mm diameter bar as bottom tension reinforcement and #8 mm diameter bar evenly spaced at 125 mm c/c as stirrups which was provided according to IS 456:2000 for the beam not to fail in shear. The deflection along the mid span was measured and the results showed higher cracking load for steel fiber reinforced beam followed by Hybrid, Glass fiber reinforced beam, and Control specimen (see Fig. 1).

Using Digital image correlation method and LVDT deflection was measured across the section at imposed load 13.7 kN for RB, 11.5 kN for GFRB, 14.4 kN for HFRB and 16 kN for SFRB specimens Rakesh and Puttaraju [11, 12] and results were as follows (see Fig. 2).

3 Problem Definition and Analysis Method

Beam is divided into $(n + 1)$ parts spaced based on the availability of reliable data subjected to constant load (p) at mid span ($l/2$) and the corresponding deflection values are measured at each of these points considered by DIC and the response equations are developed.

The problem is to find the parameters which are influencing beam output from the experimentally obtained results and compare these results mathematically. To achieve

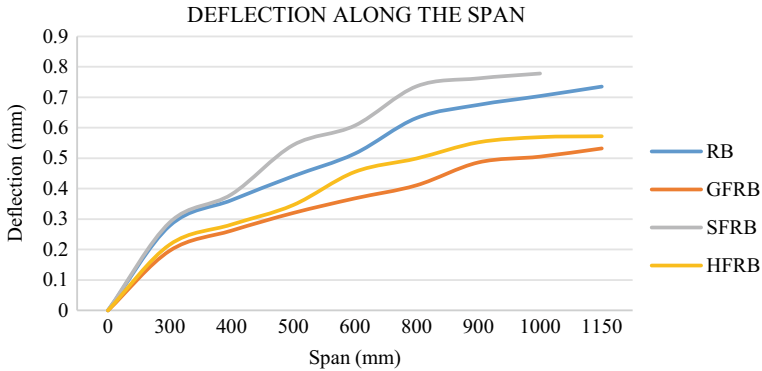


Fig. 2 Load versus deflection data of the all the beams along the span

this the considered equation is subjected to linear analysis to various constraints and boundary conditions and the results obtained are compared with experimental results.

In linear analysis, dual simplex method based on duality theory is considered as the results are better compared to other linear optimization and is mathematically more efficient. This deal simplex as a computational advantage over other methods Zarepisheh and Soleimani-Damaneh [17].

4 Algorithm

Before the start of the analysis, the algorithm is subjected to a mathematical test to check the accuracy and functioning of the algorithm. For this NTPL—IIT-K (Notes) problem is considered (Fig. 3 and Table 2).

$$\text{Maximize} = -3x_1 - 2x_2$$

Subject to,

$$x_1 + x_2 \geq 1$$

$$x_1 + x_2 \leq 7$$

$$x_1 + 2x_2 \geq 10$$

$$-x_1 + x_2 \leq 3$$

$$x_1 \geq 0, x_2 \geq 0.$$

By introducing slack variables S_1, S_2, S_3 and S_4 .

$$Z = -3x_1 - 2x_2$$

$$-x_1 - x_2 + S_1 = -1$$

$$x_1 + x_2 + 0 + S_2 = 7$$

$$-x_1 - 2x_2 + 0 + 0 + S_3 = -10$$

$$-x_1 + x_2 + 0 + 0 + 0 + S_4 = 3.$$

The same problem was solved using MATLAB for our algorithm and they are as follows in Table 3.

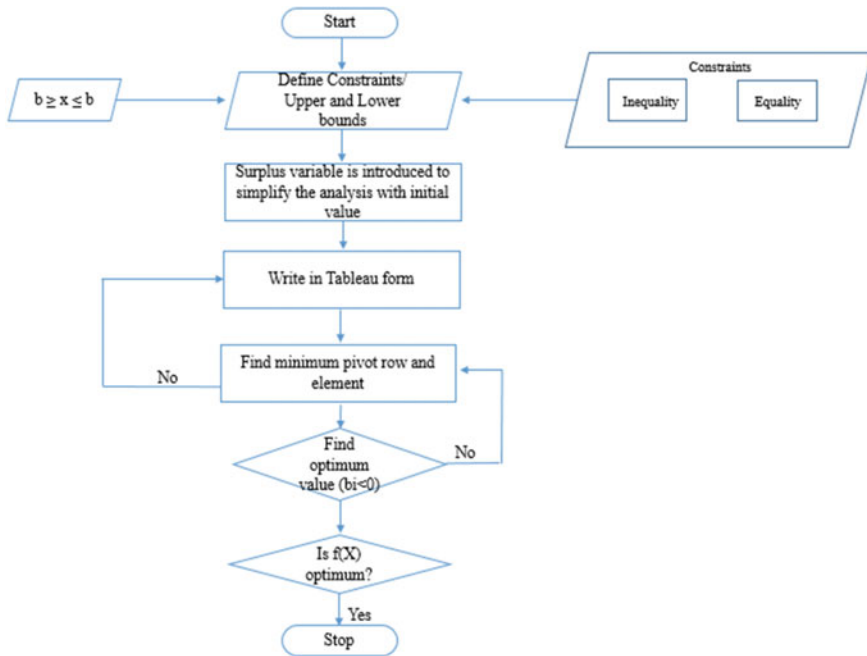


Fig. 3 Architecture of dual simplex method

The results obtained from our algorithm were as per the mathematical results hence the algorithm was good to use in our work.

5 Results and Discussion

The designed algorithm for dual simplex method is subjected to analyze the hypothetical problem with the objective to find the feasibility of the analysis method for the available data and constraints to reflect the behavior of the parameters considered in the study. To achieve this objective (see Fig. 4) in total five cases were considered for the study and they are as follows in Tables 4 and 5.

Case 1: Form the beam result output deflection is considered with second moment of inertia of the entire section with no constants defined, design parameter ($d1$) reflecting the modulus of elasticity of the beam is analyzed. The equation was subjected to inequality constrain not exceeding the modulus of elasticity of beam and lower bond at 0 and an upper bond of $1e5$. The results obtained from the dual simplex method showed no deviation from the expected results (see Fig. 5).

Case 2: In this case along with the inputs even the participation of reinforcement was studied by keeping the experimentally obtained modulus of elasticity of reinforcement as constants ($c1$) and defining parameter ($d1$) reflecting the modulus of

Table 2 Table showing iteration for the considered dual simplex problem manually

	C_j	Variables							
		-3	-2	0	0	0	0		
C_b	Basic variables	x_1	x_2	S_1	S_2	S_3	S_4	b	
0	S_1	-1	-1	1	0	0	0	-1	
0	S_2	1	1	0	-1	0	0	7	
0	S_3	-1	-2	0	0	-1	0	-10	
0	S_4	-1	1	0	0	0	-1	3	
	$Z_j = \sum C_b a_{ij}$	0	0	0	0	0	0		
	$C_j = C_j - Z_j$	-3	-2	0	0	0	0		$C_j \leq 0$
Iteration -1									
0	S_1	-1/2	0	1	0	-1/2	0	4	
0	S_2	1/2	0	0	1	1/2	0	2	
-2	x_2	1/2	1	0	0	-1/2	0	5	
0	S_4	-1/2	0	0	0	1/2	1	-2	
	$Z_j = \sum C_b a_{ij}$	-1	-2	0	0	1	0	-10	
	$C_j = C_j - Z_j$	-3	-2	0	0	0	0		$C_j \leq 0$
Iteration -2									
0	S_1	0	0	1	0	-1	-1	6	
0	S_2	0	0	0	1	1	1	0	
-2	x_2	0	1	0	0	0	1	3	
-3	x_1	1	0	0	0	-1	-2	4	
	$Z_j = \sum C_b a_{ij}$	-1	-2	0	0	3	4	-18	$bi \geq 0$
	$C_j = C_j - Z_j$	0	0	0	0	-3	-4		$C_j \leq 0$

Table 3 Table showing algorithm results solved using MATLAB

Number of iterations	2
$f(x)$	-18
X	(4, 3)

elasticity of the beam is analyzed. The equation was subjected to inequality constrain not exceeding the modulus of elasticity of beam and lower bond at 0 and an upper bond of 1e5. The results obtained from the dual simplex method showed no deviation from the expected results (see Figs. 6 and 7).

Case 3: Here the behavior check was made to know whether the considered equation is able to reflect the behavior of reinforcement. To achieve this modulus of elasticity of R.C.C Beam ($c1$) was kept constant and design parameter ($d2$) reflecting the modulus of elasticity of the reinforcement is analyzed. The equation was subjected to inequality constrain not exceeding the modulus of elasticity of beam and lower

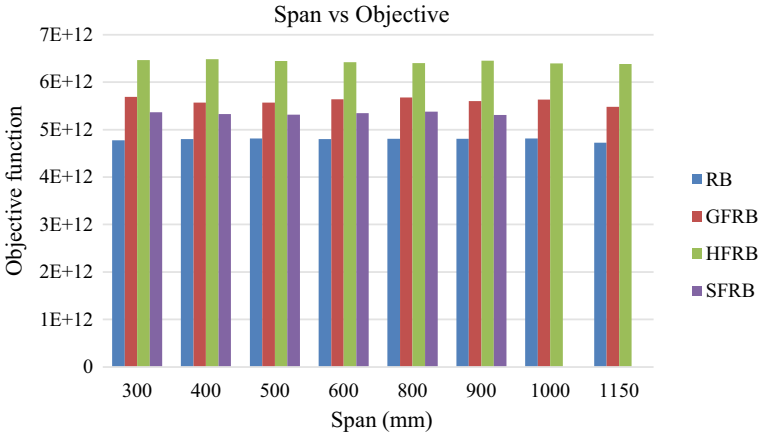


Fig. 4 Objective function variation of different types of beam along the span

Table 4 Table showing constants and parameters varied for different cases

Single variables		
Case	Constant variable	Varying parameter
1	–	$d1$
2	$d2$	$d1$
3	$d1$	$d2$
4	$d2$ and $d3$	$d3'$
5	$d2, d3$ and $d3'$	$d4$

Table 5 Table showing inputs defined in the analysis

Input		
Case	Constrains	Bounds
1	$d1 \leq E$	$0 \geq d1 \leq 1e5$
2	$d1 \leq E$	$0 \geq d1 \leq 1e5$
3	$d2 \leq Es$	$0 \geq d2 \leq 3e5$
4	$d3 \leq Ec$	$0 \geq d3' \leq 1e5$
5	$d4 \leq Eu$	$0 \geq d4 \leq 1e5$

bond at 0 and an upper bond of $3e5$. The results showed no deviation (see Figs. 8 and 9).

Case 4: Further the analysis is taken forward to account for the modulus of elasticity due to stress, Creep, and Shrinkage to achieve this modulus of elasticity of R.C.C Beam ($c2$) and Static modulus of elasticity of concrete ($c3$) were kept constants and design parameter $d3'$ reflecting the modulus of elasticity of the concrete due to stress, creep and shrinkage is analyzed. The equation was subjected to inequality constrain not exceeding the modulus of elasticity of beam and lower bond at 0 and

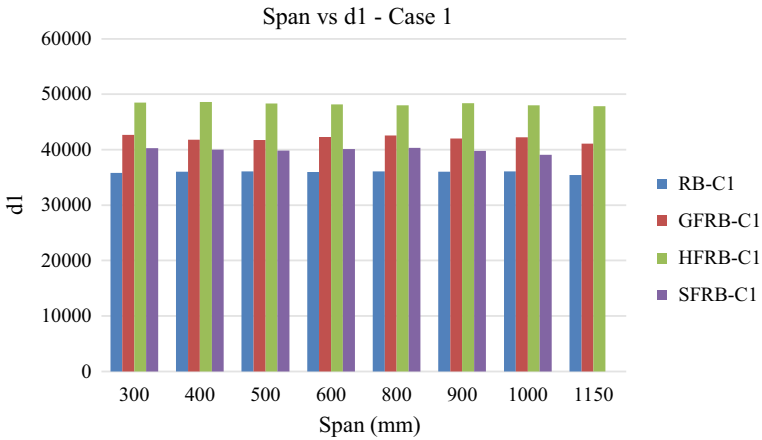


Fig. 5 Case 1—the results of variation of $d1$ along the span of the specimen

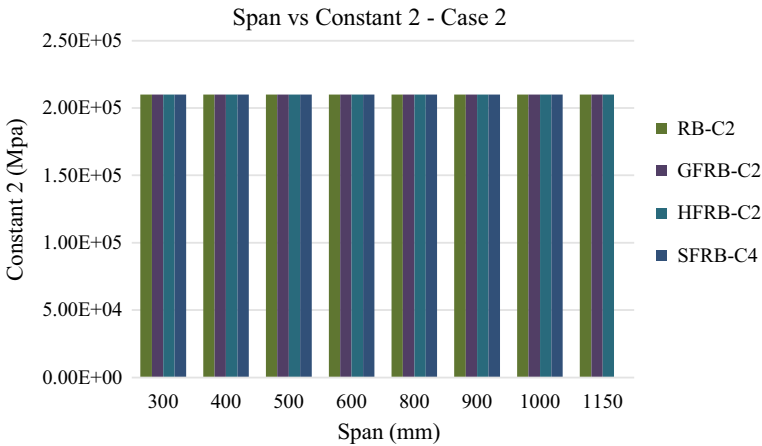


Fig. 6 Case 2—modulus of elasticity of reinforcement is kept constant along the span of the specimen

an upper bond of $1e5$. The results obtained from the dual simplex method showed no deviation from the expected results (see Figs. 10, 11 and 12).

Case 5: Finally, if there is any unaccounted parameter in case left was found in this case by keeping modulus of elasticity of reinforcement ($c2$), static modulus of elasticity of concrete ($c3$) modulus of elasticity of due to stress, creep and shrinkage ($c3'$) constants defined parameter $d4$ reflecting the unknown modulus of elasticity of the beam is analyzed. The equation was subjected to inequality constrain not exceeding the modulus of elasticity of beam and lower bond at 0 and an upper bond

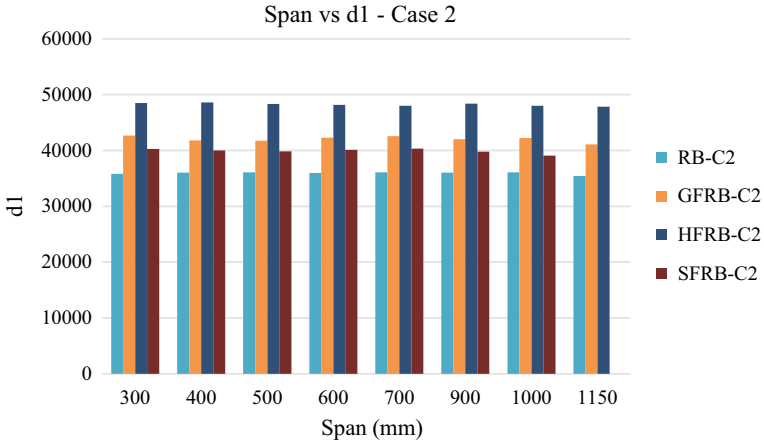


Fig. 7 Case 2—the results of variation of $d1$ along the span of the specimen

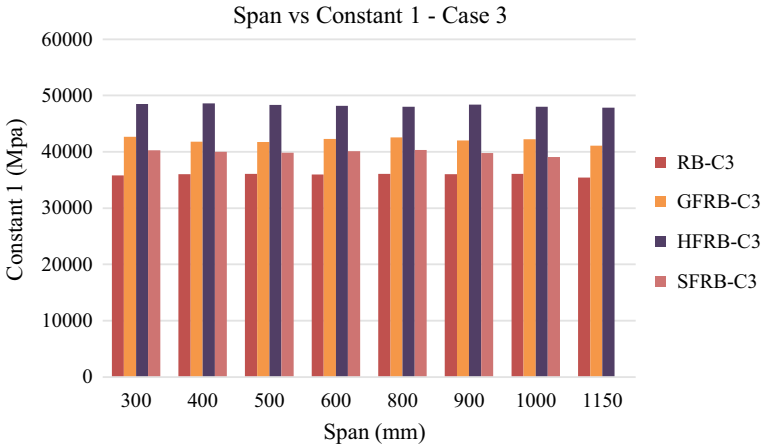


Fig. 8 Case 3—modulus of elasticity of R.C.C beam specimen is kept constant along the span of the specimen

of $1e5$. The results obtained from the dual simplex method showed no deviation from the expected results (see Figs. 13, 14, 15 and 16).

The obtained results were compared with expected experimental results and they were found to be reflecting the behavior of the Parameters with no deviation (see Figs. 5 and 17).

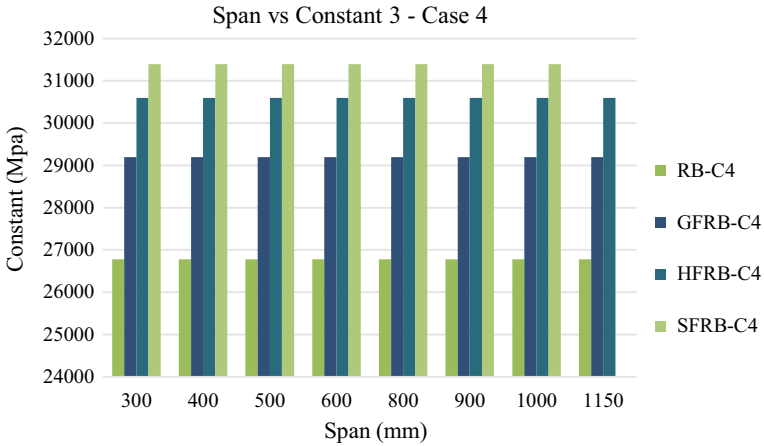


Fig. 9 Case 3—the results of variation of d_2 along the span of the specimen

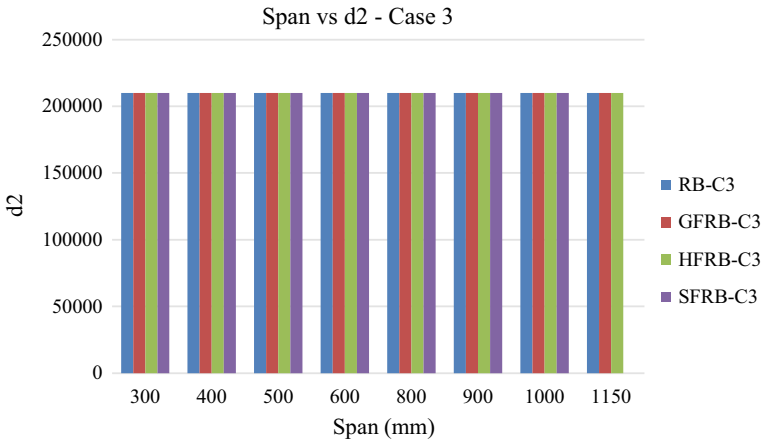


Fig. 10 Case 4—static modulus of elasticity of concrete specimen found experimentally is kept constant along the span of the specimen

6 Conclusion

In this paper dual simplex method of single variable analysis is performed for the known experimental details of R.C.C beam to get design parameters to reflect the behavior of the beam for different possible cases and compared the results with the experimental value and found that how with very less time and iterations dual simplex method is able to give the results with no deviation from the experimental results. Hence these results prove dual simplex method to be robust and an efficient method for the considered equation and for the defined constraints and boundary conditions.

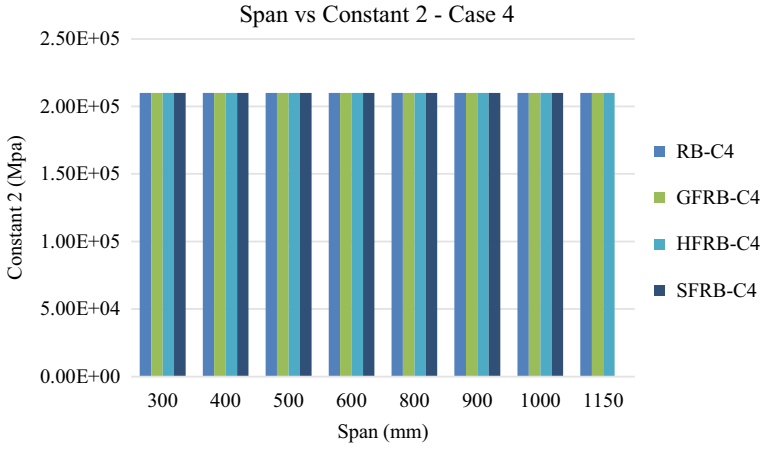


Fig. 11 Case 4—modulus of elasticity of reinforcement is kept constant along the span of the specimen

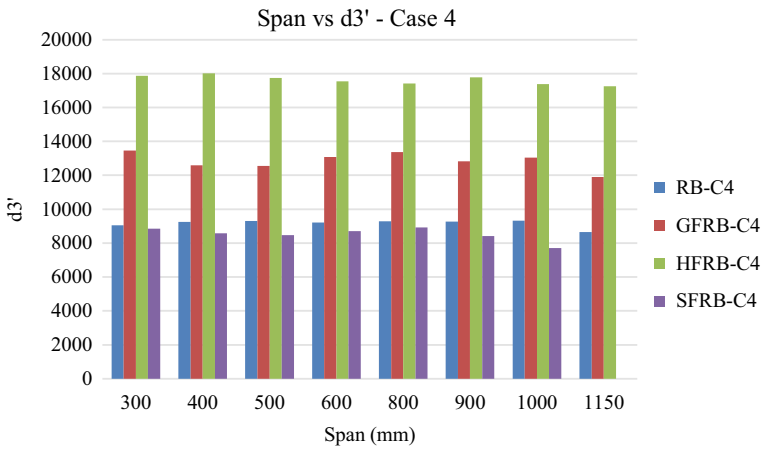


Fig. 12 Case 4—the results of variation of $d3'$ along the span of the specimen

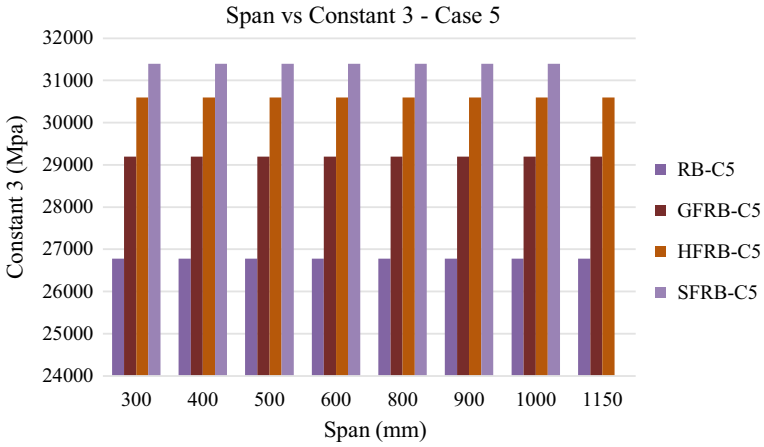


Fig. 13 Case 5—static modulus of elasticity of concrete specimen found experimentally is kept constant along the span of the specimen

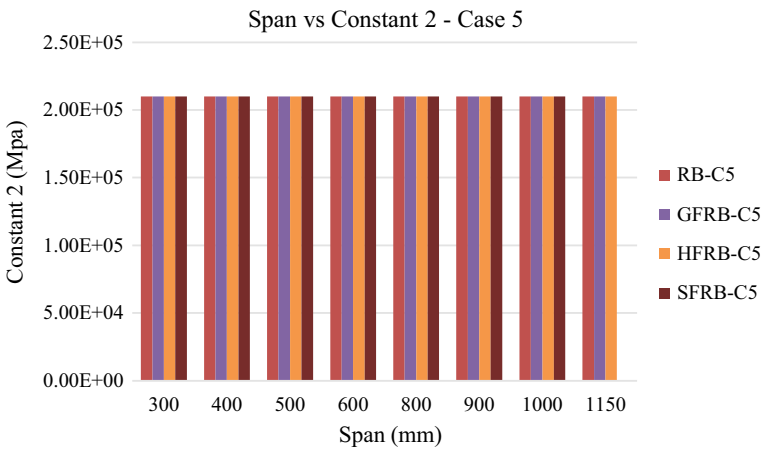


Fig. 14 Case 5—modulus of elasticity of reinforcement is kept constant along the span of the specimen

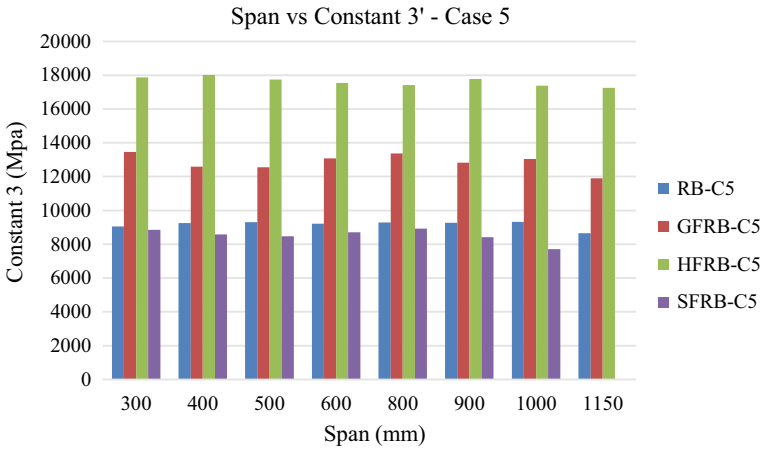


Fig. 15 Case 5—modulus of elasticity of concrete due to stress, creep and shrinkage specimen found experimentally is kept constant along the span of the specimen

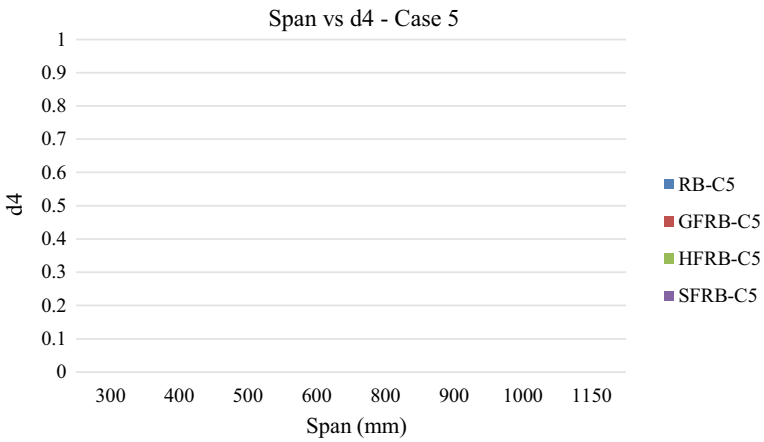


Fig. 16 Case 5—any unaccounted modulus of elasticity of concrete if any

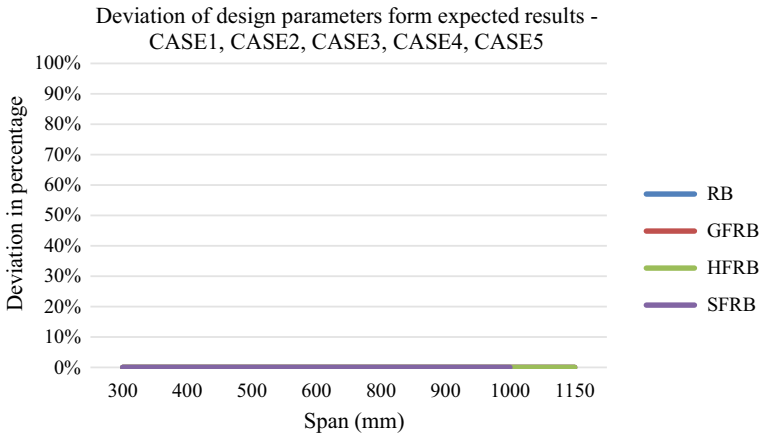


Fig. 17 Percentage deviation from expected results for RB, GFRB, SFRB, HFRB for all the five cases

References

1. F. Baby, B. Graybeal, P. Marchand, F. Toutlemonde, UHPFRC tensile behavior characterization: inverse analysis of four-point bending test results. *Mater. Struct.* **46**(8), 1337–1354 (2012). <https://doi.org/10.1617/s11527-012-9977-0>
2. H. Eiselt, Sandblom, *Linear Programming and Its Applications* (Springer, Berlin New York, 2007)
3. T. Gajewski, T. Garbowski, Calibration of concrete parameters based on digital image correlation and inverse analysis. *Arch. Civ. Mech. Eng.* **14**(1), 170–180 (2014). <https://doi.org/10.1016/j.acme.2013.05.012>
4. M.S. Jepsen, L. Damkilde, I. Lövgren, A fully general and adaptive inverse analysis method for cementitious materials. *Mater. Struct.* **49**(10), 4335–4348 (2016). <https://doi.org/10.1617/s11527-015-0791-3>
5. G. Larrea-Gallegos, I. Vázquez-Rowe, Optimization of the environmental performance of food diets in Peru combining linear programming and life cycle methods. *Sci. Total Environ.* **699**, 134231 (2020)
6. K. MacBain, W.R. Spillers, Structural optimization using incremental equations and sequential linear programming. *Struct. Multidiscip. Optim.* **32**(5), 423–426 (2006)
7. I.B. Majeed, A. Acakpovi, G. Edeful, M.B. Michael, R. Abubakar, Migration from low to high voltage distribution system: an optimization of selected unit transformers using linear programming with Matlab. *Procedia Manuf.* **35**, 552–560 (2019)
8. S. Matiz, K.E. Barner, Conformal prediction based active learning by linear regression optimization. *Neurocomputing* **388**, 157–169 (2020). <https://doi.org/10.1016/j.neucom.2020.01.018>
9. J. Planas, G.V. Guinea, M. Elices, *Int. J. Fract.* **95**(1/4), 367–378 (1999). <https://doi.org/10.1023/a:1018681124551>
10. A. Polynkin, V.V. Toropov, Mid-range metamodel assembly building based on linear regression for large scale optimization problems. *Struct. Multidiscip. Optim.* **45**(4), 515–527 (2011)
11. R. Rakesh, Nonlinear analysis for parameter estimation by multi objective single variable inverse analysis. *J. Adv. Res. Dyn. Control Syst.* **12**(SP7), 529–538 (2020). <https://doi.org/10.5373/jardcs/v12sp7/20202136>

12. R. Rakesh, Puttaraju, Effectiveness of digital image correlation method in measuring deflection of RCC beam with natural surface subjected to point loading. *Int. J. Pharm. Res.* **12**(2), 1773–1781 (2020). <https://doi.org/10.31838/ijpr/2020.12.02.230>
13. A. Ray, S. De, Polygeneration using renewable resources: cost optimization using linear programming. *Process Integr. Optim. Sustain.* **3**(1), 115–124 (2018)
14. K.M. Shawki, M.A. Emam, E.-B. Osman, Design and construction of multitier shoring towers. *J. Eng. Sci. Assiut Univ.* **40**(3), 689–700 (2012)
15. L. Wang, Z. Luo, J. Xiao, C.H. Juang, Probabilistic inverse analysis of excavation-induced wall and ground responses for assessing damage potential of adjacent buildings. *Geotech. Geol. Eng.* **32**(2), 273–285 (2013). <https://doi.org/10.1007/s10706-013-9709-4>
16. Y. Wang, L. Liu, S. Guo, Q. Yue, P. Guo, A bi-level multi-objective linear fractional programming for water consumption structure optimization based on water shortage risk. *J. Clean. Prod.* **237**, 117829 (2019)
17. M. Zarepisheh, M. Soleimani-Damaneh, A dual simplex-based method for determination of the right and left returns to scale in DEA. *Eur. J. Oper. Res.* **194**(2), 585–591 (2009). <https://doi.org/10.1016/j.ejor.2007.11.054>
18. T. Zimmermann, D. Lehký, Fracture parameters of concrete C40/50 and C50/60 determined by experimental testing and numerical simulation via inverse analysis. *Int. J. Fract.* **192**(2), 179–189 (2015). <https://doi.org/10.1007/s10704-015-9998-0>

Geopolymer a Sustainable Material: A Review



Priyanka Salunkhe, Prathamesh Balip, Tejas Deshmukh, Siddesh Gadge,
and Prasad Vhanmane

Abstract The geopolymer material is formed from geopolymerization process. The mixture of aluminosilicate material with an alkaline solution such as sodium hydroxide, sodium silicate, and calcium hydroxide completes the geopolymerization process and forms an activated alkaline solution which has the binding property. To produce geopolymer material with physical, mechanical as well as durability properties various material ratios are needed to be maintained properly and used while preparing mix design. The geopolymer material is then oven cured at controlled ambient temperature for some duration to enhance strength properties. The material is then checked or analyzed for microstructural behavior of crystalline structure produces during the geopolymerization process by XRD, SEM–EDS and FTIR test, and it is required to make changes in chemical composition if required. Finally, the physical and mechanical tests were performed and studied on geopolymer material, and the required properties are achieved. It gives the strength as well as durability properties same or near to normal brick or concrete. So, geopolymer has great binding properties and may use as the best replacer to cement.

Keywords Aluminosilicate · Alkaline activation · Geopolymerization · Microstructure analysis

1 Introduction

Concrete is a construction material widely used in the construction industry. Concrete was made from cement, sand, and coarse aggregate mixed with water to achieve maximum structural and mechanical properties. Cement is the binders used for binding the materials to form a hard and durable concrete. The manufacturing of cement requires more energy to form cement powder from rock, and while processing, 80% of CO₂ gas is evolved in the atmosphere, which causes an increase in greenhouse gas emission, which affects the ozone layer and helps to increase global

P. Salunkhe (✉) · P. Balip · T. Deshmukh · S. Gadge · P. Vhanmane
Department of Civil Engineering, Terna Engineering College, Nerul, Navi Mumbai 400706, India

© The Author(s), under exclusive license to Springer Nature Singapore Pte Ltd. 2022
M. L. Kolhe et al. (eds.), *Smart Technologies for Energy, Environment and Sustainable Development, Vol 1*, Springer Proceedings in Energy,
https://doi.org/10.1007/978-981-16-6875-3_3

warming. The forming of concrete from cement requires more natural materials, which reduces the natural resources, and it was harmful to the environment.

In nineteenth-century geopolymer material found out which was the best replacement to cement as a binder material. The geopolymer concrete is made up of industrial waste material, which is rich in aluminosilicate property with the alkaline solution by geopolymerization process. The geopolymerization is the technique that transforms various solid aluminosilicate material into a useful product. The alkaline product such as sodium silicate and aluminum silicate is prepared by heating at 900–1100 °C. So using geopolymer material at the place of cement may reduce CO₂ gas emission as well as save natural resources, and it requires 2.5–3 times less energy than cement production.

The geopolymerization process requires various aluminosilicate material and alkaline material to produce durable geopolymer material, so to achieve these various properties mixing ratios, suitability, and analysis of various testing are required as given in detail below.

2 Aluminosilicate Material and Their Properties

The industrial waste is mainly aluminosilicate materials, which are rich in silica and alumina content, and that is why they are known as aluminosilicate material. They are helpful in the generation of critical geopolymer structure, which is stable by maintaining Si/Al molar ratio. The stable structure increases all physical, chemical, and mechanical properties of geopolymer material and enhances the performance of geopolymer material under various conditions.

- **Fly Ash (F type):** The F-type low calcium fly ash with NaOH mixed bricks has excellent compressive strength [1, 2]. As we increase fly ash content and also reduce 15–20% cost than ordinary concrete [3], it has been seen that fly ash and NaOH with 10–20% red mud [4], also use of fly ash with a foaming agent makes brick lightweight, compressive strength decrease as ratio of fly ash/bottom ash increase [5–9].
- **Copper Mine Tailings:** Copper mine tailings in geopolymerization with proper molarity of alkaline solution incenses ultimate compressive strength [10, 11] as well as make lightweight brick while oven cured at 90 °C up to 84% less weight [12]. The addition of mine tailings to fine aggregate gives high ultimate compressive strength as well as greater failure strain of mine tailings geopolymer [4, 5]. When fine aggregate content increases, more critical microstructure is observed in SEM images.
- **Metakaolin:** Metakaolin can be used as a replacement material for slag by 40–50%, and also, it makes dense and critical chemical structure of geopolymer which helps to make geopolymer with increased durability properties [13, 14].
- **GGBS:** GGBS contains about 34–45% of SiO₂ and increases strength when replaced with fly ash as well as it is useful to control setting time of geopolymer

material but it emits CO₂ content in atmosphere [15]. When 60% fly ash is replaced with GGBS, it shows higher compressive strength, and also, the optimum replacement of fly ash is considered as 45% [3, 16].

- **Bottom Ash:** Fly ash and WGI glass with bottom ash reduce the cost of geopolymer brick [17], the bottom ash with 40–45% SiO₂ and 13–15% Al₂O₃ gives good compressive strength [2, 15], and coal ash has less heat transparency as 0.3 W/M K [18].
- **Rise Husk:** Rise husk is having SiO₂ content of 82%, and it was great material for geopolymerization forms critical chemical structure and produces homogeneous adhesive mixture which having great binding properties [19, 20, 21].
- **Paper Waste:** Paper waste was used in geopolymerization helpful for creating pores while the geopolymer brick oven cured at 60–105 °C, and it is useful for reducing heat transparency [22, 23].
- **Waste Brick:** Waste brick is used as fine material having less density so it also has less thermal transparency ranges from 0.62 to 0.67 W/M K [24], and as the density of the material increases, thermal transparency increases [25].
- **Pumice Aggregate:** Pumice aggregate is having a sponge structure with less density, so it also has less thermal transparency ranges from 0.2 to 0.22 W/M K [24].
- **Industrial Waste:** Industrial waste after washing sand and gravel used as fine aggregate in geopolymerization increases the compressive strength up to 76% [26].
- The fine aggregate is replaced by brick dust, sawdust or lime dust waste, coir waste, and also, they are eco-friendly, and the average compressive strength of brick using the waste is 70–75 MPa [26–34].

3 Alkaline Solution and Properties

The alkaline solutions are prepared from base material mixed with water and by heating at a temperature between 900 and 1100 °C. These alkaline solutions are rich in silica and alumina content having PH greater than 7. The alkaline solution with the proper amount of sodium silicate to sodium hydroxide molarity ratio produces the binding property and stabilizes the geopolymer chemical structure which helps in increasing all properties of the material.

- **Sodium Hydroxide (NaOH):** It was the inorganic base chemical material used to prepare activated alkaline solution while mixed with aluminosilicate material by maintaining proper molarity. The molarity maintained from 5 to 15 M useful to form a stable chemical structure with strength properties [35–40].
- **Sodium Silicate (Na₂SiO₃):** It was a colorless transparent solid which is adhesive in nature used to prepare activated alkaline solution while mixed with aluminosilicate material by maintaining proper molarity. The molarity maintained from 5 to 15 M useful to form a stable chemical structure with strength properties [35–40].

- **Calcium Hydroxide (Ca(OH)₂):** The less use of calcium hydroxide alkaline solution less than 20% gives better result and control temperature between 0.34 and 0.36 W/M K but emits CO₂ content [29, 35, 41].
- **Potassium Hydroxide (KOH):** It was highly alkaline in nature and having property to generate activated alkaline solution but it was harmful to human's life.

4 Geopolymerization Process

Demolish material or waste material from any industry is aluminosilicate material having maximum silicon dioxide (SiO₂) and aluminum dioxide (Al₂O₃) content. The mixture of alkaline solution (sodium silicate (Na₂SiO₃) and sodium hydroxide (NaOH)) with appropriate molarity ratio and waste aluminosilicate material makes activated alkaline solution which reaches in chemical binding properties [30, 42, 43]. Afterward by adding different materials in activated alkaline solution, the geopolymerization process takes place and chemical structure gets critical and geopolymer material forms as shown below by reaction and chemical structure [44].

The process involves the following steps: [3, 35–40]

- I. Mixing of solid aluminosilicate material in alkaline sodium silicate and in sodium hydroxide solution.
- II. Nucleation stage: It is the stage in which the aluminosilicates from the fly ash particle dissolve in the alkaline medium and release aluminates and silicates, known as monomers. In this process, the presence of water glass (sodium silicate) liberates hydroxide by condensation reactions and can it react again to form cycles of structure.
- III. Condensation reaction: The reaction in which molecules joins together by losing small molecules.
- IV. The alkaline activation of alkaline material such as sodium silicate and aluminum silicate is generally dependent on the linkage structure of aluminosilicate oxide (silicate oxide and aluminate oxide) as sialate bond (Si–O–Al) and siloxo bond (Si–O–Si). The ratio between Si and Al has a great contribution toward formation of geopolymer structure such as Si to Al ratio is 1 refers to poly (sialate), Si to Al ratio is 2 refers to poly (sialate-siloxo), Si to Al ratio is 3 refers to poly (sialate-disiloxo) and cross-link bridge structure which gives stability to structure [45].
- V. Formation of monomers: The nucleation stage is important to form monomers where a molecule can be bonded to other identical molecules to form a polymer.
- VI. Oligomerization: The oligomerization is the process of formation Si or Si–Al in proper sequence where dimer, trimer, and tetramer formation takes place. An oligomer is a complex molecule that is made out of few monomer units [3, 35].

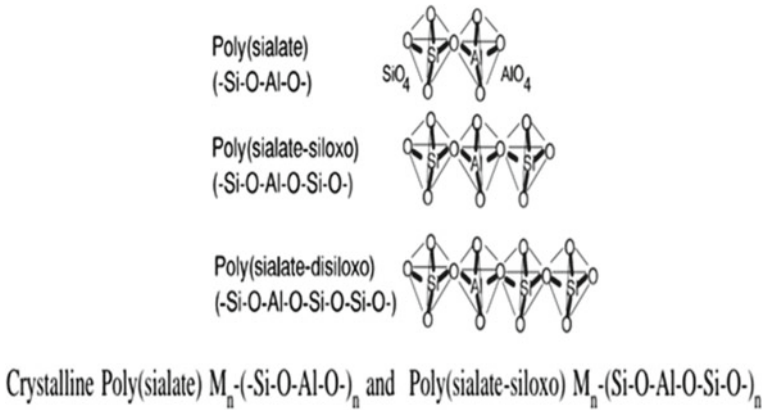


Fig. 1 Cross-link structure of aluminosilicate oxide [39]

VII. **Polymerization:** The process in which monomer molecules are linked to form a big polymer molecule is called polymerization. An polymer is a complex molecule that is made out of large number of monomers units.

The process monomer, oligomer, and polymer is continuous process in which the molecular weight of chemical structure and degree of polymerization increase [3, 35] (Figs. 1 and 2).

5 Mix Proportioning

The various factors are governed to form geopolymerization which was taken into account while preparing mix proportioning. The only use of one alkaline solution did not give effective results so use at least 2 different alkaline solutions to maintain the proper ratio to get effective results [18]. As sodium silicate and sodium hydroxide content increase, the UCS of geopolymer increases [24, 28]. The mixture of aluminosilicate (silicon dioxide (SiO₂) and aluminum dioxide (Al₂O₃)) with sodium silicate (Na₂SiO₃) is required to make water-resistant geopolymer material [36]. Maintaining the morality of alkaline solution from 5 to 15 M. Water to geopolymer binder ratio < 0.35, solution to aluminosilicate ratio < 0.35, sodium silicate to sodium hydroxide ratio equal to 1 makes geopolymer material hydrostatically stable and critical, which gives all physical and mechanical properties [4, 27, 46–50]. The UCS of geopolymer decreases as *W/Gs* ratio increases [51] (Figs. 3, 4 and 5).

Fig. 2 Conceptual model for alkaline activation process [37–39]

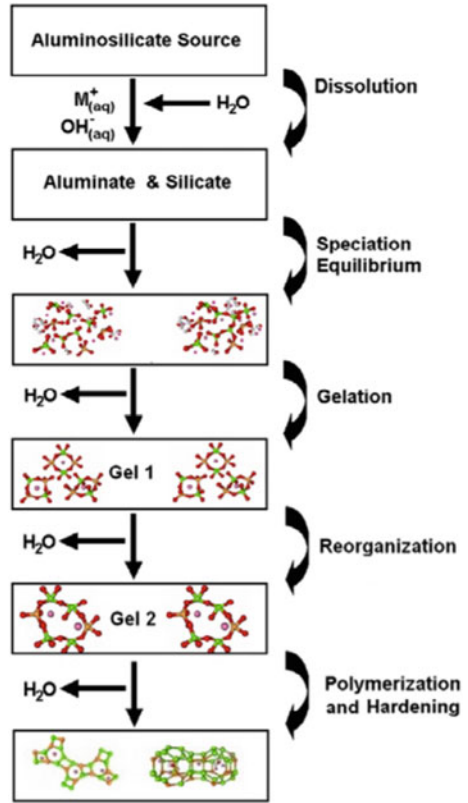
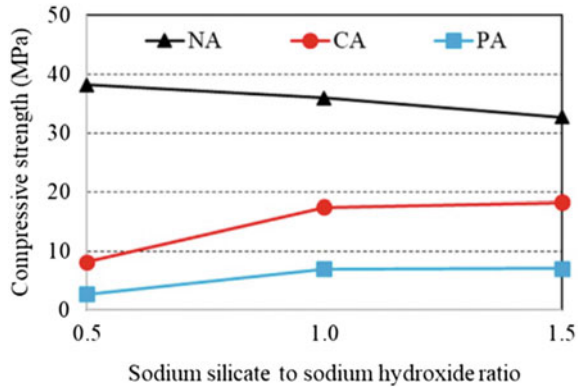


Fig. 3 Effect of Na₂SiO₃/NaOH on compressive strength [24]



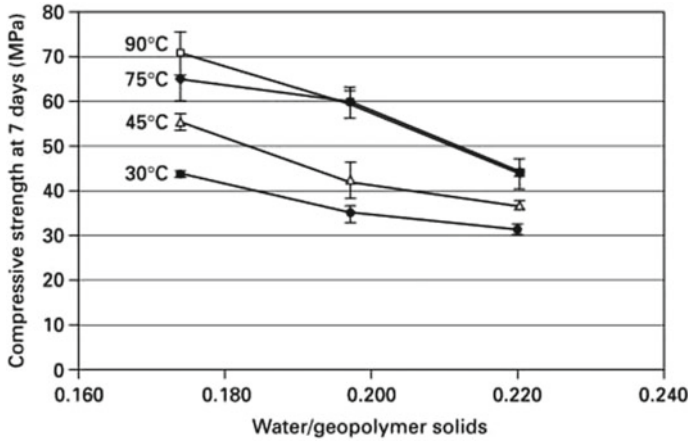


Fig. 4 Effect of W/Gs on compressive strength [51]

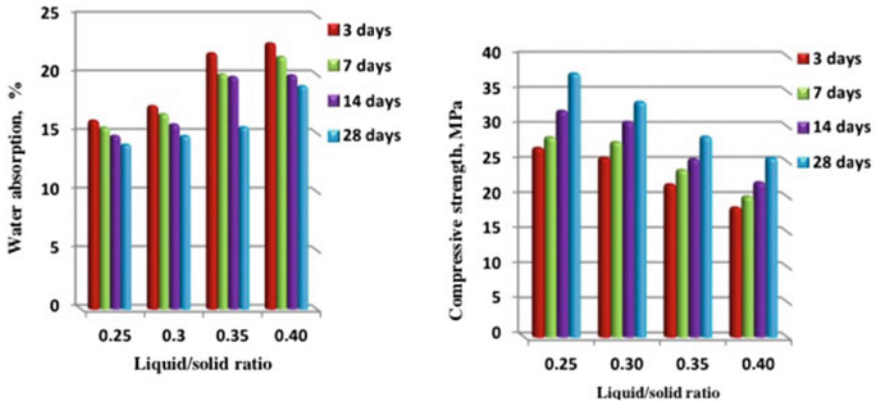


Fig. 5 Effect of liquid/solid ratio on water absorption and compressive strength [36]

6 Curing

As the amount of fly ash increases, it also increases the final setting time of geopolymer material up to 48 h [26, 33]. Weathered fly ash at 60 °C oven curing gives a remarkable effect that mechanical strength increases by 3.5 times [7]. The oven curing at temperature 60–105 °C for 1–7 days gives enhanced compressive strength up to 76% than normal curing [51] (Figs. 6, 7 and 8).

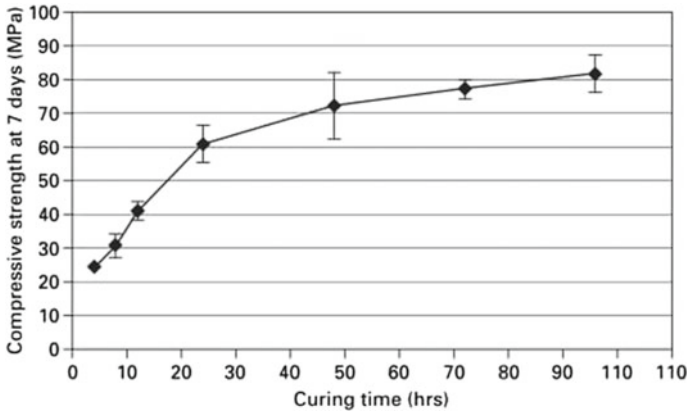


Fig. 6 Effect of curing time on compressive strength [29, 51]

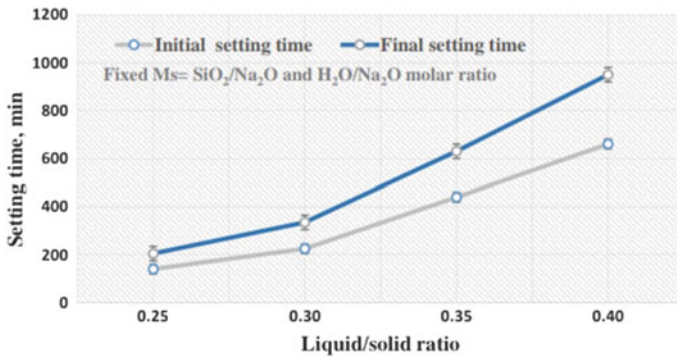


Fig. 7 Effect of liquid/solid ratio on setting time [33, 36]

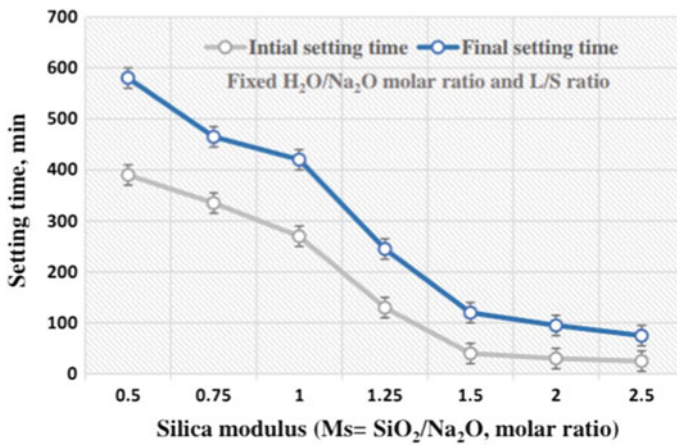


Fig. 8 Effect of silica modulus on setting time [33, 36]

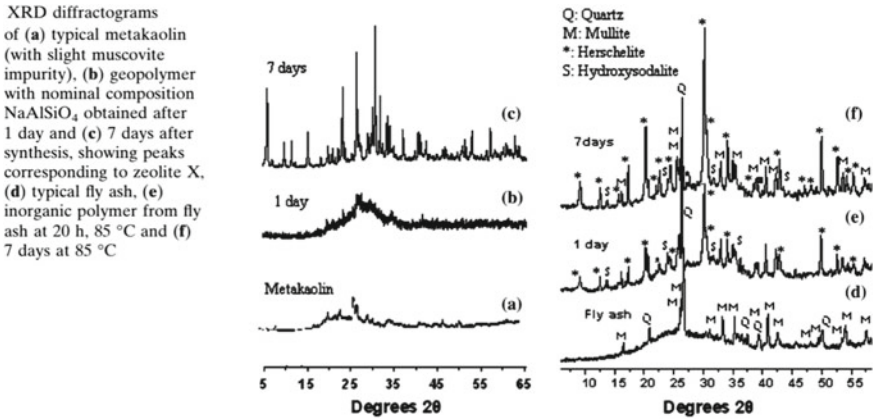


Fig. 9 XRD test analysis [42]

7 Analysis of Test

- **X-Ray Diffraction (XRD):** This test was done to analyze the structure of crystalline materials which is useful to identify crystalline phases present in material and to make changes in chemical composition if required [3, 18]. It shows the type of chemicals and nature such as N–A–S–H or C–A–S–H or C–S–H gel [42].
- **Scanning Electron Microscopy–Energy Dispersive Spectroscopy (SEM–EDS):** This testing was done to study the characterization of gel reactions in geopolymer paste such as N–A–S–H or C–A–S–H or C–S–H gel as well as to study deposited cracks and pores remaining in material [12, 42].
- **Fourier Transform Infrared Spectroscopy (FTIR):** This testing was done to study the absorption or emission of solid, liquid, and gas in geopolymer and to identify bond stretchability and strength in geopolymer material [26].
- **Thermal Conductivity Test:** This test was done by thermal conductivity meter or apparatus from which we analyze the heat conductivity and heat flow transparency in geopolymer material.
- **Physical and Mechanical Test:** All physical and mechanical tests were done on geopolymer material as per Indian standard codes to study the behavior of geopolymer material (Figs. 9, 10 and 11).

8 Discussion

The study was made on various geopolymer waste materials and their geopolymeric properties from various research papers and the further study of geopolymer material needed to be done on fracture resistance of brittle composite, different types of curing effect on hardening and strength, a ratio of alkali with geopolymer material

SEM micrographs of inorganic polymers synthesized from (a) metakaolin, (b) F class fly-ash

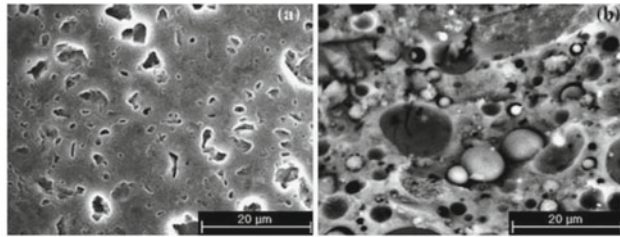
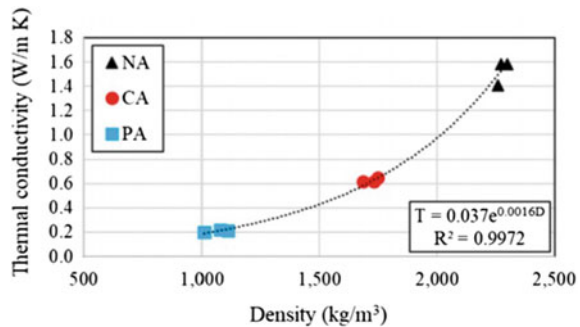


Fig. 10 SEM test analysis [42]

Fig. 11 Effect of density on thermal conductivity [24]



and in mechanical property, improve durability by improvement in heat resistance construction material up to 600–800 °C to evaluate the proper proportions of different materials used to prepare temperature controlled brick with energy production property. The entire study will then needed to be used to prepare mix design code of geopolymer brick with fine aggregate.

9 Conclusion

Waste material from industry having high amount of silica and alumina content, when mixed with alkaline solution, it gives excellent binding property. The binding property is generally formed by geopolymerization process in which the silica-to-alumina ratio plays a very important role to form stable critical structure of molecules which enhances the physical as well as mechanical properties of material.

The replacement of 10–40% of fly ash and 0–10% of GGBS in base material of geopolymer increases compressive strength [3]. 0–10% replacement of kaolin increases stability of structure as well as durability of geopolymer material [13, 14]. Rise hush 82% of SiO₂ hence, it produces greater binding property [19]. Paper waste and pumice aggregate reduce heat transparency of structure [22, 24]. To make water-resistant geopolymer material as well as durable material: maintaining morality of

alkaline solution from 5 to 15 M, water-to-geopolymer binder ratio < 0.35 , solution-to-aluminosilicate ratio < 0.35 , sodium silicate-to-sodium hydroxide ratio equal to 1 makes geopolymer material hydrostatically stable and critical which gives all physical and mechanical properties [46–50]. The oven curing at temperature 60–105 °C for 1–7 days gives enhanced compressive strength up to 76% than normal curing [51].

The geopolymer material or a geopolymer concrete has good strength and durability properties, and it can be used in civil industry. The geopolymer binder is the best replacement to cement and does not produce any greenhouse gases in environment. So, it will be the best sustainable material for civil industry.

References

1. W.M.W. Ibrahim, K. Hussin, M.M.A.B. Abdullah, A.A. Kadir, Geopolymer lightweight bricks manufactured from fly ash and foaming agent. *AIP Conf. Proc.* **1835** (2013). <https://doi.org/10.1063/1.4981870>
2. L.M. Deraman, L.Y. Ming, M.M.A.B. Abdullah, H. Kamarudin, The effect of different ratio bottom ash and fly ash geopolymer brick on mechanical properties for non-loading application. *MATEC Web Conf.* **97**, 01017 ETIC 2016 (2017)
3. A. Saludung, Y. Ogawa, K. Kawai, Microstructural and mechanical properties of FA/GGBS-based geopolymer. *MATEC Web Conf.* **195** (2018). <https://doi.org/10.1051/mateconf/201819501013>
4. A. Kumar, S. Kumar, Development of paving blocks from synergistic use of red mud and fly ash using geopolymerization. *Constr. Build. Mater.* **38**, 865–871 (2012). <https://doi.org/10.1016/j.conbuildmat.2012.09.013>
5. L. Zhang, S. Ahmari, J. Zhang, Synthesis and characterization of fly ash modified mine tailings-based geopolymers. *Constr. Build. Mater.* **25**(9), 3773–3781 (2011). <https://doi.org/10.1016/j.conbuildmat.2011.04.005>
6. A. Kumar, S. Kumar, Development of paving blocks from synergistic use of red mud and fly ash using geopolymerization. *Constr. Build. Mater.* **38**, 865–871 (2013)
7. C. Ferone, F. Colangelo, R. Cioffi, F. Montagnards, L. Santoro, Mechanical performance of weathered coal fly ash based geopolymer bricks. *Procedia Eng.* **21**, 745–752 (2011)
8. T. Subramani, P. Sakthivel, Experimental investigation on flyash based geopolymer bricks. **5**(5) (2016). ISSN 2319 – 4847
9. O. Arioz, K. Kilinc, M. Tuncan, A. Tuncan, T. Kavas, Physical, mechanical and micro-structural properties of F type fly-ash based geopolymeric bricks produced by pressure forming process. *Adv. Sci. Technol.* **69**, 69–74 (2010). TransTech Publications, Switzerland. <https://doi.org/10.4028/www.scientific.net/AST.69.69>
10. L. Zhang, S. Ahmari, J. Zhang, Synthesis and characterization of fly ash modified mine tailings-based geopolymers (2011). <https://doi.org/10.1016/j.conbuildmat.2011.04.005>
11. S. Ahmari, L. Zhang, Production of eco-friendly bricks from copper mine tailings through geopolymerization (2012). <https://doi.org/10.1016/j.conbuildmat.2011.10.048>
12. S. Ahmari, L. Zhang, Production of eco-friendly bricks from copper mine tailings through geopolymerization. *Constr. Build. Mater.* **29**, 323–331 (2012). <https://doi.org/10.1016/j.conbuildmat.2011.10.048>
13. H.M. Khater, A. El Nagar, M. Ezzat, Alkali activated eco-friendly metakaolin/slag geopolymer building bricks. *Chem. Mater. Res.* **8**(1) (2016). ISSN 2224-3224 (Print) ISSN 2225-0956 (Online)

14. J. He, J. Zhang, Y. Yu, G. Zhang, The strength and microstructure of two geopolymers derived from metakaolin and red mud-fly ash admixture: a comparative study (2012). <https://doi.org/10.1016/j.conbuildmat.2011.12.011>
15. C. Chen, Q. Li, L. Shen, J. Zhai, Feasibility of manufacturing geopolymer bricks using circulating fluidized bed combustion bottom ash. *Environ. Technol.* **33**, 1313–1321 (2012). <https://doi.org/10.1080/09593330.2011.626797>
16. A. Saludung, Y. Ogawa, K. Kawai, Microstructure and mechanical properties of FA/GGBS-based geopolymer (2018). <http://creativecommons.org/licenses/by/4.0/>
17. N.H. Thang, N.N. Hoa, D.T. Vu, P.T. Kien, M.A.B. Promentilla, Properties of geopolymer from coal bottom ash and water glass solution (2016). <https://www.researchgate.net/publication/309506286>
18. C. Freidin, Cementless pressed blocks from waste products of coal-firing power station. *Constr. Build. Mater.* (2007). <https://doi.org/10.1016/j.conbuildmat.2020.118441>
19. F. Saeeda, A. Naveedb, S. Gul, Synthesis of geopolymeric membrane using locally available rice husk ash as a source material (2020)
20. Fernando, Experimental investigation of the effect of fired clay brick on partial replacement of rice husk ash (RHA) with brick clay. *Adv. Recycling Waste* (2017)
21. J. He, Y. Jie, J. Zhang, Y. Yu, G. Zhang, Synthesis and characterization of red mud and rice husk ash-based geopolymer composites (2013). <https://doi.org/10.1016/j.cemconcomp.2012.11.010>
22. C.M.F. Vierira, R.M. Pinheiro, R.J.S. Rodriguez, V.S. Candido, S.N. Monterio, Clay bricks added with effluent sludge from paper industry: technical, economical and environmental benefits. *Appl. Clay Sci.* (2016). <https://doi.org/10.1016/j.clay.2016.07.001>
23. M. Sutcu, S. Akkuc, The use of recycled paper processing residues in making porous brick with reduced thermal conductivity. *Ceram. Int.* **35**, 2625–2631 (2009). <https://doi.org/10.1016/j.ceramint.2009.02.027>
24. A. Wongsu, V. Sata, P. Nuaklong, P. Chindapasirt, Use of crushed clay bricks and pumice aggregates in lightweight geopolymer concrete. *Constr. Build. Mater.* **188**, 1025–1034 (2018). <https://doi.org/10.1016/j.conbuildmat.2018.08.176>
25. N. Youssef, A.Z. Rabenantoandro, Z. Dakhli, C. Chapiseau, F. Waendendries, F.H. Chehade, Z. Lafhaj, Reuse of waste bricks: a new generation of geopolymer bricks. *SN Appl. Sci.* **1**, 1252 (2019). <https://doi.org/10.1007/s42452-019-1209-6>
26. H. Madani, A. Ramezaniapour, M. Shahbazinia, E. Ahmadi, Geopolymer bricks made from less active waste materials. *Constr. Build. Mater.* **247**, 118441 (2020). <https://doi.org/10.1016/j.conbuildmat.2020.118441>
27. L. Murmu, A. Patel, Towards sustainable bricks production: an overview. *Constr. Build. Mater.* **165**, 112–125 (2018). <https://doi.org/10.1016/j.conbuildmat.2018.01.038>
28. P. Turgut, M. Algin, Limestone dust and wood sawdust as brick material. *Build. Environ.* **42**, 3399–3403 (2007)
29. Aalil, D. Badreddine, K. Beck, X. Brunetaud, K. Cherkaoui, A. Chaaba, M. Al-Mukhtar, Valorization of crushed bricks in lime-based mortars. *Constr. Build. Mater.* **226**, 555–563 (2019)
30. G. Cultrone, I. Aurrekoetxea, C. Casado, A. Arizzi, Sawdust recycling in the production of lightweight bricks: how the amount of additive and the firing temperature influence the physical properties of the bricks. *Constr. Build. Mater.* **235**, 117436 (2020)
31. P. Palanisamy, P. Suresh Kumar, Effect of molarity in geo polymer earth brick reinforced with fibrous coir wastes using sandy soil and quarry dust as fine aggregate. *Case Stud. Const. Mater.* **8**, 347–358 (2018)
32. O.A. Fadele, O. Ata, Water absorption properties of sawdust lignin stabilised compressed laterite bricks (2018)
33. S. Mohammed, M.S. Liew, W.S. Alaloul, A. Al-Fakih, W. Ibrahim, M. Adamu, Development of rubberized geopolymer interlocking bricks. *Case Stud. Constr. Mater.* **8**, 401–408 (2018)
34. V.V. Kulkarni, A.K. Golder, P.K. Ghosh, Production of composite clay bricks: a value-added solution to hazardous sludge through effective heavy metal fixation (2019). <https://doi.org/10.1016/j.conbuildmat.2018.12.187>

35. D. Dimas, I. Giannopoulou, D. Papias, Polymerization in sodium silicate solution: a fundamental process in geopolymerization technology. *J. Mater. Sci.* **44**, 3719–3730 (2019). <https://doi.org/10.1017/s10853-009-3497-5>
36. R.A. Gado, M. Hebda, M. Lach, J. Mikula, Alkali activation of waste clay bricks: influence of silica modules, $\text{SiO}_2/\text{Na}_2\text{O}$, $\text{H}_2\text{O}/\text{Na}_2\text{O}$ molar ratio and liquid to solid ratio. *Mater. J.* **33**, 383 (2020)
37. I. Garcia-Loderio, A. Fernandez-Jimenez, A. Palomo, An overview of the chemistry of alkali-activated cement based binders. *Mater. DE Constr.* **64**(315) (2015). <https://doi.org/10.1533/9781782422884.1.19>
38. A. Palomo, A. Fernandez-Jimenez, Alkaline activation, procedure for transforming fly ash into new material, in *World of Coal Ash Conference* (2011)
39. *Alkaline Cement and Concrete Conference* (KIEV University, Ukraine, 1994), pp. 131–149
40. Geopolymer chemistry and applications
41. T. Cicek, M. Tanrıverdi, Lime based steam autoclaved fly ash bricks (2006). <https://doi.org/10.1016/j.conbuildmat.2006.01.005>
42. P. Duxson, A. Fernandez-Jimenez, J.K.L. Provis, G.C. Lukey, A. Palomo, J.S.J. Van Deventer, Geopolymer technology: the current state of the art. *J. Mater. Sci.* **42**, 2917–2933 (2007). <https://doi.org/10.1007/s10853-006-0637-z>
43. Pacheco-Torgal, Z. Abdollahnejad, A.F. Camões, M. Jamshidi, Y. Ding, Durability of alkali-activated binders: a clear advantage over Portland cement or an unproven issue? (2012). <https://doi.org/10.1016/j.conbuildmat.2011.12.017>
44. Palomo, M.W. Grutzeck, M.T. Blanco, Alkali-activated fly ashes: a cement for the future. *Cem. Concr. Res.* **29**(8), 1323–1329 (1999). [https://doi.org/10.1016/S0008-8846\(98\)00243-9](https://doi.org/10.1016/S0008-8846(98)00243-9)
45. K. Shrinivasan, A. Sivakumar, Geopolymer binders: a need for future concrete construction. *ISRN Polym. Sci.* **2013**. Article ID 509185 (2013). Hindawi Publications. <https://doi.org/10.1155/2013/509185>
46. S.V. Patankar, Y.M. Ghugal, S.S. Jamkar, Mix design of fly ash based geopolymer concrete (2014). <https://doi.org/10.1007/978-81-322-2187-6-123>
47. P. Pavithra, M. Srinivasula Reddy, P. Dinakar, B. Hanumanta Rao, B.K. Satpathy, A.N. Mohanty, A mix design procedure for geopolymer concrete with fly ash. *J. Clean. Prod.* **133**, 117–125 (2016). <https://doi.org/10.1016/j.jclepro.2016.05.041>
48. S. Roy, J. Sanjith, H.R. Jagath, G. Chethan, Experimental investigation on geopolymer bricks. *Int. Res. J. Eng. Technol.* **05**(08), 623–629 (2018)
49. R. Anuradha, V. Sreevidya, R. Venkatasubramani, B.V. Rangan, Modified guidelines for geopolymer concrete mix design using Indian Standard. *Asian J. Civ. Eng. (Build. Hous.)* **13**, 353–364 (2012)
50. T. Phoongernkham, C. Phiangphimai, N. Damrongwiriyapap, S. Hanjitsuwan, P. Chindaprasirt, A mix design procedure for alkali-activated high calcium fly ash concrete cured at ambient temperature. *Adv. Mater. Sci. Eng.* **2018** (2018). Article ID 2460403, PP13
51. B.V. Rangan, Engineering properties of geopolymer concrete (2006)

Effect of Creep and Shrinkage on Construction Sequence Analysis of High-Rise Building



Leroy M. Tuscano and Priyanka Jadhav

Abstract Consideration of the construction sequence of buildings will significantly change the internal forces of the structural members, especially for long span and super high-rise structures. The internal forced leads the assessment of elasto-plastic performance of building structures under earthquakes. In tall reinforced concrete building, the axial shortening of vertical members due to creep and shrinkage is non-avoidable. In design and construction of tall structures, it is necessary to pay attention for the effect of axial shortening. Mainly calculation of axial shortening is critical due to many parameters involved, viz. incorporates the grade of concrete, volume/surface ratio, sequence of construction, creep and shrinkage coefficients, and this task is not that much easy. The construction stage analysis has been carried out on fifty, sixty-five and eighty-storey building using effect of creep and shrinkage. The vertical member displacement results are compared with conventional dynamic analysis. The analysis is done for two different seismic zones, and the effect of humidity over the axial shortening is been determined. In dynamic analysis, the entire structure is considered as a lumped mass. Present study helps to understand the variation of structural load responses in construction sequence and dynamic analysis, respectively. Also the effect of creep and shrinkage after three years on the construction sequence analysis has been determined.

Keywords Elasto-plastic · Dynamic analysis · Construction sequential analysis · Creep · Shrinkage

L. M. Tuscano
Technip Energies, Mumbai, Maharashtra, India

P. Jadhav (✉)
Department of Civil Engineering, Terna Engineering College, Nerul Navi-Mumbai, Maharashtra, India

1 Introduction

In the construction sequence analysis (CSA), loads on the frame are applied stage wise construction, as construction proceeds, incremental loads can be applied and carry out nonlinear dynamic analysis. Staged construction analysis considers various stages in which load applied on the frame leads to calculation of various properties at each step. Also the order in which the various components of the building are constructed is important. In this type of analysis, limit state of serviceability of building is affected due to cycle time for floor-to-floor construction along with creep, shrinkage, span and cross section of the structural members. The main factor which is considered in this paper is creep, shrinkage and cycle time for floor-to-floor construction. Here special consideration is needed for axial deformation of columns for design and construction. But due to creep and shrinkage, column undergoes elastic and inelastic deformation. However, the elastic deformation occurs immediately after application of dead loads and live loads to the structure, but deformation due to creep and shrinkage occurs over many years. In the dynamic analysis, all structural loads are applied instantaneously on whole frame, and software considers the entire frame as Vierendeel truss. Midas Gen software is used to simulate the construction sequence of high-rise building considering effect of shrinkage and creep and estimated axial shortening of vertical members. The analysis is done using following input parameters such as compressive strength of concrete, sequence of construction, humidity of the region, slump of concrete, volume/surface ratio of the member and the axial shortening of vertical members which can be estimated. Generally, axial and lateral movements may be ignored for ordinary building, but it is important to account to overcome the adverse effect to the performance and its construction of elevators and facades. Particularly special considerations in the design as well as construction of high-rise buildings are required to account the effect of column shortening due to both elastic and inelastic, because adjacent members may experience differential shortening and it may lead to adverse effect on building. Elastic shortening decreases in the length under imposed load which is linearly proportional to load. It is independent of time-dependent properties of concrete and can be determined its dynamic analysis. Figure 1 shows the elastic shortening due to imposed load.

$$\Delta L = \frac{PL}{AE}$$

where $E = \frac{\sigma}{\epsilon}$.

The time-dependent properties of concrete (creep and shrinkage) are responsible for inelastic type of shortening. To find the value of inelastic shortening, we need to determine the creep and shrinkage coefficient. Figure 2 shows inelastic shortening.

Chakrabarti et al. [1] studied the effect on design forces based on construction sequence analysis incorporating self-weight of members. Liu et al. [2] concluded that 2D and 3D refined analyses show identical maximum slab loads. Choi and Kim [3] determined the differential column shortening due to the gravity loads. Jayasinghe

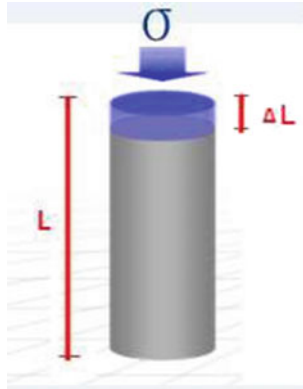


Fig. 1 Elastic shortening (<http://nptel.ac.in/courses/1052012/27>)

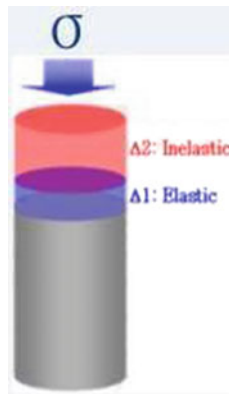


Fig. 2 Inelastic shortening (<http://nptel.ac.in/courses/105106118/10>)

and Jayasena [4] predicted possible axial shortening of columns and walls through analysis. Pranay et al. [5] presented that considerable variation is observed after simulation of construction sequence analysis and conventional analysis. Baker et al. [6] presented nonlinear time-dependent concrete effects in terms of creep and shrinkage in the construction of Burj Dubai using sequence analysis using the effects of creep and shrinkage to study the time-dependent behaviour of the structure. Ha and Lee [7] discussed that issues due to building movement both in axial and lateral direction are related to construction and maintenance issues. Pathan et al. [8] determined various responses of various forces in the transfer girder. Harsha and Vikranth [9] investigate the variation in deformation and forces for the transfer girded. Dubey et al. [10] studied the ratios of axial force and axial deformation along with the reinforcement required for critical load. They concluded that there is increase in axial force for inner columns, and less deformation is found in top columns. Shirhatti and Vanakudre [11] studied various responses of structures using time-dependent and construction

sequence analysis including P-Delta effects. Waghmare et al. [12] concluded that the effects of creep and shrinkage are to be considered because proportion of the deformations due to creep and shrinkage that contribute to the total amount of deformations is about 70%. Amin and Mahajan [13] concluded the need to improve the analysis accuracy in terms of displacement, moment and shear while doing construction sequence analysis.

2 Analysis

A typical fifty, sixty-five and eighty-storied reinforced concrete framed structure with plan asymmetry is analysed under dynamic analysis and construction sequence analysis using Midas Gen, as per the Indian standards IS 456 (2000), IS 1893 (2002), ACI 209R-92. It is done under two different cases, i.e. case I (seismic zones III) and case II (seismic zones V). Comparison is done between axial deformations in columns and shear force, axial deflection and bending moment in transfer girder (Figs. 3 and 4).

Details of building model floor-to-floor height are 3 m, slab thickness is 150 mm, beam size is 500 mm \times 750 mm (M40 concrete), transfer girder size is 1200 mm

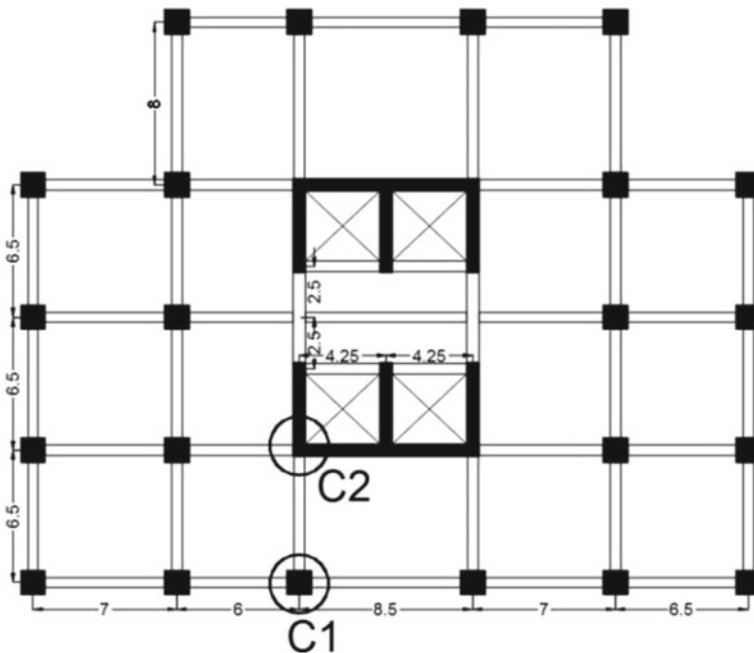
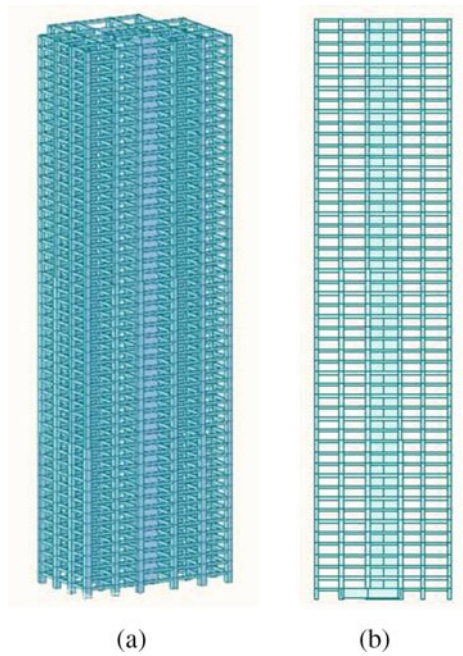


Fig. 3 Typical plan of structure

Fig. 4 a 3D model, b elevation



× 2500 mm (M50 concrete), shear wall thickness is 600 mm (M50 concrete), and column sizes are as follows:

- 1st–15th Floor—(1200 × 1200) mm (M50 concrete)
- 16th–30th Floor—(1100 × 1100) mm (M45 concrete)
- 31st–50th Floor—(1000 × 1000) mm (M40 concrete)
- 51st–65th Floor—(950 × 950) mm (M40 concrete)
- 66th–80th Floor—(900 × 900) mm (M40 concrete).

Floor finish considered is 1.25 kN/m² (IS 875 part I), live load considered is 2 kN/m² (IS 875 part I), response reduction factor (*R*) is 5, and importance factor is 1 (Figs. 5, 6 and 7).

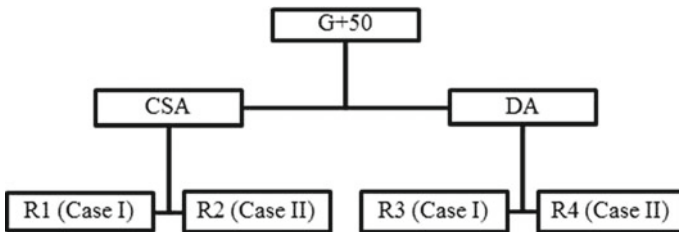


Fig. 5 Models for G + 50

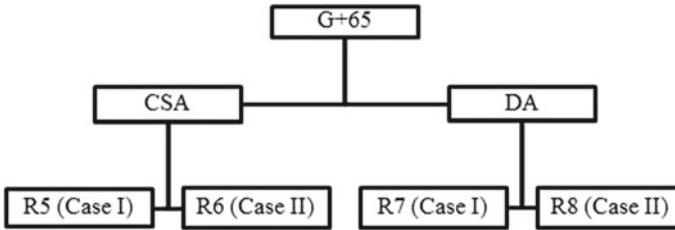


Fig. 6 Models for G + 65

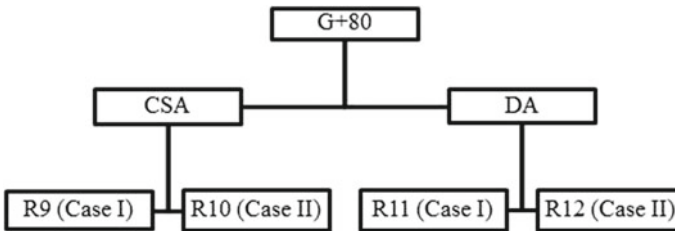


Fig. 7 Models for G + 80

3 Methodology

The construction sequence analysis and dynamic analysis are carried out on typical fifty, sixty-five and eighty-storied reinforced concrete framed structure. Two cases are considered, viz.

1. Case 1—(seismic zone III and humidity 60%)
2. Case 2—(seismic zone V and humidity 40%).

For calculation of creep and shrinkage coefficients slump of 12 cm, fine aggregate as 60% and air of 4.5% are assumed. Volume/surface (V/S) ratio is calculated as per the size of the column. Construction sequence analysis is then carried out in Midas Gen which analyses the structure step by step at every floor. Construction sequence schedule is planned in such a way that on the first day, the formwork of first floor is installed; 2 days later, the floor is being casted; after 5 days, the formwork of second floor is installed; similarly the construction of upper floors is done. On 22nd day, the formwork of first floor is removed (Fig. 8 and Table 1).

Sample calculation of creep coefficient for column (1200 × 1200) mm as per ACI 209R-92:

To calculate, the inelastic shortening in a column creep coefficient is required. Typical calculation for column 1200 mm × 1200 mm is shown below. To calculate creep coefficient, humidity is taken as 40%, slump is taken as 120 mm, fine aggregate percentage is taken as 60%, air content considered is 4.5%, and cement content is 450 kg/m³. Volume/surface (V/S) ratio is calculated as

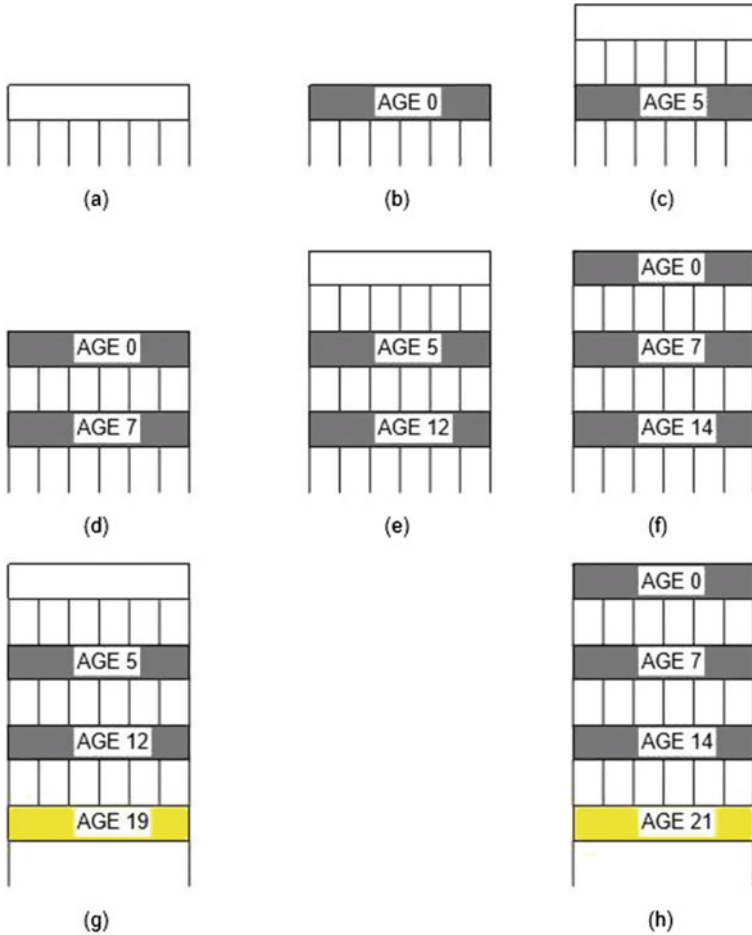


Fig. 8 Construction sequence schedule

Table 1 Material properties using ACI 209R-92

Column	Comp. strength (N/mm ²)	Humidity (%)		Slump (cm)	Fine aggregate (%)	Air (%)	Cement (kg/m ³)	V/S ratio (mm)
		Case I	Case II					
(1 ~ 15th)	50	60	40	12	60	4.5	450	300
(16 ~ 30th)	45	60	40	12	60	4.5	400	275
(31 ~ 50th)	40	60	40	12	60	4.5	380	250
(51 ~ 65th)	40	60	40	12	60	4.5	380	237.5
(66 ~ 80th)	40	60	40	12	60	4.5	380	225
Shear wall	50	60	40	12	60	4.5	450	260
Girder	50	60	40	12	60	4.5	450	405

$$\frac{V}{S} = \frac{1200 \times 1200}{2 \times (1200 + 1200)} = 300 \text{ mm}$$

- Humidity = 40% (from Table 1)
 Slump = 120 mm (from Table 1)
 Fine aggregate = 60% (from Table 1)
 Air content = 4.5% (from Table 1)
 Cement content = 450 kg/m³ (from Table 1)
 Creep coefficient = $\phi_u = 2.35\gamma_c$ (ACI 209R-92)

$$\gamma_c = \gamma_{c,t_0}\gamma_{c,RH}\gamma_{c,vs}\gamma_{c,s}\gamma_{c,\psi}\gamma_{c,\alpha}$$

- i. Age application of load factor (γ_{c,t_0})

$$\gamma_{c,t_0} = 1.25t_0^{-0.118} = 1.25(28)^{-0.118} = 0.843$$

- ii. Ambient relative humidity factor ($\gamma_{c,RH}$)

$$\gamma_{c,RH} = 1.27 - 0.67(h) = 1.27 - 0.67(0.4) = 1.002$$

- iii. Volume/surface ratio factor ($\gamma_{c,v/s}$)

$$\gamma_{c,v/s} = \frac{2}{3}(1 + 1.13e^{(-0.0213v/s)}) = \frac{2}{3}(1 + 1.13e^{(-0.0213 \times 300)}) = 0.667$$

- iv. Slump of fresh concrete factor ($\gamma_{c,s}$)

$$\gamma_{c,s} = 0.82 + 0.00264S = 0.82 + 0.00264 \times 120 = 1.1368$$

- v. Fine aggregate factor ($\gamma_{c,\psi}$)

$$\gamma_{c,\psi} = 0.88 + 0.0024\psi = 0.88 + 0.0024 \times 60 = 1.024$$

- vi. Air content factor ($\gamma_{c,\alpha}$)

$$\gamma_{c,\alpha} = 0.46 + 0.09\alpha = 0.46 + 0.09 \times 4.5 = 0.018 \leq 1 \approx 1$$

- vii. $\gamma_c = \gamma_{c,t_0}\gamma_{c,RH}\gamma_{c,vs}\gamma_{c,s}\gamma_{c,\psi}\gamma_{c,\alpha}$

$$\gamma_c = 0.843 \times 1.002 \times 0.667 \times 1.1368 \times 1.024 \times 1 = 0.6558$$

- viii. Creep coefficient = $\phi_u = 2.35\gamma_c = 2.35 \times 0.6558 = 1.54118$.

Age of loading = 28 days

$\psi = 0.6$ (ACI 209R-92)

$d = 10$ days (ACI 209R-92)

Creep coefficient @ t days $\phi(t - t_0) = \frac{(t - t_0^\psi)}{d + (t - t_0^\psi)} \phi_u$

$$f(t - t_0)@10,000 \text{ days} = \frac{(10,000 - 28)^{0.6}}{10 + (10,000 - 28)^{0.6}} \times 1.54118 = 1.482$$

Creep coefficient at 10,000 day is 1.482.

Sample calculation of shrinkage for column 1200 × 1200 mm as per ACI209R-92

To calculate, the inelastic shortening in a column shrinkage strain is important factor. Typical calculation of shrinkage strain for column 1200 mm × 1200 mm is mentioned below. Similar calculation is done for other column sizes.

Ultimate shrinkage strain (ε_{shu})

$$\varepsilon_{shu} = 780 \times \gamma_{sh} \times 10^{-6}$$

- i. Moist curing correction factor (γ_{sh,t_c}) t_c = days of curing

$$\gamma_{sh,t_c} = 1.202 - 0.2337 \log(t_c) = 1.202 - 0.2337 \log(7) = 1.005$$

- ii. Ambient relative humidity factor ($\gamma_{sh,RH}$)

$$\gamma_{sh,RH} = 1.4 - 1.02(h) = 1.4 - 1.02 \times (0.4) = 0.992$$

- iii. Volume/surface ratio factor ($\gamma_{sh,v/s}$)

$$\gamma_{sh,v/s} = 1.2e^{(-0.00472(V_s))} = 1.2e^{(-0.00472 \times 300)} = 0.2912$$

- iv. Slump of fresh concrete factor ($\gamma_{sh,s}$)

$$\gamma_{sh,s} = 0.89 + 0.00161S = 0.89 + 0.00161 \times 120 = 1.0832$$

- v. Fine aggregate factor ($\gamma_{sh,\psi}$)

$$\gamma_{sh,\psi} = 0.9 + 0.002\psi = 0.9 + 0.002 \times 60 = 1.02$$

- vi. Cement content factor ($\gamma_{sh,c}$)

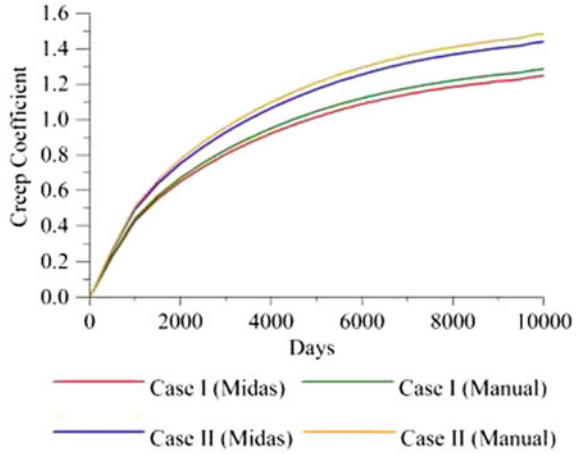
$$\gamma_{sh,c} = 0.75 + 0.00061C = 0.75 + 0.00061 \times 450 = 1.0245$$

- vii. Air content factor ($\gamma_{sh,\alpha}$)

$$\gamma_{sh,\alpha} = 0.95 + 0.008\alpha = 0.95 + 0.008 \times 4.5 = 0.986 < 1 \approx 1$$

$$\gamma_{sh} = \gamma_{sh,t_c} \gamma_{sh,RH} \gamma_{sh,v/s} \gamma_{sh,s} \gamma_{sh,\psi} \gamma_{sh,c} \gamma_{sh,\alpha}$$

Fig. 9 Creep coefficient for 1200 × 1200 mm column



$$\gamma_{sh} = 1 \times 0.992 \times 0.291 \times 1.0832 \times 1.02 \times 1.0245 \times 1 = 0.3265$$

$$\epsilon_{shu} = 780 \times \gamma_{sh} \times 10^{-6} = 780 \times 0.3265 \times 10^{-6} = 2.5467 \times 10^{-4}$$

$$\alpha = 1 \quad (\text{ACI 209R-92})$$

$$f = 35 \text{ days} \quad (\text{ACI 209R-92})$$

Age of loading = 28 days

$$\text{Shrinkage strain @ } t \text{ days} \quad \epsilon_{sh}(t - t_c) = \frac{(t - t_c)^\alpha}{f + (t - t_c)^\alpha} \epsilon_{shu}$$

$$\begin{aligned} \epsilon_{sh}(t - t_c) @ 10,000 \text{ days} &= \frac{(10,000 - 28)^1}{35 + (10,000 - 28)^1} \times 2.5467 \times 10^{-4} \\ &= 2.5377 \times 10^{-4} \end{aligned}$$

Shrinkage strain at 9000 day is 2.5377×10^{-4} .

The creep coefficients and shrinkage strains calculated manually by ACI 209-92R are compared with the results obtained from construction sequence analysis using Midas Gen software. Figures 9, 10, 11, 12, 13, 14, 15, 16, 17, 18, 19, 20, 21 and 22 given show the comparison between the manually calculated values and result obtained from CSA of creep and shrinkage.

4 Column Shortening

The maximum axial deformation is found in the top floor of the building. Axial shortening due to construction sequence analysis is the summation of shortening due to creep, shrinkage and elastic shortening. In Fig. 23, maximum shortening is found

Fig. 10 Creep coefficient for 1100 × 1100 mm column

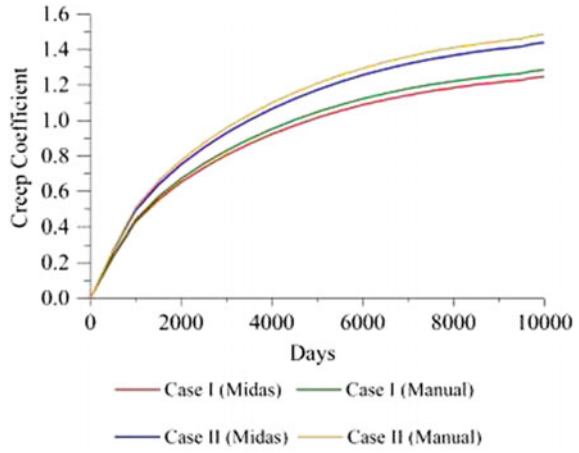


Fig. 11 Creep coefficient for 1000 × 1000 mm column

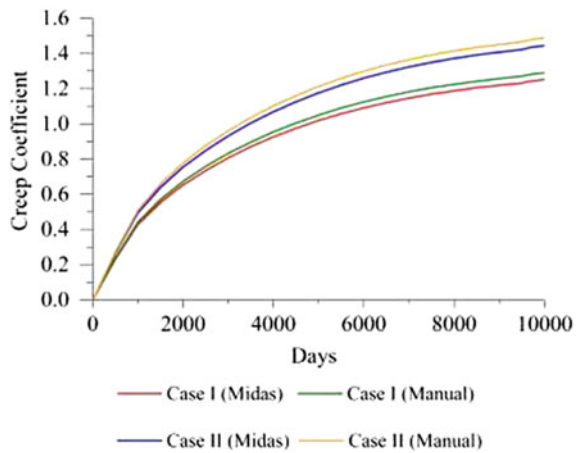


Fig. 12 Creep coefficient for 950 × 950 mm column

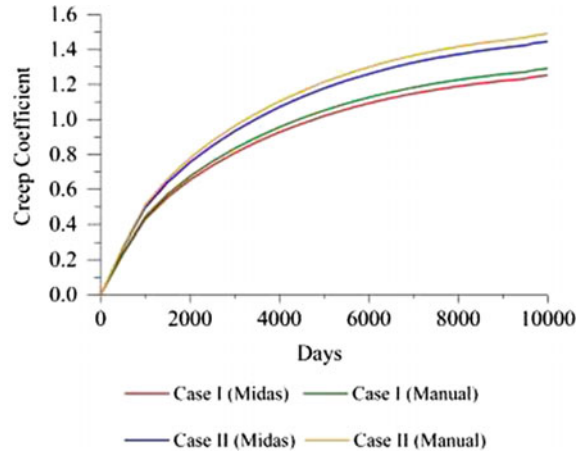


Fig. 13 Creep coefficient for 900 × 900 mm column

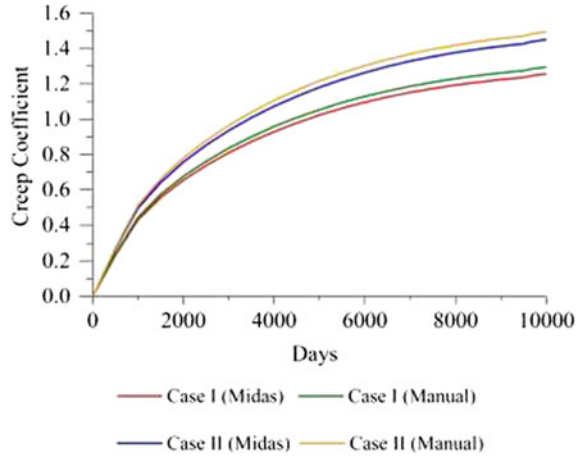


Fig. 14 Creep coefficient for shear wall

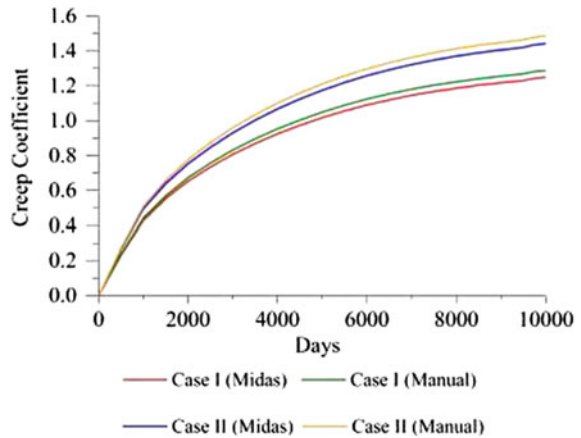


Fig. 15 Creep coefficient for transfer girder

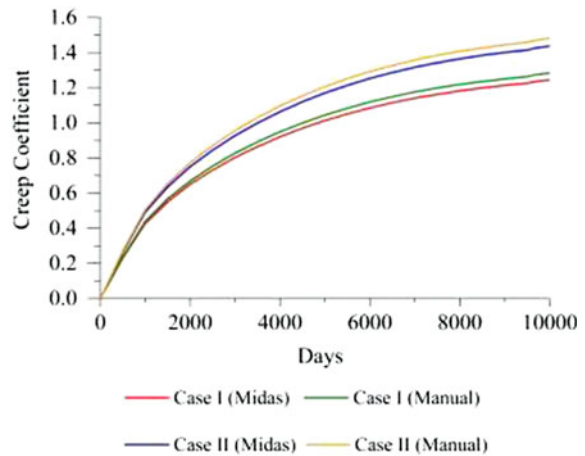


Fig. 16 Shrinkage strain for 1200 × 1200 mm column

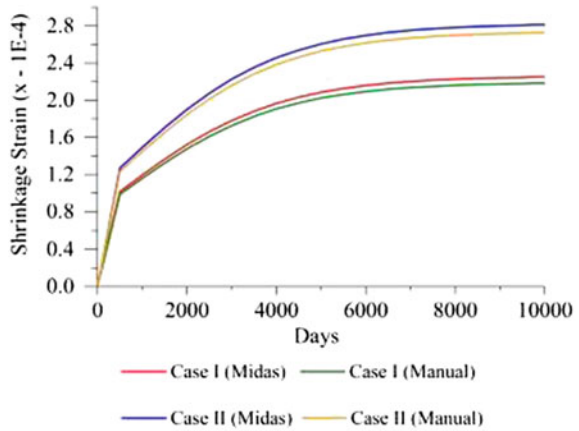


Fig. 17 Shrinkage strain for 1100 × 1100 mm column

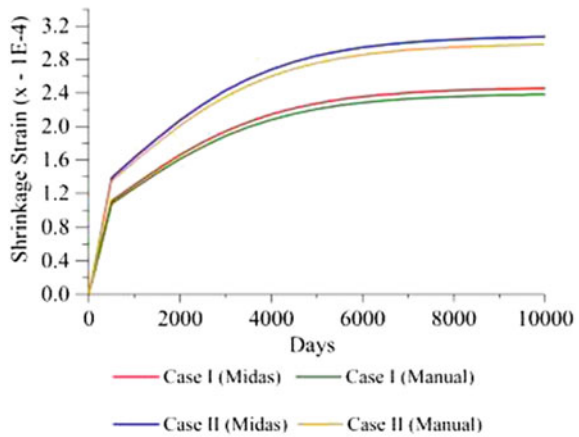


Fig. 18 Shrinkage strain for 1000 × 1000 mm column

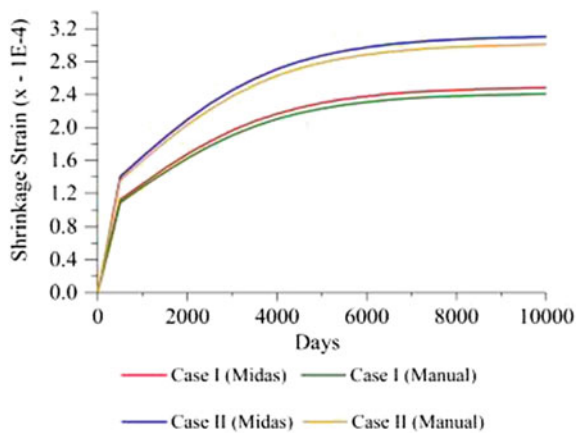


Fig. 19 Shrinkage strain for 950 × 950 mm column

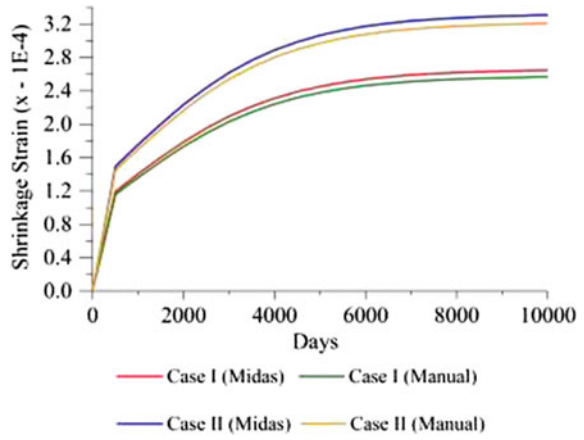


Fig. 20 Shrinkage strain for 900 × 900 mm column

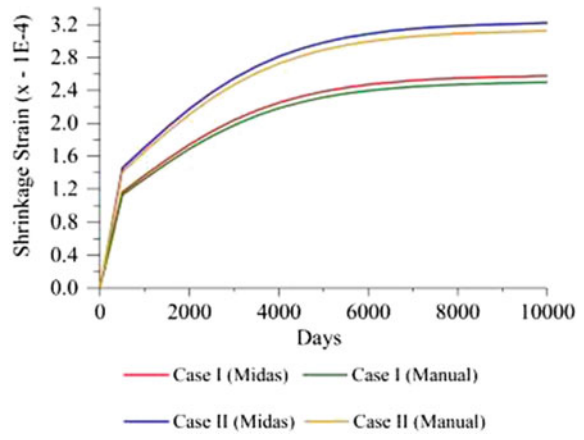
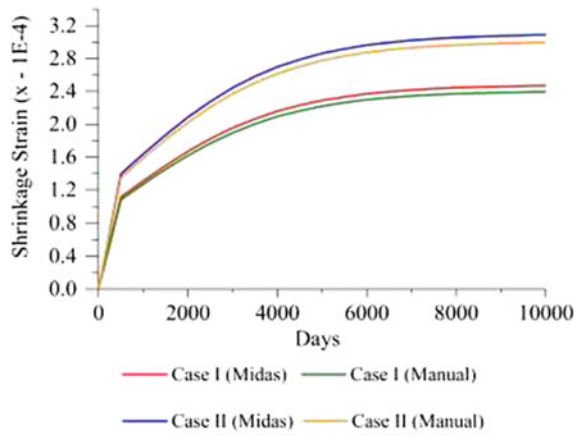


Fig. 21 Shrinkage strain for shear wall



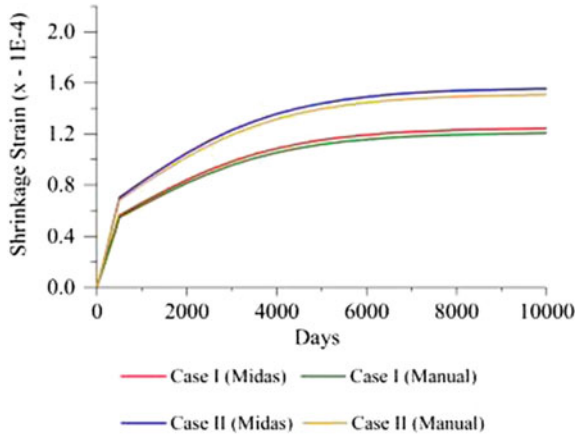


Fig. 22 Shrinkage strain for transfer girder

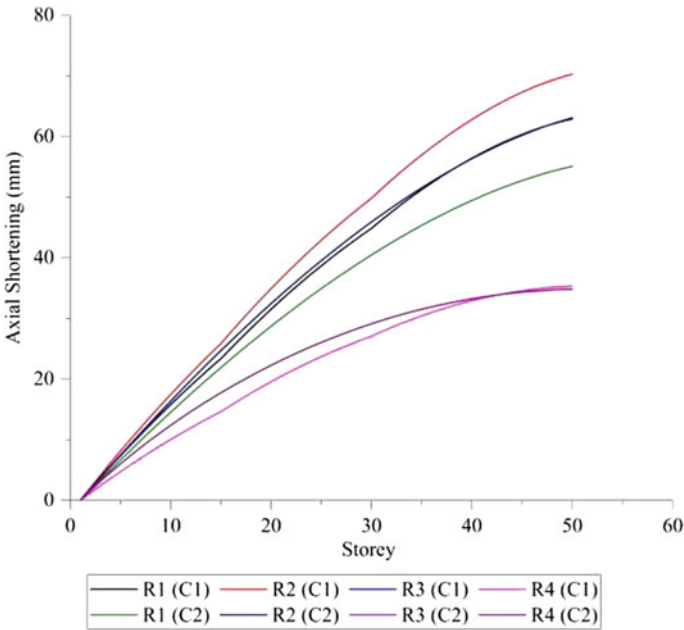


Fig. 23 Axial shortening in fifty storey

in model R2 at location C1 (70.29 mm); in Fig. 24, maximum shortening is found in model R6 at location C1 (116.6 mm), and in Fig. 25, maximum shortening is found in model R10 at location C1 (162.41 mm). Since the humidity is reduced from 60 to 40%, the axial shortening is increased by 11%.

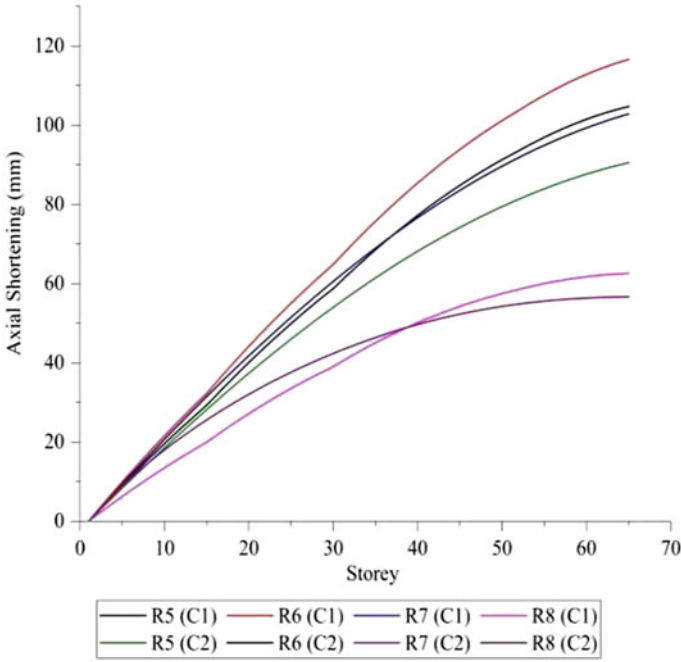


Fig. 24 Axial shortening in sixty-five storey

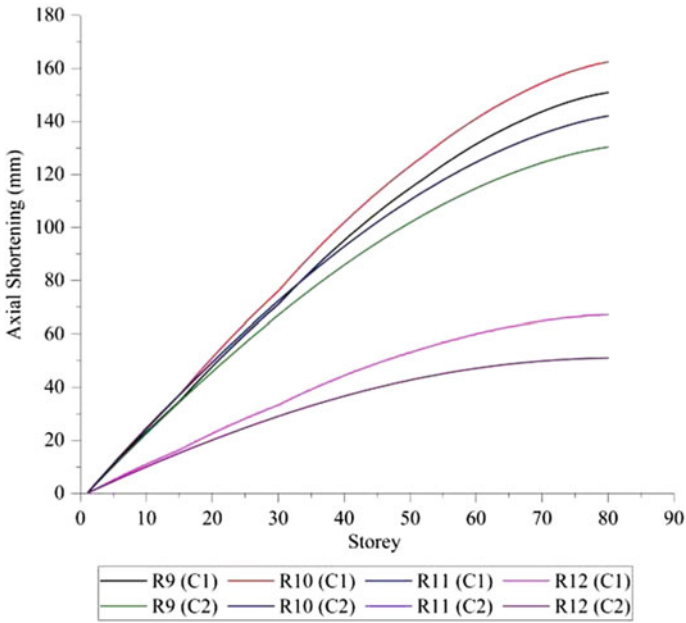


Fig. 25 Axial shortening in eighty storey

5 Transfer Girder

The maximum bending moment found in transfer girder is seen in model R10, i.e. eighty-storey building under construction sequence analysis (Fig. 26). Also due to CSA, there is 23.1% increment in bending moment as compared to the results of DA illustrated in Fig. 27. Due to case II (seismic zone V), there is 14.9% increment bending moment than R9, i.e. case I (seismic zone III). In Fig. 28, it is been seen that due to construction sequence analysis, the shear force in transfer girder is increased by 29%. Also shear force in transfer girder due to case II (seismic zone V) is 11.8% higher than case I (seismic zone III). Maximum shear force is been seen in model R10, i.e. eighty-storey building model.

The deflection seen in transfer girder is within the permissible limits. Figure 29 shows that due to construction sequence analysis, there is 13.4% increment in the deflection of transfer girder as compared to dynamic analysis. Also, deflection in transfer girder due to case II (seismic zone V) is 8.65% higher than case I (seismic zone III). Figure 30 indicates that base shear is same for DA and CSA. Also as the building height increases, there is increase in the base shear. Base shear found in the models of case II (seismic zone V) is 2.25 times the base shear found in models of case I (seismic zone III).



Fig. 26 Bending moment diagram of girder

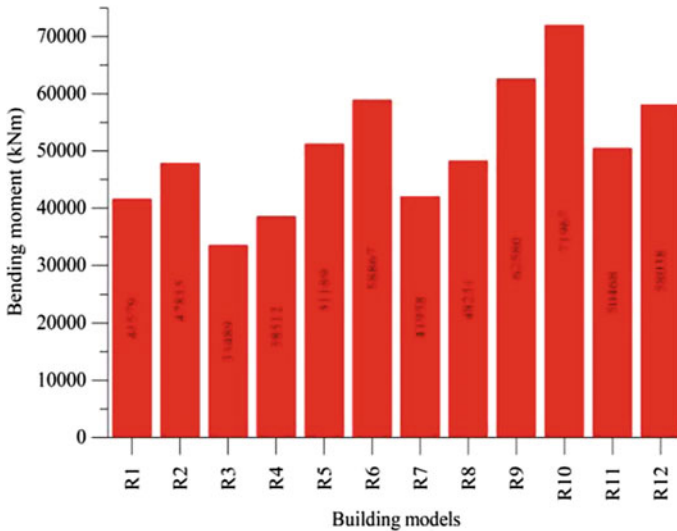


Fig. 27 Bending moment in transfer girder

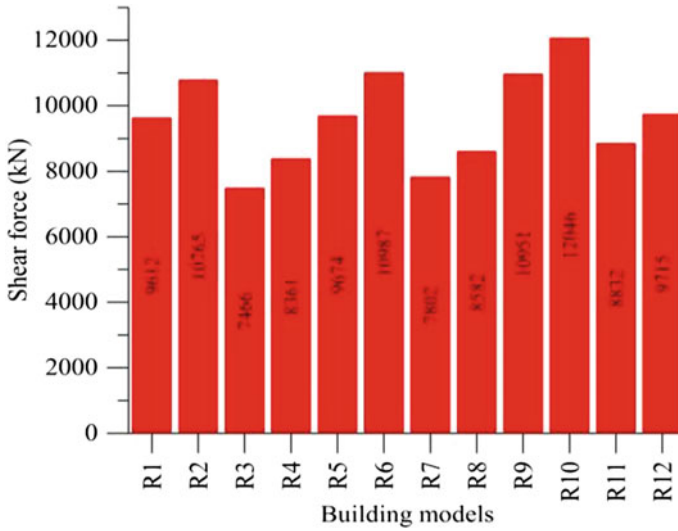


Fig. 28 Shear force in transfer girder

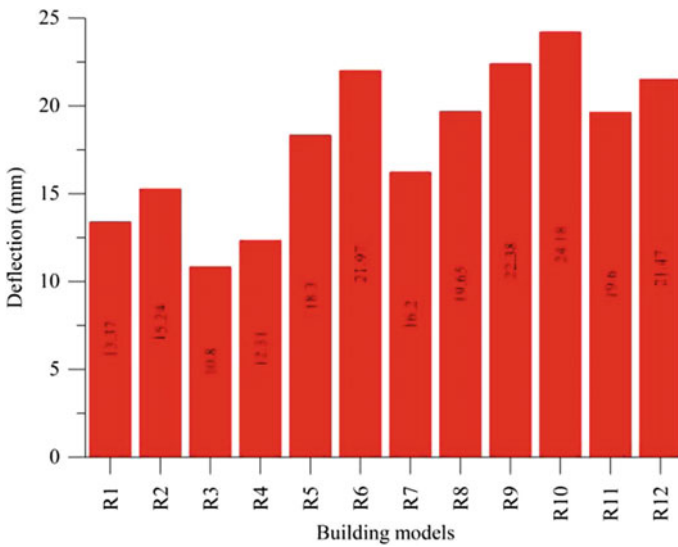


Fig. 29 Deflection in transfer girder

Figures 31 and 32 show the lateral displacement in the models. Lateral displacement seen in models due to dynamic analysis and construction sequence analysis is same. Dynamic analysis and construction sequence analysis have no effect on lateral displacement, but the difference is found due to case I (seismic zone III) and

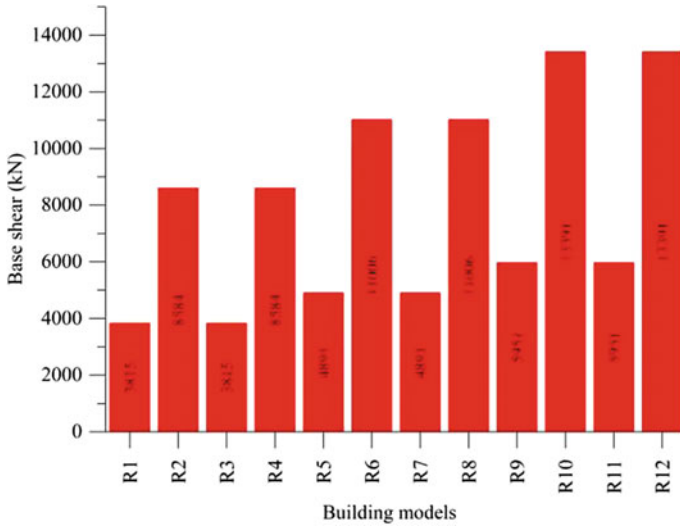


Fig. 30 Base shear

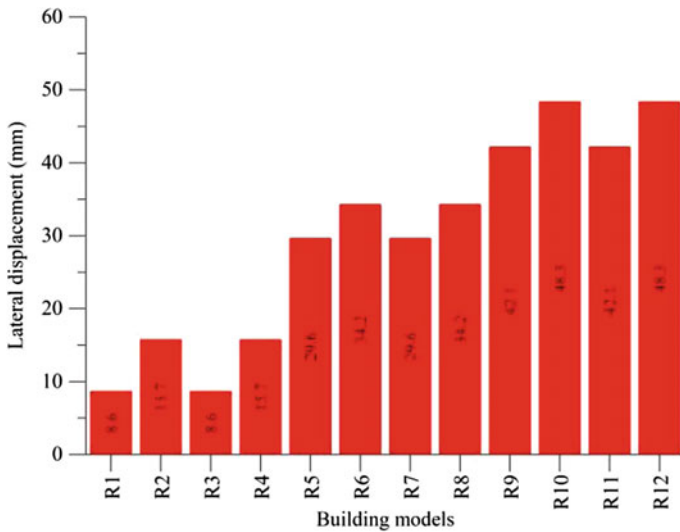


Fig. 31 Lateral displacement in x-direction

case II (seismic zone V). Due to different seismic zone, there is change in lateral displacement of building.

Figure 33 determines that time period has no change due to dynamic analysis as well as construction sequence analysis. Also the time period seen in x- and y-direction is same for all models. Due to change in humidity, the shrinkage strain and

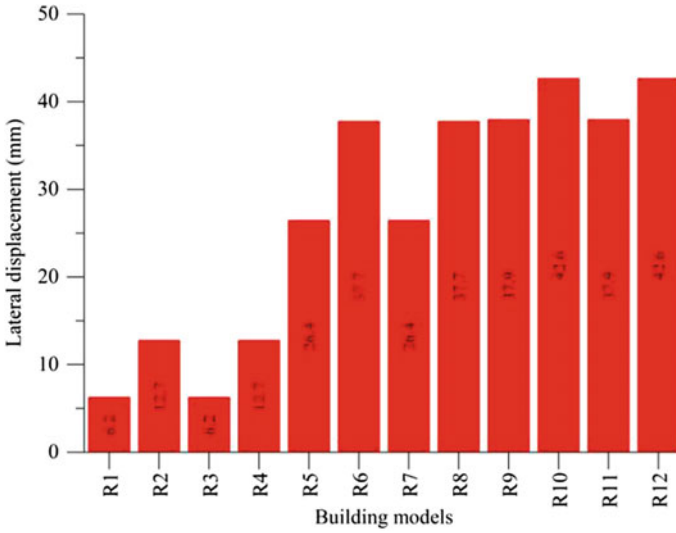


Fig. 32 Lateral displacement in y-direction

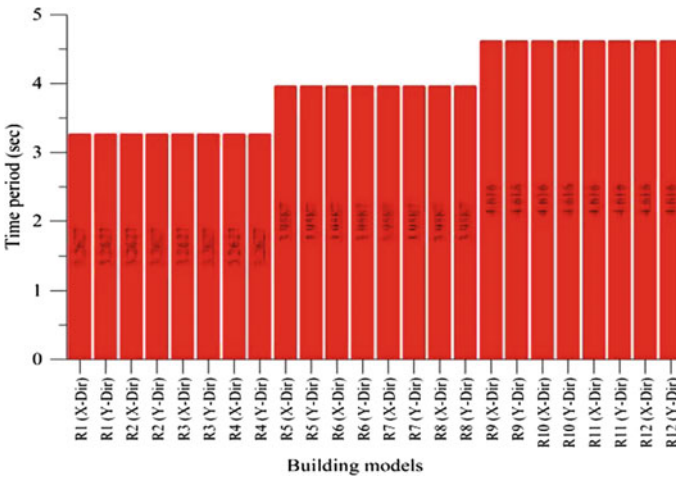


Fig. 33 Time period

creep coefficient change which directly affects the axial shortening of the column. Decrease in humidity results in increment of the axial shortening.

6 Conclusions

In the present study, analyses of fifty, sixty-five and eighty-storey reinforced concrete models are carried out using construction sequence analysis and dynamic analysis in Midas Gen software. Based on the analysis, following conclusions are drawn: axial column shortening due to construction sequence analysis is more than that of dynamic analysis due to creep and shrinkage. Differential column shortening is seen between the two adjacent columns. To compensate, the same extra reinforcement should be provided or the slab should be casted with a correction camber at the edge. Change in humidity because of different seismic zone affects the axial shortening. Humidity is inversely proportional to axial shortening. The bending moment, shear force and deflection obtained from construction sequence analysis must be used to design the transfer girder. However, due to construction sequence analysis, significant increment is seen in bending moment, shear force and deflection of transfer girder. Case 2 (seismic zone V) determines higher value of bending moment due to higher lateral forces induced in that zone. Time period has no change in the dynamic analysis as well as construction sequence analysis. Base shear has no change in the dynamic analysis as well as construction sequence analysis. Difference is seen in base shear due to case I (seismic zone III) and case II (seismic zone V). There is no change observed in lateral displacement due to dynamic analysis as well as construction sequence analysis. Because the construction sequence analysis considers the incremental loading on floor, i.e. dead load and imposed load and not the wind forces. Difference is found in lateral displacement due to different seismic zones.

However, based on above analysis, it can be observed that analysis of high-rise building after inclusion of construction sequence analysis provides more realistic design than the conventional design. Also note that considerable amount of deformations is observed due to creep and shrinkage, and it must be accounted in the analysis.

References

1. S.C. Chakrabarti, G.C. Nayak, S.K. Agarwala, Effect of sequence of construction in the analysis of multistoreyed building frame. *Build. Environ.* **13**, 1 (1978)
2. X. Liu, W.F. Chen, M.D. Bowman, Construction load analysis for concrete structures. *J. Struct. Eng.* **111**, 1019–1036 (1985)
3. C. Choi, E. Kim, Multistorey frames under sequential gravity loads. *J. Struct. Eng.* **3**(11) (1985). ISSN 0733-9445/85/0011-2373
4. M.T.R. Jayasinghe, W.M.V.P.K. Jayasena, Effects of axial shortening of columns on design and construction of tall reinforced concrete buildings. *ASCE Des. Constr.* **9**, 70–78 (2004)
5. R. Pranay, I.Y. Sreevalli, T.S. Kumar, Study and comparison of construction sequence analysis with conventional lumped analysis using etabs. *Civ. Eng. Syst. Sustain. Innov.* **78**, 7 (2007)
6. W.F. Baker, D.S. Korista, L.C. Novak, Engineering the world's tallest—Burj Dubai, in *CTBUH 8th World Congress 2007* (2007)

7. T. Ha, S. Lee, Advanced construction stage analysis of high-rise building considering creep and shrinkage of concrete, in *Advances in Structural Engineering and Mechanics (ASEM13)*, Korea, Sept 2013, pp. 8–12
8. K.M. Pathan, S.W. Ali, H.T. Khan, M.S. Mirza, M. Waseem, S. Zubair, Construction stage analysis of RCC frames. *Int. J. Eng. Technol. Res.* **2**(3), 54–58 (2014)
9. B. Harsha, J. Vikranth, Study and comparison of construction sequence analysis with regular analysis by using etabs. *Int. J. Res. Sci. Adv. Eng. [IJRSAE]* **2**(8), 218–227 (2014)
10. N. Dubey, R.S. Sonparote, R. Kumar, Effect of construction sequence analysis on seismic performance of tall buildings. *J. Civ. Eng. Environ. Technol.* **2**(11), 44–49 (2015)
11. T.G. Shirhatti, S.B. Vanakudre, The effects of p-delta and construction sequential analysis of RCC and steel building with respect to dynamic analysis. *Int. Res. J. Eng. Technol.* **2**(4), 65 (2015)
12. A.P. Waghmare, P.A. Dode, H.S. Chore, Axial shortening effect on vertical element using elastic and inelastic approach by ACI code. *Int. J. Comput. Appl.* **7**, 5–11 (2015)
13. S.R. Amin, S.K. Mahajan, Analysis of multi storied RCC building for construction sequence loading. *Int. J. Mod. Trends Eng. Res.* **7**(6), 49 (2015)

Experimental Investigation of Concrete Used in Spent Fuel Pools of Nuclear Power Plants Subjected to Boiling Water Exposure



Priyanka Jadhav, Keshav Sangle, Apurv Vaidya, Ankit Dhoot, and Siddhant Biyani

Abstract The experimental study is presented to show the effect of long term boiling water on the mechanical and chemical behaviour of concrete used in the Spent Fuel Pools (SFP) of Indian Nuclear Power Plants (NPP). Experimental investigation is performed on a simulated SFP at laboratory, which is cast using internal steel liners and concrete cube walls. The simulated SFP is subjected to long term boiling water and after successive events; tests were performed on the specimen of water tank for the purpose of damage assessment to predict the effect of long term boiling water on the physio-chemical properties of the concrete. Results revealed that compressive strength of the heated specimens was observed to be decreased on immediate testing and increased after exposure to working environmental conditions. Increase in the temperature of test specimens is well within the limitations specified in ASME standard.

Keywords Nuclear power plant · Spent fuel pool · Boiling water · Temperature variation · Compressive strength · Silica fume nano-silica

1 Introduction

Tohoku earthquake, which occurred on, March 11, 2011, caused a tsunami and hit the east coast of Japan and damaged the Fukushima Daiichi NPP and resulted in breakdown of emergency power system [1]. With reference to disaster that occurred at the Fukushima Daiichi NPP, it is necessary to estimate the safety and structural adequacy of concrete used in the SFP of NPP to gain confidence for the operator during such an event. The spent fuel issue at Fukushima Daiichi erupted with an

P. Jadhav (✉)

Terna Engineering College, Nerul, Navi Mumbai, Maharashtra, India

K. Sangle · A. Dhoot · S. Biyani

VJTI, Mumbai, Maharashtra, India

A. Vaidya

K. K. Wagh Institute of Engineering Education and Research, Nashik, Maharashtra, India

electrical failure in a switchboard which stopped cooling of water of SFP, where Unit #4, SFP contained the largest number of fuel bundles. In case, cooling of the SFP is not possible for a prolonged period, the bulk temperature of pool water may rise to reach a constant value of 100 °C and may sustain for a prolonged period.

Considering the above accidental scenario, need to access the performances of concrete walls used in SFP of the NPPs which may be exposed to elevated temperature for long period, which may help to determine and maintain its structural integrity during accidental scenario. In this direction, the author has done in depth literature review of the concrete subjected to the elevated temperature exposure from where it is concluded that, in the various elevated temperature exposure tests on concrete, SFPs of NPP structures were not modelled and analysed for representative materials as well as representative environmental conditions. Hence in order to arrive at conclusion on, effect of elevated temperature under severe accidental conditions on the walls of SFP of Indian NPPs, it is extremely necessary to test the concrete specimen under consideration at simulated desired environment and material properties.

Behaviour of concrete subjected to high temperature dependent on behaviours and alterations in the properties of the cement paste and further leads to deterioration because of moisture removal and leads to dehydration of cement paste. Also, cement gel structure breakdowns and resulted in loss of strength, durability and aggregate colour changes observed due to the number of transformations and reactions [2]. Generally, condition assessment of concrete damaged after exposure to long term fire and its corrective remedies for its rehabilitation is an important requirement. Therefore, systematic simulation and experimental investigation of concrete structures for various temperature conditions during and after exposure to accidental fire are important [3].

Handoo et al. [4] investigated the changes in pre and post fired concrete for changes in the mineralogical, physical and morphological at elevated temperature using hot air oven surface for a constant retention period of 5 h. Poon et al. [5] studied the strength and durability performance of concrete incorporating silica fume, fly ash and blast furnace slag exposed to elevated temperatures of 800 °C. Chan et al. [6] studied the effect of temperature on the residual strength and pore structure in high-performance concrete in comparison to conventional concrete. Concrete specimen was kept in an electric furnace. Zadrzil et al. [7] investigated the strength-porosity relation of concrete using the effect of temperature and age. Chini and Acquaye [8] studied the strength and durability of concrete under elevated temperatures.

Sakr and Hakim [9] studied the different types of concrete used as shielding in nuclear facilities under the exposure of accidental fire ranging from 25 to 950 °C. Husem [10] investigated experimentally effect of high temperature on the flexural and compressive strength of ordinary and high-performance micro-concrete. Arioz [11] presented experimental results to access the effect of elevated temperature on the cement paste using thermal analysis and colour image techniques using various water/cement ratios and types of aggregates. Karakoc et al. [12] studied the compressive strength of concrete containing expanded perlite aggregate and pumice aggregate which is exposed to 700 °C. After that cooled in various methods. Kizilkanat et al. [13] investigated the concrete with different types of pozzolans and aggregates

exposed to high temperatures and its effect on the thermal conductivity and moisture resistance factor of concrete. Bingol and Gul [14] investigated the effects of elevated temperatures and cooling systems on the residual bond strength. Chen et al. [15] studied the strength properties of early-age concrete under high temperatures. Mindeguia et al. [16] investigated the thermo-hydral behaviour of concrete for the possible link to spalling when exposed to high temperatures. Khan et al. [17] investigated shear strength of RC beam under the influence of cyclic thermal loading. Yaragal et al. [18] studied the behaviours of concrete during and after exposure to elevated temperature. The weight loss and residual compressive strength retention characteristics were studied on the normal strength concrete subjected to elevated temperature from 100 to 800 °C in steps of 100 °C with a retention period of 2 h.

Bastami et al. [19] investigated the effect of temperature on the properties of high-strength concrete in terms of spalling, mass loss and compressive strength. Divya and Santhanam [20] studied the effect of moderately elevated temperatures on the properties of concrete used for nuclear reactor vaults. Kizilkanat et al. [13] investigated the effect of use of different types of pozzolans and aggregates under high temperatures. Its effect on the thermal conductivity and moisture resistance factor of concrete is further studied. Tan and Nguyen [21] studied the structural responses of RC columns under elevated temperature and subjected to uniaxial bending. Bastami et al. [22] studied the mechanical and physical behaviour of nano-silica concrete under elevated temperatures. Kou et al. [23] studied the performance of recycled aggregate concrete in terms of strength and durability under the effect of high temperature. Xiao et al. [24] studied the post heating bond behaviour between high-strength concrete and high-grade rebar. Wu and Wu [25] experimentally examined the freeze–thaw resistance of ordinary concrete after high temperatures. The above scenario reveals that the numerous literatures are available on concrete subjected to elevated temperature due to accidental fire for a short duration. On the other hand, concrete subjected to elevated temperature due to boiling water for long duration is an unfocused research area. Events presented in Table 1, this research is directed to simulate the NPPs SFP concrete walls subjected to the long term boiling water exposure under accidental scenarios. Experimentation prognosticates real time scenario of the effect of elevated temperature exposure due to boiling water for 7 and 14 days on the concrete walls respectively, where M35 grade of concrete is being used.

Experimental investigations showed the effect of long term boiling water exposure on the mechanical and chemical behaviour of concrete used in the SFPs of Indian NPP. SFP is simulated in the form of water tank, which is cast with the internal steel liners and concrete walls of M35 grade concrete cube with silica fume and nano-silica. Simulated SFP is subjected to long term boiling water and after successive events; tests are performed on the concrete of SFP for the purpose of damage assessment and subsequently, results of mechanical, chemical and thermal behaviour of concrete subjected to long term boiling water are presented.

Table 1 Event sequence of Fukushima accident 2011 (<http://www.world-nuclear.org/info/safety-and-security/safety-of-plants/fukushima-accident/>)

Accident stages	Unit-1	Unit-2	Unit-3
Loss of AC power	+51 min	+54 min	+52 min
Loss of cooling	+1 h	+70 min	+36 h
Water level down to top of fuel	+3 h	+74 min	+42 h
Core damage starts	+4 h	+77 min	+44 h
Reactor pressure vessel damage	+11 h	Uncertain	Uncertain
Fire pumps with fresh water	+15 h		+43 h
Hydrogen explosion	+25 h Service floor	+87 h Suppression chamber	+68 h Service floor
Fire pumps with seawater	+28 h	+77 h	+46 h
Off-site electrical supply	+11–15 days		
Fresh water cooling	+14–15 days		

2 Materials and Methods

Systematic experimental study was planned to facilitate the investigation of the effect of elevated temperature due to long term boiling water on the physio-mechanical and chemical properties of concrete. Two types of mixes were taken into considerations as Mix 1 is a reference mix with M35 grade of concrete and Mix 2 is prepared by replacing cement with silica fume (15%) and nano-silica (2%). All tests were performed on concrete with a w/c of 0.4 with targeted workability in terms of slump was 100 mm. The concrete contained ordinary Portland cement (OPC) grade 53 with fineness 284 m²/kg. The maximum particle size of fine aggregate was 4.75 mm, specific gravity of 2.86, fineness modulus was 2.89 and water absorption was 1%. River sand was used as fine aggregate and crushed granite as coarse aggregate. Tables 2 and 3 show the properties of cement and aggregates. Potable water and a sulphonated Naphthalene base super plasticiser were used. Codal provisions of IS: 10262-2009 was followed for proportion of the concrete mix. The average compressive strength of Mix 1 concrete is 46.18 MPa and for Mix 2 concrete is 49.27 MPa at 28 days to satisfy the requirements of M35 concrete.

Table 4 show concrete mix proportions. Concrete was prepared using an electronic drum mixer. Workability of fresh concrete assessed using slump test. Concrete cubes

Table 2 Physical and chemical properties of cement

CaO—0.7SO ₃	Al ₂ O ₃ /Fe ₂ O ₃	Magnesia (% by mass)	Sulphuric anhydride (% by mass)	Total loss on ignition (% by mass)	Total chlorides (% by mass)
0.88	1.31	0.88	2.41	2.36	0.006

Table 3 Fine and coarse aggregate properties

Type	Fineness modulus	Specific gravity	Water absorption (%)	Zone
Fine aggregate	2.84	2.86	1.0	II
Coarse aggregate	2.46	2.87	0.5	—

Table 4 Concrete mixture proportions

Ingredient	Quantity	
	Mix 1	Mix 2
Cement	400 kg/m ³	332 kg/m ³ Silica fume: 60 kg/m ³ Nano-silica: 8 kg/m ³
Water	160 kg/m ³	160 kg/m ³
Superplasticiser (SNF based)	4 kg/m ³	6 kg/m ³
Fine aggregate	731 kg/m ³	733 kg
Coarse aggregate	1304 kg/m ³	1303 kg
W/C	0.4	0.4
Slump	100 mm	100 mm

with dimensions of 150 × 150 × 150 mm were cast, vibrated and cured for 28 days; these cubes were used to determine compressive strength of concrete before and after subjecting to elevated temperature due to boiling water. While casting the above specimens, RTD sensors were installed in the concrete specimens at depths of 40, 80 and 135 mm from top of the specimens. Inbuilt RTD sensors (Fig. 2) were used to monitor temperature continuously with 15-min intervals in the concrete of steel lined concrete water tank and data acquisition was done by data logger. After successive events, concrete subjected to 7 and 14 days of boiling water, whole assembly of steel lined concrete water tanks were dismantled and test was carried out on hot specimens, then balance specimens were allowed to cool for 3 and 7 days in an open environment.

SFPs were used for storage of spent fuel. These pools are robust constructions made of reinforced concrete of several feet thickness, with steel liners. Further concrete cube specimens were used to cast base and walls of the water tank with internal steel lining, to create actual scenario of SFP. The 0.75 × 0.75 × 0.75 m (24 × 24 × 24 in.) stainless steel lined concrete water tank is used to carry out experimentation. To achieve accuracy and consistency in the experimentation, in-house

automated heating system is developed. Heavy duty stainless steel lined water tank fabricated using cover on top side, inbuilt heaters, temperature sensor and water level controller with solenoid valve and control unit. Automated heating unit focused to maintain the constant temperature and constant level of boiling water in the water tank. Automated heating unit is connected to pre-heating unit to achieve the consistency in supply of boiled water and control unit maintain the temperature from the heating unit and pre-heating unit (Fig. 1) at 100 °C. First, water was heated in pre-heating unit with the help of three heaters up to a boiling point and then it was transferred to the automated heating unit of steel lined concrete water tank. Temperature in the pre-heating and automated heating unit was controlled by a controlling unit with inbuilt temperature and level sensors. Two specimens of steel lined water tank were prepared and the experimental testing program was carried. A detailed investigation was conducted to check the mechanical performance and chemical behaviour of concrete under elevated temperature for the period of 7 and 14 days.

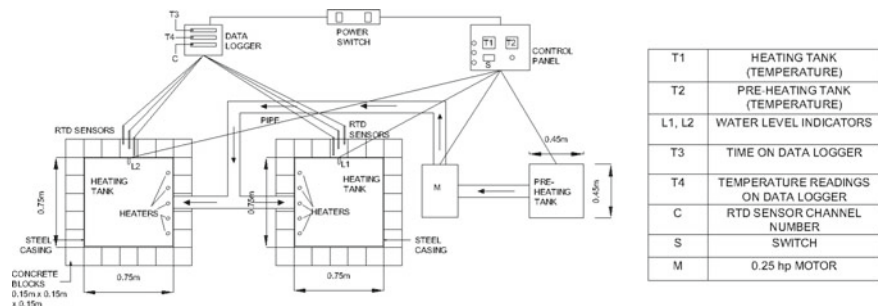


Fig. 1 Layout of automated heating unit

Fig. 2 Inbuilt RTD sensors in concrete cube



Fig. 3 Simulated SFP

Figure 2 shows inbuilt RTD sensors were used to monitor the continuous temperature in concrete cube. Figure 3 shows the actual experimental test specimen.

3 Results and Discussion

3.1 Compressive Strength

Compressive strength of M35 grade Mix 1 and Mix 2 concrete before and after subjection to elevated temperature for 7 days shown in Fig. 4. Also, it shows the compressive strength of the concrete exposed to environment for 3 and 7 days after successive events of boiling water.

Compressive strength of M35 grade Mix 1 and Mix 2 concrete before and after subjection to elevated temperature for 14 days shown in Fig. 5. Also, it shows the compressive strength of the concrete exposed to environment for 3 and 7 days after successive events of boiling water. Compressive strength was found to be decreased in the case of immediate testing of concrete after successive events of 7 and 14 days

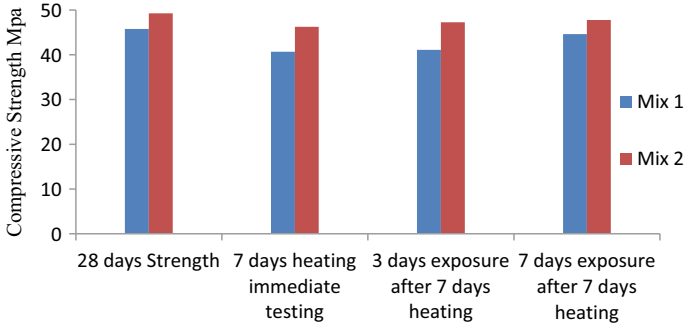


Fig. 4 Compressive strength of concrete before and after subjection to elevated temperature for 7 days

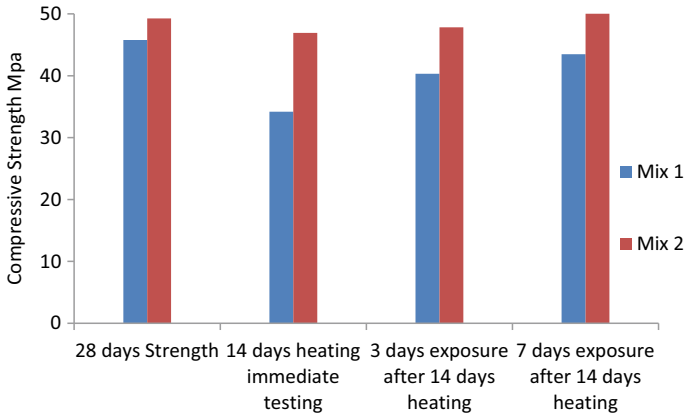


Fig. 5 Compressive strength of concrete before and after subjection to elevated temperature for 14 days

of subjecting to boiling water. But compressive strength is increased after exposure to environment for 3 and 7 days after successive events.

3.2 Temperature Variations

Figures 6 and 7 shows recorded temperature changes (15 min interval) in reference mix concrete and silica fume–nano–silica concrete during a heating program for the period of 7 days respectively. Figures 8 and 9 show recorded temperature variation for reference mix concrete and silica fume–nano–silica concrete subjecting to elevated temperature for the period of 14 days respectively. Temperature variation is recorded in RTD sensor between 35 and 58 °C at 40 mm, 36–62 °C at 80 mm and 40–72 °C at

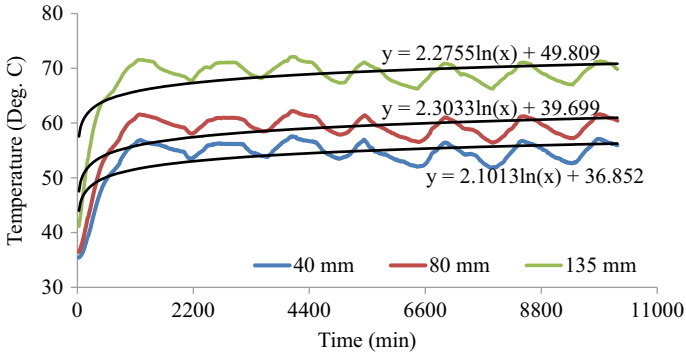


Fig. 6 Temperature record of Mix 1 concrete subjected to elevated temperature due to boiling water for 7 days

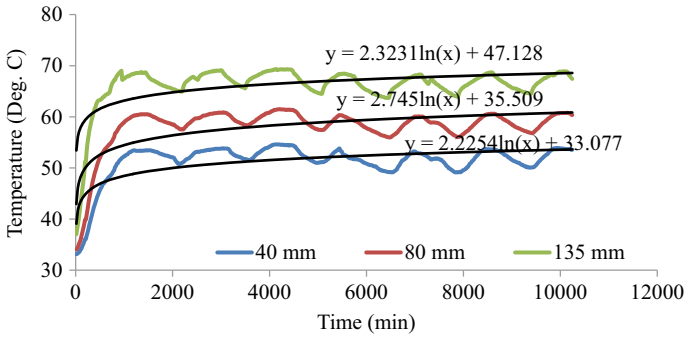


Fig. 7 Temperature record of Mix 2 concrete subjected to elevated temperature due to boiling water for 7 days

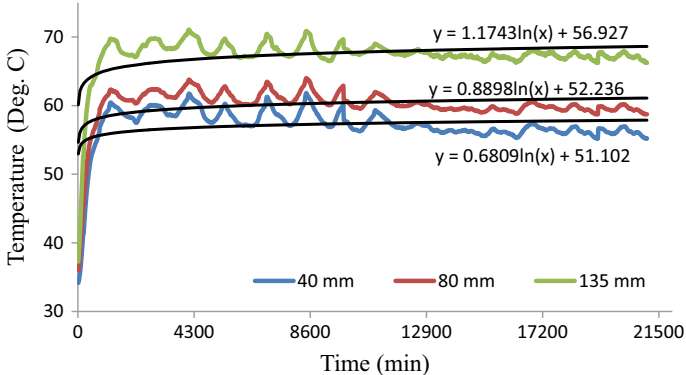


Fig. 8 Temperature record of Mix 1 concrete subjected to elevated temperature due to boiling water for 14 days

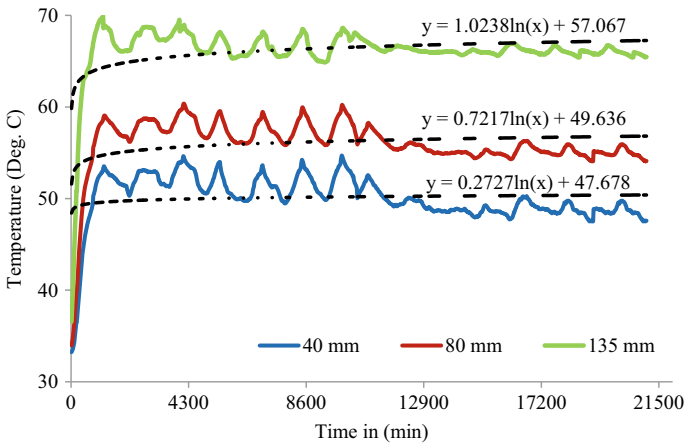


Fig. 9 Temperature record of Mix 2 concrete subjected to elevated temperature due to boiling water for 14 days

135 mm from outer face of Mix 1 concrete wall subjected to an elevated temperature due to boiling water for the period of 7 days. Temperature variations are recorded in Mix 1 concrete wall are 34–61 °C at 40 mm, 36–64 °C at 80 mm and 37–71 °C at 135 mm from outer face of concrete wall made of concrete cube samples for subjected to elevated temperature due to boiling water for 14 days. The temperature variation in Mix 2 concrete subjected to elevated temperature due to boiling water for the period of 7 days are 33–55 °C at 40, 34–62 at 80 mm, 37–69 at 135 mm from outer face of concrete wall. The temperature variation in Mix 2 concrete subjected to elevated temperature due to boiling water for the period of 14 days are 33–55 °C at 40, 34–60 at 80 mm, 37–70 at 135 mm from outer face of concrete wall.

3.3 SEM Imaging and EDS Analysis

Figures 10, 11 and 12 conveys the scanning electron microscope (SEM) results of concrete sample before, after 7 and 14 days subjecting to an elevated temperature due to boiling water respectively.

Figure 10 shows SEM image of Mix 1 concrete without heating. Here, material has undergone trans-granular fracture; this is mainly due to brittle grains. Particle size is 10–170 μm. Figure 11 Shows SEM image of Mix 1 concrete with 7 days of heating. Here particle shape is a mixture of sharp edges along with rounded grains. The grains might have changed their texture to round due to heating. Particle size has increased to 200–3000 μm. It appears nearby grains have melted and attached themselves to each other causing size increase. Material fracture has changed to inter-granular fracture. Also rather than brittleness as observed in this image, shows that it might have undergone some deformation. Figure 12 shows SEM image of Mix 1 concrete

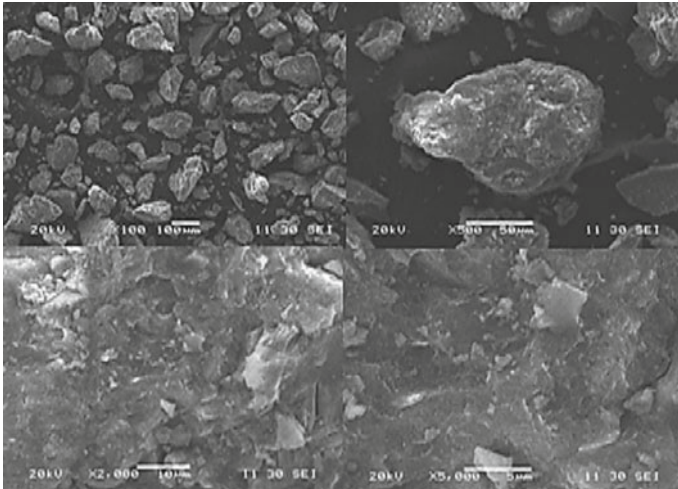


Fig. 10 SEM image of Mix 1 concrete without heating

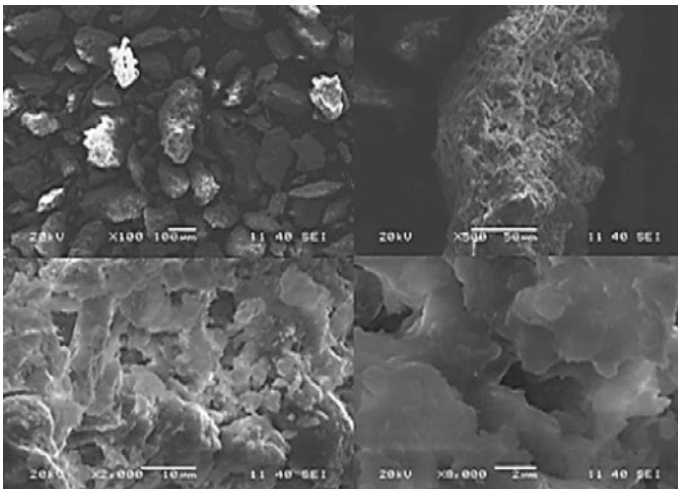


Fig. 11 SEM image of Mix 1 concrete with 7 days heating

with 14 days of heating. Particle shape is mostly rounded but with smaller size of 10–100 µ.m. Also, more uniform particle size is observed. The material fracture is mainly cleavage which seems to be due to increased brittleness of the sample. It appears that this sample should have lesser strength due to less deformation and increased brittleness among all three images.

Figures 13, 14 and 15 conveys the SEM test results of Mix 2 concrete sample before heating and after 7 days heating as well as 14 days heating event respectively.

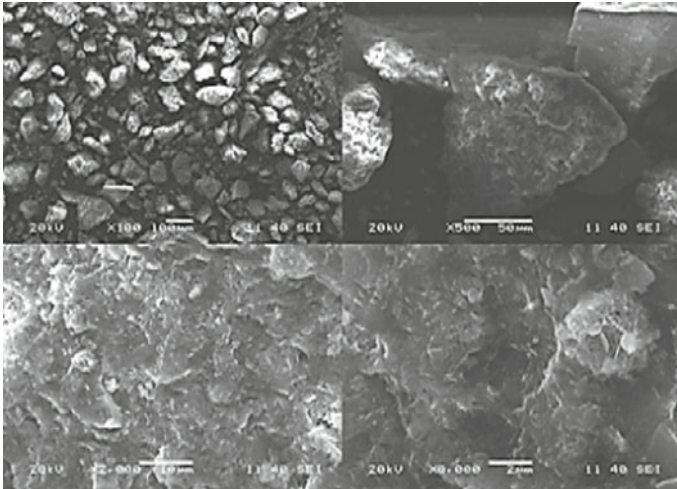


Fig. 12 SEM image of Mix 1 concrete with 14 days heating

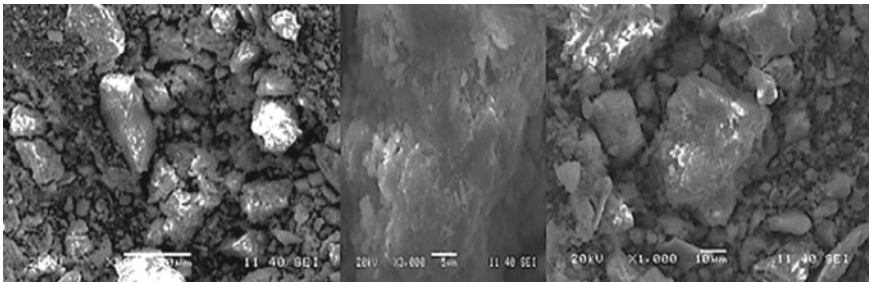


Fig. 13 SEM image of Mix 2 concrete without heating

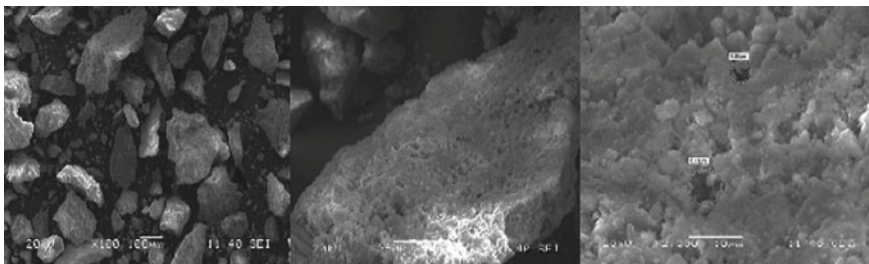


Fig. 14 SEM image of Mix 2 concrete after 7 days heating

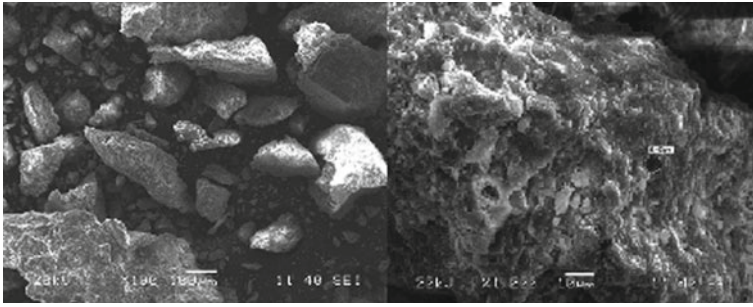


Fig. 15 SEM image of Mix 2 concrete after 14 days heating

Figure 13 Shows SEM image of Mix 2 concrete without heating. Cementitious particles formed well bonded texture resulted in higher side strength. Figure 14 Shows SEM image of Mix 2 concrete with 7 days heating. Texture shows the uniform particle distribution with fine and sharp edges due to subjecting to boiling water, but more porosity was observed and resulted in lesser strength as compared to reference mix. Figure 15 Shows SEM image of Mix 2 concrete with 14 days of heating. Higher particle size observed compared to 7 days heating event, this means that the crack path travelled is more and filled gap due to heating uniform cementitious gel is formed and shows well bonding, its strength should be higher.

4 Conclusion

An experimental investigation was carried out to check microstructural, mechanical and chemical properties of concrete subjected to elevated temperature due to boiling water. The following conclusion has been made based on the results obtained:

- Compressive strength of the heated specimens was found to be decreased in the case of immediate testing of concrete after successive events. But compressive strength of concrete is increased after exposure to working environmental conditions for 3 and 7 days.
- SEM test results presented for a concrete sample before, after 7 and 14 days subjecting to elevated temperature due to boiling water respectively.
- Temperature variation is recorded in Mix 1 concrete is between 35 and 72 °C and for Mix 2 concrete it is between 33 and 70 °C.
- The change in temperature between 33 and 72 °C for concrete subjected to boiling water for 7 and 14 days affects minimal change in mechanical properties of concrete and are within design limits enumerated by IS 456-2000 as well as ASME standard.
- This experiment predicts the real scenario of effect of elevated temperature due to boiling water on the concrete used in the SFP of the NPPs which helps operator

to gain confidence during such events and it predicts the safety and structural adequacy of concrete used in the spent fuel cooling pool of NPPs.

Acknowledgements The authors greatly appreciate the financial support of the Technical Education Quality Improvement Programme II under the Ministry of Human Resource Development, Government of India for this study. We would like to thank the technicians who helped during the experimental work.

References

1. Fukushima Accident, <http://www.world-nuclear.org/info/safety-and-security/safety-of-plants/fukushima-accident/>. Updated May 2015. World Nuclear Association
2. Z. Xing, A. L. Beaucour, R. Hebert, B. Ledesert, Influence of the nature of aggregates on the behaviour of concrete subjected to elevated temperature. *Cem. Concr. Res.* **41**, 392–402 (2011)
3. P. Mehta, P. Monteiro, *Concrete—Microstructure, Properties and Materials* (McGraw-Hill, 2006)
4. S. Handoo, S. Agarwal, S. Agarwal, Physicochemical, mineralogical, and morphological characteristics of concrete exposed to elevated temperatures. *Cem. Concr. Res.* **32**, 1009–1018 (2002)
5. C. Poon, S. Azhar, M. Anson, Y. Wong, Comparison of the strength and durability performance of normal- and high-strength pozzolanic concretes at elevated temperatures. *Cem. Concr. Res.* **31**, 1291–1300 (2000)
6. S. Chan, X. Luo, S. Wei, Effect of high temperature and cooling regimes on the compressive strength and pore properties of high performance concrete. *Constr. Build. Mater.* **14**, 261–266 (2000)
7. T. Zadrzil, F. Vodak, O. Kapickova, Effect of temperature and age of concrete on strength—porosity relation. *Acta Polytech.* **44**(1), 53–56 (2004)
8. A. Chini, L. Acquaye, Effect of elevated curing temperatures on the strength and durability of concrete. *Mater. Struct.* **38**, 673–679 (2005)
9. K. Sakr, E. Hakim, Effect of high temperature or fire on heavy weight concrete properties. *Cem. Concr. Res.* **35**, 590–596 (2005)
10. M. Husem, The effects of high temperature on compressive and flexural strengths of ordinary and high performance concrete. *Fire Saf. J.* **41**, 155–163 (2006)
11. O. Arioz, Effects of elevated temperatures on properties of concrete. *Fire Saf. J.* **42**, 516–522 (2007)
12. M. B. Karakoç, Effect of cooling regimes on compressive strength of concrete with lightweight aggregate exposed to high temperature. *Constr. Build. Mater.* **41**, 21–25 (2013)
13. A. Kizilkanat, N. Yuzer, N. Kabay, Thermo-physical properties of concrete exposed to high temperature. *Constr. Build. Mater.* **45**, 157–161 (2013)
14. A. Bingol, R. Gul, Residual bond strength between steel bars and concrete after elevated temperatures. *Fire Saf. J.* **44**, 854–859 (2009)
15. B. Chen, C. Li, L. Chen, Experimental study of mechanical properties of normal-strength concrete exposed to high temperatures at an early age. *Fire Saf. J.* **44**, 997–1002 (2009)
16. J. Mindeguia, P. Pimienta, A. Noumowe, M. Kanema, Temperature, pore pressure and mass variation of concrete subjected to high temperature—experimental and numerical discussion on spalling risk. *Cem. Concr. Res.* **40**, 477–487 (2010)
17. M. Khan, J. Prasad, H. Abbas, Shear strength of RC beams subjected to cyclic thermal loading. *Constr. Build. Mater.* **24**, 1869–1877 (2010)

18. S. Yaragal, K. Narayan, K. Venkataramana, K. Kulkarni, H. Gowda, G. Reddy, A. Sharma, Studies on normal strength concrete cubes subjected to elevated temperatures. *J. Struct. Fire Eng.* **1**(4), 249–259 (2010)
19. M. Bastami, A. Chaboki-Khiabani, M. Baghbadrani, M. Kordi, Performance of high strength concretes at elevated temperatures. *Sci. Iran. A* **8**(5), 1028–1036 (2011)
20. S. Divya, M. Santhanam, Influence of moderately elevated temperatures on engineering properties of concrete used for nuclear reactor vaults. *Cem. Concr. Compos.* **34**, 917–923 (2012)
21. K. Tan, T. Nguyen, Structural responses of reinforced concrete columns subjected to uniaxial bending and restraint at elevated temperatures. *Fire Saf. J.* **60**, 1–13 (2013)
22. M. Bastami, M. Baghbadrani, F. Aslani, Performance of nano-silica modified high strength concrete at elevated temperatures. *Constr. Build. Mater.* **68**, 402–408 (2014)
23. S. Kou, C. Poon, M. Etxeberria, Residue strength, water absorption and pore size distributions of recycled aggregate concrete after exposure to elevated temperatures. *Cem. Concr. Compos.* **53**, 73–82 (2014)
24. J. Xiao, Y. Hou, Z. Huang, Beam test on bond behaviour between high-grade rebar and high-strength concrete after elevated temperatures. *Fire Saf. J.* **69**, 23–35 (2014)
25. Y. Wu, B. Wu, Residual compressive strength and freeze-thaw resistance of ordinary concrete after high temperature. *Constr. Build. Mater.* **54**, 596–604 (2014)

Experimental and Analytical Study of Shape Memory Alloy in Civil Structures—A Review



Priyanka Salunkhe, Prajakta Agawane, Durita Chaudhari, and Sakshi Patil

Abstract Steel is embedded in concrete to carry tension and concrete will be sustaining compression. The structure is design to withstand the certain load but when the sudden load increased the beam start deflecting and structure get fail. To overcome this problem, the smart material shape memory alloy (SMA) used to minimize the deflection. Shape memory alloy is the material which has its property to regains their original shape after heating at high temperature. The material is tested with conventional steel, and the shape memory alloy gives maximum recoverable strain is 8% and steel 0.5%. The beam is tested for flexural strength for carrying heavy loads and resistance to corrosion by experimental methods. The various software used for analytical.

Keywords Shape memory alloy · Fe-SMA · Ni–Ti SMA · Superelasticity

1 Introduction

In most countries, a major portion of national wealth is added up to civil infrastructure. Most structures are subjected to loading that creates a bending moment, producing both compression and tension stresses within the structure since concrete is weak in tension so the arrangement has to be made for the tensile stresses. Concrete is reinforced with steel which is good in tension zone to support the structure [1, 2]. Due to the damaged and deteriorating conditions of the concrete, infrastructure management has become a common crisis. It needs to be repaired and surveyed at regular interval of time [1]. RC member subjected to creep and shrinkage properties which are affected by factors like variations in mix composition and quality of materials, and changes in exposure state such as humidity, temperature, etc. [3]. During earthquake buildings and bridges are subjected to destruction damage and collapse due to huge permanent deformation and yield in steel [4, 5]. To get rid of the problem of

P. Salunkhe (✉) · P. Agawane · D. Chaudhari · S. Patil
Department of Civil Engineering, Terna Engineering College, Nerul, Navi Mumbai 400706, India

infrastructure management, the smart material is to be introduced which can determine its own damage. In modern design, the smart structure as well as smart material are becoming popular [2].

In 1932, the first smart system was discovered that was “smart alloy” or “shape memory alloy”. The ability to recollect and return to the original shape gives the name “shape memory”. SMAs are a different category of metal that can regain noticeable permanent strains when they are heated above a particular temperature. In applications of civil engineering, various types of SMAs are used Cu–Zn–Al, Cu–Al–Ni, Fe–Mn–Si, etc. The structure design generally has to satisfy two conditions; strength the structure should safely carry loads over its designate service life and serviceability that the structure must be serviceable. The serviceable life and limits of serviceability includes that approved deflection. To increase life span and serviceability of the structure, the SMA material is used in RC beam [3, 6]. As per research, SMA RC beam has less deflection than conventional RC beam. The study reported in a publication by Debbarma [3] is the composition of high-strength steel and Ni–Ti has superior recovery for SMA RC beam and provides a reduced rigidity with the increasing load and has the ability to partial deformation recovery. SMA has a high recoverable strain, resilience and resist to corrosion.

2 Material Properties

SMA have the capability to undergo huge deformation and they come back to their original shape after withdrawal of stresses (superelasticity) or with an implementation of heat (shape memory effect). SMAs have two different temperature-dependent crystal structure. Martensite structure is steady at a reduced temperature phase and austenite structure is stable at an excess temperature phase. The parallelogram asymmetric structure can be shown by martensite and has a with 24 variations and this phase is weaker and easily deformed and the austenite phase is strong and has a body-centred cubic crystal structure, which increased resistance to external stress [1, 5, 7–12] (Fig. 1).

SMA as per setup in two distinct stages with three uncommon can found crystal structures such as twinned martensite, detwinned martensite, austenite (Fig. 2) SMAs are defined by four change over temperatures, i.e. A_s , A_f , M_s , M_f . When the SMA is heated, it began to convert from martensite to the austenite state. The starting temperature of austenite (A_s), where the material begin to alter from twinning of martensite to austenite, austenite-finish-temperature (A_f), where the material is fully changed to austenite, starting temperature of martensite (M_s) where austenite commence to transform into twinning of martensite, finishing temperature of martensite (M_f), where the transformation to martensite is finished [10].

The two important types of shape memory alloy are available namely copper–aluminium–nickel and nickel–titanium (Ni–Ti) alloy. SMAs can also be created by combining zinc, copper, gold and iron. Iron-based and copper-based SMAs, such as Fe–Mn–Si, Cu–Zn–Al, and Cu–Al–Ni, are economical than Ni–Ti SMAs [11].

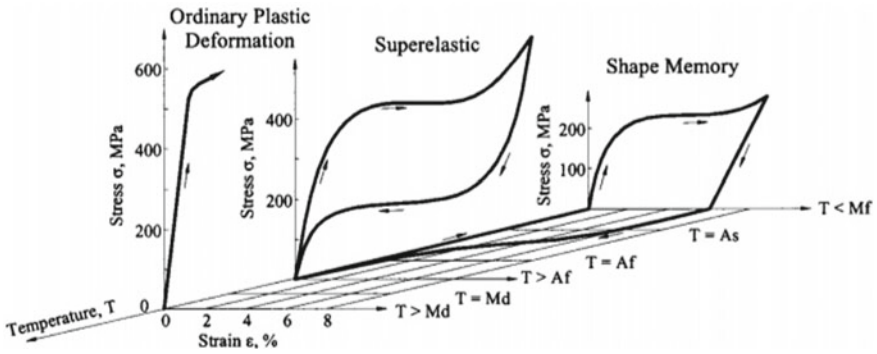


Fig. 1 3D stress–strain–temperature diagram and shape memory behaviour of Ni–Ti shape memory alloy [12]

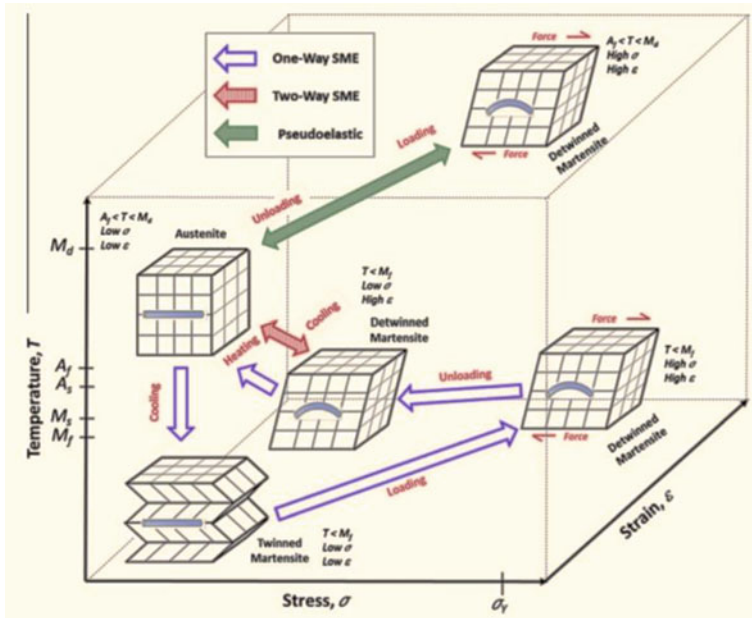
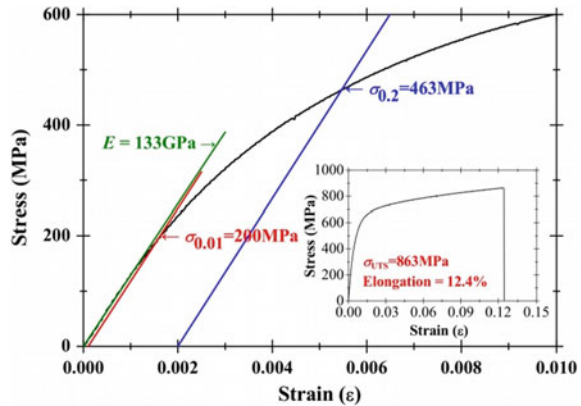


Fig. 2 SMA phases and crystal structures [10]

Ni–Ti formed shape memory alloy (SMA) has properties, such as large ultimate strength, more recovery strain about 8%, supreme anti-fatigue property and corrosion resistance, high durability and good energy dissipation capacity [1, 13].

The martensite was stated to be stable at low temperature and the values of stresses were high, whilst in the case of austenite was stable at high temperature and values of stresses were low. The purpose of temperature, stress and strain were summarized in Fig. 3 which was based on mechanical behaviour [6].

Fig. 3 Stress–strain curve of direct tensile test [6]



Ductility and self-centering without failure in mortar/concrete, Ni–Ti SMA fibres are used as reinforcement [1, 14].

The load-carrying capacity of the RC beam is increased because of the superelasticity property of SMA. Also, it reduces the long-term deflection of the beam [3].

Stress–strain action for 12.7 mm Ni–Ti (56.02% nickel and 43.98% titanium) is much greater than the 12 mm mild steel bars [8].

The percentage of Fe-SMA consists of components like Fe-17%, Si-10%, Mn-5%, Cr-4%, Ni-1% with respect to their mass [9].

Fe-SMA has sufficient bonding strength at high recovery temperature and ductility and is proved to be effective in retrofitting or strengthening structures. The Fe-SMA is less costly as compared to the ordinary Nickel-Titanium (NiTi) alloys. It has good workability and weldability properties [6, 7, 9, 10] (Table 1).

3 Analytical Results

The different finite element softwares are ATENA, ABAQUS, Hypermesh, Nastran and ANSYS. ANSYS is a systematic finite element software which is used for nonlinear design [17].

For SMA reinforced beam to carry out cyclic loading condition a schematic finite element mesh was developed as shown in Fig. 4 for the beams [18].

The finite element method is numerical technique to obtained the adjoining results which can be stated as representation of a figures and patterns by a variety of different section called as finite element [19].

Table 1 Mechanical properties of SMA

Reference No.	Material	Properties	Value
[6]	Fe-SMA	Modulus of elasticity	1.33×10^3 MPa
		Ultimate strength	863 MPa
		Elongation	12.4%
[15]	Fe-SMA	Ultimate strength	826 MPa
		Ultimate strain	41%
[4]	NiTi-SMA	Modulus of elasticity	26.7×10^3 MPa
		Ultimate strength	920 MPa
		Ultimate strain	19%
[16]	Ni-Ti fibre	Modulus of elasticity	75×10^3 MPa
		Ultimate strength	1070 MPa
		Elongation	10%
[8]	Ni-Ti bars	Modulus of elasticity	68.069×10^3 MPa
		Ultimate strength	1010 MPa
		Density	6700 KN/m ²

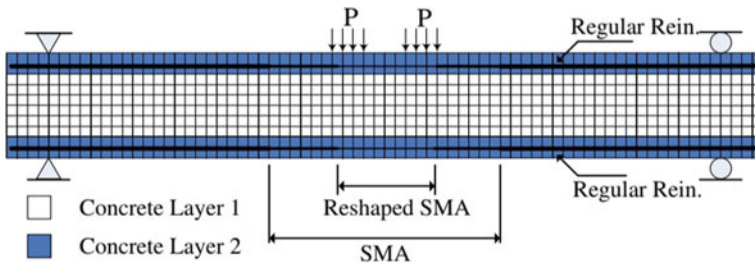


Fig. 4 SMA beam finite mesh [18]

4 Experimental Results

SMA material gets deformed beyond the particular elastic limit when they heated which add the strengthening to the RC members. The effective results of all this because of superelasticity and shape memory effect condition which takes place

because of phase transformation from martensite to austenite. The economic expense was lower in case of Fe-SMA than that of Ni-Ti SMA. The total dissipated energy was evaluated under the load–deflection curve to the critical load. The strength of RC beam in flexure was firstly increased by thermo-mechanical training and later 6% strain was observed by one cycle accompanied by 600 °C heating [15].

SMA has high-strength full recovery strain up to 8%, corrosion resistance, fatigue resistance. Reversed cyclic loading was used. Experimental and analytical study of the behaviour of steel and SMA reinforced beams-column joints subjected to crack width and crack spacing, the length of plastic hinge, moment rotation and load–displacement relationship was done. Based on results is proved that if SMA is used as reinforcement in concrete in a seismic region, it reduces the repair cost and the structure stay serviceable and safe later the earthquake [14].

Fe-SMA as the strengthening material in concrete structures. The mechanical properties were investigated by the direct tensile test which returns to a predefined shape. Fe-SMA recovery stresses were investigated with five different recovery temperature vary from 110 to 220 °C and pre-straining level ranging from 2 to 8%. The bonding strength and feasibility index of the Fe-SMAs were enhanced by mean of 8.8% with an increment in embedding length from 250 to 450 mm [6].

A performance of RC beam with Ni-Ti SMA having superelasticity behaviour were studied. At the critical section of the beam (i.e. at midspan of the beam), flexure cracks were noticed as the intensity of loading was increased. Hence after the experiment, it was stated that the highest load was required for inducing the first flexural cracks in SMA beam. The average residual crack width observed on the Ni-Ti SMA beam was lesser than the residual crack width noticed on that of the standard RC beam. The recovery deformation observed because of Ni-Ti reinforced beam displayed better results [8].

The replacement of steel reinforcement with SMA bars was explained by comparing load–displacement behaviour to standard RC beam in which most studied factors were initial load, ultimate displacement and initial stiffener. The response for load-displacement at midspan is shown in Fig. 5 for both beams [8].

Fig. 5 Monotonic load–displacement response [8]

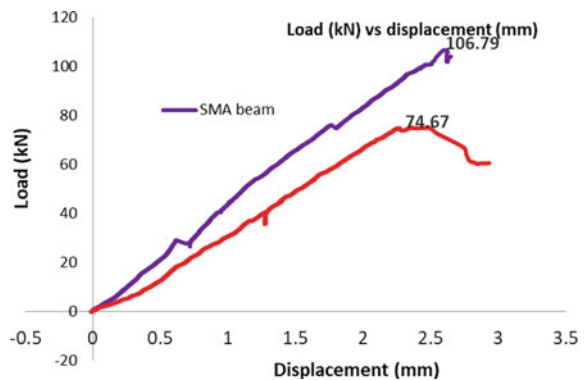


Table 2 Test results

Size of beam	Loading pattern	Displacement ductility (mm)	Conventional beam recovery (%)	SMA beam recovery (%)
2400 × 125 × 250 mm	Reverse cyclic	9.5	26	85
2400 × 125 × 250 mm	Cyclic	8.5	17	80

A detailed study was done on how the SMA fibres show the results when they have spread over the fibre reinforced concrete in a nonlinear manner. The efficiency of SMA fibres and hybrid SMA fibres was examined. On the casted concrete specimen, two important tests were conducted namely third point loading and split tensile as per ASTM C1609 and ASTM C496 testing methods, respectively. The specimen sample composed of 25% Ni–Ti SMA and 75% steel fibres resulted as the best-performed specimen which was having the highest tensile strength [16].

A test was conducted to examine the superelastic property of SMA. The combination of seven different compositions simply supported beams were cast. It consisted of the combination of only Nitinol bars and standard steel bars of different diameters. The testing of these beams was done under the monotonic, cyclic and reverse cyclic loading pattern. The specified loading was given on the critical section of the beam (i.e. at the centre of the beam). For test results refer Table 2 [18].

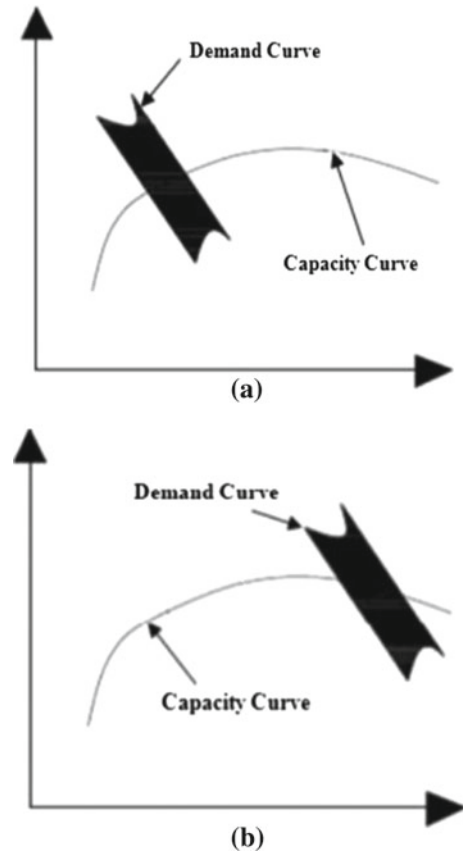
A detailed study was done on how the SMA alloy effectively behaves on implementation of loads without undergoing any distortion enough through a particular amount of energy dissipated. The results were examined based on phase transformation, i.e. from austenite to martensite and reverse transformation over loading and removal of loading respectively. A unique push over analysis theory has been presented in this content. The result enclosed that the structure reinforced with steel-SMA was more effective than standard steel bars [20].

The assumed response of a building throughout ground movement for a given designed condition is because of estimated displacement. Typical seismic demand versus capacity is shown in Fig. 6.

5 Conclusion

The shape memory alloy because of its different properties like high recovery strain, regaining original shape after heating, corrosion resistance, minimum cracking and less damage to its structures makes it a versatile material. The only disadvantages because of its high cost. But Fe-SMA is comparatively cheaper than that of Ni–Ti SMA. The bonding characteristics of this SMA makes it perfect to get embedded in different RC structures.

Fig. 6 Typical seismic demand versus capacity curve [20]



References

1. M.M. Sheriff, E.M. Khakimova, O.E. Ozbulut, D.K. Harris, H.C. Ozyildirim, Behaviour of mortar beams with randomly distributed superelastic shape memory alloy fibers. *J. Intell. Mater. Syst. Struct.* 1–12 (2017)
2. N. Mali, A. Mali, A review on shape memory alloy and its application in civil engineering. *Int. J. Adv. Res. Sci. Eng. Technol.* 4, 4395–4404 (2017)
3. S.R. Debbarma, S. Saha, Review of shape memory alloys application in civil structures, and analysis for its potential as reinforcement in concrete flexural members. *Int. J. Civ. Struct. Eng.* 2, 924–942 (2012)
4. H. Li, Z.-Q. Liu, J.-P. Ou, Study on reinforced concrete beams strengthened using shape memory alloy wires in combination with carbon-fiber-reinforced polymer plates. *Smart Mater. Struct.* 16, 2550–2559 (2007)
5. W.-S. Chang, Y. Araki, Use of shape-memory alloys in construction: a critical review. *Civ. Eng.* 169(CE2), 87–95 (2016). <https://doi.org/10.1680/jcien.15.00010>
6. K. Hong, S. Lee, S. Han, Y. Yeon, Evaluation of Fe-based shape memory alloy as strengthening material for reinforced concrete structures (2018)
7. Mishra, A.A. Ravindra, A comparison of conventional and iron-based shape memory alloy and their potential in structural applications. *Int. J. Struct. Civ. Eng. Res.* 3, 96–112 (2014)

8. N. Abd Hamid, A. Ibrahim, A. Adnan, M.H. Ismail, Behaviour of smart reinforced concrete beam with super elastic shape memory alloy subjected to monotonic loading. *AIP Conf. Proc.* **1958** (2018)
9. L. Zerbe, M. Reda, M. Dawood, A. Belarbi, A. Senouci, B. Gencturk, M. Al-Ansari, J. Michel, Behaviour of retrofitted concrete members using iron based shape memory alloy, in *Fourth Conference on Smart Monitoring, Assessment and Rehabilitation of Civil Structures* (2017)
10. J. Mohd Jani, M. Leary, A. Subic, M.A. Gibson, A review of shape memory alloy research, applications and opportunities. *Mater. Des.* **56**, 1078–1113 (2014)
11. Y.I. Elbahi, M.A. Youssef, M. Nehdi, Deflection of superelastic shape memory alloy reinforced concrete beams: assessment of existing models. *Can. J. Civ. Eng.* **37**, 842–854 (2010)
12. R. DesRoches et al., Cyclic properties of superelastic shape memory alloy wires and bars. *J. Struct. Eng. ASCE* (2004). [https://doi.org/10.1061/\(ASCE\)0733-9445\(2004\)130:1\(38\)](https://doi.org/10.1061/(ASCE)0733-9445(2004)130:1(38))
13. A. Kolekar, A. Natak, K. Navratne, A. Mali, Recent advancement in shape memory alloy. *Int. Res. J. Eng. Technol. (IRJET)* **04**(04) (2017). e-ISSN: 2395-0056 | Apr-2017 p-ISSN: 2395-0072 © 2017, IRJET
14. M.S. Alam, M.A. Youssef, M. Nehdi, Analytical prediction of the seismic behaviour of superelastic shape memory alloy reinforced concrete elements. *Eng. Struct.* **30**, 3399–3411 (2008). <https://doi.org/10.13140/2.1.3467.5200>
15. H. Rojob, R. El-Hacha, Ductility behavior of RC beams strengthened in flexure with NSM iron-based shape memory alloy bars, in *SMAR 2015* (2015)
16. E. Khakimova, M.M. Sheriff, O.E. Ozbulut, D.K. Harris, H.C. Ozyildirim, *Experimental Investigation on Shape Memory Alloy Fiber Reinforced Concrete* (University of Illinois, Urbana–Champaign, 2015)
17. S.H. Sanni, K. Girinivas, Analytical investigation on reinforced concrete beams. *IRJERT* **05** (2018)
18. A. Abdulridha, D. Palermo, S. Foo, F.J. Vecchio, Behaviour and modelling of superelastic shape memory alloy reinforced concrete beams, *engineering structures.* **49**, 893–904 (2013)
19. M.T. Islam, O. Netula, A. Singh, Study of behavior of RCC beam under impact loading and effect of hourglass energy by finite element analysis using ANSYS. *IJERT* **8**(07) (2019). ISSN 2278-0181
20. K.M. Bajoria, S.S. Kaduskar, Improvement in performance of reinforced concrete structures using shape memory alloys (2015). <https://doi.org/10.1117/12.2084192>

Effect of Aspect Ratio on Fatigue Behaviour of Steel Shear Wall



R. K. Chethan Gowda , K. Ashwini, and H. M. Rajashekaraswamy

Abstract Shear walls are secondary prominent structure that predominantly serves best in resisting lateral loads when primary structures fail to take the load. Steel shear wall is vastly used in high-rise buildings to provide resistance to lateral and seismic loads. The first phase of this study involves numerical validation of experiment on behavioural analysis and performance of steel shear wall under cyclic loading. The results of phase one are considered as inputs for further parametric study on aspect ratio. Aspect ratio for shear wall is an important parameter as it decides the shear capacity and shear distribution in a structure. Study involves variation in fatigue behavioural changes of steel shear wall with to respect change in aspect ratio. 3-D models were stimulated using CATIA and model were analysed using ANSYS Workbench. The results obtained are in form hysteresis graph which elucidates the energy-dissipating capacity of steel shear wall. Stable hysteresis graph was observed after aspect ratio 1.5. Aspect ratio 2 was found to be the best possible solution for designing steel shear wall.

Keywords Aspect ratio · Cyclic loading · Energy dissipation · Hysteresis plot

1 Introduction

The Asia continent alone has 403 tall buildings which is 63% of overall buildings round the globe. In 2016, 342 natural hazards were registered Asian continent. Alone in India, there are several such scenarios one among them are on 21st August 1988 6.7 earthquake in Himalayas which triggered landslides in Kathmandu and took life of more than 1000 people. Similarly, Uttarkashi experienced earthquake of 7.2 on Richter scale which was catastrophic. Many buildings are built in recent days keeping earthquake in mind. But buildings always fall short due to carelessness and the use of cheap materials by constructors without consultation of engineers and bribing inspectors has been practised as voodoo which is some of the reasons for building

R. K. Chethan Gowda (✉) · K. Ashwini · H. M. Rajashekaraswamy
M. S. Ramaiah University of Applied Sciences, Bengaluru, India

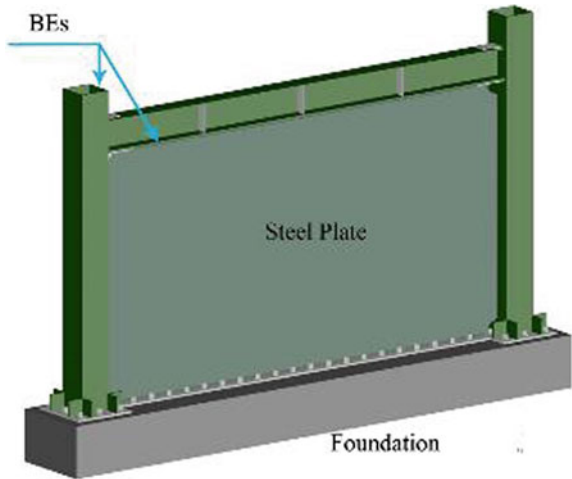
failure. According to survey, 8 out of 10 buildings are unlikely to be earthquake-resistant. There are many earthquake-resisting structures, and some are base isolators, dampers, shear walls, etc. The element we choose should be strong and ductile to act on shaking with preventable damage [1]. Secondary system that prevents structures from getting affected by lateral loads is shear walls. Shear wall is provided in tall structure to resist earthquake and wind loads and provides structural stiffness as a secondary element in building. Generally, shear walls are provided around periphery of tall structures or as shear core as in elevator shaft or stair wall providing adequate stiffness to the structure. Shear wall can be built using masonry, steel, wood and concrete. Behaviour shear walls depend on material used, wall thickness, wall length, wall positioning in building frame. Shear walls are integrated with roofs or floors, these walls have to resist the uplift forces caused by the pull of the wind and resist the shear forces that try to push the walls [2]. In the late 50s and early 60s, plywood walls were proposed simply as alternates to diagonally braced wall section. Their acceptance for this purpose was based on their ability to meet certain load or deflection criteria. Based on experiment and testing data and by incorporating knowledge gained from plywood diaphragm testing, in 1967 Uniform Building Code for first time provided allowable load tables for plywood shear walls. Then various studies were made on shear wall with various other materials such as masonry, steel, RCC. Now, RCC and steel frames are worldwide used. Steel shear walls are very popular in foreign countries due to its various advantages such as durability, strength, cost-effectiveness and easy installations.

2 Background Theory

In the past two decades, the steel shear wall is widely used in many countries as part of lateral force-resisting structure. In earlier days, it was conservative method that steel shear wall was vertically oriented plate structure. Although recent studies have erased these kinds of conservative methods of designing, a very criterion is that steel shear wall showcases high bending strength and stiffness. These members are expected to have significant effect on overall behaviour of a building [3]. High buildings are mostly soft storied and have irregularities which significantly cause difference in stiffness and resistance in structures. In the first half of the twentieth century, it was believed that of assumptions on architectural design having open story would have advantages but these were the main reasons for seismic vulnerabilities SPSW studies were carried out in 1980s and satisfactory usage of SPSW in Northern ridge and Japan has emphasized researchers and practicing engineers to use SPSW in greater extent [4] (Fig. 1).

The Canadian steel design standard has outlined design requirements of steel plate shear wall based on studies carried out by [3] and standard bolted-type shear wall by [4]. Steel plate shear was major contribution to the civil field by researchers. In spite of its robustness and ductility, they provide better resistance to seismic degradation. The low mass steel shear wall when compared with reinforced wall has lesser gravity

Fig. 1 Steel plate shear wall [5]



loads and seismic loads to be transferred foundation. From various studies, it was found that stiffened shear plate produces more energy dissipation characters but the cost of construction also increased.

3 Validation

The numerical evaluation of experimental work derived from the paper “Economical Steel Plate Shear Walls for Low-seismic Regions” [6] is used for validation work which is taken as input for parametric study. The geometry of the steel plate shear wall is modelled using the available CATIA V5 modelling software. Figure 2 indicated 3-D model created using CATIA software.

Fig. 2 Steel plate shear wall (SPSW)

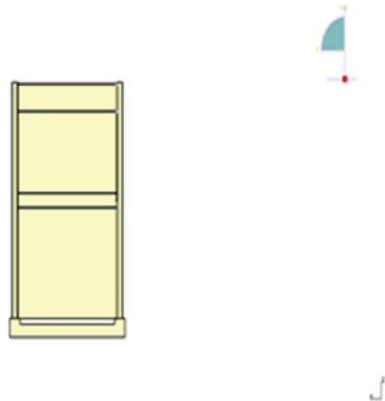


Table 1 Section details of experimental model

Section	Dimension details (mm)
Horizontal member	W 460 × 67
Vertical member	W 250 × 58
Plate	4.8 mm thick

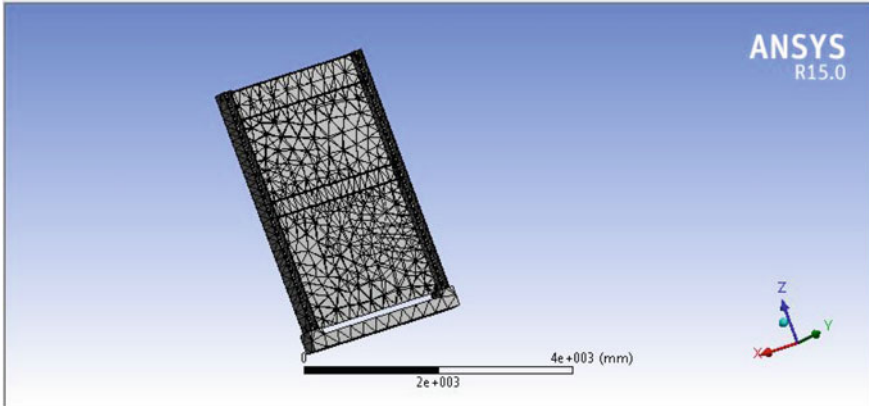


Fig. 3 Discretized model

Material properties of the steel plate shear wall.

Elastic modulus = 20,000 MPa, density of steel = 7850 kN/m³, Poisson’s ratio = 0.3. Table 1 shows details geometry used for designing.

Then imported into the ANSYS Workbench, Version 15.0 for analysis meshing is created for finite element analysis. Figure 3 shows tetrahedral meshing of structure whose sizing can be varied for refined results.

Boundary conditions the structure are fixed at bottom, axial loads of $6 + e05$ N is applied on column to resist overturning moment. Loading case details are derived from AISC (341-10) FEMA 1997. Figure 4 is stress contour obtained for structure after analysis. Experimental and numerical study results are given in Table 2, and it can be observed that percentage of difference is within the acceptable range; hence, similar methodology has been adapted for further numerical study.

4 Parametric Study

The parametric study is carried on aspect ratio to known its influence on energy dissipation. Parameters considered for study are given in Table 3. Aspect ratio is very important parameter for design of steel shear wall. Shear distribution, ductility

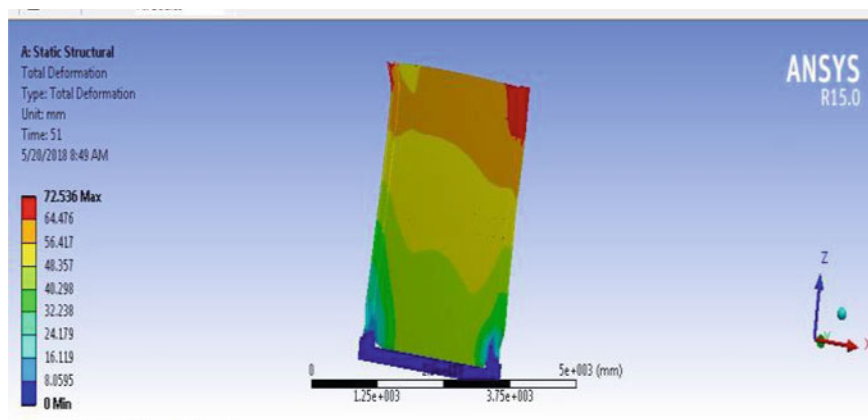


Fig. 4 Stress contour plot

Table 2 Comparison of experimental and numerical results

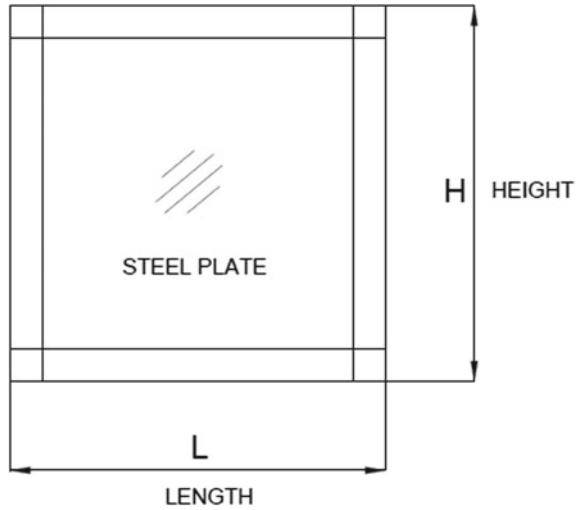
Displacement (mm)	Experimental results (load in kN)	Numerical results (load in kN)	Percentage of difference
1.5	200	185	7.5
3.2	400	378	5.5
5.2	600	570	5
6.7	800	764.5	4.43
9.2	1000	940	6
22	1920	1756.8	8.5

Table 3 Parametric study details

Aspect ratio (L/H)	Dimension details (mm)		Member details
	L	H	
0.5	$L = 950$	$H = 1900$	Vertical member ISMB 350
1.0	$L = 1900$	$H = 1900$	
1.5	$L = 2850$	$H = 1900$	Horizontal member ISMB 200
2.0	$L = 3800$	$H = 1900$	
2.5	$L = 4750$	$H = 1900$	Steel plate 4.8 mm thick
3.0	$L = 5700$	$H = 1900$	

and stiffness of steel shear wall are based on aspect ratio. Parametric model is as shown in Fig. 5, where L is length of wall and H is height of the wall. In this study, various models for varying aspect ratio are studied.

Fig. 5 Parametric model



5 Results and Discussions

Performance of all the models is compared based on the energy dissipation capacity, i.e. total area of the hysteresis loop. The hysteresis graph is plotted load versus displacement. Figure 6 shows typical hysteresis graph plotted from analysis. From the numerical study, it was found that energy-dissipating capacity was increased with increasing aspect ratio. Stable energy dissipation was seen from aspect ratio 1.5.

From Table 4, it can be observed that energy dissipation is increased with increased aspect ratio and there is gradual increase in energy dissipation after aspect ratio 1.5. It can also be observed that load-carrying capacity has gradually increased and suddenly

Fig. 6 Typical hysteresis graph

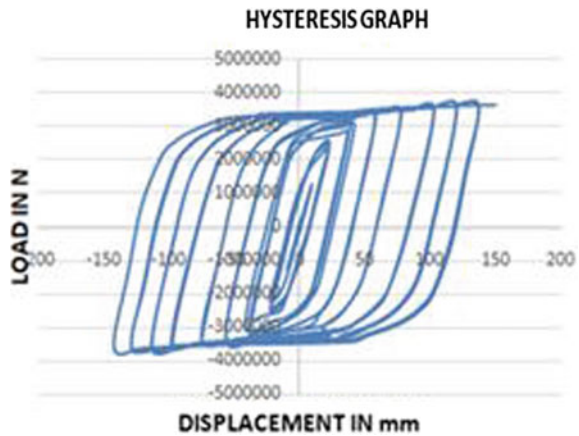
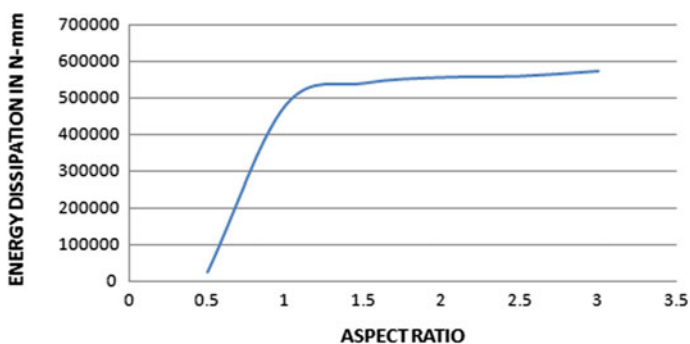


Table 4 Results of parametric study

Aspect ratio	Energy dissipation (kN-mm)	Ultimate load (kN)	Permanent deformation
0.5	24,050	978	82
1.0	482,151	1400	89
1.5	541,838	1568	93
2.0	558,146	1685	94
2.5	561,215	2276	98
3.0	575,254	1265	105

**Fig. 7** Energy dissipation versus aspect ratio

decreased for aspect ratio 3. Permanent deformation was found to be increase with increase in aspect ratio.

A comparison graph is plotted for energy dissipation and ultimate load-carrying capacity (Fig. 7) by steel plate shear wall for varied aspect ratio. From graph, it is evident that with energy dissipation is increased with increasing aspect ratio, it can be observed that there stable hysteresis graph after aspect ratio 1.5. From Fig. 8, it can observed that aspect ratio having 2.5 has the highest load-carrying capacity and it is also evident that as aspect ratio increases load-carrying capacity has decreased.

6 Conclusions

- Energy dissipation for aspect ratio initially has 9–11% variation in results, and stable energy dissipation is seen after aspect ratio of 1.5.
- Energy dissipation of aspect ratio 1.5, 2, 2.5, 3 has increased by 37%, 43%, 54% and 48%, respectively.
- Length of steel shear wall having aspect ratio of 2.5 is 20% higher than aspect ratio 2 which indirectly consumes more material than aspect ratio 2. Likewise,

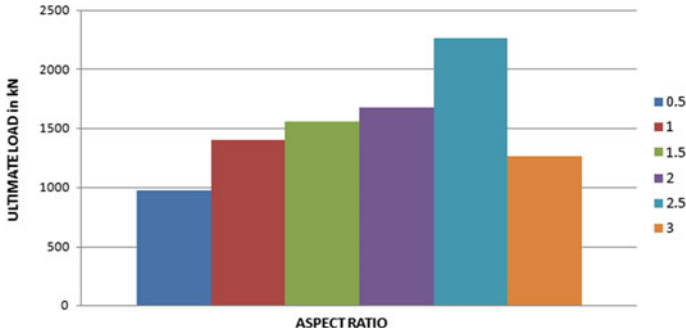


Fig. 8 Ultimate load versus aspect ratio

energy dissipation capacity of aspect ratio is only 5% lesser than aspect ratio 2.5. Since aspect ratio of 2.5 is not economical, therefore aspect ratio 2 is opted for economical designing of steel shear wall.

Acknowledgements I would like to express my sincere gratitude to my advisor I wish to extend thanks to Dr. H. M. Rajashekaraswamy, HOD Department of Civil Engineering, M. S. Ramaiah University of Applied Sciences for accepting to mentor this project.

References

1. S. Sabouri-Ghomi, C.E. Ventura, M.H. Kharrazi, Shear analysis and design of ductile steel plate walls. *J. Struct. Eng.* 12 (2000)
2. T.M. Roberts, S. Sabouri-Ghomi, Hysteretic characteristics of unstiffened perforated steel plate shear panels. *Thin-Walled Struct.* 139–151 (1992)
3. L.J. Thorburn, G.L. Kulak, C.J. Montgomery, *Analysis of Steel Plate Shear* (Department of Civil Engineering, University of Alberta, Edmonton, AB, 1983)
4. T. Hitaki, C. Matsui, Experimental study on steel shear wall with slits. *J. Struct. Eng.* 586–595 (2013)
5. P.P. Chandurkar, P.S. Pajgade, Seismic analysis of RCC building with and without shear wall. *Int. J. Mod. Eng. Res. (IJMER)* 1805–1810 (2013)
6. H. Moghimi, R.G. Driver, Economical steel plate shear walls for low-seismic regions. *J. Struct. Eng. ASCE* 379–388 (2013)

An Overview—The Effect of Radon on the Existing Building



Anil Pawade and Shrikant Charhate

Abstract Radon gas is a harmful, colorless, tasteless, and odorless gas that occurs naturally in initiate in rock and soil which is chiefly present inside the earth. The concentration of radon inside the earth therefore varies with latitude, longitude and altitudes. The earth has two sources of heat—solar energy on the surface and radioactive decay of certain materials within itself. Radon is a gas which is released during the intermediate stage of radioactive decay inside the earth. Radon gas is a harmful gas that occurs naturally in initiate in rock and soil. It leaks into households via footing, walls as well as construction joints cracks. Measured radon concentrations vary generally between houses, depending not only on time-based variability, but also on the local geology, on the details of building construction, and on the habits of the residents. There must be a radon test for every home. In many cases, prevention of lung cancer is possible specifically in the lung cancer that is caused due to radon. Furthermore, among the various primary goals one is that more precise estimations must be accommodated in the indoor environment for protecting against long-term exposures risks of radon gas. The causes for the same are analyzed and the harmful effects of the same are enumerated. It is also ensured that all the mitigation measures proposed are sustainable, eco-friendly and have the least impact on the environment.

Keywords Radon · Radioactive gas · Indoor environment · Testing

1 Introduction

The inside of the earth is similar to one huge reactor. It is dynamic and in a constant state of flux. There is a gradient in temperature from the core to the surface of the earth. The earth has two sources of heat—solar energy on the surface and the radioactive decay of certain minerals in the bowels of the earth. It is this temperature difference

A. Pawade (✉)
Amity University, Mumbai, India

S. Charhate
Amity School of Engineering and Technology, Amity University, Mumbai, India

which invokes the convection currents and incubates the various movements within the earth. Radon is a gas which is released during the intermediate stage of this radioactive decay. Its concentration is measured in terms of Becquerel per cubic meter. It can also be measured in terms of picocuries per liter–pCi/L. Due to radon exposure, Lung cancer patients are found about 21,000 in the U.S. yearly, depending on the estimation of U.S. Environmental Protection Agency. Radon, thoron, and other progeny are a large effect on the radiation's quantity acquired by humans existing in the environment naturally. There exists various components on which indoor radon depends that are occupant's behavior, ventilation, climatology, and building materials [1].

In the last 50 years, people exposing to natural radiation level is a matter of concern that is being considered as well as has taken the interest of researchers. Although, ^{222}Rn environmental radon's contribution significance in the dose of natural radiations is being concerned on in last decade as well as it becomes the relative subject matter for the current studies. It has been identified that to the world population UNSCEAR contribution of inhaled radon is greater than half of total natural environmental ionizing radiation's dosage [2]. High radon levels were measured in dwellings worldwide which includes United Kingdom, Sweden, and the United States [2], as well as a greater concern exists in relation to radon levels that its high level will have the lung cancer's increased risks. In many houses, in the above countries, international guidelines can be exceeded by high radon levels in indoors [3] as well as there exists many factors that are associated with it that includes ventilation, construction mode, building material, soil's uranium content, and soil porosity. These factor's variability accounted for the radon levels' sizeable range that is measured in houses [4]. All anthropological activities instigate and activate the release of Radon on to the surface. Human built environment predominantly comprises of indoor and/or enclosed and/or confined spaces. Due to its high density, it tends to settle down closer to the surface. Confinement in the built environment increases its potency and a simple harmless gas with among the lowest half-life among all radioactive gases becomes a potential hazard which can decimate life on our planet. Depending on the available data, in India, the concentration of indoor radon annually varied from 11 to 124 Bq m^{-3} with a GM 33.2 Bq m^{-3} [5], in response to 40 Bq m^{-3} global average [6]. In India, majority data related to indoor radon is scattered as well as in relation to indoor radon levels' effect not much work has been done in the country.

Radon presented in the rocks as well as soil gets mixed with the air and then spreads on to surfaces, on which it speedily dilutes in atmospheric concentration in open air in a low quantity. Although, when radon entered in closed areas, then in some situations, it resulted in higher concentrations. A small radioactive particle is formed by decaying of radon that can be inhaled by humans into lungs. These particles emit some radiations that can harm. There may exists some small gaps or cracks in house's walls as well as floors that resulted at times of construction or after that. These gaps or cracks helps radon to get into building from the ground such as wall cavities, wall cracks, service pipe gaps, construction joints. For the reason that generally inside the building atmospheric pressure is less as compared to underground soil pressure.

All our structures are built on the ground. They transmit the load onto the ground and also hold the structure to the ground through a system of foundations. This process of foundations involves excavations and/or boring and other allied forms of intrusions. These forms of intrusions release radon onto the surface. Since the gas is highly dense, it stays on the surface and occupies enclosed, ill ventilated spaces like caves, tunnels and all other such allied spaces. The lithosphere today is pockmarked with the foundation intrusion of various kinds and types of structures. The material used for these foundations is generally very different from the material in the earth. As the coefficients of expansions are different there will always be a hairline gap between the materials. Radon is generated continuously below the earth. This radon leaks out through these gaps and fissures on the surface. In the process, they disturb the equilibrium of the lithosphere and also pose a danger to the biodiversity on the surface.

2 Measuring Radon in Residence

As radon levels can fluctuate by the hour, from day to day, and from one season to other, levels of radon must be calculated in long periods being practically possible. Preferably, by utilizing etch-track (plastic) detectors it must be measured in every 3 months. Furthermore, for the diagnosis purpose, a week or such short-term measurements proved to be helpful; however, these may have less accurate results as well as care must be given to interpret these [7]. For these measurements, passive alpha track type ARN detector are being utilized. It comprises of “cup with membrane” that contains CR-39 Track Etch detector of 2X2 cm piece. The cup membrane restricts the airborne particulate as well as Rn daughters’ entry but Rn gas is allowed for diffusing in the sensitive volume [1].

In most of cases, generally two detectors have been used for measuring the radon levels, that are employed in the main bedroom as well as main living room, which then gives the average results for home. Until these roles are fulfilled either by basement or Cellar, than may be they need not to be monitored. Furthermore, it will not be appropriate if a detector will be placed at a place that is not used regularly or is not occupied such as basement area, the reason may be that unoccupied area may have high radon levels in comparison to the areas where occupants are being exposed regularly. Also, the risk of average occupancy is one of the main concerns, as well as thus, the measurement must be done to the rooms that are regularly occupied. However, for the basement area, there may not be any results in most of cases, because assumption is that basement may have higher radon levels in comparison with the rooms that are above the ground. Various reason for this are as:

- The basement floor as well as walls are in direct contact with the ground. Therefore, if in a building, if there exists a basement beneath its ground floor than there are chances that building may be in three times more in ground contact as

compared to building that has similar size but no basement, as well as this results in much more chances for entry of radon in the building.

- Cellars are poorly finished, and the reason is that they are utilized only for storage. Particularly, these walls features a small gap or crack myriad, and these can result in issues of radon
- Basement that exists totally beneath ground generally have poor ventilation, therefore, it results in easy entrance of the radon in the building. For aggravating such condition, timber construction is suspended often in the floor that exists between basement and room above it. It further enabled the flow of radon in the building [7].

3 Radon Exposure Control Scheme

Radon is presented worldwide, and thus, it can be detected easily in dwellings as well as workplaces but there is a difference in the radon levels from one place to other in a time. Occupational exposure control scheme for radon is different from the scheme that is used for controlling artificial sources exposure. In this section, scheme's overview is presented along with other details. Figure 1 presented the radon exposure control scheme as.

4 Remedial Action to Reduce Radon Levels

The most proven remedy is that radon entry must be prevented in homes in comparison with the actions that are used for removing radon from the homes. Practically, it implies that radon-laden air entry must be prevented in wall and floor's cracks as well as gaps. It can be achieved very easily when new house is being constructed, during the development radon barrier must be used in construction. Furthermore, there is need of remedial measures for existing dwellings. In a house, radon entering can be reduced with an underground room or basement by using given 6 ways:

- Installation of a radon sump system
- Walls and floors sealing
- Enhancing under floor ventilation
- Establishing whole-house positive pressurization or positive supply ventilation arrangement
- Enhancing the ventilation of the house
- Enhancing the ventilation of the cellar or basement.

Also, it is not necessary that these solutions will be helpful in every house type, or for every radon level, as well as in few scenarios, for solving the issue of radon, more than one solution will be required. Specifically, these solutions are applied to those

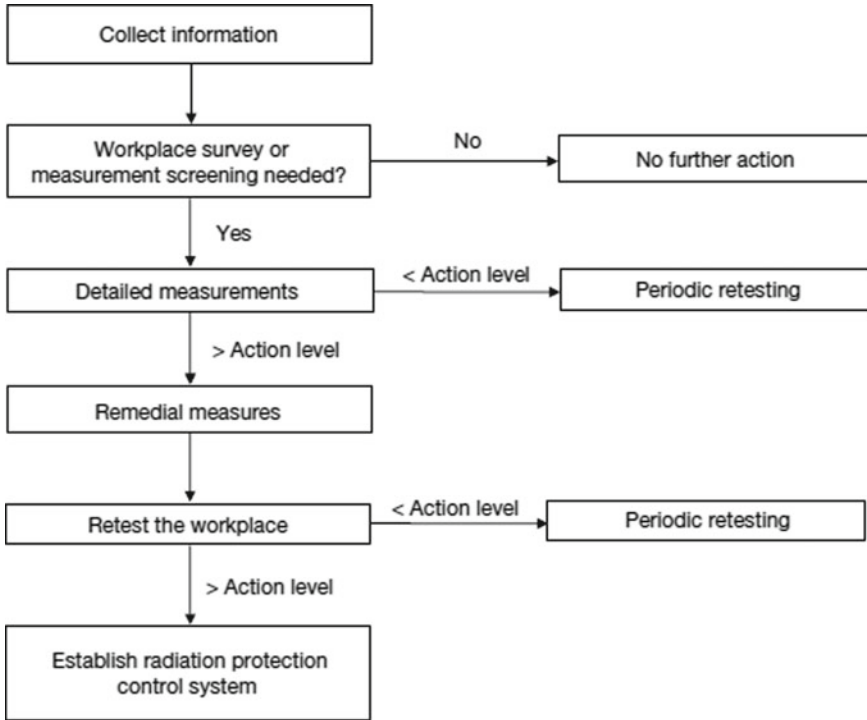


Fig. 1 Appropriate schemes for the radon level control, if radon levels are very high and their reduction is economical and easy, corrective measures are indicated. *Source* IAEA safety report series No. 33

houses that are having a basement or a cellar. Furthermore, the above six solutions are described briefly. For every solution, Fig. 2 is presented with an indication of radon level which can be decreased.

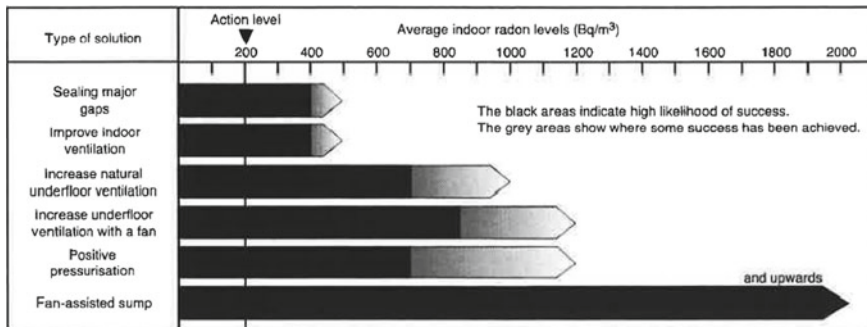


Fig. 2 Guide to the likely effectiveness of solutions. *Source* [8]

A. Radon sump

Radon-laden air can be extracted below the floors (soil depressurizing), with solid concrete ground floors by utilizing a radon sump. In general, it is considered as one of the efficient approach, whereas in most of the cases, radon levels are reduced to less than 1/10th of original level. If there is a situation where radon levels are 1200 Bq/m^3 then this solution can be used. Generally, it can be applied to the house that have solid floors, however, sump can also be utilized with suspended timber floor, in case there exists a concrete or membrane layer that covers the below soil. There exists few cases where soil pressurizing as well as sump blowing proved to be effective.

B. Walls and floors sealing

We are able to seal the floor as well as wall space exactly where they're in connection with the soil, to keep the radon from being through splits and spaces. This's apt to work solely from reasonable radon levels, up to $400\text{--}500 \text{ Bq/m}^3$. In general, it's tough to bring down the radon amount to a lot less than one half by what this means is. Full sealing of timber flooring surfaces, for instance with a consistent polyethylene (polythene) sheet, isn't advised, although the sealing of gaps that are big is actually proper. Major closing labor to floors and walls in cellars and basements is normally just a practical choice just where it forms a part of labor getting carried away to turn an unused room in space that is busy.

C. Under floor ventilation

In the case of an overhanging floor, the air flow can be increased under the floor. In general, it proved to be efficient, specifically, if a fan assists it. Up to 700 Bq/m^3 radon levels, natural ventilation is suggested, whereas up to 850 Bq/m^3 radon levels fan assistance is required. Houses with complete basements or cellars are not suggested with this solution.

D. Positive pressurization or ventilation

A house can be pressurized by utilizing a fan that pulls air from outside or loft spaces which is then blew indoors. Furthermore, again such method is useful up to about 700 Bq/m^3 moderate radon levels as well as more suitable for dwellings that are airtight.

E. Improving the ventilation of the house

There are some situations, where one can possibly modify the ventilation of whole house, for avoiding, as much possible, radon is drawn up from the walls or floors. Although, it is based on how the occupier lives in the house. In general, it is not considered as a reliable approach. Furthermore, it is useful for up to 400 Bq/m^3 radon levels.

F. Improving the ventilation of the cellar or basement

Enhanced mechanical or natural ventilation focused on a basement or maybe cellar, the place that the largest radon quantities will probably be, could show quite effective, as well as offering big radon reductions. Physical fans could be utilized to blow air flow into, or maybe draw air flow out of, a basement or perhaps cellar [8].

5 Quality Assurance and Quality Control

For any activity, there is a need of an efficient program for assuring as well as controlling the quality so that thoron as well as radon levels can be monitored. Every method (which includes detectors as well as instruments) consists of calibration traceable for international or national standards as well as traceability is maintained with the testing the quality assurance periodically. Each laboratory performs the measurement's small fraction (5–10%) that must be dedicated either to precision and accuracy estimations (as compared with duplicate measurements and traceable standards) or background determination (unexposed blanks). For each instrument, there must be routine preparation of quality chart which identifies the measurement systems' stability. Preparation of quality charts requires background sample's regular measurements as well as attest source which is trustworthy. Also, these routine measurements' results must come under acceptable limits [9].

6 Conclusion

Inside the dwellings, there exists various factors on which Rn concentration is dependent. In concern to the Rn problem, a significant role is played by the ventilation. For the ground floor house, the primary source of Rn is soil beneath the building, whereas for the higher floors the primary reason is building material.

References

1. IAEA, Radiation Protection against Radon in Workplaces other than Mines, Jointly sponsored by IAEA, ILO Safety Reports Series No. 33, International Atomic Energy Agency Vienna. (Safetyreportsseries, ISSN:1020-6450; No. 33) (2003)
2. D. Scott, UNSCEAR report sources, "effects and risks of ionising radiation", united nations scientific committee on the effects of atomic radiation, report to the general assembly, with annexes. *Int. J. Radiation Biol.* **55**(6), 1047–1048 (1988)
3. Lung cancer risk from indoor exposures to radon daughter, ICRP publication 50. *J. Radiol. Prot.* **8**(1), 55 (1988)

4. P. Shrimpton, Book reviews "International Basic Safety Standards for Protection against Ionizing Radiation and for the Safety of Radiation Sources" (IAEA Safety Series No. 115-1) (International Atomic Energy Agency, Vienna, 1994), p. 338
5. R. Ramola, R. Rawat, M. Kandari, T. Ramachandran, K. Eappen, R. Subba Ramu, Calibration of LR-115 plastic track detectors for environmental radon measurements. *Indoor Built Environ.* **5**, 364-366 (1996)
6. United Nations Scientific Committee, *On the Effects of Atomic Radiation*, UNSCEAR 1993 Report to the General Assembly, with Scientific Annexes, pp. 45-53 (1993)
7. A. Khan, A study of indoor radon levels in Indian dwellings, influencing factors and lung cancer risks. *Radiation Measure.* **32**(2), 87-92 (2000)
8. C. Scivyer, M. Jaggs, *Dwellings with Cellars and Basements*, Building Research Establishment (DETR Department of the Environment, Transport and the Regions, BR 343, 1998), pp. 1-31
9. Environmental Protection Agency (EPA), *Indoor Radon and Radon Decay Product Measurement Device Protocols*. EPA Rep. 402-R-92-004, pp. 1-48, EPA, Washington, DC (1992)

Extreme Rainfall Analysis Using Extreme Value (EV-I) Distribution Based on L-Moment Approach



Sanjay Kumar, L. N. Thakural, J. P. Patra, and Sunil Gurrapu

Abstract Extreme rainfall values are required by hydrologist and water resources professional for designing various water structures specifically for urban drainage, small and medium hydraulic structures, irrigation drainage works, etc. This study estimates annual one-day point maximum rainfall using extreme value (EV-I) distribution (Gumbel) of a small town in the foothills of the Himalayas. The parameters of the EV-I distributions are estimated using three different estimation methods, i.e. method of L-moments (LMOM), method of moments (MOM) and method of maximum likelihood (MML). Alternative approach based on frequency factor is also described. Prediction of one-day maximum rainfall is made for various return periods, i.e. 5, 10, 25, 50, 100, 200 and 500 years, using fitted EV-I distribution. A comparison of one-day maximum rainfall for various return periods using different estimation methods is also made in the analysis. However, based on the empirical and theoretical consideration it is recommended to use L-moment approach as this approach is more reliable and less sensitive to outlier and nearly unbiased. Results would be useful in designing and planning of the city drainage system which is frequently experiencing overflowing of their drainage system during monsoon period.

Keywords Extreme rainfall · Extreme value distribution · L-moment · Frequency factor · Return period · Drainage

1 Introduction

Many problems in engineering hydrology require the fitting of a probability distribution to a data sample to estimate the frequencies of extreme hydro-metrological events. Designing and planning of hydraulic and drainage structures are of specific interest, which requires estimation of extreme values of a hydro-metrological event of a specified return period (or probability) for their proper design to avoid risks of their failure [12, 17].

S. Kumar · L. N. Thakural (✉) · J. P. Patra · S. Gurrapu
Surface Water Hydrology Division, NIH Roorkee, Roorkee, India

Estimation of extreme rainfall, i.e. probable maximum precipitation (PMP), a theoretically possible precipitation that can happen at a particular location using different methods has been explained in [21]. These PMP estimations are then translated into probable maximum flood (PMF), a theoretical extreme flood that may cause extreme risks to flood control measures. In fact, these are methods used to estimate the design flood, which combines meteorology and hydrological science. This study, however, depends more on the empirical evidence to estimate the extreme rainfall at a location. To this end observed extreme rainfall observations, over previous years provide a valuable input for estimating the frequencies of extreme rainfall events corresponding to various return periods [3, 13].

Frequency analysis of observed extreme rainfall involves the selection of an appropriate probability distribution [20]. The choice of a suitable distribution has been an area of considerable research in hydrometeorology [2, 4, 6–9, 15, 16]. Frequency analysis of extreme rainfall has also been attempted in several studies [13, 14, 18].

The objective of this study is to estimate the frequencies of extreme rainfall events. This involves the selection of a suitable frequency distribution and estimation of its parameters. Three different estimation methods, i.e. method of L-moment (MLM), method of moments (MOM) and method of maximum likelihood (MML), are used to estimate the parameter of the selected distribution. Parameters, which give estimation close to the observed extreme rainfall values, are selected for the estimation of frequencies corresponding to various return periods (or probabilities). Subsequent sections explain the data, analysis steps, results and finally conclusions.

2 Data Series

Twenty-five years of daily data from NIH observatory are considered for the analysis. The highest observed daily rainfall value during a year is called the annual one-day point maximum rainfall. This series, therefore, consists of only one maximum value for each year of record. Therefore, from 25 years of daily rainfall data an extracted annual one-day maximum rainfall series will consist of 25 values, one for each year. This series, however, ignores the second and third highest values within a year, which may be higher than the maximum rainfall of other years in the series. This situation may be avoided by selecting all values above a threshold value within a year. This series is often known as partial duration series. Both types of series are used in frequency analysis. However, in this study annual one-day maximum rainfall is used for analysis. Figure 1 shows annual one-day maximum rainfall values observed at NIH observatory.

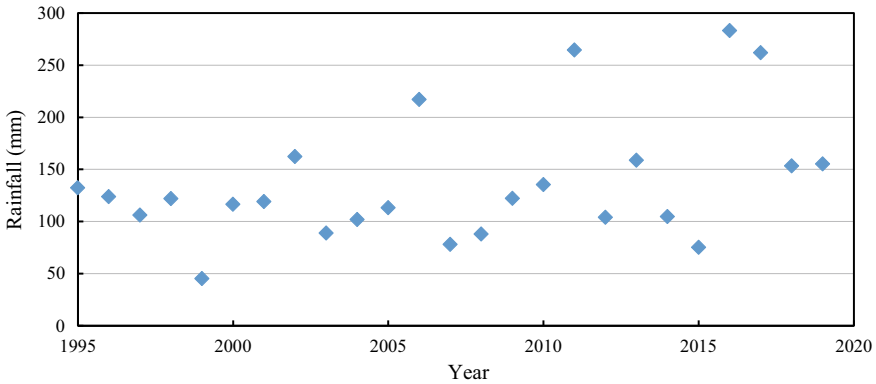


Fig. 1 Annual one-day maximum rainfall (mm) for the previous 25 years

3 Frequency Distribution

The steps involve for estimation of rainfalls for different return periods are (i) to fit a theoretical frequency distribution to the annual one-day maximum rainfall data series and (ii) estimation of parameters of the selected distribution. The choice of an appropriate distribution to fit the data is often difficult because of the many distributions in use (such as lognormal, Gumbel, log Gumbel, Pearson type III, log Pearson type III, Weibull, Gumbel extreme value). Various studies compared several frequency distributions for the determination of rainfall frequency and concluded that none of the distribution had any marked superiority over the other [6, 9, 15]. However, theoretical considerations and studies by [6, 15] suggested that Gumbel extreme value (GEV) distribution is suitable for modelling the extreme rainfall frequencies reasonably well. Therefore, GEV distribution is used to estimate the annual one-day maximum point rainfall for different return periods. The fitted distribution can be used not only for interpolation but also for the extrapolation of maximum rainfall values that were not observed during the short period of records. The subsequent subsections describe the GEV distribution and various methods of its parameter estimation.

3.1 Gumbel’s Extreme Value (EV-I) Distribution

The Gumbel extreme value distribution commonly known as Gumbel distribution is one of the most widely used probability distribution for extreme events in hydrological and meteorological studies for the prediction of floods peaks, maximum rainfall, maximum wind speed, etc. According to [4], the cumulative probability that any extreme value of a variable X will be equal to or less than x for is given by.

$$P(X \leq x) = \exp[-\exp\{-y\}] \tag{1}$$

where $y = \alpha(x - u)$, α and u are parameters of Gumbel distribution and can be estimated from observed data set. The estimated values of these parameters using MOM are shown below (σ is standard deviation and \bar{x} mean of data).

$$\frac{1}{\alpha} = \frac{\sqrt{6}}{\pi}\sigma = 0.78\sigma \quad (2)$$

$$u = \bar{x} - \frac{c}{\sigma} \quad (3)$$

Substituting $c = \text{Euler's constant} = 0.58$, the above expressions can be rewritten as

$$u = \bar{x} - 0.45\sigma \quad (4)$$

$$x = \bar{x} - 0.45\sigma + 0.78\sigma y \quad (5)$$

\bar{x} and σ of a given data series of data can be estimated to obtain the parameters α (scale parameter) and u (location parameter). The fitted distribution can be used to estimate the one-day maximum rainfall corresponding to different return periods.

Estimation of parameters by L-moments. L-moments are less sensitive to outliers and are more reliable. The LMOM calculates more accurate parameters when compared to the MOM [10]. MOM can only be applied to a limited range of parameters, whereas L-moments can be more widely used and are nearly unbiased [16]. The complete details and explanation of the L-moment approach are provided in [7]. The four L-moments ($\lambda_1, \lambda_2, \lambda_3, \lambda_4$) are derived using the four probability-weighted moments (PWMs), as below:

$$\lambda_1 = L_1 = M_{100} \quad (6)$$

$$\lambda_2 = L_2 = 2M_{110} - M_{100} \quad (7)$$

$$\lambda_3 = L_3 = 6M_{120} - 6M_{110} + M_{100} \quad (8)$$

$$\lambda_4 = L_4 = 20M_{130} - 30M_{120} + 12M_{110} - M_{100} \quad (9)$$

where $M_{100}, M_{110}, M_{120}$ and M_{130} are the four PWMs, which are computed using

$$M_{100} = \frac{1}{N} \sum_{i=1}^N Q_i \quad (10)$$

$$M_{100} = \frac{1}{N} \sum_{i=1}^N \frac{(i-1)}{(N-1)} Q_i \tag{11}$$

$$M_{100} = \frac{1}{N} \sum_{i=1}^N \frac{(i-1)(i-2)}{(N-1)(N-2)} Q_i \tag{12}$$

$$M_{100} = \frac{1}{N} \sum_{i=1}^N \frac{(i-1)(i-2)(i-3)}{(N-1)(N-2)(N-3)} Q_i \tag{13}$$

where N is the sample size, Q is the data value, and i is the rank of the value in ascending order. After estimating the L-moments ($\lambda_1, \lambda_2, \lambda_3, \lambda_4$), the Gumbel parameters α (scale parameter) and u (location parameter) can be obtained as

$$\alpha = \frac{\lambda_2}{\log 2} \tag{14}$$

$$u = \lambda_2 - \alpha c \tag{15}$$

where c is Euler’s constant (takes as 0.58).

Estimation of Parameters by Least Squares. The Gumbel method provides a straight-line fit in the x - and y -planes. It has also been found that the MOM does not give as good a fit as does the method of least squares. The use of the least square method was, therefore, recommended by [2]. The straight-line equation can be written as:

$$x = A + By \tag{16}$$

where A and B are parameters which are given by the least square method as

$$y = \log_e \left[\log_e \frac{T}{T-1} \right] \tag{17}$$

$$A = \frac{\sum x}{n} - \frac{B \sum y}{n} \tag{18}$$

$$B = \frac{\sum xy - \frac{n\bar{x}\bar{y}}{n\bar{x}\bar{y}}}{\sum y^2 - n\bar{y}^2} \tag{19}$$

The value of T can be obtained by the use of a plotting position formula. For the Gumbel model, the Weibull formula is most appropriate.

Confidence interval for different return period values bed on Gumbel distribution. The estimation by the Gumbel extreme value distribution is subject to statistical error because the estimation is made on the basis of a limited data. Therefore, it is necessary to measure the uncertainty in the estimation by calculating the confidence limits between which the estimated value can be said to lie with a certain probability. This requires an estimate of the standard error of the distribution parameters. The 95% confidence intervals for different return periods have been computed using Se of estimates as explained below. Return period value for any period can be estimated using the following equation.

$$X_T = \hat{u} + \hat{\alpha} K_T \quad (20)$$

where K_T is the frequency factor corresponding to T years of return period [1]. Lowery and Nash [11] derived the expression for standard error (S_e) for the estimated parameters of \hat{u} and $\hat{\alpha}$ as follows:

$$\text{Var}(u) = 1.168\alpha^{(2/n)} \quad (21)$$

$$V(\alpha) = 1.10\alpha^{(2/n)} \quad (22)$$

$$\text{Cov}(u, \alpha) = 0.096\alpha^{(2/n)} \quad (23)$$

where n is the sample size, using above expressions, the following equation can be deduced

$$\text{Var}(X_T) = \text{Var}(u) + K_T^2 \text{Var}(\alpha) + 2K_T \text{Cov}(u, \alpha) \quad (24)$$

and

$$S_e(X_T) = \sqrt{\text{Var}(X_T)} \quad (25)$$

Hence, the confidence limits at 95% confidence level are given as

$$\text{Lower Limit(LL)} = X_T - 1.96 S_e(X_T) \quad (26)$$

$$\text{Upper Limit(LL)} = X_T + 1.96 S_e(X_T) \quad (27)$$

Goodness of fit of Gumbel distribution was tested by chi-square test at 5% level of significance. The result shows that Gumbel distribution fitted well within the acceptance of significance level. The data of annual maximum rainfall series for durations of 1, 2 and 3 days for the stations were subjected to Gumbel's distribution and estimates of maximum 1, day rainfalls for the return periods of 2.33; 5; 10;

Table 1 Sample and L-moment statistics

Sample statistics				
Sample size (<i>N</i>)	Mean	SD	Skewness	Kurtosis
25	137.28	59.32	1.22	1.01
L-moment statistics				
Sample size (<i>N</i>)	Location (<i>L</i> ₁)	Scale (<i>L</i> ₂)	L-skewness	L-kurtosis
25	137.28	32.21	0.276	0.235

25; 50; 100; 500 were determined. The design rainfalls for different return periods together with their confidence limits are given in Table 1.

4 Analysis and Results

Twenty-five years of daily data from NIH observatory are considered for the analysis. As explained in Sect. 2, one-day annual maximum rainfall values were extracted from the daily rainfall data and are shown in Fig. 1. Table 1 shows the statistical characteristics of the annual one-day maximum data series. The L-moment statistics are also shown in Table 1. These statistics are useful in the estimation of parameters of the Gumbel extreme value distribution. The parameters (α and u) of the Gumbel extreme value distribution are estimated using MLM, MOM and MML methods, and these estimated parameters are shown in Table 2. The goodness of fit test for Gumbel extreme values distribution at 95% confidence level is also shown for three estimation methods in Table 2. It is shown that Gumbel distribution fits well to the one-day maximum rainfall values. A comparison is shown in Fig. 2 between the estimated frequencies and observed frequencies of data series. Figure 2 shows that Gumbel distribution using L-moments fits well as compared to other estimation methods although the MOM is also showing a close fit. The interpolated and extrapolated one-day maximum rainfall values for different return periods are estimated as given in Table 3. However, these values are further corrected incorporating sample size corrections using frequency factor (K) approach as Gumbel distribution is applicable when sample size (n) $\rightarrow \infty$. The frequency factor corresponding to return

Table 2 Parameter of EV-I (Gumbel) distribution

S. No.	Estimation method	EV-I (Gumbel) parameter		Chi square test statistics (CV = 24.99)
		Location	Scale	
1	Method of L-Moment (LMOM)	110.46	46.47	2.64
2	Method of moment (MOM)	110.03	47.20	2.64
3	Maximum likelihood (MML)	111.35	43.01	2.71

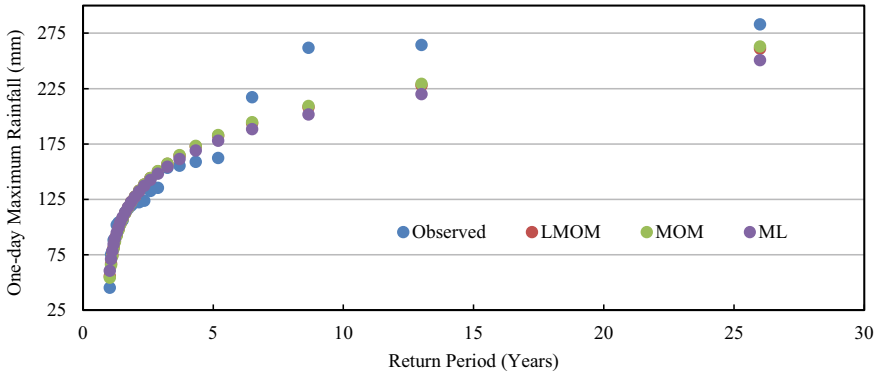


Fig. 2 Observed and expected one-day maximum rainfall using three estimation methods for the sample size (LMOM—method of L-moments; MOM—method of moments and MML—method of maximum likelihood)

Table 3 Return period and values of one-day maximum rainfall (mm)

Return period (years)	5	10	25	50	100	200	500
Estimated values (EV-I) (MLM)	180.16	215.03	259.10	291.78	324.23	356.56	399.21

period and sample size is given in [17]. These modified frequency factors are then used to estimate the modified one-day maximum rainfall corresponding to different return periods. These values are shown in Table 4. The lower and upper limits of the estimated values at 95% confidence level are also estimated and shown in Table 4. Figure 3 shows the final modified one-day maximum rainfall and their lower and upper limits at 95% confidence level.

Table 4 Corrected estimated values considering sample size of $n = 25$ [17]

Return period (years)	5	10	25	50	100	200	500
Frequency factor (K)	0.720	1.305	2.045	2.593	3.138	3.681	4.397
Modified frequency factor (K_{Modified}) (for $n = 25$)	0.888	1.575	2.444	3.088	3.728	4.365	5.206
Modified estimated values EV-I	191	233	285	324	363	402	452
Lower limit (LL) (95%)	188	228	279	316	354	391	440
Upper limit (UL) (95%)	194	237	292	332	372	413	465

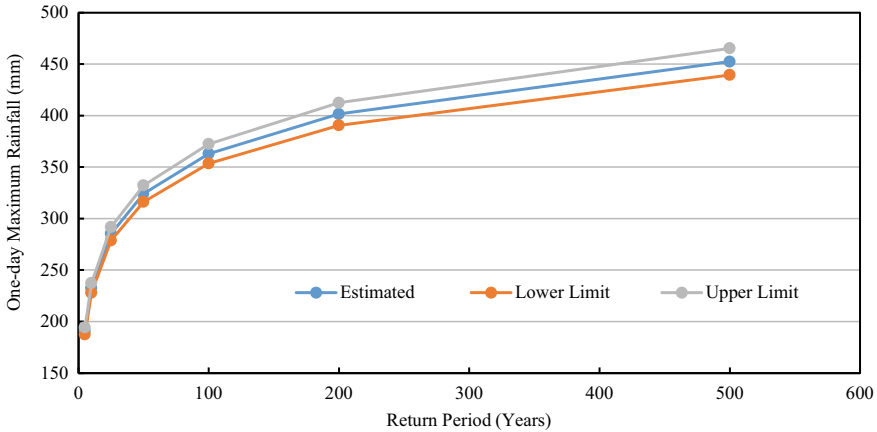


Fig. 3 Expected values of maximum one-day rainfall and their lower limit and upper limit

5 Conclusions

Frequency analysis of extreme rainfall events is important for designing and planning purposes in engineering hydrology. This study analyses the annual one-day maximum rainfall of 25 years using extreme value (EV-I) (Gumbel) distribution, which is one of the most widely used distribution for extreme values in the hydrometeorological studies for the prediction of extreme events. Three estimation methods, i.e. LMOM, MOM and MML, are described, and merits of the L-moment approach have been explained. Parameters of EV-I distribution are estimated using these three different estimation methods. A comparison of estimated frequencies and observed frequencies is made for the maximum one-day rainfall. Based on the empirical comparison and theoretical merits of L-moment approach, the estimated parameters of EV-I distribution (using LMOM) are used to predict the one-day maximum rainfall values for different return periods, i.e. 5, 10, 25, 50 100, 200 and 500 years. Alternatively, frequency factor approach is also described and estimated values are further corrected based on the sample size and modified frequency factors. The lower and upper limits of these estimated values with 95% confidence level are also evaluated to provide a measure of uncertainty in the estimated values. The current study would be useful in predicting the frequencies of extreme rainfall more efficiently using L-moment specifically when observed data is limited, which is more often the case in hydrological observations. This will eventually be helpful in designing/improving the stormwater drainage system of the city when sufficient length of observed data is lacking. Further, the study may also be extended to incorporate the effect of climate change on the observed frequencies of extreme rainfall events considering different climate change scenarios and related projections about extreme rainfalls [5, 19].

References

1. V.T. Chow, *Handbook of Applied Hydrology* (McGraw-Hill, New York, NY, 1964)
2. V.T. Chow, *Frequency Analysis of Hydrologic Data. Bulletin No. 414* (University of Illinois, Urbana, Illinois, 1953)
3. P. Guhathakurta, P.A. Menon, S.K. Dikshi, S.T. Sable, Extreme rainfall analysis of Andhra Pradesh using a probability distribution model: a regional estimate. *Mausam* **56**(4), 785–794 (2005)
4. E.J. Gumbel, *Statistics of Extremes* (Columbia University Press, New York, 1958)
5. K. Gupta, Urban flood resilience planning and management and lessons for the future: a case study of Mumbai, India. *Urban Water J.* **4**(3), 183–194 (2007)
6. D.M. Hershfield, M.A. Kohler, An empirical appraisal of the Gumbel extreme-value procedure. *J. Geophys. Res.* **65**, 1737–1746 (1960)
7. J.R.M. Hosking, J.R. Wallis, *Regional Frequency Analysis: An approach based on L-Moments* (Cambridge University Press, 1997)
8. J.R.M. Hosking, L-Moments: analysis and estimation of distributions using linear combinations of order statistics. *J. Roy. Stat. Soc. Ser. B (Methodol.)* **52**(1), 105–124 (1990)
9. F.A. Huff, J.C. Neill, Frequency relations for storm rainfall in Illinois. *Illinois State Water Surv. Bullet.* **46**, 65 (1959)
10. K. Kochanek, I. Markiewicz, W.G. Strupczewski, On feasibility of L-moments method for distributions with cumulative distribution function, and its inverse inexpressible in the explicit form, in *International Workshop on Advances in Statistical Hydrology*, Taormina, Italy (2010)
11. M.D. Lowery, J.E. Nash, A comparison of method of fitting the double exponential distribution. *J. Hydrol.* **10**(3), 259–275 (1970)
12. K.N. Mutreja, *Applied Hydrology* (Tata McGraw-Hill Publishing Company Limited, New Delhi, 1986)
13. B.P. Parida, Modelling of Indian summer monsoon rainfall using a four-parameter Kappa distribution. *Int. J. Climatol.* **19**(12), 1389–1398 (1999)
14. J.-S. Park, H.-S. Jung, Modelling Korean extreme rainfall using a Kappa distribution and maximum likelihood estimate. *Theoret. Appl. Climatol.* **72**, 55–64 (2002)
15. B.M. Reich, Short duration rainfall intensity estimates and other design aids for regions of sparse data. *J. Hydrol.* **1**(1), 3–28 (1963)
16. P.M. Rowinski, W.G. Strupczewski, V.P. Singh, A note on the applicability of log-Gumbel and log-logistic probability distributions in hydrological analyses: I. Known pdf. *Hydrol. Sci. J.* **47**(1), 107–122 (2001)
17. K. Subramanya, *Engineering Hydrology* (Tata McGraw-Hill Publishing Company Limited, New Delhi, 1984)
18. M. Unkašević, RadinovićĐ: Statistical analysis of daily maximum and monthly precipitation at Belgrade. *Theoret. Appl. Climatol.* **66**, 241–249 (2000)
19. S. Vemula, K.S. Raju, S.S. Veena, A.S. Kumar, Urban floods in Hyderabad, India, under present and future rainfall scenarios: a case study. *Nat. Hazards* **95**, 637–655 (2018)
20. WMO, *Statistical Distribution for Flood Frequency Analysis*. Operation Hydrology Report No. 33, WMO—No. 718 (Secretariat of World Meteorological Organization, Geneva, Switzerland, 1989), 128 pp.
21. WMO, *Manual on Estimation of Probable Maximum Precipitation (PMP)*. WMO—No. 1045 (World Meteorological Organization, Geneva, Switzerland, 2009), 291 pp.

Application of Machine Learning for Accuracy Improvement of Projected Precipitation of Climate Change Data with Observed Data



Lakhwinder Singh, Deepak Khare, and Nitin Mishra

Abstract General circulation models (GCMs) use a mathematical equation method for transferring energy and mass from part of the atmosphere to another part of the atmosphere. They divided the atmosphere and the sea into a series of three-dimensional cells, each cell transmitting mass and energy to its surrounding cells based on the consequence of the cell's equations. These types are essentially the same model used to forecast the weather but are used on a more comprehensive (global) scale and on a more prolonged basis than for centuries. Earth has the number of parameters controlling climatic activities. Each time when new climate control parameters found, earth simulated models are updated. But natural and physical activities on earth are so complex to make perfect copy of earth's climate in computer models. The numbers of a climate model are present. But still, no model correctly predicts daily precipitation. On the other side, some model predicts daily temperature with high accuracy. Based on literature, six models were selected. But MIROC (CPIM5) model finalised for analysis based on statics near to observed data. Representative Concentration Pathways (RCPs) 4.5 is found to relative values of observed data. It is predicting maximum and minimum temperature with 80 and 94% accuracy. But it does not correctly predicts precipitation. In this study, accuracy improved from 24 to 60% for precipitation estimation of climate change model based on a monthly scale. A new dataset was generated with improved accuracy. Support vector mechanism of advanced machine learning is used for the non-linear scenario of climate complexity. Machine learning models also depend on the number of parameters; perfect tuning of parameter is required for accurate results. So, automated parameter tuning is also used to train a machine learning model. The best set of parameters was selected for climate estimates. Observed data is used for training the model against the simulated model.

Keywords Machine learning · Support vector mechanism · Climate change · GIS

L. Singh (✉) · D. Khare

Department of Water Resources Development and Management, Indian Institute of Technology Roorkee, Roorkee, India

N. Mishra

Department of Civil Engineering, Graphic Era Deemed to be University, Dehradun, India

1 Introduction

While the models that are at the core of the IPCC study in depth, they contain all examples of coupled circulation models, which are following the current science and policy framework offers a modern view of the nature and application of them. They are partial non-linear equations systems that are based on the underlying modern physics, fluid dynamics and chemistry. To run a model, scientists partition the earth into a three-dimensional grid plus a period, use simple flow equation for wind measurement, heat transfer, sunlight, relative humidity, ocean temperature and movement, and surface hydrology inside the grid structure [1–8]. The outputs include the network-wide heat and rainfall forecasts and several other factors, which are combined to generate such high-profile outcomes as the “average regional temperature”. Emissions of greenhouse gases (including CO₂) and volcano eruptions are included (called “boundary conditions” by climate modellers). The concentration of CO₂ is a crucial intermediate variable [2, 4, 9–11]. To solve the differential equations numerically at the core of the model, the input variables and parameters should be set. Depending on the beginning point of races, many several hundreds of years earlier, the initial conditions are fixed. In the past, studies are constrained on these distances (for measurements such as ice cores), and the beginning values are thus based on plausible pre-industrial hypotheses [12–17]. The GCM function is related to physical models that often precisely describe a process, while the model utilised is a generalised approximation on other periods. Alternatively, the outcomes of a simulations “suit” the observable outputs and contextual interactions (data assimilating, in terms of climate modelling) can be “tuned” (estimated or optimised, in terms of terminology of the predictive) and remain consistent with the prior knowledge and existing physical interactions. The goal and to provide a “best” evaluation and statistical equations for modelling climate variability history and predicting of the true status of the world’s climate system [18–23]. In general, machine learning improves the dataset, so that while data is more significant to use, the measured and simulated results always vary. More tuning is used to keep the model on track again.

Moreover, data on “pressure”, including exogenous variables (known as climatic border conditions), such as CO₂ and volcano emissions, have been observed since about 1850. Other factors that may be necessary, such as shifts in land usage, usually are omitted. Owing to the sophistication of these models, the computational costs are currently expensive for implementing these steps. Because of the high level of flexibility and minimal knowledge, the decision is essential, even though it is possible. A significant proportion of the model design is thus judgmental [24–33].

Support vector support is one of the primary methods of machine learning that can also help solve problems with the data analytics classification. In a significant data context, it can aid with specific multi-domain applications. The help vector machine is therefore computer-consuming and scientifically complex. To allow readers to understand the theory, the primary purpose of this study is to apply accuracy factors to a climate model. The Lagrangian vector support with basic examples is also used on virtualisation and anti-Hadoop structures using R programming framework. In recent

decades, a large variety of computer techniques, including hydrology, have been commonly used by conventional neural networks such as the multi-layered back-propagation and radial-base structure networks. Recently, a variety of new training methods were suggested to address the limitations and efficiency of classical neural networks. One of the essential advancements of these paradigms is that of a kernel-based neural network system called SVMs, which is embedded in the theory of predictive learning, as well as the computational proper risk management approach. SVM has been broadly used in many fields, including pattern recognition, regression, imaging, bioinformatics and intelligent systems. Most recently, SVMs have been identified in the hydrological area. To distinguish automated remote data, however, for rainfall-runoff analysis and have used SVM to develop networks for groundwater head monitoring and [34–37] have used the SVM to estimate groundwater.

The basic SVM formulation for correlation is subsequently introduced. The polynomial and gamma-based SVM was used for this study. Most conventional neural network models are aimed at minimising training error by applying the concept of empirical risk minimisation. In contrast, the structural risk minimisation concept is being used by SVMs which attempts to reduce the upper limit to generalisation error by striking a proper balance between both the training error and system capability (i.e. leaven power of machines). The standard neural network will appear to collapse into an ideal local solution, while SVM is guaranteed to have the best global solution. In the model architecture, typical ANNs are considerably arbitrary, while for SVMs, the system model (number of parameters units) is the automatic preference of the training algorithm [38–45].

In comparison, conventional neural networks put little stress on the success of generalisation, while SVMs aim to resolve this problem in a strictly theoretical sense. The stability of the SVM comes from the use of clustering algorithms, which meant mappings of the data to more significant dimensional space, perhaps infinite. A linear solution of higher-dimensional parameter space is a highly non-linear solution with the initial reference space in the lower dimension. SVM is thus a promising alternative to solve several non-linear climatological problems [21, 46–53].

2 Study Area

Vadodara lies between 22° 12' 38" N and 22° 21' 33" N latitude and 73° 06' 09" E to 73° 16' 06" E of longitude. (Coordinate according to 2011 extent of Vadodara). National Highway 8, connecting Delhi and Gandhinagar with Ahmedabad to Mumbai, passes through the city. Vadodara is also connected with Ahmedabad through Indian National Expressway 1, a stretch of 97 km Super Highway with exits at Anand, Nadiad, S. P. Ring Road and finally Ahmedabad. Vadodara, formerly known as Baroda. Again in 1974, the name changed to Vadodara. Whereas for study purpose, single grid is selected located at the centre of the city. Detail map of the study area is shown in Fig. 1.

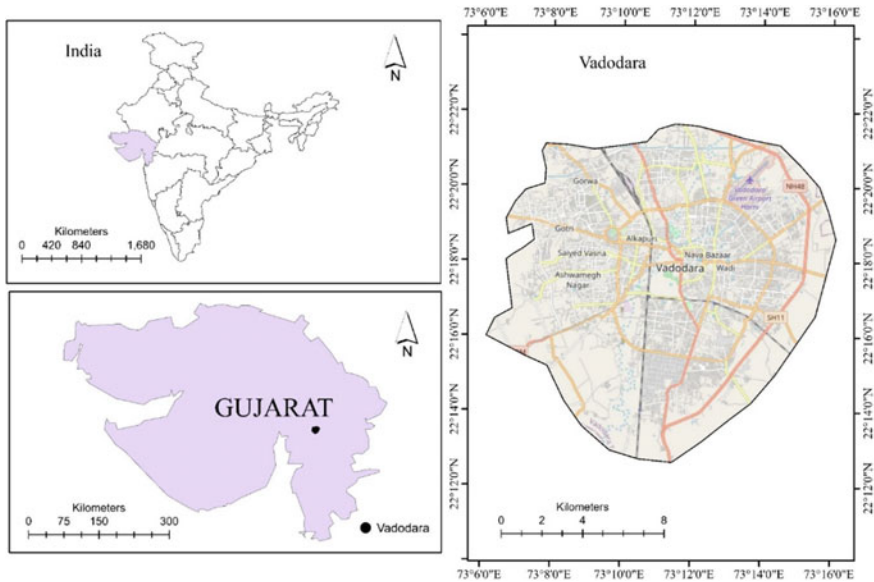


Fig. 1 Vadodara location map

2.1 Climate

In the Koppen climate classification, Vadodara features a tropical savanna climate. The winter, monsoon and summer are the primary three seasons. The weather is warm, apart from the monsoon season. The summer is 36 °C average, and the winter is 23 °C; these are the temperature between March and July. The mean daily temperature between November and February is 30 °C, and the average minimum temperature is 15 °C, with arid climates. In January, a slight chill is caused by cold northern winds. From mid-June through mid-September, the SW monsoon brings a damp environment. The mean precipitation is 93 cm, but the river is flooded by the extremely heavy rainfall. The maximum reported temperature is 47 °C and the minimum temperature is – 1 °C. Average climate value based on 1980–2018 data shown in Figs. 2 and 3

3 Methodology and Data Used

3.1 Data Used

A central location (22.25 N and 73.30 E) on the area is used for analysis. Station data collected by IMD is used from 2006 to 2017 for training and testing of the model. Data is re-gridded to 0.25° resolution. Similarly, MIROC Climate Model (CPIM5) is

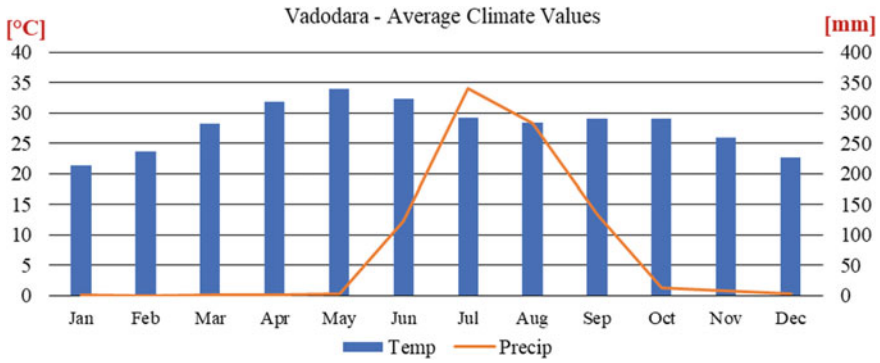


Fig. 2 Vadodara average precipitation and temperature

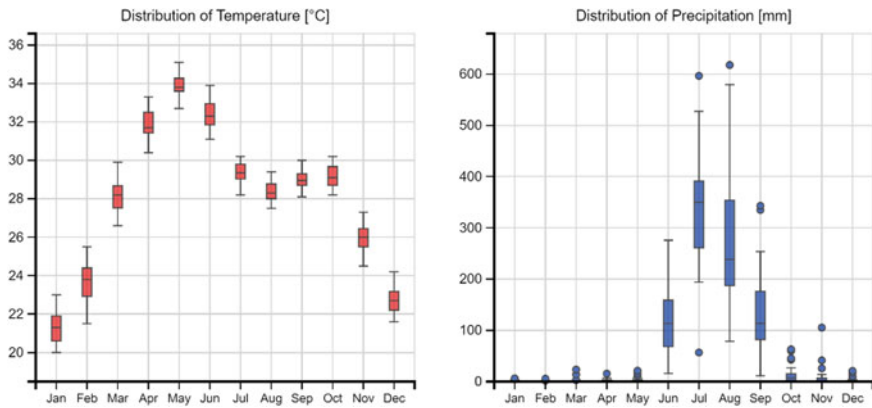


Fig. 3 Vadodara temperature and precipitation distribution

used with a re-grided resolution of 0.25. Data is downscaled and bias-corrected for India by Centre of climate change research Pune, India. After training, data is validated on the same set of training to maximise training accuracy. For prediction, only model data was available, so SVM is trained on maximum temperature, minimum temperature and simulated precipitation against IMD observed precipitation. The non-linear complexities to be studied by the SVM model. Model parameter was tuned to achieve the best results. After training the model, accurate data predicted up to 2099.

3.2 SVM Model

A higher-dimensional space in n -dimensional vector (N —the number for elements) precisely classifies its variables are found in the supporting vector machine technique. Several potential hyperplanes can be used to distinguish the two types of data points. Our goal is to locate an aeroplane with the highest limit of the data points in both groups, i.e. maximum size. Maximising the margin gap would help to boost transparency of potential data points. Hyperplanes were decision-making limits which assist in the organisation of data points. Various sections can be assigned to data points from either side of the plane. The hyperplane dimension also relies on the number of characteristics. If there are two entrance functions, the hyperplane is only one side. The hyperplane will become a two-dimensional plane when the amount of input functionality is three dimensional. Whenever the number of objects approaches 3, it becomes impossible to visualise. Help vectors are nearer data points to the hyperplane and impact hyperplane direction and orientation. We optimise the parameter of the classifier using such support vectors. The elimination of vectors of support affects the hyperplane portion. These are the aspects that enable us to build our SVM. More detail and mathematics behind that is discussed in [54].

3.3 Parameterisation and Tuning

SVM model requires perfect tuning of parameters. In this, the following parameter are used after tuning of SVM, eps-regression, polynomial kernel is used, cost value of 4, degree 3, gamma value 2 and epsilon 0.1 are used. The number of support vector generated to fit non-linear data was 79. SVM model trained using maximum and minimum values of temperature and monthly precipitation against observed precipitation values. SVM represents non-rainfall values as negative, for the month not having any rainfall, that non-rainfall negative values are filtered out during post-processing of data.

4 Model Selection Criteria

Model is selected based on statics near to observed data. As from Table 1, the climate model represents temperature value near to observed values, including maximum and minimum. As the maximum temperature is simulated is 42 °C and observed is also 41 °C both values are near. Mean and median were too similar to observed values. Same applies to minimum, 1st and 3rd Quantile values. But precipitation data is not much identical, simulated by the model. So, the improvement factor is required for this data; this study implies that the scenario with machine learning applications for climate change.

Table 1 Statistics of data used based on 2006–2017 Monthly

Statics	MIROC. Max. Temp.	MIROC. Min. Temp.	MIROC. PCP mm	IMD. Max. Temp.	IMD. Min. Temp.	IMD. PCP mm
Minimum	28.63	11.77	0.00	27.50	11.35	0.00
1st quantile	31.19	16.22	0.00	31.18	16.54	0.00
Median	33.10	22.45	0.01	32.88	23.01	0.40
Mean	34.10	20.86	82.33	33.71	21.02	86.15
3rd quantile	36.95	24.81	87.11	36.30	24.61	115.60
Max	42.15	28.01	697.15	41.04	27.16	803.60

5 Result and Discussion

It is important to discuss the comparison between simulated and observed data in depth before generating ML-based improved data. In this study, monthly datasets are used for training testing and predictions, because it is too complex to enhance data on a daily scale that also required considerable computer resources to train the model. As input parameter multiple datasets or used, to train the model using a single series was not a right approach. It is found that the MIROC model and IMD data have similar results for temperature series, but not identical for precipitation. Selected are lies in a monsoon region; monsoon is returning event on about fixed time interval in this region, i.e. June to September. So, it is possible to train the model with this non-linear relation to the simulated model. While training the model, maximum and minimum temperature with simulated precipitation of MIROC is used to train a model against unequally distributed data. Comparison of correlation between modelled temperature and observed are shown in Figs. 4 and 5. Whereas, the comparison of simulated

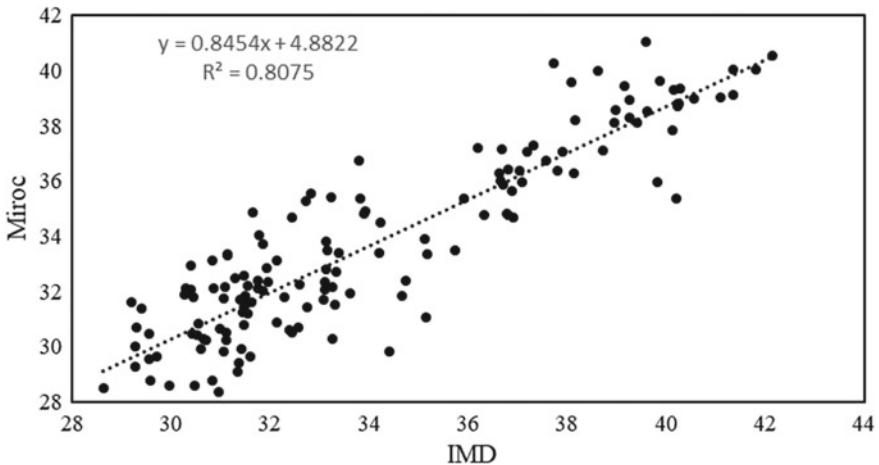


Fig. 4 Relation between observed and MIROC-simulated max temperature

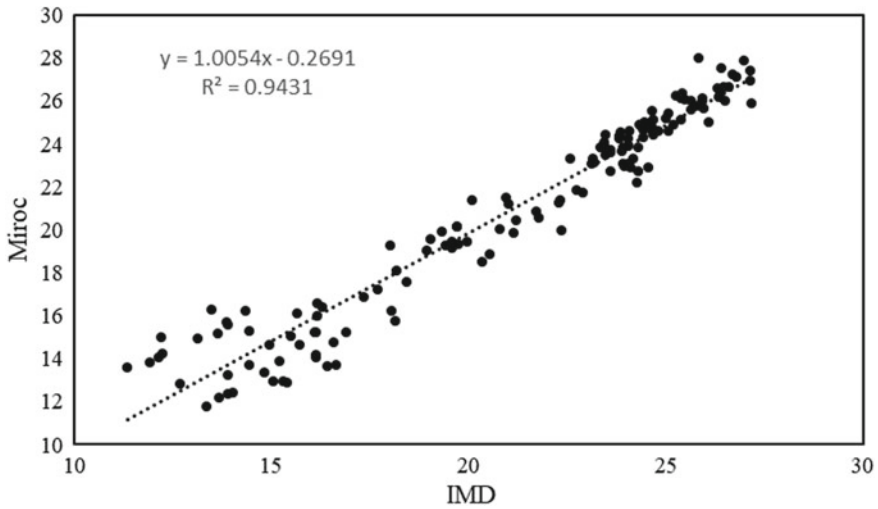


Fig. 5 Relation between observed and MIROC-simulated min temperature

and observed precipitation is shown in Fig. 6. It represents that there is a deficient relation between MIROC and observed precipitation. It has just $r^2 = 0.24$ before model training. That is not adequate to predict local weather conditions of the future. But on other side, temperature results represent a higher level of accuracy as $r^2 = 0.80$ for maximum temperature and $r^2 = 0.94$ for minimum temperature. Peak and pattern of temperature were also similar as shown in Figs. 7 and 8. But the pattern of precipitation is not similar as observed and is shown in Fig. 9.

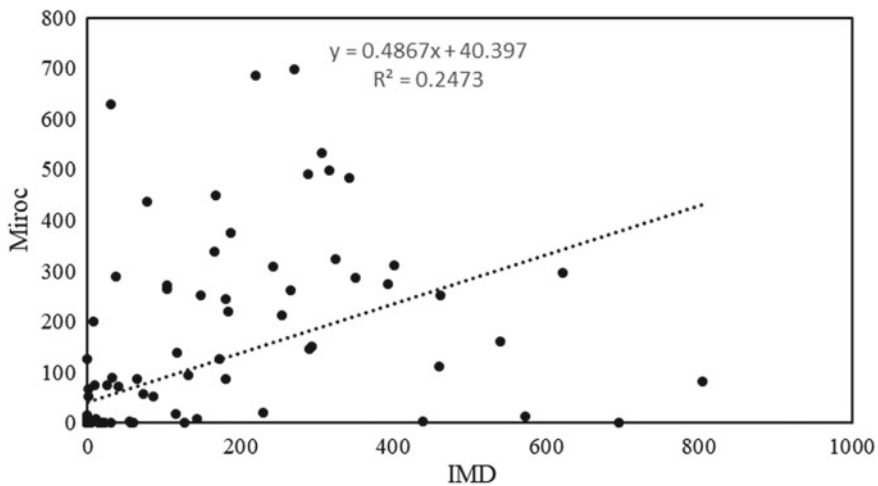


Fig. 6 The relation between observed and MIROC-simulated precipitation

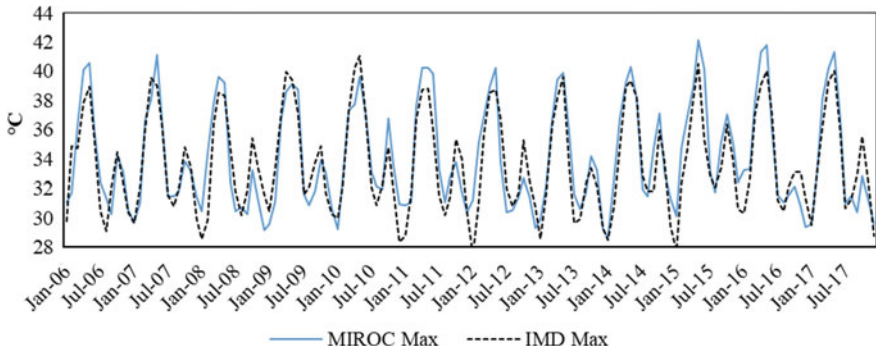


Fig. 7 The pattern of maximum temperature: observed and MIROC model simulation

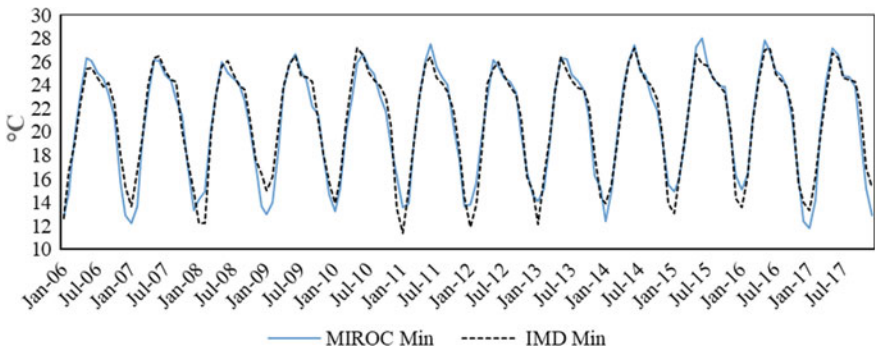


Fig. 8 The pattern of minimum temperature: observed and MIROC model simulation

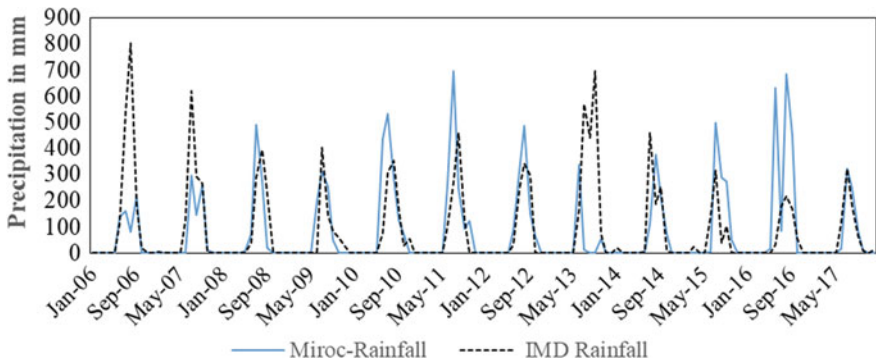


Fig. 9 The pattern of monthly precipitation: observed and MIROC model simulation

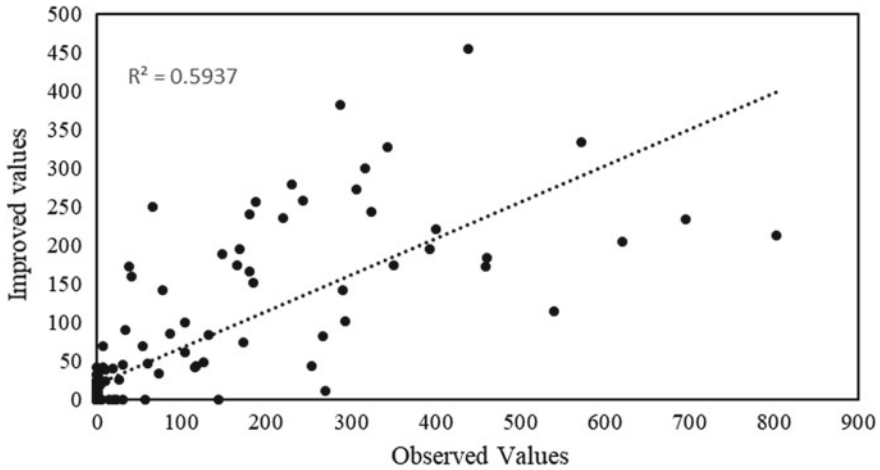


Fig. 10 Improved accuracy

However, the application of machine learning comes into action when data is complex in nature and not following any linear relation. In this term, machine learning represents significant performance for improving data accuracy to $r^2 = 0.59$ while comparing training data. It was previously $r^2 = 0.24$ on the same dataset with observed and simulated; this is also the accuracy of the model for this data. If considered mathematical regression term, then it was never possible to drive relation between this data. Almost 60% accuracy is considered to be higher accuracy in terms of the complexity of nature's "prediction". After achieving this accuracy, SVM model used further for estimation till 2099. A new dataset is generated that was near to observed data. However, it has limitations also; its best match is with RCP 4.5 scenario, but it is far away from RCP 8.5 global warming conditions. Because at present, actual observed conditions are near to RCP 4.5, and past conditions are also following this. Tested accurate data with observed data is represented in Fig. 10, and SVM-based corrected predictions are represented in Fig. 11, along with MIROC values. As from Fig. 11, MIROC estimates precipitation in 2088 about 3000 mm in a year, but actually, this area never experience precipitation more than 1500 mm, But after implication of ML SVM model, this got corrected, as represented.

6 Conclusion

Sometimes relation between two or more parameters exist but so complex in nature that fitting of regression equations appears to be inadequate. That is why, it is used in medical sciences to study the complexity of DNA and RNA. This is also used for the study of universe such as dark matter. In this study, machine learning is used to improve precipitation values of climate dataset with the help of observed

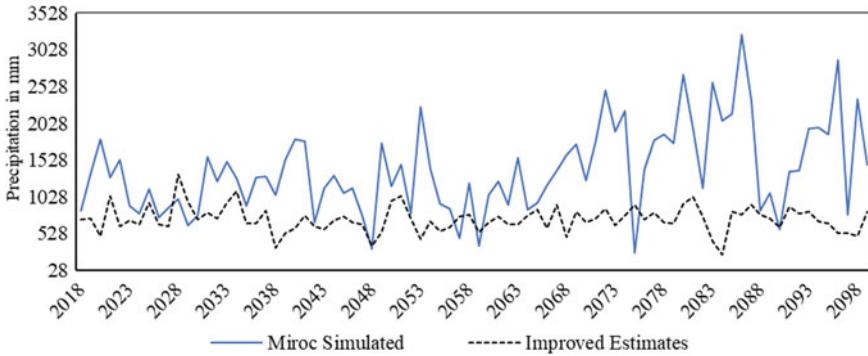


Fig. 11 Improved precipitation estimated with machine learning

weather data. Even lower relation was found between experimental and simulated data, but model improved prediction accuracy after learning and training all the data together. This advanced computing techniques are used for climate change analysis. A trained model is used to predict accurate data until 2099, as MIROC last year. Results and comparison of generated data represented a higher level of accuracy applied to climate data. On the other side, it has some limitations that sometimes need to filter out non-rain day data. To achieve the perfect result, perfect tuning of SVM parameter is required. SVM tuning is also used to automate several parameter values that best study these scenarios. It is a wider application in terms of non-linear spatial data. This study represented it.

References

1. A.E. Minarno, W.A. Kusuma, H. Wibowo, Performance comparison activity recognition using logistic regression and support vector machine, in *2020 3rd International Conference on Intelligent Automation System ICoIAS 2020*. <https://doi.org/10.1109/ICoIAS49312.2020.9081858>
2. R. Vautard, Regional climate projections. *Weather Clim. Serv. Energy Ind.* (2018). https://doi.org/10.1007/978-3-319-68418-5_10
3. J.R. Toggweiler, J. Russell, Ocean circulation in a warming climate. *Nature* (2008). <https://doi.org/10.1038/nature06590>
4. G.A. Meehl, T.F. Stocker, W.D. Collins, et al., Global climate projections. *Clim. Chang. Phys. Sci. Basis. Contrib. Work. Gr. I Fourth Assess. Rep. Intergov. Panel Clim. Chang.* (2007)
5. P.P. Sherki, V. Vala, A class-incremental classification method based on support vector machine, in *Proceedings of 14th IEEE International Conference on Semantic Computing ICSC 2020* (2020). <https://doi.org/10.1109/ICSC.2020.00012>
6. S.A. Rizwan, A. Jalal, K. Kim, An accurate facial expression detector using multi-landmarks selection and local transform features, in *3rd International Conference on Advanced Computer Science ICACS 2020* (2020). <https://doi.org/10.1109/ICACS47775.2020.9055954>
7. M.D. Mumford, T.R. Newbold, Climate. *Curated Ref. Collect Neurosci. Biobehav. Psychol.* (2016). <https://doi.org/10.1016/B978-0-12-809324-5.23522-0>

8. M. Araujo, R. Pearson, W. Thuiller, M. Erhard, Validation of species-climate impact models under climate change. *Glob. Chang. Biol.* (2005). <https://doi.org/10.1111/j.1365-2486.2005.001000.x>
9. R.A.W. Uk, Climate models and their evaluation. *Evaluation* (2007). <https://doi.org/10.1016/j.cub.2007.06.045>
10. Evaluation of climate models. *Clim. Chang. Phys. Sci. Basis Work Gr I Contrib. Fifth Assess. Rep. Intergov. Panel Clim. Chang.* (2013). <https://doi.org/10.1017/CBO9781107415324.020>
11. A. Dai, Increasing drought under global warming in observations and models. *Nat. Clim. Chang.* (2013). <https://doi.org/10.1038/nclimate1633>
12. R.J. Hijmans, C.H. Graham, The ability of climate envelope models to predict the effect of climate change on species distributions. *Glob. Chang. Biol.* (2006). <https://doi.org/10.1111/j.1365-2486.2006.01256.x>
13. P. Friedlingstein, P. Cox, R. Betts et al., Climate-carbon cycle feedback analysis: results from the C4MIP model intercomparison. *J. Clim.* (2006). <https://doi.org/10.1175/JCLI3800.1>
14. R. Knutti, R. Furrer, C. Tebaldi, J. Cermak, G.A. Meehl, Challenges in combining projections from multiple climate models. *J. Clim.* (2010). <https://doi.org/10.1175/2009JCLI3361.1>
15. T.C. Models, Country-level climate projections. *Glob. Warm. Agric. Impact Estim. Ctry.* (2007)
16. C. Bellard, C. Bertelsmeier, P. Leadley, W. Thuiller, F. Courchamp, Impacts of climate change on the future of biodiversity. *Ecol. Lett.* (2012). <https://doi.org/10.1111/j.1461-0248.2011.01736.x>
17. T. Andrews, J.M. Gregory, M.J. Webb, K.E. Taylor, Forcing, feedbacks and climate sensitivity in CMIP5 coupled atmosphere-ocean climate models. *Geophys. Res. Lett.* (2012). <https://doi.org/10.1029/2012GL051607>
18. D.W. Pierce, T.P. Barnett, B.D. Santer, P.J. Gleckler, Selecting global climate models for regional climate change studies. *Proc. Natl. Acad. Sci. USA* (2009). <https://doi.org/10.1073/pnas.0900094106>
19. M.M. Holland, C.M. Bitz, Polar amplification of climate change in coupled models. *Clim. Dyn.* (2003). <https://doi.org/10.1007/s00382-003-0332-6>
20. F. Giorgi, P. Lionello, Climate change projections for the Mediterranean region. *Glob. Planet Change* (2008). <https://doi.org/10.1016/j.gloplacha.2007.09.005>
21. D.B. Lobell, M.B. Burke, C. Tebaldi, M.D. Mastrandrea, W.P. Falcon, R.L. Naylor, Prioritizing climate change adaptation needs for food security in 2030. *Science* **80** (2008). <https://doi.org/10.1126/science.1152339>
22. R.S. Pindyck, The use and misuse of models for climate policy. *Rev. Environ. Econ. Policy* (2017). <https://doi.org/10.1093/reep/rew012>
23. A. Lupo, W. Kininmonth, Global climate models and their limitations. *Clim. Chang. Reconsidered II Phys. Sci.* (2013). <https://doi.org/10.1038/ncomms2656>
24. Global energy review 2020. *Glob. Energy Rev.* (2020). <https://doi.org/10.1787/a60abbf2-en>
25. C. Le Quéré, R.B. Jackson, M.W. Jones et al., Temporary reduction in daily global CO₂ emissions during the COVID-19 forced confinement. *Nat. Clim. Chang.* (2020). <https://doi.org/10.1038/s41558-020-0797-x>
26. S. Anand, P. Vrat, R.P. Dahiya, Application of a system dynamics approach for assessment and mitigation of CO₂ emissions from the cement industry. *J. Environ. Manage.* (2006). <https://doi.org/10.1016/j.jenvman.2005.08.007>
27. P. Friedlingstein, R.M. Andrew, J. Rogelj et al., Persistent growth of CO₂ emissions and implications for reaching climate targets. *Nat. Geosci.* (2014). <https://doi.org/10.1038/NGEO2248>
28. Y. Lei, Q. Zhang, C. Nielsen, K. He, An inventory of primary air pollutants and CO₂ emissions from cement production in China, 1990–2020. *Atmos. Environ.* (2011). <https://doi.org/10.1016/j.atmosenv.2010.09.034>
29. T. Qi, X. Zhang, V.J. Karplus, The energy and CO₂ emissions impact of renewable energy development in China. *Energy Policy* (2014). <https://doi.org/10.1016/j.enpol.2013.12.035>
30. G. Janssens-Maenhout, M. Crippa, D. Guizzardi et al., Fossil CO₂ & GHG emissions of all world countries. *Earth Syst. Sci. Data Discuss.* (2017). <https://doi.org/10.2760/709792>

31. M. Den Elzen, N. Höhne, Reductions of greenhouse gas emissions in Annex I and non-Annex I countries for meeting concentration stabilisation targets: an editorial comment. *Clim. Change* (2008). <https://doi.org/10.1007/s10584-008-9484-z>
32. R.L. Milford, S. Pauliuk, J.M. Allwood, D.B. Müller, The roles of energy and material efficiency in meeting steel industry CO₂ targets. *Environ. Sci. Technol.* (2013). <https://doi.org/10.1021/es3031424>
33. L. Losekann, G.A. Marrero, F.J. Ramos-Real, E.L.F. de Almeida, Efficient power generating portfolio in Brazil: conciliating cost, emissions and risk. *Energy Policy* (2013). <https://doi.org/10.1016/j.enpol.2013.07.049>
34. H. Yoon, S.C. Jun, Y. Hyun, G.O. Bae, K.K. Lee, A comparative study of artificial neural networks and support vector machines for predicting groundwater levels in a coastal aquifer. *J. Hydrol.* (2011). <https://doi.org/10.1016/j.jhydrol.2010.11.002>
35. S. Lee, S.M. Hong, H.S. Jung, GIS-based groundwater potential mapping using artificial neural network and support vector machine models: the case of Boryeong city in Korea. *Geocarto. Int.* (2018). <https://doi.org/10.1080/10106049.2017.1303091>
36. F. Sajedi-Hosseini, A. Malekian, B. Choubin, O. Rahmati, S. Cipullo, F. Coulon, B. Pradhan, A novel machine learning-based approach for the risk assessment of nitrate groundwater contamination. *Sci. Total Environ.* (2018). <https://doi.org/10.1016/j.scitotenv.2018.07.054>
37. B. Yadav, S. Ch, S. Mathur, J. Adamowski, Assessing the suitability of extreme learning machines (ELM) for groundwater level prediction. *J. Water L. Dev.* (2017). <https://doi.org/10.1515/jwld-2017-0012>
38. A. Mondal, D. Khare, S. Kundu, International soil and water conservation research change in rainfall erosivity in the past and future due to climate change in the central part of India. *Int. Soil Water Conserv. Res.* **4**, 186–194 (2016)
39. M. Pal, Ensemble of support vector machines for land cover classification. *Int. J. Remote Sens.* **29**, 3043–3049 (2008)
40. J.B. Swain, K.C. Patra, Impact of catchment classification on streamflow regionalization in ungauged catchments. *SN Appl. Sci.* **1**, 1–14 (2019)
41. M. Li, J. Im, C. Beier, Machine learning approaches for forest classification and change analysis using multi-temporal Landsat TM images over Huntington wildlife forest. *GIScience Remote Sens.* **50**, 361–384 (2013)
42. J. Ma, Y. Ding, J.C.P. Cheng, F. Jiang, Y. Tan, V.J.L. Gan, Z. Wan, Identification of high impact factors of air quality on a national scale using big data and machine learning techniques. *J. Clean Prod.* **244**, 118955 (2020)
43. A.E. Maxwell, T.A. Warner, M.P. Strager, Predicting palustrine wetland probability using random forest machine learning and digital elevation data-derived terrain variables. *Photogramm. Eng. Remote Sensing* **82**, 437–447 (2016)
44. R.P. Sheridan, W.M. Wang, A. Liaw, J. Ma, E.M. Gifford, Extreme gradient boosting as a method for quantitative structure-activity relationships. *J. Chem. Inf. Model* **56**, 2353–2360 (2016)
45. E. Raczko, B. Zagajewski, Comparison of support vector machine, random forest and neural network classifiers for tree species classification on airborne hyperspectral APEX images. *Eur. J. Remote Sens.* **50**, 144–154 (2017)
46. S. Drijfhout, S. Bathiany, C. Beaulieu, V. Brovkin, M. Claussen, C. Huntingford, M. Scheffer, G. Sgubin, D. Swingedouw, Catalogue of abrupt shifts in intergovernmental panel on climate change climate models. *Proc. Natl. Acad. Sci. USA* (2015). <https://doi.org/10.1073/pnas.1511451112>
47. C. Beer, M. Reichstein, E. Tomelleri, et al., Terrestrial gross carbon dioxide uptake: global distribution and covariation with climate. *Science* **80** (2010). <https://doi.org/10.1126/science.1184984>
48. B.J. Soden, I.M. Held, An assessment of climate feedbacks in coupled ocean-atmosphere models. *J. Clim.* (2006). <https://doi.org/10.1175/JCLI3799.1>
49. D. Purves, S. Pacala, Predictive models of forest dynamics. *Science* **80** (2008). <https://doi.org/10.1126/science.1155359>

50. P. Tamilarasi, R.U. Rani, Diagnosis of crime rate against women using k-fold cross validation through machine learning, in *Proceedings of 4th International Conference on Computing Methodology Communication ICCMC 2020*. <https://doi.org/10.1109/ICCMC48092.2020.ICCMC-000193>
51. S. Ghosh, SVM-PGSL coupled approach for statistical downscaling to predict rainfall from GCM output. *J. Geophys. Res. Atmos.* (2010). <https://doi.org/10.1029/2009JD013548>
52. M. Tavoni, E. Kriegler, K. Riahi et al., Post-2020 climate agreements in the major economies assessed in the light of global models. *Nat. Clim. Chang.* (2015). <https://doi.org/10.1038/nclimate2475>
53. S. Rajan, Statistical downscaling of GCM output, hydrological simulation and generation of future scenario using variable infiltration capacity (VIC) model for the Ganga Basin, India. Thesis (2014)
54. V. Vapnik, *The nature of statistical learning theory* (2013)

Statistical Downscaling of Climate Change Scenarios of Rainfall in Haridwar District of Uttarakhand, India



Gaurav Singh, Nitin Mishra, L. N. Thakural, and Sanjeev Kumar

Abstract The impact of climate change often requires climatic data of spatial resolution at a precise scale to study the ongoing scenario and future scenario as well. Climate change scenarios are evaluated on coarse spatial resolution with the help of Global Climate Models (GCMs). Different methods can be used to downscale the data present at coarser scale to the finer scale. Multiple linear regressions (MLR) technique-based SDSM was employed for downscaling the obtained data from coarser scale to finer scale. Rainfall is considered as one of the principal climate factors for environmental variation studies. Statistical downscaling technique is utilized for downscaling daily precipitation data to obtain future climate data for Haridwar District in Uttarakhand. The large-scale NCEP (National Centers for Environmental Prediction) “reanalysis” data of the interval 1961–1995 is utilized for calibration, and the data of the interval 1996–2005 is utilized for the model’s validation. The estimation of future monthly based rainfall for the period 2020s (2006–2040), 2050s (2041–2070) and 2080s (2071–2099) for Haridwar District is carried out for different RCPs (2.6, 4.5, and 8.5). This examination shows a decreasing pattern of yearly rainfall for future for the period 2020s (2006–2040) by 9–18%, 2050s (2041–2070) by 12–16%, and an increase in trend in 2080s (2071–2099) compared to the present (1961–2005) scenario.

Keywords Climate change · NCEP predictors · Future scenarios · SDSM · Rainfall · RCP · Haridwar district

1 Introduction

Various numbers of researches have been done on climate changes on the basis of climate variables. The outrageous variations in the climate pattern have prompted

G. Singh · N. Mishra (✉) · S. Kumar

Department of Civil Engineering, Graphic Era Deemed to be University, Dehradun 248001, India

L. N. Thakural

Water Resources Division, National Institute of Hydrology, Roorkee 247667, India

innumerable examinations and researches over the most recent couple of decades, particularly by observing generous variations in the pattern of precipitation at global level. Changes in the trend of rainfall which results in major climate changes require a precise consideration due to its effect on the accessibility of water and the production of food. The expanding pace of the global normal surface temperature can be observed by different pattern and lists of the atmosphere limits got from the observational data, and the best pace of variations is seen since the center of 1970s [1]. Large-scale environmental circulation designs decide the temporal and spatial dispersion of precipitation and the land surface temperature, which manages the key parts of the hydrologic cycle (e.g., stream, evaporation, soil moisture) [2]. An increment in temperature and precipitation limits will prompt drawn-out, increasingly visit dry seasons and may likewise prompt an extension of dry spell influenced territories [3]. The structure of the atmosphere is believed to keep on changing due to common activities of the human, as a result of which the mankind is going to be confronted with a greater amount of many extraordinary occasions [4]. Examination considers completed by different scientists found that the expanding patterns in air temperature have been identified with a few factors, for example, expanded concentrations of anthropogenic greenhouse gases, expanded emanations of anthropogenic aerosols, expanded cloud cover, and urbanization [5]. A proper analysis of the atmospheric variables for past as well as future situations is required for the reasonable management and improvement of water assets. Precipitation is one of the fundamental factors impacts legitimately the causes that occur due to change in the environment. The future environmental variation due to consistent increment in the amount of greenhouse gases in the air can be estimated with the help of general circulation models (GCMs) [6]. General circulation models (GCMs) in addition to large-scale circulation predictors are considered as the two most critical and significant means to study the environmental effects [7]. The GCM-based data available at coarse spatial resolution cannot be utilized directly for hydrological evaluations [6]. Downscaling techniques are required in order to overcome any issues between the climate model yields at coarse resolution and surface climate factors at better spatial resolution. Downscaling strategies go from less requesting measurable downscaling techniques depending upon the fundamental guideline and the level of complexity credited to them, which are set up based on an analytical connection between extensive atmosphere state and locally determined climate variables [4]. To obtain information about environmental change at fine resolution, statistical downscaling technique is used which develops analytical connections between extensive climatic circulation and locally present variables (such as precipitation). A freely available software SDSM version 4.2 is used for assessing the impacts of local environmental change by utilizing a powerful method of downscaling [6, 8]. Different RCPs (representative concentration pathways) length the scope of conceivable radiative forcing situations and used by climate modeling community for concentrations of aerosol and greenhouse gas together with changes in land use, that are steady with a lot of wide atmosphere results. RCP 2.6 represents a very low forcing level while RCP4.5 and RCP6 represent moderate stabilization situations and RCP 8.5 depicts a situation of a very high baseline radiation [9].

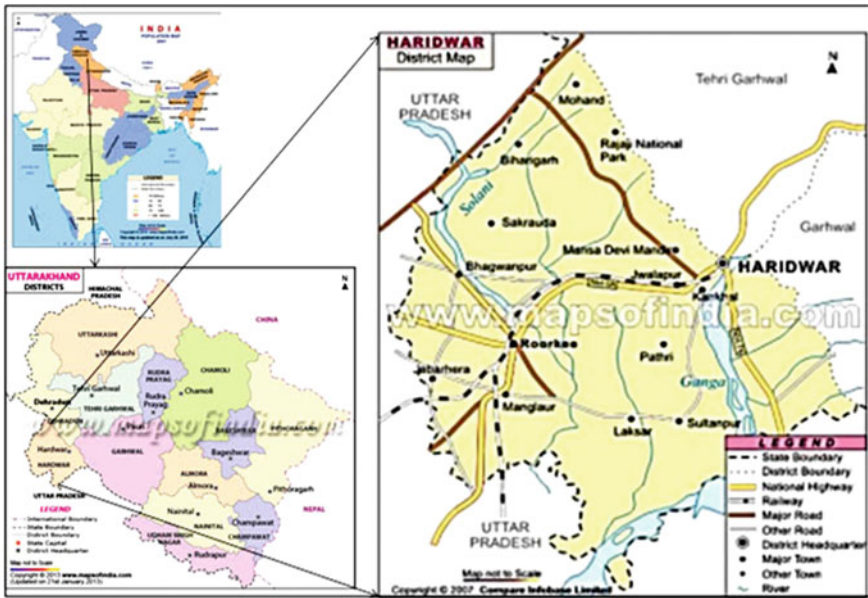


Fig. 1 Map of study area. Source www.mapsofindia.com

2 Study Area

Haridwar District is situated in the state Uttarakhand, India. This place is for nature lovers and is considered a holy place of Hinduism. As per 2011 census, Haridwar District is the most populous district of Uttarakhand. The latitudes and longitudes of Haridwar District are 29° 33'–30° 14' N and 77° 57'–78° 1' E, respectively. Geographical area of Haridwar District is approximate 2360 km² which comprises of six legislative blocks, viz. Roorkee, Bhagwanpur, Narsan, Laksar, Khanpur, and Bahadrabad (Fig. 1). The mean temperature of Haridwar District is 22 °C, and normal rainfall in Haridwar District is about 1134 mm in which most of the rainfall occurs in monsoon season (June–September).

3 Data Used and Methodology

3.1 Methodology

Statistical downscaling model (SDSM) works on multiple regression techniques to obtain future situations to evaluate the effects of environmental change (Fig. 2). Two types of data are required in this model, i.e., (i) the local data as “Predictand” (rainfall) and (ii) various atmospheric variables known as “Predictors.” In this study, multiple

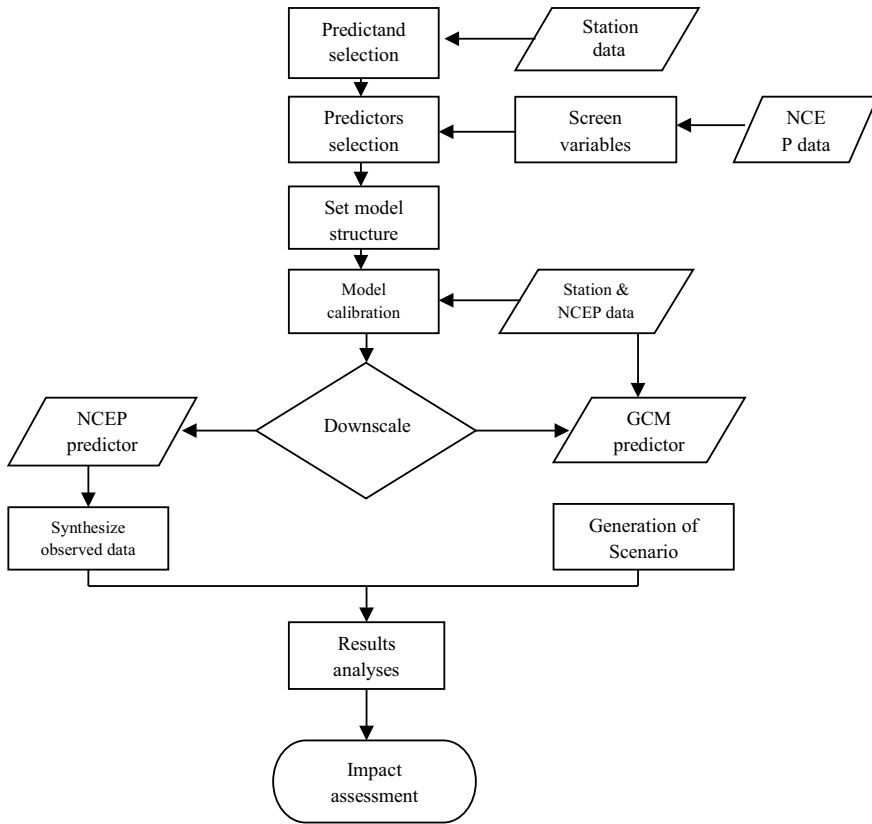


Fig. 2 SDSM climate scenario generation. *Source* [11]

linear regression method (parametric) has been used. SDSM tool version 4.2 is used for downscaling [10].

Downscaling involves the following steps:

1. Quality control and transformation of data;
2. Screening of predictor variables;
3. Calibration of the model;
4. Weather generation (utilizing observed predictors);
5. Statistical analysis;
6. Graphing output of the model;
7. Generating the scenario (utilizing climate model predictors).

3.1.1 Selection of Predictors

Both positive and negative correlation and partial correlation analysis between the predictors and the rainfall (predictand) are used for selecting the appropriate predictors. The NCEP reanalysis data on daily basis of the period 1961–2005 is utilized for selecting the appropriate predictors.

3.1.2 Calibrating and Validating the Model

Calibration of the model has been performed to establish an empirical relation between the predictors and the predictand. Multiple linear regression (parametric) technique is utilized for developing an empirical relation among the predictand and the predictors. For calibrating the model, reanalysis data of the NCEP of the period 1961–1995 is utilized, and the data of the interval 1996–2005 is utilized for validating the model.

3.1.3 Scenario Generation

Future scenarios for different RCPs emissions for the selected study area utilizing the simulated CanESM2 GCMs data are generated based on the validated regression model. In this study, it is being assumed that for the future climate conditions, this empirical relation between predictor variables and predictand (rainfall) remains valid.

3.2 Data Used

3.2.1 NCEP or NCAR “Reanalysis” Data

“Reanalysis” is a project contributed by the National Center for Atmospheric Research (NCAR) and National Center for Environmental Prediction (NCEP) together to deliver a record of 50 years of worldwide investigation of climatic information as air. It is then prepared for standard check and incorporated with a complicated and superior information integration framework that is kept unaltered over the whole “reanalysis” period. The “reanalysis” data which is considered as an intermediary to observed information has $2.5^\circ \times 2.5^\circ$ of resolution [12]. In this study, 45 years of the predictor data (reanalysis data) observed on a daily basis of atmospheric variables are used for the period of 1961–2005 from Canadian Climate Impacts Scenarios (CCIS) website (<http://www.cics.uvic.ca/scenarios/sdsm/select.cgi>).

3.2.2 Meteorological Information

The statistics of rainfall ($0.25^\circ \times 0.25^\circ$) on a daily basis for the period of 1961–2005 are obtained from Indian Meteorological Department (IMD). Statistical downscaling has been performed utilizing the day-by-day precipitation time arrangement as input predictand in SDSM software.

3.2.3 GCM Information

The general circulation model (GCM) daily precipitation simulations are obtained from Coupled Model Intercomparison Project 5 (CMIP5) climate change investigations for the period of 2006–2100. CanESM2 model output data is used in this study and is affiliated with the Canadian Centre for Climate Modeling and Analysis (CCCMA). The information is available online.

4 Results and Discussion

4.1 Predictor Variables Selection

A number of 26 predictor variables of a large scale are considered during initial screening. The predictors have been selected based on the correlation and the partial correlation of NCEP's predictors and observed climate variables in downscaling model for the interval 1961–2005. A list of predictor variable of Haridwar District is presented in Table 1.

Table 2 shows the selected predictors using the correlation coefficients values, partial correlation values, and p values between predictand (rainfall) and NCEP predictors.

4.2 Calibration and Validation Results

NCEP “reanalysis” data of the interval 1961–1995 is utilized for calibrating the model, and the data of the interval 1996–2005 is used for model validation. A good relationship between the observed and estimated monthly average statistics of rainfall is shown by the SDSM model. The value of coefficient of determination (R^2) is used during calibration and validation. Observed and estimated data during calibration (1961–1995) and validation (1996–2005) for rainfall are presented in Fig. 3a, b, respectively.

Table 1 Name and details of entire NCEP Predictors

S. No.	Predictor variable	Description
I	ncepmslpgl.dat	Mean sea level pressure
II	ncepp1_fgl.dat	1 hPa airflow strength
III	ncepp1_ugl.dat	1 hPa zonal velocity
IV	ncepp1_vgl.dat	1 hPa meridional velocity
V	ncepp1_zgl.dat	1 hPa vorticity
VI	ncepp1thgl.dat	Surface wind direction
VII	nceppzhgl.dat	Surface divergence
VIII	ncepp5_fgl.dat	500 hPa airflow strength
IX	ncepp5_ugl.dat	500 hPa zonal velocity
X	ncepp5_vgl.dat	500 hPa meridional velocity
XI	ncepp5_zgl.dat	500 hPa vorticity
XII	ncepp500gl.dat	500 hPa geopotential height
XIII	ncepp5thgl.dat	500 hPa wind direction
XIV	ncepp5zhgl.dat	500 hPa divergence
XV	ncepp8_fgl.dat	850 hPa airflow strength
XVI	ncepp8_ugl.dat	850 hPa zonal velocity
XVII	ncepp8_vgl.dat	850 hPa meridional velocity
XVIII	ncepp8_zgl.dat	850 hPa vorticity
XIX	ncepp850gl.dat	850 hPa geopotential height
XX	ncepp8thgl.dat	850 hPa wind direction
XXI	nceppzhgl.dat	850 hPa divergence
XXII	ncepprcpgl.dat	Accumulated precipitation
XXIII	nceps500gl.dat	Specific humidity at 500 hPa
XXIV	nceps850gl.dat	Specific humidity at 850 hPa
XXV	ncepshumgl.dat	Surface specific humidity
XXVI	ncepttempgl.dat	Mean temperature at 2 m

Table 2 Selected NCEP predictors and their relationship with rainfall

S. No.	Selected predictors	Correlation coefficients	Partial <i>r</i> value	<i>P</i> value
I	ncepmslpgl.dat	- 0.177	0.039	0.0072
II	nceps850gl.dat	0.261	0.015	0.2959
III	ncepprcpgl.dat	0.246	0.120	0.0000
IV	nceps500gl.dat	0.243	0.000	0.5639
V	ncepp850gl.dat	- 0.201	- 0.056	0.0001
VI	ncepshumgl.dat	0.261	0.016	0.2783

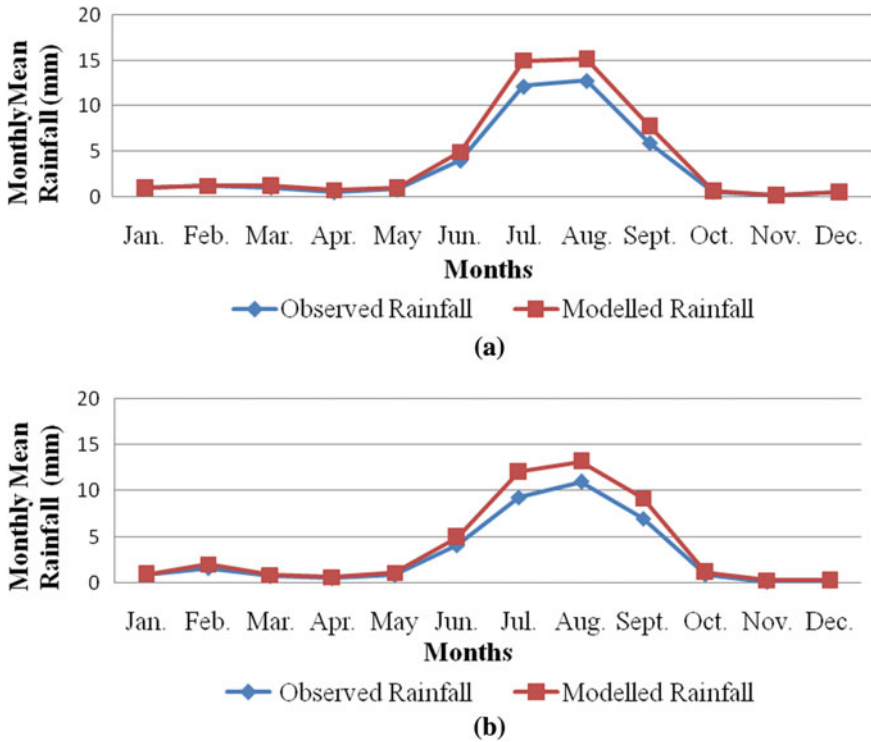


Fig. 3 a Monthly mean rainfall for calibration period (1961–1995). b Monthly mean rainfall for validation period (1996–2005)

Results of the observed and modeled monthly mean and annual (maximum, minimum, and average) data for both the period calibration and validation are presented in Table 3.

4.3 Scenario Generation

The future scenario generation of rainfall under different CanESM2 RCPs (2.6, 4.5, and 8.5) emission situations is approximated with the identified predictors by MLR-based SDSM model. The estimated rainfall is represented into three different time steps, i.e., 2006–2040 (2020s) in Fig. 4a, 2041–2070 (2050s) in Fig. 4b, and 2071–2099 (2080s) in Fig. 4c.

In Table 4, under RCP 2.6 annual rainfall varies from 590.65 to 1753 mm in 2020s, 676.68–1457.7 mm in 2050s, and 744.36–2029.4 mm in 2080s. Similarly, under RCP 4.5, rainfall varies from 624.18 mm to 1610.8 mm in 2020s, 597.99–1448.9 mm in 2050s, and 735.45–1954.4 mm in 2080s. Under RCP 8.5 rainfall

Table 3 Calibration and validation of monthly average rainfall (mm) with NCEP reanalysis data

Months	Calibration (1961–1995)		Validation (1996–2005)	
	Observed	Modeled	Observed	Modeled
Jan.	1.01	1.04	0.83	0.91
Feb.	1.16	1.20	1.58	1.99
Mar.	1.01	1.22	0.73	0.86
Apr.	0.49	0.72	0.50	0.64
May	0.79	1.00	0.85	1.09
Jun	3.99	4.94	4.11	4.97
Jul.	12.16	15.01	9.31	12.05
Aug.	12.80	15.19	10.95	13.15
Sept.	5.93	7.79	6.99	9.21
Oct.	0.54	0.64	0.93	1.15
Nov.	0.14	0.17	0.08	0.26
Dec.	0.54	0.54	0.21	0.24
Min. (annual)	482.2	1166.36	810.17	1276.66
Max. (annual)	1944.67	1857.22	1508.33	1726.95
Avg. (annual)	1243.72	1516.23	1137.90	1435.10
R^2	0.998		0.997	

varies from 735.19 mm to 1852.9 mm in 2020s, 705.50–1642.8 mm in 2050s, and 683.54–2286.4 mm in 2080s. The average annual rainfall corresponding to different RCPs (2.6, 4.5 and 8.5) scenarios of future emission is shown in Table 5.

Table 5 shows a decreasing pattern of mean annual precipitation for the interval 2020s and 2050s and an increasing trend for the period 2080s when compared with the present scenario. In 2020s, the simulated precipitation is 1111 mm for RCP 2.6, 1001 mm RCP 4.5, and 1093 mm for RCP 8.5 and decreases by 108 mm, 218 mm, and 126 mm, respectively. Similarly, 2050s show decreasing trend. In 2080s, there is increasing trend when compared with the present scenario as well as with 2020s and 2050s.

5 Conclusion

This study highlights the use of MLR-based SDSM technique for assessing the likely future monthly rainfall in Haridwar District. This study involves the generation of the daily rainfall time series corresponding to different RCPs (2.6, 4.5, and 8.5) scenarios and then utilized for estimating the monthly rainfall for different future time periods. The conclusions that can be drawn by the present study are:

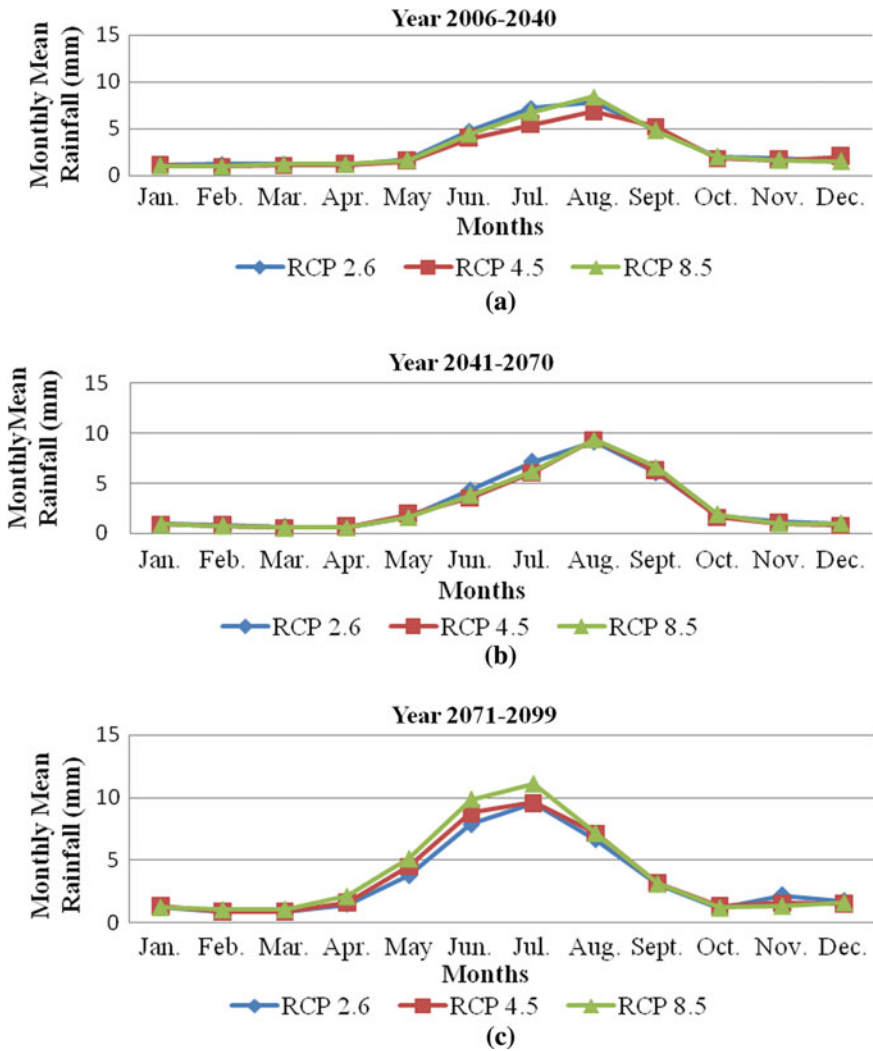


Fig. 4 **a** Monthly mean rainfall for climate scenarios 2006–2040. **b** Monthly mean rainfall for climate scenarios 2041–2070. **c** Monthly mean rainfall for climate scenarios 2071–2099

- In 2020s, there is decreasing trend in rainfall by 9–18% and by 12–16% in 2050s when compared with the present scenario.
- In 2080s, there is increase in rainfall for up to 16% when compared with the present scenario.
- This study shows a decreasing pattern in yearly rainfall for the periods of 2020s, 2050s and an increase in trend in 2080s compared to present scenario.

Table 4 Detailed monthly mean rainfall (mm) statistics for different time steps (scenarios)

Month	RCP 2.6			RCP 4.5			RCP 8.5		
	2020s	2050s	2080s	2020s	2050s	2080s	2020s	2050s	2080s
Jan.	1.08	0.94	1.25	1.07	0.91	1.40	1.04	0.90	1.27
Feb.	1.23	0.80	0.96	0.98	0.73	0.91	0.99	0.76	1.08
Mar.	1.19	0.66	0.93	1.09	0.59	0.93	1.23	0.56	1.12
Apr.	1.14	0.60	1.49	1.15	0.62	1.65	1.20	0.57	2.14
May	1.68	1.69	3.78	1.53	1.89	4.51	1.62	1.62	5.14
Jun.	4.74	4.32	7.87	3.97	3.54	8.76	4.46	3.81	9.87
Jul.	7.20	7.14	9.51	5.42	6.08	9.61	6.76	6.19	11.11
Aug.	7.83	9.12	6.66	6.80	9.38	7.17	8.39	9.36	7.18
Sept.	4.95	6.05	3.09	5.23	6.21	3.22	4.84	6.61	3.13
Oct.	1.98	1.71	1.24	1.85	1.61	1.40	2.01	1.91	1.23
Nov.	1.85	1.13	2.22	1.66	1.00	1.60	1.65	0.98	1.37
Dec.	1.50	0.95	1.76	1.99	0.83	1.55	1.54	0.96	1.64
Min. (annual)	590.65	676.68	744.36	624.18	597.99	735.45	735.19	705.50	683.54
Max. (annual)	1753.8	1457.7	2029.4	1610.8	1448.9	1954.4	1852.9	1642.8	2286.4

Table 5 Average annual rainfall for present and downscaled rainfall corresponding to RCPs (2.6, 4.5, and 8.5) scenario

Interval	RCP 2.6	RCP 4.5	RCP 8.5
<i>Mean annual rainfall (mm)</i>			
Present (1961–2005)	1219		
2020s (2006–2040)	1111	1001	1093
2050s (2041–2070)	1074	1022	1047
2080s (2071–2099)	1246	1306	1415

It is hoped that this study will serve in the effective management of present water resources in Haridwar District. Also, it will help to study the effect of changing climate on the expected rainfall in this particular region.

References

1. S. Kundu, D. Khare, A. Mondal, Interrelationship of rainfall, temperature and reference evapotranspiration trends and their net response to the climate change in Central India. *Theor. Appl. Climatol.* **130**, 879–900 (2016)
2. Y.D. Chen, Q. Zhang, X. Lu, S. Zhang, Z. Zhang, Precipitation variability (1956–2002) in the Dongjiang River (Zhujiang River Basin, China) and associated large-scale circulation. *Quatern. Int.* **244**, 130–137 (2011)
3. T. Fischer, M. Gemmer, L. Luliu, S. Buda, Temperature and precipitation trends and

- dryness/wetness pattern in the Zhujiang River Basin, South China, 1961–2007. *Quatern. Int.* **244**, 138–148 (2011)
4. Y. Hundecha, A. Bardossy, Statistical downscaling of extremes of daily precipitation and temperature and construction of their future scenarios. *Int. J. Climatol.* **28**, 589–610 (2007)
 5. D. Duhan, A. Pandey, K.P.S. Gahalaut, R.P. Pandey, Spatial and temporal variability in maximum, minimum and mean air temperatures at Madhya Pradesh in central India. *C. R. Geoscience* **345**(2013), 3–21 (2013)
 6. R. Shukla, D. Khare, R. Deo, Statistical downscaling of climate change scenarios of rainfall and temperature over Indira Sagar Canal command area in Madhya Pradesh, India, in *IEEE 14th International Conference on Machine Learning and Applications* (2015)
 7. T. Yang, H. Li, W. Wang, C.Y. Xu, Z. Yu, Statistical downscaling of extreme daily precipitation, evaporation and temperature and construction of future scenarios. *Hydrol. Processes* (2011)
 8. M.K. Goyal, C.S. Ojha, Evaluation of various linear regression methods for downscaling of mean monthly precipitation in Arid Pichola Watershed. *Nat. Resour.* 11–18 (2010)
 9. I. Jubb, P. Canadell, M. Dix, *Representative Concentration Pathways (RCPs)* (Australian Climate Change Science Program, 2013)
 10. S.K. Chandniha, M.L. Kansal, Rainfall estimation using multiple linear regression based statistical downscaling for Piperiya watershed in Chhattisgarh. *J. Agrometeorol.* **18**(1), 106–112 (2016)
 11. R.L. Wilby, C.W. Dawson, E.M. Barrow, SDSM—a decision support tool for the assessment of regional climate change impacts. *Environ. Model. Softw.* **17**, 147–159 (2001)
 12. R. Kistler, E. Kalnay, W. Collins, S. Saha, G. White, J. Woollen, M. Chelliah, W. Ebisuzaki, M. Kanamitsu, V. Kousky, H.V. Dool, R. Jenne, F. Michael, *The NCEP–NCAR 50-Year Reanalysis: Monthly Means CD-ROM and Documentation* (American Meteorological Society, 2000)

Land Use/Land Cover Change Detection of Bina River Basin, Madhya Pradesh



Gaurav Singh, Nitin Mishra, L. N. Thakural, and Amit Kumar Shrama

Abstract LU/LC (Land use/land cover) variations present a significant part in the investigation of worldwide alterations. LU/LC & regular adjustments have generally brought about biodiversity misfortune, deforestation, an unnatural weather change and increase flood events. With the create of GIS (Geographical Information System) and remote sensing approaches, LU/LC planning has specified a valuable and comprehensive approach to enhance the choice of zones intended to industrial and/or urban, agricultural regions of an area. Various strategies have been designed for land use characterizations which are commonly known as supervised and unsupervised classification. Here, supervised method of classification is used as a mode of classification. The land use/cover classification is done by using satellite images of 2000, 2009, 2014, and 2019, through ERDAS IMAGINE 2015 software. The land use has undergone major changes from year 2000–2019. The drastic increase of the built-up area or urban area from 3.12 to 20.25%, an increase in vegetation area from 8.81 to 19.60%, an increase in water bodies from 0.24 to 1.12%, a reduced in agriculture from 77.24 to 57.44% and a decrease in barren land from 10.59 to 1.59% from the year 2000–2019. This investigation clearly reveals the critical influence of population and its advancement exercises on LU/LC change. The current examination outlines that GIS and remote sensing are significant advancements for temporal examination and measurement of spatial occurrence which is generally impractical to endeavor through ordinary planning strategies.

Keywords LU/LC · Remote sensing · GIS · Bina river basin · Supervised classification

G. Singh · N. Mishra (✉) · A. K. Shrama
Department of Civil Engineering, Graphic Era Deemed to be University, Dehradun 248002, India

L. N. Thakural
Surface Water Hydrology Division, National Institute of Hydrology, Roorkee 247667, India

1 Introduction

Land Use/Land Cover is two distinct wordings which are regularly applied contrarily. Land cover indicates to the physical qualities of surface of the earth which includes distribution of soil, water, vegetation and other characteristics of the land along with those made only by human exercises, e.g., settlements whereas land-use indicates to the aspect by which land has been employed by people and their environment [1]. LU/LC (Land use/land cover) variations present a significant part in the investigation of worldwide alterations. LU/LC and regular adjustments have generally brought about biodiversity misfortune, deforestation, an unnatural weather change and increase flood events. These natural issues are much of the time related to LULC changes. In this manner, available data on LULC changes can give essential commitment to dynamic of natural management and scheduling what's to come. The increasing population and expanding financial necessities make an influence on LU/LC. This influence brings about spontaneous and unconstrained variations in LULC. The LULC changes are for the most part brought about by mishandling of urban, agricultural, range and forest lands which lead to extreme natural issues, for example, floods, landslides and so on [2]. In conditions of fast and consistently uncounted land use alteration, view of the Earth from space gives target details of human utilization of the scene. Over the earlier years, details from the Earth identifying satellites have gotten urgent in arranging the Earth's characteristics and structures, supervising regular resources and considering about natural change [3]. With the create of GIS (Geographical Information System) and remote sensing approaches, LU/LC planning has specified a valuable and comprehensive approach to enhance the choice of zones intended to industrial and/or urban, agricultural regions of an area. Use of remote sensing information made conceivable to consider the adjustments in land cover in shorter duration, demanding little effort and with finer precision in association with GIS that gives relevant platform to information examination, update and recovery [4]. Remote sensing has gotten a significant tool relevant to creating and comprehension the worldwide, physical cycles influencing the earth. Late growth in the usage of satellite details is to take benefit of extending measures of topographical details within reach related to GIS to aid understanding. GIS is a coordinated arrangement of computer hardware and software fit for catching, storing, recovering, manipulating, analyzing and showing spatial (geographically referenced) data to help advancement situated administration and dynamic cycles [5].

2 Study Area

Bina River is a significant branch of Betwa River in region Bundelkhand, Madhya Pradesh. It begins through Begumganj (Raisen region) and goes in to region Sagar (Rahatgarh area) and navigates between Khurai and Bina tehsil before conjunction with waterway Betwa close Basoda town in Vidisha region. By and by, household



Fig. 1 Map of study area

water contributes to Khurai, Rahatgarh and Bina town; railroads necessity at Junction of Bina Railway and mechanical serving for Bina Refinery and desired JP power venture is fulfilled from this waterway adjacent to restricted water system from the stream by direct siphoning. “Bina Complex-Irrigation and Multipurpose Project” has been suggested. In this task, the projected dams are the Madia dam and Chakarpar dam-cum-pickup weir on the Bina waterway in addition with one each on Dehra and Dhasan streams, branches of waterway Betwa. The watershed viable lies in between $23^{\circ} 18'$ and $24^{\circ} 15'$ N latitudes and $78^{\circ} 03'$ – $78^{\circ} 32'$ E longitudes having absolute geological territory about 2817 km^2 . The southern piece of the watershed is ruled with slopes and undulating geography with area of forest, though the northern piece of the watershed has delicate slopping and fields with prolific agricultural lands [6] (Fig. 1).

3 Land Use Classification

Various strategies have been designed for land use characterizations which are commonly known as supervised and unsupervised classification. The arrangement of Land use can be done either by an unsupervised technique in group cases on the basis of relative spectral closeness, or using supervised strategy dependent on resemblance

of cases to resource of predetermined classes which have been described spectrally. Here, supervised method of classification is used as a mode of classification.

The land use/cover classification is done by using satellite images of 2000, 2009, 2014, and 2019, through ERDAS IMAGINE 2015 software. The determination of digital land cover classification is to have a relevant information class value, which can evaluate the landscape accurately. The images are downloaded from USGS (United States Geological Survey) site and are firstly Layer stacked in the software. Land cover indicates to the cover including urban, vegetation, agriculture, barren land, water bodies and so on. Land cover is an essential variable that joins numerous pieces of the human and physical conditions. Land cover is profoundly influenced by human exercises as opposed to natural events. These days, primarily agriculture extension, consuming exercises or fuel wood utilization, deforestation, some development works and urbanization causes land cover changes.

Land use applications have significant effect on natural assets including soil, water, supplements, plants and animals. Land use data can be utilized to create answers for natural assets management issues, for example, salinity and water quality. Latest huge impacts of land use incorporate soil degradation, soil erosion and desertification. Land use alteration along with utilization of fossil fuels are the chief anthropogenic origin of carbon dioxide, a prevailing ozone depleting substance. Land use is a portrayal of how individuals use land and financial action. Urban and agriculture land utilizes are the two most ordinarily known land use classes.

4 Results and Discussion

Satellite images are acquired from the website of USGS (United States Geological Survey). Landsat 5 and Landsat 8 satellite data are used having the resolution of 30 m. Images of path and row 145/43 and 145/44 for different years are utilized as recorded in Table No. 1 with their date of acquisition for study (Table 1).

Classified images for years 2000, 2009, 2014 and 2019 are shown Figs. 2, 3, 4 and 5.

Table 1 Details of data required used

S. No.	Acquisition date	Data	Resolution (m)
1	12th February 2000	Landsat data	30
2	03rd November 2009	Landsat data	30
3	17th November 2014	Landsat data	30
4	15th November 2019	Landsat data	30

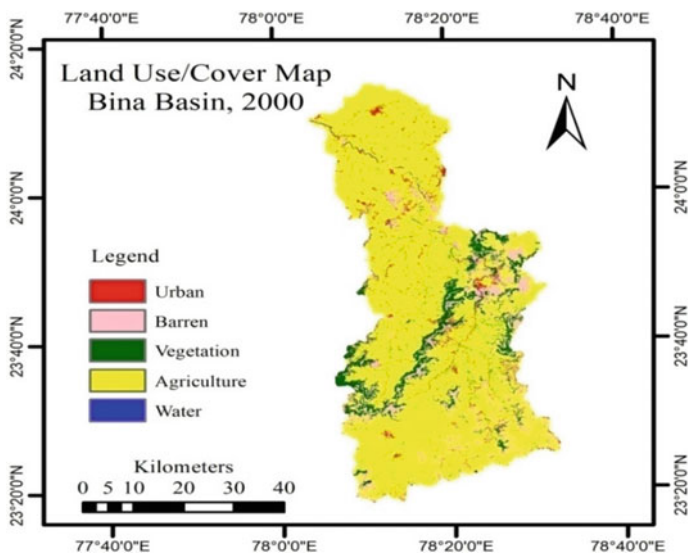


Fig. 2 Land use/land cover map of Bina Basin, 2000

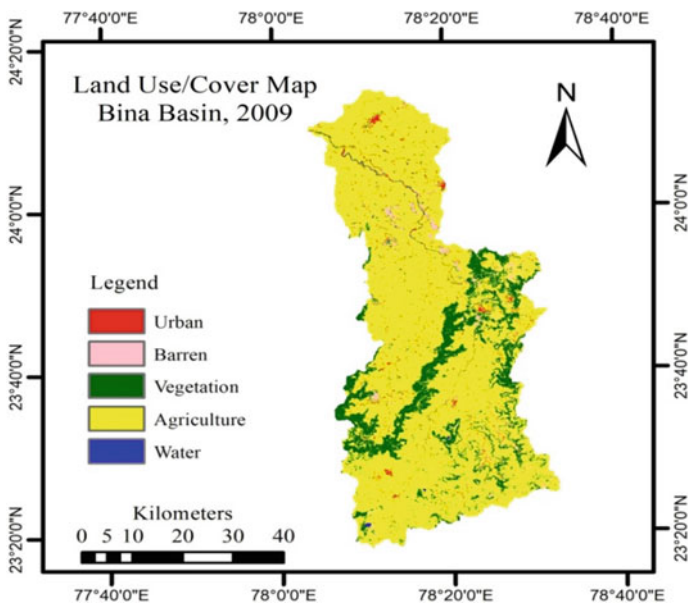


Fig. 3 Land use/land cover map of Bina Basin, 2009

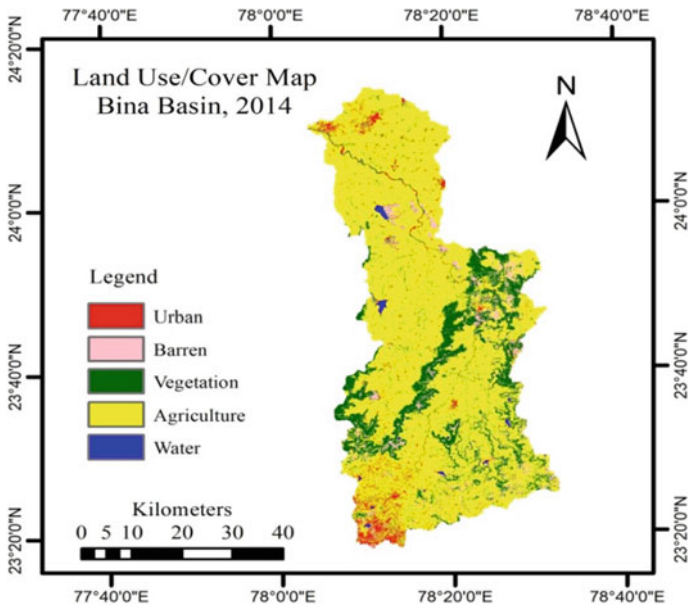


Fig. 4 Land use/land cover map of Bina Basin, 2014

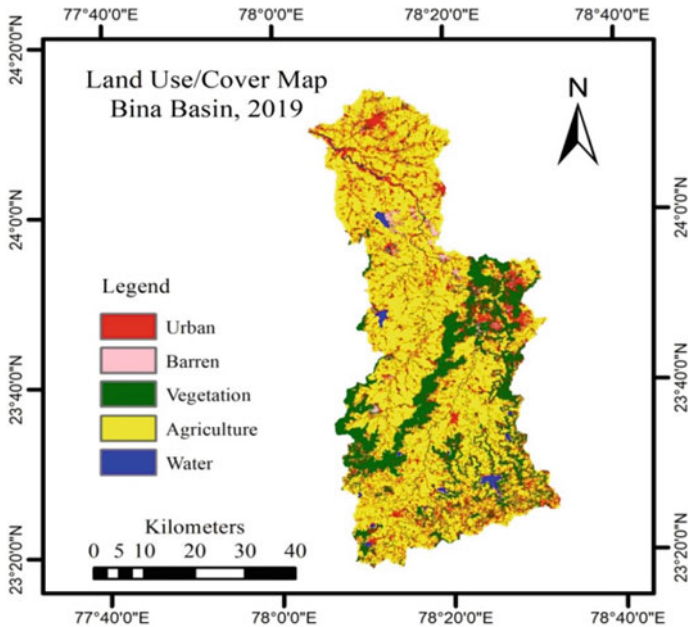


Fig. 5 Land use/land cover map of Bina Basin, 2019

The land use has undergone major changes from year 2000 to 2019. The drastic increase in the built-up area or urban area from 3.12 to 20.25%, an increase in vegetation area from 8.81 to 19.60%, an increase in water bodies from 0.24 to 1.12%, a reduced in agriculture from 77.24 to 57.44% and a decrease in barren land from 10.59 to 1.59% from the year 2000 to 2019 (Fig. 6; Table 2).

This study points examining LU/LC variations happened in Bina Basin in Madhya Pradesh between 2000 and 2019 using remote sensing and GIS. The urban area (3.12–20.25%), vegetation area (8.81–19.60%) and water bodies (0.24–1.12%) have increased and barren land (10.59–1.59%) and agriculture area (77.24–57.44%) have decreased from the year 2000 to 2019. Our outcomes distinctly show that LU/LC variations were huge during the interval from 2000 to 2019. There is noteworthy development of built-up area noticed. This investigation clearly reveals the critical influence of population and its advancement exercises on LU/LC change. The current examination outlines that GIS and remote sensing are significant advancements for

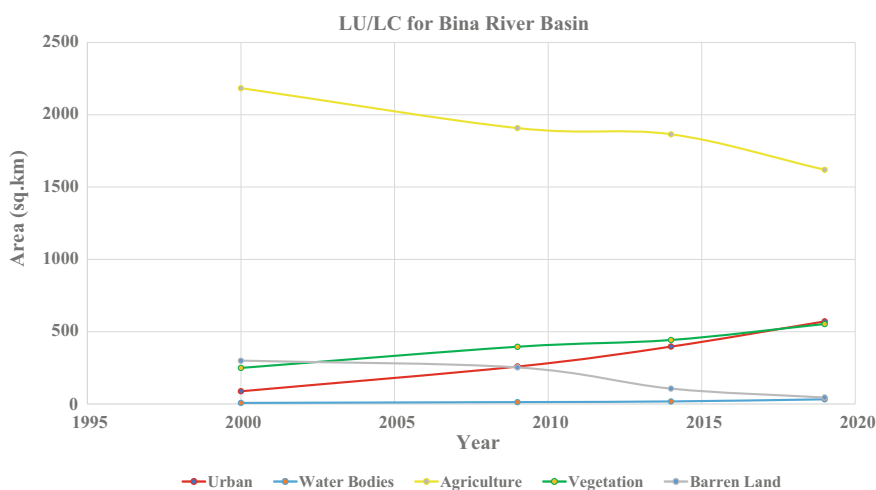


Fig. 6 Graph of land use/land cover of Bina River Basin

Table 2 Attribute table from the year 2000 to 2019

S. No.	Classes	2000		2009		2014		2019	
		Area (km ²)	%Area	Area (km ²)	%Area	Area (km ²)	%Area	Area (km ²)	%Area
1	Urban	88.08	3.12	259.17	9.16	397.02	14.04	577.68	20.25
2	Water bodies	6.99	0.24	12.54	0.44	17.15	0.61	32.67	1.12
3	Agriculture	2184.12	77.24	1907.88	67.48	1864.96	65.96	1619.75	57.44
4	Vegetation	249.05	8.81	395.42	13.99	442.07	15.63	552.73	19.60
5	Barren land	299.30	10.59	252.53	8.93	106.34	3.76	44.71	1.59

temporal examination and measurement of spatial occurrence which is generally impractical to endeavor through ordinary planning strategies. Change discovery is made conceivable by these innovations in minimum time, effortlessly and with greater precision.

5 Conclusion

The outcomes of the present study stance as scientific representation and also the spring of knowledge for collaborator operating for the planning of supportive and embellished land use/land cover management operations. Although, the land use/land cover as a topic is in its prior stages in relation to other natural resource study, and it is suggested that land use/land cover study should be taken all over for useful, elevated and embellished operation of socio-environment elements. The aberrations in land use/land cover require the adoption of technical management methods. The need for administering and controlling of these management actions will lower the rate of the effect of unusual population growth and rapid industrialization.

References

1. G. Veeraswamy, A. Nagaraju, E. Balaji, Y. Sreedhar, Land use and land cover analysis using remote sensing and GIS: a case study in Gudur area, Nellore District, Andhra Pradesh, India. *Int. J. Res.* **04**(17) (2017)
2. S. Reis, Analyzing land use/land cover changes using remote sensing and GIS in Rize, North-East Turkey. *Sensors* **2008**(8), 6188–6202 (2008)
3. H.A. Kaul, I. Sopan, Land use land cover classification and change detection using high resolution temporal satellite data. *J. Environ.* **01**(04), 146–152 (2012)
4. J.s. Rawat, M. Kumar, Monitoring land use/cover change using remote sensing and GIS techniques: a case study of Hawalbagh block, district Almora, Uttarakhand, India. *Egypt. J. Remote Sens. Space Sci.* (2015)
5. P.K. Mallupattu, J.R.S. Reddy, Analysis of land use/land cover changes using remote sensing data and GIS at an Urban Area, Tirupati, India. *Sci. World J.* **2013** (2013)
6. T.R. Nayak, S.K. Gupta, R. Galkate, GIS based mapping of groundwater fluctuations in Bina Basin, in *International Conference on Water Resources, Coastal and Ocean Engineering* (ICWRCOE, 2015)

Biocomposites and Their Applications in Civil Engineering—An Overview



Manish S. Dharek, Jagadish Vengala, Prashant Sunagar, K. S. Sreekesava, Pramod Kilabanur, and Poornachandra Thejaswi

Abstract Biocomposites or green composites are mainly defined as mixture of two or more components in which any building raw materials possess large quantity as matrix and natural fibers possess in smaller quantity as reinforcement. Due to the increase in greenhouse gas emissions and the global energy crisis, the demand for composites with natural fibers and biodegradable resins is increasing due to its low cost, renewable nature, and biodegradability. This paper presents the most comprehensive review on recent studies and development of natural fibers which includes animal-based fibers and various types of plant-based fibers and their potential applications in building materials and construction.

Keywords Biocomposites · Matrix · Natural fibers · Reinforcement · Biodegradable resins

M. S. Dharek (✉)

Department of Civil Engineering, BMS College of Engineering (Affiliated to VTU, Belagavi), Bengaluru, India

J. Vengala

Department of Civil Engineering, Prasad V. Potluri Siddhartha Institute of Technology, Vijayawada, Andhra Pradesh, India

P. Sunagar

Department of Civil Engineering, Ramaiah Institute of Technology (Affiliated to VTU, Belagavi), Bengaluru, India

K. S. Sreekesava

Department of Civil Engineering, Jyothy Institute of Technology (Affiliated to VTU, Belagavi), Bengaluru, India

P. Kilabanur

Ionidea Private Limited, Bengaluru, India

P. Thejaswi

Department of Civil Engineering, Bangalore Institute of Technology (Affiliated to VTU, Belagavi), Bengaluru, India

1 Introduction

Over the past few decades, composite materials have been developed rapidly [1, 2]. Fiber-reinforced plastic composites, typically made of glass, carbon, and aramid fiber have played a prevailing part in different applications due to their high mechanical quality and modulus. In any case, the utilization and dumping of these composites, particularly glass fiber-reinforced plastic (GFRP) composites, have been criticized due of their non-biodegradability nature which rises environmental awareness and attracting the people all over the globe to think about the future materials that could be more sustainable and eco-friendlier in nature [3, 4]. Recently, all composites which are completely biodegradable are reinforced with fibers which are extracted from nature which partially or completely rely on matrix and reinforcement, which are called green composites or biocomposites, have pulled in much interest to fathom these issues. These biocomposites are made from sustainable and renewable materials that biodegrade in an aerobic environment and are expected to utilize in non-structural and structural components. Potential applications for biocomposites comprise framing, walls and wallboard, window frames, doors, flooring, etc., within building while in construction include formwork and scaffolding. The utilization of biocomposites for short-term and adjustable components of structure would minimize landfill waste when the interior design within the structure is changed or in seismic zones where non-structural damage may be necessary after an earthquake [5–7].

2 Review of Literature

Goda et al. [8] studied about the green composites (biocomposites) of different forms like low fibers, unidirectional, textile, and cross-ply and predicted their future developmental trends which will show comparable and predominant mechanical and physical properties when compared to conventional plastic fibers especially GFRP. They also found that proper molding techniques and fiber treatments can provide better composites which can match different property requirements. Ahmed et al. [9] inspected the mechanical and physical properties of concrete using Kantharo Suter fibers as reinforcement. These fibers were used with varying proportions from 0.125 to 1.0% by weight of cement in the concrete specimens and were compared with the cement concrete specimens without fibers. From the results, it was found that addition of 0.375% of fibers was optimum as the compressive strength increased up to 59%, flexural strength up to 9%, split tensile strength up to 40% as compared to specimens without fibers. The addition of fibers also resulted in the reduction of workability up to 15% which could be enhanced by addition of different admixtures. Kavitha et al. [10] studied mechanical behavior of concrete reinforced by bamboo fibers by adding fibers upto 1.25% by weight of cement. The study demonstrated that the use of these fibers in the matrix improves strength, ductility, and post-cracking

load-carrying capacity of the concrete with reduction in the workability. However, further work is required to evaluate the long-term durability of concrete improved with bamboo fiber. Ramakrishna et al. [11] developed natural fiber biocomposites which are derived from coconut fiber powder (CFP) and walnut powder (WP) under loading with different mechanical and destructive tests and determined its behavior in terms of ultimate tensile strength (CFP-23.42% and WP-34.28% higher than steel), yield stress (CFP-26.77% and WP-58.51% higher than steel), hardness (CFP-91 and WP-94), and impact tests (same for all three specimens, i.e., 0.5 Joules) which shows that both composites performed better than the steel specimen. Strimer et al. [12] developed a mix design for the mortar emphasized the effect of addition of natural sheep's wool fibers on various properties of such cement and lime-based mortar. The results show that the fiber addition improves thermal insulation properties, reduces density and at the same time reduction in mechanical properties. As the density of the material decreases with increase in fiber volume fraction, they can be used effectively in non-load bearing applications, false ceiling, and wall partitioning.

3 Natural Fiber-Reinforced Composites

Biocomposite materials for construction must provide satisfactory firmness, quality, ductility, and also durability of buildings. While distinctive bio-based materials would comprise physical properties of special application in building, applications at particular positions because of other variations between chemical and morphological ingredients used in natural fibers and also biopolymers including polyhydroxybutyrate [13]. The large applications of utilizing natural fibers as reinforcements in various components such as cement mortar or concrete are cost-effective materials, renewable nature, and density. Different properties of fiber-reinforced composites are composed by a number of factors as given below

- fiber content, length, and orientation,
- extent and section of fiber-matrix elasticity;
- interfacial bond strength in fiber-matrix;
- class and properties of matrix such as flexible or fragile.

However, the bond strength directly relies on effectiveness of fiber in composites. The breakdown of fiber-reinforced concrete composite can be moderated with fiber and matrix alterations. Fiber changes will restorative chemical composition, dimensional stability, and bond quality in PF cementitious composites. Meanwhile, modification of the matrix containing mixed cementitious materials as a partial substitution of OPC is effective in the prevention of degradation [14]. This proposes that the future of these PF composites is seemed to be brilliant because they are less expensive, lighter, and eco-friendlier than glass fiber composites [15–17].

4 Biocomposite Formation

The uncrushed natural fibers were cleaned, dried at ambient temperature, and treated chemically with the help of isocyanate, washed with a base solution and applied hardener. After treatment, the natural fiber was dried in an oven up to 1200 °C for one or 2 days relying on the technique. Later, reduction of the size in ball is done by milling at 200–300 RPM for about 6 h. The characteristic fiber and polymer matrix were blended in the reactor or z-blade mixer. After the blending, composites were compressed and pressurized up to 150 MPa at 1500–1800 °C for 10 min, and at last dry, the composites are cured in dry atmosphere. This is indicated with a flowchart as shown in Fig 1.

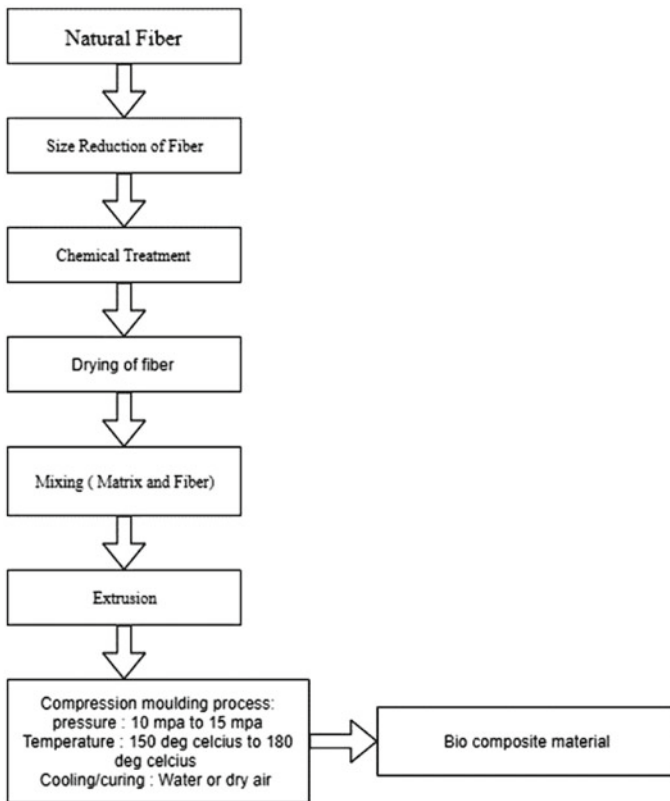


Fig. 1 Flowchart for biocomposite formation et al. [11]

5 Classification of Natural Fibers

The classification of fibers is done based on their origin and is categorized into natural and man-made (synthetic). These natural fibers are further classified into plants, mineral, and animal sources. Plants which produce natural fibers are categorized into primary and secondary relying on their utilization primary plants are raised because of their fibers (e.g., flax, jute, sisal, and kenaf) while secondary fibers, the plants are extracted from the waste product (e.g., pineapple, bagasse, coir, banana, and oil palm). Generally, plant fibers are grouped into bast fibers, leaf fibers, stalk fibers, grass fibers, seed fibers, fruit fibers, and wood fibers.

5.1 *Animal Fiber*

While the other natural fibers include mineral fibers (Asbestos) and animal fibers (spider silk, sheep's wool, and other types of hairs). Changes are found in the mechanical and physical properties of these fibers which are affected by many factors like type of fibers, humidity, and form of fibers (i.e., twined, chopped, woven, or peeled) under different experimental conditions. Animal fibers like wool, feathers, hair, silk are said to be the next most significant resource of natural fibers after plant-based fibers for reinforcing composites. Many sources from each type of animal fibers are wool, silk, hair, and feather.

- Animal hair: fur or wool obtained from animals or from hairy mammals, e.g., sheep's fur, goat's hair, horse's hair, etc.
- Silk fiber: These fibers are accrued during the preparation of cocoons from dried saliva of bugs or insects, e.g., silk obtained from silkworms.
- Avian fiber: These fibers are derived from birds, e.g., feathers and feather fiber.

5.1.1 Human Hair Fiber [18]

Human hair is essentially a biological fiber with nanocomposite microstructures that are well-defined. Hair is a protein filament that develops in the dermis or skin from follicles embedded in it. It is one of mammals defining features [18]. The key hair element is keratin that is tough, soft, insoluble, and quite strong. A crucial factor is that a single hair strand can carry about 100–150 g of load. Hair is resilient and can regain its original position once the deformation load is released. Hair is used in concrete as a fiber reinforcement material because of its greater tensile strength equal to that of the copper wire of equivalent diameter and also available in abundance with low cost. It can also minimize the problem of degradation as it is completely degradable. It can also strengthen the mortar and prevents the concrete from spalling. Human hair fibers improve mechanical behavior of concrete and can possibly be utilized with adequate proportions of cement to improve the characteristic compressive strength,

ultimate tensile strength, and bending strength of concrete. It can even reduce the inner forces by trapping the microscopic cracks from forming inside the concrete. The fineness also prevents bleeding of concrete and thereby reduces the permeability and enhances the surface characteristics of the hardened surface. The cross section of human hair is shown in Fig. 2 (Table 1).

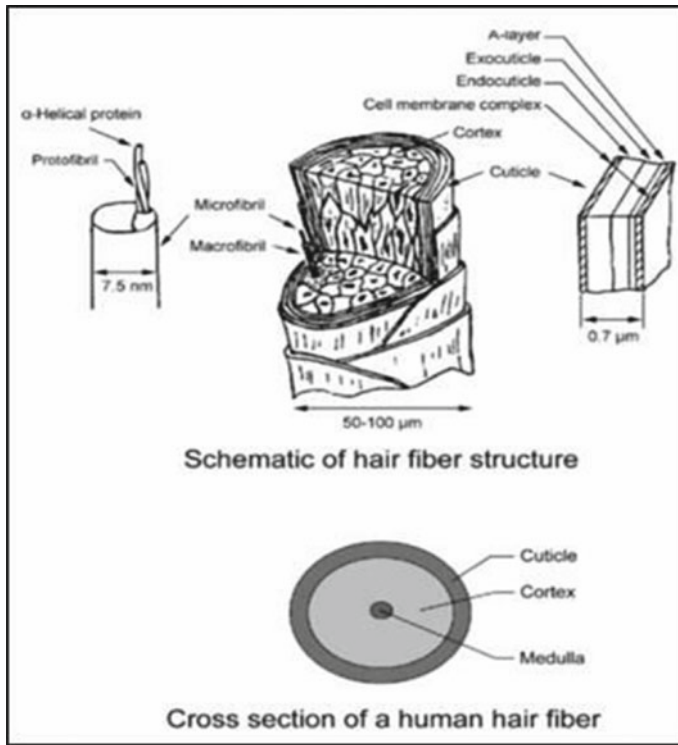


Fig. 2 Schematic of human hair fiber structure and its cross section [18]

Table 1 Physical properties of a human hair [18]

Physical properties	Values
Length (mm)	40
Diameter (mm)	60–100
Plastic modulus (GPa)	3.5
Linear density (g/cm)	1.32
Yield strength (MPa)	74.34
Breaking strength (MPa)	119
Strain at fracture (%)	29
Tensile strength (MPa)	384.79

A problem of non-uniform distribution of hairs is faced while using them as fibers and to tackle this problem, manual hair distribution method in the concrete should be implemented which is a difficult and time-consuming task. By its nature, hair is biodegradable and decomposes on contact with moisture and micro-organisms. So, in environmental conditions which do not encourage microbial attack on the structural element, hair can be utilized as a fiber reinforcement material. Harsh environmental conditions would limit the use of hair as fibers.

5.1.2 Goat Hair Fiber [9]

Goat hair is natural fiber removed from the skin of goat. It is biodegradable, eco-friendly, and elastic, soft, low cost and is available in plenty. As the disposal of hair is big headache during tannery process, hence it can be a good choice for using it as a reinforcing polymer in the biocomposites. Kantharo suter fibers shown in Fig. 3 are categorized as natural fibers, because they are derived from natural sources, i.e., animals. The local significance of the word Kantharo is “goat” and the word suter means “treated goat hair.” Cashmere is known in South Asia as "pashmina." Due to local availability in the Himalayan region, these fibers can be obtained in large amounts at a reasonable cost (at Rupees 10/kg). Historically, fine-haired Cashmere goats have been called *Caprahircus laniger*.

Kantharo suter fiber enhances the mechanical and hardened state behavior of concrete and can be utilized with proper proportions of cement to increase the characteristic compressive strength, ultimate tensile strength, and flexural strength of concrete. The properties of these fibers include preventing cracks formation due to both plastic and dry shrinkage, reducing permeability (prevents concrete bleeding), accumulating higher impact, and concrete abrasion. The fineness of the fibers helps to strengthen the concrete and thus reduces the development and expansion of cracks which ultimately enhance the surface qualities of the concrete (Table 2).



Fig. 3 Portal view of Kantharo Suter fiber [9]

Table 2 Properties of goat hair

Properties	Values
Length (mm)	42–118
Diameter (μ)	76–107
Moisture absorption (%)	7.62
Elongation in shear (%)	9.54–30.69

5.2 Plant Fibers

Plant fibers could be in the form of hair-like materials (cotton, kapok), hard fibers (coconut, sisal) which can be used in powder form or as a bundle of fibers (flax, hemp, and kenaf). These plant fibers can also be divided based on utilization for various purposes.

5.2.1 Coconut Fiber

Coconut fiber generally known as coir and scientifically can be called as *cocos nucifera* which is naturally and widely distributed in tropical countries such as India, Malaysia, Indonesia, and Sri Lanka. Coconut is a member of the palm family which is one of the world's food crops. There is a large amount of waste (coconut outer shell) which is non-food part and is one of the hard-lignocellulosic agricultural wastes. These coconut fibers in their powder form have high toughness among natural fibers. This coconut shell powdered (CSP) composite when loaded under different destructive tests, it outperforms even the steel specimen with respect to various properties such as ultimate tensile strength, yield stress and impact tests [19]. Hence, coconut fibers have potential to be used as low-cost concrete structure, especially in tropical earthquake regions such as Indonesia. Also, more sustainable concrete can be produced by using this fiber and thereby the agricultural waste can be reduced by utilizing these coirs. Whereas, if used these coirs, the specific gravity of concrete would be increased which can further affect in increased weight of concrete. Therefore, the addition of these fibers can adversely affect in the compressive strength of concrete (Fig. 4; Table 3).

5.2.2 Cotton Fiber

Gossypium is the name of the plant which is commonly known as cotton which is widely used for textiles with the help of its fibrous nature. However, cotton fibers can be used as reinforcements for composites with geopolymers. This geopolymer composite is synthesized and reinforced with short fibers of cotton and its mechanical properties such as compressive strength, impact, and hardness are found out using different fiber contents (0.3, 0.5, 0.7, and 1 wt%) [20]. The results show that the



Fig. 4 Coconut shell powder from coconut [11]

Table 3 Properties of CSP specimen and steel specimen [11]

Properties	CSP specimen	Steel specimen
Type	Flat	Flat
width (mm)	13.75	14.33
Cross-sectional area (mm ²)	178.75	189.156
Ultimate load (kN)	2.08	2.12
Ultimate tensile strength (N/mm ²)	14.64	11.21
Yield stress (N/mm ²)	9.04	6.62
Hardness test	91	93
Impact test	0.5	0.5

composite which contains 0.5 percentage of weight of cotton fibers shows optimum and better results in hardness, impact resistance, and compressive strength. Further increase in percentage of fibers may agglomerate the fibers along with reducing the mechanical properties and thereby forming of voids in composites, increasing viscosity in matrix along with weak dispersion of fibers (Table 4).

However, cotton fibers have several usage applications, which include low cost, lightweight, and sustainable with respect to synthetic and plastic fibers when used in composites. It can increase the specific gravity of composites which increase in weight than normal concrete, hence bit expensive in this case.

Table 4 Properties of coconut fiber-reinforced composites with different fiber contents [20]

Cotton fibers (wt%)	Hardness	Compressive strength (MPa)	Impact strength (kJ/m ²)
0	72	19	1.95
0.3	80	26	3.1
0.5	93	46	4.45
0.7	62	34	1.65
1	47	27	1.4

5.2.3 Sisal Fiber

Sisal is a fiber derived from the *Agave sisalana* plant's leaf portion. This plant is a shrub with short and has stocky trunk from which leaves are grown out and looks like an old pineapple plant as shown in Fig. 5. These fibers are mainly found in tropical and subtropical regions like Brazil, Mexico, China, and India (Maharashtra, West Bengal, Andhra Pradesh, Karnataka, and Bihar). Such fibers are removed through a process known as decertification in which the leaves are crushed beaten and brushed away by a rioting wheel loaded with blunt knives, leaving only the fibers. The characteristic compressive strength and flexural strength of concrete can be significantly improved using external sisal fiber wraps [21]. The tensile property of concrete is increased by addition of small volume of fibers. Additionally, increase in bond strength, decrease in permeability as well as seismic load resistance and ductility can also be obtained (Table 5).

These sisal fibers can be used in slab pavements, tunnel works, columns, and bricks. However, addition of these fibers increases workability as this fiber-reinforced concrete should be hand mixed to reduce the breakage of fibers. Therefore, the cost of this type of reinforced concrete is higher when compared to the traditional concrete.

Fig. 5 Pictorial view of sisal plant [21]



Table 5 Properties of various sisal fiber in concrete

% of sisal fiber (by weight) (%)	Grade of concrete	Characteristic compressive strength (cube test value) N/mm ²	Split tensile strength (cylinder test value) kN	Flexural strength (beam test value) N/mm ²
0.5	M20	26	184	2.8
1.0	M20	28	190	3.1
1.5	M20	36.44	250	4.357
2.0	M20	32.49	238	3.290
3.0	M20	28	220	2940

5.2.4 Jute Fiber

These fibers which are grown from jute plant (*Corchorous capsularis*) are available in mostly deltaic regions such as Bihar, West Bengal, and Bangladesh where water is in high quantity. The jute fiber originates from the plant’s stem and outer skin as shown in Fig. 6. Such fibers are extracted through a retting system consisting of bundling and immersing jute stems together in slow running water. Two types of retting are available, i.e., stem and ribbon (outer skin). The stripping process begins after the retting process wherein the non-fibrous matters are scraped off and the fibers are grabbed from within the jute stem. The properties of these fiber composites such as compressive strength, flexural strength, and tensile strength have been found to substantially improve for volume content of 0.1 and 0.25% and fiber cut length of 10 and 15 mm [22]. Therefore, integrating jute fiber into concrete to produce fiber-reinforced composites would be one of the best ways to improve concrete quality. These jute fibers in composites can be used for building columns, interior walls, tunnel works, bricks, etc., while the jute fiber composites have negative applications such as poor workability, inadequacy of roper compaction, and very high risk in fabrication process.



Fig. 6 Raw jute fibers cut length [22]

5.2.5 Kenaf Fiber

Kenaf which is scientifically called as *Hibiscus cannabinus* L. is a plant in the family Malvaceae. These are grown for their fibers and are easily available in Bangladesh, India, China, Malaysia, and some parts of Africa and Europe. These fibers are extracted from the bast (bark) and core (wood). With the use of these fibers in different proportions, eco-friendly bricks are prepared and its properties are recorded and observed. With the increase in percentage of kenaf Fibers, the water absorption capacity of the eco-bricks is increased. The results show that the bricks having 0.5 to 1.5% of fibers can perform well in moderate conditions of weather [23] (Fig. 7; Table 6).

These bricks are used in the construction and manufacturing sector to reduce overall greenhouse gas emissions. Increasing kenaf fibers in concrete bricks may also increase the development of pores in brick microstructures. Hence, these fibers are vastly used in construction sector such as building columns, beams, bricks, and tunnel

Fig. 7 Kenaf fibers [23]



Table 6 Compressive strength of different types of bricks [23]

Specimen	Characteristic compressive strength (MPa)
C73 (MW)	24.13
C73 (SW)	37.92
EB	40.78
PB	34.48
0.5% K	32.36
1.0% K	29.89
1.5% K	26.74
2.0% K	22.71

works. The challenges using these fibers can occur in polar characteristics when inadequate interfacial adhesion between reinforcement and matrix occurs resulting in poor mechanical properties. Also, some other drawbacks are poor workability and cost of fibers which when added in concrete can increase its cost compared to traditional concrete cost.

6 Case Study: The Hemp House [24]

Hemp is a sustainable plant variety belonging to the plant species. Hemp is being extensively used for a variety of applications which include paper, clothing, fabric, biodegradable plastics, insulation, paints, biofuels, food, and animal feed. Hempcrete is a sustainable building material made by combining water, hurds of hemp, and lime-based binder. This material can be utilized to produce various products like fiberboard, wallboard, roofing tiles, insulation, paneling, and bricks. The Hemp House in Mullumbimby, NSW, planned by Barefoot Sustainable Design, is a case of a home fusing hempcrete. This hemp house was worked to act as an illustration of savvy green lodging, with solid hemp being the principal building material. The 300-mm-thick dividers are built from the Australian Hemp Masonry Company (AHMC) folio and hemp. Reused materials have been utilized where practical on the 180 m² home zone, for example, reused cement and wood, while the outer entryways, interior winding flight of stairs and hardwood lumber flooring have been sourced from Gumtree. The house has a northern direction for gathering the winter sun, enormous roof to impede summer daylight and convective cooling. What is more, there is a 15,000 L water tank, sunlight-based high temp water warming and furthermore a lattice intelligent sun-oriented PV framework (Figs. 8 and 9).



Fig. 8 Hemp house in Mullumbimby designed by Barefoot sustainable design [24]

Fig. 9 Hempcrete [24]

7 Conclusion

Based on the above review, it is evident that natural fibers are good choice in reinforcing the composite matrix. Even though both animal-based and plant-based fibers are available, plant-based fibers are most promising in enhancing the properties of the given matrix. Enough studies are conducted on coconut, jute, and sisal fibers, more studies need to be conducted on kenaf fibers for various applications. Local availability of these fibers in abundance and also use of these fibers in variety of applications reduce the burden on materials which are energy-intensive. Use of plant-based materials in reinforcing the fiber composite matrix has become preferred choice for the green buildings.

References

1. M.S. Dharek et al., Experimental investigations on strength performance of the brick produced by blending demolished waste with pozzolanic materials, in *Advances in Sustainable Construction Materials*, ed. by S. Biswas, S. Metya, S. Kumar, P. Samui. Lecture Notes in Civil Engineering, vol. 124 (Springer, Singapore, 2021). https://doi.org/10.1007/978-981-33-4590-4_54
2. M.S. Dharek, K.S. Sreekeshava, J. Vengala, K. Pramod, P. Sunagar, M.V. Shivaprakash, Experimental investigations on utilization of bagasse ash in adobe bricks, in *Sustainability Trends and Challenges in Civil Engineering*, ed. by L. Nandagiri, M.C. Narasimhan, S. Marathe, S. Dinesh. Lecture Notes in Civil Engineering, vol. 162 (Springer, Singapore, 2022). https://doi.org/10.1007/978-981-16-2826-9_31

3. M.S. Dharek, P. Sunagar, K.V. Bhanu Tej, S.U. Naveen, Fresh and hardened properties of self-consolidating concrete incorporating alumina silicates, in *Sustainable Construction and Building Materials*, ed. by B. Das, N. Neithalath. Lecture Notes in Civil Engineering, vol. 25 (Springer, Singapore, 2019). https://doi.org/10.1007/978-981-13-3317-0_62
4. M.S. Dharek et al., IOP Conf. Ser.: Mater. Sci. Eng. **814**, 012040 (2020)
5. S. Christian, S. Billington, *Sustainable Biocomposites for Construction* (Stanford University, USA, 2009)
6. M.S. Dharek, S. Raghunath, P.C. Sunagar, A.H. Bhashyam, K.S. Sreekeasha, Stress strain characteristics of reinforced hollow concrete block masonry melded with mesh reinforcement. IOP Conf. Ser. Mater. Sci. Eng. **814**, 012040. <https://doi.org/10.1088/1757-899x/814/1/012040>
7. M.S. Dharek, S. Raghunath, C.P. Ashwin, Experimental behaviour of unreinforced and reinforced concrete block masonry walls under uniaxial compression, in *Materials Today: Proceedings*, vol. 46, Part 7, (2021), pp. 2462–2467, ISSN 2214-7853. <https://doi.org/10.1016/j.matpr.2021.01.398>
8. K. Goda, Y. Cao, Research and development of fully green composites reinforced with natural fibers. J. Solid Mech. Mater. Eng. **1**(9) (2007)
9. S.I. Ahmed, F.A. Shaikh, S.H. Jakhriani, M.Y. Mushtaq, J.A. Sidiqy, Mechanical behavior of normal concrete reinforced with Kantharo Suter fiber. Civ. Eng. **2**(7) (2017)
10. S. Kavitha, T. FelixKala, Effectiveness of bamboo fiber as a strength enhancer in concrete. Int. J. Earth Sci. Eng. **9**(3) (2016)
11. T. Ramakrishna, A. Sarath Kumar, Experimental investigation on natural fiber biocomposites by using destructive testing. Int. J. Latest Eng. Manage. Res. **2**, 18–25 (2017)
12. N. Štirmer, B. Milovanović, J.M. Sokol, *Cement Composites Reinforced with Sheep's Wool* (University of Zagreb, Croatia, 2014)
13. M.F.A. Yazdi, R. Zakaria, M. Mustaffar, M.Z.A. Majid, *Bio-Composites Materials Potential in Enhancing Sustainable Construction* (Universiti Teknologi Malaysia, Skudai, Malaysia, 2013)
14. R. Ahmad, R. Hamid, S.A. Osman, *Physical and Chemical Modifications of Plant Fibers for Reinforcement in Cementitious Composites* (University Kebangsaan Malaysia, Selangor, Malaysia, 2019)
15. J. Vengala, B.N. Mohanthy, S. Raghunath, Seismic performance of bamboo housing—An overview, in *Proc. of World Bamboo Congress*, vol. 1 (Damyang, Korea, 2015), pp. 389–407
16. J. Vengala, H.N. Jagadeesh, C.N. Pandey, Development of Bamboo structures in India, in *Modern Bamboo Structures*, ed. by Xiao et al (2008) pp. 51–63, ISBN 978-0-415-47597-6
17. J. Vengala, Comparison of embodied energy in different bamboo-based houses, in *Advances in Sustainable Construction Materials*, ed. by R. Pancharathi, B. Sangoju, S. Chaudhary. Lecture Notes in Civil Engineering, vol. 68 (Springer, Singapore, 2020). https://doi.org/10.1007/978-981-15-3361-7_15
18. A. Verma, V.K. Singh, S.K. Verma, A. Sharma, *Human Hair: A Biodegradable Composite Fiber—A Review* (G B Pant University of Agriculture and Technology, India, 2016)
19. S.K. Ramamoorthy, M. Skrifvars, A. Persson, *A Review of Natural fibers used in Biocomposites: Plant, Animal and Regenerated Cellulose Fibers* (Swedish Center for Research Recovery, University of Borås, Sweden, 2015)
20. T. Alomayri, I.M. Low, *Synthesis and Characterisation of Mechanical Properties in Cotton Fiber-Reinforced Geopolymer Composites* (Curtin University, Australia, 2013)
21. Y. Li, Y.-W. Mai, L. Ye, *Sisal Fibre and Its Composites: A Review of Recent Developments* (The University of Sydney, NSW, Australia, 2006)
22. M. Zakaria, M. Ahmed, M.M. Hoque, S. Islam, Scope of using jute fiber for the reinforcement of concrete material, Textiles and clothing sustainability (2011)
23. H. Abdullah, A.K. Jamaai, *Properties of Eco-Brick Manufactured Using Kenaf Fibre as Matrix* (Universiti Pendidikan Sultan Idris, Malaysia, 2015)
24. A. King, Case Study: The Hemp House, NSW, Australia. <https://build.com.au/case-study-hemp-house>

Analysis and Design of Pipe Rack Structures: A Review



Jamaluddin Maghrabi, Prerana Landge, and Riya Kotian

Abstract This study evaluates the design and analysis of pipe rack structures. Pipe rack is the most important structure in oil and gas, refineries, petrochemical projects, power plants and many other industrial structures. For most loads, the pipe racks were designed as primary critical loads and pipe loads. In this report, the analysis of the pipe rack with sufficient loads and suitable configuration was performed using various software such as STAAD Pro, ANSYS and SAP in this study. This study also aims to analyse structures considering pipe and pipe rack interaction in order to solve current issues. As per the European and Italian codes, the design and analysis of pipe rack, for both static and dynamic, were done in linear and nonlinear systems. The behaviour of pipe rack can not be judged by nonlinear static analysis. Inquisitive results reveal that scaling method was coordinated with contemporaneous model and was relevant for the design of the supporting structure.

Keywords Pipe rack · Dead load · Live load · Wind load · Pipe empty load · Pipe full load · Oil and gas · Refineries · Petrochemical projects and Power plants

1 Introduction

The foremost cause of losing life is crumbling of structures. As per the latest learnings, pipe racks lead to the damage in pipes during an earthquake which is one of the paramount causes of damage in pipes. The principal purpose of this analysis is to resolve the issues of present techniques used to design and analyse a pipe rack. In this study, a fixed nonlinear modelling in SAP and CAESAR is also used to analyse

J. Maghrabi (✉) · P. Landge · R. Kotian
Department of Civil Engineering, Terna Engineering College, Nerul, Navi Mumbai 400706, India
e-mail: jamaluddinmaghrabi@ternaengg.ac.in

P. Landge
e-mail: preranalandge@ternaengg.ac.in

R. Kotian
e-mail: riyakotian@ternaengg.ac.in

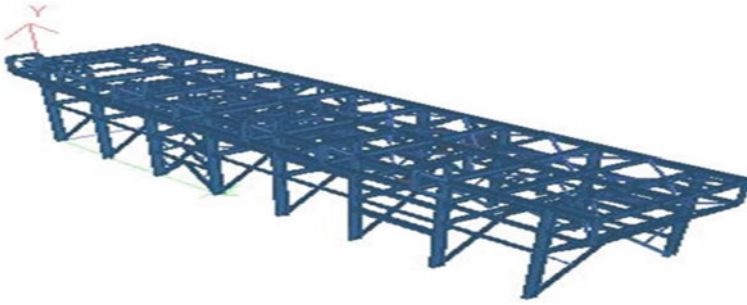


Fig. 1 Pipe rack model in 3D rendered view [1]

the techniques. The natural disasters themselves are believed to never destroy human beings; it is a poorly designed system that destroys. Thus, the system needs to be adequately tested for different natural hazards such as earthquake, cyclones, floods and typhoons. In STAAD Pro model, primary loads are applied, where appropriate to the structure and elements in the form of 46 load cases. All primary loads including dead loads, live loads, wind loads, seismic loads, test loads, working loads, etc. In these papers, each load case is defined in detail.

The aim of this study was also to carry out the check of the behaviour of structure in each approach (modular concept and normal stick-built approach) and cost comparison in terms of design results and material usage. After the STAAD analysis, the deflections found in tiers at the different levels in modular pipe rack structure were comparatively more in values than that of normal pipe rack structure. It was because of the additional analysis of the structure during transportation phases. Two separate divisions, namely serviceability check and strength design check, have placed design system in STAAD model. Various results obtained from the STAAD model were seen in the form of images. The pipe rack model is comprised of 1349 members, 1247 beams, 16 columns and 86 bracings (longitudinal, lateral and cross-bracings) as shown in Fig. 1.

2 Design Methodology

All the preceding papers state that the design of the PR18-01 pipe rack is based on standard load data from the mechanical and piping departments. In general, the architecture is followed according to the ASCE 07 and PIP (2007) STC PIP 01015 requirements.

Model Loads Considered and Code Charging Specifications:

- (1) **Dead Load—DL:** The mass of the superstructure composed of the self-pested of structural steel members, handrails and grating weight shall be called dead load. The grating self-weight shall be considered as 0.5 kN/m^2 . Additional

load of 12% of the structure's self-weight against attachment plates shall be considered [2].

- (2) Live Load—LL: Live loads on the platforms, walkways and staircases shall be considered dependent on use and design.
- (3) Fire Proofing Load—FP: The weight of the fire-proofing material used to secure the building from fire hazards shall be considered. Fireproofing weights are measured using 34-mm-thick Fendolite-MII (Unit weight = 7 kN/m^3) applied to sizes greater than 200 mm (in either dimension) in the steel profile type. For size steel profile, 200 mm or less solid fill is to be considered. Fireproofing shall be performed on the basis of measurements of fire hazards. In DL case, this load is to be included.
- (4) Pipe Empty Load—PE: The blanket load of 1.1 kN/m^2 for pipes less than 12 in. and the actual empty weight for pipes greater than or equal to 12 in. as per the piping discipline given.
- (5) Pipe Operation Load—PO: The blanket load of 0.6 kN/m^2 for pipes less than 12 in., and the actual content weight for pipes greater than or equal to 12 in. as the piping discipline provides.
- (6) Pipe Hydro-Test Load—PT: PT is the water mass within the pipe during the hydro-test. It is believed that the two biggest pipe sizes per tier on the rack are concurrently checked for hydro-test. A uniformly distributed load of $0.6 \text{ kN/m}^2 \text{ m}$ can be considered for pipes of less than 12-in. diameter where a more definite value for the weight of water in the pipes cannot be calculated. The loads from water weight in the 12-in. diameter and above lines shall be applied as concentrated loads at the pipe locations as shown in the pipe configurations and load information.
- (7) Longitudinal Pipe Friction Forces (PFL): A longitudinal horizontal force due to pipe friction equals to 10% on each pipe supporting beam of the pipe rack of the pipe operating weight (empty pipes + pipe contents) is applied. The loads above shall be taken as uniformly distributed for narrow bore lines (less than 12-in. diameter). The friction loads shall be deemed to operate on the beam at the respective pipe locations.
- (8) Transverse Pipe Friction Forces (PFT): On-pipe supporting beams of the pipe brace, a transverse horizontal force due to friction equal to 5% of the pipe operating weight (empty pipes + pipe contents) shall be applied. The loads above shall be taken as evenly distributed for narrow bore lines (less than 12 in. in diameter).
- (9) Pipe Anchor Forces—PAL & PAT: Longitudinal and transverse anchor/guide forces.
- (10) Wind loads on Pipe rack.

To analyse the conduct of the structure and to obtain the perfect superstructure and substructure sections, various simple load cases as described were contemplated that are widely utilized in the oil and gas industries. In Kuwait, piping stress load from a regular firm was used to load the present geometry for sideway conduct of

the building and above wind load and seismic framework is included in the thesis as well (Figs. 2 and 3).

Basic wind speed, $V = 45 \text{ m/s}$		Considered for Kuwait
Velocity pressure, $q_z = 0.613 \times K_z \times K_{zt} \times K_{d} \times V^2 \times I = 0.61$		Cl. 6.5.10 of ASCE7-05
Topographic factor, $K_{zt} = 1$		Cl. 6.5.7 of ASCE7-05
Wind directionality factor, $K_d = 0.85$		Table 6-4
Occupancy category = III		Table 1-1
Importance factor, $I = 1.15$		Table 6-1
Exposure, C.Cl.		6.5.6.3 of ASCE7-05
Velocity pressure exposure coefficient, $K_z = 2.01 \times (Z/Z_g)^{2/\alpha}$		Table 6-3
Height of Structure	$Z \text{ varies}$ $Z_g = 274 \text{ m}$ $\alpha = 9.5$	Table 6-2 Table 6-2

Fig. 2 Wind load data [3]

Seismic X EQX:	
Applicable Standard = UBC-97	(as per DBR Cl.7.1.6)
Seismic Zone = 1.0	(as per DBR Cl.7.1.6)
Zone Factor = 0.075	(as per Table 16-I of UBC)
Importance Factor, $I = 1.50$	(as per Table 16-K of UBC)
Response reduction factor, $R_w = 5.60$	(as per Table 16-N of UBC)
Type of soil = Medium	

Fig. 3 Seismic load data EQX [3]

3 Analytical Study

In the research of J. K. Sumanth and Dr. C. Sashidhar, its key goals were:

- (1) Study and configuration of stainless-steel pipe rack members using manual inspection according to codes specifications STC PIP 01015: ASCE 07 and PIP (2007).
- (2) Model the steel pipe rack and analyse it using STAAD Pro V8I.
- (3) Manual contrast pipe rack system with STAAD Pro V8I.

SAP and CAESAR model:

According to research by Akbar Shahiditabar (pipe and pipe rack interaction-2013), the operation of pipe steel rack supports the pipes. So, the conduct of pipe rack impacts the behaviour of pipe directly. As per his research, pipe racks lead to the damage in pipes during an earthquake which is one of the paramount causes of damage in pipes. A fixed nonlinear modelling in SAP and CAESAR was also used to compare his technique and analyse it with the present technique [4].

Different techniques have been designed to simplify the study and enable the engineer to partially comprehend the result of stability through hand calculations. The foremost cause of losing life is crumbling of buildings. Natural disasters are believed to never destroy humans; it is poorly built buildings which kills. Thus, the system needs to be properly tested for various natural disasters such as earthquake, cyclones, floods and typhoons.

In a paper by Nitesh J Singh and Mohammad Ishtiyaque, in STAAD model, primary loads are applied in 46 load cases for the structure and the components,

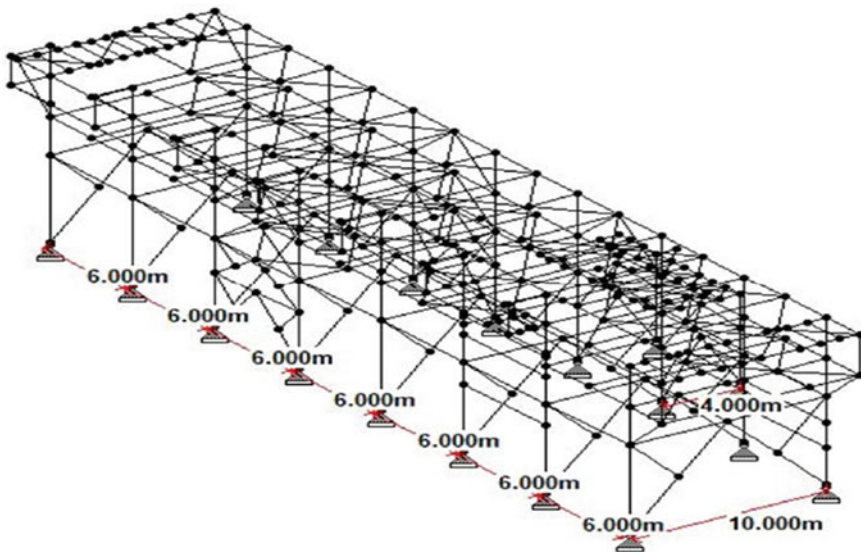


Fig. 4 View of the length of pipe rack and second bay

as necessary. Loads comprise of all the primary loads including dead loads, live loads, wind loads, seismic loads, test loads, working loads, etc. Every case of loads is detailed in these papers. Two separate divisions, namely serviceability check and strength design check, have placed design system in STAAD model. LRFD technology was used.

Seismic design consideration:

In a thesis by Luigi Di Sarno and George Karagiannakis, another aspect came into existence that the pipe rack's seismic design procedure which can be accompanied by rehearsing and executive professionals needs synchronization with various regulations just like shown by the author. As long as midstream and descending provisions are set down appearing in coastline areas to which it may be detached as well as capable of being liquefied, it is one more facet which are tested by the writers which relate to the production of soil. In his paper, the author points to clarifying design structures that differentiate the form of structure being dealt with in a more well-founded way to construct the seismic design. If the behaviour factor was calculated and the values of an interstorey drift ratio (IDR) steel pipe rack were approximated, parameters of the seismic response continuum, including recurrence time (RP), limit states (LSs), q -factors, π -factors and soil classification as indicated by EN (including Italian) and AM codes were collated to identify potential differences [5].

Comparison of methods of stability analysis:

David A. Nelson compared three stability analysis techniques of AISC 360-10 for standard pipe rack system, with the STAAD Pro V8i 3D software. For the chosen model, every technique for analysis of stability reached AISC 360–10 demands [6].

1. A method for first-order analysis
2. Effective length process
3. Direct analysis technique.

For the investigation and collation of all the three techniques of stability analysis, together pinned and fixed base support state models were evolved.

One of the researches by Preeti Rathore and Prof. D. H. Raval stated that the pipe rack [7], as an absolute construction system along its structural components should execute their tasks appropriately and carefully, with relevant grade of safety throughout design life. It has to resist all measures, comprising applied and persuaded loads as well as environmental impacts accountable to happen, holding on to its structural integrity, and also resist accidental loads and earthquake loads without giving rise to destructions. Industry practices structural design criteria (PIP STC01015) have tried to establish a steady design standard, but a code document should be noted. Steel pipe racks are widely used to promote quick and versatile construction; however, their prime demerits are fire hazard and economy. Here the purpose of the study was to develop a hybrid pipe rack made of RCC support that combines the advantages of steel and concrete (better resistant to fire).

Modularization:

One another different aspect regarding pipe rack was brought into existence by Ashit K. Kikani and Vijay R. Panchal. They stated that additional technologies and innovative methods are being traversed for a swift and economical work in construction sector. As a superior choice to this, “modularization” technique proves a lucrative option in the field of industrial sector. Modularization is falsifying and pre-gathering plant elements distant from the actual plant location. A module is a product arising from a string of far assembly actions, the great transportable unit or element of a provision and a volume contoured with all structural components, ends and process elements which are planned to occupy that area. It imparts many benefits in the construction process. They further compared (normal stick build approach and modular approach) both the structures by applying knee bracing system in STAAD Pro software [8].

Model Analysis:

Ali Reza Keyvani Boroujeni and Mehdi Hashemi said that within almost all features, designing plans were power-based as well as needed ample firmness towards every component of the resistant structure to lateral load. Hence, the seismic load has been removed from piping model and added to structural model for the supporting system design. Despite conducting the pipes and supporting structure simultaneously, pipe design and supporting structure are distinct. In this study, ASCE technique is judged in this analysis, and the scaling process has been also proposed on the basis of the same procedure. Linear and nonlinear examinations of contemporaneous model were seen like a point of reference for this evaluation [9].

4 Experimental Study

Similar thesis came when Byungyur Lee presented his paper, a modular execution strategy (MES) directs at relocation of the construction and collection pieces to potentially separate locations where the building and collection circumstances are better agreeable. After development and assembly, the modules are moved to the construction site where the final execution was managed. This theory pointed at locating the most economical way to accomplish a scalable implementation plan to construct pipe rack structures of a project that an engineering firm Fluor B. V. is currently being executed in Kuwait. A pipe rack is basically a steel structure that is built to comprehensively identify and hold several levels of pipes also provides ground clearance for industrial plants such as chemical plants, power plants or refinery.

Examination of three alternatives to different MES formats was done. In the absence of their base columns, the first alternative intends to transfer at most higher bits of the pipe racks and install the base columns at the insertion place. The second alternative intends to transfer all the pipe racks with base columns that are thickened due to provisional bracings.

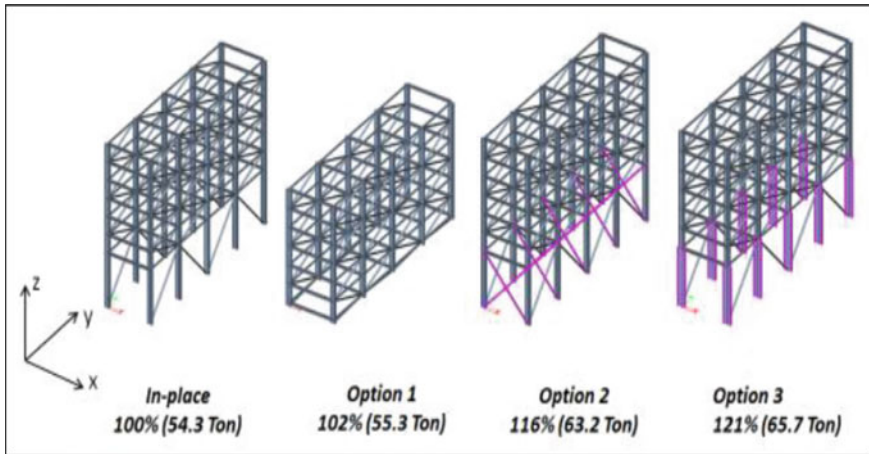


Fig. 5 Comparison of total steel quantities of options [Byungyur Lee] [10]

The last alternative intends to transfer entire pipe rack with reinforced columns with a great dimension of profile. 27 representative layouts of the theory's pipe racks were chosen in order to consider various pipe rack sizes. These pipe racks were built with a quasi-static analysis technique for resisting in-place loadings and sea-transport loadings. Owing to a vessel's movements, the sea-transport loadings are forces and vital sea-transport loads come from roll + heave and pitch + heave. Following the accomplishment of the design, steel quantities were defined for each choice (Fig. 5).

In the model by Ali Reza Keyvani Boroujeni and Mehdi, the piping structure carries three pipe racks- one pipe bridge, four flare pipes and many sleepers. In pipe racks and pipe bridge, respectively, steel bracing frames and concrete cantilever bent as lateral resistor framework are installed. The anchor positioning is examined considering design of pipe stress. There is usage of three types of pipe supports in this study. The weight along with lead support is presumed as 12 m long, and the stopper is contemplated onto fixed sleeper and pipe racks. Hence, the pipe bridge has only support for guidance and weight. Pipe bridge length is chosen as 24 m, and every bent carries five-round columns and a single cap.

5 Conclusion

The researchers concluded that in all supports, framed links connecting pipe and pipe rack were suggested. Supporting beams were placed at 6 m c/c to hold up the pipes greater than 12' diameter. Hence, the number of continual horizontal members was decreased by a huge scale. Project bracings offered in K and L shape helped in lowering the member size along with all-inclusive project costs. Also, pipes were built in all points to pipe rack, and at the same time, the pipe and supporting structure

were designed. This was evaluated by modelling in SAP and CAESAR programs with nonlinear static analysis which out-turns in the confirmation of their claims. He concluded that making use of frames including knee brace connections lowers the quantity of utilized materials up to 29%. In all supports, suggestion of framed connections between pipe and pipe rack was made.

Generally, the study revealed that the pipe rack design was hardly simple, and hence, contemplation has been stated, e.g., the approach of conduct factor selection and analysis. In case of uneven pipe racks, the reaction of which was controlled due to non-structural elements and other non-construction forms, the perfect option may probably be considered for the dynamic analysis. A significant framework in accurate and guarded design of the pipe racks was also the contact in between the rack and piping order, and therefore, a sensitivity analysis must be used to determine the contact grade.

Normally, the first-order technique shows to be intrinsically better conventional on the basis of analysis suppositions that stand up demand to description for the second-order results along with depletion in inflexibility. The fixed bottom model also tends to have lower contortions than pinned-based model even when smaller member sizes were used. When direct analysis method was compared to the first-order technique, it was observed that capacity ratio demand was somewhat much more while using the first-order technique. Modular structure possesses heavier steel design, it still proves as much economical in aspects of many benefits like saving of time, site constraints, unskilled labours and bad weather condition. Knee bracing at the base of bottom beam lowers overall deflection values in the tiers at different levels. Hence, it should be used in order to make lighter design in modular structure. Other features that are strenuous to indicate in cost expressions, such as operational struggling, protection risk as well as project plan, were never considered. Hence, in sequence to confirm the captivation of every choice in brief, it is recommended to absolutely evaluate such mentioned features.

References

1. J.K. Sumanth, C. Sashidhar, Design and analysis of pipe rack system using STAAD PRO V8i software. 6(IX). ISSN: 2321-9653; IC Value: 45.98; SJ Impact Factor: 6.887, Sept 2018. Available at www.ijraset.com
2. R. Drake, R. Walter, *Design of Structural Steel Pipe Racks* (2014)
3. N.J. Singh, M. Ishtiyaque, Optimized design and analysis of steel pipe racks for oil and gas industries as per international codes and standards (2016)
4. A. Shahiditabar, *Pipe and Pipe Rack Interaction* (2013)
5. L.D. Sarno, G. Karagiannakis, *Petrochemical Steel Pipe Rack: Critical Assessment of Existing Design Code Provisions and a Case Study* (2019)
6. D.A. Nelson, Walla University, *Stability Analysis of Pipe Racks for Industrial Facilities* (2012)
7. P. Rathore, D.H. Raval, *Comparative Study and Cost Evaluation of Combined Pipe Rack and Steel Pipe Rack* (2016)
8. A.K. Kikani, V.R. Panchal, *Comparative Study of Pipe Rack Structure with Modular Concept and Normal Stick-Built Approach Using ASCE 7-02* (2016)

9. A.R.K. Boroujeni, M. Hashemi, Linear and nonlinear analysis for seismic design of piping system. Acad. J. (2013)
10. B. Lee, *Steel Quantity and Cost Comparison of Modular Construction Options for Sea-Transported Pipe Racks* (2017)

Removal of Methylene Blue Using Activated Carbon Prepared from Waste Fruit (Orange) Peels



Shantini A. Bokil and Niraj S. Topare

Abstract Many industries such as cloth, paper, leather, plastic, and so on produce a significant amount of wastewater with color for a day now. The presence of dye materials has a direct effect on water quality, and the elimination of this form of pollutant is of prime importance. Activated orange peel carbon was prepared and used to extract methylene blue (MB) from aqueous solutions. The impacts of different factors were examined, such as adsorbent concentration (0.2, 0.4, 0.6, 0.8, 1.0 g/L), initial MB concentration (100, 200, 300, 400 ppm), temperature (40, 50, 60 °C), contact time (10, 20, 30, 40, 50, 60 min.), and pH (3, 5, 7, 9, 11). Maximum adsorption has been found to occur at an adsorbent concentration of 0.8 g/L, a dye concentration of 100 ppm, a contact time of 50–60 min, and a Ph of 11. The experimentally collected data were analyzed by a comparative study with commercial activated carbon (CAC), and it can be concluded that activated carbon prepared from orange peel gives a higher percentage of removal as compared to commercial activated carbon at 100 ppm, 60 °C, 0.8 g/L adsorbent, and pH 11. Results of this study showed that activated carbon made of orange peels could be used as an adsorbent to effectively remove MB from aqueous solutions.

Keywords Activated carbon · Methylene blue · Orange peels · Dye

1 Introduction

Adsorption has acquired significance as an industrial-scale purification, separation, and recovery method over the last few decades [1]. Maybe one of the most

S. A. Bokil (✉)

School of Civil Engineering, Dr. Vishwanath Karad MIT World Peace University, Pune 411038, India

e-mail: shantini.bokil@mitwpu.edu.in

N. S. Topare

School of Chemical Engineering, Dr. Vishwanath Karad MIT World Peace University, Pune 411038, India

e-mail: niraj.topare@mitwpu.edu.in

frequently used adsorbents for environmental applications in the industry is activated carbon (AC) [2]. Activated carbons are extremely microporous carbons with both high internal surface area and porosity, and the most common commercially used adsorbents for the removal from air and water streams of organic and inorganic contaminants [3]. Low-inorganic materials can be used as raw material for processing activated carbon for any cheap product with a high carbon level. The world demand for virgin activated carbon is forecast to expand to 1.7 million metric tons by 9% per annum through 2014 [4, 5]. Acceleration and swift industrialization will benefit from an aggressive carbon demand for the global environmental movement. The use of AC in the pharmaceuticals field provides the best prospects of growth in most emerging and industrialized countries [6, 7].

In addition, environmental problems in developing countries will drive new growth in water treatment applications which are now the biggest single field in developed countries [8]. In addition to the need for clean drinking water, government environmental regulations that differ by area often significantly affect the demand for AC in this area. The high carbon adsorption capacities of activated carbon correlate properties, such as the base, the porous volume, and the porous size distribution (PSD) [9, 10]. The specific characteristics are dependent on the form and activation process of raw material used in AC preparation. The literature review reveals that several attempts to extract low-cost activated carbons from orange peels have been made. New precursors in the preparation of AC are strongly required, response to the growing demand for AC, which should be cost-effective at around the same level as the commercially available AC [10, 11]. Whereas a range of raw materials has been investigated in earlier studies scientists also try to explore new materials for the creation of AC based on their availability and their suitability for AC processing [11]. Usage of orange peel as raw material for the preparation of activated carbon has, however, increased substantially in recent years [12].

In order to determine the suitability of prepared AC orange peel as adsorbents for dye removal. On orange peel AC, batch experiments were conducted. The purpose of this study is, therefore, to observe the impact of process parameters such as adsorbent concentration (0.2, 0.4, 0.6, 0.8, 1.0 g/L), initial dye concentration (100, 200, 300, 400 ppm), temperature (40, 50, 60 °C), contact time (10, 20, 30, 40, 50, 60 min.), and pH (3, 5, 7, 9, 11) on MB removal. However, the adsorption operation of orange peel AC for MB removal has been less recorded in comparison with other traditional adsorbents.

2 Methodology

2.1 Preparation of Activated Carbon

From nearby juice vendors, the raw material (orange peels) needed for the preparation of AC was collected. Then collected orange peels were washed through a 60-mesh

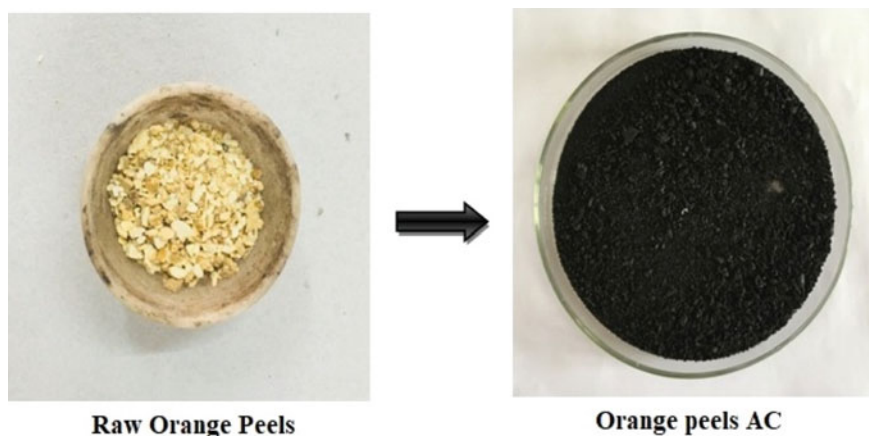


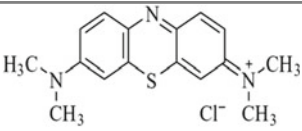
Fig. 1 Raw orange peels and orange peels activated carbon

sieve to clear soil, dried, and crushed sieve. Many acids are tested and used for the development of AC as a chemical activation agent. Analytical (AR) grade was used for all chemicals, and the glassware was cleaned with doubled distilled water. To prepare AC from raw orange peels, the chemical activation method was used. The carbonization of the materials was carried out at 200 °C for two hours in the first stage and allowed to cool at room temperature and activation is done in the second step. 50 g of each sample was combined with 50 ml of H_3PO_4 after sample preparation. The samples were impregnated for 1 h in the muffle furnace at 450 °C. To clean the base content of the prepared AC, washing of the prepared sample was carried out. The washing process continued until it reached pH 7 and then dried the samples in the oven. Figure 1 shows the raw orange peels and orange peels activated carbon prepared from chemical activation method.

2.2 MB Dye Solution Preparation

As it is readily available and typically one of the pollutants of wastewater, the dye is chosen for the current research work is MB. For this reason, to prepare a stock solution of 1000 ppm, an appropriately weighed quantity of the dye is dissolved in distilled water. The double beam UV-spectrophotometer (Model: LT-2900) was used to assess the dye concentration using absorbance values determined before and after treatment. The desired concentration was established by successive dilutions. The typical properties and structure of methylene blue as shown in Table 1.

Table 1 Typical properties and structure of MB

Chemical Formula	C ₁₆ H ₁₈ N ₃ SCl
Chemical structure	
Molecular weight	319.85 g/mole
Type of Dye	Basic blue
λ max	665 nm

2.3 Batch Adsorption Studies

The experiments were performed to study the adsorption of dye using activated carbon orange peel as an adsorbent. In batch adsorption tests, different important parameters are identified, such as the dose of adsorbents (0.2, 0.4, 0.6, 0.8, 1 g/L), the initial concentration (100, 200, 300, 400 ppm), the pH (3, 5, 7, 9, 11), the contact time (10, 20, 30, 40, 50, 60 min.), and the temperature (40, 50, 60 °C). Using a fully mixed batch reactor (CMBR) process, the adsorption experiments were carried out. Using UV–visible spectrophotometers at the respective wavelengths, the concentrations of methylene blue dye in wastewater in the supernatant solution were measured before and after adsorption. It was then measured using a normal calibration curve for wastewater concentration. Under similar conditions, every experiment was duplicated and average values were used for further calculations. Under a fixed interval of time, the suspension was subject to adsorption. A sample with the support of a pipette was taken out at various time intervals. The equilibrium adsorption quantity, q_e (mg/g), was determined by:

$$q_e = [(C_0 - C_e)V]/X \quad (1)$$

where q_e = amount of adsorbed methylene blue dye per adsorbent unit mass (mg/g), C_0 = initial methylene blue dye concentration in wastewater (mg/L), C_e = final methylene blue dye concentration in wastewater (mg/L), V = solution volume (mL), X = the dosage used for dry adsorbent (gm).

Table 2 Elemental analysis of adsorbents by XRF method

Element	Symbol	Weight in percentage
Carbon	C	48.08
Oxygen	O	43.97
Aluminum	Al	0.12
Silicon	Si	1.91
Phosphorus	P	4.92
Iron	Fe	0.33
Copper	Cu	0.39
Zinc	Zn	0.26

3 Results and Discussions

3.1 Characterization of Orange Peel AC

The adsorbents used in the current investigation were the activated carbons of orange peel. Bulk density, surface area, and calorific value are the physicochemical characteristics of the adsorbents used for their characterization. The test results show that the bulk density, specific surface area, and calorific value of activated orange peel carbons are, respectively, 0.6 g/cm³, 316.2 m²/g, and 6720 kcal/kg. In order to find out the form and concentration of crystallographic structure components, the elemental analysis was performed. The outcome shows that when the AC was used as an adsorbent, eight components were found to help enhance the adsorption process. The elemental analysis of AC generated from orange peels by the XRF method is shown in Table 2. The data show the concentration of the various elements present in the sample that may be used for the analysis of adsorption.

3.2 Effect of Orange Peel AC (Adsorbent) Dosage

Methylene blue adsorption was examined using the following constant values, 100 ppm dye concentration, 11 pH values, 60 min. contact time, 60 °C temperature, 150 rpm stirring speed, and various adsorbent concentrations (0.20–1.0 g/L). As in Fig. 2, the removal effectiveness also increases with a rising concentration of adsorbents can be seen clearly. The removal dye percentage rises from 41.60% to 96.02% as the adsorbent concentration increases from 0.2 to 1.0 g/L. It is the product of an enlarged region and activity centers with an increased adsorbent concentration. As seen in Fig. 2, the percentage change in the suspended color is very small and when the adsorbent is 0.2 g/L or higher the value is reached.

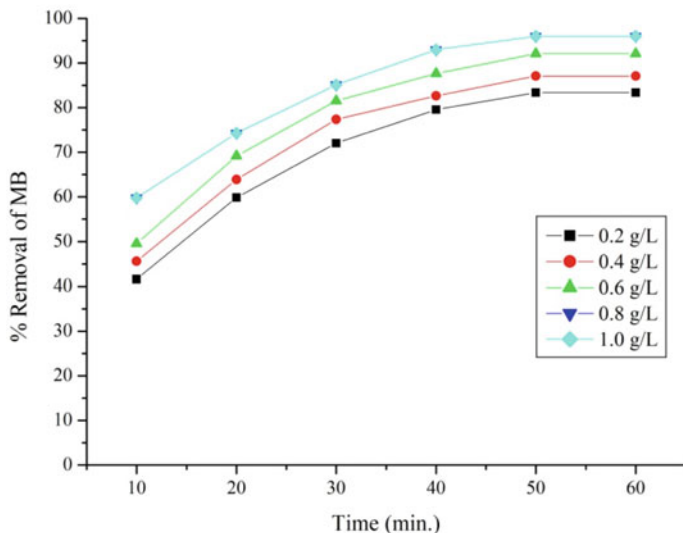


Fig. 2 Effect of adsorbent dosage at 60 °C, 11pH, 100 ppm

3.3 Effect of Concentration of MB

The following constant values were used to investigate methylene blue adsorption: adsorbent concentration of 0.8 g/L, 11 pH value, 60 min. contact time, 60 °C temperature, 150 rpm stirring speed, and various MB concentrations (100, 200, 300, 400 ppm). It is apparent, as in Fig. 3 that the removal dye percentage also increases with increasing MB concentration. The percentage of removal dye decreases from 96.80 to 81.79% as the MB concentration rises from 100 to 400 ppm.

3.4 Effect of Solution pH

In conditions of 100 ppm of dye solution concentration, 0.8 g/L of adsorbent concentration, 60 min. of contact time, 60 °C temperature, and 150 rpm of stirring speed, the pH value effect of the solution was determined for the adsorption phase. As can be seen in Fig. 4, dye solution pH ranged between 3 and 11 for MB removal. A rise in the percentage of removal dye was observed by increasing pH in this sample, as Fig. 4 indicated at pH values of 3, 5, 7, 9, and 11.

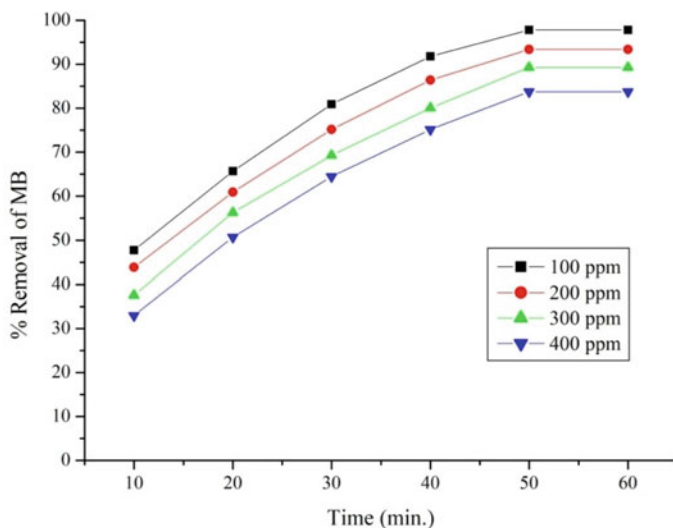


Fig. 3 Effect of concentration of MB at 11 pH, 60 °C, 0.8 g/L

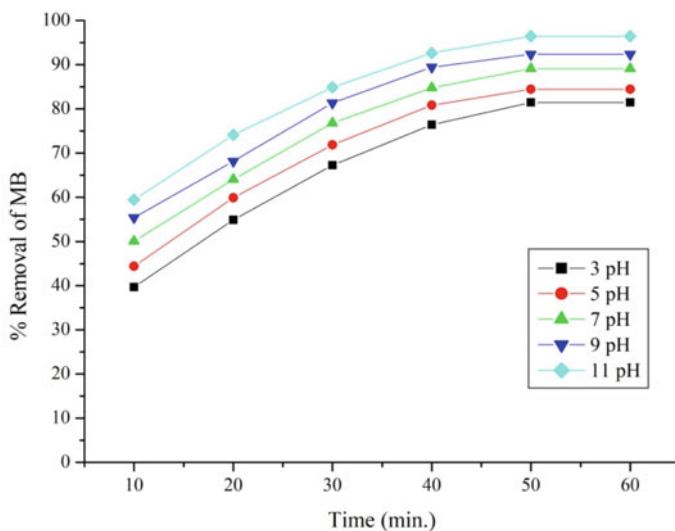


Fig. 4 Effect of solution pH at 60 °C, 100 ppm, 0.8 g/L

3.5 Effect of Temperature

The influence of temperature on methylene blue adsorption at 0.8 g/L adsorbent dose, 60 min. contact time, pH 11, and 150 rpm stirring velocity was investigated for the dye concentrations (100 ppm) shown in Fig. 5. The percentage removal of

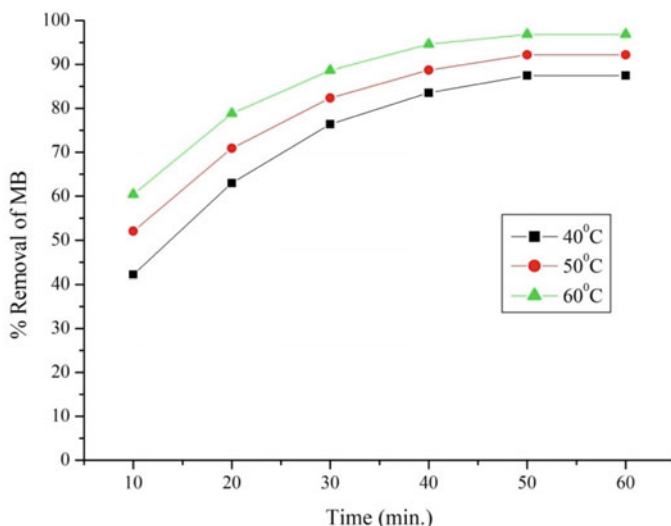


Fig. 5 Effect of temperature at 11 pH, 100 ppm, 0.8 g/L

the dye has also increased with the temperature increasing from 40° to 60 °C. The increased dissemination of adsorbed molecules through the external limit layer and the internal pores of the adsorbed particle, the adsorption potential increases with temperature, which reduces the solution's viscosity in the case of highly condensed suspensions. Furthermore, increasing the temperature will alter the adsorbent's equilibrium potential for a given adsorbate. For the 100 ppm dye concentrate, maximum percentage of dye removal at 60 °C is found to be 96.88%.

3.6 Comparative Study with CAC

Figures 6, 7 and 8 are provided in batch studies with dyes and commercial activated carbon (CAC) for a comparative assessment of the adsorption potential of orange peel activated carbon, and it can be concluded that activated carbon prepared from orange peel gives a higher percentage of removal compared to commercial activated carbon at 100 ppm, 60 °C, 0.8 g/L adsorbent, and pH 11.

4 Conclusions

MB adsorption from aqueous solution to activated carbon prepared from orange peels was examined. Due to dye content in wastewaters, adsorbent concentration, pH and temperature of the wastewater, the removal of methylene blue from wastewater is

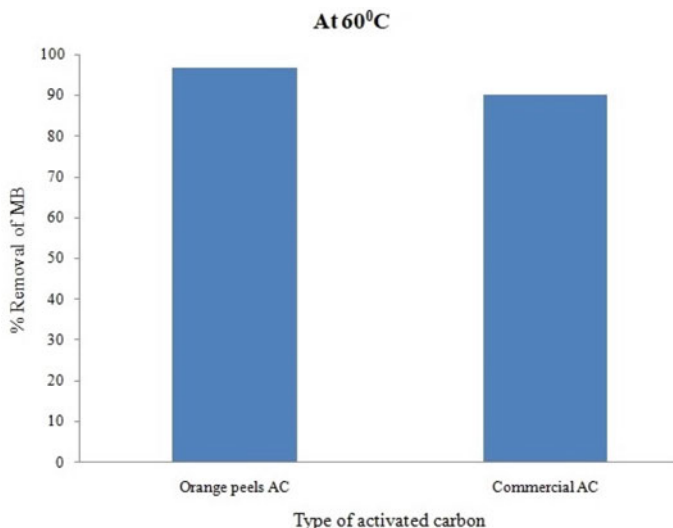


Fig. 6 Comparative study of orange peel AC versus commercial AC at 100 ppm, and 0.8 g/L

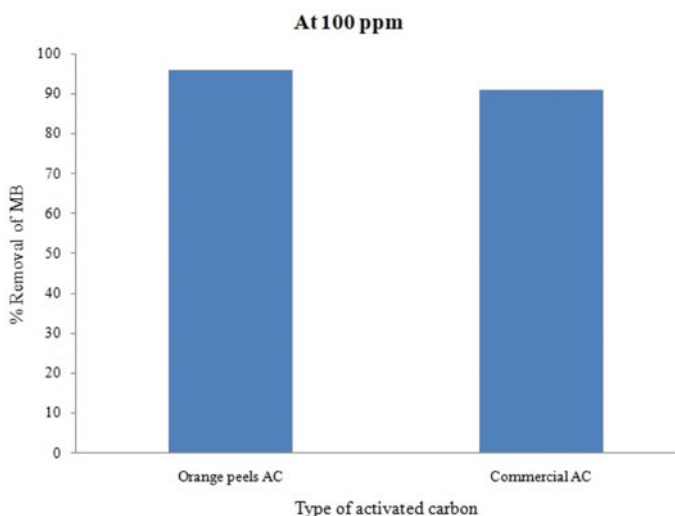


Fig. 7 Comparative study of orange peel AC versus commercial AC at 60 °C, and 0.8 g/L

mainly regulated. The percentage of the dye removal was found to decrease with a rise in the initial dye concentration with the increase in solution temperature (60 °C), contact time (60 min.), and adsorbent concentration (0.8 g/L). With an increase in pH, the percentage of dye removal was increased and the maximum adsorption was reached at pH 11. The comparative analysis with commercial activated carbon

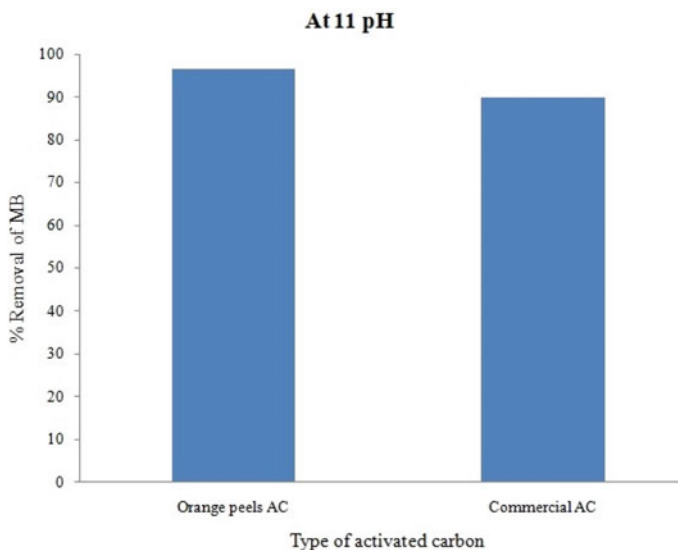


Fig. 8 Comparative study of orange peel AC versus commercial AC at 60 °C, and 0.8 g/L

shows that orange peel activated carbon gives more percentage of MB removal than commercial activated carbon.

References

1. D.N. Olowoyo, E.E. Orere, Preparation and characterization of activated carbon made from palm-kernel shell, coconut shell, groundnut shell and Obeche wood (investigation of apparent density, total ash content, moisture content, particle size distribution parameters. *Int. J. Res. Chem. Environ.* **2**(3), 16–19 (2012)
2. A.M. Khah. R. Ansari, Activated charcoal: preparation, characterization and applications: a review. *Int. J. ChemTech Res.* **1**(4), 9–10 (2009)
3. B. Sivakumar, C. Kannan, S. Karthikeyan, Preparation and characterization of activated carbon prepared from balsamodendron caudatum wood waste through various activation processes. *Rasayan J. Chem.* **5**(3), 20–24 (2012)
4. N.S. Topare, P. Joshi, Characterization of activated carbon prepared from citrus Sinensis (Orange) peels by X-Ray fluorescence spectroscopy (XRF). *Emerging Trends Chem. Eng.* **2**(3), 49–51 (2015)
5. R.K. Sharma, A. Kumar, P.E. Joseph, Removal of atrazine from water by low-cost adsorbents derived from agricultural and industrial wastes. *Bull. Environ. Contam. Toxicol.* **80**, 22–23 (2008)
6. K.S. Bharathi, S.T. Ramesh, Removal of dyes using agricultural waste as low-cost adsorbents: a review. *Appl. Water Sci.* **3**, 773–790 (2013)
7. S.A. Bokil. R.K. Rai, Preparation and characterization of activated carbon from bamboo by chemical activation. *J. Catal. Catal.* **3**(1), 1–6 (2016)
8. M. Akhtar, S.M. Hasany, M.I. Bhangar, S. Iqbal, Low cost sorbent for the removal of methyl parathion pesticide from aqueous solution. *Chemosphere* **66**(10), 23–24 (2007)

9. J.M. Salman, B.H. Hameed, Removal of insecticide carbofuran from aqueous solution by banana stalks activated carbon. *J. Hazard. Mater.* **176**(1–3), 28–29 (2010)
10. H.A. Al-Husseiny, Adsorption of methylene blue dye using low cost adsorbent of sawdust: Batch and continuous studies. *J. Babylon Univ./Eng. Sci.* **22**(2), 296–310 (2014)
11. I. Ali, M. Asim, T.A. Khan, Low cost adsorbents for the removal of organic pollutants from wastewater. *J. Environ. Manage.* **113**, 170–180 (2012)
12. S. Deshmukh, P.V. Thorat, N.S. Topare, Preparation and characterization of activated carbon from orange peels. *J. Catal. Catal.* **5**(1), 15–20 (2018)

Effect of Elevated Temperatures on Conventional Concrete



Vinayak Vaidya, Valsson Varghese, and Preeti K. Morey

Abstract Under elevated temperatures, concrete will not burn and it also will not emit any flume but there will lose its strength as temperature increases, in the presented experimental investigations, the effect of increase in temperatures on properties of concrete was done. Strength of concrete like compressive strength, split tensile strength, flexural strength was determined at 28 days. The concrete cubes, beams and cylinders samples were heated at controlled temperatures at 200, 400, 600, 800, 1000 °C for 0.5, 1 and 1.5 h and tested after 0.5 h of natural cooling. At enhanced temperature, strength of concrete and weight continuously reduces as the temperature was increasing, strength of concrete and weight of concrete reduced up to 70% and 14% at elevated temperatures, respectively.

Keywords Compressive strength · Split tensile strength · Flexure strength · Elevated temperatures

1 Introduction

Concrete fire-free structure cannot be made, as there will be a chance of having fire over lifespan of any structure. We cannot make fire-free structure, but their effect on structure can be reduced to optimize the cost of retrofitting. It is most important when we construct the buildings and structures should protect both people and property. Concrete has fire-resistive properties by which it cannot be burned, and it will not have any toxic fumes but the concrete structures should be designed for the effect of fire so that structural components of building can withstand without failure even there is reduction in strength and modulus of concrete.

V. Vaidya (✉) · V. Varghese
Department of Civil Engineering, K.D.K. College of Engineering, Nagpur 440009, India

P. K. Morey
Department of Civil Engineering, Suryodaya College of Engineering and Technology, Nagpur, India

During the elevated temperatures, there will be changed in strength of concrete, Young's modulus, Poission's ratio and volume changes [1]. The effect of elevated temperatures seen on surface of members in colour change and cracks; also, the disintegration phenomena take place at elevated temperatures which lead to the reduction of strength. To overcome this failure, concrete should be made in such a way that it will withstand during the fire, which can be possible by proper investigations on the effect of fire on concrete, so that we can choose the correct materials to be used in concrete. The effect of elevated temperatures is affected on material properties of concrete ingredients, such as aggregates, cement past and aggregate–cement past bond [2, 3].

In fire, the strength of concrete was reduced up to 80%, which may cause the failure of structures. Some structures which had fire damaged can be retrofit. The cost of retrofitting is around 60% of cost of RCC members like beams, slabs and columns, which was very high, and also, there is no guarantee of durability. In accordance with making fireproof concrete, there will be deep investigations needed [1].

Following data shows the effect of temperature on concrete [2].

- 100 °C: weight loss due to the expulsion of evaporable water from hardened cement paste and aggregate.
- 100–200 °C: Vapour pressure in the micro-pores and continuous weight loss due to evaporation of water.
- 100–500 °C: Loss in weight occurs due to the loss of water from gel pores.
- 500–700 °C: Reduction in weight loss increasing because of decomposition of calcium hydroxide in cement paste and decomposition of CSH.
- 700–900 °C: De-carbonation of calcium carbonate, which occurs at about 800 °C.
- Above 900 °C: No further measurable weight loss there and concrete was not workable.

2 Experimental Work

2.1 Methodology

For the proposed experimental work, the following methodologies were adopted.

1. Raw material Testing [3–5]
 - 1.1 Cement
 - 1.2 Fine aggregates
 - 1.3 Coarse aggregates
2. Design mix [3, 6] as per code.
3. Testing on fresh concrete [3, 5] as per code.
 - 3.1 Slum cone test
4. Casting of concrete samples [3, 5]

Table 1 Properties of ordinary Portland cement (OPC)

S. No.	Name of test	Results		
01	Fineness of cement (%)	1.448		
02	Normal consistency of cement (%)	34.92		
03	Initial setting time of cement	53.9 min		
04	Soundness of cement	0.58 cm		
05	Compressive strength (N/mm ²) of cement at	3 days	7 days	28 days
		24.7	38.34	52.46

- 4.1 Concrete cubes of size 150 × 150 × 150 mm, 48 in numbers
- 4.2 Concrete beams of size 100 × 100 × 500 mm, 48 in numbers
- 4.3 Concrete cylinders of size 150 mm Dia × 300 mm, 48 in numbers.
5. Curing of concrete samples for 28 days [3, 5]
6. Heating of concrete samples in electric furnace at controlled temperature rising up to 1200 °C [7].

2.2 Raw Material Testing [3–5]

2.2.1 Cement

In concrete, the most important ingredient is cement, which plays a role of binder to archive strength. Cement was acted a binder to fine aggregates and coarse aggregates and also to reduce the pores present between fine aggregates and coarse aggregates. Cement contributes around 20% of total volume of concrete, and therefore, it plays very active role in concrete to achieve the strength. For the proposed work, OPC 53 grade of cement was used. Properties of ordinary Portland cement (OPC) are shown in Table 1.

2.2.2 Fine Aggregate

For proposed experimentations, locally available river sand was used, conformed IS: 383-1970. The fine aggregates were conforming to grading zone II. Physical properties of fine aggregates are shown in Table 2.

Table 2 Physical properties of fine aggregates

S. No.	Name of test	Results
01	Specific gravity of F.A.	2.498
02	Fineness modulus of F.A.	2.50

2.2.3 Coarse Aggregate

Coarse aggregate plays a very important role from strength, and many investigations were carried out to examine the effect of elevated temperatures on concrete with different types of coarse aggregates. Regarding the strength of coarse aggregate crushed aggregates gives more strength because of interlocking of partials as compared to rounded aggregates which give lower internal friction. For this proposed work, crushed aggregates of 20 mm size are used. The coarse aggregates are as per IS 383-1970, well wash by water and dried to surface dry condition. Physical properties of coarse aggregates are shown in Table 3.

2.3 Concrete Design Mix [3, 4]

To achieve strength of concrete, concrete mix design was very important, and for this experimentations, mix design was done in accordance with IS: 10262:2009. The details of mix design are tabulated in Table 4.

2.4 Test on Fresh Concrete [3, 6]

Test on fresh concrete was done as per IS: 516-1959, the details are shown in Table 5.

Table 3 Physical properties of coarse aggregates

S. No.	Name of test	Results
01	Specific gravity of C.A.	2.759
02	Fineness modulus of C.A.	7.239

Table 4 Design mix for 1 m³

1	Grade of cement	M25
2	Cement mass (kg/m ³)	413
3	Water mass (kg/m ³)	185
4	Fine aggregate mass (kg/m ³)	681.98
5	Coarse aggregate mass (kg/m ³)	1022.39
6	W-C ratio	0.45

Ratio was 1: 1.649: 2.469

Table 5 Test on fresh concrete

Grade of concrete	Slump value
M 25	80 mm

Table 6 Test on fresh concrete

Type of concrete samples	Numbers of samples
Cubes	54
Beams	54
Cylinder	54

**Fig. 1** Curing of concrete samples

2.5 Casting of Concrete Samples [3, 5]

Procedure for casting of cubes, beams and cylinders was as per IS: 516-1959. Table 6 shows quantity of concrete samples casted for this research.

2.6 Curing of Concrete Samples [3, 5]

As per IS: 516-1959, to get maximum strength curing of concrete samples was very important. All concrete samples were kept in water for 28 days, Fig. 1 shows curing of concrete samples.

2.7 Specifications of Electric Furnace

Electric furnace for proposed experimentations can reach up to 1200 °C. Fire-temperature curve was used as per IS3809-1979. The details specifications of electric heating furnace are given below,

- Temperature range – 100 to 1200 °C, rate of heating is 10 °C per minutes.
- Overall size of M.S. cell (inner size)—450 mm × 300 mm × 600 mm.



Fig. 2 Electric furnace with control panel

- Electric supply—25 Amp per phase.
- Ceramic blanket—128 grade.
- Fire bricks lining confirming to I.S.
- Element brick lining.
- Thermocouple.
- Temperature setter and indicator.
- Insulation brick coated with refractory insulation cement.

2.7.1 Testing Procedure [7]

- Before putting it into furnace, the weight of concrete samples was taken.
- Samples were put in the furnace.
- Temperatures inside the furnace were set at required temperature for constant heating durations like 0.5, 1.0 and 1.5 h.
- After that, the specimen was removed from furnace and weight of samples was noted.
- Specimen was allowed to cool for 0.5 h natural cooling.
- Same procedure was adopted for temperatures ranging from 400 to 1000 °C. Experimental setup of electric furnace is shown in Fig. 2.

3 Results and Discussion

3.1 Compressive Strength of Concrete

Compressive strength of concrete is shown in Fig. 3 and percentage reduction in compressive strength is shown in Fig. 4.

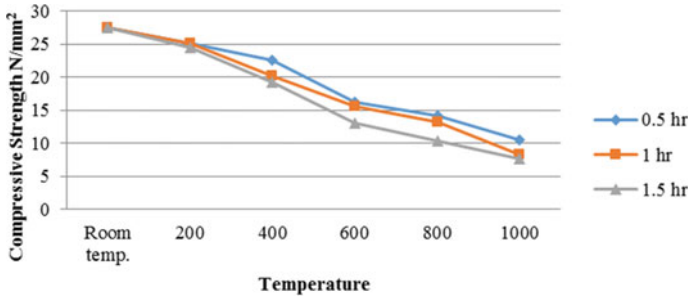


Fig. 3 Compressive strength

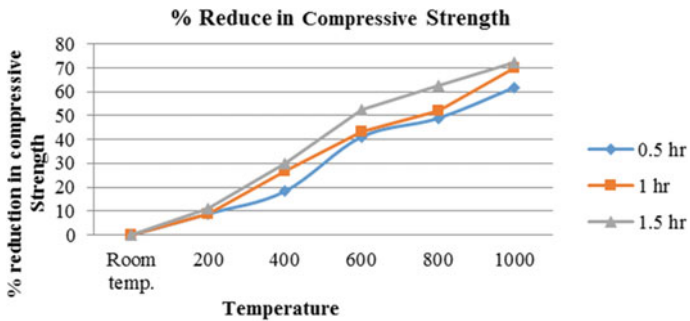


Fig. 4 Percentage reduction in compressive strength

Discussion

- As the temperature is increasing, the strength is also reducing.
- Reduction in strength is less for 0.5 h heating.
- Reduction in strength is more for 1.5 h heating.
- Strength of concrete reduces by 60%, 70% and 72% at 1000 °C for 0.5 h, 1.0 h and 1.5 h heating, respectively.

3.2 Weight Loss of Concrete

The percentage weight loss of concrete samples is shown in Fig. 5.

Discussion

- As the temperature is increasing, weight is also reducing.
- Weight of concrete reduces by 6%, 11% and 14% at 1000 °C for 0.5 h, 1.0 h and 1.5 h heating, respectively.

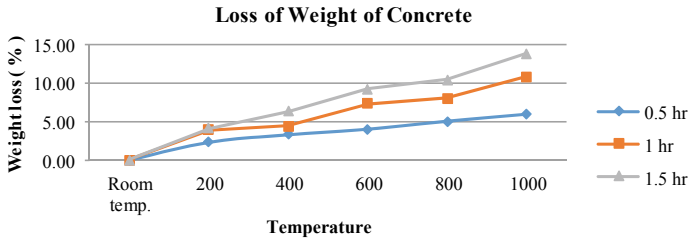


Fig. 5 Weight loss of concrete

3.3 Split Tensile Strength of Concrete

Split Tensile Strength of Concrete is shown in Fig. 6 and percentage reduction in Split Tensile Strength is shown in Fig. 7.

Discussion

- As the temperature is increasing, the strength is also reducing.

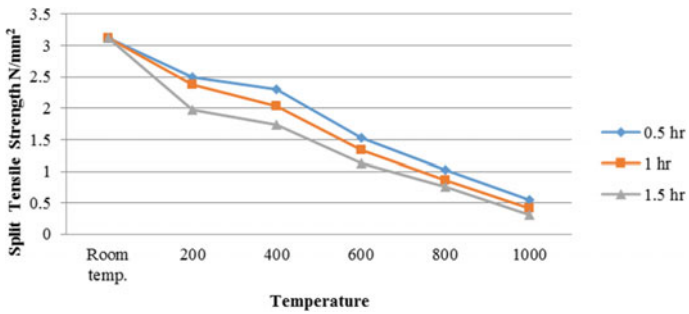


Fig. 6 Split tensile strength

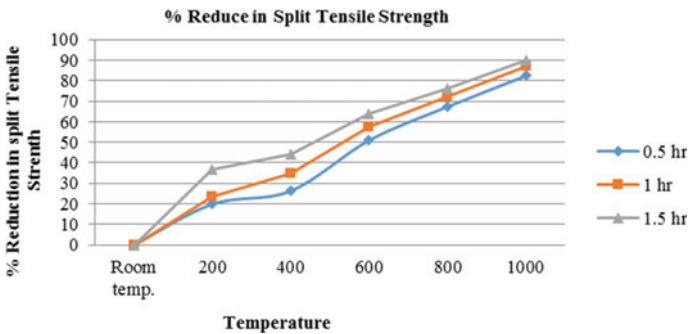


Fig. 7 Percentage reduction in split tensile strength

- Reduction in split tensile strength found less for 0.5 h heating.
- Reduction in split tensile strength found more for 1.5 h heating.
- Strength of concrete is reduced by 83, 87 and 90% at 1000 °C for 0.5, 1.0 and 1.5 h heating.

3.4 Flexural Strength

Flexural Strength of Concrete is shown in Fig. 8 and percentage reduction in Flexural Strength is shown in Fig. 9.

Discussion

- As the temperature is increasing, the strength also reducing.
- Reduction in strength is less for 0.5 h heating.
- % reduction in strength is more for 1.5 h heating.
- Strength of concrete reduces by 82, 85 and 90% at 1000 °C for 0.5, 1.0 and 1.5 h heating.

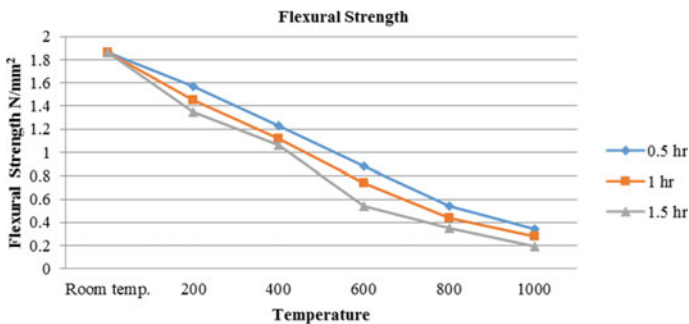


Fig. 8 Flexural strength of concrete

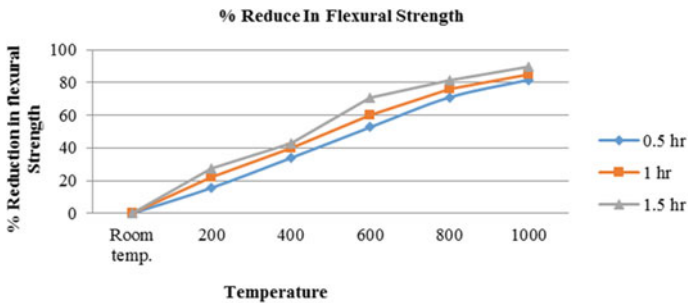


Fig. 9 Percentage reduction in flexural strength

4 Conclusions

1. With increasing in temperatures, the compressive strength, tensile strength and flexural strength of concrete get reduced with respect to elevated temperatures.
2. Effect of elevated temperatures increase with respect to temperature and exposure time increases.
3. Loss in weight of concrete get reduced up to 14% at 1000 °C for 1.5 h heating.
4. Effect of elevated temperature was observed on the surface of concrete in the form of cracks at 800 and 1000 °C.
5. From 400 to 600 °C, temperature strength loss started.
6. After 600 °C, temperature concrete was not found functioning with respect to its full structural Capacity.
7. Between 200 and 400 °C, the fracture (failure) mechanism of concrete samples was not sudden, but from temperature 600–1000 °C fracture (failure) mechanism of concrete samples happens sudden, due to evaporation of water due to which ingredients of concrete like cement, fine aggregates and coarse aggregates get disintegrated easily as the temperature increases.
8. At elevated temperatures, the colour of concrete samples turns whitish from 400 to 1000 °C.
9. Size of concrete samples (cubes, beams and cylinders) is changed around 1–2% at 800–1000 °C
10. Concrete becomes more and more stiff (brittle) and loss their strength more than 70% at 1000 °C

References

1. G.A. Khoury, Fire and Concrete Encontro Nacional Betão Estrutural, 5, 6, 7 de Novembro de 2008
2. O. Arioz, Effects of elevated temperatures on properties of concrete. *Fire Safety J.* **42**, 516–522 (2007)
3. M.S. Shetty, *Concrete Technology* (S. Chand and Co., Ltd, New Delhi, 2005)
4. IS 383-1970, Indian standard specification for coarse and fine aggregates from natural sources for concrete (2nd revision). Reaffirmed, 1997
5. IS 516-1959, Indian standard methods of test for strength of concrete, reaffirmed, 2004
6. IS 10262-2009, Indian standard concrete mix proportioning-guidelines
7. IS 3809-1979, Indian standard fire resistance test of structures, reaffirmed, 2002

Extracted Sand from Overburden of WCL Mines as Sustainable Sand Solution



B. V. Bahoria and Ashwini Badhiye

Abstract Ecological worries are being raised against exploitation of natural resources. The disagreements are mostly in related to conserving soil beds from erosion and the fact of having natural sand as a filter media for ground water. Over a period of years, coal industry in India is interfacing shortage of river sand due to new mining laws and its increasing demand in infrastructure expansion. The present study focuses on study of extraction of sand from the overburdens of opencast mines of coal fields and its feasibility as a fine aggregate in concrete. The surcharge spread over in mines needs to be removed for separation of coal to an external dump till ample space is produced for back filling by obtaining of land nearby coal carrying area. Further this surcharge waste needs to be managed at the time of closure of mine for land acquiring. In this project, physical property of extracted sand from overburden and natural sand from river bed is compared and effort is made to utilize the waste generated in tones into sustainable sand solution.

Keywords Natural sand · Extracted sand · Overburden · Sustainability

1 Introduction

Major constituent of beaches categorized as a “fine aggregate,” resulting from the erosion of siliceous and other rocks forms a major building material. At a large scale, there is scarcity of this building material, and this is the situation in many progressing nations. According to statistics, the need of sand as fine aggregate for infrastructure development in the country is about in million tonnes, and it is growing at the significant rate per year. The resources for generation of natural sand are limited. As a matter of fact, the generation is not uniform in quantity and in quality. The

B. V. Bahoria (✉)
Yeshwantrao Chavan College of Engineering, Nagpur, India
e-mail: bvbahoria@ycce.edu

A. Badhiye
Rajiv Gandhi College of Engineering and Research, Nagpur, India

state of uncertainty and unsatisfactoriness in supply, the rate of the material changes promptly leading to wrong practices. Uncontrolled exploitation of sand reserves leads to disturbing ecological balance. Complications of illegitimate excavation, environmental concerns, and variations in costs and quality of sand connected with each other are predominance across many nations. Open cast mining is a surface mining expertise of excavating hard strata or inorganic element from the earth by their separation from an open pit or earth's surface. Bhanegaon open cast mine bears a sand patch at a depth of 8–10 m. After that from overburden, sand is extracted by using sand segregation plant. In overburden, 40–50% sand are obtained and other are mud and gravel.

2 Brief Review of the Past Work

Zhengfu Bian [1], studied that the preliminary thing to treat extracted waste as lining for construction practices, and use it as building material, stuffing underground empty spaces, filling subsided basin to rejuvenate lands for forestation purpose and agricultural production and landscaping. Stolboushki [2], in his study utilized waste generated in the process of coal mining for production of bricks and fuel for their burning, carried out research of waste coal from processing plant abashevskaya and carbonaceous argillites from the lignite open-cut in korkino, and found the possibility for compound use of waste coal as a raw material for preparing ceramic bricks and as fossil energy for kilns. Parthasarathi [3], studied the effect on workability of concrete due to partial replacement of fine aggregate with gold mine remains. The residues of gold mine are extremely fine particles with a fineness modulus of 0.28 and contain around 69% of around medium and fine sand. Due to substitution of natural sand with fine tailings, there was variation in the quantity of medium and fine sand. The percentage variation of medium and fine sand in the sand resulting for 10%, 20%, and 30% substitution levels was found to be 82%, 75%, and 69%, respectively. The workability acquired for concrete for 30% replacement was found to be very low. However, the modified concrete was found to be applicable for binding, shallow sections, and pavement using pavers. Ram Chandar [4], studied gradation results marked on a semi-log plot with respect to percentage passing on (Y -axis) and sieve size on logarithmic axis (x -axis) interpreted S-curve conforming to well-graded aggregate for sandstone. The fineness modulus of the sandstone obtained as 2.25 and found it to be substitution of fine aggregate. Flow properties of concrete increased percentage variation of replacement of sand. Increased content of fly ash with constant sandstone percentage workability was found to be increased. Merbouh [5], in his study of experimental investigation on study of mines waste as sand on properties of concrete, found that the flow property of all the concrete mix decreases with increased percentage of substitution of sand by coal waste aggregate. Compressive strength of concrete increased till 4% coal waste used as sand in concrete [7, 8]. The skewed substitution of the sand by coal waste improved early compressive strength. Ibrahim [6], in his study of recycling of ash from coal as a substitute of cement, found

that the workability parameter decreased with the increasing percentage of coal ash as a cement replacement and further concluded that high fineness of ground CBA particles results in increased absorption of water. Santos [9] results showed that it was possible to process the coal waste from the carboniferous region of Santa Catarina and obtain a recycled fine aggregate that can be used in civil construction [9].

3 General Information of Bhanegaon Open Cast Mine

WCL is scrutinizing to deal with its production by separating sand while digging out coal. It has begun segregating sand from soil dug out for mining coal. A like project for manufacturing bricks has also been initiated. Surcharge, overburden as it is called in mining terms, is the earth dug out while mining activity. The same is used for backfilling of cavities created. Apart from this, surcharge soil has no other utility. Currently it has started segregating sand by mechanical means from the surcharge soil. It splits sand particles from the earth. Along with this, rocks are also crushed into sand. The company has started supplying 500 m³ per day to Nagpur Improvement Trust to be used for a low-cost housing scheme of government. WCL has got enquiry from agencies like National Highway Authority of India. WCL is looking forward to improve its overall revenues. It may lie between 5 and 105% of the public sector units' turnover regarding sand source. It sums to about 200 million tons of overburden in per annum. Although it is used to backfill mines, but a lot amount of soil is left out in process. Due to the swelling of soil, there is increase in the volume by 20% which can be used for making sand and remaining can be used for backfilling (Figs. 1 and 2).

1. Name of the subsidiary: western coalfields limited
2. Name of area: Nagpur area

Fig. 1 Bhanegaon open cast mine



Fig. 2 Sand patch at open cast mine



3. Name of mine: Bhanegaon open cast mine
4. Date of opening: 17-03-2015
5. Location: Latitude N21° 16' 37"–N21° 15' 36"
Longitude E79° 10' 12"–E79° 08' 41"
6. Total land required: 610.12 Ha
7. Excavation area: 146 Ha
8. External overburden dump area: 245
9. Area of quarry: 1.5 km * 1.0 km
10. Minimum depth of quarry: 65 m
11. Maximum depth of quarry: 215 m
12. Life of the mine: 26 years

3.1 Sand from Overburden of Coal Mines

Characteristics

The surcharge soil spread over in open areas of coal mines needs to be relocated for coal extraction to far away dumping yards in order to create an adequate space for back filling by acquiring of land near coal bearing area. Further, this surcharge soil needs to be handled properly at the time of shutting of mine reclamation of land. As per mine closure rule, 80% of the extracted surcharge utilized for backfilling of the cavity created remaining percentage to be utilized for extraction of sand.

Demerits of Overburden

1. External overburden dump is waste by products as is of no use to the company.
2. Huge quantity of land has to be acquired for overburden dump incurring huge cost to the company.

3. The external dumps always possess treat to nearby habitants that necessitates rehabilitation of villagers to a safe place which adds to additional capital investment.
4. Overburden dumps pollute the environment, flora fauna of species nereby area adjacent to the mine

3.2 Sand Segregation Plant

The main function of this plant is the separation of sand from overburden waste. Plant consists of various unit like resand bunkarhaving capacity 25 cu.m., turn screening unit, sand processing unit, rotating bucket, and conveyor belt having width 800 mm, which is used for passing the material from one unit to another unit, wing wheel 2 m length. Overall length of plant is 40 m.

WORKING OF SAND SEGREGATION PLANT

Introduction: Sand segregation plant is used to separate sand from overburden waste. The main function of segregation plant is to remove mud and bigger sizes stone.

1. The first stage involves separation of bigger size stone available in overburden waste. The overburden contains both sand as well as mud.
2. After removal of bigger size stone, the remaining overburden is passed to next unit called as screen.
3. In this unit, two types of mesh are provided that is one for course and other for fine particles. In this process, course and fine particle are properly shake. In next stage, the overburden waste is passage to sand processing unit. This unit is provided over the RRC platform. In this unit, water is applied to the overburden waste by force, and due to this action, mud is dissolved with water and is collected in tank which is provided under the mesh. Then by the use of pipe which is connected to the tank mud and water is kept outside of plant. After this remaining material called as (segregated sand) is collected in bucket. Then clean wet sand is passed to drying platform by the use of conveyor belt which is 800 mm in width and sand is collected from delivery end (Figs. 3 and 4).

Merits of Segregation of Sand from Overburden

1. Depletion in natural river sand can be stopped.
2. Sand is a national asset and recovery of sand from waste overburden is best out of waste product.
3. Land occupied by overburden can be freed for mine exploration, afforestation, cultivation, or any other economic activity that adds revenue to the company.
4. The land degradation can be minimized.
5. Indirect employment can be generated by installing a processing plant.
6. Uninterrupted supply of sand can be ensured throughout year without any seasonal affects.
7. Supply of sand can be regulated as per requirement.

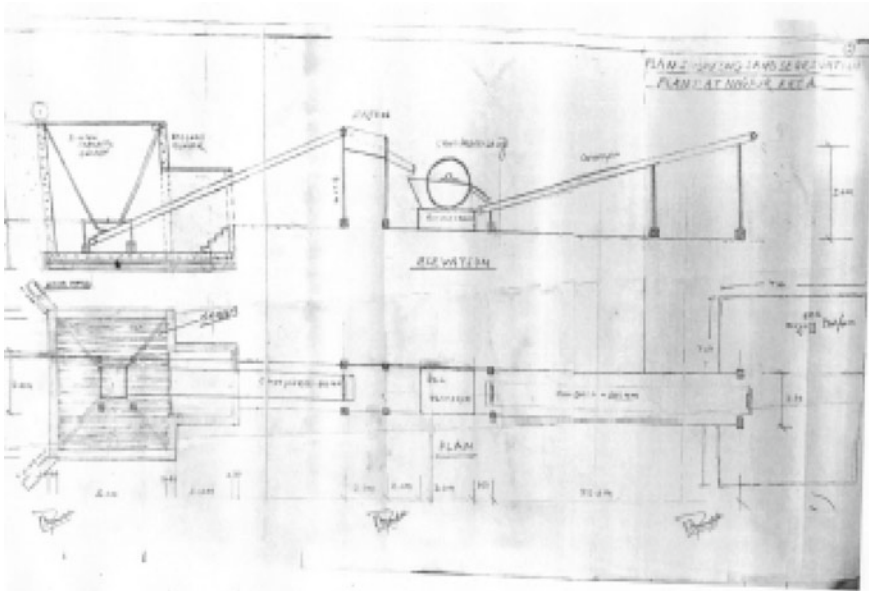


Fig. 3 Layout of sand segregation plant

- 8. The recovered sand will be supplied to government agencies as cheaper price than the prevailing market price.

4 Materials

4.1 Natural Sand

Natural sand has an ideal shape for use as fine aggregate in concrete. The natural sand particles are well rounded and are usually nearly spherical. Spherical particles decrease the percentage of voids within the concrete mixtures so no additional paste is required to fill these voids. Well-shaped natural sands are ideal for workability of mixtures. Natural sand does not require more water to enhance the workability of the mixture so that amount of bleed water in the concrete will not be increased.

4.2 Extracted Sand

In Bhanegaon open cast mine, while extracting coal, they got a sand patch at a depth of 8–10 m. After that from overburden, sand is extracted by using sand segregation plant, and this is called as the extracted sand (Figs. 5 and 6).



Fig. 4 Components of segregation plant

Fig. 5 Natural sand



Fig. 6 Extracted sand



5 Experimental Program

Fine aggregate in a concrete is structural filler, and it is a granular material used to produce concrete, and when the particles of the granular material are so fine, they pass through a 4.75 mm sieve. In the project locally available natural sand and the extracted sand had been used for experimental purpose and physical properties of fine aggregate had been determined as per IS 383-1970 [10].

Tests performed on natural sand and extracted sand

- (1) Particle size distribution
- (2) Bulking of sand
- (3) Silt content
- (4) Specific gravity and water absorption of fine aggregate (Figs. 7, 8; Tables 1, 2, 3, 4, 5 and 6).

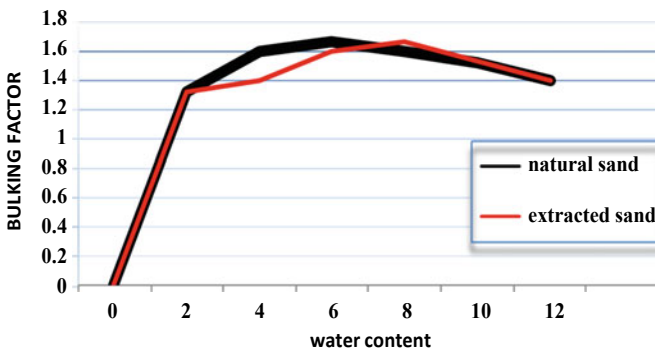


Fig. 7 Bulking of natural sand versus extracted sand

CAPACITY OF THE PLANT: 250 cum/DAY.

ANNUAL SAND RECOVERY		76250	cum	
DESCRIPTION	UNIT	AMOUNT	RS/cum	
CAPITAL EXPENDITURE				
COST OF PLANT	RS	15359376		
COST OF SEDIMENTATION POND	RS	2416707		
STOCKYARD PLAT FORM	RS	200000		
TOTAL		17976083		
COST ON CAPITAL				
PAYBACK PERIOD 5 YEAR)	MONTH	60		
CAPEX	RS	17976143	47.15	
OPERATIONAL EXPENDITURE				
COST OF MANPOWER	RS	2544798	33.37	
COST OF STORES/SPARES	RS	3071875	40.29	
COST OF POWER (170 KWH/HR)	RS	2990708	39.22	
REJECT HANDLING	RS	1026442	13.46	
COST OF ONE PAY LOADER	RS	2066680	27.10	
COST OF TRANSPORTATION OF OB FROM DUMP TO SAND PLANT	RS	4105769	53.85	
OPEX	RS	11700503.5	207.30	
COST OF SAND/cum			254.45	

Fig. 8 Approximate cost of sand segregation at Bhanegaon open cast mines

Table 1 Fineness modulus of natural sand

Is sieve	Weight of fine aggregate (gm)	Percentage of weight retained (%)	Cumulative percentage of passing (%)	Percentage passed (100-cpr)	Remark
10 mm	0	0	0	100	100
4.75 mm	5	0.5	0.5	99.5	90–100
2.36 mm	16	1.6	2.1	97.9	75–100
1.18 mm	103	10.3	12.4	87.6	55–90
600 μ	399	39.9	52.3	47.7	35–54
300 μ	393	39.3	91.6	8.4	8–30
150 μ	80	8	99.6	0.4	0–10
75 μ	2	0.2	99.8	0.2	–
Pan	2	0.2	100	0	–

6 Conclusion

- (1) The results show that both natural and extracted sand comes under the zone II.
- (2) The silt content is in permissible limits, as the extracted sand contains less silt content as compared to the natural sand, i.e., 2.52%
- (3) Specific gravity of extracted sand is 2.59 which is within permissible limits and proves to be a good replacement of natural sand.

Table 2 Fineness modulus of extracted sand

Is sieve	Weight of fine aggregate (gm)	Percentage of weight retained (%)	Cumulative percentage of passing (%)	Percentage passed (100-cpr)	Remark
10 mm	0	0	0	100	100
4.75 mm	40	4	4	96	90–100
2.36 mm	40	4	8	92	75–100
1.18 mm	170	17	25	75	55–100
600 μ	280	28	53	47	35–54
300 μ	410	41	94	6	08–30
150 μ	50	5	99	1	0–10
75 μ	0	0	0	0	–
Pan	0	0	0	0	–

Table 3 Bulking phenomena of given sample of natural sand

S. No.	Water content (%)	Initial volume of sample (v_1)	Final volume of sample (v_2)	$v_2 - v_1$	Bulking (%) = $((v_2 - v_1)/v_1) * 100$	Bulking factor = v_2/v_1
1	2	150	200	50	33.33	1.33
2	4	150	240	90	60	1.6
3	6	150	250	100	66.67	1.67
4	8	150	240	90	60	1.6
5	10	150	230	80	53.33	1.53
6	12	150	210	60	40	1.4

Table 4 Bulking phenomena of extracted sand

S. No.	Water content (%)	Initial volume of sample (v_1)	Final volume of sample (v_2)	v_3	Bulking (%) = $(v_3/v_1) * 100$	Bulking factor = v_2/v_1
1	2	150	200	50	33.33	1.33
2	4	150	210	60	40	1.4
3	6	150	240	90	60	1.6
4	8	150	250	100	66.67	1.67
5	10	150	230	80	53.33	1.533
6	12	150	210	60	40	1.4

- (4) The bulk density and the water absorption are also in the permissible limits of properties of sand and hence can be concluded that the extracted sand from the overburden of open cast mines of coal fields seems to be a sustainable substitute of natural sand.

Table 5 Silt content of natural sand and extracted sand

S. No.	Description	Natural sand sample 1	Natural sand sample 2	Extracted sand sample 1	Extracted sand sample 2
1	Volume of sample sand v2	76	82	76	82
2	Volume of silt layer v1	3	3	2	2
3	Percentage of silt	3.95	3.6	2.63	2.4
	Average (%)	3.77		2.515	

Table 6 Physical properties of natural sand and extracted sand from overburden

S. No.	Properties	Natural	Extracted	As per Indian standard code
1	Sieve analysis	Zone 1	Zone 2	Zone 1–4
2	Silt content	3.77%	2.52%	< 8%
3	Specific gravity	2.63	2.59	2.5–3.0
4	Water absorption	0.8	1.41	0.3–2.5%
5	Bulk density	1500 kg/m ³	1603 kg/m ³	1520–1680

- (5) The cost analysis of extraction at segregation plant goes to about 250/- per cumec which is much more less than the current rate of natural sand supplied for various construction activities, thus making extracted sand most economical, sustainable substitute of natural sand.

References

1. H.W. Zhengfu Bian, The impact of disposal and treatment of coal mining wastes on environment and farmland, in *International Conference "Waste Management, Environmental Geotechnology and Global Sustainable Development (ICWMEGGSD'07—GzO'07)*, Ljubljana, Slovenia, Aug 28–30, 2007
2. A.Y. Stolboushkin, Use of coal-mining and processing wastes in production of bricks and fuel for their burning. *Int. Conf. Indust. Eng. ICIE Proc. Eng.* **150**, 1496–1502 (2016)
3. N. Parthasarathi, Effect on workability of concrete due to partial replacement of natural sand with gold mine tailings. *Indian J. Sci. Technol.* **9**(35), 1–4 (2016). <https://doi.org/10.17485/ijst/2016/v9i35/99052>
4. K. Ram Chandar, B.C. Gayana, V. Sainath, Experimental investigation for partial replacement of fine aggregates in concrete with sandstone. *Adv. Concr. Constr.* **4**(4), 243–261 (2016)
5. M. Miloudi, M. Merbouh, B. Glaoui, Use of coal waste as fine aggregate on properties of concrete in hot weather. *Int. J. Civ. Eng. Technol. (IJCIET)* **8**(11), 959–966 (2017)
6. M.H. Ibrahim, Recycling of coal ash in concrete as a partial cementitious resource. *Resources* **8**, 99 (2019). <https://doi.org/10.3390/resources8020099>
7. S. Naganathan, Coal bottom ash as sustainable material in concrete. *Indian J. Sci. Technol.* **10**(36) (2017). <https://doi.org/10.17485/ijst/2017/v10i36/114595>

8. S.N. Sadon, Experimental investigation on coal bottom ash as sustainable material in concrete. *Indian J. Sci. Technol.* **10**(36), 1–10 (2017)
9. C.R. Santos, R. Tubino, Mineral processing and characterization of coal waste to be used as a fine aggregate for concrete paving blocks. *Rev. IBRACON Estrut. Mater.* **8**(1) (2015). ISSN 1983-4195, <https://doi.org/10.1590/S1983-41952015000100004>
10. IS-383, *Indian Standards Specification for Coarsse Aggregate and Fine Aggregate From Natural Sources for Concrete* (Bureau of Indian Standards, New Delhi, 1970)

Domestic Greywater Treatment by Hybrid Electrocoagulation and Filtration Method in Continuous Mode



Sanket Devikar, Khalid Ansari, Charuta Waghmare, and Mangesh Bhokar

Abstract Amassing of safe and sufficient amount of water is pushing up an attention for hybrid technologies for greywater management with felicitous handling approach of recycle and reuse. The present study examines the hybrid process of electrocoagulation and filtration with different combinations of electrode material like Al–Cu–Al–Cu and Cu–Al–Cu–Al with flow rate of 0.18 l/min and based on it the impact examinations are done on the versatility of performing at anode and cathode in continuous mode. The study reveals about 95% of COD removal at 24 V of 60 min working period of which cathode and anode isolated at 30 mm for Al–Cu with specific energy 3.85 kWh/m³ causing operational cost of 27.08 INR.

Keywords Greywater · Electrocoagulation · Electroflotation · Reaction condition · Water quality

1 Introduction

Water is crucial and important element on earth. It is primary need for plant, animals and humans. Earth's nearly 70% area is covered by water itself but only 2–3% water is fresh and drinkable [1]. The amount of greywater (GW) produced in total is about 78% of overall water consumption [2]. Researchers from many areas focus on the best solution to provide alternative treatment for less consumption and reuse facility option of water. Mainly, greywater is can be one of the alternative having low-strength characteristic directly contributing from household facilities like sinks, detergent water, bathroom sinks, showers, washing machines and dishwashers [3]. Characteristics of greywater changes according to area, social habits, different culture number of people and consumption pattern. As from researchers point of views, GW requires low treatment facility for reuse and recycle in particular areas of toilet flushing's, gardening,

S. Devikar (✉) · K. Ansari · C. Waghmare
Department of Civil Engineering, Yeshwantrao Chavan College of Engineering, Nagpur, India

M. Bhokar
Department of Civil Engineering, G.H. Rasoni College of Engineering, Nagpur, India

irrigation. Based on treatment options, greywater includes physical, chemical and biological and combination processes. One of treatment is electrocoagulation (EC) treatment which is very advance and efficient due to cations are created by disintegration of sacrificial anodes with connected electric field which actuates flocculation of scattered pollutants, by decreasing the zeta potential of suspended matter. The metal hydroxide formed coagulates the fluid impurities, and the hydrogen bubbles formed at cathode allow the floatation of floc containing organics [4–7]. As such very few publications are related to electrocoagulation treatment of greywater with hybrid electrode consumption. The prime objective of this study is to treat greywater by electrocoagulation process with different electrode materials in continuous mode.

2 Material and Methodology

2.1 Laboratory Scale Experimental Set-Up

The experimental set-up consists of laboratory-scale electrocoagulation reactors with outer dimensions 22 cm (H) × 20 cm (L) × 10 cm (W), having volume of 5.5 L, made from acrylic material, with thickness as 0.5 cm, performed with electrode materials of aluminium and copper sheets with dimensions 16.5 cm (H) × 4.5 cm (L) × 0.02 (W) cm. The gap between the anode and cathode was maintained at 4 cm to customize the energy loss. In order to take out floating material, an additional tank of the same dimensions was attached on either side of reactors. The direct current (DC) with system voltage regulators having range from 6 to 24 V was applied to electrode in mono-polar electrodes pattern, either cathode or anode with different amounts of currents flowing through the reactors. After treating from electrolytic cell the water is passed from 1.5 cm orifice opening at the 13 cm (H) through circular filter bed having dimension 65 cm (H) with 10 cm (D) made up of acrylic materials, with finer sand of effective size (0.2–0.4) mm at the top followed by granular coconut shell activated carbon with gravel of effective size (4.75 mm). The experiments were conducted at ambient room temperature with 4L greywater were gently stirred at 150 rpm. The sample was continuously monitored at 60 min time interval and passed through 12 cm (H) of tank and final effluents were transferred to filtration media by removing the precipitated flocs with flow rate 0.18 l/min continuously throughout the cycle. The removal efficiency of each parameter was calculated using equation [7].

$$\{RE(\%) = [(C_{\text{initial}} - C_{\text{final}})/C_{\text{initial}}] * 100\} \quad (1)$$

where C_{initial} and C_{final} are the initial and final concentration (Fig. 1).

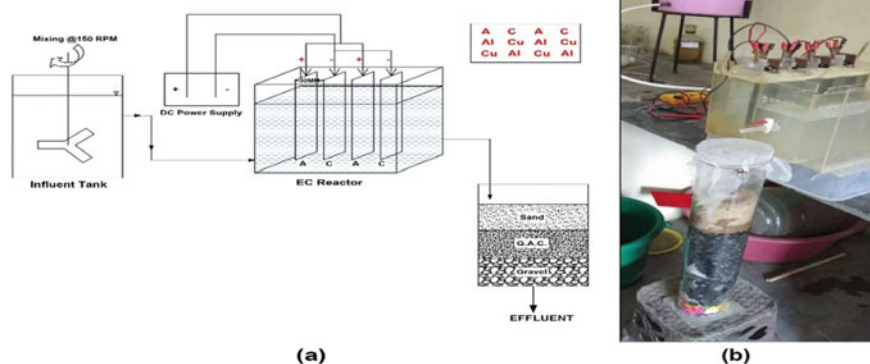


Fig. 1 Laboratory scale experimental flow diagram of electrocoagulation and filtration process

2.2 Sampling

Greywater samples were collected from household that consists of laundry, hand basins and kitchen wastewater with well stored at 4 °C in polypropylene bottles until use and were analysed within 48 h. Before each run, initial tests of greywater samples were performed for pH, conductivity, turbidity, TSS, TDS, COD and chlorides. All samples were asset with initial and final output at different tests prescribed in standard methods [4, 8–10].

3 Result and Discussion

See Table 1.

3.1 Effect of Applied Voltage

Applied voltage plays an important role for treatment of greywater by EC which directly emphasizes on efficiency. The applied voltages for electrochemical reaction cell are 12 and 24 V to eliminate the turbidity, colloidal suspended solids and organic materials. The results show that COD improved to (90–95) % removal efficiencies with higher voltages application, i.e. 24 V, with respect to operating time, which depends on conductivity of the electrode materials used [4–7, 10]. It was revealed that turbidity, suspended solids, chloride gradually dropdown with hybrid electrode combination of Al–Cu–Al–Cu to 93%, 92% and 94.65% respectively due to charge

Table 1 Greywater characteristics feed as influents to EC and *F* process, *N*: 10 samples, SD: Standard deviation

Parameter	Minimum	Maximum	Average	SD
pH	7	9	8	1.2
Turbidity (NTU)	15	170	92.5	10.6
TDS (mg/lit)	179	679	294	134
TSS (mg/lit)	18	169	76	51
COD (mg/lit)	10	400	205	195
Chloride (mg/lit)	9.2	44	22.5	9.2
Sulphate (mg/lit)	25	67	28	12.4
Ammonium nitrogen (mg/lit)	0.7	5.6	2.4	2.2
Orthophosphorus (mg/lit)	0.51	6.8	3.5	3.1

neutralization of Al^{3+} and Cu^{2+} ions resulting in passivation of electrolysis and accumulation of colloidal particles. Further, the optimum voltage must be applied in order to reflect the impact of electrode consumption, energy consumption and operation and maintenance costs. However, the removal efficiency is maintained at higher voltage consumption which is directly based on economic burden [11–13].

3.2 Effect of Material

The hybrid electrode material plays an important role in EC cell as it determines the reactions taking place due to their colloidal charges which determine by cation present in solution. In researcher's views, aluminium electrode shows greater efficiency of treatment as compared to other materials since $\text{Al}(\text{OH})_3$ forms the colloidal particles which behave as precipitates and depend upon the condition of pH in the solutions, and hence, COD removal efficiency is found greater in Al–Cu–Al–Cu combination as compared to other combinations. Again it has been seen that rapid setting of flocs was seen in 24 V Cu–Al–Cu–Al configuration (Fig. 2).

3.3 Effect of pH

The pH of a solution is also one of the key factors that govern the removal performance of greywater in EC process as it affects the stability of hydroxide species that are formed. Generally, pH of treated greywater changes during process depending upon the type of electrode, number of electrode and initial pH of solution. The properties of pH have been examined with hybrid electrode at different voltages to show maximum removal efficiency of COD, turbidity and other parameter as well as minimum energy and electrode consumptions as shown in Fig. 1b with minimum sludge formations

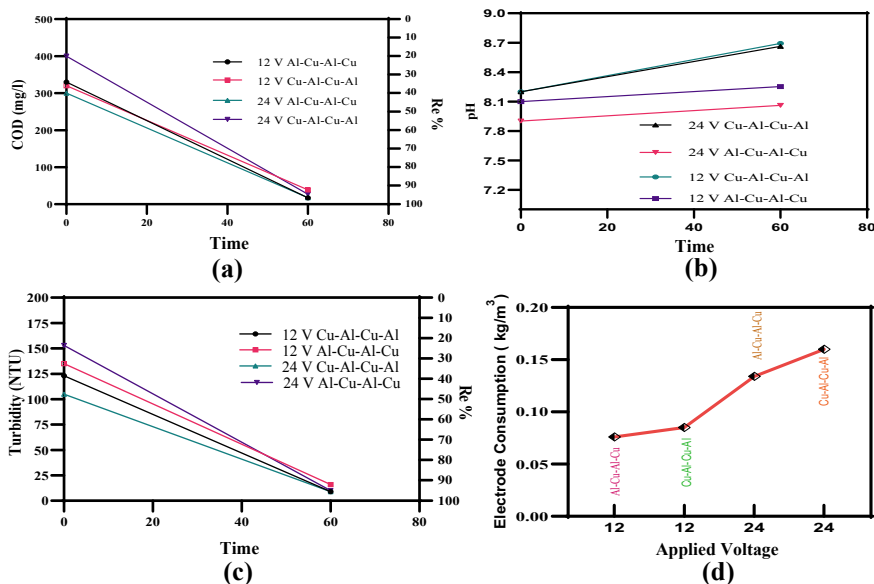


Fig. 2 **a** Effect of applied voltages and operating time for COD removal during EC and filtration process, **b** effect of pH during EC and filtration process, **c** effect of turbidity removal during EC and filtration process, **d** effect of applied voltages and operating time for electrode consumption during EC and filtration process

at pH around 7–9. Generally, the treatment efficiency clearly increased when pH is acidic, neutral or scarcely alkaline and subsequently dropped down at highly alkaline pH due to the no formation of coagulants and adsorption of organic pollutants at low and high pH values. Due to the conductivity and composition of electrode materials, pH increased energy usage. Hence in a nutshell, optimum operating pH range for greywater EC treatment is 7–9 to ascertain consummate efficiency, and thus, initial pH of waste needs no adjustments to final pH to avoid operational costs [14, 15].

3.4 Effect of Operating Time

Working time is another vital factor in ECF process, which is important to give adequate current connected to the electrodes where the metal particles are produced by the disintegration to form metal hydroxide species. Operating time is taken to be constant is 1 h/60 min for electrocoagulation and 1 h for electrofloatation. In this way, sensible electrolysis times ought to be given in the ECF reactor. From the figure, it is found that when polarity of electrodes is changed; i.e. when Cu is anode and Al is cathode, COD and turbidity removal increases with increase in time but TSS and TDS removal was decreased. For an electrolysis time beyond optimum time, the

pollutant evacuation proficiency does not increment as adequate quantities of flocs are accessible. Besides, evacuation effectiveness does not increment; unexpectedly, it diminishes because of the anodic passivation and cathodic polarization which can obstruct the execution of ECF.

4 Operating Cost Estimation

For practical execution of EC process on real basis, it is important to be economical and the major factor responsible for maintaining the same is cost of operation. Operational rate (OPc) of EC and filtration process include electrical energy used, cost of electrode consumption and maintenance cost for the disposal of sludge on landfill, filtration media and other fixed charges which are expected to be INR 2.1 per kg/m³. Operating cost mainly is evaluated by adding cost for electrical energy and electrode material with maintenance cost, and their equations are given below.

$$OPc = \text{Cost energy} + \text{Cost electrode} + \text{Cost maintenance} \tag{2}$$

$$\text{Cost of energy, Cost energy} \{ \text{kWh/m}^3 \} = \{ U * i * t_o \} / V \tag{3}$$

$$\text{Cost of Electrode, Cost electrode} \{ \text{kg/m}^3 \} = \{ i * t_o * M_w \} / (z * F * V) \tag{4}$$

EC + filtration	U (V)	CD (A)	C _{energy} (KWh/m ³)	C _{electrode} (kg Al/m ³ kg Cu/m ³)		C _{Main} (INR) (kg/m ³)	OP _c in INR/m ³
Al-Cu-Al-Cu	12	0.4	1.0	0.0074	0.0263	2.1	12.57
Al-Cu-Al-Cu	24	0.8	3.84	0.0149	0.0351	2.1	27.08
Cu-Al-Cu-Al	12	0.5	1.2	0.0093	0.0329	2.1	19.89
Cu-Al-Cu-Al	24	0.9	4.32	0.0251	0.0592	2.1	32.18

where *U* = cell voltages (V); *i* = current (A); *t_o* = operating time (h); *V* = wetted volume of reactor (m³); *F* = faradays constant (96,455 C/mol); CD = current density (A). Electrical unit price was taken as Rs. 6/unit of kWh for the Nagpur area, June 2020 and price of electrode material were Rs. 285 and 130/kg for copper and aluminium, respectively. It is found that electrocoagulation process depends upon many treatment conditions for the estimation of operational cost such as current density, volume of treated effluents, electrode material and connection, EC reactors, and type of power supply.

5 Conclusion

In this study, the electrocoagulation process along with filtration strategy was led to dissect the achievability of greywater evacuation with hybrid electrode combination aluminium and copper cathodes in continuous flow mode with working time of 60 min to show the flexibility, vitality proficiency and cost adequacy. The outcomes showed that blends of Al–Cu–Al–Cu with 24 V are sufficiently proficient to give great evacuation efficiencies of almost acquiring 95% with operating cost of INR 27.08/m³. At the outcome of pH, 8.5 show that hybrid electrode for both combinations reflects great strength in removal efficiency with increase in applied voltage to working time. Economical figure of operating cost at 24 V, the combination of Al–Cu–Al–Cu required less electrical energy than Cu–Al–Cu–Al, respectively, which results in higher COD current efficiencies. The additional performance of filtration process indicated the reduction of colour and other inert organic matter. The experiment results show that the performance of EC and sand bed filtration process can be alternative choice for onsite greywater treatment and reuse for low-strength greywater.

References

1. D.T. Moussa, M.H. El-Naas, M. Nasser, M.J. Al-Marri, A comprehensive review of electrocoagulation for water treatment: potentials and challenges. *J. Environ. Manage.* **2016**, 1–18 (2016)
2. B. Lesjean, R. Gnriss, Grey water treatment with a membrane bioreactor operated at low SRT and low HRT. *Desalination* **199**(1–3), 432–434 (2006)
3. H.I. Abdel-Shafy, M.A. El-Khateeb, M. Shehata, Greywater treatment using different designs of sand filters *Desalin. Water Treat.* **52**, 28–30, 5237–5242 (2014)
4. D.M. Ghaitidak, K.D. Yadav, Characteristics and treatment of greywater—a review. *Environ. Sci. Pollut. Res.* **20**(5), 2795–2809 (2013)
5. F. Li, K. Wichmann, R. Otterpohl, Review of the technological approaches for grey water treatment and reuses. *Sci. Total Environ.* **407**, 3439–3449 (2009)
6. M. Pidou, F.A. Memon, T. Stephenson, B. Jefferson, P. Jeffrey, Greywater recycling: treatment options and applications. *Proc. Inst. Civil Eng.* **160**, 119–131 (2007)
7. K.A. Vakil, M.K. Sharma, A. Bhatia, A.A. Kazmi, S. Sarkar, Characterization of greywater in an Indian middle-class household and investigation of physicochemical treatment using electrocoagulation. *J. Separation Purif. Technol.* **130**, 160–166 (2014)
8. Metcalf & Eddy, *Wastewater Engineering Treatment, Disposal, and Reuse*, 3rd edn. (McGraw-Hill, New York, 2003)
9. R. Otterpohl, A. Albold, M. Oldenburg, Source control in urban sanitation and waste management ten systems with reuse of resources. *Water Sci. Technol.* **39**, 153–160 (1999)
10. B. Sibel, O. Turkay, Domestic greywater treatment by electrocoagulation using hybrid electrode combinations. *J. Water Process Eng.* **10**, 56–66 (2016)
11. L. Hernandez, H. Temmink, G. Zeeman, A. Marques, C. Buisman, Comparison of three systems for biological grey water treatment, in *Proceedings of Sanitation Challenge: New Sanitation Concepts and Models of Governance*, pp. 357–364, 2008
12. Z. Li, H. Gulyas, M. Jahn, D.R. Gajurel, R. Otterpohl, Greywater treatment by constructed wetland in combination with TiO₂-based photocatalytic oxidation for suburban and rural areas without sewer system. *Water Sci. Technol.* **48**(11), 101 (2003)

13. C.-J. Lin, S.-L. Lo, C.-Y. Kuo, C.-H. Wu, Pilot-scale electrocoagulation with bipolar aluminium electrodes for on-site domestic greywater reuse. *J. Environ. Eng.* **2005**, 491 (2005)
14. S. Sostar-Turk, I. Petrinic, M. Simonic, Laundry wastewater treatment using coagulation and membrane filtration. *Resour. Conserv. Recycl.* **44**(2), 185–196 (2005)
15. K. Ansari, A.N. Shrikhande, Feasibility of greywater treatment by electrocoagulation process: a review. *Int. J. Emerging Technol.* **10**(1), 92–99
16. J.H.T. Winneberger (ed.), *Manual of Grey Water Treatment Practice* (Ann Arbor Science Publishers Ltd., Ann Arbor, Michigan, USA, 1974)
17. E. Eriksson, K. Auffarth, M. Henze, A. Ledin, Characteristics of grey wastewater. *Urban Water* **4**, 85–104 (2002)

Computing the Compressive Strength of Fly Ash Concrete by Using Machine Learning



Lomesh S. Mahajan and S. R. Bhagat

Abstract The construction field basically identifies with the most renowned materials like concrete and cement in all the region of globe. The mechanical strength is only the property by which concrete power should be assessed. **In the traditional method of computing strength by using CTM machine is time consuming in the control laboratory observations.** Also most of the study has been successfully done on OPC concrete but in the era of twenty-first century, the concrete behavior assessing modern tools are available. In this study, the machine learning method is used for predicting the compressive strength of fly ash concrete. A total of 324 sets of fly ash concrete is tested for compressive strength test, and this results used to train and test the machine system. The machine is trained by considering a few parameters as inputs, i.e., cement, water-cement ratio, binder content, fly ash and curing period, etc. The obtained experimental readings of compressive strength are set for output. After using machine learning application, the training prediction accuracy compared with experimental data sets, it is found that 90% of total data set of training results are within the acceptable range. Machine learning has the emerging field to be proposed due to their undamaging applicability.

Keywords Materials · Fly ash · Concrete · Compressive strength · Machine learning

1 Introduction

All the civil engineering concrete structure basically consume cement for binding the other constituents of concrete and the identity of potential building material is due to their binding engineering properties [1]. If alternative material like fly ash or bottom ash found similar binding characteristics, then partially can be used in concrete making. Specially, concrete has been provided multiple advantages like reliability,

L. S. Mahajan (✉) · S. R. Bhagat
Department of Civil Engineering, Dr. Babasaheb Ambedkar Technological University,
Maharashtra, India

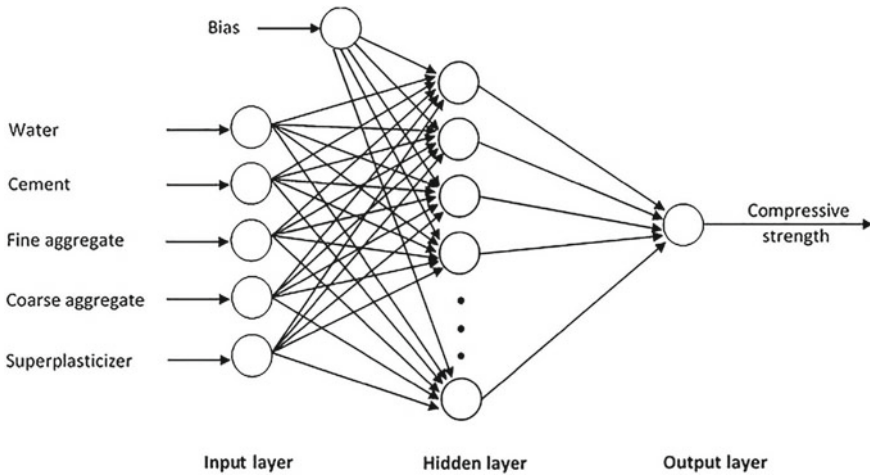


Fig. 1 A typical machine learning tool architecture

robustness, cheaper substance, density, etc. [2, 3]. In the various characteristics of properties of concrete, the compressive strength parameter is the basic one because every structure needed safety and strength performance. The concrete usually made up by mixing Portland Cement (P.C.), Coarse Aggregate (C.A.), Sand (S.), and water. Now a days, the sustainable concrete has been also in boom because it has made by various attentions of alternative materials. The ordinary Portland cement positive source of CO₂ emission and the alternative materials are helping hands for reducing this concentration of CO₂ in construction field. Fly ash, bottom ash, Rice Husk ash are the good feature of supplementary cementitious materials [4]. It is prove that concrete is the complicated system due to their random speeding of filler and binder component [5, 6]. In such challenging matrix, the identification of role of individual constituents is difficult to judge by general test. It has also challenge to predict accurate compressive strength of any concrete mix [7, 8]. In every country, the popular method to predict compressive strength of concrete is laboratory compressive testing machine physical exercise. This is direct method adopted by observing some specific size cube and cylinder specimens according to specification recognized by countries national code. The instrument used for compressive strength are required manpower and time-consuming process, ultimately become costlier as it has been depend on curing period of specimens. If decided time frame of curing not complete then it's not feasible to work out experiment for that particular curing age and the specimens obtained readings suffers due to maturity problem. If we switch from traditional approach for predict compressive strength, the regression method has also in practice which used by some empirical formulae [9, 10]. Due to nonlinear behavior between concrete mix and compressive strength, the method of applying regression model is insufficient to provide accurate equation [5, 11, 12]. The splitting and compressive strength are the majorly check for every concrete structure [13]. The

typical architectural method of applicability of machine learning is shown in Fig. 1. Input parameter includes all raw materials which influencing the strength property.

2 Methodology and Results

The primary level raw materials were identify for making concrete mass. The result of laboratory testing initially carried out and after that machine learning tool was applied successfully. For this study, a proper comprehensive dataset has required which having many mixture proportions of fly ash and cement. The reliability of model somehow depends on binder variations and mix proportioning of large dataset [14]. For the generation of dataset, a proper experimentation results was needed and due to requirement of these dataset an experimental outline was designed for 54 concrete mixes. OPC 53 grade cement, *F* type Fly ash was used for experimentation and locally available natural sand was used as a fine aggregates. 20 mm size well-graded coarse aggregate were used in the whole concrete mixes. A total of 324 sets of fly ash concrete is tested for compressive strength test and this results used to train and test the machine system. The machine is trained by considering a few parameters as inputs, i.e., cement, water-cement ratio, binder content, fly ash and curing period, etc. The obtained experimental readings of compressive strength are set for output. Table 1 and Fig. 2 are show the machine learning inputs and output, respectively.

Table 1 A index variables [binder content, w/c ratio, natural sand, cement, fly ash, curing period, compressive strength]

Data out [4]							
Sample No	Binder content	W/C ratio	Natural sand	Cement	Fly ash	Curing period	Compressive strength
0	300	0.5	100	100	0	3	25.61
1	300	0.5	100	90	10	3	23.21
2	300	0.5	100	80	20	3	18.21
3	300	0.5	100	70	30	3	16.35
4	300	0.5	100	60	40	3	13.22
319	450	0.4	100	90	10	180	49.18
320	450	0.4	100	80	20	180	55.84
321	450	0.4	100	70	30	180	47.23
322	450	0.4	100	60	40	180	41.66
323	450	0.4	100	50	50	180	32.71

324 rows × 7 columns

```

In [21]:
reg.coef_

Out[21]:
array([[ -3.84320988e-03,  -1.14639815e+02,   0.00000000e+00,
         1.90771164e-01,  -1.90771164e-01,   1.51116706e-01]])

In [22]:
y_pred=reg.predict(X_test)

```

Fig. 2 Output obtained in the form of final solution

3 Conclusion

The traditional computational method of laboratory testing and machine learning method gives nearly same results. The method of determining the role of ingredients has difficult in traditional computational methods but by considering multiple index variable as Binder Content, w/c ratio, Natural sand, Cement, Fly ash, Curing Period, Compressive Strength for machine learning technique it's become easy to develop relation between them. The machine learning output in the form of exact equation is more reliable as it involves less manual interference. The using obtained equation we can calculate prediction of compressive strength for any type of binder content and for any ingredients. Machine learning approach can be used for time and cost saving benefits.

References

1. L.S. Mahajan, S.R. Bhagat, Strength assessment of concrete using fly ash and metakaoline, in *Proceeding: International Conference on Advances in Concrete Technology Materials and Construction Practices* (Excel India Publishers, New Delhi, 2016), pp. 113–114
2. L. Mahajan, S. Bhagat, Hardened behaviour of fly ash incorporated concrete with bottom ash as partial replacement of fine aggregate. *Int. J. Innov. Technol. Explor. Eng.* **9**(4), 2898–2907 (2020)
3. L. Mahajan, S. Bhagat, *The Contribution of Bottom Ash Toward Filler Effect with Respect to Mortar, Lecture Notes in Civil Engineering*, vol. 72 (Springer Nature, 2020), pp. 145–154. 978-981-15-3676-2
4. L. Mahajan, S. Bhagat, Fly ash effects on fresh concrete. *Int. J. Innov. Technol. Explor. Eng.* **9**(5), 1247–1252 (2020)
5. M. Lessard, O. Challal, P.-C. Aticin, Testing high-strength concrete compressive strength. *ACI Mater. J.* **90**(4), 303–307 (1993)
6. D.-C. Feng, J. Li, Stochastic nonlinear behavior of reinforced concrete frames numerical simulation. *J. Struct. Eng.* **142**(3), 04015163 (2015)

7. L.S. Mahajan, S.R. Bhagat, Sustainability of concrete using flyash and metakaolin to save CO₂ emission, in Proceeding. UKIERI Concrete Congress, Associate with RILEM Publisher, Dr. B.R. Ambedkar NIT, Jalandhar, Punjab, India (2019)
8. H.-S. Shi, B.-W. Xu, X.-C. Zhou, Influence of mineral admixtures on compressive strength, gas permeability and carbonation of high performance concrete. *Constr. Build. Mater.* **23**(5), 1980–1985 (2009)
9. B. Bharatkumar, R. Narayanan, B. Raghuprasad, D. Ramachandramurthy, Mix proportioning of high performance concrete. *Cem. Concr. Compos.* **23**(1), 71–80 (2001)
10. S. Bhanja, B. Sengupta, Investigations on the compressive strength of silica fume concrete using statistical methods. *Cem. Concr. Res.* **32**(9), 1391–1394 (2002)
11. D.C. Feng, X.D. Ren, J. Li, Softened damage-plasticity model for analysis of cracked reinforced concrete structures. *J. Struct. Eng.* **144**(6), 04018044 (2018)
12. D.-C. Feng, Z. Wang, G. Wu, Progressive collapse performance analysis of precast reinforced concrete structures. *Struct. Des. Tall Special Build.* **28**(5), e1588 (2019)
13. L. Mahajan, S. Bhagat, Investigation of the relationship between splitting tensile strength and compressive strength for prediction of splitting tensile strength of fly ash concrete, in *Proceedings, 3rd International Conference on Innovative Technologies for Clean and Sustainable Development at NITTTR* (Chandigarh, India, 2020)
14. M.F.M. Zain, S.M. Abd, Multiple regression model for compressive strength prediction of high performance concrete. *J. Appl. Sci.* **9**(1), 155–160 (2009)

Water Budget Allocation for Curing of Residential Bungalow and Self-curing Concrete as a Smart Material for Construction



Mahesh Navnath Patil and Shailendrakumar Dubey

Abstract Million litres of water are consumed by construction industry for curing. To save water, it is need of time to invent concrete without curing. This research aims to catch the eye over wastage of water through case study. It explores modest method for quantification of water. Self-curing concrete is proposed as a remedy over elimination of water wastage through curing. Self-curing material mitigates autogenous shrinkage and reduces water evaporation from body the concrete. Water holding capacity of concrete increases with a significant proliferation in mechanical properties of concrete.

Keywords Curing · Quantification · Self-curing concrete · Shrinkage

1 Introduction

Yearly construction industry depleted huge quantity of water around the world. Down to Earth Magazine depicted and figured out annual rate of consumption of water by construction industry. Astonishingly it is eye opening. It reveals water consumption of 145 km³ of water per year. It is extremely essential to go with concrete without curing. It will ultimately result in saving of million litres of the water. This paper aims to propose modest method for quantification of water required for curing of building structure. Relevance of fact regarding water wastage in curing is also prime objective of the study.

Appropriate curing process can produce strong and durable concrete [1]. Many times it is difficult to achieve desired curing condition due to negligence, due to scarcity of water, due to inaccessibility, etc. It is need of the time to obsolete traditional methods of curing with any alternative competent method to avoid wastage

M. N. Patil (✉)
Research Scholar, KBC NMU, Jalgaon, Maharashtra, India

S. Dubey
Professor and Head of Civil Engineering Department, SSVPS BSD College of Engineering,
Dhule, India

of water. Concreting is cast in situ process and one of the biggest challenging areas which suffers from shortage of water. Self-curing concrete can be the best solution to eliminate wastage of water for curing and to produce concrete with desired properties.

Self-curing concrete generates source of water within body and subsequently made available for the hydration process [2, 3]. In the traditional method of curing, situation is formed in such a way that loss of water from the surface is prevented. Curing takes place from outside to inside. In self-curing concrete, curing is processed from inside to outside through internal source of water [4]. Self-curing concrete is an admixture-based concrete. Super-absorbent polymer (SAP) [5, 6], shrinkage reducing admixtures such as polyethylene glycol (PEG) [7], light expanded clay aggregate (LECA) [8], and pumice stone (PC) can be the best admixtures for the formation of self-curing concrete. Surface coating of curing compound (CC) can also be used to create adiabatic conditions. Judicious dosage of polyethylene glycol helps to reduce crack formation to reduce drying shrinkage.

Utilization of porous aggregates like LECA [9] and pumice stone builds water resource inside the concrete. It served hydration of cement. In the present study, all the mentioned admixtures and curing compound were tried. The excellent results of self-curing concrete can be risen as superior alternative to the conventional concrete.

The present paper intended for water budget allocation, provision of authentic data and guideline for the researcher, professional engineers for effective use of self-cured concrete.

2 Quantification of Water

2.1 General

Quantification of water requirement for curing purpose is done for $G + 1$ building. Figure 1 shows plan of $G + 1$ building used for case study. Total 150 m^2 of plan area is exposed. In present study, distinct calculation is performed for slab + beam and columns + foundation. Water charges are calculated as per rates applicable for Municipal Corporation of Shirpur, Maharashtra, India.

2.2 Calculations for Quantity of Water Required for Curing of Slab and Beams

Following are the details of water budgeting for curing of slab and beam.

- Total area of slab exposed = 150 m^2
- Depth of water required for ponding on slab = $50 \text{ mm} = 0.05 \text{ m}$
- Total volume = $150 \times 0.05 = 7.5 \text{ m}^3$

Fig. 1 Determination of velocity through pipe by actual observation



- Rate of evaporation = 10 mm per day = 0.010 m per day... (By actual observation)
- Total evaporation loss = $7.5 \times 0.010 = 0.075 \text{ m}^3$
- Water required for curing = $7.5 + 0.075 = 7.575 \text{ m}^3/\text{day} = 8 \text{ m}^3/\text{day}$ (approx.)
- For 10 days of curing, quantity of water can be calculated as $8 \times 10 = 80 \text{ m}^3 = 80,000 \text{ L}$.
- Considering 10% of wastage, total quantity of water required for curing of slabs = $80,000 + (80,000 \times 10/100) = 88,000 \text{ L}$.

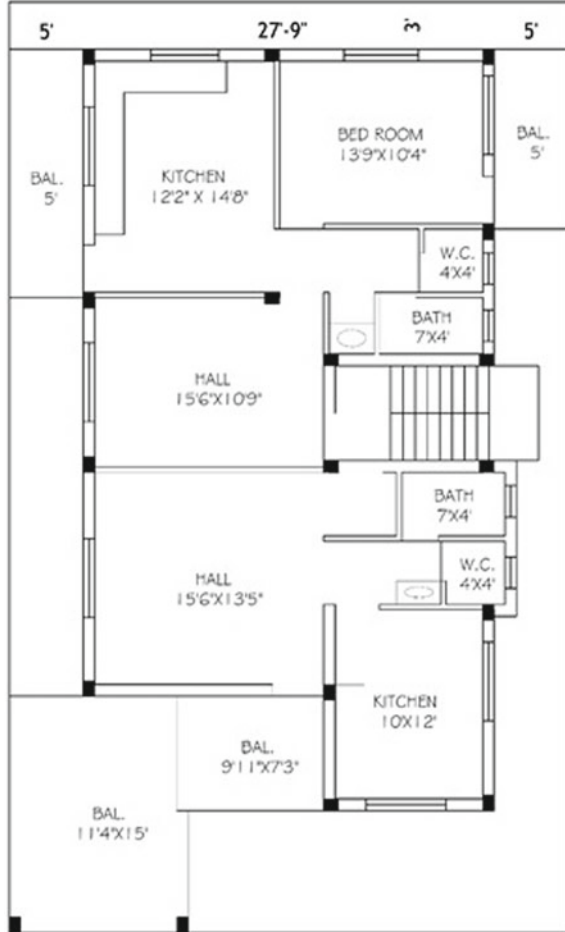
2.3 Calculations for Velocity of Water Through Pipe

Velocity of water used for curing on site is measured by actual observation.

- Volume of bucket = 15 L
- Time required to fill bucket completely with water = 18 s
- $Q = \text{Volume}/\text{time} = (15 \times 10^{-3}/18)$
- $Q = 0.833 \times 10^{-3} \text{ m}^3/\text{s}$
- Discharge = area \times velocity
- $Q = A \times V$
 $= 0.833 \times 10^{-3}$
 $= (\pi/4 \times 0.0254^2) \times V$
 $V = 1.64 \text{ m/s} \approx 2 \text{ m/s}$.

Velocity of water through pipe is 2 m/s.

Fig. 2 Plan of bungalow



2.4 Details of Columns

Details of the columns referred from Fig. 2 are tabulated in Table 1

2.5 Calculations for Quantity of Water Required for Curing of Columns

- Diameter of pipe = 1 in. = 0.0254 m.
- Discharge = area \times velocity [10].
- $Q = A \times V = \pi/4 \times (0.0254)^2 \times 2 = 0.001 \text{ m}^3/\text{s}$.
- Curing done for 10 min and 3 times a day.

Table 1 Details of columns

Group No.	Size (mm)	Height of column (m)	Total nos	Volume of column (m ³)
1	230 × 300	4.5	9	2.7945
2	230 × 380	4.5	4	1.5732
3	230 × 450	4.5	5	2.328
Total number of columns			18	
Total no. of columns provided = 18			6.6957 m ³ = 7 m ³	
Total volume				

- $Q = 0.0010 \times 60 \times 10 \times 3 = 1.8 \text{ m}^3$.
- From Table 1 total volume of columns = 7 m³.
- Total volume of water required $V = 7 + 1.8 = 8.8 \text{ m}^3$.
- Loss of water due to evaporation = $8.8 \times 0.011 = 0.0968 \text{ m}^3$.
- Water required for curing = $8.8 + 0.0968 = 8.8968 \text{ m}^3 = 8896.8 \text{ L} \approx 9000 \text{ L}$.
- For 10 days = $9000 \times 10 = 90,000 \text{ L}$.
 Considering 10% of wastage, total water required for curing of columns.
 = $90,000 + (90,000 \times 10/100)$.
 = 99,000 L.

3 Estimation of Water Charges

3.1 Water Charges

According to Municipal Corporation, Shirpur, and District: Dhule, water charges for domestic use are tabulated as Table 2.

Table 2 Water charges for domestic use

No. of units	Charges in rupees/unit
For first 54 units	5.5
For next 18 units	6.5
For next 18 units	7
For next 18 units	7.5
For all further units	8

Where 1 unit = 1000 L

Table 3 Water charges for curing of slab and beams

No. of units	Charges in rupees/unit	Charges in rupees
For first 54 units	5.5	297
For next 18 units	6.5	117
For next 16 units	7	112
		Total charges = Rs. 526/-

Expenditure for 10 days curing of slab = Rs. 526/-

Table 4 Water charges for curing of columns

No. of units	Charges in rupees/unit	Charges in rupees
For first 54 units	5.5	297
For next 18 units	6.5	117
For next 16 units	7	112
For next 9 units	7.5	67.5
		Total charges = Rs. 594/-

Expenditure for 10 days curing of columns = Rs. 594/-

3.2 Water Charges for Curing of Slab and Beam

Total quantity of water required for curing of slabs = 88,000 L (Table 3).

3.3 Water Charges for Curing of Columns

Total quantity of water required for curing of columns = 99,000 L (Table 4).

3.4 Total Quantity and Expenditure of Water for Curing of Bungalow

For the execution of bungalow with exposed area of 150 m² and with 18 no. of columns.

- Total quantity of water required for curing of slabs = **88,000 L**.
- Total quantity of water required for curing of columns = **99,000 L**.
- Total quantity of water required for curing = quantity of water for slab and beam + column from foundation level = 88,000 + 99,000 = **187,000 L**.

- Expenditure on 10 days continuous curing of slab as per Shirpur Municipal Corporation = **Rs. 526/-**.
- Expenditure on 10 days continuous curing of columns as per Shirpur Municipal Corporation = **Rs. 594/-**.
- Total expenditure on 10 days continuous curing as per charges of Shirpur Municipal Corporation = Expenditure on curing for slab and beam + expenditure on water for columns from foundation level = $526 + 594 =$ **Rs. 1120/-**.

4 Self-curing Concrete: A Smart Construction Material

4.1 Introduction of Self-curing Concrete

Construction industry is a sector which consumes a huge quantity of water every year. According to Down to Earth Magazine (dealing with environmental protection), whole world consumes 145 cubic kilometres of water every year. It is need of time to invent concrete without curing which can saves million litres of the water. Self-curing concrete can be the best solution.

Self-curing concrete is an admixture-based concrete. In self-curing concrete, suitable curing conditions are produced with the help of admixtures. Reservoirs of water are formed inside body of concrete to facilitate hydration of cement [2]. Reliability of concrete on externally supplied water for curing is completely eliminated. Self-curing concrete prevents loss of moisture from the surface. In self-curing concrete, curing is carried out from “inside to outside” instead of “outside to inside” of concrete. It can be made possible by a creating water source inside the body of concrete. Admixtures such as lightweight expanded clay aggregates (LECA) [11], pumice stone (PS), super-absorbent polymer (SAP) [12, 13], polyethylene glycol (PEG) are added proportionately inside concrete [8].

Self-curing material mitigates autogenous shrinkage and reduces water evaporation from body the concrete [5, 14]. Water holding capacity of concrete increases with a significant proliferation in mechanical properties of concrete [15].

The objective of the study is to generate substantial statistics and mix design guideline for the researcher and professional engineers in the whole world to eliminate wastage of water during conventional curing process.

4.2 Preliminary Study

The present study aims to assess effect of self-curing agent on mechanical properties of normal strength concrete. M40 grade self-curing concrete (compressive strength 40 N/mm^2) is prepared using different curing agent. Self-curing agent and their dosage are the crucial parameters of the study (Fig. 3).

Fig. 3 Self-curing material

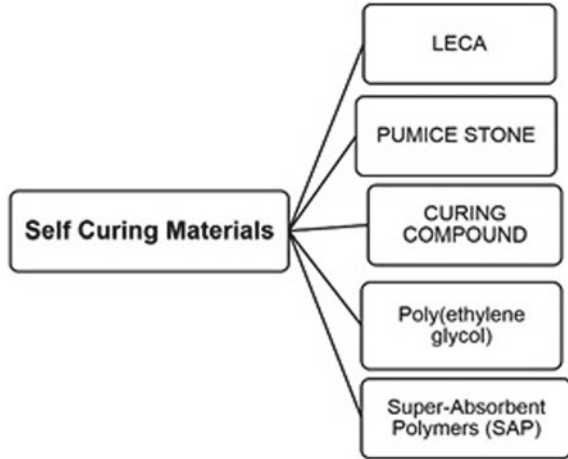


Table 5 Dosage of admixtures

Admixture	Replacement percentage of admixtures by weight of cement (%)
Sodium polyacrylate	0.05, 0.15, 0.20, 0.25 and 0.3
Polyethylene glycol	1, 2, 3, 4 and 5
Light expanded clay aggregate (LECA)	1, 2, 3, 4 and 5
Pumice stone (PS)	1, 2, 3, 4 and 5

Self-curing admixtures used in the present study are sodium polyacrylate, i.e. super-absorbent polymer (SAP) [16, 17], shrinkage reducing admixtures, i.e. polyethylene glycol (PEG) [9, 18], light expanded clay aggregate (LECA), pumice stone (PS) and with the surface coating of curing compound (CC). Dose of admixture is kept variable with M40 as a grade of the concrete. The dosage of admixtures was used as a percentage by the weight of cement as shown in Table 5 (Fig. 4).

4.3 Experimental Programme

M40 grade normal strength concrete is designed as per IS 10262:2019. Compressive strength of concrete with tested for four different water cement ratios. Water cement ratio 0.3, 0.36, 0.40 and 0.45 is considered for trial. Out of these, 0.36 is finalized for further study on the basis of workability and strength characteristics of concrete. The flowchart of the experimental programme is as shown in Fig. 5.

FAIRCURE WC curing compound was applied as coating like paint on the surface of concrete cube. It forms a layer over the surface of the concrete to produce adiabatic



Light Weight Expanded Clay Aggregates (LECA)



Pumice Stone (PS)



Super Absorbent Polymer (SAP)



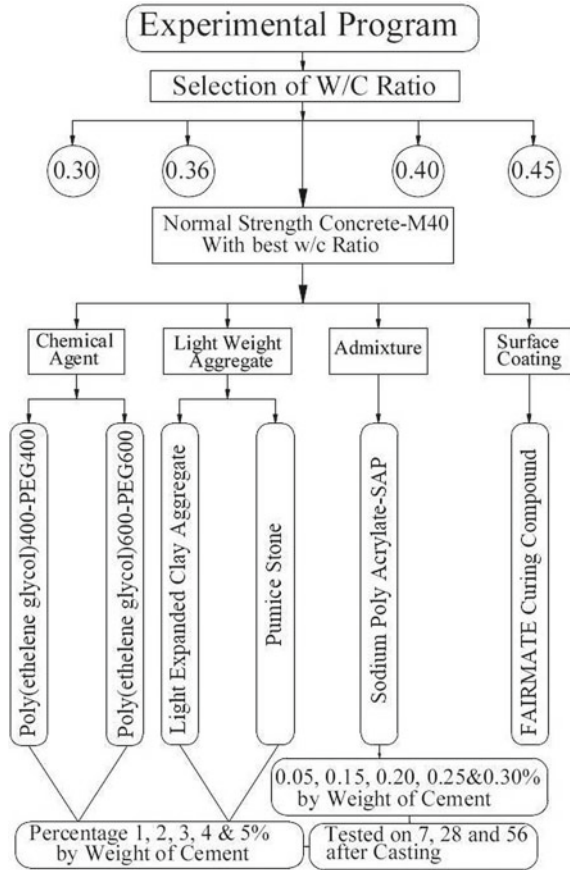
Poly Ethylene Glycol (PEG)

Fig. 4 Self-curing material

action. The layer arrests the water content of concrete which was already present in concrete as mixing water. The impermeable layer prevents loss of moisture.

Standard size mould of dimension 150 mm × 150 mm × 150 mm was used to determine compressive strength, cylinders of 150 mm diameter and 300 mm length to determine split tensile strength. The beam of dimensions 150 mm × 150 mm × 7000 mm determines flexural strength of concrete. All the mould used for testing are confirming to the specifications of IS 10086:1982.

Fig. 5 Experimental programme



5 Results

5.1 Preliminary Discussion

In present study, mechanical properties, i.e. compressive strength and split tensile strength of M40 grade self-curing concrete are determined. The results are represented in graphical form. The abbreviations used in comparative analysis are as shown in Table 6.

Table 6 Dosage of admixtures

Admixture	Replacement percentage of admixtures by weight of cement (%)
Sodium polyacrylate	0.05, 0.15, 0.20, 0.25 and 0.3
Polyethylene glycol	1, 2, 3, 4 and 5
Light expanded clay aggregate (LECA)	1, 2, 3, 4 and 5
Pumice stone (PS)	1, 2, 3, 4 and 5

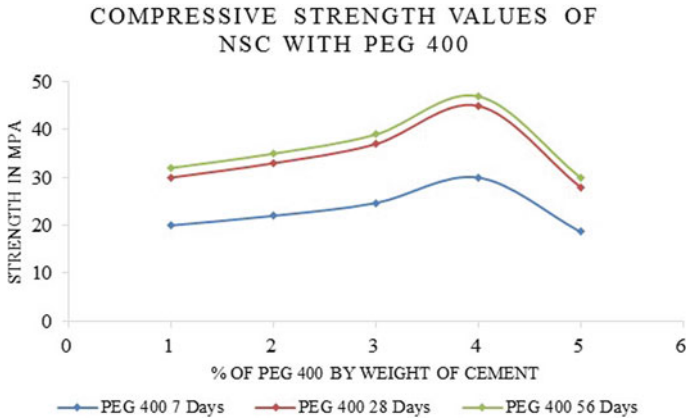


Fig. 6 Compressive strength of NSC-PEG 400

5.2 Graphical Representation

Results of tests as discussed in section V-A are shown below in the form of graphs (Figs. 6, 7, 8, 9, 10, 11, 12, 13, 14 and 15).

6 Concluding Remark

This research work is carried out in two distinct stages. In stage-I, quantification of curing water for residential bungalow is carried out. Following can be the conclusions of stage-I.

1. Total exposed plan area is 150 m². 99,000 L of water are wasted on curing for period of 10 days.
2. As per charges of Shirpur Municipal Corporation, total charges levied on water used for curing purpose are Rs. 1120.

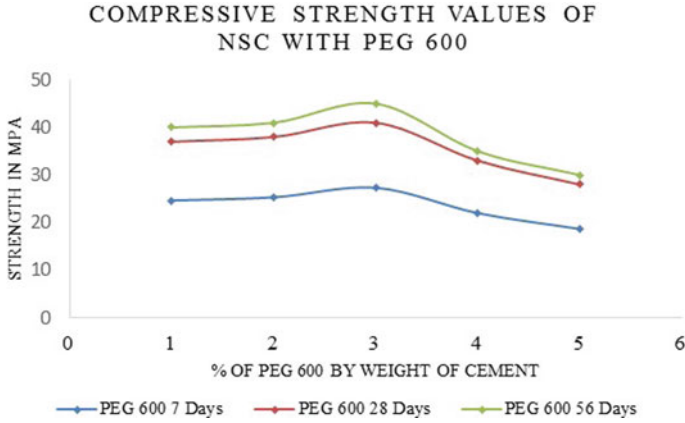


Fig. 7 Compressive strength of NSC-PEG 600

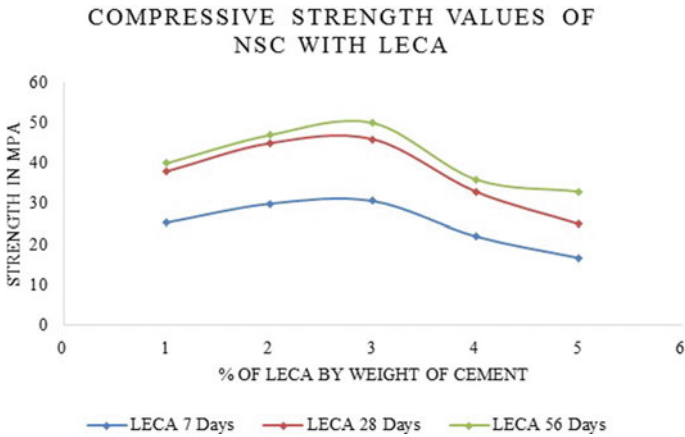


Fig. 8 Compressive strength of NSC-LECA

3. Levied charged for water are least as compared to volume of water used. Need to increase charges per litre to check wastage of water.
4. Need to find out permanent solution on this wastage of water around the globe.
5. Self-curing concrete can be the best solution to eliminate wastage of water on curing of concrete.

In stage-II, M40 grade self-curing concrete is prepared using five different self-curing admixtures. Curing compound is used as coating to produce adiabatic condition. Sodium polyacrylate also known as super-absorbent polymer, polyethylene glycol of concentration 400 and 600 (PEG 400 AND PEG 600), lightweight expanded clay aggregates (LECA), pumice stone (PS) are used as a self-curing admixture. Following can be the conclusions of stage-II.

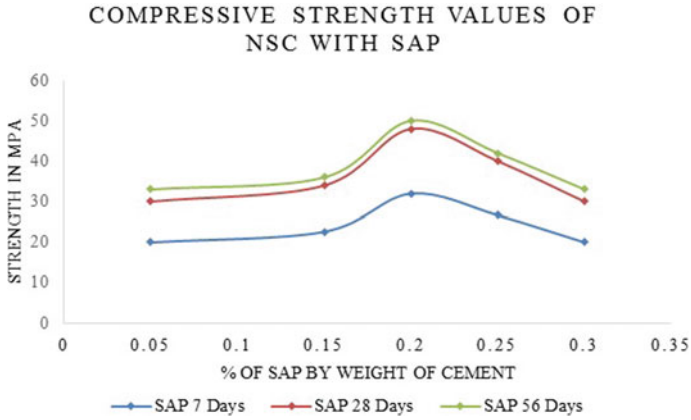


Fig. 9 Compressive strength of NSC-SAP

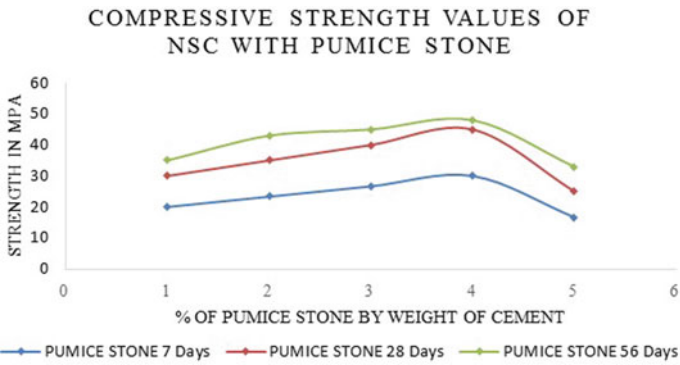


Fig. 10 Compressive strength of NSC-PS

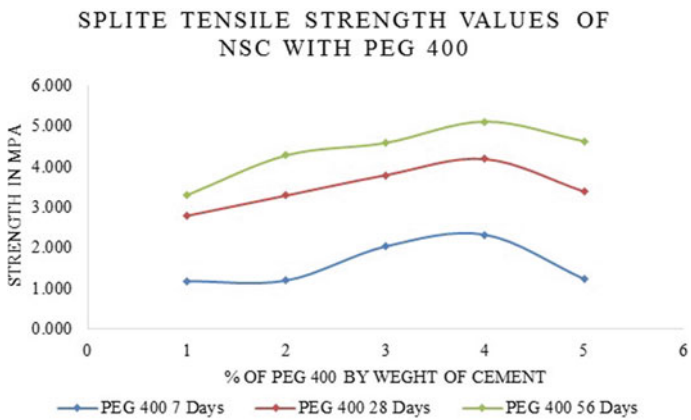


Fig. 11 Split tensile strength of NSC-PEG 400

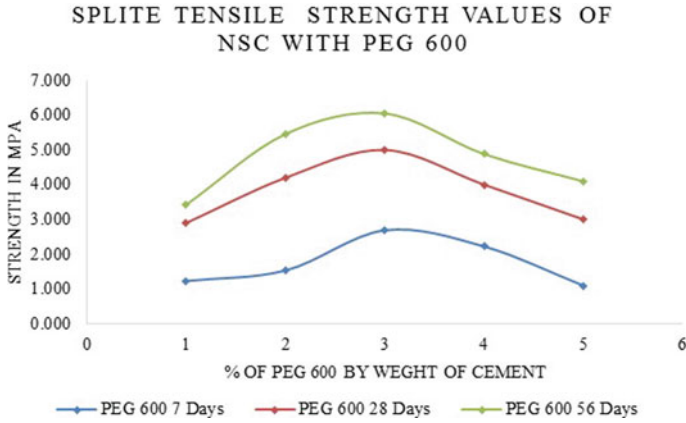


Fig. 12 Split tensile strength of NSC-PEG 600

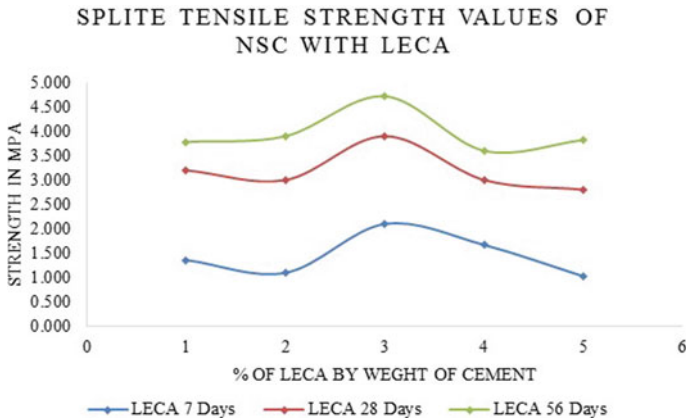


Fig. 13 Split tensile strength of NSC-LECA

- Initially mix design of M40 grade concrete is carried out as per IS 10262:2019. Water–cement ratio 0.3, 0.36, 0.4 and 0.45 is tried. Out of these four w/c ratio 0.36 is selected for further study based on its best result with respect to compressive strength and split tensile strength.
- Workability of the self-curing concrete directly depends on the type of the curing agent used.
- Curing compound-based self-curing concrete shows best results followed by LECA, PUMICE STONE, SAP, PEG600 and PEG 400.
- The optimum value was obtained at 0.2% SAP, 4% PEG 400 and 3% of PEG 600, 3% of LECA, 4% of pumice stone percentage by the weight of the cement in terms of compressive strength as well as split tensile strength.

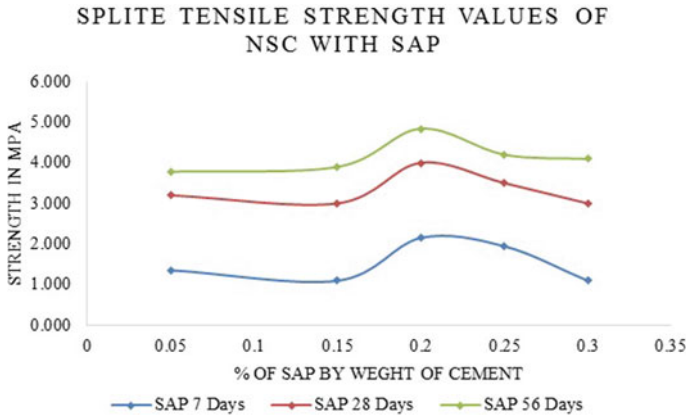


Fig. 14 Split tensile strength of NSC-PEG 400

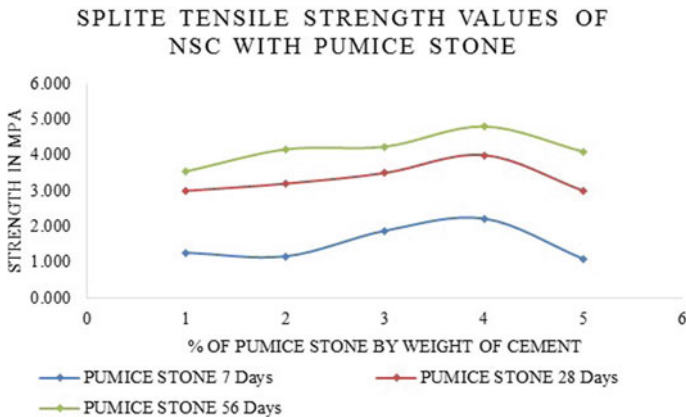


Fig. 15 Split tensile strength of NSC-pumice stone

10. The externally applied curing compound gives the best result. Curing compound should be applied under strict supervision such that no area on the surface of concrete should remain blank.

References

1. H. Aruntas, S. Cemalgil, O. Şimşek, G. Durmuş, M. Erdal, Effects of super plasticizer and curing conditions on properties of concrete with and without fiber. *Mater. Lett.* **62**(19), 3441–3443 (2008)
2. R. Dhir, P. Hewlett, T. Dyer, Durability of ‘self-cure’ concrete. *Cem. Concr. Res.* **25**(6), 1153–1158 (1995)

3. A. El-Dieb, Self-curing concrete: water retention, hydration and moisture transport. *Constr. Build. Mater.* **21**(6), 1282–1287 (2007)
4. D. Varga, R. Spragg, C. Bella, J. Castro, D. Bentz, J. Weiss, Fluid transport in high volume fly ash mixtures with and without internal curing. *Cem. Concr. Compos.* **45**, 102–110 (2014)
5. C. Song, Y. Choi, S. Choi, Effect of internal curing by superabsorbent polymers—internal relative humidity and autogenous shrinkage of alkali-activated slag mortars. *Constr. Build. Mater.* **123**, 198–206 (2016)
6. D. Shen, X. Wang, D. Cheng, J. Zhang, G. Jiang, Effect of internal curing with superabsorbent polymers on autogenous shrinkage of concrete at early age. *Constr. Build. Mater.* **106**(1), 512–522 (2016)
7. S. Madduru, S. Pallapothu, Effect of self curing chemicals in self compacting mortars. *J. Immunol.* **188**(2), 753–764 (2012)
8. D. Cusson, T. Hoogeveen, Internal curing of high-performance concrete with pre-soaked fine lightweight aggregate for prevention of autogenous shrinkage cracking. *Cem. Concr. Res.* **38**(6), 757–765 (2008)
9. M. Kamal, M. Safan, A. Bashandy, A. Khalil, Experimental investigation on the behavior of normal strength and high strength self-curing self-compacting concrete. *J. Build. Eng.* **16**, 79–93 (2018)
10. R. Bansal, *A Text Book of Fluid Mechanics and Hydraulic Machines*, 9th rev edn. (Laxmi Publication Pvt Ltd, 2018). ISBN 978-81-318-0815-3
11. D. Zou, K. Li, W. Li, H. Li, T. Cao, Effects of pore structure and water absorption on internal curing efficiency of porous aggregates. *Constr. Build. Mater.* **163**, 949–959 (2018)
12. J. Justs, M. Wyrzykowski, D. Bajare, P. Lura, Internal curing by superabsorbent polymers in ultra-high performance concrete. *Cem. Concr. Res.* **76**, 82–90 (2015)
13. H. Lee, H. Wong, N. Buenfeld, Self-sealing of cracks in concrete using superabsorbent polymers. *Cem. Concr. Res.* **79**, 194–208 (2016)
14. M. Mousa, M. Mahdy, A. Reheem, A. Yehia, Self-curing concrete types; water retention and durability. *Alexandria Eng. J.* **54**(3), 565–575 (2015)
15. A. Karthik, K. Sudalaimani, C. Kumar, Investigation on mechanical properties of fly ash-ground granulated blast furnace slag based self-curing bio-geopolymer concrete. *Constr. Build. Mater.* **149**, 338–349 (2017)
16. D. Shen, H. Shi, X. Tang, Y. Ji, G. Jiang, Effect of internal curing with superabsorbent polymers on residual stress development and stress relaxation in restrained concrete ring specimens. *Constr. Build. Mater.* **120**, 309–320 (2016)
17. D. Shen, M. Wang, Y. Chen, W. Wang, J. Zhang, Prediction of internal relative humidity in concrete modified with super absorbent polymers at early age. *Constr. Build. Mater.* **149**, 543–552 (2017)
18. J. Liu, C. Shi, X. Ma, K. Khayat, J. Zhang, D. Wang, An overview on the effect of internal curing on shrinkage of high performance cement-based materials. *Constr. Build. Mater.* **146**, 702–712 (2017)

Applications of Engineering Mathematics in Real Life Civil Engineering: Practical Examples



Mahesh Navnath Patil, Vinay Ashok Rangari, Aakash Suresh Pawar, and Shailendrakumar Dubey

Abstract Mathematics is part of our day-to-day life. Many field works employ extensive use of mathematics knowingly or unknowingly. Engineering field cannot be imagined without involvement of mathematics, and it forms the backbone of mother branch ‘civil engineering.’ For many peoples, applying mathematics to engineering problems found a little difficult. The reason behind this, in most of cases, civil engineering problems are not discussed with respect to their compatibility with basic mathematics which makes difficult for people to understand interlinking. The aim of this paper is to exhibit some applications of mathematics to various fields of civil engineering. Some simple and basic examples are discussed to build a bridge between civil engineering and engineering mathematics. This paper is divided into three case studies. Each case study represents application mathematics with examples in particular field of civil engineering.

Keywords Engineering · Mathematics · Civil · Applications

1 Introduction

Mathematics is part of our day-to-day life. Many field works employ extensive use of mathematics knowingly or unknowingly [1]. Engineering field cannot be imagined without involvement of mathematics, and it forms the backbone of mother branch ‘civil engineering.’ Engineering mechanics, essential part of civil engineering, is the extension of various applications of mathematics along with physics [2]. Research and development in the field of civil engineering cannot be imagine without mathematics [3]. Matrices, linear algebra, differential equations, integration (double and

M. N. Patil (✉) · A. S. Pawar
Department of Civil Engineering, RCPIT, Shirpur, Maharashtra, India

V. A. Rangari
Department of Civil Engineering, Sree Vidyanikethan Engineering College, Tirupati 517102, India

S. Dubey
Department of Civil Engineering, SSVPS BSD College of Engineering, Dhule 424001, India

triple integration) numerical analysis calculus, statistics, probability are taught as they are essential to realize numerous civil engineering fields such as structural engineering, fluid mechanics, water resource engineering, geotechnical engineering, foundation engineering, environmental engineering and transportation engineering to name a few. However, it becomes necessary to correlate basic mathematics to its real life applications of civil engineering [4]. The theory of matrices can be implemented to structural analysis to perform stability checks [5]. Similarly, differential equations are used to solve complex networks involved in fluid mechanics as well as structural analysis [6]. Concepts of probability and statistics have direct application in water resource engineering [4].

For many peoples, applying mathematics to engineering problems found a little difficult. The reason behind this, in most of cases, civil engineering problems are not discussed with respect to their compatibility with basic mathematics which makes difficult for people to understand interlinking [3]. The aim of this paper is to exhibit some applications of mathematics to various fields of civil engineering. Some simple and basic examples are discussed to build a bridge between civil engineering and engineering mathematics. This paper is divided into three case studies. Each case study represents application mathematics with examples in particular field of civil engineering.

2 Case Studies

Mathematics is widely used in many real life problems associated civil engineering. Few applications of engineering mathematics various fields of civil engineering are explained in subsequent paragraph.

2.1 *Water Resources Engineering*

Data availability and data consistency are of utmost importance in water resources engineering [7]. Statistics and probability help in analysis of data and checking the quality of available data. Many hydraulic engineering applications concerned with rainfall events and floods requires the estimation of probability of occurrence of a particular event. Frequency analysis of such events provides useful information regarding the rainfall/runoff data. The probability of occurrence of an event is studied using frequency analysis of annual data series of rainfall. The occurrence probability of an event is denoted by ' P ,' while, the non-occurrence probability of the same event is given by $q = (1 - P)$. The recurrence interval (return period) is given by Eq. 1. Then, occurrence probability of the event ' r ' times in ' n ' successive years ' $P(r, n)$ ' is given by the binomial distribution as represented by Eq. 2.

$$T = \frac{1}{P} \quad (1)$$

$$P_{r,n} = {}^n C_r P_r q^{n-r} = \frac{n!}{(n-r)!r!} P^r q^{n-r} \quad (2)$$

2.2 Structural Engineering

Use of mathematical equations to find solutions of various problems related to structural design is a traditional practice used by man-kinds from ages. For example, curve fitting can be used to formulate graphical relationship between two parameters to form the basic laws (laws of load vs. deflection, load vs. effort, etc.) is common practice [8]. Similarly, the differentiation and integration methods are primarily used in analysis of determinate as well as indeterminate structures. Matrices have distinguished application in stiffness method and flexibility method (matrix method of structural analysis) of structural analysis [9]. Stiffness is defined as the action required at the simply supported end of the member to cause a unit displacement, whereas the flexibility is the displacement produced due to application of unit force on the member.

2.3 Stiffness Matrix

Stiffness equation in the matrix form can be written as:

$$\Delta = k^{-1}[P - P'] \quad (3)$$

$$\begin{bmatrix} \Delta_1 \\ \Delta_2 \\ \Delta_3 \end{bmatrix} = k^{-1} \left\{ \begin{bmatrix} P_1 \\ P_2 \\ P_3 \end{bmatrix} - \begin{bmatrix} P'_1 \\ P'_2 \\ P'_3 \end{bmatrix} \right\} \quad (4)$$

where,

- Δ_1 Slope or deflection at co-ordinate 1.
- Δ_2 Slope or deflection at co-ordinate 2.
- Δ_3 Slope or deflection at co-ordinate 3.
- P_1 External Slope or external moment at co-ordinate 1.
- P_2 External Slope or external moment at co-ordinate 2.
- P_3 External Slope or external moment at co-ordinate 3.
- P'_1 Fixed end moment at co-ordinate 1.
- P'_2 Fixed end moment at co-ordinate 2.
- P'_3 Fixed end moment at co-ordinate 3.

2.4 Application of Integration and Differential Equations

Macaulay’s method used for estimating the slope and deflections in a beam uses integration and differential equations, represents wide application of mathematics in civil (structural) engineering [10]. Equation 5 represents the differential equation of elastic curve, the ‘EI’ is known as flexural rigidity of beam. By integrating the differential equation of elastic curve, we get slope of the beam (Eq. 6). Whereas deflection of beam (Eq. 7) is obtained by integrating the slope Eq. 6.

$$EI \frac{d^2y}{dx^2} = M \tag{5}$$

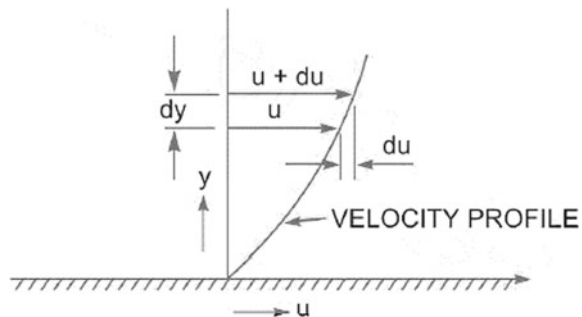
$$EI \frac{dy}{dx} = \int M dx + C_1 \tag{6}$$

$$EI y = \int \int M dx + C_1x + C_2a \tag{7}$$

2.5 Fluid Mechanics

Mathematics has wide applications in fluid mechanics branch of civil engineering. The simple application of ordinary differential equations in fluid mechanics is to calculate the viscosity of fluids [11]. Viscosity is the property of fluid which moderate the movement of adjacent fluid layers over one another [4]. Figure 1 shows cross section of a fluid layer. Consider two fluid layers ‘dy’ distance apart moving with velocities ‘u’ and ‘u + du,’ respectively. The movement of fluid layers will produce in shear stress ‘τ’ on the contact surface. This shear stress is proportional to the rate of change of velocity with respect to ‘y’ and is given by Eq. 8.

Fig. 1 Fluid profile



$$\tau \propto \frac{du}{dy} \quad \text{Therefore, } = \mu \frac{du}{dy} \tag{8}$$

where, ‘ μ ’ is constant of proportionality.

2.6 Applications of Bernoulli’s Differential Equations

The Bernoulli’s Differential Equations is most commonly used application of mathematics in fluid mechanics branch of civil engineering [4]. The Bernoulli’s Differential Equations are used to calculate the head loss in pipe flows under different conditions [12]. For instance, due to sudden enlargement of pipe the fluid flow will lose its energy. Consider two sections as shown in Fig. 2. The Bernoulli’s Equation (Eq. 9) can be applied between the two sections. Solving Eq. 9, the head loss due to sudden enlargement can be estimated as shown in Eq. 10.

$$\frac{P_1}{\rho g} + \frac{v_1^2}{2g} + Z_1 = \frac{P_2}{\rho g} + \frac{v_2^2}{2g} + Z_2 + h_e \tag{9}$$

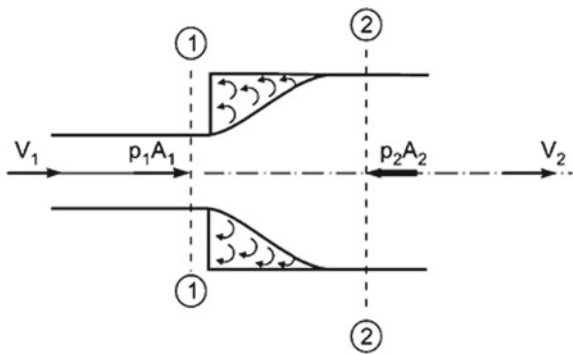
where h_e = head loss due to sudden enlargement.

$Z_1 = Z_2$...For Horizontal Pipe.

$$\frac{P_1}{\rho g} + \frac{v_1^2}{2g} = \frac{P_2}{\rho g} + \frac{v_2^2}{2g} + h_e$$

$$h_e = \left(\frac{P_1}{\rho g} - \frac{P_2}{\rho g} \right) + \left(\frac{v_1^2}{2g} - \frac{v_2^2}{2g} \right) \tag{10}$$

Fig. 2 Sudden enlargement of pipe



2.7 Applications of Vector, Scalar, Continuity Equation, Laplace Equation and Partial Derivative

Vector, Scalar, Continuity Equation, Laplace Equation, and Partial Derivative are basic forms of mathematical equations widely used to explain many physical phenomenon's [6]. A common example elaborating use of all these applications of mathematics together is explained using velocity potential function (\emptyset) and stream function (φ).

2.8 Velocity Potential Function (\emptyset)

Velocity potential function is function of space and time. It is denoted by ' \emptyset .' Velocity of fluid in any direction can be obtained by negative partial differentiation of velocity potential function with respect to that direction.

By mathematical expression we can write, $\emptyset = f(x, y, z)$.

$$u = -\frac{\partial \emptyset}{\partial x}, v = -\frac{\partial \emptyset}{\partial y}, w = -\frac{\partial \emptyset}{\partial z} \quad (11)$$

where u is component of velocity in x direction, v is component of velocity in y direction, w is component of velocity in z direction.

For incompressible fluid, continuity equation of steady flow is (Eq. 12).

$$\frac{\partial u}{\partial x} + \frac{\partial v}{\partial y} + \frac{\partial w}{\partial z} = 0 \quad (12)$$

After substitution of u , v and w from Eqs. 1 in 2, we get:

$$\frac{\partial}{\partial x} \left(-\frac{\partial \emptyset}{\partial x} \right) + \frac{\partial}{\partial y} \left(-\frac{\partial \emptyset}{\partial y} \right) + \frac{\partial}{\partial z} \left(-\frac{\partial \emptyset}{\partial z} \right) = 0$$

Therefore,

$$\frac{\partial^2 \emptyset}{\partial x^2} + \frac{\partial^2 \emptyset}{\partial y^2} + \frac{\partial^2 \emptyset}{\partial z^2} = 0 \quad (13)$$

This (Eq. 13) is known as Laplace equation.

2.9 Stream Function (φ)

Stream function is scalar function. Velocity perpendicular to any direction can be obtained by partial differentiation of stream function with respect to that direction [6]. For instance, $\varphi = f(x, y)$,

$$u = -\frac{\partial\varphi}{\partial y}, v = \frac{\partial\varphi}{\partial x} \quad (14)$$

The continuity equation for 2-D flow:

$$\frac{\partial u}{\partial x} + \frac{\partial v}{\partial y} = 0 \quad (15)$$

From Eqs. 4 in 5, we get:

$$\begin{aligned} \frac{\partial}{\partial x} \left(-\frac{\partial\varphi}{\partial y} \right) + \frac{\partial}{\partial y} \left(\frac{\partial\varphi}{\partial x} \right) &= 0 \\ -\frac{\partial^2\varphi}{\partial x\partial y} + \frac{\partial^2\varphi}{\partial x\partial y} &= 0 \end{aligned} \quad (16)$$

Equation 16 is known as Laplace equation. Any equation satisfying the Laplace equation shows the possible case of fluid flow.

3 Examples

Applications of mathematics in civil engineering as explained in back forth paragraphs. Few crucial application based examples are as follows.

1. Maximum one day rainfall for 50 years return interval in Delhi is found to be 280 mm. what is the possibility of one day rainfall more than 280 mm depth
 - (i) One time in 20 consecutive years,
 - (ii) Twice in 15 consecutive years,
 - (iii) At least once in 20 consecutive years.

Solution

Here,

$$\begin{aligned} P &= \frac{1}{T} = \frac{1}{50} = 0.02 \\ q &= (1 - P) = (1 - 0.02) = \mathbf{0.98} \end{aligned}$$

Case (i): $n = 20, r = 1$

$$P_{1,20} = \frac{20!}{(20-1)!1!} P^1 q^{20-1}$$

$$P_{1,20} = \frac{20!}{19!1!} (0.02)^1 (0.98)^{20-1} = 20 \times (0.98)(0.98)^{19}$$

$$P_{1,20} = 20 \times 0.02 \times 0.68123 = 0.272$$

Case (ii): $n = 15, r = 2$

$$P_{2,15} = \frac{15!}{(15-2)!2!} (0.02)^2 (0.98)^{15-2}$$

$$P_{2,15} = \frac{15!}{13!2!} (0.02)^2 (0.98)^{13} = 15 \times \frac{14}{2} \times 0.0004 \times 0.769$$

$$P_{2,15} = 0.323$$

Case (iii): $n = 20$

$$P_1 = 1 - q^n = 1 - (1 - P)^n$$

$$P_1 = 1 - (1 - 0.02)^{20} = 0.332$$

2. A river catchment consists of four rain-gauges with average yearly rainfall of 800, 620, 400, and 540 mm.
- The optimal rain-gauge stations required to limit the error up to 10%.
 - Calculate the extra rain-gauges required.

Solution

Mean annual average precipitation

$$\bar{P} = \frac{\sum P}{n} = \frac{(800 + 620 + 400 + 540)}{4} = \mathbf{590 \text{ mm}}$$

Mean of squares

$$\overline{P^2} = \frac{\sum P^2}{n} = \frac{(800^2 + 620^2 + 400^2 + 540^2)}{4} = \mathbf{369,000}$$

Sample Standard Deviation

$$\sigma = \sqrt{\frac{n}{n-1} [\overline{P^2} - (\bar{P})^2]}$$

$$\sigma = \sqrt{\frac{4}{4-1} [369000 - (590)^2]}$$

$$\sigma = \mathbf{166.93}$$

Calculation of coefficient of variation of the rainfall

$$C_v = \frac{100\sigma}{\bar{P}}$$

$$C_v = \frac{100 \times 166.93}{590}$$

$$C_v = \mathbf{28.29}$$

Optimum number of rain-gauges (N) are calculated using following equations:

$$N = \left(\frac{C_v}{E}\right)^2$$

$$N = \left(\frac{28.29}{10}\right)^2 = 8.004 \approx 8$$

Additional gauges required = 8-Existing gauges (4) = 4 Numbers.

- Simply supported beam carries a concentrated load ‘ P ’ at its middle point. Corresponding to various values of ‘ P ,’ maximum deflection is tabulated as below. Find law in the form $Y = ap + b$ using least square method, (where, ‘ a ’ and ‘ b ’ are constants) (Table 1).

P	100	120	140	160	180	200
Y	0.90	1.10	1.20	1.40	1.60	1.70

Solution

We have,

$$Y = ap + b \tag{17}$$

Table 1 Load and distribution table

S. No.	p	Y	pY	p^2
1	100	0.9	90	10,000
2	120	1.1	132	14,400
3	140	1.2	168	19,600
4	160	1.4	224	25,600
5	180	1.6	288	32,400
6	200	1.7	340	40,000
Sum	900	7.9	1242	142,000

The normal equations are given as:

$$\sum Y = a \sum p + nb \tag{18}$$

$$\sum pY = a \sum p^2 + b \sum p \tag{19}$$

From Eq. 18,

$$7.9 = 900a + 6b \tag{20}$$

From Eq. 19,

$$1242 = 142,000a + 900b \tag{21}$$

Solving Eqs. 20 and 21

$$a = 8.14 \times 10^{-3} \text{ and } b = 0.095$$

Therefore, Eq. 17, can be written as:

$$Y = (8.14 \times 10^{-3})p + 0.095$$

4. Analyze the continuous beam as shown in Fig. 3.

Solution

Slope at point B, C and D, i.e., $\theta_B, \theta_C, \theta_D$ can be calculated by using Stiffness Equation

$$\Delta = k^{-1}[P - P']$$

$$\begin{bmatrix} \Delta_1 \\ \Delta_2 \\ \Delta_3 \end{bmatrix} = k^{-1} \left\{ \begin{bmatrix} P_1 \\ P_2 \\ P_3 \end{bmatrix} - \begin{bmatrix} P'_1 \\ P'_2 \\ P'_3 \end{bmatrix} \right\}$$

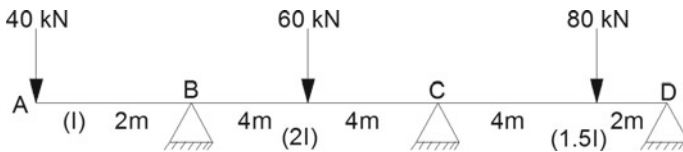


Fig. 3 Point load on continuous beam

where

$$\begin{aligned} \Delta_1 &= \theta_B, \Delta_2 = \theta_C, \Delta_3 = \theta_D \\ P_1 &= -80 \text{ kN m}, P_2 = 0, P_3 = 0 \\ P'_1 &= -60 \text{ kN m}, P'_2 = 24.44 \text{ kN m}, P'_3 = 71.11 \text{ kN.m} \end{aligned}$$

$$\begin{bmatrix} \theta_B \\ \theta_C \\ \theta_D \end{bmatrix} = k^{-1} \left\{ \begin{bmatrix} -80 \\ 0 \\ 0 \end{bmatrix} - \begin{bmatrix} 60 \\ 24.44 \\ 71.11 \end{bmatrix} \right\}$$

where,

$$K^{-1} = \frac{1}{1.5EI} \begin{bmatrix} 1.75 & -0.5 & 0.25 \\ -0.5 & 1 & -0.5 \\ 0.25 & -0.5 & 1.75 \end{bmatrix}$$

Solving matrix, we get

$$\theta_B = \frac{-27.038}{EI}, \theta_C = \frac{14.077}{EI} \text{ and } \theta_D = \frac{-78.15}{EI}$$

- For given simply supported beam subjected to point load at center find slope at support and deflection at the mid span of beam (Fig. 4) [5].

Let us consider FBD of the beam (Fig. 5).

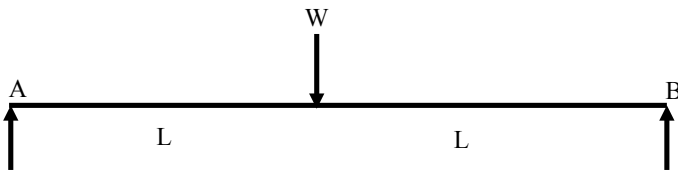
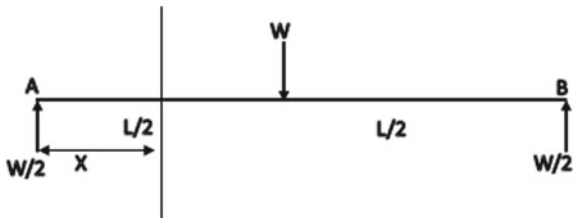


Fig. 4 Point load acting at the center

Fig. 5 Free body diagram of beam



Solution

Differential equation of elastic curve of beam is given by

$$EI \frac{d^2y}{dx^2} = M = \frac{W}{2} \times X \tag{i}$$

By integrating above Eq. (i) we get slope of the beam:

$$EI \frac{dy}{dx} = \frac{W}{2} \times \frac{X^2}{2} + C_1 = \frac{WX^2}{4} + C_1 \tag{ii}$$

Again integrating equation to (ii) we get,

$$EI.y = \frac{WX^3}{12} + C_1X + C_2 \tag{iii}$$

At point at center of beam, $X = \frac{L}{2}$ and $\frac{dy}{dx} = 0$. Applying Eq. (ii), we get:

$$EI(0) = \frac{W}{4} \times \frac{L^2}{4} + C_1$$

Therefore,

$$C_1 = \frac{-WL^2}{16} \tag{iii}$$

Put C_1 in Eq. (ii)

$$EI \frac{dy}{dx} = \frac{WX^2}{4} + \frac{-WL^2}{16} \tag{iv}$$

At point A, $X = 0$, Therefore,

$$EI \frac{dy}{dx} = \frac{-WL^2}{16}$$

$$\left(\frac{dy}{dx} \right)_A = \frac{-WL^2}{16EI}$$

Therefore,

$$\theta_A = \frac{WL^2}{16EI} \curvearrowright \text{Clockwise rotation.}$$

By symmetry

$$\theta_B = \frac{WL^2}{16EI} \curvearrowright \text{Clockwise rotation.}$$

Let us consider Eq. (iii)

$$EI.y = \frac{WX^3}{12} + C_1X + C_2 \quad (\text{iiia})$$

At point A $X = 0$, $Y = 0$, we get $C_2 = 0$ and we have $C_1 = \frac{-WL^2}{16}$.
Therefore,

$$EI.y = \frac{WX^3}{12} - \frac{WL^2}{16} \quad (\text{v})$$

At point C, $X = L/2$.

Put in Eq. (v), we get

$$EI.y = \frac{WL^3}{48} \quad (\text{vi})$$

Deflection at the center of simply supported beam

$$y = \frac{WL^3}{48EI} \quad (\text{vii})$$

6. Calculate slope at the support and deflection at the center of simply supported beam of span 10 m subjected to point load of 50 kN at the center of the span [13]. Take $EI = 31,300 \text{ kN m}^2$

Solution

See Fig. 6.

$$\begin{aligned} \theta_A = \theta_B &= \frac{WL^2}{16EI} \\ \theta_A = \theta_B &= \frac{50 \times 10^2}{16 \times 31,300} = 9.984 \times 10^{-3} \text{ Radian} \\ &= 9.984 \times 10^{-3} \times \frac{180}{\pi} = 0.572^\circ \\ \delta_C &= \frac{WL^3}{48EI} = \frac{50 \times 10^3}{48 \times 31300} = 0.0333 \text{ m} = 33.28 \text{ mm} \end{aligned}$$

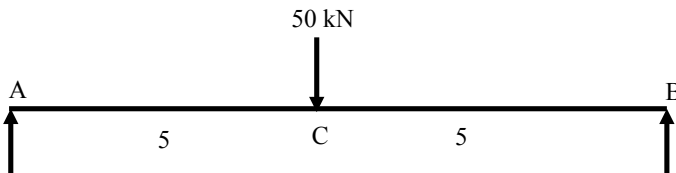


Fig. 6 Point load of 50 kN at the center of the span

7. For given cantilever beam subjected to point load at end find slope and deflection at the end span of beam.

Solution

Let's consider reaction at a distance 'x' as shown in Figs. 7 and 8.

Using Eq. (i),

$$EI \frac{d^2y}{dx^2} = M = Wx - WL \tag{i}$$

On integrating,

$$EI \frac{dy}{dx} = \frac{W \cdot x^2}{2} - WLx + C_1 \tag{ii}$$

Again integrating,

$$EI \cdot y = \frac{W \cdot x^3}{6} - \frac{WLx^2}{2} + C_1 \cdot x + C_2 \tag{iii}$$

Consider boundary conditions, $x = 0, \frac{dy}{dx} = 0$.

Substituting in Eq. (ii), we get

$$C_1 = 0$$

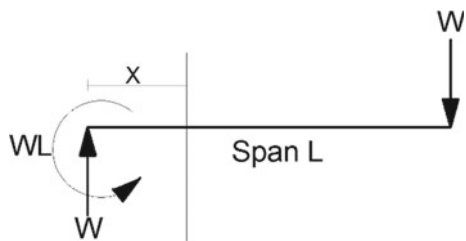
Substituting in Eq. (iii), we get

$$C_2 = 0$$

Fig. 7 Cantilever beam subjected to point load



Fig. 8 Free body diagram Cantilever beam subjected to point load



Therefore, Eqs. (ii) and (iii) can be written as:

$$EI \frac{dy}{dx} = \frac{W.x^2}{2} - WLx \quad (\text{iv})$$

$$EI.y = \frac{W.x^3}{6} - \frac{WLx^2}{2} \quad (\text{v})$$

Put $x = L$ in Eq. (iv) to calculate slope at free end of beam.
Therefore,

$$EI \frac{dy}{dx} = \frac{W.x^2}{2} - WLx \quad (\text{iv})$$

$$EI \frac{dy}{dx} = \frac{W.L^2}{2} - W.L.L$$

$$EI \frac{dy}{dx} = \frac{W.L^2}{2} - WL^2$$

$$\frac{dy}{dx} = -\frac{W.L^2}{2EI} = \theta \quad (\text{vi})$$

Put $x = L$ in Eq. (v) to calculate deflection at free end of beam.
Therefore,

$$EI.y = \frac{W.x^3}{6} - \frac{WLx^2}{2} \quad (\text{v})$$

$$EI.y = \frac{W.L^3}{6} - \frac{W.L.L^2}{2}$$

$$y = \frac{W.L^3}{3EI}$$

8. For given cantilever beam subjected to point load at end find slope and deflection at the end span of beam.

$$\text{Slope: } \theta_B = \frac{W.L^2}{2EI} = \frac{2500}{EI},$$

$$\text{Deflection: } Y_B = \frac{W.L^3}{3EI} = \frac{16666.67}{EI}$$

9. The discharge through a level pipe is $0.25 \text{ m}^3/\text{s}$. The pipe diameter is 0.2 m and suddenly enlarged to 0.4 m so that the intensity of pressure reduced to 11.772 N/cm^2 . If $h_e = 1.816 \text{ m}$. Estimate the intensity of pressure in large pipe.

Solution

$$Q = 0.25 \text{ m}^3/\text{s}.$$

Diameter of small pipe, $D_1 = 200 \text{ mm} = 0.20 \text{ m}$

$$\text{Area } A_1 = \frac{\pi}{4} D_1^2 = \frac{\pi}{4} 0.2^2 = 0.03141 \text{ m}^2$$

$$D_2 = 400 \text{ mm} = 0.4 \text{ m}$$

$$A_2 = \frac{\pi}{4} D_2^2 = \frac{\pi}{4} 0.4^2 = 0.12564 \text{ m}^2$$

$$Q = 250 \text{ L/s} = 0.25 \text{ m}^3/\text{s}$$

$$V_1 = \frac{Q}{A_1} = \frac{0.25}{0.03141} = 7.96 \text{ m/s}$$

$$V_2 = \frac{Q}{A_2} = \frac{0.25}{0.12564} = 1.99 \text{ m/s}$$

$$P_1 = 11.772 \frac{\text{N}}{\text{cm}^2} = 11.772 \times 10^4 \frac{\text{N}}{\text{m}^2}$$

Loss of head due to enlargement = $h_e = 1.816 \text{ m}$

$$\frac{P_1}{\rho g} + \frac{v_1^2}{2g} + Z_1 = \frac{P_2}{\rho g} + \frac{v_2^2}{2g} + Z_2 + h_e$$

$Z_1 = Z_2 \dots$ For Horizontal Pipe.

$$\frac{11.772 \times 10^4}{1000 \times 9.81} + \frac{7.96^2}{2 \times 9.81} = \frac{P_2}{1000 \times 9.81} + \frac{1.99^2}{2 \times 9.81} + 1.816$$

$$P_2 = 12.96 \times 10^4 \frac{\text{N}}{\text{m}^2}$$

10. The velocity potential function (\emptyset) is given by an expression:

$$\emptyset = -\frac{xy^3}{3} - x^2 + \frac{x^3y}{3} + y^2$$

Find: (1) velocity components in x and y directions. (2) Show that \emptyset represents a possible case of flow.

Solution

Given

$$\emptyset = -\frac{xy^3}{3} - x^2 + \frac{x^3y}{3} + y^2$$

The partial derivatives of \emptyset w.r.t. x and y are

$$\frac{\partial \emptyset}{\partial x} = -\frac{y^3}{3} - 2x + \frac{3x^2y}{3}$$

$$\frac{\partial \emptyset}{\partial y} = -\frac{3xy^2}{3} + \frac{x^3}{3} + 2y$$

We know that

$$u = -\frac{\partial \emptyset}{\partial y} = -\left(-\frac{y^3}{3} - 2x + \frac{3x^2y}{3}\right)$$

$$u = \frac{y^3}{3} + 2x - x^2y \quad \text{(i)}$$

$$v = -\frac{\partial \emptyset}{\partial x} = -\left(-\frac{3xy^2}{3} + \frac{x^3}{3} + 2y\right)$$

$$v = xy^2 - \frac{x^3}{3} - 2y \quad \text{(ii)}$$

\emptyset Must satisfy Laplace equation for the possible case of fluid flow.
Laplace equation for two-dimensional flow:

$$\frac{\partial^2 \emptyset}{\partial x^2} + \frac{\partial^2 \emptyset}{\partial y^2} = 0 \quad \text{(iii)}$$

$$\frac{\partial \emptyset}{\partial x} = -\frac{y^3}{3} - 2x + x^2y$$

Therefore,

$$\frac{\partial^2 \emptyset}{\partial x^2} = -2 + 2xy \quad \text{(iv)}$$

$$\frac{\partial \emptyset}{\partial y} = -xy^2 + \frac{x^3}{3} + 2y$$

$$\frac{\partial^2 \emptyset}{\partial y^2} = -2xy + 2 \quad \text{(v)}$$

Substituting value of (iv) and (v) in (iii), we get

$$\frac{\partial^2 \emptyset}{\partial x^2} + \frac{\partial^2 \emptyset}{\partial y^2} = (-2 + 2xy) + (-2xy + 2) = 0$$

Laplace equation is satisfied. Hence, \emptyset represents a possible case of flow.

11. A stream function is given by $\varphi = 5x - 6y$. Calculate the velocity components in x and y directions. Also find magnitude and direction of the resultant.

Solution

$$\varphi = 5x - 6y$$

$$u = -\frac{\partial\varphi}{\partial y} = 6 \text{ Unit/s}$$

$$v = \frac{\partial\varphi}{\partial x} = 5 \text{ Unit/s}$$

$$\text{Resultant velocity} = \sqrt{u^2 + v^2}$$

$$\text{Resultant velocity} = \sqrt{6^2 + 5^2} = 7.81 \text{ Units/s}$$

$$\tan\theta = \frac{v}{u} = \frac{5}{6} = 39^\circ 48'$$

$$\theta = \tan^{-1}(0.833) = 39^\circ 48'$$

4 Conclusion

This paper presents a brief discussion on real time application of mathematics in the various field of civil engineering (water resources, structural engineering and fluid mechanics). Applications of mathematics such as matrices, probability, statistics, differentiation, and integration are explained with suitable examples. These examples will help civil engineers to visualize the real time use of mathematics in day-to-day activities. The paper also serves the motto to boost the interest, confidence and create a joyful mathematical environment among students.

References

1. A. Ahmad, *Applications of Mathematics in Everyday Life* (Third Cambridge-Sultan Qaboos Universities Symposium (CAMSQU2019) on Mathematical Modelling, Muscat, Sultanate of Oman, 2019)
2. E. Popov, *Engineering Mechanics of Solids* (Prentice-Hall, New Jersey, 1990)
3. J. Caldwelland, Y.M. Ram, *Mathematical Modelling* (Springer Science + Business Media. Dordercht, 1999)
4. R.K. Bansal, *A Text Book of Fluid Mechanics and Hydraulic Machines* (Laxmi Publications, 2018). ISBN: 9788131808153
5. J.E. Connor, S. Faraji, *Fundamentals of Structural Engineering* (Springer-Verlag, Berlin Heidelberg, 2012)

6. A.P.S. Selvadurai, *Partial Differential Equations in Mechanics I*. ISBN 978-3-642-08666-3 (2000)
7. R.C. Reid, J.M. Prausnitz, B.E. Poling, *The Properties of Gases and Fluids* (McGraw-Hill Inc., New York, 1987)
8. M.A. Aiello, L. Ombres, Load-deflection analysis of concrete elements reinforced with FRP rebars. *Mech. Compos. Mater.* **35**, 111–118 (1999)
9. P. Antosik, C. Swartz, *Matrix Methods in Analysis* (1985). ISBN 978-3-540-39266-8
10. K.D. Hjelmstad, *Fundamentals of Structural Mechanics*, 2nd edn. (Springer-Verlag, New York, 2005)
11. M. Braun, *Differential Equations and Their Applications* (Springer Science + Business Media, New York, 1993)
12. R.T. Jacobsen, S.G. Penoncelo, E.W. Lemmon, *Thermodynamic Properties of Cryogenic Fluids* (Springer Science + Business Media, New York, 1997)
13. J.M. Gere, S.P. Timoshenko, *Mechanics of Materials*, 3rd edn. (Springer Science Business Media, Dordrecht, 1991)

Shear Strength Improvement of Black Cotton Soil Reinforced with Waste Plastic Bottle Strips



Nilesh Shirpurkar, Dhanraj Saste, Vaibhav Varpe, and Bhaskar Wabhitkar

Abstract India generates an average of 26,000 tons of plastic a day. The plastic processing industry is producing 13.4 MT in 2015 and growing to 22 million tons (MT) a year by 2020 (TOI article 2019) [1]. Black cotton soil has a very low-bearing capacity. Due to its characteristics, it forms a very poor foundation material. Black cotton soil falls under a major constituent of soil in India. The soil undergoes volumetric changes when soil is present on the water table. Increase in water content causes the swelling of the soils and loss of strength. Decrease in moisture content resulting in soil shrinkage. BC soil comes under category of expansive soil, and it causes differential settlements of soil resulting in severe damage to the foundations. In this research, we are trying to improve the shear strength of BC soil by adding waste plastic bottle (PET) strips as a reinforcement material. Waste plastic bottles were used in soil by 0.2, 0.4, 0.6, 0.8, 1% to its dry weight of soil. The length of strips is 1 and 2 cm with 2 mm constant width. Also, we test the reinforced BC soil with mixture of plastic strips (i.e., 1 cm length and 2 cm length of the same width). The direct shear test was performed on BC soil (reinforced and un-reinforced) to improve the shear strength. We also find out the properties of BC soil-like, specific gravity, Atterberg's limit (LL, PL, SL), and density of soil (standard proctor test).

Keywords Black cotton soil · PET—plastic bottle strips · Direct shear test · Atterberg's limit · SPT

N. Shirpurkar (✉) · D. Saste · V. Varpe · B. Wabhitkar
Department of Civil Engineering, MIT Academy of Engineering, Pune, India
e-mail: nsshirpurkar@mitaoe.ac.in

D. Saste
e-mail: dhanrajsaste@mitaoe.ac.in

V. Varpe
e-mail: vaibhavvarpe@mitaoe.ac.in

B. Wabhitkar
e-mail: bdwabhitkar@civil.mitaoe.ac.in

1 Introduction

Waste plastic bottles are widely spread around the world. We are identifying the coca-cola plastic bottles, made up of polyethylene terephthalate (PET) which is being increasingly used as a packaging purpose for drinks. Most of these bottles are specifically made for spot use, having a short life span and which are being discarded immediately after use. Though at many places PET is being collected for recycling or reuse, it is still not up to the mark. These cause many environmental problems, while on the other hand, cohesive soils are weak in shear. To improve the weaker zone of cohesive soil (i.e., shear zone) by adding the polyethylene terephthalate (PET) waste plastic bottle strips with various percentages in it research carried by Alshkane [2].

We are trying to improve the Shear strength parameter of black cotton soil as it is cohesive in nature. The basic property of black cotton soil is swelling and shrinking because of the presence of clay minerals, especially montmorillonite. Due to this, the differential settlements resulted in severe damage to the foundations of civil engineering structures. Uses of waste coca-cola plastic bottles as a soil reinforcement are recommended to reduce the amount of plastic waste, which creates a disposal problem. Waste plastic bottle strips are prepared by us and used as reinforcement to improve the shear strength of black cotton soil. The main advantage of waste plastic bottle material is easily available and cost-effective. The addition of plastic bottle strips in black cotton soil acts as a composite material. The strips mobilize tensile resistance to loading, which improves the shear zone of black cotton soil. It is one of the most effective soil reinforcement techniques and can be effectively used to meet the challenges to reduce plastic bottle waste.

2 Literature Review

There were lot of ground improvement techniques (like fly ash, lime, cement, etc.) while executing the construction on poor quality of soil. Later over the new advanced technology introduced by Adili [2] objective to improve the strength behavior of sandy soil reinforced with randomly included papyrus fiber. The direct shear tests were conducted on both unreinforced and reinforced soil. The direct shear test was conducted on reinforced sandy soil. It was observed that the improvement in cohesion for 10% papyrus was highest among the different percent (i.e., 5, 15, and 20%). The compression ratios of the reinforced soil were reduced for 5, 15, and 25% additions, while they increased with a 10% addition. After a year Asst. Lec. Nsaif [3] carried out his research on the utilization of industrial plastic as reinforcement in clayey and sandy soil. The plastic waste is used in circular pieces having diameter 1–2 and 5 mm thick with specific gravity 0.93. The waste plastic pieces of 0, 2, 4, 6, and 8% were used to prepare the test samples to its dry weight of soil [4]. The test soil was poorly graded sand with $C_c = 1.43$ and $C_u = 3.92$ and specific gravity 2.66. The test results were found to be significant improvement in the strength of soil due to increase in

internal friction. The percentage of angle of internal friction is slightly more in sandy soil than clayey soil. Mohankar and Pidurkar [5] were used the waste plastic fibers added in ratio of weight of fiber to the weight of soil. The fibers weight are 1.09, 2.03, 2.82, 3.44 gm and the soil weight 109.34, 101.53, 93.72, 85.91 gm. The soil samples were prepared for the water content of 24.38, 22.64, 20.90, 19.16 gm. The observed value of shear strength was to increase from 0.075 to 0.108 kg/cm² and from 0.044 to 0.091 kg/cm² for 1 kg normal loading.

Sodhi and Pal [6] worked on polypropylene of 10, 20, 30 mm in length are used by percent weight of dry soil sample. The test was conducted on plain soil, mixed soil and reinforced soil at different percentages 0, 0.15, 0.25, and 0.35% of waste fiber. The obtained shear parameter, cohesion 53.12 kPa, and angle of internal friction were 23.77° for polypropylene fiber of 20 mm length and 0.35% of waste plastic fiber. Peddaiah and Burman [7] research was carried out for the improvement of sandy soil using cut plastic bottle strips having sizes (15 mm × 15 mm), (15 mm × 25 mm), and (15 mm × 35 mm). The soil was reinforced with plastic strips of 0.2, 0.4, 0.6, and 0.8% by dry weight of soil. The observed proctor value is 16.75 kN/m³ and 16.8%. The plastic content increases from 0.6 to 0.8%, MDU decreases. In the case of OMC, it is just reversed therefore 0.4%. The obtained shear value is 19 kPa and 23.2°. Furkhan and Syed [8] observed that shear strength property of BC soil is improved when the use of different percentages, i.e., 0.5, 0.7, 0.9%, of plastic bottles strips along with admixture as cement lime, waste materials (like fly ash, phosphogypsum) to increase the shear strength of soil.

3 Material

3.1 Natural Soil

Locally available black cotton soil was collected for the test. It is one of the major soil deposits of India, which covers more than 20% geographical area of India. It is spread over Maharashtra, Madhya Pradesh, Andhra Pradesh, Gujarat, Tamil Nadu, Karnataka, and some other parts of India as well. The black cotton soil is very fine and dark which contains tremendously argillaceous, calcium, and magnesium carbonate. When the BC soil is wet, they are extremely adhesive and tenacious of moisture. The BC soil is from montmorillonitic and beidellitic groups of clay minerals. These clay minerals contain very high expensive characteristics. Construction of any civil engineering structure on cohesive soil (i.e., black cotton soil) is the biggest challenge, due to its property, i.e., swelling and shrinking. Because of high rates of montmorillonite in this soil, which leads to forming cracks in soil without any warning which is too dangerous for any construction structures, as this soil is directly connected to engineering structures.

3.2 Waste Plastic Bottle

In day-to-day life, plastic bottles are most commonly used and generate non-degradable waste causing land pollution. It is lightweight and durable, which makes them a popular packaging choice for transporting liquids. Plastic bottles are used to sell mineral drinking water, aerated drinks, juices, sodas, syrups, squashes, and more. It causes both land and water pollution. The disposal and dumping of the used and unwanted plastic have become a major threat to the civilized society, which also poses a risk to marine life. Since plastic is a non-biodegradable material. Plastic bottle and plastic bag recycling have not kept pace with the dramatic increase in virgin resin polyethylene terephthalate (PET) sales. The aspect of reduce/reuse/recycle has emerged as the one that needs to be given prominence. India generates nearly 26,000 tons of plastic waste every day.

PET is reported as one of the most abundant plastics in the solid urban waste, whose effective reuse/recycling is one of the critical issues. We are using coca-cola plastic bottle strips as soil reinforcement will help to minimize the waste.

4 Methodology

The waste plastic bottles strips of size 1, 2 cm in length with 2 mm constant thickness and the combination of 1 and 2 cm (equal percentage used) length strips were added in soil. The sizes of strips are measured using digital vernier caliper for accuracy. The strips are used to prepared soil sample for testing in 0.2, 0.4, 0.6, 0.8, 1% to its dry weight of soil. The variation in percentage of use of waste plastic bottle is based on the literature survey.

The standard proctor test and box shear test are conducted on un-reinforced BC soil. The SPT test is carried out on black cotton soil. The test soil samples are prepared using water content which is obtained from SPT, i.e., OMC and MDD. The series of box shear test was conducted on reinforced soil, with varying percentage of plastic strip, i.e., 0.2, 0.4, 0.6, 0.8, 1% for 1 and 2 cm length and combination of both. The normal stress is applied to perform the box shear test is 0.5, 1 and 1.5 kg/cm² (Table 1).

5 Experimental Study

5.1 Box Shear Test (IS-2720-Part13-1986) [9]

The waste plastic bottles strips are used to prepare the reinforced BC soil samples. The various percentage of waste plastic bottle strips (i.e., 0.2, 0.4, 0.6, 0.8, 1%) were added in test soil sample. The plastic strips were mixed in such a way that there will

Table 1 Properties of black cotton soil

Properties of tested black cotton soil	Value	IS code
Specific gravity (<i>G</i>)	2.268	IS 2720-part3-1980 [10]
Liquid limit (%)	83.33	IS 2720-part5-1985 [11]
Plastic limit (%)	45.33	IS 2720-part6-1972 [12]
Shrinkage limit (%)	23.29	
Optimum moisture content (%)	21.8	Compaction of soil IS 2720-part7-1980 [13]
Maximum dry density (γ_d) (gm/cc)	1.527	

be no formation of lumps in soil and strips spread effectively throughout the soil. The normal stress 0.5, 1, and 1.5 kg/cm² was applied to carry out the series of box shear test. The area of shear box was 36 cm². The loading rate to perform the shear test was 0.002 mm/s. The shear stress and the horizontal displacement were recorded till the failure of sample for the applied normal stress. The direct shear test was carried on both the samples 1 and 2 cm length with constant thickness 2 mm and combination of both lengths strip samples for the same percentage.

6 Observation and Discussion

6.1 Direct Shear Test on Un-Reinforced Black Cotton Soil

The un-reinforced BC soil sample was prepared using the 21.8% of water content (OMC value of SPT test). The direct shear test was performed on plain soil sample by giving the applied normal stress 0.5, 1, and 1.5 kg/cm². Figure 1 shows the failure

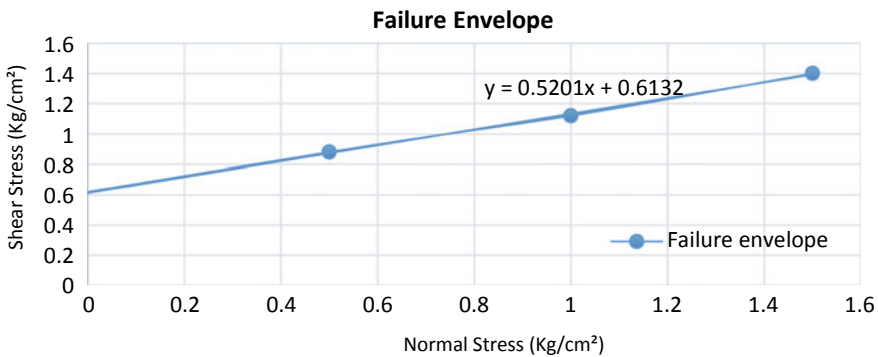


Fig. 1 Failure envelope-un-reinforced BC soil

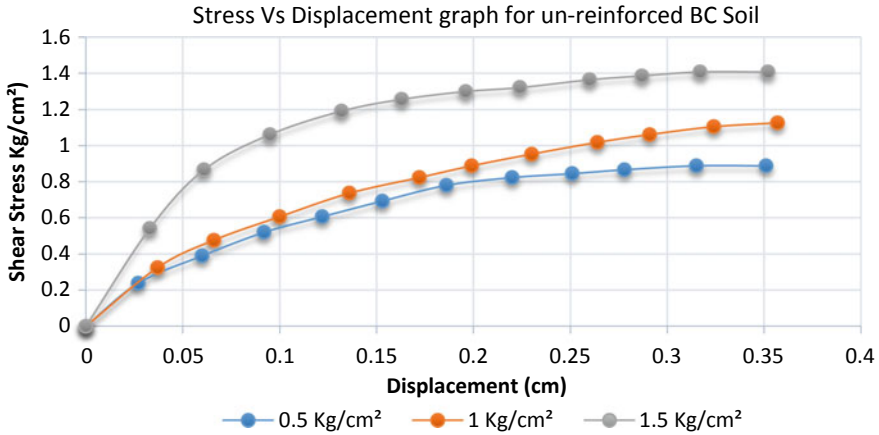


Fig. 2 Stress versus displacement graph of un-reinforced BC soil for applied normal stress

Table 2 Shear stress and displacement values

Normal stress (kg/cm ²)	Shear strength (kg/cm ²)	Displacement (cm)
0.5	0.888	0.351
1	1.126	0.357
1.5	1.408	0.352

envelope of un-reinforced black cotton soil and Fig. 2 stress versus displacement graph of un-reinforced BC soil for applied normal stress.

The obtained values of cohesion (C) = 0.613 kg/cm² and angle of internal friction (ϕ) 27.47° of black cotton soil.

The obtained values of shear strength and displacement for the applied normal stress are shown in Table 2

6.2 Direct Shear Test on Reinforced Black Cotton Soil

For the reinforcement of plastic strip, 0.2, 0.4, 0.6, 0.8, and 1% by weight of dry soil sample is taken for the length of 1, 2 cm, and combination of waste plastic fiber (1 cm + 2 cm) with 2 mm constant thickness.

For 1 cm length of plastic strip

From Fig. 3, the improvement observed for 1% addition of waste plastic strips, cohesion is 1.017 kg/cm² and angle of internal friction is 12.24°.

The max. shear stress is 1.0183 kg/cm² and displacement 0.56 cm for addition of 1% plastic bottle strips as shown in Fig. 4.

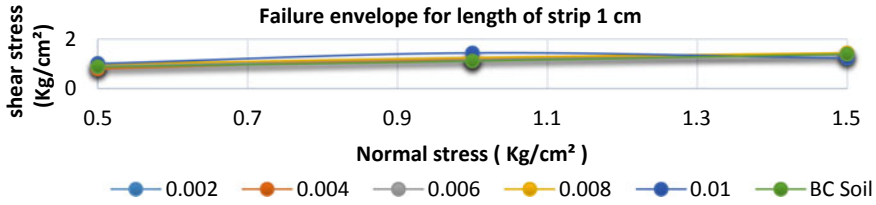


Fig. 3 Shear stress versus normal stress of soil reinforced with 1 cm length of strips

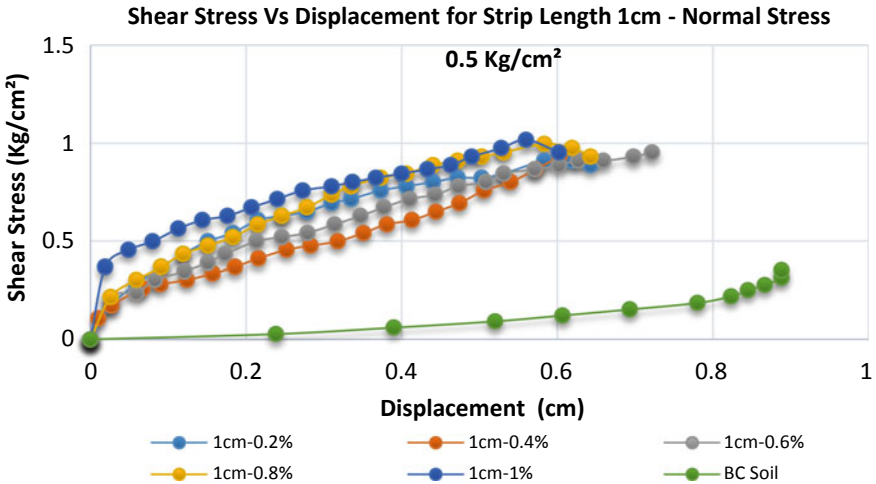


Fig. 4 Shear stress versus displacement for strip length 1 cm—normal stress 0.5 kg/cm²

The max. shear stress is 1.4516 kg/cm² and displacement 0.436 cm for addition of 1% waste plastic strips shown in Fig. 5.

From Fig. 6, there is no improvement in shear strength of reinforced BC soil for the applied normal stress 1.5 kg/cm².

For 2 cm length of plastic strip

From Fig. 7, observed value of cohesion is 0.859 kg/cm² and angle of internal friction is 24.46° for 1% addition of plastic bottle strips in BC soil.

The obtained values of shear stress 1.0833 kg/cm² and displacement 0.506 cm for 1% addition of plastic strips are shown in Fig. 8.

From the graph, the maximum shear strength of reinforced BC soil was 1.321 kg/cm² with horizontal displacement of 0.589 cm by adding 1% waste plastic bottle strips observed from Fig. 9.

Figure 10 shows the maximum shear strength of reinforced BC soil is found equal of 1.668 kg/cm² with horizontal displacement of 0.513 cm by adding 0.6% plastic strips in BC soil.

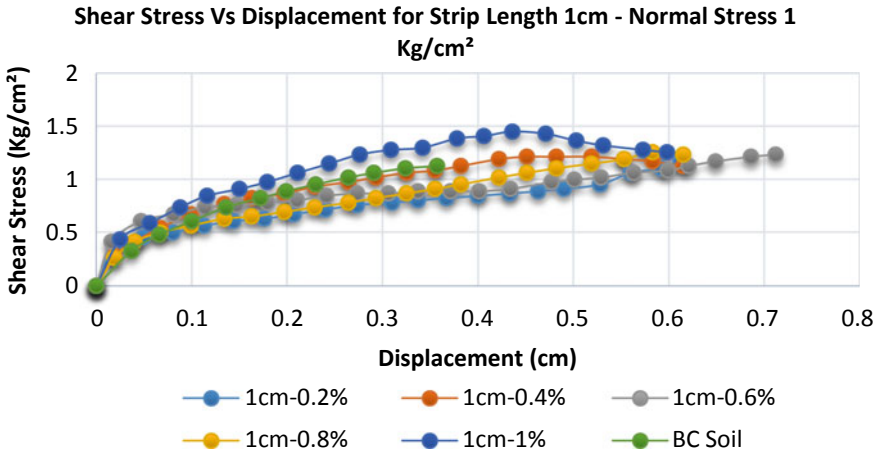


Fig. 5 Shear stress versus displacement for strip length 1 cm—normal stress 1 kg/cm²

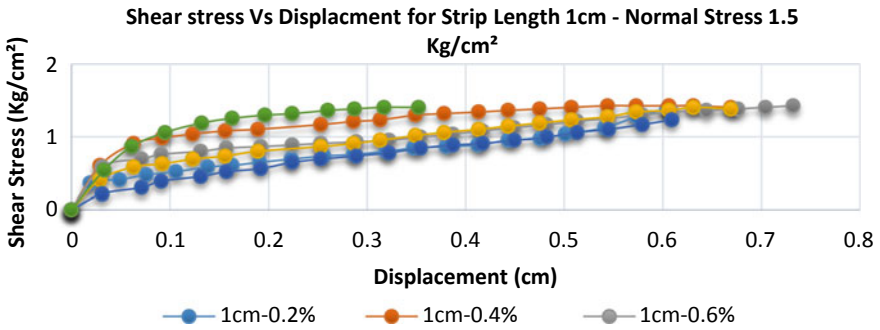


Fig. 6 Shear stress versus displacement for strip length 1 cm—normal stress 1.5 kg/cm²

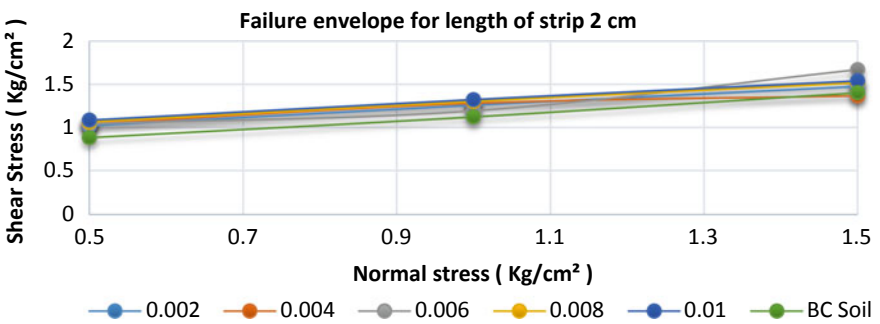


Fig. 7 Shear stress versus normal stress of soil reinforced with 2 cm strips

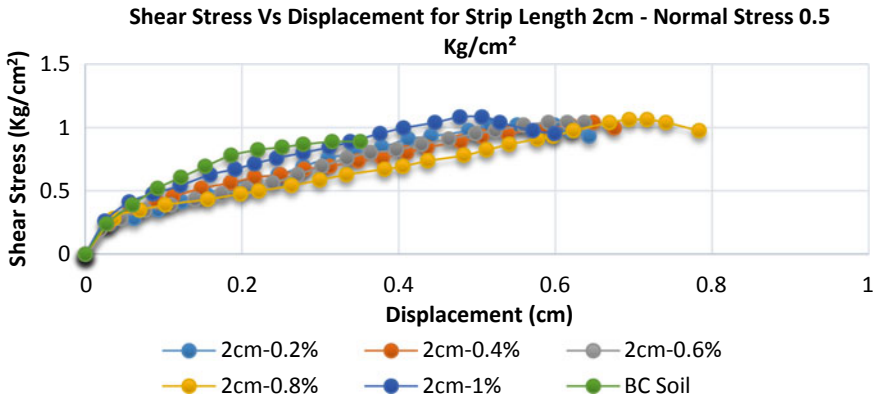


Fig. 8 Shear stress versus displacement for strip length 2 cm—normal stress 0.5 kg/cm²

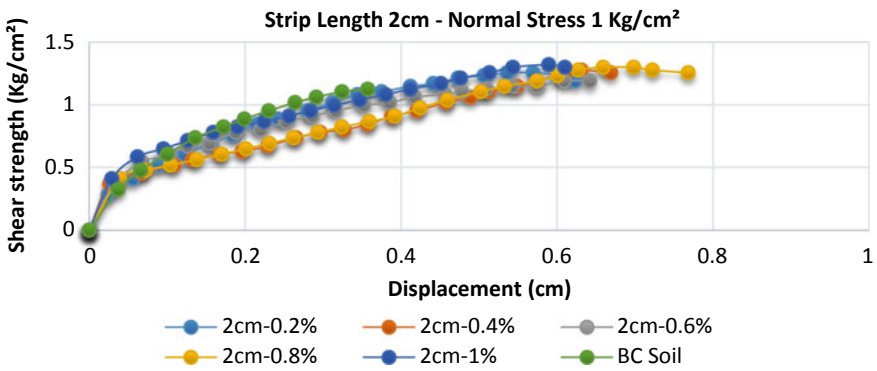


Fig. 9 Shear stress versus displacement for strip length 2 cm—normal stress 1 kg/cm²

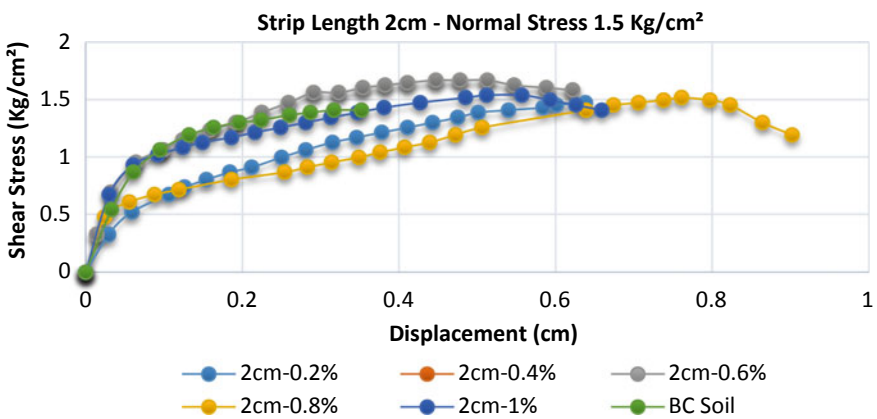


Fig. 10 Shear stress versus displacement for strip length 2 cm—normal stress 1.5 kg/cm²

For combined (1 and 2 cm) length of plastic strips

The failure envelope of combined length (1 and 2 cm) waste plastic bottle strips for the various used of percentage, i.e., 0.2, 0.4, 0.6, 0.8, and 1%. The maximum improvement observed for 1% addition of waste plastic strips as shown in Fig. 11.

The maximum shear strength of reinforced BC soil is 1.278 kg/cm² with horizontal displacement of 0.639 cm by adding 1% of plastic strips as shown in Fig. 12.

From Fig. 13, the observed values of maximum shear strength reinforced BC soil are 1.668 kg/cm² with horizontal displacement of 0.513 cm by adding 1% of combined strip length, i.e., 1 and 2 cm with constant thickness of 2 mm.

The maximum shear strength of reinforced BC soil is 1.863 kg/cm² with horizontal displacement of 0.541 cm by adding 0.8% of mixed strip length as shown in Fig. 14.

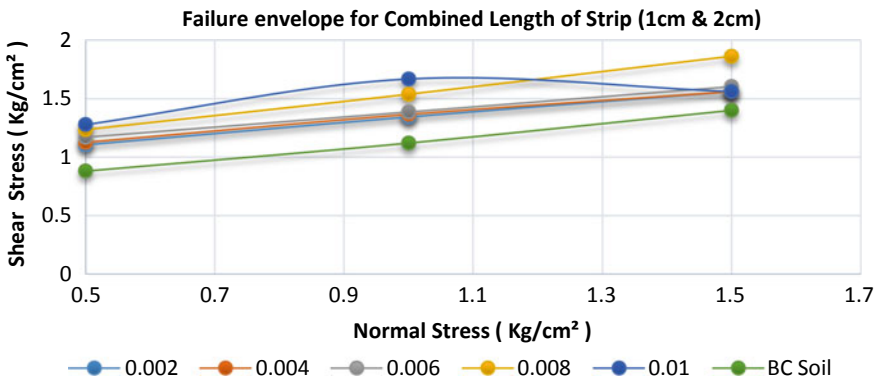


Fig. 11 Shear stress versus normal stress of soil reinforced with 1 and 2 cm strips

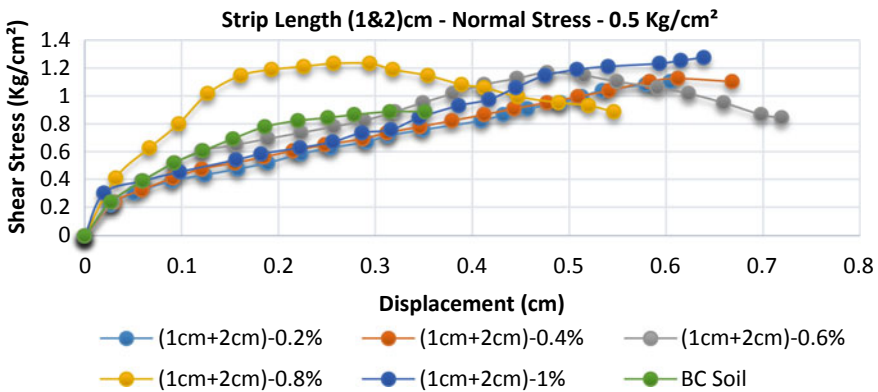


Fig. 12 Shear stress versus displacement for strip length 1 and 2 cm—normal stress 0.5 kg/cm²

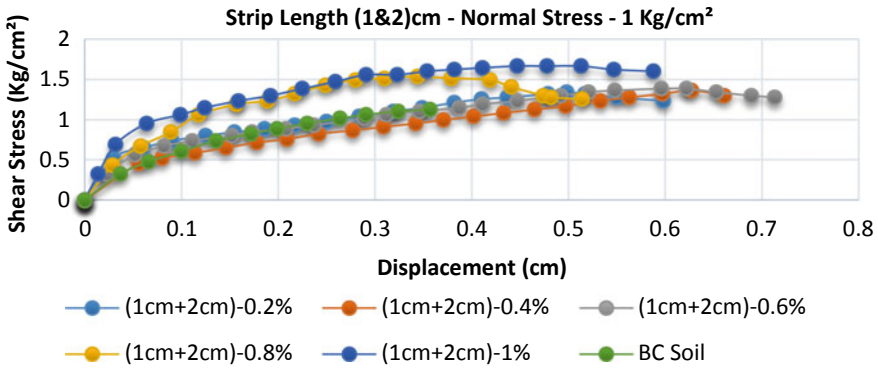


Fig. 13 Shear stress versus displacement for strip length 1 and 2 cm—normal stress 1 kg/cm²

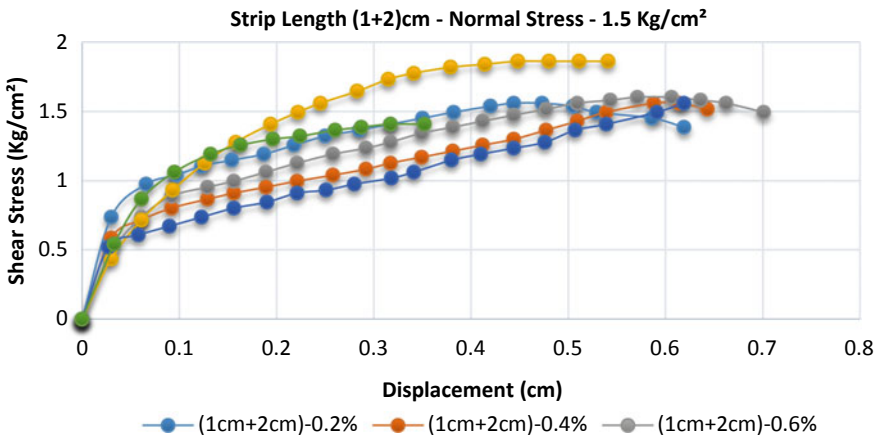


Fig. 14 Shear stress versus displacement for strip length 1 and 2 cm—normal stress 1.5 kg/cm²

7 Conclusion

In the present study, the attempt was made to evaluate shear strength of BC soil using waste plastic bottle strips. The strips are reinforced into the soil. The tests show that reinforcing black cotton soil with PET bottle strips enhances its strength. The variation of plastic strip was considered as 0.2, 0.4, 0.6, 0.8, and 1%. Moreover, the comparison was made in between reinforced soil with plastic strip and unreinforced soil. Based on the experimental work carried out, the following conclusions are made regarding the aspect of shear strength improvement of BC soil. The shear strength and cohesion value were found to be maximum in case of plastic mix with combination of 1 cm + 2 cm strips.

The shear strength is found to be increased as the percentage of plastic strip increases up to 0.8%, and after this mix, the shear strength starts decreasing. This

means the maximum shear strength is occurred at 0.8% mix (combination of 1 cm + 2 cm strips). The maximum shear strength with this proportion is found to be 1.863 kg/cm² with horizontal displacement of 0.541 cm on direct shear test machine.

The cohesion increases as the plastic mix increases. The value for cohesion of black cotton soil is found to be 0.613 kg/cm² when the soil is unreinforced. The cohesion value for BC soil with 1% of plastic mix increases to 1.22 kg/cm². Hence, it is concluded that the addition of plastic strip increases cohesion almost double.

References

1. Times of India, article on Nov 25, 2019. <https://www.indiatimes.com/amp/news/india/india-generates-nearly-26-000-tonnes-of-plastic-waste-every-day-40-remains-uncollected-says-government-501097.html>
2. Y.M. Alshkane, Reinforcement of sandy soil using plastic fibres made from waste plastic bottles. *Iraqi J. Civ. Eng.* **11**(2), 45–54 (2017)
3. M.H. Nsaif, Behavior of soils strengthened by plastic waste materials. *J. Eng. Sustain. Dev.* **17**(4), 182–194 (2013)
4. A. Al Adili, R. Azzam, G. Spagnoli, J. Schrader, Strength of soil reinforced with fiber materials (Papyrus). *Soil Mech. Found. Eng.* **48**(6), 241–247 (2012)
5. R.H. Mohankar, M.D. Pidurkar, R.S. Bute, Y.D. Chintanwar, Behaviour of soil reinforced with plastic waste. *Int. J. Res. Appl. Sci. Eng. Technol.*
6. N.S. Sodhi, S. Pal, V.K. Sonthwal, Soil strengthening using waste materials. *Int. Res. J. Eng. Technol. (IRJET)* (2017). e-ISSN, 2395-0056
7. S. Peddaiah, A. Burman, S. Sreedeeep, Experimental study on effect of waste plastic bottle strips in soil improvement. *Geotech. Geol. Eng.* **36**(5), 2907–2920 (2018)
8. M. Furkhan, S. Syed, M. Ahmed, M. Mohiuddin, Improving the strength of soil by using plastic bottles. *Int. J. Res. Anal. Rev.* **6**(2), 2019 (2019)
9. IS 2720-part3-1980, Code of practice specific gravity of soils
10. IS 2720-part5-1985, *Code of Practice Methods of Test for Soil* (Determination of Liquid Limit & Plastic Limit)
11. IS 2720-part6-1972, Code of practice methods of test for soil—determination of shrinkage factors
12. IS 2720-part7-1980, Code of practice methods of test for soil—determination of water content-dry density relation using light compaction
13. IS 2720-part 13-1986, Code of practice methods of test for soil—direct shear test

A Study on Behaviour of Pedestrians to Improve the Riding Quality and Comfortability Through Metro Rail System: A Review



Vamsi Kommanamanchi, Jyoti Prakash Giri, and Koorma Rajendra Babu

Abstract Increased pedestrian volume in metro railway stations is enveloping unnecessary results like loss in the comfortability of the service, increased passenger density inside train car units, etc. Especially in developing countries like India, urban commuters use the facility on a daily basis. Compared to the surface mode of transport, metro railway system have less turbulence in movement from other modes of transport along its alignment-enabling it to be relatively fastest mode of transport. As metro rail system is economic in many aspects urban commuters pool at metro stations in metropolitan cities for their purpose of travel. Pooling at massive rates also distracts a few of the using population from the metro railway system, because of discomfort that may arrive in the process of travelling. In this study, an attempt is made to consolidate pedestrian characteristics and practices that are found to be beneficial by different metro stations around the world, that offer great amount of ridership with comfortability to passenger.

Keywords Pedestrian behaviour · Walking speed · Reaction time

1 Introduction

Metro Rail Transit System (MRTS) is the most commonly noticed mass transit system in any urban region due to its functional benefits. These are inexpensive in reducing travel time when they are prepared by grade separation with other traffic unit paths. Capital cost for installation of the MRTS system in urban regions is high and requires massive infrastructure units to operate the construction. Since it drastically reduces travel time, many urban citizens prefer to reach their destination with less delays

V. Kommanamanchi (✉) · J. Prakash Giri · K. Rajendra Babu
Department of Civil Engineering, GMR Institute of Technology, Rajam 532127, India

J. Prakash Giri
e-mail: jyotiprakash.g@gmrit.edu.in

K. Rajendra Babu
e-mail: rajendrababu.k@gmrit.edu.in

Fig. 1 Metro rail transit [1]

during the journey. Overcrowding metro stations always have operational problems associated with strength demanding it. Due to the limited capacity, pooling of passengers at the station and in the service units: MRTS is becoming a discouraging option for urban commuters due to discomfort in travel. Such a situation probes authorities of MRTS to run the service at a great amount of frequency during peak hours; which in turn demands an investment of huge capital as an expense.

Figure 1 shows the difference between the roadways and the elevated ways, in which the average speed of the metro rail is 30–35 kmph. The metro rail system has a very advanced control system with high frequency of operations. Also, the metro rail will have high affinity. The metro rail is very expensive when compared to the other transit systems [2].

Movement of goods and passengers occupies utmost importance in saturating urban regions in many developing countries. To cater for the movement of passengers and goods, different modes in transportation system serve the purpose at different levels of serviceability. Among them, Mass Transit System by metro is significant and is predominant for safe and faster movement. Due to curbing problems by tolling traffic on arterial streets and other major streets within a city during the peak hour, urban populations tend to use metro mass transit system. Metro mass transit systems are facilitated by grade separation and alignment which enables it to be conflict free mode among mass transiting modes, hence eventually it reduces travel time [3]. The success story of the Delhi metro sets an example to the other developing urban cities for the management of the crowd. The metro network in Delhi is named as Delhi metro rail corporation with an operational network of 389 km. Over 285 metro stations sprawl in the entire Delhi Metro Rail Network which also includes Noida-Greater Noida Corridor and Gurugram. The DMRC has over 300 trains with 4, 6 and 8 coaches. To avoid ambiguity within passengers boarding at different stations in Delhi Metro Rail Network, different metro channels are displayed within metro rail as well at stations to ease the movement of pedestrians. Display of such metro network maps at suitable locations can yield better performance of stations as well as pedestrians,

Fig. 2 Snap of pedestrians at a metro [6]



saving time on route decisions and ticketing policies. To help the sustainability of Delhi metro rail corporation, bus rapid transit systems are connected with visiting frequency of minimum 13 number of buses at each station. A partnership of Hyundai Rotem, Mitsubishi Motors and Mitsubishi electric company created its first range of rolling stock. Rotem in South Korea installed initial sets while Bharat Earth Movers Limited (BEML) completed the corresponding units in India. BEML was also liable under a technology transfer deal for manufacturing coaches [4]. The rolling stock in the Delhi metro rail for the second phase was constructed by MOVIA. DMRC is the largest fleet of MOVIA metro cars in the world. The mobility plan was successfully implemented by DMRC for the commonwealth games in 2010. The system is capable of transporting 184 passengers by four cars, 284 passengers by six cars and 384 by eight cars [5].

In the present study, the factors that affect the pedestrians are considered as pedestrian speed, pedestrian reaction time and train movements. The activity of the passengers during the loading and the landing will be based solely on features, such as passenger numbers, the spatial spread across platforms and passenger conduct, as well as the internal vehicle and stationary characteristics, which will play an essential role in congestion. Also, the interweaving passengers can cause interruptions for the stock [7]. Figure 2 shows the headway reduction between the passengers which reduces the level of comfortability among the passengers. For the imprudent of the ridership and the comfortability of the passengers the metro rail crowd management and the passenger speed at the metro premises. For this reason, the estimation of the travel time from the entry to the destination in the crowded areas. When the pedestrian speed was reduced within the entrance and destination then the managing administrations can make some other alternative plans to alter the crowd and the speed of the pedestrians.

The pedestrian's perception reaction times were analyzed at the signalized cross sections, the pedestrians will attain a constant walking velocity after a certain time and average walking speed is determined. Gait analysis was used to know about the pedestrian's movement gait analysis is the systematic study of animal locomotion, more specifically the study of human motion, using the eye and the brain of observers. Therefore we can adopt the gait analysis for the optimization of the passenger or

Table 1 Factors influencing the pedestrians

Qualitative characteristics	Quantitative characteristics
Gender	Age
Qualification	Number of trips per day
Type of trip	Trip length
Type of luggage	Waiting time
Distractions	Passengers volume
Fare collection system	Station capacity

pedestrian movement. Data of the pedestrians have been analyzed at a variety of intersections ranging from small busy towns to suburban intersections. Mean acceleration and time to steady state walking velocity is determined by the digital video. Authors considered the sample of 288 which shows a significant percentage of the pedestrians, who will initiate the movement within one second of walk light illumination. Also, the authors stated that the width of the street will not show any effect on the steady state velocities of the pedestrians [8]. Therefore, the qualitative and quantitative characteristics that affect the pedestrian movement are tabulated in Table 1.

The level of serviceability affects with increase in the volume of pedestrians who travel within the transit service. To maintain and manage the passenger fleet and serviceability in the crowding conditions the study on pedestrian characteristics is much needed to maintain comfort and serviceability, the major characteristics that affect the pedestrian movement and reaction are waiting time, travelling alone or in a group, etc. [9]. In this regard, for instance, it is essential to highlight the need for a transaction methodology that stresses the role played by physical, financial, psychological and cultural factors in determining the behaviour of the pedestrians [10]. The structures for the physical factors include the function of signs and screens for each affiliation. The user’s perceptions and the ground characteristics for each position have been registered and compiled [11]. Figure 3 indicates the crowd in one of the major metro networks of India. The increased ridership increases the congestion which results in the colliding of pedestrians in boarding and alighting of

Fig. 3 Crowded metro station—Delhi [13]



the passengers, to understand cluster boarding the model of passenger behaviour and an easy mechanism is developed [12].

2 Movement of the Pedestrians

Movement of the pedestrians will highly influence the traffic operations in the mass gatherings. During the process of walking the movement of the pedestrians will be based on the gap acceptance between the pedestrians and the behaviour of the pedestrians. The authors have analyzed the 36 variables in six types, which can be regarded as a consideration when the drivers respond for geometry details, driver, vehicle, pedestrian, environment, crash event. The peak category includes the amount of people, age, race, alcohol and/or drug trafficking to help find the extent of foot injury. Engaging with alcohol or drugs decreases the reaction time of the pedestrians and vision which contributes to crashes [14]. In the urban transit systems, passenger alighting and boarding plays a crucial role in managing the crowd, to manage this crowd the crowd dynamics were to be analyzed quantitatively through the video surveillances recorded in several metro stations. Also, several statistical methods were used to determine the burst size and the headways between two passengers. The passenger data was collected from the seven Beijing subway stations, China. The train dwelling time and the order degree were recorded in the peak hours, i.e. from 07:00 AM to 10:00 AM. The order degree of the passengers/pedestrian's was determined by the flow consumption and the time, smaller the order degree (i.e. both alighting and boarding passengers were same) the situation at the doors is a bottleneck. Further, illustrating the three types of headway's like alighting headway, boarding headway and general time headway is done through considering the flow consumption between 0 and 1. The major observations are when the board time headway is increased initially and then it decreased with increasing of the order and degree, while alight time headway kept constant. Regarding the average burst size, when it increased from 0.5 to 4 s, the average time headway is decreased from 1 to 0.5 s. Finally, the increase in the burst size would improve the order degree of the crowd which helps in increasing the efficiency. Finally, the crowd dynamics are estimated through the time gap, which alters the crowd behaviour [6].

The management of the pedestrian movement at the crowdy areas is a very difficult task, to manage the crowd one should know the pedestrian movements for better results in the Safety, Security, attractiveness and efficiency of the respective area. For counting the pedestrian, some of the adapted methods are

- Manual counting, done by humans in which an error between 8 and 25% is observed.
- Automatic single file movement counting method, a sensor is fixed at a line in which the sensor will count the pedestrians that passes the line and switching mats and infrared beams which are the alternatives for the turnstiles.

- Active infrared based counting, which provides accurate data where the bottleneck situations are absent using DILAX and IRIRS sensors.
- Video based counting is done by recording the scene through the video and the analysis is done through the pedestrians who crossed the virtual line.
- Recording the pedestrian movements with the help of the geovisual analytical tool [15].

To differentiate between the different methods a case study at Vienna International Airport and represented with the help of graphs to find out the accuracy. Finally, author states that there is a data hungry in the planning and management of infrastructures. The tracking technology is much more mature than counting most of the systems are not developed with real-world scenarios. Regarding this situation, author suggests that there should be much research work should be done [16].

The investigations of the visual efficiency of male vs. female Stroop-like test was performed with 30 subjects were presented with female and male. Accuracy and response times across all subjects did not differ for the female vs. male signs, indicating that Ampelfrau and Ampelmann (a signal that indicates the traffic signs) signs have equal visual efficiency. More than 50 years ago, in 1961, German traffic psychologist Karl Peglau noticed the increasing degree of traffic, which leads to the confusion and making of the wrong decisions pedestrians concludes to the collisions. The experiment studies the pedestrians of the German country. A total of 30 subjects, between 19 and 26 years of age, 15 male and 15 females have participated, an experiment with a colour-form stroop task applied in four blocks, in which the samples have to respond in time for the signals. The signals were, two different traffic light figures the East German male traffic figure and its female counterpart. The simulation results were plotted on a 27 in. back-lit TFT monitor with a fast response time of nominally 1 with the custom written C-Programme which also acquired responses from a custom-built response box that was monitored via the parallel port with a temporal resolution of 1000 Hz. The processing was done with the corrections of the reaction times. The raw data for the first sample showed far outlying response times of RT greater than 700. The second subject had a low overall accuracy of only <75%. All the 30 subjects in the pool responded with an accuracy of 95.1% and mean RTs of 435 [17].

A generalized statement is made about the collisions of the pedestrians will occur more in winter, more collisions occur on Saturday, at the same time the collisions are seen more in the single travellers [18]. Experimental study for estimating the passenger space at metro stations with platform edge doors studies states that the pedestrian spacing will play a major role in the pedestrian boarding and alighting in metro station, snipping. In any standing area (e.g. metro stations and surroundings) a pedestrian can be represented as an ellipse of area 0.30 comprising a body depth of 50 cm and a shoulder breadth of 60 cm.

However, when the pedestrian starts to walk, this area increases to 0.75 m² because there is extra space used for leg and arm movements and therefore a “face to face” distance between pedestrians of less than 0.5² will be considered as intimate. Platform train interface can occur when there are two persons and five passengers [19].

In order to judge pedestrian evacuation, the writers prepared an adjustment to the cellular automaton model by adding local intensity region and distance field costs. The pedestrian decision-making process should rely on the visual range of the pedestrians. Simulation results show that the involvement of evacuation communities of too many cooperatives or defectors is not conducive to safe disposal. The heterogeneous pedestrian speeds have been shown to increase to some degree the evacuation performance. When 20% of people slow down, the overall exit period may be limited [20].

For the improvement of the ridership and the comfortability of the passengers the metro rail crowd management and the pedestrian speed at the metro premises. For this reason, the estimation of the travel time from the entry to the destination in the crowded areas. When the pedestrian speed is reduced within the entrance and destination then the managing administrations can make some other alternative plans to alter the crowd and the speed of the pedestrians. The authors have considered the factors like the travel time and source–destination traffic flow and the factors influencing the moving persons and finally analyzed through the regression modelling using the statistical study, the authors said that the traffic flow between the origin and destination is affected by the influential activities near the walking routes. To create the relation between the scene locations and the source–destination traffic flows, the activate areas (R) were considered which may overlap for different sources and destinations respectively, such that we can predict the probable increase of travel time between source and destination of the pedestrians. Finally, the influential weightage for the R is given using Gaussian kernel bandwidth. The temporary source and destination for the pedestrians were considered to be as a window. Each window is divided into 10 and the average time of each passenger was considered to be the true value for the regression modelling. The authors introduced a method for finding the travel time of the pedestrians by simulation using

- Social force model (an indicator of human internal motives for such acts)
- Using the pedestrian's trajectories considered from tracking
- Based on the person reidentification

The question of the pedestrian travel time estimation, for the daunting challenge consisting of active area development, moving/stationary function architecture and regression, a new travel time evaluation approach is introduced. The approximate time of travel offers valuable knowledge to grasp the crowd situation and to evaluate pedestrian behaviour and includes three applications focused on the methodology suggested, although further important applications on details regarding travel times tend to be discovered [21]. For finding the travel trends, pedestrian speeds play an important role. Since the pedestrian walking speed is important for determining the pedestrian collisions and vehicular pedestrian collisions have a major significance in the research. For analyzing the pedestrian characteristics considered by the authors are: age, sex, temperature, time of the day, crosswalk markings, signal type and pedestrian length roadway width and number of lanes. A video camera was used to take videos of pedestrians and total of 5235 samples were collected. The walking speed is computed by the equation:

$$S_w = \frac{L}{T_w} \quad (1)$$

where,

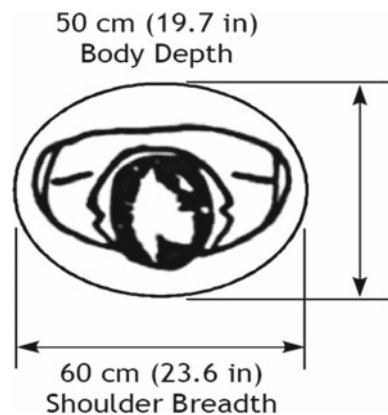
L : Length of the detection range.

T_w : Crossing time of the detected pedestrians.

By analysis, in most cases, the mean speed of the adults is higher than the female adults and the crossing speed of the individuals is higher than the mean speeds of the group of two are more also the 15th Percentile speed was less than the designed speed. Finally, the statistical tests like integrating t test and the one-way ANOVA test are done. For multiple comparisons between categories, Scheffe's S test is adopted. Also, the authors proposed to do the analysis on the children and elderly pedestrian's and to develop a database that can analyze the walking speeds of the pedestrians with one and more factors [22]. The Manual on Uniform Traffic Control Devices (MUTCD) (Federal Highway Administration) states that the pedestrian clearance time should be sufficient to allow a pedestrian to travel at a walking speed of 1.2 m (4 ft.) per second. Federal Highway Administration recommends the pedestrian dimensions for standing areas like for standing area design a simplified body ellipse of 50 cm by 59.9 for standing areas, with a total area of 0.3 m² (3.2 (ft²)) (Fig. 4).

It is very difficult for understanding the movement of the pedestrians, the movement of the pedestrians can be based on several factors such as activity choice, mode choice, destination choice, walking behaviour (speed, reaction time), interactions and collision avoidance. The authors have done the discrete choice modelling for each factor, regarding the activity choice the choice of going to the educational institution, office purpose and the recreational purpose. Usually, the people will get rush into the trains while going back to the home or during the late hours to their work, then there will be a high impact on the decisions that the pedestrians may take. Also, the authors state that the time of the day and the weather conditions will also play a major role in the decision making. Finally, the author concluded that the single logit model may not be appropriate since the attributes are shared by many [24]. Also, the

Fig. 4 Recommended pedestrian dimensions [23]



behaviour of pedestrians with respect to age is analyzed by the modelling and stated that there is a significant difference in the walking speeds of the male and female at the survey points except some. Regarding the crossing distance, the author found that there is no significant difference between the male and female pedestrians with respect to the 15th, 50th and 85th percentile speeds. Also, the risk assessment of the pedestrians is given by

$$R = (L + vT)/G \text{ (includes the gap length)} \quad (2)$$

where,

V = Average velocity of the flow.

L = Average length of the vehicles.

t = Average crossing time of the pedestrians.

G = Average gap length in metres.

Some of the results stated the differences between female and male with respect to perception and distractions.

- Pedestrians who were directly looking at the walk signal, the perception–reaction time was similar for males and females, males appearing 0.21 s faster than the females.
- Pedestrians who were distracted, the males get distracted about 0.4 s longer than the females.
- The pedestrians who were less than 55 years will have a lower perception reaction time than the pedestrians of age greater than 55 years [25].

3 Modelling of the Pedestrian Characteristics

The scale of the pedestrian infrastructures has a direct effect on crowded areas, especially in transport in fractures. Foot transport comprehension is essential to accurately calculate the system's ability, particularly in transport terminals, such as train stations, bus terminals, airports and so on, where large crowds gather and move. Foot activity habits must be carefully studied and modelled in order to ensure healthy and relaxed travel in a natural environment as well as a swift escape in an emergency (Fig. 5).

The methodology was adopted for the data collection to analyse the pedestrian with the help of the Traffic-Analyzer software at on second interval. The centroid of the body can be taken as the reference point. The intersection points were calibrated using the real-world coordinates concentrating from the GIS database obtained. Simultaneously the passenger entry and exits were recorded. Overall, 121 passengers have been considered and the 59 pedestrians behaved illegally and were not considered in the analysis. With the help of the IBM SPSS 23.0 with the confidence interval of 95% and the statistical analysis shows that 23.69% of the pedestrians crossed the section within the pedestrian flashing green time and the rest have crossed during the red signal. Using ANOVA, the analysis of the crosswalk speeds at three cross walks

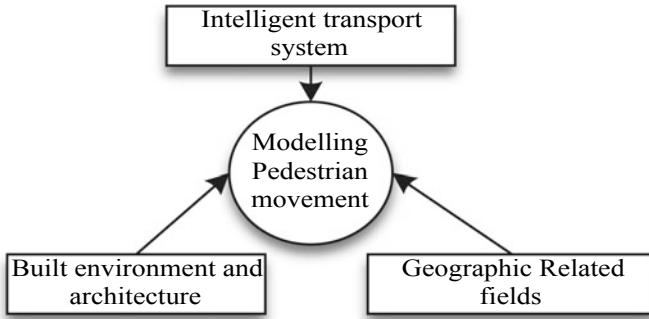


Fig. 5 Approach to the modelling of pedestrian movements

shows significant and different results with respect to the single stage and two stage cross walks, with the speeds 1.27, 1.60 and 1.13 m/s, respectively [26].

While coming to the children the management of the pedestrians carrying a child is a challenging task. To examine the children behaviour with adults in the cross walks with the grid pattern behaviour survey with 269 samples at an elementary school is considered. A grid pattern of having three combinations with child alone, child holding the adult’s hand and the child holding adults’ hand along with the adult hand. A Chi Square test is performed to differentiate the unsafe behaviour of the children among the respective groups. The authors stated that the greatest proportion of the child behaviour is unsafe with the child lead with an adult. Considering the overtaking of the pedestrians, the overtaking points in which we can see in reality is at the railway stations. Since this study represents the optimization of pedestrian behaviour. The walking speed of the pedestrians could be considered in the study. Also, the movement of the pedestrian’s flow is shown in a rectangular field (Fig. 6).

The movement model, an extension model of the initial social force model is adopted.

$$m_i \frac{d^2 \vec{x}_i(t)}{dt^2} = m_i (\vec{v}_i^0 - \vec{v}_i) + \sum_{j \neq i} (\vec{f}_{ij}^{soc} + \vec{f}_{ij}^c) + \sum_w (\vec{f}_{iw}^{soc} + \vec{f}_{iw}^c) + \vec{\xi}_i(t) \quad (3)$$

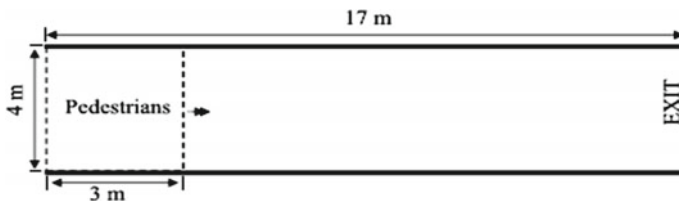


Fig. 6 Schematic illustration of the unidirectional pedestrian flow [27]

where $x_i(t)$ is the position of pedestrian i . The velocity of pedestrian i at time t is given by

$$v_i t = \frac{dx_i t}{dt} \tag{4}$$

Overtaking model is the modelling that shows how the fast-moving pedestrians can overtake the slow-moving pedestrians, an assumption that the counterflow, i.e. the opposite direction. Overtaking cannot be an option for the pedestrians in the crowds. To avoid these circumstances, one has enough mobility for the movements, therefore an optimization equation is derived for the pedestrian movement, which can also specialize in detecting the responsiveness of accepting the space in the crowd.

$$\sum_{j \in S_i} \frac{k_{in} v_i^h |\vec{v}_j - v_i, u_{ii}^0| - c_{ot}}{\max(0.2, d_{ij} - r_{ij})} \tag{5}$$

k_{in} a parameter and c_{ot} are a constant. The inner products $(v_j - v_i)$ of the arguments, $(v_j - v_i)$ and, are used to weight the effect of pedestrian agent j on the score of the sector depending on his velocity. For exploring the model quantitatively, the values derived are 0.98 and 1.31 m/s are the respective speeds that were assigned for the slow- and fast-moving pedestrians with the speed ratio of 0.75 and a premovement time are 1.0 s and if the premovement time is considered as 0.1 the fast pedestrians are informed to walk normally [28] (Fig. 7).

For the pedestrian facilities, the modelling of the passengers is important for various situations the movement of the pedestrians is determined by using the discretized floor into the tools by dividing each tile into 40 cm by 40 cm. The initial distribution of the passenger is determined. The probability function for the passengers who are moving from one cell to the other is given as

$$P_{ij} = N_i \exp(kSS_{ij} + kD D_{ij})(1 - n_j) \chi_{ij} \tag{6}$$

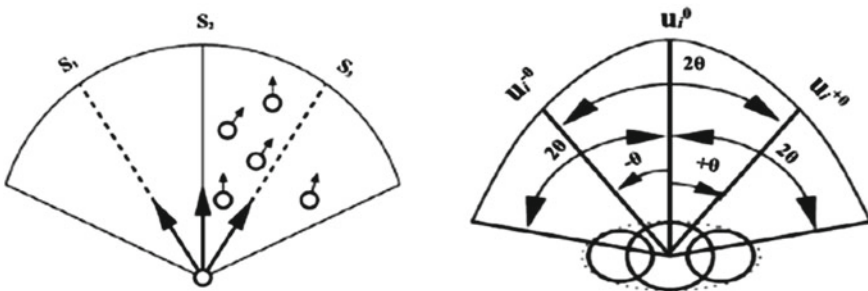


Fig. 7 Visual area in front of the current pedestrians [27]

Since the authors are willing to analyze the movement around 90° and 180° the comparison between the static and dynamic floor tests are done. Every person will enter into the blocks and was entered into each block randomly [29]. Assessment of passenger satisfaction from the systematic and quantitative procedure and aims to establish the passenger satisfaction model for urban rail transit. The structural equation modelling and partial least squares are used to establish the modelling, the indicator system which includes the level of indicators to measure the passenger's satisfaction the structural evaluation modelling (SEM) combined with the PLS estimation gives the solution for the urban rail transit. By forming the relationship between the latent variables and the manifest variables the model which is formed can be used for the study, a case study on suzhou urban rail transit has done, the questionnaire was prepared and the surveys were done. From this, we can adapt the methodology for the modelling by considering the latent variables and manifest variables from the urban metro passengers [30]. The passenger flow organization in the subway stations the station's service capacity are divided into three types of demands, these three demands are solved by the mathematical modelling, the three different types of demand scenarios considered by the authors are

- Dynamic concept for estimating the level of service (LOS)
- By the uncertain demand, the authors derived a model for the station service capacity
- Unified simulation based approach

The types of passengers that the authors considered were gathering passengers and scattering passengers, the gathering and scattering process were involved in the inbound, outbound and alighting the passengers. The mathematical model for the uncertain demand condition is made for the station service capacity by considering the distinct types of passengers. For the mathematical modelling the assumptions made were the "the arrival distributions of the inbound passengers is constant and the passengers moment is time based with stochastic distribution" and "the total number of passengers that are alighting are time independent and deterministic in each model" [27].

4 Simulation

Modification of cellular automata model by introducing the local density field and density field cost to judge the pedestrian evacuation. Decision-making process of the pedestrians will depend on the visual range of the pedestrians which is anticipated by the pedestrians the hesitation time cost can be used for the payoff. Simulation results show that either the presence of too many cooperators or defectors in the evacuation group is not conducive to the safe evacuation. It is found that heterogeneous pedestrian speeds can improve evacuation efficiency to a certain extent. The total evacuation time can be reduced if 20% of the pedestrians slow down [31].

Cellular automation, each of a set of units in a mathematical model which has simple rules governing their replication and destruction, is used to model complex systems composed of simple units such as living things or parallel processors. Each pedestrian considered as a single body. Movement of pedestrians will look like coins moving on the chess board as Fine grid Cellular Automata Simulation is used to predict the efficiency of the system and performance issues, to estimate evacuation time. In the adopted the fine grid cellular automata to simulate straight line movement towards a target. Pedestrians will walk in a straight way writer projects the basics of fine grid cellular automata and formulated the variation of least effort movement and discrete event simulation methods for simulating the actions of the pedestrians. Large scale behaviour of pedestrians like wayfinding and navigational aids are dealt with in the separate model. Navigational and wayfinding movements are the macroscopic element. Crowd is considered as the liquid entity with varying densities and speeds and can be solved by the differential equations. Simulation of the pedestrian will transit into the neighbouring cells and some others will remain. Considering the size of the cell as 40×40 cm and pedestrians can move 1, 2, 3, 4 cells at a time with speeds of 0, 0.4, 0.8, 1.2 and 1.6 m/s. The average speed of the pedestrians will be 1.3 m/s.

In the proposed new method pedestrians can have different sizes, shapes and speeds also can be divided into groups (adults teenagers, children) by applying the cellular automata settings and modelling the collisions and overlapping the pedestrians are avoided. Cellular grid automata can accommodate up to 7–8 passengers [32] (Fig. 8).

The speed and the movements of the pedestrians in the metro stations in the rush hours are being analyzed and an expected velocity model and attractive force model were introduced that fits the best results. The results of the simulation show that

Fig. 8 Representation of pedestrian in cellular grid automata [32]

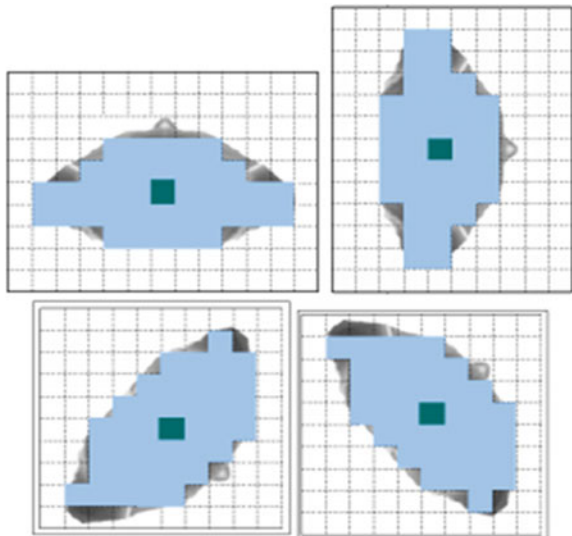
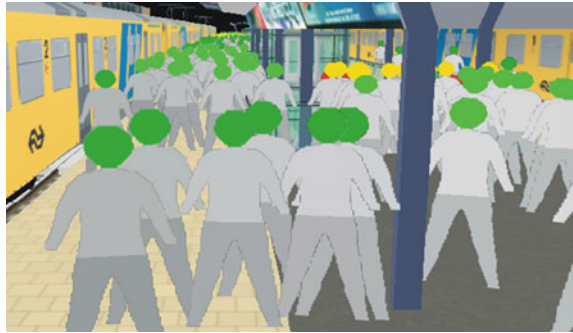


Fig. 9 Pedestrian flow using
StiPend [32]



models and algorithms proposed are best suited with the conclusions, fast followed by slow [33]. The pedestrians flow at the stations can be done using a simulation tool SimPed by considering the walking speed, densities over space and results of the walking speed on the staircase is 10% higher than the simulation tool (Fig. 9).

For the imprudent of the ridership and the comfortability of the passengers the metro rail crowd management and the passenger speed at the metro premises. For this reason, the estimation of the travel time from the entry to the destination in the crowded areas. When the pedestrian speed was is reduced within the entrance and destination then the managing administrations can make some other alternative plans to alter the crowd and the speed of the pedestrians. The factors like the travel time and source–destination traffic flow and the factors influencing the moving persons and finally analyzed through the regression modelling. It is a valid approach to model and simulates the movement of passengers at underground stations. The models on foot dynamics can be divided into macroscopic and microscopic models and were proposed by [32].

Also, in simulation of the pedestrian motion, the movement of the pedestrian is related to fluid movement and other hydromechanical concepts are used. Instead, in the field of crowd evacuation science, the microscopic models based on the movement of each peasant were far more commonly used. The paradigm of collective force and actor-based simulation are both effective solutions to crowd dynamics [34, 35]. The model of social force is suggested by summing up the combination of cognitive and emotional forces affecting the pedestrian, which assesses the speed of the pedestrian. One of the most key findings of the social force model is the “speedy-is-slower” concept that has been reviewed and assessed by experiments and simulations [36, 37]. Functional relationship with both expected speed and evacuation time in the case of a single exit based on the model of social force and the mechanism for the formation of exit block clusters and their impact on the efficiency of crowd evacuation is explained and agent-based simulation is also a typical technique for the identification of microscopic walking behaviour of the pedestrians (Table 2).

The table indicates the differentiation of the major writings from various countries about the passengers in metro areas from the previous lines there is an aperture at finding the passenger speed and the passenger reaction times in the metro transit

Table 2 Differentiating the works of authors

Authors	Location	Facility	Remarks
AI-Gadhi [2]	Crowded areas	Crowd management at special events	Study of the pedestrian movements regarding 1. Steady state pedestrian movement under normal conditions and 2. Crowd behaviour was presented Which affect the movement of the pedestrians in the crowd
Qu et al. [39]	Metro stations	Metro platform	Study of the microscopic boarding and alighting process of the passengers and the time headways of the individuals are analyzed with the help of the Statistic methods. Comparison between the alight time headway and the board time headway is done
Tang [33]	Railway station	Platform of high speed railway station	The modelling of the pedestrian flow theory at the high speed railway stations with the help of cellular automation and the passenger inflow rate and the choice of entrance into the station has been developed
Thomas and Fugger [32]	Cross walks and footpaths	Signal-controlled cross walk sections and side walks	Perception and reaction data of the pedestrians with the steady state acceleration and mean state acceleration is a valuable tool for the recreation of the accidents in which the pedestrians and the vehicles are involved

(continued)

Table 2 (continued)

Authors	Location	Facility	Remarks
Brown [3]	Guided walks at light rail stop	Guided side walks	States the importance of the subjective experience of the pedestrians and their problems which can overcome the problems in the urban design
Mehta [26]	Main streets	Walk ways for pedestrians	Integration of the user perceptions and subjective measures that impact the characteristics of the walking behaviour on the streets
Hool [21]	Railway station	Railway platform	Pedestrian platform interface and a mathematical modelling approach to know the pedestrian behaviour while boarding the train
McArdle [15]	Pedestrian facilities	Car parking	The pattern of the movement data can predict the future movement of the pedestrians that can use the spaces and identify the trajectories with the help of the Geo-visualising tool
Bauer [11]	Junctions at pedestrian infrastructures	Infrastructures like shopping complexes, railway platforms	The methods of pedestrian counting and pedestrian tracking deals with the planning and management of the urban pedestrian facilities
Farid and Kandil [12]	Pedestrian traffic signalings	Traffic signalings	The reaction times of the pedestrians regarding the traffic signs. The robustness, accuracy and speed of the pedestrians can differentiate the male and female

(continued)

Table 2 (continued)

Authors	Location	Facility	Remarks
Wei-Hua Lin and Chenghong Wang [40]	Crowded areas with pedestrians	Shopping mall	The complex human behaviour of the pedestrians with pedestrian simulation flow model (attention-based exploratory movement module)

premises. Such that to overcome the passenger delays there is a need in finding the procedure for finding the passenger speed and the passenger reaction time.

5 Summary

In this paper, the movements of the pedestrians, reaction times, modelling of the speeds and the simulations were studied and some of them were written accordingly. From this, we can conclude the characteristics of the pedestrians while walking in crowded places. Since the research on the pedestrian reaction time and the walking speed at the metro railway stations are very less, there is a provision to do more and more research on the reaction times and walking speeds that can develop the management of the crowded pedestrians, especially in the metro stations. More detailed dynamics characteristics have to be investigated to further reveal the pros and cons of the pedestrians in the metro train stations and the cross walks. This research helps in finding out the velocity and the moving path of the passengers especially in the metro trains during the peak hours by analyzing the characteristics through the qualitative and quantitative data that was obtained through surveys. The characteristics of the pedestrians and the simulation procedures were discussed in this paper. The simulation that shows the passenger motion in the respective areas will be useful. From this work one can research their work on the characteristics of the pedestrians who were travelling during the peak hours, the characteristics of the passengers on the different places like stairways, platform, concourse during train arrivals and the departures, different types of approaches for simulating the pedestrians in the respective places in which the optimization the passenger movements and improvement of the riding quality and the comfortability of the passengers.

Therefore, there are several methods for counting the passengers in the metro premises, for finding the Queue lengths, finding the delays to quantify them there are several modelling methods and simulation tools. But the major drawback and no method is there for finding a reaction time of the passengers in the metro rail transit. If we overcome the procedure for finding the reaction time of the passengers, we can regulate the group sizes through the consolidated reaction times of the passengers.

From that, we can regulate the delays of the passengers by creating a relationship between age, passenger reaction time and passenger speed and we can increase the level of service of the respective metro transit.

References

1. P.N. Agency, Phillipine Canadian Inquirer (2011, August 02). Retrieved February 2020, from <https://www.canadianinquirer.net/2014/05/06/articulated-bus-to-help-decongest-edsa-starting-wednesday-ltfrb/>
2. S.A. Al-Gadhi, A review study of crowd behavior and movement. *Eng. Sci.* **8**, 77–107 (1995). Retrieved February 2020
3. B.B. Brown, Walkable route perceptions and physical features: converging evidence for en route walking experiences. *Environ. Behav.* **39**, 34–61 (2007). <https://doi.org/10.1177/0013916506295569>
4. C.L. Baobao Zou, Effect of pedestrian judgement on evacuation efficiency considering. *Physica A*, **17** (2013, August). <https://doi.org/10.1016/j.physa.2019.122943>.
5. C.L. Baobao Zou, Effect of pedestrian judgement on evacuation efficiency considering hesitation. *Physica A* (2019). <https://doi.org/10.1016/j.physa.2019.122943>
6. B. Steffen, A. Seyfried, Modeling of pedestrian movement around 90 and 180 degree bends (2009). arXiv preprint [arXiv:0912.0610](https://arxiv.org/abs/0912.0610)
7. C.Y. Chang, T.H. Woo, S.-F. Wang, Analysis of pedestrian walking speeds at crosswalks in Taiwan. *J. East. Asia Soc. Transp. Stud.* **9**, 1186–1200. Released October 31, 2011, Online ISSN 1881-1124 (2011). <https://doi.org/10.11175/easts.9.1186>
8. D.R. Parisi, C.O. Dorso, Microscopic dynamics of pedestrian evacuation. *Physica A* **354**(1–4), 606–618. <https://doi.org/10.1016/j.physa.2005.02.040>
9. D. Muley , W. Alhajyaseen, M. Kharbeche, M. Al-Salem, Pedestrians’ speed analysis at signalized crosswalks. *Procedia Comput. Sci.* **130**, 567– 574 (2018). <https://doi.org/10.1016/j.procs.2018.04.102>
10. W.A.-S. Deepti Muleya, Pedestrians’ speed analysis at signalized crosswalks. *Proc. Comp. Sci.* **130**, 567–574 (2018). <https://doi.org/10.1016/j.procs.2018.04.102>
11. N.B. Dietmar Bauer, Measurement of pedestrian movements: a comparative study on various existing systems. *Emerald Insight*, 325–344 (2016). <https://doi.org/10.1108/9781848557512-015>
12. I. Farid, B.O. Kandil, Female vs. male Ampelmännchen-gender-specific reaction times to male and female traffic light figures. *Front. Psychol.* **8**, 1–9 (2017, May 23). <https://doi.org/10.3389/fpsyg.2017.00690>
13. X.H. Fasheng Qiu, Modeling group structures in pedestrian crowd simulation. *Simul. Model. Pract. Theory* **18**, 190–2005 (2009). <https://doi.org/10.1016/j.simpat.2009.10.005>
14. S.S. Fujiyama, Experimental study for estimating the passenger space at metro stations with platform edge doors. *Transport. Res. Rec.* **9** (2018). <https://doi.org/10.1177/03611981187820>
15. U.D. Gavin McArdle, Interpreting pedestrian behaviour by visualising and clustering movement data (2016)
16. L.F. Henderson, *The Statistics of Crowd Fluids* **229**(5284), 381–383 (1971). <https://doi.org/10.1038/229381a0>
17. J.B. Hendrik Vermuyten, A review of optimisation models for pedestrian evacuation and design problems. *Saft. Sci.* **87**, 167–178 (2016). <https://doi.org/10.1016/j.ssci.2016.04.001>
18. Hindustan Times (1996, August 08). Retrieved February 2020, from <https://www.hindustanimes.com/gurgaon/government-nod-to-extension-of-metro-line-up-to-udyog-vihar-with-25-new-stations/story-BI56DjGLFfDfhpXF33uALP.html>

19. I. Zuriguel, D.R. Parisi, R.C. Hidalgo, C. Lozano, A. Janda, Clogging transition of many-particle systems flowing through bottlenecks. *Sci. Rep.* **4**(7324) (2014). <https://doi.org/10.1038/srep07324>
20. X.C. Jia Liua, Simulation of passenger motion in metro stations during rush hours based on video analysis. *Autom. Const.* **107** (2019). <https://doi.org/10.1016/j.autcon.2019.102938>
21. G. Dell'Asin, J. Hool, Pedestrian patterns at railway platforms during boarding: evidence from a case study in Switzerland. *Hindawi, J. Adv. Transport.* **11** 2018. <https://doi.org/10.1155/2018/4079230>
22. J.L. Kefan Xie, Escape behavior in factory workshop fire emergencies: a multi-agent simulation. *Inf. Technol. Manag.* **15**, 141–149 (2014). <https://doi.org/10.1007/s10799-014-0185-1>
23. A. Martin, *Factors Influencing Pedestrian Safety: A Literature Review* (TRL Limited, London, 2006). Retrieved February 2020
24. V. Media, Delhi Metro Rail System, India (Railway Technology, 1997). Retrieved February 2020, from <https://www.railway-technology.com/projects/delhi-metro/>
25. V. Mehta, Walkable streets: pedestrian behaviour, perceptions and attitudes. *J. Urbanal. Int. Res. Placemaking Urban Sustainability*, 217–245 (2008). <https://doi.org/10.1080/175491708.02529480>
26. H.O. Park, Main factor causing “faster-isslower” phenomenon during evacuation: rodent experiment and simulation. *Sci. Rep.* 1–14 (2017). <https://doi.org/10.1038/s41598-017-14007-6>
27. Pedestrian Characteristics, In Federal Highway Administration University Course on Bicycle and Pedestrian Transportation (pp. 1–22) (2006). Georgetown Pike: Federal Highway Administration. Retrieved February 2020, from <https://www.fhwa.dot.gov/publications/research/safety/pedbike/05085/chapt8.cfm>
28. C.D. Phil Fouracre, Mass rapid transit systems for cities in changing world. *Trans. Rev. A Transnat. Transdisciplinary J.*, 299–310 (2003). <https://doi.org/10.1080/0144164032000083095>
29. M.B. Robin, *Pedestrian Behaviour Models, Data Collection and Applications* (Emerald, Eindhoven, 2009). Retrieved January 2020
30. Yi. Shuai, Li. Hongsheng, Li, X. Wang, Pedestrian travel time estimation in crowded scenes. *Int. Conf. Comp. Vision.* 3137–3145 (2015). Retrieved February 2020, from {syi,hsli,xgwwang}@ee.cuhk.edu.hk
31. F. Thomas, J.B. Fugger, Analysis of pedestrian gait and perception–reaction at signal-controlled crosswalk intersections. *Transport. Res. Rec.* **1705**, 20–25 (2000). <https://doi.org/10.3141/1705-04>
32. T.-Q. Tang, Y.-X. Shao, L. Chen, H.-Y. Shang, Modeling passengers’ boarding behavior at the platform of high speed railway station. *Hindawi, J. Transport. Eng.* **2017**, 11 (2017). <https://doi.org/10.1155/2017/4073583>
33. T. Rosenbloom, A. Ben-Eliyahu, D. Nemrodov, Children’s crossing behavior with an accompanying adult. *Saft. Sci.* **46**, 1248–1254 (2008). 10.1016/j.ssci.2007.07.004. <https://doi.org/10.1016/j.ssci.2007.07.004>
34. B. Transportation, Bombardier Movia Metro (1995). Retrieved February 2020, from bombardier.com/content/dam/Websites/bombardiercom/Projects/supporting-documents/BT-MOVIA-Metro_Delhi.pdf
35. W. Shen, W. Xiao, X. Wang, Passenger satisfaction evaluation model for Urban rail transit: a structural equation modeling based on partial least squares. *Transp. Policy* **46**, 20–36 (2016). <https://doi.org/10.1016/j.tranpol.2015.10.006>
36. X.-Y. Xua, J. Liu, H.-Y. Lia, J. Man, Capacity-oriented passenger flow control under uncertain demand: algorithm development and real-world case study. *Transport. Res. Part E*, **87**, 130–148 (2016). <https://doi.org/10.1016/j.tre.2016.01.004>
37. XU, X.-b. D.-f. (2010). Simulating crowd movements using fine grid cellular automata. *Int. Conf. Comp. Modell. Simulat.* <https://doi.org/10.1109/UKSIM.2010.85>
38. Y. Qu, Y. Xiao, H. Liu, H. Yin, J. Wu, Q. Qu, D. Li, T. Tang, Analyzing crowd dynamic characteristics of boarding and alighting process in urban metro stations. *Physica A* **526**, 121075 (2019). <https://doi.org/10.1016/j.physa.2019.121075>

39. Y. Zheng, [American Society of Civil Engineers Second Transportation & Development Congress 2014 - Orlando, Florida (June 8-11, 2014)] T&DI Congress 2014 - Analysis of Factors Influencing Pedestrian Injury Severity in Pedestrian-Vehicle Crashes, 448–457 (2014). <https://doi.org/10.1061/9780784413586.043>
40. W.H. Lin, C. Wang, An enhanced 0-1 mixed-integer LP formulation for traffic signal control. IEEE Trans. Intell. Transp. Syst. **5**(4), 238–245 (Dec. 2004). <https://doi.org/10.1109/TITS.2004.838217>

Improvement in Liquid and Plastic Limit for Black Cotton Soil by Addition of RBI Grade 81



Prashant Khedkar, Shraddha Shinde, Sakshi Wayal,
and Bhaskar Wabhitkar

Abstract Civil engineering structures constructed in black cotton (BC) soil are quite difficult. Engineers all over the world are researching on various ways of stabilizing the BC soil. To enhance the properties of BC soil, we have used RBI Grade 81 soil stabilizer. RBI Grade 81 is inorganic and inexpensive. RBI Grade 81 is used as an additive to study the change in the specific gravity, liquid, and plastic limit of BC soil. The test was performed on BC soil with the percentage addition of RBI Grade 81, such as specific gravity, LL, and PL. The used percentages of RBI Grade 81 were 2, 4, 6, 8 and 10% to improve the specific gravity, LL, and PL of black cotton soil, i.e., low value of LL and PL (water content). Lower the value of LL and PL will indicate higher in shear strength of BC soil. The tests conducted showed outcomes as expected, which give a conclusion that the RBI Grade 81 can be used to decrease the permissible value of LL and PL of BC soil.

Keywords RBI Grade 81 · Specific gravity (G) · Liquid limit (LL) · Plastic limit (PL) · Plasticity index (PI) · Black cotton soil

1 Introduction

The state of Maharashtra has black cotton (BC) soil over its entire region. The analysis on black cotton soil may be a necessity because of the swelling and shrinkage ability. Civil engineers are facing many on-site problems with black cotton soil. BC soil has

P. Khedkar (✉) · S. Shinde · S. Wayal · B. Wabhitkar
Department of Civil Engineering, MIT Academy of Engineering, Pune, India
e-mail: pbkhedkar@mitaoe.ac.in

S. Shinde
e-mail: svshinde@mitaoe.ac.in

S. Wayal
e-mail: sawayal@mitaoe.ac.in

B. Wabhitkar
e-mail: bdwabhitkar@civil.mitaog.ac.in

high compressibility, low shear strength, and bearing capacity, and these properties depend upon the LL and PL of BC soil. Higher the LL and PL, lower will be the shear strength of soil. Many soil stabilizers are available worldwide. But, the challenge involved is to select the one which is easily available and also economical. The previous study done by researcher on RBI Grade 81 is to improve the characteristics of BC soil. RBI Grade 81 is eco-friendly, inorganic, hydration-activated powder-based stabilizer. RBI Grade 81 can be expanded as Road Building International 81.

2 Literature Review

Alhassan [1], soil test collected from the Maikunkele region by Minna, named an A-7-6 lateritic soil on AASHTO arrangement was balanced out with 2–12% rice husk debris (RHA) by dry soil weight. Utilizing BSL compaction vitality level, execution of the dirt RHA was researched as to compaction attributes, CBR and unconfined compression strength tests. The obtained test results show the small decrease in dry density and increase in water content as RHA content increases in soil, i.e., MDD decreases and OMC increases. There was slight enhancement in the CBR and unconfined compression strength test with increment in the RHA content. Madurwar et al. [2], as age increases, the strength of soil is treated with RBI Grade 81. Due to the environmental and safety compatibility, the sodium silicate is found to be most popular grouts. RBI Grade 81 was added into the dry soil with varying percentage of 2–6%. The percentage of 3–6% sodium silicate solution was used in mix as molar concentration. The results were obtained. Liquid limit decreases as the admixture content increases. As the admixture increase the PL also increases, due to their will be decreases in plasticity index.

Gunturi et al. [3], most definitely, strong clayey soil is an intense test for parkway builds because of its growing and shrinkage qualities which are the sole purposes behind asphalt disappointments. The target of the investigation manages the correlation of the quality and micro-structural changes of virgin soil test. The RBI Grade 81 is balanced out the soil at different restoring days blended in with different measurements, i.e., 2, 4 and 6%. RBI Evaluation 81 stabilizer gives good outcomes for both the dirt as far as quality and swelling.

Basha et al. [4], adjustment of leftover soils is concentrated by artificially utilizing concrete and rice husk debris. The obtained test results show for both concrete and husk debris reduces the soil property. In terms of compatibility, expansion of rice husk debris and concrete declines the increase in the dry density of soil and expand the water content. From the perspective of versatility, compaction and quality attributes, and economy, expansion of 6–8% concrete and 10–15% rice husk debris is prescribed as an ideal sum.

Brooks [5], LL of clayey soil is largely affected by ion accumulation ionic valency. The characteristic of soil such as compressibility and expansion is reduced as the LL

of soil also reduces. It was recorded that there was an improvement in LL of BC soil after adding RBI 81 into it.

3 Methodology

Addition of RBI Grade 81 in BC soil, the properties like specific gravity, LL, and PL can be improved. The soil sample preparation was made in the percentage of RBI addition with BC soil, i.e., 2, 4, 6, 8 and 10%. The specific gravity, LL, and PL tests were conducted on pure BC soil to compare the results. The test was performed using standards IS 2720-Part 5 [6] and IS 2720-Part 3 [7].

4 Observation and Discussion

4.1 Effect of RBI 81 on the Specific Gravity of Black Cotton Soil

The specific gravity of soil is a principal parameter in deciding void ratio, porosity, degree of saturation, and other parameters of soil. It is helpful to determine the aptness of a soil as a construction material as a higher value of specific gravity gives more toughness to foundations and roads. Tests of specific gravity of the soil using pycnometer gave following results with various proportions of RBI 81 as shown in Fig. 1.

It is noticed that initially, the specific gravity of the soil improves with an increase in the percentage of RBI 81 added. The maximum specific gravity of 2.75 is for 6% addition of RBI 81, then gradually, it is decreasing in gravity of BC soil.

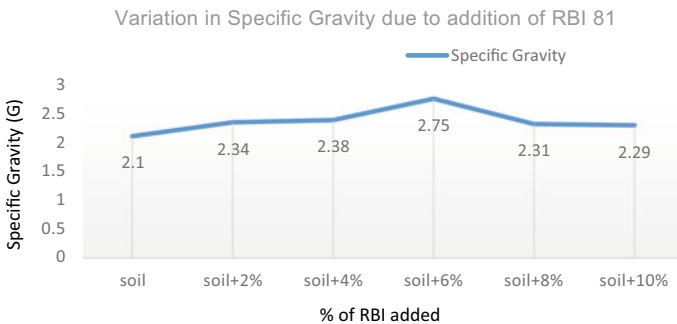


Fig. 1 Effect of RBI 81 on specific gravity of BC soil

4.2 Effect of RBI 81 on Liquid Limit and Plastic of BC Soil

In general, the LL is having greater attention as compared to plastic limit as it directly affects the structure if higher. Graph in Fig. 2 shows that the LL is improved by the addition of RBI Grade 81 in BC soil.

The PL of soil is useful to determine the consistency of fine-grained soil. A soil with a low plastic limit is more likely to undergo excessive settlement and may lead to reduce the strength. Figure 3 shows the values of the plastic limit of BC soil and various percentages of RBI 81 added to it.

The plastic limit of BC soil increases as the quantity of RBI added is increased. It is 21.16% for black cotton soil and increases to 28.34% with the addition of 10% RBI.

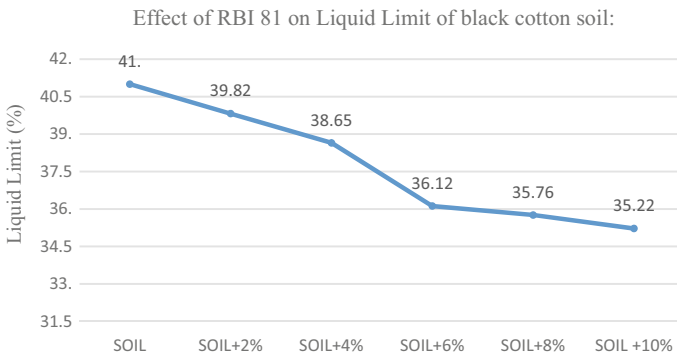


Fig. 2 Effect of RBI 81 on liquid limit of BC soil

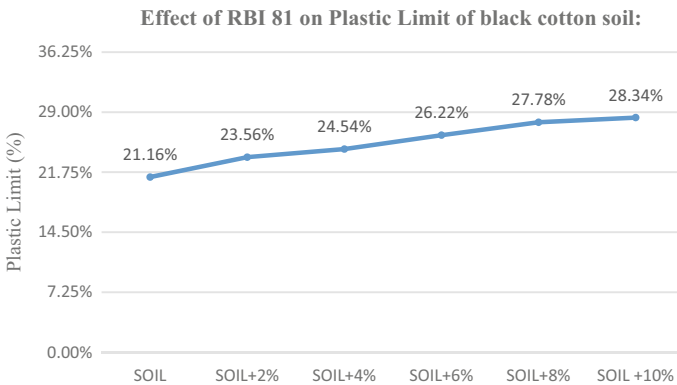


Fig. 3 Effect of RBI 81 on plastic limit of BC soil

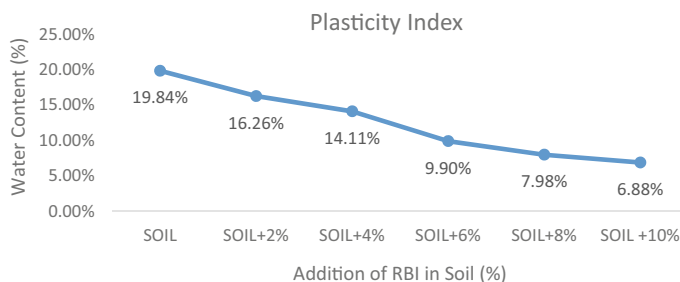


Fig. 4 Effect of RBI 81 on the plasticity index of BC soil

4.3 Effect of RBI 81 on Plasticity Index of Black Cotton Soil

Plasticity index (PI) is the variation between the LL and PL of soil. Plasticity index in its graph shows the range of water content of soil in plastic state. The PI depends on the amount of clay present in the soil. PI shows the fineness and property to change the shape with no change in volume of soil. It is an indication of soil compressibility. Greater the plasticity index, greater is the soil compressibility (Fig. 4).

The plasticity index of BC soil reduces as the quantity of RBI added is increased. It is 19.84% for soil taken by us and decreases to 6.88% with the addition of 10% RBI.

5 Conclusion

The experimental study was carried out on black cotton soil after addition of RBI 81 in percentage variation. The conclusions made on the basis of experimental investigation are as follows:

1. The liquid limit of black cotton soil decreases as the percentage of RBI Grade 81 increases. It is seen that, with addition of 10% RBI Grade 81, the LL decreases from 42 to 35.22%.
2. The plastic limit of BC soil increases from 21.16 to 28.34% after addition of 10% of RBI Grade 81. This means, if percentage increases for RBI Grade 81, the PL also increases.
3. Plasticity index (PI) of soil is reduced from 19.84 to 6.88% when 10% of RBI Grade 81 is added.

References

1. M. Alhassan, Potentials of rice husk ash for soil stabilization. *AU J. Technol.* **11**(4), 246–250 (2008)
2. K.V. Madurwar, P.P. Dahale, A.N. Burile, Comparative study of black cotton soil stabilization with RBI Grade 81 and sodium silicate. *Int. J. Innov. Res. Sci. Eng. Technol.* **2**(2), 493–499 (2013)
3. M. Gunturi, P.T. Ravichandran, R. Annadurai, K.D. Krishnan, Effect of RBI-81 on CBR and swell behavior of expansive soil. *Int. J. Eng. Res.* **3**(5), 336–339 (2014)
4. E.A. Basha, R. Hashim, H.B. Mahmud, A.S. Muntohar, Stabilization of residual soil with rice husk ash and cement. *Constr. Build. Mater.* **19**(6), 448–453 (2005)
5. R.M. Brooks, Soil stabilization with fly ash and rice husk ash. *Int. J. Res. Rev. Appl. Sci.* **1**(3), 209–217 (2009)
6. IS 2720-Part 5 (1985), Code of practice, methods of test for soils, Part 5. Determination of liquid limit and plastic limit
7. IS:2720-Part-3 (1980), Code of practice, methods of test for soils, Part 3. Determination of specific gravity

Effect of Infill Wall on Reinforced Concrete Frame



Swati D. Ambadkar and Vinayak S. Dakre

Abstract In open ground storey buildings, along the building height, sudden change of stiffness takes place. Therefore, the storey is more flexible than adjacent storey. As a result, beams and column in these storey get heavily stressed. The behaviour of building gets changed due to infill walls under lateral loads. However, in industry, while analysing the framed building, the stiffness of infill wall is ignored. To compensate for stiffness, discontinuity IS1893:2002 allows analysis of open ground storey building with a multiplication factor of 2.5 without considering infill walls. According to design office, for low-rise building, the multiplication factor of 2.5 is not real. This gives a call for review and assessment of code recommendation on multiplication factor for low-rise buildings with open ground storey. The present study deals with the modelling of the reinforced concrete structure with infill walls in the software. The results shall be studied for the fully infill wall, partially infill walls and without infill wall.

Keywords Infill wall · Storey stiffness · Lateral displacement · Time period · Storey shear · Storey drift

1 Introduction

In earthquake-prone regions of Turkey, the most common building types are reinforced concrete (RC) frames with infill walls. Due to the difficulties encountered in modelling of infill walls, they are generally neglected in structural design process. Stiffness, strength and seismic behaviour of structure get affected due to presence of infill wall [1]. Infill walls may be either detrimental or beneficial under seismic loading depending on the capacity demand ratios. The stiffness and strength of the

S. D. Ambadkar (✉)

Department of Civil Engineering, G.H. Raisoni University, Amravati, India
e-mail: swati.ambadkar@ghru.edu.in

V. S. Dakre

Department of Mechanical Engineering, G.H. Raisoni University, Amravati, India
e-mail: vinayak.dakre@ghru.edu.in

© The Author(s), under exclusive license to Springer Nature Singapore Pte Ltd. 2022
M. L. Kolhe et al. (eds.), *Smart Technologies for Energy, Environment and Sustainable Development, Vol 1*, Springer Proceedings in Energy,
https://doi.org/10.1007/978-981-16-6875-3_25

299

structure get increased due to infill walls. Upon certain limits, this situation is helpful for non-ductile building. On the contrary, brittle nature infill walls may cause unforeseen and irreversible damages [2]. At lower stories of multistorey structure, soft-storey mechanism may occur due to drift concentration. To waive the negative effects of the infill walls, along height of the structure, stiffness distribution is done by using infill walls with different stiffness and strength properties [3].

The aim of the study is to find out the stiffness variation in infill walls with seismic loading. A five-storey five-bay RC frame is designed according to RC Codes and Turkish Earthquake. With the typical deficiencies observed in residential building in Turkey, the stirrup spacing of the members at the confinement regions was designed.

Stilt building or soft storey building is the building in which the ground storey consists of open space. Such space is used for retail and commercial purpose or parking. In these buildings, the storey is more flexible than the adjacent storey due to sudden change of stiffness along the height of building [4]. In other words, soft storey is the storey in which there is significant reduction of stiffness. As a result, beams and column in these storey get heavily stressed. Hence, sufficient strength and adequate ductility are necessary for the ground storey column [5].

2 Modelling

The different parameters considered for modelling are as follows, and the plan and elevation are also presented in the following Figs. 1, 2 (Table 1). Infill walls are modelled by using diagonal struts pinned at both the ends. As self-weight of wall is considered already in model, and density of strut material is taken as zero.

3 Results

Symmetrical building: The analysis is carried out in the ETAB software for the symmetrical building as in Figs. 3, 4, 5, 6, 7.

Unsymmetrical building: Figs. 8, 9, 10, 11, 12, 13.

4 Conclusion

Infill wall increases the lateral stiffness and seismic resistance of the building. It also increases the strength and rigidity of the building. Following are the conclusions drawn after analysing and studying the various parameters like lateral displacement, storey drift, time period, storey shear, storey stiffness the symmetrical and asymmetrical building with infill wall.

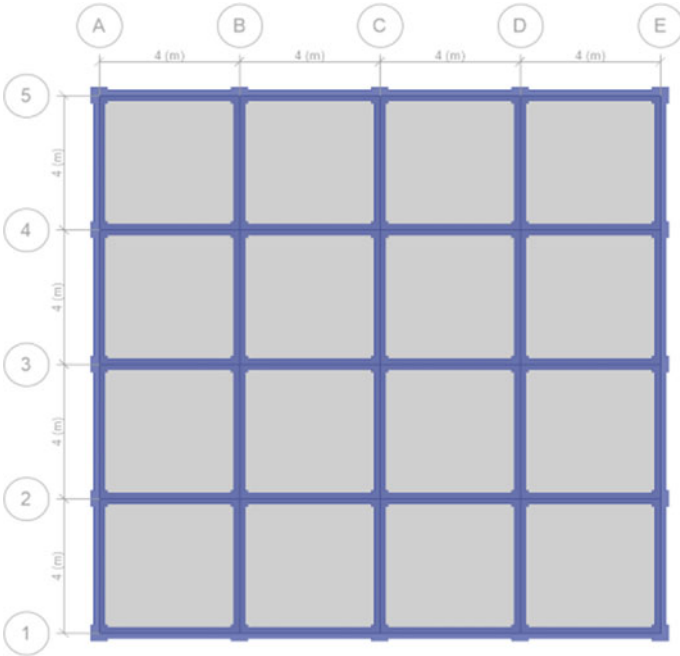


Fig. 1 Plan of the symmetrical building

Fig. 2 Elevation of the symmetrical building

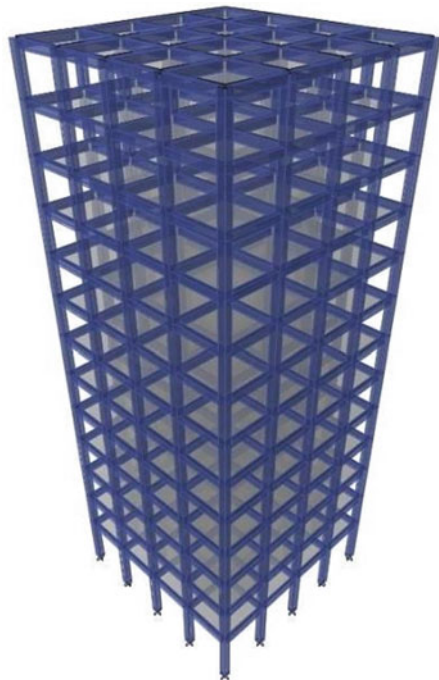


Table 1 Parameters considered for modelling

Plane dimensions	24 × 24 m
Total building height	42.9 m
Each storey height	3.2 m
Parapet height	1 m
Foundation depth	1.3 m
Beams size	300 × 500 mm
Columns size	500 × 500 mm
Slab thickness	150 mm
External wall thickness	230 mm
Internal wall thickness	115 mm
Seismic zone	III
Soil condition	Medium
Response reduction factor	5
Importance factor	1
Floor finishes	1.5 kN/m ²
Floor live load	3 kN/m ²
Concrete grade	M25
Steel grade	Fe500
Concrete density	25 kN/m ³
Brick masonry density	20 kN/m ³

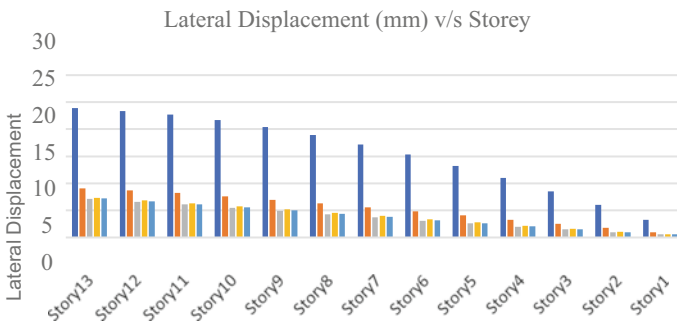


Fig. 3 Lateral displacement versus storey

- i. Top storey shows maximum lateral displacement, i.e. on 13th storey.
- ii. Storey drift is maximum for lower storey as storey drift is greater for storey 1 when compared with other storey.
- iii. Time period (s) is maximum for mode 1 for all the models.
- iv. Storey shear is maximum for storey 1 as compared to other model.
- v. Storey stiffness is maximum for storey 2.

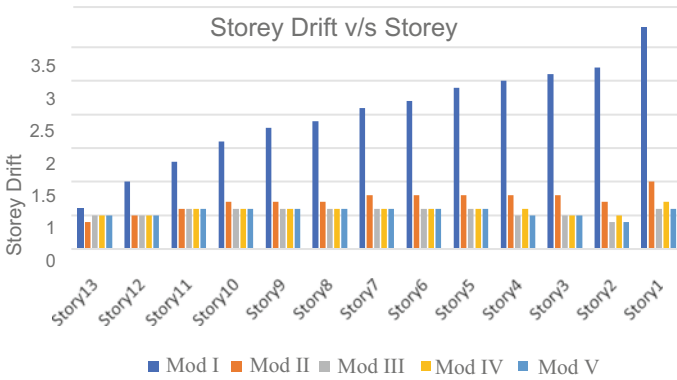


Fig. 4 Storey drift versus storey

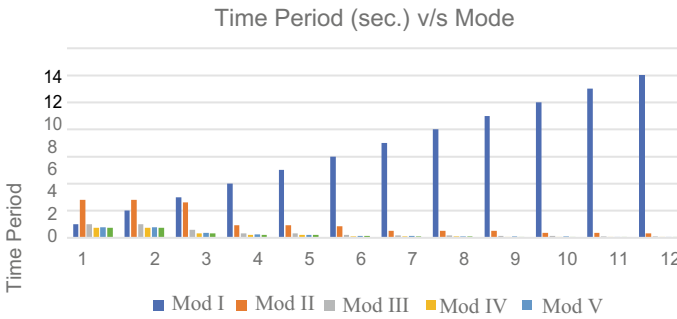


Fig. 5 Time period versus mode

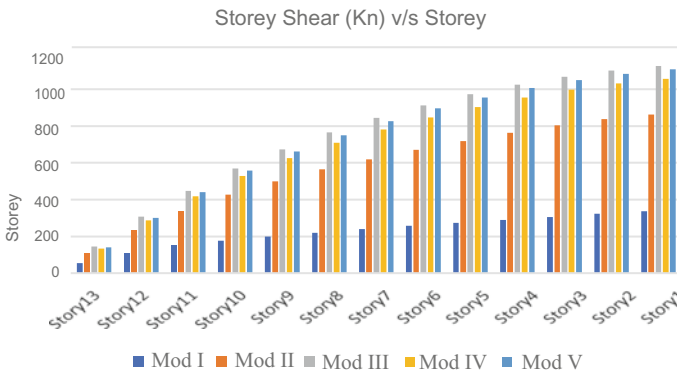


Fig. 6 Storey versus Storey Shear (Kn)

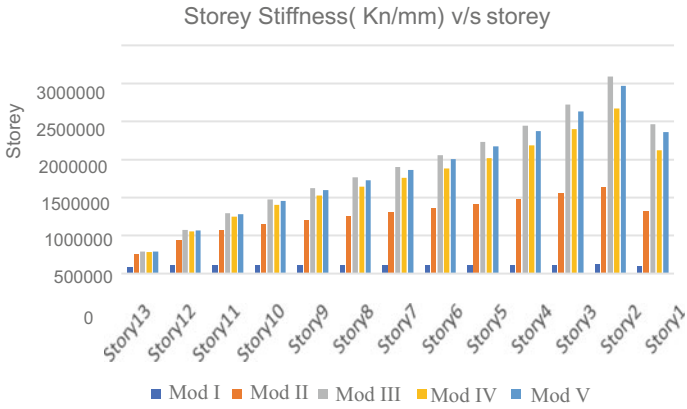
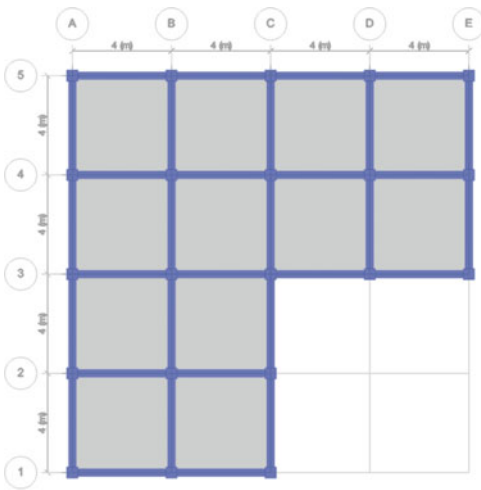
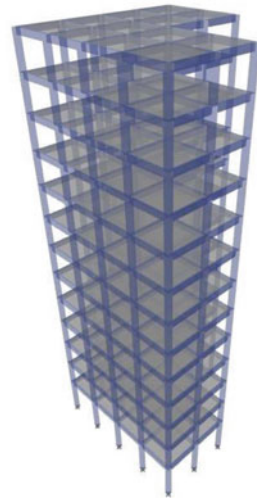


Fig. 7 Storey stiffness versus storey



(a) : plan of unsymmetrical building



(b) : Elevation of unsymmetrical building

Fig. 8 a Plan of unsymmetrical building. b Elevation of unsymmetrical building

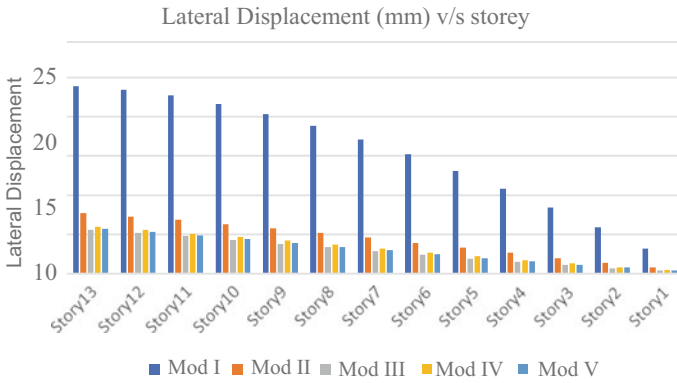


Fig. 9 Lateral displacement versus storey

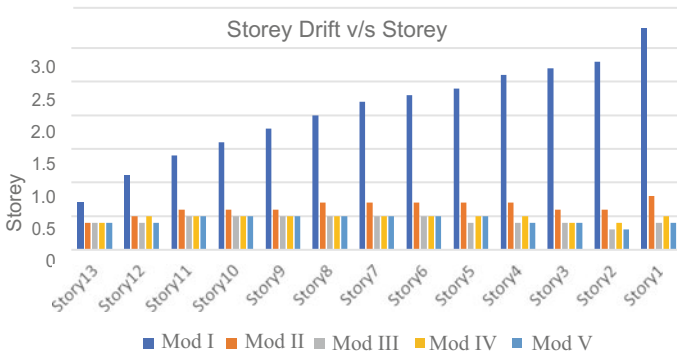


Fig. 10 Storey drift versus storey

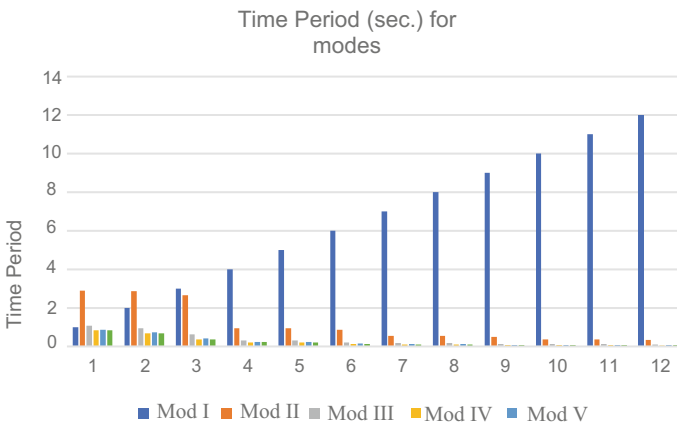


Fig. 11 Time period for modes

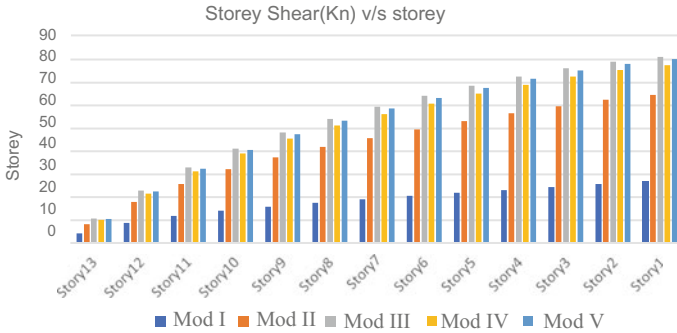


Fig. 12 Storey shear versus storey

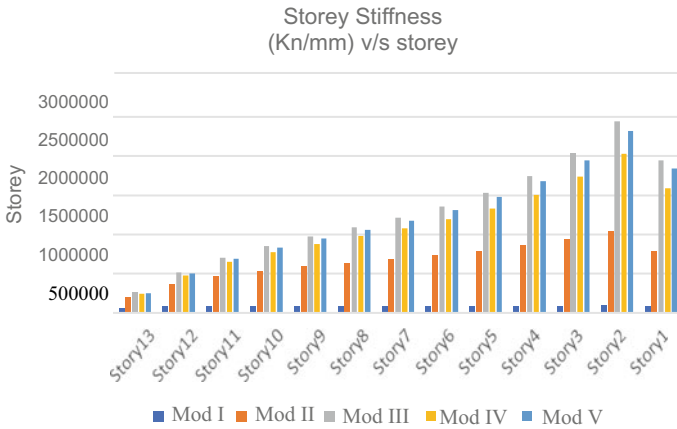


Fig. 13 Storey stiffness versus storey

References

1. S. Suryawanshi et al., Study & comparison of structures having different infill material using E-Tabs. International Journal of Engineering & Technology (IRJET) 7(08) (2020)
2. X. Zhou et al. Influence of Infill wall configuration on failure modes of RC Frame. Shock & Vibration 2018, Article ID 6582817
3. F. Mohiuddin, Behaviour of infill wall under seismic loading in RC Framed structure. International Journal of Engineering & Research (IJETR) 7(7) (July-2017)
4. A. Ahmed et al., in Role of masonry infill wall on the seismic behavior of typical four story building in Pakistan. 1st International Conference on Advances in Engineering & Technology (ICAET -2018). Material Science & Engineering (2017), vol. 414 (Baleli Quetta, 87300, Pakistan, 2-3 April 2018)
5. P. Paudel, Effect of infill walls in performance of reinforced concrete building structures. Int. J. Eng. Res. Gen. Sci. 5(4) (July-Aug 2017)
6. S.S. Sankhla et al. A comparative study on the effect of Infill walls on RCC frame structure. International Journal of Mechanical & Civil Engineering (IOSR-JMCE) 13(6), Version VI (Nov.-Dec. 2016)

7. L.M. Thomas, P.E. Kavitha, Effect of infill walls on the seismic performance of the multistoried buildings. *International Journal of Research in Engineering & Technology (IJRET)* **4**(10) (Oct.-2015)
8. E. Sönmez, C. Dönmez, Effect of infill wall stiffness variations on the behavior of reinforced concrete frames under earthquake demands. In: 2nd European conference on earthquake engineering and seismology, Istanbul, August 2014
9. S. Attajkani, A. Khamlichi, A. Jabbouri, Modelling the effect of infill walls on seismic performance of reinforced concrete buildings. *Int. J. Eng. Res. Appl.* **3**(1) 1178–1183 (2013)
10. M.A. Çankaya, Dynamic behavior of reinforced concrete frames with infill walls (Master's thesis), Civil Engineering Department, Izmir Institute of Technology, İzmir, Turkey, 2011
11. M. Mohammadi, V. Akrami, R. Mohammadi-Ghazi, Methods to improve infilled frame ductility. *J. Struct. Eng.* **137**(6), 646–653 (2011)
12. S. Das, Seismic design of vertically irregular reinforced concrete structures. Ph.D. Thesis. North Carolina State University. Raleigh. NC (2000)
13. M. Dolsek, P. Fajfar, Soft story effects in uniformly infilled reinforced concrete frames. *J. Earthq. Eng.* **5**(1) 1–12 (2001)
14. C.V.R. Murthy, S.K. Jain, Beneficial influence of masonry infill on seismic performance of RC frames buildings. In: Proceedings of 12th world conference on earthquake engineering, New Zealand, paper no. 1790, 2000
15. F. Danesh, V. Behrang, The influence of masonry infill walls on dynamic behaviour of concrete structures. In: 13th World conference on earthquake engineering, Vancouver, B.C., Canada, August 1–6, 2004, paper no. 1984

Development of Eco-Friendly Pervious Concrete Utilizing Granite Cutting Sludge Waste



Yash Agrawal, Manish Varma, Trilok Gupta, and Ravi K. Sharma

Abstract Solid industrial waste by-products increased with rapid industrial growth in recent years. Using these wastes in the construction sector, a huge contribution would be made towards sustainable and cleaner production. The extensive use of concrete is increasing in the construction sector for urban development, and therefore, demand of the alternative constituents of concrete like cement and sand has also been increased. The granite cutting sludge waste is generated during the cutting operation of dimensional stone into pieces, and these wastes are having a detrimental effect on the environment and humans. In this experimental work, the feasibility of granite cutting sludge waste as a partial replacement of cement in no-fine pervious concrete production is examined for eco-friendly construction. The experimental study is carried out by using granite cutting sludge waste as partial replacement of OPC cement at 0, 5, 10, 15, 20, 25 and 30% levels. To evaluate the performance of no-fine permeable concrete, various tests have been carried out like compressive strength test, flexural strength test, water permeability test and ultrasonic pulse velocity test. The test results showed that the properties of no-fine pervious concrete were enhanced with the use of 5% granite cutting sludge waste as partial replacement of cement.

Keywords Granite cutting sludge waste · Pervious concrete · No-fine concrete · Sustainability

1 Introduction

Today in this modern world concrete demand is very high so we have to find out sustainable and eco-friendly construction material. In the concrete main ingredients, cement and aggregate are used most commonly. However, cement production

Y. Agrawal (✉) · T. Gupta · R. K. Sharma
Department of Civil Engineering, College of Technology and Engineering, MPUAT, Udaipur,
Rajasthan, India

M. Varma
Department of Civil Engineering, Geetanjali Institute of Technical Studies, Udaipur, Rajasthan,
India

© The Author(s), under exclusive license to Springer Nature Singapore Pte Ltd. 2022
M. L. Kolhe et al. (eds.), *Smart Technologies for Energy, Environment and Sustainable Development, Vol 1*, Springer Proceedings in Energy,
https://doi.org/10.1007/978-981-16-6875-3_26

309

produces a large amount of CO₂ emission (7% of total) [1–5]. That is, why sustainable development has become a necessity particularly in a country like India where flooding and water-logging problems are the major environmental issue. To deal with these issues, diverse sustainable and eco-friendly resources and things are being implemented where permeable concrete pavement is among them [6, 7].

In India and other countries, stormwater surface runoff has rapidly increased due to infrastructure development which has decreased unpaved open land area for seepage of the water [8]. As an effect of this road transport is interrupted by drainage system overload and flood foreseeable. To avoid this engineered solution like permeable concrete is needed to manage the stormwater runoff. Pervious concrete directly captured stormwater and allow the seepage of water which also recharge the underground water to achieve environmental sustainability [9–11].

In this experimental study, the effect of granite cutting sludge waste as partial replacement of cement on eco-friendly no-fine permeable concrete is evaluated.

An effort must be applied to obtain desired properties, which include strength and permeability. It is essential to optimize the effective void content in the cement paste of concrete to achieve both strength and permeability [12, 13]. The desired void content may be achieved either by modifying the level of compactive effort or by adjusting the aggregate proportions and properties.

There are no standard specifications for achieving the desired strength and permeability in the field of concrete. Therefore, it is more beneficial to modify the permeable concrete with such of these wastes which makes it sustainable and eco-friendly.

In this study, concrete mixes were made with the granite cutting sludge waste to ensure proper packing/bonding between cement paste and aggregate along with full penetration of water and to find a sustainable way for making eco-friendly concrete with sludge waste in an innovative manner.

2 Experimental Programme

In this experimental study, seven permeable concrete mixes were cast based on trial mixes. Various tests were carried out to investigate the properties of no-fine permeable concrete with or without granite cutting sludge waste as replacement of cement. On no-fine permeable concrete, different tests have been carried out to evaluate mechanical and durability properties. For mechanical properties, the compressive strength test and flexure strength test were determined, and for durability properties, the water permeability test was determined. For quality assessment of concrete, a non-destructive test (UPV) was done.

2.1 Materials

In the study, cement binder ordinary Portland cement (OPC) of 43-grade was used as per the specification mentioned in IS 8112:2013 [14]. The specific gravity of the cement was found by the Le Chatelier flask. The specific gravity of the cement was found with the following formula

$$\text{Specific gravity of cement} = W5(W3 - W1)/(W5 + W3 - W4)(W2 - W1)$$

Here $W1$ = Weight of flask (kg)

$W2$ = Weight of flask + water (kg)

$W3$ = Weight of flask + kerosene (kg)

$W4$ = Weight of flask + kerosene + cement (kg)

$W5$ = Mass of cement (kg).

The standard consistency and initial and final setting time of cement were found with the Vicat apparatus. The specific gravity of the granite cutting sludge waste and coarse aggregate was found by the pycnometer bottle and glass flask. The specific gravity of the granite cutting sludge waste and coarse aggregate was found with the following formula

$$\text{Specific gravity of granite cutting sludge waste} = (W2 - W1)/((W4 - W1) - (W3 - W1))$$

Here $W1$ = Weight of Container (kg)

$W2$ = Weight of container + aggregate (kg)

$W3$ = Weight of container + aggregate + water (kg)

$W4$ = Weight of container + water (kg)

$W5$ = Mass of cement (kg).

Granite cutting sludge waste of specific gravity 2.19 was used in this study as a replacement of cement in no-fine permeable concrete. Coarse aggregate ranging from 10 to 20 mm having specific gravity 2.71 was used in this experimental work. Other physical properties of cement, aggregates and granite cutting sludge waste are shown in Table 1.

2.2 Mix Proportions

No-fine permeable concrete was cast with different concrete mix proportions such as 1:4 and 1:6 in trial mixes. The trial mixes were made with varied w/c ratio. The compressive strength was found first to get the proper mix for desired strength. From the trial mixes, the results were found and the mix proportion for no-fine pervious concrete was adopted. The results of trial mixes are given in Table 2.

Table 1 Physical properties of cement, aggregates and granite cutting sludge waste

Characteristics	Cement (OPC)	Granite cutting sludge waste	Coarse aggregate
Specific gravity	3.13	2.19	7.6
Water absorption %	–	2.9	5%
Consistency	32%	37%	–
Initial setting time (min)	113	–	–
Final setting time	245		
Compressive strength (MPa)		–	–
7 days	34.5		
28 days	45.1		

Table 2 Trial mixes

S. No.	Cement/aggregate ratio	w/c ratio	Average compressive strength for 28 days (MPa)	Remarks
1.	1:4	0.3	–	Improper mix
2.	1:4	0.33	15.0	Proper mix
3.	1:4	0.35	12.5	Proper mix
4.	1:6	0.3	–	Improper mix
5.	1:6	0.33	8.5	Proper mix
6.	1:6	0.35	5.2	Proper mix

The mix of no-fine permeable concrete was designed with a 1:4 cement to aggregate ratio and 0.33 w/c ratio so that no fine concrete would achieve the compressive strength around 15 N/mm². Using this mix ratio, different mixes were made to cast different specimens as shown in Fig. 1. In this study, cement was partially replaced with granite cutting sludge waste from 0 to 30% in incremental order as shown in Table 3.

3 Testing Programme

The following tests were carried out to assess the properties of no-fine permeable concrete.

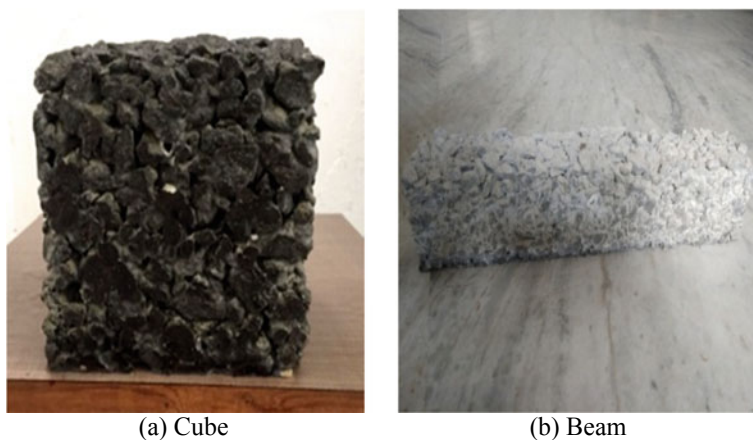


Fig. 1 No-fine pervious concrete specimens

Table 3 Mix proportion casted

S. No.	Cement	w/c ratio	Cement (in %)	Percentage of granite cutting sludge waste
1.	OPC	0.33	100	0
2.	OPC	0.33	95	5
3.	OPC	0.33	90	10
4.	OPC	0.33	85	15
5.	OPC	0.33	80	20
6.	OPC	0.33	75	25
7.	OPC	0.33	70	30

3.1 Compressive Strength Test

The crushing strength of hardened concrete was found as per the guidelines of IS 516 [15]. The specimen size of the cube 150 mm × 150 mm × 150 mm was used for this test (Fig. 2).

3.2 Flexural Strength Test

Flexural strength of concrete as per IS: 516 [15]. The flexural strength for three points loading was calculated as follows:

$$F_{cf} = fl/bd^2$$



Fig. 2 Compressive strength test

F_{cf} = Flexural strength (MPa)

F = Maximum load at failure (N)

l = Distance b/w axes of supporting rollers (mm)

b = Width of specimen (mm)

d = Depth of the specimen (mm).

3.3 Water Permeability Test

The water permeability of specimens was determined as per the guidelines of DIN 1048 (Fig. 3) with the specimens of size (150 mm × 150 mm × 150 mm) [16]. The depth of water penetration was determined by 72 h of a testing period after spilling the cube into two parts.

3.4 Ultrasonic Pulse Velocity Test

UPV test was conducted on specimens of size 150 mm × 150 mm × 150 mm (Fig. 4) as per IS 13311(Part 1) [17].



Fig. 3 Water permeability test



Fig. 4 Ultrasonic pulse velocity test

4 Results and Discussion

In the succeeding parts, the results for compressive strength, flexure strength, water permeability test and ultrasonic pulse velocity test (UPV) were presented. Analysis and discussions on the above-discussed tests have also been reported.

4.1 Compressive Strength

The compressive strength of concrete specimens was determined after 7 and 28 days of standard curing. From the test results, the highest compressive strength was found at 5% partial replacement of cement (OPC) by granite cutting sludge waste with a different interval of water curing period 11.2 MPa and 15.9 MPa, respectively, for 7 days and 28 days. An increase in the compressive strength of concrete has been observed with 5% inclusion of granite cutting sludge waste as partial replacement of cement (OPC) as shown in Fig. 5.

The compressive strength of concrete was decreasing after 10% partial replacement of OPC at a w/c ratio of 0.33. This reduction in compressive strength was increased with the increment in the percentage of granite cutting sludge waste.

The cement particles and coarse aggregate cannot pack together as efficiently as to make the proper bonding due to the wall effect in fresh concrete. Granite cutting sludge waste has fine particles that make the proper cement paste ensure effective packing and better bonding in the permeable concrete matrix, which increases the

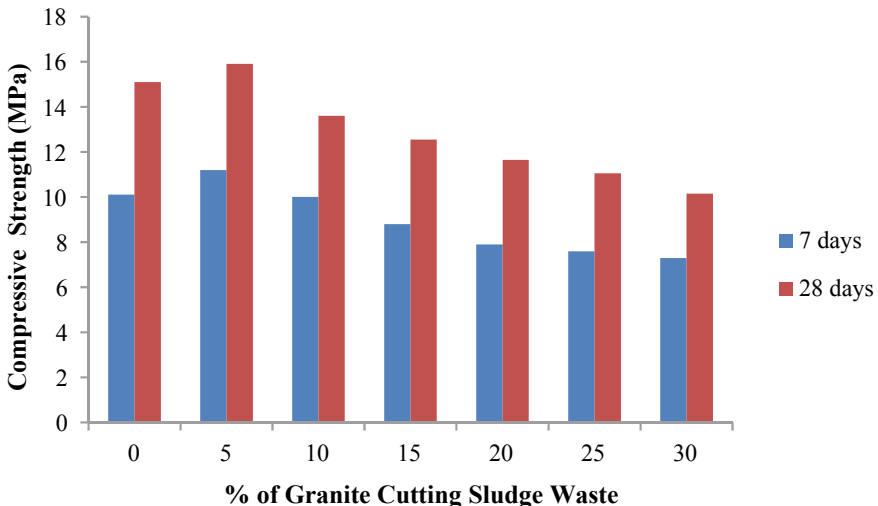


Fig. 5 Variation in compressive strength of permeable concrete containing granite cutting sludge waste

strength of permeable concrete and due to the use of granite cutting sludge waste as a partial replacement of cement excessively the permeable concrete strength decrease.

4.2 Flexural Strength

The flexural strength of concrete specimens was determined after 7 and 28 days of standard curing. The result of the flexural strength of permeable concrete containing cement (OPC) with different percentage levels of granite cutting sludge waste is shown in Fig. 6.

It can be observed from Fig. 6 at a w/c ratio of 0.33, maximum flexural strength has been obtained at 5% partial replacement of cement (OPC) by granite cutting sludge waste for curing at 7 and 28 days. The flexural strength at this replacement level increases to 2.22 MPa (at 28 days) from 1.82 MPa of the control sample (replacement level 0%). From this Fig. 6, the flexural strength of permeable concrete is decreasing after 5% partial replacement of cement (OPC) at a w/c ratio of 0.33.

Granite cutting sludge waste has effective packing (microstructure), wall effect between aggregate and cement paste was reduced and excessive use of granite cutting sludge waste as cement replacement decreased the flexural strength.

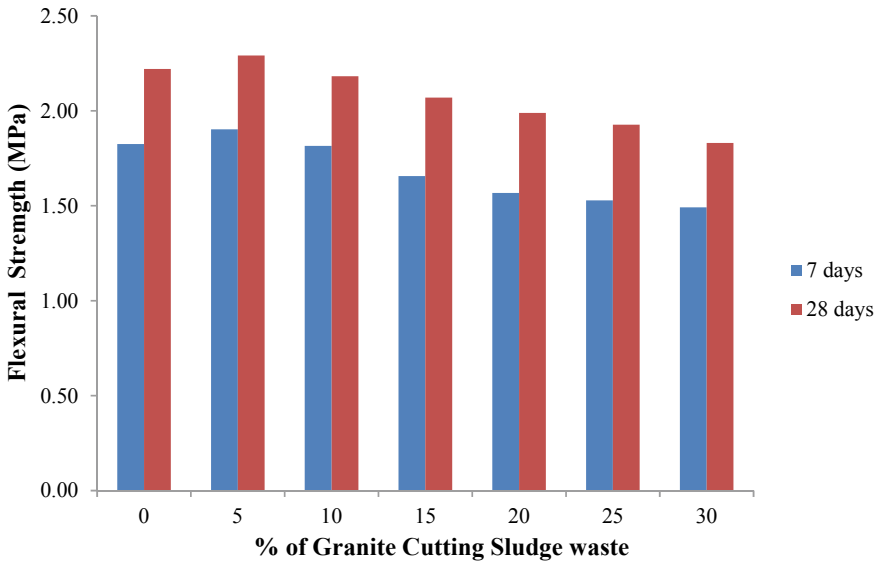


Fig. 6 Variation in flexural strength of permeable concrete containing granite cutting sludge waste

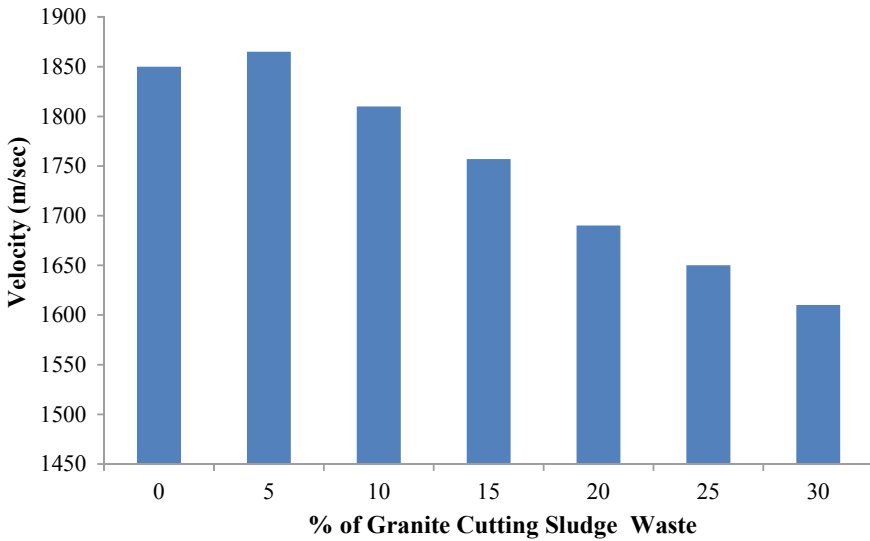


Fig. 7 Variation in pulse velocity of permeable concrete containing granite cutting sludge waste

4.3 Water Permeability of Concrete

The water penetration depth for all the specimens was found same because the water was fully penetrate in the specimens with different percentage of granite cutting sludge waste as partial replacement of cement (OPC).

4.4 Ultra Sonic Pulse Velocity of Concrete

UPV results obtained for various mixes are shown in Fig. 7. It can be observed from Fig. 7 that the UPV value of permeable concrete increases at a 5% replacement of cement with granite cutting sludge waste after that reduction was observed as compared to the control mix.

It can be further seen that the maximum value of UPV for the mix containing 5% granite cutting sludge was 1865 m/s. As per IS 13311 (Part 1), the quality of permeable concrete was found bad for the various mixes containing granite cutting sludge (0–30%).

5 Conclusion

The following conclusions can be drawn from the discussion of the results of no-fine pervious concrete:

1. The compressive strength of permeable concrete was increased due to effective packing and depending upon the replacement level of granite cutting sludge waste as partial replacement of cement (OPC). For w/c ratio 0.33, the increase in compressive strength was observed at a replacement level of 5% for OPC replacement by granite cutting sludge waste.
2. The flexure strength of permeable concrete increased depending upon the replacement level of granite cutting sludge waste as partial replacement of cement (OPC). For w/c ratio 0.33, the increase in compressive strength was observed at a replacement level of 5% for OPC replacement by granite cutting sludge waste.
3. The water penetration depth for the entire specimen is the same as the concrete is permeable.
4. The UPV results showed that with the increase of granite cutting sludge waste as replacement of cement in concrete UPV values decreases after 5%.
5. The granite cutting sludge waste can be used in the construction of permeable pavement. The use of granite cutting sludge as the construction material can also reduce the carbon footprint as compared to cement production.

References

1. M.L. Berndt, Properties of sustainable concrete containing fly ash, slag and recycled concrete aggregate. *Constr. Build. Mater.* **23**(7), 2606–2613 (2009)
2. A. Bilodeau, V.M. Malhotra, High-volume fly ash system: concrete solution for sustainable development. *Mater. J.* **97**(1), 41–48 (2000)
3. C. Meyer, Concrete and sustainable development. *ACI Spec. Publ.* **206**, 501–512 (2002)
4. N. Tošić, S. Marinković, A. Stojanović, Sustainability of the concrete industry: current trends and future outlook. *Tehnika* **72**(1), 38–44 (2017)
5. L. Bragança, H.H. Koukkari, R. Blok, H. Gervasio, M. Veljkovic, R.P. Borg, C. Schaur, Sustainability of constructions: towards a better built environment, in *Proceedings of the Final Conference of COST Action C25* (2011)
6. M. Scholz, P. Grabowiecki, Review of permeable pavement systems. *Build. Environ.* **42**(11), 3830–3836 (2007)
7. L.N.N. Jayasuriya, N. Kadurupokune, M. Othman, K. Jesse, Contributing to the sustainable use of stormwater: the role of pervious pavements. *Water Sci. Technol.* **56**(12), 69–75 (2007)
8. R. Sriravindrarajah, N.D.H. Wang, L.J.W. Ervin, Mix design for pervious recycled aggregate concrete. *Int. J. Concr. Struct. Mater.* **6**(4), 239–246 (2012)
9. M.A. Alam, S. Naz, M.E. Student, Experimental study on properties of no-fine concrete. *Int. J. Inf. Futuristic Res. (IJIFR)* **2**, 3687–3694 (2015)
10. P.R. Teware, S.M. Harle, Mix proportion of cementitious material in pervious concrete. *J. Recent Act. Arch. Sci.* **1**(3) (2016)
11. P.S. Patil, I.P. Sonar, S. Shinde, No fine concrete. *Int. J. Concr. Technol. (IJCT)* **3**(2) (2017)

12. M. Neamitha, T.M. Supraja, Influence of water cement ratio and the size of aggregate on the properties of pervious concrete. *Int. Ref. J. Eng. Sci* **6**, 9–16 (2017)
13. L.K. Crouch, J. Pitt, R. Hewitt, Aggregate effects on pervious portland cement concrete static modulus of elasticity. *J. Mater. Civ. Eng.* **19**(7), 561–568 (2007)
14. *BIS: 8112 Ordinary Portland Cement, 43 Grade-Specification* (Bureau of Indian Standards, New Delhi, 2013)
15. *BIS: 516 Methods of Tests for Strength of Concrete* (Bureau of Indian Standards, New Delhi, 1969)
16. *DIN 1048 Water Permeability Test* (1991)
17. *BIS: 13311 Methods of Non Destructive Testing of Concrete: Part-1: Ultrasonic Pulse Velocity* (Bureau of Indian Standards, New Delhi, 1992)

Strength and Durability of Nano-silica Added Cement Composites—A Way Forward



Babalu Rajput and S. S. Pimplikar

Abstract Documented literature shows that nano-silica is a substance capable of constructing durable composites of cement with improved performance. The current state of the use of nano-silica in cement composites is discussed in this article. Literature has been studied to understand the impact of nano-silica on cement composites' fresh and mechanical properties. The durability attributes of the nano-silica added cement composites are also evaluated. Analysis findings have shown that the inclusion of nano-silica to cement composites may improve its strength and durability. It is suggested that stronger and more stable cement composites can be produced using nano-silica as partial cement replacement with or without mineral admixtures.

Keywords Nano-silica · Mechanical properties · Durability properties · Cement composites

1 Introduction

Cement concrete is commonly used all over the world for building and infrastructure projects. Due to colossal construction development, the demand for concrete material is growing. Indian building projects are getting more dynamic in architecture, design, construction, and subject to adverse environmental conditions; thus, they demand high strength, durable, and sustainable concrete. Mora had earlier clarified the significance of durability. It was claimed that the growing durability of concrete from 50 to 500 years would minimize its effect on the environment by a factor of ten [1]. Normal strength concrete needs regular maintenance or conservation [2]. Traditional concrete ingredients cannot produce durable, high strength, and sustainable

B. Rajput (✉)

Research Scholar, Department of Technology, Savitribai Phule Pune University, Ganeshkhind Rd, Aundh, Pune 411077, Maharashtra, India

S. S. Pimplikar

Research Guide, SPPU and Program Head, Dr. Vishwanath Karad MIT World Peace University, Pune, Maharashtra, India

concrete. Research has been carried out to improve environmental sustainability and concrete quality in the past.

Since its inception, nanotechnology has a significant impact on every area of science [3]. Nanotechnology advances have allowed researchers to study the impact of various nanomaterials on cement composites. Recently, researchers have analyzed the different properties of concrete produced using various nanomaterials. Nanomaterials include nano-clay, nano-silica, nano-iron oxide, nano-titanium dioxide, nano-aluminum oxide, nano-calcium carbonate, and carbon nanotubes. This paper examines available knowledge on the strength and durability of nano-silica added cement composites. This analysis will provide a clearer understanding of nano-silica application in concrete and will steer future investigations in this field.

2 Nano-silica and Cement Composites

Using nano-silica in cement composites, it is one of the leading research fields and has drawn significant interest from the research community. It is essential to review the current literature on nano-silica added cement composites to know the mechanism of hydration, microstructural, and mechanical properties. A systematic analysis of the literature has been carried out to understand nano-silica's role in cement composites over the past twenty years. The information available on the impact of nano-silica on various properties of cement composites is given in the following section of the paper.

2.1 *Nano-silica and Cement Paste*

Several investigators studied cement paste produced using nano-silica as a partial substitute for cement. The names of the researchers and descriptions of the analysis are displayed in Table 1.

Cement paste made with nano-silica reveals a dense microstructure [9]. Nano-silica serves as filler in cement composites, improves microstructure, and encourages pozzolanic reaction [12, 13]. The amount of calcium hydroxide (CaOH_2) in cement paste is lowered with the rise in the percentage of nano-silica, as shown in Fig. 1 [9, 10].

Calcium leaching dramatically decreases, which creates a thick calcium-silicate-hydrate gel by applying nano-silica particles to cement paste. Calcium leaching reduces due to the chemical reaction between nano-silica and CaOH_2 . Nano-silica accelerates the hydration process of cement paste and mortar, according to the literature [5, 6, 14, 15]. Accelerated hydration is due to smaller particles of nano-silica. However, cement paste's quick hydration is based on nano-silica's chemical reactivity or related to its surface behavior has not yet been determined [4].

Table 1 Reviewed literature on the properties of nano-silica added cement paste

References	Paste	Nano-silica percentage	Other admixtures	w/c ratio	The particle size of nano-silica (nm)	Properties studied
[4]	C ₃ S paste	1–5	–	0.4	5	Rate of hydration
[5]	Paste	0, 1, 2, 3, 5	2.5% (superplasticizer)	0.22	15	Consistency, setting time, compressive strength (CS), bond strength
[6]	Paste	0, 2.5	2% (superplasticizer)	0.35	9	Rheology, fresh properties
	Mortar	0, 1, 1.5, 2, 2.5	2% (superplasticizer)	0.35	9	Rheology, fresh properties
[7]	Paste	0, 0.5, 1.5, 3, 4.5	Silica fine	0.5–0.7	5–156	Water demand, workability
[8]	Paste	0, 0.2, 0.5, 1, 2.5, 5		0.30–0.33	100	Setting time, compressive strength, morphology
[9]	Paste	0, 0.5, 1, 2, 5		0.342–0.566	14	Microstructure, flexural and compressive strength
	Paste	0, 0.5, 1, 2, 5	1% (superplasticizer)	0.333–0.513	14	Microstructure, flexural and compressive strength
[10]	Paste	0, 5			50	CH content
	Mortar	0, 0.5, 1, 2, 3		0.4	50	Compressive strength, CH content, chloride permeability
[11]	Paste	0, 5		0.4	10	Cement hydration and gel properties

The inclusion of nano-silica to cement paste raises its water requirement [6]. Table 2 shows an improvement in the nano-silica added cement paste's compressive strength (CS) relative to cement paste's compressive strength made without nano-silica [8, 9]. It indicates that the percentage increase in cement paste's compressive strength ranges from 20 to 35 at 28 days, with the change in nano-silica content.

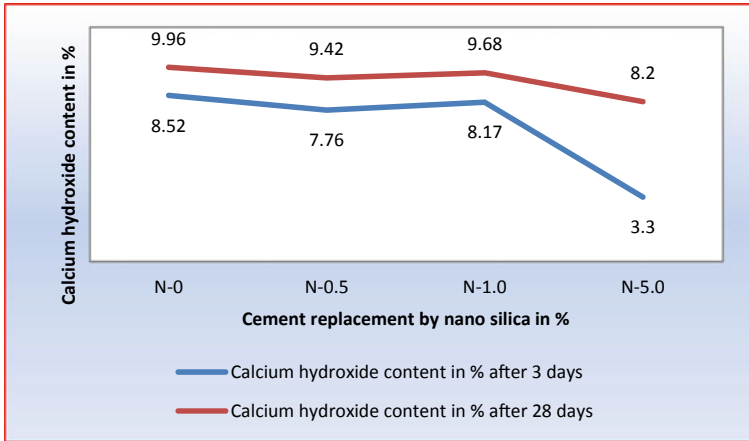


Fig. 1 The amount of calcium hydroxide in a nano-silica added cement paste [9, 10]

Table 2 Percentage increase in compressive strength of cement paste at 28 days

Nano-silica in %	Percentage increase in compressive strength of cement paste at the age of 28 days	References
0.50	25	[9]
1.0	20	[9]
2.0	20	[9]
5.0	35	[8]

On one day, the cement paste’s compressive strength containing 5% nano-silica was 64% more than the control mix, whereas, at 28 days, it was 35% higher [8]. Compared to the control sample’s compressive strength, cement paste’s compressive strength produced using 5% nano-silica and 2.5% superplasticizer increased by 8, 41, 25, and 15% at one day, three days, twenty-eight days, and sixty days [5]. Cement paste generated using 0.5–2% nano-silica without superplasticizer showed a 20–25% rise in compressive strength, and the same was 30–35% with 1% superplasticizer [9].

2.2 Cement Mortar with Nano-silica

Cement mortar made using nano-silica has been studied by numerous researchers. The list of available literature and information about the research is shown in Table 3.

Various researchers have reported an improvement in cement mortar compressive strength by nano-silica [10, 12–17]. Table 4 indicates a percent rise in the nano-silica added cement mortar’s compressive strength relative to the compressive strength of cement mortar formed in the absence of nano-silica [12, 15, 17]. It shows that the

Table 3 List of reviewed literature on the properties of nano-silica added cement mortar

References	Nano-silica percentage	Other admixtures	w/c ratio	Particle size of nano-silica	Properties studied
[12]	0, 3, 5, 10	Water reducing agent and defoamer	0.5	15 ± 5 nm	Microstructure, flexural strength, compressive strength
[13]	0, 3, 6, 10, 12	1.2, 1.8, 2.4, 2.9, 3.3% (superplasticizer)	0.5	40 nm	Rate of heat evaluation, microstructure, compressive strength
[14]	0, 3, 10		0.5	9 nm	Setting time, flexural strength, compressive strength
[15]	0, 0.5, 1.0, 1.5, 2.0	1.6, 2.1, 2.4% (superplasticizer)	0.3	20 nm	Cement hydration, microstructure, compressive strength, water sorptivity, chloride migration, drying shrinkage
	0, 0.5, 1.0, 1.5, 2.0		0.5	20 nm	
[16]	0, 3, 6, 10, 12	1.2, 1.8, 2.4, 2.9, 3.3% (superplasticizer)	0.48	40 nm	Microstructure, compressive strength
[17]	0, 0.25	0.1% (superplasticizer)	0.3	5–70 nm	Compressive strength, flexural strength

Table 4 Percentage increase in cement mortar’s compressive strength at 28 days

Nano-silica in %	Percentage increase in compressive strength of cement mortar at the age of 28 days	Use of water reducer/superplasticizer in the mix	References
0.25	20.0	Yes	[17]
0.5	9.0	No	[15]
1.0	8.0	No	[15]
1.5	10.0	No	[15]
2.0	11.0	No	[15]
3.0	13.8	Yes	[12]
5.0	17.0	Yes	[12]
10.0	26.0	Yes	[12]

rise in compressive strength at 28 days varies from 8 to 26, with a shift in nano-silica content.

Cement mortar manufactured with 0.5, 1.0, 1.5, and 2.0% and nano-silica demonstrated a rise in compressive strength by 9%, 8%, 10%, and 11% at 28 days, respectively [15]. The CS of cement mortar made of cement and the 1.2% superplasticizer at 7th and 28th day is 18.3 and 25.6 MPa. On the other side, with 3% nano-silica and 1.8% superplasticizer, the CS of cement mortar was 27.5 and 42.3 MPa at 0.48 w/c. As the nano-silica content raised from 3 to 12%, mortar CS was found to increase [16]. Even so, it is important to adjust the water dosage with a higher percentage of nano-silica. Otherwise, the strength of the cement composite can be reduced [14]. It was noticed that nano-silica up to 3% in cement mortar greatly enhances the compressive strength. Beyond 3%, there is no substantial improvement in CS [10]. Cement mortars with 0.25% nano-silica and 0.1% superplasticizer showed a 20% rise in compressive strength at one day than the compressive strength of plain cement mortar, reaching 63.9 MPa. A small quantities (0.25%) nano-silica, cement mortar's compressive, and flexural strength were improved [17]. Cement mortar produced using 10% nano-silica and 5% water-reducing agent revealed a rise in compressive strength by 26% relative to CS of control mix [12]. Compressive strength of three mortars, i.e., mortar 1 (cement and 1.2% superplasticizer), mortar 2 (cement, 15% silica fume and 2.2% superplasticizer), and mortar 3 (cement, 3% nano-silica and 1.8% superplasticizer) was observed as 18.3, 26.1, 39.5 MPa and 25.6, 38.0, 54.3 MPa at 7 days and 28 days, respectively [13].

2.3 Concrete Properties and Nano-silica

Researchers examined the various properties of the nano-silica added fresh and hardened concrete. Researchers' names and research descriptions are displayed in Table 5.

The inclusion of nano-silica to concrete benefits of a homogenous and compact microstructure [18, 27]. The interfacial transition zone is also denser with the inclusion of nano-silica [18]. For nano-silica used HVFAC, the initial and final setting time decreased [22].

Nano-silica integrated concrete displayed higher CS than normal concrete [25, 27]. The modulus of elasticity, tensile properties improved, and the compressive strength increased by 20% at 28 days, including 3% nano-silica [27]. Mortar and concrete developed with 1.5 and 2% nano-silica dosage showed improved performance. These dosages increased the compressive strength by 90 and 70%, increasing the tensile strength and chloride penetration resistance by 57 and 70% at 28 days [28]. The CS of nano-silica added concrete changes due to changes in a specific surface area of nano-silica [26]. Coarse nanoparticles (264 nm) produce long-lasting and durable mortar and concrete compared to mortar and concrete formed by finer nanoparticles (36 nm) [28]. A study of concrete's mechanical properties with nano-silica, silica fume, superplasticizer, and crushed dolomite aggregate showed improvement. It was

Table 5 List of documented literature concerning properties of nano-silica added concrete

Author(s)	Nano-silica percentage	Other admixtures	w/c ratio	The particle size of nano-silica (nm)	Properties studied
[18]	0, 3.5	Fly ash, superplasticizer	0.48	15 ± 5	Water permeability, microstructure
[19]	0, 2	Silica fume, superplasticizer, viscosity modifying agent	0.38	15 ± 3	Chloride penetration, water absorption, electrical resistivity
[20]	0, 3, 5, 10, 15	Silica fume, viscocrete	0.23–0.30	40–80	Compressive strength, resistance against chloride ion penetration
[21]	0, 3	Superplasticizer	0.33–0.5		Abrasive strength, porosity, and permeability
[22]	0, 2	Fly ash, slag, silica fume, superplasticizer	0.45	12	Setting time, strength
[23]	0, 3, 6, 9	Micro silica, superplasticizer	0.45	20 ± 5	Water permeability, compressive strength, microstructure
[24]	0, 0.3, 0.9	Superplasticizer	0.48	13	Microstructure, compressive strength, water penetration depth, water sorptivity, chloride migration coefficient, chloride diffusivity
[25]	0, 1, 2, 3, 4, 5	Silica fume, viscocrete, superplasticizer	0.20, 0.24	15	Compressive strength, split tensile strength, Flexural strength, Modulus of elasticity

(continued)

Table 5 (continued)

Author(s)	Nano-silica percentage	Other admixtures	w/c ratio	The particle size of nano-silica (nm)	Properties studied
[26]	0, 0.25, 0.5, 0.75, 1.0, 1.25, 1.5, 2, 3, 5, 10	Superplasticizer	0.4, 0.5, 0.6	5, 15, 98.7	Workability, microstructure, compressive strength, water absorption
[27]	0, 0.75, 1.5, 3		0.4	8–20	Fresh concrete properties, compressive strength, nondestructive parameters, water absorption, density and microstructure
[28]	0, 0.5, 1.0, 1.5, 2.0	Superplasticizer	0.58	264, 36.5	Setting time, fluidity, compressive strength, tensile strength, chloride penetration resistance

reported that the optimal nano-silica dosage should be 3% by weight of the cement content [25]. Few researchers have concluded that higher compressive strength will result from nano-silica and microsilica [20, 23]. A 45% rise in compressive strength was seen in the concrete mix created by using 10% nano-silica and 5% silica fume, and after that, strength was reduced. Consequently, the study proposed that the nano-silica content in concrete should not exceed 10% [20]. Concrete containing 15% micro silica and 3% nano-silica showed an improvement in compressive strength of 67.5% relative to the control concrete mix, while it was 39.6% for samples containing just 15% micro silica [23].

2.4 Nano-silica and Durability of Concrete

Concrete durability requires concrete resistance to various environmental and other attacks such as corrosion resistance, resistance to water entry, freezing and thawing resistance, resistance to acid and alkali attacks, and abrasion resistance. With 3% nano-silica in concrete, the decrease in water absorption was observed from 4.74 to 3.21% [27]. For concrete developed with nano-silica and superplasticizer, [21]

observed a reduction in permeability, porosity, and increased strength and abrasive resistance. For concrete manufactured with 3% nano-silica, with a reduction in w/c ratio from 0.5 to 0.33, concrete abrasive strength increased by 36%, concrete hydraulic conductivity coefficient dropped from 31.71×10^{-15} to 2.0×10^{-15} m/s, and concrete porosity decreased by 13% [21]. Jalal et al. [19] found lower water absorption, capillary absorption, and chloride ion in concrete mixes of silica fume and nano-silica. Water absorption decreased by 46%, 43%, and 50% for binder material 400, 450, and 500, respectively, for samples containing 10% silica fume and 2% nano-silica. It therefore led in a decline in capillary water absorption by 66%, 65%, and 66%, a decrease in chloride ion penetration by 62%, 60%, and 56%, respectively, for 400, 450, and 500 binders [19]. It was concluded that the inclusion of nano-silica could improve the resistance of the water penetration of concrete [18]. Concrete water penetration depth, chloride migration coefficient, and diffusion coefficient were lowered by 45%, 28.7%, and 31%, respectively. Marginal changes in water sorptivity and water absorption of concrete due to nano-silica have been noted [24].

2.5 Application of Nano-silica for Producing Different Concretes

Various properties of the other concrete made using nano-silica have been investigated by researchers. Table 6 contains the names of the researchers and the specifics about the study.

A compact and dense UHPC were formed with the inclusion of nano-silica and relatively less binder quantity. It was also observed that the viscosity and porosity of UHPC increased significantly [32]. Compared with the reference mix, the inclusion of 3% nano-silica to UHPC improved the CS of concrete by 8% and 6.5% at 28 and 90 days, respectively. However, when the replacement level reached 4%, CS decreased marginally [30]. The inclusion of nano-silica to UHPC was found to have the lowest corrosion rate (up to 0.1 mm/y) compared to HPC (0.36 mm/y) and UHPC without nano-silica (0.17 mm/y) mixtures. Therefore, it was concluded that the nano-silica in UHPC stopped corrosion from occurring in steel bars embedded in such concrete [33]. For HVFAC, a drop in initial and final setting times of 90 min and 100 min, respectively, was observed by adding 2% of nano-silica. A 25% rise in CS was observed for HVFAC after 7 days of curing [22]. An enhancement in the strength properties of concrete has been observed in SCC generated with nano-silica particles [31]. The SCC mix produced using 2% nano-silica exhibited a strength rise of 9.28% over 90 days [36]. The inclusion of nano-silica to SCC reduced the slump value, demonstrated improved tensile strength, resistance to capillary rise, increased resistance to chloride ion penetration, and improved resistance to sulfate attack [37]. SCC durability parameters, such as permeability, conductivity, migration of chloride, diffusion coefficients, and resistance to freezing and thawing, were significantly

Table 6 List of literature published on different types of nano-silica added concrete

Author(s)	Concrete type	Nano-silica percentage	Other admixtures	w/c or w/b ratio	The particle size of nano-silica	Properties studied
[22]	High volume fly ash concrete (HVFA)	0, 2	Fly ash, slag, silica fume, superplasticizer	0.45	12 nm	Setting time, strength
[25]	High strength concrete (HSC)	0, 1, 2, 3, 4, 5	Silica fume, viscocrete	0.20, 0.24	15 nm	Compressive strength, flexural strength, split tensile strength, modulus of elasticity
[29]	Self-compacting concrete (SCC)	0, 10	Limestone powder, superplasticizer, viscosity agent	0.5		Compressive strength
[30]	Ultra-high performance concrete (UHPC)	0, 1, 2, 3, 4	Silica fume, superplasticizer	0.198	15 ± 5 nm	Fresh and hardened properties, transport properties, microstructure
	Paste	0, 3		0.2	15 ± 5 nm	Pozzolanic reactivity
[31]	Self-compacting concrete		Superplasticizer	0.45		Microstructure, fresh concrete properties, mechanical properties, durability properties
[32]	Ultra-high performance concrete	0, 1, 2, 3, 4, 5	Limestone powder, superplasticizer	0.4	0.12 μm	Microstructure, mechanical properties, slump
[33]	Ultra-high performance concrete	0, 3	Silica fume, superplasticizer	0.20, 0.33	15 ± 5 nm	Corrosion resistance
[34]	Lightweight concrete (LWC)	0, 1, 2	Superplasticizer	0.42	12.4 nm	Mechanical and transport properties

(continued)

Table 6 (continued)

Author(s)	Concrete type	Nano-silica percentage	Other admixtures	w/c or w/b ratio	The particle size of nano-silica	Properties studied
[35]	Lightweight concrete	0, 1, 2, 4	Superplasticizer, stabilizer	0.4	Less than 150 nm	Mechanical properties, thermal properties, transport properties
[36]	Self-compacting concrete	0, 1, 2, 3	Superplasticizer	0.38	17 nm	Fresh concrete properties, mechanical properties
[37]	Self-compacting concrete	0, 1, 2, 3	Superplasticizer	0.44	17 nm	Fresh concrete properties, split tensile strength, water absorption, sorptivity, rapid chloride penetration, drying shrinkage, resistance to sulfate attack, microstructure

improved by 3.8% of nano-silica [31]. In SCC's case, produced with nano-silica and silica fumes, electrical resistivity was much more significant. With age and binder content, electrical resistivity increased [19]. Concrete made using recycled concrete aggregates and nano-silica has greater compressive strength than concrete produced with traditional aggregates [29]. An investigation on the mechanical and transport properties of LWC manufactured using nano-silica showed a reduction in water penetration and sorptivity [34]. A substantial rise in the strength of nano-silica added lightweight concrete had been observed. However, the increase in strength would only be significant if the nano-silica quantity is more than 1%. Nano-silica also reduced such lightweight concrete's consistency and therefore requires mixing of workability admixtures [35].

3 Analysis of the Review

A comprehensive literature review suggests the following aspects:

- Researchers have shown some interest in studying nano-silica applications in cement composites in recent years. Nano-silica in cement composites improves its microstructure, promotes the pozzolanic reaction, and accelerates hydration of cement [5, 9, 10, 12–14]. However, cement paste's quick hydration is based on nano-silica's chemical reactivity or related to its surface behavior has not yet been determined [4].
- The favorable effect of nano-silica on cement composites' mechanical properties was reported in a few studies [5, 9, 10, 12, 22, 25, 30, 32]. However, only limited research related to nano-silica concrete's durability properties is available [18–21, 23, 24, 26–28]. The durability of cement mortar or concrete, in addition to the compressive strength, depending upon various factors such as permeability, adsorption, chloride ingress, sulfate resistance, acid and alkali resistance, abrasion resistance, carbonation resistance, thermal properties, acoustic properties, fire resistance, impact resistance, and electrical and magnetic fields. The impact of nano-silica on these parameters also needs to be evaluated.
- Based on cement concrete/mortar/paste performance, the researchers reported varying and conflicting optimal nano-silica quantities. Hence, it is necessary to find an optimum amount of nano-silica with a reasonable permissible variation percentage for generalizing durable concretes' mass-scale production.
- Though some research has been conducted on nano-silica added concrete, the adoption rate of this concrete by users in India has been prolonged. To promote the use of such concrete techno-commercially, one must gain confidence in the nano-silica incorporated concrete. Thus, it is needed to carry out a complete comprehensive systematic experimental investigation focusing on durability aspects.

4 Conclusion

The impact of nano-silica particles was examined in cement composites by using a literature review. From the study, the following conclusions can be drawn:

- Based on cement composites' performance, the researchers reported varying and conflicting optimal quantities of nano-silica. It can be inferred from the literature that 3–10% cement replacement by nano-silica in the development of cement composite is considered. It gives satisfactory results concerning the strength and durability of cement composites. Replacement of cement by nano-silica will reduce the consumption of cement, which helps in protecting the environment.
- Nano-silica does have a greater specific surface area as compared to cement. Hence, the inclusion of nano-silica in cement composites accelerates the cement hydration process.

- Nano-silica in cement composites controls calcium leaching and makes cement paste dense with less porous spaces. Nano-silica behaves as a filler and acts as an activator to promote the pozzolanic reaction, which increases the overall durability of cement composite.
- The incorporation of nano-silica to cement composites decreases its workability. The workability of cement composites can be controlled by using workability admixtures. Admixtures like fly ash and superplasticizers are suitable for nano-silica added mortar/concretes.
- For nano-silica, added mortar/concrete improvement in mechanical properties was observed.
- Only a few studies concerning the durability properties of nano-silica added concrete are available. The effect of nano-silica on these parameters also needs to be evaluated.
- Nano-silica appears to be a promising building material for the production of high strength, durable, and sustainable concrete. Concrete produced with high strength and durability creates any structure with longer service life, reduces repair, and maintenance cost, and would achieve the economy in construction.

References

1. E.P. Mora, Life cycle, sustainability, and the transcendent quality of building materials. *Build. Environ.* **42**, 1329–1334 (2007)
2. T. Martins, F.P. Torgal, S. Miraldo, J.B. Aguiar, C. Jesus, An experimental investigation on nano-TiO₂ and fly ash based high performance concrete. *Indian Concr. J.* **90**(1), 23–31 (2016)
3. L.P. Singh, S.R. Karade, S.K. Bhattacharyya, M.M. Yousuf, S. Ahalawat, Beneficial role of nano silica in cement based materials—a review. *Constr. Build. Mater.* **47**, 1069–1077 (2013)
4. J. Bjornstrom, A. Martinelli, A. Matic, L. Borjesson, I. Panas, Accelerating effects of colloidal nano silica for beneficial calcium-silicate-hydrate formation in cement. *Chem. Phys. Lett.* **392**, 242–248 (2004)
5. Y. Qing, Z. Zenan, K. Deyu, C. Rongshen, Influence of nano-SiO₂ addition on properties of hardened cement paste as compared with silica fume. *Constr. Build. Mater.* **21**, 539–545 (2007)
6. L. Senff, J.A. Labrincha, V.M. Ferreira, D. Hotza, W.L. Repette, Effects of nano silica on rheology and fresh properties of cement pastes and mortars. *Constr. Build. Mater.* **23**, 2487–2491 (2009)
7. G. Quercia, G. Husken, H.J.H. Brouwers, Water demand of amorphous nano silica and its impact on the workability of cement paste. *Cem. Concr. Res.* **42**, 344–357 (2012)
8. L.P. Singh, S.K. Bhattacharyya, S. Ahalawat, Preparation of size controlled silica nano particles and its functional role in cementitious system. *J. Adv. Concr. Technol.* **10**, 345–352 (2012)
9. M. Stefanidou, I. Papyianni, Influence of nano-SiO₂ on the portland cement pastes. *Compos. Part B Eng.* **43**, 2706–2710 (2012)
10. L.P. Singh, S.K. Bhattacharyya, U. Sharma, G. Mishra, S. Ahalawat, Microstructure improvement of cementitious system using nanomaterials: a key for enhancing the durability of concrete, in *Ninth International Conference on Creep, Shrinkage, Durability Mechanics* (2013), pp. 293–301
11. P. Hou, S. Kawashima, D. Kong, D.J. Corr, J. Qian, S.P. Shah, Modification effects of colloidal nano SiO₂ on cement hydration and its gel property. *Compos. Part B Eng.* **45**, 440–448 (2013)

12. H. Li, H. Xiao, J. Yuan, J. Ou, Microstructure of cement mortar with nano particles. *Compos. Part B Eng.* **35**, 185–189 (2004)
13. B. Jo, C. Kim, G. Tae, J. Park, Characteristics of cement mortar with nano-SiO₂ particles. *Constr. Build. Mater.* **21**, 1351–1355 (2007)
14. M. Ltifi, A. Guefrech, P. Mounanga, A. Khelidj, Experimental study of the effect of addition of nano silica on the behaviour of cement mortars. *Procedia Eng.* **10**, 900–905 (2011)
15. H. Du, S.D. Pang, High performance cement composites with colloidal nano silica. *Constr. Build. Mater.* **224**, 317–325 (2019)
16. B. Jo, C. Kim, J. Lim, Investigations on the development of powder concrete with nano-SiO₂ particles. *KSCE J. Civ. Eng.* **11**(1), 37–42 (2007)
17. K. Sobolev, I. Flores, L.M. Torres-Martinez, P. Valdez, E. Zarazua, E.L. Cuellar, Engineering of SiO₂ nanoparticles for optimal performance in nano cement-based material, in *Nanotechnology in Construction Proceedings of NICOM3* (2009), pp. 139–148
18. T. Ji, Preliminary study on the water permeability and microstructure of concrete incorporating nano SiO₂. *Cem. Concr. Res.* **35**, 1943–1947 (2005)
19. M. Jalal, A.R. Pouladkhan, H. Norouzi, G. Choubdar, Chloride penetration, water absorption and electrical resistivity of high performance concrete containing nano silica and silica fume. *J. Am. Sci.* **8**(4), 278–284 (2012)
20. Jonbi, I. Pane, B. Hariandja, I. Imran, The use of nano silica for improving of concrete compressive strength and durability. *Appl. Mech. Mater.* **204–208**, 4059–4062 (2012)
21. A. Shamsai, S. Peroti, K. Rahmani, L. Rahemi, Effect of water cement ratio on abrasive strength, porosity and permeability of nano-silica concrete. *World Appl. Sci. J.* **17**(8), 929–933 (2012)
22. M.H. Zhang, J. Islam, Use of nano silica to reduce setting time and increase early strength of concretes with high volumes of fly ash and slag. *Constr. Build. Mater.* **29**, 573–580 (2012)
23. J. Esmaeili, K. Andalibi, Investigation of the effects of nano silica on the properties of concrete in comparison with micro silica. *Int. J. Nano Dimens.* **3**(4), 321–328 (2013)
24. H. Du, S. Du, X. Liu, Durability performances of concrete with nano silica. *Constr. Build. Mater.* **73**, 705–712 (2014)
25. M. Amin, K. Abu el-hassan, Effect of using different types of nano materials on mechanical properties of high strength concrete. *Constr. Build. Mater.* **80**, 116–124 (2015)
26. M. Alhawati, A. Ashour, A. El-Khoja, Properties of concrete incorporating different nano silica particles. *Mater. Res. Innov.* **24**(3), 133–144 (2020)
27. B. Mukharjee, S. Barai, Influence of incorporation of colloidal nano-silica on behaviour of concrete. *Iran. J. Sci. Technol. Trans. Civ. Eng.* **44**, 657–668 (2020)
28. J.D.P. Suárez, S.L. Uribe C., J. Lizarazo-Marriaga, J. Cárdenas-Pulido, Optimal nanosilica dosage in mortars and concretes subject to mechanical and durability solicitations. *Eur. J. Environ. Civ. Eng.* (2020). <https://doi.org/10.1080/19648189.2020.1731715>
29. S. Salkhordeh, P. Golbazi, H. Amini, The improvement of 28 day compressive strength of self compacting concrete made by different percentages of recycled concrete aggregate using nano silica. *World Acad. Sci. Eng. Technol.* **59**, 874–877 (2011)
30. E. Ghafari, H. Costa, E. Julio, A. Portugal, L. Duraes, The effect of nano silica addition on flowability, strength and transport properties of ultra high performance concrete. *Mater. Des.* **59**, 1–9 (2014)
31. G. Quercia, P. Spiesz, G. Huskan, H.J.H. Brouwers, SCC modification by use of amorphous nano silica. *Cem. Concr. Compos.* **45**, 69–81 (2014)
32. R. Yu, P. Spiesz, H.J.H. Brouwers, Effect of nano silica on the hydration and microstructure development of ultra high performance concrete with a low binder amount. *Constr. Build. Mater.* **65**, 140–150 (2014)
33. E. Ghafari, M. Arezoumandi, H. Costa, E. Julio, Influence of nano silica addition on the durability of UHPC. *Constr. Build. Mater.* **94**, 181–188 (2015)
34. H. Du, S. Du, X. Liu, Effect of nano silica on the mechanical and transport properties of lightweight concrete. *Constr. Build. Mater.* **82**, 114–122 (2015)
35. M.A. Elrahman, S. Chung, P. Sikora, T. Rucinska, D. Stephan, Influence of nanosilica on mechanical properties, sorptivity, and microstructure of lightweight concrete. *Materials* **12**(19), 3078, 1–16 (2019)

36. K. Nandhini, V. Ponmalar, Effect of blending micro and nano silica on the mechanical and durability properties of self-compacting concrete. *Silicon*. **13**, 687–695 (2021)
37. K. Nandhini, V. Ponmalar, Investigation on nano-silica blended cementitious systems on the workability and durability performance of self-compacting concrete. *Mater. Express* **10**(1), 10–20 (2020)

Controller for the Power Injection from a Grid-Interfaced Energy Storage within an AC Micro Grid



D. J. K. Dassanayake, H. M. A. P. Ruwanthi, K. K. D. I. Karunanayaka, K. M. S. Y. Konara, P. D. C. Perera, and Mohan Lal Kolhe

Abstract AC microgrids can work in either grid-connected or isolated mode. In the grid-connected operation, the power flow between the grid should be controlled. For this purpose, an accurate power flow controller is needed. The main focus of the study is to design an innovative power flow controller which is capable of injecting controlled power to the grid through a three-level neutral point clamped inverter integrated with a battery storage. The control strategies are developed in the d-q synchronous frame. The controller comprises of four main control blocks serving four major functions. Conversion of natural frame parameters into d-q synchronous reference frame, phased locked loop strategy to track grid frequency, generation of current references, current controlling loops to control active and reactive power, generation of voltage references and pulse generation with sinusoidal pulse width modulation scheme are the functions handled by the control blocks. The proposed controller is capable of handling power injection under both fixed and varying power demands from the grid.

Keywords Distributed generation · Energy storage · Microgrid control · Multilevel inverter · Grid following strategy

D. J. K. Dassanayake (✉) · H. M. A. P. Ruwanthi · K. K. D. I. Karunanayaka · K. M. S. Y. Konara · P. D. C. Perera
Faculty of Engineering, Department of Electrical and Information Engineering, University of Ruhuna, Galle, Sri Lanka
e-mail: dassanayake.djk@eie.ruh.ac.lk

K. M. S. Y. Konara
e-mail: konara@uia.no

P. D. C. Perera
e-mail: chandana@eie.ruh.ac.lk

K. M. S. Y. Konara · M. L. Kolhe
Faculty of Engineering and Science, University of Agder, PO Box 422, No 4604, Kristiansand, Norway
e-mail: mohan.l.kolhe@uia.no

© The Author(s), under exclusive license to Springer Nature Singapore Pte Ltd. 2022
M. L. Kolhe et al. (eds.), *Smart Technologies for Energy, Environment and Sustainable Development, Vol 1*, Springer Proceedings in Energy,
https://doi.org/10.1007/978-981-16-6875-3_28

1 Introduction

The gradual depletion of fossil fuel and the recognition of adverse effects of it on the environment have made the man move toward renewable energy sources (RES) in the sector of power generation. Consequently, distributed power generation systems (DPGS) with RES have been established in countries all over the world to produce more clean energy. Microgrid concept has become an important improvement for DPGS where several RES with different electrical behaviors can be integrated in the same grid, expanding system capacity and providing more controllability of power generation [1]. Due to the intermittent nature of RES, renewable energy integration causes fluctuations in grid voltage and frequency, thus creating instability. Therefore, microgrids consist of an energy storage for proper integration of RES with the demand-side management improving the power quality [2]. To overcome the intermittency of RES and to avoid the unstable conditions of the grid, an active and reactive power flow controller is needed for the controlled injection of power between the microgrid and the utility grid [3].

Some possible control structures for DPGS connected to the utility network and different reference frames in which these control structures can be implemented are discussed in [4]. Additionally, PI controllers in d-q frame, PI controllers in natural frame, resonant controller and dead beat predictive controller are the types of controllers discussed in details in [4]. Optimum design of PI controllers of dynamic systems can be achieved by a computational intelligence approach named as particle swarm optimization [5]. Particle swarm optimization algorithm to optimally tune controllers during real-time operation of a PV system has been investigated in [5]. Furthermore, in [6], a comparison of direct power control and grid voltage modulated direct power control strategies are presented. The paper [7] presents a photo-voltaic (PV) system utilizing neutral point clamped inverter (NPC). A current control loop is proposed in [7] which is capable of calculating reference currents in a fast manner, hence contributes to overcome problems associated with intermittent nature of in grid-connected PV systems. A voltage controller is presented which can be used for low voltage ride through (LVRT) control on DPGS. The proposed controller in [8] can be applied to different voltage control algorithms and prevents overcurrent transients during a fault.

This paper presents a power flow controller for the active power compensation in grid-connected mode using three-level NPC multilevel inverter embedded with an energy storage. The performance of the power flow controller is analyzed using MATLAB® SIMULINK® environment for both fixed and varying active power demands. The paper is organized into four sections. Initially, the overview of the system is presented in Sect. 2. The control structure and the proposed design of the power flow controller is described subsequently in Sect. 3. The analysis and the simulation results are discussed in Sect. 4. The simulations include the performance of the power controller under two cases of active power and a harmonic analysis is done for the system. Finally, the conclusion of the study is presented in Sect. 5.

2 System Overview

The system includes a DC battery bank, a boost converter, a three-level NPC inverter and an LCL filter. The DC link is accomplished by boosting the voltage of the DC battery bank. DC energy is transferred to the grid through the three-level NPC inverter. The inverter is controlled with sinusoidal pulse width modulation (SPWM) scheme at a constant switching frequency. In order to filter the inverter current and reduce harmonics content, an LCL filter is used between the inverter and the grid. The grid frequency and voltage are 50 Hz and 400 V, respectively. Figure 1 depicts the overall system.

In the last few decades, multilevel converters have been employed usually for medium-voltage and high-power applications. They have become a mature solution in the renewable energy sector. A three-level NPC is employed in this study due to its improved output waveform quality, fault-tolerant capability and reduced output filter sizing [9].

Three-level NPC inverters contain less harmonic content than conventional inverters. Upon employing SPWM for a three-level NPC inverter, it has been studied that the fifth and seventh harmonics are eliminated [10]. Furthermore, the content of the eleventh and thirteenth harmonics are less compared to the conventional inverter [10].

The connection of the inverter to the grid is done through a filter. For this purpose, either a pure L filter or an LCL filter can be used. LCL filter is more preferred compared to the L filter due to its better attenuation of switching frequency harmonics of the inverter, reduction in current ripple of the grid-side current and the decrease in total size and weight of the filter [11]. Even though LCL filters are superior to L filters, controlling a system with an LCL filter becomes complex due to the resonant pole pair created between the filter elements [12]. Therefore, proper damping methods should be introduced to avoid the possible instability of the system. Two methods

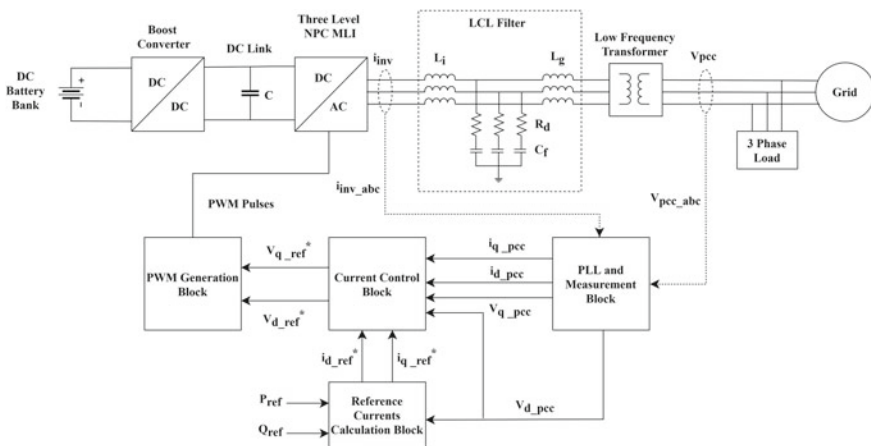


Fig. 1 Overview of the system

can be used to damp the resonance of the LCL filter. Passive damping is a method in which a passive resistor is used in series or parallel with the filter inductor or filter capacitor. Out of these, a series resistor with the filter capacitor has been widely adopted for its low power loss behavior [13]. An analysis of passive damping types of the LCL filter is done in [13]. Active damping methods can be used to eliminate the power loss resulted from the passive filters. The characteristics and design methods of active damping for LCL filters are discussed in [11]. For the model of this paper, passive damping using a resistor in series with the filter capacitor has been used. The design equations and the procedure are as follows.

It is considered that the rated current through the filter is allowed to have a fluctuation of 10% of the maximum current for the design. Equations for maximum current I_{\max} , allowable variation in rated current ΔI_{\max} and inverter-side filter inductance L_i are obtained from Eqs. (1), (2) and (3).

$$I_{\max} = \frac{\sqrt{2} P}{3 V_{\text{fil}}} \quad (1)$$

$$\Delta I_{\max} = \%10 I_{\max} \quad (2)$$

$$L_i = \frac{V_{\text{DC}}}{6 f_{\text{sw}} \Delta I_{\max}} \quad (3)$$

f_{sw} is the switching frequency and V_{DC} is the DC link voltage. The capacitor value is limited by the reduction of the power factor (less than 5%) in the rated capacity. The filter capacitance is given from Eq. (4) where C_b is the base capacitance.

$$C_{\text{fil}} = 0.05 C_b \quad (4)$$

Attenuation factor k_a , is taken as 0.2 (20%). The grid-side filter inductance can be calculated as,

$$L_g = \frac{\sqrt{\frac{1}{k_a^2} + 1}}{C_f \omega_{\text{sw}}^2} \quad (5)$$

$$\omega_{\text{res}} = \sqrt{\frac{L_i + L_g}{L_i L_g C_f}} \quad (6)$$

$$f_{\text{res}} = \frac{\omega_{\text{res}}}{2 \pi} \quad (7)$$

where L_g is the grid-side inductance, ω_{res} is the resonance angular velocity and f_{res} is resonance frequency. In order to avoid the resonance problems, the resonance frequency should satisfy the below condition.

$$10 f_g < f_{\text{res}} < 0.5 f_{\text{sw}} \quad (8)$$

A series resistor with the filter capacitor is used to prevent the resonance and reduce a part of ripple at the switching frequency. The resistor (R_d) value can be calculated using Eq. (9).

$$R_d = \frac{1}{3 C_f \omega_{\text{res}}} \quad (9)$$

3 Power Flow Controller

Grid-connected voltage source inverters have two main control methods which are voltage mode control and current mode control. In voltage mode control, the output voltage is considered as the control variable and it is controlled to have same frequency and phase as the grid voltage, while current mode control method considers the control variable as the inductive current output of the inverter and controls it to have the same frequency and phase as the grid voltage. The main grid can be regarded as a voltage source that has infinite capacity [15]. If voltage control is employed, then the total system is equivalent to a voltage source of finite capacity is made parallel a voltage source with infinite capacity. In order to make the system stable, phase-locked loop (PLL) is used to form the grid with the required frequency, amplitude and phase [15]. However, there is no controlled injection power in this scenario, and as the active power of the voltage source of finite capacity is changing, this requires high demands for PLL response time and the system stability is poor [15]. In contrast, if the current mode control method is utilized, PLL is used to extract the grid frequency. The output current of the inverter is kept in the same frequency and phase as the grid voltage ensuring the grid synchronization. Furthermore, in this scenario, the power injected to the grid will be controlled.

The control strategies are designed in synchronous reference frame in this study. This is known as d-q frame control where the current and voltage waveforms are transformed into a reference frame that rotates synchronously with the grid voltage [1]. By means of this, the control variables are converted into DC values which make it easier to implement current controllers. For the conversion of natural frame parameters to the synchronous reference frame parameters, Clark and Park transformation is used. The Park transformation (abc to dq transformation) is defined as

$$\begin{bmatrix} v_d \\ v_q \end{bmatrix} = \frac{2}{3} \begin{bmatrix} \cos(\omega t) & \cos(\omega t - \frac{2\pi}{3}) & \cos(\omega t + \frac{2\pi}{3}) \\ -\sin(\omega t) & -\sin(\omega t - \frac{2\pi}{3}) & -\sin(\omega t + \frac{2\pi}{3}) \\ \frac{1}{2} & \frac{1}{2} & \frac{1}{2} \end{bmatrix} \begin{bmatrix} v_a \\ v_b \\ v_c \end{bmatrix} \quad (10)$$

v_a , v_b and v_c are the three-phase voltage components of natural frame, while v_d and v_q are the components of voltage in the synchronous reference frame.

In order to design the current controllers, a mathematical model is required. System components after the inverter are used to derive the transfer function of the plant of the system. Considering the LCL filter, in the frequencies below the resonant

frequency, the LCL filter can be considered as a simple L filter [16]. Therefore, the plant can be simplified into a resistive and inductive element. Resistive element R_{tot} , represents the per phase resistance, the inductive element L_{tot} corresponds to the addition of the inverter-side inductance (L_i), the cumulative value of the grid-side inductance (L_g) and the transformer inductance (L_{tr}).

Considering the voltage drop across R_{tot} and L_{tot} , the following equations can be developed. Let v_{inv} and v_{pcc} be the voltages at inverter output and the voltage at the point of common coupling (PCC) respectively, and the output voltage of the inverter can be expressed as in Eqs. (11), (12) and (13) respectively.

$$v_{\text{a_inv}} = (R_{\text{tot}})i_{\text{a}} + (L_{\text{tot}}) \frac{di_{\text{a}}}{dt} + v_{\text{a_pcc}} \quad (11)$$

$$v_{\text{b_inv}} = (R_{\text{tot}})i_{\text{b}} + (L_{\text{tot}}) \frac{di_{\text{b}}}{dt} + v_{\text{b_pcc}} \quad (12)$$

$$v_{\text{c_inv}} = (R_{\text{tot}})i_{\text{c}} + (L_{\text{tot}}) \frac{di_{\text{c}}}{dt} + v_{\text{c_pcc}} \quad (13)$$

The natural frame model coordination in matrix form is expressed in Eq. (14).

$$[V_{\text{inv}}] = [R_{\text{tot}}][I] + [L_{\text{tot}}] \frac{d}{dt} [I] + [V_{\text{pcc}}] \quad (14)$$

The dq transformation is given by Eq. (15). Here, matrix T is the transformation matrix.

$$[X_{dq}] = [T][X_{abc}]$$

$$\begin{bmatrix} v_{\text{d_inv}} \\ v_{\text{q_inv}} \end{bmatrix} = \begin{bmatrix} R_{\text{tot}} & -\omega_{\text{g}} (L_{\text{tot}}) \\ \omega_{\text{g}} (L_{\text{tot}}) & R_{\text{tot}} \end{bmatrix} \begin{bmatrix} i_{\text{d}} \\ i_{\text{q}} \end{bmatrix} + \begin{bmatrix} (L_{\text{tot}}) & 0 \\ 0 & (L_{\text{tot}}) \end{bmatrix} \frac{d}{dt} \begin{bmatrix} i_{\text{d}} \\ i_{\text{q}} \end{bmatrix} + \begin{bmatrix} v_{\text{d_pcc}} \\ v_{\text{q_pcc}} \end{bmatrix} \quad (15)$$

where ω_{g} is the angular velocity of the grid.

The inverter output voltages in d-q frame are expressed in Eqs. (16) and (17).

$$v_{\text{d_inv}} = R_{\text{tot}}i_{\text{d}} + (L_{\text{tot}}) \frac{d(i_{\text{d}})}{dt} - \omega_{\text{g}} (L_{\text{tot}}) i_{\text{q}} + v_{\text{d_pcc}} \quad (16)$$

$$v_{\text{q_inv}} = R_{\text{tot}}i_{\text{q}} + (L_{\text{tot}}) \frac{d(i_{\text{q}})}{dt} + \omega_{\text{g}} (L_{\text{tot}}) i_{\text{d}} + v_{\text{q_pcc}} \quad (17)$$

The Laplace transform of Eqs. (16) and (17) are given in Eqs. (18) and (19).

$$v_{\text{d_inv}} = R_{\text{tot}}i_{\text{d}} + s(L_{\text{tot}})i_{\text{d}} - \omega_{\text{g}} (L_{\text{tot}}) i_{\text{q}} + v_{\text{d_pcc}} \quad (18)$$

$$v_{q_inv} = R_{tot}i_q + s(L_{tot}) i_q + \omega_g (L_{tot}) i_d + v_{q_pcc} \tag{19}$$

In order to implement the above model in the power flow controller, a combination of four control blocks is used.

3.1 Generation of Park Components and PLL

This block is used to convert the voltage at the PCC (v_{abc_pcc}) and line current (i_{abc_inv}) into Park components ($v_{d_pcc}, v_{q_pcc}, i_{d_pcc}, i_{q_pcc}$) in pu values as shown in Fig. 1.

For the synchronization purpose, PLL is used to extract the phase of the grid voltage [3]. PLL is implemented in synchronous reference frame where the grid voltage is transformed into DC components which are V_{pcc_d} and V_{pcc_q} as shown in Fig. 2. V_{pcc_q} is set to zero to thereby locking the PLL. PI controller (loop filter) is used to control this variable by bringing the phase error to zero. The nominal angular frequency of the grid (ω_{ff}) is then added to the output of the PI controller, and a voltage controlled oscillator (VCO) which acts as an integrator is used to achieve the phase-locked angle of the grid [20]. The angle is used to generate the frequency of the grid and used for the synchronization of the inverter with the grid. The relationship of voltage vectors in dq rotating coordinate system and abc coordinate system is shown in Fig. 3.

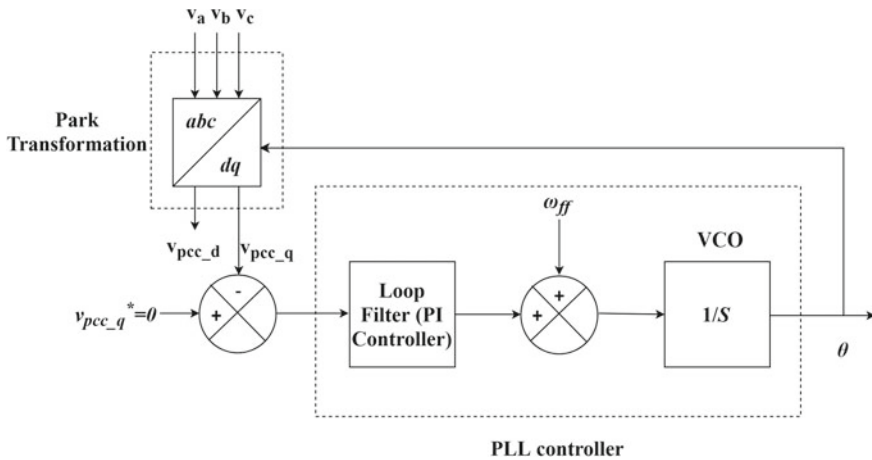
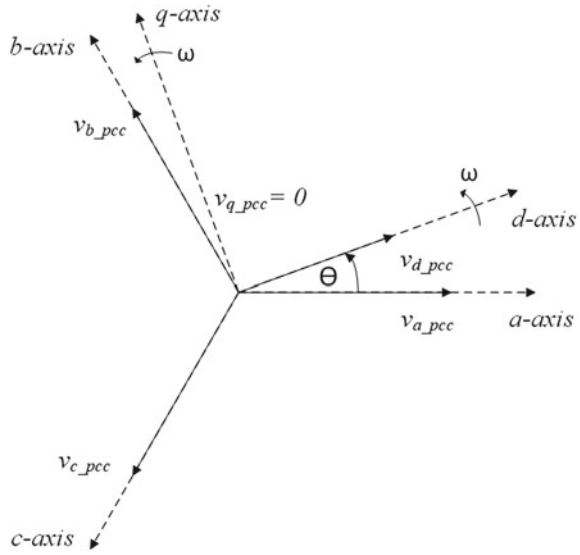


Fig. 2 Structure of PLL for grid synchronization

Fig. 3 Voltage at PCC (grid voltage) in dq rotating coordinate system and abc coordinate system



3.2 Reference Currents Calculation Block

The function of this block is to generate the current references for the current controller block as depicted in Fig. 1. The active and reactive power reference set points are given, and the current references are calculated using Eqs. (20) and (21).

$$P_{ref} = \frac{3}{2}(v_{d_pcc} i_{d_ref}) \tag{20}$$

$$Q_{ref} = -\frac{3}{2}(v_{d_pcc} i_{q_ref}) \tag{21}$$

3.3 Current Mode Controller

Equations (18) and (19) are further used to develop the model for the current mode controller. v_d and v_q terms are defined in order to simplify Eqs. (18) and (19).

$$v_d = (R_{tot}i_d + s(L_{tot})i_d) \tag{22}$$

$$v_q = (R_{tot}i_q + s(L_{tot})i_q) \tag{23}$$

Therefore, Eqs. (18) and (19) are simplified into,

$$v_{d_inv} = v_d - \omega_g (L_{tot}) i_q + v_{d_pcc} \tag{24}$$

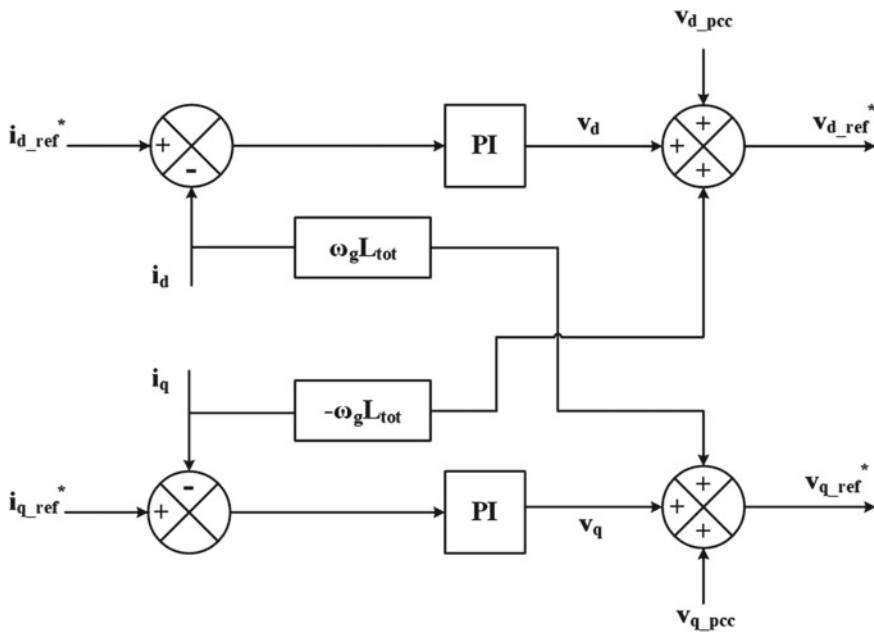


Fig. 4 Current control loops of the current mode controller

$$v_{q_inv} = v_q + \omega_g (L_{tot}) i_d + v_{q_pcc} \tag{25}$$

The v_d and v_q voltages are obtained using two PI controllers where the input to the PI controllers are the static error between the measured current at the PCC and the reference currents from the active and reactive power controller. The above relationship is shown in Eqs. (26) and (27). The terms $K_d(s)$ and $K_q(s)$ are equal to $k_{id,p} + \frac{K_{id,i}}{s}$ and $k_{iq,p} + \frac{K_{iq,i}}{s}$ respectively, where $k_{id,p}$, $K_{id,i}$, $k_{iq,p}$ and $K_{iq,i}$ are PI controller gains.

$$v_d = (i_{d_ref} - i_d)K_d(s) \tag{26}$$

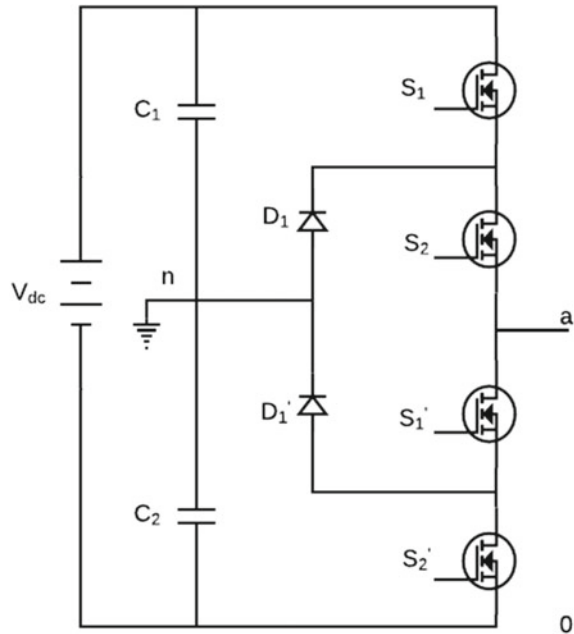
$$v_q = (i_{q_ref} - i_q)K_q(s) \tag{27}$$

The overall structure of the current controllers is shown in Fig. 4.

3.4 PWM Generation for the Three-Level NPC Inverter

The outputs of the current controller block are v_{d_ref*} and v_{q_ref*} . These are transformed into natural frame and used as sinusoidal references for pulse generation

Fig. 5 One leg of the three-level NPC inverter



using SPWM. The required PWM signals for switches of the inverter are generated by comparing reference sinusoidal signal with two-level shifted triangular signals. The frequency of the triangular signal determines the switching frequency of the PWM generation.

Schematic diagram of one leg of the inverter is depicted in Fig. 5. PWM generation for one leg of the inverter is shown in Figs. 6 and 7.

3.5 Tuning of PI Controllers

There are several methods of tuning PI controller parameters. Many PI controller tuning methods are discussed in the literature. The tuning method depends on the nature of the requirement. If the plant is complicated, that its mathematical model cannot be easily obtained, then an analytical or computational approach to design the PI controller is not possible. More experimental approaches to tuning of PI controllers should be employed [17]. Even though tuning parameters are obtained from computational methods, fine tuning of the system should be done using trial and error method. Ziegler and Nichols (Z-N) method have had a strong impact on the practice of control, and it is widely used in the industry [18]. The design criterion of Z-N method is quarter amplitude damping. Two methods of damping are presented in Z-N method [18].

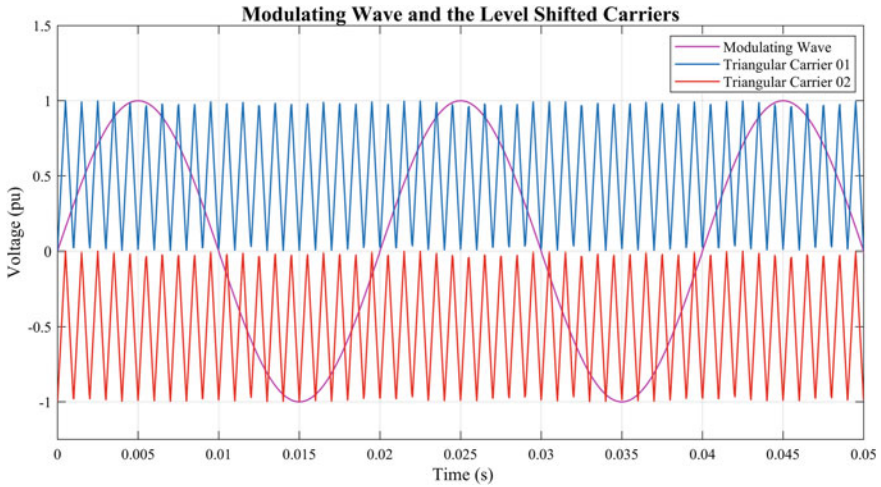


Fig. 6 Modulating signal and the level-shifted carrier waves

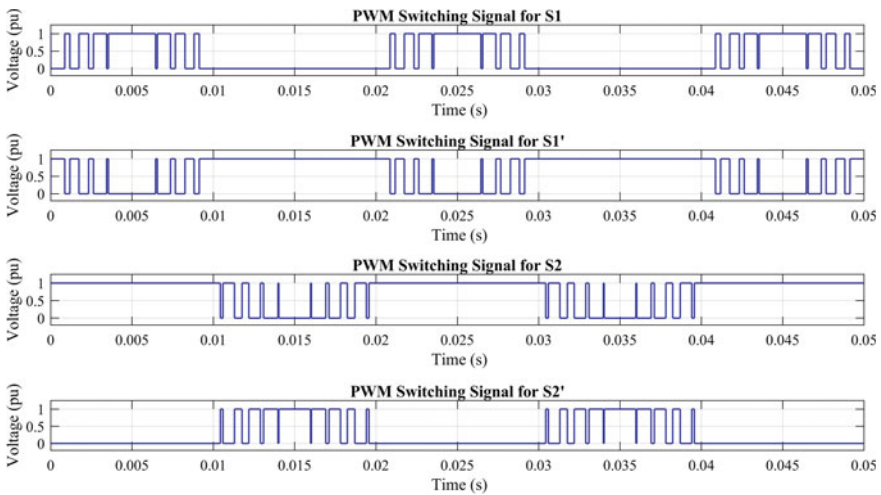


Fig. 7 PWM switching patterns for the switches of one leg of the inverter

The first method is based on experimental step responses and the latter based on the value of K_p that results in marginal stability when only proportional control action is used [17]. Several drawbacks exist in Z-N method. Lack of information to characterize process dynamics, the design criterion, quarter amplitude damping chosen by Ziegler and Nichols gives close-loop systems with poor damping and poor robustness [18]. Further modifications of the Z-N methods can give a substantially improved system performances.

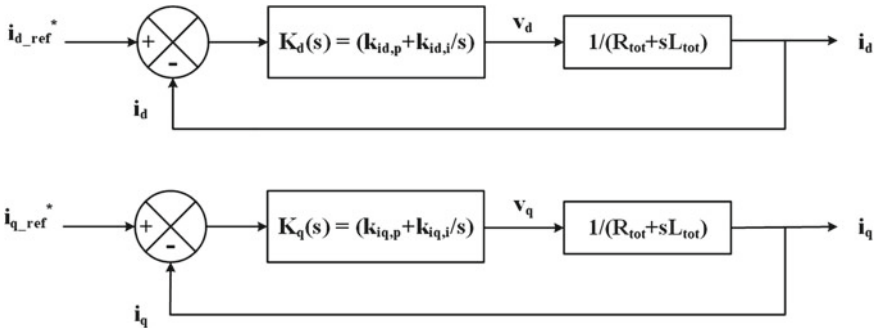


Fig. 8 Model for designing PI controllers

The initial step is identifying the model for tuning the PI controllers. The closed loop transfer functions of the model are given in Eqs. (28) and (29). The model which is used to tune PI controllers is depicted in Fig. 8.

$$\frac{i_d(s)}{i_{dref}(s)} = \frac{sk_{id,p} + k_{id,i}}{s^2L_{tot} + s(R_{tot} + k_{id,p}) + k_{id,i}} \tag{28}$$

$$\frac{i_q(s)}{i_{qref}(s)} = \frac{sk_{iq,p} + k_{iq,i}}{s^2L_{tot} + s(R_{tot} + k_{iq,p}) + k_{iq,i}} \tag{29}$$

Due to the complex nature and the dynamic behavior of the mode, for the tuning of the PI controllers, control system designer tool in MATLAB® is used. The root locus, bode plots and the step response of the plant can be obtained. These plots can be used to analyze the stability of the system. The following design criteria are set in order to create a stable system [21].

- Percent Overshoot = 40%
- Rise time < 0.1 s
- Settling time < 1 s
- Phase Margin > 30°
- Gain Margin > 20 dB.

A real zero and a integrator term are added to the root locus of the plant transfer function to implement the compensator, thereby achieving the design requirement. Compensator transfer function can be derived with the k_p and k_i obtained after tuning the controllers. The performance of the controller is then verified by giving a step response to the closed loop transfer function and observing its behavior.

4 Results and Discussion

The closed loop transfer functions of the system are given from Eqs. (28) and (29).

The system is simulated for a case of 1 kW rated NPC inverter connected to a grid of 400 V through a low-frequency transformer with a voltage ratio of 63.5 V/230 V. The simulation parameters of the system are given in Table 1.

The step response for the closed-loop transfer function is shown in Fig. 9 for the above system parameters. The response has the following criteria.

- Percent Overshoot = 29.8%
- Rise time = 0.02 s
- Settling time = 0.15 s
- Phase Margin = 51.8°
- Gain Margin = 45.8 dB.

Table 1 System parameters used in the simulation

Output power (P)	1 kW
DC link voltage (V_{DC})	300 V
Phase-to-phase RMS voltage (E_n)	110 V
Switching frequency (f_{sw})	10 kHz
Inverter-side inductance (L_i)	3.9 mH
Grid-side inductance (L_g)	115 μ H
Filter capacitance (C_f)	13.15 μ F
Damping resistance (R_d)	0.974 Ω
Proportional gain (k_p)	0.15
Integral gain (k_i)	30

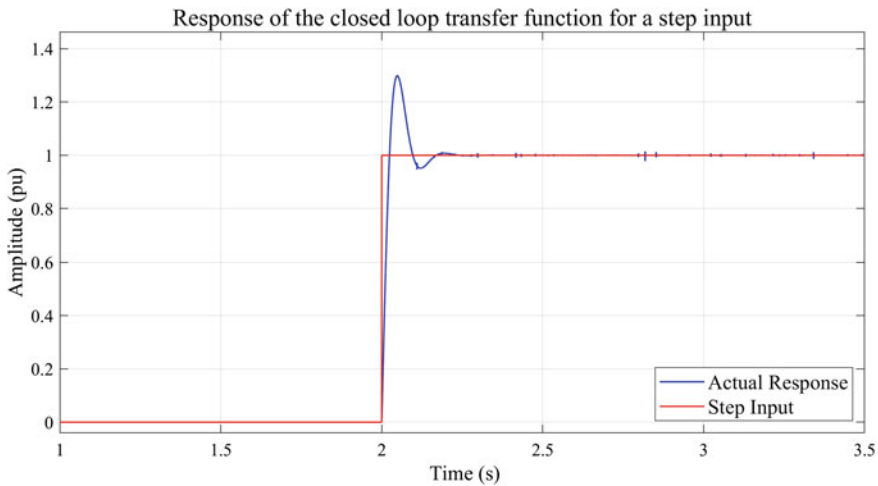


Fig. 9 Step response of closed-loop transfer function Eq. (28)

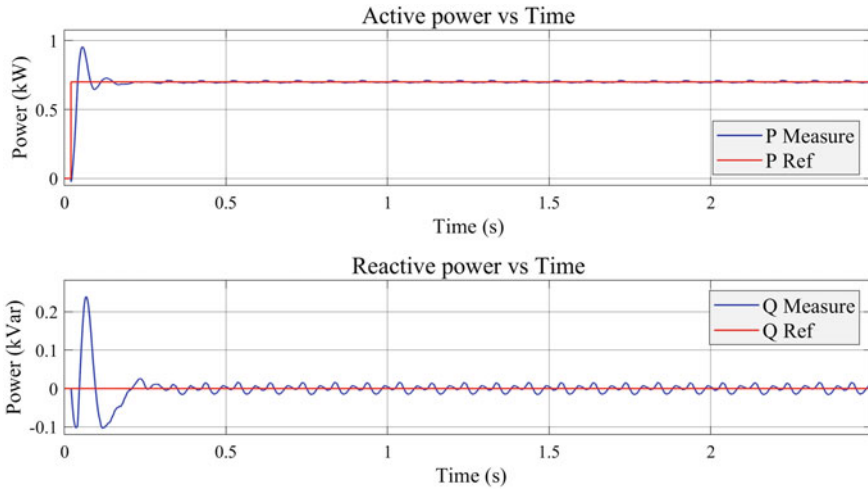


Fig. 10 Waveforms for fixed active power requirement

It can be observed that the phase margin and gain margin are both positive and phase margin is larger than the gain margin. Therefore, it can be concluded that the system has achieved closed-loop stability [17].

The simulation studies the injection of active power to the grid. Hence, the reactive power reference is made as zero. Furthermore, a harmonic analysis is done at the PCC.

4.1 Case 01: The Performance of the Controller for a Constant Active Power Requirement

The waveforms for fixed active power requirement are shown in Fig. 10.

4.2 Case 02: The Performance of the Controller for a Varying Active Power Requirement

The waveforms for varying active power requirements are shown in Fig. 11.

Figure 12 presents the variation of grid voltage and grid current of Phase A at PCC for a step change in active power from 0 to 0.7 kW.

In addition, the robustness of the method to grid voltage which is the LVRT capability is checked. Initially, the active power reference is set as 0.7 kW. When the fault occurs, the active power reference instantly decreased to 0 kW. After the fault clears, the active power reference is taken back to the original set point. Figure 13 depicts how the controllers perform under a 100% balanced voltage sag.

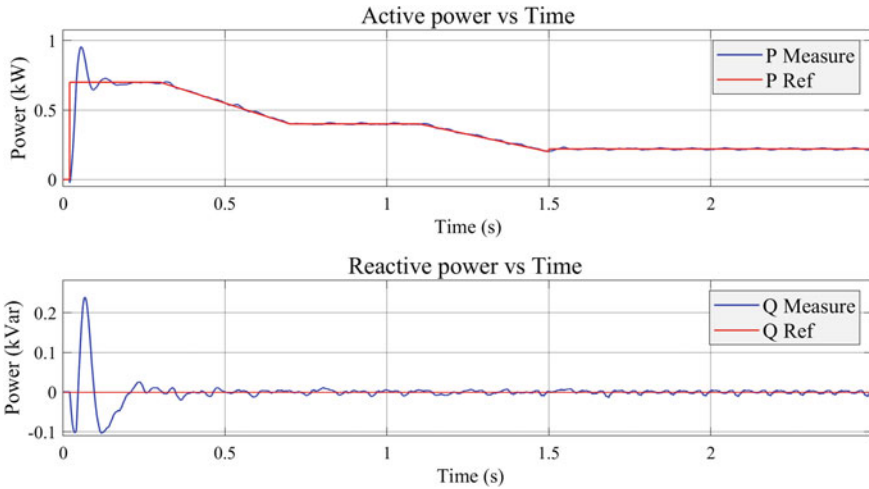


Fig. 11 Waveforms for varying active power requirement

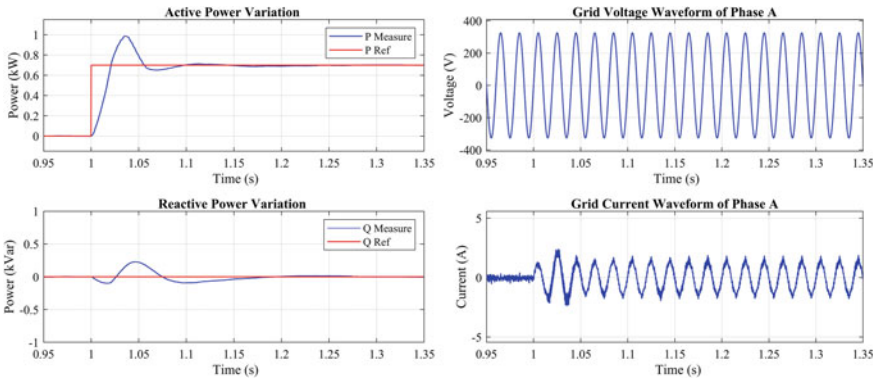


Fig. 12 Variation of grid voltage and grid current for a step change in active power

4.3 Harmonic Analysis

IEEE-519 includes the recommended harmonic voltage limits and recommended current distortion limits for systems nominally rated 120 V through 69 kV. For the simulated model, harmonic content is checked at PCC.

According to the standard, systems under 1 kV the total harmonic distortion (THD) should be below 8.0% [19]. From Fig. 14, it can be observed that the THD of voltage waveform is 5.6%. Furthermore, in order to determine the THD of current waveforms, the ratio between maximum short-circuit current at the output of the filter (I_{sc}) and the fundamental frequency component (I_L) is needed. It is found that

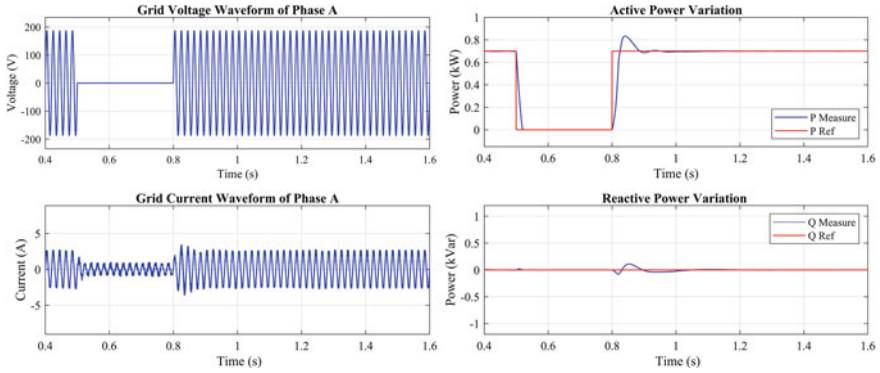


Fig. 13 LVRT performance for a 100% voltage sag

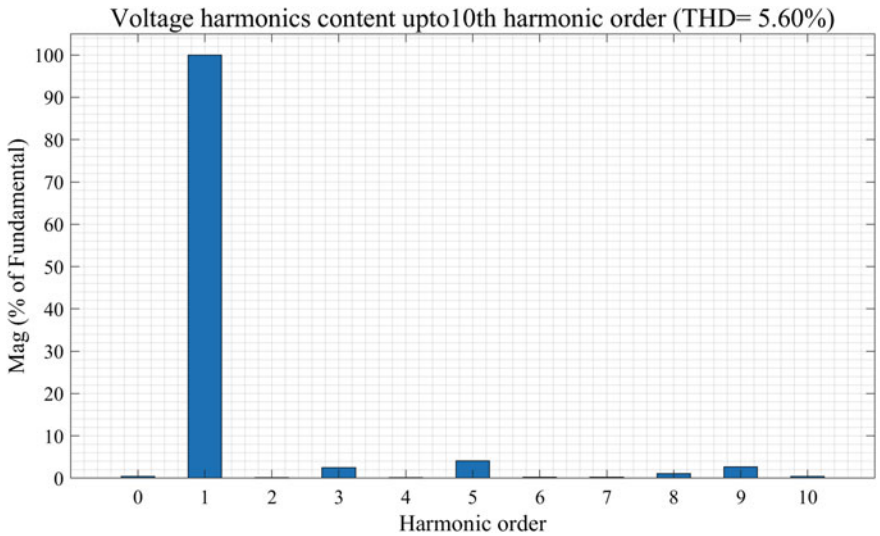


Fig. 14 Harmonic spectrum of the voltage waveform of the filter output

the I_{sc}/I_L ratio is 508.2 from calculations and lies between the range of 100 and 1000. Therefore, according to the standard, the THD of current should be less than 15% [19]. The THD of current waveform of the simulated model is 7.81% and can be observed from Fig. 15.

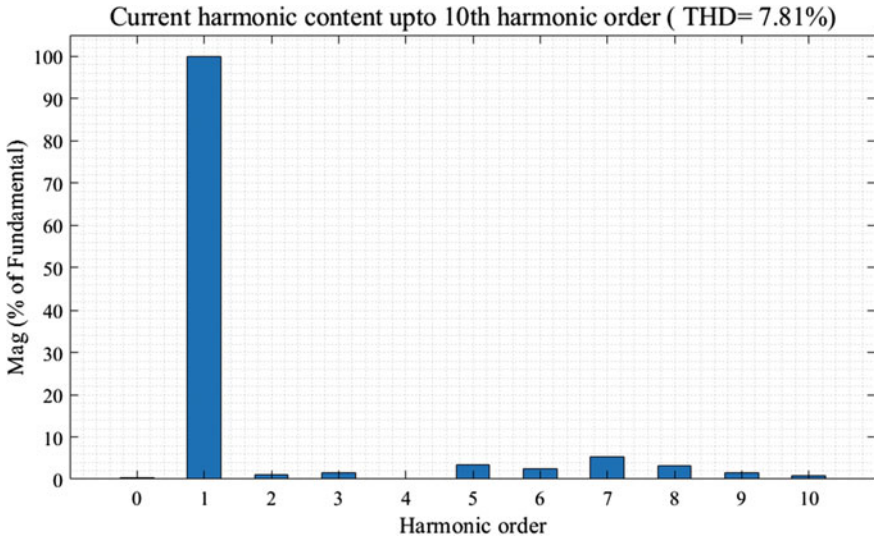


Fig. 15 Harmonic spectrum of the current waveform of the filter output

5 Conclusion

Multilevel inverters are extensively utilized as the interface between RES and AC grid lately in the industry. As the concept of microgrid is emerging, proper controlling schemes are needed for the stable between the RES and the grid. In this paper, an innovative power flow control method with a three-level NPC inverter has been discussed. In order to increase the stability of the system and to eliminate harmonics, LCL filter with passive damping is used. Two PI controllers are used for current controlling and ultimately following the active power and reactive power references. Simulation results illustrate the performance of the controller under constant active power requirement and varying active power requirement. The harmonic study presents that THD of voltage is 5.6% and THD of current is 7.81%. It can be seen that the voltage and current THD are well under IEEE harmonic guidelines. It can be concluded that with the proposed architecture, active power injection can be realized with a three-level NPC inverter integrated with an energy storage. For future work, this energy storage system with the power controller will be used combined with a PV system to supply grid power requirement according to time-based tariff system. This study is important for countries who are still moving toward renewable energy systems and also microgrids.

References

1. F. Blaabjerg, R. Teodorescu, M. Liserre, A. Timbus, Overview of control and grid synchronization for distributed power generation systems. *IEEE Trans. Ind. Electron.* **53**, 1398–1409 (2006). <https://doi.org/10.1109/tie.2006.881997>
2. K. Konara, M. Kolhe, W. Sankalpa, Grid synchronization of DC energy storage using voltage source inverter with ZCD and PLL techniques, *2015 IEEE 10th International Conference on Industrial and Information Systems (ICIIS)* (2015). <https://doi.org/10.1109/iciinfs.2015.7399055>
3. K. Konara, M. Kolhe, Charging management of grid integrated battery for overcoming the intermittency of RE sources, in *IEEE International Conference on Information and Automation for Sustainability (ICIAfS)*, vol. 2016 (2016), pp. 1–6
4. A. Timbus, M. Liserre, R. Teodorescu et al., Evaluation of current controllers for distributed power generation systems. *IEEE Trans. Power Electron.* **24**, 654–664 (2009). <https://doi.org/10.1109/tpe.2009.2012527>
5. A. Arzani, P. Arunagirinathan, G.K. Venayagamoorthy, Development of optimal PI controllers for a grid-tied photovoltaic inverter, in *IEEE Symposium Series on Computational Intelligence*, vol. 2015 (2015), pp. 1272–1279. <https://doi.org/10.1109/ssci.2015.182>
6. Y. Gui, X. Wang, F. Blåbjerg, D. Pan, Control of grid-connected voltage-source converters: the relationship between direct-power control and vector-current control. *IEEE Ind. Electron. Mag.* **13**(2), 31–40 (2019). <https://doi.org/10.1109/MIE.2019.2898012>
7. L. Campanhol, S. da Silva, A. de Oliveira, V. Bacon, Dynamic performance improvement of a grid-tied PV system using a feed-forward control loop acting on the NPC inverter currents. *IEEE Trans. Ind. Electron.* **64**(3), 2092–2101 (2017)
8. P. Piya, M. Ebrahimi, M. Karimi-Ghartemani, S. Khajehododin, Fault ride-through capability of voltage-controlled inverters. *IEEE Trans. Ind. Electron.* **65**(10), 7933–7943 (2018)
9. J. Leon, S. Vazquez, L. Franquelo, Multilevel converters: control and modulation techniques for their operation and industrial applications. *Proc. IEEE* **105**, 2066–2081 (2017). <https://doi.org/10.1109/jproc.2017.2726583>
10. A. Nabae, I. Takahashi, H. Akagi, A new neutral-point-clamped PWM inverter. *IEEE Trans. Ind. Appl.* **IA-17**, 518–523 (1981). <https://doi.org/10.1109/tia.1981.4503992>
11. C. Bao, X. Ruan, X. Wang et al., Step-by-step controller design for LCL-type grid-connected inverter with capacitor-current-feedback active-damping. *IEEE Trans. Power Electron.* **29**, 1239–1253 (2014). <https://doi.org/10.1109/tpe.2013.2262378>
12. E. Kantar, S.N. Usluer, A.M. Hava, Design and performance analysis of a grid connected PWM-VSI system, in *2013 8th International Conference on Electrical and Electronics Engineering (ELECO)* (2013), pp. 157–161. <https://doi.org/10.1109/eleco.2013.6713823>
13. B.-G. Cho, S.-K. Sul, LCL filter design for grid-connected voltage-source converters in high power systems, in *IEEE Energy Conversion Congress and Exposition (ECCE)*, vol. 2012 (2012), pp. 1548–1555. <https://doi.org/10.1109/ecce.2012.6342629>
14. M. Dursun, M.K. Dosoglu, LCL filter design for grid connected three-phase inverter, in *2018 2nd International Symposium on Multidisciplinary Studies and Innovative Technologies (ISM-SIT)* (2018), pp. 1–4. <https://doi.org/10.1109/ismsit.2018.8567054>
15. H. Zheng, X. Chang, X. Wang, Study on the control strategy of grid connected and disconnected of microgrid with photovoltaic and storages, in *International Conference on Materials for Renewable Energy and Environment*, vol. 2013 (2013), pp. 115–118. <https://doi.org/10.1109/icmree.2013.6893627>
16. J.-Y. Lee, Y.-P. Cho, H.-S. Kim, J.-H. Jung, Design methodology of passive damped LCL filter using current controller for grid-connected three-phase voltage-source inverters. *J. Power Electron.* **18**, 1178–1189 (2018). <https://doi.org/10.6113/JPE.2018.18.4.1178>
17. K. Ogata, Y. Yang, *Modern Control Engineering* (Prentice Hall, UpperSaddle River, NJ, 2010)
18. H. Wu, W. Su, Z. Liu, PID controllers: design and tuning methods, in *2014 9th IEEE Conference on Industrial Electronics and Applications* (2014), pp. 808–813. <https://doi.org/10.1109/iciea.2014.6931273>

19. IEEE Standards Association et al., *519-2014-IEEE Recommended Practices and Requirements for Harmonic Control in Electric Power Systems* (IEEE, New York, 2014), p. 2014
20. A. Abdalrahman, A. Zekry, A. Alshazly, Simulation and implementation of grid-connected inverters. *Int. J. Comput. Appl.* **60**, 41–49 (2012). <https://doi.org/10.5120/9683-4117>
21. K. László et al., *Control Engineering: MATLAB Exercises* (Springer, 2019)

Economic Load Dispatch in Power System by Using Elephant Herding Optimization Technique



Leena Daniel, Krishna Teerth Chaturvedi, and Mohan Lal Kolhe

Abstract The goal of economic load dispatch (ELD) is to cut the generator's fuel consumption rate by which reducing the operating cost of the power system by defining the output power of each generator with consideration of different constraints to meet the load demands of the connected network. Economic load dispatch is a most communal problem that comes upon in power system studies. ELD is always formulated as nonlinear optimization problem with various constraints. This work proposes a metaheuristic optimization method for the solution of ELD-related issues. The name of this method is elephant herding optimization (EHO). This technique is primarily stimulated by the navigation nature of elephant cluster. During the journey of any elephant's life, it belongs to many diverse fraternities. The group of elephants is always following their leader, and usually, elder female elephant leads the group. When male elephants mature, they isolate from origin cluster and live separately. These are the two different behaviors and can be exhibited in two operators, i.e., clan updating operator and separating operator. Each clan of the elephants is updated and modified by their current position and matriarch by clan updating operator. To establish its effectiveness, EHO is applied on 13-unit test system and compared with GSA and CEP. The outcomes display that the EHO gives better results as compared to other metaheuristic algorithms.

Keywords Economic load dispatch (ELD) · Elephant herding optimization (EHO) · Valve point loading effect

L. Daniel (✉) · K. T. Chaturvedi
UIT, RGPV, Bhopal, M.P., India

K. T. Chaturvedi
e-mail: kteerth@rgtu.net

M. L. Kolhe
Faculty of Engineering and Science, University of Agder, Kristiansand, Norway
e-mail: Mohan.L.Kolhe@uia.no

1 Introduction

The daily arising struggle and actual-life hitches inspire the investigators to hunt and advance beneficial approaches for discovery and improving the solutions of composite and optimization difficulties [1]. Optimization process is a systematic mathematical approach to discover the finest policy for solution of any problem among numerous probable solutions under given constraints. It can also be explained that any mathematical equation is optimized when the variable values are finding out, so the value of that equation becomes maximum or minimum. Nowadays, optimization is required in every fields like engineering, economics, science, medical, chemistry, and physics [2]. In each field, only the aim of optimization is to design a product or process by available resources, which should be economic and gives optimal decision making. Several conventional methods have been implemented for the solution of economic load dispatch difficulties [3]. Many linear and nonlinear problems can be resolved by traditional scientific program design created on the basis of optimization methods such as gradient method, dynamic programming method, and lambda iteration method. All these methods were used in early days, and they are simple and effective [4]. However, these methods need continuously differentiable objective functions which puts a restriction on problems to be solved. The nature of these methods can be oscillatory for the systems consisting of several generators which result in longer computation time. Last few years have witnessed the blooming of numerous non-conventional practices based on soft computational techniques for resolving the ELD problems. Owing to the presence of different ELD problems like prohibited operating zones (POZ), valve point loading effects, and ramp rate limits (RRL), the cost curves for contemporary generating units embrace various interruptions and interventions which translate the ELD difficulties into a nonlinear, discontinuous, and nonconvex problem. The conservative approaches are suitable for linear statements but not competent to solve practical nonconvex ELD problem. Due to the ability of parallel random search and independence of convexity assumptions, techniques for instance evolutionary programming, tabu search, artificial intelligence, bee colony optimization, particle swarm optimization (PSO), artificial neural network, and genetic algorithm are very efficient in handling nonlinear ELD problems with slight calculation period. These search approaches are not all the time assure global finest results although are often realizing a speedy and close to global optimal solution.

Day-by-day increasing demand of electrical energy motivates the electrical engineers to provide the electricity on the best possible low cost [5].

In this paper, elephant herding optimization (EHO) is used to run optimization process for 13-unit system at different load demands. Cost curves are compared with the other metaheuristic techniques for the same load.

2 Economic Load Dispatch (ELD)

A high price of fossil fuel still plays a major role for variation in the cost of electrical generation, and it proportionally replicated in the electrical energy consumption bill of the consumer [6]. ELD can be defined as sharing of demand to the connected generating units in the most fiscal or lucrative mode, whereas incessantly complying with the actual limitations of the interconnected network. The real ELD difficulties are not convex due to generator nonlinear characteristics like POZ, RRL, and valve point loading effects. The presented work is done with valve point loading effect for optimization of economic load [7].

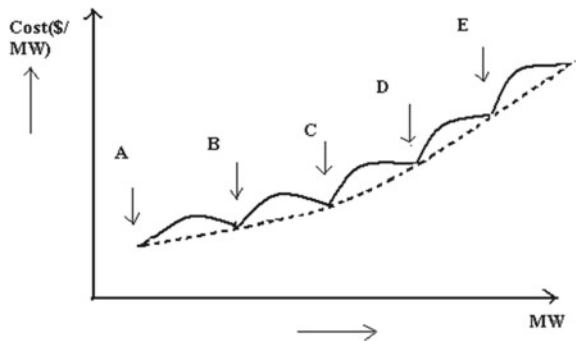
3 Valve Point Loading Effect

There are many valves are associated with generation process, and these valves are operated synchronously as per the load demand. This on/off process of valves introduces ripples as shown in Fig. 1. Due to these throttling losses in the heat characteristic of generator, the objective function is nonconvex and intermittent with several minima [8]. A sinusoidal function is included to equation for introducing the valve point effect in the main objective function. After inclusion of sinusoidal function, the cost function can be given in equation:

$$F_j(P_j) = a_j P_j^2 + b_j P_j + c_j + |e_j \times \sin(f_j \times (P_j^{\min} - P_j))|$$

Here cost coefficients of fuel for the j th unit are represented by a_j , b_j , and c_j . The cost coefficients of fuel for j th unit with valve point effects are given by e_j and f_j .

Fig. 1 Effect on generator with valve point loading



4 Problem Formulation

The modern power generation system may consist of multiple generation units, and it is essential to minimize the overall operating cost of all load schedules. The entire cost function is specified by Eq. (1), formulated as objective function, which needs to be minimized [7]

$$F(P_g) = \sum_{i=1}^n (a_i P_{gi}^2 + b_i P_{gi} + c_i) \quad (1)$$

Below-mentioned constraints are considered to minimize the cost function.

(1) **Power balance equation**

Overall power generated by all generating units should be equal to the total losses and entire power demand, it can be formulated by Eq. (2).

$$\sum_{i=1}^n P_{gi} - P_D - P_L = 0 \quad (2)$$

where output power of unit i is given by P_{gi} (MW), total interconnected network loss of the system is given P_L (MW), and all load demand of the system is given by P_D (MW), N gives total connected online generating units.

(2) **Generator limit constraint**

For smooth conduction of entire system with all constraints, all generators should be operated within upper and lower bounds. These operating limits can be given by Eq. (3) [9]

$$P_{gi \min} \leq P_{gi} \leq P_{gi \max} \quad i = 1, 2, \dots, N_g \quad (3)$$

5 Elephant's Herding Behavior

Elephants are unique and the biggest creatures on the earth [10]. The behavior of elephant is very complex, although elephants are social animals. Elephants usually move in large groups which consist of many clans under the command of matriarch [11]. An elephant's fraternity contains a feminine with her calves or other correlated females. Female elephants choose to always be with family groups, but paternal or male elephants be inclined to be in quarantine, and hence as they grow up, they quit their family unit. The driving or herding nature of the elephants can be derived into two operators, which are used as objective function for different optimization processes [12].

6 Elephant Herding Optimization

To solve the different optimization challenges, the herding nature of the elephants is used, but there are few rules preferred which are as follows [13]

- (1) Elephants live in small groups or clans, here it is considered that in a clan a static number of elephants are grouped [14].
- (2) A specific number of elephants (male) moved away from their own family clan and stay in isolation. After separation, each generation of male elephants live at very long distance from their origin group [15].
- (3) Each clan of elephant moves under the supervision and guidance of matriarch [16].

Based on the above rule, two operators can be defined

- (i) Clan updating operator
- (ii) Separating operator.

(i) Clan updating operator

Initially, male elephant stays with their family clan under the surveillance of a matriarch. So, in a clan C_i , every elephant location is categorized by matriarch C_i .

In a clan C_i , the j th elephant can be updated as new C_{ij} which is given by Eq. (4)

$$X_{\text{new,ci,j}} = X_{\text{ci,j}} + \alpha \times (X_{\text{best,ci}} - X_{\text{ci,j}}) \times r \quad (4)$$

Here old position of elephant in clan C_i is given by $X_{\text{ci,j}}$, and new updated position of elephant is given by $X_{\text{new,ci,j}}$. The effect of matriarch C_i on $X_{\text{ci,j}}$ is stated by scale factor $\alpha \in [0, 1]$. In clan C_i , fittest elephant is given by $X_{\text{best,ci}}$. r lies in the range of $[0, 1]$.

For the fittest elephant, updating can be done by Eq. (5)

$$X_{\text{new,ci,j}} = \beta \times X_{\text{center,ci}} \quad (5)$$

$\beta \in [0, 1]$, which find out the influence of $X_{\text{center,ci}}$ on $X_{\text{new,ci,j}}$.

Center of clan C_i is represented by $X_{\text{center,ci}}$ for the range of d th dimension, given by Eq. (6)

$$X_{\text{center,ci,d}} = \frac{1}{n_{\text{ci}}} \sum_{j=1}^{n_{\text{ci}}} X_{\text{ci,j,d}} \quad (6)$$

Here D is total dimension, and d th is current dimension ($1 \leq d \leq D$). n_{ci} gives the number of elephants in clan C_i . $X_{\text{ci,j,d}}$ is d th dimension of the specific elephant $X_{\text{ci,j}}$.

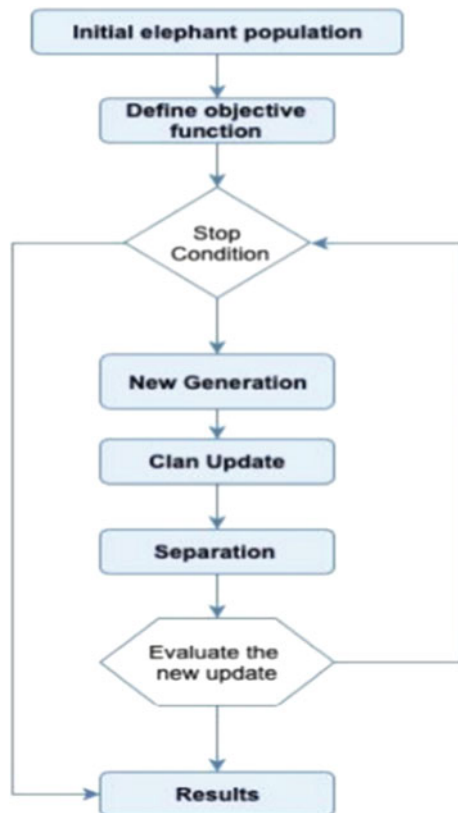
(ii) **Separating operator**

As earlier mentioned, male elephants quit their origin clan and stay away, when they step to adolescence [17]. This method of separation is exhibited by separating operator at the time of optimization process [18]. It enhances the hunt capability of elephant herding optimization technique. To implement the separating operator for individual generation, let assume worst fitness of different elephant in a clan, which can be represented by Eq. (7).

$$x_{\text{worst,ci}} = x_{\text{min}} + (x_{\text{max}} - x_{\text{min}} + 1) \times \text{rand} \tag{7}$$

rand is in the range of [0, 1]. x_{max} is upper limit and x_{min} is lower limit of the elephant. In clan C_i , $x_{\text{worst,ci}}$ gives the worst elephant. Figure 2 shows the steps involved in the EHO.

Fig. 2 Flowchart for EHO



7 Results and Discussions

As EHO is implemented to resolve the ELD problem [19], different load demands are being taken into consideration. It is applied on 13-generating unit test system. 5000 iterations are performed for each demand, and population considered in each case is 100. Three generating unit test systems are given in Tables 1 and 2 which show

Table 1 Thirteen generating units

Unit	P^{\min}	P^{\max}	a	b	c	e	f
1	0	680	550	8.10	0.00028	300	0.035
2	0	360	309	8.10	0.00056	200	0.042
3	0	360	307	8.10	0.00056	200	0.042
4	60	180	240	7.74	0.00324	150	0.063
5	60	180	240	7.74	0.00324	150	0.063
6	60	180	240	7.74	0.00324	150	0.063
7	180	150	240	7.74	0.00324	150	0.063
8	60	180	240	7.74	0.00324	150	0.063
9	60	180	240	7.74	0.00324	150	0.063
10	40	120	126	8.6	0.00284	100	0.084
11	40	120	126	8.6	0.00284	100	0.084
12	55	120	126	8.6	0.00284	100	0.084
13	55	120	126	8.6	0.00284	100	0.084

Table 2 Economic load dispatch 13 units

Power demand	1800	2000	2200	2400	2600
P1	42.92	0	0.0015	72.282	55
P2	66.60	60	91.02	91.56	60.13
P3	91.54	60.03	92.35	92.82	104.62
P4	92.80	93.37	110.06	107.14	116.05
P5	107.31	93.60	113.51	109.82	116.59
P6	111.79	108.92	114.37	110.08	159.41
P7	111.98	110.13	116.04	114.80	159.43
P8	112.04	112.03	158.22	154.93	160.06
P9	114.25	114.80	158.35	159.80	160.22
P10	159.18	160.83	159.54	161.15	160.70
P11	220.17	161.07	160.60	298.63	359.55
P12	270.15	298.118	300.12	299.77	359.88
P13	299.37	627.08	627.74	627.49	628.46
Cost (\$)	18,336.22	19,928.94	21,649.69	23,277.84	25,218.64

Table 3 Comparison with other techniques for $P_D = 1800$ MW (13-unit system)

Technique	Cost (\$)
GSA [20]	18,910.31
CEP [21]	18,404.04
EHO	18,336.227

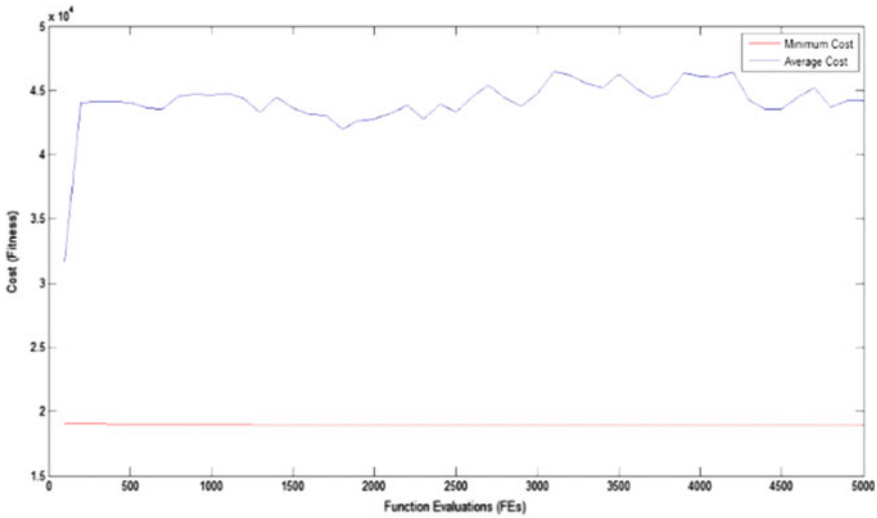


Fig. 3 Function evaluation for 1800 MW

the optimal fuel cost at different loads for 13-unit generating model. GSA and CEP are compared with EHO in Table 3. Figures 3, 4, 5, 6, 7, and 8 show the simulation curves of function evaluation and generation curves for different loads.

8 Conclusion

This work presented the results of ELD problem with EHO technique. All outcomes of 13 units for different load demands are presented, and their economic loading is also given with their costs. For programming the EHO algorithm, MATLAB (2013a) software is used. EHO is a modest, competent, consistent, and specific technique for resolving the ELD problems in interconnected modern power system. Moreover, a comparison of results of EHO compared to other optimization algorithm is presented based on previous work results. We conclude that EHO has a good characteristic as optimization algorithm, and it would give better performance for solving complex optimization problems.

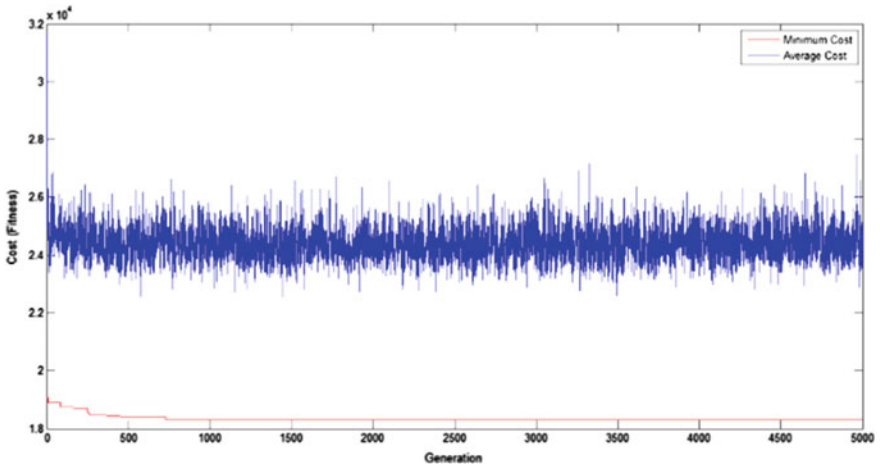


Fig. 4 Generation curve for 1800 MW

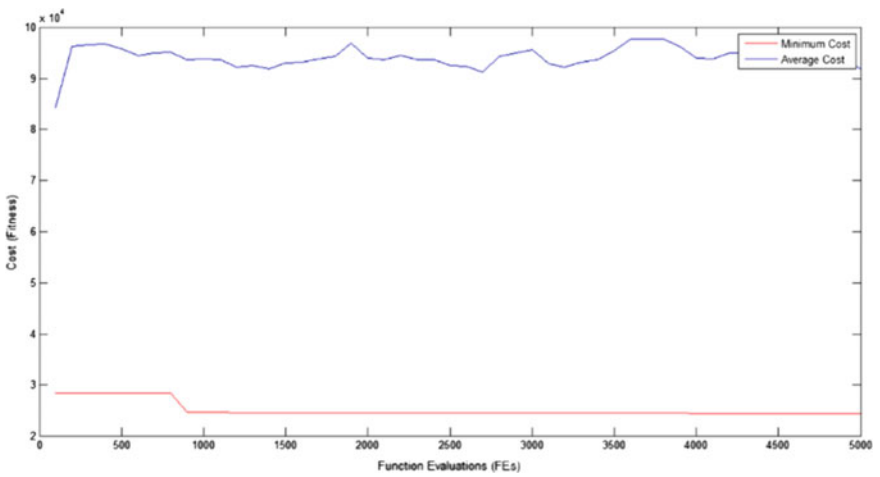


Fig. 5 Function evaluation 2400 MW

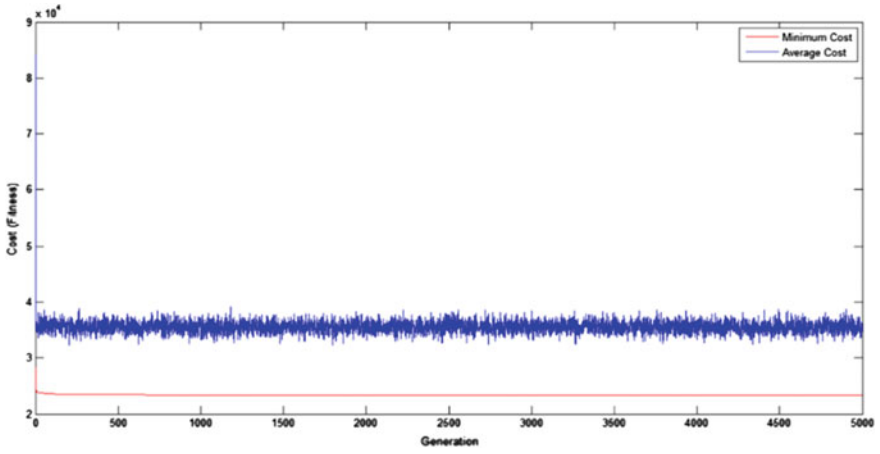


Fig. 6 Generation curve for 2400 MW

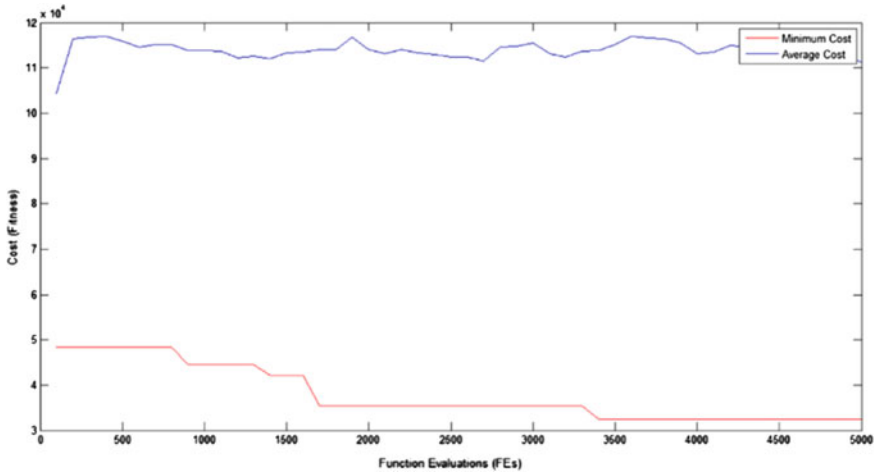


Fig. 7 Function evaluation for 2600 MW

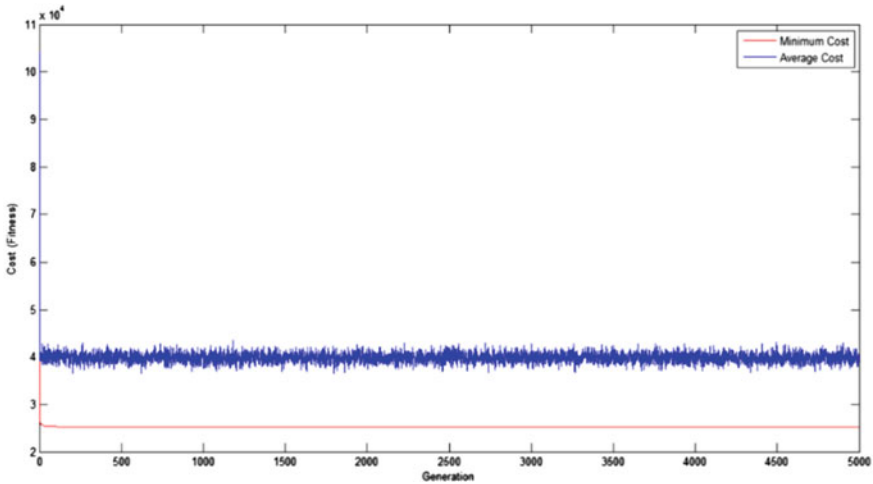


Fig. 8 Generation curve for 2600 MW

References

1. K.T. Chaturvedi, M. Pandit, L. Srivastava, Self-organizing hierarchical particle swarm optimization for nonconvex economic dispatch. *IEEE Trans. Power Syst.* **23**(3), 1079–1087 (2008)
2. S. Almufti, R. Marqas, V. Saeed, Taxonomy of bio-inspired optimization algorithms. *J. Adv. Comput. Sci. Technol.* (2019)
3. L. Daniel, K.T. Chaturvedi, Economic load dispatch using ant lion optimization. *Int. J. Eng. Trends Technol.* **67**(4), 81–84 (2019)
4. S. Kosalairaman, T. Elango, K. Bharathi, Economic load dispatch with valve point effect using quantum inspired particle swarm optimization. *J. Comput. Theoret. Nanosci.* **16**, 2307–2310 (2019)
5. M.A. Elhosseini, R.A. El Sehiemy, Y.I. Rashwan, X.Z. Gao, On the performance improvement of elephant herding optimization algorithm. *Knowl.-Based Syst.* **166**, 58–70 (2019). ISSN 0950-7051
6. V. Hosseinneshad, E. Babaei, Economic load dispatch using θ -PSO. *Int. J. Electr. Power Energy Syst.* **49**, 160–169 (2013). ISSN 0142-0615
7. P. Veeramanikandan, S. Selvaperumal, A fuzzy-elephant herding optimization technique for maximum power point tracking in the hybrid wind-solar system. *Int. Trans. Electr. Energy Syst.* (2020)
8. L. Daniel, K.T. Chaturvedi, M.L. Kolhe, Dynamic economic load dispatch using Levenberg Marquardt algorithm. *Energy Procedia* **144**, 95–103 (2018)
9. L. Daniel, K.T. Chaturvedi, A crazy particle swarm optimization with time varying acceleration coefficients for economic load dispatch. *Int. J. Eng. Adv. Technol. (IJEAT)* **9**(2) (2019). ISSN: 2249 – 8958
10. B. Bentouati, C. Saliha, R. El-Sehiemy, G.-G. Wang, Elephant herding optimization for solving non-convex optimal power flow problem. *J. Electr. Electron. Eng.* **10**, 31–40 (2017)
11. S. Parashar, A. Swarnkar, K.R. Niazi, N. Gupta, Modified elephant herding optimization for economic generation co-ordination of DERs and BESS in grid connected micro-grid. *J. Eng.* **2017**(13), 1969–1973 (2017)

12. N.K. Meena, S. Parashar, A. Swarnkar, N. Gupta, K.R. Niazi, Improved elephant herding optimization for multiobjective DER accommodation in distribution systems. *IEEE Trans. Ind. Inf.* **14**(3), 1029–1039 (2018)
13. W. Li, G.-G. Wang, A.H. Alavi, Learning-based elephant herding optimization algorithm for solving numerical optimization problems. *Knowl.-Based Syst.* (2020)
14. A.A.K. Ismaeel, I.A. Elshaarawy, E.H. Houssein, F.H. Ismail, A.E. Hassanien, Enhanced elephant herding optimization for global optimization. *IEEE Access* **7**, 34738–34752 (2019)
15. S.M. Almufti, R.R. Asaad, B.W. Salim, Review on elephant herding optimization algorithm performance in solving optimization problems. *Int. J. Eng. Technol.* **7**(4), 6109–6114 (2019)
16. R. Vijay, M. Abhilash, Elephant herding optimization for optimum allocation of electrical distributed generation on distributed power networks. *Asian J. Electr. Sci.* **7**, 70–76 (2018)
17. C. Cahig, J.J. Villanueva, R. Bersano, M. Pacis, Optimal virtual power plant scheduling using elephant herding optimization, in *2018 IEEE 10th International Conference on Humanoid, Nanotechnology, Information Technology, Communication and Control, Environment and Management (HNICEM)*, Baguio City, Philippines (2018), pp. 1–6
18. R. Vijay, Optimal allocation of electric power distributed generation on distributed network using elephant herding optimization technique. *CVR J. Sci. Technol.* **15**, 73–79 (2018). ISSN 2277-3916
19. J. Li, L. Guo, Y. Li, C. Liu, Enhancing elephant herding optimization with novel individual updating strategies for large-scale optimization problems. *Mathematics* **7**(5), 395 (2019)
20. S.M.A. Bulbul, P.K. Roy, Quasi-oppositional gravitational search algorithm applied to complex economic load dispatch problem, in *2014 1st International Conference on Non-Conventional Energy (ICONCE 2014)*, Kalyani (2014), pp. 308–313
21. N. Sinha, R. Chakrabarti, P.K. Chattopadhyay, Evolutionary programming techniques for economic load dispatch. *IEEE Trans. Evol. Comput.* **7**(1), 83–94 (2003)

Role of Subsidies for PV Solar Installations in India: A Cost–Benefit Analysis



Pooja Sharma, Mohan Lal Kolhe, Stina Torjesen, and Arvind Sharma

Abstract The paper highlights the role of subsidies in the PV solar installments both from the lenders and from the receiver’s perspective, evaluating the existing financial incentives contributing to the adoption of PV solar technology. It evaluates the costs and benefits accumulated by the installation of grid-connected PV solar panel of size 2.5 and 10 kW using the method of cost–benefit analysis and net present value. The paper observes a significant role of subsidies in realizing the benefits in case of PV solar installations. The results of cost–benefit analysis reveal that the internal rate of return is greater in case of subsidy than without subsidy indicating the role of subsidies in incentivizing the investment in PV solar systems. An internal rate of return is 13% for smaller plant and 19.94% for larger plant with subsidy. However, the slow growth in investment observed in past years reflects the vulnerability of the PV solar system on the financial structure. The PV solar costs that are highly vulnerable to technological innovations, and the subsidies in such cases are bound to accumulate financial liabilities for government in terms of opportunity cost foregone by not investing in new technology. Moreover, the reduction in the costs of PV solar technology is contributing in shorten the gestation period and achieving break even hinders investors in making investment decisions. The present situation of PV solar development in India needs not only a periodic assessment process to tackle the issue

P. Sharma (✉)

Department of Economics, Daulat Ram College, University of Delhi, New Delhi, India

M. L. Kolhe · A. Sharma

Faculty of Engineering and Science, University of Agder, PO Box 422, 4604 Kristiansand, Norway

e-mail: mohan.l.kolhe@uia.no

A. Sharma

e-mail: arvind.sharma@uia.no

S. Torjesen

School of Business and Law, University of Agder, PO Box 422, 4604 Kristiansand, Norway

e-mail: stina.torjesen@uia.no

of rapid innovation in technology but also relevant policies and procedures promoting buyback options to integrate upgradation of technology.

Keywords PV solar installations · Cost–benefit analysis · Financial liabilities · Subsidies · Buyback options

1 Introduction

Climate change has placed itself as an epitome of all challenges faced by the world in present times. A grid-connected solar PV system has several benefits such as it not only reduces electricity consumption from the grid but also tends to feed excess power to the grid. As a result, the Ministry of New and Renewable Energy (India) has undertaken ambitious targets under the National Solar Mission [1]. Increase in energy demand for a growing economy like India coupled with clean and sustainable energy use becomes a challenge. However, India is still heavily dependent on fossil fuels for energy generation. To visualize a clean and sustainable energy, source option becomes an immense need of the hour. India is endowed with rich solar radiation, and it falls within the sunny geographical locations in the world. Many geographical locations within India receive three hundred days of sunshine a year [2].

India obtains a substantial quantity of solar energy that has the potential to produce more than 500,000 TWh per year of electricity energy, with 10% PV module's conversion efficiency [3]. In this regard, the Government of India has also updated the PV installation target from 20 to 100 GW by 2022 through Jawaharlal Nehru National Solar Mission [3]. PV systems are mainly installed on rooftops of commercial, institutional, industrial, and residential buildings and as grid-connected rooftop PV system [4]. The successful deployment of PV system requires understanding and expertise of operational performance assessment under variable climate conditions [5]. The rooftop PV solar reduces land requirement and transmission and distribution losses, and conversion losses are also dissolved at the point of generation. For the consumers, it reduces dependency on grid power and diesel generators and provides long-term reliable energy source, while for the commercial complexes, the roof top PV generates maximum energy during the peak usage time.

Financial instruments or incentives play a critical role in successful adaptability of solar technology. Cash incentives such as rebates and grants experience the rapid deployment of PV solar technology along with the state renewable energy portfolio standards [6]. Solangi et al. [7] and Hsu [8] conclude that feed-in-tariffs, renewable portfolio standards and incentives are most beneficial in implementing renewable energy deployment at a large scale. There has been a rapidly declining trend in the cost of solar PV technology since 2010, while the adoption is more skewed toward wealthy and heavy electricity consuming households [9] and large-scale solar project in Pakistan can feed substantial energy to the grid [10]. Kolhe et al. [11] assessed a hybrid system in comparison to grid-connected system and concluded that the hybrid

system was found to be more economically viable irrespective of off-grid or grid-connected operation. While Liu et al. [12] as well as Lang et al. [13] analyzed the hybrid system, but, however, failed to consider the effect of future grid connections as well as grid electricity tariffs on their techno-economic operational performance. Kolhe et al. [14] asserts the viability of PV system as compared to conventional diesel-powered system. Kolhe et al. [15] concluded that the cost of PV module, investment rate, PV module efficiency, and battery efficiency would have significant impact on energy generation, price, and payback period with PV integration. Sharma et al. [16] concluded that during the appropriate monthly grid power supply limits the battery storage with the PV system has been functioning much better by enhancing battery participation (battery energy throughput) compared to the other reported scenarios.

Jeon et al. [17] and Frisari and Stadelmann [18] proposed a method of optimizing financial subsidies along with public research and development to reduce subsidy. Decision makers, investors, and advisory services play a critical role in witnessing technological shifts in the industry [19]. The techno-economic viability of PV installation projects is growing as the installation costs of PV system continue to drop while the grid tariff continues to rise [20]. Martin and Rice [21] critically analyze the feed-in tariff policy, highlighting lessons for policymakers.

Rooftop PV solar installation is a public utility investment which is inherently based on the financial support extended by several other sources. Therefore, it is imperative to examine the vulnerability of the deployment of rooftop PV solar installations on the sources of finance, examining the challenges and shortcomings. The study examines the financial structure for the deployment of PV solar rooftop installations in India. The study evaluates and compares the rooftop PV solar installations of the threshold size of 2.5 and 10 kW with and without subsidy. To evaluate the economic feasibility of installing the rooftop PV solar projects, the study deploys cost–benefit approach, while to examine the technical feasibility, the paper deploys the methodology of net present value (NPV) and internal rate of return (IRR).

The paper is organized in the following sections. Apart from Sect. 1, which is Introduction, Sect. 2 describes the methodologies deployed in the study, mainly the cost–benefit approach, net present value and internal rate of return, and provides an account of various models and variety of combinations of policies existing in India, while Sect. 3 describes the financial structure or regime for rooftop PV solar deployment in India. Section 4 presents the results of cost–benefit and net present value analysis, and gives a brief account of discussions based on results. Finally, Sect. 5 concludes the study by providing relevant policy recommendations.

2 Methodology

The study deploys two types of approaches, cost–benefit analysis and net present value. The cost–benefit approach involves the computation of costs and benefits in the installation of PV solar. The first step is to generate the total cost that is required that incorporates cost of panel, battery, inverter, and controller, while benefits are in the

form of reduced electricity bill for 25 years (lifetime of rooftop solar) environmental benefits are in the form of reduced carbon-di-oxide emissions. The steps involved in cost–benefit analysis have been compiled in Appendix.

Net present value (NPV) is the return the solar plant will make accounting for the time value of money. It accounts for opportunity cost, inflation, and risk to evaluate the overall value of the project in today's time. Net present value is the present value of the cash inflow minus the present value of cash outflow. It is the absolute value gained or lost on a project. NPV compares the value of a currency today to the value of that same currency in the future, taking inflation into account.

A positive value of NPV indicates that the project is profitable over a period considered, while a negative value is an indicator that it is not worthwhile to invest in the project concerned. Lohmann and Baksh [22] investigated the effects of errors in risk assessment and decision strategy to reduce the exposure to the risk of the capital invested by deploying the measures such as net present value, internal rate of return, and payback period.

Present value (PV) = Cash flow n years in the future * Discounted present value factor.

Let cash flow n years in future be F_n ,

Discount rate = d , discounted present value factor: $1/(1 + d)^n$.

Present value (PV): $F_n * 1/(1 + d)^n$.

Total present value: $\sum_n [F_n * 1/(1 + d)^n]$.

2.1 Cash Flow Calculations

The amount of electricity generated over the year:

Electricity generated (kWh) = Installed capacity (kWp) * Capacity utilization factor (%) * 8760 (h) where installed capacity is the peak installed capacity and 8760 is the number of hours in a year. Cash flows are both positive and negative. Negative cash flows are upfront capital costs and later as operation and maintenance cost throughout the lifetime of the plant. The cash flows that are positive are given by

Annual revenue (Rs.) = Electricity generated in a year (kWh) * applicable electricity tariff (Rs./kWh).

In case of third-party model, the operational cash flow is calculated as:

Operational annual cash flow = Annual revenue – Annual expenses due to operation and maintenance. The third-party model involves equity and debt. The annual amortization for servicing debt will be computed as:

$$A = P [1 + r/n]^n$$

P : the amount of loan

r : annual rate of interest

n : number of installments.

Earnings before interest and taxes = (Operational cash flow) – (Depreciation tax)
= Corporate tax at 34% on (earnings before interest and taxes – interest)

Free cash flows = operational cash flow – interest – tax amortization.

Total earnings = Free cash flows + tax benefits due to AD.

Internal rate of return is that rate of return that brings the total net present value NPV to zero. For the cash flow calculations, the following types of costs are considered.

Energy generation cost of PV system

For calculating the energy generation cost, PV modules and inverter are considered the part of PV system. The battery’s cost is not considered in the calculations as battery is separate energy source. The energy generation cost can be computed by the following equation:

$$E_{pv} = \frac{C_{NCF,PV} * CRF}{\sum_{m=1}^{12} N_d * L_m} \tag{1}$$

where N_d is the total days in a month, L_m energy by the PV system in a month, and CRF is the capital recovery factor. The CRF is calculated by Eq. (2)

$$CRF = \left(\frac{d}{1 - (1 + d)^{-N}} \right) \tag{2}$$

The total cash flow ($C_{NCF,PV}$) of a PV system is the total investment cost ($C_{PV,SYS}$), the present value of O&M cost (OM_{PV}), and the present value of replacement cost (R_{PV}). Equation (3) defines the total cash flow ($C_{NCF,PV}$) and its other cost of components

$$C_{NCF,PV} = C_{PV,SYS} + OM_{PV} + R_{INV} \tag{3}$$

The total investment ($C_{PV,SYS}$) is the sum of the each element of the PV system; i.e., PV module cost (C_{PV}), inverter cost (C_{INV}), and I&C cost ($C_{I\&C}$) are described in Eq. (4).

$$C_{PV,SYS} = C_{PV} + C_{INV} + C_{I\&C} \tag{4}$$

Operation and maintenance costs of PV system

O&M costs (OM_{PV}) include indemnity, maintenance, levies (tax), regular (recurring) costs, etc. It is given as a percentage (say m) of the total capital cost. All operational costs are increased at a rate e_0 and reduced at rate d . The life-cycle cost for a lifetime of N years is described by Eq. (5):

$$OM_{PV} = OM_0 \left(\frac{1 + e_0}{d - e_0} \right) * \left[1 - \left(\frac{1 + e_0}{d - e_0} \right)^N \right] \text{ if } d \neq e_0 \tag{5}$$

$$OM_{PV} = OM_0 * N \text{ if } d = e_0 \tag{6}$$

where $OM_0 = m(C_{PV, SYS})$.

Replacement cost of PV system components

The replacement cost (R_{INV}) includes the number of inverter replacements (v) throughout the system lifetime, without taking the salvage value of inverter (replaced one). It is described by Eq. (7).

$$R_{INV} = \sum_{j=1}^v C_{INV} * \left(\frac{1 + e_0}{1 + d} \right)^{\frac{N_j}{v+1}} \quad (7)$$

In Eq. (7), v is the number of inverter's replacements over a period of N years (i.e., project lifetime 25 years). For inverter, replacement period is taken 15 years and efficiency is 95%.

3 Solar Photovoltaic System's Finance Structure

Based on how electricity is billed, the investments of PV installations vary. To completely avail the advantages of the PV installations, the users must reap the maximum benefits out of the metering system. There are two types of metering systems available: net metering and gross metering. Smart metering and net metering offer an opportunity to the consumers to reduce their bills. Net metering is the most common method in which owners of distributed generation may offset electricity consumption from the grid with local generation [23], while on the other hand gross metering is a system where rooftop owners or third-party investors sell energy to DISCOM using the electricity generated by roof top PV solar installation by the roof owners or third party. Such a system is also called as feed-in-metering where all energies are exported to the grid and recorded through a 'feed-in meter.' The solar energy is transferred to the distribution grid at a feed-in-tariff (FIT) approved by the regulator. The project developers and investors participate into a long-term purchase agreement with the distribution grid. A PV system can be grid connected and gross-metered.

These two types of metering system are applicable under two main business models: capital expenditure model (CAPEX) and renewable energyservice company model (RESCO). When the capital expenditure is provided by rooftop owner, it is CAPEX model. In this model, the consumer buys the PV system by making 100% payment either directly or invest in the system through bank. However, in the RESCO model, the capital expenditure is covered by the third party.

There exist two types of models for acquiring finance or funds based on consumption choice. First is the rooftop leasing where the RESCO developer contracts for the roof and pays a fixed amount (rental) to the landlord over the time of the contract lease period for installing the PV modules, while in power purchase agreement (PPA), the RESCO developer puts their money in PV rooftop system and offers the generated

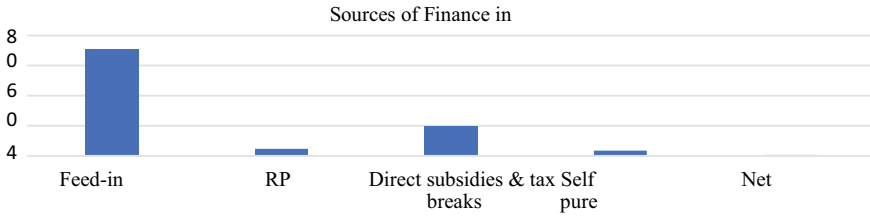


Fig. 1 Sources of finance in India. Source: <https://mnre.gov.in/>

electricity to the owner in at lower tariff compare to grid. The excess of solar power could be sold by the building owner to the utility through the metering system.

It is evident that there are five routes of financing the investments in solar PV in India, feed-in-tariffs are the most favored source among others such as renewable portfolio standards (RPS), direct subsidies and tax-breaks, self-consumption and pure competitive PV, and net-metering. Various agencies that release funds are State Nodal Agencies and State Nodal Departments, Solar Energy Corporation of India (SECI), channel partners, financial institutions or financial instigators and other government agencies for government projects. These agencies extend up to 30% of eligible central finance assistance (CFA) and services charges at the time of the project proposal, and about 10% advance is given at the time of allocation of targets, while the balance of 70% after the successful commissioning of the project (MNRE). The subsidy is disbursed directly by MNRE to the channel partners or through State Nodal Agencies (SNAs). MNRE specifies an accounting system, monitoring mechanism and uses SECI or SNAs for subsidy disbursement to channel partners (Fig. 1).

4 Results and Discussion

The results of cost–benefit analysis are compiled in Table 1 for the rooftop grid-connected solar PV of two different sizes, one smaller with the size 2.5 kWh, and the other with a greater size 10 kWh.

The cost of a solar PV installation comprises of cost of panel per kW, cost of the inverter, the total cost of the structure, other accessories, and installation cost. The results of cost–benefit analysis reveal that the total cost of large size solar PV plant is much greater, almost double the cost of the smaller size plant of 2.5 kWh; after deducting the subsidy of 30%, the cost after subsidy of solar PV plant of 10 kWh is about 224,385 kWh greater than the solar PV plant of size 2.5 kWh.

From the benefits side, the total electricity bill without solar for the lifetime of the plant 25 years is considered as a benefit. Apart from the monetary benefit from saving on electricity bill for a lifetime, another crucial benefit derived from the deployment of solar PV grid-connected system is the environmental benefit. The environmental benefit is estimated by the reduction in carbon dioxide emissions in 25 years. From the environmental perspective, the smaller size plant 2.5 kWh can reduce CO₂ emissions

Table 1 Cost–benefit analysis of rooftop grid-connected solar PV

Costs per kW	Amount (Rs.)	Total costs (2.5 kWh)	Total costs (10 kWh)	Benefits	Amount (2.5 kWh)	Amount (10 kWh)
Total cost of panel per kW	27,300	68,250	273,000	Total electricity bill without solar in 25 years	357,000	486,000
The total cost of the inverter	252,000	252,000	252,000		105,805	10,420
The total cost of the structure per kW	6000	15,000	60,000	Total profit using solar power (without subsidy)	(–1850)	(–193,400)
Other accessories and installation cost per kW	9440	23,600	94,400	Total CO ₂ emission reduction in 25 years	187.0625 tons	7482.333 tons
Total cost		358,850	679,400	Payback period	Approximately 9 yrs	Approximately 8–10 yrs
Subsidy 30%		107,655	203,820			
Cost after subsidy	251,195		475,580			

Source: <https://www.bijlibachao.com/solar/solar-panel-cell-cost-manufacturer-price-list-in-indiahtml>

by about 187.0625 tons, while the plant of size 10 kWh reduces the CO₂ emissions by 7482.333 tons. The payback period which refers to the time required to recover the initial cost of investment is more in case of small size plant as compared to a large size plant (Table 2).

Considering the above parameters, the internal rate of return (IRR) is estimated which reveals around 13% of IRR with a subsidy for a solar PV of size 2.5 kWh and about 20% of IRR with a subsidy for 10 kWh, While in the case of no subsidy, the IRR is much lesser of about 9% for smaller size plant and 14.5% for bigger plant size of 10 kWh.

Table 2 Description of variables

S. No.	Variables	Size of the plant (2.5 kWh)	Size of the plant (10 kWh)
1.	Capital cost (INR 100/Wp)	250,000	1,000,000
2.	Annual operation and maintenance expenses (INR 23 million/MW)	3075	12,300
3.	Applicable grid tariff (INR/kWh)	5.95	8.1
4.	Capacity utilization factor (%)	19	19
5.	Plant life (years)	25	25
6.	Loan duration (years)	12	12
7.	Cost of debt or rate of interest (%)	13	13
8.	Corporation tax rate (%)	34	34
9.	Depreciation (%)	90	90

5 Conclusion

The results of cost–benefit analysis reveal that the internal rate of return is larger in case of subsidy than in the case without subsidy. The work highlights the role of subsidies in incentivizing the investment in PV solar systems and yields an internal rate of return (IRR) is substantially smaller for a small plant while larger for a large plant with subsidy. A rapid change in technology reduces the cost, thus affecting the IRR and the net benefits reducing the payback period; this discourages the investment in solar PV plants in making any investment decisions on the present technology. The paper, therefore, recommends a financial scheme where subsidies are linked to the technology used. This will provide not only an incentive to the investors by reducing the risks due to vulnerability of change in technology but also reduce the burden of subsidies on government.

Appendix

The subsidy can be disbursed in the following ways:

- 20% after completion of I&C of the PV system.
- 5% after effective operation of the solar project after 1 year.
- Balance 5% after the 2 years of reliable operation of the project. Techno-economic evaluation of roof top PV system has given in [14].

The first step is to generate the total energy that is required by using the following formula. Energy per day is given by:

$$\text{Energy day} = \sum (H_i P_i N_i) / 1000 \text{ kWh} \tag{8}$$

where i is the indicator type of load required, for example light, AC, Fan, etc. H_i is the number of hours equipment is utilized per day, and P_i is the power of i th equipment type,

N_i is the number of devices being utilized.

Therefore, the total PV (TPV) generation capacity required can be calculated as

$$\text{TPV} = \text{Energy day} / (\text{Sun} * d) \text{ kW} \tag{9}$$

where, sun is the average number of hours the sun shines at the site, d is the de-rating factor, effect of efficiency and changes in the solar generation during the day.

Let P_c be the power output capacity of each panel, the number of solar panels required can be calculated as

$$N_{\text{panel}} = \text{TPV} / P_c \tag{10}$$

Economic profit involved in shifting from grid power to rooftop solar power. Assume cost grid be the cost of power from the grid. Cost solar be the cost of rooftop solar system taking into account the subsidy. Considering the lifetime as (yrs) and cost of unit of energy charged by utility as cost utility, the cost of power from the grid can be calculated as

$$\text{Cost grid} = 365 * \text{Energy day} * \text{Cost utility} * \text{yrs} \tag{11}$$

The rooftop PV system involves mainly four components PV module, battery, charge controller, and inverter. The total cost of the PV system cost solar ^ without considering any subsidy can be calculated as:

$$\text{Cost solar} \wedge = \text{Cost panel} + \text{Cost battery} + \text{Cost inverter} + \text{Cost controller} \tag{12}$$

Let subsidy be the percentage subsidy by the government. The total cost of the roof top solar system cost solar is given as:

$$\text{Cost solar} = (1 - \text{Subsidy}) * \text{Cost solar} \wedge \tag{13}$$

where cost battery = $N_{\text{battery}} * \text{cost per battery}$

$$\text{Cost panel} = N_{\text{panel}} * \text{cost per PV panel} \tag{14}$$

Therefore, the overall profit achieved by moving from grid to PV system is

$$\text{Profit} = \text{Cost grid} - \text{Cost panel} \tag{15}$$

It is evident that the benefit of shifting to roof top solar eventually implies independence from the grid. All the shortcomings of grid-connected electricity supply can therefore be avoided. In order to calculate the time period needed to achieve the savings equivalent to the amount financed can be obtained as follows.

$$\text{Energy day} * \text{Cost utility} * 365 * \text{Yrspayback} = \text{Cost panel} \quad (16)$$

where Yrs is the payback in years. Based on the above equation, payback period can be calculated as

$$\text{Yrspayback} = \text{Cost panel} / \text{Energy day} * \text{Cost utility} * 365 \quad (17)$$

According to Central Electricity Authority (CEA) under Ministry of Power, Government of India, the weighted average emission factor for PV system is 0.82 tons of CO₂ per MWh of energy generated. By going with rooftop PV system, CO₂ emissions can be cut for next 25 years with the below-mentioned equation.

$$\text{CO}_2 \text{ emission} = \text{Energy day} * 0.82 * 365 * 25 / 1000 \text{ ton/MWh} \quad (18)$$

References

1. <https://powermin.gov.in/en/content/annual-reports-year-wise-ministry>
2. A. Enayat et al., India's on-grid solar power development: historical transitions, present status and future driving forces. *Renew. Sustain. Energy Rev.* **69**, 239–247 (2017)
3. MNRE, *State Wise Estimated Solar Power Potential in the Country* (Ministry of New & Renewable Energy, Government of India, 2015). <http://mnre.gov.in/file-manager/UserFiles/StateWise-Solar-Potential-NISE.pdf>
4. M.K. Hairat, S. Ghosh, 100 GW solar power in India by 2022—a critical review. *Renew. Sustain. Energy Rev.* **73**, 1041–1050 (2017)
5. G. Makrides, B. Zinsser, M. Norton, G.E. Georghiou, M. Schubert, J.H. Werner, Potential of photovoltaic systems in countries with high solar irradiation. *Renew. Sustain. Energy Rev.* **14**, 754–762 (2010)
6. A. Sarzynski, J. Larriue, G. Shrimali, The impact of state financial incentives on the market deployment of solar technology. *Energy Policy* **46**, 550–557 (2012)
7. K.H. Solangi, M.R. Islam, R. Saidur, N.A. Rahim, H. Fayaz, A review of global solar energy policy. *Renew. Sustain. Energy Rev.* **15**(4), 2149–2163 (2011)
8. C.W. Hsu, Using a system dynamics model to assess the effects of capital subsidies and feed-in tariffs on solar PV installations. *Appl. Energy* **100**, 205–217 (2012)
9. S. Borenstein, Private net benefits of residential solar PV: the role of electricity tariffs, tax incentives, and rebates. *J. Assoc. Environ. Resour. Econ.* **4**(S1), S85–S122 (2017)
10. J.Z. Irfan Jamil, Evaluation of energy production and energy yield assessment based on feasibility, design and execution of 3×50 MW grid—connected solar PV pilot project in Nooriabad. *Int. J. Photoenergy* (2017)
11. M. Kolhe, K.M.I.U. Ranaweera, A.G.B.S. Gunawardana, Techno-economic sizing of the off-grid hybrid renewable energy system for rural electrification in Sri Lanka. *Sustain. Energy Technol. Assess.* **11**, 53–64 (2015)

12. G. Liu, M.G. Rasul, M.T. Amanullah, M.M. Khan, Techno-economic simulation and optimization of residential grid-connected PV system for the Queensland climate. *Renew. Energy* **146**–155 (2012)
13. T. Lang, D. Ammann, B. Girod, Profitability in absence of subsidies: a techno-economic analysis of rooftop photovoltaic self-consumption in residential and commercial buildings. *Renew. Energy* **87**, 77–87 (2016)
14. M. Kolhe, S. Kolhe, J.C. Joshi, Economic viability of the stand-alone solar photovoltaic system in comparison with the diesel-powered system for India. *Energy Econ.* **24**, 155–165 (2002)
15. M. Kolhe, J.C. Joshi, G. Agnihotri, A.M. Shandilya, Market penetration and pay-back period analysis of a solar photovoltaic system under Indian conditions. *Int. J. Energy Technol. Policy* **1** (2002)
16. P. Sharma, M. Kolhe, A. Sharma, Economic performance assessment of building integrated photovoltaic system with battery energy storage under grid constraints. *Renew. Energy* **145**, 1901–1909 (2020)
17. C. Jeon, J. Lee, J. Shin, Optimal subsidy estimation method using system dynamics and the real options model: photovoltaic technology case. *Appl. Energy* **142**, 33–43 (2015)
18. G. Frisari, M. Stadelmann, De-risking concentrated solar power in emerging markets: the role of policies and international finance institutions. *Energy Policy* **82**, 12–22 (2015)
19. M. Bazilian, I. Onyeji, M. Liebreich, I. MacGill, J. Chase, J. Shah et al., Re-considering the economics of photovoltaic power. *Renew. Energy* **53**, 329–338 (2013)
20. K. Branker, M.J.M. Pathak, J.M. Pearce, A review of solar photovoltaic levelized cost of electricity. *Renew. Sustain. Energy Rev.* **15**(9), 4470–4482 (2011)
21. N. Martin, J. Rice, The solar photovoltaic feed-in tariff scheme in New South Wales, Australia. *Energy Policy* **61**, 697–706 (2013)
22. J.R. Lohmann, S.N. Baksh, The IRR, NPV and payback period and their relative performance in common capital budgeting decision procedures for dealing with risk. *Eng. Econ.* **39**(1), 17–47 (1993)
23. C. Eid, J.R. Guillén, P.F. Marín, R. Hakvoort, The economic effect of electricity net-metering with solar PV: consequences for network cost recovery, cross-subsidies and policy objectives. *Energy Policy* **75**, 244–254 (2014)

An Efficient Ensemble-Based Protection Technique for Transmission Line Protection



Murli Manohar, Prema Diagavane, and Sunil Kumar Shukla

Abstract Fast and reliable protection is the prerequisite for any protection scheme for providing protection to the transmission network. The detection and classification of transmission line faults are the main challenge for the power engineers. In this regard, an efficient protection approach for transmission line protection has been proposed in this paper. The proposed protection strategy involves the development of protection algorithm into two stages, i.e. feature extraction and fault detection/classification. The raw time-domain voltage and current signals at the relaying bus are pre-processed using discrete wavelet transform (DWT) to derive discriminatory attributes and the features so obtained is further used as input to train the ensemble of K-nearest neighbour (KNN) classifier to perform detection/classification of fault. The ensemble-based approach gives improved performance as compared to the single classifier. The performance evaluation of proposed protection scheme under varying fault parameters and other operating conditions clearly ascertains its applicability in providing reliable protection to the transmission line.

Keywords Transmission line protection · Discrete wavelet transform · Machine learning · Ensemble classifier · Feature extraction

1 Introduction

With considerable development and growing advancements in the lifestyle, the electrical power requirement at the receiving end has witnessed the subsequent need to

M. Manohar (✉)

National Institute of Technology, Raipur, Raipur, CG, India

P. Diagavane

G H Raisoni College of Engineering, Nagpur, MH, India

e-mail: hodee.ghrce@raisoni.net

S. K. Shukla

Nirma University, Ahmedabad, Gujarat, India

e-mail: sunilkumar.shukla@nirmauni.ac.in

expand the existing power infrastructure to meet the demand. Since the electrical energy has emerged as an essential ingredient behind all kinds of the development, in order to drive the progress, it is required to ensure the adequate availability of power to the end-user. In order to fulfil the demand of electric power, it is needed to generate extra power to cater load centre through existing transmission line network. If the same situation prevails further, it will be extremely challenging for the power system engineers to accommodate the transmission of additional power through existing power framework. In order to avoid such situation, the generation of electric power and its transmission to the load centre is changing all around the globe. For the satisfactory operation of power transmission network, it is important to ensure the maximum power transfer through the transmission lines without violating the maximum power transfer capability criteria. The power infrastructure in the developing countries such as India, in spite of being capable in generating the surplus power, are quite unable to satisfy the rising power demand due to unavailability of adequate transmission and distribution network. The existing power transmission network is not enough to fulfil the power demand in the near future due to its limited ability to transfer power.

Though the three-phase transmission system provides various advantages but owing to the lack of accurate and fast protection technique, it has not yet gained so much popularity. The transmission lines spread over large distances to transmit the generated electrical power from generating stations to the load centres undergo various climatic abnormalities such as speeding wind, snowfall and rain, based on the environmental conditions of the place. The abnormalities associated with the environment are mainly responsible for the occurrence of faults in transmission lines leading to power interruptions at the load centre. The protection schemes developed so far are not appropriate to ensure the suitable protection to the three-phase system.

With the advancements in the field of power electronics and to cater to the needs of modern lifestyle, the use of nonlinear loads has increased considerably in recent times. The switching activity in nonlinear loads leads to distortion in the current–voltage waveform, due to the nonlinear relation among the current–voltage [1]. The harmonic current drawn from the nonlinear loads causes subsequent distortion in the voltage–current profile. Due to this reason, the classical protection algorithms commonly influence under such conditions. In other words, the conventional relays quite often fail to detect and classify the faults under poor power quality condition [2, 3]. The harmonics arising due to the switching of nonlinear loads increase the apparent impedance, thereby increasing the probability of under-reach of distance relay [4]. Thus, in this regard, an effective protection technique is required to be developed which is immune to the presence of harmonics.

In this regard, various protection schemes related to protection of three-phase line [5–10] have been documented in the literature. A data mining model-based approach to analyse the unsymmetrical faults in three-phase system is reported in [7]. A comprehensive review on the protection of transmission line is presented in [11]. A adaptive network-based fuzzy inference approach for analysing the probable shunt faults is discussed in [12]. The wavelet transform and neural network-based fault analysis approach for three-phase line protection is reported in [9]. A decision

tree-based algorithm for providing protection to the FACTS-based transmission line is reported in [10].

Over the last few decades, artificial neural network (ANN) has been exploited for the protection of three-phase transmission system. In this context, a protection scheme based on modular ANN and discrete Fourier transform (DFT) to perform the planned tasks of fault finding/categorization and location approximation against all probable faults in three-phase system has been reported in [3, 13]. However, DFT considers the fault signal as stationary and also fails in preserving the time–frequency information of the signal. To have remedy of the limitation of DFT-based scheme, another relaying approach based on discrete wavelet transform and ANN has been proposed in [14]. The selection of the number of decomposition level and the type of mother wavelet is a tedious task. However, the accuracy of ANN-based scheme is greatly affected by the selection of suboptimal architecture. The K-nearest neighbour (KNN)-based protection schemes have been widely adopted in the recent time, due to their inherent merits including wider stability, easier generalization, accurate prediction for different scenarios and simpler implementation [14, 15]. With the aim of further enhancing, the mapping capability of KNN, instead of single KNN classifier, ensemble of kNN has been preferred for performing the classification task [14, 16]. However, the approach has not been extended for imparting protection to the three-phase system. With the aim of overcoming the drawbacks associated with the reported protection schemes for three-phase transmission system, in the present work, the hybrid framework of ensemble of KNN and discrete wavelet transform (DWT) has been proposed in the present work. The results obtained through the performance evaluation carried out under the diverse fault scenarios clearly indicate the effective, accurate and reliable execution of the proposed scheme in performing the planned tasks of fault finding, categorization and location inference.

2 Power System Model

The single line diagram of power system model simulated under MATLAB/Simulink environment is depicted in Fig. 1. The power system model includes a three-phase double-circuit transmission line with total line length of 200 km and two sources (400 kV, 50 Hz) connected at both extremes of the line. In order to replicate the actual loading profile in the system, both linear and nonlinear loads have been connected at the sending and receiving ends of the line. The nonlinearity in the loads has been achieved by modelling the three-phase rectifier fed load. In order to analyse the performance of proposed scheme under harmonic distortion in the current–voltage profile, the switching of nonlinear is performed.

In order to demonstrate the behaviour of nonlinear loading and fault, a scenario has been generated involving the switching of nonlinear load at $t = 0.1$ s followed by the inception of three phase to ground (ABCG) fault at a distance of 5 km from the relaying point, on three-phase transmission line, which is assumed to be uniformly distributed. The three-phase voltage waveform is analysed to see the effect of this

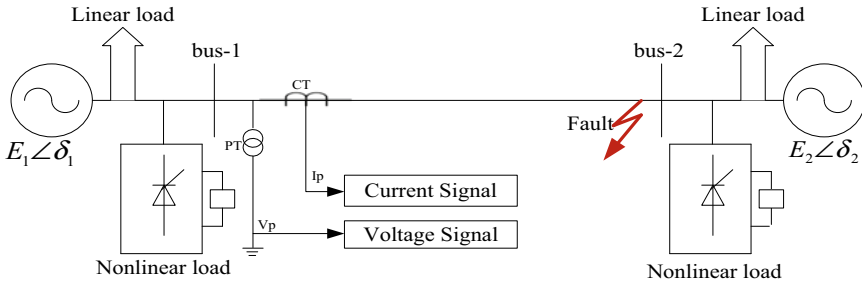


Fig. 1 Single line diagram of three-phase transmission system considered under study

shunt fault. It has been observed from Fig. 2 that before the occurrence of fault the current and voltage waveforms of three phases are balanced, but after the initiation of fault, there is considerable change in the magnitude of voltage waveform of the faulty phase A.

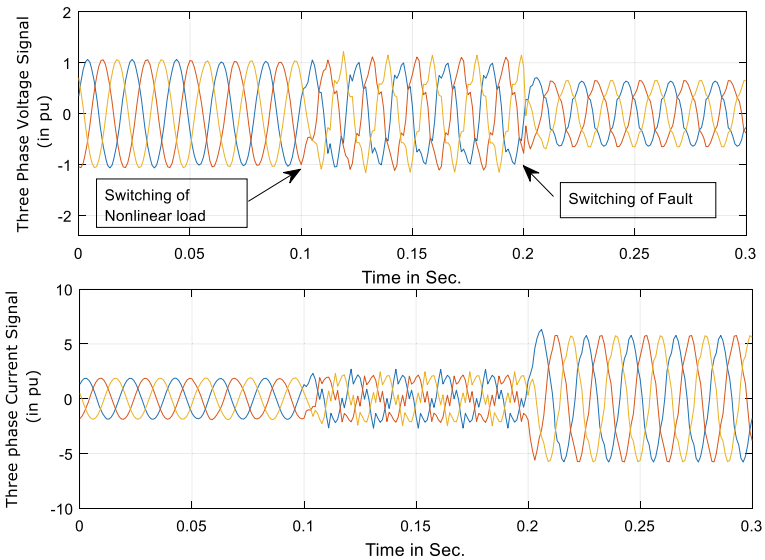


Fig. 2 Waveforms representing three-phase voltage and current during 'ABCG' fault

3 Discrete Wavelet Transform (DWT)-Based Pre-processing and Feature Extraction

In present times, wavelet transform has come up as the dominant technique for analysis of non-stationary signals such as fault current–voltage signals. In the proposed work, the widely used discrete wavelet transform (DWT) has been adopted for extraction of discriminatory features from the instantaneous currents and voltage signals, since it offers the information in time–frequency domain [3, 17]. The pre-processing of raw current and voltage signals obtained from the relaying location is carried out using DWT. The approximate coefficients of the signals are derived using the Daubechies Db3 mother wavelet. The signals so obtained undergo decomposition up to three levels thereby eliminating the higher frequency components, while the lower frequency components are retained in the signals.

The scaling function $\phi_j(t)$ used to perform the complete decomposition of any time-series signal into approximations is given by:

$$\phi_j(t) = 2^{-j/2} \phi(2^{-j}t - n) \quad (1)$$

where $n \in Z$, j represents an integer.

The approx. coefficients of signals obtained using (1) are used to estimate the standard deviation (SD) which is further utilized as input data set for the classifier.

4 Ensemble of KNN Classifier

Data-mining methods are aimed at implementing a comprehensive network by analysing the data set effectively in order to make it useful to analyse the system response. Various data-mining methods such as support vector machine, decision tree, neural network, etc., have been reported in the literature for detecting and classifying the faults [18–20]. However, all the reported methods have invariably adopted a single individual classifier for carrying out the task of detecting the fault and the discriminating the fault type. The incapability of single individual classifiers in performing the classification tasks of complex data is well documented in the literature [21, 22].

In this context, the idea of exploiting the set of multiple classifiers (ensemble) for dealing with complex classification problems is mostly preferred [23]. The ensemble-based multiclassifier involves a group of classifiers to obtain the input–output mapping, and the individual decisions of each classifier are further combined and weighted to obtain the final prediction.

The feature extraction stage is followed by the classification of output using the input data set. The classification stage involves the formation of smaller data sets formed by random selection process. Further, the subset of selected features is suitably weighted to maximize the rate of classification [24]. The feature weighting

process is followed by the training of each subset using the individual KNN-based base classifiers. Post-training, predicted output of each individual classifier is combined and utilized to obtain the final prediction.

Considering an unknown test case X , which is being fed as input to the trained network, the predicted output class of each KNN classifier (ω_j) assigned based on the classification type. The prediction of t_{th} classifier considered to be $d_{t,j} \in \{0,1\}$, if $t = 1 \dots, T$ and $j = 1, \dots, C$, where C represents the number of classes. The final prediction of ensemble classifier is done on the basis of polling strategy as represented below:

$$\sum_{t=1}^T w_t d_{t,j} = \max_{j=1}^C \sum_{t=1}^T w_t d_{t,j} \quad (2)$$

5 Proposed Protection Scheme

Considering the limitation of single classifier in achieving the satisfactory performance, a scheme based on ensemble of classifier has been proposed in the present work. The steps involved in the development of proposed protection scheme are depicted in Fig. 3. The current signals retrieved at the relaying bus are pre-processed through the discrete wavelet transform (DWT) for the extraction of the useful attributes. A moving window of one cycle is considered for estimating the input attributes. The standard deviation of approximate coefficient is used as the feature vector for the development of ensemble of KNN (EC)-based fault detector/classifier and zone identifier. The generation of training as well as the testing data has been accomplished by varying the fault parameters, and other operating contingencies including load variation are summarized in Table 1.

6 Results and Discussions

In this section, the ensemble classifier-based protection scheme has been tested against diverse fault situations to evaluate the efficacy of the developed scheme. Diverse fault parameters which have been varied during testing data generation include the fault type, instant of fault, fault resistance along with the fault location. The critical fault cases like high resistance faults and faults occurring at near as well as the far end have also been included during testing. The faultwise performance evaluation results of the proposed ensemble of KNN-based fault detector/classifier in terms of the reliability indices, i.e. dependability and security, have been summarized in Table 2. The observations made from the table clearly indicate that the performance of the ensemble three based proposed protection scheme is immune to the variations in fault parameters.

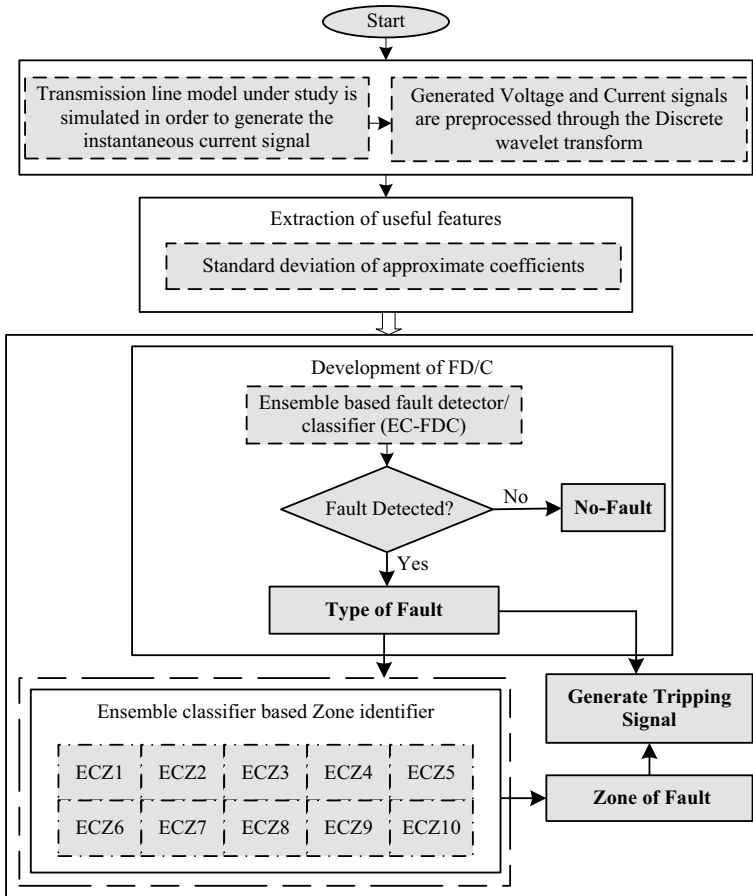


Fig. 3 Flowchart of proposed ensemble-based protection scheme

Table 1 Pattern of training and testing data generation

Type of cases	Fault type					No fault cases
	<i>LG</i>	<i>LLG</i>	<i>LLLG</i>	<i>LL</i>	<i>LLL</i>	
Training cases	1368	1368	456	1368	456	18
Testing cases	600	600	200	600	200	40

In order to validate the performance of proposed ensemble-based zone identifier, the assessment has been carried out for both types of loading conditions, i.e. linear and nonlinear loading in Table 3. The higher overall accuracy obtained in each case ascertains its applicability for providing suitable protection to the transmission line without being influenced by the harmonics caused due to nonlinear loading.

Table 2 Test results of ensemble-based fault detector/classifier in terms of the reliability indices

Fault/no fault	Type of fault	Accuracy (%)	Dependability (%)	Security (%)	Max. response time (ms)
Phase(s) to ground fault	LG	99.33	99.61	–	13
	LLG	99.63	99.12	–	14
	LLLG	99.03	99.51	–	15
Phase(s) to phase fault	LL	99.48	99.20	–	14
	LLL	99.31	99.21	–	14
No fault	variation in linear and nonlinear loading	100	–	100	–

Table 3 Overall performance of ensemble-based zone identifier

Type of load	Total no. of test cases	Total no. of correctly predicted cases	Overall accuracy (%)
Linear load	4950	4913	99.25
Nonlinear load	4950	4898	98.94

7 Conclusions

The present works aim at improving the performance of relaying schemes in terms of operating reliably under varying operating scenarios. In this regard, stress has been laid on exploiting the effectiveness of digital relaying scheme for providing the adequate protection to the three-phase transmission system. The variable voltage–current behaviour during load variation may lead to relay maloperation. In this context, a novel protection approach has been proposed involving the combined framework of ensemble of KNN classifier and discrete wavelet transform, which utilizes the approximate coefficient of voltage and current signal as input feature. The developed scheme is capable of avoiding the nuisance tripping by discriminating between load variation and fault, while performing the task of FD/C accurately within one cycle. It can be clearly observed from the obtained test results that the developed scheme is able to successfully perform the task of fault detection/classification and zone identification with high accuracy. The proposed scheme has been found to be unaffected by the nonlinearity and variation in fault parameters including fault type, location, inception angle and fault resistance.

References

1. P.K. Ray, N. Kishor, S.R. Mohanty, Islanding and power quality disturbance detection in grid-connected hybrid power system using wavelet and S-transform. *IEEE Trans. Smart Grid* **3**(3), 1082–1094 (2012)
2. P.K. Dash, S.R. Samantaray, G. Panda, Fault classification and section identification of an advanced series-compensated transmission line using support vector machine. *IEEE Trans. Power Delivery* **22**(1), 67–73 (2007)
3. S. Shukla, E. Koley, S. Ghosh, A hybrid wavelet—APSO—ANN-based protection scheme for six-phase transmission line with real-time validation. *Neural Comput. Appl.* **3456789**(123) (2018)
4. E. Koley, K. Verma, S. Ghosh, An improved fault detection classification and location scheme based on wavelet transform and artificial neural network for six phase transmission line using single end data only (2015)
5. K. Chen, J. Hu, J. He, Detection and classification of transmission line faults based on unsupervised feature learning and convolutional sparse autoencoder. *IEEE Trans. Smart Grid* **9**(3), 1748–1758 (2016)
6. A. Prasad, J. Belwin Edward, K. Ravi, A review on fault classification methodologies in power transmission systems: part—I. *J. Electr. Syst. Inf. Technol.* (2017)
7. S.R. Samantaray, A data-mining model for protection of FACTS-based transmission line. *IEEE Trans. Power Delivery* **28**(2), 612–618 (2013)
8. E. Koley, R. Kumar, S. Ghosh, Low cost microcontroller based fault detector, classifier, zone identifier and locator for transmission lines using wavelet transform and artificial neural network: a hardware co-simulation approach. *Int. J. Electr. Power Energy Syst.* **81**, 346–360 (2016)
9. P.S. Bhowmik, P. Purkait, K. Bhattacharya, A novel wavelet transform aided neural network based transmission line fault analysis method. *Int. J. Electr. Power Energy Syst.* **31**(5), 213–219 (2009)
10. S.R. Samantaray, Decision tree-based fault zone identification and fault classification in flexible AC transmissions-based transmission line (2009)
11. K. Chen, C. Huang, J. He, Fault detection, classification and location for transmission lines and distribution systems: a review on the methods. *High Volt.* **1**(1), 25–33 (2016)
12. M.J.B. Reddy, D.K. Mohanta, Performance evaluation of an adaptive-network-based fuzzy inference system approach for location of faults on transmission lines using Monte Carlo simulation. *IEEE Trans. Fuzzy Syst.* **16**(4), 909–919 (2008)
13. F. Martin, J.A. Aguado, Wavelet-based ANN approach for transmission line protection. *IEEE Trans. Power Delivery* **18**(4), 1572–1574 (2003)
14. M. Manohar, E. Koley, S. Ghosh, Reliable protection scheme for PV integrated microgrid using an ensemble classifier approach with real-time validation. *IET Sci. Meas. Technol.* **12**(2), 200–208 (2018)
15. P. Ray, B.K. Panigrahi, N. Senroy, Extreme learning machine based fault classification in a series compensated transmission line, in *IEEE International Conference on Power Electronics, Drives and Energy Systems* (2012), pp. 1–6
16. M. Manohar, E. Koley, S. Ghosh, Microgrid protection under wind speed intermittency using extreme learning machine. *Comput. Electr. Eng.* **72**, 369–382 (2018)
17. M.A.S. Masoum, S. Jamali, N. Ghaffarzadeh, Detection and classification of power quality disturbances using discrete wavelet transform and wavelet networks. *IET Sci. Meas. Technol.* **4**(4), 193–205 (2010)
18. H. Wang, W. Keerthipala, Fuzzy-neuro approach to fault classification for transmission line protection. *IEEE Trans. Power Delivery* **13**(4), 1093–1104 (1998)
19. S. Kar, S.R. Samantaray, M.D. Zadeh, Data-mining model based intelligent differential microgrid protection scheme. *IEEE Syst. J.* **PP**(99), 1–9 (2015)

20. J.M. Johnson, A. Yadav, Complete protection scheme for fault detection, classification and location estimation in HVDC transmission lines using support vector machines. *IET Sci. Meas. Technol.* **11**(3), 279–287 (2017)
21. R. Polikar, Ensemble based systems in decision making. *IEEE Circuits Syst. Mag.* 21–45 (2006)
22. T.K. Ho, The random subspace method for constructing decision forests. *IEEE Trans. Pattern Anal. Mach. Intell.* **20**(8), 832–844 (1998)
23. S.R. Samantaray, Ensemble decision trees for high impedance fault detection in power distribution network. *Int. J. Electr. Power Energy Syst.* **43**(1), 1048–1055 (2012)
24. L. Nanni, A. Lumini, Evolved feature weighting for random subspace classifier. *IEEE Trans. Neural Netw.* **19**(2), 363–366 (2008)

Electric Vehicle (EV) Powertrain Modeling and Optimization



Vinay Pawar and Shridhar Rakhonde

Abstract The electric vehicle power train is consisting of subsystems, for the power transmission of electric vehicles (EV). This paper provides comparative study about EV powertrain subsystems and their modeling. The subsystem has components like motors, accumulators, and gear drives. Selection of proper components to be used in an EV has specific criteria depending on vehicle dynamics and drive type. EV modeling and optimization are very important aspects while working with electric vehicles. Stability of the system and performance of DC motor and electric vehicle subsystems can easily analyze by modeling and optimization. The proposed system model is simulated and developed in Scilab X-cos and MATLAB. The simulation model is described in this paper to elaborate powertrain modeling technique for EV. The results obtained from the powertrain simulation give various electrical and mechanical parameters as discussed in this paper. This paper also provides a brief study about powertrain optimization which is a very important aspect in powertrain modeling for effective sustainable mobility. The optimization of EV powertrain consists of power prediction, energy prediction, and lifecycle analysis with the consideration of efficiency region of specific subsystem.

Keywords Electric vehicles (EV) · EV powertrain · Optimization · Worldwide harmonized light vehicles test procedure (WLTP) · Scilab X-cos

1 Introduction

Electric vehicles are the automotive machines which use electrical energy for vehicle movement. The electric vehicles are coming with high torque and high-speed characteristics used for different applications. The electrical vehicle uses electrical energy

V. Pawar (✉)

Bhiwarabai Sawant College of Engineering and Research, Pune, India

S. Rakhonde

Vidyapratishthans Kamal Nayan Bajaj Institute of Engineering, Baramati, India

stored in batteries, and generally, these batteries are rechargeable. The electric vehicles are seen as green automobile, in order to address the issues like emission of gases causing air pollution, global warming, limited natural reserves, and many more. The concept of electric vehicles became popular in twentieth century; it has drawn a considerable amount of interest as technology has grown up. Electrical vehicles can actively control rising carbon footprint and many environmental adverse effects of fuel-based IC vehicles.

In powertrain modeling of electrical vehicles, the power sizing of electric motors and batteries is done by analyzing vehicle application. It requires a drive cycle to model and simulate. Drive cycle required to characterize the required electrical power of the motor as function of its variable mechanical load. Drive cycle data type used is decided vehicle type and its purpose of usage that enables the characterization of mechanical load so-called to be tractive load. The definition of powertrain modeling is to design an EV subsystem model with more effective power management for the traction load on electrical components such as accumulator battery and traction motor. However, the drive cycle is specific for vehicle type and purpose of usage [1].

The modeling method is to determine the power route during the motoring and its power transfer. For the simulation of this electric vehicle powertrain, a BLDC (Brushless DC) tractive motor, motor controller, mechanical transmission gearbox, and rechargeable Li-ion battery are used. The results of this model are used to optimize the powertrain components and to achieve maximum efficiency for optimum speed and torque under dynamic load conditions [2].

The electric vehicle power train modeling has the proper selection of EV subsystem components. For the selection of EV subsystem, the model must be gone through the right selection criteria which depends on vehicle dynamics and drive cycle type. Electric vehicle traction motors generally offer quieter operation and faster acceleration as compared to conventional motors. Further, the EV traction does not require multi-level gearbox like conventional vehicles because the electric motor has a more favorable performance that can provide the highest torque even at the lowest speed.

The BLDC motor is also known as PMSM permanent magnet AC synchronous motor. The battery has DC power stored, and hence, there is the necessity of inverter controller. This BLDC motor controller also controls the BLDC motor by varying its speed and performance. Lithium-ion batteries are more preferable for electrical vehicles as they have more energy densities than lead–acid batteries or nickel–metal hydride (NMH) batteries, so it is possible to make the Li-ion battery size compact in size than others while can adjust size and shape for the same storage capacity. The focus on the development of hybrid electric vehicles (HEV) and electrical vehicles (EV) batteries is on higher energy densities, compact size, safety of battery pack, and cell lifecycle.

2 Powertrain System Model

The powertrain modeling and simulation of the electric vehicles have a specific scenario of conclusion. For the powertrain system model, the user type and the purpose of vehicle usage are the factors that taken into consideration. The required outcomes of the vehicle are derived with the help of drive cycle. The system model provides technological advancements in areas, such as system designing and power train development are focused on reducing cost and weight and improving life and operation of traction motors, thus making the EVs more affordable.

The powertrain system model developed for this system has defined the workflow in aspect of developing an electric vehicle. The electric vehicles are usually assumed to work as rigid bodies for performance analysis. There are some structural deflections in powertrain which are generally ignored. So, this should not be ignored. In most cases, there is a good assumption, and it simplifies analysis considerably.

The working of the electric vehicle powertrain modeling is shown in Fig. 1. First requirement of this modeling is the user requirement and the drive cycle selection. The drive cycle data is different for different vehicles and their purpose. Vehicle data is referred to shape, weight, and capacity of the vehicle. Vehicle performance is the study of the resistive forces and the motion of a vehicle. The motion of any vehicle depends upon all the forces that act upon it when a vehicle tends to move. These forces and moments, for the most part, are caused by the interaction of the vehicle with various environmental quantities. Transmission is a mechanical system present in the electric vehicle which is used to increase torque or speed at the wheel. The transmission is connected between the motor and the wheels. From transmission calculations and iterations for the selection of different transmission ratios, the motor it is obtained w.r.t. drive cycle. The battery subsystem contains all the calculations related to the battery. The battery power, battery voltage, battery current, battery C-rate, and state of charge (SOC) are calculated in the battery. The calculation of powertrain components allows to obtain both voltage and current behavior of the

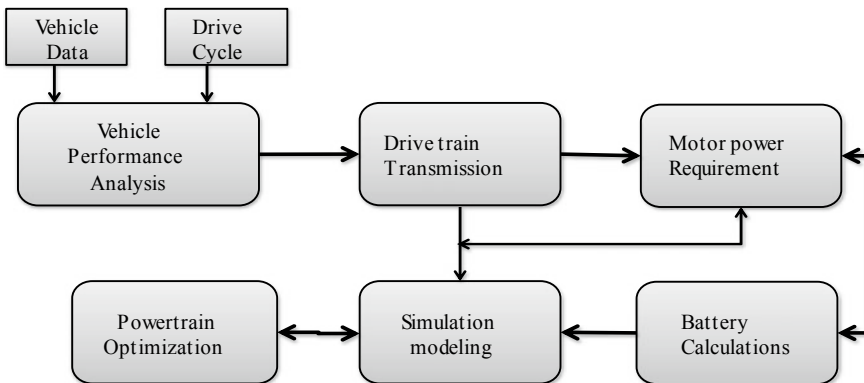


Fig. 1 Block diagram of system model

accumulator, which is useful for sizing and selection of subsystem components of the electric vehicle [3].

3 Drive Cycle and Vehicle Performance Analysis

The drive cycle is a point data or a set of various points where the values are velocity versus time. The drive cycle data is used for testing purpose or diagnosis of vehicles. There are different types of drive cycles, and they vary with different vehicles and loading conditions.

There are many drive cycles, e.g., NEDC, FTP 75, WLTP, MNEDC, and many more. For this modeling, Worldwide Harmonized Light Vehicles Test Procedure (WLTP) drive cycle is used.

The WLTP drive cycle is referred to the world harmonized light-duty vehicles test procedure.

Time duration—1477 s.

Distance—14.6 km.

Max. speed—85.2 km/h (Fig. 2).

The WLTP includes special provisions for testing of various categories of hybrid electric and electric vehicles off-vehicle chargeable hybrid electric vehicles, not off-vehicle chargeable hybrid electric vehicles, and battery electric vehicles. The WLTP replaces the old New European Driving Cycle (NEDC) [4]. Main difference is that model cycles are a compilation of straight acceleration and constant velocity periods, and a real driving behavior is not represented, whereas transient cycles contain many speed variations, on-road driving conditions.

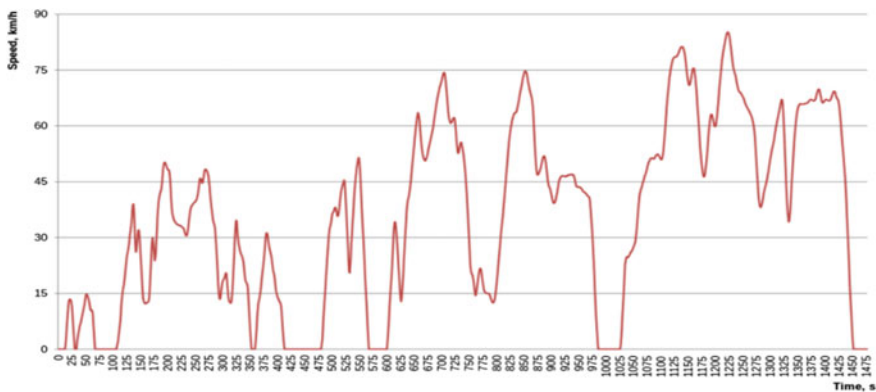


Fig. 2 WLTP drive cycle

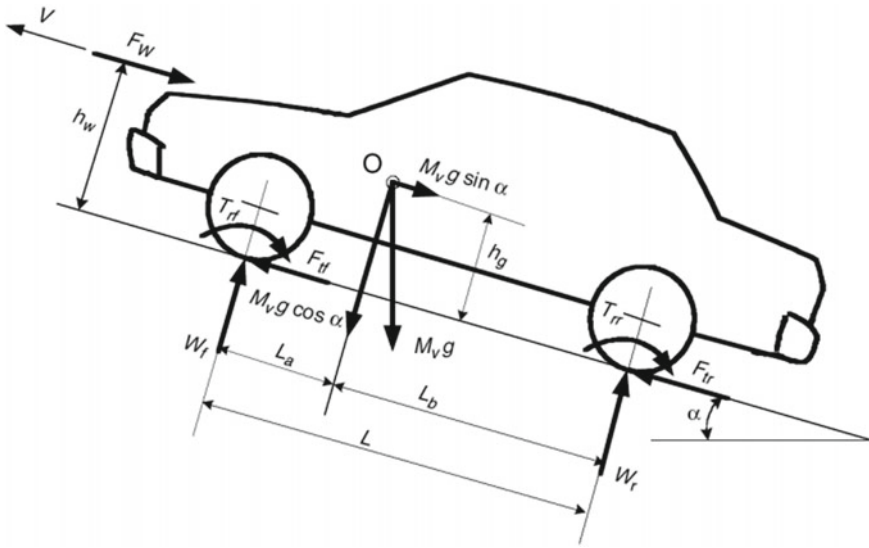


Fig. 3 Free body diagram of vehicle in motion

This is the analysis of various resistive forces acting upon the vehicle, and these forces resist the motion of the vehicle. These forces are as rolling, gradient, aerodynamic, and acceleration force. The above-mentioned forces are motion resistance forces.

Figure 3 shows the various forces acting upon the vehicle. The vehicle dynamics play an important role in powertrain development. The following equations show the calculation of motion resistive forces.

$$F_{rolling} = \frac{C1 * GVW}{R} \tag{1}$$

$$C1 = 0.005 + \left(\frac{1}{P}\right) + \left((0.01 + 0.0095) \frac{v^2}{100^2}\right)$$

$$F_{aero.} = \frac{1}{2} * \rho * Cd * A * v^2 \tag{2}$$

$$Cd = \frac{2 * Fa}{\rho * v^2 * A}$$

$$F_{grade} = GVW * \sin(\alpha) \tag{3}$$

$$F_{acc.} = GVM * a \tag{4}$$

From the above Eqs. 1, 2, 3, and 4.

Total tractive Efforts

$$F_{tractive} = F_{rolling} + F_{grade} + F_{aero.} + F_{acc.} \quad (5)$$

3.1 Transmission

T_w is torque required at wheels.

$$T_w = F_{tractive} * R_w \quad (6)$$

Wheel speed is the speed of the wheel in rpm.

$$N_w = \frac{v * 60}{2 * \pi * R_w} \quad (7)$$

Motor torque

$$T_m = \frac{T_w}{\text{Gear Ratio} * N_{eff}} \quad (8)$$

Motor speed

$$N_m = N_w * \text{Gear ratio} \quad (9)$$

3.2 Traction Motor

From Eqs. (6), (7) given above,

Motor power can be calculated as

$$P_{motor} = \frac{2 * \pi * N_m * T_m}{60 * N_{eff}} \quad (10)$$

3.3 Battery Calculations

From Eq. 11, battery power can be calculated.

$$\text{Battery power} = \frac{\text{Motor Power}}{C_{\text{eff.}} * B_{\text{eff.}}} \quad (11)$$

$$\text{Power/km} = \frac{\int \text{Battery Power}}{D * 3.6 * 10^6} \quad (12)$$

From Eq. 12, battery capacity can be obtained

$$\text{Battery Capacity (w/h)} = P/\text{km} * \text{Range} \quad (13)$$

Battery capacity in Ah is given as:

$$\text{Ah} = \frac{\text{Battery Capacity}}{\text{voltage}} \quad (14)$$

Battery Cell C-rating:

The term ‘C-rate’ is referred to the discharge current and will discharge the battery completely in hour. For a battery with a capacity of Ah, this equates to a discharge current of A.

$$\text{C-rate} = \frac{I}{\text{Ah}} \quad (15)$$

State of charge can be calculated as

$$\text{SOC} = 100 * \pm \int \frac{i}{3600 * \text{Ah}} dt \quad (16)$$

For the modeling of electric vehicle power train, some specification values of an electric bike are considered as an example for the simulation model.

The technical specifications of the considered model are given as follows:

The above specifications are used for the modeling of power train model. These are the values of electric bike considered as for modeling of electric vehicle powertrain.

4 Simulation and Modeling

The simulation is done in software’s like Scilab 6.0.2 and MATLAB R2019b with their simulation tool X-cos and Simulink, respectively. Modeling of EV powertrain is done with respect to WLTP drive cycle. This is mathematical equation-based graphical dynamic model. The mathematical Eqs. (9)–(16) are used to develop this simulation model.

As shown in Fig. 4, there are four subsystems for simulation model and that are:

- a. Vehicle dynamics
- b. Transmission

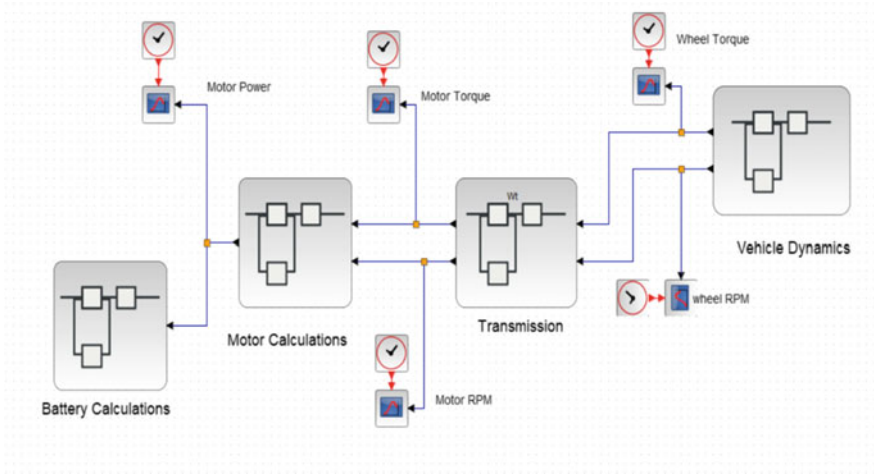


Fig. 4 Power train simulation modeling

- c. Motor calculation
- d. Battery calculation.

The resistive force modeling (Fig. 5) gives total tractive force required. Vehicle resistive forces like rolling, gradient, aerodynamic, and acceleration forces are simulated as per mathematical equation of vehicle performance analysis.

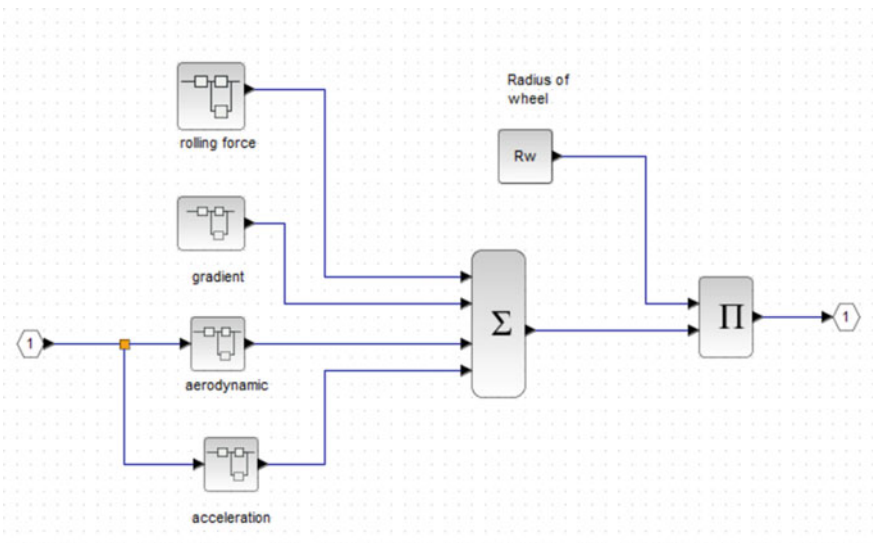


Fig. 5 Resistive force modeling

Battery current, discharge C-rate, battery power, and state of charge can be simulated as shown in Fig. 6.

Figure 7 shows model of state of charge (SOC) estimation. There are some methods for SOC estimation.

1. Coulomb counting/current integration method
2. Kalman filter-based method
3. Voltage measurement method.

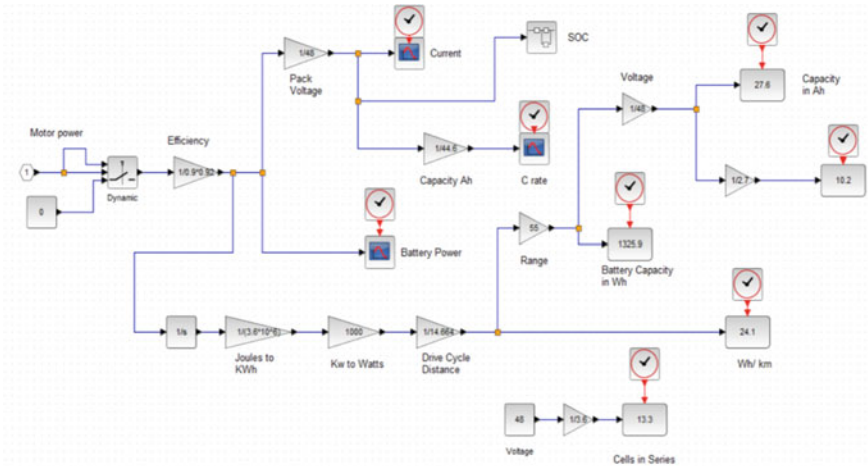


Fig. 6 Battery calculation simulation modeling

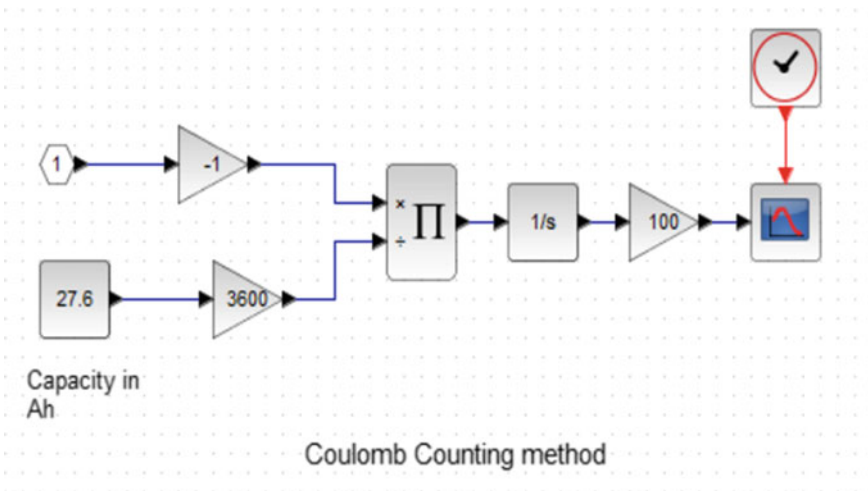


Fig. 7 Battery state of charge model

This simulation model shows Coulomb counting method.

5 Simulation Results

The results of powertrain simulation are obtained in graphical form. Values obtained by simulation are as per WLTP drive cycle data and vary as per technical specifications (Table 1) and vehicle data (Figs. 8 and 9).

- Nominal torque—4 Nm
- Peak torque—5 Nm
- Motor RPM—11,000 RPM (for 7.8).

Transmission gear ratio should be changed depending on wheel RPM and efficiency explained further (Figs. 10 and 11).

Table 1 Technical specifications of system model

Sr.	Specifications	Values
1	Mass of the vehicle	110 kg
2	Load on the vehicle	80 kg
3	Required speed	From WLTP drive cycle data in m/s
4	Frontal area	0.875 m ²
5	Battery voltage	48 V
6	Range	55 km
7	Transmission gear ratio	7.8: 1

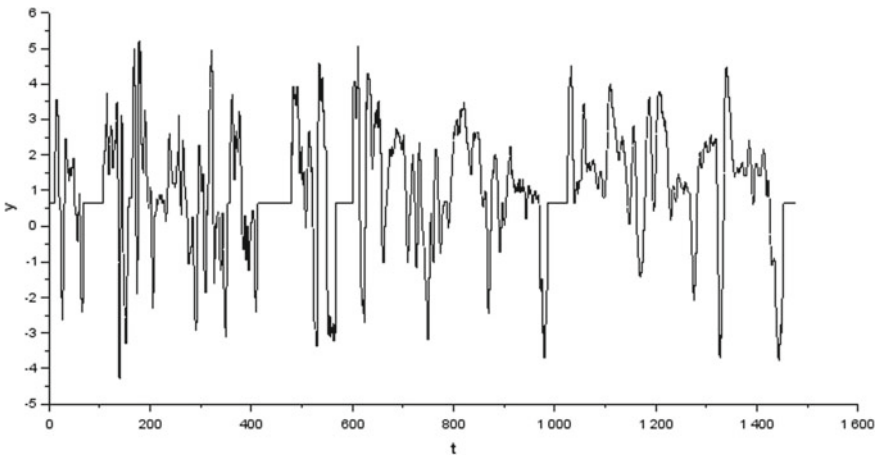


Fig. 8 Motor torque (nm)

- Nominal torque - 4 Nm
- Peak torque - 5 Nm

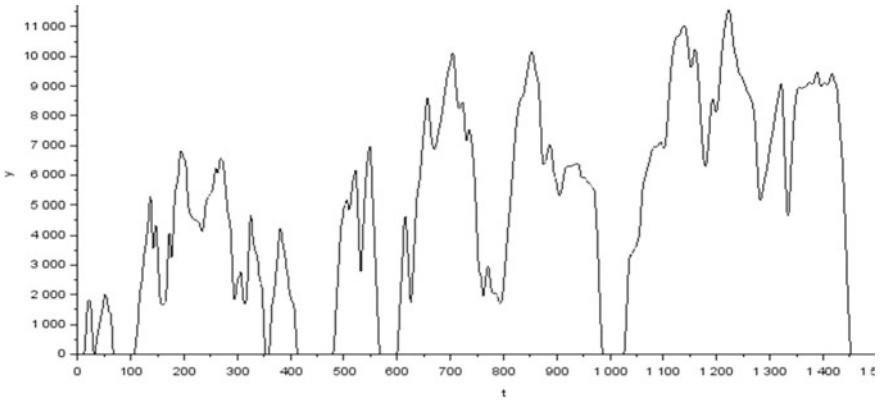


Fig. 9 Motor speed (RPM)

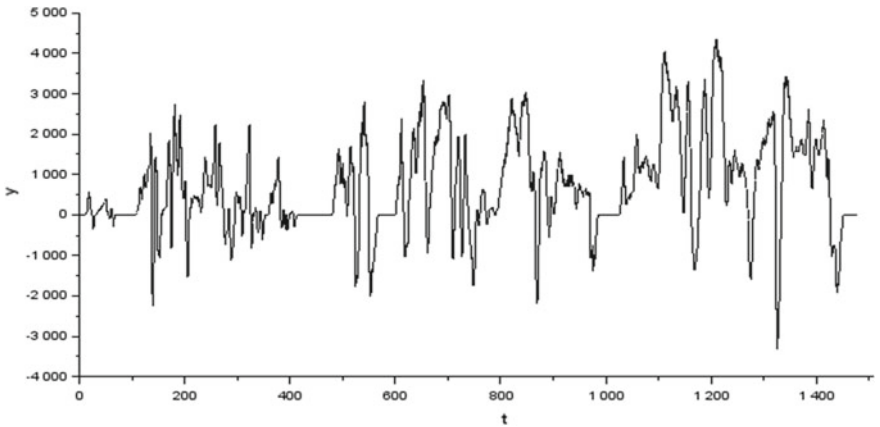


Fig. 10 Motor power (W)

- Nominal power—3 kW
- Peak power—5 kW
- Battery power—3 kW
- Battery peak power—5 kW.

Battery discharge power is the same as motor power while considering motor and controller efficiencies (Figs. 12 and 13).

- Nominal discharge current—70 A
- Peak discharge current—100 A
- Discharge C-rate—1.5

- Nominal power - 3 kw
- Peak Power – 5 kw

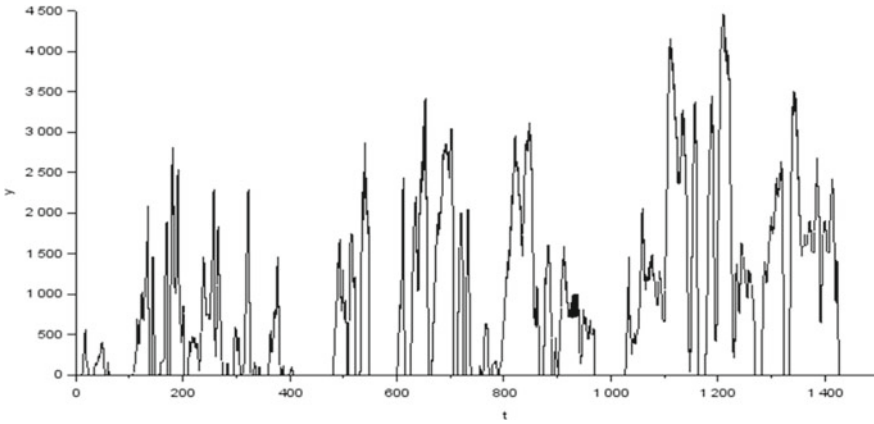


Fig. 11 Battery power (W)

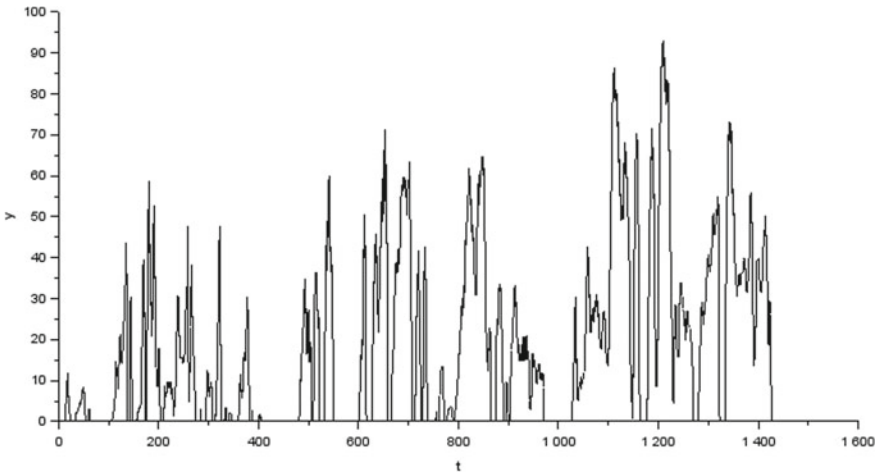


Fig. 12 Battery current (A)

- Peak C-rate—2.

Discharge C-rate should not exceed cell C-rate value and that should be under 3C (Fig. 14).

This state of charge (SOC) graph shows battery discharge up to 84% for 1400 s of WLTP drive cycle vehicle run.

- Nominal discharge current - 70 A
- Peak discharge current - 100 A

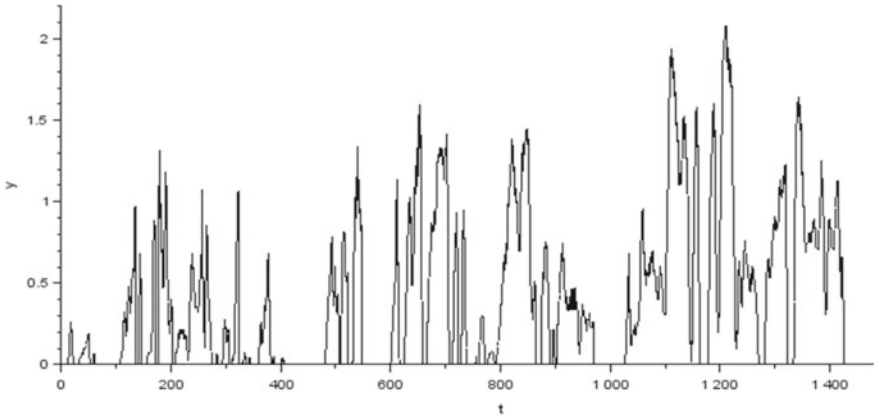


Fig. 13 Battery discharge C-rate

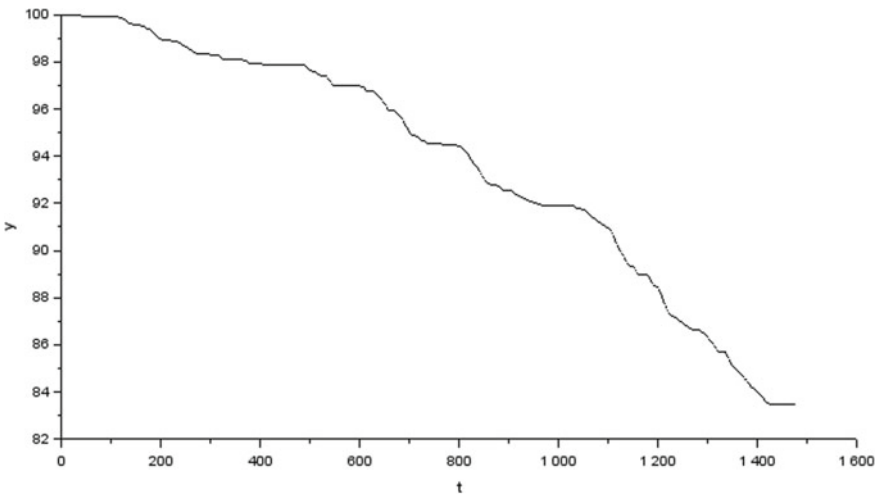


Fig. 14 State of charge (SOC) %

6 Powertrain Optimization

The EM efficiency model was developed with data obtained from the smart electric vehicle trial for efficiency modulation. The negative values shown in this efficiency map denote the regenerative energy developed in electric machine. The combined electric motor and inverter controller are represented as an efficiency map and as a function of torque and speed, as shown in figure.

The diagram given here (Fig. 15) shows the efficiency map of electrical motor. This map is obtained from MATLAB/Simulink simulation model. This is speed versus torque graph of electric machine showing the efficiency region (Fig. 16).

For the component sizing of electric motor, some measures must be taken into consideration such as weight of vehicle, acceleration required for total load, top speed and grade ability of the system. For battery pack optimization, pack energy, pack power, cell C-rating, and thermal equilibrium of battery can be optimized as per efficiency map. The battery discharge current, cell C-rating, state of charge and

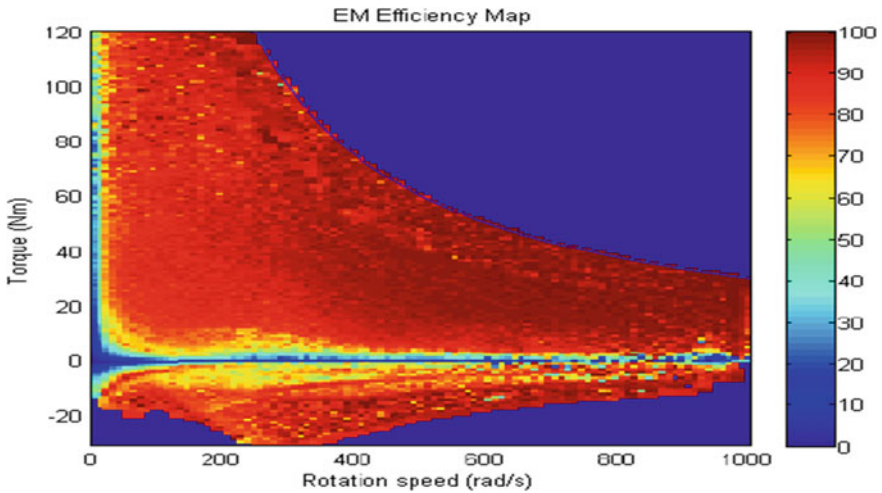


Fig. 15 Efficiency map of electrical machine

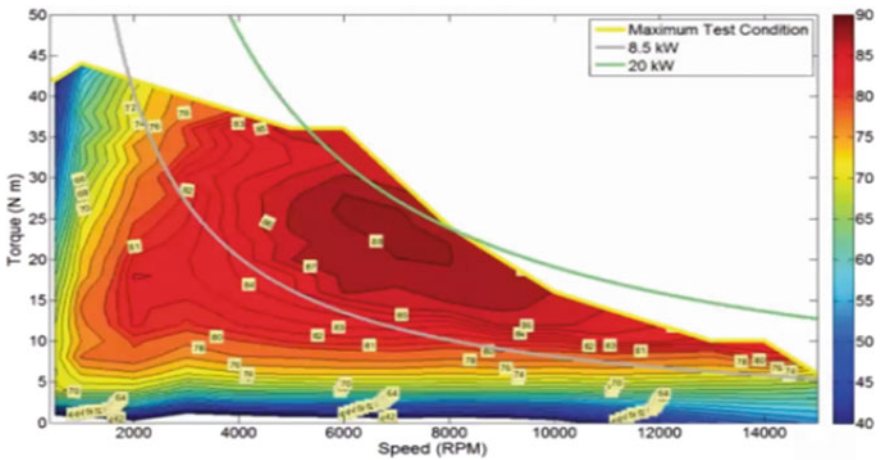


Fig. 16 Efficiency region of electrical motor

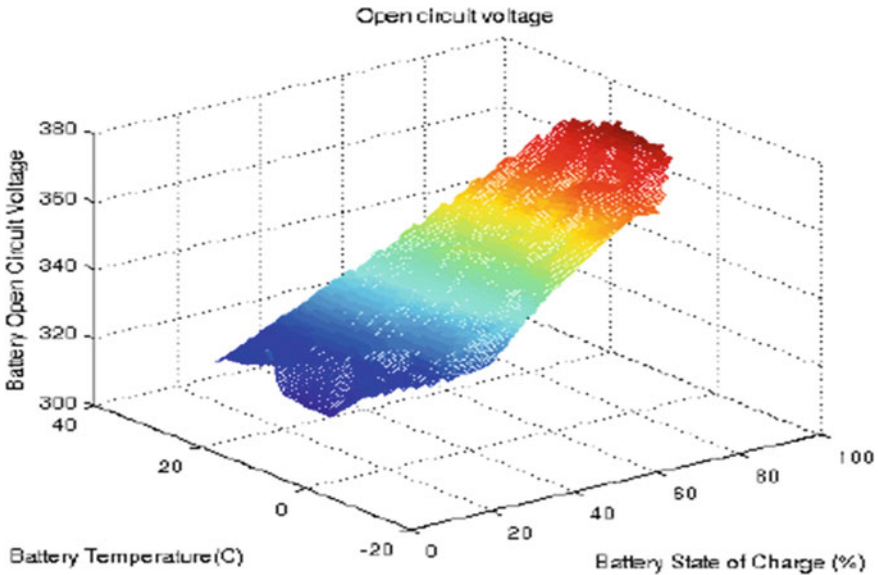


Fig. 17 Efficiency map of battery

cell current measurements of the accumulator battery pack were obtained from the controller area network (CAN) interface. Control area network is information protocol used in the battery management system (BMS).

The three-dimensional graph (Fig. 17) shows the efficiency graph of the electric vehicle battery pack with respect to the cell open-circuit voltage (OCV), battery state of charge (SOC), and battery temperature.

For the optimization of the electric vehicle power train, the following measures describe the scenario to achieve maximum efficiency.

- Prediction of sub-system and EV components behavior.

From the simulation model of powertrain, it is observed that the behavior of electrical components changes with the change in dynamic conditions of the vehicle.
- Prediction and calculation of component sizing.

The size or the power rating of the electrical subsystem components are predicted by results obtained and by calculating power requirements.
- Prediction of energy consumption by the component with considering drive cycle part.

Accurate power rating of sub-system components is obtained. This power rating selected w.r.t. drive cycle part of the vehicle as WLTP drive cycle has max speed of 85.2 kmph.
- Optimization of component sizing with respect to efficiency of the component.

As the prediction of motor and battery power is done with the help of simulation results. Then optimization of subsystem components is required, in order to achieve maximum efficiency.

- Prediction of energy consumption.

The power prediction is to be done as the vehicle specification and requirement. The figure shows that battery power is predicted by comparing with vehicle specification. The shaded part denotes the predicted battery power after optimization.

- Lifecycle analysis.

The lifecycle of powertrain subsystem is an important aspect especially for the battery pack. The Li-ion cells of battery pack have specific life cycles such as 1000–5000 charge discharge cycles.

This analysis of lifecycle is done by calculating energy density of the cell and state of health (SOH). Battery structure optimization is possible with:

- parameterized cell modeling of battery
- Cells connected in series
- Cells connected in parallel [5].

7 Conclusions

In this model, we have designed the electric vehicle powertrain and to achieve efficiency and performance of EV with some optimization techniques. When developing a powertrain of electric vehicle, there is necessity as it the dynamic model as it is important for the modeling and simulation as it gives value data of critical dynamic conditions. In powertrain sizing, the vehicle range and performance are taken into interest. The powertrain is designed to improve range of the vehicle and maximize the performance output. The variation in powertrain calculations is considered while modeling with dynamic conditions. The proposed method of electric vehicle powertrain modeling is for improving the stability of the system and the performance of system under dynamic condition. Powertrain can be designed to work at high efficiency to reduce the powertrain losses and achieve desired power outputs. The optimization of power train is most efficient and important for component sizing and modeling. We can build up battery pack and optimize electrical machine by using static efficiency maps. The efficiency maps are obtained by MATLAB simulation. The data was obtained by the vehicle testing and diagnosis. This paper is developed with the intention to achieve the optimized performances and powertrain efficiency.

References

1. M. Karamuk, Review of electric vehicle powertrain technologies with OEM perspective, in *2019 International Aegean Conference on Electrical Machines and Power Electronics*
2. L. Gangurde, A. Gawande, S. Khanvilkar, A. Khochare, P. Dave, Modelling and control of electric car powertrain, in *2019 1st International Conference on Innovations in Information and Communication Technology (ICIICT)*
3. I. Husain, *Electric and Hybrid Vehicles Design Fundamentals*, 2nd edn. (CEC Press). ISBN: 978-1-4398-1175
4. Drive cycle data analysis, <https://www.sciencedirect.com/topics/engineering/driving-cycle>
5. N. Janiaud, F.-X. Vallet, M. Petit, G. Sandou, Electric vehicle powertrain simulation to optimize battery and vehicle performances, in *2010 IEEE Vehicle Power and Propulsion Conference* (2010). <https://doi.org/10.1109/vppc.2010.5729141>

Static 2D-Finite Element Analysis of Eccentricity Fault in Induction Motor



E. Fantin Irudaya Raj  and M. Appadurai 

Abstract Thanks to its robust design and versatile operating characteristics, the three-phase induction motor is increasingly popular in high-power applications. One of the most critical and extreme faults that often occur in the induction motor is eccentricity. This is primarily due to shaft dislocation or friction between the shaft and the rotor. In industrial applications, eccentricity detection and analysis are, therefore, essential to prevent production losses. This paper explores how to model the induction motor using the Ansys Maxwell finite element software package and Infolytica MagNet software package for eccentricity fault analysis. The present work focuses on the identification of static eccentricity fault. For this purpose, the static 2D analysis was conducted for faulty and healthy conditions. Comparisons are made between the conditions by considering different parameters such as stored magnetic energy, flux linkage, and flux density.

Keywords Induction motor · Eccentricity fault · Induction motor · Finite element analysis

1 Introduction

In all modern industries, rotating machines play a significant role. Several types of rotating machines are used in industries in which the induction machine is the highly used one because of its reduced economic cost and flexible operating characteristics. The three-phase induction motor is desired when going for high-power ratings. A recent study says 75% of the electric motor used in industry is induction motor. Due to the failure of mechanical components such as gears and bearings, mechanical faults in electrical machines may occur. In electric machines, mechanical faults are normal

E. Fantin Irudaya Raj (✉)

Department of Electrical and Electronics Engineering, Dr. Sivanthi Aditanar College of Engineering, Tiruchendur, India

M. Appadurai

Department of Mechanical Engineering, Dr. Sivanthi Aditanar College of Engineering, Tiruchendur, India

© The Author(s), under exclusive license to Springer Nature Singapore Pte Ltd. 2022
M. L. Kolhe et al. (eds.), *Smart Technologies for Energy, Environment and Sustainable Development, Vol 1*, Springer Proceedings in Energy,
https://doi.org/10.1007/978-981-16-6875-3_33

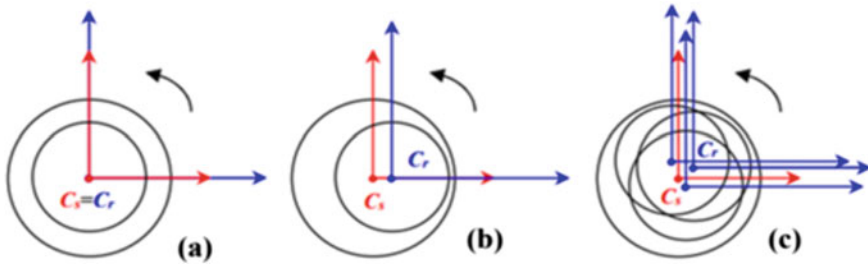


Fig. 1 a Induction motor cross-sectional view in normal state b in the state of static eccentricity c in the state of dynamic eccentricity

and reflect up to 50–60% of the defects. The critical and harmful faults between the stator and the rotor include bearing faults and eccentricity faults [1]. Static, dynamic, and mixed eccentricities are various types of eccentricities. Figure 1 displays the different cross-sectional views of the healthy condition of the induction motor with various forms of eccentricities happened in machine.

In normal healthy condition of the motor, the rotor geometric axis and stator geometric axis are the same. Figure 1a shows the induction motor in a healthy state. At the time of static eccentricity, the stator and rotor geometric axis are not the same. The rotor tends to rotate about its own geometric axis. Figure 1b shows the static eccentricity of the induction machine. At the time of dynamic eccentricity, the rotor is not concentric. It starts to rotate around the geometric axis of the stator. Due to eccentricity, mechanical vibrations can occur in the motor, which will decrease the machine's life span. Vibrations will also lead to acoustic problems. There would be an unbalanced magnetic pull that contributes to winding damage resulting from stator and rotor rub. In order to protect induction motors against failure and permanent damage, identification of such faults is therefore necessary.

By using the finite element model, the conventional equivalent circuit model is defined. For a three-phase squirrel cage induction motor, it is used to evaluate the equivalent circuit components. Fast execution time is obtained by using minimal models. They used distinct finite element models for the rotor and the stator separately in this process [2]. By using finite element methodology and online current monitoring system, eccentricity level determination of the faulty motor and the current in stator coils is computed. The current amplitude is predicted by using the frequency component analysis which excludes the fifth- and seventh-order harmonics [3]. Induction motor modeling and analysis are carried out using the winding function method and the method of finite element analysis. Harmonics analysis for stator current is carried out, and the findings are compared for both healthy and defective machines. The finite element method has been shown to be the best strategy [4]. In the study, in three-phase induction motor, the inter-turn fault is noted and analyzed. The static analysis is achieved by using finite element analysis for healthy condition of the motor and the different eccentricity fault conditions, then after the measurements

Table 1 Induction machine data

Components	Dimensions
Core length (in inches)	2.5
Outer diameter of stator (in inches)	8.188
Airgap length (in inches)	0.013
Length of rotor slot (in inches)	0.532
Shaft diameter (in inches)	1.357
Inner diameter of stator (in inches)	4.875
Skew	0.425
Rated voltage, V	415
Rated power, hp	30
Rated frequency, Hz	50
The number of rotor slots	28
The number of stator slots	36
Number of poles	4

are tabulated [5]. In this paper, the three-phase induction machine in the closed-loop system is used and the rotor eccentricity fault is identified. The artificial neural network is used to distinguish harmonics in voltage and current waveforms [6]. In this work, the method of high-frequency pulse injection is utilized to locate the different types of eccentricities. It is done by calculating variance in the current of switched reluctance motor [7]. In this work, voltage source inverter fed three-phase induction motor is designed using FEA and the electromagnetic functionality at the time of different fault condition is analyzed [8]. In this paper, the authors presented and criticized several eccentricity fault diagnosis indices. The benefits, disadvantages, and unclear points of each index are discussed, as well as the potential basis for the development of these techniques [9]. In this paper, parameters such as torque, radial airgap flux density, and FFT spectrum are monitored and analyzed for healthier and eccentricity fault conditions using finite element method, and a three-phase PWM inverter fed induction motor is modeled [10].

To find the eccentricity fault, the above papers used different methodologies. In the present work, through static 2D finite element analysis of the induction motor in healthy and defective environments, detecting the eccentricity faults. The investigation is carried out using the Ansys Maxwell finite element software package and Infolytica MagNet software package. The induction motor is designed by using the Ansys Maxwell, and the static 2D analysis is carried out by using MagNet. To carry out the analysis, we made certain assumptions. They are (1) The magnetic field is negligible outside the periphery of the motor, (2) The effects of hysteresis are ignored, (3) The magnetic field is axially distributed in the direction of the motor and it is constant, (4) Disregarded the currents of displacement [11–14].

Table 1 displays the design information of the three-phase induction motor. The methodology is more focused on field solutions. In this model, the motor is considered to be having a double cage winding. The adopted configuration in stator is star

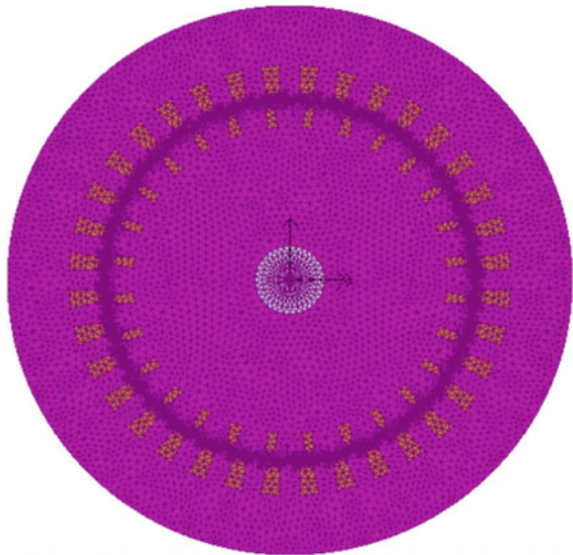
connection. It is assumed that the slots/pole per phase is 3 and 0.7 mm is set to be as air gap length. It is assumed that each portion of the field quantity varies sinusoidally with respect to time. For the high-quality design model, length-to-pole pitch ratio is also assumed as 1 and 0.45 Wb/m^2 is taken as the average flux density [15, 16].

2 Finite Element Model of the Three-Phase Induction Motor

Finite element modeling is becoming ever more popular nowadays. It is all because of the freedom in the simulation of finite elements in terms of geometry distribution and reinforcement, interface, and mechanical properties. It is the most widely used method for solving problems of engineering and mathematical modeling. The finite element method (FEM) is a basic computational process for solving partial differential equations in more than one space variables. In FEM, a large structure is subdivided into smaller parts, it is known as finite elements. In the FEM formulation of a boundary value, a system of algebraic equations finally results. This method approximates the function over the unknown domain [17, 18].

Figure 2 shows the prototypical of the three-phase induction motor developed by using the Maxwell finite element analysis software package. The shaft of the induction motor is made by using stainless-steel material which is in S430 grade, and the stator and the rotor are made up of silicon steel stampings. The stator and rotor carry copper windings. Depending upon the analysis, the number of stator and rotor windings and the turns are engineered.

Fig. 2 Induction motor model by Maxwell



3 Static Analysis

The 2D static analysis is carried out by using MagNet software package. The induction motor, which is designed by using the Maxwell, is imported into MagNet. The simulated results for the three-phase squirrel cage induction motor with static analysis of the motor without eccentricity fault and the defective motor with 10, 20, and 30% of eccentricity at the time of full-load condition are presented in the below section.

3.1 Flux Distribution and Magnetic Field

In the healthy condition of the motor, under full-load operation, the magnetic field and flux distribution of the induction motor are symmetrical. At the time of different eccentricity conditions—10, 20, and 30% eccentricity, we can observe unsymmetrical flux distribution [19, 20]. We can conclude that a lower degree of magnetic saturation and higher degree of magnetic saturation is detected in the maximum air gap and minimum air gap sections, respectively. It can be seen from Figs. 3 and 4 that as the eccentricity level increases, plots tend to change their symmetry dramatically.

The same simulation work is carried forward against a three-phase induction motor's half load and no-load conditions. We can sense the change in stored magnetic energy at the time of different load conditions and with various eccentricities. As eccentricity increases, the stored magnetic energy is also getting increased. The simulated results are listed out in Table 2. A graphical representation shown in Figs. 5 and 6 represents the magnetic energy stored in Joules and change in the stored magnetic energy in percentage.

From the above graphs, we can observe the value of magnetic energy stored is increasing at the time when eccentricity value gets augmented.

3.2 Field Profile and Flux Profile

When the motor is in normal healthy state, the flux density and the distribution of flux function are symmetrical, while at the time of eccentricity fault occurs, these become unsymmetrical [21]. The field and flux distribution are evaluated with respect to the circumference that is measured in millimeters.

It is observed from Figs. 7 and 8 that as the eccentricity percentage increases, in the minimum and maximum airgap, the waveform alters its symmetry nature. The same type of analysis is carried forward toward the three-phase induction motor with half load and no-load conditions. The values obtained through simulation are listed in Table 3.

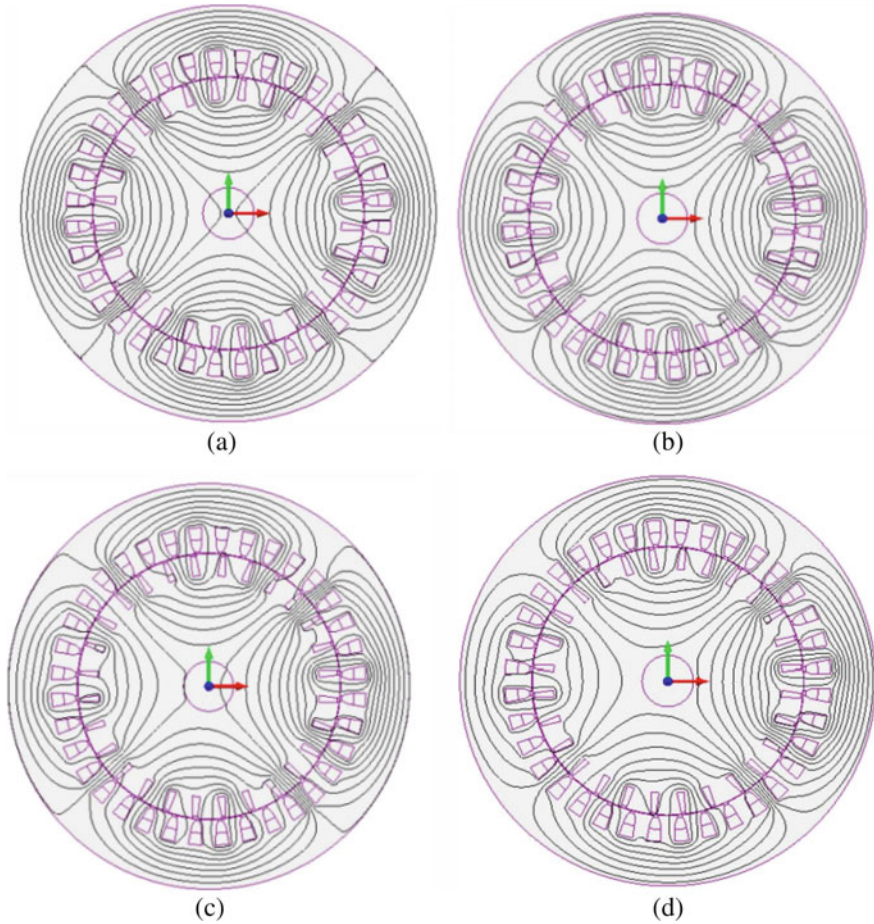


Fig. 3 Distribution of magnetic field—full-load condition **a** motor in healthy condition, **b** motor with 10% of eccentricity fault, **c** with 20% of eccentricity fault, **d** with 30% of eccentricity fault

From Table 3, it is observed that under different load conditions and different levels of eccentricities, flux function has been increased in minimum air gap and decreased in maximum air gap. Figures 9 and 10 show the graphical representation of flux function at a minimum and maximum air gap, respectively.

Figures 9 and 10 display the flux function change at the minimum airgap and maximum air gap, respectively. At the maximum air gap section, the flux function and flux density are decreased and they are increased at the minimum air gap, as can be seen from the graphs.

In normal healthy conditions, the values of flux density and flux function are calculated using an experimental setup in the laboratory. These values are compared with the simulated values. The simulated values are allied with the theoretically calculated values. From this point, we can validate our induction motor model, which

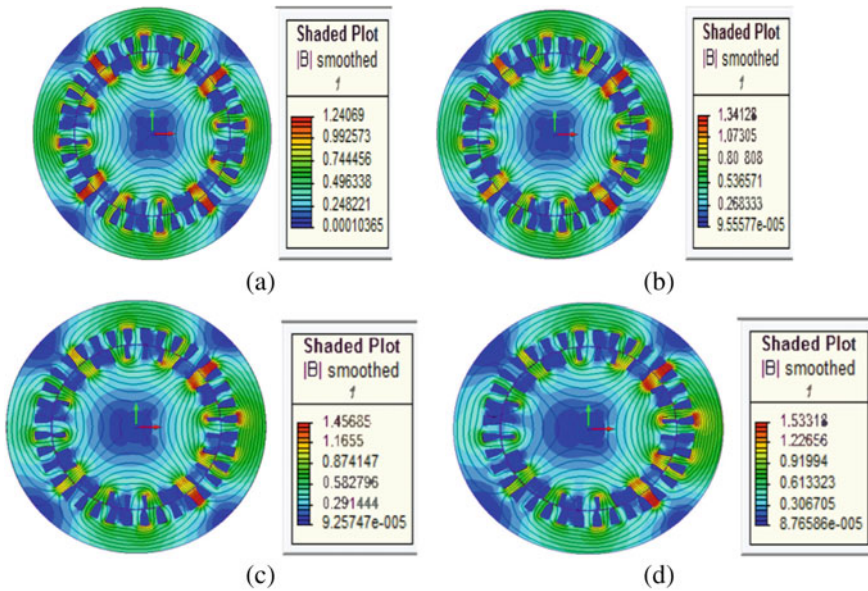


Fig. 4 Distribution of flux—full-load condition **a** motor in healthy condition, **b** motor with 10% static eccentricity, **c** 20% static eccentricity, **d** 30% static eccentricity

is designed by using Maxwell and analysis carried out by MagNet software packages. From this, we can conclude that the values obtained at the time of eccentricity faults are also more reliable. The values of flux density and flux function under healthy condition obtained through simulation and experimental setup in the laboratory are listed in Table 4.

4 Conclusion

The static 2D analysis is conducted under healthy and different eccentricity fault conditions for the three-phase induction motor. Through this analysis, we can obtain the results such as whenever the percentage of eccentricity increased the stored magnetic energy also get increased. In a similar way, through the static analysis we also obtain the results as at the minimum air gap position, the flux density, and flux function are increased. And, when the eccentricity percentage is increased, the value of flux density and flux function is decreased in maximum air gap position. In order to validate the simulated value such as flux density and flux function, the simulated results are experimentally tested. The results are more convincing. The work is further extended to static 3D and transient 2D and 3D analysis.

Table 2 Induction machine data

Motor condition		Magnetic energy stored (J)	Change in Percentage (%)
Full-load condition	Healthy motor	0.05210	Nil
	Motor with 10% eccentricity	0.05531	7.6
	Motor with 20% eccentricity	0.05712	8.8
	Motor with 30% eccentricity	0.05821	10.3
Half load condition	Healthy motor	0.01213	Nil
	Motor with 10% eccentricity	0.01422	3.8
	Motor with 20% eccentricity	0.01512	5.1
	Motor with 30% eccentricity	0.01631	7.4
No-load condition	Healthy motor	0.00051	Nil
	Motor with 10% eccentricity	0.00053	3.8
	Motor with 20% eccentricity	0.00054	5.7
	Motor with 30% eccentricity	0.00055	7.6

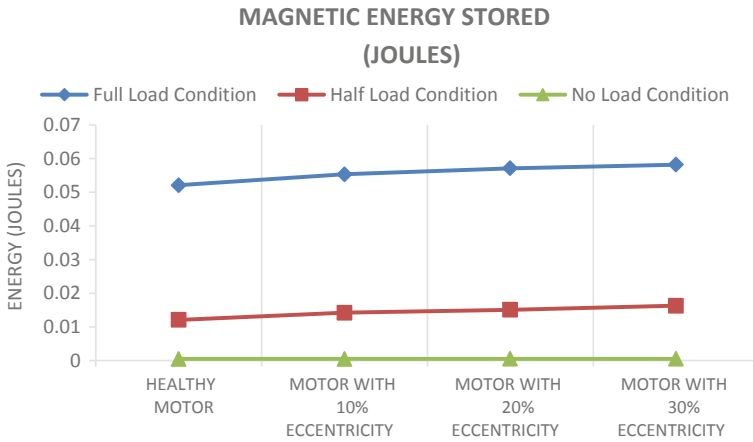


Fig. 5 Stored magnetic energy (J) under different load conditions and eccentricities

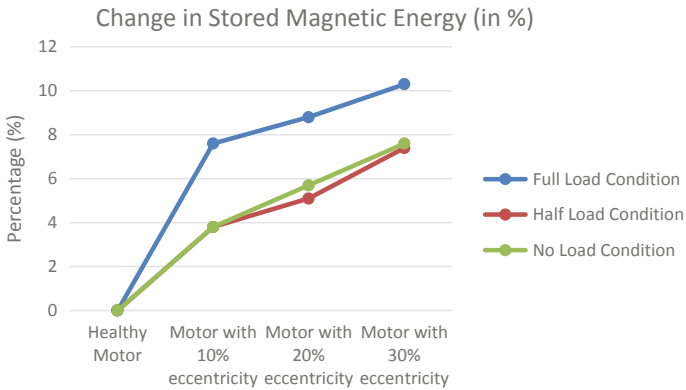
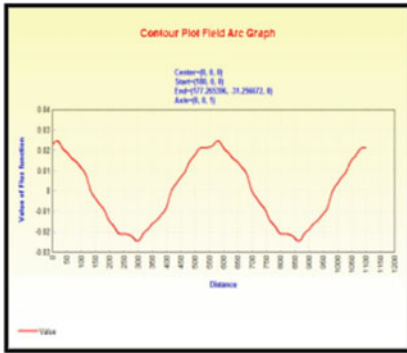
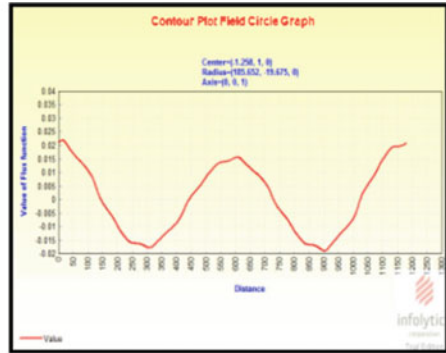


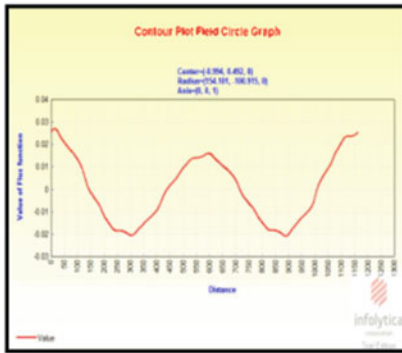
Fig. 6 Change in stored magnetic energy in percentage at the time of different load conditions and various eccentricities



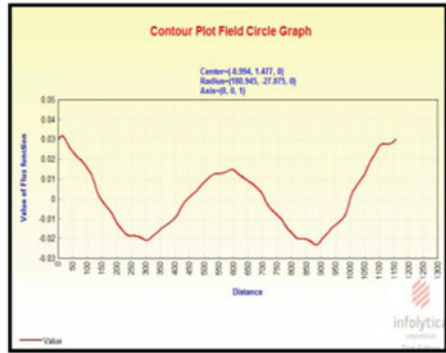
(a)



(b)



(c)



(d)

Fig. 7 Field distribution—full-load condition **a** motor in normal condition, **b** motor with 10% eccentricity fault, **c** with 20% eccentricity fault, **d** with 30% eccentricity fault

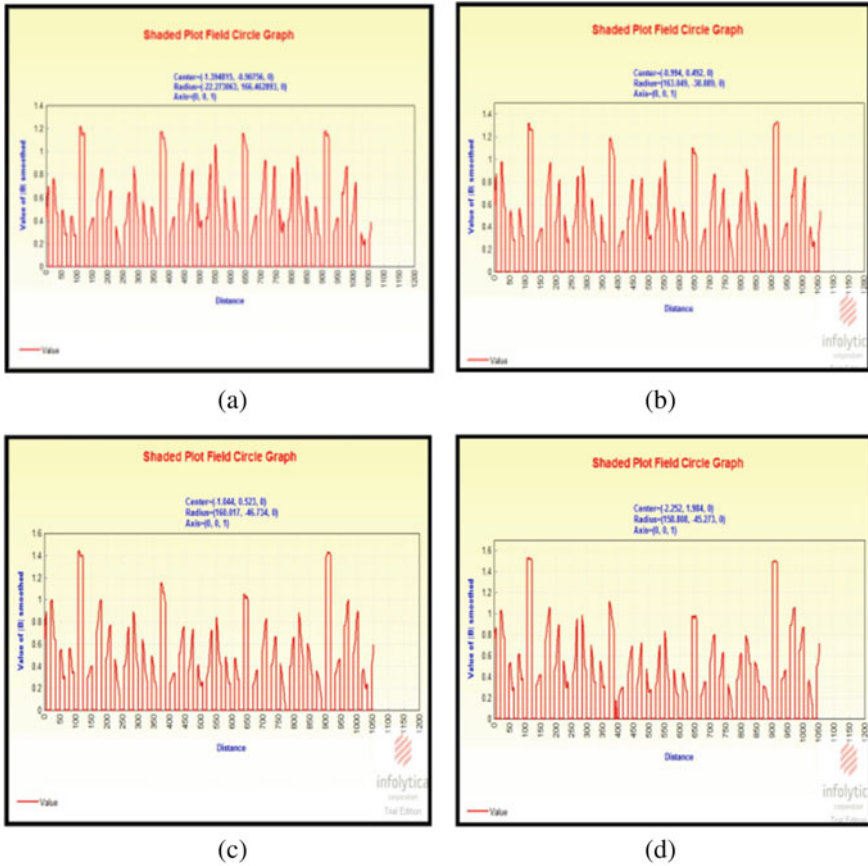


Fig. 8 Flux distribution—full-load condition **a** motor in normal condition, **b** motor with 10% eccentricity fault, **c** motor with 20% eccentricity fault, **d** motor with 30% eccentricity fault

Table 3 Flux function

Motor condition		Flux function (Wb) in minimum air gap	Change in percentage (%)	Flux function (Wb) in maximum air gap	Change in percentage (%)
Full-load condition	Healthy motor	0.0282	Nil	0.0284	Nil
	Motor with 10% eccentricity	0.0331	18.01	0.0269	-6.01
	Motor with 20% eccentricity	0.0384	34.12	0.0243	-12.96
	Motor with 30% eccentricity	0.0431	65.42	0.0209	-24.34
Half load condition	Healthy motor	0.0147	Nil	0.0147	Nil
	Motor with 10% eccentricity	0.0169	16.10	0.0136	-12.06
	Motor with 20% eccentricity	0.0181	24.90	0.0126	-17.96
	Motor with 30% eccentricity	0.0291	41.62	0.0106	-27.99
No-load condition	Healthy motor	0.0027	Nil	0.0027	Nil
	Motor with 10% eccentricity	0.0031	13.69	0.0023	-5.91
	Motor with 20% eccentricity	0.0035	18.10	0.0021	-14.01
	Motor with 30% eccentricity	0.0039	42.13	0.0019	-26.36

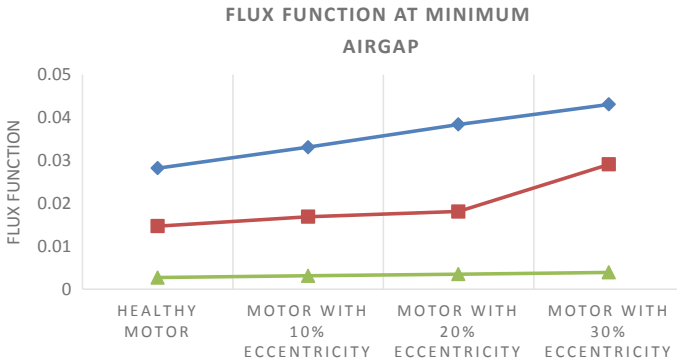


Fig. 9 Flux function at minimum air gap—a graphical representation

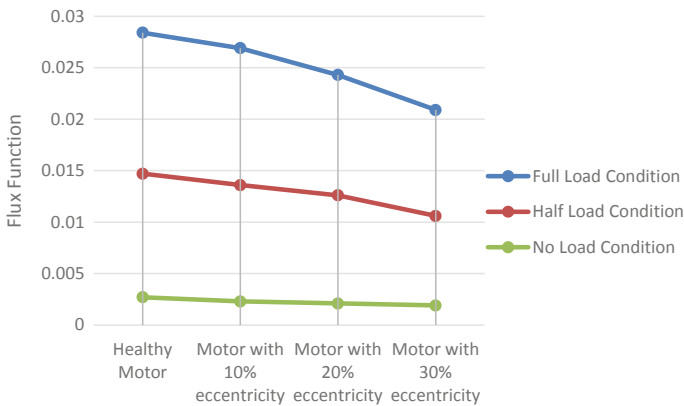


Fig. 10 Flux function at maximum air gap—a graphical representation

Table 4 Validation of results

When the motor in healthy condition	Flux density (Wb/m ²)	Flux function (Wb)
Experimental value	0.6741	0.0224
Simulated value	0.6902	0.0228

References

1. A.M. Trzynadlowski, M. Ghassemzadeh, S.F. Legowski, Diagnostics of mechanical abnormalities in induction motors using instantaneous electric power. *IEEE Trans. Energy Convers.* **14**(4), 1417–1423 (1999)
2. S. Williamson, M.J. Robinson, Calculation of cage induction motor equivalent circuit parameters using finite elements. *IEE Proc. B (Electr. Power Appl.)* **138**(5), 264–276 (1991)
3. W.T. Thomson, A. Barbour, On-line current monitoring and application of a finite element method to predict the level of static airgap eccentricity in three-phase induction motors. *IEEE*

- Trans. Energy Convers. **13**(4), 347–357 (1998)
4. J. Faiz, B.M. Ebrahimi, H.A. Toliyat, Effect of magnetic saturation on static and mixed eccentricity fault diagnosis in induction motor. *IEEE Trans. Magn.* **45**(8), 3137–3144 (2009)
 5. K. Yamazaki, S. Kuramochi, N. Fukushima, S. Yamada, S. Tada, Characteristics analysis of large high-speed induction motors using 3-D finite element method. *IEEE Trans. Magn.* **48**(2), 995–998 (2012)
 6. X. Huang, T.G. Habetler, R.G. Harley, Detection of rotor eccentricity faults in a closed-loop drive-connected induction motor using an artificial neural network. *IEEE Trans. Power Electron.* **22**(4), 1552–1559 (2007)
 7. H. Torkaman, E. Afjei, Comprehensive detection of eccentricity fault in switched reluctance machines using high-frequency pulse injection. *IEEE Trans. Power Electron.* **28**(3), 1382–1390 (2012)
 8. B.H. Priya, R. Karthick, B. Lokprakash, S. Vasanth, N.K. Praveen, Static eccentricity fault analysis in inverter fed induction motor using finite element method. *IOP Conf. Ser. Mater. Sci. Eng.* **872**(1), 012049 (2020)
 9. J. Faiz, H. Nejadi-Koti, Eccentricity fault diagnosis indices for permanent magnet machines: state-of-the-art. *IET Electr. Power Appl.* **13**(9), 1241–1254 (2019)
 10. S. Viswanath, N.P. Kumar, T.B. Isha, Static eccentricity fault in induction motor drive using finite element method, in *Advances in Electrical and Computer Technologies* (Springer, Singapore, 2020), pp. 1291–1302
 11. M. Appadurai, E. Fantin Irudaya Raj, Finite element analysis of lightweight robot fingers actuated by pneumatic pressure, in *Recent Advances in Manufacturing, Automation, Design and Energy Technologies* (pp. 379–385). Springer, Singapore (2022)
 12. M. Appadurai, E. Raj, Epoxy/silicon carbide (sic) nanocomposites based small scale wind turbines for urban applications. *Int. J. Energy Environ. Eng.* 1–16 (2021)
 13. M. Appadurai, E.F.I. Raj, Finite element analysis of composite wind turbine blades, in *2021 7th International Conference on Electrical Energy Systems (ICEES)* (pp. 585–589). IEEE (2021, February)
 14. M. Appadurai, E.F.I. Raj, K. Venkadeshwaran, Finite element design and thermal analysis of an induction motor used for a hydraulic pumping system. *Mater. Today Proc.* **45**, 7100–7106 (2021)
 15. E.F.I. Raj, M. Balaji, Analysis and classification of faults in switched reluctance motors using deep learning neural networks. *Arab. J. Sci. Eng.* **46**(2), 1313–1332 (2021)
 16. E.F.I. Raj, M. Appadurai, The hybrid electric vehicle (HEV)—an overview, in *Emerging Solutions for e-Mobility and Smart Grids*, pp. 25–36 (2021)
 17. A.C. Sijini, E. Fantin, L.P. Ranjit, Switched reluctance motor for hybrid electric vehicle. *Middle-East J. Sci. Res.* **24**(3), 734–739 (2016)
 18. E.F.I. Raj, V. Kamaraj, Neural network based control for switched reluctance motor drive, in *2013 IEEE International Conference on Emerging Trends in Computing, Communication and Nanotechnology (ICECCN)* (pp. 678–682). IEEE (2013, March)
 19. E. Fantin Irudaya Raj, M. Appadurai, Minimization of torque ripple and incremental of power factor in switched reluctance motor drive, in *In Recent Trends in Communication and Intelligent Systems: Proceedings of ICRTCIS 2020* (pp. 125–133). Springer Singapore (2021)
 20. V. Gampala, M.S. Kumar, C. Sushama, E.F.I. Raj, Deep learning based image processing approaches for image deblurring, in *Materials Today: Proceedings* (2020)
 21. K. Priyadarsini, E.F.I. Raj, A.Y. Begum, V. Shanmugasundaram, Comparing DevOps procedures from the context of a systems engineer, in *Materials Today: Proceedings* (2020)

The Saturated Core Fault Current Limiter in Modern Power Systems—A Laboratory Model Test Results



Vittesh Naphade, Kiran Naphade, and Vilas Ghate

Abstract Recently, the power sector across the world had seen substantial growth in power demand and generation. The use of local power resources (distributed generation) is also trending along with the paralleling of power networks. These traits led to a rise in short-circuit current in the power system networks. The level of short-circuit current became so high, nowadays, that it reached or nearing the breaking capacity of the circuit breakers. The components of the system are, in turn, overstressed. The protection from these damaging short-circuit current becomes inevitable and a challenge before the power engineers. The power industry is looking at the development of fault current limiter (FCL) technology as a solution to the problem. The introduction of reliable fault current limiter technology can lengthen the service life of equipment in the power industry. This paper reports the experiment on saturated core fault current limiter (SCFCL) technology. The results have demonstrated that the short-circuit peak fault current has reduced with a significant clipping factor. Also, the insertion voltage drop lies within the general limit for different DC bias. An optimum DC bias is required to cause an agreement between the clipping ability and the device contribution to the insertion voltage drop in the system.

Keywords Clipping factor · Fault current limiter · Insertion impedance

V. Naphade (✉)

Department of Electrical Engineering, R. H. Sapat College of Engineering, Nashik, Maharashtra, India

K. Naphade

Department of Electrical Engineering, LOGMIEER, Nashik, Maharashtra, India

V. Ghate

Department of Electrical Engineering, Government College of Engineering, Amravati, Maharashtra, India

1 Introduction

The growth in demand and generation, the influx of power quality sensitive loads, distributed generations, and interconnections have characterized the modern power systems. Though these traits increased flexibility and economy, it posed a severe challenge in terms of escalation of short-circuit current. The level of short-circuit current, at places, even exceeds the circuit breaker capacity [1]. These short-circuit currents, traditionally, have been controlled with the help of apparatus measures like the use of series reactors, high impedance transformers, fuses, and large rating circuit breakers. Also, the busbar splitting, splitting of grid networks, etc., have been the topological measures to control these currents. But, all these measures had possessed with drawbacks. Like, series reactors and high impedance transformers have losses and contribute to voltage drops, fuse requires manual replacements and is limited to low voltage applications, and circuit breakers operate at current zeros. The splitting measures, however, decrease the economy and reliability of supply systems.

Power engineers, therefore, felt a need for a solution that can control the magnitude of these short circuit current and, at the same time, allow optimized power system operations. An enabling technology option in terms of fault current limiters has recently been a topic of research. FCL imposes low impedance in its steady-state and high impedance during transient state. It can limit the magnitude of these high short-circuit currents and prolong the upgradations or replacements of costly circuit breakers.

There are many types of FCLs like superconducting resistive FCLs [2, 3] solid-state FCLs [4], and saturated core type FCLs [5]. The superconducting FCLs relies on the superconductor property of low resistance at the steady-state condition and very high resistance at the transient condition. As its operation involve a transition from low-impedance state to high-impedance state, they suffer from slow reaction and recovery after having a short circuit. The solid-state FCLs use power electronic switches (IGBTs) that triggers after a current crosses a preset value. Although it offers low impedance during normal steady-state operation, they have high power losses during limiting-state operations.

The research on SCFCL has been at the center stage in recent years, particularly for MV and HV applications. The technology is still not commercialized, and major work has only been carried out on the modeling and simulation of the device to date. The SCFCL is a variable nonlinear inductor that offers negligible impedance under steady-state and trigger high impedance under fault-state of the system. It has, comparatively, negligible losses during the un-faulted, steady-state condition and has fast response and recovery from the short circuit [6]. In [7], the inductance versus current characteristics is obtained with the FEA simulations as well as experimental measurements with good agreements. A nonlinear inductance model, then incorporated in the grid is simulated to show that the limiting current has a dynamic component that significantly contributes to the current controlling property of the device. As an alternative to the FEM solution, the equivalent magnetic circuit which can accommodate the varying core dimensions employable in the commercial software

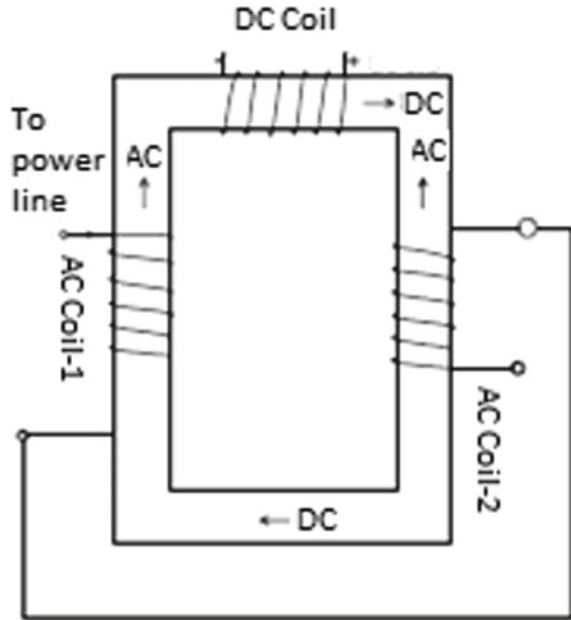
such as MATLAB/PSCAD has been suggested [8]. The transient performance in the grid is then calculated using MATLAB by introducing the NR method in the study. Some research studies suggested an application of permanent magnet (PM) bias for core saturation. But, the application of PM bias may be endangered by high power losses due to eddy currents and subsequent heating. The 2-D FEM analysis with the coupled 3-D analytical model of PM evaluated the performance in terms of eddy current losses. It has been demonstrated in the work that the PM width segmentation improves the eddy current losses in the device [9]. The research in [10] suggests a modeling methodology in terms of the nonlinear flux linkage-current characteristics to study the dynamic behavior of the device. The characteristic is plotted with FEM simulations initially and then the analytical and fast numerical solution is proposed. Experimental validation is also carried out in this work. The conventional SCFCL dual-core design suffers from huge core material requirements for the practical realization of the device. The authors [11] proposed the novel 5-leg configuration, and the performance of the existing dual-core topology and the 3-leg configuration have been compared in this work. The research in [12] has investigated and compared the performance in terms of current reduction ability, voltage drop contribution, and losses with two compatible models, one with conventional DC bias and the other with the application of PM bias. The COMSOL Multiphysics simulations have shown that the PM bias can improve the losses and coupling problems in the conventional design.

As most of the research had done with simulations and modeling, the focus of this work was experimentation. Although the SCFCL offers the most viable technology option to control short-circuit current, it poses challenges in terms of reducing the mass, weight, and volume of the device. Also, there has been a transformer coupling problem between its AC–DC electrical circuits. Therefore, in this paper, a novel concept of SCFCL configuration with reduced volume and coupling has been addressed [13]. The commercial deployment of this SCFCL technology will relieve power network components such as circuit breakers, transformers, T&D lines, etc., from their over-duty due to uncontrolled short-circuit currents. It can prolong the service life of these costly power network components. In this work, we report the performance of a small-scale SCFCL model characterized in terms of its current clipping ability and voltage drop contribution. The results of the experiment carried out with the single-phase, single-core configuration test model are presented.

2 Saturated Core Fault Current Limiter: Principle of Operation

The SCFCL with Closed DC-Open AC (CDOA) configuration uses an elongated magnetic core. The DC winding has been placed on the shorter limb and the two AC coils on longer limbs of the magnetic core (see Fig. 1). The DC coil is supplied power with an isolated DC source. The two AC coils are differentially connected in series with the circuit to be protected and carry line current.

Fig. 1 Closed DC-open AC configuration of the SCFCL



Under the steady-state operation of the system, the core has maintained at deeper saturation with (explicit) the DC biasing source. The magnetic pressure established due to the un-faulted load current (AC) is insufficient to drive the core out of saturation. As the magnetic core has been at deeper saturation under steady-state operation, the inductance of the AC coils is low enough (due to the low value of the core permeability) to activate the device as transparent to the system. It is equivalent to an inductance with air as a core.

Under the fault condition of the system, the elongated core legs are alternately taken out of saturation in each half cycle by the high magnitude of the magnetization forces affected with large fault current. It results in a substantial increase in the permeability of the cores. Hence, the impedance of the AC coils also increases, subsequently limiting the fault current. The total inductance offered by the AC coils, in this case, is very high as one of the legs is forced out of saturation and operating in the linear region (high value of the core permeability) of the magnetization. This inductive impedance of the SCFCL limits the prospective fault current to a desired controllable value.

3 Experimental Details

An actual picture of the laboratory setup for the experiment (see Fig. 2) consists of a controlled DC source, autotransformer, a computer system, MicroLabBox,

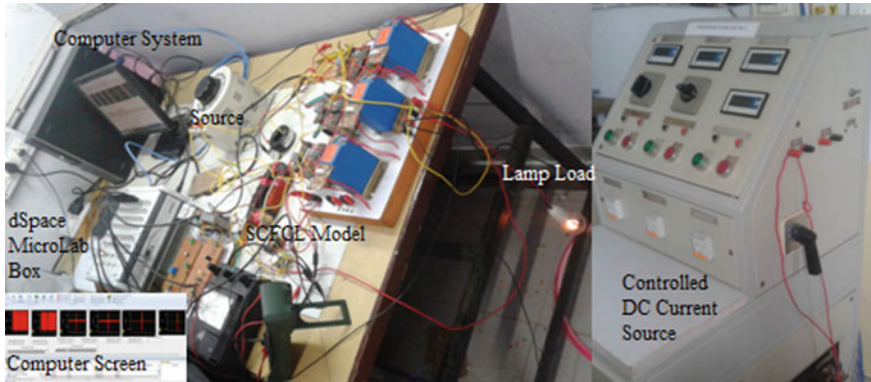


Fig. 2 An actual picture of test setup for the SCFCL model

Table 1 The physical parameters of the SCFCL model

Core dimensions in mm	
Leg_width	16
Leg_depth	30
Mean_width	54
Mean_height	138
Area_CS (mm ²)	480
Mean_length	384
Turns_DC	150
Turns_AC	100

Lamp, and SCFCL model. A single-phase autotransformer has worked as a source in the simple power system created to include the SCFCL model. A 200 W lamp in the laboratory act as a single-phase load. The L&T make contactor has been digitally controlled to create an artificial short circuit across the load. The dSpace, MicroLabBox used to acquire fault event data with the different biasing of the core. The core material used for the SCFCL model is high-grade CRGO steel (M4 electrical steel). The physical properties of the magnetic core and the coils are given in Table 1.

4 Test Results

The magnetic properties of the SCFCL model core have initially explored as it uses nonlinear magnetization for affecting the current limiting performance. The experimentally plotted B–H curve (see Fig. 3) has indicated that the magnetizing force of 400 A/m saturates take the core well ahead of the knee of the curve. It was,

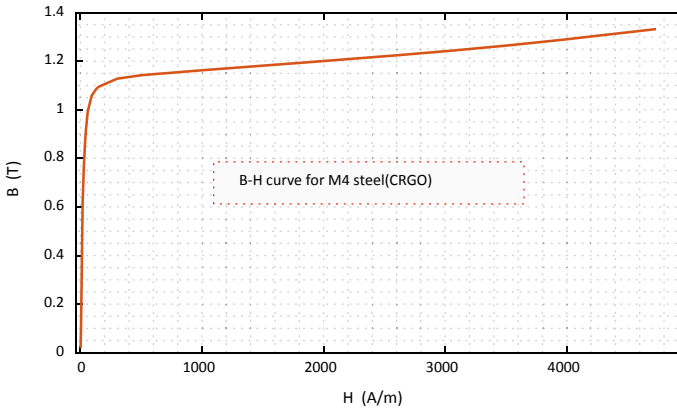


Fig. 3 Experimental B–H curve for high-grade core material

therefore, confirmed to apply a bias of 1 A for affecting the saturation of the magnetic core during the steady-state operation of the SCFCL.

Also, the SCFCL reactance under steady-state (un-faulted) for different bias, varying from 0 to 8 A in steps of 1 A, has been measured. It decreases as the bias level increases (see Fig. 4). The maximum reactance value is evident for unbiased (0 A-DC bias) core operation.

The SCFCL model has then tested for short-circuit performance. A fault has been created across the load without the inclusion of SCFCL in the circuit. The prospective short-circuit current (maximum peak), at the working voltage of 60 V rms, measured (see Fig. 5) was 104.84 A. The low voltage has been selected to ensure the safety of instruments and the wiring.

The inclusion of the SCFCL model has then limited the short-circuit current at a substantially low value with a maximum peak of 24.34 A (see Fig. 6). As the SCFCL exploits the nonlinear magnetization of the core for affecting current limitation, the bias level further varies to 0 A (unbiased operation) on the lower side and 3 A on

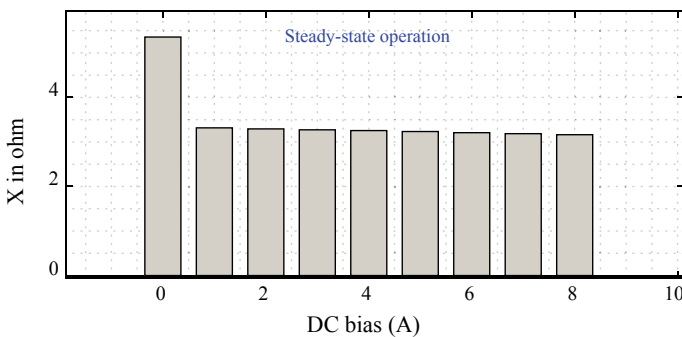


Fig. 4 The steady-state reactance of SCFCL with respect to bias

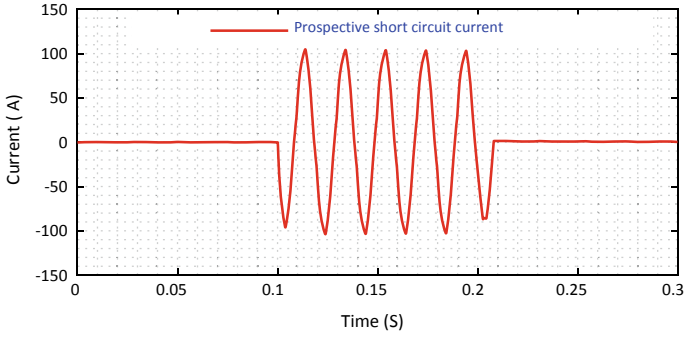
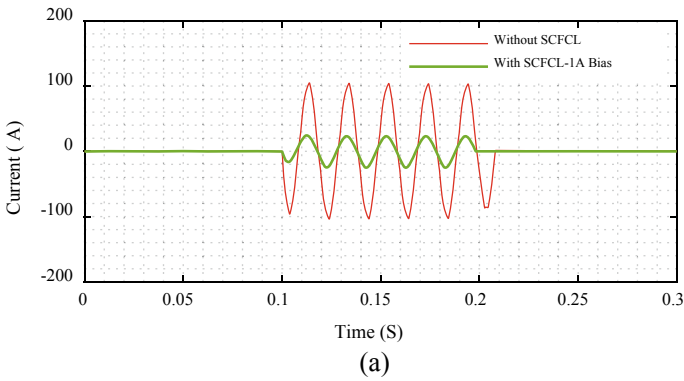
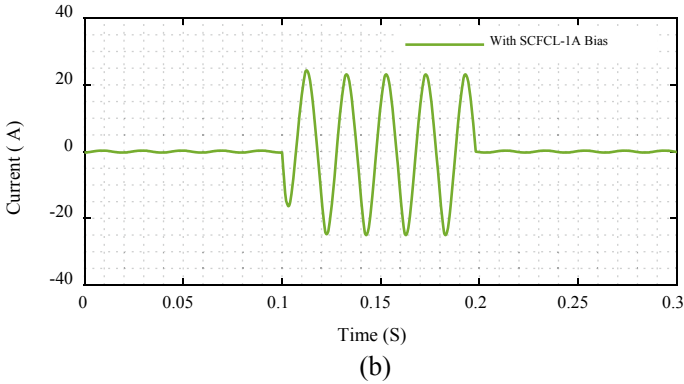


Fig. 5 The prospective short-circuit current without SCFCL model



(a)



(b)

Fig. 6 The short-circuit current (a) prospective current superimposed with the limited current and (b) the limited current (zommed) at 1 A bias

Table 2 The performance parameters of the SCFCL model at designated bias levels

Prospective current maximum peak: 104.846 (A)			
DC bias (A)	Max. peak (A)	Current reduction rate (%)	Voltage drop (%)
0	23.33	77.75	14.52
1	24.34	76.79	4.23
3	26.92	74.33	3.78

the higher side. It has been done to check the effect of changing the bias on the performance of the core. The performance indices, therefore, at the three different bias levels have been presented in Table 2.

It had observed that the current reduction rates [1] decrease as the bias level increases. It is because, with the higher bias, the deeper is the saturation of the magnetic core. It leads to the shifting of the operating point toward right on the magnetization curve. Consequently, the net demagnetizing force remains available to push the magnetic core toward linearity during short circuits reduces. It results in less permeability of the magnetic core that leads to lower impedance to the AC coils and reduction in current clipping.

The voltage drops also decreased with the increasing bias (see Table 2). As the steady-state reactance decrease with higher bias, the voltage drop thus decreases.

5 Conclusion

The B–H curve plotted experimentally was found useful in selecting the bias level of the magnetic core. The working state of the magnetic core has a significant influence on the performance of the device. A maximum current reduction has been noted for the unbiased operation of the SCFCL model. However, the same reduces with the increasing bias. It has been affected due to the shifting of the operating point to the right on the magnetization curve. Subsequently, the net demagnetizing force remains available to push the magnetic core toward linearity for affecting current limitations reduce. It results in less permeability of the magnetic core that leads to lower impedance to the AC coils. However, the clipping (current) does not drop significantly to lower values as the bias changed from the 1 A level to the 3 A level.

Also, the voltage drop under the steady-state operation of the SCFCL noted unacceptable at unbiased state (0 A) of the magnetic core. However, the same has substantially dropped to lower value from the 0 A bias to 1 A bias operation. The further increase of the bias does not result in significant change. The optimum bias selection, therefore, has compelling importance in the SCFCL design as under bias contributes a large voltage drop, and an excessive bias may yield more losses with trivial performance improvement.

References

1. Y. Jia, Z. Shi, H. Zhu, L. Hao, J. Zou, J. Yuan, Cognition on the current-limiting effect of saturated-core superconducting fault current limiter. *IEEE Trans. Magn.* **51**(11), 1–4, Art no. 8003004 (2015). <https://doi.org/10.1109/tmag.2015.2436715>
2. L. Kovalsky, X. Yuan, K. Tekletsadik, A. Keri, J. Bock, F. Breuer, Applications of superconducting fault current limiters in electric power transmission systems. *IEEE Trans. Appl. Supercond.* **15**(2) PART II, 2130–2133 (2005). <https://doi.org/10.1109/tasc.2005.849471>
3. Y. Xin, J.Z. Wang, H. Hong, W.Z. Gong, J.Y. Zhang, X.Y. Niu, A.L. Ren, D.J. Si, M.R. Zi, Z.Q. Xiong, F. Ye, Field tests on a 35 kV/90 MVA superconducting fault current limiter, in *International Conference on Power System Technology: Technological Innovations Making Power Grid Smarter*, POWERCON2010 (2010), pp. 1–5. <https://doi.org/10.1109/powercon.2010.5666578>
4. J. Patterson, P. Gomez, M. Gravely, M. Jones, Development of fault current controller technology prototyping, laboratory testing, and field demonstration. CEC Report, June 2011
5. H. Schmitt, Fault current limiters report on the activities of CIGRE WG A3.16, in *2006 IEEE Power Engineering Society General Meeting*, vol. 10 (2006), p. 5. <https://doi.org/10.1109/pes.2006.1709205>
6. B.P. Raju, K.C. Parton, T.C. Bartram, A current limiting device using superconducting D.C. bias: applications and prospects. *IEEE Trans. Power Apparatus Syst.* **PAS-101**(9), 3173–3177 (1982). <https://doi.org/10.1109/tpas.1982.317531>
7. S. Wolfus, Y. Nikulshin, A. Friedman, Y. Yeshurun, Dynamic inductance in saturated cores fault current limiters. *J. Supercond. Novel Magn.* (2014). <https://doi.org/10.1007/s10948-014-2717-7>
8. B. Li, F. Guo, J. Wang, C. Li, Electromagnetic transient analysis of the saturated iron-core superconductor fault current limiter. *IEEE Trans. Appl. Supercond.* **25**(3), 1–5 (2015). <https://doi.org/10.1109/tasc.2014.2374191>
9. C. Tian, Y. Zhong, J. Yuan, Y. Lei, B. Chen, K. Muramatsu, A coupled method for evaluating eddy current loss of NdFeB permanent magnets in a saturated core fault current limiter, in *2016 IEEE Conference on Electromagnetic Field Computation (CEFC)*, Miami, FL (2016). <https://doi.org/10.1109/cefc.2016.7816085>
10. N. Vilhena, P. Arsénio, J. Murta-Pina, A. Pronto, A. Álvarez, A methodology for modeling and simulation of saturated cores fault current limiters. *IEEE Trans. Appl. Supercond.* **25**(3) (2016). <https://doi.org/10.1109/tasc.2014.2374179>
11. M. Eladawy, I.A. Metwally, A novel five-leg design for performance improvement of three-phase presaturated core fault-current limiter. *IEEE Trans. Mag.* **54**(7), 1–10 (2018). <https://doi.org/10.1109/tmag.2018.2827000>
12. M. Eladawy, I.A. Metwally, A comparative investigation of presaturated core fault current limiters biased by DC current and permanent magnet. *IEEE Trans. Magn.* **55**(11), 1–10, Art no. 8002310 (2019). <https://doi.org/10.1109/TMAG.2019.2926658>
13. Y. Nikulshin, Y. Wolfus, A. Friedman, Y. Yeshurun, Improving the performance of saturated cores fault current limiters by varying winding density in the AC coils. *IEEE Trans. Appl. Supercond.* **25**(3) (2015). <https://doi.org/10.1109/tasc.2014.2386323>

Double Stage Voltage Lift Switched Capacitor Converter for High-Voltage Applications in DC Microgrids



Md. Samiullah, Imtiaz Ashraf, and Atif Iqbal

Abstract A typical DC microgrid has generating sources such as solar photovoltaic and fuel cells which do not maintain a suitable voltage profile to be directly interfaced to this grid structure. Therefore, a DC-to-DC converter is needed to develop a proper communication and energy exchange. The low-voltage terminal outputs of the generating stations need high gain DC converters as the traditional converter would fail to give a suitable higher voltage at a reasonable duty ratio. Many unwanted issues such as higher losses, increased EMI, impaired transients, and diodes reverse recovery concerns are related to operation of a converter at extremely large duty ratio. This paper presents a novel topology for a high gain DC-to-DC converter which has been realized by a systematic coupling of diode capacitor-based voltage lift circuit to the switched inductor network. Along with being simple a transformerless structure with only a single active switch, the converter gives a significantly high gain at very low duty ratio and finds its suitability with the DC microgrids. The analysis is done in CCM, and behavior is verified through simulation results at a frequency of 10 kHz.

Keywords DC–DC converter · DC microgrid · High gain · Switched capacitor

1 Introduction

The continuous growing demand of electricity has laid down a strong foundation for renewable energy sources. Solar photovoltaic and fuel cells have got particular attention owing to its energy density and availability in abundance. Microgrids and distributed generations are simultaneously being promoted as surplus for the conventional energy sources [1, 2].

Md. Samiullah (✉) · I. Ashraf
Aligarh Muslim University, Aligarh, India
e-mail: md_samiullah@zhcet.ac.in

A. Iqbal
Qatar University, Doha, Qatar

Power electronics converters have always been the backbone for these generating cradles as they shape the voltages and power according to the demand. A DC-to-DC converter is required at the output of photovoltaic and fuel cell to lift the voltage up to the level of a bus voltage in a DC microgrid [3]. A conventional boost converter does serve the purpose but with a compromise of operating it at the above normal range of prescribed duty ratio. This operation of available converters at large duty ratio dawns many unwanted issues with the converter performance such as undesirable voltage perturbations and overshoots, impaired transients, more losses and increased EMI [2, 4–7]. Moreover, diodes in the circuit experience reverse recovery issues. Therefore, high gain efficient DC-to-DC converter is needed for a proper and competent integration of generating sources with the microgrids.

In the available literature, many converters have been reported serving the purpose of high gain at low duty cycle. These converters are broadly classified among isolated and non-isolated ones. Isolated converters have transformers which make the purpose to be easily attained by simply varying the turn ratio along with the duty ratio. However, these converters have limitations of its bulky structure, core saturation, more leakage inductances losses, and higher cost [8–11]. These drawbacks pull non-isolated converters to be explored. A non-isolated converter uses voltage lifting circuits for boosting up the low voltage. These circuit structures include switched inductor, diode capacitor type voltage multiplier, switched capacitor, voltage lift circuits, or coupled inductor structure [8, 12–15]. Sometimes, it also involves cascaded or quadratic structures for stepping up the voltage. The reported converters have pros and cons on one another. The cascaded or interleaved structure has large size and cost [16]. Some of the converters need clamping circuits better response, while others have increased input current ripples [17]. Most of the converters compromise with the complexity and cost when they have to deal with higher voltage applications.

This paper proposes a transformerless non-isolated converter which contributes the following:

- (a) Significantly high gain at very reasonable and low duty ratio.
- (b) Low-voltage stress on the active switches.
- (c) Simple structure with low current ripples at the input.
- (d) Utilization of switched inductor and switched capacitor in an efficient manner (Fig. 1).

2 The Double Stage Voltage Lift Switched Capacitor Converter

The converter circuit topology is shown in Fig. 2. It is a single MOSFET switch-based converter designed particularly for high-voltage gain. The circuit is composed of four inductors L_{x_1} , L_{x_2} , L_{x_3} , and L_z , four capacitors, one in the switched inductor network and two in the voltage lift circuit named as C_{y_1} and C_{y_2} along with one at the output terminal for maintaining a ripple-free constant output voltage. This configuration of

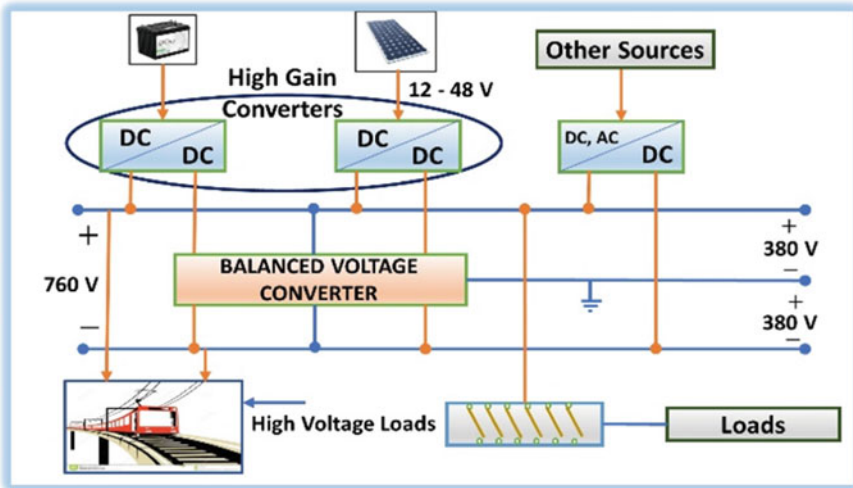


Fig. 1 Layout of a typical DC microgrid

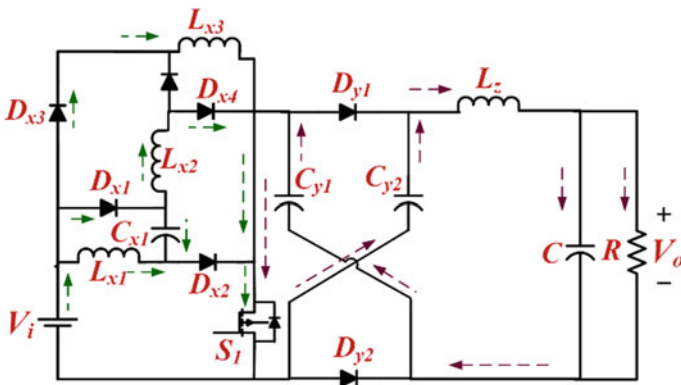


Fig. 2 Proposed converter topology for high-voltage applications

the circuit enables the converter to easily attain a significantly high-voltage gain. The switched capacitor network is fascinated with inductors which are being charged in parallel and discharge in series. A single switch in only used which is highly advantageous and can be controlled without any complexity. For analysis purpose, the inductors chosen are identical such as $L_{x1} = L_{x2} = L_{x3} = L_z$. Moreover, some important assumptions are also made before the experimentation is done in order to make the analysis simple by taking care of the originality of the converter. The ON-state potential drop has been neglected in the switch, forward voltage drop across the diodes are assumed to be negligible, and trivial ESR of the inductors and capacitors have been taken into consideration. The switching frequency and the time period of

the switch are assumed as f_s and T_s , respectively. The converter is analyzed in CCM in the subsequent section in order to come up with the voltage gain expression and other important design aspects of the converter.

2.1 Steady-State Analysis During CCM

The steady-state analysis of the proposed converter during continuous conduction mode is done in this section. The assumptions made has already been discussed in the aforementioned paragraph. Since there is only a single switch, therefore it is quite easy to describe the performance in duty and off-duty modes. Identical inductors have similar characteristics, and a single waveform describes their voltage and current relations.

Mode I: (Duty period) from 0 to t_1 : This is the duty mode of the converter when the switch S_1 is closed. The circuit configuration during this mode of operation is shown in Fig. 3. Diodes D_{y1} , D_{y2} , and D_{x5} in the voltage lift circuit are OFF, and the remaining diodes are forward biased. The output capacitor maintains a constant voltage across the load R .

$$\begin{cases} v_L^I = v_{Lx1}^I = v_{Lx2}^I = v_{Lx3}^I = V_i \\ v_{Cx1}^I = V_g \end{cases} \quad (1)$$

$$i_i = i_{Lx1} + i_{Lx2} + i_{Lx3} + i_{Cx1} \quad (2)$$

$$v_{Lz}^I = 2v_{Cy}^I - V_o, \{v_{Cy1}^I = v_{Cy2}^I = v_{Cy}^I\} \quad (3)$$

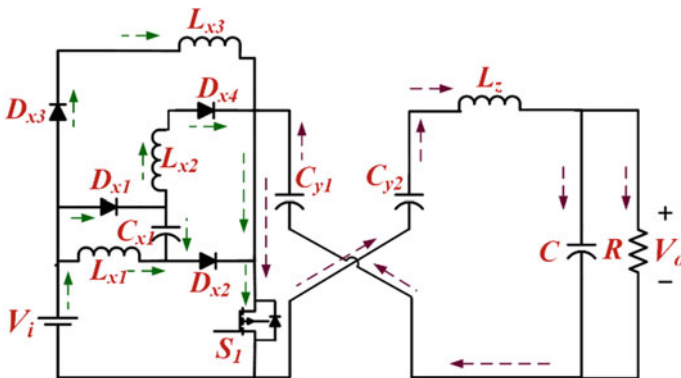


Fig. 3 Converter layout when the switch is ON

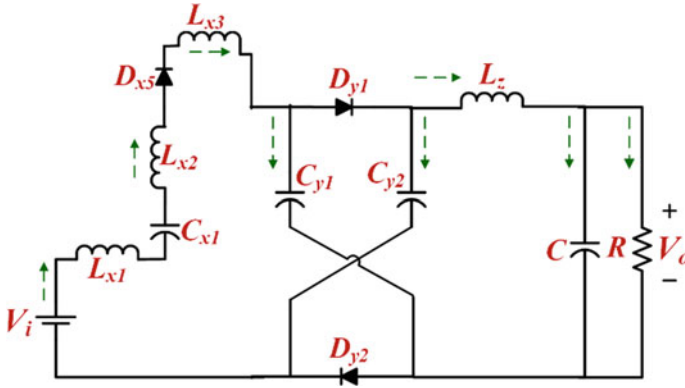


Fig. 4 Converter layout during OFF state of the switch

Mode II: (OFF-Duty period) from t_1 to T_s : This is the OFF duty mode of the converter when the active switch is kept OFF. The circuit configuration during this mode has been presented in Fig. 4. The diodes which were turned OFF in the duty period are forward biased in this mode and vice-versa. The converter exhibits the following relations:

$$v_L^{\text{II}} = v_{Lx1}^{\text{II}} = v_{Lx2}^{\text{II}} = v_{Lx3}^{\text{II}} = \frac{2V_i - v_{Cy}^{\text{II}}}{3}$$

$$v_{Ca}^{\text{II}} = v_{Cy1}^{\text{II}} = v_{Cy2}^{\text{II}} \tag{4}$$

$$v_{Lz}^{\text{II}} = v_{Cy}^{\text{II}} - V_o \tag{5}$$

Since the capacitor is chosen with sufficiently high value, it keeps the constant voltage across them given as;

$$v_{Cy}^{\text{I}} = v_{Cy}^{\text{II}} = V_{Cy} \tag{6}$$

The principle of volt-second balance gives the following relation with k being the duty cycle of the converter;

$$\left\{ \int_0^{kT_s} V_i dt + \int_{kT_s}^{T_s} \frac{2V_i - V_{Cy}}{3} dt = 0 \right. \tag{7}$$

Solving Eq. (7), the following relation is obtained

$$\frac{V_{Cy}}{V_i} = \frac{2 + k}{1 - k} \tag{8}$$

The volt-second balance principle is applied on the inductor L_z which gives the following important relation (Fig. 5):

$$\left\{ \int_0^{kT_s} (2V_{Cy} - V_o)dt + \int_{kT_s}^{T_s} (V_{Cy} - V_o)dt = 0 \right. \quad (9)$$

$$\Rightarrow \frac{V_{Cy}}{V_o} = \frac{1}{1+k} \quad (10)$$

After solving Eqs. (8) and (10), the voltage gain expression of the converter is obtained and given as:

$$M_{CCM} = \frac{V_o}{V_i} = \frac{2 + 3k + k^2}{1 - k} \quad (11)$$

3 Results and Discussion

The simulation of the double stage voltage lift switched capacitor converter is done in MATLAB with the parameters given in Table 1. Inductors are chosen just above their critical values to keep the conduction in continuous mode only. The capacitors are also chosen suitably for the voltage to be constant and ripple-free. An input voltage of 10 V is applied to the converter, and the results are analyzed for medium and high duty ratios, e.g., 60 and 90%. The output voltage has a steady-state value of 103.8 V at a duty ratio of 60% as shown in Fig. 6, which is almost the same as the calculated analytical value of 104 V.

Similarly, the output voltage at a duty ratio of 90% is also shown in Fig. 7. This also proves the suitability at high duty ratio although not advisable to operate at this range of duty cycle. Switch voltage and capacitor current are also shown in Figs. 9 and 10, respectively. The switch voltage is low as expected, and the inductor current follows the natural characteristics with ripples of less than 1% (Fig. 8).

4 Conclusion

A novel converter named as double stage voltage lift switched capacitor converter has been proposed in the paper which is highly suitable for high-voltage applications owing to its inherent characteristics of high-voltage gain at a significantly low duty ratio. This particular converter finds its application in integrating of low-voltage output solar photovoltaic to the high-voltage DC bus of a DC microgrid. The

Fig. 5 Different characteristics waveforms of the converter parameters during CCM

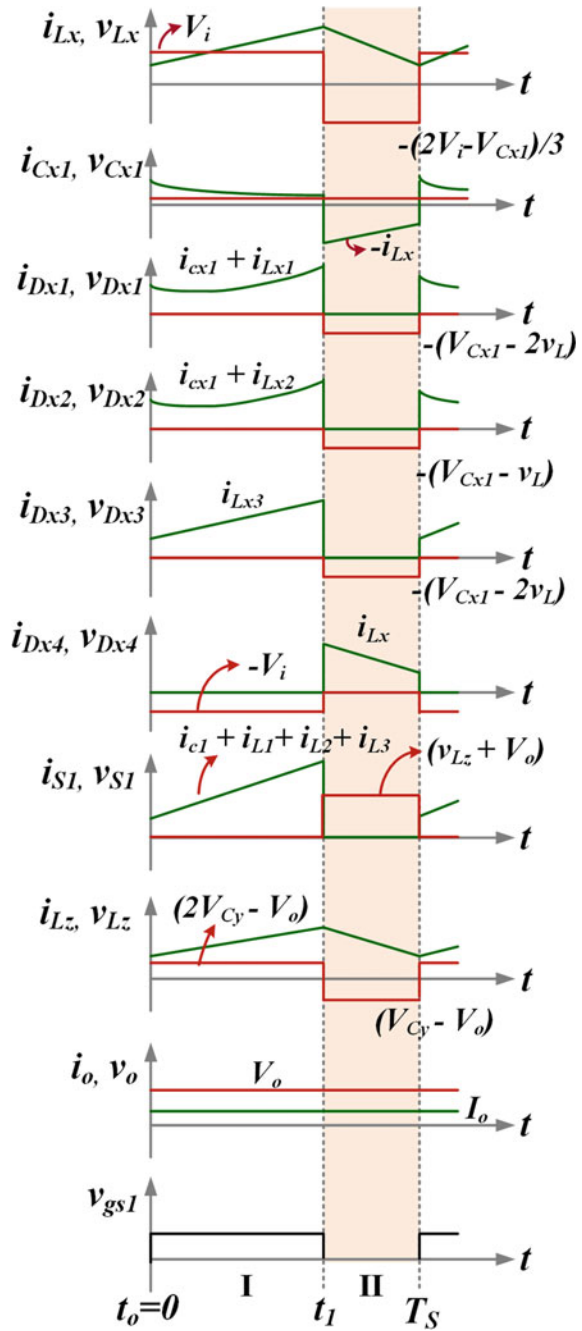


Table 1 Parameter values for simulation

Parameters	Values
Input voltage	10 V
Duty ratio	0.6 and 0.9
Switching frequency	10 kHz
Inductances	$L_{x1} = L_{x2} = L_{x3} = L_z = 450$ mH
Capacitances	$C_{y1} = C_{y2} = 220$ μ F, $C_{x1} = 100$ μ F

Fig. 6 Input and output voltages obtained at a duty ratio of 0.6

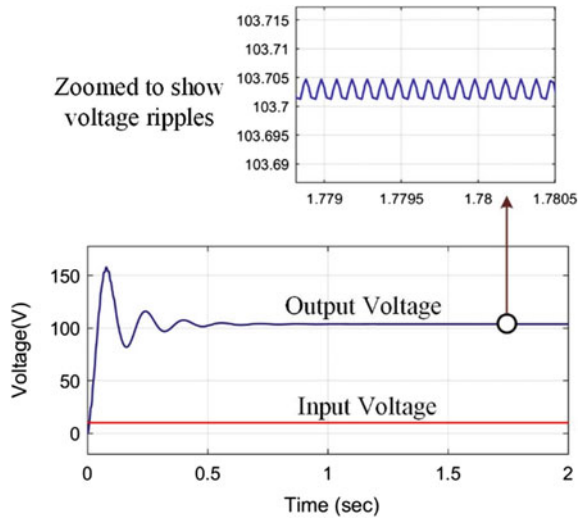
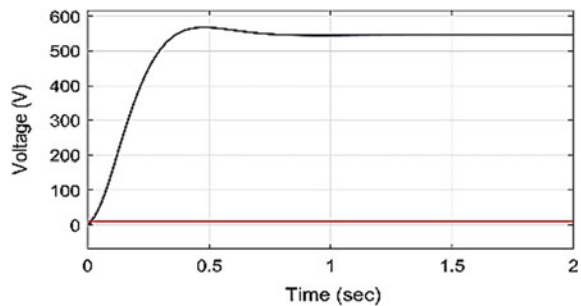


Fig. 7 I/P and O/P voltages at a duty ratio of 0.9



proposed converter has been realized using voltage lift circuit and switch inductor–capacitor coupled together. The advantages of these basic circuits are utilized in an efficient manner such that low-voltage appears across the switching device and diodes. Compared to other topologies, this converter has significantly high-gain factor and low switching stress with only a single switch in the circuit. The behavior of the

Fig. 8 Inductor current waveform

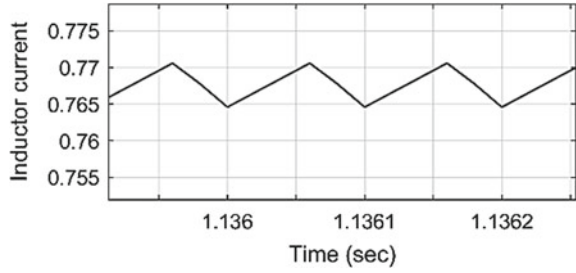


Fig. 9 Switch voltage stress when the duty ratio is 0.6

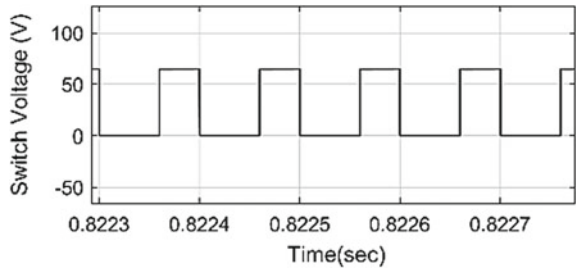
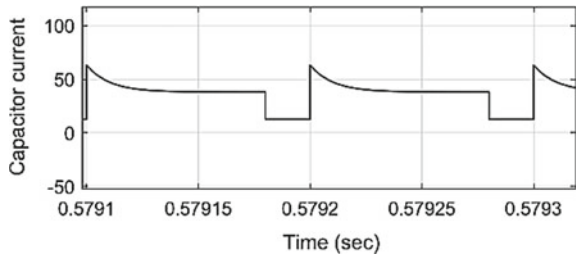


Fig. 10 Capacitor current $I_{C_{x1}}$ at a duty ratio of 0.9



converter is analyzed through simulation at a frequency of 10 kHz and the results justified the analytical studies in continuous conduction mode.

References

1. M. Lakshmi, S. Hemamalini, Nonisolated high gain DC-DC converter for DC microgrids. *IEEE Trans. Ind. Electron.* **65**, 1205–1212 (2017). <https://doi.org/10.1109/TIE.2017.2733463>
2. B. Sri Revathi, M. Prabhakar, Non isolated high gain DC-DC converter topologies for PV applications—a comprehensive review. *Renew. Sustain. Energy Rev.* **66**, 920–933 (2016). <https://doi.org/10.1016/j.rser.2016.08.057>
3. M.S. Bhaskar, M. Meraj, A. Iqbal et al., High gain transformer-less double-duty-triple-mode DC/DC converter for DC microgrid. *IEEE Access* **7**, 36353–36370 (2019). <https://doi.org/10.1109/ACCESS.2019.2902440>

4. W. Qian, D. Cao, J.G. Cintron-Rivera et al., A switched-capacitor DC-DC converter with high voltage gain and reduced component rating and count. *IEEE Trans. Ind. Appl.* **48**, 1397–1406 (2012). <https://doi.org/10.1109/TIA.2012.2199731>
5. L.S. Yang, T.J. Liang, J.F. Chen, Transformerless DC-DC converters with high step-up voltage gain. *IEEE Trans. Ind. Electron.* **56**, 3144–3152 (2009). <https://doi.org/10.1109/TIE.2009.2022512>
6. Y. Cao, V. Samavatian, K. Kaskani, H. Eshraghi, A novel nonisolated ultra-high-voltage-gain DC-DC converter with low voltage stress. *IEEE Trans. Ind. Electron.* **64**, 2809–2819 (2017). <https://doi.org/10.1109/TIE.2016.2632681>
7. S.J. Chen, S.P. Yang, C.M. Huang, C.K. Lin, Interleaved high step-up DC-DC converter with parallel-input series-output configuration and voltage multiplier module, in *Proceedings of the IEEE International Conference on Industrial Technology* (pp. 119–124) (2017). <https://doi.org/10.1109/ICIT.2017.7913069>
8. F.M. Shahir, E. Babaei, M. Farsadi, Analysis and design of voltage-lift technique based non-isolated boost dc-dc converter. *IET Power Electron.* **11**, 1083–1091 (2018). <https://doi.org/10.1049/iet-pel.2017.0259>
9. F.L. Tofoli, D. de Castro Pereira, W.J. de Paul, D.S. Oliveira, Survey on non-isolated high-voltage step-up dc-dc topologies based on the boost converter. *IET Power Electron.* **8**, 2044–2057 (2015). <https://doi.org/10.1049/iet-pel.2014.0605>
10. E.H. Ismail, M.A. Al-Saffar, A.J. Sabzali, A.A. Fardoun, High voltage gain single-switch non-isolated DC-DC converters for renewable energy applications, in *2010 IEEE International Conference on Sustainable Energy Technologies, ICSET 2010* (2010)
11. L.H.S.C. Barreto, P.P. Praça, G.A.L. Henn et al., Single stage high voltage gain boost converter with voltage multiplier cells for battery charging using photovoltaic panels, in *Conference Proceedings—IEEE Applied Power Electronics Conference and Exposition—APEC* (2012), pp. 364–368. <https://doi.org/10.1109/APEC.2012.6165845>
12. Y. Jiao, F.L. Luo, M. Zhu, Voltage-lift-type switched-inductor cells for enhancing DC-DC boost ability: principles and integrations in Luo converter. *IET Power Electron.* **4**, 131–142 (2011). <https://doi.org/10.1049/iet-pel.2010.0021>
13. M. Forouzesh, Y.P. Siwakoti, S.A. Gorji et al., Step-up DC-DC converters: a comprehensive review of voltage-boosting techniques, topologies, and applications. *IEEE Trans. Power Electron.* **32**, 9143–9178 (2017). <https://doi.org/10.1109/TPEL.2017.2652318>
14. H. Liu, F. Li, A novel high step-up converter with a quasi-active switched-inductor structure for renewable energy systems. *IEEE Trans. Power Electron.* **31**, 5030–5039 (2016). <https://doi.org/10.1109/TPEL.2015.2480115>
15. F.L. Luo, Switched-capacitor DC/DC converters. *Appl. Mech. Mater.* **310**:453–465 (2013). <https://doi.org/10.4028/www.scientific.net/AMM.310.453>
16. A. Mostaan, S.A. Gorji, M.N. Soltani, M. Ektesabi, A novel single switch transformerless quadratic DC/DC buck-boost converter, in *2017 19th European Conference on Power Electronics and Applications, EPE 2017 ECCE Europe 2017-January* (2017), pp. P1–P6. <https://doi.org/10.23919/EPE17ECCEEurope.2017.8099120>
17. M. Prudente, L.L. Pfitscher, G. Emmendoerfer et al., Voltage multiplier cells applied to non-isolated DC-DC converters. *IEEE Trans. Power Electron.* **23**, 871–887 (2008). <https://doi.org/10.1109/TPEL.2007.915762>

Impact Analysis of Different Gap on CIGS Photovoltaic Device with MoSe₂ as Tunnel Layer



R. Akter, R. A. Anonto, K. Nahreen, A. A. Badhon, T. Mahbub, M. J. Alam, and S. S. Mahtab

Abstract Through this research, we have gone for various bandgap and thickness of the CIGS solar cell's absorber layer to identify the highest possible efficiency as well as other components. And hopefully with the Solar Cell Capacitance Simulator (SCAPS) program, we have been able to improve performance. The determined value was ranged from 8.70% < efficiency < 28.15%, 0.4464 < open-circuit voltage < 1.4592, 25.87 < short-circuit voltage < 38.197 as well as various form factor. These values were collected for various bandgap and thickness. Bandgap was ranged to 1.02–1.75 as wider bandgap decreases the efficiency so we have keep that in mind while simulating. The thickness was ranged to 100–3000 nm. While studying we have found great efficiency of CIGS solar cell. The structure of reference solar cell consists of ZnO, CdS, CIGS, Mo, SLG, and the cell we have used is the glockre's CIGS reference solar cell. And in our proposed structure, we have MoSe₂ beneath the CIGS absorber layer.

1 Introduction

Copper indium gallium selenide (CIGS) is a kind of thin-film solar cell that is also acknowledged in photovoltaic (PV) technology for its greater performance and

R. Akter (✉) · K. Nahreen

Department of EEE, Mymensingh Engineering College, Mymensingh, Bangladesh

R. A. Anonto

Department of EEE, American International University Bangladesh, Dhaka, Bangladesh

A. A. Badhon

Department of ECE, Khulna University of Engineering and Technology, Khulna, Bangladesh

T. Mahbub

Department of EEE, Independent University Bangladesh, Dhaka, Bangladesh

M. J. Alam · S. S. Mahtab

Department of EEE, Feni University, Feni, Bangladesh

greater absorption facility and requires less substance than silicon cells, lower manufacturing rate, and stability [1, 2]. Also, the efficiency of CIGS solar cell has reached over 20%, 20.3% on the glass, and 20.4% on the flexible polymer substrate [1]. The efficiency has also been increased up to 25% by adding an extra layer by some investigate groups [2]. CIGS thin-film solar cell is based on the chalcopyrite p-type absorber layer $\text{Cu}(\text{In}_{1-x}\text{Ga}_x)\text{Se}_2$ [3]. The performance of CIGS solar cells principally depends on the bandgap as well as thickness of the absorber layer. The broader bandgap aids the CIGS cell to manage higher alteration efficiency and also progresses the working conditions. So, we varied the bandgap and thickness of the absorber layer to simulate the cell's output parameters like open-circuit voltage, short-circuit current density, form factor, and most importantly the efficiency. A numerical simulation study of CIGS cell with the Solar Cell Capacitance Simulator (SCAPS) software has been done, and we were able to improve the efficiency of CIGS cell through the software. A performance study for different bandgap and thickness in the CIGS solar cells with the CdS buffer layer has also been discussed in this paper.

2 Device Structure and Simulation Details

The three-dimensional of reference solar cell of CIGS solar cell has been represented in Fig. 1. Here, here for this paper, we have gone for a reference cell, which is structured as ZnO/CdS/CIGS/Mo/SLG. According to M. Gloeckler, the numerical simulation can be done only with limited information of basic participation factors. For convenient comparisons between laboratories and simulations, it is very helpful to have a mutual preliminary idea. The base case structure was proposed by M. Gloeckler, which is further optimized is shown in Fig. 1 [4].

Fig. 1 Reference CIGS solar device

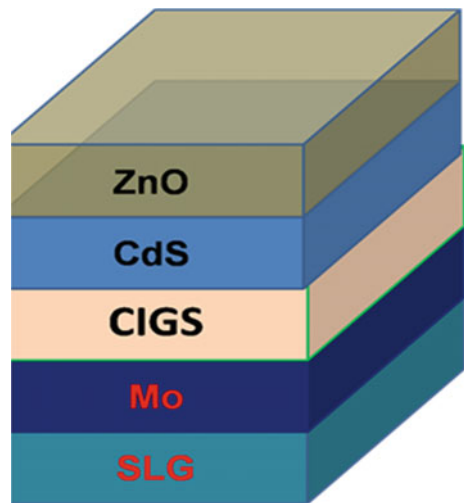
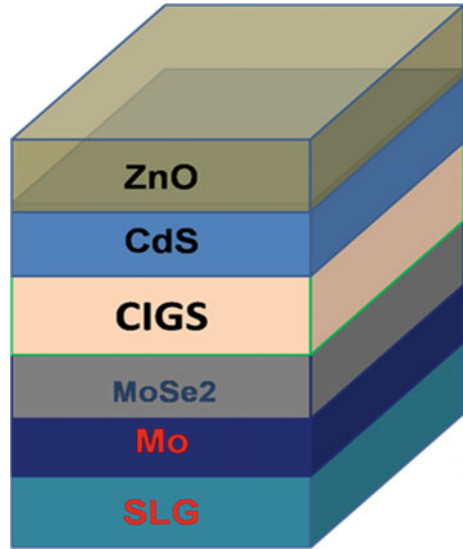


Fig. 2 Proposed CIGS solar device



For any particular solar cell or photovoltaics, the most important thing is its absorber layer/active layer which plays the vital role here. For this work, CIGS plays this vital role. For our work, we have taken as well as considered a single active layer with its constant values (properties). The constant values were doping concentrations, energy gap, etc., like there is in formal/conventional CIGS photovoltaics. After that, we have considered into our system a new structure that has been proposed for obtaining more efficiency. The proposed structure can be seen in Fig. 2. After having the optimized structured of reference cell, we have introduced a very thin tunneling layer, which has been placed between the region of CIGS active layer (absorber) and molybdenum back contact (BC). In our proposed cell, everything is almost except the extra tunnel layer. We used MoSe_2 as tunnel layer here to observe the impact of it.

CIGS is a compound semiconductor alloy of group I–III–VI, and it has a possibility of bandgap engineering within the range 1.01–1.67 eV according to the equation [5, 6]:

$$E_g = 1.011 + 0.421x + 0.244 \times 2.$$

where the bandgap is E_g in eV and x is the percentage of Ga in CIGS sample ($x = \text{Ga}/(\text{Ga} + \text{In})$). CIGS has high absorption coefficient of about $I \sim 10^7 \text{ m}^{-1}$, makes this material more attractive and efficient for photovoltaic applications, and it can absorb most of the incident photons within $2 \mu\text{m}$ thickness of CIGS absorber [7–14] (Tables 1 and 2).

Table 1 Properties of material used during simulation

	<i>p</i> -CIGS	<i>n</i> -CdS	<i>N</i> -ZnO
Thickness (μm)	variable	0.05	0.05
Bandgap (eV)	variable	2.4	3.3
Electron affinity (eV)	4.5	4.2	4.45
Dielectric permittivity (relative)	13.6	10	9
CB effective density of states (1/cm ³)	2.200E+18	2.200E+18	2.200E+18
VB effective density of states (1/cm ³)	1.800E+19	1.800E+19	1.800E+19
Electron thermal velocity (cm/s)	1.000E+7	1.000E+7	1.000E+7
Hole thermal velocity (cm/s)	1.000E+7	1.000E+7	1.000E+7
Electron mobility (cm ² /Vs)	1.00E+2	1.00E+2	1.00E+2
Hole mobility (cm ² /Vs)	2.500E+1	2.500E+1	2.500E+1

Table 2 Properties of contact layers used during simulation

	Front	Back
Metal work function	4.45	5.4
Relative to E_f	0	0.2000
Relative to E_v or E_c	-0.0204	0.0238
Electrons	1.00E+7	1.00E+7

3 Simulation Details

In the simulation model, the method below for calculating system parameters is considered.

Efficient bandgap— E_g . The made-in capacity is determined by using the majority carrier quantities on the interfaces *n* and *p* and the effective state densities in the conduction band N_{cond} and the valence band N_{valen} . It is possible to write the potential for the conduction and valence band using unit geometry as follows:

$$E_{\text{cond}} = -\chi - q\varphi \quad (1)$$

$$E_{\text{valen}} = -\chi - E_g - q\varphi \quad (2)$$

The concentration of minority carriers can also be estimated using

$$n_l = N_c \exp\left(\frac{F_n - E_{\text{cond}}}{kT}\right) \quad (3)$$

where in *n*-side F_n is the Fermi equilibrium stage.

The charge carrier transport was determined using the bipolar formulas of drift-diffusion as follows: for electron,

$$J_n = q\mu_e n_f \frac{\partial E_{\text{cond}}}{\partial x} + qD_n \frac{\partial n_f}{\partial x} \quad (4)$$

And for holes,

$$J_p = q\mu_h p_f \frac{\partial E_{\text{valen}}}{\partial x} + qD_p \frac{\partial p_f}{\partial x} \quad (6)$$

For the measurement of carrier trapping, the Shockley–Read–Hall (SRH) recombination principle was used [19]. The efficiency of the unit was theoretically determined by using the formula

$$\text{FF} = \frac{P_{\text{max}}}{I_{\text{sc}} \times V_{\text{oc}}}$$

$$\eta = \frac{I_{\text{sc}} \times V_{\text{oc}} \times \text{FF}}{P_{\text{light}}}$$

where fill factor is FF, maximum power is P_{max} , open-circuit voltage is V_{oc} , and short-circuit current is I_{sc} . The values were taken from the curve of I – V characteristics. P_{light} is the input power of 100 mW/cm² under 1 illumination with sunlight intensity 1.5 a.m.

4 Results and Discussion

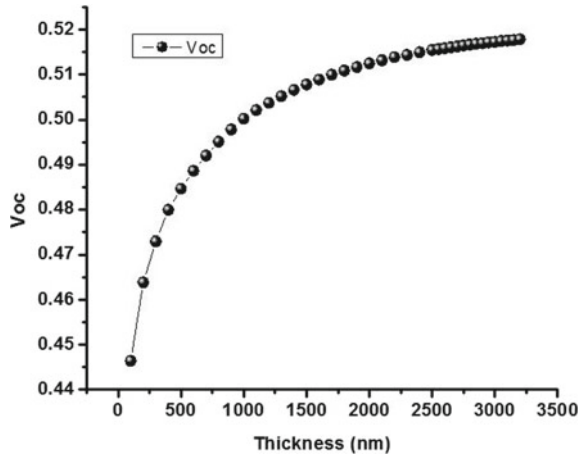
In this research paper, we have varied the bandgap as well as thickness of the p -CIGS layer among p -CIGS, n -CIGS, and N -ZnO layers of the CIGS solar cell. The purpose of this is to grow the efficiency mainly. In the p -CIGS layer, by varying the bandgap to 1.02, 1.15, 1.18, 1.26, 1.41, and 1.75 eV also the thickness from 100 to 3200 nm, we have collected data to investigate the value of open-circuit voltage, short-circuit current density, form factor, and mostly the efficiency. As we used SCAPS software for simulation, the results are given as below.

4.1 Bandgap 1.02

Relation of Thickness and Open-Circuit Voltage

From the following diagram, in place of thickness 100 nm, the open-circuit voltage is 0.4464 V. On behalf of thickness 200 nm, the open-circuit voltage is 0.4639 V and so on. Finally, for thickness 3200 nm, the open-circuit voltage develops at 0.5179 V. Hence, the rising thickness also rises the open-circuit voltage; thus, we can say the open-circuit voltage is proportional to thickness. Aimed at changing thickness, the changing open-circuit voltage is in the diagram as per specified in Fig. 3.

Fig. 3 Change of V_{oc} (open-circuit voltage) with absorber layer's thickness at bandgap-1.02



Relation of Thickness, Short-Circuit Current Density, and Form Factor

From the following diagram, in place of thickness 100 nm, the short-circuit current density is 25.87 mA/cm² and form factor is 75.39%. On behalf of thickness 200 nm, the short-circuit current density is 31.88 mA/cm² with form factor 76.14%, and for 300 nm thickness, the form factor becomes 76.02% and later the form factor is 76.15%. After that the form factor increases as accordingly but the short-circuit current density keeps expanding with growing thickness from the beginning. Finally, for thickness 3200 nm, the short-circuit current density develops at 37.93 mA/cm² and form factor develops at 78.23%. Hence, the rising thickness rises both the short-circuit current density and form factor; thus, we can say the short-circuit current density is proportional to thickness. Aimed at changing thickness, the changing short-circuit current density besides form factor is in the diagram as per specified in Fig. 4.

Fig. 4 Change of J_{sc} (short-circuit current density) and form factor with absorber layer's thickness at bandgap-1.02

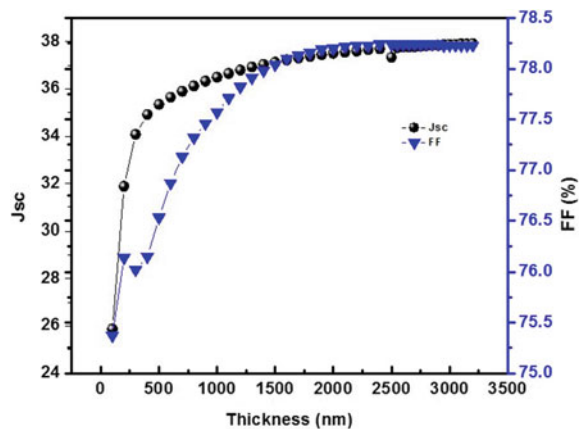
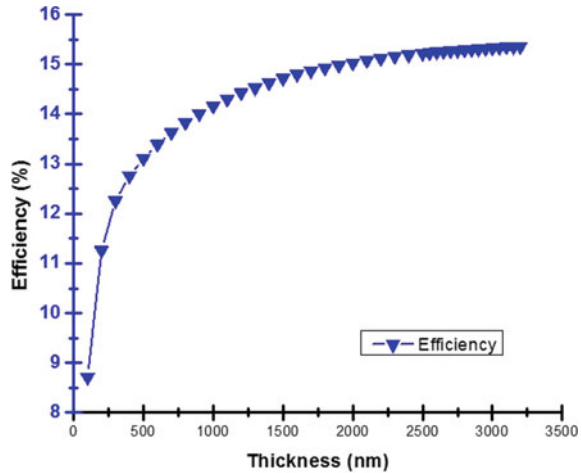


Fig. 5 Change of η (efficiency) with absorber layer thickness at bandgap-1.02



Relation of Thickness and Efficiency

From the following diagram, in place of thickness 100 nm, the efficiency is 8.71%. On behalf of thickness 200 nm, the efficiency is 11.26% and so on. Finally, for thickness 3200 nm, the efficiency develops at 15.36%. Hence, the rising thickness also rises the efficiency, thus we can say the efficiency is proportional to thickness. Aimed at changing thickness, the changing efficiency is in the diagram as per specified in Fig. 5.

4.2 Bandgap 1.15

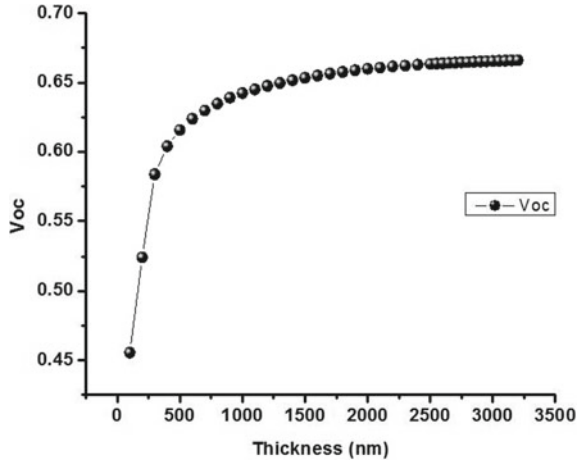
Relation of Thickness and Open-Circuit Voltage

From the following diagram, in place of thickness 100 nm, the open-circuit voltage is 0.4556 V. On behalf of thickness 200 nm, the open-circuit voltage is 0.5243 V and so on. Finally, for thickness 3200 nm, the open-circuit voltage develops at 0.6661 V. Hence, the rising thickness also rises the open-circuit voltage; thus, we can say the open-circuit voltage is proportional to thickness. Aimed at changing thickness, the changing open-circuit voltage is in the diagram as per specified in Fig. 6.

Relation of Thickness, Short-Circuit Current Density, and Form Factor

From the following diagram, in place of thickness 100 nm, the short-circuit current density is 25.79 mA/cm² and form factor is 74.58%. On behalf of thickness 200 nm, the short-circuit current density is 31.4099 mA/cm² with form factor 71.54%. For thickness 300 nm, we get 32.21 mA/cm² short-circuit current density along with 73.84% form factor. After that the form factor increases as accordingly but the short-circuit current density keeps expanding with growing thickness from the beginning. Finally, for thickness 3200 nm, the short-circuit current density develops at

Fig. 6 Change of V_{oc} (open-circuit voltage) with absorber layer's thickness at bandgap-1.15



37.99 mA/cm² and form factor develops at 81.08%. Aimed at changing thickness, the changing short-circuit current density besides form factor is in the diagram as per specified in Fig. 7.

Relation of Thickness and Efficiency

From the following diagram, in place of thickness 100 nm, the efficiency is 8.76%. On behalf of thickness 200 nm, the efficiency is 11.78% and so on. Finally, for thickness 3200 nm, the efficiency develops at 20.52%. Hence, the rising thickness also rises the efficiency thus we can say efficiency is proportional to thickness. Aimed at changing thickness, the changing efficiency is in the diagram as per specified in Fig. 8.

Fig. 7 Change of J_{sc} (short-circuit current density) and form factor with absorber layer's thickness at bandgap-1.15

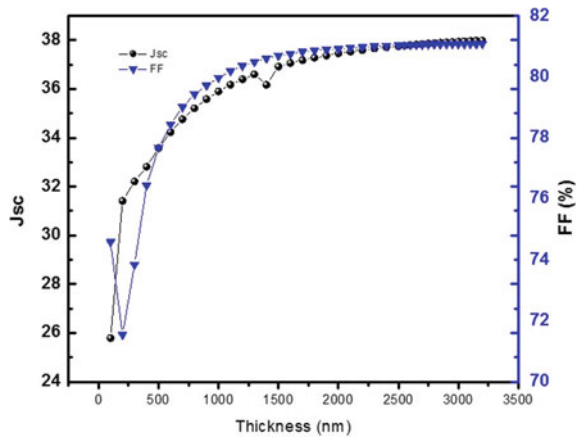
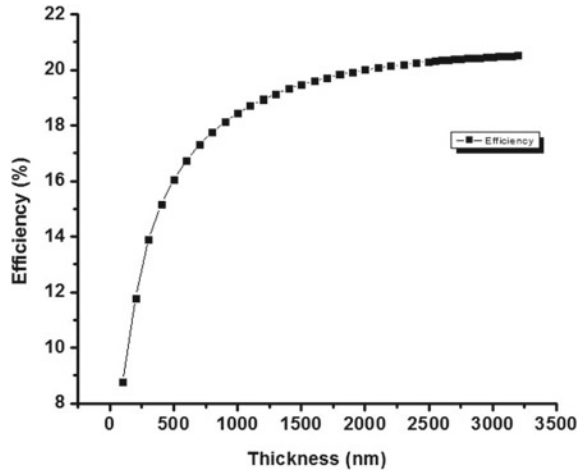


Fig. 8 Change of η (efficiency) with absorber layer thickness at bandgap-1.15



4.3 Bandgap 1.26

Relation of Thickness and Open-Circuit Voltage

From the following diagram, in place of thickness 100 nm, the open-circuit voltage is 0.4556 V. On behalf of thickness 200 nm, the open-circuit voltage is 0.5310 V and so on. Finally, for thickness 3200 nm, the open-circuit voltage develops at 0.7758 V. Hence, the rising thickness also rises the open-circuit voltage; thus, we can say the open-circuit voltage is proportional to thickness. Aimed at changing thickness, the changing open-circuit voltage is in the diagram as per specified in Fig. 9.

Fig. 9 Change of V_{oc} (open-circuit voltage) with absorber layer's thickness at bandgap-1.26

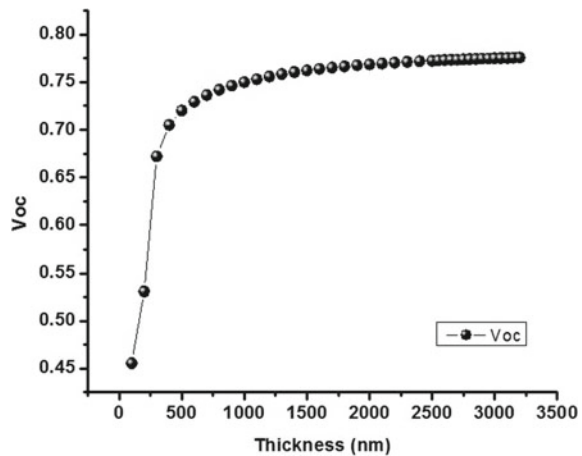
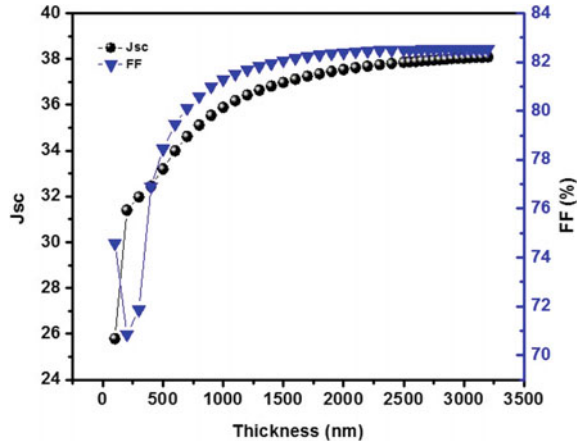


Fig. 10 Change of J_{sc} (short-circuit current density) and form factor with absorber layer's thickness at bandgap-1.26



Relation of Thickness, Short-Circuit Current Density, and Form Factor

From the following diagram, in place of thickness 100 nm, the short-circuit current density is 25.79 mA/cm² and form factor is 74.58%. On behalf of thickness 200 nm, the short-circuit current density is 31.40 mA/cm² with form factor 70.85%. For thickness 300 nm, we get 31.98 mA/cm² short-circuit current density along with 71.86% form factor. After that the form factor increases as accordingly but the short-circuit current density keeps expanding with growing thickness from the beginning. Finally, for thickness 3200 nm, the short-circuit current density develops at 38.09 mA/cm² and form factor develops at 82.53%. Aimed at changing thickness, the changing short-circuit current density besides form factor is in the diagram as per specified in Fig. 10.

Relation of Thickness and Efficiency

From the following diagram, in place of thickness 100 nm, the efficiency is 8.76%. On behalf of thickness 200 nm, the efficiency is 11.82% and so on. Finally, for thickness 3200 nm, the efficiency develops at 24.39%. Hence, the rising thickness also rises the efficiency; thus, we can say efficiency is proportional to thickness. Aimed at changing thickness, the changing efficiency is in the diagram as per specified in Fig. 11.

4.4 Bandgap 1.41

Relation of Thickness and Open-Circuit Voltage

From the following diagram, in place of thickness 100 nm, the open-circuit voltage is 0.4556 V. On behalf of thickness 200 nm, the open-circuit voltage is 0.5311 V and so on. Finally, for thickness 3200 nm, the open-circuit voltage develops at 1.36 V. Hence, the rising thickness also rises the open-circuit voltage thus we can say the open-circuit voltage is proportional to thickness. Aimed at changing thickness, the changing open-circuit voltage is in the diagram as per specified in Fig. 12.

Fig. 11 Change of η (efficiency) with absorber layer thickness at bandgap-1.26

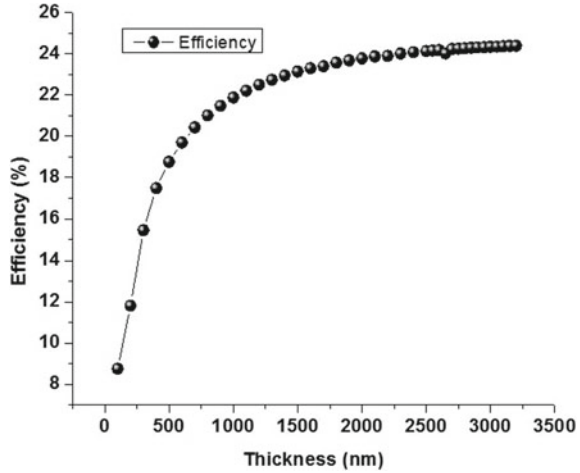
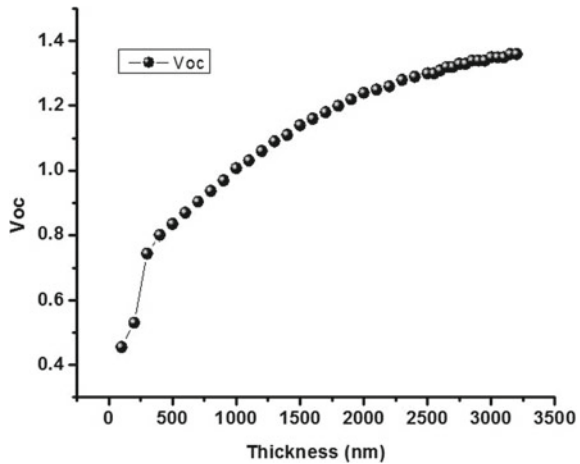


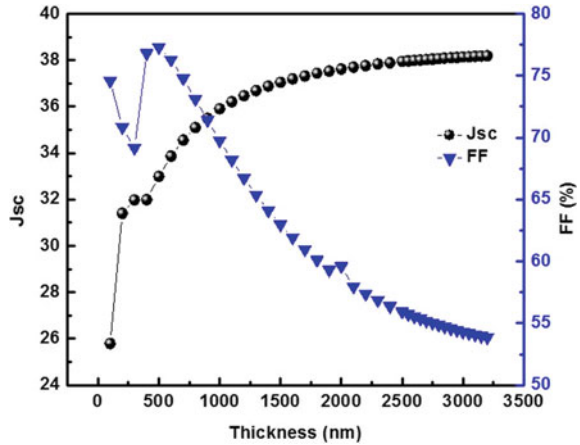
Fig. 12 Change of V_{oc} (open-circuit voltage) with absorber layer's thickness at bandgap-1.41



Relation of Thickness, Short-Circuit Current Density, and Form Factor

From the following diagram, in place of thickness 100 nm, the short-circuit current density is 25.79 mA/cm² and form factor is 74.58%. On behalf of thickness 200 nm, the short-circuit current density is 31.40 mA/cm² with form factor 70.84%. For thickness 300 nm, we get 31.98 mA/cm² short-circuit current density along with 69.16% form factor. After that the form factor becomes 76.81% for 400 nm thickness and increases as accordingly but the short-circuit current density keeps expanding with growing thickness from the beginning. Finally, for thickness 3200 nm, the short-circuit current density develops at 38.19 mA/cm² and form factor develops at 53.85%. Aimed at changing thickness, the changing short-circuit current density besides form factor is in the diagram as per specified in Fig. 13.

Fig. 13 Change of J_{sc} (short-circuit current density) and form factor with absorber layer's thickness at bandgap-1.41



Relation of Thickness and Efficiency

From the following diagram, in place of thickness 100 nm, the efficiency is 8.76%. On behalf of thickness 200 nm, the efficiency is 11.82% and so on. Finally, for thickness 3200 nm, the efficiency develops at 28.00%. Hence, the rising thickness also rises the efficiency, thus we can say efficiency is proportional to thickness. Aimed at changing thickness, the changing efficiency is in the diagram as per specified in Fig. 14.

Fig. 14 Change of η (efficiency) with absorber layer thickness at bandgap-1.41

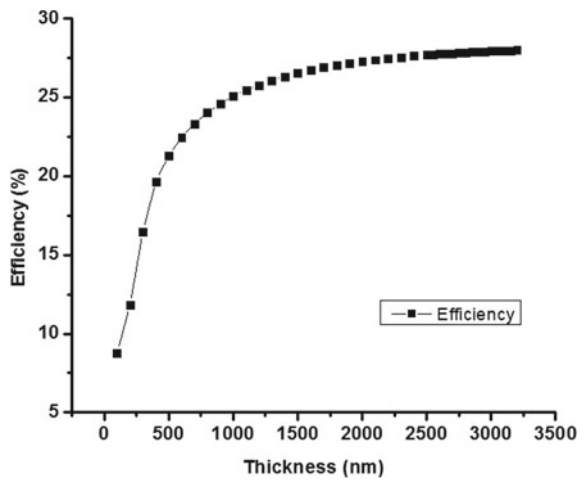
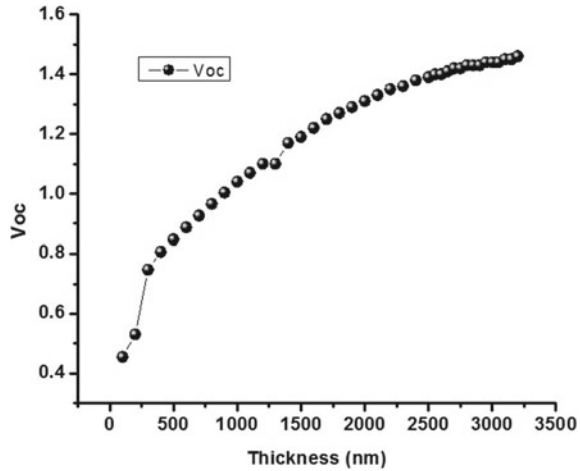


Fig. 15 Change of V_{oc} (open-circuit voltage) with absorber layer's thickness at bandgap-1.75



4.5 Bandgap 1.75

Relation of Thickness and Open-Circuit Voltage

From the following diagram, in place of thickness 100 nm, the open-circuit voltage is 0.4556 V. On behalf of thickness 200 nm, the open-circuit voltage is 0.5311 V and so on. Finally, for thickness 3200 nm, the open-circuit voltage develops at 1.4592 V. Hence, the rising thickness also rises the open-circuit voltage; thus, we can say the open-circuit voltage is proportional to thickness. Aimed at changing thickness, the changing open-circuit voltage is in the diagram as per specified in Fig. 15.

Relation of Thickness, Short-Circuit Current Density, and Form Factor

From the following diagram, in place of thickness 100 nm, the short-circuit current density is 25.79 mA/cm² and form factor is 74.58%. On behalf of thickness 200 nm, the short-circuit current density is 31.40 mA/cm² with form factor 70.84%. For thickness 300 nm, we get 31.98 mA/cm² short-circuit current density along with 69.02% form factor. After that the form factor becomes 76.59% for 400 nm thickness and increases as accordingly but the short-circuit current density keeps expanding with growing thickness from the beginning. Finally, for thickness 3200 nm, the short-circuit current density develops at 38.197 mA/cm² and form factor develops at 50.51%. Aimed at changing thickness, the changing short-circuit current density besides form factor is in the diagram as per specified in Fig. 16.

Relation of Thickness and Efficiency

From the following diagram, in place of thickness 100 nm, the efficiency is 8.76%. On behalf of thickness 200 nm, the efficiency is 11.82% and so on. Finally, for thickness 3200 nm, the efficiency develops at 28.15%. Hence, the rising thickness also rises the efficiency, thus we can say efficiency is proportional to thickness. Aimed at changing thickness, the changing efficiency is in the diagram as per specified in Fig. 17.

Fig. 16 Change of J_{sc} (short-circuit current density) and form factor with absorber layer's thickness at bandgap-1.75

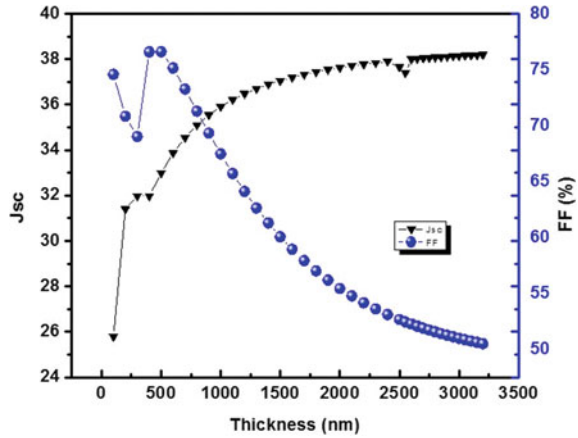
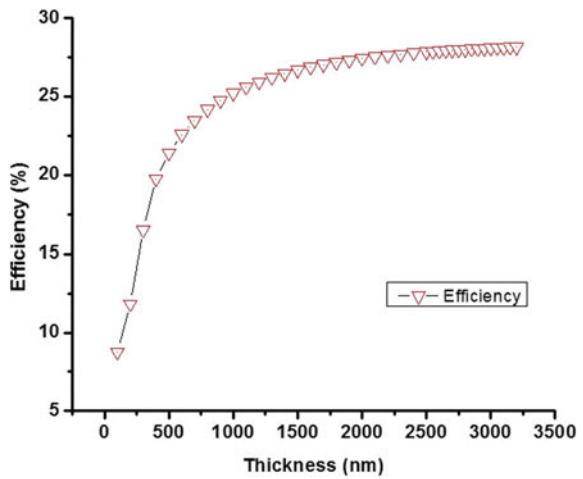


Fig. 17 Change of η (efficiency) with absorber layer thickness at bandgap-1.75



5 Conclusion

For different bandgap and thickness, the CIGS cell with CdS buffer layer has been discussed in this paper. By simulating, we have found out that, increasing thickness and bandgap increases efficiency, open-circuit voltage, and short-circuit current density but form factor shows different changes with the variation; normally decreases but for some conditions it also shows increased values which we have found through our study. We also know that higher bandgap decreases efficiency so we have chosen our highest bandgap to be 1.75. This paper shows all results for SCAPS software. Further studies and work should be done in this research field for both theoretical and practical.

References

1. N. Khoshsirat, N.A.M. Yunus, M.N. Hamidon, S. Shafie, N. Amin, Analysis of absorber layer properties effect on CIGS solar cell performance using SCAPS. *Optik* **126**(7–8), 681–686 (2015). <https://doi.org/10.1016/j.ijleo.2015.02.037>; <http://www.sciencedirect.com/science/article/pii/S0030402615000753>
2. A.K. Daoudia, E.H. Youssef, A. Benami, Investigation of the effect of thickness, band gap and temperature on the efficiency of CIGS solar cells through SCAPS-1D. *Int. J. Eng. Tech. Res.* **6**(2) (2016). ISSN: 2321-0869 (O) 2454-4698 (P)
3. M. Asaduzzaman, M. Hasan, A.N. Bahar, An investigation into the effects of band gap and doping concentration on Cu(In, Ga)Se₂ solar cell efficiency. *SpringerPlus* **5**, 578 (2016). <https://doi.org/10.1186/s40064-016-2256-8>
4. M. Gloeckler, J.R. Sites, Potential of submicrometer thickness Cu(In,Ga)Se₂ solar cells. *J. Appl. Phys.* **98**, Article ID 103703 (2005)
5. M. Gloeckler, J.R. Sites, Band-gap grading in Cu(In, Ga)Se solar cells. *J. Phys. Chem. Solids* **66**(11), 1891–1894 (2005)
6. T. Minemoto, T. Matsui et al., Theoretical analysis of the effect of conduction band offset of window/CIS layers on performance of CIS solar cells using device simulation. *Sol. Energy Mater. Sol. Cells* **67**, 83–88 (2001)
7. B.J. Stanbery, Copper indium selenides and related materials for photovoltaic devices. *Crit. Rev. Solid State Mater. Sci.* **27**(2), 73–117 (2002)
8. S.S. Mahtab, M.J. Alam, Numerical modeling and simulation of high-efficiency thin Cu(In,Ga)Se photovoltaic by WxAMPS, in *International Conference on Communication, Computing and Electronics Systems* ed. by V. Bindhu, J. Chen, J. Tavares. Lecture Notes in Electrical Engineering, vol. 637 (Springer, Singapore, 2020). https://doi.org/10.1007/978-981-15-2612-1_40
9. S.S. Mahtab, A. Monsur, S.S. Ahmed, R. Chakma, M.J. Alam, Design and optimization of perovskite solar cell with thin ZnO insulator layer as electron transport, in *2018 International Conference on Advancement in Electrical and Electronic Engineering (ICAEEE)*, Gazipur, Bangladesh (2018), pp. 1–4. <https://doi.org/10.1109/ICAEEE.2018.8643012>
10. R. Chakma et al., Navigation and tracking of AGV in ware house via wireless sensor network, in *2019 IEEE 3rd International Electrical and Energy Conference (CIEEC)*, Beijing, China (IEEE, 2019), pp. 1686–1690. <https://doi.org/10.1109/CIEEC47146.2019.CIEEC-2019589>
11. M.F.S. Khan et al., PLC based energy-efficient home automation system with smart task scheduling, in *2019 IEEE Sustainable Power and Energy Conference (iSPEC)*, Beijing, China (IEEE, 2019), pp. 35–38. <https://doi.org/10.1109/iSPEC48194.2019.8975223>
12. I.S. Emon, S.S. Ahmed, S.A. Milu, S.S. Mahtab, Sentiment analysis of Bengali online reviews written with English letter using machine learning approaches, in *Proceedings of the 6th International Conference on Networking, Systems and Security (NSysS'19)*, Association for Computing Machinery, New York, NY, USA (2019), pp. 109–115. <https://doi.org/10.1145/3362966.3362977>
13. S.A. Milu et al., Sentiment analysis of Bengali reviews for data and knowledge engineering: a Bengali language processing approach, in *International Conference on Communication, Computing and Electronics Systems* ed. by V. Bindhu, J. Chen, J. Tavares. Lecture Notes in Electrical Engineering, vol. 637 (Springer, Singapore, 2020). https://doi.org/10.1007/978-981-15-2612-1_8
14. S.S. Milu et al., Opinion mining of Bengali review written with English character using machine learning approaches, in *International Conference on Communication, Computing and Electronics Systems* ed. by V. Bindhu, J. Chen, J. Tavares. Lecture Notes in Electrical Engineering, vol. 637 (Springer, Singapore, 2020). https://doi.org/10.1007/978-981-15-2612-1_5

A Review on Architecture of Hybrid Electrical Vehicle and Multiple Energy Storage Devices



Kiran H. Raut and Asha Shendge

Abstract The usage of integrated energy storage devices in recent years has been a popular option for the continuous production, reliable, and safe wireless power supplies. In adopting these techniques, there are many advantages to the energy storage devices may be correctly integrated and an adequate supply of electricity for different applications possible. This need has encouraged the growing introduction of distributed generation systems and predominantly renewable energy sources. In today's power networks, the widespread usage of these energy sources may be unquestionable and minimize the thread of climate change and global warming. This paper aim is to describe an architecture of hybrid electric vehicles and technology use for storing electrical energy. The article addresses the role of the technology for mechanical, thermal, electrochemical, and chemical storage.

Keywords Architecture of HEV · Concept of energy storage · Multiple energy storage devices

1 Introduction

Provides well designed and organized transport mobility for citizen and products. The transport sector comprises mainly of road, rail, ships, and aircraft, where road transportation occupies 75% of the overall resources expended. The automobile sector plays a vital part, the place of the economic prosperity of the nation, and so this affects culture as a whole. Since vehicles are mainly powered by the internal combustion engine (ICE), transport industry accounts for 25–30% of the total greenhouse gas emissions [1]. ICE operates in fuel cycle combustion which results in the development of different gases same as CO₂, NO₂, NO, and CO [2], which affect the

K. H. Raut (✉)

Electrical Engineering Department, G H Raisoni University, Amravati, India

A. Shendge

Electrical Engineering Department, G H Raisoni Institute of Engineering and Technology, Pune, India

e-mail: Asha.shendge@raisoni.net

atmosphere degradation by greenhouse influence and responsible for the harmful human health consequences.

Scientists, academics, and policy-makers have been compelled to center them on beginning to learn of renewable technologies or devices that can interrupt the negative effects of its just nature occurring. As a consequence, the twenty-first century will become a century evolution of the various systems with the primary emphasis on automotive sector. The innovations that would turn the automotive industry face will be “hybrid electric car,” “hybrid solar car,” “hydrogen fuel cell,” etc. All this hybrid electric vehicle is known to be the most industrially developed technology and has more capacity than petrol or diesel or CNG vehicles, while hybrid solar vehicle has lower output than petrol or diesel or CNG vehicles.

The first registered hybrid vehicles were exhibited at Paris Salon in 1899 [1]. They were founded by Vendovelli and the French Priestly Electric Carriage Company in Liège, Belgium, and by the Pieper establishments. The Pieper vehicle was a dual hybrid powered by a powerful air-cooled petrol engine electric motor and lead battery-acid tank.

Frenchman Camille Jenatzy introduced a similar construction car at Paris in 1903. This vehicle coupled a 6 hp gasoline engine with a 14 hp gasoline engine mechanical unit that can either charge the battery on the motor.

During a period from 1899 to 1914, other parallel and series-type hybrid vehicles were constructed. The biggest challenge is to compete with those early prototypes. It was the electric computer controlling complexity. It offered a limited operational spectrum incoherent of successful operation. Because of these restrictions, the interface conforms to the usage of an electric vehicle.

Dr. Victor Wouk designed a parallel model version of a Buick Skylark in 1975 along with his colleagues [1]. The motor was a Renault rotary. Engine accompanied by a manual transmission. Separately, enthralled DC unit was assisted by a 15 hp located in front of the transmitter. Eight to 12 V car batteries were common for storing electricity. Fast speed of 80 mph (129 km/h) was reached in 16 s with acceleration from 0 to 60 mph.

HEVs and EVs are now making a return in the traditional market conveyance. Global large population density cities are considering usage of IC engines a safety problem. In certain instances, smoking indoors are banned in Western nations. Similarly, usage of IC engines in potential cities may be outlawed: The European Union aims to phase down conventionally tanked vehicles in towns by 2050 [3].

2 Architecture of Hybrid Vehicle

The hybrid vehicle design is defined as the link between the various components and comprises primarily of the power source routes and control ports. HEVs are classified in three forms: series hybrid, parallel hybrid, and series and parallel hybrid systems [4].

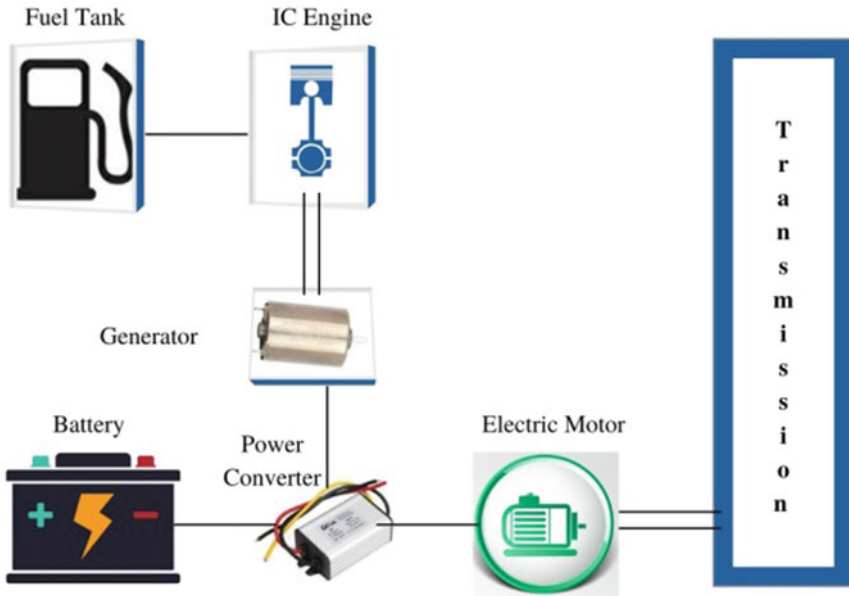


Fig. 1 Series Hybrid System [1]

2.1 Series Hybrid Vehicle

A series hybrid vehicle, the power of a single electric motor, is supplied for propelling the unit by two electric motors. The HEV system's main components include an IC generator, battery, electric motor, and a power converter. The IC engine, together with the electric motor, is powered by a fuel tank. The electric generator output is connected via power converter (rectifier) to electric power bus. The traction motor may either be powered in forward or reverse direction as an engine or generator. The drive will need a adapter to charge the batteries from the power network with a wall plug-in. A hybrid sequence of emissions reduction, a simple control scheme, and better efficiency. The challenge the EV faces is its short driving range, generator contributes extra weight, and expense, and the engine's energy is transferred twice. In the driving cycle, the energy transfer in the drive train is either linear or in sequence (Fig. 1).

2.2 Parallel Hybrid Vehicle

The engine is operated by an IC engine or electronic traction motor which is linked in parallel with the train motion HEV system. Both ICE and electric motors are attached to the same drive shaft and with specific drive power at the same time.

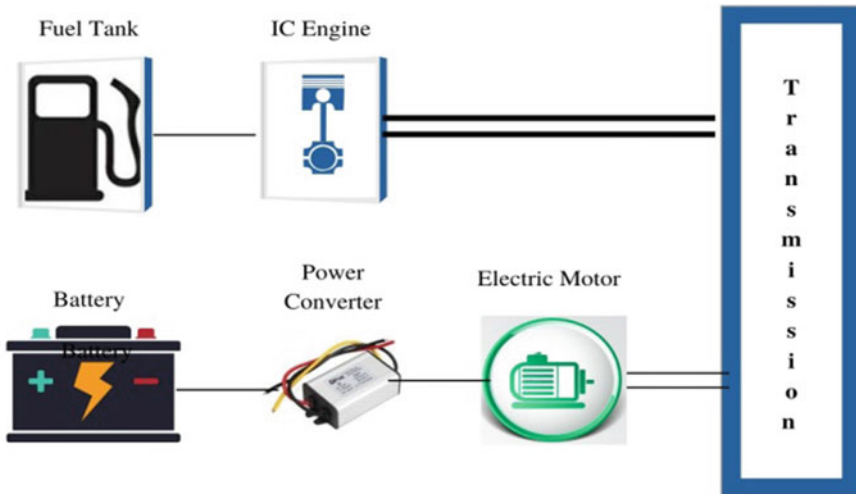


Fig. 2 Parallel Hybrid System [1]

The mechanical connection links the IC engine with electric motor in Fig. 2. HEV is easily available in the sector throughout the business, for example Honda, Civic Hybrid, and Honda Insight ICE are two-wheelers specifically related. In the cycle of regenerative braking and driving, the battery is recharged. The electrical unit serves as a generator during engine braking and supplies the battery with electricity. ICE's need for energy is greatly reduced by choosing the right battery power and ensuring good cooperation across primary agencies, too secondary a source of strength. This system is less costly but the drive issue cannot be charged as a series drive train and ICE cannot be mounted somewhere as it needs to be connected to the propulsion system.

2.3 Series and Parallel or Combine Hybrid Vehicle

Parallel system or combination mix or phase split integrates the sequence characteristics with parallel configuration. This mechanism consists basically of two control paths which are supplied to the wheels. The parallel route involves transferred energy to the same shaft from engine to wheel and the associated motor power. The series route includes an IC engine and control generator controller [4]. This lightweight drive can be powered in nature and batteries on electric mode while the vehicle is in motion. The complexity of this drive is currently growing with the usage of several components in the system (Fig. 3).

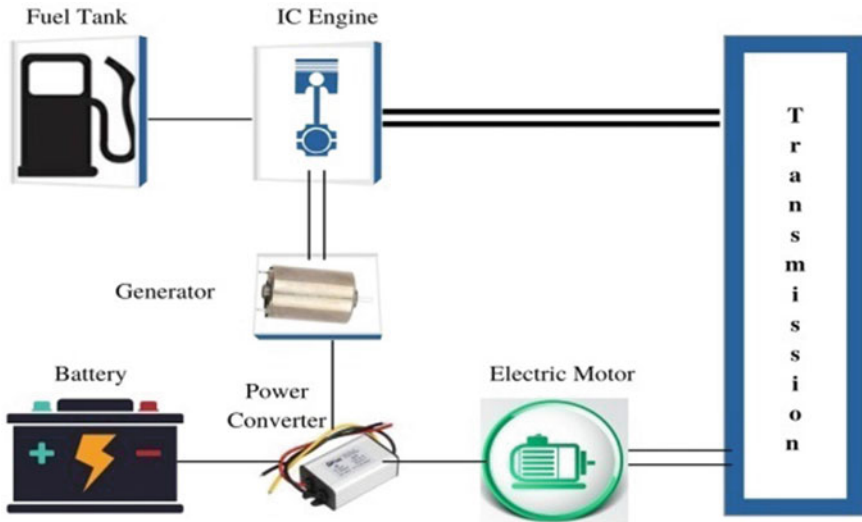


Fig. 3 Series and Parallel Hybrid Vehicle [1]

3 Concept of Energy Storage

According to the energy conservation act, in a close network, cumulative capacity is set and electricity cannot be produced or lost. It can only be converted from one form to another, or modified. The basic theory serves as the foundation of virtually all energy transport and storage methods. The bulk of storage systems is grouped into four generic categories according to the literature analysis: mechanical energy storage, chemical energy storage, electrochemical energy storage, and electrical energy storage.

The highest amount of electrical work that can be withdrawn from a production plant is given by

$$G = H - TS \tag{1}$$

G indicates the average energy required for mechanical or electrical operation, H is enthalpy, T is temperature, and S is entropy.

3.1 Mechanical Energy Storage

Mechanical energy may be either kinetic energy or potential energy, for example pumped hydro is expressed by potential, $E_{\text{potential}}$, and/or kinetic, K_{kinetic} , energies that can be describe by

$$E_{\text{potential}} = f d \quad (2)$$

Here, f stands for power, d is distance

$$K_{\text{kinetic}} = (1/2)mv^2 \quad (3)$$

In these cases, m is mass and v denotes velocity. The kinetic energy for a spinning object, like a flywheel or a wind turbine, is represented in a similar expression

$$E_{\text{kinetic}} = (1/2) m\omega^2 \quad (4)$$

3.2 *Chemical Energy Storage*

Chemical storage is based on the energy contained in the chemical bonds of fuels which are inherently stable and thus have very large electricity densities. Nonetheless, usually one needs the use of electrical or thermal energy to generate the fuels for chemical storage. The control equation for optimum chemical storage function is given by above Eq. 1.

3.3 *Electrochemical Energy Storage*

Electrochemical storage systems are designed to load electrodes with battery or electric interface with electrochemical condensers or super condensers or chemical bindings of fuels, like fuel cells. Electrochemical energy storage provides intrinsically high efficiencies as the theoretical output for electrochemical energy transfer is described by the ration of $(\Delta G/\Delta H)$.

3.4 *Electrical Energy Storage*

Electrical energy storage (EES) can enable facilitate the accelerated transition of the global electricity system through innovations in sustainable technology, achieve effective load-leveling and control, promote widespread renewable energy deployment, understand distributed generation and municipal grids, and boost energy protection. Several key important benefits occur in energy. First of all, the electricity production is isolated from the load or energy consumption which allows power supply and demand. Secondly, it improves the efficiency of the mains and hence the electricity performance of integrated storage networks for municipal grids or micro grids.

4 Classification of Energy Storage

Energy storage system as for large or small energy storage devices plays a crucial role in a variety of industrial applications. The main criteria for selecting different energy devices are specific power, lifetime, energy-specific, reliability, and safety. Energy storage devices are the most costly device in the traditional standalone network for different power applications, but have just a short charge / discharge duration, making them economically unsustainable. Hybrid electric storage systems (HESSs) have started to appear, incorporating the advantages of two or more technologies. The detailed ESS classification is given Fig. 4. Classification is made based on the energy stored.

Recently, a number of electrical storage technologies have been developed including pumped hydropower, compressed air energy storage (CAES), batteries, flywheels, superconducting magnetic energy storage (SMES), super capacitors, and hydrogen storage.

4.1 Pump Hydro Energy Storage

Since 1929, pumped hydro is used as an electric storage method, rendering it the oldest device used. Pump hydro storage (PHS) consists of two reservoirs, each of which is built on two separate stages. It operates by storing energy in the upper reservoir in water, which is transferred from the second reservoir to the lower reservoir when the network has excess power. When there is energy demand, the water in the

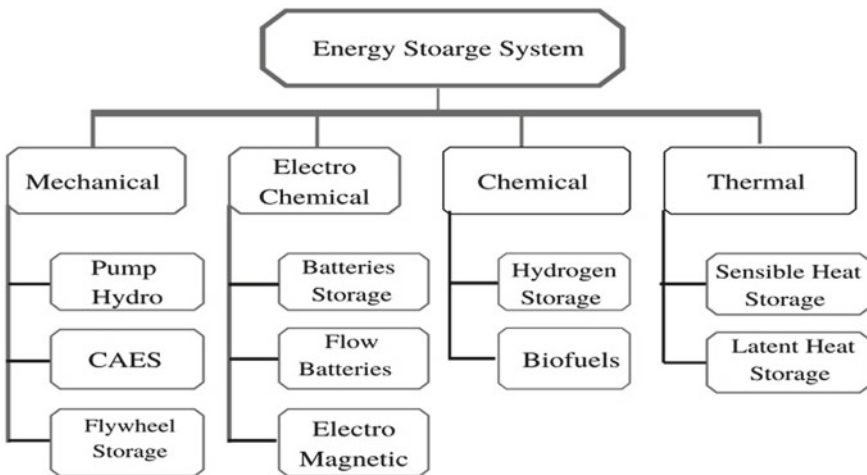


Fig. 4 Classification of ESS [5]

upper reservoir is released, and when it falls, it spins turbines that generate the electricity.

Case study: In 1999, a pumped hydroelectric power plant was first constructed in Japan (Yanbaru, 30 MW). There are more than 90 GW of pumped storage in operation worldwide, which is around 3 percent of global electricity production. Kadamparai (Tamil Nadu), Bhira (Maharashtra), Srisailem (Andhra Pradesh), Ghatghar (Maharashtra), Purulia (West Bengal), and Paithan are some of the pump storage projects in India (Maharashtra). The power plant’s installed capacity is 2612 MW (source: CEA, IEEFA).

4.2 Compress Air Energy Storage

Additional to PHES is the compressed air energy storage (CAES). Another evolving platform suitable for use as a wide storage device, within the hundreds of MW background [6, 7] which have a similar working principle to modern gas turbine technology in which uses the elastic potential of compressed air save the energy. At off-peak load, the CAES enters in to charging mode when the air is compressed and stored in underground or sealed storage tanks vessel room. When the peak load is compressed hours, when electricity is to be supplied to the grid air and is drawn from storage tanks, gradually heated, and then released by high-pressure turbine, which converts much of the compressed air energy into the device kinetic rotational energy, which is converted to electricity by turbine-coupled power unit as shown in Fig. 5.

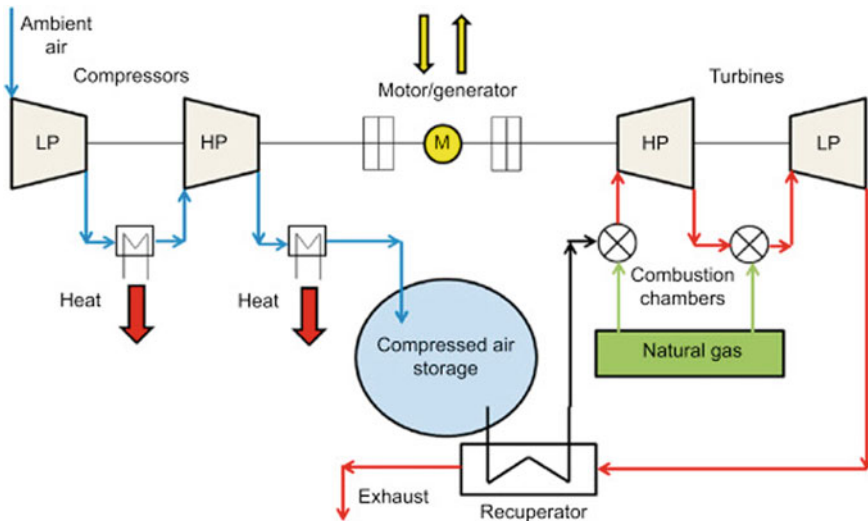


Fig. 5 CAES system

Case study: As industrial, CAES networks are actually running around the globe in the United States (US) and Germany. At the highest of these, which has been working at Huntorf in Germany since 1978, a cavern of $0.3 \times 106 \text{ m}^3$ is pressurized utilizing 60 MW of surplus nuclear power produced for 8 h per day cycle and the compressed air supplies a gas-fired turbine to produce 320 MW for 2 h during the high demand time [8].

There are actually two CAES facilities in service around the globe. Both utilize common concepts of architecture and service and storage devices. Many other potential CAES programs are being developed and completed at separate phases. The functioning of established CAES facilities provides for prior research with which to build a second generation CAES facility in Gwalior, India. Several CAES projects are already being planned in India. Other projects in Louisiana, New York and California are in consideration, but preparation for these facilities remains in the early stages.

4.3 Flywheel Energy Storage

FES is used to store energy in form of kinetic energy through the angular momentum of the flywheel mass. For short-term uses such as energy demands of more than 80 kW and 1–100 s [9], they are typically used. The benefit of the flywheel provides an infinitesimal amount of charge-discard cycles with high strength and energy density and is used for voltage and frequency stability, reliability, low maintenance, and reduced environmental effects. They are also very costly to produce.

The quantity of energy (E) retained by FES depends on the moment of inertia (I) and the rotating velocity of the mass (ω), as given by equation

$$E_{\text{kinetic}} = (1/2)mI^2 \quad (5)$$

Case study: The Grobus was the flywheel system used in transport, operated by a 1500 kg flywheel built in Switzerland during the 1950s [10]. The main uses for flywheel energy storage systems are frequency regulation of the power quality, monitoring voltage falls, renewable, and satellites.

Integrated technologies of battery and flywheel boost performance and increasing the weight and expense of spacecraft. NASA's proposed flywheel configuration includes a compound rotor and magnetic bearings capable of maintaining peak power of 15 MJ and 4.1 kW, with net output of 93.7% [11] (Table 1).

Table 1 Comparison of low to high level FES [11]

Specifications	Low speed FES	High speed FES
Material	Steel	Composite
Electrical machine	Induction, permanent magnet synchronous and reluctance machine	Permanent magnet synchronous and reluctance machine
Quarantine atmosphere	Partial vacuum and partial gas	Absolute vacuum
Required weight of enclosure	Double of flywheel weight	Half of flywheel weight
Applications	Power quality improvement	Aerospace and traction
Economy	Low cost and commercial	High cost and specific usage

4.4 Batteries

Batteries generally provide attractive solutions for cost-effective and compact storage, non-moving-parts pollution-free operation, high overall performance, good cycle life, substantial shelf life, and service life. Several batteries are indicated in Fig. 6. They have resources from seasonal renewable sources for centralized cooling and controlling frequencies. Unfortunately, some of these devices are now too costly to effectively be utilized for large-scale energy storage and need major improvements in material capacity, reliability, versatility and longevity, as well as cost savings. [12]. Nevertheless, their growing dominance of the industry is projected to drive down battery costs.

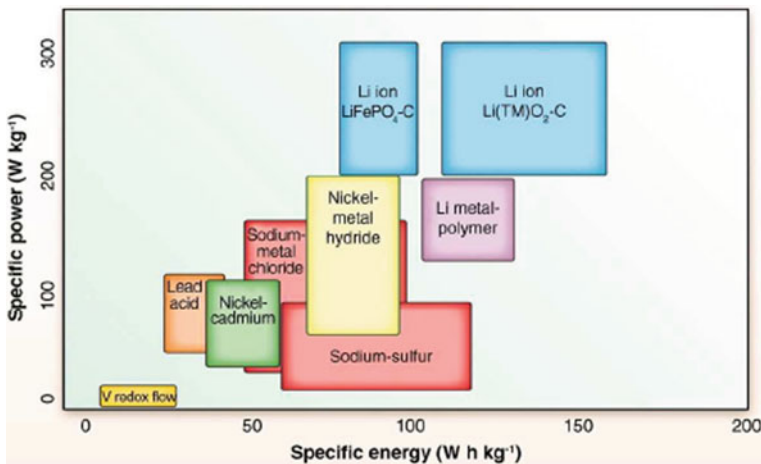


Fig. 6 Diagram of specific energy versus specific power for major rechargeable battery systems [12]

Nearly, all vehicles are currently used as battery storage for chemical batteries. The state of the battery modules currently accessible for both EVs and HEVs is shown in Table 2.

Case study: In 1800, Italian scientist Alessandro Volta developed the first real battery. Volta stacked copper (Cu) and zinc (Zn) disks divided by fabric that was immersed in salty water. In 1859, the lead-acid battery was developed several of the most common batteries which are still the device used to power most internal combustion engine automobiles today.

Batteries now come with a large range of sizes from large megawatt capacities that store the electricity from solar panels or substations to maintain reliable supply of whole towns or islands, down to tiny batteries such as those found of electronic devices.

Table 2 System status for EV and HEV batteries [6]

	Specific energy (kW/kg)	Peak power (W/kg)	Energy efficiency (%)	Cycle life	Cost (\$/kWh)
Acidic aqueous solution					
Lead-acid	35–50	50–400	> 80	500–1000	120–150
Alkaline aqueous solution					
Nickel/cadmium	40–60	80–150	75	800	250–350
Nickel/iron	50–60	80–150	65	1500–2000	200–400
Nickel/zinc	55–75	170–260	70	300	100–300
Ni-metal-hydride	70–90	200–300	70	750–1200+	200–350
Aluminum/air	200–300	90	< 50	–	–
Iron/air	80–120	90	60	500+	50
Zinc/air	100–200	30–80	60	600+	90–120
Flow					
Zinc/bromine	70–85	90–110	65–75	500–2000	200–250
Vanadium redox	20–30	110	75–85		400–450
Molten salt					
Sodium/sulfur	150–240	230	85	800+	250–450
Sodium/Ni/Cl	90–120	130–160	80	1200+	230–345
Li-ion-sulfur (FeS)	100–130	150–250	80	1000+	110
Organic/lithium					
Lithium-ion	80–130	200–300	> 95	1000+	200
Li-ion high power*	85–95	~ 4000	–	–	–
Li-ion high energy*	135–150	~ 600	–	–	–

Table 3 SMES-technical evidence [5]

Energy density	Rated power capacity (MW)	Duration	Cycle efficiency	Energy cost (\$/kWh)	Power capacity cost (\$/kW)	Life (year)
0.2–5 Wh/L	0.1–10	8 ms	90–97	200–350	200–350	20–30

4.5 Superconducting Magnetic Energy Storage (SMES)

Superconducting magnetic energy storage (SMES) systems keep electricity under the magnetic field. A constant current flowing across a superconducting wire creates a magnetic field. In a typical cable, energy is lost as heat when electrical current flows through the metal due to electrical strength. However, the wire is a superconducting material in a SMES system and is cooled under its critical stage. This means the electric current can be stored in a SMES system for a longer period through the wire with virtually no resistance. The rising coil ingredients are mercury, vanadium, and niobium-titanium. The energy collected on a SMES device is discharged by linking the AC power converter to the conductive coil. SMES systems are highly efficient storage technology but they have very low energy densities and are far from economically viable.

Case study: Superconducting magnetic energy storage (SMES) was initially developed as an energy supply to satisfy the diurnal variability in the demand for electricity. In 1969, Ferrier introduced a single wide device to accommodate the regular power variation in France. The initial design consisted of a three-component. Superconducting magnet and a cooling mechanism for controlling operating temperature and a connection between direct current in magnet and power grid.

The latest accelerated development of SMES technology is in progress. A great deal of interest linked to the common usage of silicon-based three phase adjustable motor drives (ASDs) and FACT drives appliances that can be seen as supporting technology introduction of SMES (Table 3).

4.6 Super Capacitor

A super capacitor, functionally lies, is somewhere between the conventional batteries and condensers. As for the batteries, super condensers are two electrodes separated by one separator and energy storage in the form of an electrostatic field like a conventional condenser but they can store a large amount of energy per unit volume (10–100 times more than a conventional condenser) and have a very fast response (10 times faster than batteries). Super condenser capacitance (C) is determined by the electrode surface area (A).

The surface area is far greater than traditional condenser electrodes owing to porous design, isolation of the separator's electrodes (d), and dielectric constant (π),

Table 4 Generalized features of super capacitor [13]

Sr. No.	Technology	Standards
1	Model	BMOD0430 E016
2	Rated voltage	16 V
3	Capacitance	430 F
4	Operating temperature range	− 40 °C to + 65 °C
5	Number of cell	6
6	Voltage across individual cell	2.7 V
7	Mass	5.50 kg
8	ESR DC (moh-m)	3.5 (moh-m)
9	ESR 1 kHz (moh-m)	2.8 (moh-m)

as shown by equation.

$$C \propto \epsilon A/d \tag{6}$$

Super condensers are divided into three main types: double layer (DL) condensers, pseudo-capacitors, and hybrid condensers. Transparent activated carbon serves as electrodes, recently chemical aerosols and still using carbon nanotubes [7] (Table 4).

Case study: The new hybrid capacitor development comprises primarily of hybrid condensers of composite form, asymmetric form, and battery type. The cumulative power installed for the grid linked capacitor program is 30.903 MW. Using super capacitor for energy storage applications, it is not very popular nowadays and there is still demonstration of research and development (RandD) and pre-commercial period of this technology. The energy range of the capacitors is 0.001–10 kWh, regardless of the very small period of storage time. In comparison, power prices (300–2000 \$/kWh) are very small capacitor capacity which enables them to switch into their own promotion.

4.7 Hydrogen Storage

Power in the form of hydrogen may be extracted and transported. The hydrogen and oxygen degradation of water require electrical energy. These gasses must be processed and shipped, and then mixed again to release the collected steam. Oxygen is usually removed from the soil to combine the two. Hydrogen is found in the form of a gas (hydrogen pressure), stable shape, and in the shape of hydride-metal. In deep caverns, hydrogen is found in a gaseous shape as dry as NG reservoirs. The liquid supply of hydrogen by low hydrogen boiling point (20 K) is challenging to manage. A ventilation system is expected to maintain the need for air storage [14].

Case study: Six MW Audi e-gas ESS and six MW Energy Park Mainz, Germany are the major hydrogen storage projects connected to the grid. ADLE163 (Switzerland), BOR4STORE (Germany), Ideal Hy (Netherlands), Sapphire (Norway), Smart Cat (France), etc., are designed the latest hydrogen storage and FC undertakings [15].

5 Conclusion

There are several specific energy storage systems available, each providing its own beneficial capabilities while used for a specific application. All power storage devices have undergone and continue to be in the cycle of development, to improve performance and efficiency. This paper systematically explored state-of-the-art modern hybrid vehicle technology that includes architecture and various devices for energy storage. The systems more frequently use parallel and series-parallel systems. The design of series hybrids is often used by large trucks, combat equipment, and buses, with their own benefits and disadvantages. Parallel and series-parallel, on the other side, are primarily found in compact vehicles such as passenger cars. From the study, storage technologies are developed with a very fast response suitable for applications of power quality such as small and medium-sized businesses and super capacitors; FES, BESS, and FBESS are favored alternatives for these systems.

References

1. M. Ehsani, *Modern Electric, Hybrid Electric and Fuel Cell Vehicles: Fundamentals, Theory and Design* (CRC Press, Boca Raton, 2005)
2. N. Khan, S Dilshad et al., Review of energy storage and transportation of energy. *Energy Storage* 1–49 (2019). <https://doi.org/10.1002/est2.49>. www.wileyonlinelibrary.com/journal/est2
3. A. Karki, S. Phuyal et al., Status of pure electric vehicle power train technology and future prospects. *Appl. Syst. Innov.* (2020). <https://doi.org/10.3390/asi3030035>
4. K.V. Singh, H.O. Bansal, D. Singh, A comprehensive review on hybrid electric vehicles: architectures and components. *J. Mod. Transp.* 77–107 (2019). <https://doi.org/10.1007/s40534-019-0184-3>
5. O. Krishan, S. Suhag, An updated review of energy storage systems: Classification and applications in distributed generation power systems incorporating renewable energy resources. *Int. J. Energy Res.* 1–40 (2018). <https://doi.org/10.1002/er.4285>. wileyonlinelibrary.com/journal/er
6. www.saftbatteries.com/automotive/uk/f/f.htm. SAFT Batteries.
7. M.E. Şahin, F. Blaabjerg, A hybrid PV battery/supercapacitor system and a basic active power control proposal in MATLAB/Simulink. *Electronics* 1–19 (2020). <https://doi.org/10.3390/electronics9010129>. www.mdpi.com/journal/electronics
8. S.A. Rackley, *Carbon Capture and Storage*, 2nd edn. (2017), pp. 471–488
9. M.E. Amiryar, K.R. Pullen, *Applied sciences a review of flywheel energy storage system technologies and their applications* (2017)
10. M.E. Amiryar*, K.R. Pullen, A review of flywheel energy storage system technologies and their applications. *Appl. Sci.* (2017). <https://doi.org/10.3390/app7030286>. <https://www.mdpi.com/journal/applsci>

11. H. Liu, J. Jiang, Flywheel energy storage. An upswing technology for energy sustainability. *Energy Build.* **39**, 599–604 (2007)
12. T.M. Gur, Review of electrical energy storage technologies, materials and systems: challenges and prospects for large-scale grid storage. *Energy Environ. Sci.* 1–154 (2018). <https://doi.org/10.1039/C8EE01419A>
13. V. Tibude, S.G. Tamekar, Co-working of solar panel – battery – super capacitor for electric vehicle. *Int. J. Eng. Res. Electr. Electron. Eng. (IJEREEE)* **2**(3), 7–13 (2016)
14. M. Kopp, D. Coleman, C. Stiller, K. Scheffer, J. Aichinger, B. Scheppat, Energiepark Mainz: technical and economic analysis of the worldwide largest power-to-gas plant with PEM electrolysis. *Int. J. Hydrogen Energy* **42**(19), 13311–13320 (2017)
15. The first industrial PtG plant—“Audi e-gas as driver for the energy turnaround” (2018) <http://www.cedec.com/files/default/8-2014-05>

Comprehensive Topological Analysis of Solar Integrated Multilevel Inverter for Power Filters



Bipasa Patra and Pragya Nema 

Abstract According to the present situation, it is observed that the energy demands are increasing day by day. This is the outcome of our growing population and henceforth it is increasing energy demands. So there arises the need of many different and varied energy resources that can be renewed. At this point, more stress is being laid on the green and environment-friendly technical advances. At present time, the demand at load end is growing at an alarming rate while the non-renewable sources (mostly fossil resources like coal etc.) are getting depleted and nearing extinction, so it becomes essential to introduce and work more in the field of renewable energy like the solar, water etc. Above all, the most substantial development is in the arena of development of PV with MLI domain so as to procure the voltages at several levels if summarized against inverter with a conventional circuitry. This paper presents a complete detailed discussion of methodological, financial and strategic aspects of control methodologies related to MLI. This paper also presents a valuation of the advanced trends in the domain of quality power dependent on the available conditions depending on the capability for improved efficiency with lowered harmonics.

Keywords Solar photovoltaic (PV) systems · Multilevel inverter (MLI) · Control designs and algorithms · Power drives · Fundamental and high switching frequency · Reduced harmonics

1 Introduction

Energy demands are increasing day by day. Nature has provided humans with plenty of free gifts which if used properly can suffice the present as well as the future energy demands; these are termed as renewable energy resources. The renewable system can convert energy from the sources like water, wind, sunlight etc., into electricity. It has been found that the main source of energy from sun estimates approximately 20,000 times the global requirement. The extraction for maximum possible energy

B. Patra (✉) · P. Nema
Oriental University, Indore, Madhya Pradesh, India

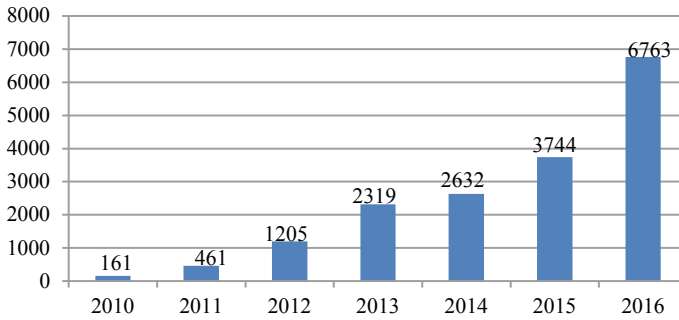


Fig. 1 Year cumulative capacity (in MW) of installed solar PV

can be carried out with the MPPT scheme so as to maintain the balance with the load demands, irrespective of the weather constraints. In huge interconnected power systems, the cascaded H Bridge MLI needs a separate source (DC) for maintaining the power at HV that needs to be remote [1]. Figure 1 shows the year cumulative capacity (in MW) of installed solar PV.

It is a proven fact that for required power semiconductor converter devices, the solar PV systems are good to produce low-voltage to maintain the balance with the load demands, irrespective of the weather constraints without compromising on efficiency [2]. For inverting the DC, the converter serves the purpose, by receiving the same from any PV source. As of the charge, controller serves the purpose of interfacing by linking the PV source and utility web end. Generally, CSI or VSI function for the same. In case of traditional two-level converter at the output, we have the voltage as a function of Voltage 0, $+V_{dc}$ or $-V_{dc}$ [3].

The multilevel inverter's history started finding its importance as early as in the middle of 1970s. Then in 1975, the patent was first filed by Baker and Bannister which elaborated the inverter configuration that utilized the DC sources to generate the output in a multilevel pattern. They worked on multilevel configuration with three levels and five levels. Then in 1980, Baker introduced a different model with series allied clamping diodes with the five-level topology. This way, the DCMLI came into existence. After that in mid 1990s, the conceptual topologies took more focus. Then in 1992, Meynard and Foch patented the flying capacitor MLI. Later in 1997, a much-developed model CHB-MLI was presented by Hammond. Then the issues regarding control strategies and modulations were significantly worked for multilevel voltage source modulation PWM, including modulation in the sinusoidal triangle and modulation by space vector technique by Bowes in 1975 and Bhagwat and Stefanovic in 1983, respectively. Utility and drive systems use power electronic drives that were used widely and gaining acceptance as demonstrated successfully by Tolbert and Peng 1998, 1999, 2002. This further established the direct dependency of increase in voltage level with the betterment in efficiency. This helped to understand that the conventional inverters can be switched to every input or output connections

in the two possible voltage or current levels only. But MLI on the other hand had the flexibility to switch between different levels of voltage and current.

2 Classification and Types

2.1 *Multilevel Inverter*

Relating to this, present-day pros and cons for the MLI have come into existence. The final quality of the output is superb, having improved profile as far as power quality issues are concerned. This has been proved with the relative study of MLI with the traditional two-level inverter [4]. It was in 1981 that Nabae explored multilevel inverter as a potential in this domain. As the amplification of counted stages of aforesaid inverter is done, generation of a staircase waveform w.r.t. the output voltage with minimal harmonics content is observed [5]. It is also found beneficial for the lowered stress content in voltage. The content of ratio of dv to dt with minimal common mode voltage leads less disturbances in output power quality [6]. MLI serves best for medium-voltage and high-power applications.

Pros and Cons of Multilevel Inverter

The domain of multilevel inverter is gaining popularity because of the proven potential with uniqueness of ideas implemented, that get it contrasted from the conventional design. Most prominently, the fact that it can be collaborated with resources like solar is the best part since we can harness this as a DC source to the maximum extent. Hence, the high-powered ratings with MLI configuration are employed to get better voltage profile as well. Thus, we can avoid bulky and spacious transformers for the requirement of HV with conventional two-level converters that finally tend to increase the overall cost. Also, a lot can be worked out well by using many DC buses and hence the lowering of electromagnetic interference by employing the multiple level inverters by lowering voltage hassles with low voltage of steps. This leads to higher efficiencies for devices employing switching at lowered frequencies.

But the bitter side of this technology is still into existence and is being worked upon. Actually, a greater number of separate and remote power supplies are needed for individual MLI. Hence, huge count of devices may lead to increased risk of failure of components. So, a lot of work is being carried out to overcome these issues, and it is always one of the areas with greater interest for the researchers.

2.2 *Topologies of Multilevel Inverter*

Renewable energy resources can be easily increased due to the lower switching frequencies in multilevel inverter, causing lower disturbances in its operation. As

the amplification of counted stages of multiple level inverters is done, generation of a staircase waveform w.r.t. the output voltage with minimal harmonics content is observed. This proves that level count has an inverse relation THD content of harmonics. In other words, if number of levels tend to infinity THD to an extent progressively tends to zero. While increasing the MLI levels of the numerous components, also enhancing and execution of control become more difficult. So the necessary topology, which is accurate, is needful to overcome this disadvantage. Most commonly used domains with three different multilevel of inverter designs are like: DCMLI—Diode clamped MLI, FCMLI—Flying capacitor MLI, CMLI—Cascaded MLI. It is also interesting to find out that lesser number of switches introduced helps to reduce the component count to be employed for gate drives. Further, as the switch count is reduced that accounts to improving the efficiency and supports the minimization of complexities involved in control techniques [7] (Fig. 2).

Multilevel Inverter with Diode Clamped Topology

In a multilevel inverter having diode clamped configuration, the point that is neutral is clamped with a diode. This clamp is provided so as to assist the DC voltage source with the ability to produce the output waveform in steps [9]. So as to obtain any count of levels (N) for the formulation of double the switches $(N - 1)$, $(N - 1)(N - 2)$ diodes and $(N - 1)$ number of capacitors are being employed for clamping. The voltage source V_{dc} , then by use of capacitor $C_1 - C_N$ in series, is further divided into numerous levels of voltage [10].

Multilevel Inverter with Flying Capacitor Topology

This is constructionally much more similar to the configuration of inverter clamped with a diode as discussed above, hence following the name capacitor clamped MLI, wherein the capacitor replaces the diode [11]. Due to the involvement of capacitor, the functioning now is evaluated by the charging characteristics. Then it follows the discharging cycle of the flying capacitor that is linked with the neutral tip [12, 13]. The changes or variation in the charging and discharging times of each clamping capacitor causes an output waveform of voltage as a multiple level format. Similar ratings of the capacitors as in the diode clamped are required for this purpose for obtaining the N level output, with requirement of capacitors as half of the product of $(N - 1)$ and $(N - 2)$ are required for clamping.

Multilevel Inverter with Cascaded Topology

This is the simplest and extensively used configuration for a number of uses in power quality controls. It is also termed H Bridge Inverter due to its configuration setup where for N levels, $(N - 1)/2$ sources will be needed. This configuration includes a Bridge with H configuration and the linking of four semiconductor switches. The connection altogether is series so-called cascaded. Here, the upper part provides the output from of primary bridge and the lower branch of the final bridge. With the beginning of the switch cycle bridge works in a cascaded pattern wherein 1st Bridge is functional, which causes the DC voltage from first source to generate an altitude and when 2nd Bridge is functional, both the bridges add up together in output to give

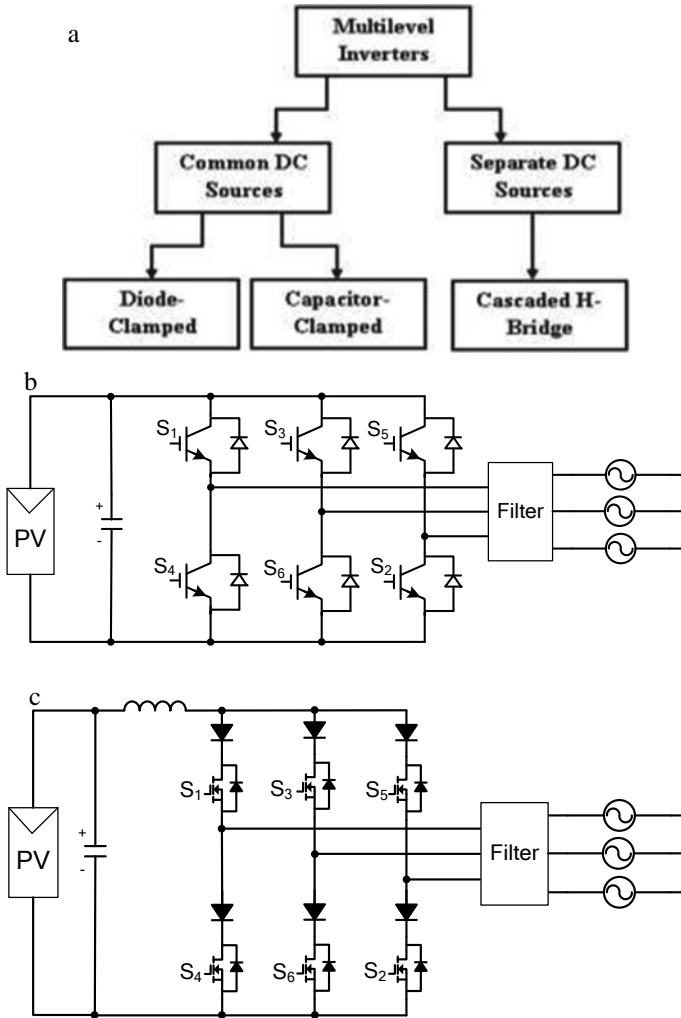


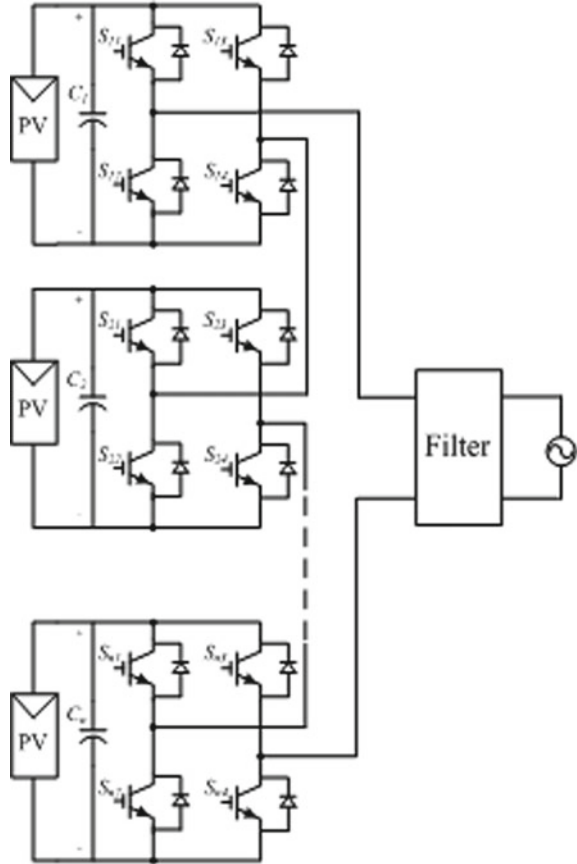
Fig. 2 a Multilevel inverter topologies. b 3-phase voltage source inverter. c Multilevel inverter topology three-phase current source inverter [8]

next level [14]. Hence, for number of bridges (N) as START, the cascaded total gives the maximum voltage at output with these \tilde{N} levels (Fig. 3).

Hybrid or Mixed Multilevel Inverter

Any two topologies when combined together from the above-mentioned lead to the formulation of the so-called hybrid or mixed type of MLI. This type of topology was a specific area of interest as it tries to eliminate the disadvantages of each or the other type. Significantly, the hybrid model with an H bridge cascaded type with a flying capacitor inverter can be developed for the five-level output [15, 16]. The

Fig. 3 Multilevel inverter with cascaded topology



advantage of this type will include a reduced switch count and apparatus with an improved productivity in terms of power quality [17] (Table 1).

3 Harmonics Reduction Technique

3.1 Switching Topology

One of the most followed and preferred techniques to control the MLI started since 1960s. It is believed to eradicate the selective disturbance of harmonic profile in case of resultant waveform of half bridge as well as full bridge inverter. This is sometimes renamed as the preprogrammed pulse width modulation optimized to obtain an enhanced and better harmonic profile as and when reduced switching is concerned. It is advantageous due to the following facts:

Table 1 Research contribution in this field of topologies of MLIs till date

Parameters	DCMLI [18]	FCMLI	CHB-MLI
Count of switches w.r.t. count of levels N	$2(N - 1)$	$2(N - 1)$	$2(N - 1)$
Source connected (DC)	1	1	$(N - 1) \div 2$
No. of diodes	$(N - 1) \times (N - 2)$	0	0
For Generation of 0 level Capacitor count	$(N - 1)$ Diodes for clamping and switches	$(N \times (N - 1)) \div 2$ Capacitors for clamping and switches	0 Just semiconductor switches with diodes
Key features	<ul style="list-style-type: none"> • Only source is DC I/P • Increased reliability • Better efficiency • Balancing voltage is tough 	<ul style="list-style-type: none"> • Suitable for active and reactive power control • Only 1 remote separate DC source 	<ul style="list-style-type: none"> • Lesser components • Scalable • Greatly modular network ckt.
Shortcomings	<ul style="list-style-type: none"> • Increased level requires more count of capacitors and Diodes • Balancing voltage is tough 	<ul style="list-style-type: none"> • Increased level requires more count of capacitors • Heavy circuitry • Costly for Higher power requirements 	<ul style="list-style-type: none"> • Semiconductor switches requirement of large • Isolated DC sources more in number [19]
Applications	<ul style="list-style-type: none"> • Low moderate voltage AC motor drive • Photovoltaic applications 	<ul style="list-style-type: none"> • Low medium voltage • For motor drive 	<ul style="list-style-type: none"> • Voltage Moderate high • Applied in EV, Drives and renewable sector

1. When the frequency is fundamental and operation is carried out, the losses due to switching losses are minimized.
2. Output voltage can be directly moderated and controlled for improved harmonics and hence power quality.
3. Reduced Triplen harmonics with better connections of circuit and improved control strategies (Table 2).

Then, it was very essential to explore the design features and work for the switching of low or fundamental level (mostly preferred scheme was SHE). So, the domain of the findings and conclusions from each depended on the design and mainly on the control strategies Table 3 includes the summarized points w.r.t. frequency in the low and fundamental switching patterns of the MLI.

Table 2 High switching frequency of MLIs research findings [20, 21]

Criteria	Switching frequency is high (w.r.t. PWM)			
	Sinusoidal	Level shift	Phase shift	Space vector
Methodology applied for reference switching	Sine wave-based	Carrier based		Ref vector with changing magnitude and fundamental frequency is rotating constantly
Benefits	<ul style="list-style-type: none"> • Rigorous calculation in offline mode can be avoided • Easy implementation • No optimization technique required 	<ul style="list-style-type: none"> • Performs superiority in THD minimization • Easy implementation 	<ul style="list-style-type: none"> • DC voltage ripples can be minimized • Less loss • Mostly applied for FC and CHB 	<ul style="list-style-type: none"> • Switching redundancy is more • Controlled switching sequence • Low THD
Constraints	<ul style="list-style-type: none"> • Switching loss is more 	<ul style="list-style-type: none"> • Complexity in control over capacitor voltage balance problem • Not suitable for FC and CHB based 	<ul style="list-style-type: none"> • More THD • Synchronization Issue 	<ul style="list-style-type: none"> • Complex Switching • Clarke’s Transformation required. For 1 ph.

Table 3 Fundamental/low switching frequency of MLIs research findings

Parameters	Fundamental/low switching frequency		
	Selective harmonic elimination	Nearest level control	Space vector configuration
Operational scheme	Dependent on calculations made online or offline	Dependent on reference as sinusoidal	Switching dependent on reference
Benefits	<ul style="list-style-type: none"> • Minimized loss due to Switching and EMI • THD can be precisely regulated • Applied mainly for high-power sectors 	<ul style="list-style-type: none"> • Improved voltage profile • Minimal ripples • Easy to configure 	<ul style="list-style-type: none"> • Used for high-power applications with minimal THD and Ripples in o/p voltage
Constraints	<ul style="list-style-type: none"> • Techniques of optimization are complex • Larger count of levels increases the non-linear equations 	<ul style="list-style-type: none"> • Poor performance in dynamic state • Nearest level can’t be found easily and THD not satisfactorily mitigated 	<ul style="list-style-type: none"> • Dominant low-order harmonics pose a threat and difficult to remove • Mathematical synthesis is quite difficult

4 Contributions in Comparative Analysis

In 2006, some new findings have been recommended for MLI by Martins et al. for high-power devices, which uses topology having lowered frequency of switching. Even though the design has some alteration to minimize disturbed output voltage waveform, the major drawback being that it has considerable current harmonics of low-order.

In 2009, Song et al. have proposed a new approach, which reduces the count of employed DC inputs in the MLI by inserting transformer instead. The main shortcoming of this idea is that involving numerous transformer windings will cause to the hike complete volume and cost of the inverter [22].

Another approach for MLI was selection based on a defined motive which can be either the reduced switching or the reduced DC input. However, disadvantage of the above structure is that the control switches with semiconductor diodes must have different ratings. Jagdish Kumar has discussed a modified Newton Raphson (NR) method to find out the switching angles for harmonic reduction in output waveforms of MLI. But, it did not give all solution space in terms of MI [23]. The proposed topology in this research work is based on symmetrical topologies since the value of all voltage sources in the MLI are same. Inclusively, there are asymmetrical methodologies which need variable input supply. For cascaded multilevel inverter, there are only one or two circuit topologies which are currently available today [24]. Also, only few switching schemes are used at present for CMLI such as sine PWM with triangular carrier waveform and space vector pulse width modulation (SVPWM). The SVPWM is used for three-level and five-level CMLI and for higher level CMLI, SVPWM technique becomes more complex for practical implementation. In this research work, new PWM techniques are developed for CMLI and also new circuit topologies that utilize less number of switches are developed for CMLI [25] (Fig. 4).

Recent research works lead to the introduction of newer converter methodologies and exceptional modulation technologies [11]. However, the most recently used MLI

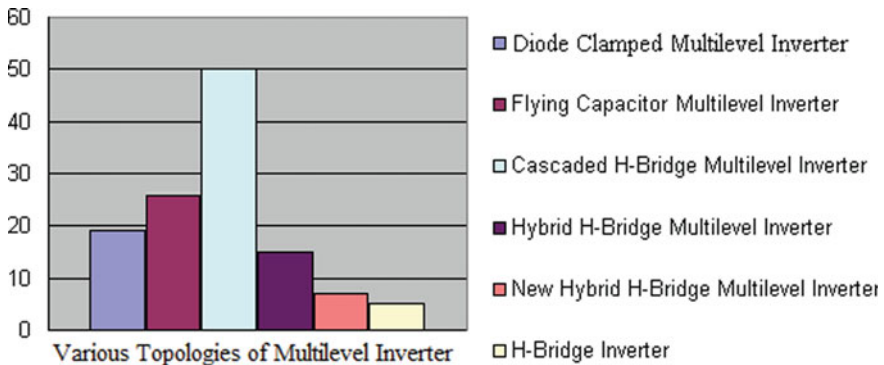


Fig. 4 Various topologies of MLI

strategies include NPC, flying capacitor inverter and cascaded designs. Among them, cascaded inverter gains interest since it needs fewer components and enhances the level count by the addition of full bridge inverter modules without employing greater ratings on discrete switching as shown in the graph [26].

5 Conclusion

This paper and research demonstrate and elaborate the proven advantage and potential in the domain of MLI when paired up with Solar PV. This proves best for eradication of harmonics in order to improvise the power quality to a larger extent. Thus, more interest as a researcher lies in the fact as this would lead to a better green and technically competent future supporting sustainability. This paper gives a clear idea as to develop a relation between the reductions in THD with increase in the voltage level counts. It also brings all the unique ideas, innovations and advances in the sector of power quality improvement as per the present-day needs w.r.t. the availability of potential resources without compromising on quality of the output and efficiency of the utility so as to lower the THD and get a perfectly sinusoidal output.

References

1. R. Ramaprabha, G. Ramya, Implementation of photovoltaic fed single phase nine level hybrid cascaded modular multilevel inverter with reduced number of devices, in *IEEE PEDS* (2017), pp. 493–496
2. N. Kumar, T.K. Saha, J. Dey, Multilevel inverter (MLI)-based stand-alone photovoltaic system: modeling, analysis, and control. *IEEE Syst. J.* **14**(1), 909–915 (2020)
3. A. Salem, E.M. Ahmed, M. Orabi, M. Ahmed, New three-phase symmetrical multilevel voltage source inverter. *IEEE J. Emerg. Sel. Top. Circ. Syst.* **5**(3), 430–442 (2015)
4. V. Sharna, Diode clamped multilevel inverter switching topology. *Int. J. Ind. Electron. Electr. Eng.* **5**(11), 31–35 (2017). ISSN: 2347-6982, 2349-204X
5. H. Fujita, N. Yamashita, Performance of a diode-clamped linear amplifier. *IEEE Trans. Power Electron.* **23**(2), 824–831 (2008)
6. S. Bhattacharya, V. Dewangan, Improvement of power quality using multilevel inverter based shunt active power filter. *Int. J. Eng. Sci. Res. Technol.* **6**(3) (2017)
7. N. Prabakaran, K. Palanisamy, New hybrid asymmetric multilevel inverter with reduced number of switches, in *International Conference on Power Electronics, Drives and Energy Systems (PEDES)* (IEEE, 2016)
8. Md. Mubashwar Hasan, A. Abu-Siada, S.M. Islam, S.M. Muyeen, A novel concept for three-phase cascaded multilevel inverter topologies. *Energies MDPI Open Access J.* **11**(2), pp. 1–16 (2018)
9. S. Srinivas, Uniform overlapped multi-carrier PWM for a six-level diode clamped inverter. *Int. J. Electr. Electron. Eng.* 763–768 (2009)
10. E. Ozdemir, S. Ozdemir, L.M. Tolbert, Fundamental-frequency-modulated six-level diode-clamped multilevel inverter for three-phase stand-alone photovoltaic system. *IEEE Trans. Power Electron.* **56**(11), 4407–4415 (2009)

11. M.M. Renge, H.M. Suryawanshi, Five-level diode clamped inverter to eliminate common mode voltage and reduce dv/dt in medium voltage rating induction motor drives. *IEEE Trans. Power Electron.* **23**(4), 1598–1607 (2008)
12. M.D. Manjrekar, T.A. Lipo, A hybrid multilevel inverter topology for drive applications, in *Proceedings of Applied Power Electronics Conference and Exposition 1998, APEC'98*, vol. 2 (1998), pp. 523–529
13. M.D. Manjrekar, P.K. Steimer, T.A. Lipo, Hybrid multilevel power conversion system: a competitive solution for high-power applications. *IEEE Trans. Ind. Appl.* **36**(3), 834–841 (2000)
14. S. Salehahari, E. Babaei, A new hybrid multilevel inverter based on coupled inductor and cascaded H-bridge, in *International Conference on Electrical Engineering/Electronics, Computer, Telecommunications and Information Technology (ECTI-CON)* (IEEE, Sept 2016)
15. C. Rech, J.R. Pinheiro, Hybrid multilevel converters: unified analysis and design considerations. *IEEE Trans. Ind. Electron.* **54**(2), 1092–1104 (2007)
16. J. Rao, Y. Li, Power flow management of a new hybrid cascaded multilevel inverter, in *Proceedings of International Conference on Electrical Machines and Systems*, Seoul, Korea (2007), pp. 58–63
17. J. Bangarraju, V. Rajagopal, N. Bhoopal, M. Priyanka, Power quality improvement using solar PV H-bridge based hybrid multilevel inverter, in *Proceedings of the 6th IEEE India International Conference on Power Electronics (IICPE 2014)*, NIT Kurukshetra (2014)
18. X. Yuan, I. Barbi, Fundamentals of a new diode clamping multilevel inverter. *IEEE Trans. Power Electron.* **15**(4), 711–718 (2000)
19. C.M. Nirmal Mukundan, P. Jayaprakash, Cascaded H-bridge multilevel inverter based grid integration of solar power with PQ improvement, in *2018 IEEE International Conference on Power Electronics, Drives and Energy Systems (PEDES)*, Chennai, India (2018), pp. 1–6
20. B. Farid, A study of new techniques of controlled PWM inverters. *Eur. J. Sci. Res.* **32**(1), 77–87 (2009). ISSN 1450-216X
21. B. Cougo, G. Gateau, T. Menyard, M.B. Rafal, M. Cousineau, PD Modulation scheme for three phase parallel multilevel inverters. *IEEE Trans. Ind. Electron.* **59**(2), 690–700
22. N. Hatti, K. Hasegawa, H. Akagi, A 6.6-KV transformer less motor drive using a five-level diode-clamped PWM inverter for energy savings of pumps and blowers. *IEEE Trans. Power Electron.* **24**(3), 796–803 (2009)
23. J. Kumar, B. Das, P. Agarwal, Selective harmonic elimination technique for a multilevel inverter, in *Fifteenth National Power Systems Conference (NPSC)*, IIT Bombay (2008), pp. 607–613
24. S. Mariethoz, Design and control of high-performance modular hybrid asymmetrical cascade multilevel inverters. *IEEE Trans. Ind. Appl.* **50**(6), 4018–4027 (2014)
25. P. Palanivel, S.S. Dash, Control of three phase cascaded multilevel inverter using various novel multicarrier pulse width modulation techniques, in *Proceeding of TENCON* (2010), pp. 70–79
26. A.K. Koshti, M.N. Rao, A brief review on different multilevel inverter topologies, in *2017 International Conference on Data Management, Analytics and Innovation (ICDMAI)*, Zeal Education Society, Pune, India, 24–26 Feb 2017, pp. 187–193

Implementation of Scalable Low Cost Industrial IoT GATEWAY for Uninterrupted Monitoring and Data Acquisition of Industrial Machines



Suraj Satyawan Dudhe, Amit Khawse, Pankaj Ramtekkar, and Ankur Gupta

Abstract Internet of Things is the backbone of Industry 4.0. Monitoring and data acquisition of Industrial equipment on online cloud platforms or online servers is today's need. Artificial intelligence and data science platforms work on cloud platforms for monitoring and predictive analysis of the data. Uninterrupted Data Acquisition systems on the online server using IoT technology is the main challenge. Unavailability of the internet for small intervals or unavailability of online servers because of maintenance are the main reasons for the same. In this paper, the design and implementation of a low cost IoT System elaborate based on my experience during implementation of the IoT System in industry name as Kapilansh Dhatu Udyog Pvt. Ltd., Nagpur.

Keywords Php · PhpMyadmin · MySQL · VPS · WAMP Server · NodeMCU · Access point · MQTT HTTP · RTU · GUI · TCP · UPS

1 Introduction

In 2020, various IoT startups are jumping into the market. For startups, the main challenge is commercial subscription of IoT cloud platforms [1, 2] which is available free of cost for developer subscription only and a system based on developer subscription will not fulfil lots of continuous data storing facilities. If they use commercial subscription which is actually required for startups then it requires lots of money for subscription which is not possible without Government funding or Angel Investors. This paper is for the design of a low cost industrial IoT System [3] using a combination offline server and online server for uninterrupted data Acquisition system for

S. S. Dudhe (✉) · P. Ramtekkar · A. Gupta
G. H. Raison College of Engineering, Nagpur, India
e-mail: suraj.dudhe@raisoni.net

A. Khawse
Kapilansh Dhatu Udyog Pvt Ltd., Nagpur, India

Industrial IoT even if online server down because of server maintenance or internet facility stop because of internet service provider failure which are not in our control.

2 Related Work

2.1 Research Paper Study

In [4] Author proposed Mobile Cloud Computing (MCC), cloudlet computing, mobile clouds, mobile IoT computing, IoT cloud computing, fog computing, Mobile Edge Computing (MEC), edge computing, the Web of Things (WoT), the Semantic WoT (SWoT), the Wisdom WoT (W2T), participatory sensing, mobile crowd sensing and mobile crowdsourcing for Storing data using IoT System.

In [5] Author proposes MQTT (Message Queue Telemetry Transport for protocol for Machine to machine communication.)

2.2 Our Approach System

In our System, Wi-Fi based Microcontroller is sending data using HTTP (Hypertext Transfer Protocol) [6] or MQTT Protocol [7] to the local server. Local Server stores data in the local database and forwards the same data to Online Server (in our case, online VPS-Virtual Private Server hosted by Hostinger). In this approach, local servers continuously store all transmitted values without fail. If the online server is not available for some reason then it will update data from the local server when it comes online. Similar operations can be done through storing data (during unavailability of an online server) in the memory card interface to microcontroller and later on updates to online servers when the server comes online. Which is very simple but useful for small scale projects, But in the case of startup companies, large data with complex operations cannot be handled through a microcontroller based offline storage system.

3 Methodology

3.1 Software/Programing Language

3.1.1: WAMP Server is used for development of local servers for window machines or LAMP server can be used if raspberry pie is used for local server development.

This Platform provides all necessary tools in one package like Apache server, MySQL Database and PhpMyadmin.

3.1.2: Hostinger is a virtual private server (VPS) that has been used as an online receiving end which is at a very low price provides all tools similar to WAMP in online Environment.

3.1.3: Arduino IDE is used for programming NodeMCU as RTU for sensing industrial parameters and communicating with a server using HTTP protocol over Wi-Fi network.

3.1.4: Php and SQL language has been used for communication (receiving data) with RTU to Offline server as well as offline server to Online Server.

3.2 Hardware

3.2.1 IoT GATEWAY

Window based PC accompanied with WAMP [8] server has been used as IoT GATEWAY. This machine is used because it is already installed in the company which runs 24 by 7 with 4 h. UPS (Uninterrupted Power Supply) backup. In case of low cost product development for a startup company, Raspberry pie accompanied with LAMP (Linux Apache MySQL Pph-Myadmin) Server, 12 V 2 AH battery and voltage converter would be the best option. Coding of the GATEWAY will remain the same for any type of OS based machine used in GATEWAY. Use a Unique GATEWAY ID while sending data to VPS [9] (Online Server) so that it will be uniquely identified on VPS when multiple GATEWAY sends data to common VPS.

3.2.2 RTU (Remote Terminal Unit)

NodeMCU is ESP-8266 Wi-Fi based microcontroller used in development of RTU. RTU connect to a common Access point where GATEWAY is connected for transmitting sensor values to GATEWAY.

3.2.3 Access Point (Wi-Fi Router)

TP-Link Wi-Fi router is used as Access Point for Wi-Fi connectivity between IoT GATEWAY and RTU. We used this router because it was already installed in the company.

3.3 *Our Approach*

In our System, RTU based on NodeMCU (ESP 8266 based Microcontroller) is sensing parameters using various sensors and holding value into variables. Using HTTP (Hyper Text Transfer Protocol) or MQTT Protocol, all variable values are sent to a local WAMP (Windows Apache MySQL, PHP) server which is connected to a common access point (Wi-Fi Router). HTTP server has MySQL database [8] and GUI. Store all variables using the receiving end of the server (Insert query using a php file directed by IP Address) into MySQL database and call it on GUI for user interface using a Computer machine connected to the same Access Point. In addition to that, create a new php variable at receiving end in php file and forward all variables to the online MySQL database (in our case, VPS-Virtual Private Server hosted by Hostinger). In this approach, local servers continuously store all transmitted values without fail but if the online server is not available for some reason then it will update data from the local server when it comes online.

4 Implementation

4.1 *Theory*

In Industry, centrifugal casting method is used for metal pipe manufacturing. Manufacturing losses happen because of operator error and other unavoidable factors like power failure. Operators do not take entry on manual log sheets when a fault occurs and loss of pipe. According to the owner, mistakes can be minimized if we monitor the system without human intervention. With the help of Engineers, we observed the manufacturing process and sequence of control signals for development of algorithms for RTU that capture pipe casting intervals automatically. Operator controls three command signals from operator panel to control manufacturing process. (1) Hopper is used for Pouring Molten Metal into mould using Star delta starter operated machine. (2) Hydraulic system control through star delta starter for forward and reverse movement of pipe mould on rail guided track. (3) Pulley system is used for applying centrifugal force by rotating pipe mould using VFD speed Controller.

4.2 *Block Diagram*

4.2.1 RTU Hardware Block Diagram

See Fig. 1.

Fig. 1 RTU hardware block diagram

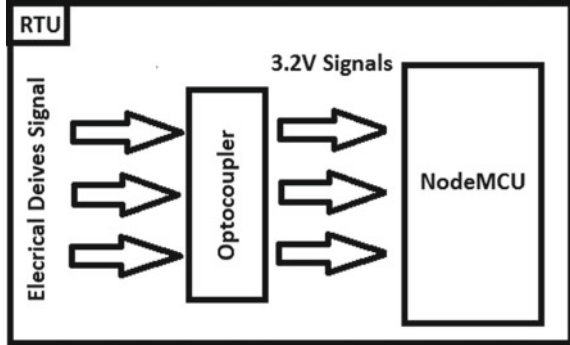
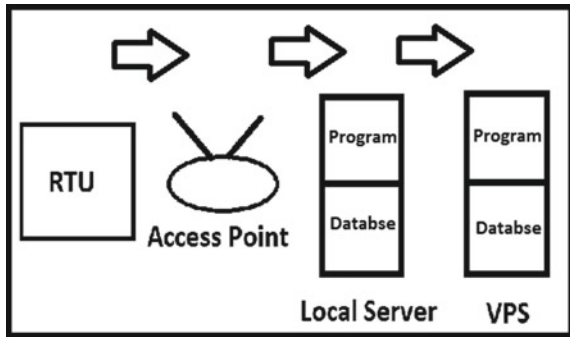


Fig. 2 System block diagram



4.2.2 System Block Diagram

See Fig. 2.

4.3 Working of System

4.3.1 Working of Pipe Casting Machine

Machine is controlled by an operator using three control signals (Hopper, Hydraulic and Pulley) mentioned in 4.1 point and diagrammatically shows in Fig. 1. Step1: all machines are in off condition at the beginning. Step2: At the beginning, first of all, Pulley starts for rotating mould. Step3: Then the hopper starts tilting to pour molten metal into rotating mould through the cannel. Step4: After the hopper, the hydraulic system started moving forward direction for equal distribution of molten metal into pipe mould and hydraulic system stops at the end. Step5: when hydraulic complete forward movement, the operator stops the pulley. Step6: When hydraulic start moving back toward its original position, casted pipe is removed from its mould

by holding with a pneumatic pinch. Step7: When the Hydraulic system reaches its original location, then the operator stop Hopper and Hydraulic. From all steps, it has been observed that the Pipe casting interval is indicated by the high status of all three signals. In this way, pipe casting intervals can be captured by RTU.

4.3.2 Working of RTU

Based on the Operation of the pipe casting machine, RTU monitors all steps 1–7 and sends the status of all three signals to GATEWAY using HTTP protocol via Access Point.

RTU Steps: Step A: When all three Signals are in low states, RTU sends “ONLINE” continuously to GATEWAY. Step B: When a minimum of one signal is in High state, RTU sends “IDLE” continuously to GATEWAY Step C: When all signals are at High States, RTU sends Casting to GATEWAY. Step D: When RTU Starts or is reset, RTU sends “RESET” to GATEWAY.

4.3.3 Working of GATEWAY

According to Fig. 2 in 4.2.2, all steps indicated that RTU repeatedly sends data to the IoT GATEWAY. IoT GATEWAY accompanied with HTTP server (WAMP/LAMP/XAMP) for HTTP based communication with RTU receives data using HTTP protocol then saved it to MySQL database of local server as well as forward it to an online server for the same action on an online server.

If the very fast data sampling rate is required (example—10 data sample/s) then HTTP based communication is not efficient in the term of microcontroller based RTU. To increase communication speed, MQTT protocol can be used between GATEWAY and RTU. IN addition to WAMP, mosquito servers must be installed for MQTT communication. GATEWAY machine will host MQTT environment on the local network as well as php or python language based script of GATEWAY will act as MQTT subscriber with wild card subscription for fetching all MQTT topic data on MQTT network. Then GATEWAY saves data to the local MySQL server and forwards the same data to the online server using HTTP.

4.3.4 Working of Virtual Private Server-VPS

VPS server is used for receiving data from GATEWAY and saving it to an online MySQL database. GATEWAY receives data from RTU using HTTP or MQTT protocol and forwards data with GATEWAY id and RTU id to the online server pointed by the website address. PHP based files receive all data and save all data into an online MySQL server.

5 Conclusion

Http based RTU to GATEWAY communication is accurate but the speed of operation is slow as compared to MQTT protocol. Personal IoT network using a VPS server and Raspberry-pi based GATEWAY is very economical and customizable. In Arduino programming of RTU, removing the Serial.print command leads to very low heating of the microcontroller and it is an advantage in the long run.

References

1. P. Ganguly, in *Selecting the right IoT cloud platform*. 2016 International Conference on Internet of Things and Applications (IOTA), pp. 316–320 (2016). <https://doi.org/10.1109/IOTA.2016.7562744>
2. P.P. Ray, A survey of IoT cloud platforms. *Future Comput. Inf. J.* **1**(1–2), 35–46, ISSN 2314-7288 (2016)
3. W. Li, B. Wang, J. Sheng, K. Dong, Z. Li, Y. Hu, A resource service model in the industrial IoT system based on transparent computing. *Sensors* **18**, 981 (2018). <https://doi.org/10.3390/s18040981>
4. H. Elazhary, Internet of Things (IoT), mobile cloud, cloudlet, mobile IoT, IoT cloud, fog, mobile edge, and edge emerging computing paradigms: Disambiguation and research directions. *J. Netw. Comput. Appl.* **128**, 105–140, ISSN 1084-8045 (2019)
5. P. Bellavista, A. Zanni, in *Towards better scalability for IoT-cloud interactions via combined exploitation of MQTT and CoAP*. 2016 IEEE 2nd International Forum on Research and Technologies for Society and Industry Leveraging a better tomorrow (RTSI) (2016), pp. 1–6. <https://doi.org/10.1109/RTSI.2016.7740614>
6. G. Mois, S. Folea, T. Sanislav, in *Analysis of three IoT-based wireless sensors for environmental monitoring*. *IEEE Transactions on Instrumentation and Measurement*, vol. 66, no. 8 (Aug. 2017), pp. 2056–2064. <https://doi.org/10.1109/TIM.2017.2677619>
7. M. Singh, M. A. Rajan, V. L. Shivraj, P. Balamuralidhar, in *Secure MQTT for Internet of Things (IoT)*. 2015 Fifth International Conference on Communication Systems and Network Technologies, pp. 746–751 (2015). <https://doi.org/10.1109/CSNT.2015.16>
8. M. Musaruddin, M. Zaporoshenko, R. Zivanovic, in *Remote protective relay testing*. 2008 Australasian Universities Power Engineering Conference, pp. 1–4 (2008)
9. M. Niswar, A. A. Sabri, E. Warni, M. N. Musa, in *Memory sharing management on virtual private server*. International Conference on ICT for Smart Society, pp. 1–4 (2013). <https://doi.org/10.1109/ICTSS.2013.6588079>

Verification of Microprocessor Using Universal Verification Methodology



Sarabjeet Singh Tieth and P. M. Menghal

Abstract Integrated circuits have become more complex every year, and their verification has become more time-consuming. Therefore, effective and new verification methodology needs to be learnt. This paper covers an efficient exercise to develop a methodology that lets us formally verify functional correctness of a digital design (microprocessor) using system UVM at appropriate abstraction level with emphasis on ALU verification and the flow of instruction in the pipeline only, abstracting away from the details such as the exact implementation of execution units, branch prediction units etc. It allows the design to be verified in its full generality rather than permitting only a fixed instantiation of the design to be verified. This avoids the need of re-verification of the design when some parameters such as the number of registers or the numbers of execution units are changed. It supports error localization either at RTL or testbench to facilitate debugging and verifying the correctness of a microprocessor at the micro architectural level of abstraction. Traditional verification methods do not guarantee that they uncover all the design bugs, and hence a need for a well suited properly structured verification methodology, i.e., UVM for the functional verification of digital hardware (16-bit microprocessor) primarily using simulation and log file has been carried out.

Keywords Verification · RTL · Testbench · Universal verification methodology · Log file

1 Introduction

Technological changes are nothing new, but this round of changes is happening at a rate faster than ever before. Similarly, ICs are growing rapidly which allowed electronics to expand at an amazing rate with advantage such as compactness, higher speed, lower power consumption, high reliability and low cost due to which we

S. S. Tieth · P. M. Menghal (✉)
Faculty of Electronics, Military College of Electronics and Mechanical Engineering,
Secunderabad, Telangana 500 015, India
e-mail: prashant_menghal@ieee.org

© The Author(s), under exclusive license to Springer Nature Singapore Pte Ltd. 2022
M. L. Kolhe et al. (eds.), *Smart Technologies for Energy, Environment and Sustainable Development, Vol 1*, Springer Proceedings in Energy,
https://doi.org/10.1007/978-981-16-6875-3_41

witness many portable devices available today. This transformation is brought by VLSI design, which in design industry caters from designing to manufacture as per ASIC design flow which consist of functional verification at front-end techniques. This paper aims at verifying the functional correctness of 16-bit, 5-staged pipelined microprocessor by utilizing the testbench architecture offered by UVM verification environment and verifies the correctness by simulation and log file by utilizing Xilinx ISE and EDA playground with the novelty of designing the verification environment for an above-mentioned microprocessor.

The term **VLSI Verification** is a functional check of the design/specification written using Verilog/SV to find functional bugs and subsequently correcting it. By **bugs**, we refer to a particular functionality of the design not giving desired output. It is important to remove these bugs in the design before it is approved for synthesis and fabrication as the relative cost to fix bugs is directly proportional to the time of detection due to which [1] verification forms 70% of the entire chip designing process consisting of Test Planning, Testbench development, creating Test and Running Simulation and debug. The most important step being the **testbench** development which is again a code which generate input/stimulus, apply to design under test (DUT), capture response and check with the expected results to determine the correctness of 16-bit, 5-staged pipeline processor by verifying its ALU block functionality of arithmetic, logical and shifting operation and various stages of pipelining (Fig. 1).

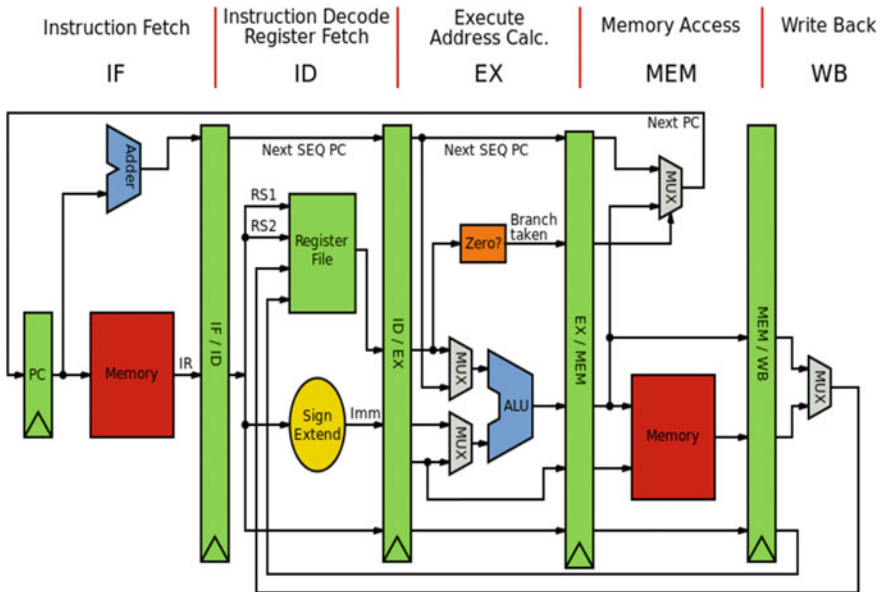


Fig. 1 Basic processor architecture

Table 1 Comparison between languages

Verilog	System Verilog
Before 2009, Verilog was the main language and used for RTL design and modeling	After 2009, System Verilog has emerged to be the main language and used for RTL design and modeling as well as verification
New test has to be created. Though \$ random can provide random numbers	It provides randomization
Disadvantage: Tedious process for complex design and consumes lot of time	Disadvantage: Its verification environment is not reusable and synthesis tools are limited

2 Different Verification Approaches

There are various techniques available today for functional verification and to select best for your project is not so simple and is seldom confusing and costly [2]. Few of the bottlenecks which need to be addressed while selecting any approach are.

- (a) Design bottleneck
- (b) Verification bottleneck
- (c) Functional complexity
- (d) Higher system reliability.

In traditional hardware descriptive language, **Verilog** is basically used for gate/RTL design and modeling. With increased complexity of digital system, **SystemVerilog** with added language extension covering the verification functionalities was quite prominent in verification world. A small comparison between Verilog and SystemVerilog is given below in Table 1.

3 Universal Verification Methodology

The UVM standard was engineered between EDA vendors and customers which was created potentially by the robust foundation of data and skill that was given the standardization effort within the style of the present OVM code. The UVM standard utilizes OOP and class inheritance in conjunction with many new technologies like resources, TLM2, Phasing etc., all developed to create UVM as we all know it today. These options combine give robust, versatile technology and methodology to assist you produce reusable and practical testbenches [3]. With the OVM at its core, the UVM already embodies years of object-oriented style and methodology expertise, all of which may be applied instantly to a UVM project. So, it should be clear that UVM is a factory standard for verifying designs. It brings automation to SV, i.e., it is utilizing SV for writing RTL codes/Testbench as it provides a method/protocols which one has to follow for connecting various entities involved. Hence, it reduces verification

Table 2 Comparison between methodologies

	Traditional testing	UVM
Stimulus structure	Procedural code	Constrained random variable
Reusability	Not reusable	Reusable
Type	Static	Dynamic
Test redundancy	None	Yes
Stimulation overhead	None	10–40% to solve constraint
Controllability	Coarse grained	Fine grained
Observability	Lower	Higher
Maintainability	Hard	Easy

Table 3 UVM environment

Component	Description
Sequencer	Generate different stimulus to be driven to DUT
Interface	Contains design signals that can be driven or monitored
Driver	Drives the generated stimulus to design
Monitor	Monitor design input–output port to capture design activity
Scoreboard	Check output from design with expected behavior
Environment	Contain all verification component mentioned above
Test	Contains environment that can be tweaked with different configuration settings

coding effort because of its pre-built architecture and allows its reusability [3]. The comparison of UVM with other traditional testing are tabulated in Table 2.

UVM Verification environment consists of the components such as sequencer, driver, monitor, scoreboard, environment and test with their function described as in Table 3 [1, 3, 4], and all these modules are connected with each other as shown in Fig. 2 [1, 5]. We can compare the result from the simulation result and can come to conclusion that either my testbench or environment is faulty or my RTL code is faulty.

4 Simulation and Results

The microprocessor is designed and simulated using Xilinx ISE. The UVM-based testbench is created for verification of the ALU of the microprocessor. Functional verification is verified in three phases via simulation, log file and coverage analysis and could achieve good coverage analysis as per the coverage plan. The simulation result for verification of ALU is depicted by ADD, logical AND, Shift Right operation along with code in Figs. 3, 4, 5, respectively. The linear pipelining which assist in

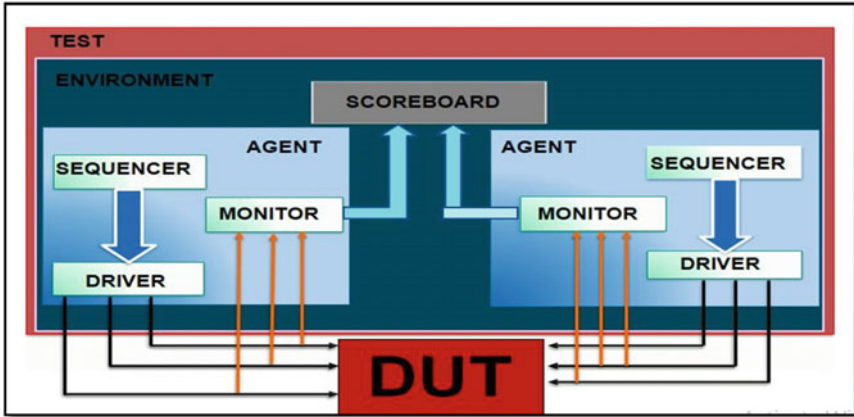


Fig. 2 UVM verification environment

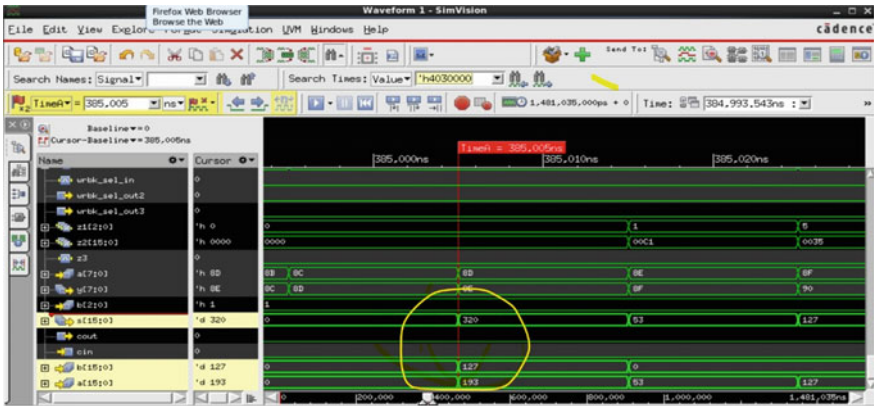


Fig. 3 ADD operation

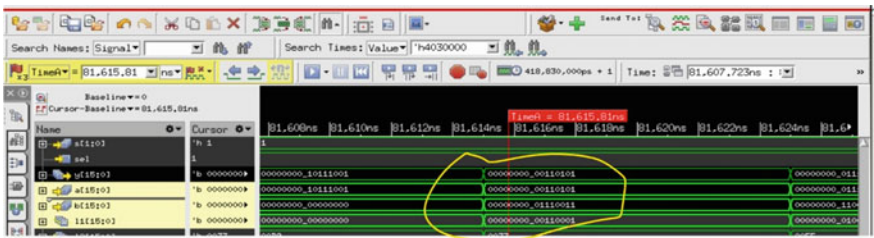


Fig. 4 AND operation

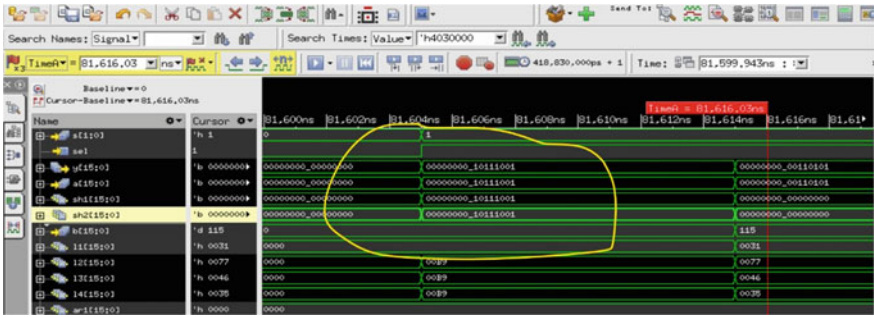


Fig. 5 Shift right

verifying the microprocessor in totality is verified by the simulation result shown in Fig. 6.

From Figs. 3, 4 and 5, it is clearly brought out that addition, logical AND and Shift Right that is arithmetic, logical and shifting operation, respectively, of ALU are completely verified as we get the desired output in each case which can be checked with different values also.

The second phase of the results consists of log file which depicts the scoreboard result when constrained random variables are applied to it. Since it does not show any error, then the design has passed the stress under which it has been put to.

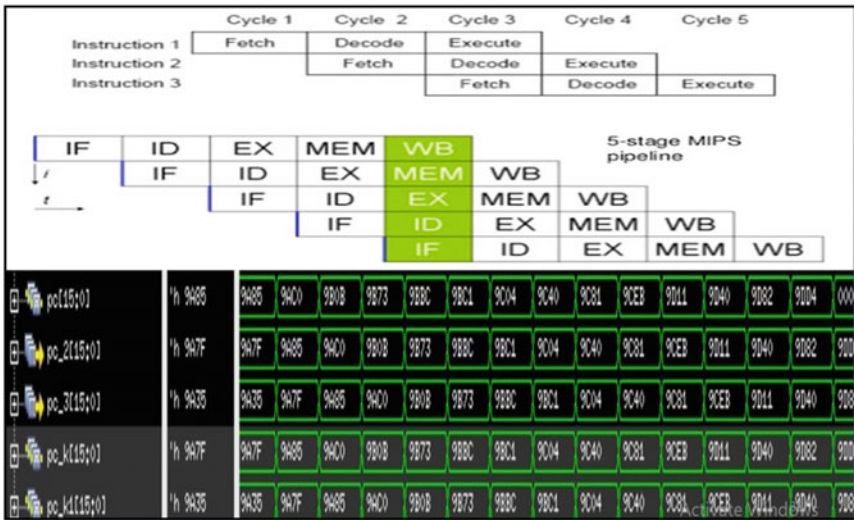


Fig. 6 Linear pipelining

Table 4 Coverage summary

Name	Score	Line	Conditional	Toggle
ALU	98.3	97.8	100	100
CPU	94.5	95.1	97.6	96.62

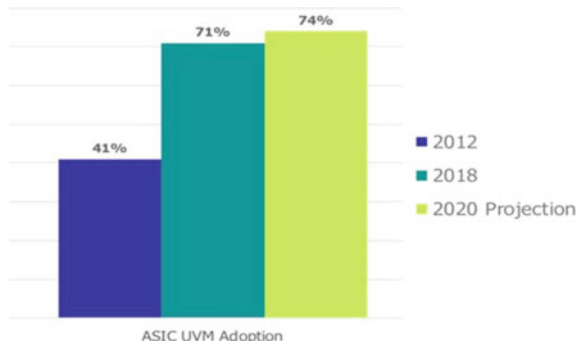
The last phase of the result is the coverage analysis which is the metric of completeness of verification which measures the quality of suite and tells verification engineers when to stop verification [6]. The coverage includes line, toggle and conditional coverage. UVM allows defining all cover-groups and different tests are written to remove the coverage holes in verification. Line coverage checks whether all lines of codes are being checked. Similarly, toggle coverage checks for the transition of signals from 0 to 1 and vice versa. Conditional coverage makes sure that all the conditional statements are being tested with all possible combination. The total coverage summary is depicted in Table 4 [1].

5 Drawback and Opportunities of UVM

As we are aware that synthesis tool for SV is limited which restricts designers to accept SV as a design language. There are also limitations for using UVM with emulators. Moreover, UVM is very complicated, so it does not make sense with small projects. UVM provides no links between testbenches and code running in the embedded processors. Steep learning curve makes it less user friendly and is attributable for its lesser adoption, but it is picking up and is being widely adopted as shown in Fig. 7 [7].

UVM methodology can be enhanced to offer a flexible framework for the virtual prototyping of multi-discipline testbenches that support both digital and analog

Fig. 7 UVM adoption



Source : Wilson Research and group mentor, A Siemens Business, 2018 Functional Verification Study

mixed-signal (AMS) at the architectural level UVM is a promising solution in verifying 3D-SoC which has many IPs and heterogeneous systems [3].

6 Conclusion

In this paper, UVM-based architecture for logic sub-system verification is outlined with the example of microprocessor design, clearly bringing out the importance of verification since more than 70–80% of project cycle time is spent for verification and UVM methodology with strong base class, and power of system Verilog helps in reducing the verification time. The use and advantages of testbench along with constraint randomization feature significantly helps in defining input stimulus. The UVM-based testbench offers reusability of verification of components. The design is then verified with the help of simulation results, log file and coverage-driven analysis. Still it has got a few drawbacks which if overcome can assist to achieve 100% coverage. For verification methodology implementation, the Universal Verification Methodology (UVM) was used as a guideline. By dividing the implementation phase in multiple sub-stages, UVM seems to be a structured methodology to ensure correct results.

As Bangalore and Hyderabad are growing as the R&D for entire chip design industries all around and massive demand for VLSI resource around the world, verification is becoming an endless field in growth and development.

References

1. T.M. Pavithran, R. Bhakthavatchalu, UVM based testbench architecture for logic sub-system verification, in *2017 International Conference on Technological Advancements in Power and Energy (TAP Energy)*, pp. 1–5 (2017)
2. P.P. Chu, *System Verilog vs. Verilog in RTL Design* (2018)
3. K. Salah, *A UVM-Based Smart Functional Verification Platform: Concepts, Pros, Cons, and Opportunities*, pp. 94–99 (2015). <https://doi.org/10.1109/IDT.2014.7038594>
4. UVM user guide 1.1 and 1.2
5. J. Kolour, N. Reddy, V. Siva Reddy, Design verification of UMC IP core using system Verilog architecture. *Int. Res. J. Eng. Technol.* (2019)
6. Wei, X. Wang, Functional coverage-driven UVM-based UART IP verification, in *2015 IEEE 11th International Conference on ASIC (ASICON)*, pp. 1–4 (2015)
7. J. Bromley, *If System Verilog is So Good, Why Do We Need UVM*. Uploaded on 2017 and avl on <https://www.esearchgate.net/publication/261399083>

Optimal Operation Strategy for A. A. Energy Ltd. 10 MW Cogeneration Power Plants, Wadsa



Sachin Shedmake, Ramchandra Adware, and Dhanraj Rajurkar

Abstract This paper is intended to optimize the total power generation capacity of cogeneration power plant based at Wadsa town located in eastern region of Maharashtra. The total power generation capacity of power plant is up to 10 MW which needs to be optimizing as the power deliverable is less than power generated by the plant. The paper uses renewable power generation and reduced switched-inverter topology-based distribution techniques for optimization of given power plant.

Keywords Power optimization · Renewable energy sources · Reduced switch inverter

1 Introduction

Electricity is one of the important needs in our day to day life. Generation and distribution of electricity are two important aspects in utilization of electrical energy. The power generated by the power plants is usually generated at high potential and in an alternating current form which cannot be stored as that of DC power. This leads to maintain the balance between power generation and utilization of electricity produced by the plants. Thus, power plants are essential part of today's world as electricity is one of the most demanding commercial forms of energy.

Most of the power plants generate electrical energy to their rated capacity, but some of the power is utilized as auxiliary supply for the plant itself. This leads in the change in rated power generation capacity of plant to some extends. Though this change is less as compared to power generated and delivered to the grid, but this can affect on cost of the power generation for generation company. A. A. Energy Ltd.

S. Shedmake (✉) · R. Adware

Department of Electrical Engineering, G. H. Raisoni College of Engineering, Nagpur, India

R. Adware

e-mail: ramchandra.adware@raisoni.net

D. Rajurkar

A. A. Energy Pvt. Limited, Wadsa, Gadchiroli, India

10 MW cogeneration power plant uses rice husks as its fuel. But, the power generated by the plant is not completely deliverable to the grid as nearly 1.5 MW of power is used by the power plant itself. This auxiliary power can be generated separately using renewable energy sources like solar and wind energies. The power generated by this newly proposed system will be in DC form to make the power generation more cost-effective. Though the power generated by this renewable energy sources is in DC form, we can use new reduced switched-inverter topology-based inverters array to deliver the auxiliary AC power needed by the plant.

2 Problem Statement

The objective of the study is to optimize the power of cogeneration power plant to its rated capacity. Interfacing of renewable energy power generation and newly proposed inverter system into the existing power plant is the key point to overcome the problem in existing system.

The company has set up a flyash bricks manufacturing unit in Desaiganj Wadsa, District Gadchiroli, and the project reduces the burden to dispose the flyash generated by the existing 10 MW power plant [1]. The plant runs on rice husk as its primary fuel along with other available biomass. This biomass and the raw material for fueling supply are presently purchased from the open market by the company. The auxiliary power supply used by power plant for its own operation is taken from power generated by the plant itself.

This auxiliary power supply is needed to be generated by some other alternative power source. Use of renewable energy sources may lead to unevenness in the power quality for auxiliary supply. New type of inverter system is proposed to avoid such power quality issues in auxiliary power generation.

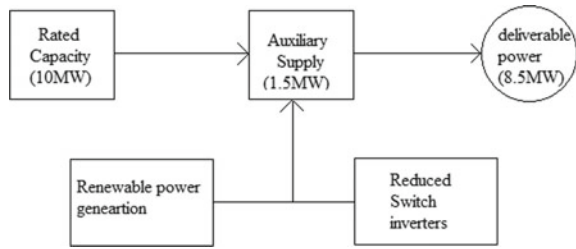
3 Methodology

The A. A. Energy Ltd. cogeneration power plant uses rice husk as its fuel. Along with rice husk, other biomass products such as flower seed husks, products, and by-products produced by oil companies are used as raw material for development of fuel for the plant. This helps in reducing the cost of conventional energy sources consumed by the plants to generate electricity.

Total power generation capacity of the plant is of 10 MW, among which nearly 1–1.5 MW of power is being used by the power as an auxiliary supply for its own operation and electricity required for safety measures. The block diagram below shows the requirement of auxiliary supply requirement and its compensation using renewable energy sources along with reduced switch-type multilevel inverters (Fig. 1).

The rated capacity of power generation by the plant is achieved by fully condensing steam turbine with alternator. This power plant is based on Rankin cycle. The steam

Fig. 1 Block diagram



alternator is designed to run on combination of rice husk along with coal as fuel. The high-pressure boiler is fed into a single bleed cum condensing steam turbine generator of 10 MW capacities. The boiler is of fluidized bed combustion type and has the advantage of high thermal and combustion efficiency reducing quantity of husk needed, to a minimum. Steam turbine of fully condensing mode with suitable alternator generator is installed for generating electricity. The turbine is of the single cylinder, single exhaust fully condensing type, designed for high reliability (Fig. 2).

The newly proposed system compensates the power used as auxiliary supply for the plant. This auxiliary supply amount of power which is up to 1.5 MW can be generating using solar power plant.

Formula for fuel utilization efficiency

$$FUE = (W + Q)/E$$

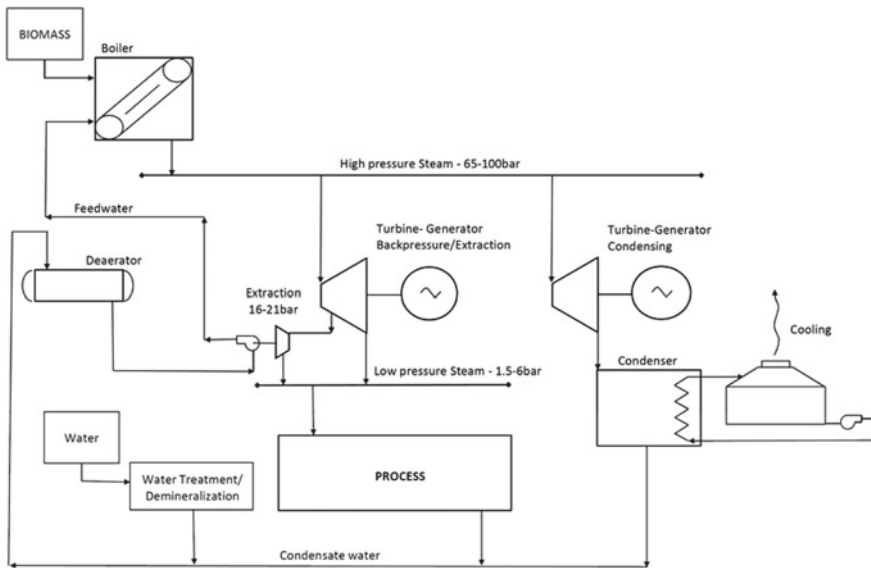


Fig. 2 Process flow diagram of biomass cogeneration plant

where

W = overall electric work done

Q = overall useful heat

E = overall fuel energy.

This solar plant along with other DC power generation techniques such as wind turbine, biogas plants, diesel plant will be together having power generation capacity up to 1.5 MW. The concept of multilevel inverters will be useful in AC power distribution as auxiliary supply for given power plant. This concept can be used in many other power plants as only the initial set up cost is high, but the payback period can be calculated as we get higher efficiency toward power deliverable toward grid. The solar plant uses solar panels which generate DC power which can be used to charge series of batteries. This stored power can be then boosted to get higher current value and better power quality for distribution and utilization purpose (Fig. 3).

An inverter is utilized to transform a direct current (DC) source into an alternating current (AC) source using electronic component like controlled switches. While converting DC to AC, it is conceivable to acquire the preferred output voltage and frequency by two types of inverters, one is two level, and another one is multilevel inverter (MLI).

Minimum total harmonic distortion, reduced number of EMI are the advantages of MLI, and it can be operated on different voltage levels. Here, MOSFETs are used as switches. In the real world, all loads (appliances/machines) do not use direct current (DC) power supply as their sources. If the only available supply is DC, then the conversion of DC to AC is needed when the loads or any applications require AC

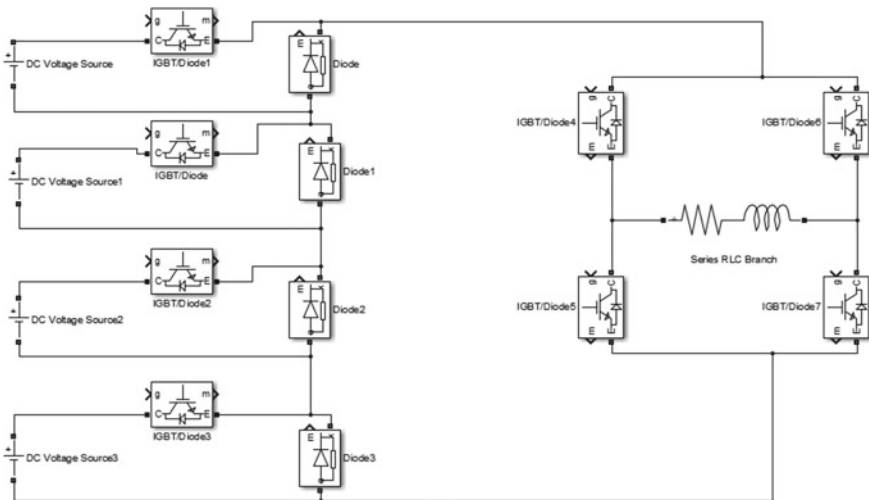


Fig. 3 Circuit diagram of the proposed single-phase 21-level reduced numbers of switches and sources MLI

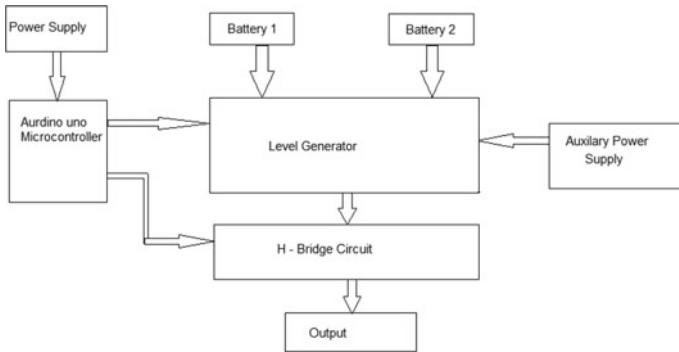


Fig. 4 Block diagram for reduced switch and source inverter

power source. In these situations, there is a need of inverters. So, the inverters show a very significant character in the real world (Fig. 4).

The block diagram of single-phase 7-level multilevel inverter topology with reduced numbers of switches and sources consists of power supply for microcontroller. There are two batteries of different ratings used as a DC input power supply to the level generator. A microcontroller is used for the programming of gate triggering of MOSFETs in level generator and H-bridge circuit. Level generator is used for the generation of voltage levels in inverter. H-bridge is used for positive and negative generation of levels. Output block is used for measuring the output. Auxiliary power is used for switching of level generator MOSFETs.

4 Results and Discussion

As we discussed earlier in the paper, newly proposed system consists of external renewable power generation arrangement. This system is mainly based on solar and wind turbine-based generation mini plants. The cost of these plants may be higher in initial stage, but the increasing efficiency toward power deliverable by the main plant can recover the cost of external mini power generation plant. The power quality of this system depends on the configuration of multilevel inverter.

Multilevel inverters provide better power quality as compared to other conventional inverters. Also, the maintenance cost of these MLI is less than conventional inverters. The single-phase multilevel inverter with reduced number of switches and sources requires minimum switching devices and minimum separate DC sources for generating multilevel output voltage compared to the conventional one. All the current as well as voltage signals obtained in MATLAB/SIMULINK for both conventional topology of single-phase multilevel cascaded H-bridge MLI and the proposed single-phase multilevel multilevel inverter with reduced number of switches and

sources with the results of the simulated MLI come in diminished size, lesser loss, along with low installation cost (Fig. 5).

The initial cost for external plant used for auxiliary power generation may increase the total cost of main power plant. This can be recovered in definite period of time. This time period depends on the total installation cost of external mini plant and the per unit rate of power deliverable to the grid. The amount of auxiliary power used by the main power plant will be no more used from main plant capacity which will benefit in the cost generation by the plant (Fig. 6).

Per unit cost of AA Ltd. biomass cogeneration power plant is approximately 6.80 Rs. As we know, the power generation capacity of this plant is up to 10 MW per

Fig. 5 Voltage output of proposed single-phase 21-level reduced numbers of switches and sources MLI

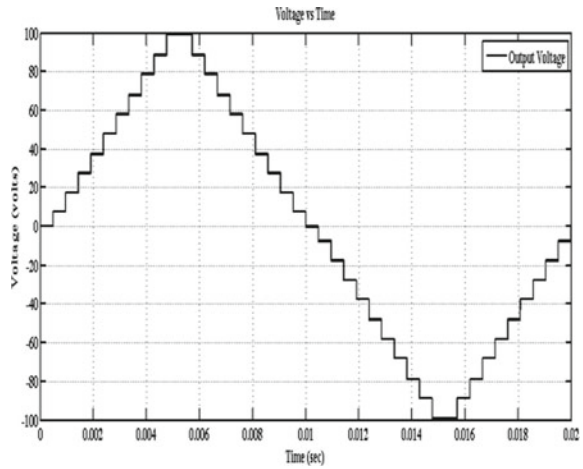


Fig. 6 System on-site observations

day. Thus, the amount of auxiliary power supply which up to 1–1.5 MW can be the additional profit for the company on daily basis.

5 Conclusion

The change in rated power generation capacity of plant to some extends leads in financial loss for the plants like biomass cogeneration as the customer or consumer of these types of plants is low-utility-type consumers. Thus, external power generation plant based on renewable energy sources can be useful for compensation of auxiliary power supply required for the plants. Following conclusions are made on the basis of researches made above.

1. Conservation of mass and energy
Use of renewable energy sources for auxiliary power generation benefits in conservation of mass and other forms of energy. Also, the efficiency of biomass cogeneration plant helps in more energy conservation considering the several environmental factors.
2. More calibrated system
Total power generation capacity of 10 MW of power per day can be achieved only with highly calibrated system. Replacement of auxiliary power supply source leads in increase in calibration of main plant.
3. More stability in output voltage
Use of multilevel inverters provides stability in the power quality for auxiliary power used by the parent plant. The DC power generation at low cost and distributing it in AC form with the help of multilevel inverters are key point toward optimization of power generation and operation strategy for these types of plants.
4. Greater overall plant efficiency

Compensating the auxiliary power required by the power generation plant use for its own operation leads in greater overall efficiency of the plant. Also, the cost-effectiveness helps in financial point of view.

Reference

1. K. Moslehi, M. Khadem, R. Bernal, G. Hernandez, Optimization of multiplant cogeneration system operation including electric and steam networks. *IEEE Trans. Power Syst.* **6**(2), 484–490 (1991)

Analysis of Ferroresonance in a Transformer with B-H Loop Having Variable Core Loss



Rajat Shubhra Pal 

Abstract Ferroresonance is a nonlinear oscillatory phenomenon, which occurs in capacitor-coupled saturable core transformers under certain conditions in a power system. The major part of the ferroresonance analysis is to find out the appropriate model of the B-H loop of the transformer. The magnetizing branch of the transformer at no load is modeled by nonlinear equation. R. Rudenburge in his graphical approach, proposed in the year 1950, took the magnetizing curve as a single line. Then, the occurrence of ferroresonance was examined by varying different circuit parameters. In this paper to incorporate the variable core loss, two separate equations are used to represent the B-H loop. Then, the new model is used to verify the occurrence of ferroresonance with the variation of different circuit parameters.

Keywords Ferroresonance · B-H loop · Transformer's nonlinear characteristics · Variable core loss

1 Introduction

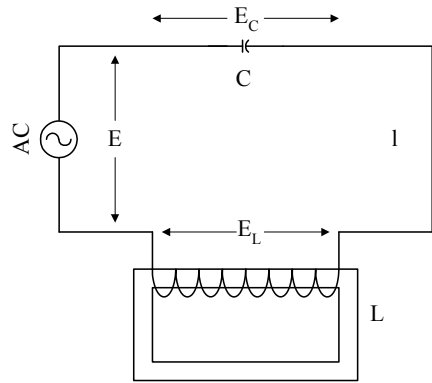
Ferroresonance is a nonlinear oscillation in a power system leading to dangerous overvoltages across transformers and line capacitance [1]. This overvoltages or over-currents may cause the equipment damage and the malfunctioning of the protective and measuring devices connected to the system. Nonlinearity is introduced due to magnetic characteristics of the core of a transformer or a power transformer at no load conditions, in series with the line capacitance as shown in Fig. 1.

In the graphical approach of Rudenburge [2], the voltage across the inductance is considered as proportional to the frequency and represented by

$$E_L = \omega f(I) \quad (1)$$

R. S. Pal (✉)
Institute of Engineering & Management, Kolkata, India
e-mail: rajatshubhra.pal@iemcal.com

Fig. 1 Ferroresonance series circuit



where $f(I)$ is a function of current, which is characteristic of the inductor and is solely dependent on the number of turns of the winding and the dimensions of the iron core and its magnetic characteristics. The voltage across the capacitor is proportional to the current and inversely proportional to frequency and capacitance. These relations lead to a simple graphical solution of the circuit response under AC source. In Fig. 2, the voltages are plotted against the current.

The capacitor line will intercept the magnetic characteristic at three different points 'a', 'b' and 'c'. However the points 'a' and 'b' represent stable states of operation of the circuit, whereas point 'c' indicates an unstable performance. The operation at 'a' in the third quadrant represents stable state of operation of the circuit generating large voltages (E_L & E_C) across the circuit elements due occurrence of ferroresonance. At this stage, an appropriate magnitude of operating alternating voltage can force the transformer to operate in nonlinear region of magnetizing characteristics and ferroresonance oscillations occur if circuit capacitance and initial conditions match.

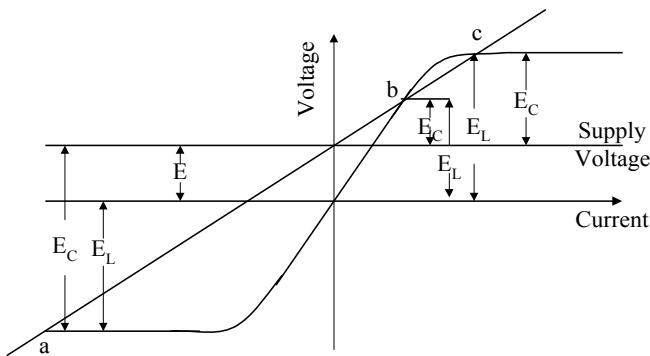


Fig. 2 Rudenberg's graphical method for inductor and capacitor characteristics [2]

2 System Equation and Transformer Model

The most critical aspect regarding the study of ferroresonance is the modeling of the transformer’s core characteristics. To accurately represent a transformer requires all of the parameters of the transformer to be known. For most simulation cases, the hysteresis and Eddy currents are approximated using a nonlinear resistor representation in the core losses. The saturation behavior, i.e., magnetizing circuit of the transformer, is represented by a nonlinear inductor based on the B-H curve or open circuit test results. Different approaches can be found out in [3–5]. A hysteresis model of an unloaded transformer has been introduced in [6]. Preisach theory is used to model the core magnetization characteristic of transformer [7]. Jiles–Atherton (JA) hysteresis model is applied to represent the hysteresis behavior of a nonlinear ferromagnetic core [8, 9].

The anhysteretic curve [10] is the core characteristic without taking any loss into account, and it is represented by the dotted curve labeled as ‘aob’ which is situated in the first and third quadrants of λ - i plane of Fig. 3.

The curve is represented by a p th order polynomial which has the following form:

$$i_m = a\lambda + b\lambda^p \tag{2}$$

where $p = 1, 3, 5, \dots$, and the exponent p depends on the degree of saturation.

Fig. 3 **a** Anhysteretic curve.
b Equivalent circuit

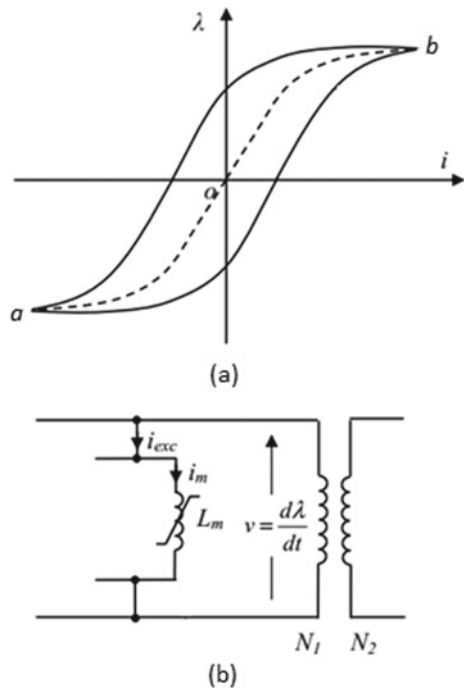
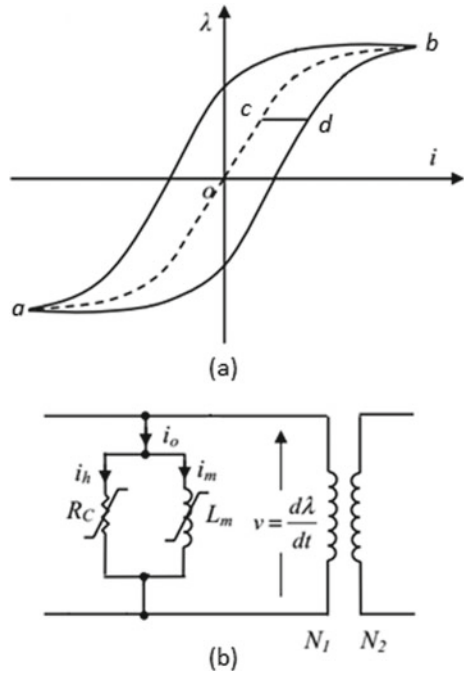


Fig. 4 a Hysteretic curve. b Equivalent circuit



Based on (2), the magnetizing branch can be represented by a nonlinear inductance, L_m , which is used to characterize the saturation effect without hysteresis effect.

In order to represent saturation with hysteresis effect (i.e., hysteresis loop) in the core, a parameter called a loss function is introduced in Fig. 4 by drawing a distance of ‘cd’ in the hysteresis loop. This corresponds to adding a resistor, R_C , connected in parallel with the nonlinear inductor, L_m .

To fit this loop in the working model, two separate equations, one for the falling edge and one for the rising edge, are used.

$$i_m = a_1\lambda^7 + a_2\lambda^6 + a_3\lambda^5 + \dots + a_7\lambda + a_8 \tag{3}$$

$$i_m = b_1\lambda^7 + b_2\lambda^6 + b_3\lambda^5 + \dots + b_7\lambda + b_8 \tag{4}$$

where (a_1, a_2, \dots, a_8) and (b_1, b_2, \dots, b_8) are the coefficients that can be determined from curve fitting tool.

Figure 5 shows the hysteresis loop along with mean curve (dashed).

To find the B-H loop, an experimental arrangement has been set up with a single phase 450 VA, 50 Hz transformer [11] as shown in Fig. 6. The voltage across the capacitor is proportional to the magnetic flux (φ), and they are in same phase. The voltage across the resistor r is proportional to the magnetizing current.

Fig. 5 Hysteretic curve; (1) falling edge (2) rising edge (3) mean curve

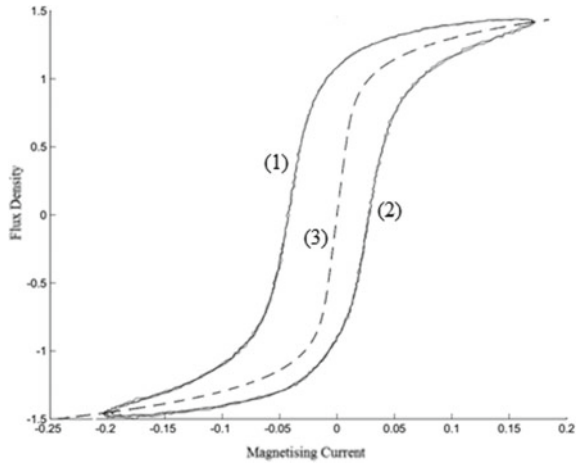
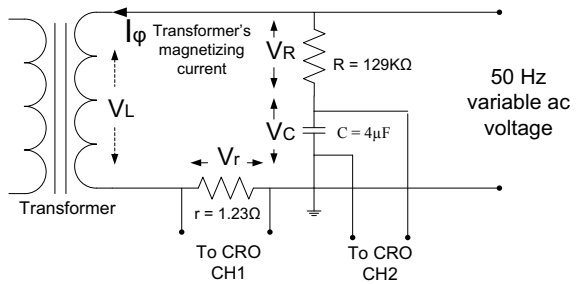


Fig. 6 Transformer B-H loop measurement circuit [11]



The data is then plotted in MATLAB [12], and using MATLAB plotting tool, the equation for the falling edge and rising edge of the B-H loop is obtained.

With the supply voltage $E(t) = V_s \sin(\omega t)$ via grading capacitance C , the transformer circuit in Fig. 1 can be described by the following equation using K.V.L.

$$\frac{d^2\lambda}{dt^2} = \frac{dE}{dt} - \frac{1}{C} \left(\frac{v}{R} \right) - \frac{1}{C} (i_m) \tag{5}$$

3 Results and Analysis

Using Eq. 5, a study is performed to find the regions in parameters where ferroresonance oscillations may exist. The parameters are (i) V_s : the magnitude of the source voltage, (ii) C : the coupling capacitances and (iii) ω : the angular frequency of the source. These are varied to show influence on ferroresonance of them.

3.1 Variation in Source Voltage

Simulation started with the following parameters:

$V_s = 100$ V; peak value of source voltage

$f = 50$ Hz; supply frequency

$C = 1.27$ μ F; series capacitance.

Value of the supply voltage is increased gradually in small steps. Figure 7 shows that there is a clear jump in the system voltages when ferroresonance occurs in the system.

The behavior well matches with the analysis given by R. Rudenburge. In Fig. 8, several capacitor lines are plotted for varying supply voltage E . At a certain increasing

Fig. 7 Variation of transformer voltage (V_L) and capacitor voltage (V_C) with source voltage

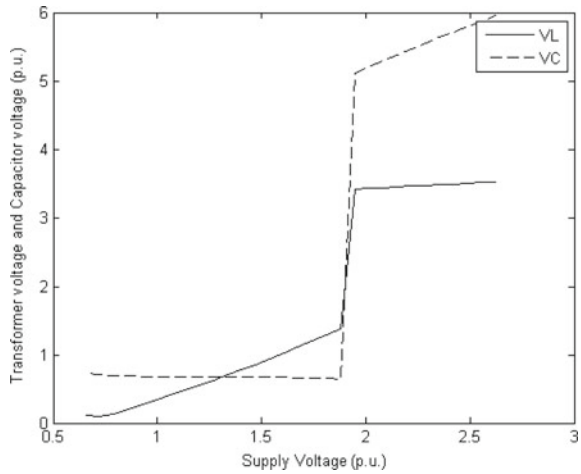
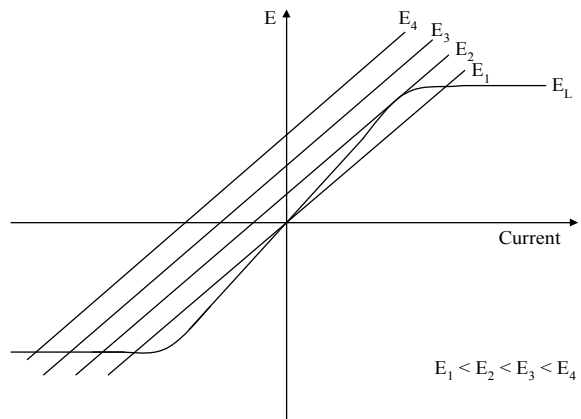


Fig. 8 Intersection of coil and capacitor characteristics with variation of supply voltage [2]



voltage between E_2 and E_3 , the performance of the circuit suddenly changes over from the inductive to the capacitive state, a ferroresonance jump which is not reversible if the voltage is decreased.

3.2 Variation in Series Capacitance

Simulation started with the following parameters:

$V_s = 100$ V; peak value of source voltage

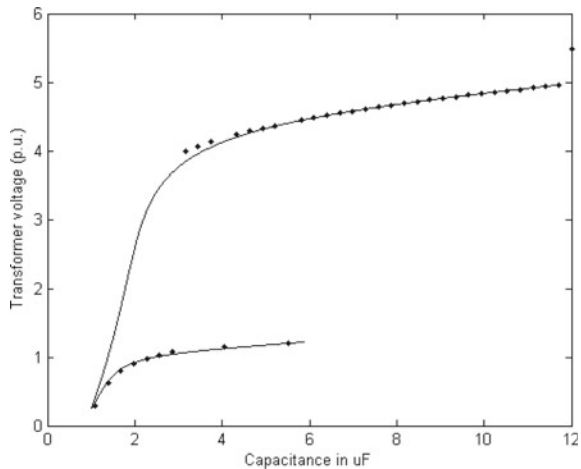
$f = 50$ Hz; supply frequency

$C = 0.5$ μ F; series capacitance.

Value of the capacitor is varied gradually up to 12 μ F. Figure 9 shows the variation of transformer voltage with the series capacitance.

As per Rudenburge [2], large capacitor with large charging current acts nearly like a conducting connection and the inductive voltage becomes equal to the impressed voltage V_s . Decreasing capacitance shifts the working point on the magnetic characteristics to higher voltages. However, there will be a point where the capacitor line no longer intersects the characteristics but touches it as a tangent at the first quadrant. For still smaller capacitance, no operation of the circuit is possible in the first quadrant, but a second point will be obtained in the third quadrant. In this state, the current in the circuit has changed direction from lagging magnetizing current to a leading charging current and the magnitude of which will greatly increase. With ever smaller capacitance, the working point shifts upward on the negative branch of the characteristics (Fig. 10), the voltages at the inductance and capacitance become

Fig. 9 Variation of transformer voltage (V_L) with capacitance



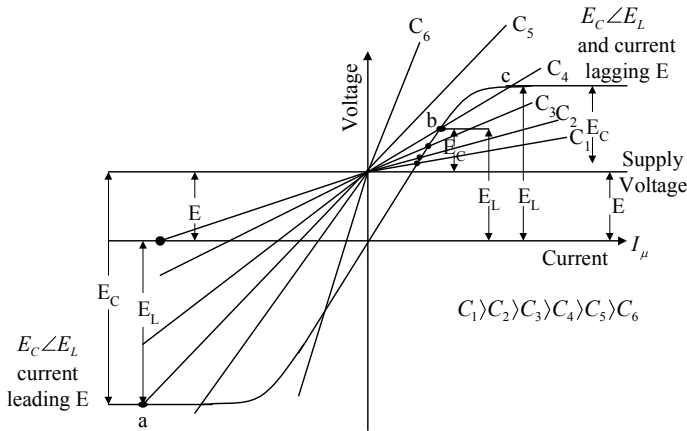


Fig. 10 Intersections of coil and capacitor characteristics with variation of capacitance [2]

smaller, and finally, with very small capacitance, the inductive voltage disappears, and the capacitor voltage coincides with the impressed voltage.

3.3 Variation in Frequency

Simulation started with the following parameters:

$V_s = 100$ V; peak value of source voltage

$f = 10$ Hz; supply frequency

$C = 1.27$ μ F; series capacitance.

Value of the frequency is varied gradually up to 80 Hz. Figure 11 shows the variation of capacitor voltage with the angular frequency.

Figure 12 represents the plot for different frequencies. The position and slope of the capacitor line change with the frequency. For low frequency ω_1 , the capacitor line is steep and intersects the magnetic characteristic on the negative branch. Thus, the circuit carries leading charging current, and state is single-valued. With increase in frequency, the capacitor line at first touches and then intersects also the positive branch of the magnetic characteristic so that with high frequency, for example ω_3 , two more possible states appear. They both operate with lagging magnetizing current in the circuit, and with further increasing frequency as for example ω_5 , the stable point moves downward on the characteristic.

Fig. 11 Variation of capacitor voltage (V_C) with frequency

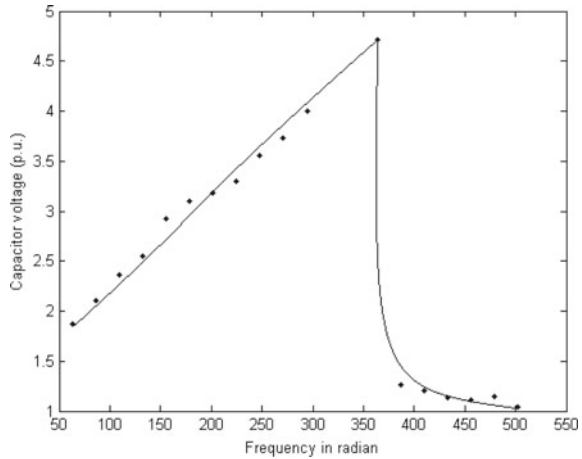
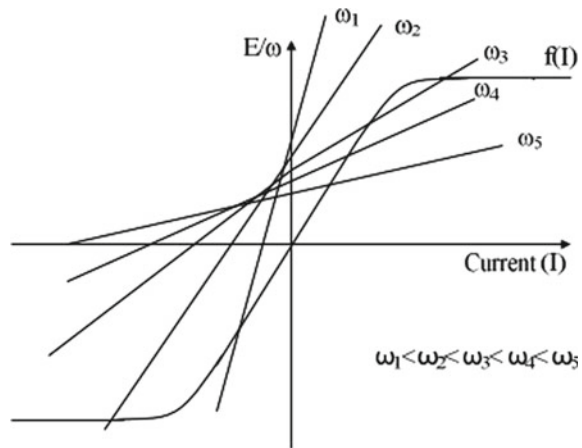


Fig. 12 Intersections of coil and capacitor characteristics with variation of supply frequency [2]



4 Conclusion

The use of the mean curve Eq. (2) does not represent the hysteresis loss of the transformer properly as it approximated core loss as a constant. To capture the variable core loss, here in this paper, an attempt has been made to represent the B-H curve by two equations, one for falling edge and another for rising edge. Two polynomial equations have been incorporated in a single MATLAB/Simulink model, and switching between the equations has been made carefully depending on the source voltage phase status.

The variation of different circuit parameters, keeping other parameter constant, shows the occurrence of fundamental ferroresonance at a certain instant. The analysis also matches with the graphical analysis proposed by Rudenburg [2].

References

1. C. Hayashi, *Nonlinear Oscillations in Physical Systems* (Princeton University Press, Princeton, 1985)
2. R. Rudenberg, *Transient Performance of Electric Power System* (McGraw-Hill, New York, 1950), pp. 642–656
3. T. Tran-Quoc, L. Pierrat, A. Montmeat, O. Huet, A dynamic model of power transformers, in *Proceedings of 8th Mediterranean Electrotechnical Conference on Industrial Applications in Power Systems, Computer Science and Telecommunications (MELECON 96)*, pp. 313–316 (1996)
4. S. Ray, Digital simulation of B/H excursions for power system studies. *IEE Proc. C—Gener. Transm. Distrib.* **135**(3), 202–209 (1988). <https://doi.org/10.1049/ip-c.1988.0026>
5. T. Tran-Quoc, L. Pierrat, An efficient non linear transformer model and its application to ferroresonance study. *IEEE Trans. Magn.* **31**(3), 2060–2063 (1995). <https://doi.org/10.1109/20.376449>
6. B. Patel, S. Das, C.K. Roy, M. Roy, Simulation of ferroresonance with hysteresis model of transformer at no-load measured in laboratory, in *TENCON 2008–2008 IEEE Region 10 Conference, IEEE*, pp. 1–6 (2008). <https://doi.org/10.1109/TENCON.2008.4766386>
7. A. Rezaei-Zare, R. Irvani, M. Sanaye-Pasand, H. Mohseni, S. Farhangi, An accurate hysteresis model for ferroresonance analysis of a transformer. *IEEE Trans. Power Deliv.* **23**(3), 1448–1456 (2008)
8. J.C. LacerdaRibas, E.M. Lourenco, J. VianeiLeite, N. Batistela, Modeling ferroresonance phenomena with a flux-current Jiles-Atherton hysteresis approach. *IEEE Trans. Magn.* **5**, 1797–1800 (2013)
9. M.M. Beyranvand, B. Rezaeealam, Finite element study of ferroresonance in single-phase transformers considering magnetic hysteresis. *J. Magn.* **22**(2), 196–202 (2017). <https://doi.org/10.4283/JMAG.2017.22.2.196>
10. M. Nowicki, An hysteretic magnetization measurement methods for soft magnetic materials. *Materials* (2018). <https://doi.org/10.3390/ma11102021>
11. M. Roy, C.K. Roy, A study on ferroresonance with a varying initial conditions using a nonlinear model of transformer, in *Proceedings of Third International Conference on Power Systems*, no. 213, India, 2009
12. MATLAB, MathWorks, Online: <https://in.mathworks.com/>

A Brief Review of Cathode Materials for Li-ion Batteries



D. Saritha

Abstract A crucial quantity of battery research is happening to realize the idea of electric vehicle applications. Incredible advancement has accomplished in the improvement of Li-ion batteries in modern eras. Nanostructured materials are attention presently for Li-ion batteries owing to their huge surface area, porosity, and little diffusion length. Exploration of nanomaterials as electrodes is obligatory to boost the electrochemical results. Nanotechnology procedures have confirmed several profits for superior energy and power density. This review enlightens various modern advancement in the formation, characterization, and performance of nanostructured materials including layered oxides, spinel oxides, and polyanion oxides as cathodes.

Keywords Review · Cathode · Electrode · Batteries · Li-ion batteries · Energy storage

1 Introduction

CO₂ footmark decline is a chief dynamic strength for the progress of greener and talented alternative energy sources [1]. Worldwide warming, restricted fossil-fuel provisions, and contaminations unite to formulate the employ of renewable energy. Energy storage is a vital constituent of the total scenery of energy processes out of energy production, transmission, and usage. Superior energy density, lesser expenses as well as enhanced shield is extremely enviable for the progress of Li-ion batteries. Predictable intercalation electrode resources have performed a decisive position in allowing the prevalent accessibility of customer electronics. Conversely, still they have limitations in their performance. The manifestation and intensification of nanotechnology in the last few years have created novel approaches to aim for battery resources on the nanoscale [2–4].

The battery comprises three major parts anode, electrolyte, and a cathode [5]. The performance of Li-ion battery is basically attained via the cathode and anode

D. Saritha (✉)

Department of Chemistry, Chaitanya Bharathi Institute of Technolygy, Hyderabad, India
e-mail: dsaritha_chm@cbit.ac.in

constituents. Researchers have paid attention to advancement in the production, optimization, and description of nanostructured materials as electrode materials for Li-ion batteries. Whittingham established the initial rechargeable Li-battery with a TiS_2 cathode, a Li-metal anode [6]. The performance of the battery openly depends on the construction, composition, and properties of cathode and anode materials.

LiCoO_2 , LiMn_2O_4 , LiFePO_4 , V_2O_5 are the resources used for producing cathode [7]. Metallic Lithium, graphitic carbon, Lithium titanate, Sn-alloys, Si-based resources are utilized for generating anode [8, 9]. The progress of cathode materials is less than the anode materials [10]. We will concentrate on the huge diversity of nanostructured cathode materials in this article. There are mainly three categories of cathode constituents, i.e., layered materials, spinel, polyanionic compounds. Protection cycle time, environmental benignity, and rate ability of the materials are reasonable for the performance of cathodes. Current trends in nano cathode resources, pioneering approach of cathode production and electrochemical act for Li-ion batteries is discussed in this mini review.

1.1 Layered Oxides

Good enough proposed and Sony commercialized the mainly victorious layered transition metal oxide LiCoO_2 as a cathode [11]. Better cycling routine, the reasonable theoretical specific capacity of 274 mAh g^{-1} , little self-discharge, high voltage forms the LiCoO_2 as attractive cathode material [12, 13]. Co and Li atoms are positioned in octahedral sites to form a hexagonal regularity of Layer LiCoO_2 . Thermal stability is the limiting factor of LiCoO_2 . Several metal oxide coverings progress the constancy and routine of LiCoO_2 [14, 15]. LiCoO_2 is mainly admired among the feasible cathode materials because of the ease and effortlessness preparation. LiCoO_2 is produced via solid-state and chemical ways [16, 17]. Li_xCoO_2 reveals admirable cyclability ($1 > x > 0.5$). Hence, the specific capacity of the substance is restricted to 140 mAh g^{-1} , even though the LiCoO_2 theoretical capacity is 273 mAh g^{-1} [18].

Conversely, its attainable theoretical capacity is 130 mAh g^{-1} moderately low, and this material is extremely pricey. Broad particle size allocation, asymmetrical morphology and non-homogeneity are the distinctiveness of the solid-state reaction which affects the electrochemical assets of LiCoO_2 [19]. Numerous novel synthetic approaches are mandatory to prepare the nano LiCoO_2 to boost the electrochemical outcomes of the material. Spray deposition [20, 21], sol-gels [22], emulsion drying method [23], emulsion process were implemented to obtain the particles with size below 100 nm. A customized sol-gel scheme via the triblock copolymer surfactant (P123) template is utilized to acquire the nano-sized LiCoO_2 with 50–100 nm particle size [24]. Superior primary discharge capacity 150 mAh g^{-1} is achieved with adequate cycling constancy [24]. Capacity fading is the core preventive fact for the nano-sized LiCoO_2 . A metal oxide coating on the superficial of LiCoO_2 particles is an appropriate selection in order to conquer this barrier [25]. Aluminum phosphate coating is a fine replacement coating owing to an additional consistent coating layer

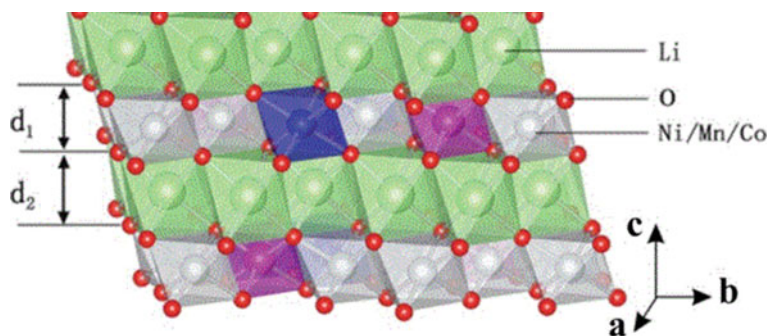


Fig. 1 Graphical illustration of layered structure (green atoms: Li; red atoms: O; silver/purple/blue atoms: Ni/Co/Mn transition metals) [27]. Reprinted with permission from John Wiley & Sons

as judge against other coatings (Al_2O_3 , ZrO_2). AlPO_4 coating on nano-sized LiCoO_2 has revealed the preservation of capacity and better thermal stability [26].

The crystal structure of LiNiO_2 is matching with the LiCoO_2 structure. Low price and high-energy density is the motivating strength to exploit as a cathode. Conversely, the thermal stability of LiNiO_2 is less than the LiCoO_2 [27]. Replacing minute amount of Co with Ni decreases the cationic disorder in LiNiO_2 [28]. Al doping boosts the thermal stability and electrochemical presentation [29]. Consequently, the $\text{LiNi}_{0.8}\text{Co}_{0.15}\text{Al}_{0.05}\text{O}_2$ cathode has been commercially used thanks to its extended almanac life and high capacity.

LiMnO_2 is an accepted electrode owing to less price and low toxicity of Mn compared to Co or Ni. Conversely, the cycling appearance of LiMnO_2 is not reasonable as the layered assembly has an affinity to alter into spinel structure throughout Li-ion extraction [30]. Steadiness of cycles can be better by cation doping [31]. $\text{LiNi}_{0.33}\text{Co}_{0.33}\text{Mn}_{0.33}\text{O}_2$ is an eminent range of NMC and is extensively explored in the battery market. Macro porous NMC exhibited superior cycle steadiness and a reversible specific capacity is 234 mAh g^{-1} [32]. The graphical illustration of layered structure is revealed in Fig. 1.

1.2 Spinel Oxides

An abundant resource, low toxicity levels, environmental geniality are the rewards of LiMn_2O_4 compared to LiCoO_2 and LiNiO_2 [33]. Thackeray et al. initially projected the spinel cathode LiMn_2O_4 and improved by several authors [33, 34]. LiMn_2O_4 is an admired cathode material owing to its benefit of low price, high voltage, and a theoretical capacity of 148 mAh g^{-1} [33].

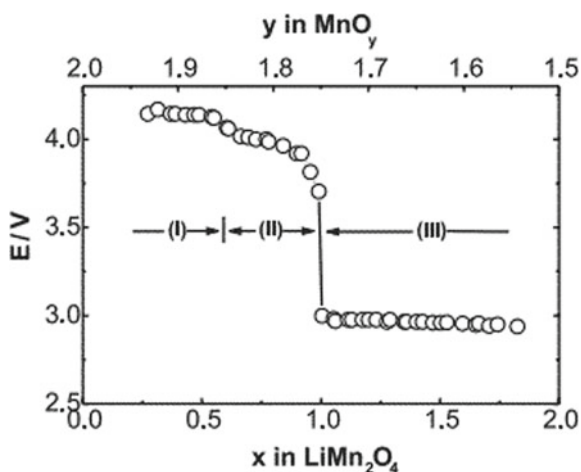
The anion lattice of the LiMn_2O_4 is correlated to the R- NaFeO_2 layered structure. It surrounds cubic close-packed oxygen ions, whereas the allotments of the cations are varied. The space group of LiMn_2O_4 is $\text{Fd}\bar{m}3$. Li^+ ions dwell in the 8a tetrahedral

sites and the $\text{Mn}^{3+/4+}$ ions reside in the 16d octahedral sites of the spinel skeleton through a cubic close-packed display of oxide-ions [35]. Edge-shared octahedra of Mn_2O_4 produces a three-dimensional Li-ion diffusion path with rapid conductivity [35]. Li-ions enroll into the empty 16c sites if the Li^+ mole fraction go beyond 1 [36]. The three-dimensional path for Li^+ diffusion is generated via 8a and unfilled 16c sites in spinel LiMn_2O_4 . Since it recommends the lowest energy barrier [36].

$\text{Li}_x\text{Mn}_2\text{O}_4$ shows two plateaus around 4 V at the I and II region and 3 V at region III which resulting in the formation of $\text{Li}_2\text{Mn}_2\text{O}_4$ [37] (Fig. 2). The cubic structure retains at 4 V as the x range varies from 0 to 1. If $1.0 < x < 2.0$, then the phase alteration occurs from the cubic spinel to the tetragonal rock salt phase [37]. Consequently, degradation happens at a voltage below 3.5 V. The poor cycle life of LiMn_2O_4 also owing to the Jahn–Teller effect. It causes due to uneven expansion and compression takes place in the lattice through cycling [38]. Downscale the material size to accomplish little diffusion distance and massive surface area which improves the poor rate capability of $\text{Li}_x\text{Mn}_2\text{O}_4$. Various production ways are employed to produce nano LiMn_2O_4 to overcome the above issues [39]. Various dissimilar groups have synthesized nanowires and mesoporous shapes of LiMn_2O_4 , which confirmed a gifted outcome [39].

The substitution of metal ions in LiMn_2O_4 also improves the electrochemical performance. $\text{LiNi}_{0.5}\text{Mn}_{1.5}\text{O}_4$ produced by the Pechini process displays acceptable electrochemical characteristics once cycled among 3.5 and 5 V [40]. ZrO_2 coated LiMn_2O_4 shows the most excellent cycling steadiness compared to Al_2O_3 and SiO_2 coated LiMn_2O_4 [41]. The characteristic charge–discharge curves of LiMn_2O_4 microspheres exhibit two voltage plateaus at around 3.9–4.0 V and 4.1–4.2 V, correspondingly. LiMn_2O_4 is altered into $\text{Li}_{0.5}\text{Mn}_2\text{O}_4$ and finally converted into $\lambda\text{-MnO}_2$ at high voltage plateau during the charging route [33]. Substituting a tiny quantity of Li in LiMn_2O_4 reduces the dissolution of Mn from the lattice into the electrolyte [33]. Rate of diffusion for rate for Li^+ ion in LiMn_2O_4 is 10^{-6} – 10^{-10} sq cm/s [42].

Fig. 2 Discharge curve of $\text{Li}_x\text{Mn}_2\text{O}_4$ [42]. Reprinted with permission from © 2001, Elsevier



The capacity reduction is the leading concern upon various cycling. Cycling stability can be enhanced in LiMn_2O_4 by doping with metal ions Al, Co, Cr, Fe, Mg, Ni, Mg, etc. [39]. In recent times, a novel ordered mesoporous $\text{Li}_{1.12}\text{Mn}_{1.88}\text{O}_4$ spinel was established to superior electrochemical presentation compare to bulk spinel [39]. The electrochemical performance can be optimized in LiMn_2O_4 via doping with cations like Li, B, Mg, Al, Fe, Co, Ni, and Zn [39].

1.3 Polyanion Oxides

Polyanionic compounds have been explored as a choice to the layered and spinel compounds owing to their environmental acceptance, better electrochemical features, and small-price for Li-ion batteries [43]. Manthiram and Goodenough projected the phosphates of polyanion oxides $\text{LiTi}_2(\text{PO}_4)_3$, $\text{LiZrTi}(\text{PO}_4)_3$, $\text{NbTi}(\text{PO}_4)_3$, and $\text{SbTi}(\text{PO}_4)_3$ as electrode sources. $\text{Li}_2\text{Ni}_2(\text{MoO}_4)_3$ and $\text{Li}_2\text{Co}_2(\text{MoO}_4)_3$, $\text{Fe}_2(\text{MoO}_4)_3$ compounds belong to Nasicon-type have been experienced as optimistic electrodes [44]. Nasicon $\text{Li}_3\text{Fe}_2(\text{PO}_4)_3$, olivine LiFePO_4 , amorphous FePO_4 are widely studied polyanionic compounds [45]. LiFePO_4 as a remarkable electrode because of its abundance, economically viable, ecologically receptive, thermal constancy and a theoretical capacity of 170 mAh g^{-1} [45].

On the other hand, olivine LiFePO_4 has poor conductivity, charging voltage goes down below 4 V and its electrochemical act is restricted [46]. Decrease in cathode particle and employ nanocomposites of LiFePO_4 with carbon has been anticipated to progress this challenge [46]. Adapted solid-state reaction, emulsion drying process, and citric acid support sol–gel routes were utilized to produce nano-sized LiFePO_4/C composites [39]. These nanocomposites have revealed admirable performance. Rho et al. introduced the metallic coating $\text{Fe}_2\text{Pon C-LiFePO}_4$ which facilitates the high capacity at a high C rate [47]. Carbon xerogel based nanocomposite LiFePO_4 can be formed via resorcinol–formaldehyde precursor. It attained a 90% theoretical capacity at a C/2 rate with exceptionally fine steadiness and an admirable electrochemical act [48].

Various metal oxidation states, structural steadiness, and superior theoretical specific capacity formulate the vanadium- and molybdenum-based polyanion as fascinating electrodes [49]. AlVMoO_7 structure is made-up of tetrahedral polyanionic groups linked by corner-sharing. It generates a three-dimensional network connected by Al_2O_{10} octahedral dimmers and corner-shared $(\text{Mo}/\text{V})_2\text{O}_7$ tetrahedral clusters [50] (Fig. 3). The exhibited initial discharge capacity was 310 mAh g^{-1} and matches to the response of 3.3 Li per formula unit (Fig. 4). The originated leading charge capacity was 245 mAh g^{-1} and equivalent to the extraction of 2.6 Li. Three plateaus were stated at 2.8, 1.9 and 1.8 V in the differential capacity plot which resembles to the reduction of $\text{V}^{5+}/\text{V}^{4+}$, $\text{Mo}^{6+}/\text{Mo}^{5+}$ and $\text{Mo}^{5+}/\text{Mo}^{4+}$. The outcome of cycling information exposed that the AlVMoO_7 phase displays a superior reversible capacity and it was 180 mAh g^{-1} still after 20 cycles. AlVMoO_7 provide accommodation 3.3 Li per formula unit [50]. Recently, Saritha et al. explored structurally

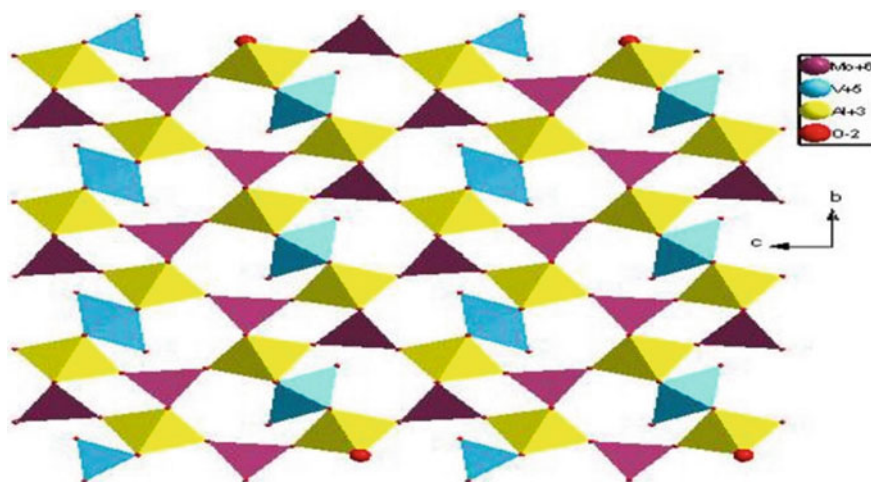


Fig. 3 Crystal structure of AlVMoO_7 along bc -plane [Draw using diamond software]

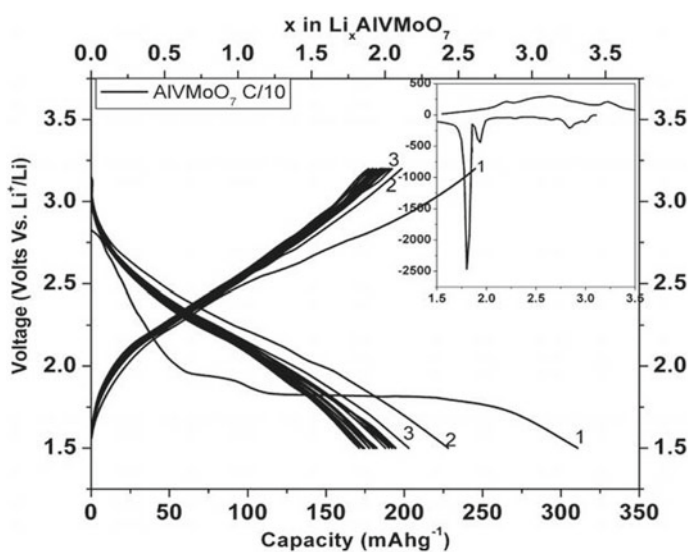


Fig. 4 Charge–discharge behavior of AlVMoO_7 and the insert displays the analogous differential capacity plot (dQ/dV)

related polyanion compounds FeVMoO_7 , CrVMoO_7 as electrode materials for Li-ion batteries [51]. These phases were made by hiring sol–gel way. Preliminary electrochemical studies revealed the superior reversible capacity was 160 mAh g^{-1} still after 20 cycles in the case of FeVMoO_7 [51].

2 Conclusions

The Li-ion battery research persists on novel electrode materials to acquire energy density, power density, protection, and cycle existence. The growth of Li-ion batteries can profit from the discrete assets of nanomaterial's, i.e., high surface areas, short diffusion paths and autonomy for volume alter through charging–discharging cycles. An extensive variety of synthetic procedures is employed to produce nanomaterials. Marvelous research works have been ready to alleviate the intrinsic issues of cathode materials. This article carries out a brief analysis of the advancement of various cathode materials extensively engaged.

References

1. V. Ruiz, A. Pfrang, A. Kriston, N. Omar, P. Van den Bossche, L.A. Boon-Brett, Review of international abuse testing standards and regulations for lithium-ion batteries in electric and hybrid electric vehicles. *Renew. Sustain. Energy Rev.* **81**, 1427–1452 (2017)
2. H.C. Zhou, J.R. Long, O.M. Yaghi, Introduction to metal–organic frameworks. *Chem. Rev.* **112**, 673–674 (2012)
3. A.K. Geim, K.S. Novoselov, The rise of graphene. *Nat. Mater.* **6**, 183–191 (2007)
4. A.P. Alivisatos, Perspectives on the physical chemistry of semiconductor nanocrystals. *J. Phys. Chem.* **100**, 13226–13239 (1996)
5. V. Etacheri, R. Marom, R. Elazari, G. Salitra, D. Aurbach, Challenges in the development of advanced Li-ion batteries: a review. *Energy Environ. Sci.* **4**, 3243 (2011)
6. M.S. Whittingham, Electrical energy storage and intercalation chemistry. *Science* **192**, 1126–1127 (1976)
7. A. Mishra, A. Mehta, S. Basu, S.J. Malode, N.P. Shetti, S.S. Shukla, M.N. Nadagouda, T.M. Aminabhavi, Electrode materials for lithium-ion batteries. *Mater. Sci. Energy Technol.* **1**(2), 182–187 (2018)
8. W. Xu, J. Wang, F. Ding, X. Chen, E. Nasybulin, Y. Zhang, J.G. Zhang, Lithium metal anodes for rechargeable batteries. *Energy Environ. Sci.* **7**, 513–537 (2014)
9. N. Nitta, F. Wu, J.T. Lee, G. Yushin, Li-ion battery materials: present and future. *Mater. Today* **18**, 252–264 (2015)
10. A.S. Arico, P. Bruce, B. Scrosati, J.M. Tarascon, W.V. Schalkwijk, Nanostructured materials for advanced energy conversion and storage devices. *Nat. Mater.* **4**, 366–377 (2005)
11. K. Mizushima, P.C. Jones, P.J. Wiseman, J.B. Goodenough, Li_xCoO_2 ($0 < x < 1$): a new cathode material for batteries of high energy density. *Mater. Res. Bull.* **15**(6), 783–789 (1980)
12. R. Yazami et al., New trends in intercalation compounds for energy storage and conversion, in *Proceedings of the International Symposium*, The Electrochemical Society, p. 317 (2003)
13. A. Du Pasquier, I. Plitz, S. Menocal, G. Amatucci, A comparative study of Li-ion battery, supercapacitor and nonaqueous asymmetric hybrid devices for automotive applications. *J. Power Sources.* **115**(1), 171–178 (2003)
14. J. Cho, Y.J. Kim, T.J. Kim, B. Park, Zero strain intercalation cathode for rechargeable Li-ion cell. *Angew. Chem.* **113**(18), 3471–3473 (2001)
15. I.D. Scott, Y.S. Jung, A.S. Cavanagh, Y. Yan, A.C. Dillon, S.M. George, S.H. Lee, Ultra thin coatings on Nano- LiCoO_2 for Li-ion vehicular applications. *Nano Lett.* **11**(2), 414–418 (2011)
16. J.N. Reimers, J.R. Dahn, Electrochemical and Insitu X-ray diffraction Studies of Lithium Intercalation in Li_xCoO_2 . *J. Electrochem. Soc.* **139**, 2091–2097 (1992)
17. P.N. Kumta, D. Gallet, A. Waghay, G.E. Blomgren, M.P. Setter, Synthesis of LiCoO_2 powders for lithium-ion batteries from precursors derived by rotatory evaporation. *J. Power Sour.* **72**, 91–98 (1998)

18. T. Ohzuku, A. Ueda, Why transition metal (di) oxides are the most attractive materials for batteries. *Solid State Ionics* **69**, 201–211 (1994)
19. H. Liu, Y.P. Wu, E. Rahm, R. Holze, H.Q. Wu, Cathode materials for lithium ion batteries prepared by sol-gel methods. *J. Solid State Electrochem.* **8**, 450–466 (2004)
20. C. Chen, E.M. Kelder, P.J.J.M. van der Put, J. Schoonman, Morphology control of thin LiCoO_2 films fabricated using the electrostatic spray deposition (ESD) technique. *J. Mater. Chem.* **6**, 765–771 (1996)
21. C.H. Chen, A.A.J. Buysman, E.M. Kelder, J. Schoonman, Fabrication of LiCoO_2 thin film cathodes for rechargeable lithium battery by electrostatic spray pyrolysis. *Solid State Ionics* **80**, 1–4 (1995)
22. Y.K. Sun, Cycling behaviour of LiCoO_2 cathode materials prepared by PAA-assisted sol-gel method for rechargeable lithium batteries. *J. Power Sour.* **83**, 223–226 (1999)
23. S.T. Myung, N. Kumagai, S. Komaba, H.T. Chung, Preparation and electrochemical characterization of LiCoO_2 by the emulsion drying method. *J. Appl. Electrochem.* **2000**(30), 1081–1085 (2000)
24. Q. Wu, W. Li, Y. Cheng, Z. Jiang, Homogenous LiCoO_2 nanoparticles prepared using surfactant P123 as template and its application to manufacturing ultra-thin-film electrode. *Mater. Chem. Phys.* **91**, 463–467 (2005)
25. J. Cho, H. Kim, B. Park, Comparison of overcharge behavior of AlPO_4 -coated LiCoO_2 and $\text{LiNi}_0.8\text{Co}_0.1\text{Mn}_0.1\text{O}_2$ cathode materials in Li-Ion cells. *J. Electrochem. Soc.* **151**, A1707–1711 (2004)
26. J. Cho, Y.W. Kim, B. Kim, J.G. Lee, B. Park, A breakthrough in the safety of lithium secondary batteries by coating the cathode material with AlPO_4 nanoparticles. *Angew. Chem. Int. Ed.* **42**, 1618–1621 (2003)
27. S.H. Cui, Y. Wei, T. Liu, W. Deng, Z. Hu, Y. Su, H. Li, M. Li, H. Guo, Y. Duan, W. Wang, M. Rao, J. Zheng, X. Wang, F. Pan, Optimized temperature effect of Li-ion diffusion with layer distance in $\text{Li}(\text{Ni}_x\text{Mn}_y\text{Co}_z)\text{O}_2$ cathode materials for high performance Li-ion battery. *Adv. Energy Mater.* **6**, 1501309 (2016)
28. H. Arai, S. Okada, Y. Sakurai, J. Yamaki, Thermal behavior of $\text{Li}_{1-y}\text{NiO}_2$ and the decomposition mechanism. *Solid State Ionics* **109**(3), 295–302 (1998)
29. C.H. Chen, J. Liu, M.E. Stoll, G. Henriksen, D.R. Vissers, K. Amine, Aluminum-doped lithium nickel cobalt oxide electrodes for high-power lithium-ion batteries. *J. Power Sour.* **128**(2), 278–285 (2004)
30. M. Gu, I. Belharouak, J. Zheng, H. Wu, J. Xiao, A. Genc, K. Amine, S. Thevuthasan, D.R. Baer, J. Zhang, N.D. Browning, J. Liu, C. Wang, Formation of the spinel phase in the layered composite cathode used in li-ion batteries. *ACS Nano* **7**(1), 760–767 (2012)
31. G. Ceder, S. Mishra, The stability of orthorhombic and monoclinic-layered LiMnO_2 . *Electrochem. Solid State Lett.* **2**(11), 550–552 (1999)
32. K.M. Shaju, P.G. Bruce, Macroporous $\text{Li}(\text{Ni}_1/3\text{Co}_1/3\text{Mn}_1/3)\text{O}_2$: a high-power and high-energy cathode for rechargeable lithium batteries. *Adv. Mater.* **18**(17), 2330–2334 (2006)
33. Z. Chen, W. Zhang, Z. Yang, A review on cathode materials for advanced lithium ion batteries: microstructure designs and performance regulations. *Nanotechnology* **31**, 012001 (2020)
34. D. Guyomard, J.M. Tarascon, The carbon/ $\text{Li}_{1+x}\text{Mn}_2\text{O}_4$ system. *Solid State Ionics* **69**, 222–237 (1994)
35. E. Lee, K.A. Persson, First-principles study of the nanoscaling effect on the electrochemical behavior in $\text{LiNi}_{0.5}\text{Mn}_{1.5}\text{O}_4$. *Nanotechnology* **24**, 424007 (2013)
36. O.K. Park, Y. Cho, S. Lee, H.C. Yoo, H.K. Song, J. Cho, Who will drive electric vehicles, olivine or spinel? *Energy Environ. Sci.* **4**, 1621–1633 (2011)
37. T. Ohzuku, M. Kitagawa, T. Hirai, Electrochemistry of manganese dioxide in lithium nonaqueous cell. *J. Electrochem. Soc.* **137**(3), 769–775 (1990)
38. Z. Jiang, K.M. Abraham, Preparation and electrochemical characterization of micron-sized spinel LiMn_2O_4 . *J. Electrochem. Soc.* **143**(5), 1591–1598 (1996)
39. F. Fernanda, C. Bazito, R.M. Torresi, Cathodes for lithium ion batteries: the benefits of using nanostructured materials. *J. Braz. Chem. Soc.* **17**(4), 627–642 (2006)

40. M. Kunduraci, G.G. Amatucci, Synthesis and characterization of nanostructured 4.7 V $\text{Li}_x\text{Mn}_{1.5}\text{Ni}_{0.5}\text{O}_4$ spinels for high-power lithium-ion batteries. *J. Electrochem. Soc.* **153**, A1345–A1352 (2006)
41. J.S. Kim, C.S. Johnson, J.T. Vaughey, S.A. Hackney, K.A. Walz, W.A. Zeltner, M.A. Anderson, M.M. Thackeray, The electrochemical stability of spinel electrodes coated with ZrO_2 , Al_2O_3 , and SiO_2 from colloidal suspensions. *J. Electrochem. Soc.* **151**, A1755–A1761 (2004)
42. M. Wakihara, Recent developments in lithium ion batteries. *Mater. Sci. Eng. R: Rep.* **33**(4), 109–134 (2001)
43. J. Shirakawa, M. Nakayama, M. Wakihara, Y. Uchimoto, Changes in electronic structure upon lithium insertion into $\text{Fe}_2(\text{SO}_4)_3$ and $\text{Fe}_2(\text{MoO}_4)_3$ investigated by X-ray absorption spectroscopy. *J Phys. Chem. B.* **111**, 1424–1430 (2007)
44. A. Manthiram, An outlook on lithium ion battery technology. *ACS Cent. Sci.* **3**, 1063–1069 (2017)
45. M. Armand, J.M. Tarascon, Building better batteries. *Nature* **451**, 652–657 (2008)
46. A.K. Shukla, T. Prem Kumar, Materials for next generation lithium batteries. *Curr. Sci.* **94**(3), 317–327 (2008)
47. F. Croce, A.D. Epifanio, J. Hassoun, A. Deptula, T. Olczac, B. Scrosati, A novel concept for the synthesis of an improved LiFePO_4 lithium battery cathode. *Electrochem. Solid-State Lett.* **5**, A47–A50 (2002)
48. H. Huang, S.C. Yin, L.F. Nazar, Approaching theoretical capacity of LiFePO_4 at room temperature at high rates. *Electrochem. Solid-State Lett.* **4**, A170–A172 (2001)
49. M. Morcrette, P. Rozier, L. Dupont, E. Mugnier, L. Sannier, J. Galy, J.M. Tarascon, A reversible copper extrusion–insertion electrode for rechargeable Li batteries. *Nat. Mater.* **2**, 755–761 (2003)
50. D. Saritha, Sol-gel Synthesis and electrochemical analysis of the three dimensional structure of AlVMoO_7 . *Bull. Mater. Sci.* **41**, 64 (2018)
51. D. Saritha, Electrochemical study of the two structurally related compounds FeVMoO_7 and CrVMoO_7 synthesized by sol-gel method. *J. Chem. Sci.* **130**, 7 (2018)

A Review of Electric Vehicle Components



Mali Rohini and Shendge Asha

Abstract An EV (Electrical Vehicle) uses battery for driving vehicle with 0% emission. EV has different component such as electric motor, battery, connector, etc. This paper will give you basic concept of each component, principle, uses, advantages, disadvantages, EV in India, etc. Also, various types of charging modes, charging time, battery swapping, Vehicle to Grid (V2G) concept is explained. From that we can define the more efficient way for EV for proper selection of charging battery system such as for motor cycle, cars, trucks, auto rickshaw, bus, trains, etc. However, EV uses have many challenges to overcome in upcoming years.

Keywords EV (Electrical Vehicle) · Battery · Battery swapping · Connector · Electrical motor · V2G (vehicle to grid)

1 Introduction

The first EVs came into presence in the mid-nineteenth century. EV uses electrical motor for driving vehicle with the help of battery storage system. The battery storage was main issue at that time, so EV production and use stopped [1].

After at twenty-first century, EV comes again in the form of cars, since the need for the 0% emission of carbon dioxide is needed. EV is clean and 0% emission of CO₂ [2]. EV takes the power from battery which can rechargeable from charging station with electrical supply from electricity or renewable energy [3].

Nowadays, Government is giving incentives to increase the EV modes and renewable energy us. EV can increase from 2 to 22% in global market [4].

In twenty-first century, the electricity may be stored in form of using a battery, flywheel, or super capacitors. From 2008, more than 50,000 electrical car and utility vehicle have sold out in world. In 2018, the cars which are capable to run on highway,

M. Rohini (✉) · S. Asha
GHRIT, Electrical Department, Savitribai Phule University, Wagholi, Pune, India

S. Asha
e-mail: asha.shendge@raisoni.net

Fig. 1 Edison and Detroit electric model



Fig. 2 The Nissan Leaf EV (red) and the Tesla EV (black)



is produced, that are of 45 types of series in various countries. In December 2015, the Leaf sold 200,000 cars, Tesla Model S sold 100,000 cars, in a worldwide, India also have rapid increasing market for Ev (Figs. 1 and 2).

1.1 Electrical Vehicle Manufacturer in India

See Table 1.

2 Electrical Vehicle Battery

EV battery can convert chemical energy into electrical energy which gives to EV for propulsion. The working principle of a battery is, when it supply electric energy, the negative terminal which carries the electrons to the positive terminal through an external electric circuit [36]. When a battery is used to give electric energy, a

Table 1 EV in India

S. No.	Electrical vehicle	Electrical vehicle manufacturing companies
1	Electrical cars	Hyundai-Kona [5], Mahindra-e-Verito [6] and e2o, MG ZS EV, Tata-Tigor [7], Nexon EV, Maruti Omani-ISRO-Solar Hybride Car [8]
2	E-Motorcycles	Revolt (RV400 & RV300) [9–13], Tork Mtorcycle [14], Emflux [15, 16], Ultraviolette Automotive [17]
3	E-Scooters	Hero-Electric Photon 48 V, Ather Energy [18, 19], Bajaj-Chetak, TVS-iQube, Okinawa, Yakuza-Rubie, Evolet Pony
4	E-Buses	India's first E-bus-Bangalore [20], Ashok Leyland [21], Tata-Starbus Electric 9 m [22], Goldstone Infratech-Himachal Pradesh [23], First intercity electric bus between Mumbai–Pune by MSRTC [24]
5	E-MiniPickup Trucks	Mahindra [25], Tata Motors-Ace [26], Ashok Leyland-Dost India first electric cargo light truck- Croyance Automotive, ELECRO 1.t [27]
6	Heavy duty trucks, semi-trailer and tractor trucks	Infraprime Logistics Technologies Pvt. Ltd. heavy duty truck (tractor-tipper-trailer) [28]
7	E-Rickshaws	Mahindra [29], MAuto Electric Mobility-Retrofit EV [30], Entice Impex Pvt Ltd–Gatti rickshaw [31], Oculus, Kerala Automobiles Limited [32]
8	E-Railway	By 2022, whole rail system in the country will be electrified [33]. Solar trains: panel mounted on trains uses in lighting and fans in the train [34]
9	E boat/Solar boat	Aditya-NavAlt
10	Old to battery vehicles	Maruti E-trio, Alto, Wagno R [35]
11	Hybrid Cars	Toyota–Prius, Honda–Camryand Glanza, MG Hector, Maruti Suzuki-Ciaz, Swift, Ertiga and Baleno, Mahindra-Scorpio, BMW i8-Volvo XC90 T8 Excellence

chemical reaction occurs which changes high-energy reactants to low energy, and the residual energy is given as electrical energy.

The battery have two type, primary and secondary (rechargeable). The batteries used in EV are generally rechargeable (secondary) batteries. These are Li-ion, lead–acid nickel cadmium, nickel metal hydride, zinc–air and sodium nickel chloride (zebra) [37–40]. The batteries for EV have specification as high ampere-hour (or

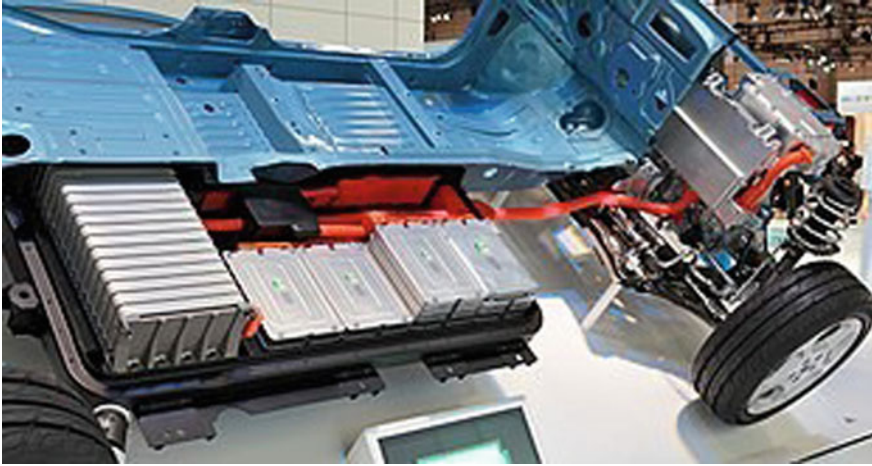
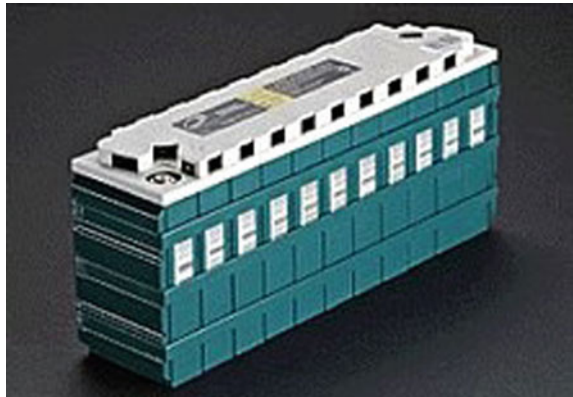


Fig. 3 The simplified view of Nissan Leaf battery

Fig. 4 The Lithium ion battery



kilowatt-hour) capacity, high power-to-weight ratio, specific energy and energy density [41]. Mainly in EV, smaller, light weight batteries are used because, decrease in the weight of the vehicle and increases its performance. The recent batter have low specific energy, and hence this effects the electric range of the vehicles [42] (Figs. 3, 4, 5 and Table 2).

3 Charging Station

An EV charging station is, where electrical vehicle can charge with the help of different level of charger for different vehicle according to battery capacity, EV can

Fig. 5 GM Ovonix NiMH Battery



charge. There are different charging modes, charging level, time for charging, etc. The charger like AC and DC charging are available. Types of charger are AC fast charging, DC rapid charging, multi-standard chargers armed with two or three of the Combined Charging System (CCS), CHAdeMO.

The charging station can be located at parking level, residential level, public charging station. Charging can be from electricity supply or renewable energy sources (Fig. 6).

3.1 Different Charging Modes

As per the International standard IEC 61851-1, EV charging system has defined different Modes of charging.

Mode 1: Residential socket with cable [53].



An EV is connected through socket at residential. This electrical installation is done with safety guidelines and earthing system. A circuit breaker is provided as protection against overload and an earth leakage. The limitation of this mode is, the risks of heating of socket and cables. Fire risk if any electrical accident happens. The installation’s power management mean, tripping of CB, stopping charging.

Table 2 Commonly used EV batteries and there comparison

Battery type	Cell voltage	Spe. Energy (KJ/KG)	Cycles	Years	Comment
Lead-Acid	2.1	140	300–500 [43]	3 [44]	<ul style="list-style-type: none"> – Flooded type are cheaper, less capacity to start up – Battery of deep cycle used in continuous energy to run forklifts/golf carts – Battery life is 50% and efficiency 70–75% – The emission H₂, O₂ and sulphur in charging/discharging – E.g.: Modern, EV1 [45]
Ni-MH (Nickel metal hydride)	1.2	360	< 2000	43	<ul style="list-style-type: none"> - Efficient 60–70% than lead acid, long lives [38, 46] -Latest batteries has low self-discharge rate approximate 25% [47], Poor performance in cold weather [48] - E.g.: 2nd model EV-1, Toyota RAV4 EVs
Zebra	1.3	120	< 400	1	<ul style="list-style-type: none"> – Electrolyte is a molten sodium chloroaluminate (NaAlCl₄) salt [49] – Poor specific power, potentially hazard, charge cycles for a few thousand and are non-hazardous – E.g: The Modec

(continued)

Table 2 (continued)

Battery type	Cell voltage	Spe. Energy (KJ/KG)	Cycles	Years	Comment
Li-ion	3.6	460	> 4000	> 10 [50]	<ul style="list-style-type: none"> - a lithium cobalt oxide cathode and a graphite anode [37, 51] - Sensitivity to lower temperature, performance get down with life of battery [52], Li-ion gives specific energy power to give fire resistance, environmental friendly, rapid charging in few minutes, and long lifespans - Battery can regain 90% of its initial capacity after 6 years - Li-iron-phosphate (with A123 types) have life more than 10 years and charge/discharge cycles > 7000, Li-manganese spinel batteries lifespan up to 40 years

Mode 2: A private/commercial socket with cable [54]



A private or commercial scheme for a fee or free use this mode. An EV is attached to the main household/private socket. The charging via a type 1 or type 2 network is performed. A protection devices are in the cable with earthing. This is costly than Mode 1 due to the cable [55, 56].



Fig. 6 A solar powered charging station

Mode 3: Fixed network socket [57].



An EV is coupled to the electrical network with socket and plug and a network. A control and protection devices are installed. The standards regulating electrical installations (IEC 61851) are used to during charging or can enhance charging time [58].

Mode 4: DC Connection

An EV is connected to the power grid through an external charger. The control and protection devices are installed [59].



3.2 Different Charging Levels

The Society of Automotive Engineering (SAE) decided the rules for the EV charging systems as in North America. It is called SAE J1772. The different charging levels

based on the voltage, current and power, the charging levels in North America are of three types [37]:

- Level 1: The voltage is 120 V, the current of 12–15 A and maximum power of 1.44–1.92 kW. This is on-board charger.
- Level 2: The AC voltage level is up to 240 V, current of 80 A and a maximum power of 19.2 kW. This is on-board charger.
- Level 3: The voltage is up to 480 V. The charger is off board means the vehicle is charged with DC in charging station to the battery via a DC connector.

For light trucks, the CCS DCFC standard is used for commercial vehicles, called as High-Power Charging for Commercial Vehicles (HPCCV) with the operating range of 200–1500 V and 0–3000 A for power of 4.5 MW [38].

3.3 Charging Time

The charging time to charge EV depends on the battery size and the charging power. The charge timing depends on the charging level used. The charging level depends on the voltage in the batteries and charger. The SAE International defines Level 1 as the slow charge rate, Level 2 in the middle charge rate and Level 3 as super charging, 480 V DC or higher as the fastest. Level 3 charging level can charge battery in just 30 minutes for an 80% charge. The charging time can be calculated by using the formula [46]:

$$\text{Charging Time}(h) = \text{Battery Capacity(kWh)}/\text{Charging Power (kW)}$$

For charging up to 8 kW, car have a battery charger into the car only. For faster charging about 22, 43 kW and more, manufacturers have applied as: (1) The built-in charger, for range from 3 to 43 kW at 230 V single phase or 400 V three- phase. (2) The charger which converts AC current into DC current and power up to 50 kW. E.g., Nissan Leaf, Tesla Model S120-135 Kw (Fig. 7 and Table 3).

Fig. 7 Renault EV charging stations



Table 3 Charging time for 100 km of Bharat electrical vehicle

Power supply	Power (Kw)	Voltage (V)	Current (A)	Charging time
AC-single phase	3	230	16	5–6 h
	7	230	32	2–3 h
AC-three phase	11	400	32	1–2 h
	22	400	63	1 h
	43–50	400	63	30 min
DC	50	400–500	100–125	30 min
	12	400–500	300–350	10 min

3.4 Types of Charging Station

Depending upon the charger is connected or not to the vehicle, the charging station have two types. The charging will be done via charger connected to connector called conductive charging. Other type is wireless type also called inductive type [60].

3.4.1 Conductive Charging System

The direct contact between electric vehicle connector and charger. Two methods used in using conductive method: AC and DC charging [61–63] (Fig. 8).

AC Conductive Charging: AC charging is by AC chargers. This is further categorized into various levels as level-1, level-2 and level-3 [64].

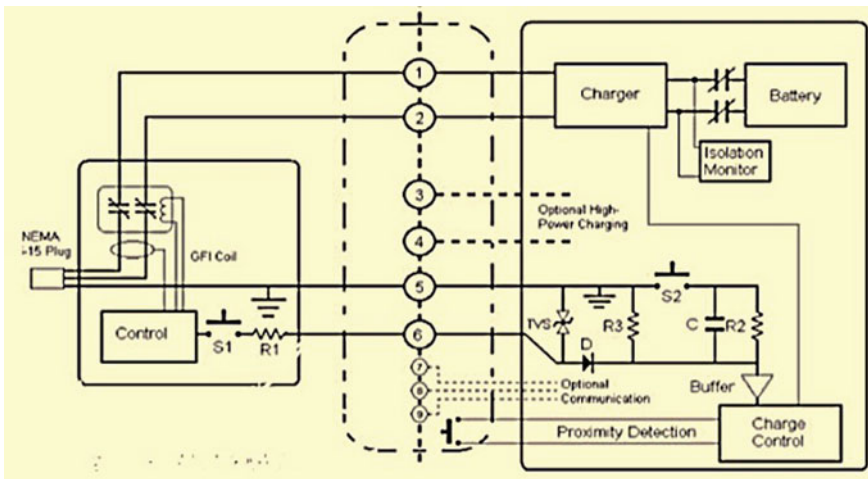


Fig. 8 AC conductive charging

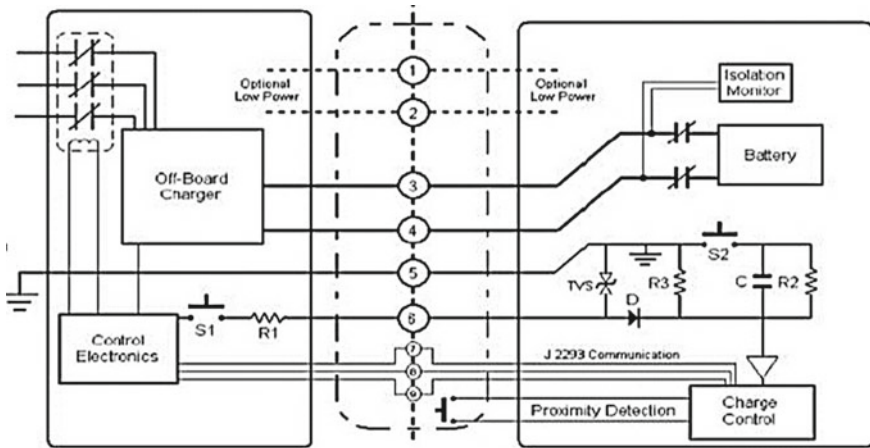


Fig. 9 DC conductive charging

DC Conductive Charging: DC charging by using DC charger. It uses DC supply equipment to provide energy from off board charger to EV in either private or public locations. It is known as fast DC charging. It is used up to 50 kW and charging time is 20 min from empty to 80% full [65]. Example: The Honda car of voltage of DC 375 V, current 300 A, 100 kW of power, and speed of 70 km/h [65] (Fig. 9).

3.4.2 Inductive Charging System

An inductive charging uses electromagnetic field principle to transfer energy. With induction coil to create an alternating electromagnetic field and energy is transmitted through inductive coupling to the device to charge batteries [66, 67].

The device such as cars or trucks use second induction coil to receive the EM field. These EM fields are revert back as current in order to charge the battery of EV. The electrical vehicle in which inductive charging is used are:

1. The General Motors EV1 electric car
2. General Motors–Chevrolet S-10 eV and Toyota RAV4 EV, AUDI [68]
3. Bombardier-Transportation PRIMOVE [69]
4. Transport in London for double-decker buses [70], Magne Charge [71], Evatran–the Plugless L2 Wireless charging system. Volvo Group’s [72, 73], BRUSA Elektronik AG module ICS with 3.7 kW power [74] (Fig. 10).

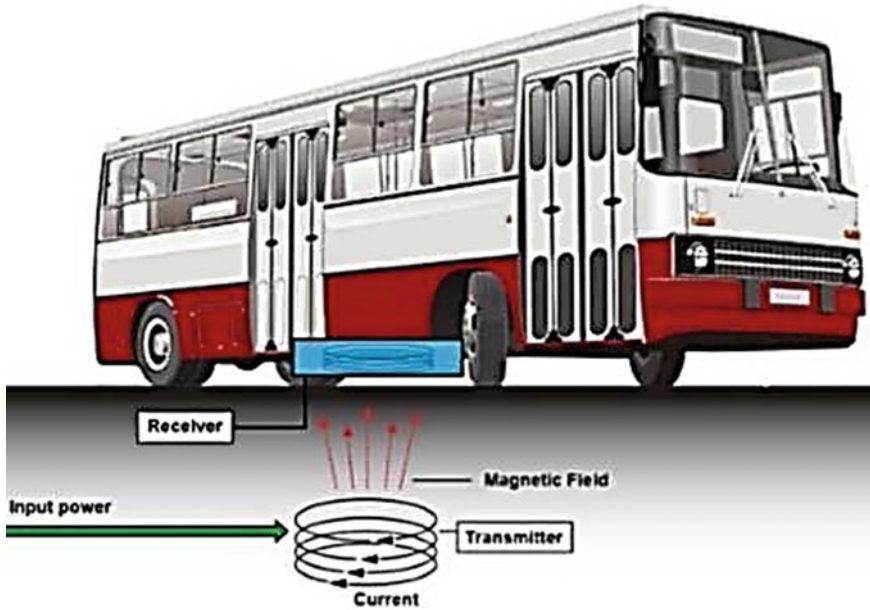


Fig. 10 Inductive charging

4 An EV Charging Connector Types

An EV is using mainly two types of charger Type 1 and Type 2. The Type 1 have single phase supply and Type 2 have both single phase and three phase supply [75]. The plug and charger varies according to different vehicle requirement. This also varies according to geographical area and model of EV.

The Combined Charging System (CCS) uses in North America and Europe, CHAdeMO uses in Japan and GB/T uses in China has the world's largest electric vehicle market [76]. The SAE have standard for connector of J1772 connector, also known as the J-plug, for Level 1 and Level 2 charging. But Tesla have different connector, it gives their own adapter cable with every car that allows their cars to use charging stations with a J1772 connector (Fig. 11).

4.1 CCS (Combined Charging System)

CCS is the combination of the J1772 connector with the high-speed charging pins. CCS is the accepted standard in North America, and developed and recommended by the Society of Automotive Engineers (SAE). The companies that are using this type of connector General Motors (all divisions), Ford, Chrysler, Dodge, Jeep, BMW,

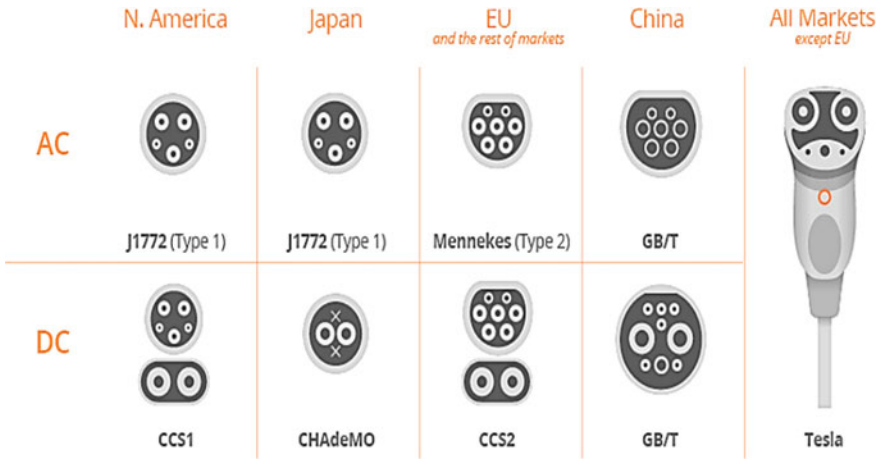


Fig. 11 EV charging connector

Mercedes, Volkswagen, Audi, Porsche, Honda, Kia, Fiat, Hyundai, Volvo, smart, MINI, Jaguar Land Rover, Bentley, Rolls Royce and others [76].

4.2 CHAdeMO

It is used in Japan as DC fast connector also for Nissan and Mitsubishi, Kia, etc. [76] (Figs. 12 and 13).

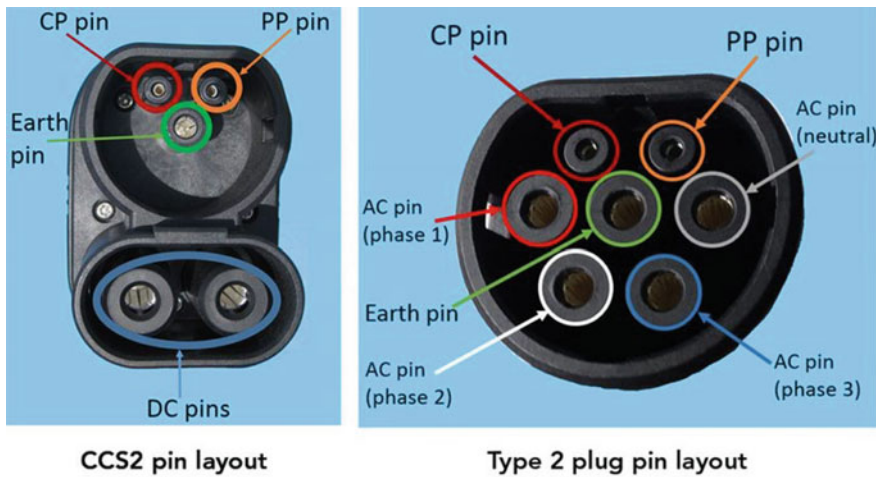


Fig. 12 CCS (combined charging system)

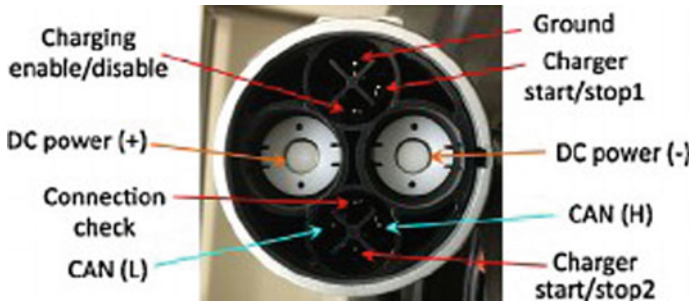


Fig. 13 CHAdEMO pin diagram

4.3 Charger and Connector in India

In India, BHARAT EV standard is mainly used for charger and connector. The Committee on standardization of protocol for Electric Vehicles Charging Infrastructure specifications for AC and DC charging. These standards are called - Bharat EV Charger AC-001 and Bharat EV Charger DC-001 [77]. The types of charging:

1. **4.3.1 Home Charging:** Bharat EV recommends using the IEC 60309 Industrial connector uses 230 V/15 A single phase plug gives maximum of up to 2.5 kW of power. The meter billing done at home meter.
2. **4.3.2 Public Charging:** The charging at outside the home area.
3. **4.3.3 AC Slow Charging:** The AC current to the vehicle's on-board charger which converts the AC power to DC to charge the battery.

Example: Mahindra e2o or e2o plus electric car. A Li-Ion based e- Scooter using a 15 Amp socket or a smart charger.

There are 2 categories of charging:

- **Normal AC charging:** An electric 2-wheelers, 3-wheelers and 4-wheeler vehicles have on-board charger with power 2.5–3 kW. The AC 2.5 kW or 3 kW fast charger, charges a 2-wheeler in an hour's time. The 4-wheeler or larger vehicles batteries of 12 KWh or more can charges in 5–6 h.
- **Fast AC charging:** The Nissan Leaf and Tesla have fast charging with a faster rate, from 7.7 to 22 kw.

@@4.3.4 DC Fast Charging: The DC Charging Specifications have power rating of fast chargers are 10, 15, 30, 50 kW or even higher capacity. The voltage rating are 48–72 V for electric cars like the Mahindra e2o Plus P8, Mahindra e-Verito and upcoming Tata electric cars. Up to 750 V or even higher rating charger used by global electric cars like Nissan Leaf and others. Fast charging mode gives the 100 or more km's of range per hour of charging.

- **Level 1 DC Chargers:** The DC Chargers at output voltage of 48–72 V, power outputs of 10–15 kW and current of up to 200 A.

- **Level 2 DC Chargers:** This DC Chargers at output voltage up to 1000 V and power outputs of 30–150 kW.

4.4 AC Plug Connectors

An Indian electric cars uses the IEC 60309 Industrial Blue connectors and Bharat EV specifications recommend using this plug. The worldwide EVs use the IEC 62196 Type 2 connector. The European Commission referred it as official charging plug in (Figs. 14, 15 and 16).

Fig. 14 IEC 60,309 Industrial Socket



Fig. 15 IEC 62,196 Type 2



Fig. 16 3 pin connector with a 15 Amp



4.5 DC Plug Connectors

There are four types of DC Fast Charging connectors which are used all over the world.

- i. CHAdeMO–Nissan, other Japanese companies like Mitsubishi.
- ii. SAE Combo Charging System (CCS)–BMW, GM, VW, and other carmakers.
- iii. Supercharger–Tesla standard connector.
- iv. GB/T-BYD among other Chinese companies, Mahindra and Tata (Figs. 17, 18 and 19).

Fig. 17 CHAdeMO



Fig. 18 CCS



Fig. 19 GB/T



5 Battery Swapping and Vehicle to Grid Concept

5.1 Battery Swapping

Battery Swapping means, the exchange station where the EV can change battery of vehicle to reduce the required time for charging the battery. By changing single battery or entire battery chassis, EV vehicle can be fully charged with battery package. Swapping is faster than charging. It can be placed in just 60 s. Customer have to pay cost for swapping of battery [78].

But swapping is concern with battery performance and battery life. The cost of a Li-ion battery amounts to 40% to the vehicle cost. But life is more years longer. The negative point of battery swapping is, battery should be fully charged. But the battery have self-discharging property because of its own chemical reaction. Another one is,



Fig. 20 Battery swapping station

if battery remain in discharge, the chemical reaction can reduced in battery. This is challenging issue for swapping model [78].

Otherwise battery swapping is best option as business model. Battery swapping station can swap 15–20 battery pack, like petrol pump. For battery swapping, location can be installed at any crowded place such as at restaurant, at an ATM, at gym, any parking area, at commercial structure [78]. Li-ion battery are safer for replacement since low heating is there (Fig. 20).

The Companies in India in battery swapping market are SUN Mobility Pvt. Ltd., Lithion Power Pvt. Ltd., Exicom Tele-Systems Ltd., Twenty Two Motors Pvt. Ltd. (22KYMCO), Panasonic India Pvt. Ltd., E-Charge Up Solutions, EVI Technologies Pvt. Ltd. (EVIT), Bharat Sanchar Nigam Ltd. (BSNL).

5.2 *Vehicle to Grid (V2G) Concept*

In V2G (Vehicle to Grid), an EV sells there electricity to the power grid when there is excess electricity [79–81]. Mainly, the electricity can obtain from non-conventional sources (renewable energy) like solar, wind, etc. [82].

The vehicle venders can earn upto \$454 per year by selling power to grid depending on daily drive up to 97 km [82]. In V2G the remaining power is sold, while there is

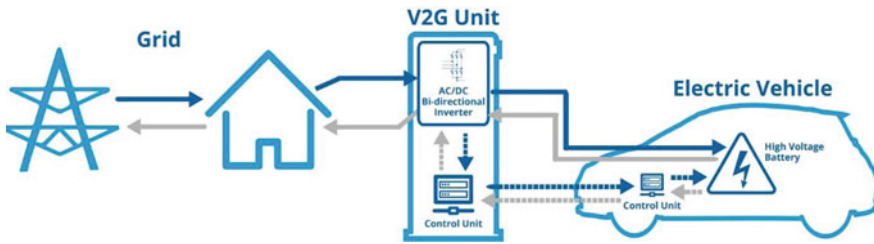


Fig. 21 Vehicle to Grid (V2G)

no loading condition and can bring power from grid when there is loading condition [83–85] (Fig. 21).

5.3 Types of V2G

Unidirectional V2G or V1G: In V1G, have variable time at which an EV is charged, while V2G have reverse power flow. In V1G, can charge in the midday to get excess of solar generation, or to vary the charge rate of EV.

Bidirectional local V2G (V2H, V2B, V2X): It makes stability within the local environment [86]. The EV holds up the residential power supply during periods of power limit.

Bidirectional V2G: In this V2G, EV provided electricity to the grid.

5.4 EV Uses V2G

Hyundai ix35 FCEV 10 kW DC V2G output [87], Nissan Leaf and Nissan e-NV200 [88–90]

5.5 Advantages of V2G

V2G have advantages like:

- Less concerns for grid overload, cheap and fast energy storage.
- Making use of existing resource as supporting electrical grid.
- Reduction of environmental impact.

6 Electrical Vehicle Motor

An EV is using electrical motor for vehicles like cars, trucks, rails. The types of electrical motors are AC and DC motor. Today's EV uses the BLDC motor, brushed DC motor, and AC induction motor. Tesla uses the Induction Motor for EV [91]. Electric Motors used in EV: There are mainly 5 types of electric motors which are used in EVs [92, 93].

6.1 DC Series Motor

Dc motor have high starting torque. Their speed control is easy and can withstand in increase in load. The disadvantages is high maintenance cost because of brushes.

6.2 Brushless DC Motor

The BLDC motors are the most preferred motors for the EV. BLDC motors does not have the commutator and brush arrangement. BLDC motors are maintenance free. BLDC motors have characteristics like high starting torque, high efficiency around 95–98%, suitable for high-power density design. The disadvantage is high cost due to permanent magnets. Mostly used in 2-Wheeler and 3-Wheeler EVs like Electric Scooters and Electric Motorcycles.

- Electric Scooters: Ather Energy Scooters, TVS Creon, Hero Electric, 22 Motors Niu Electric Scooters, Yamaha EC-03.
- Electric Motorcycles: Tork Motors, eMotion Motors, Chinese Evoke.
- In all e-Rickshaws and e-Auto Rickshaws.

BLDC motors have two types:

6.2.1 Out-Runner Type BLDC Motor

This type of motor have rotor on outside and stator inside. It is also called Hub Motor because wheel is directly connected to outer part. No external gear requires.

EV that uses this motor in Hullikal, Tronx, Spero, light speed bicycles, etc. Used by two-wheeler manufacturers like 22 Motors, NDS Eco Motors.

6.2.2 In-Runner Type BLDC Motor

In this type, the rotor of the motor is present inside and the stator is outside. The transmission system requires to transfer the power to the wheels, because of this the out-runner configuration is heavy. EV uses this motor, Three-wheeler: Goenka Electric Motors, Speego Vehicles, Kinetic Green, Volta Automotive. Low and medium performance scooter (Figs. 22 and 23).

Fig. 22 Bosch's BLDC Hub Motor



Fig. 23 BLDC In-runner type



Fig. 24 Permanent magnet synchronous motor



6.3 Permanent Magnet Synchronous Motor (PMSM)

This motor has permanent magnets on the rotor and also has traction characteristics like high-power density and high efficiency, higher power ratings. PMSM has sinusoidal back EMF. Mainly used in applications like cars, buses. PMSM has a high cost than BLDC, increased efficiency. Most of the automotive manufacturers use PMSM motors for their hybrid and electric vehicles. PMSM are used by many EV Manufacturers for their High-Performance.

- Electric Motorcycle: Energica Motors, Brammo Empulse R, Toyota Prius, Chevrolet Bolt EV, Ford Focus Electric, Zero motorcycles S/SR, Nissan Leaf, Honda Accord, BMW i3
- Electric Cars: Chevy Bolt EV, Nissan Leaf EV, Hypercar Pininfarina Battista.
- Electric Buses: TATA Ultra Urban 6/9 and 6/12 (Fig. 24).

6.4 Three Phase AC Induction Motors

The starting characteristic of this motor is useful in EV. An induction motor does not have a high starting, this characteristic can be used by various control techniques like v/f methods. By using control methods, the maximum torque and current at the starting of the motor is gained suitable for traction application. Induction motors operate up to an efficiency of 92–95%.

The limitation is that its complex inverter circuit and control of the motor.

AC Induction Motor is used by some EV Manufacturers in 2-wheeler and 4-wheeler.

- For 2-Wheeler: Emflux Motors-Emflux One.

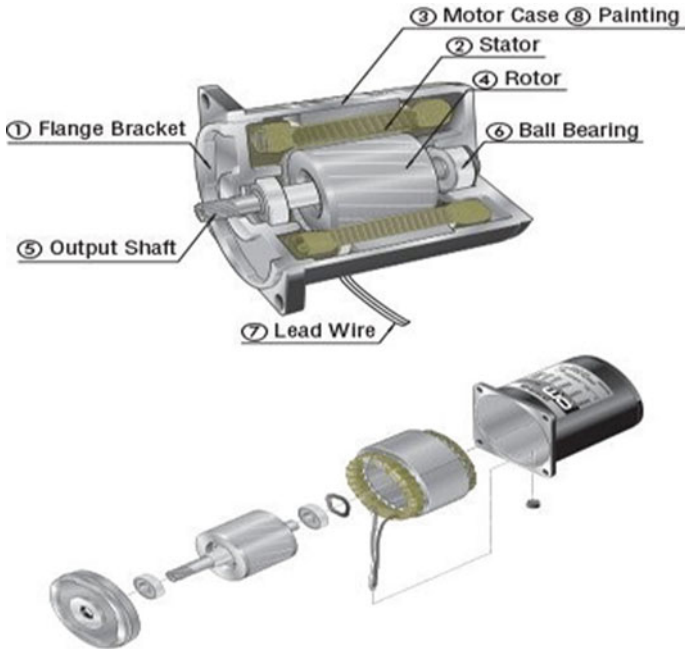


Fig. 25 Induction motor

- For 4-Wheeler: Tesla Roadster, Tesla Model S, Tesla Model X, Tesla Model 3, Mahindra e Verito, Mahindra e2o, Mahindra e-Supro, TATA Tigor, TATA Tiago (Fig. 25).

6.5 Switched Reluctance Motors (SRM)

SRM have variable reluctance, simple in construction and robust for the high-speed application and made up of laminated steel with no windings or permanent magnets on it. SRM have high power density. The heat generated in the stator, it is easier to cool the motor. The drawback of the SRM is the difficult control and increase in the switching circuit, has some noise issues.

This motor used by EV as Interior Permanent Magnet Motor (IPMM) are being used by 2-Wheeler EV Motorcycle. Zero Motorcycles (Model S/SR, DS/DSR, FX, FXS, 'SR/F'), Lightning Motorcycles (Model LS218). Permanent Magnet Switched Reluctance Motor (PMSRM) is used in Tesla Model 3 (Fig. 26).

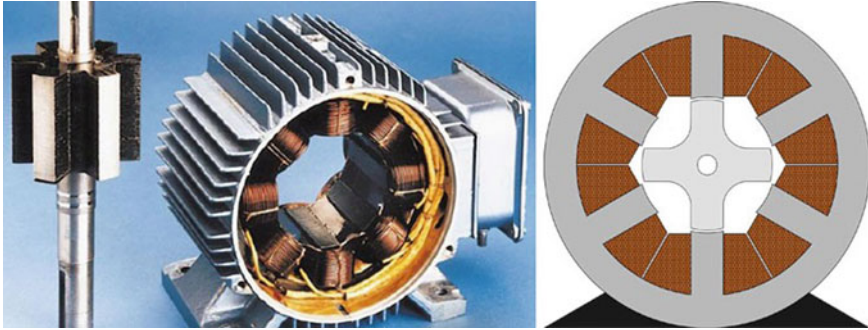


Fig. 26 Switched Reluctance Motor

7 Advantages, Disadvantages, Future of EV

EV have wide scope in now days, since there is shortage of Petroleum fuels. But EV have advantages, disadvantages also.

7.1 Advantages

- i. EV is clean source of energy since there is no emission of carbon dioxide.
- ii. Compared to the vehicle which uses Conventional fuel, EV have same energy or it can be more efficient then IC engine vehicle.
- iii. The Regenerative breaking in EV can save energy up to 30–50%.
- iv. Electrical vehicle uses electricity produced from non-polluting renewable energy sources.
- v. In EV, electric motors delivers high torque at low speeds, hence performance of EV is improved.

7.2 Disadvantages

- i. EV has to find charging point whenever required.
- ii. The charging time required for EV is more.
- iii. The battery pack will decide the range of driving EV.
- iv. Eventhough research on battery is going on, the initial cost for battery is more.

7.3 Future

Nowadays, EV has increasing market. Battery prices falling 73% since 2010, so electric cars are expected to be cheap in future. The International Energy Agency cites that by 2020, up to 20 million electric vehicles will be on the road, and that is expected to go up to 70 million by 2025.

Under the Make in India program, the manufacturing of EV and their components is expected to increase. The charging infrastructure is increasing. The Government is also giving initiative to charging station. NTPC which is India's largest power generation utility, has commissioned its first EV charging station—designed in-house with a capacity to charge three EV simultaneously in Vishakhapatnam.

An Ola company have announced 'Mission Electric', have aims to put one million electric vehicles on the road by 2021. Li-ion battery have long life, better performance, safe in operation, so it is best option in EV. The charging time required is main concern about EV. So the battery swapping station will be the solution. Otherwise, EV is the best option for e-mobility.

8 Conclusion

In this paper, the review of EV component and drives, working principle, types, advantages, disadvantages of it have studied. An EV has Li-ion battery as best solution over another battery for performance. Also, AC induction motor is good for EV because of regenerative braking. For charging of EV, the charging station and battery swapping station are required, and it is a big business opportunity.

References

1. A. Faiz, C.S. Weaver, M.P. Walsh, *Air Pollution from Motor Vehicles: Standards and Technologies for Controlling Emissions* (World Bank Publications, p. 227) ISBN 978-0-8213-3444-7 (1996)
2. Obama Administration Announces Federal and Private Sector Actions to Accelerate Electric Vehicle Adoption in the United States
3. EU Policy-Makers Seek to Make Electric Transport a Priority
4. Auto & Mobility Trends in 2019, *CB Insights Research. Hyundai KONA Electric Highlights | SUV | Hyundai Motor India* (Hyundai Motors, 2019)
5. Mahindra Electric Launches eVerito. carindia.in
6. Tata Tigor EV Launched, *Prices Start from Rs 9.99 Lakh after FAME Incentive* (The Financial Express)
7. ISRO Converts a Maruti Omni Into a Solar Hybrid Electric Car, | Digit.in
8. First Revolt Electric Bike Rolls Off the Assembly Line in Manesar. Timesnownews.com
9. I. Shahjul, Pradeep, *Revolt RV 400 Crosses 2500 Bookings in 15 days: India's 1st Smart Electric Bike Launching This Month* (The Financial Express, India, 2019). 10 July 2019
10. Staff, *Revolt RV 400 AI-Enabled Electric Motorcycle India Launch on August 28* (BGR India, 2019), 7 Aug 2019


11. ETAuto.com, *Does Rahul Sharma of Micromax Have the Recipe to Crack Electric 2W Market?*—ET Auto. ETAuto.com. www.ETAuto.com
12. Tork Motors Unveils India's First Electric Bike. Economic Times
13. Emflux-Home
14. Electronic Vehicles Company Emflux Motors Raises Rs 2 Crore from Fabian Brian Crain, Samar Singhla and Others (The Financial Express)
15. TVS Motor Invests in e-Mobility Firm Ultraviolette (The Hindu Business Line)
16. Siddharth, Chauhan 2020-01-28T11:44:40Z, *Ather Energy Zooms into 10 Indian Cities with the 450X Electric Scooter* (TechRadar India)
17. D. Govind, *Ather Energy Begins Delivery of Its Electric Scooters* (Livemint)
18. India's First Electric Bus Launched in Bangalore (The Times of India)
19. S. Elizabeth, *Ashok Leyland Unveils India's First Indigenous Electric Bus*. (The Economic Times, 2016) 20 Oct 2016
20. Tata Motors Launches Electric, *Hybrid Buses Priced up to Rs 2 Crore* (The Economic Times)
21. Goldstone Infratech Buses Join HRTC Fleet. thehindu.com
22. Maharashtra Gets its First Intercity Electric Bus Services, Leads the Way for Other States
23. Electric Truck—Time to Move Things. pluginindia.com
24. Tata Ace Electric Review, Prices, Mini Truck, Van, 2015 Specs. speedmasti.com
25. Croyance Auto. croyanceauto.com
26. India's First Electric Heavy Truck is in Operation! <https://www.financialexpress.com>
27. Electric Vehicles, a Silent Uprising. The Financial Express
28. MAuto Electric Rickshaws | Electric Rickshaw. MAuto Electric
29. 48 Percent Rail Tracks Electrified. Aim to Double it in 5 years. Govt. The Indian Express
30. Gatti E-RICKSHAW | Electric Rickshaw. Gatti E-Rickshaw
31. Entice Impex Pvt Ltd. "Kerala Neem G"
32. http://eprints.iisc.ac.in/49769/1/cur_sci_107-2_255_2014.pdf
33. Rail Coaches With Rooftop Solar Photovoltaic Systems: A Feasibility Study. Researchgate.net
34. Indian Solar Powered Rail Coaches. PV Magazine India
35. This Telangana Startup's Aftermarket Kits Let You Convert Your Old Petrol Car To Electric!
36. Top 5 Hybrid/Electric Cars in India 2016. NDTV. 25 May 2017
37. T. Sakai, I. Uehara, H. Ishikawa, R&D on metal hydride materials and Ni–MH batteries in Japan. J. Alloys Compound **293–295**, 762–769 (1999)
38. P. Ruetschi, F. Meli, J. Desilvestro, Nickel-metal hydride batteries. The preferred batteries of the future? J. Power Source (1995)
39. Patent: High power nickel-metal hydride batteries and high power electrodes for use therein
40. Electric Vehicle Charging Levels, Modes and Types Explained | North America Vs. Europe Charging cables and plug types
41. T.R. Crompton, *Battery Reference Book*, 3rd ed. Newnes. p. Glossary 3, 20 Mar 2000
42. L. Pauling, *15: Oxidation-Reduction Reactions; Electrolysis* (General Chemistry, Dover Publications, Inc., New York, 1988)
43. K. Schmidt-Rohr, How batteries store and release energy: explaining basic. electrochemistry. J. Chem. Educ. **95**, 1801–1810 (2018)
44. G. Pistoia, *Batteries for Portable Devices* (Elsevier, 2005)
45. Lithium Iron Disulfide Handbook and Application Manual (PDF). energizer.com
46. Excludes the Mass of the Air Oxidizer
47. Elektroautos von BYD: FENECON startet Verkauf des e6. Sonne Wind&Wärme (in German)
48. 10 Years Guaranty for Battery. byd-auto.net
49. HowStuffWorks Lithium-ion Battery Cost and Longevity. auto.howstuffworks.com
50. P. Gifford, J. Adams, D. Corrigan, S. Venkatesan, Development of advanced nickel metal hydride batteries for electric and hybrid vehicles. J. Power Sources **80**, 157–163 (1999)
51. U. Kohler, J. Kumpers, M. Ullrich, High Performance Nickel-Metal Hydride and Lithium-ion Batteries. J. Power Sources (2002)
52. I. Uehara, T. Sakai, H. Ishikawa, The state of research and development for applications of metal hydrides in Japan. J. Alloys Compounds **253–254**, 635–641 (1997)

53. <https://insideevs.com/news/372749/charin-hpccv-over-2-mw-power>
54. D.A. Notter, K. Kouravelou, T. Karachalios, M.K. Daletou, N.T. Haberland, Life cycle assessment of PEM FC applications: electric mobility and μ -CHP. *Energy Environ. Sci.* **8**(7), 1969–1985
55. Charging at Home. Energy.gov
56. P. Stenquist, *Electric Chargers for the Home Garage* (The New York Times, 11 July 2019)
57. J. Savard, *Is it Time to Add Electric Vehicle Charging Stations to Your Retail Shopping Center?* Metro Commercial, 16 Aug 2018
58. Alternative Fuels Data Center, *Workplace Charging for Plug-In Electric Vehicles*. afdc.energy.gov
59. F. Siddiqui, *There are Now More Places to Charge Your Electric Vehicle in Maryland for Free* 14 Sept 2015
60. A Simple Guide to DC Fast Charging. Fleetcarma.com
61. Guide to Buy the Right EV Home Charging Station. US: Home Charging Stations
62. Inductive vs. Conductive Charging. St. Louis Post Dispatch, 8 August 2010
63. MWC 2013: Kirk H&J Shows New Wireless Charging System [sic] Inpofi at Showstoppers
64. N. Ken, *Wireless Charging: Inductive or Conductive?* 15 Feb 2011
65. K. Boehret, It's hard to cut the charging cord. Wall Street J. 16 February 2011
66. <https://energysquare.co/power-by-contact-charging-technology>
67. T. Tajima, H. Tanaka, T. Fukuda, Y. Nakasato, et al., *Study of High Power Dynamic Charging System*. SAE Technical Paper 2017-01-1245 (2017)
68. <https://news.stanford.edu/2017/06/14/big-advance-wireless-charging-moving-electric-cars/>
69. Wireless Charging: The State of Disunion
70. M. Treffers, History, current status and future of the wireless power consortium and the Qi interface specification. *IEEE Circuit. Syst. Mag.* **15**(2) (2015)
71. AUDI, *Fast Charging and Audi Wireless Charging*. AUDI, 17 Sept 2015. Archived from the original on 2016-04-05
72. Bombardier Mannheim, *Experts Convinced by PRIMOVE Solution for Cars*. Bombardier, 17 Sept 2015. Archived from the original on 2016-04-05
73. Sybille Maas-Müller, *SITE FACT SHEET Mannheim Germany* (PDF). Bombardier, 12 Mar 2015
74. New Hybrid Bus Charging Technology Trial Announced. Transport for London
75. P. Bacque, *Evatran to Begin Shipping Its Plugless Electric Vehicle Charging System*. Richmond.com, 6 Jan 2014
76. Volvo is Interested in Wireless Charging
77. Das Induktivladesystem ICS115 von BRUSA basiert auf einer weltweit einzigartigen FRAME®-Technologie. www.brusa.biz. Retrieved 28 May 2020
78. https://www.mobilityhouse.com/int_en/knowledge-center/charging-cable-and-plug-types
79. <https://evreporter.com/battery-swapping/>
80. <https://thebluecircle.co/2020/03/12/battery-swapping-future-of-electric-vehicle-ev-charging-in-india/>
81. <https://www.psmarketresearch.com/market-analysis/india-electric-vehicle-battery-swapping-market>
82. C.J. Cleveland, C. Morris, *Dictionary of Energy* (Elsevier, Amsterdam, 2006), p. 473. ISBN 978-0-08-044578-6
83. Pacific Gas and Electric Company Energizes Silicon Valley With Vehicle-to-Grid Technology. Pacific Gas & Electric
84. C.B. Robledo, V. Oldenbroek, F. Abbruzzese, Ad J.M. van Wijk, Integrating a hydrogen fuel cell electric vehicle with vehicle-to-grid technology, photovoltaic power and a residential building. *Appl. Energy* **215**, 615–629 (2018)
85. T. Lindeman, J. Pearson, E. Maiberg, *Electric School Buses Can Be Backup Batteries For the US Power Grid*. Motherboard, 15 May 2018
86. Y. He, P. Bhavsar, M. Chowdhury, Z. Li, Optimizing the performance of vehicle-to-grid (V2G) enabled battery electric vehicles through a smart charge scheduling model. *Int. J. Autom. Technol.* **16**(5), 827–837 (2015)

87. S.G. Liasi, M.A. Golkar, Electric vehicles connection to microgrid effects on peak demand with and without demand response, in *2017 Iranian Conference on Electrical Engineering (ICEE)*, Tehran
88. K. Uddin, M. Dubarry, G., B. Mark, The viability of vehicle-to-grid operations from a battery technology and policy perspective. *Energy Policy* **113**, 342–347 (Feb 2018)
89. P. Paulraj, *What Are V1G, V2G and V2H/V2B/V2X Smart Charging? | Integrating Electric Vehicles Into Power Grid*. E-Mobility Simplified, 10 Dec 2019
90. J. Wassink, *Hydrogen Car as Power Backup* (Delta TU Delft, 2016)
91. B. Mattucci, *Nissan and Enel Present an Agreement for Two-Years of Electric Mobility Services Included in the Price of a New Nissan LEAF* (Enel, Italy, 2017)
92. <https://circuitdigest.com/article/different-types-of-motors-used-in-electric-vehicles-ev>
93. <https://electricvehicles.in/types-of-motors-used-in-evs-and-why-bldc-motors-are-widely-used>
94. Types of Hybrid Cars. CarSangrah
95. A. Taniguchi, N. Fujioka, M. Ikoma, A. Ohta, Development of nickel/metal-hydrate batteries for EVs and HEVs. *J. Power Sources* **100**, 117–124 (2001)
96. US: Home Charging Stations, Guide to buy the right EV home charging station, *Sustainable Transportation Based on EV Concepts: A Brief Overview* ed. by U. Eberle, R. von Helmolt, Energy & Environmental Science, 14 May 2010. Retrieved 1 Sept 2018
97. <https://evcharging.enelx.com/eu/about/news/blog/552-ev-charging-connector-types>
98. <https://www.pluginindia.com/blogs/bharat-ev-specifications-for-ac-and-dc-charging-everything-you-need-to-know>

Contribution Generation of Electricity from Treadmill Using Piezoelectric Transducers



L. Divakar , Dheeraj Mohan, Dimpa Moni Kalita, and P. V. Abhishek

Abstract The electricity has been an essential lifeline for the sustenance and well-being of human beings. The modern lifestyle of humans has a greater dependency on electronic devices and gadgets. Thus, there is a greater demand for electrical power for various operations. Also, due to the population growth around the globe, energy demand is increasing exponentially. In compensating the increasing energy demand, there is a huge burden on non-renewable sources of energy like coal leading to environmental pollution. Recent advances have allowed practical applications of various power harvesting systems to meet energy demand. One of the most important strategies to reduce the environmental impact is to use clean and renewable energy instead of fossil fuels. Energy from solar power, wind, hydroelectric, geothermal, marine energy and piezoelectricity are few examples. The power output from the piezos not only depends upon the weight but also the impact made by the individual also matters.

Keywords Piezoelectric transducers · Bridge rectifier · Capacitors · Treadmill · Series–parallel connection

1 Introduction

We know that exercises play an important role in maintaining the well-being of humans. Hitting the gym has become so much of a trend these days because it not only helps in reducing the excess calories but also annihilates the metabolic activities of the human body. A large amount of human energy gets wasted when doing exercise. At the same time, the lights in gyms and fitness centers run all day long and consume a lot of power, thus becoming one of the major power consumers of late. This, in

L. Divakar (✉) · D. Mohan · P. V. Abhishek
Ramaiah University of Applied Sciences, Bangalore, Karnataka 560058, India

D. M. Kalita
The Assam Royal Global University, Assam, India

turn, increases the electricity bill and consequently reduces the profit of the owner. Maintaining the Integrity of the Specifications.

Electricity generation from human footsteps using a piezoelectric transducer has been popular in the last few years. This technology works on the principle of the piezoelectric effect, where pressure and strain applied on certain materials generate an electric charge in response. Quartz, Berlinite, sucrose, Rochelle salt and topaz are a few examples of piezoelectric materials. Piezoelectric transducers find their application in floorings of railway stations, airports, dance clubs, sidewalks, gyms workspaces, etc. One of the main civil engineering applications of these transducers is in the highways where the vibrations produced by the vehicular movement can be converted into electrical energy and used for lighting the streets.

The advent of new technology and gadgets has increased the energy need. This has led to the exhaustion of a lot of energy resources. Currently, there is an urge to utilize alternative forms of energy especially at the passenger terminals like bus stops, railways and airports for the lightings to cut down the power consumption costs. The other major power-consuming industry is the IT sector where the light runs all day, thereby increasing the electricity consumption. Other major power consumers are hotels, restaurants, pubs and discos. On comparing the estimated electricity consumption in India during 2007–2008 to 2016–2017, an appreciable increase is observed from 5,01,977 to 10,66,268 GWh. It can be observed that electricity consumption is high in the industry sector followed by domestic, agriculture and commercial sectors [1]. Majority of electricity is consumed by industry, domestic and agriculture, then rest for the traction, commercial uses and miscellaneous. So, it is crucial to look for alternative energy harvesting methods.

2 Literature Review

Sodano et al. continued their work and considered another piezoelectric device bimorph quick pack (QP) actuator in addition to PZT and MFC to compare their effectiveness. Power efficiency, charging time and maximum charging capacity of each device when subjected to realistic ambient vibration source were compared. PZT was found more efficient for power harvesting than MFC or QP as current output was high. However, QP and PZT were capable of recharging the batteries.

Lefeuvre et al. [2] proposed a new approach to convert mechanical energy to electrical energy by embedding piezoelectric materials in vibrating structures. Based on nonlinear voltage processing three novels high performance techniques were derived—The first one was “SSDS” technique (Synchronous Switch Damping on Short) that helps in removing the electrostatic charges from the capacitor when it was charged maximum; the second one was “Parallel SSHI” (Synchronized Switch Harvesting on Inductor) that inverts the electric charge polarity from the blocking capacitor. The third one was called “Series SSHI” which is similar to parallel SSHI; the only difference is the voltage processing device that was connected in series with the piezoelectric material and the input from rectifier along with the switch in series.

Mehedi et al. [3] focused on the generation of electricity from a treadmill using piezoelectric transducers during the activity of walking or running on the track of the treadmill. The output from the transducers was stored in a battery and was used to charge small power-consuming devices. The system consisted of a wooden board with ten piezoelectric transducers (five on each row) with cork pieces housed in the treadmill.

3 Literature Review

The study focused on mounting piezoelectric transducers on the treadmill track for the generation of electricity during human activity. Experiments were conducted for choosing the right number and connection for the piezoelectric transducers. Various bridge rectifier circuits were compared, and the one with minimum losses was selected. Also, the charging and discharging rates of capacitors of different capacitances were compared, and the most optimum one was selected (Figs. 1, 2 and 3).

Certain materials tend to generate a voltage when mechanical stress or force is applied on them, or conversely, when the voltage supplied to them, a change in their dimensions is observed. Such materials are known as piezoelectric transducers, and the mechanism is known as piezoelectric effect.

Figure 4 shows a simple graphical representation of the electrical circuit. In the circuit board, input voltage in the form of AC from the piezoelectric transducer was converted to DC voltage by passing it through a bridge rectifier (made with four OA79 diodes). The positive and the negative terminals of the input AC voltage were directly connected to the positive and the negative side of the bridge rectifier in the circuit board. From the bridge rectifier, one line was grounded, and the other line was connected to an SPDT switch. SPDT switch was used to connect two different paths of voltage flow. One terminal of the switch was directly connected to the LED across a 100 Ω resistor for direct discharge. The other terminal of the switch was

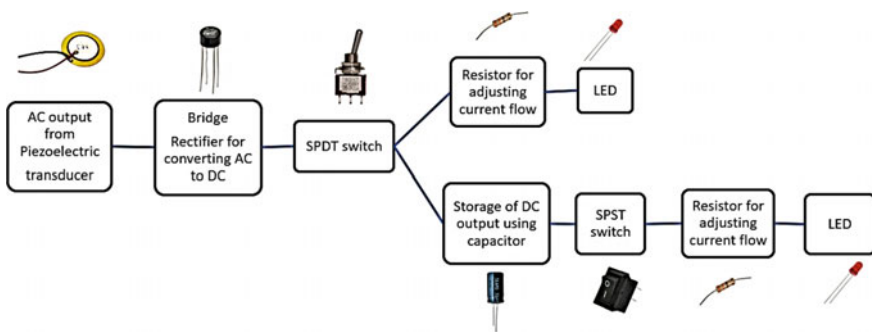


Fig. 1 Block diagram

Fig. 2 Piezoelectric transducer

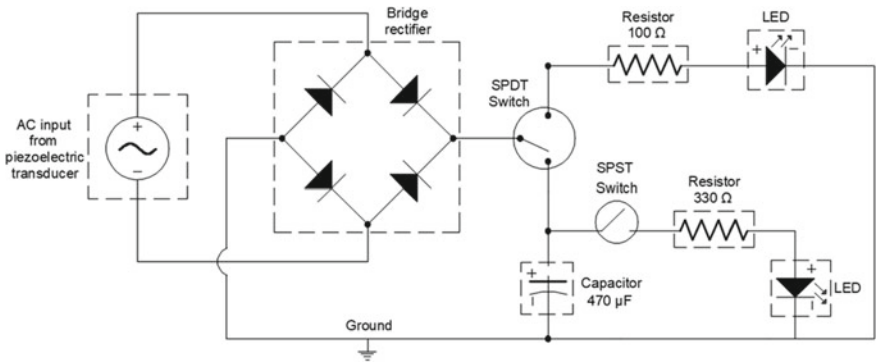
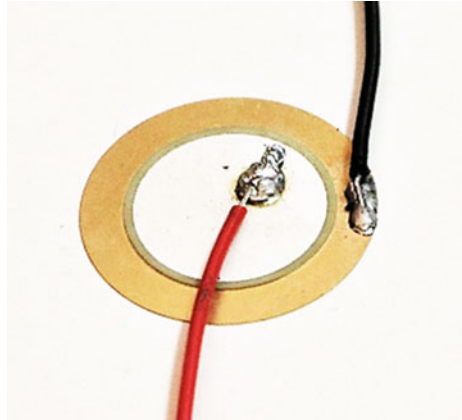


Fig. 3 Circuit diagram

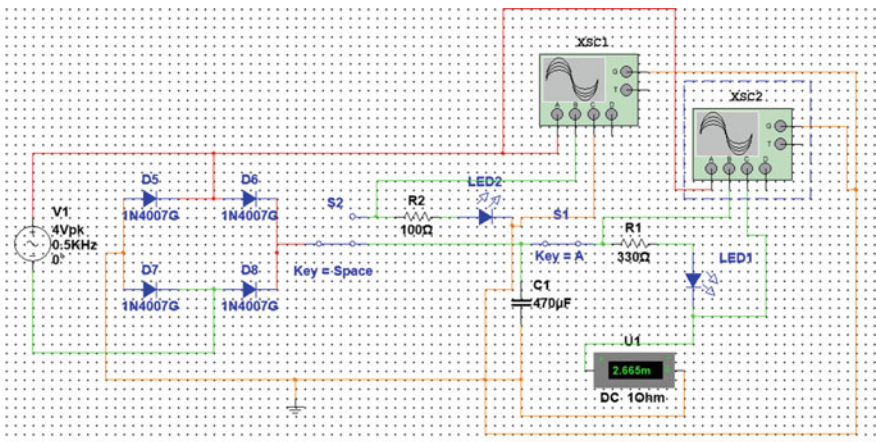


Fig. 4 Graphical representation of the electrical circuit

connected to a capacitor for smoothing the DC output and storing the charge which was further connected to an SPST switch. SPST switch was connected to regulate the flow of voltage to the LED across a $330\ \Omega$ resistor when required.

The working of the circuit was analyzed using “NI Multisim 14.1” software. The AC and DC waveforms were analyzed, and the corresponding voltages and current through the circuit were observed. The input AC voltages were varied from 4 to 12 V, and the resultant DC voltage and current were observed. From Fig. 4, it can be seen that at 4 V AC input, LED2 blinks due to the discontinuous flow of current through the circuit.

Figure 5 shows waveform of AC input (orange) and DC output (green). The readings from channel A correspond to AC input, and channel B corresponds to DC output. It can be observed that the DC output is unsteady and requires smoothing. Hence, a capacitor of $470\ \mu\text{F}$ was used.

Various individuals of different weights were asked to walk over the treadmill track, and the maximum output voltage was recorded in both the cases, i.e., parallel and series–parallel connections. From Fig. 6, it can be observed that the output voltage is maximum for the same individual in the case of series–parallel connection. Hence, the series–parallel connection of piezoelectric transducers was chosen.

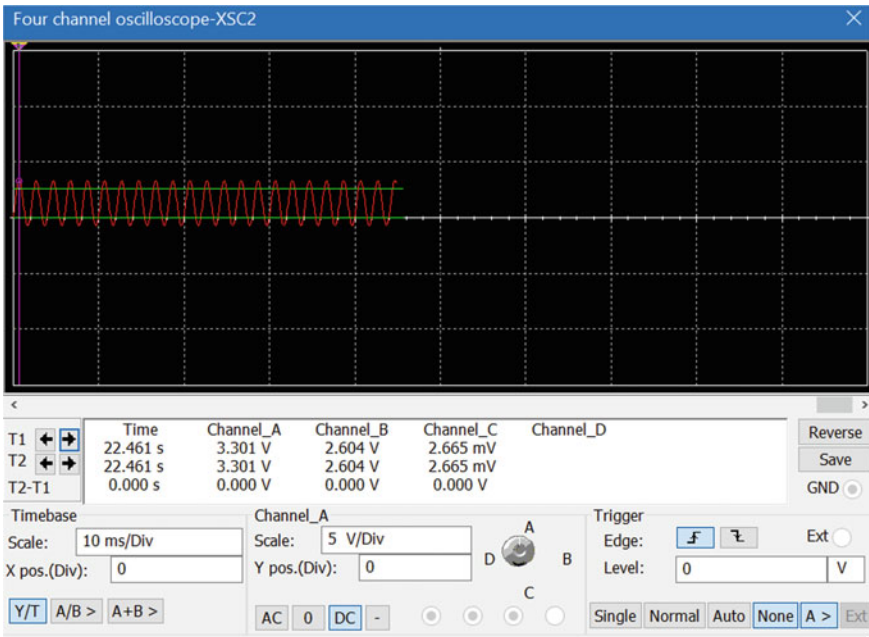


Fig. 5 Waveform of AC input (orange) and DC output (green)

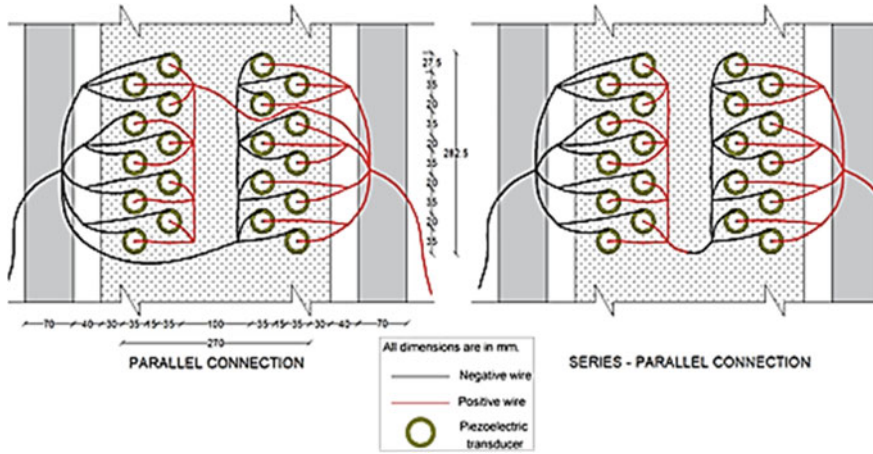


Fig. 6 Connection of the transducer

4 Results

The capacitor was charged during the activity of walking or running, and the respective DC voltage and current were recorded. $V \propto I \propto P$ (Table 1).

We know that voltage \propto current \propto power. It is verified with the output from the experimental setup. Figures 7 and 8 show the graph of variation of current with output voltage and variation of power with the current, respectively.

The average charging rate of the capacitor is 0.08 v/s during walking. In one minute, the capacitor can be charged up to $0.08 \times 60 = 4.8$ v say 4 v considering the delay in stepping on the treadmill.

From Table 2, power corresponding to 4 v is 7.12 mw. Minimum energy generated in one hour is

$$E = (7.12 \times 60)/1000 = 0.48 \text{ Wh} = (0.48 \times 1000)/4 = 120 \text{ m Ah}$$

In most of the fitness centers, the treadmill will run for about 6 h in a day.

Table 1 Charging and discharging rates of capacitors

Capacitance (μF)	Charging rate during (V/s)		Discharging rate (V/s)
	Walking	Running	
47	0.25	0.55	0.08
100	0.15	0.25	0.06
470	0.08	0.10	0.01
1000	0.065	0.08	0.005
2200	0.03	0.05	0.00125

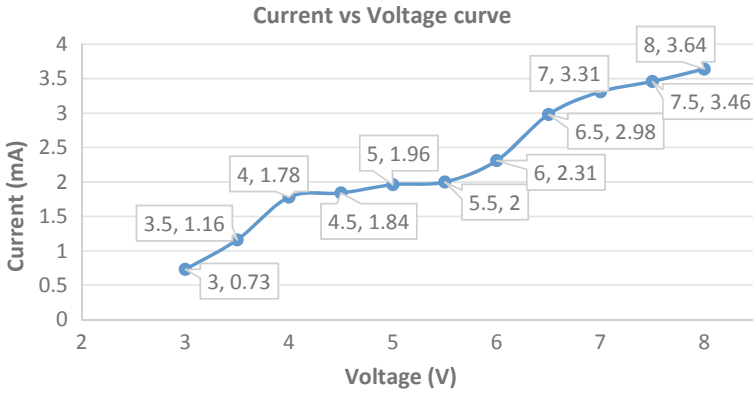


Fig. 7 Variation of current with output voltage

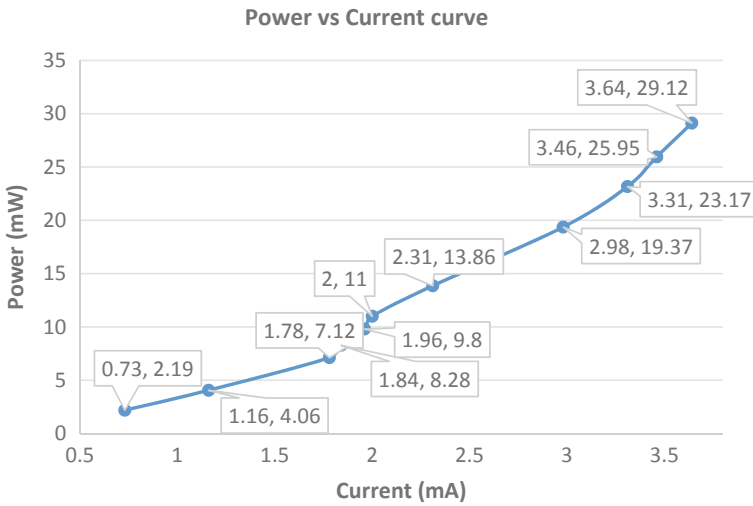


Fig. 8 Variation of power with the current

Hence, total energy generated in 6 h is

$$E = 0.48 \times 6 = 2.88 \text{ Wh} = (2.88 \times 100)/4 = 720 \text{ m Ah}$$

Table 2 Power output

Observation no.	Voltage (V)	Current (mA)	Power (mW)
1	3	0.73	2.19
2	3.5	1.16	4.06
3	4	1.78	7.12
4	4.5	1.84	8.28
5	5	1.96	9.8
6	5.5	2	11
7	6	2.31	13.86
8	6.5	2.98	19.37
9	7	3.31	23.17
10	7.5	3.46	25.95
11	8	3.64	29.12

5 Conclusion

1. Piezoelectric transducers have low power output.
2. Series–parallel connection of the transducers has higher power output than series or parallel connections alone.
3. W04 rectifier has performed better compared to bridge rectifier made from silicon, germanium diodes and three-stage voltage multiplier by 2.5, 12.8 and 23%, respectively.
4. The power output from the piezos not only depends upon the weight but also the impact made by the individual also matters.
5. This concept can be applied to a motorized treadmill.
6. Studies can be conducted on the ability to charge a battery from the stored energy in the capacitor.
7. Piezoelectric transducers can be introduced in other gym equipments like leg press, cross trainer and bench press.
8. This concept can be used in public areas like railway stations, shopping malls, roadways, walkways, etc.
9. Piezoelectric transducers can be used in road stud reflectors.

References

1. Central Statistics Office ENERGY STATISTICS (Ministry of Statistics and Programme Implementation, Government of India, New Delhi, 2018)
2. E. Lefeuvre, A. Badel, A. Benayad, L. Lebrun, C. Richard, D. Guyomar, A comparison between several approaches of piezoelectric energy harvesting. *J. Phys. IV* **12**(8), 177–186 (2005)
3. A.B. Mehedi, A. Masuma, U.A. Husna, Electricity generation from Treadmill using piezoelectric transducer. *International Conference on Mechanical, Industrial and Materials Engineering, 2017 (ICMIME2017)*, RUET (2017)

Influence of Pyrolysis Technologies on Biofuel Production and Its Physicochemical Properties: A Review



Ashish Pawar and N. L. Panwar

Abstract Agricultural biomass mostly comes from crop residues, and it can be converted into a clean and green liquid fuel, i.e. bio-oil, through thermo-chemical conversion routes. Bio-oil is a promising renewable alternative of crude oil and booming interest in recent years as increases the cost of fuel. It is a basically destructive distillation process where biomass is heated at an elevated temperature in inert atmospheric conditions. The heating rate and residence time of vapour during the process play a major role in bio-oil yield and process identification. This paper is described focusing on different pyrolysis processes for bio-oil production. Flash pyrolysis process reveals maximum bio-oil yield (75–80 wt%) with very low residence time (<0.5 s). In most of the pyrolysis processes, fine biomass particle's size was recommended for better yield. Furthermore, the paper covers different types of pyrolysis reactors that are extensively used for bio-oil from biomass / crop residues, which include rotating cone, fluidized bed, vacuum pyrolyzer, fixed bed and auger reactors. This overview is providing a general summary of different pyrolysis technologies, physicochemical properties of bio-oil and their applications in commercial sector.

Keywords Pyrolysis · Bio-oil · Biomass · Diesel engine · Auger reactor

Abbreviations

BTG Biomass Technology Group

GC-MS Gas Chromatography–Mass Spectrometry

A. Pawar (✉) · N. L. Panwar

Department of Renewable Energy Engineering, College of Technology and Engineering, Maharana Pratap University of Agriculture and Technology, Udaipur, Rajasthan 313001, India

1 Introduction

Today, energy distribution and environmental issues have developed into international threats. Demand for alternative fuels increases every day due to rapid population growth, rising living standards and economic sustainability. With its massive population, India has become the fourth largest energy-consuming country in the world after the USA, China and Russia [1]. Because most nations use fossil fuels to fulfil their energy demands, they create negative impacts on the environment, including rising global temperatures, pollution, acid rain and other effects. As such, the quest for alternative fuels derived from renewable resources has captured significant attention throughout the world [2]. In the present context, thermal power plants represent 70% of the total installed capacity in India [3]. Over dependency on these plants requires massive fossil-fuel inputs, which adversely affect the environment as well as human beings. The major question is: How to meet the power demands of the upcoming generation while minimizing fossil-fuel consumption, creating renewable alternative fuels and preserving sustained economic development? The use of organic waste material, known simply as “biomass”, represents a potential source of clean, renewable energy, abundant, easily available and low in CO₂, it has stoked interest throughout the world [4]. According to Renewable Global Status Report 2017 [5], bioenergy has grown to become the largest renewable energy source and currently represents almost 13% of total global energy demand. Globally, the utilization of biofuels such as bio-oil, bio-ethanol and biodiesel has been reached up to 0.55×10^{20} J/yr in 2012, which accounts for the worlds 80% share in renewable energy generation. It is forecast that by 2050, the biomass-derived biofuels such as bio-oil, biodiesel and bio-ethanol would be presiding fuels in heavy vehicle and public transportation system.

Converting biomass to green fuel production can mitigate carbon dioxide in the atmosphere and combat global greenhouse effects because the carbon dioxide that is liberated during biomass combustion can be captured by growing trees, plants and so on through photosynthesis. Due to this property, biomass represents a promising alternative to fossil fuels for power generation, heat production, fuel transportation and the preparation of chemicals and other bio-materials [6]. There are different biomass conversion routes are available such as combustion, pyrolysis, liquefaction and gasification for the preparation of energy-rich fuels. Although the biomass combustion process is a very traditional and simple process for generating heat and power, it is not eco-friendly due to its emissions, lower conversion efficiency and problem in ash handling [7]. Another process of biomass conversion is gasification, which is known to the industrial sector for the generation of combustible gas (i.e. producer gas) from biomass, although it requires a high capital investment. Another main drawback is the produced gas has to be quick to be used because it becomes economically inevitable or costly for storage and transportation [8]. As compared to the above-discussed processes, the pyrolysis process has been received a remarkable identity as a potential method for the conversion of any organic biomass into valuable energy-rich products due to its simplicity in operation and also required a reasonable

cost for conversion process [3]. Pyrolysis is the thermal decomposition of biomass at a temperature range from 400 to 700 °C in the absence of air producing, namely three end products, liquid (bio-oil or pyrolytic oil), solid (biochar) and syngases. Bio-oil or pyrolytic oil is composed of organic substances like phenol, amines, ketones, ethers, esters, furans, aromatic hydrocarbons, alcohols and water [9, 10]. Due to these salient properties bio-oil possess, many applications in the commercial sector, for example, in the boiler for electricity and heat generation, gas turbine or in diesel engine for power generation, it may be used as a binding material to make briquettes, pellets, etc., and as a transportation fuel in a diesel engine. Despite advantages that include being eco-friendly, having a low-cost requirement mostly the cost required to produce a litre of bio-oil is about 0.50–0.70 US\$/l, and having high conversion efficiency, bio-oil is facing some technical challenges and limitations for use in the commercial sector due to its high-water content (15–30%) and high composition of oxygenated compounds (35–60%). Therefore, to overcome these problems, bio-oil can be produced using efficient and effective pyrolysis technologies, which are discussed in the current review paper. The current technical status of biomass in India, different pyrolysis technologies, properties of bio-oil and various applications of pyrolytic oil have been thoroughly discussed in the present review paper. In addition, the present overview may show the appropriate path to research communities, which are meticulously working on waste management, especially biomass handling, bio-oil production and its extensive applications in various sectors.

2 Current Technical Status of Biomass in India

In India, people are consuming nearly 32% primary energy obtained from biomass and almost 70% of people in the country are depending upon the energy derived from biomass. In developing countries like India, biomass has a huge potential and considered as inexpensive, carbon neutral and abundant source of energy. Mainly available biomass material from agriculture waste includes rice husk, bagasse, straw, soya husk, groundnut shell, sawdust, coffee waste, etc. However, according to the Ministry of New and Renewable Energy (MNRE) [11], the current potential production of biomass in India is about 500 million metric tonnes per annum; among this, only small fraction of biomass has been further utilized as an animal feedstuff, in small-scale industrial application, and most commonly used as domestic cooking fuel. Among the total available biomass, most of the biomass is remained unutilized known as surplus biomass nearly \approx 120–150 MT, and however, it creates a disposal-related problem. This surplus biomass quantity is nearly equal to 25 Exajoule (EJ) of the total energy potential, which is about 10% of India's total primary energy requirement. Otherwise, as a result, a very common solution preferred by some peasants is the burning of surplus residue in an open field which significantly creates health issues throughout the living organisms. As per the information from Intergovernmental Panel on Climate Change (IPCC), almost 25% surplus residue from crop residue is put through for field burning all around the world, which subjected to about

36 EJ of energy is being wasted annually [12]. According to MNRE, the agriculture or forest surplus residue has the potential to generate power about 18,000 MW. Therefore, there is an urgent need to manage biomass by converting it into value-added products.

3 Classification of Pyrolysis Process

Pyrolysis process is significantly influenced by various operating conditions such as type of feedstock, pyrolysis temperature, heating rate and residence time. Organic waste material such as agro-waste, forest waste and woody biomass is considered as promising raw material for the pyrolysis process. The biomass classification takes place according to the availability of organic waste, energy crops, natural vegetables and crops by-products. Biomass pyrolysis is carried out in two ways: one is at under atmospheric pressure and second in vacuum pyrolysis condition at low pressure [13]. Panwar [14] has classified the biomass feedstock according to the source of availability such as energy crops, organic waste, crop by-products and natural vegetables as shown in Fig. 1. The pyrolysis processes have been classified as slow, intermediate, fast and flash pyrolysis.

3.1 Slow Pyrolysis

The slow pyrolysis of biomass conveys several advantages because it produces a primary end product, biochar, which is an organic carbon-rich product that can act as a carbon sequester and improve the soil quality. Slow pyrolysis is performed at

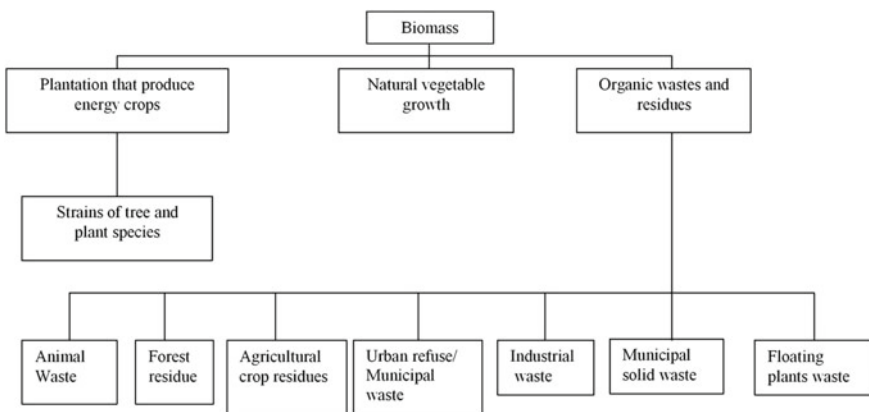


Fig. 1 Biomass classification [14]

a moderate temperature, with long residence time and a low heating rate; therefore, biochar is the primary end product of this process. The most commonly used reactors for slow pyrolysis are rotary kilns, drums and screw reactors. However, according to Marshall [15] an auger/screw reactor is considered to be more suitable for both slow and fast pyrolysis processes. Generally, biochar is the main end product of slow pyrolysis or carbonization process obtained at a temperature range between 300 and 350 °C in the absence of air and required longer residence time (5–30 min) with a lower heating rate (0.1–0.8 °C/s), respectively [16]. The yields for biochar and bio-oil are greatly influenced by the processing temperature, the feedstock properties, the pyrolysis environment (including the availability of inert media) and the residence time. Goyal et al. [2] recorded yield of pyrolysis products, among which biochar showed higher yield (35 wt%), bio-oil (30 wt%) and syngases (35 wt%), respectively. In addition, Yu et al. [17] used fixed bed reactor to perform a slow pyrolysis experiment by using hinoki cypress (*chamaecyparis obtusa*) as a feedstock at a temperature range from 350 to 600 °C and observed that as the pyrolysis temperature increased the biochar yield significantly dropped, while bio-oil yield increased from 28.8% (350 °C) to 35.5% (600 °C), respectively. Despite these advantageous results, the produced bio-oil contained a higher proportion of water. The biochar produced by slow pyrolysis (350–450 °C) fulfils the quality criteria for agricultural soil [18]. In addition, biochar produced by slow pyrolysis can act as a carbon sequester because it contains the maximum amount of organic carbon (> 50%), O/C molar ratio (< 0.4) and H/C molar ratio (< 0.7). The authors also observed that the biochar produced from hinoki cypress at 350 °C temperature showed the highest energy yield (52.7%), on the other side energy yield of bio-oil was found 39.80% at 600 °C temperature. This happened due to maximum energy content available in biomass or enrichment of carbon with depletion of oxygen in the case of pyrolysis products. The higher surface area of biochar indicated that produced biochar had a good adsorption capacity due to its micro-porous structure as well as the availability of large pores [19].

3.2 Intermediate Pyrolysis

Presently, intermediate pyrolysis has gained significant attention due to its satisfactory raw bio-oil production (50% from woody biomass) at a pyrolysis temperature 500 °C with the minimum residence time of 10–30 s [20]. However, this kind of pyrolysis allows making use of larger particle size of feedstock (including chips and pellets) while in case of fast pyrolysis required finely ground raw material [21]. Therefore, this process is considered as most robust and reliable because of its suitability in small- and medium-scale industries. Funke et al. [22] compared the yield of bio-oil obtained from intermediate and fast pyrolysis of a biomass feedstock by keeping pyrolysis temperature 500 °C. The fast pyrolysis experiment showed higher bio-oil yield (26–51%) as compared to intermediate pyrolysis (17–21%), the lower bio-oil yield might be occurred due to the formation of secondary products includes

char, water vapours and pyrolysis syngases. Mohammed et al. [23] studied the effect of operating conditions such as pyrolysis temperature, gas flow rate, residence time and heating rate on the bio-oil produced from intermediate pyrolysis by using Napier grass as a feedstock. The optimum bio-oil yield was recorded about 50.57 wt% at a pyrolysis temperature of 600 °C, by keeping heating rate 50 °C/min and 5 l/min of nitrogen flow rate. The produced organic phase liquid oil is composed of some benzene derivatives such as methoxyphenols, phenols, methoxy-benzene, ethylphenols, methylphenol. In addition, the produced bio-oil contains about 60% of the total organic phase. Therefore, the produced bio-oil exhibits strong agreement of organic constituents [24].

3.3 *Fast Pyrolysis*

Fast pyrolysis is considered as the cheapest biomass conversion route for biofuel production [25]. In the fast pyrolysis process, thermal decomposition of biomass takes place in the absence of oxygen at a temperature range from 450 to 600 °C in a short residence time (< 2 s). The major resulting end product in fast pyrolysis is an initial dark brown-coloured viscous liquid known as bio-oil or pyrolytic oil followed by biochar and syngases. The fast pyrolysis of biomass recorded higher conversion efficiency and a maximum yield of about 75% on dry basis [6]. In addition, the authors also observed that secondary products such as char and gas can provide necessary heat or power after combustion to complete the pyrolysis reaction. Therefore, as compared to other biofuel production processes, bio-oil produced through a fast pyrolysis process is considered a cost-effective thermochemical conversion route. The profitability of the fast pyrolysis process depends on parameters such as product yield, quality of the product, feedstock cost and production scales [26]. The fast pyrolysis reactors such as a bubbling fluidized bed, rotating cone, screw/auger, ablative and vacuum pyrolysis are considered suitable technologies for bio-oil production, although the configuration of the fluidized bed and rotating cone reactors is viewed as the most cost-effective and commercialized technologies of the group [27]. In a fast pyrolysis process, the syngas yield has a bad effect on biochar and the bio-oil yield because as syngas yield increases, the yield of biochar and bio-oil drops suddenly [28]. The bio-oil produced from woody biomass shows a higher yield than agricultural by-products, forest residue and energy crops because clean woody biomass contains a high percentage of cellulose and hemicellulose, which is more favourable for bio-oil production [29, 30]. The selection of feedstock particle size in a fast pyrolysis process can adversely affect bio-oil, char and syngas yield because as the used particle size is more, the heat transfer rate slightly decreases so it causes raising the biochar yield, while the drop in both bio-oil and syngas yield [31]. Therefore, for getting the maximum yield of bio-oil small particle size feedstock should be preferred.

Xue et al. [32] performed the fast pyrolysis of waste plastic and biomass in a fluidized bed reactor at a pyrolysis temperature from 525 to 675 °C. The maximum

bio-oil yield 57.6% was obtained at 625 °C, and here it was observed that due to co-pyrolysis resulted bio-oil possesses a higher heating value of 36.6 MJ/kg respectively. Recently, Park et al. [33] examined the different properties of bio-oil obtained from fast pyrolysis fruit waste in the fluidized bed reactor at 500 °C, resulting bio-oil showed a higher heating value (13–17 MJ/kg), viscosity (14–18 mm²/s), water content (20–29%), flash point (46–49 °C), sulphur content (0.04–0.05 wt%) and pour point (−17.5 to −22.5 °C), respectively. In particular, viscosity, heating value, ash content and the total amount of acid content in obtained bio-oil were significantly affected by the moisture content of biomass. Authors also observed that non-condensable gases are highly composed of carbon dioxide and carbon monoxide, which were almost 80%. In addition, Duanguppama et al. [34] carried out fast pyrolysis of sawdust in circulating fluidized bed reactor and recorded maximum yield of 67 wt% at 500 °C and had calorific value 30 MJ/kg, also at same pyrolysis temperature biochar yield was 18 wt% with a calorific value, 18 MJ/kg and gas yield was almost 15 wt% with a heating value 28 MJ/Nm³, respectively. The authors also noticed that as pyrolysis temperature increased, the water content and stability of bio-oil significantly reduced, while there was an improvement in the heating value and viscosity of bio-oil.

3.4 Flash Pyrolysis

In case of flash pyrolysis process, thermal heating of biomass takes place at a moderate temperature at a higher heating rate (from 10³ to 10⁴ °C/s) and carried out with a very short residence time (< 0.5 s), giving the highest bio-oil yield (75–80 wt%) [35, 36]. If maximum bio-oil production is the goal, then flash/fast pyrolysis is a more recognized process as compared to others. Generally, flash pyrolysis reaction takes place with a fraction of seconds, but it requires a higher heating rate so due to instant heating; biomass particle size should be small [37].

According to Balat et al. [38], the higher bio-oil yield (75 wt%) at a maximum pyrolysis temperature (800–1000 °C), might be due to the selection of very small particle size of feedstock material about the 200-micron metre. Owing to this, Raja et al. [39] used jatropa oil cake as a feedstock having a particle size ranged between 0.6 and 1.18 mm in a fluidized bed reactor for the production of bio-oil through the flash pyrolysis process. It was observed that the maximum bio-oil yield was obtained when the feedstock particle size was 1.0 mm. Various reactor configurations such as the fluidized bed, rotating cone, circulating fluidized bed, ablative, vacuum moving bed reactors and others are more suitable for bio-oil production through flash pyrolysis [40, 41]. Makibar et al. [42] conducted a flash pyrolysis experiment in a conical spouted bed reactor by using poplar (*Populus nigra*) as a feedstock and recorded bio-oil yield in two fractions at a temperature range between 425 and 525 °C. Authors observed that in first fraction bio-oil yield was about 85 wt% and contained a higher proportion of water, while another fraction gave a bio-oil yield (25 wt%) with lower water content. In addition, authors also noticed that produced

bio-oil with low water content had a higher heating value (HHV) in the range of 16–18 MJ/kg, respectively.

4 Case Studies

The pyrolyzers have been broadly classified as the fluidized bed, rotating cone, fixed bed, vacuum, ablative, catalytic, conical spouted bed and auger reactors. The output of pyrolysis products it may be solid, liquid and gases was significantly varied according to the type of pyrolyzer, heating rate, duration of pyrolysis, pyrolysis temperature and feedstock. As, if the aim is to acquire the maximum yield of biochar through the pyrolysis process, then pyrolyzer should be operating at moderate temperature, slow heating rate and required longer residence time. On the other hand, if the main objective is to achieve the maximum yield of bio-oil and syngas, then pyrolysis temperature, residence time and heating rate have to be chosen accordingly. Table 1 lists the selection of feedstock, heating rate, source of heat, residence time, pyrolysis temperature for estimating the yield of different pyrolysis by-products.

4.1 Rotating Cone Reactor

In the case of a rotating cone reactor, instead of using the inert gas medium, the pyrolysis process is carried out by mixing raw material and hot sand. Therefore, heat transfer takes place efficiently and resulting bio-oil have a maximum yield, although the design of rotating cone reactor is complex in nature [48].

Wagenaar et al. [49] designed rotating cone reactor for a capacity of 260 kg/h, exceeding the rated capacity by 30% and noted a bio-oil yield of about 70% on a dry basis. The performance of the reactor was carried out for 4 days continuously, which was the longest run, and 20 tonnes of bio-oil had been produced by various end-users. In the rotating cone reactor, intensive mixing of biomass and hot inert particles takes place and due to this rapid heating was possible with a very short residence time. BTG [50] has successfully commercialized a fast pyrolysis plant with a 2-tonnes/h capacity in Malaysia. The commissioned plant operates on empty fruit bunches of palm and produces about 1.2 t/h pyrolysis oil. The flow diagram of a BTG fast pyrolysis process is shown in Fig. 2.

4.2 Catalytic Pyrolysis

Biomass co-pyrolysis can be done by using the catalytic pyrolysis process, depending on the type of catalyst utilized for the pyrolysis process. The fundamental principle of a catalytic pyrolysis process is to break down the feedstock components and

Table 1 Characteristics of each pyrolyzer at different operating conditions

S. No.	Type of reactor	Feedstock	Temperature (°C)	Heating rate (°C/min)	Residence time	Source of heat	Oil yield (%)	Char yield (%)	Non-condensable gas yield (%)	References
1	Auger-type reactor	Pine needles	500	–	15 min	Electric coil	28	31.7	21.6	[43]
2	Fixed bed reactor	Rice straw	400	20	1 h	Electric coil	34.5	38	27.5	[44]
3	Ablative pyrolysis reactor	Corn cobs	500	–	7 min	LPG stove	72	25	–	[45]
4	Fluidized bed reactor	Sawdust	500	–	–	Electric coil	60	15	25	[33]
5	Vacuum pyrolysis reactor	Lignocellulosic biomass	480	20	–	Electric heat	65	–	–	[46]
6	Microwave pyrolysis reactor	Sugarcane bagasse	550	–	30 min	Microwave power (W)	14–22	61–83	2.4–16.1	[47]
7	Conical spouted bed reactor	Poplar	455	15	–	Sand	69	–	16	[42]

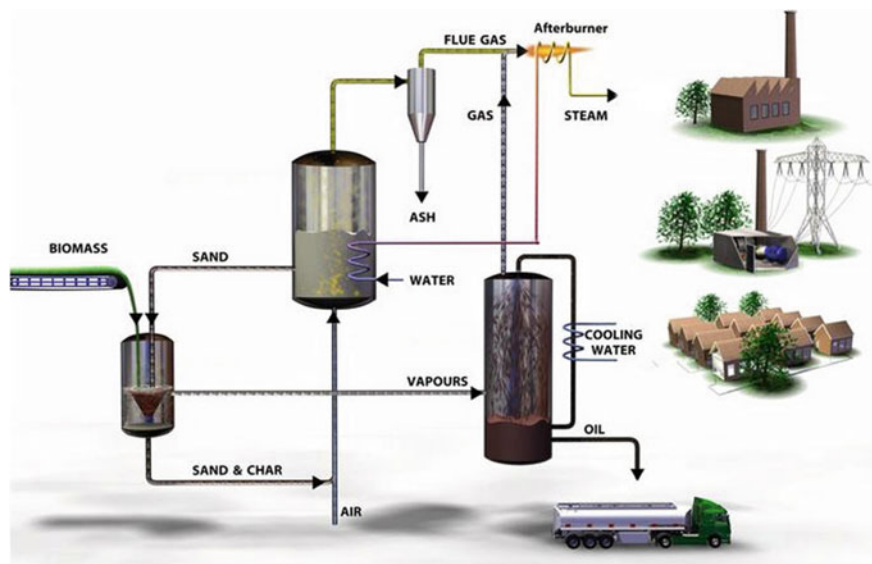


Fig. 2 Process flow diagram of BTG's rotating cone fast pyrolysis [50]

increase the bio-oil yield. The performance of a catalytic pyrolysis process varies according to the composition of feedstock and sort of catalyst [51]. Addition of catalyst during biomass pyrolysis, bio-oil yield decreases, whereas qualities of bio-oil in terms of higher heating value, oxygenated group removal and uniform hydrocarbon distribution were considerably increased [52]. Authors pyrolyzed cottonseed in a tubular fixed bed reactor as shown in Fig. 3 and recorded maximum bio-oil was about 49.30% under the sweeping gas conditions at the rate of 200 mL min^{-1} . Further, it was also concluded that as an increasing amount of catalyst, lower the oil yield, and increases the gas and char yield.

French and Czernik [53] performed catalytic pyrolysis experiments using various types of feedstocks, such as cellulose, lignin and wood, fed in a semi-continuous flow reactor with physical contact with a catalyst that belongs to the ZSM-5 group and maintained pyrolysis temperatures range from 400 to 600 °C. During the experiment, the maximum hydrocarbon yield from wood was recorded about 16 wt% including 3.5 wt% toluene, and the produced hydrocarbons could be treated as a fuel or fuel blend.

The aromaticity in bio-oil was found to be noticeably increased because of catalyst. As pyrolysis temperature increases, aromaticity was also subsequently increased meanwhile the experiment. Besides, Williams and Nugranad [54] investigated that during the catalytic pyrolysis, the oxygen content in bio-oil was manifestly reduced and polycyclic aromatic hydrocarbons were present in the produced bio-oil at very low concentration.

Catalytic hydro-processing of bio-oils from different feedstocks was investigated in a fixed bed reactor system [55]. The research was aimed to produce petroleum

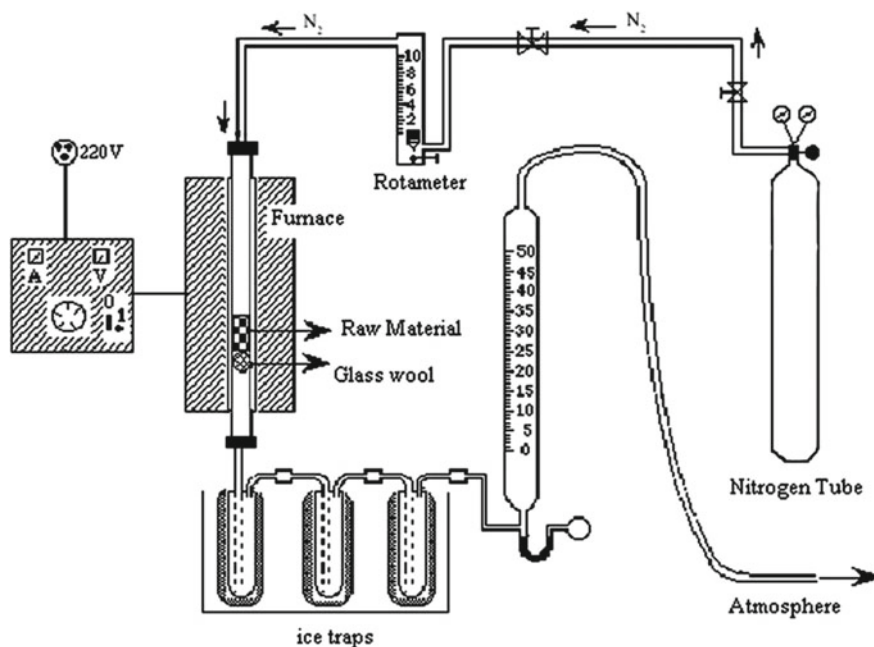


Fig. 3 Catalytic pyrolysis of biomass in tubular fixed bed reactor [52]

refinery products to supplement the fossil energy sources. During the hydrocracking (high temperature) and hydrotreating (low temperature) experiment in the fixed bed reactor, the bio-oil and hydrogen gas were fed under high pressure, and the resulting product was collected and cooled in a dual cylinder. Aho et al. [56] carried out the catalytic pyrolysis using pine wood as a feedstock in a fluidized bed reactor at a temperature of about 450 °C, and acidic zeolite catalysts were used as bed material in a fluidized bed reactor. Meanwhile, the effect of different acidic zeolite catalysts on the yield of final pyrolysis products, and maximum bio-oil yield was recorded by using H-ZSM-5-23 zeolite catalyst.

4.3 Fluidized Bed Reactors

A fluidized bed reactor is one of the best and most efficient technologies for the conversion of biomass into clean and good quality bio-oil [57]. In a fluidized bed reactor, carrier gas moves through sand bed media into the reactor and a downstream cyclone separator can easily separate the char and sand from the pyrolysis product [58].

Araza et al. [59] carried out fast pyrolysis of dry sewage sludge in a fluidized bed reactor for bio-oil production. During the experiment, it was observed that the

process temperature, the vapour residence time and the sludge particle size have a significant impact on bio-oil yield, higher heating value (HHV) and moisture content in oil. The results demonstrate that high bio-oil yield (26–35%) was obtained with an HHV ranged from 26 to 37 MJ/kg by keeping particle size between 0.2 and 1.0 mm, residence time between 1 and 2 s at a temperature between 425 and 500 °C. Here, the results indicate that the bio-oil yield and its HHV increased according to pyrolysis temperature and particle size of feedstock, while the water/moisture content was mostly influenced by pyrolysis temperature. According to several sources, the fluidized bed reactor usually works on fast/flash pyrolysis mode. However, recently Qureshi et al. [60] developed a novel helical screw-fluidized bed reactor that peacefully works on slow pyrolysis mode. The developed reactor has high conversion efficiency and recorded a maximum bio-oil yield of about 50 wt% by using palm shell as a feedstock at a temperature of 500 °C without using any inert gas. Apart from this, the developed reactor has positive salient features like operating at slow pyrolysis mode, fast vapour formation, no agglomeration of feedstock particle and producing good quality biochar. In addition, it was also observed that the resulting bio-oil possessed significant physiochemical characteristics such as high energy density, high organic phases and low water content.

Generally, the fluidization velocity and pyrolysis temperature notably affect the quality as well as quantity of bio-oil. Furthermore, the higher heating value and pH of bio-oil have been given notable attention because it could potentially be used directly for power and heat generation through boilers or gas turbines [61]. The authors produced bio-oil by using macroalga (*saccharina japonica*) as a feedstock in the fluidized bed reactor. They recorded a maximum bio-oil yield of nearly 45% having a higher heating value in the range of 24.80–28.27 MJ/kg and also a high pH value (4.68–6.08) as compared to bio-oil derived from lignocellulosic biomass by keeping pyrolysis temperature at 350 °C and fluidization velocity as 4.0 Umf.

VTT (Technical Research Centre of Finland) developed a fluidized bed reactor having a capacity of 20 kg/h. In the developed system, a screw conveyor is used to feed the feedstock to the reactor (Fig. 4). The operating temperature was varied 480–520 °C and the vapour residence time kept 0.5–2 s. During the experimental study with pine wood, 62% organic liquid, 12 wt% product water (chemically dissolved in organic liquids), 14 wt% char and 12 wt% non-condensable gases were obtained. Furthermore, the developed unit has produced 42 tonnes of liquid in 3100 h during 1996–2011 [62].

Heo et al. [63] carried out an experiment for the production of bio-oil using sawdust as a feedstock from waste furniture in a small fluidized bed reactor at different operating conditions including temperatures (400–550 °C), the flow rate of nitrogen gas (3–5 L/min) as a fluidizing agent and particle sizes (0.3–1.3 mm) of feedstock. In each test case, approximately 150 g of sawdust was fed into the bed for 75–100 min. After completing the experiment, maximum bio-oil yield about 65% was observed at pyrolysis temperature of 450 °C and by keeping the particle size of feedstock about 0.7 mm. Heo et al. [63] also concluded that a higher gas flow rate due to more feeding rate was found more suitable for maximum bio-oil yield because of its reduced vapour residence time. Jung et al. [64] produced bio-oil from rice straw and

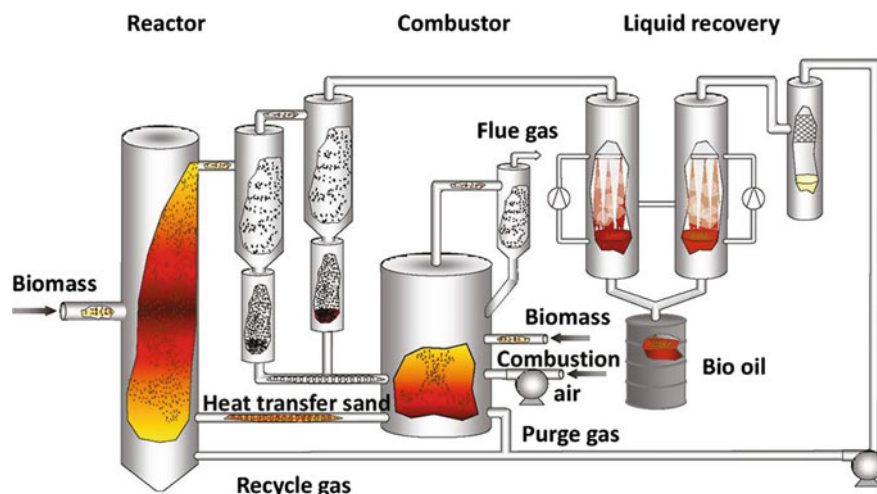


Fig. 4 VTT PDU unit, 20 kg/h [62]

bamboo sawdust as feedstocks using a fluidized bed reactor at pyrolytic temperatures between 440–500 °C and 405–450 °C and noted that produced bio-oil having a higher heating value was about 19 MJ/kg, respectively. The bio-oil produced from rice straw was heterogeneous in nature. The bio-oil obtained from fluidized bed reactor was impure organic material and had maximum water content analysed by Jung et al. [64]. Bio-oil yield, char yield and gas yield produced during pyrolysis of rice straw and bamboo sawdust are presented in Table 2.

In the case of a fluidized bed reactor for the production of bio-oil, the temperature is inversely proportional to the yield of char; as temperature increases, yield of char decreases. The maximum bio-oil yield has occurred at a temperature of 500 °C [65], and they carried out an experiment for the production of bio-oil using jute sticks as a feedstock in a fluidized bed reactor, at various temperatures ranging from 300 to 600 °C. The water, solid and ash contents in the produced bio-oil were found 16, 0.02 and 0.03 wt%, respectively. A fluidized bed reactor is reliable in operation according to Boateng et al. [66], consistently produce bio-oil by using switchgrass as a feedstock and found a bio-oil yield more than 60% along with energy conversion efficiency in the range from 52 to 81%. During the experiment, authors realized that

Table 2 Different products produced during pyrolysis process [64]

Feedstock's	Bio-oil yield (%)	Char yield (%)	Gas yield (%)
Rice straw (440–500 °C)	68	20	18
Bamboo sawdust (405–450 °C)	72	18–20	10

the feedstock, i.e. switchgrass and bio-oil, has similar heating values, but bio-oil had a specific gravity in the range of 1.2–1.3, which indicates benefits of transportation of liquid to overcome the problems associated with handling and transporting bulky biomass.

Pattiya [67] conducted an experiment using biomass crop residues such as cassava stalk and cassava rhizome, in a fluidized bed reactor for the production of bio-oil and acquired that maximum yield of bio-oil derived from cassava stalk and rhizome were 62 and 65 wt%, which occurred when the pyrolysis temperature varied in a range of 475–510 °C. The rhizome feedstock was found a more capable material for the production of bio-oil, having a greater yield than (approximately 2–4 wt%) cassavas stalk.

4.4 Fixed Bed Reactor

The fixed bed pyrolysis technology is quite simple, reliable in operation consist of a reactor along with a separate gas cleaning and cooling system. The fixed bed pyrolysis is well proven for biofuels (recorded 54% oil yield from municipal solid waste), although removal of tar becomes a major problem [48]. Recently, Chandrasekaran et al. [68] pyrolyzed wood chips in the fixed bed reactor by keeping the temperature of 600 °C, heating rate 20 °C/min and recorded the highest yield of both bio-oil and char notably 38.3 and 36.8%, respectively. In addition, authors also observed that acetic acid content was dropped up to 14.2% at a high heating rate (20 °C/min) and resulting biochar at a high temperature showed higher heating value of 30.53 MJ/kg.

Ates et al. [69] investigated the fast pyrolysis process to produce bio-oil from wheat straw through a well-swept fixed-bed reactor by keeping a heating rate of 300 °C/min. The pyrolysis temperature varied from 300 to 800 °C in a nitrogen atmosphere. The experimental results revealed that the maximum oil yield of 31.9% was obtained at a pyrolysis temperature of 500 °C in non-catalytic procedure. Morali and Sensoz [70] pyrolyzed hornbeam shell (*Carpinus betulus L*) residues in a fixed-bed reactor and assessed the physical and chemical properties of bio-oil as well as biochar. Choi and Meier [71] developed a TI mini-scale fast pyrolyzer, which consisted of a small quartz pipe, movable heating oven and rapid condensation tube as shown in Fig. 5. The developed system was used to pyrolyze Kraft lignin. During the operation, the movable heating oven was preheated to 500 °C or 600 °C. As targeted pyrolysis temperature was reached, it quickly and automatically moved to the lignin sample ensuring rapid uniform heating.

In the case of a fixed bed reactor, pyrolysis temperature and sweeping gas are deciding factors of bio-oil and char yield. Ertaş and Alma [72] characterized bio-oil produced from (*Laurus nobilis L.*) extraction residues. The maximum bio-oil yield was reported about 21.91 wt% at 500 °C under the sweeping gas of N₂ with a flow rate of 100 mL min⁻¹ and heating rate was kept about 10 °C min⁻¹.

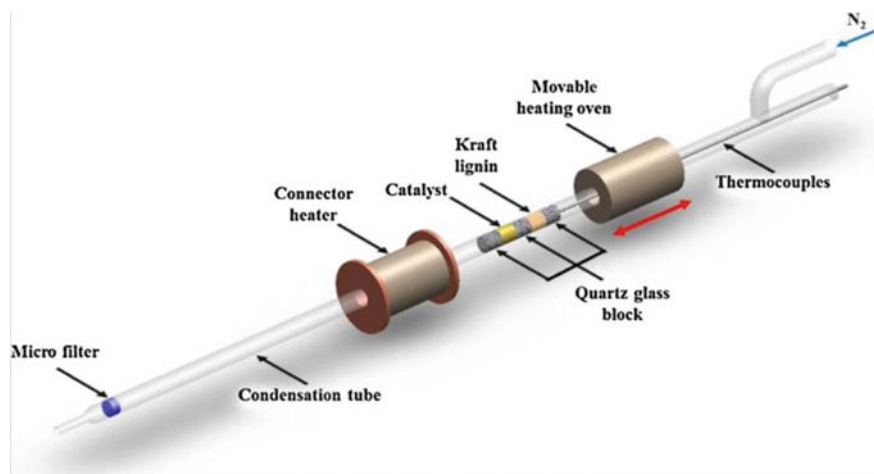


Fig. 5 TI-mini fast pyrolyzer system [71]

4.5 Auger Reactor

Presently, auger-type pyrolyzer has a large potential to increase the production of bio-oil by reducing the operating cost. The main principle of this reactor is continuous pyrolysis of biomass, which takes place by using a heat carrier material such as sand studied [73]. In auger reactor, the particle size of feedstock has a minor influence on bio-oil yield, whereas process temperature and nitrogen flow rate greatly affect on bio-oil yield as well as physicochemical properties of bio-oil [74].

Kelkar et al. [75] studied that a pilot-scale auger reactor pyrolyzer was competent to process 1–6 kg of biomass or any residues per hour, depending upon the type of feedstock. Here they used expanded coffee grounds as a feedstock in a screw reactor at a pyrolysis temperature of about 500 °C and recorded maximum bio-oil yield approximately 61.8%. The yield of bio-oil increased in the presence of a short residence time and raising the operating temperature up to 505 °C. The produced bio-oil from laboratory-scale auger reactor had outstanding properties such as higher heating value, less water content, lower acid values and low densities were reported [76]. Authors demonstrated a laboratory-scale auger reactor which had a capacity of 2 kg/h and used pine wood and waste plastic (including polystyrene, high-density polythene and polypropylene each pyrolyzed simultaneously with wood) as a feedstock in 50:50 wt ratios at pyrolyzing temperatures of 450 and 525 °C to produce upgraded modified bio-oil. Meanwhile, another study found that the produced bio-oil contained a maximum percentage of carbon and hydrogen due to the presence of plastic, along with wood, as a feedstock during the pyrolysis. This simultaneously increased the heating value of bio-oil.

Thangalazhy-Gopakumar et al. [77] studied the physical (such as pH, water content, higher heating value [HHV], solid and ash contents) and chemical properties of bio-oil produced from pine wood as a feedstock in an auger reactor at different pyrolysis temperatures from 425 to 500 °C and reported that necessary temperature required for obtaining maximum bio-oil yield was to be 450 °C. During the study, the author investigated the increasing concentration of phenol in bio-oil concerning increase in the pyrolysis temperature and simultaneous decrease in the guaiacol concentration as well as pH values in the bio-oil.

4.6 Vacuum Pyrolysis Reactor

Vacuum pyrolysis is the thermal decomposition of biomass in the absence of air under low pressure and high temperature, resulting in liquid yield (bio-oil), biochar and syngases. The pressure maintained during vacuum pyrolysis usually varies from 0.05 to 20 MPa, and pyrolysis temperature is in between 450 and 900 °C [78]. The heating rate of vacuum pyrolysis is distinguished from that of slow pyrolysis due to vacuum condition inside the reactor it is to be characterized by quick removal of pyrolytic gases within a short residence time. Therefore, due to the rapid removal of syngases, the primary pyrolysis process significantly minimized secondary char formation and cracking reaction [79]. As a result, vacuum pyrolysis ensures high bio-oil yield usually 40% [80]. In addition vacuum pyrolysis not only increased the bio-oil yield but become much suitable for improving the physicochemical properties of biochar in terms of surface area, porosity (macro/micro), functional groups, etc. Generally, organic vapours and bio-oil yield tend to be improved by raising the pyrolysis temperature [81]. Zheng et al. [82] carried out vacuum co-pyrolysis of fermentation residue and woody sawdust in a vacuum reactor by keeping temperature 900 °C, provided a vacuum nearly 5 kPa for 2 h. During the experiment, the authors observed maximum gas yield 54.7%, followed by char yield 14.3%, respectively. Further Li et al. [80] pyrolyzed rape straw in a vacuum pyrolyzer at a temperature of 500 °C, vacuum pressure 5.0 kPa, heating rate 20 °C/min and hold time 45 min. They recorded maximum bio-oil yield 39.57% and gas yield about 32.07%, respectively. In addition, the authors also analysed the physicochemical properties of bio-oil in terms of density (1.18 g/cm⁻³), pH (2.10), HHV (28.44 MJ/kg), viscosity (6.45 mm² s⁻¹), respectively.

4.7 Ablative Pyrolysis Reactor

In ablative pyrolysis, woody biomass undergoes a melting reaction as similar to the melting of butter, when we kept it in an open pan. Here, biomass melting/ sublimation reaction occurred due to direct contact of a hot plate under pressure [83]. As the woody biomass is pressed in contact with a hot plate by adding some pressure, pyrolysis

reaction takes place within a residual oil get to evaporate as pyrolysis vapour. This thin layer of oil is contacting only hot surfaces and move towards the heart of biomass with constant velocity. Therefore, pyrolysis reaction in an ablative pyrolysis process only happened at a superficial layer rather than whole biomass [84]. For this reason, ablative pyrolysis is considered more suitable for large size biomass rather than small particle size. Therefore, this salient feature can reduce the grinding cost of nearly 7–9% of the overall cost [85]. Luo et al. [84] carried out ablative pyrolysis using wood chips (5×15 mm), at pyrolysis temperature of 500 °C, wood chips layer (< 5 mm), pressure on wood chips (< 0.5 bar) and recorded maximum bio-oil yield about 60 wt%. The main feature of this reactor is the suitability towards the large size of biomass feedstock and no need for any carrier gas. The performance of the ablative pyrolysis reactor mainly depends on surface temperature, plate pressure, etc.

5 Properties of Bio-oil

Bio-oil, an organic mixture with many components, which is obtained by the fragmentation and depolymerization of biomass that contains hemicelluloses, cellulose and lignin [86]. The physicochemical properties of bio-oil mainly depend on the feedstock type and pyrolysis condition. The chemical species in the bio-oil play a significant role in determining its quality, suitability and stability towards further upgrading. The pyrolytic oil termed bio-oil is composed of numerous organic compounds (it may be several hundred), which exhibit good chemical functionalities. Therefore, bio-oil can be used either as a fuel or as a valuable chemical. Oyebanji et al. [87] analysed chemical species in bio-oil produced from fast pyrolysis of west African cordia and African birch sawdust as energy biomass. The authors analysed different phenolic compounds, aromatic hydrocarbons, oleic acid and nitrogen-containing compounds. The level of oleic acid and phenolic compounds were higher in bio-oil derived from cordia biomass than birch sawdust. The aromatic hydrocarbons present in bio-oil are mainly indene, benzene, naphthalene, tolyene and methylnaphthalene. The availability of phenolic compounds in bio-oil subjected to replacement for fossil phenol for the preparation of different chemicals. The bio-oil produced from mango waste at 650 °C is composed of phenols (32.6%), hydrocarbons (7.2%), acid content (16.8%) and ketones (22.9%), respectively [88]. The physical properties of bio-oil, i.e. higher heating value, pH, density, viscosity, and its water, solid and ash contents, as well as its elemental properties, i.e. carbon, hydrogen, nitrogen, oxygen and sulphur contents, derive due to the different composition of feedstock's used, and the operating conditions are summarized and presented in Table 3. Instruments used during assessing the physical properties of bio-oil, main drawbacks, reasons, benefits and solutions to overcome the problems are summarized and presented in Table 4.

Table 3 Elemental analysis of bio-oil produces from different feedstocks

S. No.	Type of feedstock	Operating condition (mode of pyrolysis)	Water content (%)	Solid content (%)	Ash content (%)	Viscosity	HHV MJ/kg	pH	Density	Elemental analysis				References	
										C (%)	H (%)	N (%)	O (%)		S (%)
1	Com stover	Novel microwave pyrolysis	15.2	0.22	0.04	185 mPa.s (at 40 °C)	17.5	2.87	1.25 g/m L	60.66	7.70	2.02		0.15	[89]
2	Wood sawdust	Cyclone reactor (606–946 °C)	20	0.14		0.05–0.15 Pa.s		2.6 ± 0.1	1270 ± 10 kg/m ³			0.004–0.005			[90]
3	Bark residue (softwood bark)	Continuous feed pilot plant unit (~530 °C)	13	0.55	0.3	15–62 cSt	27.9	3	1188 kg/m ³	62.6	7.0	1.1		0.07	[91]
4	Rice husk	Fluidized bed pyrolysis reactor (~475 °C)	28	0.5	0.25	13.2 cSt (at 40 °C)	16.5	3.2	1.14 gm/ml	39.92	8.15	0.67		0.03	[92]
5	Pine wood	Auger pyrolysis reactor (~450 °C)	16	0.19	0.20	60.9 (cSt, 50 °C)	21.9	3.1	1.19 g/cc	52.64	7.53	0.09		39.5	[93]
6	Rapeseed cake	Fixed bed reactor (~500 °C)	0.001		0.30	62 (cSt, 37.8 °C), 38 (cSt, 50 °C)	36.4		993 kg/m ³ at 15 °C	73.74	10.69	4.65		10.51	[94]
7	Rapeseed cake	Fixed bed reactor (~650 °C)	0.001		0.1	198 SSU (cSt, 50 °C)	26.7		964 at 20 °C	63.56	8.89	3.6		23.74	[95]
8	Com straw	Fluidized bed reactor (525 °C)				9.01–9.58 (cSt, 20 °C)	9,027–9,477		1.04–1.12 at 20 °C						[96]
9	Herbaceous biomass	Tubular furnace pyrolysis equipment (300–450 °C)						<6		48.09	7.691				[97]
10	Wood	Fast pyrolysis (450–550 °C)		0.2–1.0	0–0.2	40–100 cp, 773 k	16–19	2.5	1.2	54–58	5.5–7.0	0–0.2		35–40	[98]

(continued)

Table 3 (continued)

S. No.	Type of feedstock	Operating condition (mode of pyrolysis)	Water content (%)	Solid content (%)	Ash content (%)	Viscosity	HHV MJ/kg	pH	Density	Elemental analysis					References
										C (%)	H (%)	N (%)	O (%)	S (%)	
11	Oak, Eucalyptus, Pitch Pine, Japanese Cedar	Fluidized bed reactor (~500 °C)	20–26		0.4–0.8	10.3–45.9 (cSt, 40 °C)	15.5–19	1.7–2.4		38–50	6–7		45.1–48.3		[99]
12	Palm and Jatropha waste	Fluidized bed reactor (380–530 °C)	1–15				30.2–30.9		1.13–1.23	65.8–71.5	8.92–10.3	5.62–2.82	11.5–18.8	0.01–0.19	[100]
13	Wheat straw	Flash pyrolysis (525 °C)	17.8		1.6	91.4 (cP, 20 °C) 27.4 (cP, 40 °C)	16.4	3.20	1.19 g/cm ³	50.2	6.2		43.6		[101]
14	Grape bagasse	Fixed bed reactor (550 °C)					32.95		992 kg/m ³ at 15 °C	>1.72	8.69	2.69	16.90		[102]

Table 4 Properties of bio-oil assessed through methods and their benefits, drawbacks and solutions to improve its properties

S. No.	Properties of bio-oil	Method/instrument	Range	Reasons	Benefits	Drawbacks	Solutions
1	Water content	Karl Fischer (KF) analysis (Cole-Parmer Model EW-25800-10) [77] Dean-Stark distillation (ANSI/ASTM D 95-70) [103] ASTM D 1744	High (30–35%) [104]	Moisture content in feedstock and dehydration reaction took place during fast pyrolysis [105]	Can reduce the viscosity of bio-oil and also ensure the uniform temperature distribution in chamber [106] Provides facility for atomization [105]	Reduce the heating value of bio-oil as well as problem in phase separation [107]	Drying of feedstock to achieve moisture level up to zero [106] To increase the size of biomass particle (smaller size of feedstock particle increases the water content) [108]
2	Viscosity	Capillary-type viscometer [99] Rheometer (Bohlin, model CVO 100) [77] Rotational viscometer equipped with NVST spindle (Haake Model VT 550) [109] ASTM D 445 [110]	High/low	Flexibility in feedstock. Water content and amount of light ends collected [35] Pyrolysis temperature (as temperature increased viscosity decreased) [77]	Reduction in viscosity greatly reduce engine operation problem Low viscous oil can be used in IC engine for generation of power and transportation [65]	High viscosity in bio-oil affects pumping and atomization [111] Due to high viscosity, bio-oil does not reach in commercial standards [35]	Viscosity of oil can be reduced by addition of methanol [103] Transesterification, pyrolysis and dilution can resolve the problem in case of high viscous bio-oil [112]

(continued)

Table 4 (continued)

S. No.	Properties of bio-oil	Method/instrument	Range	Reasons	Benefits	Drawbacks	Solutions
3	pH	pH metre Digital pH metre (Oakton, model PC 50) [77]	<6 (Acidic)	Bio-oil contains volatile acids, such as acetic acid, formic acid and diluted water [113] Aldehyde also contributes to low pH [65]	The produced acidic bio-oil is non-corrosive to stainless steel [114]	Storage material like carbon steel and aluminium became corrosive Bio-oil becomes unstable Degradation of hemicelluloses and lignin take place during pyrolysis and results in increasing the concentration of acidic components	Need some chemical treatment to low the pH and further application in sophisticated engine [65] Careful material selection during storage and piping system Increase the pyrolysis temperature (pH increases with increasing pyrolysis temperature) [115]
4	Density	Densimeters [98] Density measurement bottles [65]	High (larger than gasoline and diesel)	Raw material and pyrolysis condition Occurrence of Aromatic hydrocarbon [116] More oxygen and water content [117] Presence of Macromolecules such as cellulose, hemicelluloses, oligomeric, phenolic compounds [114]	Due to the higher density of bio-oil than hydrocarbon fuel oil, heating value on volumetric basis is about 60% of that diesel oil [118]	Density of oil has a major impact on the atomization quality of spray [119]	Density of bio-oil can be reduced by increasing the concentration of methanol [103] Lower density ends up at high pyrolysis temperature. (breakdown of large compounds at higher temperature) [115]

(continued)

Table 4 (continued)

S. No.	Properties of bio-oil	Method/instrument	Range	Reasons	Benefits	Drawbacks	Solutions
5	Heating Value	Oxygen –bomb calorimeter [111] $HHV(MJ/kg) = 338.2 \times C + 1442.8 \times (H - \frac{O}{8})$ [120] LECO AC 350 instrument (ASTM D 3286-91a) [94] $HHV(MJ/kg) = -1.3675 + 0.3137C + 0.7009H + 0.03180$ [121]	Low calorific value of bio-oil as compared to conventional fossil fuel [122]	Aqueous phase reduces the calorific value of bio-oil, i.e. high water and oxygen content [123]	Application in engine after upgrading of bio-oil	Decreasing the combustion rate [123] Due to minimum calorific value increases ignition delay [105]	Calorific value can be raised by catalytic deoxygenation [124] Some modifications are required in combustor and especially in nozzle [125] Quality of bio-oil should be improved by catalytic upgrading to be suitable for transportation fuel [99]

6 Applications of Bio-oil

The main applications of bio-oil produced from pyrolysis processes are in boiler for electricity and heat generation, gas turbine or in diesel engine for power generation, and it may be used as a binding material to make briquettes, pellets, etc., and as a transportation fuel in diesel engine. Presently, bio-oil has extensive applications in small- and large-scale industrial and commercial sector for power and heat generation. Due to some intrinsic properties of bio-oil, the minor modifications are necessary for boilers, gas turbine, furnace and in compression ignition (CI) or diesel engine to enrich the combustion efficiency of bio-oil.

6.1 Furnace/Boiler/Co-firing

The biomass-derived fuel as bio-oil is used to generate heat and power instead of using fossil fuels like diesel in stationary applications such as boiler and furnace. The furnaces, boiler can operate with a wide range of fuels but less competent than engine and turbine. Lujaji et al. [126] studied the combustion characteristics of bio-oil in a horizontal combustion chamber named as box furnace. An air-fed external mixed nozzles were provided for the atomization of bio-oil in a redesigned 100 kW burner for getting full utility of bio-oil combustion in furnace. Combustion performance was carried out at different air–fuel equivalence ratio of 0.46, 0.53 and 0.68, respectively, results showed that externally assisted nozzles could successfully atomized and also provided the stable combustion.

Existing industrial boiler can be run on bio-oil by replacing the fossil fuel is possible by few modifications in existing combustion chamber in order to enhance the combustion stability. As bio-oil can be co-fired with a conventional fossil fuels for exploring the advantage of maximize the overall efficiency by reducing the emission of CO_2 , SO_x and NO_x [35]. With respect to the above findings, Hou et al. [127] carried out co-firing of pyrolysis oil and heavy fuel oil (HFO) blends in a 300 kW_{th} furnace for investigation of combustion characteristics and its emission pattern in atmosphere. The results showed that instability in combustion operation occurred as increase in bio-oil (more than 5%) emulsion. In addition, combustion of bio-oil and HFO blend (2.5:97.5) indicated similar furnace interpretation, with a lowering the SO_x and NO_x emission level as compared to combustion of pure HFO. Still, it is not known to human being how the fuel affects or alters the individual health due to emission. Therefore, recently, Sippula et al. [128] conducted a comparative detailed health-related emission study of bio-oil, fossil oil and wood-fired boiler. The total suspended and fine particulate matters were more in bio-oil boiler flue gases, which was higher as compared to HFO boiler and probably similar to wood-fired boiler. In case of toxicological analysis, bio-oil flue gas particles consist of ash species and less presence of polycyclic aromatic hydrocarbons (PAH), heavy metals as compared to

HFO combustion. This feature denoted that, toxicological properties of bio-oil flue emission create a less impact than HFO combustion particle.

6.2 Diesel Engine

The boiler and furnace are commonly used to produce the heat, but diesel engine generates power at a maximum efficiency (45%), and it can also adapt in a cycle that generates both heat and power. Bio-oil can be used at a slow and medium speed of a conventional diesel engine; however, sometimes it creates a problem when used in the engine application directly. These problems included the deposition of carbon on piston as well as on components of engine combustion chamber, gum and wax formation, injector coking, poor atomization, engine wear, and starting difficulty in cold weather, among others. Recently, Yuan et al. [129] were combusted bio-oil emulsion with diesel in direct injection (DI) diesel engine for investigation of bio-oil properties in engine performance and to check the emission index. They observed that as compared to diesel, synthetic bio-oil causes increase in brake-specific fuel consumption (BSFC) and energy consumption, although break power remained same for emulsion.

In the compression ignition (CI) engine 50–80% of rubber seed oil can substitute for diesel fuel easily without any changes, modifications, engine structure and operational difficulties, as studied [130]. During the experiment, they tested performance and emission level of the CI engine using a blend of rubber seed oil and diesel fuel. They found that the blend-fuelled CI engine had more carbon deposition inside the combustion chamber as compared to a diesel-fuelled engine. Van de Beld et al. [131] studied the effect of different parameters on performance of a one-cylinder 20 kW diesel engine for power generation, installed using a stainless-steel fuel injection system and injector to enable the fuelling of bio-oil and upgraded bio-oil. They found very promising results during the experiment when they filled the pyrolysis oil in the diesel engine for duration of 40 h and found that there was a notable effect on fuel consumption as well as flue gas emissions. They also estimated the cetane number of pyrolysis oil in the range of 20–25 and reported that pyrolysis oil is easily accessible to ignite in the engine as compared to butanol and bio-ethanol. As noticed in many studies have reported various technical challenges associated with the application of bio-oil in heat and power generation, such as deposition of coke, ash or carbon in the combustion chamber, poor ignition quality, injector clogging and polymerized material and corrosion. In addition, Costro et al. [132] carried out fractional distillation of bio-oil produced from pyrolysis of lignin cellulose residue at 450 °C temperature. The GC-MS analysis of bio-oil showed that it was composed of hydrocarbons (21.52 wt%) and oxygenate (78.48 wt%) in which phenols (35.16%), carboxylic acid (8.52%), ester (4.06%), ketones (3.53%), furans (5.75%) and 0.91% aldehydes made it desirable for further fractional distillation to prepare a fossil fuel-like fractions (kerosene, gasoline and light diesel oil).

6.3 Gas Turbine

Gas turbines are extensively used in power plant to generate electric power, which operates on petroleum fuels. It can be modified to make them compatible with bio-oil. Owing to this, Buffi et al. [133], checked the performance of micro-gas turbine by using fast pyrolysis bio-oil blends with ethanol, included a modified combustor and new fuel injection line. The demonstration of micro-gas turbine for a test as 20:80 and 50:50 (volume fraction) of bio-oil blend with ethanol performed a stable and efficient engine operation. Authors are also observed that engine performed an overall electrical efficiency more than diesel fuel, it occurred due to redesigned combustor and fuel line. In addition, authors also highlighted the emission status, as bio-oil volume fraction was increased; carbon monoxide emission happened very rapidly, probably it occurred due to high viscous bio-oil along with a large droplet size. Finally, they also checked performance on 100% bio-oil, found as unstable fuel combustion, deposition of carbon particles, showing that it required further modifications to reach at desired goal. The testing of the first gas turbine J69-T-29 using biomass-derived pyrolysis oil was carried out at Teledyne CAE (USA) [134]. During the testing, the combustion efficiency of pyrolysis oil as a fuel was reported about 95%, but it was expected that it would exceed up to 99% in the engine at the optimum condition.

6.4 Chemicals

The bio-oil derived from the pyrolysis process has the potential to produce high-grade chemicals that are used to make fertilizers, acetic acid, food flavourings, phenol and sugars, as well as for industrial applications. Bio-oil is a complex mixture of different compounds including phenols, acids, ketones, aldehydes, hydrocarbon, sugars, ethers, ester, etc. [88]. Therefore, bio-oil has a potential to produce different chemicals for further industrial application, e.g. levoglucosan for the preparation of pharmaceuticals, phenolic compounds used in phenolic resins, surfactant, biodegradable polymer and hydroxyacetaldehyde, considered as meat browning agents [135].

7 Conclusion

Biomass has been recognized as a clean and green energy source. It extensively used for both heat and power generation; hence, it reduces the dependency on fossil fuels. The bio-oil can be used as transport fuel. Petrol fuel, diesel oil and valuable fractional products can be obtained using destructive distillation. The heating rate, type of reactor, feedstocks and particle's size are deciding factor for quality of bio-oil,

yield and by-products. Fast pyrolysis is one of the economical processes for bio-fuel production where thermal decomposition of biomass takes place in the absence of oxygen at a temperature range from 450 to 600 °C in a short residence time (< 2 s). In flash pyrolysis process, bio-oil can be obtained at a higher heating rate (from 10^3 to 10^4 °C/s) and with a very short residence time (< 0.5 s). Bio-oil yield highly depends on operating temperature, moisture content of feedstock, particles size, heating rate and types of the pyrolysis process. It has been observed that in most of the studied pyrolysis processes and reactors the yield of bio-oil increases with increasing the temperature up to 500 °C. The biochar yield decreased with increasing the temperature. However, syngas yield increase with increasing the temperature. Bio-oil has extensive applications in small- and large-scale industrial and commercial sector for power and heat generation.

Acknowledgements The authors are grateful to the Indian Council of Agricultural Research, Government of India, for providing financial support for design and development of vacuum pyrolysis reactor for biochar and bio-oil production from biomass under Consortium Research Platform on energy from agriculture. The author (Ashish Pawar) is also thankful to the Council for Scientific and Industrial Research (CSIR), Government of India, for providing research fellowship.

References

1. EIA, US energy information administration, <http://www.eia.gov/countries/analysisbriefs/India/india.pdf>. Accessed on May 01 2020
2. H.B. Goyal, D. Seal, R.C. Saxena, Bio-fuels from thermochemical conversion of renewable resources: a review. *Renew. Sustain. Energy Rev.* **12**, 504–517 (2008)
3. CEA, Central Electricity Authority, Ministry of Power, Govt of India. <http://www.cea.nic.in/>. Accessed on 25 Apr 2020
4. N. Zhao, B.X. Li, The effect of sodium chloride on the pyrolysis of rice husk. *Appl. Energy*. **178**, 346–352 (2016)
5. Renewable 2017 Global Status Report. 2017. Available at: <http://www.ren21.net/status-of-renewables/global-status-report/>
6. A.V. Bridgwater, Renewable fuels and chemicals by thermal processing of biomass. *Chem. Eng. J.* **91**, 87–102 (2003)
7. H.V. Ly, J. Kim, S.S. Kim, Pyrolysis characteristics and kinetics of palm fiber in a closed reactor. *Renew. Energy*. **54**, 91–95 (2013)
8. N.E. Bassam, *Handbook of Bioenergy Crops: A Complete Reference to Species*, 1st edn. (Earthscan, London, 2010)
9. M. Asadullah, N.S. Ab Rasid, S.A. Kadir, A. Azdarpour, Production and detailed characterization of bio-oil from fast pyrolysis of palm kernel shell. *Biomass Bioenerg.* **59**, 316–324 (2013)
10. J. Alvarez, M. Amutio, G. Lopez, J. Bilbao, M. Olazar, Fast co-pyrolysis of sewage sludge and lignocellulosic biomass in a conical spouted bed reactor. *Fuel* **159**, 810–818 (2015)
11. Ministry of New Renewable Energy, Govt of India, <https://mnre.gov.in/biomass-powercogen>. Accessed on 26 Aug 2019
12. B. Chaitanya, V. Bahadur, A.-D. Thakur, R. Raj, Biomass-gasification-based atmospheric water harvesting in India. *Energy* **165**, 610–621 (2018)
13. X. Zhang, T. Wang, L. Ma, J. Chang, Vacuum pyrolysis of waste tires with basic additives. *Waste Manag.* **28**, 2301–2310 (2008)

14. N.L. Panwar, Biomass for domestic and agro industrial applications, in *Wood: Types, Properties, and Uses*, ed. by L.F. Botannini (Nova Science Publisher, Inc., New York, 2011)
15. A.J. Marshall, *Commercial Application of Pyrolysis Technology in Agriculture* (2013). www.ofa.on.ca/uploads/userfiles/files/pyrolysis%20report%20final.pdf.
16. A. Hornung, *Transformation of Biomass: Theory to Practice* (Wiley, 2014)
17. S. Yu, J. Park, M. Kim, C. Ryu, J. Park, Characterization of biochar and byproducts from slow pyrolysis of hinoki cypress. *Bioresour. Technol. Rep.* **6**, 217–222 (2019)
18. J.A. Albuquerque, M.E. Sánchez, M. Mora, V. Barrón, Slow pyrolysis of relevant biomasses in the Mediterranean basin. Part 2. Char characterisation for carbon sequestration and agricultural uses. *J. Clean. Prod.* **120**, 191–197 (2016)
19. A. Mandal, N. Singh, T.J. Purakayastha, Characterization of pesticide sorption behaviour of slow pyrolysis biochars as low cost adsorbent for atrazine and imidacloprid removal. *Sci. Total Environ.* **577**, 376–385 (2017)
20. I.D.V. Torri, V. Paasikallio, C.S. Faccini, R. Huff, E.B. Caramão, V. Sacon, C.A. Zini, Bio-oil production of softwood and hardwood forest industry residues through fast and intermediate pyrolysis and its chromatographic characterization. *Biores. Technol.* **200**, 680–690 (2016)
21. A.K. Hossain, P.A. Davies, Pyrolysis liquids and gases as alternative fuels in internal combustion engines—a review. *Renew. Sustain. Energy Rev.* **21**, 165–189 (2013)
22. A. Funke, M.T. Morgano, N. Dahmen, H. Leibold, Experimental comparison of two bench scale units for fast and intermediate pyrolysis. *J. Anal. Appl. Pyrol.* **124**, 504–514 (2017)
23. I.Y. Mohammed, Y.A. Abakr, S. Yusup, F.K. Kazi, Valorization of Napier grass via intermediate pyrolysis: optimization using response surface methodology and pyrolysis products characterization. *J. Clean. Prod.* **142**, 1848–1866 (2017)
24. C.H. Lim, I.Y. Mohammed, Y.A. Abakr, F.K. Kazi, S. Yusup, H.L. Lam, Novel input-output prediction approach for biomass pyrolysis. *J. Clean. Prod.* **30**, 1–11 (2016)
25. M. Sadeqzadeh, M. Guo, T.N. Borhani, N.M. Konda, M.C. Garcia, N. Shah, The multi-scale challenges of biomass fast pyrolysis and bio-oil upgrading: Review of the state of art and future research directions. *Prog. Energy Combust. Sci.* **71**, 1–80 (2019)
26. P. Roy, G. Dias, Prospects for pyrolysis technologies in the bioenergy sector: a review. *Renew. Sustain. Energy Rev.* **77**, 59–69 (2017)
27. D. Vamvuka, Bio-oil, solid and gaseous biofuels from biomass pyrolysis processes—an overview. *Int. J. Energy Res.* **35**, 835–862 (2011)
28. S. Li, S. Xu, S. Liu, C. Yang, Q. Lu, Fast pyrolysis of biomass in free-fall reactor for hydrogen-rich gas. *Fuel Process Technol.* **85**, 1201–1211 (2004)
29. D.J. Stevens, C. Kinchin, S. Czernik, *Production of Gasoline and Diesel from Biomass Via Fast Pyrolysis, Hydrotreating and Hydrocracking: A Design Case* (Pacific Northwest National Laboratory, Richland, WA, 2009)
30. M.F. Demirbas, M. Balat, Biomass pyrolysis for liquid fuels and chemicals: a review. *J. Sci. Ind. Res.* **66**, 797 (2007)
31. A. Sharma, S. Wang, V. Pareek, H. Yang, D. Zhang, Multi-fluid reactive modeling of fluidized bed pyrolysis process. *Chem. Eng. Sci.* **123**, 311–321 (2015)
32. Y. Xue, S. Zhou, R.C. Brown, A. Kelkar, X. Bai, Fast pyrolysis of biomass and waste plastic in a fluidized bed reactor. *Fuel* **156**, 40–46 (2015)
33. J.Y. Park, J.K. Kim, C.H. Oh, J.W. Park, E.E. Kwon, Production of bio-oil from fast pyrolysis of biomass using a pilot-scale circulating fluidized bed reactor and its characterization. *J. Environ. Manage.* **234**, 138–144 (2019)
34. K. Duanguppama, N. Suwapaet, A. Pattiya, Fast pyrolysis of contaminated sawdust in a circulating fluidised bed reactor. *J. Anal. Appl. Pyrol.* **118**, 63–74 (2016)
35. M.I. Jahirul, M.G. Rasul, A.A. Chowdhury, N. Ashwath, Biofuels production through biomass pyrolysis—a technological review. *Energies* **5**, 4952–5001 (2012)
36. M. Amutio, G. Lopez, R. Aguado, J. Bilbao, M. Olazar, Biomass oxidative flash pyrolysis: autothermal operation, yields and product properties. *Energy Fuels* **26**, 1353–1362 (2012)
37. R.E. Guedes, A.S. Luna, A.R. Torres, Operating parameters for bio-oil production in biomass pyrolysis: a review. *J. Anal. Appl. Pyrol.* **129**, 134–149 (2018)

38. M. Balat, M. Balat, E. Kirtay, H. Balat, Main routes for the thermo-conversion of biomass into fuels and chemicals. Part 1: pyrolysis systems. *Energy Convers. Manag.* **50**, 3147–3157 (2009)
39. S.A. Raja, Z.R. Kennedy, B.C. Pillai, C.L.R. Lee, Flash pyrolysis of jatropha oil cake in electrically heated fluidized bed reactor. *Energy* **35**, 2819–2823 (2010)
40. D. Meier, B. Van de Beld, A.V. Bridgwater, D.C. Elliott, A. Oasmaa, F. Preto, State-of-the-art of fast pyrolysis in IEA bioenergy member countries. *Renew. Sust. Energy. Rev.* **20**, 619–641 (2017)
41. G.S. Miguel, J. Makibar, A.R. Fernandez-Akarregi, New advances in the fast pyrolysis of biomass. *J. Biobased Mater. Bioenergy* **6**, 193–203 (2012)
42. J. Makibar, A.R. Fernandez-Akarregi, M. Amutio, G. Lopez, M. Olazar, Performance of a conical spouted bed pilot plant for bio-oil production by poplar flash pyrolysis. *Fuel Process. Technol.* **137**, 283–289 (2015)
43. S. Mandal, J. Haydary, T.K. Bhattacharya, H.R. Tanna, J. Husar, A. Haz, Valorization of pine needles by thermal conversion to solid, liquid and gaseous fuels in a screw reactor. *Waste and Biomass Valorization* 1–13 (2018)
44. B. Biswas, R. Singh, J. Kumar, R. Singh, P. Gupta, B.B. Krishna, T. Bhaskar, Pyrolysis behavior of rice straw under carbon dioxide for production of bio-oil. *Renew. Energy* **129**, 686–694 (2018)
45. N. Khuenkao, N. Tippayawong, Production and characterization of bio-oil and biochar from ablative pyrolysis of lignocellulosic biomass residues. *Chem. Eng. Commun.* 1–8 (2019)
46. Y.M. Ju, K.C. Oh, K.Y. Lee, D.H. Kim, Performance analysis of a vacuum pyrolysis system. *J. Biosyst. Eng.* **43**, 14–20 (2018)
47. B.J. Lin, W.H. Chen, Sugarcane bagasse pyrolysis in a carbon dioxide atmosphere with conventional and microwave-assisted heating. *Front. Energy Res.* **3**, 4 (2015)
48. P. Madhu, H. Kanagasabapathy, I.N. Manickam, Cotton shell utilization as a source of biomass energy for bio-oil by flash pyrolysis on electrically heated fluidized bed reactor. *J. Mater. Cycles Waste Manage.* **18**, 146–155 (2016)
49. B.M. Wagenaar, R.H. Venderbosch, J. Carrasco, R. Strenziok, B.J. van der Aa, Rotating cone bio-oil production and applications, in *Progress in Thermochemical Biomass Conversion*, ed. by A.V. Bridgwater, pp. 1268–80 (2001)
50. BTG, <http://www.btgworld.com/en/rtd/technologies/fast-pyrolysis>. Assessed on 6 June 6 2019
51. S.P. Bhagat, P. Gera, A. Bhavanam, Catalytic co-pyrolysis of *Pterospermum acerifolium* and plastic waste. *J. Mater. Cycles Waste Manage.* **20**, 1923–1933 (2017)
52. E. Pütün, Catalytic pyrolysis of biomass: effects of pyrolysis temperature, sweeping gas flow rate and MgO catalyst. *Energy* **35**, 2761–2766 (2010)
53. R. French, S. Czernik, Catalytic pyrolysis of biomass for biofuels production. *Fuel Process. Technol.* **91**, 25–32 (2010)
54. P.T. Williams, N. Nugranad, Comparison of products from the pyrolysis and catalytic pyrolysis of rice husks. *Energy* **25**, 493–513 (2000)
55. D.C. Elliott, T.R. Hart, G.G. Neuenschwander, L.J. Rotness, A.H. Zacher, Catalytic hydroprocessing of biomass fast pyrolysis bio-oil to produce hydrocarbon products. *Environ. Prog. Sustain. Energy* **28**, 441–449 (2009)
56. A. Aho, N. Kumar, K. Eränen, T. Salmi, M. Hupa, D.Y. Murzin, Catalytic pyrolysis of woody biomass in a fluidized bed reactor: influence of the zeolite structure. *Fuel* **87**, 2493–2501 (2008)
57. S. Suranani, V.R. Goli, Combustion characteristics of sawdust in a bubbling fluidized bed, in *International Conference on Chemistry and Chemical Process, IPCBEE*, vol. 10, pp. 167–172 (2011)
58. M. Ringer, V. Putsche, J. Scahill, *Large-Scale Pyrolysis Oil Production: A Technology Assessment and Economic Analysis* (National Renewable Energy Laboratory, Golden, CO, USA, 2006)

59. R.O. Arazo, D.A. Genuino, M.D. de Luna, S.C. Capareda, Bio-oil production from dry sewage sludge by fast pyrolysis in an electrically-heated fluidized bed reactor. *Sustain. Environ. Res.* **27**, 7–14 (2017)
60. K.M. Qureshi, F. Abnisa, W.M.A.W. Daud, Novel helical screw-fluidized bed reactor for bio-oil production in slow-pyrolysis mode: a preliminary study. *J. Anal. Appl. Pyrolysis* **142**, 104605 (2019)
61. H.V. Ly, S.S. Kim, H.C. Woo, J.H. Choi, D.J. Suh, J. Kim, Fast pyrolysis of macroalga *Saccharina japonica* in a bubbling fluidized-bed reactor for bio-oil production. *Energy* **93**, 1436–1446 (2015)
62. Y. Solantausta, A. Oasmaa, K. Sipila, C. Lindfors, J. Lehto, J. Autio, P. Jokela, J. Alin, J. Heiskanen, Bio-oil production from biomass: steps toward demonstration. *Energy Fuels* **26**, 233–240 (2012)
63. H.S. Heo, H.J. Park, Y.K. Park, C. Ryu, D.J. Suh, Y.W. Suh, S.S. Kim, Bio-oil production from fast pyrolysis of waste furniture sawdust in a fluidized bed. *Bio Resour. Technol.* **101**, S91–S96 (2010)
64. S.H. Jung, B.S. Kang, J.S. Kim, Production of bio-oil from rice straw and bamboo sawdust under various reaction conditions in a fast pyrolysis plant equipped with a fluidized bed and a char separation system. *J. Anal. Appl. Pyrol.* **82**, 240–247 (2008)
65. M. Asadullah, M.A. Rahman, M.M. Ali, M.A. Motin, M.B. Sultan, M.R. Alam, M.S. Rahman, Jute stick pyrolysis for bio-oil production in fluidized bed reactor. *Biores. Technol.* **99**, 44–50 (2008)
66. A.A. Boateng, D.E. Daugaard, N.M. Goldberg, K.B. Hicks, Bench-scale fluidized-bed pyrolysis of switchgrass for bio-oil production. *Ind. Eng. Chem. Res.* **46**, 1891–1897 (2007)
67. A. Pattiya, Bio-oil production via fast pyrolysis of biomass residues from cassava plants in a fluidised-bed reactor. *Biores. Technol.* **102**, 1959–1967 (2011)
68. A. Chandrasekaran, S. Ramachandran, S. Subbiah, Modeling, experimental validation and optimization of *Prosopis juliflora* fuelwood pyrolysis in fixed-bed tubular reactor. *Biores. Technol.* **264**, 66–77 (2018)
69. F. Ates, S. Tophanecioglu, A.E. Putun, The evaluation of mesoporous materials as catalyst in fast pyrolysis of wheat straw. *Int. J. Green Energy* **12**, 57–64 (2015)
70. U. Morali, S. Sensoz, Pyrolysis of hornbeam shell (*Carpinus betulus* L.) in a fixed bed reactor: characterization of bio-oil and bio-char. *Fuel* **150**, 672–678 (2015)
71. H.S. Choi, D. Meier, Fast pyrolysis of Kraft lignin—vapor cracking over various fixed-bed catalysts. *J. Anal. Appl. Pyrol.* **100**, 207–212 (2013)
72. M. Ertaş, M.H. Alma, Pyrolysis of laurel (*Laurus nobilis* L.) extraction residues in a fixed-bed reactor: characterization of bio-oil and bio-char. *J. Anal. Appl. Pyrol.* **88**, 22–29 (2010)
73. W.N.R.W. Isahak, M.W. Hisham, M.A. Yarmo, T.Y.Y. Hin, A review on bio-oil production from biomass by using pyrolysis method. *Renew. Sustain. Energy Rev.* **16**, 5910–5923
74. T.L. Duong, D.T. Nguyen, H.H.M. Nguyen, B.M.Q. Phan, H.L. Nguyen, T.M. Huynh, Fast pyrolysis of Vietnamese waste biomass: relationship between biomass composition, reaction conditions, and pyrolysis products, and a strategy to use a biomass mixture as feedstock for bio-oil production. *J. Mater. Cycl. Waste Manag.* 1–9 (2019)
75. S. Kelkar, C.M. Saffron, L. Chai, J. Bovee, T.R. Stuecken, M. Garedew, R.M. Kriegel, Pyrolysis of spent coffee grounds using a screw-conveyor reactor. *Fuel Process. Technol.* **137**, 170–178 (2015)
76. P. Bhattacharya, P.H. Steele, M.H. El Barbary, B. Mitchell, L. Ingram, C.U. Pittman, Wood/plastic co pyrolysis in an auger reactor: Chemical and physical analysis of the products. *Fuel* **88**, 1251–1260 (2009)
77. S. Thangalazhy-Gopakumar, S. Adhikari, H. Ravindran, R.B. Gupta, O. Fasina, M. Tu, S.D. Fernando, Physiochemical properties of bio-oil produced at various temperatures from pine wood using an auger reactor. *Biores. Technol.* **101**, 8389–8395 (2010)
78. M. Carrier, T. Hugo, J. Gorgens, H. Knoetze, Comparison of slow and vacuum pyrolysis of sugar cane bagasse. *J. Anal. Appl. Pyrolysis* **90**, 18–26 (2011)

79. M. Tripathi, J.N. Sahu, P. Ganesan, Effect of process parameters on production of biochar from biomass waste through pyrolysis: a review. *Renew. Sustain. Energy Rev.* **55**, 467–481 (2016)
80. X. Li, X. Zhang, S. Shao, L. Dong, J. Zhang, C. Hu, Y. Cai, Catalytic upgrading of pyrolysis vapor from rape straw in a vacuum pyrolysis system over La/HZSM-5 with hierarchical structure. *Biores. Technol.* **259**, 191–197 (2018)
81. K.B. Ansari, V.G. Gaikar, Investigating production of hydrocarbon rich bio-oil from grassy biomass using vacuum pyrolysis coupled with online deoxygenation of volatile products over metallic iron. *Renew. Energy* **130**, 305–318 (2019)
82. Y. Zheng, Y. Zhang, J. Xu, X. Li, C.C. Xu, Co-pyrolysis behavior of fermentation residues with woody sawdust by thermogravimetric analysis and a vacuum reactor. *Biores. Technol.* **245**, 449–455 (2017)
83. S. Thangalazhy-Gopakumar, S. Adhikari, Fast pyrolysis of agricultural wastes for bio-fuel and biochar, in *Recycling of Solid Waste for Biofuels and Bio-chemicals*, pp. 301–332 (Springer, Singapore, 2016)
84. G. Luo, D.S. Chandler, L.C. Anjos, R.J. Eng, P. Jia, F.L. Resende, Pyrolysis of whole wood chips and rods in a novel ablative reactor. *Fuel* **194**, 229–238 (2017)
85. A.A. Kumar, conceptual comparison of bioenergy options for using mountain pine beetle infested wood in Western Canada. *Bioresour. Technol.* **100**, 387–399 (2009)
86. X. Lian, Y. Xue, Z. Zhao, G. Xu, S. Han, H. Yu, Progress on upgrading methods of bio-oil: a review. *Int. J. Energy Res.* **41**(13), 1798–1816 (2017)
87. J.A. Oyebanji, P.O. Okekunle, O.A. Lasode, S.O. Oyedepo, Chemical composition of bio-oils produced by fast pyrolysis of two energy biomass. *Biofuels* **9**(4), 479–487 (2018)
88. E. Lazzari, T. Schena, C.T. Primaz, G.P. da Silva Maciel, M.E. Machado, C.A. Cardoso, E.B. Caramão, Production and chromatographic characterization of bio-oil from the pyrolysis of mango seed waste. *Ind. Crops Prod.* **83**, 529–536 (2016)
89. F. Yu, S. Deng, P. Chen, Y. Liu, Y. Wan, A. Olson, R. Ruan, Physical and chemical properties of bio-oils from microwave pyrolysis of corn stover. *Appl. Biochem. Biotechnol.* **137**(1–12), 957–970 (2007)
90. J. Lédé, F. Broust, F.T. Ndiaye, M. Ferrer, Properties of bio-oils produced by biomass fast pyrolysis in a cyclone reactor. *Fuel* **86**(12–13), 1800–1810 (2007)
91. T. Ba, A. Chaala, M. Garcia-Perez, D. Rodrigue, C. Roy, Colloidal properties of bio-oils obtained by vacuum pyrolysis of softwood bark, Characterization of water-soluble and water-insoluble fractions. *Energy Fuels* **18**(3), 704–712 (2004)
92. Q. Lu, X.L. Yang, X.F. Zhu, Analysis on chemical and physical properties of bio-oil pyrolyzed from rice husk. *J. Anal. Appl. Pyrol.* **82**(2), 191–198 (2008)
93. L. Ingram, D. Mohan, M. Bricka, P. Steele, D. Strobel, D. Crocker, C.U. Pittman, Pyrolysis of wood and bark in an auger reactor: physical properties and chemical analysis of the produced bio-oils. *Energy Fuels* **22**(1), 614–625 (2007)
94. D. Özçimen, F. Karaosmanoğlu, Production and characterization of bio-oil and biochar from rapeseed cake. *Renew. Energy* **29**(5), 779–787 (2004)
95. E. Çulcuoglu, E. Ünay, F. Karaosmanoglu, D. Angin, S. Şensöz, Characterization of the bio-oil of rapeseed cake. *Energy Sources* **27**(13), 1217–1223 (2005)
96. R. Liu, C. Deng, J. Wang, Fast pyrolysis of corn straw for bio-oil production in a bench-scale fluidized bed reactor. *Energy Sour. Part A: Recovery, Util. Environ. Effects* **32**(1), 10–19 (2009)
97. L. Li, H. Zhang, Production and characterization of pyrolysis oil from herbaceous biomass (*Achnatherum Splendens*). *Energy Sour. Part A: Recovery Util. Environ. Effects* **27**(4), 319–326 (2005)
98. Q. Zhang, J. Chang, T. Wang, Y. Xu, Review of biomass pyrolysis oil properties and upgrading research. *Energy Convers. Manage.* **48**(1), 87–92 (2007)
99. K.H. Kim, T.S. Kim, S.M. Lee, D. Choi, H. Yeo, I.G. Choi, J.W. Choi, Comparison of physicochemical features of biooils and biochars produced from various woody biomasses by fast pyrolysis. *Renew. Energy* **50**, 188–195 (2013)

100. S.W. Kim, B.S. Koo, J.W. Ryu, J.S. Lee, C.J. Kim, D.H. Lee, S. Choi, Bio-oil from the pyrolysis of palm and Jatropha wastes in a fluidized bed. *Fuel Process. Technol.* **108**, 118–124 (2013)
101. N. Ibrahim, P.A. Jensen, K.K. Dam-Johansen, M. Ka, Experimental investigation of flash pyrolysis oil droplet combustion. *Chem. Eng.* **32** (2013)
102. I. Demiral, E.A. Ayan, Pyrolysis of grape bagasse: effect of pyrolysis conditions on the product yields and characterization of the liquid product. *Biores. Technol.* **102**(4), 3946–3951 (2011)
103. M.E. Boucher, A. Chaala, C. Roy, Bio-oils obtained by vacuum pyrolysis of softwood bark as a liquid fuel for gas turbines. Part I: Properties of bio-oil and its blends with methanol and a pyrolytic aqueous phase. *Biomass Bioenergy* **19**(5), 337–350 (2000)
104. D. Radlein, Study of levoglucosan production—a review fast pyrolysis of biomass. *A Handbook* **2**(6), 205–241 (2002)
105. Q. Lu, W.Z. Li, X.F. Zhu, Overview of fuel properties of biomass fast pyrolysis oils. *Energy Convers. Manage.* **50**(5), 1376–1383 (2009)
106. R.J. Westerhof, N.J. Kuipers, S.R. Kersten, W.P. van Swaaij, Controlling the water content of biomass fast pyrolysis oil. *Ind. Eng. Chem. Res.* **46**(26), 9238–9247 (2007)
107. R. Fahmi, A.V. Bridgwater, I. Donnison, N. Yates, J.M. Jones, The effect of lignin and inorganic species in biomass on pyrolysis oil yields, quality and stability. *Fuel* **87**(7), 1230–1240 (2008)
108. M. Garcia-Perez, X.S. Wang, J. Shen, M.J. Rhodes, F. Tian, W.J. Lee, C.Z. Li, Fast pyrolysis of oil mallee woody biomass: effect of temperature on the yield and quality of pyrolysis products. *Ind. Eng. Chem. Res.* **47**(6), 1846–1854 (2008)
109. F. Abnisa, W.W. Daud, W.N.W. Husin, J.N. Sahu, Utilization possibilities of palm shell as a source of biomass energy in Malaysia by producing bio-oil in pyrolysis process. *Biomass Bioenerg.* **35**(5), 1863–1872 (2011)
110. M. Asadullah, M.A. Rahman, M.M. Ali, M.S. Rahman, M.A. Motin, M.B. Sultan, M.R. Alam, Production of bio-oil from fixed bed pyrolysis of bagasse. *Fuel* **86**(16), 2514–2520 (2007)
111. A. Oasmaa, E. Leppawaki, P. Koponen, J. Levander, E. Topola, Physical characterisation of biomassbased pyrolysis liquids, in *Application of Standard Fuel Oil Analyses* (VTT OFFSETPAINO, 1997)
112. M.A. Nazha, R.J. Crookes, Combustion characteristics at elevated pressures of plant derived oils, in *Proceedings of Applied Energy Research Conference*, pp. 91–102 (1989)
113. Y. Xu, X. Hu, W. Li, Y. Shi, Preparation and characterization of bio-oil from biomass, in *Progress in Biomass and Bioenergy Production* (InTech, 2011)
114. A. Oasmaa, S. Czernik, Fuel oil quality of biomass pyrolysis oils state of the art for the end users. *Energy Fuels* **13**(4), 914–921 (1999)
115. R. He, X.P. Ye, B.C. English, J.A. Satrio, Influence of pyrolysis condition on switchgrass bio-oil yield and physicochemical properties. *Biores. Technol.* **100**(21), 5305–5311 (2009)
116. S. Yin, R. Dolan, M. Harris, Z. Tan, Subcritical hydrothermal liquefaction of cattle manure to bio- oil: effects of conversion parameters on bio-oil yield and characterization of bio-oil. *Biores. Technol.* **101**(10), 3657–3664 (2010)
117. A. Oasmaa, C. Peacocke, *A Guide to Physical Property Characterisation of Biomass-Derived Fast Pyrolysis Liquids* (Technical Research Centre of Finland, Espoo, 2001)
118. A. Oasmaa, D. Meier, Analysis, characterization and test methods of fast pyrolysis liquids. *Fast Pyrolysis of Biomass: A Handbook* **2**, 23–40 (2002)
119. R. Yin, R. Liu, Y. Mei, W. Fei, X. Sun, Characterization of bio-oil and bio-char obtained from sweet sorghum bagasse fast pyrolysis with fractional condensers. *Fuel* **112**, 96–104 (2013)
120. T. Milne, A.H. Brennan, B.H. Glenn, *Source Book of Methods of Analysis for Biomass and Biomass Conversion Processes* (Springer Science & Business Media, 1990)
121. C. Sheng, J.L.T. Azevedo, Estimating the higher heating value of biomass fuels from basic analysis data. *Biomass Bioenerg.* **28**(5), 499–507 (2005)
122. J. Wildschut, F.H. Mahfud, R.H. Venderbosch, H.J. Heeres, Hydrotreatment of fast pyrolysis oil using heterogeneous noble-metal catalysts. *Ind. Eng. Chem. Res.* **48**(23), 10324–10334 (2009)

123. R.H. Liu, C.J. Shen, H.J. Wu, C.J. Deng, S.Y. Liu, Characterisation of bio-oil from fast pyrolysis of rice husk in a fluidised bed reactor. *J. Energy Inst.* **84**(2), 73–79 (2011)
124. B.S. Kang, K.H. Lee, H.J. Park, Y.K. Park, J.S. Kim, Fast pyrolysis of radiata pine in a bench scale plant with a fluidized bed: influence of a char separation system and reaction conditions on the production of bio-oil. *J. Anal. Appl. Pyrol.* **76**(1–2), 32–37 (2006)
125. R. Andrews, P.C. Patnaik, Q. Liu, R. Thamburaj, Firing fast pyrolysis oil in turbines. In *Biomass Pyrolysis Oil Properties and Combustion Meeting* (1994)
126. F.C. Lujaji, A.A. Boateng, M.A. Schaffer, C.A. Mullen, I.S. Mkilaha, P.L. Mtui, Pyrolysis oil combustion in a horizontal box furnace with an externally mixed nozzle. *Energy Fuels* **30**(5), 4126–4136 (2016)
127. S.S. Hou, W.C. Huang, F. Rizal, T.H. Lin, Co-firing of fast pyrolysis bio-oil and heavy fuel oil in a 300-kWth furnace. *Appl. Sci.* **6**(11), 326 (2016)
128. O. Sippula, K. Huttunen, J. Hokkinen, S. Kärki, H. Suhonen, T. Kajolinna, P. Yli-Pirilä, Emissions from a fast-pyrolysis bio-oil fired boiler: comparison of health-related characteristics of emissions from bio-oil, fossil oil and wood. *Environ. Pollut.* **248**, 888–897 (2019)
129. X. Yuan, X. Ding, L. Leng, H. Li, J. Shao, Y. Qian, G. Zeng, Applications of bio-oil-based emulsions in a DI diesel engine: the effects of bio-oil compositions on engine performance and emissions. *Energy* **154**, 110–118 (2018)
130. A.-S. Ramadhas, S. Jayaraj, C. Muraleedharan, Characterization and effect of using rubber seed oil as fuel in the compression ignition engines. *Renewable Energy* **30**(5), 795–803 (2005)
131. B. Van de Beld, E. Holle, J. Florijn, The use of pyrolysis oil and pyrolysis oil derived fuels in diesel engines for CHP applications. *Appl. Energy* **102**, 190–197 (2013)
132. D.-A.-R. de Castro, H.J. da Silva Ribeiro, C.C. Ferreira, M. de Andrade Cordeiro, L.H.H. Guerreiro, A.M. Pereira, R.L. Oliveira, Fractional distillation of bio-oil produced by pyrolysis of Açaí (*Euterpe oleracea*) seeds, in *Fractionation* (IntechOpen, 2019)
133. M. Buffi, A. Cappelletti, A.M. Rizzo, F. Martelli, D. Chiaramonti, Combustion of fast pyrolysis bio-oil and blends in a micro gas turbine. *Biomass Bioenerg.* **115**, 174–185 (2018)
134. J.M. Kasper, G.B. Jasas, R.L. Trauth, Use of pyrolysis-derived fuel in a gas turbine engine, in *ASME 1983 International Gas Turbine Conference and Exhibit (1983, March)*, pp. V003T06A016–V003T06A016 (American Society of Mechanical Engineers, 1983)
135. A.V. Bridgwater, Biomass fast pyrolysis. *Therm. Sci.* **8**, 21–50 (2014)

Bayesian Regularization Neural Network-Based Fault Detection System in HVDC Transmission System



Aditya S. Londhe, Aashutosh S. Ingale, and Chetan B. Khadse

Abstract The artificial neural network-based fault detection system in the HVDC transmission line is proposed in this paper. The Bayesian regularization neural network is used to detect as well as classify the faults. The training and testing are done in the MATLAB/Simulink. A model of the HVDC transmission line is simulated to get the data of the healthy as well as faulty conditions. This data is used for the training of the neural network. The neural network model is generated after training is used for the testing. The faults considered in this paper are line-to-line and line-to-ground fault for the DC link. The faults at the converter side are AC faults like a line-to-ground, line-to-line, double-line-to-ground, triple-line, and triple-line-to-ground faults. The detection and classification of these faults are also considered in this paper.

Keywords Fault detection · HVDC system · Neural network

1 Introduction

The HVDC transmission system is known for the transfer of bulk power over a distance of 500 km in an efficient manner. In the case of long distances, DC transmission is proved to be superior to AC transmission due to the fewer line losses. However, the faults like line-to-ground fault and line-to-line fault in the DC line severely affect the operation of the transmission in the HVDC system. These two faults are dominant as well as frequently occurring faults. Along with these faults, symmetrical and unsymmetrical AC faults occur at the converter side. These faults affect the HVDC system stability which may result in a malfunction of valves, misfiring of power electronics switches, and short circuit across converter stations.

Various methods are reported in the literature for the clearing of faults such as use of fast circuit breakers, fast protective relaying algorithms, open grid protection, and grid splitting protection. The reliability of these all fault clearing methods depends

A. S. Londhe (✉) · A. S. Ingale · C. B. Khadse
MIT World Peace University, Pune, Maharashtra, India

© The Author(s), under exclusive license to Springer Nature Singapore Pte Ltd. 2022
M. L. Kolhe et al. (eds.), *Smart Technologies for Energy, Environment and Sustainable Development, Vol 1*, Springer Proceedings in Energy,
https://doi.org/10.1007/978-981-16-6875-3_48

601

upon the fast detection and classification of faults on either DC side or an AC side. The accurate and fast estimation of faults lead to the fast clearing of faults. The fault detection system based on machine learning is proposed in [1]. The K-nearest neighbour (KNN) and support vector machine (SVM) are used as machine learning methods. These two methods eliminated the signal processing of fault which results into fast detection and classification. Fuzzy logic-based fault analysis is reported in [2]. In this paper, a fuzzy inference engine is proposed for the fault detection of voltage source-controlled HVDC system. In [3], the rate of change of voltage (ROCOV) is compared to determine the direction of fault currents. The local measurement and this ROCOV-based fault detection system are proved to be effective.

The artificial neural network (ANN) is proved to be the best in many pattern-based detection and classification systems. As there is a pattern of signal changes for healthy and faulty conditions in HVDC system, ANN can be used to estimate the faults. In literature, neural network is used for various applications such as medical, engineering, astronomy, and many more. The power quality disturbances are detected and classified with the help of neural network in [4–6]. The scaled conjugate backpropagation is used to identify the disturbances like sag, swell, harmonics, and interruption. A diffuse optical tomography and convolutional neural network-based breast cancer detection is proposed in [7]. An ensemble classifier and deep neural network-based lung cancer detection are proposed in [8]. Neural pattern recognition-based fault diagnosis of bevel gears is proposed in [9]. Hence, artificial neural network is proved to be the best tool for the automatic detection in various applications.

In this paper, artificial neural network is used for the detection of DC line faults as well as AC line faults in HVDC system. A system is modelled in MATLAB which provides the data for the training and testing of the neural network. In the second section of the paper, HVDC system in which fault is created and fault data acquisition is explained. In the third section, neural network training and testing is explained. In the fourth section, conclusion remarks are given.

2 HVDC System for Data Generation

The neural network proposed here is based on supervised learning. Hence, input and target matrices are known. The input matrix is generated with the help of the HVDC system modelled in MATLAB/Simulink. The model is built with the following components: three-phase voltage source, transformer, three-phase V-I measurements, universal bridge rectifiers and converters, fault creation block, three-phase harmonic filter, and three-phase load. The power begins to flow from three-phase voltage sources. It is being monitored by the three-phase V-I measurement block. Further, the power will flow towards the converter transformer. The configuration of this transformer is star-delta, and the purpose of this transformer is to step up the voltage. This power will continue towards the first universal converter block (rectifier). The AC power will be converted into DC power that will flow through the DC link (conductor). During this interval, there is an introduction to the various types of

faults carried on the DC link. These faults are mostly line to line (L-L) and line to ground (L-G). After this, the power from the DC link will flow towards the second universal converter block (inverter). The DC power is again converted into AC power (Fig. 1).

The generation of the power is shown by the three-phase source block. In this block, the parameter of the voltage is set to 380 kV (AC) and the frequency is set 50Hz. The internal impedance such as resistance and inductance is configured accordingly. Then, there is a three-phase V-I measurement block where voltage and current are monitored by connecting it to the scope. After that, the power will flow towards the three-phase transformer block. This transformer consists of two windings. The voltage is stepped up from 380 kV to 500 kV. The frequency is set 50Hz. The configuration of the magnetizing resistance and inductance is done accordingly. The value of nominal power is set to 1500 MW. Next, there is a three-phase harmonic filter block which will protect the circuit from harmonics. Now the AC power is converted to DC power with the help of a universal bridge rectifier block. This block consists of three bridge arms on the input and two outputs. The internal resistance is adjusted to 5500 for the flowing of 500 kV on the DC link. After that, the two types of faults are introduced by a fault block which is line to line and line to ground. The power is again inverted into AC by using a universal bridge inverter. Then, it will pass through the three-phase transformer block again to step down to the 360 kV, and then it will be monitored by the three-phase VI measurement block. Now the power will flow to the load block.

3 The Neural Network for the Fault Detection

The fault data generated from the simulation model is used to train the network. The simulation is run for 10s with 10,000 samples. As the fault is created for the limited time such as 4–6s, the pattern is changed for the time. The pattern for the healthy condition is different and the pattern for 4–6s is different. Hence, the input matrix is of 10,000 samples with healthy and faulty pattern. Healthy samples are from 1 to 4000 and 6001 to 10,000. Faulty samples are from 4001 to 6000. According to this input matrix, a target matrix is built in the workspace of MATLAB of the dimension $10,000 \times N$. Where N is the number of faults considered. If only 1 fault is considered, then the dimension of target matrix will be $10,000 \times 1$. In this case, the elements of the target matrix are 0 for 1–4000 and 6001–10,000 samples. The elements in faulty conditions, i.e. from 4001 to 6000, are put as 1, hence 0 or low signal for healthy condition and 1 or high for faulty conditions.

These input and target matrices are given as an input to the training of neural network. The neural network toolbox, *nprtool* is used for the training. The input data samples are divided into training sample, testing sample, and validation sample in the proportion of 70, 15, and 15%, respectively. The learning algorithm used is *Bayesian Regularization*. The training performance, gradient and validation checks are shown in Figs. 2 and 3. The neural network parameters and its specifications are

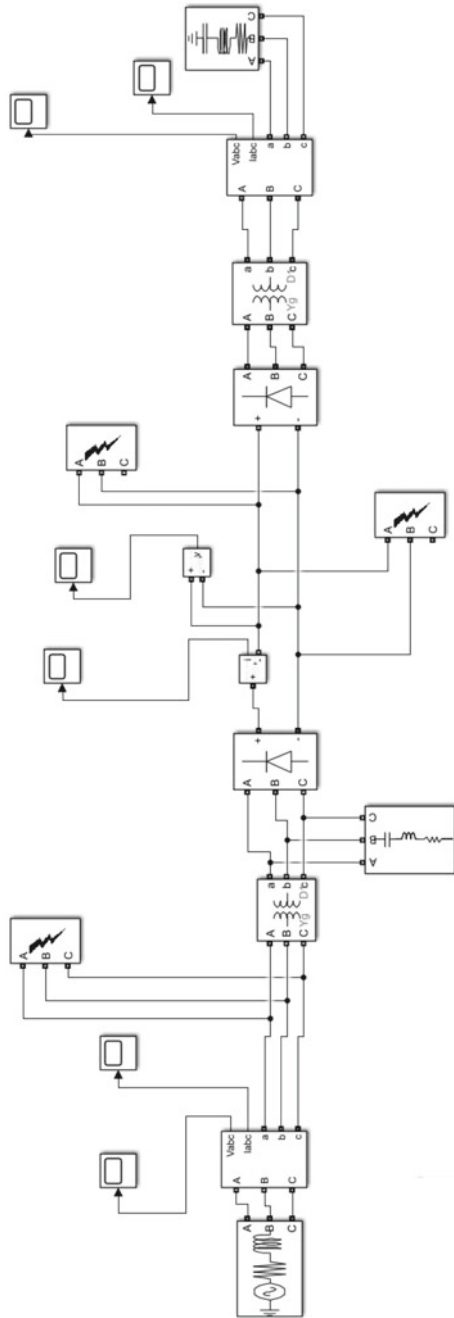


Fig. 1 HVDC system for fault creation

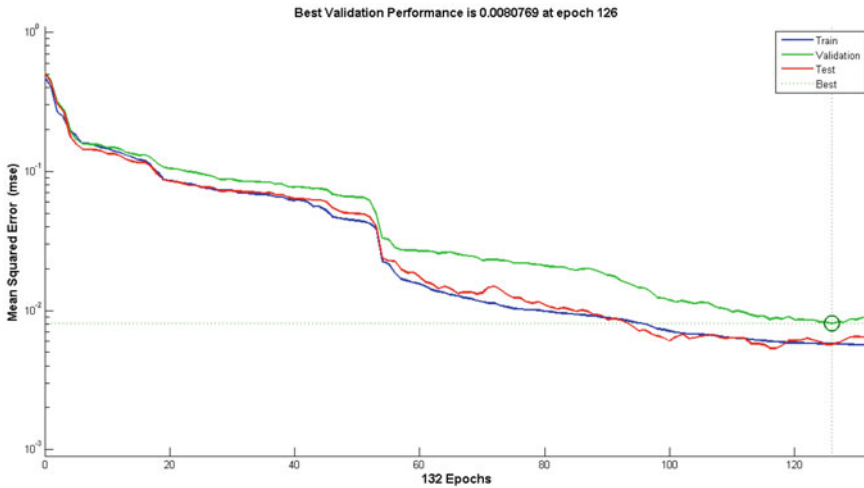
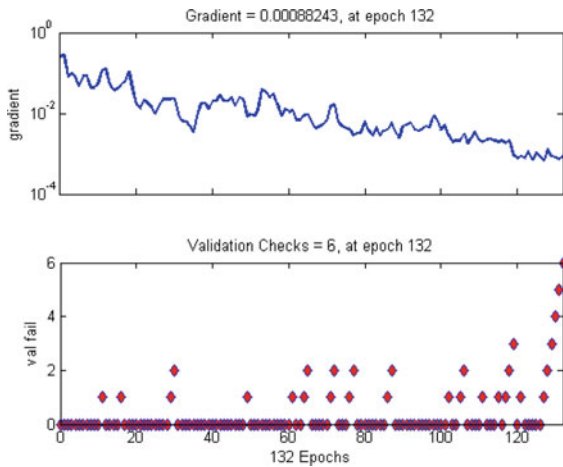


Fig. 2 Performance curve of training

Fig. 3 Gradient and validation checks



mentioned in Table 1. The iterations or epochs required to train the networks are 126 in which minimum gradient and validation checks are achieved. The training is done, and the simulation model of the trained network is created using *gensim* command. This generated model is used with HVDC system for the testing.

The testing of the neural network is performed by considering two DC line faults and five AC line faults. In DC line faults, DC line-to-ground and DC line-to-line faults are considered. In AC line faults, line-to-ground, line-to-line, double-line-to-ground, triple-line, and triple-line-to-ground faults are considered. The testing results are shown in Table 2. The triple-line-to-ground fault is detected and classified most accurately with the proposed system. However, double line to ground is identified

Table 1 The neural network training parameters

Network parameter	Specification
Algorithm	Bayesian regularization
Activation function	logsigmoid
No. of neurons	30
Data split-up method	Random
Performance	Mean squared error

Table 2 The testing results of trained neural network

Fault type	Accuracy in percentage
DC line to line	92
DC line to ground	94
Line to ground	94
Line to line	92
Double line to ground	90
Triple line	94
Triple line to ground	96

least accurately, i.e. with 90% accuracy. The accuracy is calculated by the ratio of number of accurate cases to the total number cases. A total of 50 different cases of faults are considered for the testing. Hence, out of 50 cases how many cases are detected and classified accurately gives the accuracy of the proposed method.

4 Conclusion

The proposed neural network-based fault detection system accurately detected the DC line as well as AC line faults. The training of the neural network with Bayesian regularization algorithm is proved to be successful for the HVDC system. The triple-line-to-ground AC fault is detected accurately with 96% of accuracy with the proposed method. However, the least accuracy is observed in case of double-line-to-ground fault which is 90%. The feature extraction process before the training may increase the accuracy of the proposed system.

References

1. M. Chen, S. Lan, D. Chen, Machine learning based one-terminal fault areas detection in HVDC transmission system, in *8th International Conference on Power and Energy Systems (ICPES)* (IEEE Press, Sri Lanka, 2018), pp. 278–282. <https://doi.org/10.1109/ICPESYS.2018.8626976>
2. B. Paily, S. Kumaravel, M. Basu, M. Conlon, Fault analysis of VSC HVDC systems using fuzzy logic, in *IEEE International Conference on Signal Processing, Informatics, Communication and Energy Systems* (IEEE Press, Kozhikode, 2015), pp. 1–5. <https://doi.org/10.1109/SPICES.2015.7091543>

3. N.M. Haleem, A.D. Rajapakse, Application of new directional logic to improve DC side fault discrimination for high resistance faults in HVDC grids. *J. Mod. Power Syst. Clean Energy* **5**, 560–573 (2017). Springer. <https://doi.org/10.1007/s40565-017-0301-4>
4. C. Khadse, M. Chaudhari, V. Borghate, Comparison of seven backpropagation algorithms for three phase power quality assessment, in *IEEE Region 10 Conference (TENCON)* (IEEE Press, Malaysia, 2017), pp. 2548–2553. <https://doi.org/10.1109/TENCON.2017.8228291>
5. C. Khadse, M. Chaudhari, V. Borghate, A laboratory set-up for power quality disturbance generator and real time power quality monitoring, in *IEEE International WIE Conference on Electrical and Computer Engineering* (IEEE Press, Pune, 2016), pp. 61–64. <https://doi.org/10.1109/WIECON-ECE.2016.8009088>
6. C. Khadse, M. Chaudhari, V. Borghate, Electromagnetic compatibility estimator using scaled conjugate gradient backpropagation based artificial neural network, in *IEEE Transaction of Industrial Informatics* (IEEE Press, June, 2017), pp. 1036–1045. <https://doi.org/10.1109/TII.2016.2605623>
7. Q. Xu, X. Wang, H. Jiang, Convolutional neural network for breast cancer diagnosis using diffuse optical tomography. *Vis. Comput. Ind. Biomed. Art* **2**, 1 (2019). <https://doi.org/10.1186/s42492-019-0012>
8. P.M. Shakeel, M.A. Burhanuddin, M.I. Desa, Automatic lung cancer detection from CT image using improved deep neural network and ensemble classifier. *Neural Comput. Appl.* (2020). <https://doi.org/10.1007/s00521-020-04842-6>
9. C. Keleşoğlu, H. Küçük, M. Demetgül, Fault diagnosis of bevel gears using neural pattern recognition and MLP neural network algorithms. *Int. J. Precis. Eng. Manuf.* **21**, 843–856 (2020). <https://doi.org/10.1007/s12541-020-00320-0>

Revisited the Design Technique of Hybrid Dielectric Resonator Antenna



Dipali Soren and Nilesh Tamboli

Abstract This article provides a focused review on Dielectric Resonator Antennas (DRAs) and Microstrip patch Antennas suitable for modern wireless communications. The DRA is having several advantages as compared to the conventional microstrip antennas in many aspects like its compact size as well as very high efficiency. There are various fields in which UWB has been used such as communications and sensors, Radar, home network applications and also huge researches are applying UWB technology to the military and defense sectors. Looking into the various factors, many researchers have analyzed various new geometries and methods to design broadband as well as ultra wideband DRAs. One of the present author investigated a new technique where fractal geometry has been incorporated in conventional shape DRA and achieved enhanced bandwidth for X-band, WiMax and WLAN applications. In this article, all the noteworthy fraction of new techniques along with few recent contributions will be discussed by the present authors.

Keywords Dielectric resonator antenna · Patch antenna · Hybrid DRA

1 Introduction

A fast and revolutionary growth has been seen in the field of wireless communications in the past years. Some 15 years ago, the invention of portable mobile phones attributed the growth in wireless communications. After the 2G technologies which enabled the various cellular networks to provide the efficient communication services, the development of 3G technologies which provides high-speed bandwidth and high-data transfer rates to cellular phones and other services like IR wireless communication, satellite communication, broadcast radio, Microwave radio, Bluetooth, wireless local area networks, home RF, etc., gives the new directives. The

D. Soren (✉)

ETCE Department, Christian College of Engineering Technology, Bhilai, Chhattisgarh, India

N. Tamboli

ETCE Department, Lakhmi Chand Institute of Technology, Bilaspur, Chhattisgarh, India

fundamental component is the antenna for a wireless network or device. To maintain safety and portability, the highly preferable wireless devices are of low power, multi-functional and multi-band. All these severe requirements that can be made embedded into wireless products which demand the development of antenna with reasonable size, i.e., small height and width, high efficiency, lower VSWR, high-impedance matching, high gain, wide bandwidth, etc.

Two types of innovative antennas have been investigated and broadly reported on in the last 2 decades. They are the dielectric resonator antenna and the microstrip patch antenna. Both the antennas plays a significant role in the development of contemporary wireless communications. Recently, due to the attractive features of dielectric resonator antenna compared to more conventional microstrip antennas researchers studied extensively and analyzed various broad banding technique of DRA.

As a substitute to the microstrip patch antenna the DRA started its journey in 1983 [1, 2]; since then, it has been investigated extensively due to various features like its small dimension, high-radiation efficiency, simple coupling, wide operating bandwidth and simple feeding techniques. In modern microwave and wireless communication there are two alternatives antennas, i.e., microstrip patch antenna and dielectric resonators antennas (DRAs). Although DRA having several inherent limitations, like substantial properties of the material, their fabrication and measurement for various application still the antenna researchers has been greatly involved in DRA research in recent years.

The microstrip antenna initiated in 1953 [3] but a decade before the inception of DRA between 1972 and 1974 [4, 5] microstrip antenna earned attention by the antenna researchers. After the inception of DRA in 1980s, a revolutionary changes have been observed. Almost in every sector of wireless and microwave communications, dielectric resonator antenna occupied even in our day-to-day life. Although some inbuilt limitations were there like narrow bandwidth, high cross-polarization radiation, etc., which has been addressed and resolved [6–12]. At higher frequencies due to several other attractive features, the DRA appears to be a possible substitution for the microstrip patch antenna.

In reality, microstrip patch antenna and dielectric resonator antenna are very close to each other in some aspects like feeding mechanisms, radiation patterns, etc. But both of them are their individual potential and qualities. So far very few works [13–15] have addressed their comparative study.

2 Various Geometries

A review of some research work on microstrip patch and dielectric resonator antenna over last three decades are presented in this article. Significant research activities of each decade are summarized and focused here. It may act as a reference for researchers who are new in the field of microwave communication will get better

understanding, considering them as alternatives for new designs and compare the performance with new designs. This section is broadly classified in three categories.

Dielectric Resonator Antenna (DRA)

In 1939, Ritchmyer showed that a block of dielectric material whose dielectric constant is very high would resonate in free space and these resonators exhibits radiation damping [16]. Since in late 1960s, the development of low loss ceramics, in microwave applications dielectric resonators with high Q-factor have been used as antennas. In early eighties, research upon microstrip patch antenna were on full swing around the globe. But various problems arise with microstrip patch antenna while trying to increase the bandwidth. In microstrip, narrow bandwidth can be achieved for electrically thin substrate. But electrically thicker substrate supports surface waves which decreases radiation efficiency and ohmic losses is also high. When dielectric resonators used as antenna how to determine the resonant frequencies has been calculated analytically and verified in [17, 18] which greatly facilitated advancements in design of dielectric resonator antennas (DRAs).

Long et al. developed a dielectric resonator antenna in early 1980s [2]. Dielectric resonator antenna avoids the disadvantages of patch antennas at millimeter wave frequencies. Dielectric resonator antenna is a resonant antenna made with high-dielectric constant material having dielectric constant between 6 and 100, fixed on a ground plane and fed by a coaxial probe, microstrip line or slot coupling in the ground plane. The DRAs are often excited by coaxial probe, microstrip line, aperture coupling or coplanar waveguide feed. To allow the flexibility in design investigations of different shapes like rectangular, cylindrical, hemispherical structures have been carried out theoretical and experimentally. The impedance bandwidth of dielectric resonator antenna is a function of aspect ratio, i.e., length to height ratio of DRA and dielectric constant of the material [19]. To provide low-profile, compactness, broadband the aspect ratio may be adjusted for a specified material permittivity. Antenna size can be reduced using high-dielectric material, while bandwidth can be increased using low-dielectric material. Luk et al. [20] focused the basic properties of dielectric resonator antenna for a variety of common shape and simple feed mechanisms. Dipali et al. presented review on various shape of DRA, feeding mechanisms, bandwidth of DRAs in wideband, multiband, ultra wideband have been explored, since the inception of the concept [21].

Microstrip Patch Antenna with Slot

A microstrip patch antenna is investigated by P.A. Ambers et al. [22]. They have obtained reduced size, high gain, low VSWR and good radiation pattern when a slotted conducting patch is introduced in which as dielectric medium air is filled.

To enhance the bandwidth chia ping lee et al. [23] incorporated a diamond slot in microstrip patch antenna in which they observed bandwidth from 3.28 to 19.64 GHz. For Wi MAX application a compact microstrip patch antenna with multiple T Slot by Rajan Mishra et al. [24] was proposed. In this, they have obtained improved return loss by 22.5 dB at middle frequency range of Wi MAX application and VSWR < 2. A microstrip patch antenna with slot in E and U shapes are combined to make an array

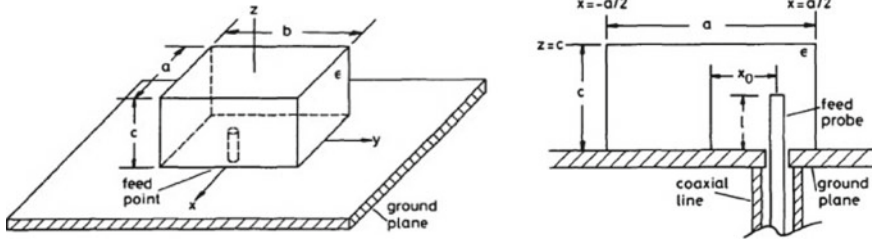


Fig. 1 Rectangular DRA antenna with geometry and feed mechanism [1]

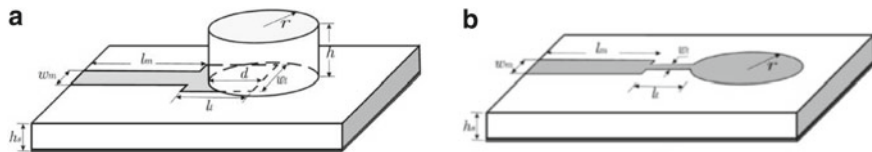


Fig. 2 Configuration of a cylindrical DRA and a circular disk MSA [15]

was proposed by G Aswan Kumar et al. [25]. It gives better result when compared with a rectangular patch antenna and gain and bandwidth is also increased. Tahsin firdous et al. [26] observed improved bandwidth of 506 MHz ranging from 9.872 to 10.378 MHz in an X band rounded patch antenna where a slot of diamond shaped surrounded by the ring of diamond shaped.

To enhanced band width, efficiency, directivity Neelesh Dixit et al. [27] implemented a multiple square slot in microstrip patch antenna. Dual-Band Hexagonal-shaped Microstrip Patch Antenna with L shaped slot proposed by Tanuj Garg et al. [28]. They optimized antenna design with the horizontal length of L slot at which return has highest negative value. An U-shaped slot introduced in a microstrip antenna was proposed where ground structure has been modified to improve the return loss. [29]. For Wi Fi and WMAX application S. Kannadhasan [30] proposed a microstrip patch antenna of U-shaped with improved bandwidth at operating frequency of 3.8 GHz. A parasitic patch along with the main patch antenna was proposed by Mekala Harinath et al. [31]. On study they obtained that hexagonal slot in main patch gives better performance. Xiao Zhang et al. [32] proposed a patch antenna where a straight slot is incorporated in central line of patch and a shorting pin was placed longitudinally. They observed that gain and directivity of the antenna was enhanced.

Dielectric Resonator Antenna with Patch

A dielectric resonator of cylindrical shape and microstrip patch which are arranged in a stacked configuration a unique dual-frequency circularly polarized antenna is presented by Y. Lee et al. [33]. By using four coax feeds in phase quadrature circular polarization is obtained. Leung et al. proposed a aperture-coupled hemispherical

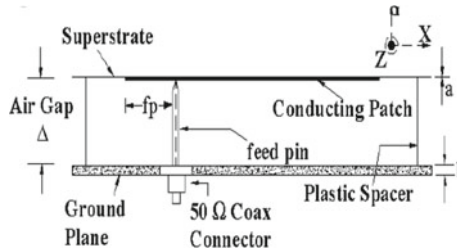


Fig. 3 Slots are loaded on the conducting patch element with thick air dielectric medium sandwiched between superstrate patch and ground plane is excited through single-coax feed arrangement [22]

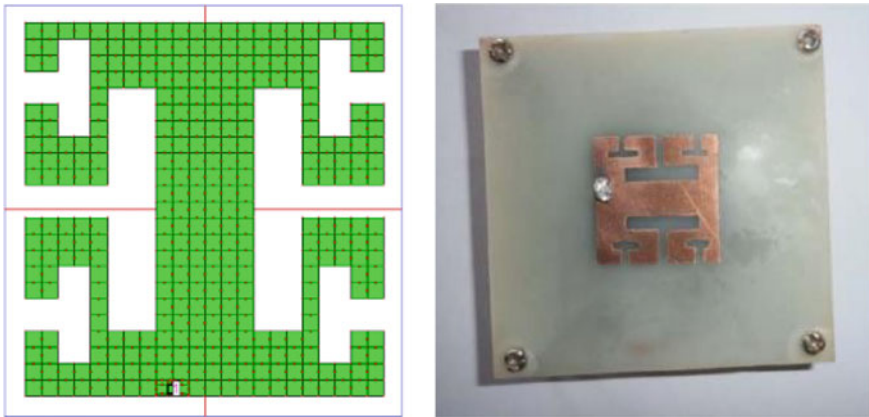


Fig. 4 Simulated geometry of multiple T-slot Antenna and front view of fabricated antenna [24]

dielectric resonator antenna (DRA) with a parasitic patch [34]. It is a linearly polarized antenna and obtained wider bandwidth of 22% compare to without parasitic patch. Since then to design practical DRA patch is applied to DRAs. By varying the size of the loading cap, the resonant frequency of the antenna can be tuned is investigated in a hemispherical dielectric resonator antenna which is slot-coupled, and the antenna is top loaded by a conducting patch [35].

The top of a dielectric resonator when loaded with patch antenna and excited by a coaxial cable is proposed [36]. A wide impedance bandwidth of 57.1% from 3.75 to 6.75 GHz is obtained and a peak gain of 11.5 dB at the center of frequency is seen from the measured results. While compare with the common dielectric resonator antenna an average gain improvement of 3 dB is occurred. Moreover, it offers other advantages also like high gain, large bandwidth and low-fabrication cost compared to other high gain, low bandwidth, complex structured DRAs.

An unique and compact omni-directional circularly polarized (CP) cylindrical dielectric resonator antenna top loaded with a Alford loop is investigated [37]. The DRA is excited by an coaxial probe, which acts as a electric monopole vertically

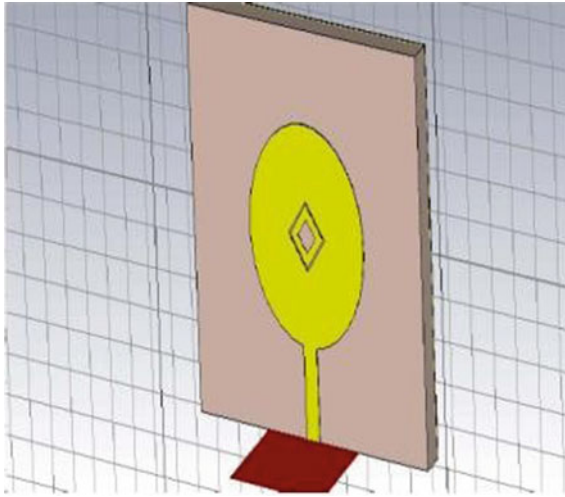


Fig. 5 Front view of a X Band Circular Patch Antenna with Diamond-Shaped Slot and Ring in Patch for UWB Applications [26]



Fig. 6 U-shaped microstrip patch antenna [30]

polarized. The modified Alford loop consists of a rounded patch in center and four curved parts placed on the top of the DRA and an corresponding polarized magnetic dipole provided horizontally. When broadside mode of the DRA excited by a balanced slot and fed by a microstrip line then the broadside radiation pattern is obtained. For WLAN applications, both dielectric resonator antennas (DRA) were designed at 2.4 GHz. Different parameters like reflection coefficients, axial ratios, radiation characteristics, gains, VSWR, efficiencies are studied. Observed closed agreement between the simulated and measured results.

A large bandwidth and high-gain cylindrical Dielectric resonator antenna (DRA) is proposed by F. Kuisheng et al. [38]. To obtain large bandwidth and high gain they used a cylindrical shaped dielectric resonator, a double ring-shaped patch and a metallic cylinder. From the measured results, it has been observed that the DRA with this arrangement achieves a wide bandwidth of 23% from 5.3 to 6.8 GHz, VSWR < 2 and a high gain about 11 dBi.

A common Dielectric Resonator Antenna fed by microstrip patch is investigated for wireless and radar applications [39]. Adjacent resonant modes have been shifted close to each other and merged to enhance the bandwidth. To find the radiation characteristics of antenna using microstrip patch and dielectric resonator with slots a detailed study has been carried out. To improve the radiation characteristics cutting the slot in the best possible position on patch the field distribution has been changed.

Chun-Hsing Li et al. proposed a low-cost and high-gain terahertz on-chip dielectric resonator antenna [40]. The antenna consists of dielectric resonator (DR) which is low loss and made of high-resistivity silicon material. For excitation, the desired electromagnetic (EM) mode a feeding patch is realized on-chip using CMOS technology. To get the required dimension the dielectric resonator antenna is fabricated by wafer dicing method which improves the antenna gain. Moreover, its ground plane which also enhance the antenna efficiency by preventing the electromagnetic field from leaking into the lossy CMOS silicon substrate. The simulated antenna gain is obtained 7.9 dBi, radiation efficiency of 74% at 341 GHz with 7.3% bandwidth.

Pan et al. [41] investigated a one-sided probe-fed rectangular dielectric resonator antenna (RDRA) with a very small ground plane. In that the small ground plane acts as an excitation patch which excites the fundamental mode of the DRA, i.e., TE_{111} mode, the same as magnetic dipole. It has the same e-field and h-field patterns with low back radiation.

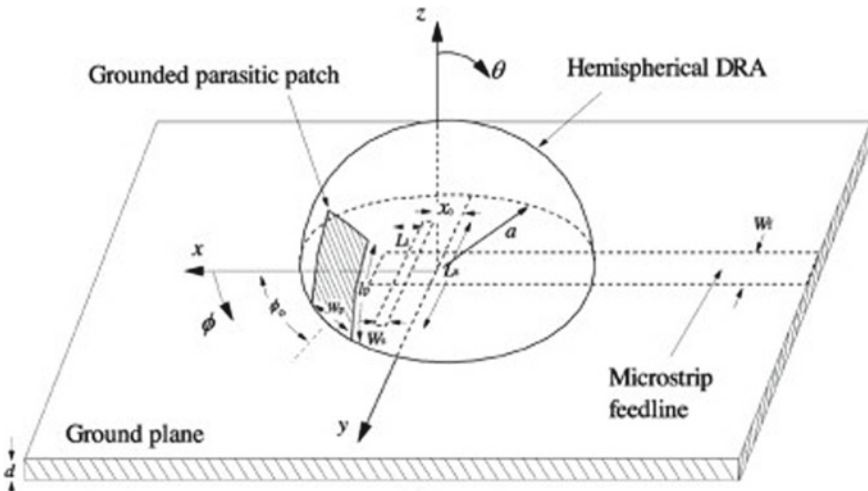


Fig. 7 Perspective view of the aperture-coupled hemispherical DRA with a parasitic patch [34]

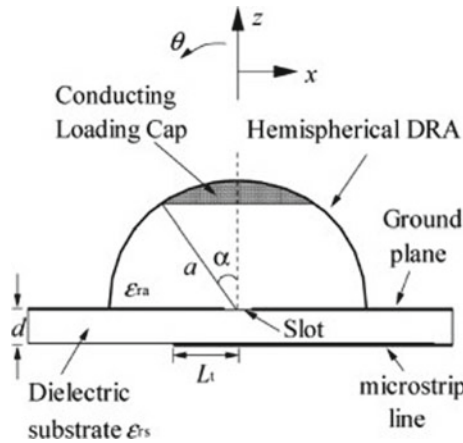


Fig. 8 Side view of the slot-coupled DRA with a conducting loading cap [35]

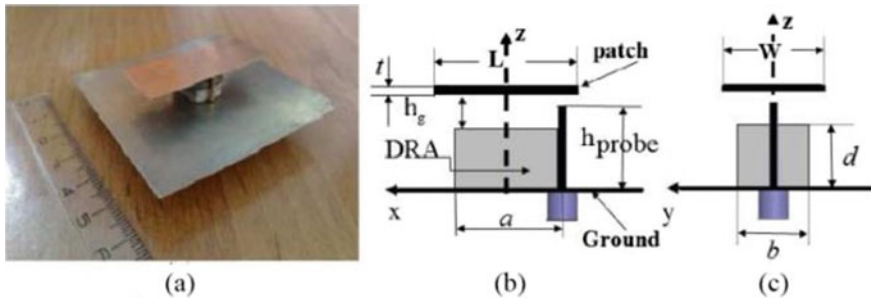


Fig. 9 Structure of a dielectric resonator with top loaded patch antenna, a 3D view, b side view (XZ plane), c side view (YZ plane) [36]

3 Physical Insight into the Wideband DRA Design

Dielectric resonator antenna (DRA) showing broadband performance was introduced [1] and subsequently various papers has been studied. Motivated by various design for broad banding, present authors proposed an hybrid antenna consists of a patch with slot in which a rectangular-shaped DRA is placed in that slot. By doing this, the ultra wideband response has been obtained. The antenna consists of a rectangular patch on FR4 (lossy) material $\epsilon = 4.3$, dimension 50×55 mm, height of $h_s = 1.6$ mm, to enhance the bandwidth a rectangular shaped slot is drilled out and is excited by microstrip feed line. A DRA, ϵ DRA = 2.1 is placed on that slot and both being fitted on a common ground plane as shown in Fig. 10. The impedance bandwidth has improved significantly and ultra wideband is obtained in this method. First, we observed the return loss characteristics of exclusively for patch incorporated on the same ground plane. Then, the return loss characteristic of slot incorporated in patch

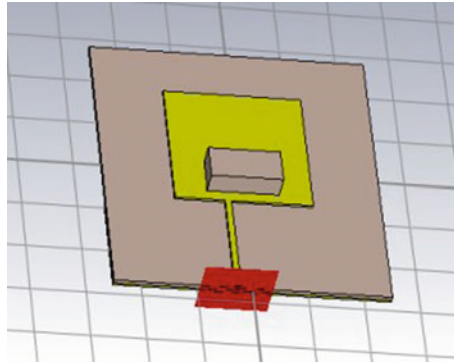


Fig. 10 Panoramic view of hybrid dielectric resonator antenna

has been observed. Finally, a DRA of rectangular shaped placed on slot, and there is an air gap between DRA and inner boundary of the patch. It has been observed from the simulated return loss response that ultra wideband occurs from 2 to 10.5 GHz shown in Fig. 11 when the air gap is introduced with all other parameters being unchanged.

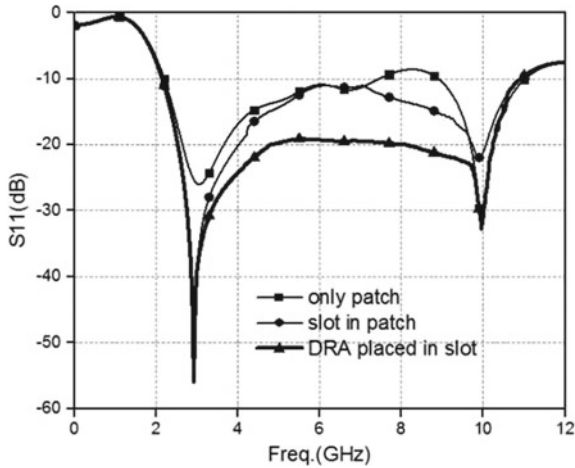


Fig. 11 Simulated return loss characteristics of proposed hybrid dielectric resonator antenna

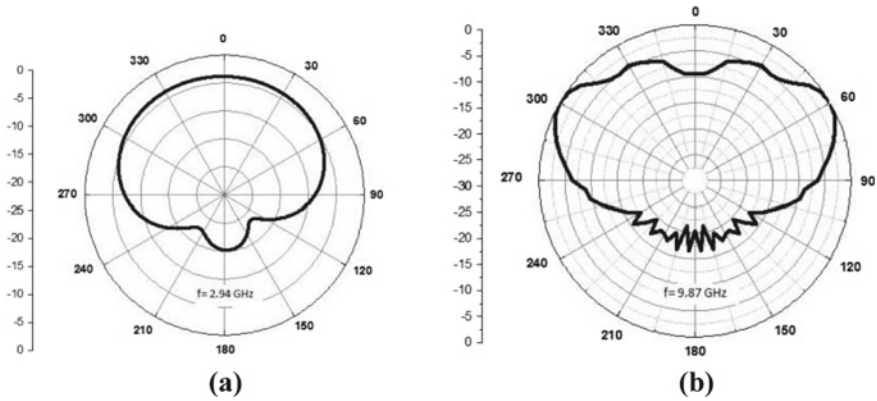


Fig. 12 Simulated E-theta pattern for $\phi = 90^\circ$ at **a** 2.94 GHz and **b** 9.87 GHz, respectively

4 Radiation Characteristics

In all wideband DRA designs which are mentioned in this section, the consistent broadband radiation patterns have been analyzed using experimental as well as simulated results. Some representative results are given here. In our proposed hybrid antenna, the radiation pattern in E-theta for $\phi = 90^\circ$ at $f = 2.94$ GHz and at $f = 9.87$ GHz is appeared in Fig. 12. These outcomes show the broadband radiation qualities inside the band in both cut planes. The antenna peak gain obtained from 5.45 to 6.75 dBi inside the band. The computed efficiency is found to be above 90%.

5 Conclusion

A review on hybrid DRA design techniques are briefly presented in this article. The physical insights of bandwidth enhancement techniques are also discussed. The various techniques mentioned in this article for enhancement of bandwidth provide the antenna designers the wide choice flexibility and design guidance for the implementation of wideband DRAs. The objective is that the information given in this article will allow antenna designer who are new in the field of DRA, to show signs of improvement comprehension of their latent capacity and maybe think about them as options when undertaking new design. For new researcher who are interested in DRA field they can take it as a reference, providing a summarized outline of the design and along with listing benchmark which might help to compare the performance of recent DRA designs.

Acknowledgements This work is supported by the Chhattisgarh Swami Vivekananda Technical University (CSVTU), Bilalai, as Collaborative Research Project under TEQIP-III project number CSVTU/CRP/TEQIP-III/46 Date 05/09/2019.

References

1. M.W. McAllister, S.A. Long, Rectangular dielectric resonator antenna. *IEE Electron. Lett.* **19**(6), 218–219 (1983)
2. S.A. Long, M.W. McAllister, L.C. Shen, The resonant cylindrical cavity antenna. *IEEE Trans. Antennas Propagat.* **31**, 406–412 (1983)
3. G.A. Deschamps, Microstrip microwave antennas, Presented at the 3rd USAF Symposium on Antennas (1953)
4. J.Q. Howell, Microstrip antennas, in *Digital IEEE International Symposium on Antennas Propagation* (1972), pp. 177–180
5. R.E. Munson, Conformal microstrip antennas and microstrip phasedarrays. *IEEE Trans. Antennas Propagat.* **22**(1), 74–78 (1974)
6. R. Garg, P. Bhartia, I. Bahl, A. Ittipiboon, *Microstrip Antenna Design Handbook* (Artech House, Norwood, 2001)
7. D. Guha, Y.M.M. Antar (eds.), *Microstrip and Printed Antennas New Trends, Techniques and Applications* (Wiley, Hoboken, 2010)
8. D.M. Pozar, Microstrip antennas. *Proc. IEEE* **80**(1), 79–91 (1992)
9. A. Petosa, A. Ittipiboon, N. Gagnon, Suppression of unwanted probe radiation in wideband probe-fed microstrip patches. *Electron. Lett.* **35**(5), 355–357 (1999)
10. K.L. Wong, C.L. Tang, J.Y. Chiou, Broad-band probe-fed patch antenna with a W-shaped ground plane. *IEEE Trans. Antennas Propagat.* **50**(6), 827–831 (2002)
11. Z.N. Chen, M.Y.W. Chia, Broad-band suspended probe-fed plate antenna with low cross-polarization level. *IEEE Trans. Antennas Propagat.* **51**(2), 345–346 (2003)
12. C. Kumar, D. Guha, Nature of cross-polarized radiations from probe fed circular microstrip antennas and their suppression using different geometries of defected ground structure (DGS). *IEEE Trans. Antennas Propagat.* **60**(1), 92–101 (2012)
13. A. Petosa, S. Thirakoune, M. Zuliani, A. Ittipiboon, Comparison between planar arrays of perforated DRAs and microstrip patches. *IEEE Antennas Propag. Soc. Int. Symp.* **2A**, 168–175 (2005)
14. R. Chair, A.A. Kishk, K.F. Lee, D. Kajfez, Performance comparisons between dielectric resonator antennas and printed microstrip patch antennas at X-band. *Microwave J.* **49**, 90–104 (2006)
15. Q. Lai, G. Almpanis, C. Fumeaux, H. Benedickter, R. Vahldieck, Comparison of the radiation efficiency for the dielectric resonator antenna and the microstrip antenna at Ka band. *IEEE Trans. Antennas Propagat.* **56**(11), 3589–3592 (2008)
16. R.D. Richtmyer, dielectric resonator. *J. Appl. Phys.* **10**, 391–398 (1939)
17. P. Gullon, Y. Garault, Accurate resonant frequencies of dielectric resonators. *IEEE Trans. Antenna Propag.* **25**(11), 916–922 (1939)
18. J.F. Legier, P. Kennis, S. Toutain, J. Citerne, Resonance frequencies of rectangular dielectric resonators. *IEEE Trans. Microwave Theory Tech.* **28**(9), 1031–1034 (1980)
19. A. Petosa, A. Ittipiboon, Y.M.M. Antar, Roscoe, M. Cuhasi, Recent advances in dielectric resonator antenna technology. *IEEE Antenna Propag Mag* **40**(3):33–47 (1998)
20. K.-M. Luk, K.-W. Leung, *Dielectric Resonator Antenna* (Research Studies Press Ltd., England, 2003)
21. D. Soren, R. Ghatak, R.K. Mishra, D.R. Poddar, Dielectric resonator antennas: design and advances. *J. Prog. Electromagn. Res. B (PIER B)* **60**, 195–213 (2014)
22. P.A. Ambresh, P.M. Hadalgi, P.V. Hunagund, Effect of slots on microstrip patch antenna, characteristics, in *International Conference on Computer, Communication and Electrical Technology* (2011)
23. C.P. Lee, C.K. Chakrabarty, Ultra wideband microstrip diamond slotted patch antenna with enhanced bandwidth. *Int. J. Commun. Netw. Syst. Sci.* 468–474 (2011)
24. R. Mishra, N. Muchhal, R.S. Mishra, Multiple T slot compact & ultra wide band microstrip patch antenna for Wimax applications, in *IEEE Students' Conference on Electrical, Electronics and Computer Science* (2014)

25. G. Aswan Kumar, I.B.A. Sarath, Design and simulation of EU slot microstrip patch antenna for broadband applications. *Int. J. Eng. Sci. Comput.* (2016)
26. T.F.A. Nayna, E. Haque, F. Ahmed, Design of a X band defected ground circular patch antenna with diamond shaped slot and ring in patch for UWB applications, in *International Conference on Signal Processing, Communication, Power and Embedded System (SCOPES)* (2016), pp. 559–562
27. A.A.K.P. Neeleshdixit, Implementation of multiple square slot in microstrip rectangular patch antenna for S-band application, in *Symposium on Colossal Data Analysis and Networking (CDAN)* (2016)
28. T. Garg, Hexagonal shaped slotted microstrip patch antenna. *Int. J. Eng. Sci. Comput.* 2172–2175 (2016)
29. N. Mittal, R. Khanna, J. Kaur, Performance improvement of U-slot microstrip patch antenna for RF portable devices using electromagnetic band gap and defected ground structure. *I.J. Wirel. Microwave Technol.* **3**, 20–28 (2016)
30. S. Kannadhasan, A.C. Shagar, Design and analysis of U-shaped microstrip patch antenna, in *3rd International Conference on Advances in Electrical, Electronics, Information, Communication and Bio-Informatics (AEEICB17)* (2017)
31. M.H. Reddy, R.M. Joany, M. Jayasaichandra Reddy, M. Sugadev, E. Logashanmugam, Bandwidth enhancement of microstrip patch antenna using parasitic patch, in *IEEE International Conference on Smart Technologies and Management for Computing, Communication, Controls, Energy and Materials (ICSTM)* (2017), pp. 295–298
32. X. Zhang, L. Zhu, Gain-enhanced patch antenna without enlarged size via loading of slot and shorting pins. *IEEE Trans. Antennas Propag.* (2017)
33. Y. Lee, J. Yea, R. Mittra, A dual frequency circularly polarized antenna design using a combination of DRA and microstrip patch (2003). 0-7803-7846-6/03IEEE
34. K.W. Leung, H.K. Ng, The slot-coupled hemispherical dielectric resonator antenna with a parasitic patch: applications to the circularly polarized antenna and wide-band antenna. *IEEE Trans. Antennas Propag.* **53**(5) (2005)
35. H.K. Ng, K.W. Leung, Frequency tuning of the dielectric resonator antenna using a loading cap. *IEEE Trans. Antennas Propag.* **53**(3) (2005)
36. S. Fakhte, H. Oraizi, M.H. Vadjed Samiei, A high gain dielectric resonator loaded patch antenna. *Prog. Electromagn. Res. C* **30**, 147–158 (2012)
37. W.W. Li, K.W. Leung, Omnidirectional circularly polarized dielectric resonator antenna with top-loaded Alford loop for pattern diversity design. *IEEE Trans. Antennas Propag.* **61**(8) (2013)
38. K. Feng, N. Li, Q. Meng, Y. Wang, J. Zhang, Study on dielectric resonator antenna with annular patch for high gain and large bandwidth. *Chin. J. Electron.* **24**(4) (2015)
39. G. Varshney, P. Mittal, V.S. Pandey, R.S. Yaduvanshi, S. Pundir, Enhanced bandwidth high gain micro-strip patch feed dielectric resonator antenna. in *International Conference on Computing, Communication and Automation (ICCCA2016)* (2016). ISBN: 978-1-5090-1666-2/16/\$31.00 ©2016 IEEE 1479
40. C.-H. Li, Member, IEEE, T.-Y. Chiu, 340-GHz low-cost and high-gain on-chip higher order mode dielectric resonator antenna for THz applications. *IEEE Trans. Terahertz Sci. Technol.* (2017)
41. Y.M. Pan, K.W. Leung, L. Guo. Compact laterally radiating dielectric resonator antenna with small ground plane. *IEEE Trans. Antennas Propag.* (2017)

A Review on Different Technology Used in Battery Management System of Electric Vehicle



Madina S. Tamboli and Asha Shendge

Abstract The batteries are mostly preferred in wide range of applications such as electric vehicle (EV) due to which managing battery operations become a crucial key factor for better performance as well as their safe and reliable operation. This paper gives a brief review on electric vehicle model, issues related with battery management system, and how they function in overall system, EV main components, and battery cell balancing methods. Firstly, various components and problems associated with battery management system which is used in electric vehicle and are elaborated after which battery management system functions are surveyed, and finally, cell balancing methods are discussed.

Keywords Electric vehicle model · Battery management system · Battery balancing methods

1 Introduction

Electric vehicle (EV) has been widely used in order to provide most promising solution to replace the ongoing internal combustion (IC) engine-based vehicle. Electric vehicles are less common than regular vehicles. The traditional vehicle is heavy-duty, and the electric car is quiet and invisible compared to the conventional car. Electric vehicles have no difficulty whatsoever. There are just a few wiring connections for each unit. Battery has been widely used in electric vehicles as it provides high energy efficiency, low environmental emissions, and a long life cycle [1]. Battery management system (BMS) is used to manage battery operation. Improper operation such as overcurrent and overvoltage causes to battery safety, therefore, the battery management system plays vital role to check whether battery is safe and to get optimized battery performance. Recent problem surveyed firstly on key function of BMS including the battery pack protection performance optimization and health monitoring. This paper

M. S. Tamboli (✉) · A. Shendge
Department of Electrical Engineering, G.H. Rasoni Institute of Engineering and Technology,
Wagholi, Pune, India

© The Author(s), under exclusive license to Springer Nature Singapore Pte Ltd. 2022
M. L. Kolhe et al. (eds.), *Smart Technologies for Energy, Environment and Sustainable Development, Vol 1*, Springer Proceedings in Energy,
https://doi.org/10.1007/978-981-16-6875-3_50

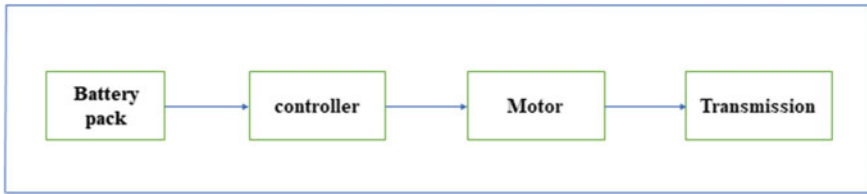


Fig. 1 Standard electric vehicle system

aims to focus on the cell balancing methods especially active and passive balancing methods [1, 2].

2 Electric Vehicle

In internal combustion engine vehicle production, many vehicles used in the world are causing severe environmental and human lives problems. Current challenges are air pollution, global warming, and oil wealth depletion. There are several parts to the electric vehicle. The main electric vehicle part is the battery pack, battery management system (BMS), controller, engines, and transmission unit (Fig. 1).

In battery pack, there are hundreds of cells arranged to form a battery pack. It is required to monitor those cells it can use battery monitoring circuit. The DC voltage from battery cannot be used to drive a motor so it needs to use controller which drives the motor. In the transmission system, rotational energy is transferred from engine to wheel through the gear mechanism.

3 Battery Management System

The battery management system is an electronic system that controls operations to ensure safe and effective operation. With the battery pack and its individual cells, BMS is designed to control all parameters and optimizes battery output [3, 4].

3.1 Function of BMS

The battery management system continuously focuses on parameter such as voltage, current, and temperature. Primary function of BMS is to protect battery cell and it provides thermal management. BMS is sensing electrical isolation in that vehicle chassis and is completely isolated from the high voltage battery pack. All times user prevents from getting an electric shock. The BMS uses collected parameter

temperature, voltage, and current to estimate the state of charge (SOC) and state of health (SOH). BMS is responsible for communication with other electronic control unit in the vehicle. It provides the monitoring and communicate with other display and controls unit of vehicle.

“Secondary function of BMS is balances all cells in battery pack. This provides maximum amount of energy from battery pack to the weakest cell. Monitor the temperature of battery pack and controls battery fan. They provide real-time information and values to other devices.”

3.2 Issues of BMS

BMS consists of several functional units. Currently, several battery management system challenges or difficulties. Issues include accurate cell voltage measurement, battery pack estimate, power, and contact process [3].

3.2.1 Measurement of Cell Voltage

The more difficulties of measurement of cell voltage in battery pack of electric vehicle hundreds of cells connected in series. The voltage is calculated. If each cell is different to the other, potential is stored and coherent prediction methods cannot be available. Difficulties are posed in constructing the measuring circuit [3].

3.2.2 Estimation of Battery Pack

In that battery, state consists of state of charge (SOC) and state of health (SOH) [5]. “In this SOC, battery degradation models are based on specific materials, condition of environments, and cycle of charge-discharge battery. Estimation of battery state when discharging at constant current and temperatures is related to discharge voltage” [2]. In this SOH, AC impedance, self-discharge rate, and power density are derived by energy, internal resistance, and the other battery parameter. Decreasing the battery cell SOH due to aging and deterioration of the battery results in a challenging battery module longevity issue and SOH issues. Decreased battery module capacity will lead to a reduction in battery module capacity by each cell [3].

3.2.3 Communication Mechanisms

Battery communications through CAN bus should be made with the internal panel, charger and external surroundings. System management bus is built to connect smart battery charger. Due to different suppliers, the battery data is difficult to interact with a uniform charger. Furthermore, the advancement of wireless technology [2].

3.3 Battery Management System in EV

The BMS consists of a number of functional blocks. In this, the signals are continuously transferred from one block to another. They can communicate by using CAN bus (Fig. 2).

Battery module

“The battery cells are connected to the module in the vehicle design. The module consists of cell count. Number of modules connected in series to create the vehicle battery pack with total voltage. Each battery module has sensors mounted. Connection and power lines are included in the battery module” [2].

Measurement unit block

Battery modules consist of a voltage, current, and temperature measuring unit. The temperature of the atmosphere can be calculated in digital format.

Battery equalization unit

Each of battery cells is needed to balance voltage for eliminating the risk of over voltage transfer of energy between the cells by using switched-mode power converter. Resistive dummy load is used to discharge the overvoltage cell. Transfer excess charge to other cells. The voltage of each cell battery module and battery pack is measured, monitoring controlled to cell balancing.

MCU: Estimation unit

MCU consists of estimation unit for battery condition. In this voltage, current, temperature, and other parameter are used to calculate SOC and SOH of battery. Cells temperatures are measured. Also, it regulates thermal control such as cooling and heating system.

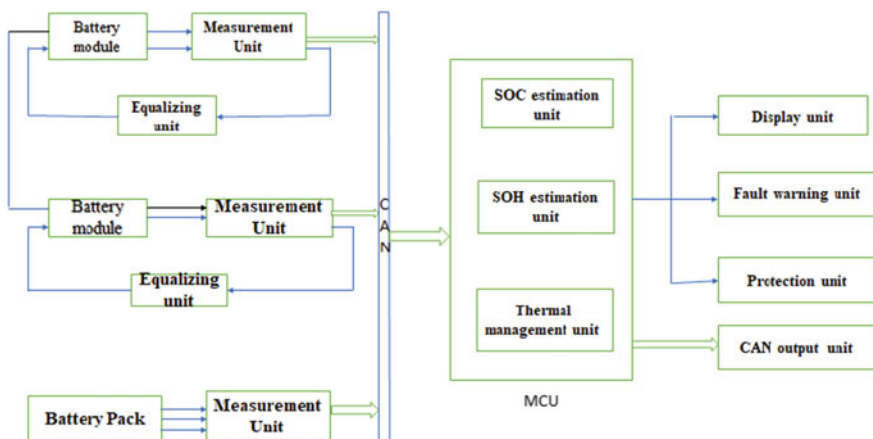


Fig. 2 Battery management system in EV

Display unit

“In this unit, SOC, SOH, temperature, maximum temperature, maximum voltage of cells, and minimum voltage of cells to display. It shows current status of the vehicle battery units” [2].

Fault warning block

“The parameters are over the range of the setting, it will trigger the warning decision to give a warning procedure. This will be sent to the display unit” [2].

4 Cell Balancing Methods

Generally, the EV battery pack consists thousands of cells combined together in series and parallel connections to provide sufficient operating voltage, power, and energy to electric vehicle. The battery charge pack consists of the serially connected cells, which can be unbalanced by overloading the stronger cells or the weakest cells in the bag. After many cycles of battery charging and uploading, the power losses and a shorter life cycle of the cells in the pack will increase [1]. To solve this unbalanced charging problem in cells in the pack, battery balancing methods were developed. Battery balance strategies have been developed to overcome the battery pack’s imbalance charge issue [1]. The main cell balancing methods are active and passive balancing.

4.1 Active Balancing

“Capacitive or inductive charge for transfer of charge between battery cells is used for active cell balancing. The cell bypass system is split into three methods: absolute shunting, shunt resistor, and shunt transistor. This method is easy to implement, easy to modularize, and cost-effective but is used at the end of the charging process and active balancing strategies are categorized into the six energy flow classes” [6].

- Cell bypass
- Cell to cell
- Cell to pack
- Pack to cell
- Cell to energy storage tank to cell
- Cell to pack or pack to cell.

4.1.1 Cell Bypass

In this balancing method, individually each cell controlled by two switches. One cell reaches its cut-off voltage for charge that time cell is completely shunted by

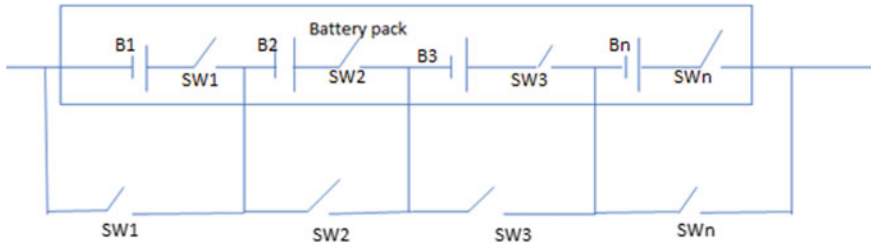


Fig. 3 Cell bypass balancing circuit

using two switches associated with this cell. The last cell in the pack is fully charged then charge finishes. “The benefits of this technique are comparatively low cost and high performance. Modularization is simple. The key drawback is that the higher voltage of the battery (i.e., the greater number of cells), the greater currents that pass through the switches, the less efficient switches are due to their resistance” [3]. In this cell controller method, the bypass current for cells reaching their high/minimum voltage waiting to reach the maximum/minimum voltage for the remaining cells [6]. “This approach is relatively cost-effective and reliable. Modularization is simple. The higher voltage of the battery pack will be used with low power battery pack. The larger currents passing through the switches, the less resistance of the switches can affect the operation” [3].

4.1.2 Cell to Cell

“The number of methods for transmitting energy from cell to cell has been developed. They can be applied in two operating modes using the flipped condenser. Each condenser is first attached to the corresponding upper cell in parallel. The capacitor is programmed to transfer energy from these cells to the cell voltage” [1] (Fig. 3).

In second mode, capacitor is connected in parallel with corresponding to lower cell. The capacitor is set to cell voltage which transfers energy from these respective cells in order to reach the new voltage. After this process, voltage of cell will be equalized. This method is highly efficient, low complexity, and possibility. It can be used in high power application. There is no required for closed loop control and sensing (Fig. 4).

4.1.3 Cell to Pack

This method is developed by transfer energy from cell to pack. They can be implemented based on shunt inductors. In shunt inductor balancing method, the balancing circuits work on two modes. In first mode, the voltage is higher than other cell of the pack then cell is detected. “By activating the appropriate cell switches, this cell is chosen parallel to the inductor. Additional cell energy is passed to the inductor” [1].

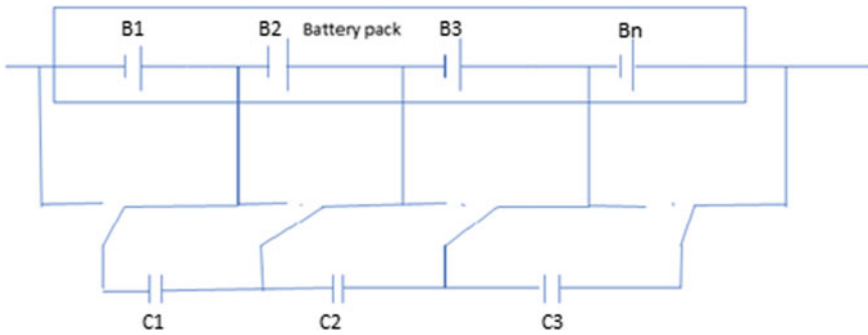


Fig. 4 Switched capacitor-based cell balancing circuit

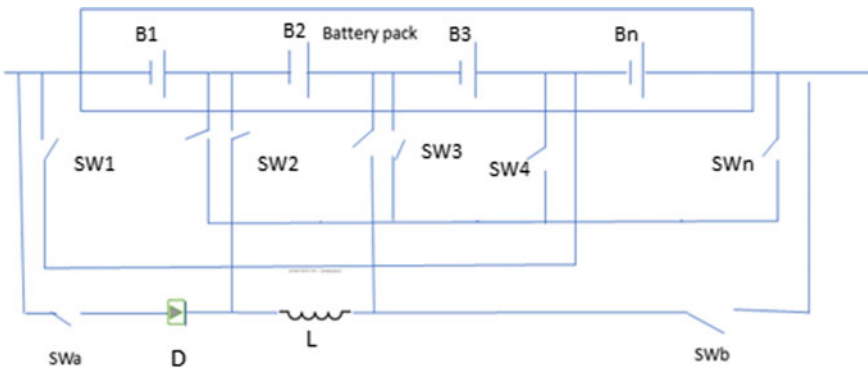


Fig. 5 Shunt inductor-based cell balancing circuit

In second mode, higher voltage cell corresponding the switches is turned off while switches SWa and SWb are activated. After, which connect inductor to battery pack. In this method, extra energy is transferred from higher voltage cell to pack. This method can be used for high power application (Fig. 5).

4.1.4 Pack to Cell

There are numbers of methods developed to transfer energy from pack to cell. Multiple secondary winding transformers can be implemented. In this method, single magnetic core of the transformer shared with secondary sides connected in each cell. Imbalance condition is detected when current from the pack is switched into the primary side of transformer. Induce current presents in each of secondary side which is provided to the cell with low voltage through diode (Fig. 6).

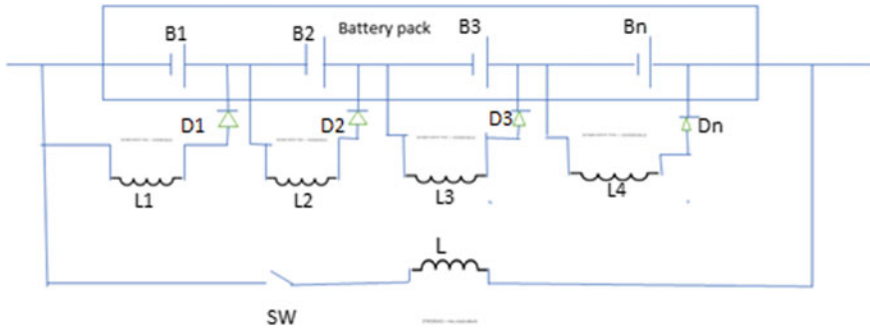


Fig. 6 Cell balancing circuit based on multiple secondary winding transformer

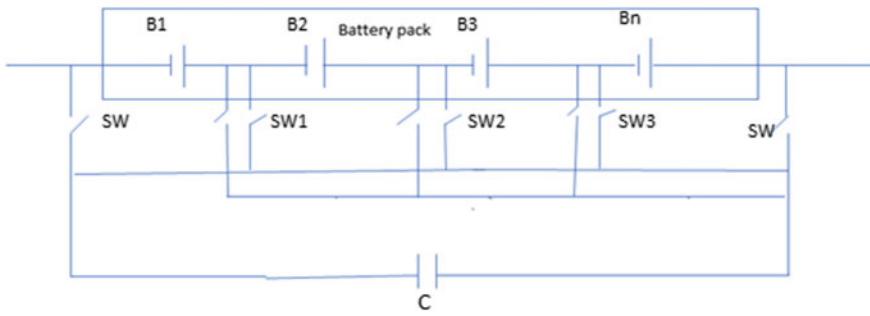


Fig. 7 Single switched capacitor-based cell balancing circuit

4.1.5 Cell to Energy Storage Tank to Cell

“Many methods are developed to transfer energy from high cell to the energy storage tank and then to low cell” [1]. This methods implementation is based on single switch capacitor. In this method, the controller selects switches and capacitor in parallel with highest cell. Capacitor is reaching the cell voltage, the controller selects switches and capacitor gets connected in parallel with the lowest voltage cell. After, which the excessive energy is transferred in the higher cells through capacitor to lower cell. This method cost is low and high efficiency (Fig. 7).

4.1.6 Cell to Pack or Pack to Cell

“This method is based on a bidirectional transformer. In this method, one transformer is used to transfer energy from the higher cell to the packet or from the packet to the lower cell by choosing the appropriate switches” [3] (Fig. 8).

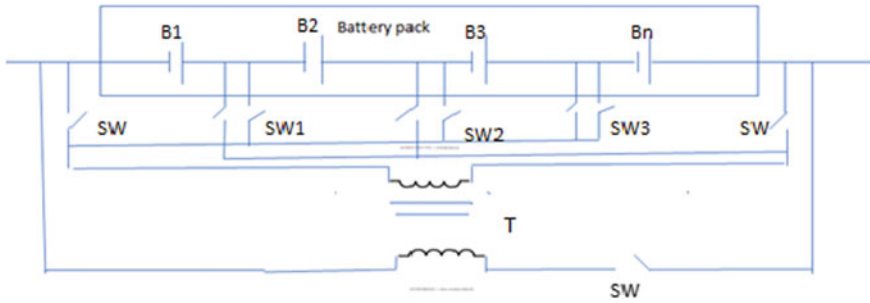


Fig. 8 Bidirectional switched transformer-based cell balancing circuit

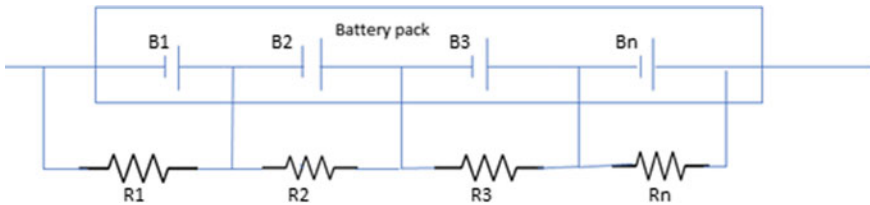


Fig. 9 Fixed shunt resistor-based cell balancing circuit

4.2 Passive Balancing

“Passive cell balancing methods are simple as compared to active cell balancing method. In passive balancing, charge drains from the cell having high charge and dissipate drained energy as heat. Passive balancing method no distribution of energy between cells. Cell energy is wasted as heat by using resistor. The conventional passive balancing when high SOC is distributed as heat across resistor resulting energy efficiency reduced. There are two types of passive cell balancing methods. They can be identified as fixed shunt resistor and switched shunt resistor” [7].

4.2.1 Fixed Shunt Resistor

“In this method, resistors are connected in parallel with individual cell in battery pack. In charging process, the current is passed from cells through resistor and continuously passing current. Energy dissipates into heat from the cells are continuous” [1] (Fig. 9).

4.2.2 Switched Shunt Resistor

“This system switches connected to each cell in a battery pack in a resistor series and parallel to each cell. There are two operating modes. All switches are on first

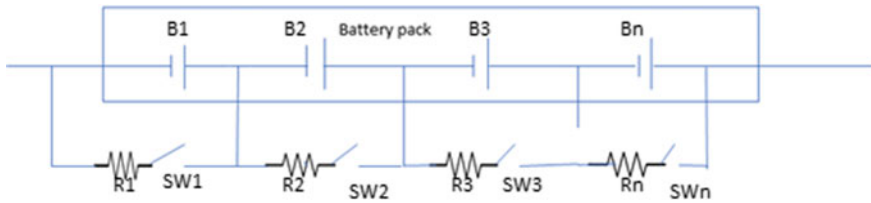


Fig. 10 Switched shunt resistor-based cell balancing circuit

mode when necessary. When a cell has a higher voltage more current passes through the capacitor rather than draining the battery. Pick the resistance factor so the lower cells efficiently balance the higher cells” [1] (Fig. 10).

“Tension sensing and dynamic transition management are used in second mode. Each voltage of the cell is sensed. The higher voltage of cells, the greater amount of energy that is dissipated” [1].

5 Conclusion

The reliability and safety of the battery are very critical for the BMS, status monitoring, and evaluation are usable. The main issues in the battery management system for EV have been presented. We have described battery management system function. This paper focuses on the study of battery cell balance processes, electric vehicle, and BMS. The principal approach to cell modeling includes a satisfactory solution for cell life prediction was also explored. As well as, we have focused on battery cell life to improve its life and protect from overcharge and bottom charge. Implementation of cell balancing process has been properly discussed.

References

1. J. Gallardo-Lozano, E. Romero-Cadaval, M. Isabel Milanes-Montero, M.A. Guerrero-Martinez, Battery equalization active methods. *J. Power Sources* (2014)
2. Z.B. Omariba, L. Zhang, D. Sun, Review of battery cell balancing methodologies for optimizing battery pack performance in electric vehicles. *IEEE Access* (2019)
3. Y. Xing, E.W.M. Ma, K.L. Tsui, M. Pecht, Review battery management systems in electric and hybrid vehicles. *Energies* **4**, 1840–1857 (2011). <https://doi.org/10.3390/en4111840energies>. ISSN 1996-1073
4. J. Cao, N. Schofield, A. Emadi, Battery balancing methods: a comprehensive review, in *2008 IEEE Vehicle Power and Propulsion Conference*. <https://doi.org/10.1109/vppc.2008.4677669>
5. S. Abada, G. Marlair, A. Lecocq et al., Safety focused modeling of lithium-ion batteries: A review. *J. Power Sources* **306**, 178–192 (2016)
6. K.T. Chau, W. Li, Overview of electric machines for electric and hybrid vehicles. (Invited Paper) *Int. J. Veh. Des.* **64**(1), 46–71 (2014)

7. J. Cao, N. Schofield, A. Emadi, Battery balancing methods: a comprehensive review, in *Vehicle Power and Propulsion Conference*, 2008. VPPC '08. IEEE, 2008, pp. 1–6
8. Z. Rao, S. Wang, A review of power battery thermal energy management. *Renew. Sustain. Energy Rev.* **15**(9), 4554–4571 (2011)
9. L. Lu, X. Han, J. Li et al., A review on the key issues for lithium-ion battery management in electric vehicles. *J. Power Sources* **226**, 272–288 (2013)
10. M.A. Rahman, S. Anwar, A. Izadian, Electrochemical model parameter identification of a lithium-ion battery using particle swarm optimization method. *J. Power Sources* **307**, 86–97 (2016)
11. W. Sung, C.B. Shin, Electrochemical model of a lithium-ion battery implemented into an automotive battery management system. *Comput. Chem. Eng.* **76**, 87–97 (2015)

Power Quality Analysis of Grid Connected Solar Farm with FC-TCR and UPFC



Abhishek Kumar Sinha, Sachin Mishra, and Javed Dhillon

Abstract This paper gives an insight about the effect of fixed capacitor-thyristor controlled reactor (FC-TCR) and unified power flow controller (UPFC) in the grid stability connected with solar farm. The model of solar farm has been developed in MATLAB by using the standard equations of the PV cell. The series and parallel connection of these PV cells enhance the magnitude of power output from solar farm. Fuzzy logic-based maximum power tracking (FL-MPPT) technique has been used to maximize power from the solar farm. The FL-MPPT controls the on-off duration of the boost converter switch. The results of the system without FC-TCR and UPFC have been compared with the results of system with FC-TCR and UPFC. The total harmonic distortion (THD) in these cases has been analyzed.

Keywords Solar farm · UPFC · FC-TCR · MPPT · Fuzzy logic

1 Introduction

The heat and radiant light from sun are the source of solar energy. This energy can be utilized by using large range of technologies like solar thermal energy, solar heating, artificial photosynthesis, molten salt power plants, and photovoltaic cells. Solar energy is an important and abundant source of renewable energy. There are two techniques, namely active and passive solar techniques used to capture this solar energy. Photovoltaic systems, solar water heating and concentrated solar power, are considered as active solar techniques while passive solar techniques include selection of materials which have favorable light dispersing characteristics and design of spaces which have characteristic to circulate the air naturally. The annual potential of solar energy is several times larger than the total requirement of world energy consumption. The factors which affect the solar energy includes geography, cloud, land availability,

A. K. Sinha · S. Mishra (✉) · J. Dhillon
School of Electronics and Electrical Engineering, Lovely Professional University, Phagwara,
Punjab, India
e-mail: sachin.20444@lpu.co.in

© The Author(s), under exclusive license to Springer Nature Singapore Pte Ltd. 2022
M. L. Kolhe et al. (eds.), *Smart Technologies for Energy, Environment and Sustainable Development, Vol 1*, Springer Proceedings in Energy,
https://doi.org/10.1007/978-981-16-6875-3_51

633

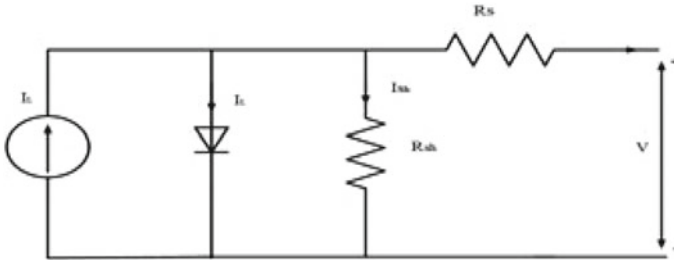


Fig. 1 Single cell model of photovoltaic cell

and time variation. The effect of geography factor among these affects mostly the potential of solar potential energy.

2 Solar Farm

PV cell is building block of solar farm. These PV cells are then connected in parallel and series to make module. The individual module is then connected to make an array. Solar farm is the obtained by these arrays to get desired power output. In this work, basic equation of solar cell is used in MATLAB to model the solar cell. Figure 1 represents the equivalent circuit of a PV cell. The mathematical equation for the PV module output current may express as [1]

$$I = n_p I_{pv} - n_p I_0 \left[e^{\frac{V + IR_c}{aT_i - I}} \right] - \frac{V + IR_c}{R_p} \tag{1}$$

where I is current of photovoltaic module, V is voltage of the PV cell, I_{pv} is photo-current of cell, I_0 is reverse saturation current of cell, n_p and n_s represent cells in parallel and series, R_p and R_s are to include shunt and series resistance.

3 UPFC

UPFC is FACTS device which offers a unique combination of series as well as shunt compensation [2]. Figure 2 represents the basic arrangement of this controller with the static synchronous compensator (STATCOM) and a static synchronous series compensator (SSSC) which are coupled by means of a DC connection. This DC connection allows the flow of “P;” the real power P linking shunt output terminals of the STATCOM, and the series output terminals of SSSC bidirectionally. These are controlled to give simultaneous real as well as reactive line compensation without

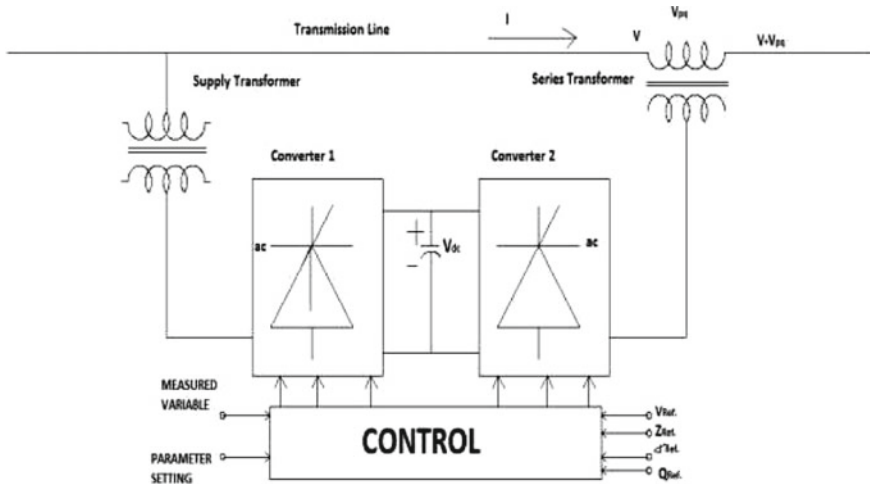


Fig. 2 Basic arrangement of UPFC

any external source of energy [3]. UPFC controls the flow of P (real power) and Q (reactive-power) by the injecting series voltage in transmission line [4, 5].

4 FC-TCR

FC-TCR can be used to obtain lagging VARs which can be controlled through the thyristor control. This control of thyristor controls the reactor current. Two or more varying capacitor bank provide leading VARs. The variable current is provided by the series connected phase angle-controlled pair of thyristors (connected back to back). Due to inclusion of FC-TCR, the system has increased power exchange capability and decreased losses. The voltage profile of the system is flat under various operating conditions of the system. This improves the dynamic behavior of grid system. Figure 3 represents the general arrangement of FC-TCR.

5 Maximum Power Point Tracking (MPPT)

It is an electronic system that adjusts modules and the working so that they can deliver maximum power. In this work, fuzzy-based MPPT technique has been used. Figure 4 represents the block diagram of MPPT [6]. MPPT is most effective under conditions like cold climate, shady, or hazy days along with the conditions when battery is used. MPPT enhances the performance of the energy storage system by controlling current and charge of the battery.

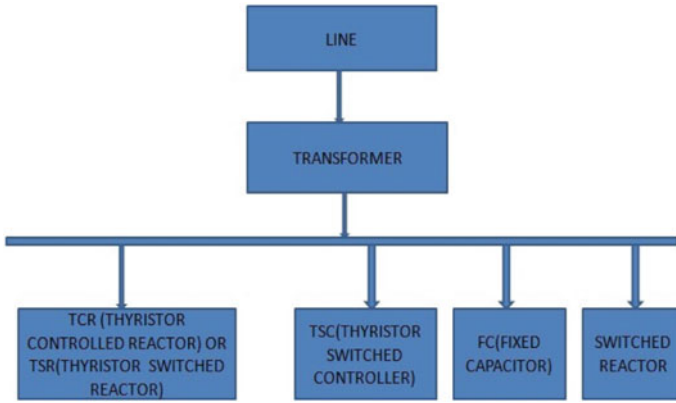
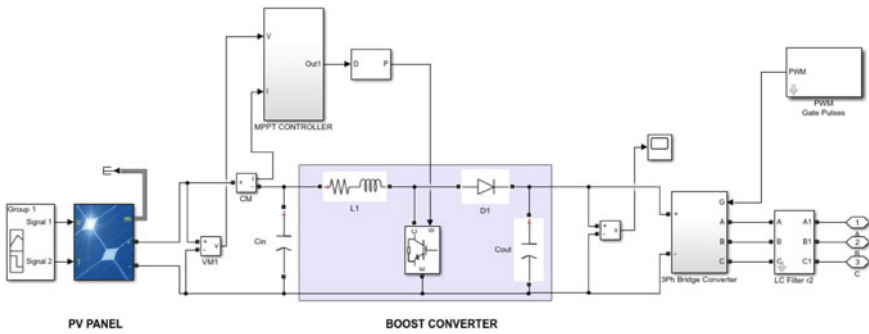
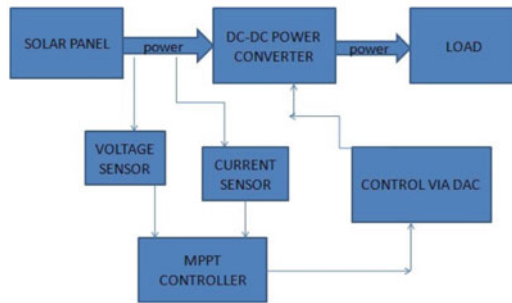


Fig. 3 Basic arrangement of FC-TCR



(a)



(b)

Fig. 4 a Simulation model of MPP, b block diagram of MPP

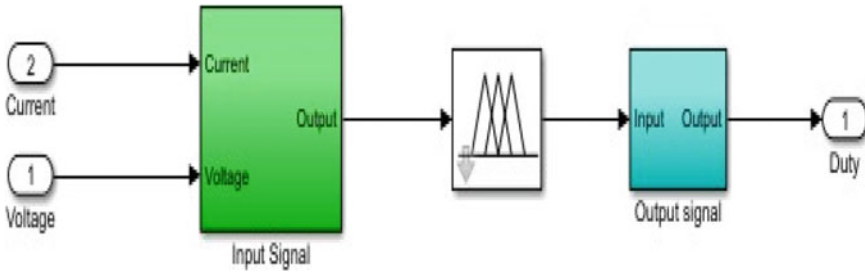


Fig. 5 Fuzzy logic-based MPPT

Table 1 Rule base for fuzzy logic MPPT

E = DP/DV	CE = DEL. DP/DV				
	N/B	N/S	Z/E	P/S	P/B
N/B	Z/E	Z/E	P/B	P/B	P/B
N/S	Z/E	Z/E	P/S	P/S	P/S
Z/E	P/S	Z/E	Z/E	Z/E	P/S
P/S	N/S	N/S	N/S	Z/E	Z/E
P/B	N/B	N/B	N/B	Z/E	Z/E

6 FI-MPPT

The basic block diagram of MPPT is shown in Fig. 4. The MATLAB model of a MPPT based on fuzzy logic has been shown in Fig. 5. The power output from FL-MPPT is constant which is desired. This also enhances the stability of the system. The rule base used for the fuzzy logic-based MPPT has been mentioned in Table 1.

7 Simulation Model and Results

The THD values of the solar PV system connected to grid are calculated and have been observed as (Figs. 6, 7, 8, 9, 10 and 11)

8 Conclusion

The THD values in the PV system have been concluded in Table 2 which indicates that the THD of the PV system with UPFC is much lesser than the same PV system with FC-TCR. Due to this, the system has better stability with UPFC and thus this

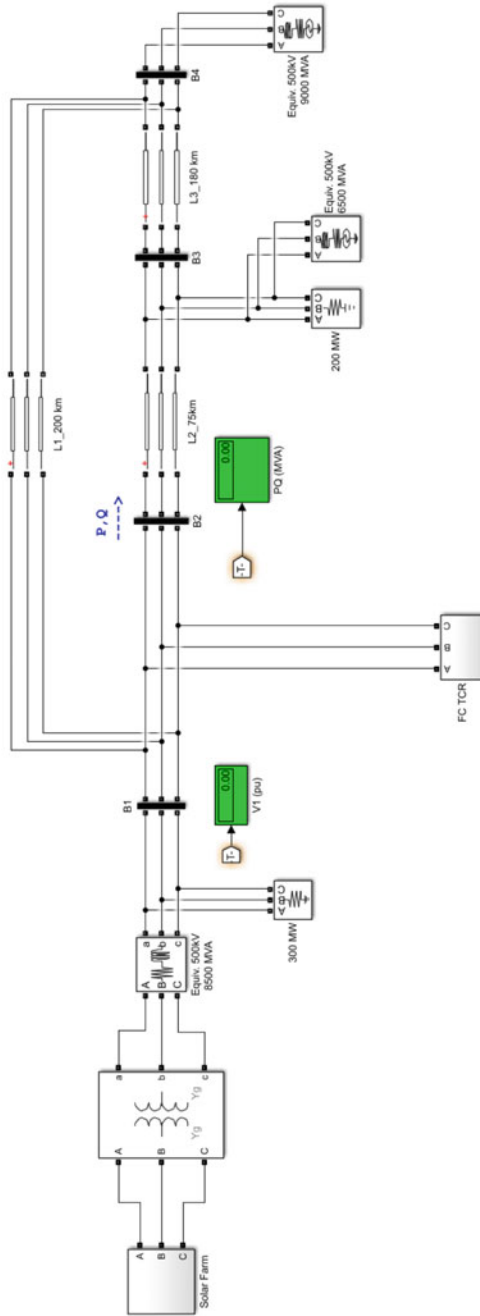


Fig. 7 Model of solar farm grid system with FC-TCR

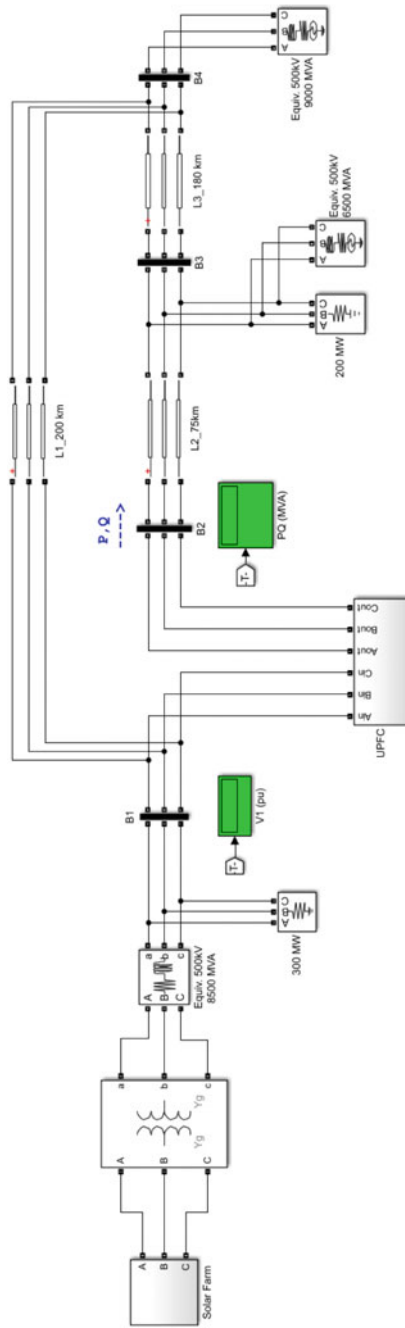


Fig. 8 Model of solar farm grid system with UPFC

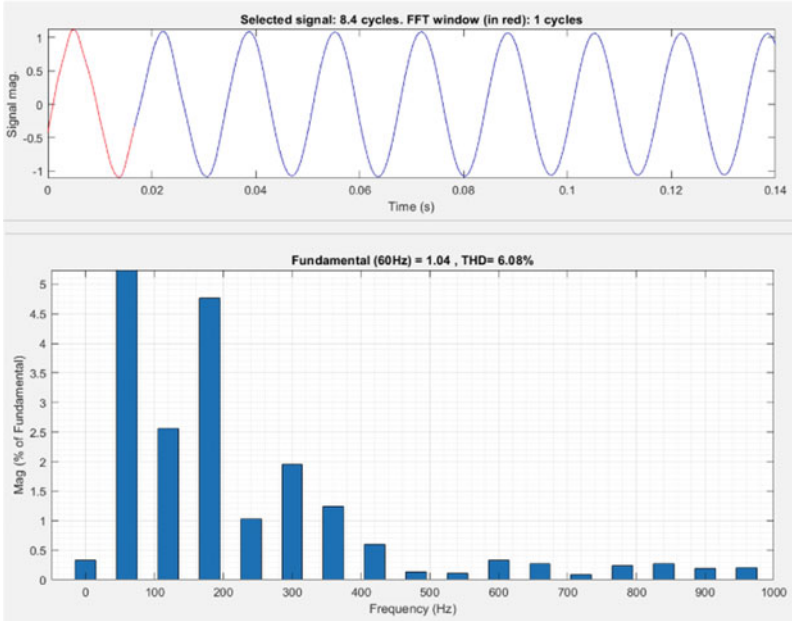


Fig. 9 THD value of solar farm grid system without compensator

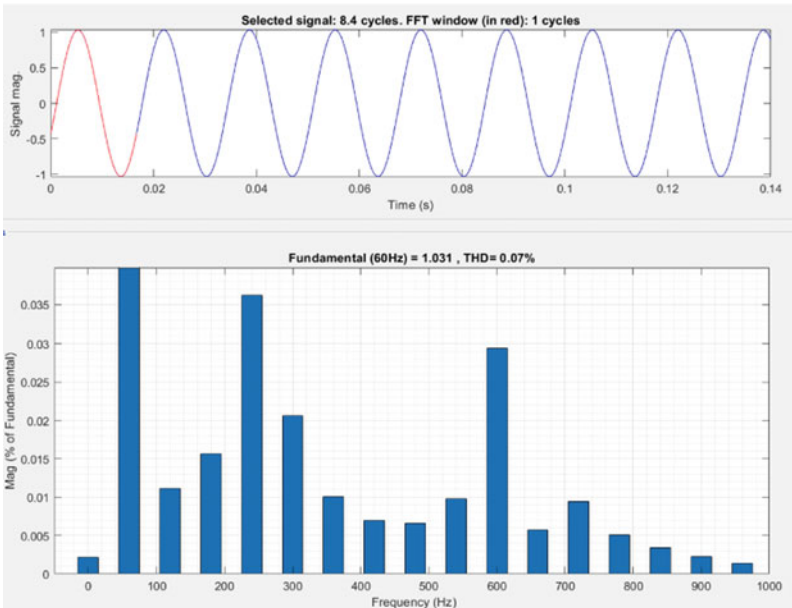


Fig. 10 THD value of solar farm grid system with FC-TCR

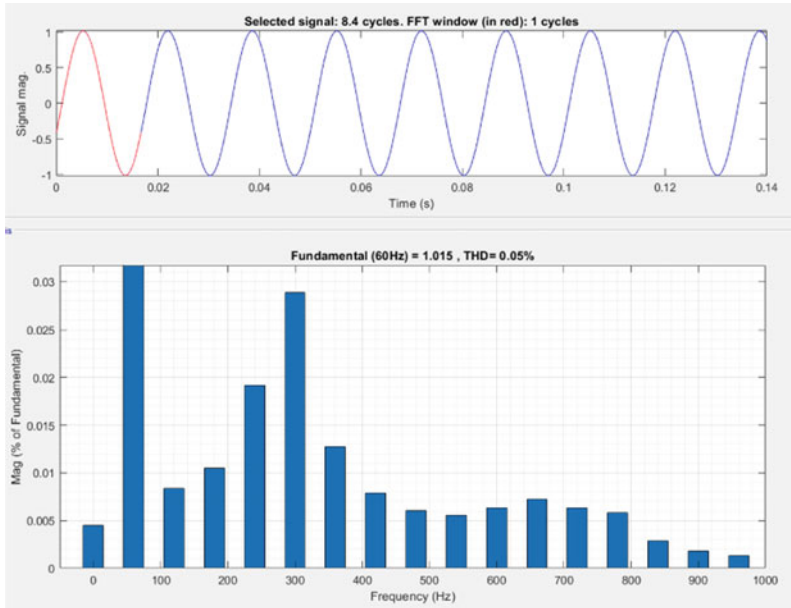


Fig. 11 THD value of solar farm grid system with UPFC

Table 2 THD values of photovoltaic system

THD of photovoltaic system in absence of compensator	6.08%
THD of photovoltaic system with FC-TCR	0.07%
THD of photovoltaic system with UPFC	0.05%

also indicates that this system can be utilized in various grids for power quality improvement.

References

1. D.R. Espinoza-Trejo, Associate Member, IEEE, E. Bárcenas-Bárcenas, Member, IEEE, D.U. Campos-Delgado, Senior Member, IEEE, C.H. De Angelo, Senior Member, IEEE, IEEE Trans. Ind. Electron. **62**(6) (2015)
2. N.K.Sharma, P.P. Jagtap, Modelling and application of Unified Power Flow Controller (UPFC), in *Third International Conference on Emerging Trends in Engineering and Technology* (2010)
3. K. Han, D. Shin, Y. Choi, Efficiency of solar cell at relatively high temperature. Int. J. Emerg. Technol. Adv. Eng. **2** (2012)
4. S. Marlin, S.D. Sundarsingh Jebaseelan, B. Padmanabhan, G. Nagarajan, Power quality improvement for thirty bus system using UPFC and TCSC. Indian J. Sci. Technol. **7**(9), 1316–1320 (2014)

5. P. Sanpoung, P. Boonchiam, B. Plangklang, Analysis and control of UPFC for voltage compensation using ATP/EMTP. *Asian J. Energy Environ. Res. Article* (2009)
6. P. Molleti, B.D.S. Prasad, Power quality improvement for PV/battery hybrid system using fuzzy logic controlling technique. *Int. J. Sci. Eng. Adv. Technol. IJSEAT* **3**(12) (2015)

Five-Phase Induction Motor Modeling and Its Analysis Using MATLAB/Simulink



Sandip A. Gaikwad and S. M. Shinde

Abstract Induction motors with more than three phases, or high phase machines have several advantages over conventional three-phase motors. With the innovations and cheapness of power electronics components, the so-called frequency inverters have become feasible, allowing their development in a more promising way. The use of more phases provides a series of advantages such as the reduction of amplitude of torque pulsations, as well as increasing their frequency. That way the mechanical performance at lower operating frequencies becomes superior. Another advantage is its reliability due to the fact that the motor can continue operating even with one of its damaged phases. Electric motors with more than three phases are currently used in critical operation, where the supply is not necessarily three-phase and where the three-phase motor does not meet desirable specifications. Examples of use are in airplanes, ships, trains, high-power compressors, electric cars, etc. In this paper, mathematical modeling of five-phase induction motor is done and this mathematical model is implemented in MATLAB/Simulink. Various performance characteristics of five-phase induction motor with different conduction modes in five-phase voltage source inverter are measured with the help of MATLAB/Simulink.

Keywords Multiphase machine · Total harmonic distortion · Arbitrary reference frame · MATLAB/Simulink · Five-phase inverter

1 Introduction

The first known record of multiphase motors comes from 1969, when the issue dealt with the authors of E. E. Ward and H. Harer in the article “Preliminary investigation of an inverter fed 5-phase induction motor.” The real development of research in this

S. A. Gaikwad (✉) · S. M. Shinde
Electrical Engineering Department, Government College of Engineering, Aurangabad,
Maharashtra, India

S. M. Shinde
e-mail: smshinde.ee@geca.ac.in

sector is at the beginning of this century. This is mainly related to the use of favorable properties that are highlighted above three-phase motors. They are used in security applications that require resistance to faults and higher system reliability, such as electric boats, electric and hybrid vehicles, electric aircraft, compressors, or pumps [1].

Comparison of the properties of a multiphase machine with a three-phase machine:

Greater fault tolerance. If one phase is open, the machine can be started again in normal mode without performing a service repair.

1. The stator winding creates a field with a lower harmonic content in multiphase machines, so the efficiency of a multiphase machine is lower than that of a three-phase machine.
2. They are less sensitive than three-phase machines which excite the waveform of the time-harmonic components,
3. which cause an increased pulsating torque.
4. It is possible to use power components with lower values to achieve high-performance propulsion (e.g., marine propulsion).
5. Improves the noise characteristics of the machine.

Machines with more than three phases are similar in their properties to three-phase asynchronous machines [2]. Multi-phase machines, e.g., in the version with a five-phase power supply, have a winding in space as well time-shifted by 72° .

The opening section of this paper presents mathematical modeling of five-phase induction machine with speed and torque equations. Five-phase inverter modeling is shown below of modeling of motor. Finally, the simulation models and the results obtained through MATLAB/Simulink software, at the end conclusion of the paper are given.

2 Five-Phase Induction Motor

2.1 Block Diagram

The entire system consists of the three-phase supply, controlled rectifier, LC filter, five-phase inverter, and five-phase induction motor. Five-phase supply obtained from the inverter is fed to motor. Working principle of five-phase induction motor is identical to the three-phase induction motor, and only difference is five-phase motor has five stator terminal and phase displacement between two winding.

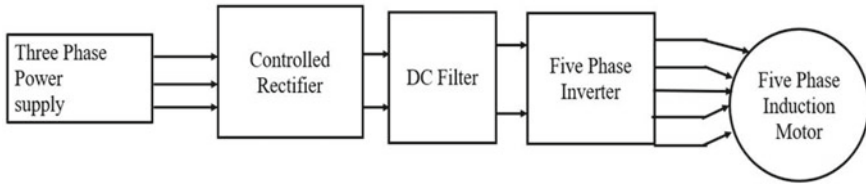


Fig. 1 System block diagram

2.2 Modeling

The model in phase variables of the induction machine is also known as a physical model. The five-phase induction machine is built by ten sinusoidally distributed coils for each pair of poles P around the surface cylindrical stator and electrically displaced 72° ($\vartheta = 2\pi/5$) between consecutive phases of the same pole [3].

The voltages and torque equations of five-phase induction motor vary with respect to the time because it contains mutual inductances. Five-phase quantities of machines are converted to two-phase dynamic quantities. Five-phase model of induction motor is represented as $dxy0$ model in arbitrary reference frame. In this model, dq component is credible for torque, power, and fluxes. The x - y components are responsible for losses in machine. The mathematical modeling of five-phase induction motor is done using the following equation [4],

Stator winding voltages of five-phase induction motor under balance condition are given below,

$$v_{as} = V_m \sin(2\pi ft) \tag{1}$$

$$v_{bs} = V_m \sin\left(2\pi ft - \frac{2\pi}{5}\right) \tag{2}$$

$$v_{cs} = V_m \sin\left(2\pi ft - \frac{4\pi}{5}\right) \tag{3}$$

$$v_{ds} = V_m \sin\left(2\pi ft + \frac{2\pi}{5}\right) \tag{4}$$

$$v_{es} = V_m \sin\left(2\pi ft + \frac{4\pi}{5}\right) \tag{5}$$

The model described in phase variables can be simplified, to eliminate the dependence of mutual inductance with time, by means of the Clarke transformation. The model would be redefined by means of five new variables obtained by means of the power-invariant transformation of the original variables using the matrix of Clarke decoupling

$$A = \sqrt{\left(\frac{2}{5}\right)} \begin{bmatrix} 1 & \cos\left(\frac{2\pi}{5}\right) & \cos\left(\frac{4\pi}{5}\right) & \cos\left(\frac{4\pi}{5}\right) & \cos\left(\frac{2\pi}{5}\right) \\ 0 & \sin\left(\frac{2\pi}{5}\right) & \sin\left(\frac{4\pi}{5}\right) & \sin\left(\frac{4\pi}{5}\right) & \sin\left(\frac{2\pi}{5}\right) \\ 1 & \cos\left(\frac{4\pi}{5}\right) & \cos\left(\frac{8\pi}{5}\right) & \cos\left(\frac{8\pi}{5}\right) & \cos\left(\frac{4\pi}{5}\right) \\ 0 & \sin\left(\frac{4\pi}{5}\right) & \sin\left(\frac{8\pi}{5}\right) & -\sin\left(\frac{8\pi}{5}\right) & -\sin\left(\frac{4\pi}{5}\right) \\ 1/\sqrt{2} & 1/\sqrt{2} & 1/\sqrt{2} & 1/\sqrt{2} & 1/\sqrt{2} \end{bmatrix}$$

The equation of five-phase machine model in arbitrary reference frame is given below.

Stator voltages in d - q reference frame are given as,

d - q reference frame is given as,

$$V_{ds} = R_s i_{ds} - \omega_a \psi_{qs} + p \psi_{ds} \quad (6)$$

$$V_{qs} = R_s i_{qs} + \omega_a \psi_{ds} + p \psi_{qs} \quad (7)$$

$$V_{xs} = R_s i_{xs} + p \psi_{xs} \quad (8)$$

$$V_{ys} = R_s i_{ys} + p \psi_{ys} \quad (9)$$

$$V_{0s} = R_s i_{0s} + p \psi_{0s} \quad (10)$$

Rotor side voltages in d - and q -reference frame are given as,

$$V_{dr} = R_r i_{dr} - (\omega_a - \omega) \psi_{qr} + p \psi_{dr} \quad (11)$$

$$V_{qr} = R_r i_{qr} - (\omega_a - \omega) \psi_{dr} + p \psi_{qr} \quad (12)$$

$$V_{xr} = R_r i_{xr} + p \psi_{xr} \quad (13)$$

$$V_{yr} = R_r i_{yr} + p \psi_{yr} \quad (14)$$

$$V_{0r} = R_r i_{0r} + p \psi_{0r} \quad (15)$$

Flux equations of stator side of five-phase induction motor are given as,

$$\psi_{qs} = L_{ls} + L_m i_{ds} + L_m i_{dr} \quad (16)$$

$$\psi_{ds} = L_{ls} + L_m i_{qs} + L_m i_{qr} \quad (17)$$

$$\psi_{xs} = L_{ls} i_{xs} \quad (18)$$

$$\psi_{ys} = L_{ls} i_{ys} \quad (19)$$

$$\psi_{0s} = L_{ls} I_{0s} \quad (20)$$

Flux equation of rotor side of five-phase induction motor is given as,

$$\psi_{qr} = L_{lr} + L_m i_{dr} + L_m i_{ds} \quad (21)$$

$$\psi_{dr} = L_{ls} + L_m i_{qr} + L_m i_{qs} \quad (22)$$

$$\psi_{xr} = L_{lr} i_{xr} \quad (23)$$

$$\psi_{yr} = L_{lr} i_{yr} \quad (24)$$

$$\psi_{0r} = L_{lr} i_{0r} \quad (25)$$

By solving equations from (16) to (25), we will get the current equations of machine in d - q reference frame as follows,

Stator currents:

$$i_{ds} = \frac{(L_r \psi_{ds} - L_m \psi_{dr})}{(L_s L_r - L_m^2)} \quad (26)$$

$$i_{qs} = \frac{(L_r \psi_{qs} - L_m \psi_{qr})}{(L_s L_r - L_m^2)} \quad (27)$$

$$i_{xs} = \frac{\psi_{xs}}{L_{ls}} \quad (28)$$

$$i_{ys} = \frac{\psi_{ys}}{L_{ls}} \quad (29)$$

Rotor currents:

$$i_{dr} = \frac{L_s \psi_{dr} - L_m \psi_{ds}}{(L_s L_r - L_m^2)} \quad (30)$$

$$i_{qr} = \frac{(L_s \psi_{qr} - L_m \psi_{qs})}{(L_s L_r - L_m^2)} \quad (31)$$

$$i_{xr} = \frac{\psi_{xr}}{L_{lr}} \quad (32)$$

$$i_{yr} = \frac{\psi_{yr}}{L_{lr}} \quad (33)$$

Torque equation of five-phase induction motor can be expressed as: t

$$T_e = PL_m(i_{dr}i_{qs} - i_{ds}i_{qr}) \quad (34)$$

$$\omega_r = \int \frac{P}{2J}(T_e - T_L) \quad (35)$$

where

$$L_s = L_{ls} + L_m \quad (36)$$

$$L_r = L_{lr} + L_m \quad (37)$$

In the above equations, $p = d/dt$ and subscript s, r denotes the parameter that is associated with stator and rotor, respectively. V_{ds}, V_{qs}, V_{xs} , and V_{ys} are arbitrary stator voltages and V_{dr}, V_{qr}, V_{xr} , and V_{yr} are rotor voltages in arbitrary reference frame. Likewise i_{ds}, i_{qs}, i_{xs} , and i_{ys} are stator currents and i_{dr}, i_{qr}, i_{xr} , and i_{yr} are rotor currents in arbitrary reference frame.

L_{ls} and L_{lr} are stator and rotor leakage inductances, respectively. L_m is the magnetizing inductance. R_s and R_r are stator and rotor resistances, respectively. $\psi_{ds}, \psi_{qs}, \psi_{xs}$, and ψ_{ys} are stator flux and $\psi_{dr}, \psi_{qr}, \psi_{xr}$, and ψ_{yr} are rotor flux in arbitrary reference plane [5].

Torque developed by motor, i.e., electromagnetic torque, is represented by T_e . “ P ” represents the number of pole in machine. T_L is the load torque which is applied to machine. J is the moment of inertia, and ω_r is the rotor speed.

3 Five-Phase Inverter

In Fig. 3, the basic diagram of the inverter with five phases and two levels, consisting of ten power switches, one pair for each inverter branch, powered by a direct current source of Vdc voltage such as DC link, and whose output would in turn feed a balanced pentaphase load, it is eminently inductive type. For this study, it is also assumed that the load fed by the investor is always balanced.

In general, three-phase power supplies are easy to use, but it is difficult to generate a multiphase power supply as the power cannot be generated beyond the three-phase power supply. Therefore, you will use a voltage source inverter to get a

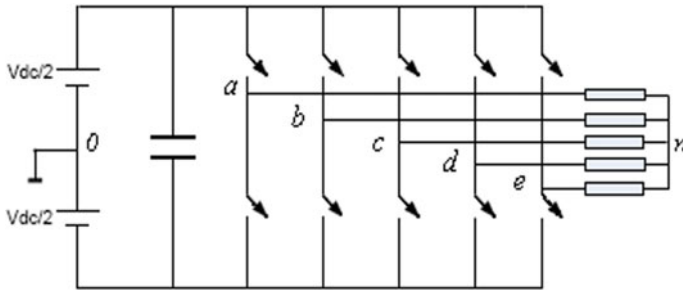


Fig. 2 Five-leg inverter

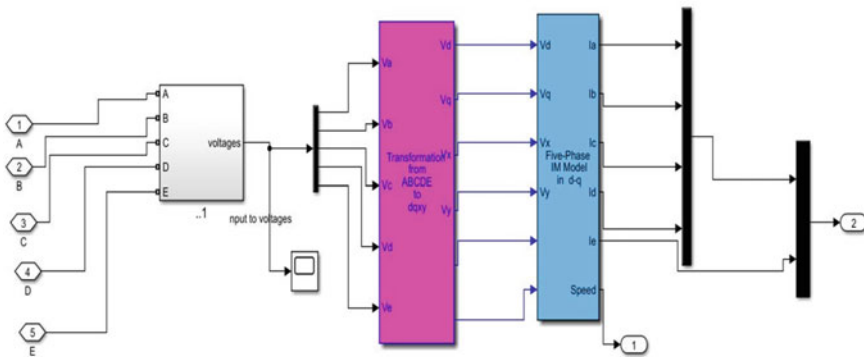


Fig. 3 Simulation model of five-phase induction motor

three-phase to five-phase power supply. The objective of a five-phase inverter is to generate alternating current electrical energy from a direct current power source, with desired magnitudes and frequencies [6]. It is mainly constituted by power electronic devices, which work as switches operating in cut-off and saturation with an appropriate sequence to obtain five balanced and symmetrical output voltages. Any type of inverter (multiphase or three-phase) uses devices with controlled activation and deactivation (i.e., BJT, MOSFET, IGBT, MCT, SIT, GTO) or forced commutation thyristors, depending on the application [7] (Fig. 2).

4 Simulation Model and Result

In Sect. 2, mathematical equation of five-phase induction motor is discussed and by using this equations MATLAB/Simulink model of five-phase induction motor is developed. A five-phase inverter is designed to obtain a five-phase supply with different conduction modes. Pulse width of gate signal is varied by changing the pulse width parameter of pulse generator.

Table 1 Parameter of five-phase induction motor at 180° conduction mode of inverter

S. No.	Load torque (%)	Speed (in rpm)	Input current THD (%)
1	12.5	1491	124.5
2	37.5	1470	119.2
3	100	1415	89.8
4	150	1365	65.04
5	200	1208	40.36

Five-phase inverter is simulated by using the “simpowersystem” block in MATLAB/Simulink. Five-leg inverter model consists of ten IGBT switches with antiparallel diodes (Fig. 3).

Tables 1, 2, 3 and 4 represent the motor performance during different load conditions and during different conduction modes. Parameter measured from the simulation is rotor speed and input current THD (%). Here 100% load torque is considered as rated torque, and 200% load torque is considered as maximum load torque. Five-phase inverter.

Here, various parameters of five-phase induction motor are noted for different load torques and for different conduction modes of five-phase inverter. Torque applied to motor is from range from 12.5 to 200%. Under different load torque conditions, motor performance is observed and readings are taken according to operation. Input current THD is measured.

Table 2 Parameter of five-phase induction motor at 144° conduction mode of inverter

S. No.	Load torque (%)	Speed (in rpm)	Input current THD (%)
1	12.5	1489	80.32
2	37.5	1473	73.92
3	100	1411	51.85
4	150	1341	35.68
5	200	–	–

Table 3 Parameter of five-phase induction motor at 153° conduction mode of inverter

S. No.	Load torque (%)	Speed (in rpm)	Input current THD (%)
1	12.5	1493	91.74
2	37.5	1469	92.58
3	100	1401	71.52
4	150	1334	50.26
5	200	–	–

Table 4 Parameter of five-phase induction motor at 171° conduction mode of inverter

S. No.	Load Torque (%)	Speed (in rpm)	Input current THD (%)
1	12.5	1493	121.4
2	37.5	1473	116.3
3	100	1419	83.96
4	150	1367	32.78
5	200	1199	38.43

5 Conclusion

This paper has analyzed a five-phase induction machine, as a multiphase drive of great interest for high performance and reliability applications. The behavior of the system has been studied by modeling five-phase induction motor under different load conditions and at different conduction modes. Various advantages of five-phase induction motor are also discussed in this paper.

It has seen that motor operation at 144° gives better performance with high speed and less THD in input current at rated load torque condition. For better performance of five-phase induction motor, it should be operated at 144 conduction mode.

Appendix

Five-phase induction motor parameters used in MATLAB/Simulink software,

Stator resistance (R_s)	10 Ω
Rotor resistance (R_r)	6.3 Ω
Stator leakage reactance (L_{ls})	0.46 mH
Rotor leakage reactance (L_{lr})	0.46 mH
Magnetizing reactance (Lm)	0.4 mH
Moment of inertia (J)	0.00488 kg m ²
Number of pole (P)	4
Frequency (f)	50
Friction coefficient (B)	0.01 m s

References

1. N. Dattu, M.R. Rashmi, Modeling of five phase induction motor drive, in *IEEE International Conference on Technological Advancements in Power and Energy (TAP Energy)*, 2017

2. [Online]. Available: <https://medwelljournals.com/abstract/?doi=ijsr.2008.288.292>
3. N. Bianchi, M. Dai Pre, E. Fornasiero, Post-fault operations of the five-phase motor using a full-bridge inverter, in *Power Electronics Specialists Conference*, 2008. PESC 2008. IEEE Rhodes, Greece, 15–19 June 2008, pp 2528–2534
4. A.N. Dhanagare, M.P. Bulbule, G.H. Mane, K.S. More, O.B. Chavare, Performance analysis of inverter fed mathematical modeling of five phase induction motor. *Int. J. Adv. Res. Electr., Electron. Instrum. Eng.* **7**(10) (2018)
5. P.G. Sharma, S. Rangari, Simulation of inverter fed five phase induction motor. *Int. J. Sci. Res. (IJSR) India* **2**(2) (2013). ISSN: 2319-7064
6. D. Uma, K. Vijayarekha, Modeling and simulation of VSI fed induction motor drive in Matlab/Simulink. *Int. J. Electr. Comput. Eng. (IJECE)* **7**(2), 584–595 (2017)
7. S.A. Gaikwad, S.M. Shinde, Review on five-phase induction motor fed by fivephase voltage source inverter with different conduction mode, in *2020 International Conference on Industry 4.0 Technology (I4Tech)*, Vishwakarma Institute of Technology, Pune, India, 13–15 Feb 2020

Air Writing-Based Automated Room



Sagnik Ghosh and Aniruddha Mitra

Abstract One of the most commonly studied subjects in today's world is air writing or gesture recognition in the air. Gesture recognition in the air requires the detection of the alphabet or number that is being written and correctly predicted. In this paper, if a person makes a specific gesture with a finger, the gesture is recognized, and all gestures correspond to a certain alphabet that triggers certain actions in the surrounding area, such as turning on the appliances. Here, we have built a cheap and powerful motion capture device at home to execute a desired operation with the flick of our finger. Using a standard night vision camera (a modified Raspberry Pi camera), Raspberry Pi, CNN, OpenCV computer vision library and machine learning, we have achieved a device that recognizes characters in a three-dimensional space with six degrees of freedom. The proposed system achieves 94.77% accuracy in the recognition rate when tested with English alphabets and numbers.

Keywords Air writing · Gesture control · Deep learning · Raspberry Pi · CNN · OpenCV

1 Introduction

English handwritten character recognition has become a challenging and exciting field of research with the emergence of artificial intelligence and soft computing. This adds greatly to the relationship between humans and computers and enhances the interface between the two. There are also other great areas of study like face, speech and thumb print recognition. The identification of characters may normally be interpreted in two forms: offline and (ii) online. In the offline mode, the pattern is obtained as an image and taken for testing purposes. Strain, time, slopes, movements and other physical parameters are a function of each point of the pattern in the case of an online approach. In the field of machine learning, all approaches are effective depending on their use. A key precondition for the method of pattern recognition is to

S. Ghosh (✉) · A. Mitra
St. Thomas College of Engineering and Technology, Kolkata, India

have the highest accuracy with a minimum cost of time. Therefore, the identification of handwritten characters continues to be a wide area of study. The gestures are performed with one finger. The motion capture system perceives what we humans interpret as a not-so-distinctive tip of the finger moving in the air as a bright blob that can be easily separated and tracked in the video stream to identify the pattern drawn by the individual and perform the appropriate action. In real time, all this processing takes place and makes use of computer vision and machine learning. In our method for motion capture, a basic web camera is used, and the camera video stream is fed into a Python program running OpenCV code that is used for fingertip detection, isolation and tracking. The prediction is made, and the pattern drawn is recognized. This result is fed into the Raspberry Pi in which the GPIOs are controlled accordingly to perform some activities. In this case, four relays which turn the electrical appliances on and off are regulated by the GPIOs.

2 Literature Survey

In recent years, in order to address a range of supervised, unsupervised and reinforcement learning issues, deep learning-based approaches have gained considerable interest in the research community. Convolution neural networks (CNNs), a specific type of neural networks, possess the capability to extract relevant features from the given input. It is one of the most highly used neural networks. The ability of convolution neural networks to retrieve features from multidimensional inputs makes them a very interesting way out towards resolving computer vision problems. Computer vision has literally been a test bed for the validation of novel CNN methods and technologies. More specifically, a certain dataset has been extensively used for this purpose: the MNIST dataset. MNIST, with separate training and test sets, is a database of numbered handwritten digits and is therefore a domain that can be effectively understood. This enables various techniques to be rapidly compared. LeCun et al. [1], authors of the initial MNIST article, released the first ranking, which covered works as recent as 2012. To the best of our knowledge, the most recent ranking was published by Beneson [2], revised as of 2016. MNIST is perceived to have already been resolved. As a result, the extended MNIST database (EMNIST) was published in April 2017 by Cohen et al. [3], comprising both handwritten digits and letters and having the same structure as the MNIST database. Most hand gesture recognition systems use different classification techniques, preprocessing, extraction of characteristics and essentially simple/statistical matching or machine learning techniques which require massive computing resources using a mathematical approach. In Hinton's paper [4], deep learning has been put in order to build a hand gesture recognition system. Likewise, Deng has developed a large-scale visual recognition system with deep convolution neural networks [5]. Gulshan has developed a deep learning system to identify diabetic retinopathy in retinal fundus photography [6]. According to Kuprel, a dermatologist-level segmentation of skin cancer has been developed using deep neural networks [7]. In Johannes' paper, he developed a deep

learning system to spot breast cancer in women [8]. Sundaram established a device that detected tuberculosis in chest radiographs using DCNN [9]. Likewise, Yasaka introduced a method using CNN to separate liver masses from dynamic contrast enhanced computed tomography [10]. Established hand gesture recognition systems function on the basis of hand signals. As a result, we have taken the convolutional neural network to recognize alphabets that are drawn mid-air with a finger to perform desired operations.

3 Work Description

Step 1: Training a model using convolutional neural network

1.1 Loading dataset and preliminary work

We load the EMNIST dataset from storage and import other necessary files. The data is segmented into the train and test sets followed by standardizing the images, and preprocessing is completed.

1.2 Defining the Model

In Keras, models are described in the form of several consecutive layers. First, we initialize the ‘sequential model’, and then, the corresponding neurons are added to the layers. The model, in our case, takes 28×28 pixels.

1.3 Compiling the Model

We use the ADADELTA optimizer.

1.4 Fitting Model

Model variables of batch size and epochs influence the efficiency of our model so that they are taken into account.

1.5 Evaluate Model

The test accuracy for the dataset model was 94.77%.

1.6 Taking all of it together

Summing up everything, we obtain a CNN model trained on EMNIST dataset to get desired results.

Step 2: Initialization

We initialize things after which the recognition code is executed. First, the models designed in the previous stage are loaded. A dictionary of letters, red lower and red upper bounds are created in order to detect the reflected object from the video stream, a kernel to smoothen operations, a blackboard for placing the writings in white (just

like an alphabet in the EMNIST dataset), a stack for storing all the points created by the light and a few default variables.

Step 3: Capturing the writings

We begin to read the input video frame by frame using the `cv2.VideoCapture ()` method of OpenCV (using a time loop), from the web camera in real time. When we start reading the webcam stream, with the assistance of the `cv2.inRange ()` process, we continuously scan for a blue colour object in the frames and use the previously initialized red upper and red lower variables. We will do a sequence of image operations after we have located the contour to make it smooth. Smoothing makes our lives simpler. We will do a sequence of image operations after we have located the contour, to make it smooth. Smoothing simplifies our lives. The basic definition of erosion is just like soil erosion; the foreground entity boundaries are torn down (always strive to keep the white foreground). The kernel (as in the 2D convolution) will slide through the image. In the original image, a pixel (either 1 or 0) is deemed to be 1 only if all the pixels in the kernel are 1; otherwise, it will be eroded (made to zero).

Step 4: Scraping the writing and passing it to the model

As soon as a user finishes writing, the points that were stacked earlier are placed on a blackboard and further moved to the models. Control goes in the `elseif` block when writing is paused (since no contours are detected). Now, a blackboard photo is taken to do short contours search again. Once found, we shape it appropriately and resize it to meet the input dimensions of the model we built, i.e. 28×28 pixels.

Step 5: Showing model predictions

On the frame pane, the predictions that are given by our model are displayed. The results are also displayed in the console using the `cv2.imshow ()` process. We call the relay control function with the expected value, and the particular operation is performed according to the sent letter. The parameter 'L' turns the relay on GPIO pin number 2. After exiting the while loop that we moved in to read data from the web camera, we locked the web camera and destroyed all the screens.

Convolutional Neural Networks (CNNs)

Convolution neural networks are very analogous to conventional neural networks. They consist of neurons with weights and preferences that can be trained. Each neuron receives those inputs, executes a dot product and follows it with a nonlinearity optionally. A single distinguishable score feature is now represented by the entire network: from the raw image pixels on one end to class scores on the other. They have a loss function on the last (full-connected) layer (e.g. SVM/Softmax), and the CNN also has all the attributes or schemes for a regular neural network. ConvNet architectures specifically claim that the inputs are pictures, which help one to represent those properties in the architecture. This would allow implementing the forward function more efficiently and greatly reduce the number of network parameters.

Layers used to build ConvNets

- ConvNet is a series of layers, and each layer of ConvNet uses a differentiating function to transform one volume of activations to another. For creating ConvNet architectures, we use three major layer types: Convolutional layer, pooling layer and fully connected layer. To form a completely connected ConvNet architecture, we are going to club these layers.
- INPUT $[28 \times 28 \times 3]$ —it includes the raw image pixel numbers, and in this case, the image width is 28, the image height is 28, and the three colour channels are R, G and B.
- The CONV layer (Fig. 1)—it calculates the output of the neurons associated to the local regions in the data, each measuring a product between their weights and the small area to which they are associated in the input volume. If we intend to use 12 filters, this can result in volumes such as $[28 \times 28 \times 12]$.
- The element-wise activation function, such as the $\max(0, x)$ threshold at zero, is used by the RELU layer. The volume scale remains ($[28 \times 28 \times 12]$) unchanged.
- The POOL layer (Fig. 2) conducts a downstream sampling operation along the spatial dimensions (width and height) resulting in volumes such as $[14 \times 14 \times 12]$.
- Class scores can be determined by the FC (i.e. fully connected) layer, resulting in size volume $[1 \times 1 \times 10]$ where each of the ten numbers correlates to class scores, such as those of the 10 CiFAR-10 classes. As in normal neural networks, each neuron in this layer would be related to all the numbers in the previous amount.

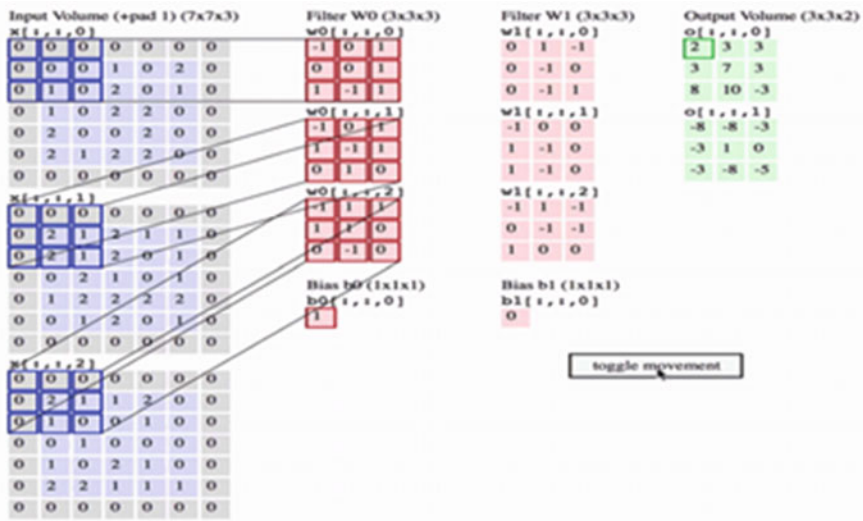


Fig. 1 CNN layer working. Source Towards datascience

Fig. 2 Pooling layer diagram. *Source* Towards datascience



In this way, ConvNets transforms the original image layer by layer to the final class scores from the original pixel values. The CONV/FC layers, in particular, perform transformations that are a function not only of the input volume activation, but also of the parameters (neuron weights and biases). In the other side, a fixed function may be carried out by the RELU/POOL layers (Fig. 3).

3.1 Equipment Requirements

Relay for switching electrical appliances

A digital switch and relays are designed to regulate voltages and currents much higher than regular Arduino boards do. The relay flips to allow the current to transfer or to break depending on the wiring since the logical voltage is input. A relay usually consists of a common terminal, a terminal that is normally closed and a terminal that is normally open. The common terminal and the normally opened terminal will have continuity since the coil is energized (Fig. 4).

4 Raspberry Pi 3 Model B

Developed in United Kingdom by Raspberry Pi foundation, Raspberry Pi is a series of small single-board computers made in order to encourage basic computer science education in schools and developing countries. It does not contain peripherals (e.g. keyboards) or instances. In a number of official and unofficial sets, however, some of the accessories have been included. The third version of the Raspberry Pi is the Raspberry Pi 3 Type B. This strong single-board machine-sized credit card can be utilized for multiple uses, replacing the original Raspberry Pi Model B+ and Model B Raspberry Pi 2 (Fig. 5).

Fig. 3 Architecture of our applied CNN

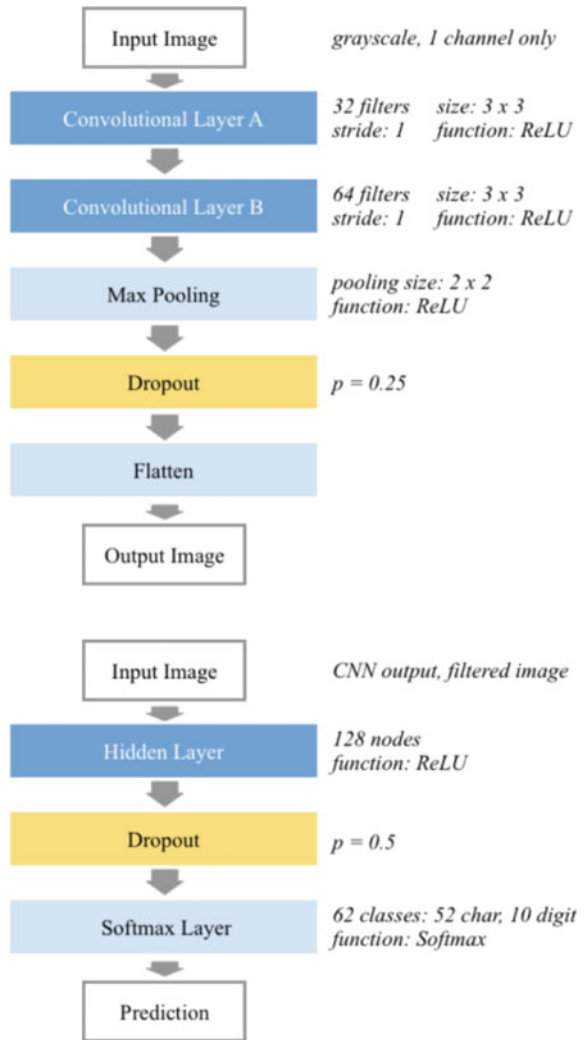


Fig. 4 Relay

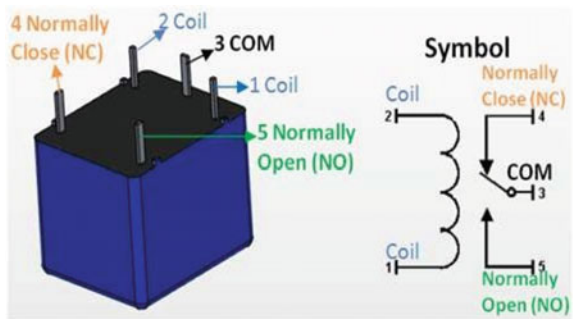


Fig. 5 Raspberry Pi



4.1 Flow Chart

The circuit diagram of the proposed system is shown in Figs. 6 and 7.

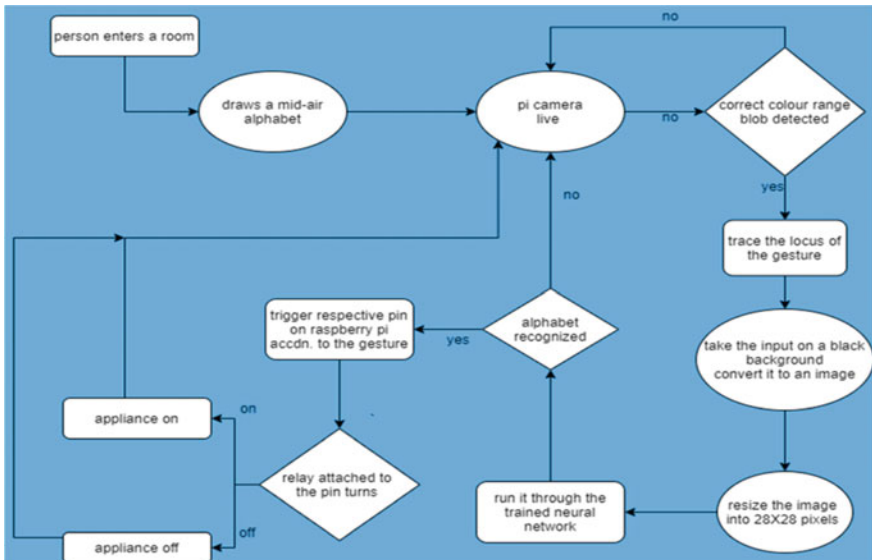


Fig. 6 Flow chart

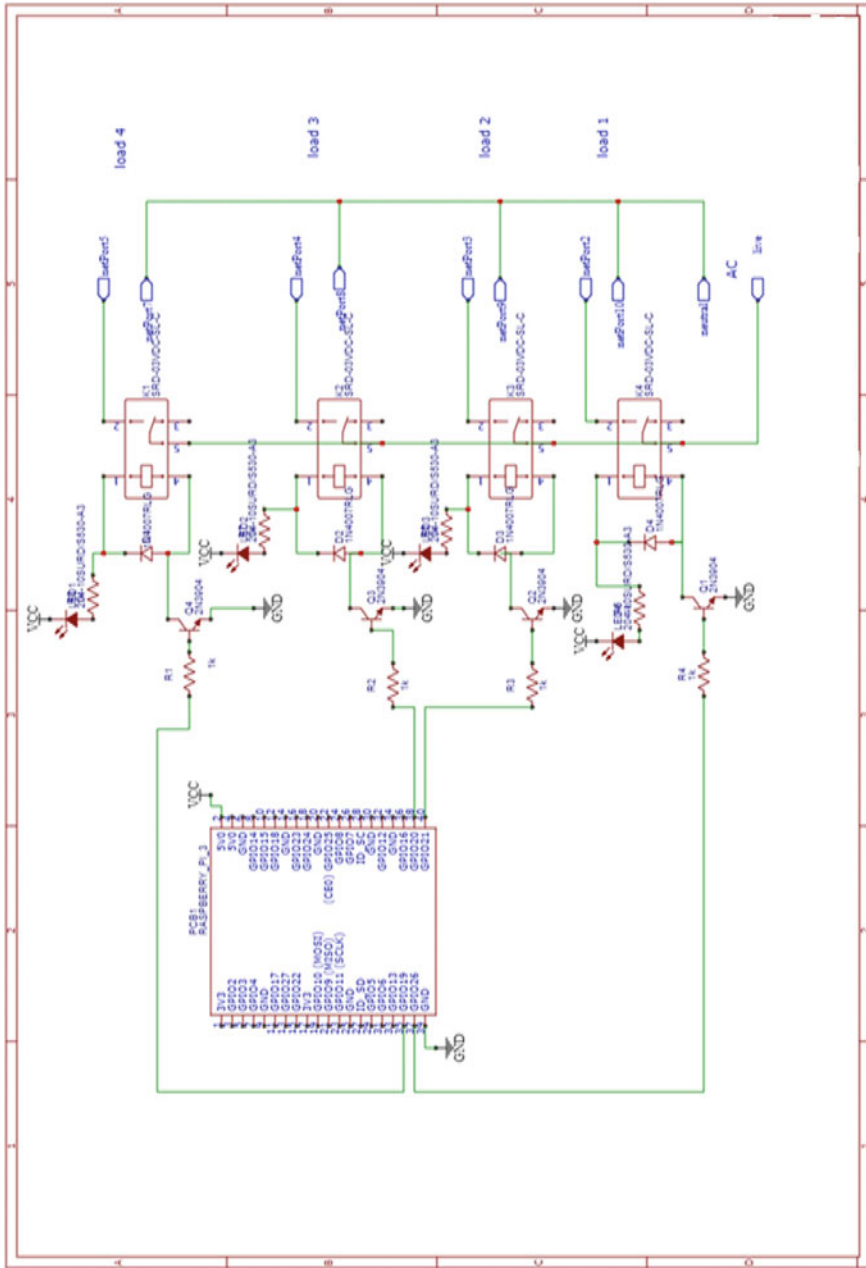


Fig. 7 Schematic of the system

5 Results

When our neural network was initially trained on 731,668 samples of EMNIST data (split 8:2 between datasets for testing and evaluation), a training accuracy percentage of 82.65% was obtained, and an evaluation accuracy of 84% was obtained. There was a training loss percentage of around 47% and an evaluation loss of around 40%. It was found that the evaluation data actually performed better than that of training data, and when checked on the initial 10% test data, we got 85.43% test accuracy and 37% test loss. It was necessary to achieve higher accuracy in order for our model to perform better. This was done by training more number of epochs and increasing one more layer of the neural network. Finally, test accuracy achieved on checking with the test data was around 94.77%. It is shown in Fig. 8. We noticed that when running the program from beginning to end, the accuracy of the real prediction is slightly lower than that of only the model used for classification of alphabets and numbers. This may be because the pictures produced during the processing stage as stated earlier have characteristics dissimilar from those of EMNIST, since the created images also have more noise and user errors. Moreover, during tuning our hyperparameters for improving accuracy of the images, some noise may have been introduced.

The results obtained in real time are displayed in Fig. 9. On drawing a specific pattern on the stream captured by the web camera, we obtained satisfactory results. The model was tested on sentences like ‘I am a boy’, and surprisingly, it detected the air written content correctly. The segmentation mask or the pointer followed by the estimated indicator path is shown in Fig. 10. These steps are very vital towards detection of air writing. This data which was obtained was passed on to the Raspberry Pi for operating home appliances like lights and fans. The appliances were connected

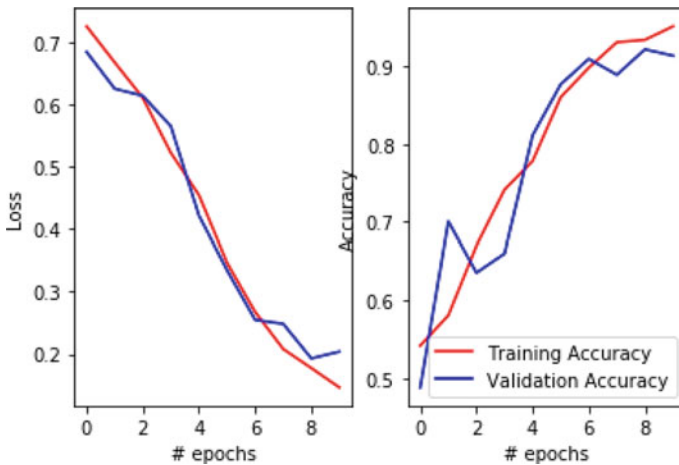


Fig. 8 Model loss (left) and accuracy (right)



Fig. 9 Air writing detection

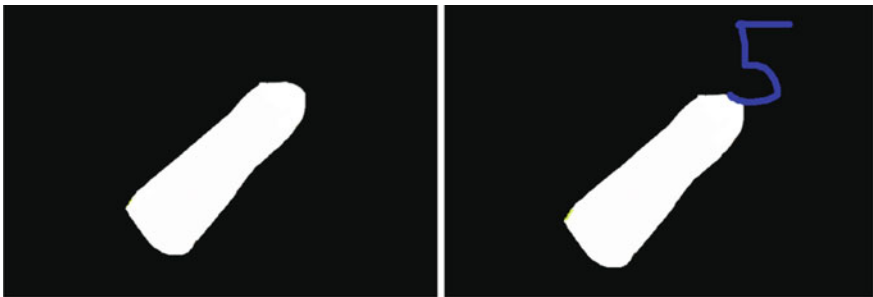


Fig. 10 Left: Segmentation mask. Right: Segmented indicator and estimated indicator path

to a relay for proper operation. The circuit diagram for connecting the appliances is shown in Fig. 11.

As seen in Figs. 9 and 10, the concept of air writing with the help of gesture recognition is satisfied. When a figure is drawn using a marker, the predicted output of the digit or alphabet is given successfully. Following this, the correct trigger is given for a pin on the Raspberry Pi, and ultimately, an appliance starts. The accuracy obtained is 94.77%, and our system detects the numbers and alphabets properly followed by operating the lights and fans.

6 Conclusion

The above proposed method is highly cost effective. Moreover, this proposed technique is different from other proposed methods, and this is may be one of the first

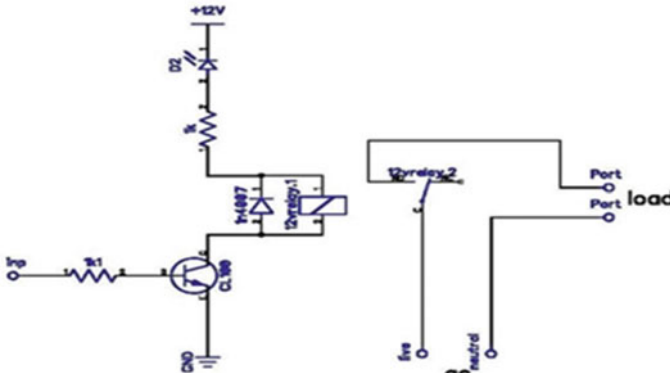


Fig. 11 Relay connection. Load is the light/fan

and inexpensive implementation of a smart gesture-based automated room that can operate irrespective of the lighting conditions. Its utility lies in the fact that it will be highly beneficial for the visually impaired or handicapped people. As soon as they draw a pattern on a camera, the light or fan turns on. There is absolutely no need to find the switchboard. Furthermore, if we use a night vision camera, the above system can be easily functional in the night. It would be a one of its kind systems.

References

1. Y. LeCun, Y. Bengio, G. Hinton, Deep learning. *Nature* **521**, 436–444 (2015). Classification Dataset Results, https://rodrigob.github.io/are_we_there_yet/build/classification_datasets_results.html
2. R. Benenson, Classification Datasets Results. 2016. Available online: http://rodrigob.github.io/are_we_there_yet/build/classification_datasets_results.html. Accessed on 21 May 2018
3. G. Cohen, S. Afshar, J. Tapson, A. Schaik, EMNIST: extending MNIST to handwritten letters, in *2017 International Joint Conference on Neural Networks (IJCNN)* (2017), pp. 2921–2926
4. A. Krizhevsky, I. Sutskever, G.E. Hinton, ImageNet classification with deep convolutional neural networks. *Adv. Neural. Inf. Process. Syst.* **25** (2012)
5. O. Russakovsky, J. Deng, H. Su et al., ImageNet large scale visual recognition challenge. *Int. J. Comput. Vis.* **115**, 211–252 (2015)
6. V. Gulshan, L. Peng, M. Coram et al., Development and validation of a deep learning algorithm for detection of diabetic retinopathy in retinal fundus photographs. *JAMA* **316**, 2402–2410 (2016)
7. A. Esteva, B. Kuprel, R.A. Novoa et al., Dermatologist-level classification of skin cancer with deep neural networks. *Nature* **542**, 115–118 (2017)
8. B. Ehteshami Bejnordi, M. Veta, P. Johannes van Diest et al., Diagnostic assessment of deep learning algorithms for detection of lymph node metastases in women with breast cancer. *JAMA* **318**, 2199–2210 (2017)

9. P. Lakhani, B. Sundaram, Deep learning at chest radiography: automated classification of pulmonary tuberculosis by using convolutional neural networks. *Radiology* **284**, 574–582 (2017)
10. K. Yasaka, H. Akai, O. Abe, S. Kiryu, Deep learning with convolutional neural network for differentiation of liver masses at dynamic contrast-enhanced CT: a preliminary study. *Radiology* **286**, 887–896 (2018)

Reliability Assessment of Smart Grid with Renewable Energy Sources, Storage Devices, and Cyber Intrusion



Lalit Tak, Atul Kumar Yadav, Neeraj Kumar Singh,
and Vasundhara Mahajan

Abstract Aiming at the series of problems existing in current power system this paper evaluates the reliability indices by considering the cyber intrusion phenomenon at the distribution side of smart grid infrastructure using MATLAB software. Modernization of grid will help to improve the reliability and promote energy efficiency. This will allow the customer to generate and store electricity and use it in case of an outage. Furthermore, the paper also discusses the cyber-attack modeling and its impact on reliability indices. The reliability indices such as system average interruption frequency index (SAIFI), system average interruption duration index (SAIDI), customer average interruption duration index (CAIDI), average service availability index (ASAI), average service unavailability index (ASUI), energy not supplied index (ENS), average energy not supplied (AENS), annual customer interruptions (ACI), customer interruption duration (CID) for each case are evaluated and the impact of cyber intrusion on reliability indices is also taken into consideration. Assessment is carried out on IEEE 14 bus system for the following four cases: Case 1: System with conventional sources, Case 2: System with renewable energy sources (RES), Case 3: System with conventional, renewable energy sources, and storage devices (SDs), Case 4: System with conventional, renewable sources, and storage devices, including cyber intrusion (CIs).

Keywords CAIDI · Cyber-attacks · Cyber physical system · ENS · Reliability assessment · Renewable energy sources · Smart grid · Storage devices · SAIDI · SAIFI

1 Introduction

Development in the world economy and population, combined with rapid urbanization, fuels energy consumption, and energy demands on a daily basis. In order to maintain a healthy ecosystem, in addition to the challenges of meeting rising

L. Tak · A. K. Yadav · N. K. Singh · V. Mahajan (✉)
SVNIT, Surat, Gujarat, India

demand, greater reliability, security, productivity, and a safe environment are also important. Technological change and innovation, “technological change and innovation” in order to make the grid process smarter and smarter smart grids, the strides into digital technology were introduced [1].

The smart grid provides an unparalleled opportunity for the energy industry to step into the new age of reliability, availability, and efficiency, adding to the power infrastructure that enables electricity to be stored and generated by consumers, enabling faster electricity restoration after disconnection from the utility.

In recent decades, the advent of many technical advances as well as environmental and economic issues has made conventional electricity systems redundant and not well-suited to meet the requirements of reliability, performance, and sustainability, not just because the complexities of the electricity grid also pose a challenge to the production and distribution of electricity [1, 2].

The implementation of a new smart grid concept or the automation of the grid makes it smarter through the use of various types of equipment and controls that interact and function together to deliver power more effectively and efficiently to restore services more quickly when outages occur [2].

The smart grid technology encompasses various new technologies and application that interacts to create a more secure and reliable system. Electricity distribution systems are undergoing a revamp; moving toward smarter utilities with innovations such as electric vehicles and home appliances. The modern grid allows electricity and data to flow in two forms, consisting of two distinctive and complex networks, cyber and power. Each network has its own set of rules and standards defined and is regulated exclusively by physical and logical laws belonging to that network. There is a security issue with the emergence of cybercrime, especially where communication is concerned, which is critical in fault detection, isolation, and restoration from the reliability point of view and not only should recognize and isolate the faulty region, automatically reenergize the non-faulty component and boost reliability metrics [3].

Architecture of smart grid has been shown in Fig. 1. It visualizes each component, i.e., bulk generation, energy storage, a two-way communication system, transmission, distribution, and customer sections.

From a cyber security viewpoint, the implications of malicious commands can be modeled for risk management and early mitigation. Steps that are taken when a cyber-attack takes place in a network component are that the affected area is isolated and measures are taken to restore supplies, such as closing points usually open. At higher loading speeds, reliability becomes more critical because supply restoration can be unfeasible or limited when failure occurs. In order to have more practical reliability, network limitations, e.g., line capacity and voltage limits, and various other steps need to be taken into account [4].

The design and technologies used for transmission and distribution grids and their device interactions would need to be modified. The demands of this transition will increase over the next 10–15 years as a result of energy efficiency initiatives in buildings with an increased presence of zero or positive energy buildings,

i.e., equipped with their own energy sources for self-consumption or for selling part of their excess output to electricity operators and the complete integration of

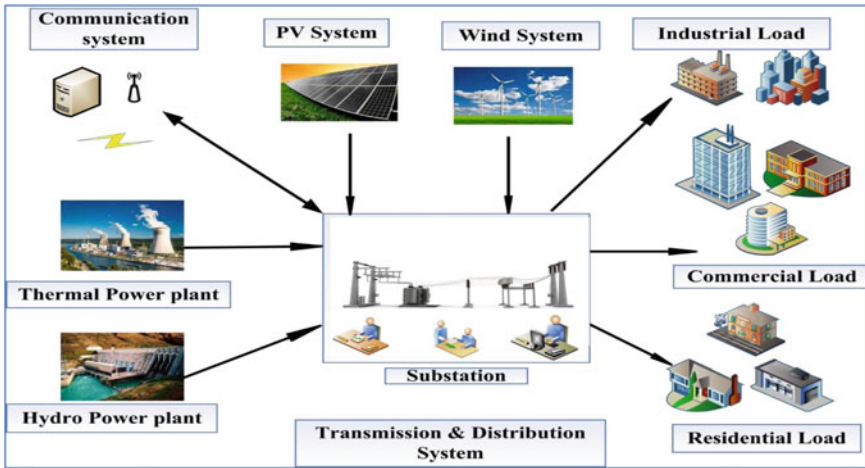


Fig. 1 An example of architecture of smart grid

renewable energy sources (RES) which, by their very nature, display fluctuations in availability and productivity [5]. Energy storage would be needed in order to effectively cover the mismatch between energy needs and the generation of RES and the use of electric vehicles and their need for both to be sluggish.

This paper deals with the reliability of a smart grid based on a different mix of power grid systems such as traditional power grids, renewable energy grids, power grids connected with storage devices, and cyber intrusions (CIs). The MATLAB software program is used for the simulation and study of electrical power systems. Results show that more efficient and sustainable electricity can be supplied to end-users when the power grid is combined with traditional, renewable energy sources, and storage devices.

This paper is structured as follows. Section II briefly describes the smart grid and cyber threats. Section III describes basic principles for the evaluation of reliability indices. Section IV addresses the case analysis of four incidents. The findings for these cases are compared in Section V. Finally, the inference drawn from the discussions in this paper is set out in Section VI.

2 Smart Grid with Cyber Intrusion

Electrical grids power our day-to-day life, but it is time to smarten up!

“A self-healing grid” or “smart grid” is an electrical grid based on the design idea of “Demand Follows Supply.” It is the digital technology that helps in meeting the complex power demand by providing two-way communication between the customer and utilities with the increased flow of information and energy.

A smart grid is a developing network of communications controls, computers, automation, and new technologies and tools working together to make the grid more efficient, more reliable, more secure, and greener. With more advancement in this field, the smart grid will replace today’s grid’s aging infrastructure, and utilities can better communicate with us to help manage our electricity needs [6].

The benefits associated with the smart grid include:

1. Helps in the identification and to monitor any glitches or problems that may arise, i.e., real-time availability status
2. Improving outage management: restore power in less time.
3. Actively manage energy consumption.
4. A small electrical device, i.e., in-home display, is paired up with a smart meter to give you all kinds of data about your energy use.
5. The dynamic pricing of power in the smart grid enables the user to adjust their demand according to time-varying pricing.

Separating myths from reality allows us to benefit from all the benefits that a smarter, efficient, secure, and more modernized electric grid (smart grid) offers. It is essential to stay acquainted and learn about your utility’s different ways to deploy a smart grid to improve their electric service [5, 6].

The smart grid permits the authority to connect/ disconnect the consumers remotely for not paying bills, without going to their houses/industries. A smart meter in the smart grid context records the consumer’s power usage and communicates this data on time to the utility center, which enables them to generate the electricity bills with that data. It can be inferred that the smart meters replaced the meter readers in this new era of power generation [7]. Analytics platforms are built, which enables to control or monitor the peak load of the grid. Monitoring structure of smart grid is shown in Fig. 2. In grid monitoring, it will monitor the storage available in energy storage devices and it will also communicate with the advanced metering infrastructure.

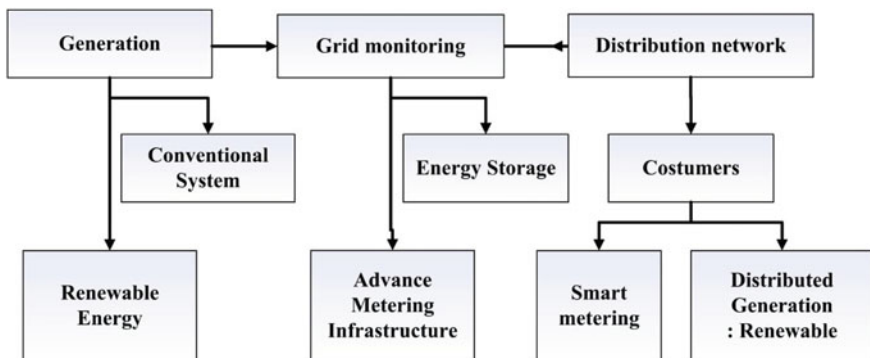


Fig. 2 Monitoring structure of smart grid

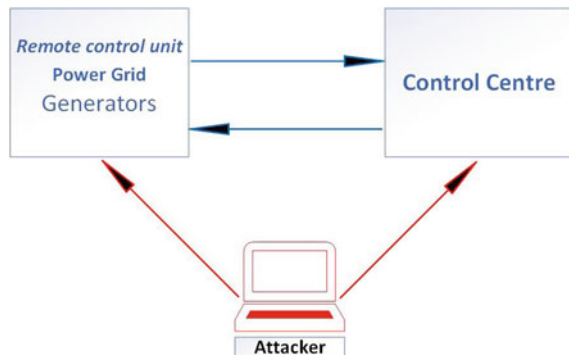
The SCADA-OMS (outage management system) method allows for the rapid identification of faults and their position directly on the portal. This reduces the time required to clear the fault (tree collapse, transformer burst, etc.). The demand response system allows the utility to run a load-reduction program (automated). Say, if the consumer consumes more power than the prescribed value, he or she will be physically removed from power, and this will happen 2–3 times to remind the consumer of his or her consumption so that the consumer decreases his or her load at specific intervals. If it still does not reduce its load, the power supply would be limited for the entire load limitation duration. Provision may be temporarily disconnected by the user using the portal if the supply is not needed for a few months. The entire electrical grid is superimposed on the “geographic information system,” which monitors feeders, transformers, and houses. Supervising the violation of the sanctioned load by the consumers helps in generating revenues to the utility [5–7].

The smart grid can solve many problems, but it also poses many challenges. These problems are related to a lack of understanding and adaptation to emerging technologies among citizens, electrical infrastructure at the distribution level and do not promote the full automation of the grid. Significant investment is required in the rehabilitation of the infrastructure or in the implementation of remote monitoring (PMU) technology. The smart grid faces a variety of challenges, but also offers excellent opportunities [8].

Cyber intrusion in power grid and control center is shown in Fig. 3.

Owing to high penetration of the Internet, cyber protection is one of the most critical needs in the world, as cyber security threats are perilous. In the smart grid system, the vulnerability of the system renders it vulnerable to cyber-attacks. Cyber-attacks in the smart grid system rely on a number of factors that enable the attacker to reduce the information security of the system [9]. In the smart grid system, cyber-attacks target sensitive information to unauthorized users, who exploit the information to hurt others and take advantage of it. Cyber-attacks often target the unauthorized deletion or alteration of information in the network system and the transmission of false information to the customer. Most cyber security experts agree that malware is a key

Fig. 3 Cyber intrusion in power system



weapon option for malicious intent to infringe cyber security efforts in cyberspace [9].

Malware may be distributed to utility center servers or the organization to extract certain sensitive pieces of information by inserting those functions by malware. The aim of the attacker could also be to conduct a denial-of-service attack, which puts the power supply at a standstill—creating outages and difficulties in restoring the power supply [10–12].

Researchers in the field of power systems have recently increased their emphasis on power interruption by malware attacks, which is the leading cause of device unreliability. If the alarm is not activated immediately after the malicious data has been detected, the device will be exposed to the risk of unauthorized access to the data [10–12].

A comprehensive study of sources of threat helps in achieving smart grid security. Smart grid security threats classification by sources is as follows [13]:

2.1 Technical Sources of Threat

The three salient points of the technical sources of threat are identified, and these are:

1. Infrastructural security

The smart grid system is a very complex system that is geographically and economically distributed, interconnecting users, utilities, power stations, substations, ICT devices, etc., needs protection because bypassing any of these by unauthorized users makes the system prone to cyber-attack and weakens the system making it unreliable.

2. Technical, operational security

It covers the infrastructural installations and operation procedures. It also ensures that routine check occurs because the identification and diagnosis of the problem beforehand make the system reliable, secure, efficient, and uninterruptible operations.

3. Systems' data management security

This aspect covers real-time supervision and monitoring of the data and storing the necessary information and data. It also provides security against cyber-attacks by injection of false information, malware attacks, terrorism, etc. The main concern is the customer's privacy breach by access to their personal information. Various protocols and guiding policies are made against this to provide customer satisfaction in terms of privacy assurance.

2.2 Non-Technical Sources of Threat

This includes;

1. Environmental security

The environmental hazards such as earthquakes, floods, falling of trees, and bush burning are factors that can prevent the smart grid’s deployment. So while installing the smart grid, various environmental factors of that location should be a matter of concern. Furthermore, a smart response system should be set up to tackle the situation as soon as possible to restore the power supply.

2. Government regulatory policies and implementation

The government should introduce various policies to create awareness among the peoples about the new technologies that are emerging for the country’s socio-economic development. The various organizations should raise funds under the government to set up the smart grid system’s infrastructure by replacing the aging electric power system. Investment should also be made in the research and development sector by the government.

3 Reliability Assessment of Smart Grid with Consideration of Cyber Intrusion

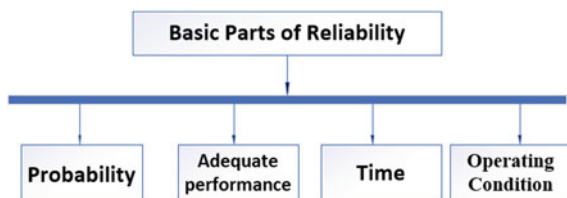
Reliability is the possibility that the system can perform its task in an acceptable manner for the period of time intended under the operating conditions encountered. The description of reliability is broken down into the following sections as shown in Fig. 4.

The block one, probability, provides the numerical input for the reliability evaluation as well as the first device adequacy index. The remaining three blocks are all engineering parameters, and probability theory is not helpful in this part of the assessment [14].

Generally, only the engineer responsible for a particular system can satisfactorily supply information relating to these. For reliability evaluation, the following steps involved are as follows:

1. Recognize the way of system operation,

Fig. 4 Basic parts of reliability



2. Analyze the ways in which system can fail,
3. Reduce the consequences of the failures,
4. Obtain models to exemplify these characteristics.

After that select the reliability evaluation technique. Reliability evaluation can be done with these two techniques: analytical and simulation.

Analytical techniques exemplify the system by a mathematical model and evaluate the reliability indices from this model using mathematical solutions. Monte Carlo simulation methods, however, estimate the reliability indices by simulating the actual process and random behavior of the system [14].

3.1 Reliability Evaluation at Generation Side

Availability means the percentage of time that the system remains operational under normal circumstances in order to serve its intended purpose.

$$\text{Mean time to repair(MTTR)} = \frac{1}{\mu} \quad (1)$$

$$\text{Mean time to failure(MTTF)} = \frac{1}{\lambda} \quad (2)$$

$$\text{Forced outage rate(FOR)} = \frac{\lambda}{\lambda + \mu} \quad (3)$$

Here forced outage rate (FOR) is also called “Unavailability” of the system.

$$\text{Availability of the System} = 1 - \text{FOR} \quad (4)$$

$$\text{Availability} = \frac{\mu}{\lambda + \mu}; \quad (5)$$

where λ is expected failure rate, μ is expected repair rate, mean time between failures can be calculated as

$$\text{MTBF} = \text{MTTF} + \text{MTTR} \quad (6)$$

Availability can also determine in terms of MTTF & MTTR.

$$\text{Availability} = \frac{\text{MTTF}}{\text{MTTF} + \text{MTTR}} \quad (7)$$

3.2 Reliability Evaluation at Distribution Side

When a customer is connected at load point, he requires all system components in between supply side and himself. For evaluation of reliability indices for such situation, we are using a classical concept that includes three basic parameters such as average failure rate, average repair duration, and average annual unavailability or average annual outage time [15]. Here we can evaluate the following values as shown below:

$$\text{Failure rate } \lambda = \sum_{i=0}^n \lambda_i \tag{8}$$

$$\text{Annual unavailability } U = \sum_{i=0}^n \lambda_i r_i \tag{9}$$

$$\text{Repair time } r = \frac{U}{\lambda} = \frac{\sum_{i=0}^n \lambda_i r_i}{\sum_{i=0}^n \lambda_i} \tag{10}$$

$$\text{Annual Customer Interruptions} = \sum N_i \lambda_i \tag{11}$$

$$\text{Customer Interruption Duration} = \sum N_i U_i \tag{12}$$

1. Customer-orientated indices

The customer indices are calculated by the following expressions:

$$\text{SAIFI} = \sum N_i \lambda_i / \sum N_i \tag{13}$$

$$\text{SAIDI} = \sum N_i U_i / \sum N_i \tag{14}$$

$$\text{CAIDI} = \sum N_i U_i / \sum N_i \lambda_i \tag{15}$$

$$\text{ASAI} = (\sum N_i * 8760 - \sum N_i U_i) / \sum N_i \lambda_i \tag{16}$$

$$\text{ASUI} = 1 - \text{ASAI} \tag{17}$$

where λ_i is the failure rate, N_i is the total number of customers at load point i , and U_i is the annual outage duration at load point i .

2. Load-orientated indices

The load indices are calculated by the following expressions:

Fig. 5 Two-state model of cyber intrusion



$$ENS = \sum LiUi \tag{18}$$

$$AENS = ENS / \sum Ni \tag{19}$$

where Li is average load at load point i .

3.3 Cyber Intrusion Modeling and Calculation

For cyber intrusion, two-state model is used as shown in Fig. 5.

$$\text{Mean time to cyber intrusion} = 1/\alpha \tag{20}$$

Whenever cyber intrusion occurs in the system, the operator will follow two steps:
 Step 1: Identify and block the intrusion.

Step 2: Introduce a new method to handle the blockage when any other intrusion came in the future.

$$\text{Repair time to recover cyber intrusion } \beta = 1/2\alpha \tag{21}$$

4 Case Studies

The performance evaluation conducted is based on the IEEE 14 bus system. Average load data taken from Appendix A [16] and number of customers assumed are given in Table 1:

Case 1: A system with Conventional Sources

Data sheet for case 1 is shown in Table 2. Customer- and load-orientated indices evaluated for case 1 as follows:

$$\text{Annual Customer Interruptions} = 36,771$$

$$\text{Customer Interruption Duration} = 111,922.4$$

$$\text{SAIFI} = 1.751 \text{ interruption/customer}$$

$$\text{SAIDI} = 5.329637 \text{ h/customer}$$

Table 1 Details of the distribution system

S. No.	Bus No.	Load point	No. of costumers (N)	Avg. load demand, <i>L</i> (kW)
1	2	Lp1	2000	21,700
2	3	Lp2	7000	94,200
3	4	Lp3	4000	47,800
4	5	Lp4	700	7600
5	6	Lp5	900	11,200
6	9	Lp6	3000	29,500
7	10	Lp7	800	9000
8	11	Lp8	400	3500
9	12	Lp9	600	6100
10	13	Lp10	1000	13,800
11	14	Lp11	600	14,900
Total			21,000	259,300

Table 2 Reliability indices for case 1

Load point	λ (failures/yr)	<i>r</i> (hr/failure)
Lp1	1.98	2.58
Lp2	1.84	3.63
Lp3	1.69	2.77
Lp4	1.44	2.46
Lp5	1.69	3.13
Lp6	1.58	2.54
Lp7	1.99	2.75
Lp8	1.75	3.20
Lp9	1.69	2.48
Lp10	1.48	3.10
Lp11	1.86	2.89

= 319.7782 min/customer

CAIDI = 3.043767 h/customer interruption

= 182.62600 min/customer interruption

SAI = 0.9993916

ASUI = 0.0006084060

ENS = 1,406,182.02 kWh

Table 3 Reliability indices for case 2

Load point	λ (failures/yr)	r (hr/failure)
Lp1	1.70	2.61
Lp2	1.82	1.76
Lp3	1.42	1.82
Lp4	1.62	1.92
Lp5	1.21	1.73
Lp6	1.39	1.54
Lp7	1.46	1.96
Lp8	1.11	2.60
Lp9	1.32	2.28
Lp10	1.16	2.20
Lp11	1.21	1.90

AENS = 66.96105 kWh/customer

Case 2: A system with renewable energy sources

Data sheet for case 2 is shown in Table 3. Customer- and load-orientated indices evaluated for case 2 as follows:

Annual Customer Interruptions = 32,503

Customer Interruption Duration = 60,494.55

SAIFI = 1.547762 interruption/customer

SAIDI = 2.880693 h/customer

= 172.8416 min/customer

CAIDI = 1.861199 h/customer interruption

= 111.6719 min/customer interruption

ASAI = 0.9996712

ASUI = 0.0003288462

ENS = 747,301.9 kWh

AENS = 35.58580 kWh/customer

Case 3: A system with conventional, Renewable energy sources, and storage devices

Data sheet for case 3 is shown in Table 4. Customer- and load-orientated indices evaluated for case 3 as follows:

Annual Customer Interruptions = 27,883

Customer Interruption Duration = 47,929.62

Table 4 Reliability indices for case 3

Load point	λ (failures/yr)	r (hr/failure)
Lp1	1.40	1.11
Lp2	1.32	1.70
Lp3	1.22	1.85
Lp4	1.42	1.64
Lp5	1.11	1.18
Lp6	1.50	1.69
Lp7	1.46	1.76
Lp8	1.21	2.30
Lp9	1.32	1.98
Lp10	1.36	2.60
Lp11	1.11	2.10

SAIFI = 1.327762 interruption/customer

SAIDI = 2.282363 h/customer
 = 136.9418 min/customer

CAIDI = 1.718955 h/customer interruption
 = 103.1373 min/customer interruption

ASAI = 0.9997395

ASUI = 0.0002605437

ENS = 592,480.9 kWh

AENS = 28.21338 kWh/customer

Case 4: A system with conventional, renewable sources, and storage devices, including cyber intrusion

Data for the cyber interruption in terms of intrusion time of the system α , recovery time of the system β is shown in Table 6. Reliability indices for this case were calculated using failure and repair rate of the systems with intrusion and recovery time of the system, as shown in Table 5.

Customer- and load-orientated indices evaluated for case 4 as follows:

Annual Customer Interruptions = 45,382

Customer Interruption Duration = 43,475.04

SAIFI = 2.161048 interruption/customer

SAIDI = 2.070240 h/customer
 = 124.2144 min/customer

Table 5 Reliability indices for case 4

Load point	λ (failures/yr)	r (hr/failure)
Lp1	1.70	0.68
Lp2	2.16	0.93
Lp3	2.61	0.98
Lp4	1.21	1.07
Lp5	1.55	1.07
Lp6	2.25	0.92
Lp7	2.73	0.94
Lp8	1.60	1.27
Lp9	1.16	1.24
Lp10	2.68	1.36
Lp11	2.05	1.13

Table 6 Data sheet of cyber interruption

Load point	α (failures/yr)	β (hr/failure)
Lp1	2	0.250
Lp2	3	0.166
Lp3	4	0.125
Lp4	1	0.500
Lp5	2	0.250
Lp6	3	0.166
Lp7	4	0.125
Lp8	2	0.250
Lp9	1	0.500
Lp10	4	0.125
Lp11	3	0.166

CAIDI = 0.957979 h/customer interruption

= 57.47879 min/customer interruption

ASAI = 0.9997637

ASUI = 0.0002363288

ENS = 543,603.4 kWh

AENS = 25.88588 kWh/customer

5 Result and Discussion

Since innovation and technology have ushered in a new era of energy, healthier, smarter, and greener, while this transformation offers opportunities, it also poses challenges to “meet the customer.” The electric utility industry defines various reliability indices to measure the system performance and distribution system reliability. In the below-given figure, the performance evaluation is done on IEEE 14 bus system, and the comparison is performed among various indices, i.e., customer-oriented indices and load-oriented indices.

System average interruption duration index (SAIDI): the most often used performance measurement indices. On comparing the data of SAIDI from all the four cases mentioned above and from the bar chart (Fig. 6), it can be analyzed that the reduction in the value of SAIDI took place by 45.94% on switching to the system with renewable energy source from the conventional energy source. Further, it is reduced by 57.14% for the system which includes conventional with renewable energy sources and storage devices. In comparison with case 1, a decrease of 61.15% in the SAIDI value is seen for the system, including cyber intrusion.

System average interruption frequency index (SAIFI): These customer-oriented indices give the average number of times a customer experiences an outage during the time under study.

From the comparison of data and the bar chart (Fig. 6), it can be seen that a decrease of 11.67% in the outage value is obtained in a system with a renewable energy source (compared to case 1). When conventional with renewable energy sources and storage devices are considered, a higher decrease of 24.17% is seen in the outage that customer experiences. But the trend shows an increase of 23.41% in the number of outages on the system, including cyber intrusion.

Customer average interruption duration index (CAIDI): Once an outage occurs, the average time to restore service is found by CAIDI. In case 2, the value of CAIDI

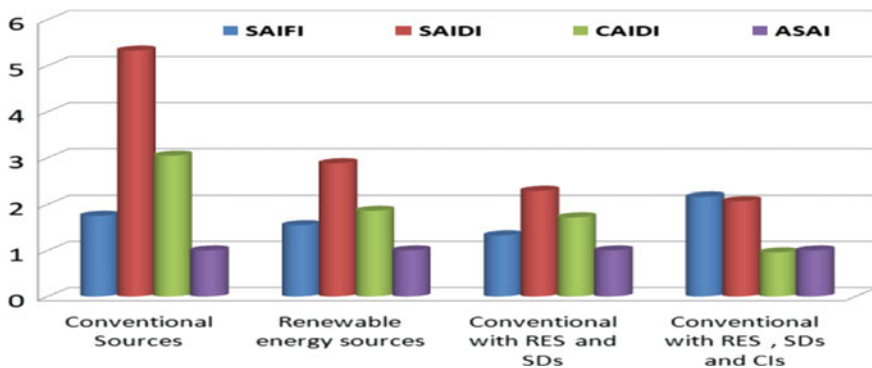


Fig. 6 Reliability assessment of power grid system

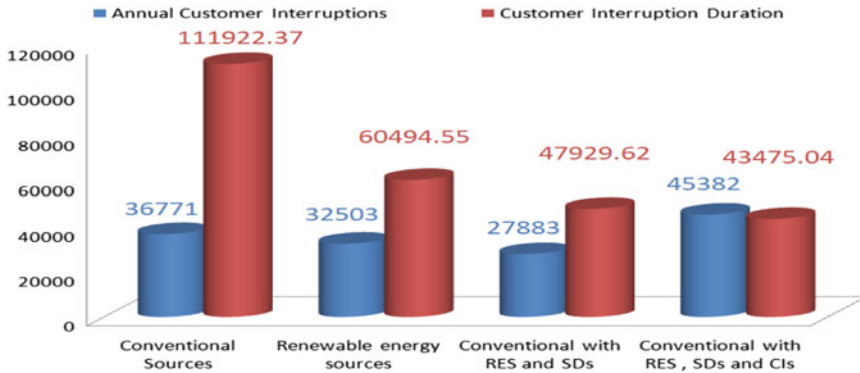


Fig. 7 Customer interruption for different cases

is enhanced by 38.85% compared to case 1. Moreover, a 43.52% improvement was noticed in the value of CAIDI in case 3 when storage devices are integrated.

Average service availability index (ASAI): ASAI is the total number of customer hours that service was available during a given time to the total customer hours demanded. No appreciable change is observed in ASAI’s value while making a comparison among all the four systems.

From the comparison of data of the annual customer interruption and customer interruption duration, it can be inferred that a decrease of 11.60% is seen in annual customer interruption between conventional sources and renewable sources. In comparison, a reduction of 24.17% is observed in conventional with renewable energy sources and storage devices. But on cyber intrusion, the interruption value rises by 23.41%. On calculating the percentage decrease in customer interruption duration, a decrease of 45.94% is seen between conventional sources and renewable sources, and the trend shows that the percentage goes on decreasing for both 2 and 3 cases as shown in Fig. 7. In comparison, an increase of 61.15% in customer interruption duration is seen in conventional with renewable energy sources and storage devices, including cyber intrusion.

6 Conclusion

This paper has analyzed the reliability indices of smart grid taking four different systems: a conventional energy source, renewable energy source, conventional with renewable energy source and storage devices, and conventional with renewable energy source and storage devices, including cyber intrusion. The performance evaluation is carried out on IEEE 14 bus system, and simulation is done on MATLAB software. According to the results, as stated above, it can be inferred that the most efficient system is “conventional with renewable energy sources and storage devices.” But on cyber intrusion, the system’s efficiency decreases, it becomes less secure and

unreliable, resulting in unexpected outages and difficulty in the restoration of power supply. Cyber-attacks are becoming more sophisticated and thereby presenting challenges to the electric utility industry. As future work, the performance evaluation will be conducted on a large scale to detect cyber intrusion and implementation of secure architecture to recover faster.

References

1. K. Moslehi, R. Kumar, A reliability perspective of the smart grid. *IEEE Trans. Smart Grid* **1**, 57–64 (2010)
2. B. Falahati, Y. Fu, Reliability assessment of smart grids considering indirect cyber-power interdependencies. *IEEE Trans. Smart Grid* **5**, 1677–1685 (2014)
3. A. Escalera, B. Hayes, M. Prodanovic, Reliability assessment of active distribution networks considering distributed energy resources and operational limits, in *CIREN Workshop 2016*, pp. 1–4
4. G. Celli, E. Ghiani, F. Pilo, G.G. Soma, Reliability assessment in smart distribution networks. *Electr. Power Syst. Res.* **104**, 164–175 (2013)
5. M.L. Tuballa, M.L. Abundo, A review of the development of Smart Grid technologies. *Renew. Sustain. Energy Rev.* **59**, 710–725 (2016)
6. M. Fadaeenejad, A.M. Saberian, M. Fadaee, M.A.M. Radzi, H. Hizam, M.Z.A. AbKadir, The present and future of smart power grid in developing countries. *Renew. Sustain. Energy Rev.* **29**, 828–834 (2014)
7. M.E. El-Hawary, “The smart grid” state-of-the-art and future trends. *Electr. Power Compon. Syst.* **42**, 239–250 (2014)
8. A. Bari, J. Jiang, W. Saad, A. Jaekel, Challenges in the smart grid applications: an overview. *Int. J. Distrib. Sens. Netw.* **10**, 974682 (2014)
9. D.B. Rawat, C. Bajracharya, Cyber security for smart grid systems: status, challenges and perspectives, in *SoutheastCon 2015*, pp. 1–6
10. Y. Liu, P. Ning, M.K. Reiter, False data injection attacks against state estimation in electric power grids. *ACM Trans. Inf. Syst. Secur. (TISSEC)* **14**, 1–33 (2011)
11. A. Abur, A.G. Exposito, *Power System State Estimation: Theory and Implementation* (CRC Press, 2004)
12. E. Handschin, F.C. Schweppe, J. Kohlas, A. Fiechter, Bad data analysis for power system state estimation. *IEEE Trans. Power Appar. Syst.* **94**, 329–337 (1975)
13. A.O. Otuoze, M.W. Mustafa, R.M. Larik, Smart grids security challenges: classification by sources of threats. *J. Electr. Syst. Inf. Technol.* **5**, 468–483 (2018)
14. R. Billinton, R.N. Allan, *Reliability Evaluation of Engineering Systems* (Springer, Berlin, 1992)
15. T.L. Laubst, Reliability evaluation of power systems, in *Quality and Reliability Engineering International*, ed. by R. Billinton, R.N. Allan, vol. 1 (Plenum Press, New York and London, 1984, 1985), pp. 141–141
16. J. Rajathy, Data sheets for IEEE 14 bus system, 2003

Development of Unstructured Kinetic Model for Bioethanol Production by *Saccharomyces cerevisiae* MTCC 171 from Sorghum Grain Waste



Sheetal Deshmukh and Dheeraj Deshmukh

Abstract In the present study, a kinetic model was developed by batch fermentation for bioethanol production using *Saccharomyces cerevisiae* MTCC 171 from sorghum waste grains. For simulating the experimental value for biomass, ethanol production and substrate utilization, unstructured kinetic models were studied. Biomass production and bioethanol production were evaluated by Logistic Model and Luedeking Piret model respectively. The predicted values of the parameters from these models had good agreement with experimental data. Thus they were capable of calculating the fermentation profile of ethanol estimation from waste (jowar) sorghum grains. High values of coefficient of determination (R^2) values of 0.978, 0.959 and 0.985 were found for cell biomass, product formation and raw material utilization. For scaling up of bioethanol production process with consistency from waste grains this kinetic model could be a very convenient tool.

Keywords Waste Sorghum grain · Bioethanol · Growth kinetics · Substrate utilization kinetics · Production kinetics

1 Introduction

Bioethanol is gaining importance over the last few years as a viable fuel source due to its potential as a substitute for conventional fossil fuel. Bioethanol is used as gasoline additive and as an unusual source of fuel [1–3]. Huge quantity of various grains is rotten every year in India. This is due to severe climatic conditions and a lack of proper storage facilities. Food grains get spoiled or wasted during harvesting and improper handling. High moisture levels and temperature, causes decay of grains heavily. Utilization of waste sorghum grains is renewable feedstock. Sorghum could

S. Deshmukh (✉)
Department of Food Technology, L.I.T., RTMNU, Nagpur, MS, India

D. Deshmukh
Department of Mechanical Engineering, G H Raisoni College of Engineering, Nagpur,
Maharashtra, India
e-mail: dheeraj.deshmukh@raisoni.net

© The Author(s), under exclusive license to Springer Nature Singapore Pte Ltd. 2022
M. L. Kolhe et al. (eds.), *Smart Technologies for Energy, Environment and Sustainable Development, Vol 1*, Springer Proceedings in Energy,
https://doi.org/10.1007/978-981-16-6875-3_55

contribute to the requirement of country's fuel ethanol [4]. Cost of raw material for ethanol production by fermentation is to be taken into consideration as the economics of the process is a very crucial part of this process. More than half of production cost is dependent on cost of raw material. In previous research work, utilization of inexpensive agricultural resources like damaged food grains for ethanol production was carried out [5–7]. Higher production and more efficient bioprocesses need to be discovered in order to fulfil the increasing demand for ethanol production. Thus to operate and control ethanol production process, a thorough knowledge of static and dynamic behaviour is necessary [8]. Formulation of mathematical model enables to perform optimization of any process for further improvement in desirable outcomes that is ethanol production. Different models are utilized for determining constants for the variables involved in the process. Kinetic expressions for the process derived from different models are investigated also mass balance equations are utilized. Model kinetic parameter values have to be determined very precisely so that consistent predictions can be made [9].

The present study targets developing and validating, Logistic and Luedeking Piret mathematical models for predicting the dynamics of biomass, ethanol production and substrate utilization from waste sorghum grains using *Saccharomyces cerevisiae* MTCC 171 and to assess the suitability of the projected mathematical model.

2 Materials and Methods

2.1 *Microorganism and Favourable Culture Conditions for Fermentation Process*

Saccharomyces cerevisiae MTCC 171 strain for investigation was obtained from the Microbial Type Culture Collection (MTCC), Institute of Microbial Technology, Chandigarh, India. Yeast extract, peptone, dextrose and agar medium was used for maintenance of slants. The strain was grown under sterile conditions at a temperature of 30 °C for a time period of 8 h. Immediately after 8 h, it is used for inoculating previously sterile medium in a 5 L batch fermenter (B-Lite, Lab Fermenter, Satorius, India Pvt. Ltd.). Batch process of fermentation was used to perform experiments in a 5 L batch fermenter containing half of its volume that is 2.5 L of fermentation medium. The medium was stirred at 250 rpm for uniform distribution of constituents of medium for growth of yeast cells. Previously enzymatically liquefied and saccharified sorghum waste wort was used as fermentation medium as it was an adequate source of carbon and energy for metabolism of yeast cells. In the medium, mineral nutrients and yeast extract were added as nitrogen sources. In order to maintain aseptic conditions the fermenter containing the medium was sterilized by autoclaving at 121 °C for 35 min. To maintain sustainability/viability of cell, aeration was given to bioreactor/fermenter with 0.45 vvm air and the temperature was kept at 30 °C. Initially, pH of the medium was 4.5 and reducing sugar (S_0) and

biomass (X_0) concentrations in the experimental work were $S_0 = 1.467$ g/L, $X_0 = 1.893$ g/L. Liquefying enzyme diastase (α -amylase) was procured from Hi-media Laboratories Pvt. Ltd. The enzyme used for hydrolysis of starch was glucoamylase from fungus *Aspergillus niger* (NCIM 1248) procured from the National Collection of Industrial Microorganisms, National Chemical Laboratory, Pune, India possessing activity of 44 U/ml. Potato dextrose agar (PDA) slants were used for maintaining fungal culture. All medium components and laboratory tools used in experimentation were autoclaved (121 °C, 15–30 min). Samples were removed from fermenter every 12 h for analysis. These samples were centrifuged in a variable speed research centrifuge at 5000 r min⁻¹. After centrifugation, the supernatants were analyzed for residual sugar, biomass and bioethanol concentrations.

Biomass concentration (grams/litre) was estimated as dry weight using spectrophotometer at wavelength of 570 nm. Remaining/residual sugar concentration stated as grams/litre was estimated by the 3, 5-Dinitrosalicylic acid (DNS or DNSA) method [10]. Viability of cells was determined by the classical method of staining with methylene blue [11]. Estimation of ethanol was done by spectrophotometer [12]. All the testing were repeated thrice and the average values are obtained.

2.2 Mathematical Modelling

Performance of any cellular process can be predicted using a kinetic model through probable mathematical equations. Modelling of kinetic process can efficiently analyze as well as optimize a fermentation process. Previously various kinetic models have been studied for growth of microorganisms, carbohydrate utilization and ethanol formation. When microbial cells are treated as a multicomponent system, it is known as a structured model where when microbial cells are treated as one component in the whole system then it becomes an unstructured model. While exploring the growth of microbial cells, unsegregated model is the best ideal solution [13].

Logistic kinetic equation which is used to analyze the rate of microbial growth of cells, when there is no inhibition by substrate as well as product, during optimum conditions of growth is given by

$$\frac{dx}{dt} = \mu_m X \left(1 - \frac{X}{X_m} \right) \quad (1)$$

where X is concentration of cells or biomass (grams/litre), X_m is the cell or biomass concentration at maximum level (grams/litre), μ_m or μ_{\max} is the maximum specific growth rate (/hour) and t is the time required (hour). Using the initial conditions of $X = X_0$ at $t = 0$ and on integration of Eq. (1) will give Eq. (2):

In the above equation is the specific growth rate of microorganisms and concentration of cell or biomass is represented by μ and X respectively.

Rearranging

$$\ln \frac{X}{X_m - X} = \mu_m t - \ln \left(\frac{X_m}{X_0} - 1 \right) \quad (2)$$

Above equation has can be plotted by taking $\ln \frac{X}{X_m - X}$ on y axis and time (t) on x axis which gives the slope as μ_m and value of X_0 can be obtained from the intercept. Experimental data gives the value of maximum biomass concentration X_m .

By alteration of Luedeking Piret model kinetics of substrate consumption (utilization) can be obtained which takes into consideration substrate transformation to biomass, ethanol (product) and maintenance of substrate utilization

$$\frac{dS}{dt} = \frac{1}{Y_{X/S}} \frac{dx}{dt} - \frac{1}{Y_{P/S}} \frac{dP}{dt} + ke^x \quad (3)$$

$Y_{x/s}$ is yield coefficient for biomass production (g biomass produced/g substrate consumed).

$Y_{p/s}$ is the yield coefficient for product formation (g product formed/g substrate consumed).

Equation 3 changes to Eq. 4 when second and third terms are neglected when quantity of carbon sources used for formation of ethanol (product) that is $\frac{dP}{dt}$ and constant k for maintenance of substrate are insignificant and the mathematical model converts to,

$$\frac{dS}{dt} = \frac{1}{Y_{X/S}} \frac{dx}{dt} \quad (4)$$

Leudeking-Piret model defines kinetics of product formation $\frac{dP}{dt}$. According to this model rate of product formation $\frac{dP}{dt}$ simultaneously depends on both biomass concentration and rate of microbial growth which is given by the following equation:

$$\frac{dP}{dt} = \alpha \frac{dX}{dt} + \beta X \quad (5)$$

P is the concentration of product (grams/litre), the constants α and β can change with operating conditions and they are to be evaluated [14].

3 Result and Discussion

3.1 Microbial Growth

A normal growth form was observed in ethanol fermentation by *Saccharomyces cerevisiae* 171 using waste food grains. All the phases of growth lag, log or exponential, stationary and death were found in growth patterns. In order to fit microbial

Table 1 Model parameter for ethanol production

Logistic model		Luedeking piret model						
Cell concentration		Substrate consumption				Product formation		
μ_m	X_0	k	R^2	$Y_{x/s}$	Error%	α	β	Error%
0.151	0.199	0.09126	0.9829	10.22	6.63	0.5	0.0808	3.05

growth kinetics information of batch fermentation Logistic equation (Eq. 1) is used. There was no remarkable increase in ethanol concentration during the first 6 h of fermentation process. However, rise in ethanol production was found after 6th hour of fermentation. It reached maximum to the peak and then reduced slowly. Maximum cell concentration or biomass (12.364 g/litre) was attained at 72th hour of fermentation and then it remains constant due to depletion of reducing sugar in the medium. By taking $X_m = 12.364$ g/litre from the performed experimental data in Eq. (2), maximum specific growth rate μ_m and initial cell concentration X_0 were obtained as 0.151 h^{-1} and 0.199 g/litre respectively (Table 1). Calculated X_0 value shows good agreement with model predicted value. From these values, it was observed that the recommended logistic model was satisfactory to explain the exponential growth pattern of yeast cells.

3.2 Substrate Utilization

In ethanol fermentation, it was found that while depletion in reducing sugar, there was a simultaneous increase in cell mass (biomass) concentration from the medium. Initially, sugar consumption by yeast cells was very slow but it increased steadily and maximum reduction of reducing sugar was found at 12 h of fermentation. Reducing sugar kinetics was represented in Eq. 3. The initial level of reducing sugar concentration used was 1.467 g/L. Yield coefficient $Y_{x/s}$ for biomass with respect to substrate consumed was found to be 10.22 and constant k for substrate consumption kinetics was obtained as 0.09126.

3.3 Product Formation

Ethanol production was evaluated by Luedeking- Piret model and the kinetic parameters were studied using Eq. (5) at stationary phase when growth rate dX/dt is zero. From Table 1 it was observed that value of α and β are 0.5 and 0.0808 respectively. These results showed that the value α is more than β . Thus growth related constant ' α ' is more than the non-growth related rate constant β . Thus, the bioethanol production in this work was found to be as growth associated product formation and similar findings were reported with ethanol production from banana and pineapple waste by

Peng and Zhong [15]. Similar results were also reported by Germec et al. [16]. On the other hand, Ahmed et al. [17] has shown in his work that ethanol production is not growth related product [17].

3.4 Data Analysis and Modelling

Biomass production by growth of microbial cells, reducing sugar consumption and product formation were evaluated and simulated with the lab scale experimental data for bioethanol production by *S. cerevisiae* MTCC 171 using food waste grains. For microbial yeast cell growth kinetic study the logistic equation was used whereas for reducing sugar consumption and ethanol production, Luedeking Piret model was used. Minitab software was used to estimate kinetic parameters. The estimated parameters were used to test the model. Microsoft Office Excel 2016 was used to evaluate the model by graphical method. A comparison of experimental and predicted data is shown in Figs. 1, 2 and 3 for cell concentration, substrate consumption and product formation. R^2 value is generally used to describe the accuracy of the model by examining the goodness of fit for the experimentally conducted data and model predicted data. In this study, R^2 values for cell concentration (biomass), bioethanol production and reducing sugar consumption were found to be 0.978, 0.959 and 0.985 respectively. These R^2 values certified that the recommended model gives superior estimates. Thus high significance of coefficient of determination (R^2) shows the reliability and validity of model with the experimental and predicted results.

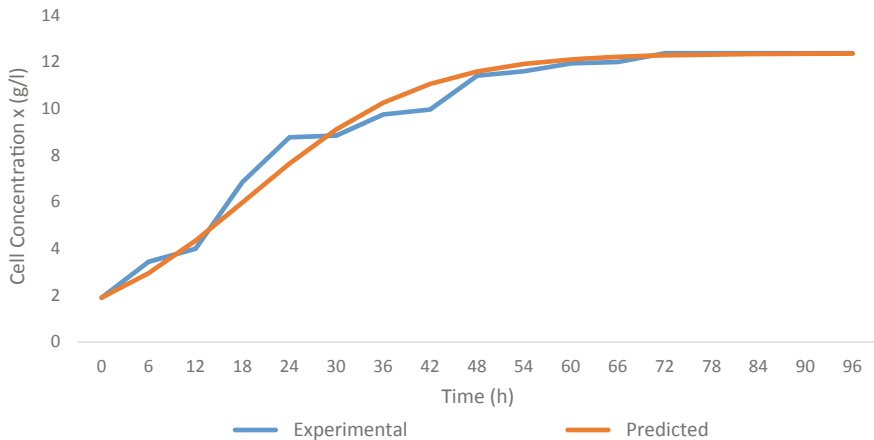


Fig. 1 Comparison of experimental and predicted data for modelling growth kinetics of *Saccharomyces cerevisiae* MTCC 171

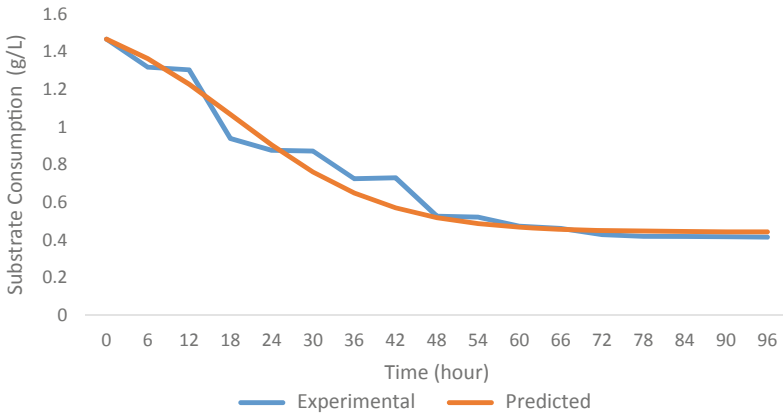


Fig. 2 Comparison of experimental and predicted data for modelling substrate consumption using *Saccharomyces cerevisiae* MTCC 171

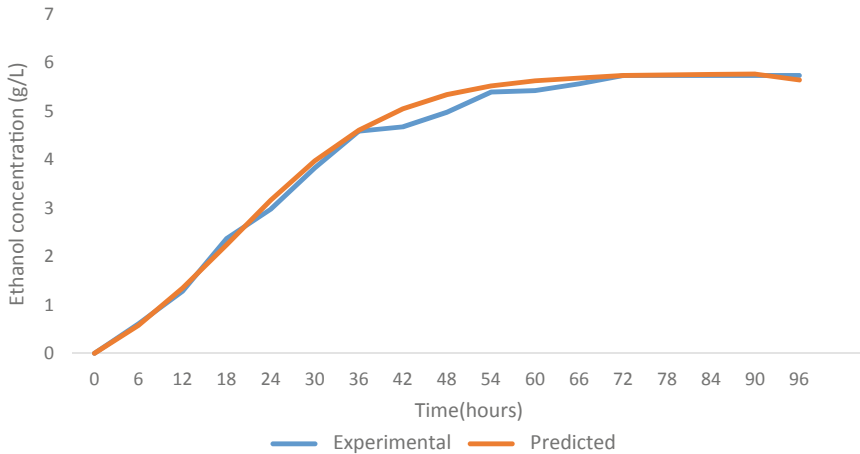


Fig. 3 Comparison of experimental and predicted data for modelling Ethanol production from food grain waste using *Saccharomyces cerevisiae* MTCC 171

4 Conclusion

During study and further experimental work for development of an unstructured kinetic model of bioethanol Production following conclusions could be stated. Kinetics of fermentation process from waste sorghum grains is very complex in any biochemical reaction and thus it is difficult to define the most appropriate model for fermentation process. However, it was found that the mathematical model developed in this investigation predicts the biomass, ethanol production and substrate utilization with process time in a very precise manner to support ethanol production industry


economically. Ethanol production performance was evaluated by Luedeking Piret model whereas biomass production was by Logistic Model. On the basis of estimated kinetic parameter values, it was concluded that ethanol production by *Saccharomyces cerevisiae* 171 was growth associated. With these results obtained in the present work, it can be concluded that developed model may be a useful tool for controlling and optimizing the growth, bioethanol production and substrate consumption kinetics in an industrial level fermentation process using *Saccharomyces cerevisiae* 171 from waste food grains.

References

1. B.H. Davison, C.D. Scott, Operability and feasibility of ethanol production by immobilized *Zymomonas mobilis* in a fluidized-bed bioreactor. *Appl. Biochem. Biotechnol.* **18**(1), 19 (1988)
2. J. Rass-Hansen, H. Falsing, B. Jorgensen, C. Christensen, Perspective bioethanol: fuel or feedstock. *J. Chem. Technol. Biotechnol.* **82**, 329–333 (2007)
3. J.W. Worley, D.H. Vaughan, J.S. Cundiff, Energy analysis of ethanol production from sweet sorghum. *Bioresour. Technol.* **40**(3), 263–273 (1992)
4. W.L. Rooney, J. Blumenthal, B. Bean, J.E. Mullet, Designing sorghum as a dedicated bioenergy feedstock. *Biofuels, Bioprod. Biorefin.* **1**(2), 147–157 (2007)
5. K. Suresh, L. Venkateswar Rao, Utilization of damaged sorghum and rice grains for ethanol production by simultaneous saccharification and fermentation. *Bioresour. Technol.* **68**(3), 301–304 (1999)
6. K. Suresh, N. Kiransree, L. Venkateswar Rao, Production of ethanol by raw starch hydrolysis and fermentation of damaged grains of wheat and sorghum. *Bioprocess Eng.* **21**(2), 165–168 (1999)
7. S. Yan, X. Wu, J. Dahlberg, S.R. Bean, F. MacRitchie, J.D. Wilson, D. Wang, Properties of field-sprouted sorghum and its performance in ethanol production. *J. Cereal Sci.* **51**(3), 374–380 (2010)
8. I.C.P. Astudillo, C.A.C. Alzate, Importance of stability study of continuous systems for ethanol production. *J. Biotechnol.* **151**(1), 43–55 (2011)
9. S.C. Oliveira, R.C. Oliveira, M.V. Tacin, E.A.L. Gattás, Kinetic modeling and optimization of a batch ethanol fermentation process. *J. Bioprocess. Biotech.* **6**(266), 2 (2016)
10. G.L. Miller, Use of dinitrosalicylic acid reagent for determination of reducing sugar. *Anal. Chem.* **31**(3), 426–428 (1959)
11. S. Sadasivam, *Biochemical methods* (New age international, 1996)
12. A. Caputi Jr., M. Ueda, T. Brown, Spectrophotometric determination of ethanol in wine. *Am. J. EnolVitic* **19**(3), 160–165 (1968)
13. J.E. Bailey, D.F. Ollis, *Biochem. Eng. Fundamentals* **28** (1986)
14. R. Luedeking, E.L. Piret, A kinetic study of the lactic acid fermentation. Batch process at controlled pH. *Biotechnol. Bioeng.* **67**(6), 636–644 (2000)
15. Y.P. Teoh, Z.X. Ooi, Evaluation of unstructured kinetic models for the production of bioethanol from banana and pineapple wastes. *BioResources* **11**(2), 4295–4305 (2016)
16. M. Germec, I. Turhan, M. Karhan, A. Demirci, Kinetic modeling and techno-economic feasibility of ethanol production from carob extract based medium in biofilm reactor. *Appl. Sci.* **9**(10), 2121 (2019)
17. F. Ahmad, A.T. Jameel, M.H. Kamarudin, M. Mel, Study of growth kinetic and modeling of ethanol production by *Saccharomyces cerevisiae*. *Afr. J. Biotechnol.* **10**(81), 18842–18846 (2011)

Experimental Investigation on RCCI Engine Operated with Dairy Scum Oil Methyl Ester and Producer Gas



V. S. Yaliwal, P. A. Harari, and N. R. Banapurmath 

Abstract The impact of producer gas (PG) on performance, combustion, and emission characteristics of dairy scum oil methyl ester (DSOME) fueled common rail direct injection (CRDI) engine worked under reactivity controlled compression ignition (RCCI) mode of operation were examined. During suction stroke, producer gas was injected into the intake manifold as low reactive fuel (LRF); meanwhile, diesel, DSOME B20 and DSOME B100 blends were injected during compression stroke as high reactive fuels (HRF). The experimentation was performed on CRDI engine at a constant speed of 1500 rpm with 75% of the rated power. The results showed that, brake thermal efficiency (BTE) of the engine significantly increased up to 40% of gaseous fuels energy share (GFES) for D + PG fuel combination. As compared with other fuel combinations, hydrocarbon (HC), carbon monoxide (CO), and smoke emissions of D + PG in all energy shares were lower. Meanwhile, nitric oxide (NO_x) emissions of D + PG in all energy shares were higher as compared with other fuel combinations.

Keywords Dairy scum oil methyl ester · Gaseous fuels energy share · Producer gas · Reactivity controlled compression ignition

1 Introduction

The electric vehicles can be considered as a likely innovation to advance the change from regular portability to e-versatility. The genuine advantages regarding carbon dioxide emissions rely upon an incredible degree on their method of utilization,

Present Address:

V. S. Yaliwal · P. A. Harari (✉)

Department of Mechanical Engineering, SDM College of Engineering and Technology, Dharwad, Karnataka 580002, India

N. R. Banapurmath

Department of Mechanical Engineering, BVB College of Engineering and Technology, Hubballi, Karnataka 580031, India

design of vehicle, and power source. Over the most recent couple of years, low-temperature combustion mode such as RCCI combustion is an interesting topic for various researchers due to its lower soot and NO_x emissions [1]. In a RCCI combustion, when the premixed proportion of low reactive fuel was high, inadmissible high pressure rise rate is consistently developed [2]. Dual fuel direct injection was most encouraging approaches for controlling the blending process in a dual fuel engine [3]. Pan et al. [4] found that, as compared with RCCI diesel/gasoline combustion mode, RCCI diesel/iso-butanol combustion mode had later combustion phase, longer ignition delay and combustion duration, higher indicated thermal efficiency, and lower pressure rise rate. Duraisamy et al. [5] found that, use of polyoxymethylene dimethyl ether as high reactive fuel with methanol as low reactive fuel under RCCI mode reduced the ignition delay and resulted in shorter combustion duration as compared with diesel/methanol RCCI mode of combustion. Raza et al. [6] found that, in-cylinder pressure rise rate and heat release rate of RCCI were efficient by utilizing physical and chemical properties of multisegment substitute fuel for both diesel and gasoline. Nazemian et al. [7] found that, with the expansion of diameter of piston bowl and depth of piston bowl, because of higher the heat transfer exergy increased and total exergy decreased. Wang et al. [8] found that, thermal efficiency of RCCI gasoline/polyoxymethylene dimethyl ether combustion could be adequately improved with exhaust gas recirculation and intake air. Yu et al. [9] found that, kernels of low-temperature combustion created in n-heptane stream inside the blending layer and advance into flames of low-temperature combustion increased into moderately fuel-rich mixtures. Dadsetan et al. [10] found that, minimum swirl proportion was the best for HC and CO decrease. The exhaust gas temperature was most extreme around the swirl proportion of 1.2. The ideal swirl proportion for that engine was in the scope of 0.95–1.2 which prompts higher efficiency and most reduced NO_x. Kakoei et al. [11] found that, high flame speed and high heating value hydrogen lead to expanding pressure rise rate. Due to increment of temperature of in-cylinder combustion, great consuming of methane and accordingly, there was a plummet of HC emissions at 50% of hydrogen addition. Wenming et al. [12] found that, emissions of soot dropped fundamentally by 75%, with methanol expansion rate from 0 to 60% because of efficient blending between air and fuel. Liu et al. [13] found that, initial low-temperature combustion of RCCI was constrained by spray combustion of high reactive fuel, along with essential heat release rate originating from n-heptane low-temperature combustion process that improved the system reactivity. Ebrahimi et al. [14] found that, addition of hydrogen to the landfill gas, mass of fuel per each cycle was decreased and pressure rise rate was increased. Addition of hydrogen to landfill gas improved the methane dissociation rate; subsequently the combustion duration was diminished considerably. Zheng et al. [15] found that, expanding n-butanol proportion leads to decrease of soot emissions and prompts higher HC and CO emissions for RCCI mode.

2 Materials and Methods

2.1 *Production of Biodiesel from Dairy Scum*

In this present work, well-known conventional transesterification was employed to achieve DSOME. Experimental setup used for transesterification is shown in Fig. 1. Initially the scum was purified and heated to about 100 °C. Heating removes the moisture content and filtered. The dairy scum is then subjected fatty acid test and acid value was recorded. Based on this acid value of scum, acid-catalyzed transesterification is carried out, in which the known quantity of methanol and sulfuric acid is taken in a beaker. In the next step, the known quantity of dairy scum is mixed with methanol and sulfuric acid mixture. Then transesterification process is carried out using round flask apparatus. Further, base-catalyzed transesterification is done and creation of biodiesel from dairy scum is followed according to the method. Noteworthy consideration was taken during glycerin removal and water washing. Washing of transesterified item with 30% warm water eliminates the metallic mixes.

2.2 *Properties of Test Fuels*

Different types of fuels have been used in the experimental work, and they are categorized into liquid fuels and gaseous fuels. The fuel properties are provided in Tables 1 and 2.

3 Experimental Setup

The tests were conducted on a CRDI engine with single cylinder and rated power 5.2 kW which runs at 1500 rpm. The engine was changed in accordance with run under RCCI mode by introducing producer gas during suction stroke by utilizing electronic control unit. Diesel, B20 DSOME, and B100 DSOME were used as pilot fuels during compression stroke. The injection of pilot fuel was controlled by electronic control unit. The test engine was equipped with exhaust gas analyzer for measuring of NO_x , CO, and HC emissions. To evaluate smoke emissions, the smoke meter was used. Information acquisition system was used to accumulate data of in-cylinder pressure rise and heat release rate in a computer. The schematic representation of experimental setup is shown in Fig. 2. The detail specifications of the test engine are presented in Table 3.

Fig. 1 Transesterification setup for the production of biodiesel from dairy scum



(a) Round flask apparatus for Transesterification



(b) Separation of DSOME and Glycerin



(c) Diary sum oil methyl ester



(d) DSOME washing and moisture removal

Table 1 Properties of liquid fuels [16]

Properties	Diesel	DSOME B20	DSOME B100
Density (kg/m ³)	830	840	870
Viscosity at 40 °C (CST)	2.9	2.98	4.36
Calorific value (MJ/kg)	43	40.89	38.012
Flash point (°C)	50	58	130

Table 2 Producer gas properties [17]

Properties	Values
Gas calorific value ratio (MJ/m ³)	5.6
Mixture calorific value (MJ/m ³)	2.6
Stoichiometric air fuel ratio	1.12:1
Adiabatic flame temperature (K)	1546 ± 25
Laminar burning velocity (m/s)	0.5 ± 0.05
Energy density (MJ/m ³)	2.6

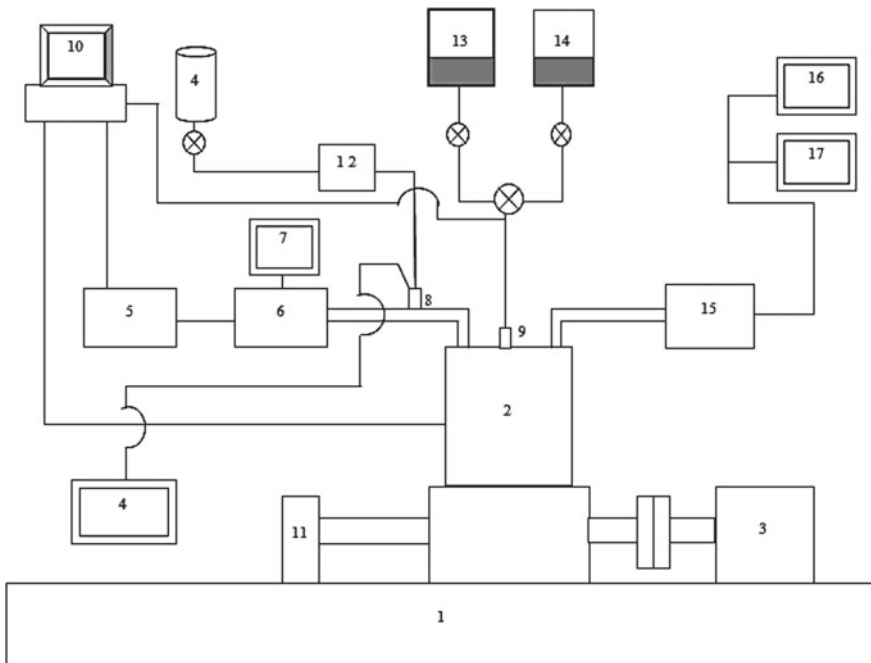


Fig. 2 Schematic diagram of experimental setup. 1—Base; 2—CRDI engine; 3—Eddy current dynamometer; 4—Producer gas cylinder; 5—Air box; 6—Electric air heater; 7—Temperature controlling unit; 8—Gas fuel injector; 9—Diesel injector; 10—Computer interfaced to engine; 11—Crank angle sensor; 12—Injector driver for gaseous fuel; 13—Diesel tank; 14—Biodiesel tank; 15—Calorimeter; 16—Exhaust gas analyzer; 17—Smoke meter

Table 3 Test engine specifications

Engine parameters	Specifications
Engine	TV1 Kirloskar
Software used	Engine soft
No. of cylinder	1
No. of strokes	4
Bore × stroke (mm)	87.5 × 110
Compression ratio	17.5:1
Dynamometer	Eddy current
Combustion chamber	Toroidal
Governor type	Mechanical centrifugal type
Rated power	5.2 kW
Dynamometer arm length	0.180 m
Manifold injector opening pressure	5 bar
Direct injector opening pressure	900 bar

Table 4 Measurement precision and uncertainties in the measured parameters

Measured variable	Accuracy (\pm)
Load (N)	0.1
Engine speed (rpm)	2
Temperature ($^{\circ}$ C)	1
Measured variable	Uncertainty (%)
Smoke	± 1.1
HC	± 1.2
CO	± 2.5
NOx	± 4
Calculated parameters	Uncertainty (%)
BTE (%)	± 1.3

3.1 Uncertainty Analysis for the Experimental Data

The measurement precision and the uncertainties of the measured parameters were provided in Table 4. Six readings have been reported to eliminate measurement errors and averaged out results were only presented for the purpose of plotting the graphs and the analysis.

4 Results and Discussions

In the primary stage, the test engine was run under RCCI mode powered with D + PG. The tests were conducted on the engine at 75% of rated power. The primary fuel was changed with B20 + PG and B100 + PG with same rated power. The performance, combustion, and emission characteristics of RCCI engine powered with producer gas as low reactive fuel and diesel, B20 and B100 blends of DSOME as high reactive fuels are presented in this section.

Figure 3 shows variation of BTE with GFES. The BTE of the engine is improved for RCCI combustion mode with up to 40% of GFES while it diminished with further increment in GFES. This is due to reduced reactivity of the dual fuel charge by domination of charge dilution effect with increase in specific heat capacity of the charge. The BTE of the engine improved for D + PG-powered RCCI combustion mode with all GFES when compared with B20 + PG and B100 + PG.

Figure 4 shows variation of HC emissions with GFES. HC emissions diminished for D + PG-powered RCCI combustion mode when compared with B20 + PG and B100 + PG. This is due to, incomplete combustion prevailing inside the combustion chamber. Also, incomplete combustion caused by ignition of small pilot fuel quantities of biodiesel can lead to higher HC emissions. Biodiesel has fuel bound oxygen which improved oxidation pace of HC. Higher HC emissions were found for biodiesel powered RCCI combustion.

Figure 5 shows variation of CO emissions with GFES. CO emissions were increased as GFES increased which may be due to abatement of in-cylinder pressure and temperature because of deficient reaction rate. Reduction in the quantity of pilot liquid fuels leads to poor ignition. Partial combustion due to lean mixture at high energy share of gaseous fuels could further lead to increased CO. The CO emissions

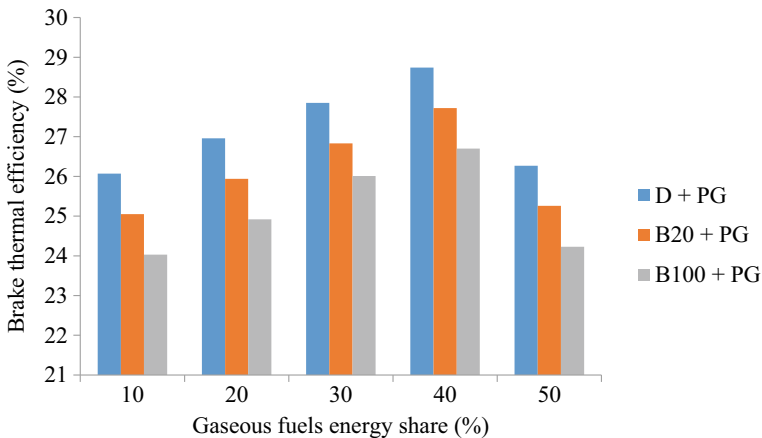


Fig. 3 Variation of brake thermal efficiency with gaseous fuels energy share

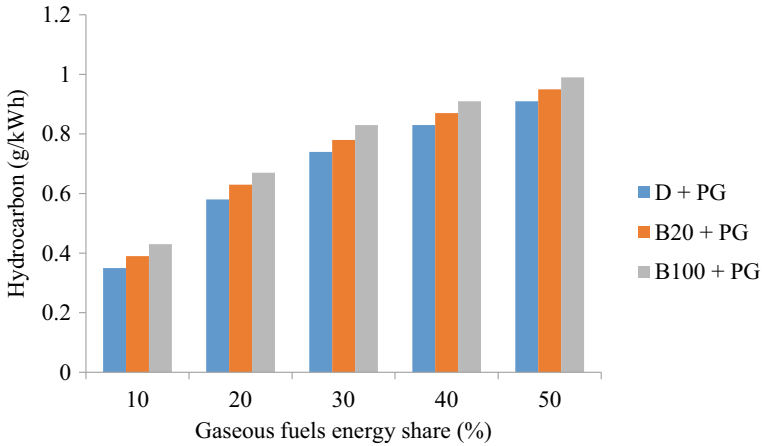


Fig. 4 Variation of hydrocarbon emissions with gaseous fuels energy share

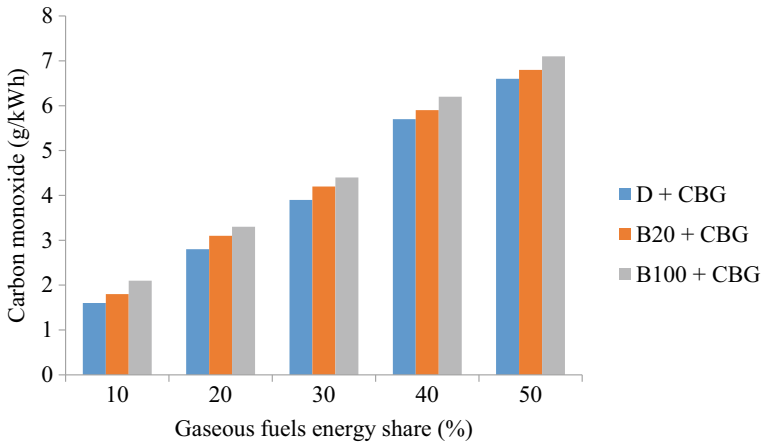


Fig. 5 Variation of carbon monoxide emissions with gaseous fuels energy share

diminished for D + PG-powered RCCI combustion mode when compared with B20 + PG and B100 + PG.

Figure 6 shows variation of NO_x emissions with GFES. NO_x emissions were diminished as the GFES increased. RCCI engine powered with D + PG discharged higher NO_x emissions as compared with B20 + PG and B100 + PG. For biodiesel, fewer NO_x emissions were seen because of expanded residual time, additionally higher density and viscosity results into deficient ignition which brings down in-cylinder pressure and temperature which in turn brings down NO_x emissions.

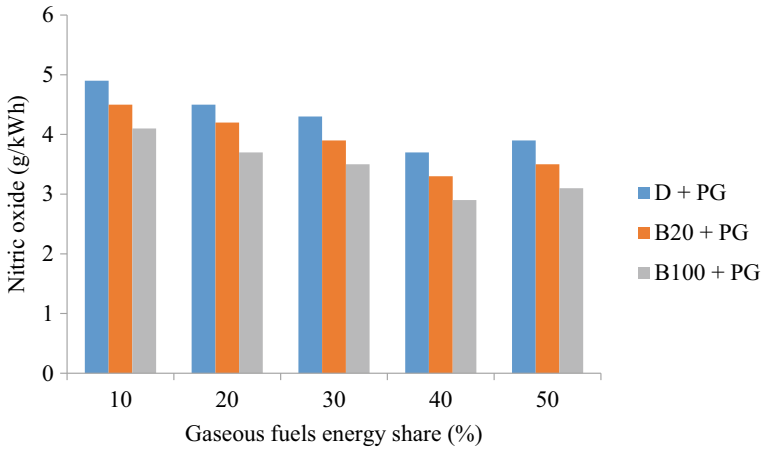


Fig. 6 Variation of nitric oxide emissions with gaseous fuels energy share

Figure 7 shows variation of smoke emissions with GFES. Smoke emissions were diminished as the GFES increased. RCCI engine powered with D + PG transmitted lower smoke emissions as compared with B20 + PG and B100 + PG. Higher smoke was found for biodiesel activity. The primary explanation behind this could be heavier structure of molecules, higher density and viscosity, and deficient air–fuel mixture formation compared with diesel.

Figure 8 shows the variation of in-cylinder pressure with crank angle at 40% GFES. Highest pressure is found for D + PG fuel combination mode as compared with other tested fuels. The reason for this is, better combustion of fuel and air blends

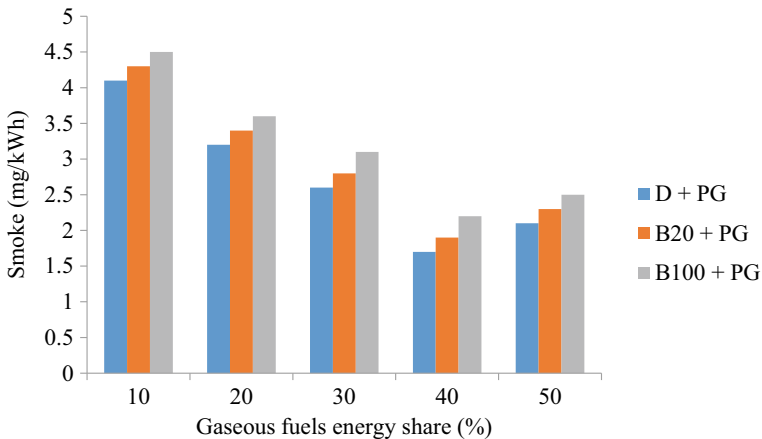


Fig. 7 Variation of smoke emissions with gaseous fuels energy share

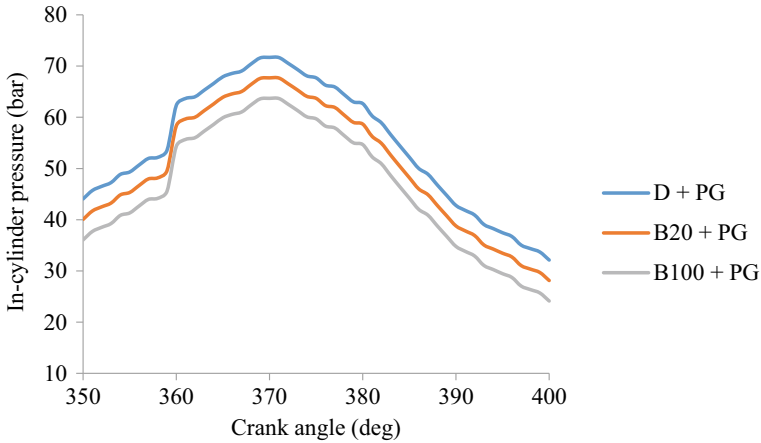


Fig. 8 Variation of in-cylinder pressure rise with crank angle at 40% gaseous fuels energy share

inside the cylinder when producer gas was injected into suction stroke and it is well mixed with diesel and hence it burns effectively.

Figure 9 shows variation of HRR with crank angle at 40% GFES. Highest HRR was found for D + PG fuel combination mode as compared with other tested fuels. This is due to, diesel had more calorific value than biodiesel, and hence, it burns effectively with the injection of producer gas.

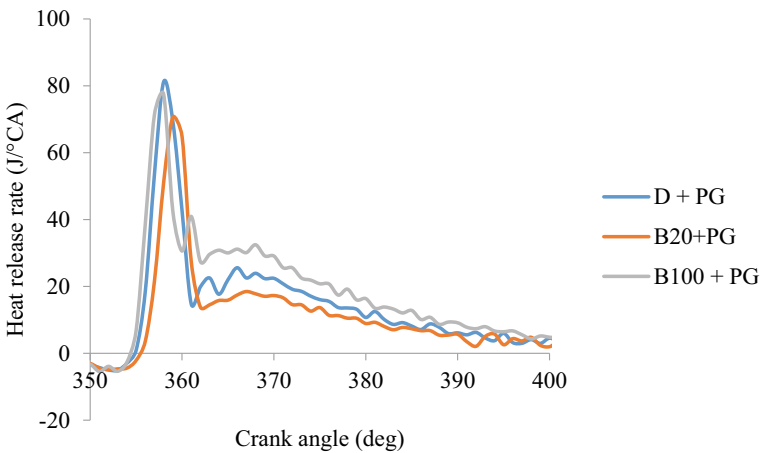


Fig. 9 Variation of heat release rate with crank angle at 40% gaseous fuels energy share

5 Conclusions

The following conclusions are made based on experimental results.

- BTE of RCCI engine powered with D + PG was higher as compared with B20 + PG and B100 + PG fuel combinations. Highest BTE was obtained at 40% GFES.
- HC, CO, and smoke emissions were increased with the percentage of GFES increased. HC and CO emissions of RCCI engine powered D + PG were less as compared with B20 + PG and B100 + PG.
- NO_x and smoke emissions were decreased as the percentage of GFES increased. NO_x emissions of RCCI engine powered with D + PG were more as compared with B20 + PG and B100 + PG.
- In-cylinder pressure rise and heat release rate of RCCI engine powered with D + PG were more as compared with B20 + PG and B100 + PG.
- Finally, it can be concluded that, at 40% of GFES with D + PG resulted into highest thermal efficiency and lower emissions.

References

1. J. Benajes, A. Garcia, J.M. Serrano, S.M. Boggio, Emissions reduction from passenger cars with RCCI plug-in hybrid electric vehicle technology. *Appl. Thermal Eng.* **164**, 114430 (2020)
2. J. Li, X. Yu, J. Xie, W. Yang, Mitigation of high pressure rise rate by varying IVC timing and EGR rate in an RCCI engine with high premixed fuel ratio. *Energy* **192**, 116659 (2020)
3. B. Yang, Q. Duan, B. Liu, K. Zeng, Parametric investigation of low pressure dual-fuel direct injection on the combustion performance and emissions characteristics in a RCCI engine fuelled with diesel and CH₄. *Fuel* **260**, 116408 (2020)
4. S. Pan, X. Liu, K. Cai, X. Li, W. Han, B. Li, Experimental study on combustion and emission characteristics of iso-butanol/diesel and gasoline/diesel RCCI in a heavy-duty engine under low loads. *Fuel* **261**, 116434 (2020)
5. G. Duraisamy, M. Rangasamy, N. Govindan, A comparative study on methanol/diesel and methanol/PODE dual fuel RCCI combustion in an automotive diesel engine. *Renew. Energy* **145**, 542–556 (2020)
6. M. Raza, H. Wang, M. Yao, Numerical investigation of reactivity controlled compression ignition (RCCI) using different multi-component surrogate combinations of diesel and gasoline. *Appl. Energy* **242**, 462–479 (2019)
7. M. Nazemian, E. Neshat, R.K. Saray, Effects of piston geometry and injection strategy on the capacity improvement of waste heat recovery from RCCI engines utilizing DOE method. *Appl. Therm. Eng.* **152**, 52–66 (2019)
8. H. Wang, D. Liu, T. Ma, L. Tong, Z. Zheng, M. Yao, Thermal efficiency improvement of PODE/Gasoline dual-fuel RCCI high load operation with EGR and air dilution. *Appl. Thermal Eng.* **159**, 113763 (2019)
9. G.H. Yu, M.B. Luong, S.H. Chung, C.S. Yoo, Ignition characteristics of a temporally evolving n-heptane jet in an iso-octane/air stream under RCCI combustion relevant conditions. *Combust. Flame* **208**, 299–312 (2019)
10. M. Dadsetan, I. Chitsaz, E. Amani, A study of swirl ratio effects on the NO_x formation and mixture stratification in an RCCI engine. *Energy* **182**, 1100–1114 (2019)

11. A. Kakoe, Y. Bakhshan, A. Gharehghani, M.M. Salahi, Numerical comparative study of hydrogen addition on combustion and emission characteristics of a natural-gas/dimethyl-ether RCCI engine with pre-chamber. *Energy* **186**, 115878 (2019)
12. Y. Wenming, Y. Meng, Phi-T map analysis on RCCI engine fueled by methanol and biodiesel. *Energy* **187**, 115958 (2019)
13. X. Liu, S. Kokjohn, Y. Li, H. Wang, H. Li, M. Yao, A numerical investigation of the combustion kinetics of reactivity controlled compression ignition (RCCI) combustion in an optical engine. *Fuel* **241**, 753–766 (2019)
14. G. Xu, M. Jia, Y. Li, Y. Chang, H. Liu, T. Wang, Evaluation of variable compression ratio (VCR) and variable valve timing (VVT) strategies in a heavy-duty diesel engine with reactivity controlled compression ignition (RCCI) combustion under a wide load range. *Fuel* **253**, 114–128 (2019)
15. M. Ebrahimi, S.A. Jazayeri, Effect of hydrogen addition on RCCI combustion of a heavy duty diesel engine fuelled with landfill gas and diesel oil. *Int. J. Hydrogen Energy* **44**, 7607–7615 (2019)
16. M.N. Channappagoudra, K. Ramesh, G. Manavendra, Influence of compression ratio on diesel engine fueled with dairy scum oil methyl ester. *AIP Conf. Proc.* **2039**, 020007 (2018). <https://doi.org/10.1063/1.5078966>
17. N.R. Banapurmath, P.G. Tewari, Comparative performance studies of a 4-stroke CI engine operated on dual fuel mode with producer gas and Honge oil and its methyl ester (HOME) with and without carburetor. *Renew. Energy* **34**, 1009–1015 (2009)

A Study on Women Police Bullet-Proof Jacket Considering Anthropometry Data, Comfort and Safety in Pune, India



Chinmayanand Prakash Jagtap, Shilpi Bora, Pranjal Arun Patil, Abhijeet Malge, and Mahesh Goudar

Abstract An effective study was held with a survey carried out by interacting with a number of lady police about the current Bullet-Proof vest available, which are bullet resistant to a particular threat level. These are not manufactured according to the concern of women. This study helps in figuring out the need for a new bullet-proof vest for women. The survey gave many aspects which need to be changed. The paper flows by briefing today's availability and condition for women's working in various defence sectors. With current scenarios and the changes need to be done with the women police personnel located in Pune district of Maharashtra state. A motive for designing a bullet-proof vest for women is basically giving them equal importance, comfort, joy and stress free duty while serving the nation. A questionnaire was developed for the survey analysis of 15 women police in Pune district. The development of the armour which can provide better protection considering comfort, weight, fitness as major factors is a demand. As a result of this study, the need of improving the armour led to various design changes like the section under the arm, neck portion, and weight reduction. These were the major aspects of the reforming strike by the women police.

Keywords Women police · Comfort · Bullet-proof vest · Safety · Anthropometry

1 Introduction

Protection and comfort play a vital role in body armour for both men and women. This body armour helps in protecting from various injuries due to physical assaults, traffic accidents and criminal conflicts as well as on the battlefield. Flexibility in

C. P. Jagtap (✉) · P. A. Patil · M. Goudar
School of Mechanical Engineering, Academy of Engineering (MITAOE), Dehu Phata, Alandi (D), Pune, Maharashtra 412105, India

S. Bora · A. Malge
School of Design, MIT, Academy of Engineering (MITAOE), Dehu Phata, Alandi (D), Pune, Maharashtra 412105, India
e-mail: shilpi.bora@adypu.edu.in

design, corrosion resistant, good mechanical properties, wear and impact resistance and ease in fabrication are requirements of design of suitable body armour which can be achieved by fibre-reinforced composite materials. These materials are used in a wide range of applications due to their properties. These can be used to produce efficient lightweight bullet-proof jackets where weight is reduced and at the same time provides high strength. Multiple layers of the fabric which are arranged in a specific manner would increase protection to absorb all the energy from the attack to dissipate it uniformly over the surface. But it will also add undesirable weight and increase flexibility. Increased number of protective layers also increases the cost of the jacket.

Involvements of women in wide areas which involve physical stress have increased in recent years. Also their employment in the military, security fields have increased. Considering such women's involvement there is needed to carry out research to develop women friendly body armour design. Light weight and comfort are the two main factors according to women centric body armour design. Many times women working in the military field are ordered to wear bullet-proof jackets which are smaller in size and same as males. Due to many psychological differences between men and women, the armour jackets which were designed for male body were obviously not accepted by the female body. In order to reduce the weight of the jackets, it is mandatory to reduce the number of layers and also the weight. Jackets can be categorized based upon threat conditions whether it's minimum or maximum. In case of minimum threat conditions normal bullet-proof jackets with less number of layers can be used whereas in situations of high risk additional separate jackets can be worn over bullet-proof for better protection levels.

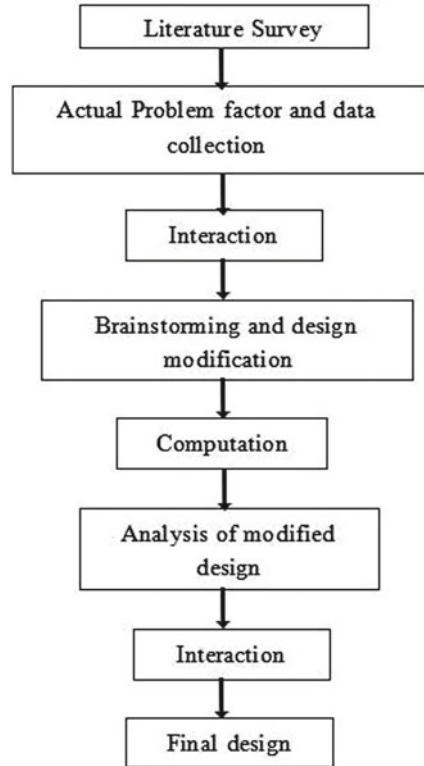
Looking at the current scenario when women wear male designed body armours, there is a lot of free space between protection layers and body due to different body shapes. In some cases, it becomes large enough creating additional risks such as difficulty in breathing for women soldiers. The smallest size of bullet-proof vest is too wide or too long for 85% of female personnel (US Department of Defense (DoD)). Body adjustment designs would also prove helpful in order to fit according to women's body shapes. This would also reduce the cost by reducing the number of exact sizes of jackets.

2 Integrated Methodology for Data Collection

This paper consists of the following content (Fig. 1):

The motive of the study was to access the current bullet-proof jackets and how it can be modified for the convenience of women police. The main reasons for discomfort, vest design and weight were some of the parameters which were analyzed strictly. We tried to reach the people who possibly owned bullet-proof armours, police departments, court offices, gun stores, body armour stores, military organizations and their offices. These surveys included 15 female participants and were selected randomly. In contrast to this, there were only 15 women police were selected because

Fig. 1 Flowchart reflecting the methodology



no other police women ever tried the bullet-proof vest and mentioned that it is not required for them. Thus, 15 women police officers were interviewed as they were available based upon their working shifts therefore the researcher has to only select those police ladies who have sometimes used the vest in their duty.

The aim of the research was to develop and modify a new protective women centric bullet-proof jacket which provides comfort, flexibility, adjustment possibilities, considering its strength similar to those providing high protection levels of existing body armours.

The covering page of the questionnaire consisted of the basic information of the interviewer including job details and family details. Based on the scale from strongly agree to strongly disagree ranging from 1 to 5 opinions were taken individually.

The questionnaire consisted of:

- Occupational and environmental stress related scales to determine how work is affected by wearing armours.
- On-job burnout to determine their views on major barriers faced during stressful conditions.

- Anthropometric measurement of women police body dimension for bullet-proof vest of Shivajinagar Police Station.

3 Occupational Well-Being Issues and Assessment

Police women have issues with a defensively covered vest fit that is not a mystery. They feel compressed, the vest moves around on the body, the Velcro sides bust open constantly, the vest spreads way out before them which brings about lost ballistic inclusion and their thoracic back encounters huge weight from wearing this substantial unbalanced structure for significant stretches of time. In the midst of an increasing chart against ladies in the nation, there is 8.98% of women police power across India, as indicated by BPR&D's most recent information on police associations [1].

The need for suitable gender-friendly defensive vests is progressively becoming a reason for unease amid policewomen in this area. The body protective layer being used right now was planned carefully for men with no thought for female physiological make up [1]. The firmness of the defensive layer is unbearable to the point that it causes uneasiness for women police as they think that it's exceptionally hard to put their chest while their patrolling duty, which is a normal piece of their schedules without almost dropping. Another zone for concern is that this female cordial body defensive layer doesn't give sufficient insurance to women police. At the point when woman police with an adequate bust wears the vest, her chest is left uncovered by sides, in this way leaving her defenceless. Bigger vests are not superior; they appear to be free and are unsafe to women cops.

3.1 Occupational and Environmental Stress Related Scales to Determine How Work is Affected by Wearing Armours

Policing, because of the one of a kind stressors, has been broadly viewed as an upsetting calling, which thus results in a disturbance of the emotional and physiological homeostasis of the individual, prompting degenerate working in the workplace. According to Vivek et al. [2], there was a very high pervasiveness of occupational stress—90% reported operational stress (high anxiety by 70% and moderate anxiety by 20%) and 80% reported organizational stress (both high stress and moderate stress by 40% each). This calls for assured consideration from the authorities as occupational strain can have an awfully negative effect on the physical, mental and social well-being as well as professional life of the women cops.

It can be seen in Table 1. That shift work affects the performance of the women police based upon rating. Their energy level is different during different times of day; hence efficiency also varies based upon their performance. Secondly, the highly rated problem of lack of a modern system affects mostly the police department, where they rely on age-old technologies. Heavy weight can be seen as a major

Table 1 Survey results on exposure to occupational and environmental stress related scales to determine how work is affected by wearing armours

Respondents	Qa	Qb	Qc	Qd	Qe	Qf	Qg	Qh	Qi	Qj	Qk	Ql	Qm	Qn	Qo
1	1	2	1	3	4	5	2	1	3	3	1	2	2	2	2
2	1	2	2	4	3	3	2	2	3	3	1	2	1	1	2
3	2	1	1	3	5	4	3	2	2	2	2	1	2	2	3
4	2	2	2	4	3	2	2	3	4	2	2	2	2	3	3
5	1	1	3	2	3	3	1	2	2	3	1	2	3	2	2
6	2	3	2	3	4	3	1	1	2	1	2	1	2	1	3
7	2	2	1	4	2	2	2	2	2	3	1	2	1	1	2
8	2	2	1	2	3	2	2	3	3	2	1	3	2	2	3
9	1	2	2	3	2	4	3	3	3	2	1	2	2	1	2
10	2	1	2	4	4	3	3	2	2	2	2	2	1	2	2
11	1	3	3	3	5	4	1	2	4	3	1	2	2	2	3
12	2	2	2	4	4	3	3	2	3	2	1	1	2	3	2
13	2	2	2	4	5	3	3	3	4	1	2	3	1	2	2
14	2	3	1	3	3	2	2	2	2	2	1	2	2	1	3
15	1	1	2	2	2	4	1	1	3	3	2	2	3	2	2

Questions Qa. Law Enforcement is a masculine job; Qb. Staff Shortages; Qc. Shift Work; Qd. Social Life; Qe. Boredom; Qf. Noisy work area; Qg. Poor equipment/maintenance; Qh. Lack of modern system; Qi. Lack of prompt utilities; Qj. Basic amenities; Qk. Less efficiency due to heavy weight; Ql. Fitting issues of the armour; Qm. Restriction in movement due to armour; Qn. On field Restrictions; Qo. Outdoor Activities

Here the numbers indicate as 1. Strongly Agree; 2. Agree; 3. Neither agree nor disagree; 4. Disagree; 5. Strongly Disagree

problem, where almost every lady police suggested that it should be reduced during the survey. Many other problems such as fitting issues, restriction in movement, on-field restrictions were rated equally. However, the body posture of the women police needs to be analyzed in detail to eliminate stress like musculoskeletal, neck pain, arms and shoulder pain, etc. Social life, basic amenities although were rated low do affect their performance level. Noisy work area and boredom can be considered self-centred based upon the individual level of each lady police.

The respondents have also revealed that bullet-proof or body protection vests provided to them are too tight, rigid and heavy that they cause breathlessness and suffocation, as they are made according to the physical requirements of a male counterpart. Moreover, the women police have also incorporated smaller palms, it is like a confrontation for them to get a solid grip on the weapon given to them, like a revolver or an INSAS rifle. Consequently, they have also sought after gender-friendly clothes and arms and armours.

From Table 2 and Fig. 2. It was found that the majority of the women police reveal that police job is a masculine job and everything is designed according to their body dimension. 60% of the women police suggested reducing weight of the

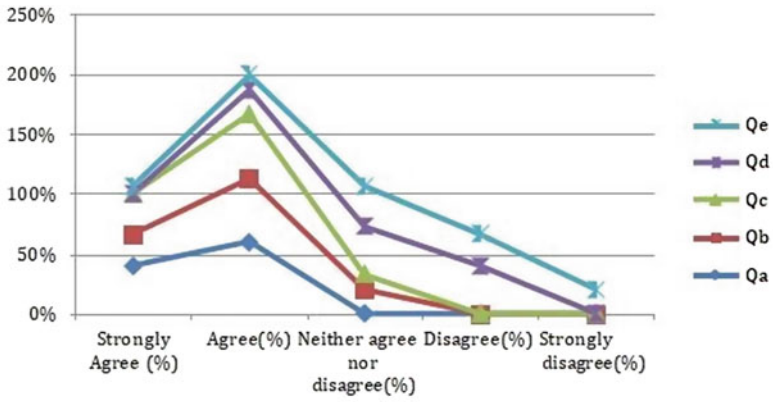
Table 2 Percentage wise analysis of Table 1

Questions	Total respondent	Strongly agree' (%)	Agree (%)	Niether agrees nor disagree (%)	Disagree (%)	Strongly disagree (%)	Total (%)
Scales		1	2	3	4	5	
Qa	15	40	60	0	0	0	100
Qb	15	27	53	20	0	0	100
Qc	15	33	53	13	0	0	100
Qd	15	0	20	40	40	0	100
Qe	15	7	13	33	27	20	100
Qf	15	7	20	40	27	7	100
Qg	15	33	33	33	0	0	100
Qh	15	27	47	27	0	0	100
Qi	15	7	33	40	20	0	100
Qj	15	13	47	40	0	0	100
Qk	15	60	40	0	0	0	100
Ql	15	20	67	13	0	0	100
Qm	15	27	60	13	0	0	100
Qn	15	33	53	13	0	0	100
Qo	15	0	60	40	0	0	100

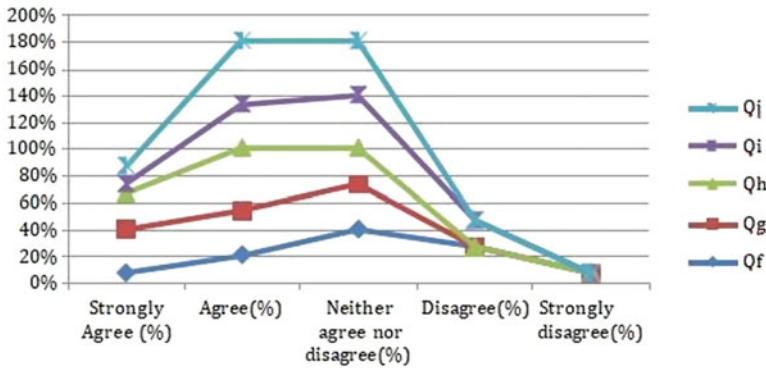
Questions Qa. Law Enforcement is a masculine job; Qb. Staff Shortages; Qc. Shift Work; Qd. Social Life; Qe. Boredom; Qf. Noisy work area; Qg. Poor equipment/maintenance; Qh. Lack of modern system; Qi. Lack of prompt utilities; Qj. Basic amenities; Qk. Less efficiency due to heavy weight; Ql. Fitting issues of the armour; Qm. Restriction in movement due to armour; Qn. On field Restrictions; Qo. Outdoor Activities

Here the numbers indicate as 1. Strongly Agree; 2. Agree; 3. Neither agree nor disagree; 4. Disagree; 5. Strongly Disagree

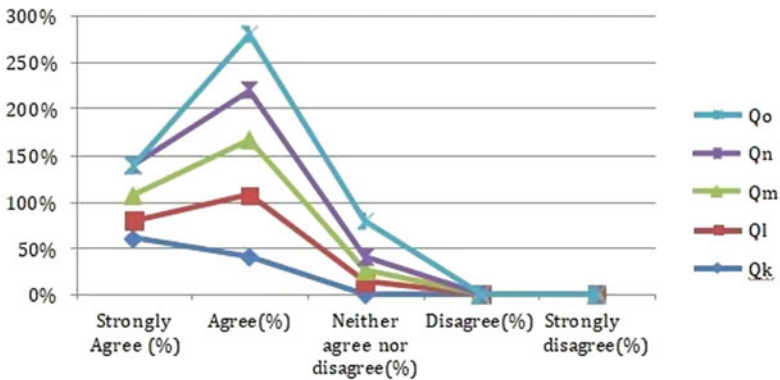
bullet-proof vest and including all the other body armour. This can be a major factor to be considered. Further, the fitting issue is faced by almost all of them as nobody disagreed with that point. Subsequently, 60% of the women police faced field restrictions because of the current bullet-proof jacket design. The women police integrated that they faced restrictions in movement which was quite surprising (67% of women police agreed). This would eventually affect their performance level. Other parameters like social life, boredom, noisy work area affected very less. These can be therefore neglected currently. Modern systems are obviously the need for the current



(a) Graphical representation of Table 1.2. From Qa to Qe



(b) Graphical representation of Table 1.2. from Qf to Qi



(c) Graphical representation of Table 1.2. From Qk to Qo

Fig. 2 Statistical distribution of occupational and environmental stress related scales to determine how work is affected by wearing armours from Table 2. **a** Graphical representation of Table 2 from Qa to Qe. **b** Graphical representation of Table 2 from Qf to Qi. **c** Graphical representation of Table 2 from Qk to Qo.

scenario of the police departments, as they must constantly try to keep updated with the latest technologies in their field.

On-job burn out to determine their views on major barriers faced during stressful conditions

Job satisfaction is a most explored issue amid industrial and organizational psychologists but police organizational scholars have all but unobserved the part of job satisfaction [3]. It is an essential factor of an organization's effective and proficient efficiency [4]. According to Rizvi [5], most women in the police force are not satisfied with their working conditions because of various reasons. It has been exposed by Alexopoulos et al. [6] more elevated levels of pressure are identified with the hazard of announcing imperfect occupation fulfilment and Quality of Life (QoL). The range of this organization differed relying upon age, sexual orientation and rank, featuring the requirement for stress-management instruction.

Adequate workplace support will lead to augmenting the intensity of job satisfaction and occupational well-being among the women cops. It is recommended that in this workplace one should maintain the programs that will persuade the women police and allow them to work with assurance, fortitude and vitality in intimidating circumstances. This intrusion will assist the women police to lessen the stress. In contrast to this, it can be proved that workplace support is considered as an opportunity to boost job satisfaction among the women police. As a result, it is suggested to diminish the hectic circumstances and to get better job satisfaction among the women police with more attention.

Table 3 explains the on-job problems faced by women police in Pune district due to various problems. The problem such as excessive workload, discomfort with the arms and ammunition including the uniform (mainly designed for male counterparts), heavy materials to be carried and held during a long period of time. The discomfort caused by wearing currently available armours is the highest rated problem where most of them strongly agree. Hence, a new bullet-proof armour design considering a woman's body posture is a necessity. Excessive workload isn't always a major problem as it depends on the area of the police station in which state it is. Going from south to north in India, the need for bullet-proof armour goes on increasing, counting highest in the extreme north and eastern region of India. Work frustration is also a similar kind of problem. Both excessive workload and work, frustration have been rated between 3 and 4 on a scale. Further, burn out during job due to armour can also be studied in order to work on the design point of view.

The respondents have also disclosed that job satisfaction of the women police is inclined by promotion, salary and place of work. The women in police are an essential part of policing. The women in Shivajinagar Police Station and other areas of Pune district have acknowledged that they are glad about the etiquettes of a male colleague in their workplace which is an excellent precursor in a male-dominated police society. It is fundamental to confirm the job satisfaction of women police to know about the assorted problems of women in policing culture. They have also mentioned that there are still a variety of difficulties for women in policing at police stations for e.g. duty belts, heavy bullet-proof vests, basic amenities, uniform, helmet, etc. Redesigning of

Table 3 Survey results on-job burn out to determine their views on major barriers faced during stressful conditions

Respondent	Qa	Qb	Qc	Qd	Qe	Qf
1	3	2	3	3	2	1
2	2	2	2	2	1	2
3	3	3	3	3	1	1
4	2	2	4	2	2	1
5	1	3	2	1	2	1
6	2	2	1	1	2	1
7	2	2	2	2	1	2
8	2	3	2	1	2	1
9	3	2	2	3	1	1
10	2	3	3	1	2	1
11	2	3	2	2	2	1
12	2	2	4	1	1	2
13	1	2	3	1	1	2
14	3	3	2	3	2	1
15	2	2	4	2	2	2

Questions Qa. Feels burnout while doing the job; Qb. Work frustrates; Qc. Excessive workload; Qd. Discomfort while wearing the arms and armour and the equipment; Qe. Heavy weight of the arms and armour and the equipment while carrying for a long period of time; Qf. Basic necessities for women in the police station

Here the numbers indicate as 1. Strongly Agree; 2. Agree; 3. Neither agree nor disagree; 4. Disagree; 5. Strongly Disagree

Table 4 Percentage wise analysis of Table 2

Questions	Total respondent	Strongly agree (%)	agree(%)	Neither agree nor disagree(%)	Disagree (%)	Strongly disagree (%)	Total (%)
Scale		1	2	3	4	5	
Qa	15	13	60	27	0	0	100
Qb	15	0	60	40	0	0	100
Qc	15	7	47	27	20	0	100
Qd	15	40	33	27	0	0	100
Qe	15	40	60	0	0	0	100
Qf	15	67	33	0	0	0	100

Questions Qa. Feels burnout while doing the job; Qb. Work frustrates; Qc. Excessive workload; Qd. Discomfort while wearing the arms and armour and the equipment; Qe. Heavy weight of the arms and armour and the equipment while carrying for a long period of time; Qf. Basic necessities for women in the police station

Here the numbers indicate as 1. Strongly Agree; 2. Agree; 3. Neither agree nor disagree; 4. Disagree; 5. Strongly Disagree

equipment is still in its initial stage, where the respondents requested the researchers to redesign user friendly equipment for the women. On the other hand, the working conditions are still needed to be enhanced so that it can increase productivity and a healthy working atmosphere at the workplace to work for a longer period of time.

Table 2 and Fig. 3 specify that this graph shows that 40% of women police faced discomfort after wearing a bullet-proof jacket while remaining were confused. No one fully disagreed to the point. Comfort should be the priority in finalizing the design as it would directly increase their performance level. Almost all women police felt that the bullet-proof jacket was too heavy with respect to their body weight. This would drastically reduce their energy level affecting performance. Also, 60% of women police felt burn out after wearing a bullet-proof jacket. Work frustration and excessive workload were not much highly rated because the other parameters dominated over them.

Anthropometry measurement of women police body dimension for bullet-proof vest of Shivajinagar Police Station

Most of the women police complained that the bullet-proof jackets are heavy and ill fitting; physically they are made for flat-chested, which causes pain, breathlessness and hence can wear only for a limited time or for an hour. Clearly, it can be observed that the woman's body figure is different from that of a man. Hence women police need bullet-proof vests made particularly according to their shapes and size. The specialists can't talk about the plan of agreeable and ergonomic impenetrable gear, giving the equivalent or prevalent assurance level, without performing in detail anthropometric examinations [7].

Anthropometric Study

In order to get an overview of the design of overall shape and size, the 3D model of paint 3D helped to analyze it. Using a 3D mannequin the average size of the woman's

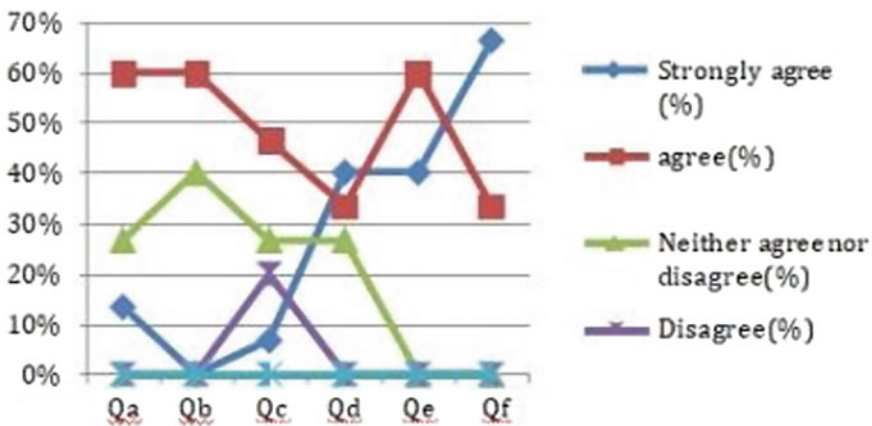


Fig. 3 Statistical distribution on-job burn out to determine their views on major barriers faced during stressful conditions from Table 4

physiological shape was easy to denote. The further process of designing in Blender and Gemini CAD editor was easy because of this mannequin design [8]. Chest (mid tidal) on bust, Chest (mid tidal) below bust, Abdominal extension, waist, hip and neck are the regions denoted on a mannequin. Due to unavailability of anthropometry kit the researcher used the measuring tape to measure the selected parameters for the bullet-proof vest.

Figure 4 shows the average readings of the parameters measured during the survey. Each participant was asked to stand erect on the floor board. The heels of the feet were placed together with both heels touching the base floor board. The arms were made to hang freely by the sides of the trunk with palms facing towards the thighs. All these measurements are taken in inches. These parameters were selected based upon most of the problems found out during the survey taken. The average readings were found out as Neck-32.8, Chest (mid tidal) on bust-29.533, Chest (mid tidal) below the bust-26.4, Abdominal extension-31.6, Waist-27.166, Hip-32.8. These data collected helped in further analysis.

Table 5 represents anthropometric measured data of women body parts. The various parameters measured were Chest (mid tidal) on bust, Chest (mid tidal) below bust, Abdominal extension, Waist, Hip, Neck. Unit was taken in inches. Based upon the average values of Table 5 a certain range of adjustable size can be selected while deciding final size of the bullet-proof armour. Considering these average values for experiment purpose sizes can be classified as S, M, L, XL, 2XL and 4XL. The height obviously plays a crucial part in considering respective sizes. As it should be kept into consideration that bullet-proof armour is not stretchable, proper body posture analysis is much needed in each size design.

Fig. 4 Anthropometric body dimension of women police

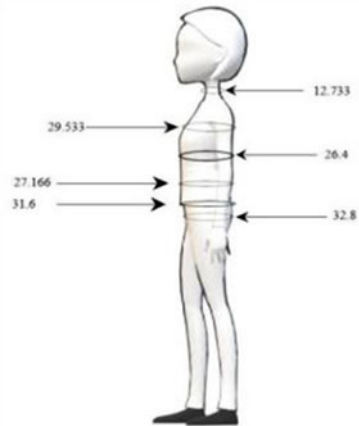


Table 5 Anthropometric body dimension of women police

Respondents	Chest (mid tidal) on bust	Chest (mid tidal) below bust	Abdominal extension	Waist	Hip	Neck
1	29	25	31	25	34	12.5
2	29	27	33	28	34	12
3	27	24	29	24	30	12
4	28	26	32	30	33	12
5	30	27	31	28	32	13.5
6	31	29	32	30	33	14
7	29	26	30	26.5	34	12.5
8	33	29	34	30	36	14
9	34	30	36	33	35	12
10	27	24	30	26	30	13
11	30	27	32	26	32	13
12	31	27	32	27	34	13.5
13	28	25	30	24	31	12
14	30	26	33	26	33	13
15	27	24	29	24	31	12
Average	29.533	26.4	31.6	27.166	32.8	12.733

4 Discussion: Key Issues for Development of Bullet-Proof Vest for Women Police

Efforts have been made to improve the performance of the body armours based on the factors such as comfort, breathability, ballistic protection which are primarily concerned according to males. As involvement of females is increasing in this sector, development in the female body armour is a need. Due to the physiological differences between the men and women, directly using male bullet-proof jackets would be inappropriate. It may cause the imbalance of the whole body during obstacle crossing due to the overweight of the armour. Also, limited movements of the upper body parts would also affect emergency conditions.

These bullet-proof jackets could be categorized as soft body jackets and hard body jackets. These soft body armours are used to absorb impact energy. These include many layers of flexible fabrics. Layers can vary from 7 to 50. Using minimal required layers considering weight as an important factor will surely benefit to reducing the overall weight of the bullet-proof jacket. Hard body armours are used against rifles and other metallic threats. Along with layers of fabric plates of metal, plastic or ceramics are inserted in the pockets of the jacket for increased protection. This increases the weight of the bullet-proof jacket to much extent. Weight needs to be balanced from both front and the back side for easy convenience.

By interviewing many of those women police, they suggested many changes which according to them can be identified as in common and changes in design can be suggested accordingly. This armour average weight goes around 15 kg. Along with this, they have to carry other heavy objects such as rifle guns, pistols, grenades, other kits, etc. Due to this overall body weight has increased to a large extent.

The collected database allowed the anthropometric body assessment of women to establish a primary database required in the current design of bullet-proof armour.

Almost 90% of women police felt armour was not suitable for them. They felt discomfort in the neck, shoulder and chest where they suggested many changes. Weight had been the major problem based upon all the observations.

Design according to female physique and adjustability are the other problems that need to be focused on based upon observations. From Fig. 5 it can be seen that the women police were wearing a vest that is oversize with heavyweights. They have included that carrying this weight they suffer from musculoskeletal disorder, fatigue and low performance. The women police have also exposed that they suffer a lot during the summer season which felt breathlessness and suffocation. In this figure, it can be witnessed that the bullet-proof vest they were wearing was designed for their counterparts. They have also integrated that the neck portion is very uncomfortable for them.



Fig. 5 Women police with arms and ammunition and body armour

5 2D Design Processes for Women Bullet-Proof Jacket

Lightweight bullet-proof vests are commonly used among police, military and government special forces. Considering such women involvement in the field and their unique body shapes, various researcher and body armour designer have been working on the design and developments of women bullet-proof vests considering not only ballistic protection but also breathability, cost, safety, fitness and comforts to the wearer. The above 2D design (Fig. 6) of body armour is currently used everywhere by men and women so, the proposed changes located in the 2nd image which are particularly highlighted to get is more specifically women-oriented design.

The bullet-proof vest with good ballistic resistance, lightweight and comfortable is extremely important for the women personnel working for long hours at various threat levels. Today, in view of their unique body shapes, there is the various designing approach used in developing bullet-proof vests for women personnel. Such design also affects the comfort and personnel mobility due to much allowance for bullet-proof vest deformation that leads to the panel being thicker especially in the armpit region. The ballistic protection garment ought to be designed considering not solely flight resistance toward projectile penetration however conjointly moderately lightweight in weight and versatile to produce comforts.

The bullet-proof vest with good ballistic resistance, lightweight and comfortable is extremely important for the women personnel working for long hours at various threat levels. Today, in view of their unique body shapes, there is the various designing approach used in developing bullet-proof vests for women personnel. Such

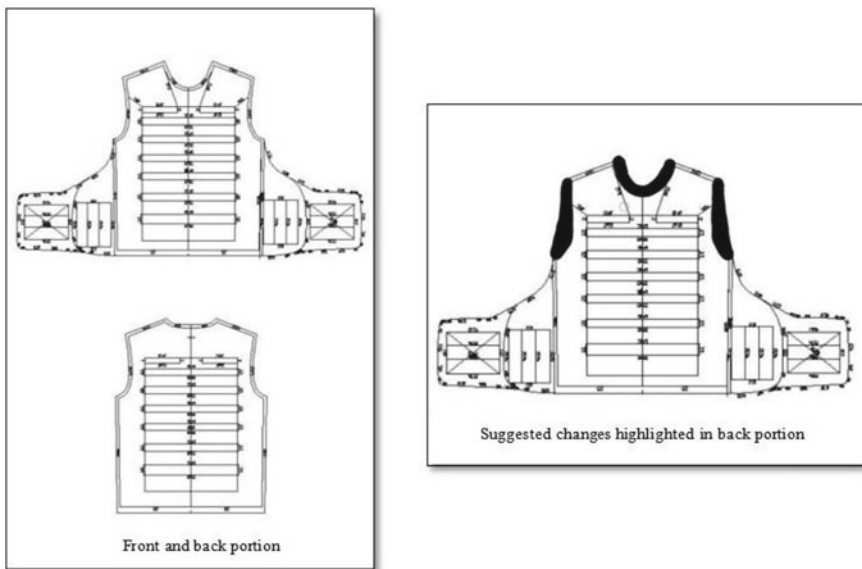


Fig. 6. 2D bullet-proof vest feature measurement, using Gemini pattern editor model

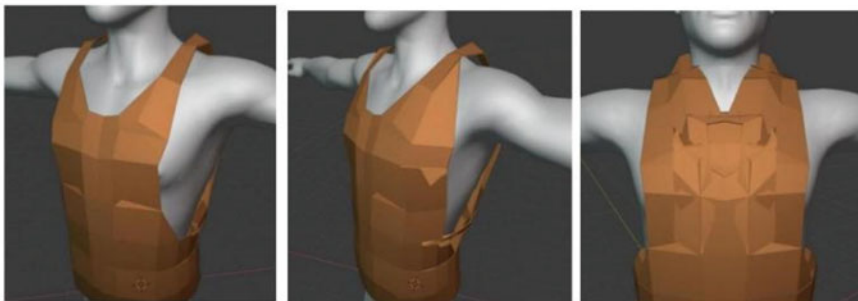
design also affects the comfort and personnel mobility due to much allowance for bullet-proof vest deformation that leads to the panel being thicker especially in the armpit region. The ballistic protection garment ought to be designed considering not solely flight resistance toward projectile penetration however conjointly moderately lightweight in weight and versatile to produce comforts.

6 3D Design Processes for Women Bullet-Proof Jacket

Design in virtual atmosphere is a locality of nice interest, each for computer aided graphics and industrial products and goods, or clothes. Figure 7 are representing the variations of existing jackets and the new design created with the help of a survey conducted. A simulation variant however is partitioned with a bullet-proof on a mannequin so as to verify the pattern style, coverage and protection space that might be offered. In the beginning, the main questions were added and the answer to them given by lady police cleared the view of problems faced due to existing design



a. Existing Designs



b. New Designs

Fig. 7 Both the existing and new design of a bullet-proof vest. **a** Existing designs. **b** New designs

by them. These helped us to form a concept and work on the design based on the problems countered. The main problems listed were Neck belt, Stomach flexibility, Breast adjustment.

The above new designs are women anthropometric oriented designs proposed according to the issues listed. The simulation in a virtual house of body armour dressed on a mannequin permits the manufacturer to optimize the quantity of physical prototypes required to validate it and to ascertain the optimum level of technological parameters for producing methods. The pattern vests are designed to know the values of several dimensions. These patterns are made either using parametric design programs or specialized design systems. Knowing the values of characteristic dimensions, the final shape of bullet-proof armour is designed with a 3D Blender Design System.

The standard structure of a bullet-proof vest includes multiple layers of ballistic material protection, assembled in a so-called “ballistic package”. This package is inserted into a pouch made of nylon or cotton fabric. These ballistic packages can be permanently fixed in or removable cover. Where in Fig. 6 (front neck) the main aspect of the neck has been solved, this design will help in their neck protection with flexibility movement for the neck. The other Fig. 6. (Side added) represents the stomach flexibility area so that even if any pregnant or obsessed women wear this jack would not feel uncomfortable or stressful. This will help to work efficiently and comfortably.

The overall design proposed for lady police is to help them work efficiently and comfortably in all circumstances. This will also help them to contribute equally and protect themselves easily. The important parameters to be kept in mind are:

1. Balance thermo-physiological comfort for survival in extreme conditions.
2. Reduce weight and bulk of materials.
3. Increase comfort and flexibility near the breast, neck and tummy area.
4. Adjustable height of armour.
5. Fewer complexes to wear.
6. More gripped to access.

7 Conclusion

The body armour for women police should provide a balance of protection and comfort. The above research is the novelty in the bullet-proof design consisting in taking into account the size of the female body and the technical solution of their issues. The necessary data obtained from the survey has been used to make ergonomic changes in bullet-proof vests, specially dedicated to female staff. The survey gave the conclusion of various issues faced by the women police which are weight, breast and stomach area flexibility and side underarm and constraint neck movement. A systematic 3D design process was used to develop and solve the issues for the ballistic protective armour for women police. Conversely, a far design and

development, potential works is very essential to develop the jacket and experimental testing of the design intervention for comfort, robustness and ballistic performances.

Acknowledgements This paper has been supported by the Police organization of Pune, Maharashtra, Shivajinagar Police Station. The researcher would like to acknowledge all the women police for their kind support to complete this paper.

References

1. R. Tripathi, Women police personnel constitute a meagre 8.98% of police force across India: BPR&D (2020). <https://economictimes.indiatimes.com/news/defence/womenpolice-personnel> by Scott Burton, A call for female friendly body armour, body armour news
2. S. Vivek, R.G. Varghese, K.S. Neethumol, S.S. Sameena, R.S. Reju, P. James, S. Vijaysankar, Occupational stress among female police officers in an urban setting in South Kerala. *Int. J. Commun. Med. Public Health* **6**(1), 325 (2019)
3. M.L. Dantzker, M.A. Surrette, The perceived levels of job satisfaction among police officers: a descriptive review. *J. Police Crim. Psychol.* **11**(2), 712 (1996)
4. S. Bora, A. Chatterjee, P. Rani, D. Chakrabarti, On-the-job stress: interventions to improve the occupational well-being of policewomen in Assam, India. *J. Int. Women's Stud.* **18**(1), 260–272 (2016)
5. F. Rizvi, Challenges for women in Indian police system. *Int. J. Manage. Soc. Sci.* **3**(2), 816–821 (2015)
6. E.C. Alexopoulos, V. Palatsidi, X. Tigani, C. Darviri, Exploring stress levels, job satisfaction, and quality of life in a sample of police officers in Greece. *Saf. Health Work* **5**(4), 210–215 (2014)
7. C. Lăzăroaie, T. Zecheru, M. Lăzăroaie, D. Toma, Design and performance characteristics of new female bulletproof vests, in *International conference Knowledge-Based Organization*, vol. 23, no. 3 (Sciendo, 2017), pp. 204–207
8. M. Avădanei, I. Dulgheriu, R.D. Cezar, Virtual prototyping design of bullet-proof vests (De Redactie, 2012), p. 290

Scrap Reduction and Proper Utilization of Raw Materials During Cutting Operations in SMEs



Arpita R. Shukla, A. M. Khalatkar, and Inayat Ullah

Abstract Manufacturing industries are one of the major drivers of the economic growth, employment and innovations of both developing and developed countries. In India, there are millions of manufacturing industries, majority of which belongs to medium and small-sized segments. The medium and small-scale industries contribute to manufacturing outputs about 45%, exports about 40% and also provide employment to more than 120 millions (i.e., about 40%) of working population of the country. Although these industries are making significant contribution to the socio-economic growth of the country, their productivity performance has been observed as somewhat poor. Therefore, efforts are required for enhancing their operational and financial performance as well as productivity. To this end, this study attempts to identify the main sources of scraps and proposes guidelines and corrective measures to minimize the waste and enhance the productivity as well as organizational performance. For the purpose of this research, a case study of medium-sized manufacturing industry has been conducted. The study develops guidelines for reduction of scrap that is produced during manufacturing. By using cause and effect diagram and five whys method, the main source of scrap generation is identified. The proper cutting plan is created by using cutting optimization software.

Keywords Scrap reduction · Productivity · Fabrication work · Productivity enhancement · Economic growth

1 Introduction

The manufacturing industries are the backbone, responsible for the economic growth of any country. These industries act as the building block of the developing countries to become established economic power in the world. In India, majority of manufacturing industries belongs to small and medium-sized segments. These industries are one of the major employment providing sectors in India. Medium-sized industries

A. R. Shukla (✉) · A. M. Khalatkar · I. Ullah
Department of Mechanical Engineering, G.H. Rasoni College of Engineering, Nagpur,
Maharashtra 440016, India

© The Author(s), under exclusive license to Springer Nature Singapore Pte Ltd. 2022
M. L. Kolhe et al. (eds.), *Smart Technologies for Energy, Environment and Sustainable Development, Vol 1*, Springer Proceedings in Energy,
https://doi.org/10.1007/978-981-16-6875-3_58

725

not only play a critical role in providing significant employment opportunities at comparatively lower cost of capital as compared to large industries, but they also help to industrialize remote and backward regions.

Some industries are the complementary to large enterprises as ancillary unit. Due to some major issues and challenges, the growth and development of these industries are hindered, and due to this, many times they are on the verge of closure. Some major issues and challenges are lack of skilled manpower, lack of formal plan for training of worker, etc.

The first step is to recognize the root cause to minimize scrap in manufacturing industries that leads to defects. The use of Pareto charts, Fishbone diagrams and Five whys methodologies help to distinguish the main root causes [1–3]. The five whys methodology offers a structured approach to identify the issues to effectively minimize and remove defects at zero cost [4]. Continuous process control is necessary to enhance productivity and minimize the unnecessary generation of scraps during the manufacturing process. The process improvements can be carried out by using DMAIC procedures, i.e., define, measure, analyze, improve and control [2, 5–7].

Using management and industrial engineering tools such as Total Quality Management, Total Productive Maintenance, Just-in-Time, Kaizen and Lean manufacturing can minimize operating costs by using raw materials in a proper way to eliminate waste [8]. During laser cutting of mild steel, [9] author concentrated on improving cutting efficiency. Some input process variables are considered for evaluation such as laser, cutting speed and material thickness [9]. Raju used the Taguchi approach to optimize the machining parameters of the plasma arc cutting machine and concentrated on the various process parameters (such as current and cutting speed) that affect the cutting efficiency [10].

2 Methodology

A case study-based approach has been adopted for the present work. This qualitative data collection study technique has a certain benefit over other quantitative techniques. Advantages—According to Bryn Farnsworth [11], qualitative approaches can be used to identify and access the deep understanding of thoughts, trends, points of view as well as other individual experiences as compared to quantitative techniques [11].

Some of the data collection techniques are as follows:

- Individual interviews
- Group discussions, etc.

3 Data Collection

The data for the present study is collected by field visits as well as the semi-structured interview of industry personnel, manager, project manager and other employees. The machines and equipment's present in the workshop are automatic, semi-automatic and manual machines. The staff is semi-skilled for operating manual operations. Owing to lack of expertise and training, they were not involved in the participative decision making.

This is the main reason behind the ineffective total production maintenance (TPM). Employees should be encouraged for successful TPM.

3.1 Case Description

The case industry is a fabrication and service provider industry of stainless steel and mild steel grills, sheds, railings, power plant structures and tank fabrication to clients—Ambuja Cements, GMR Power Plant, MPPGCL, NTPC, MAHAGENCO, SAIL, BHEL, Reliance Energy, TATA, Ultratech Cements, etc. (see Table 1). The purpose of this industry is to provide high-quality fabrication work and services. This industry consists of a large workshop (see Fig. 1) with various types of machines and operates on the orders as defined by the client. After each and every phase, the inspection is carried out by the client and the quality engineer to ensure that the quality of the job is up to the mark or not. If the work is up to the mark, it will be forwarded to another stage of development as required, otherwise the same operation will be carried out until the work is finished well.

The industry supplies the range of manufacturing services of mild steel, stainless steel and other materials as required by the customer. The industry practices mixed production strategies as per the customer's requirement, i.e., engineer to order and make to order.

Table 1 General information regarding the case industry

Demographics	Case
Firm size	Medium
Business type	Metal fabrication and service provider
Product category	Mild steel grills, sheds, railings, power plant structures and tank fabrication
Number of employees	101–500
Years of operation	11 yrs
Number of facilities	01
Types of clients	Ambuja cement, GMR power plant, MPPGCL, NTPC, MAHAGENCO, SAIL, BHEL, Reliance energy, TATA, Ultratech cement, etc.

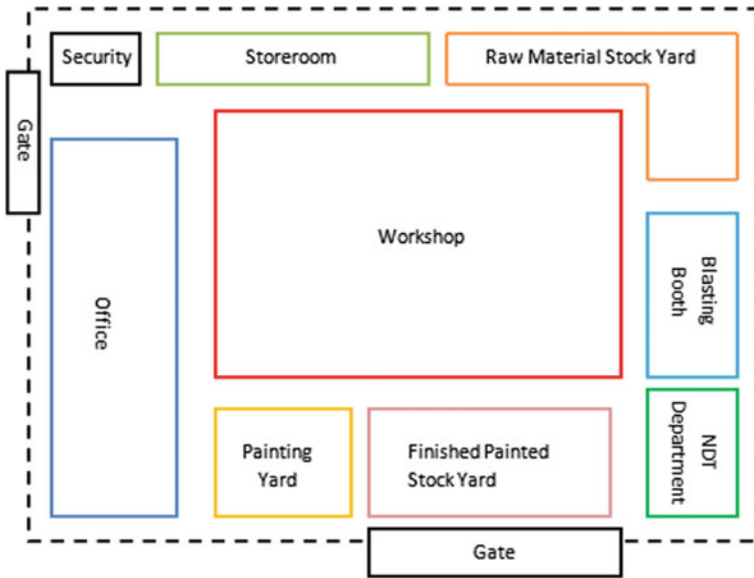


Fig. 1 Plant layout

3.2 Fabrication Flow

There are a large variety of raw materials required for manufacturing operations, and knowing which supplies to keep on hand will greatly improve the production process by ensuring that the workers/laborers have what they require at all times. The selected raw materials are kept as a stock in a stockyard. The materials are verified in compliance with the purchase order. The purchasing order (PO) is a document listing the type, quantity of goods and services that the vendor offers, as well as the accepted price for the purchasing. Materials are also verified by the Material Test Certificate (MTC).

MTC is a quality assurance document used in the manufacturing sector. Material Testing Certificate certifies the physical and chemical properties of the material and specifies that the fabricated metal component (steel, aluminum, brass or other alloys) satisfies the basic criteria of the international standards organization (such as ANSI and ASME). The inspection may be carried out by the customer using the MTC. Raw materials delivered to workers for starting various fabrication operations. Drawing sheets are forwarded to workers for marking measurements and dimensions, etc. Marking inspection takes place after marking different dimensions and measurements. If the markings and dimensions are up to the mark, it is allowed for cutting. The assembling of separate pieces of raw materials takes place as per the drawing.

Assembly inspection is carried out to check whether the assembled pieces are correctly positioned or not. After inspection, if the assembly is found up to the mark, the welding process is permitted. After welding, the finishing of the welded sections

takes place to minimize roughness on the surface. Final inspection is carried out by the customer with respect to weld, finishing, measurements, etc., with the help of drawing sheets. The permission for blasting is given after the final inspection of the product. The surface of metal, stone, concrete and other materials is thoroughly cleaned and shaped by blasting method (e.g., grit blasting). After blasting, the painting above the surface takes place as per the client's order. When all the processes have been finished, the entire completed product is finally delivered to the address of the customer.

3.3 Solution Space Development

It is noted that the case industry is working on the design provided by the customers. Often the customer offers the specifications and allows them freedom to select the correct material according to the specifications. Designs can be prepared with the guidance of Freelancer Designer because they have not appointed skilled Draftsmen within the industry. The workers are semi-skilled and few of them have years of experience in performing procedures to produce the finished product.

3.4 Scrap Reduction Techniques

Scrap generation is entirely based on the design of the project and the quantity of raw materials required for the manufacturing of the desired product. The maximum amount of scrap is created during the cutting process of metal sheets, beams, etc. The removal of scrap during production is an essential aspect of the lean and efficient manufacturing process. Optimizing the production process is one of the easiest ways to minimize the generation of scrap. Proper documentation of ordering goods and used resources can also minimize scrap during the manufacturing process.

4 Analysis

The root causes of scrap generation can be identified by using Ishikawa/Fishbone diagrams, and using Five whys, we can determine the main root cause.

4.1 Ishikawa/Fishbone Diagram

Ishikawa diagrams are often referred as Fishbone diagrams and cause and effect diagrams. These diagrams are created by Kaoru Ishikawa to show the causes of a single event. The popular use of Ishikawa diagrams is to identify possible factors

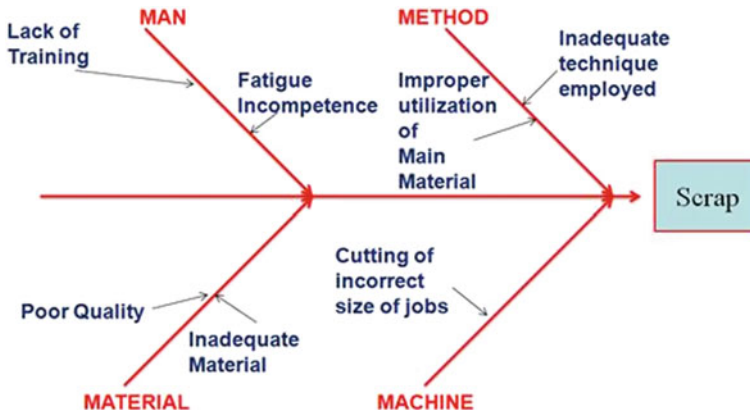


Fig. 2 Ishikawa diagram or cause and effect diagram

that trigger an overall effect in the design and prevention of quality defects. Figure 2 shows the main sources of generation of scrap in the manufacturing sector.

The head of the fish is created by listing the main problem, i.e., scrap. The horizontal arrow is drawn with an arrow pointing to the head, which represents the backbone of the fish. Man, method, material, and machine are the four main causes that contribute to the problem. These generic categories show the different causes in the form of small branches that are lack of training, fatigue incompetence, improper utilization of main material, inadequate technique employed, poor quality of material, inadequate material and cutting of incorrect size of jobs.

4.2 Five Whys

The five whys technique was developed in the 1930s by Sakichi Toyoda, a Japanese industrialist and inventor of Toyota Industries. It was popular in the 1970s, and today, Toyota continues to use it to solve problems.

Table 2 illustrates the decision-making process, which is based on a thorough study of what is currently happening on the manufacturing floor. By using this iterative interrogative technique, the root cause of scrap generation can be identified by repeating the question “why?” again and again. The questions can be taken more than five iterations, but five iterations of asking “why” is enough to uncover the main root cause.

Benefits of using five whys technique are as follows:

- It helps to identify the root causes of the problem.
- It is used to identify the relations between various causes of the problem.
- It is one of the simplest and easiest tools without statistical analysis.
- It can be used when problem involves human interactions and factors.

Table 2 Whys decision-making process

Why's	Why's	Why's	Why's	Why's
MAN	Lack of training	Time constrains training of new employees	Employees needed to start working as soon as possible	Large amount of work and short lead time
	Fatigue incompetence	High physical demand	Heavy components handled manually	Lack of handling equipment
METHOD	Inadequate technique employed	Operator using technique they are familiar with to perform operation	Not defined/documented technique for performing operation	Lack of standardization
	Improper utilization of material	Lack of supervision	Lack of skills	Not defined cutting plans for proper utilization
MA CHINEST	Cutting of incorrect size of jobs	Specifications not given in proper format	Job positioning incorrect	Job holders are not available
MATERIAL	Inadequate material	As per order based on faulty forecasting	Lack of data collection	Documentation is not proper

- It can be used in day-to-day business with a Six Sigma project.

5 Problem Identification

Using five whys technique, the main root cause of scrap generation during cutting operation is identified, i.e., faulty planning and forecasting. The cutting plan can be prepared using the measurements and quantities of the main material and the required parts. Industries with CNC automatic cutting machines are well programmed and execute cutting operations as per programme instructions. Whereas, industries in which cutting processes are mainly manual, the cutting strategy plays a very important role.

Normally, drawing sheets are provided with measurements and dimensions, in which it is not clearly specified how to cut the pieces using the main material without producing scrap. It is very difficult to prepare cutting plans without contacting any professional.

6 Solution

The cutting plan can be prepared by using the cutting software tools. These software are commonly used for the cutting of rectangular sheets of woods, glass, plastic and metal and are often used to achieve optimum cutting layouts for 1D and 2D parts used in industrial applications. Some software are Cutting Optimization Pro, 1DCutX, etc.

a) Cutting Plan Solutions for Steel Bars

In order to create a cutting plan for steel bars, consider the data given Table 3. We have taken various cutting lengths as per the specifications. We required 400 quantities of parts for each cutting length.

The cutting plan (see Fig. 3) is generated by filling the required dimensions of cutting length and stock details. It shows the proper utilization of raw materials in order to minimize wastage. It also shows the usage and wastage of materials in the form of diagrammatic representation which can help the workers to perform manual cutting operations without creating unnecessary wastage of raw materials.

The details of utilized parts and bars are also generated (see Fig. 4) and show the exact quantity of stock to get parts of different cutting lengths as per the requirements. The detail of waste and cuts (see Fig. 5) shows the unavoidable waste of raw material after cutting all the parts with proper utilization.

(b) Cutting Plan Solutions for Metal plates -

In order to generate the cutting plan for metal plates, let us consider the data given Tables 4 and 5.

After filling the necessary stock and part information, the software generates the cutting plan with appropriate usage of stock material (see in Figs 6 and 7). The cutting strategy also identifies the unavoidable waste of material from the stock and the exact quantity of stock to get parts of different cutting dimensions as per the requirements.

Table 3 Required data for generating cutting plan solution

Length of the bar	Cutting lengths (in m)	Quantity of parts
12 m	2	400
	2.5	400
	3	400
	3.5	400
	4	400
	4.5	400
	5	400
	5.5	400
	6	400
	6.5	400

Length	Material	Quantity	Label	Waste	Graphic: 1D
12	Bar	200		0	
12	Bar	400		0	
12	Bar	133		0	
12	Bar	1		0	
12	Bar	199		0	
12	Bar	199		0	
12	Bar	50		0	
12	Bar	1		0	
12	Bar	100		0	
12	Bar	99		0	
12	Bar	1		0	
12	Bar	1		0	
12	Bar	32		0	
12	Bar	1		4	

Fig. 3 Cutting plan for steel bar

Fig. 4 Details of utilized parts and bars

Utilized parts

Length	Width	Quantity	Material
6	0	400	Bar
6.5	0	400	Bar
5.5	0	400	Bar
4	0	400	Bar
4.5	0	400	Bar
3.5	0	400	Bar
5	0	400	Bar
3	0	400	Bar
2.5	0	400	Bar
2	0	400	Bar

Utilized bars

Length	Width	Quantity	Material
12	0	1417	Bar

Waste

Length	Material	Quantity
4	Bar	1

Details of Cuts

Length	Material	Quantity	Label	Waste	Cuts
12	Bar	200		0	6+6
12	Bar	400		0	6.5+6.5
12	Bar	133		0	4+4+4
12	Bar	1		0	4.5+4+3.5
12	Bar	199		0	5+3.5+3.5
12	Bar	199		0	4.5+4.5+3
12	Bar	50		0	3+3+3+3
12	Bar	1		0	5+4.5+2.5
12	Bar	100		0	5+5+2
12	Bar	99		0	2.5+2.5+2.5+2.5+2
12	Bar	1		0	3+2.5+2.5+2+2
12	Bar	1		0	3.5+2.5+2+2+2
12	Bar	32		0	2+2+2+2+2+2
12	Bar	1		4	2+2+2+2

Fig. 5 Details of waste and cuts

Table 4 Data for stock details

Length	Width	Quantity	Material
2000	2000	4	Metal Plate

Table 5 Data for parts details

Length	Width	Quantity	Material
600	600	4	Metal Plate
900	900	4	Metal Plate
300	500	5	Metal Plate
700	400	4	Metal Plate

7 Conclusions

The cutting plan is very important for the small and medium scale industries, where cutting operations are often manual, in order to minimize scrap and to utilize stock properly. Without consultation with any professional, it is very difficult to prepare cutting plans. The increase in scrap caused by a faulty cutting plan contributes to a decline in productivity. The cutting plan can be created by using various cutting optimization software for 1D and 2D parts and can be used by workers to utilize the proper stock without producing excess scrap.

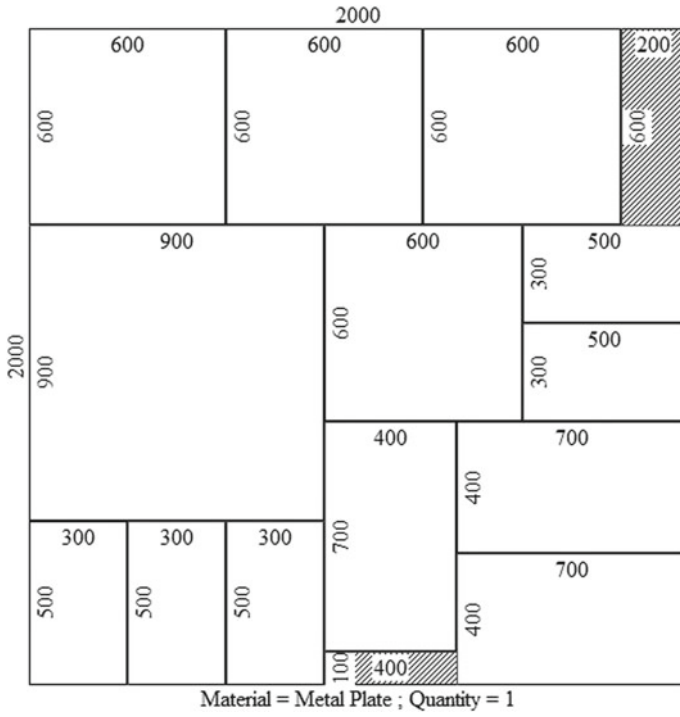


Fig. 6 Cutting plan for metal plate (Page 1)

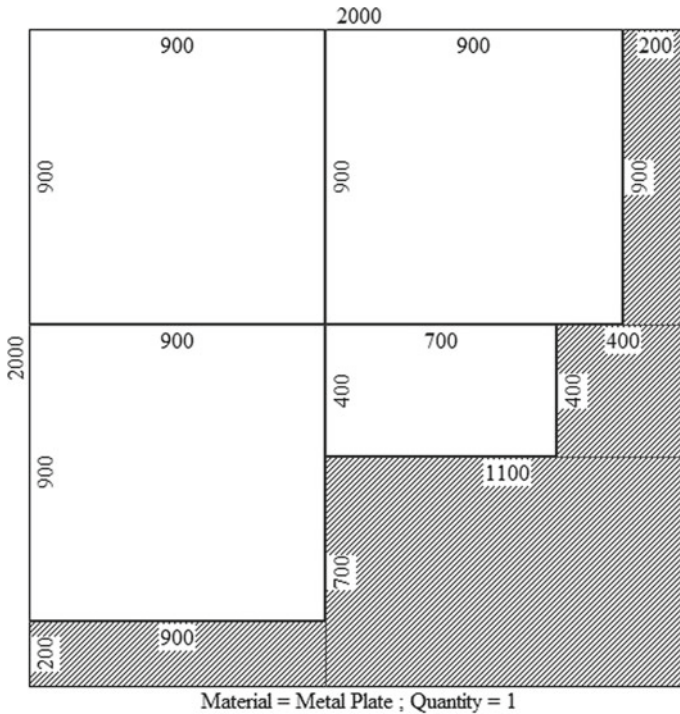


Fig. 7 Cutting plan for metal plate (Page 2)

References

1. Z. Mpanza, Identifying the root causes contributing to defects in order to minimize scrap, in *International Conference on Industrial Engineering and Operations Management* (2016), pp. 1139–1146
2. L. Huda, The effect of material productivity on scrap reduction on aluminium reduction pot process. *IOP Conf. Ser.: Mater. Sci. Eng.* **309** (2018). <https://doi.org/10.1088/1757-899x/309/1/012117>
3. P. Shinde, S. Shinde, A. Kalunge, S. Rokade, Scrap reduction techniques. *Int. Res. J. Eng. Technol. (IRJET)* **06**, 312–314 (2019)
4. U. Murugaiah, S. Benjamin, M. Marathamuthu, S. Muthaiyah, Scrap loss reduction using the 5-whys analysis. *Int. J. Qual. Reliab. Manage.* (2010). <https://doi.org/10.1108/02656711011043517>
5. A. Shokri, Reducing the scrap rate in manufacturing SMEs through lean six sigma methodology: an action research. *IEEE Eng. Manage. Rev.* **47**, 104–117 (2019)
6. D. Kumar, D. Kaushish, Scrap reduction in a piston manufacturing industry: an analysis using six sigma and DMAIC methodology. *IUP J. Oper. Manage.* **14**(2), 7–24 (2015)
7. B. Chaurasia, D. Garg, A. Agarwal, Lean six sigma approach: a strategy to enhance performance of first through time and scrap reduction in an automotive industry. *Int. J. Bus. Excellence* **17** (2018). <https://doi.org/10.1504/IJBEX.2019.096903>
8. A. Athalye, P. Gera, A. Madan, Study and analysis of cost reduction techniques by scrap utilization of press part production: a case study of stamping unit. *Int. J. Sci. Res. (IJSR)* **4**(4), 3247–3252 (2015)

9. N. Abhimanyu, B. Satyanarayana, Optimization of CNC laser cutting process parameters. *Int. Adv. Res. J. Sci. Eng. Technol.* **3**(5), 206–210 (2016)
10. D. Raju, Optimization of process parameters of plasma arc cutting using Taguchi's robust design methodology. *IOSR J. Mech. Civ. Eng.* **16**(053), 124–128 (2016)
11. B. Farnsworth, Qualitative vs quantitative research – what is the difference?, in *imotions* (2019). <https://imotions.com/blog/qualitative-vs-quantitative-research>

Fuel-Purpose Bioethanol from Agricultural Waste: A Step Towards Sustainable Environment and Energy Security



Debasmita Dash and Bhabani Prasanna Pattanaik 

Abstract The increasing demand for fossil fuel owing to rapid growth in civilization, industries, automobiles etc., not only depletes the conventional energy sources, but also responsible for global climate change. In this context, biofuels in recent years have emerged as potential substitute for the conventional fuels. There are growing opportunities for development and application of bioethanol as a promising substitute in automotive engines. However, too much focus on bioethanol production as automotive fuel may considerably affect the food supply chain. Thus, production of bioethanol from lignocellulosic biomass, such as various plants and agricultural crop residue, is plentifully available and low in harvesting cost is likely to contribute a significant role in fulfilling future energy demands. This work presents an expatiated review concerning the current and potential conversion of starch into sugar and ethanol following separate hydrolysis and fermentation (SHF) process. The residual lignin portion is converted into petrochemical feedstock by thermal catalytic and chemical conversion along with the exposure to some modelling aspect that reduce the emission of greenhouse gases (GHGs). The stability of the ethanol conversion reaction is controlled by the multiplicity and oscillation that has to be controlled because of inhibition effect during fermentation in the presence of furfural and formic acid. On the other hand, bioethanol usage as engine fuel significantly lowers CO, HC and NO_x emissions. Thus, bioethanol produced from waste biomass may be a potential alternative to the presently used conventional fuels owing to its significant characteristics, such as energy security, waste utilization and environmental sustainability.

Keywords Bioethanol · Agricultural waste · GHGs · Fermentation · Hydrolysis · NO_x emissions

D. Dash

Department of Chemistry, KMBB College of Engineering and Technology, Khordha
Bhubaneswar, Odisha 752056, India

B. P. Pattanaik (✉)

Department of Mechanical Engineering, KMBB College of Engineering and Technology,
Khordha, Bhubaneswar, Odisha 752056, India

1 Introduction

In the twenty-first century, the world energy demand continues to increase day by day and is projected to keep rising owing to growth in population, urbanization, industrialization and unpredictable oil supplies. The global energy dependency, in terms of fuel for automotive engines and power production, is primarily focused on fossil-based sources in the present day. In this regard, there is the need to develop alternative fuels to meet the future energy demand using a sustainable and environment-friendly approach. In recent years, biofuels have drawn significant global attention as potential alternatives for some of the major fossil fuels. However, production of biofuels from edible sources may seriously affect the food production chain [1]. Thus, production of biofuels from waste biomass has become an area of significant research interest in the present time. Further, waste biomass has the potential to become one of the leading bioenergy resources for future due to its greater conversion rate and higher hydrocarbon content of the produced biofuel. Furthermore, production of biofuel from waste biomass significantly contributes to address the waste management and environmental issues. From the perspective of carbon neutrality, bioethanol produced from sugar and starch containing waste biomass is regarded as extremely environment friendly as its combustion has very little contribution to global warming [2].

The use of crop biomass such as grains, roots and tubers for the production of bioethanol may compete with food chain. The renewable resource such as lignocellulosic biomass, which are rich in starch and sugar through metabolic enzymatic process can be converted to alcohol. A focused attention on lignocellulosic biomass is an alternate approach for the synthesis of bioethanol. Lignocellulose has a complex structure and is composed of lignin, hemicellulose and cellulose. Figure 1 [3] illustrates the structural components of lignocellulose, and Fig. 2 [4] presents the percentage composition of lignocellulosic biomass. Again, Fig. 3 [5] represents the structures of cellulose and hemicellulose.

The chemical structure of cellulose and hemicellulose as depicted in Fig. 3 reveals that it is convenient to hydrolyse hemicellulose for production of bioethanol [6]. The role of lignin is to establish cross-linking between hemicellulose and cellulose within

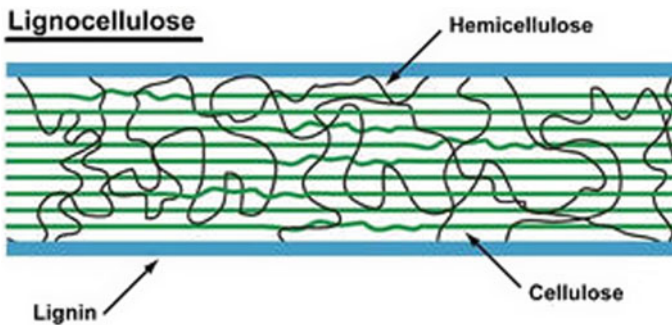


Fig. 1 Lignocellulose and its components [3]

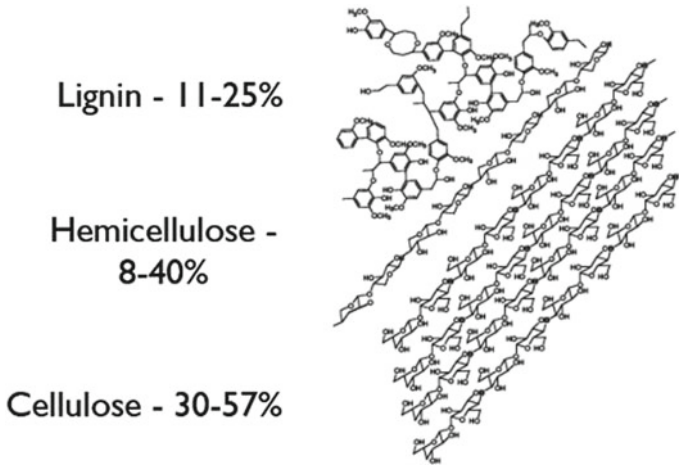


Fig. 2 Structural percentage composition of lignocellulosic biomass [4]

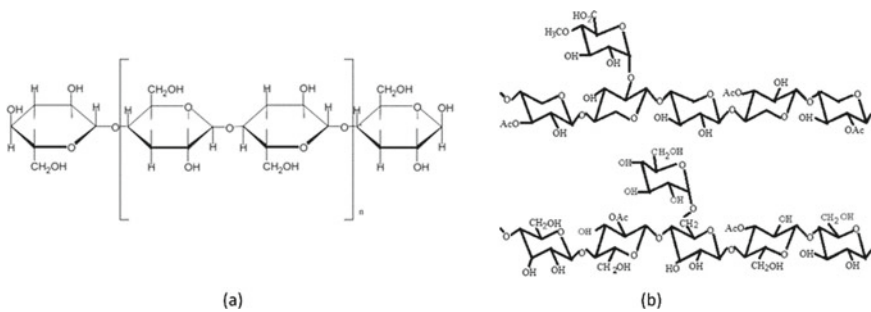


Fig. 3. Structure of **a** cellulose and **b** hemicellulose [5]

the carbohydrate matrix. The solubility of lignin depends on the precursors, as it is soluble in acidic and alkaline medium, which makes lignocellulosic materials too hard that requires a pre-treatment process for conversion into ethanol [6, 7] (Table 1).

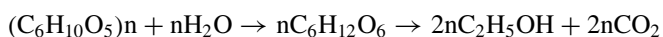
The total process of agricultural waste includes (1) Pre-treatment followed by hydrolysis of lignocellulosic biomass to monomeric sugar; (2) Formation of inhibitors, which will block fermentation process; (3) Fermentation of pentoses and hexoses to ethanol. The left residual portion of lignin is then thermochemically converted to hydrogen fuel and valuable chemicals. Fermentation process is carried out efficiently by strains such as *Saccharomyces cerevisiae* and *Zymomona* [13].

Table 1 Composition of common agricultural residue and energy crops [8–12]

Biomass residue of energy crop	Lignin (%)	Hemicellulose (%)	Cellulose (%)
Rice straw	17–18	26	46–47
Wheat straw	22–23	27–28	39–40
Bagasse	18–19	26	44–45
Hardwood	18–25	25–40	40–56
Softwood	25–35	26–35	45–50
Corn cobs	15	35	45
Corn stover	19–20	30–31	42–43

2 General Process to Convert Lignocellulosic Biomass to Bioethanol

The general chemical conversion of lignocellulosic mass to bioethanol is given by:



Brewery residues like straw, woods, grasses and bagasse are taken as input material (Fig. 4).

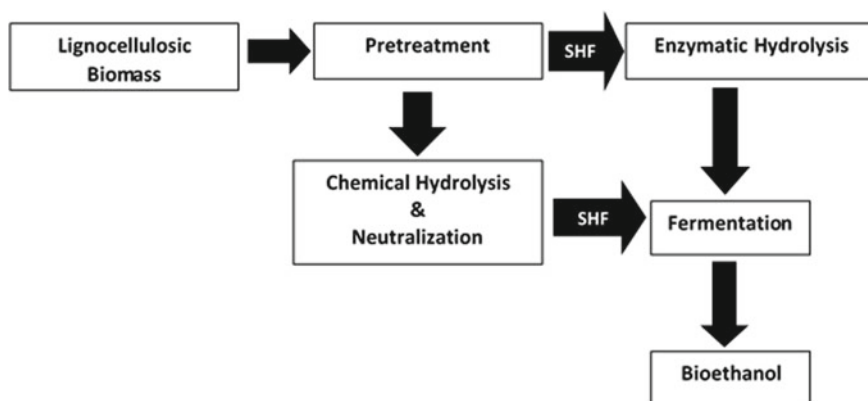


Fig. 4 Steps towards production of bioethanol

2.1 Pre-treatment for Lignocellulosic Biomass Size Reduction

It is a key step to convert lignocellulosic mass to sugars, which is to be fermented later. The main effective pre-treatment process must meet the ability to make the cellulosic component to vigorous enzyme attack, and the most important point is that it should not break hydrolysed sugars and less genetic inhibitor is produced. Objective of pre-treatment is to alter the structural as well as chemical composition so that enzymatic hydrolysis of carbohydrate portion will be converted to monomeric sugar in a larger proportion with better yield. This will also separate the hemicellulosic portion from lignin. The solubility of lignin is high in aqueous acid and alkali in economic point of view. In acidic pre-treatment, H_2SO_4 and HCL are preferred; high cones are always avoided due to hydrolysis of both cellulosic and hemicellulosic portion in pre-treatment and it is toxic by nature. Much diluted acids are also not taken into consideration due to the formation of furfural acid that acts as genetic inhibitor. Diluted aqueous solution of sulphuric acid with conc. of 2.0, 4.0, 6.0 wt% at 80, 60, 120 °C are found to be effective [14–16]. Alkaline pre-treatment is more favourable as it stops furfural formation and promote the hydrolysis by removing acetyl group. NaOH is the most popular one due to low cost and high efficiency [17].

2.2 Generation and Removal of Inhibitor

During pre-treatment process of lignocellulosic biomass with sulphuric acid at high temperature, some of the released sugar reacts to form chemicals that will inhibit the growth of cell as well as fermentation process. Some examples of these inhibitors are hydroxymethyl furfural, furfural acids like vanillic and syringic. Some detoxifying method, like use of XAD resins or use of modified generic culture which metabolize the inhibitor, is employed [13, 17, 18].

2.3 Size Reduction

Size of lignocellulosic biomass is reduced to 0.5–2.0 mm diameter by employing chipping and milling. The objective of size reduction is to increase the surface area of lignocellulosic biomass, which provides larger site of contact for polymer and enzymes and an easy pathway to hydrolysis of cellulosic mass to fermented sugar [19, 20].

3 Conversion of Pre-treated Lignocellulose to Bioethanol

The pre-treated lignocelluloses can be converted to bioethanol by direct method conversion (DMC) and enzymatic fermentation process. Enzymatic process is more efficient and has better yield performance [20, 21].

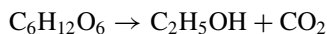
3.1 *Enzymatic Conversion of Cellulosic Mass to Sugar (Saccharification)*

After pre-treatment, the lignocellulosic polysaccharide material is converted to monosaccharide such as hexose and pentose. More knowingly, the enzyme cellulase derived from microorganism is used in saccharification. The role of enzyme is to cleave glycosidic link present in carbohydrate via retention mechanism or inversion. Retention proceeds through enzyme–glycosil intermediate [22]. In between cellulose and hemicelluloses, latter will be hydrolysed more easily, whereas cellulosic portion shows resistance to depolymerization up to some extent by maintaining slightly stable crystalline structure. For efficient conversion and better yield, more than one enzyme is collectively employed [9, 23].

The enzyme 1, 4- β -D-glucan-4-glucanohydrolase with Exo-1, 4- β -D glucanase is used to hydrolyse D-cellobiose slowly and to remove D-glucose from 1, 4- β -D-glucan. Enzyme 1, 4- β -D-glucan cellobiohydrolase is employed to separate 1, 4- β -glucan from cellobiose. Enzyme β -D-Glucosidase is used to apart D-glucose from cellobiose. EG (Endo-1, 4- β -glucanases) is used to break 1, 4- β -glucan bonds randomly. The function of enzymatic hydrolysis is to provide better development and growth to microorganism for fermentation process.

3.2 *Fermentation*

The single sugar produced in saccharification step is converted to ethanol in the presence of enzyme is known as fermentation. Metabolically the single sugar known as glucose (both pentose and hexose) is converted to ethanol. The chemical reaction for the same process is given as below.



There are two methods commonly used for preparation of bioethanol; one is separate hydrolysis and fermentation (SHF), in which after completion of hydrolysis, microorganism is used for fermentation process and other is simultaneous hydrolysis and fermentation (SSF), in which both hydrolysis and addition of microorganism are carried out at a time. SSF process is more efficient with high percentage yield in

Table 2 Various fermentation processes [24, 25]

Process of fermentation	Function	Merits	Drawbacks
SHF	Hydrolysis of glucose is carried out first enzymatically to produce bioethanol	Optimize temperature both hydrolysis and fermentation	Contamination, long process, generation of inhibitor
SSF	Hydrolysis and fermentation simultaneously enzymatically	Short time, less equipment, economically efficient, less enzyme requirement	Temperature required for hydrolysis is more than fermentation temperature; hence, reuse of enzyme is not possible

a short time involving less contamination and less equipment [14]. Modified *Saccharomyces cerevisiae*, *Thermoanaerobacter ethanolicus* and *Thermoanaerobacterium saccharolyticum* are commonly used in generation of bioethanol during fermentation process because of biologically high conversion rate, ability to ferment both pentose and hexose sugar along with decreased viscosity high solubility of substrate and less contamination. Most important is that these have high resistance to inhibitor. They will also generate hemicellulase and cellulose enzyme, which will convert biomass to bioethanol (Table 2).

4 Thermochemical Conversion of Residual Lignin Mass

The residual lignin is treated as a biological renewable source to produce aromatic chemicals and biofuel along with water gas as the composition of lignin is p-hydroxyphenyl, 4-hydroxy-3-methoxyphenyl and 3, 5-dimethoxy-4-hydroxyphenyl which are connected to each other by ethereal C–O and condensed C–C bonds [9, 26, 27]. Some of the techniques adopted in the said thermochemical conversion process are depicted as below.

4.1 Solvolysis

One of the most promising methods for the conversion of lignin into different type of value-added aromatic chemicals is involving depolymerization of lignin in H-donor solvent. The lignin depolymerization in formic acid and ethanol solvent at 380 °C is very effective, producing a greater yield of liquid hydrocarbon and phenol [27, 28].

4.2 *Hydrothermal Conversion in Water Medium*

For this purpose, aqueous alkaline solution is used. The depolymerisation of lignin in this solution at either critical or super critical condition of very low temperature (280–400 °C) at pressure 20–25 MPa for few seconds to few hours. Different types of phenols, catechol and methoxy phenol are produced due to hydrolysis of ether bonds [29, 30].

4.3 *Pyrolysis*

Pyrolysis is a major pathway to derive bio-oil from biomass. It is carried out under an inert environment with a controlled oxygen supply in an economical method. Presence of small quantity of oxygen promotes the thermolytical breaking of lignin that increases the cleavage on the side chain. Reaction between the lignin-derived phenol and oxygen produces phenolic ketones and aldehydes. As pyrolysis process is endothermic, the required process heat may be reduced by oxidative pyrolysis. Auto-thermal pyrolysis is achieved by either combustion of pyrolysis char or by introducing oxidative exothermic reaction. From pyrolysis of lignin biomass, bio-char is produced that enhances the economy and environmental sustainability. Pyrolysis via solid–gas reaction of residual bio-char and oxygen with limited supply of steam produces gaseous fuel [27, 31]. The gasification of lignin will produce CO and H₂ that is used as a substitutive fuel.

5 **Bioethanol as a Commercial Fuel and its Environmental Aspects**

Bioethanol has been popular in recent years due to its adaptability as an engine fuel. However, too much focus on bioethanol production for fuel purpose may give rise to food crisis [32]. Hence, fuel-purpose bioethanol production from waste and lignocellulosic biomass has been a major research area in the present time. Yoon and Lee [33] studied the influence of undiluted bioethanol on combustion and emissions of a spark ignition (SI) engine and reported higher volumetric and thermal efficiencies, lower specific fuel consumption along with reduced carbon monoxide (CO) and unburned hydrocarbon (HC) emissions. Noh and No [34] carried out an excellent review on effect of bioethanol on combustion and emissions of compression ignition (CI) engines. According to them, bioethanol use in CI engines produces lower nitrogen oxides (NO_x) and soot emissions. In another work, use of bioethanol along with isobutanol and gasoline blends in an SI engine resulted in higher brake power, torque and volumetric efficiency, whereas the HC and CO emissions were reported to be lower [35]. Tan et al. [36] in their study reported that sorghum-based bioethanol

production can significantly contribute towards petroleum fuel savings as well as lowers the GHG emissions by 35% compared to the same for conventional gasoline. In another study, Silitonga et al. [37] reported lower NO_x, CO₂ and CO emissions with diesel–biodiesel–bioethanol blends compared to neat diesel in a CI engine. In their work on use of use of bioethanol as an additive with diesel–biodiesel blends in a CI engine, Silitonga et al. [37] reported lower brake specific fuel consumption and higher brake thermal efficiency along with lower CO emissions and reduced smoke opacity. Addition of bioethanol with diesel or diesel–biodiesel blends decrease the octane number, increase the aromatic hydrocarbons. Another advantage of using bioethanol as fuel is that the amount of CO₂ released to the atmosphere is absorbed by the natural sink by photosynthesis, as there is a fixed proportion of carbon in carbohydrate prepared by the plant. Hence, no net accumulation of CO₂ takes place to the atmosphere. Thus, the use of bioethanol as fuel of fuel additive in engines will lead to significantly lower emissions, thereby enhancing the environmental sustainability for future.

6 Conclusion

The emission of GHGs from carbon footprint of fossil fuel not only increases the global warming but also responsible for environmental pollution. Thus, the need of the hour is an eco-friendly and low-cost biofuel for future energy security and a sustainable environment. Bioethanol could serve this purpose with its inherent characteristics and significant potential. The agricultural waste derived biomass, which is plentifully available and cheap, is considered to be the most favourable raw material for bioethanol production. Bioethanol production from agro-wastes is considered as a sustainable and eco-friendly waste minimization and energy recovery strategy. The commercial use of bioethanol as engine fuel seems to be extremely promising due to its excellent fuel properties that tends to reduce the viscosity and cetane number of the fuel blend, thereby lowering the engine emissions. However, research attention must be focused on low-cost fuel-purpose bioethanol production from waste biomass, to address simultaneously the issues related to environmental degradation as well as waste disposal.

References

1. B.P. Pattanaik, R.D. Misra, Effect of reaction pathway and operating parameters on the de-oxygenation of vegetable oils to produce diesel range hydrocarbon fuels: a review. *Renew. Sustain. Energy Rev.* **73**, 545–557 (2017)
2. S.H. Yoon, C.S. Lee, Effect of undiluted bioethanol on combustion and emissions reduction in a SI engine at various charge air conditions. *Fuel* **97**, 887–890 (2012)
3. Y. Yun, *Alcohol Fuels: Current Technologies and Future Prospect* (BoD–Books on Demand, 2020).

4. The Lignocellulosic Biorefinery, Vision and implementation, <https://www.iche.org/sites/default/files/community/444416/aiche-community-site-page/467701/aicherials.pdf>. Last accessed 2020/10/15
5. C. Tezara, J.P. Siregar, H.Y. Lim, F.A. Fauzi, M.H. Yazdi, L.K. Moey, J.W. Lim, Factors that affect the mechanical properties of kenaf fiber reinforced polymer: a review. *J. Mech. Eng. Sci.* **10**(2), 2159–2175 (2016)
6. E. Palmqvist, B. Hahn-Hagerdal, Fermentation of lignocellulosic hydrolysates. II: inhibitors and mechanism of inhibition. *Bioresour. Technol.* **74**, 25–33 (2000)
7. J. Sheehan, *Glycosyl Hydrolases for Biomass Conversion* (American Chemical Society, Washington D.C., 2001)
8. M.A. Hansen, J.B. Kristensen, C. Felby, H. Jørgensen, Pretreatment and enzymatic hydrolysis of wheat straw (*triticum aestivum* L.)—the impact of lignin relocation and plant tissues on enzymatic accessibility. *Bioresour. Technol.* **102**(3), 2804–2811 (2011)
9. T.C. Ezeji, N. Qureshi, H.P. Blaschek, Acetone butanol ethanol (ABE) production from concentrated substrate: reduction in substrate inhibition by fed-batch technique and product inhibition by gas stripping. *Appl. Microbiol. Biotechnol.* **63**(6), 653–658 (2004)
10. S.S. Kelley, R.M. Rowell, M. Davis, C.K. Jurich, R. Ibach, Rapid analysis of the chemical composition of agricultural fibers using near infrared spectroscopy and pyrolysis molecular beam mass spectrometry. *Biomass Bioenerg.* **27**(1), 77–88 (2004)
11. M. Moniruzzaman, B.S. Dien, B. Ferrer, R.B. Hespell, B.E. Dale, L.O. Ingram, R.J. Bothast, Ethanol production from AFEX pretreated corn fiber by recombinant bacteria. *Biotech. Lett.* **18**(8), 985–990 (1996)
12. S. Reshamwala, B.T. Shawky, B.E. Dale, Ethanol production from enzymatic hydrolysates of AFEX-treated coastal bermudagrass and switchgrass. *Appl. Biochem. Biotechnol.* **51**(1), 43 (1995)
13. J. Perez, J. Munoz-Dorado, R. de la Rubia, J. Martinez, Biodegradation and biological treatments of cellulose, hemicellulose and lignin: an overview. *Int. Microbiol.* **5**, 53–63 (2002)
14. D.F. Root, J.F. Saeman, J.F. Harris, Kinetics of the acid catalyzed conversion of xylose to furfural. *For. Prod. J.* **158**, 165 (1959)
15. X.B. Lu, Y.M. Zhang, J. Yang, Y. Liang, Enzymatic hydrolysis of corn stover after pre-treatment with dilute sulfuric acid. *Chem. Eng. Technol.* **30**, 938–944 (2007)
16. C. Cara, E. Ruiz, M. Ballesteros, P. Manzanares, M.J. Negro, E. Castro, Production of fuel ethanol from steam-explosion pre-treated olive tree pruning. *Fuel* **87**(6), 692–700 (2008)
17. V.S. Chang, M.T. Holtzapple, *Twenty-First Symposium on Biotechnology for Fuels and Chemicals* (Humana Press, Totowa, New Jersey, 2000)
18. H. Itoh, M. Wada, Y. Honda, M. Kuwahara, T. Watanabe, Bioorganosolve pre-treatments for simultaneous saccharification and fermentation of beech wood by ethanolysis and white rot fungi. *J. Biotechnol.* **103**(3), 273–280 (2003)
19. Q.D. Nguyen, T.K.P. Le, T.A.T. Tran, A technique to smartly re-use alkaline solution in lignocellulose pre-treatment. *Chem. Eng. Trans.* **63**, 157–162 (2018)
20. C.E. Wyman, Ethanol from lignocellulosic biomass: technology, economics, and opportunities. *Bioresour. Technol.* **50**(1), 3–15 (1994)
21. L. Zertuche, R.R. Zall, A study of producing ethanol from cellulose using clostridium thermocellum. *Biotechnol. Bioeng.* **24**(1), 57–68 (1982)
22. B.C. Knott, M. Haddad Momeni, M.F. Crowley, L.F. Mackenzie, A.W. Götz, M. Sandgren, G.T. Beckham, The mechanism of cellulose hydrolysis by a two-step, retaining cellobiohydrolase elucidated by structural and transition path sampling studies. *J. Am. Chem. Soc.* **136**(1), 321–329 (2014)
23. R. Chosdu, N. Hilmy, T.B. Erlinda, B. Abbas, Radiation and chemical pre-treatment of cellulosic waste. *Radiat. Phys. Chem.* **42**(4–6), 695–698 (1993)
24. K. Olofsson, A. Rudolf, G. Lidén, Designing simultaneous saccharification and fermentation for improved xylose conversion by a recombinant strain of *Saccharomyces cerevisiae*. *J. Biotechnol.* **134**(1–2), 112–120 (2008)

25. L.R. Lynd, W.H. Van Zyl, J.E. McBride, M. Laser, Consolidated bioprocessing of cellulosic biomass: an update. *Curr. Opin. Biotechnol.* **16**(5), 577–583 (2005)
26. M. Kleinert, J.R. Gasson, T. Barth, Optimizing solvolysis conditions for integrated depolymerisation and hydrodeoxygenation of lignin to produce liquid biofuel. *J. Anal. Appl. Pyrol.* **85**(1–2), 108–117 (2009)
27. A. Vuori, Thermal and catalytic reactions of the CO bond in lignin and coal related aromatic methyl ethers. *Acta Polytech. Scand. Chem. Technol. Ser.* **176**, 1–131 (1986)
28. O. Bobleter, Hydrothermal degradation of polymers derived from plants. *Prog. Polym. Sci.* **19**(5), 797–841 (1994)
29. B. Zhang, H.J. Huang, S. Ramaswamy, *Biotechnology for Fuels and Chemicals* (Humana Press, Totowa, New Jersey, 2007)
30. J. Barbier, N. Charon, N. Dupassieux, A. Loppinet-Serani, L. Mahé, J. Ponthus, F. Cansell, Hydrothermal conversion of lignin compounds. A detailed study of fragmentation and condensation reaction pathways. *Biomass Bioenergy* **46**, 479–491 (2012)
31. M. Kleinert, T. Barth, Towards a lignin-cellulosic biorefinery: direct one-step conversion of lignin to hydrogen-enriched biofuel. *Energy Fuels* **22**(2), 1371–1379 (2008)
32. M. Shukla, S. Singh, S.A. Siddiqui, A. Shukla, *Energy Sustainability Through Green Energy* (Springer, New Delhi, 2015)
33. H.K. Noh, S.Y. No, Effect of bioethanol on combustion and emissions in advanced CI engines: HCCI, PPC and GCI mode—a review. *Appl. Energy* **208**, 782–802 (2017)
34. A. Elfasakhany, Engine performance evaluation and pollutant emissions analysis using ternary bio-ethanol–iso-butanol–gasoline blends in gasoline engines. *J. Clean. Prod.* **139**, 1057–1067 (2016)
35. H. Cai, J.B. Dunn, Z. Wang, J. Han, M.Q. Wang, Life-cycle energy use and greenhouse gas emissions of production of bioethanol from sorghum in the United States. *Biotechnol. Biofuels* **6**(1), 141 (2013)
36. Y.H. Tan, M.O. Abdullah, C. Nolasco-Hipolito, N.S.A. Zauzi, G.W. Abdullah, Engine performance and emissions characteristics of a diesel engine fueled with diesel-biodiesel-bioethanol emulsions. *Energy Convers. Manage.* **132**, 54–64 (2017)
37. A.S. Silitonga, H.H. Masjuki, H.C. Ong, A.H. Sebayang, S. Dharma, F. Kusumo, W.H. Chen, Evaluation of the engine performance and exhaust emissions of biodiesel-bioethanol-diesel blends using kernel-based extreme learning machine. *Energy* **159**, 1075–1087 (2018)

Bio-Dielectric as an Alternative Degradable and Sustainable Fluid in EDM: A Review



Tapas Chakraborty  and Amitava Mandal 

Abstract Electro-discharge machining (EDM) process is an essential non-traditional machining process that allows the machining of harder materials with exceptional accuracy. In this thermal erosion process, extra material is removed by the action of regulated spark generated between the electrodes which are immersed into the dielectric. During ionization of hydrocarbon dielectric fluid the harmful gases emerge out of the dielectric tank at elevated temperature. Nowadays, the harmful environmental effect of hydrocarbon dielectric fluid is overcome with the replacement of bio-dielectric fluids, an inevitable issue of the present decade. This paper focuses on the comparative review of the output performance of bio-dielectrics over conventional dielectrics and also concentrates on environmental hazards, personnel health, operator's safety, bio-degradability and sustainability issues. The thorough literature survey depicts that bio-dielectric can be considered as a unique alternative of conventional hydrocarbon oil. Finally, the future scope of work is mentioned appropriately.

Keywords EDM · Hydro-carbon · Bio-dielectric · Biodegradability · Sustainability

1 Introduction

Electro-discharge machining is an abundantly used non-conventional material removing process. In 1694, Sir Robert Boyle first explored the discharge phenomena between two electrodes. Then, in 1770, Joseph Priestly observed the erodic incident in EDM. Two scientists, Lazarenko brothers in Russia, invented this electro-discharge machining process in 1943, and the circuit was named as Lazarenko circuit [1]. This

T. Chakraborty (✉)

Department of Mechanical Engineering, Saroj Mohan Institute of Technology, Hooghly, West Bengal 712512, India

A. Mandal

Department of Mechanical Engineering, Indian Institute of Technology (Indian School of Mines), Dhanbad, Jharkhand 826004, India

circuit has been used in the power supply of EDM. Their resistance-capacitance type power transmission system was abundantly used in the 1950s in EDM machines. The past problems with weaker electrodes were diminished with further development of pulse and solid state generators in the 1960s. Later, wire electrodes were introduced commercially with the EDM machine in 1967. In 1976, the CNC wire EDM was developed in the USA [2]. The materials which are too hard to machine by the conventional machining process, can be machined comfortably by non-conventional machining process with higher accuracy. In EDM, additional material is eliminated by thermal erosion process using a controlled DC spark created in the gap between the conductive electrodes. Either straight polarity or reverse polarity is opted based on the type of electrode materials used. The work-piece and tool tip both are dipped into the dielectric fluid. Now, high voltage is applied between two electrodes. Spark starts to flow through a small gap between the electrodes. The electric field intensity at the gap exceeds the dielectric strength of the fluid when the voltage is increased gradually. Then, the atoms of dielectric begin to be ionized and current flows through the tool work-piece gap. Due to successive electrical discharges, huge amounts of heat are created and material is removed from that zone where the sparks strike. The shape of the cavity which is formed in machining on the work surface is an absolute mirror image of the tool electrode [3, 4]. A constant gap between the electrodes is maintained by a servo mechanism for avoiding the short circuit due to tool work-piece contact. With expeditious academic and industrial growth, fabrication of complex harder materials, alloys and composite materials has been easier in electro-discharge machining basically in moulding die manufacturing, nuclear engineering, making of prototype, aerospace. In EDM, outstanding strength to weight ratio, high hardness, extensive wear and heat endurance capability are maintained. Although researchers have conducted several researches earlier, EDM process has been competently systematized for various work-tool-dielectric combinations and also extensively being used in modern manufacturing industries. Dielectric fluid takes an important part for achieving the required improved outcome. Researchers have used various dielectrics in different times in order to achieve the most favourable performance in EDM. Hence, ongoing development of the dielectric properties has been happening focussing on intensity of environmental pollution, effect on operator's health, biodegradability and overall sustainability. At elevated temperature some of the dielectrics such as kerosene oil, other hydrocarbon oils and mineral oils emit harmful poisonous gases like acetylene, ethylene, olefins, oxides of carbon and nitrogen. Due to continuous discharge, huge temperature is raised in the machining area which leads to dissociation of dielectric. Consequently, carbon layer deposits on tool surface causing deterioration of conductivity. It results in reduction of tool wear and MRR. Moreover, continuous reuse of dielectrics generates sludge and waste. This segregated sludge and filtration cartridges pollute land and water. Hence, nowadays sorting out of perfect dielectric is the major concern. Sustainability is a term which is used in manufacturing a product focussing on minimization of environmental hazards, paying attention to operator's health issues, recycling and treatment of waste.

Based on the term 'sustainability' numerous research scientists have exercised different dielectrics like oil-in-water emulsions, deionized water, water mixed with organic compound, tap water, distilled water, high velocity air or gas and bio-dielectric [5–9]. Although in concern with water dielectric, the chances of inflammability are removed but here productivity is less compared to EDM oil. Because of lower viscosity, water generates a small restriction to the discharge channel which results in decrease of energy density. Hence, MRR decreases. Distilled water as a dielectric depicts some beneficial points over conventional kerosene oil. It presents better material removal performance, greater surface finish, and minimum tool wear ratio and eliminates the chances of carbon deposition on the machined cavity. Conversely, it produces low-accuracy machined components [6, 10].

2 Literature Review

Bio-dielectrics do not produce any harmful toxic volatile and semi-volatile organics, poisonous halogens, aromatic compounds or hazardous inorganic gases compared to mineral oils or hydrocarbon dielectrics [11]. Vegetable oils are eco-friendly and readily biodegradable in both aerobic and anaerobic situations [12]. Moreover, EDM with vegetable oil dielectrics is a more sustainable machining process concerned with deposition of lesser amount of solid and liquid wastes causing friendlier pollution free environment, lesser machining cost, safety operation in concern with operator's health [13, 14]. It was also observed by the researchers that vegetable oils have almost 70–100% capability of biodegradability in 28 days span [15].

Rajurkar et al. [16] had kept an overview on sustainability of the EDM process. They have pointed out some benchmarks on sustainable manufacturing processes concerning public health, operational protection, environmental impact, manufacturing cost, type of material, energy consumption rate and also waste management. They have also described the important dielectric properties and evaluated their values which are mostly responsible for achieving the excellent quality of manufactured product, performance, productivity and trouble free operation. Similarly, Singaravel et al. [17] also assessed the essential electro-chemical and electro-physical properties of four dielectric fluids and compared the respective values of canola oil, sunflower oil and Jatropha oil with kerosene oil. They obtained the surface roughness values of almost mixed results for all dielectrics. Moreover, from another experiment with same dielectrics they concluded that these bio-dielectrics are superior to kerosene oil considering the operator's health and safety issue, pollution free environment that recommends sustainability [18]. Likewise, the waste vegetable oil also explores nearly identical results to conventional kerosene dielectric concerning material removal rate (MRR), electrode wear ratio (EWR) and tool wear rate (TWR). Here, vegetable oil is also assessed to be more preferable for sustainability issues in electro-discharge machining [19]. Biodiesel ameliorates material removal rate and reduces electrode wear rate with respect to kerosene oil. It is more economic. Researchers observed biodiesel and transformer oil emits less smoke and smells

[20, 21]. Vegetable oil based esters bestow more recommended dielectric properties than hydrocarbon oils and synthetic oils [22]. Bio-fluids present superior dielectric properties like excellent biodegradability, noble flash point, distinguished oxygen content, higher breakdown voltage, inferior volatility and minor poisonous emissions [23, 24]. Valaki et al. [25] witnessed the superior MRR, finer surface finish and harder work piece surface employing *Jatropha* biodiesel instead of kerosene oil. Ng et al. [26] also found outstanding results enhancing MRR and decreasing tool wear ratio using Canola and Sunflower biodiesel compared to conventional dielectric. Using transesterified neem dielectric oil Das et al. [27] attained 6.2%–15.6% more MRR and achieved 12.25%–15.45% finer surface in comparison with kerosene and proved the justification of neem oil as a sustainable dielectric. Besides, it was noted that waste vegetable oil named *Pongamia pinnata* presented 32% higher MRR but employing blended used vegetable oil EWR lowered 8% compared to conventional hydrocarbon oil. EDM with mixed reused vegetable oil yields smoother surface quality than obtained using waste vegetable oil [28]. Radu et al. [29] selected sunflower oil and soyabean oil in their study of sustainability. On the basis of a series of careful testing of refractive index, dynamic viscosity and with the result of spectra analysis no structural variation in these bio-oils were detected. From the environmental aspect, they pointed out that these oils have extreme biodegradability as there exists no harmful ingredients. They found these bio-dielectrics are more than 95% biodegradable, whereas mineral oils are less than 30%. Rao et al. [30] also estimated MRR for Canola oil and EDM oil separately and concluded MRR for Canola oil is more than EDM oil. They also established its biodegradability. Das et al. [31] carried out an experiment with transesterified *Jatropha*, Canola and Neem oil and observed their comparative influences with respect to kerosene oil. They found all of these bio-dielectrics depicted more MRR and lesser SR than Kerosene oil. They also found the flushing velocity range 0.30–0.40 m/s is more acceptable for obtaining preferable output results. Moreover, neem dielectric depicted more over cut and taper cut with respect to kerosene. Researchers also noted that biodiesel exhibits more MRR and less SR than bio oil [32]. *Jatropha* oil has high-kinematic viscosity. At 38 °C, it exhibits nearly 41 cSt which is more than conventional kerosene oil 2.5 cSt [33]. However, the viscosity of *Jatropha curcas* oil is excessively high because of higher molecular mass [34]. Hence, Khan et al. [35] described nicely the transesterification process by which the viscosity is reduced for smooth functioning as dielectric. He also investigated the transesterified *Jatropha* oil as a sustainable dielectric. Although researchers have worked on various bio-dielectrics namely *Jatropha curcas* oil, canola oil, sunflower oil, soyabean oil, waste vegetable oil, palm oil, however, till now a very few work have been recognized. There is still much more scope remaining to investigate the green parameters focussing on the sustainability index in EDM. Hence, a critical review of the present literature has been carried out which includes comparative discussion and analysis of the effect of various dielectrics over conventional dielectric from different aspects and issues such as output responses, sustainability and biodegradability and also investigated an appropriate research gap in EDM process in the present scenario.

3 Essential Dielectric Properties of Bio-Dielectric Compared to Conventional Dielectrics

Bio-dielectric includes edible oil, non-edible oil and waste vegetable oil. Dielectric properties are very essential for spark generation to remove extra material from the work-piece, to increase material removal rate, to decrease manufacturing cost, to achieve finer surface finish, surface quality, high accuracy, safety operation in electro-discharge machining. The essential electro-physical properties and electro-chemical properties are stated in Table 1.

Here, we are watching in most of the cases the essential properties are favourable in bio-dielectrics compared to conventional oil [17].

Dielectric properties are essential characteristics of dielectric fluid required to improve output responses like MRR, EWR, RWR, SH and SR. Manufacturing cost is related to MRR, EWR and RWR. Higher amount of material removed per unit time leads to increased production efficiency and to decrease production time. Similarly, electrode wear rate is related to tooling cost. It should be reduced. Surface hardness should be more and more for increasing wear resistance of the specimen. For achieving prolonged satisfactory service life, lower surface roughness value is preferable. At elevated current value with higher breakdown voltage and high viscosity of

Table 1 Comparison of level of dielectric properties between bio-dielectrics and conventional dielectrics Singaravel et al. [17]

Sl. no.	Dielectric properties	Required for	Bio-dielectrics	Conventional oil
1	Elevated break down voltage	Avoiding break down of dielectric easily	Higher	Lower
2	Acidic numbers	Better human health	Lower	Higher
3	Low viscosity	Better cooling action, effective flushing	Higher	Lower
4	High flash point	Safety from fire, stable sparking	Higher	Lower
5	High fire point	Safety from fire, stable sparking	Higher	Lower
6	High pour point	For better flow ability in cold atmosphere, stable sparking	Higher	Lower
7	Low oxygen value	Avoiding oxidation	Lower	Higher
8	High thermal conductivity	Carrying away excess heat from discharge area stopping thermal damage	Higher	Lower
9	Low Density	Better flushing effect	Higher	Lower
10	Specific heat	Better heat utilization	Higher	Lower
11	Bio-degradability	Pollution free environment	Higher	Lower

vegetable oil, MRR increases due to higher energy density with respect to conventional dielectric. From this discussion, it can be assured that vegetable oil and its properties depict high MRR value [36]. Higher viscosity clears out debris effectively leading to enhancing MRR. High thermal conductivities of dielectric also circulate more heat energy to the sparking zone to increase erosion. Low specific heat also enhances more heat utilization causing prolong ionizing duration. Higher percentage of oxygen in the dielectric enhances oxidation rate which increases impact on electrode surface. It increases EWR. Electrode wear rate also increases due to high breakdown voltage of dielectric which results in delayed ionization. High viscosity also may result to enhance EWR. Relative wear rate is evaluated by dividing work-piece material removal rate with tool wear rate. Hence, higher RWR is preferred. At elevated current level, due to high energy penetration on the work-piece surface, it presents deeper and wider crater. Then, high-surface roughness value is obtained for vegetable dielectric fluid [36]. Vegetable oil with larger thermal conductivity and lower specific heat tends to form deep craters on the work-piece due to lower energy density. Surface hardness increases due to higher oxygen value, which enhances melting and erosion. SH value also increases due to quenching operation for higher thermal conductivity. Lower specific heat utilizes heat perfectly and solidification for high viscosity leads to formation of higher surface hardness [17].

4 Bio-Dielectric as an Alternative Degradable and Sustainable Fluid for the Future

In EDM, a question arises that unsaturated fatty acids in vegetable oils may spoil its stability because of exposure to oxygen, high temperature and heat for long operating time [37, 38]. Researchers investigated the physico-chemical change if any occurred in vegetable oils. The report of spectra analysis, dynamic viscosity and refractive index of Sunflower oil and soyabean oil uncovered that no structural conversion took place. This is very much encouraging from the viewpoint of EDM sustainability. Moreover, the production rate of many vegetable oils are rapidly increasing throughout the world. It was reported that the production rate of soybean oil enhanced by 20% in 2019/2020 with respect to 2013/2014, whereas sunflower oils production increased by 30%, respectively [39]. Considering the economic aspect, vegetable oils are mostly cheaper than mineral oils. In addition, vegetable oil bestows higher MRR than EDM oil and also transesterified vegetable oil removes more material than conventional kerosene oil [30, 31, 35]. Consequently, productivity increases besides decreasing cost. Polanga bio-dielectric contributes better results in MRR, REWR and achieves finer quality of surface finish with improved micro-structure. Employing this bio-dielectric 6.46% enhancement of surface hardness became possible [40]. Based on environmental perspective, bio-dielectrics are free from detrimental materials. Moreover, bio-dielectrics are highly biodegradable in 28 days [15] and renewable [11, 12]. It was observed that sunflower oil and soybean oil are more than 50%

biodegradable, whereas mineral oils are less than 30%, respectively. The chances of explosion for bio-dielectric are less and safe for operators due to high flash and fire point [41]. The aerosol releasing rate for Polanga bio-dielectric decreases remarkably by 17.33% in comparison with conventional dielectric. It also calls for its good recyclability for next machining operation [40]. Based on the benchmarks regarding sustainability mentioned by Rajurkar et al. [16], bio-dielectric almost attains all the criteria. Hence, after thorough literature survey, it is concluded that bio-dielectric can be considered as an alternative degradable and sustainable fluid for the coming days.

5 Conclusion

The literature review leads to the conclusion that bio-dielectric can replace conventional hydrocarbon oil. It may be feasible to use as an essential dielectric in industry due to following benefits:

1. Generally used hydrocarbon oil releases harmful gases which cause acute environmental pollution. Also the price of synthetic oil is higher. Safe and environmental cleanliness may be ensured by employing eco-friendly and biodegradable dielectric. So, EDM with bio-dielectric provides a sustainable manufacturing process. Besides, personnel health and operator safety are perfectly maintained.
2. Vegetable oil based dielectrics present machining efficiency and surface finish quality almost equal or little more improved than using conventional dielectric.
3. Viscosity is one of the most essential properties for selection of dielectric. Using pure *Jatropha* oil as dielectric is a problem due to high viscosity. So this problem can be eliminated by transforming into biodiesel through reduction of viscosity in transesterification operation.

6 Future Scope

Various research works have been conducted using different dielectrics and also adding different additives to acquire favourable output performance. The literature survey depicts that bio-dielectric may be an alternative to the conventional hydrocarbon based oil considering free of pollution due to absence of harmful organics, sustainability, biodegradable and safety operation. Hence, more investigation is required using other different bio-dielectrics purely or in blended form to achieve more improved output responses. More research can be conducted by adding different metallic powders such as nickel, molybdenum, vanadium, manganese, cadmium with the variation of size, concentration and shape of the particles to the dielectric in order to obtain more fruitful outcomes. The impacts of different bio-dielectrics on surface texture, recast layer thickness, heat affected zone, micro-hardness, crack length and

crack density to be studied thoroughly before being ensured as alternative dielectric. More investigation is also required in the area of sustainable electro-discharge machining process. In material processing of some metals such as stainless steel, magnesium alloy the variation in viscosity of dielectric is an important phenomenon [29]. The variation of oil quality of vegetable oil dielectric should be tested more thoroughly for long processing time and at elevated temperature.

References

1. B.R. Lazarenko, To invert the effect of wear on electric power contacts (Dissertation of the All-Union Institute for Electro Technique in Moscow/CCCP, Russian, 1943).
2. Y.Y. Tsai, C.T. Lu, Influence of current impulse on machining characteristics in EDM. *J. Mech. Sci. Technol.* **21**, 1617–1621 (2007). <https://doi.org/10.1007/BF03177384>
3. C.J. Luis, I. Puertas, G. Villa, Material removal rate and electrode wear study on the EDM of silicon carbide. *J. Mater. Process. Technol.* **164–165**, 889–896 (2005). <https://doi.org/10.1016/j.jmatprotec.2005.02.045>
4. J. Marafona, J.A.G. Chousal, A finite element model of EDM based on the Joule effect. *Int. J. Mach. Tools Manuf.* **46**(6), 595–602 (2006). <https://doi.org/10.1016/j.ijmactools.2005.07.017>
5. W. König, L. Jörres, Aqueous solutions of organic compounds as dielectrics for EDM sinking. *CIRP Ann. Manuf. Technol.* **36**, 105–109 (1987). [https://doi.org/10.1016/S0007-8506\(07\)62564-5](https://doi.org/10.1016/S0007-8506(07)62564-5)
6. M.L. Jeswani, Electrical discharge machining in distilled water. *Wear* **72**(1), 81–88 (1981). [https://doi.org/10.1016/0043-1648\(81\)90285-4](https://doi.org/10.1016/0043-1648(81)90285-4)
7. S.T. Jilani, P.C. Pandey, Experimental investigations into the performance of water as dielectric in EDM. *Int. J. Mach. Tool Des. Res.* **24**(1), 31–43 (1984). [https://doi.org/10.1016/0020-7357\(84\)90044-1](https://doi.org/10.1016/0020-7357(84)90044-1)
8. S.L. Chen, B.H. Yan, F.Y. Huang, Influence of kerosene and distilled water as dielectrics on the electric discharge machining characteristics of Ti-6Al-4V. *J. Mater. Process. Technol.* **87**, 107–111 (1999). [https://doi.org/10.1016/S0924-0136\(98\)00340-9](https://doi.org/10.1016/S0924-0136(98)00340-9)
9. B.H. Yan, H.C. Tsai, F.Y. Huang, The effect in EDM of a dielectric of a urea solution in water on modifying the surface of titanium. *Int. J. Mach. Tools Manuf.* **45**(2), 194–200 (2005). <https://doi.org/10.1016/j.ijmactools.2004.07.006>
10. Y.C. Lin, H.M. Chow, B.H. Yan, H.J. Tzeng, Effects of finishing in abrasive fluid machining on micro-holes fabricated by EDM. *Int. J. Adv. Manuf. Technol.* (2007). <https://doi.org/10.1007/s00170-006-0485-7>
11. S. Howell, Promising industrial applications for soybean oil in the US (American Soybean Association, National Biodiesel Board, 2007)
12. L.A.T. Honary, Biodegradable/bio-based lubricants and greases. *Machinery Lubrication Magazine*, Issue no. 200109 (Noria Corporation, 2004). www.oilmaintenance.com
13. I.S. Jawahir, P.C. Wanigarathne, X. Wang, Product design and manufacturing processes for sustainability, in *Mechanical Engineer's Handbook: Manufacturing Management*, vol. 3, 3rd edn, ed. by K. Myer (2006), pp. 414–443
14. G. Rotella, T. Lu, L. Settineri, O.W. Dillon, I.S. Jawahir, Dry and cryogenic machining: a comparison from the sustainability perspective, in *International 9th Global Conference on Sustainable Manufacturing*, ed. by G. Seliger (Springer, Heidelberg, 2012), pp. 95–100
15. P. Broekhuizen, D. Theodor, K. Le Blanch, S. Ullmer, *Lubrication in Inland and Coastal Water Activities*, 1st edn. (A. A. Balkema Publishers, Tokyo, 2003)
16. K.P. Rajurkar, H. Hadidi, J. Pariti, G.C. Reddy, Review of sustainability issues in non traditional machining processes. *Proc. Manuf.* **7**, 714–720 (2017)

17. B. Singaravel, K. Chandra Shekar, K.M. Rao, G.G. Reddy, Study of vegetable oil and their properties for as an alternative source to mineral oil based dielectric fluid in electric discharge machining. *Int. J. Mod. Eng. Res. Technol. Nat. Conf. Adv. Mech. Eng. Nanotechnol. (AMENT)* **5** (2018)
18. B. Singaravel, K. Chandra Shekar, G.G. Reddy, S.D. Prasad, Experimental investigation of vegetable oil as dielectric fluid in electric discharge machining of Ti-6Al-4V. *Ain Shams Eng. J.* **11**(1) (2019). <https://doi.org/10.1016/j.asej.2019.07.010>
19. J.B. Valaki, P.P. Rathod, Assessment of operational feasibility of waste vegetable oil based bio-dielectric fluid for sustainable electric discharge machining (EDM). *Int. J. Adv. Manuf. Technol.* **87**, 1509–1518 (2016). <https://doi.org/10.1007/s00170-015-7169-0>
20. K. Dincer, Lower emissions from biodiesel combustion. *Energy Source A* **30**(10), 963–968 (2008)
21. P. Sadagopan, B. Mouliprasanth, Investigation on the influence of different types of dielectrics in electrical discharge machining. *Int. J. Adv. Manuf. Technol.* **92**, 277–291 (2017). <https://doi.org/10.1007/s00170-017-0039-1>
22. Z.H. Shah, Q.A. Tahir, C.J. Town, Dielectric properties of vegetable oils. *J. Sci. Res.* **3**(3), 481–492 (2011)
23. U.U. Abdullahi, S.M. Bashi, I. Member, R. Yunus, H.A. Nurdin, *The Potentials of Palm Oil as a Dielectric Fluid, National Power and Energy Conference (PECON) Proceedings* (Kuala Lumpur, Malaysia, 2004), pp. 224–228
24. D. Martin, I. Khan, J. Dai, An overview of the suitability of vegetable oil dielectrics for use in large power transformers. *Euro. Tech. Con.* 4–23 (2006)
25. J.B. Valaki, P.P. Rathod, C.D. Sankhavara, Investigations on technical feasibility of *Jatropha curcas* oil based bio dielectric fluid for sustainable electric discharge machining (EDM). *J. Manuf. Process.* **22**, 151–160 (2016)
26. P.S. Ng, S.A. Kong, S.H. Yeo, Investigation of biodiesel dielectric in sustainable electrical discharge machining. *Int. J. Adv. Manuf. Technol.* **90**(9–12), 2549–2556 (2016)
27. S. Das, S. Paul, B. Doloi, Investigation of the machining performance of neem oil as a dielectric medium of EDM: a sustainable approach. *IOP Conf. Ser. Mater. Sci. Eng.* (2019). <https://doi.org/10.1088/1757-899X/653/1/012017>
28. H.S. Mali, N. Kumar, Investigating feasibility of waste vegetable oil for sustainable EDM, in *6th International and 27th All India Manufacturing Technology Design and Research Conference* (2016)
29. M.C. Radu, R. Tampu, V. Nedeft, O.I. Patriciu, C. Schnakovszky, E. Herghelegiu, Experimental investigation of stability of vegetable oils used as dielectric fluids for electrical discharge machining. *J. Process.* **8**(9), 1187 (2020). <https://doi.org/10.3390/pr8091187>
30. K.M. Rao, D.V. Kumar, K.C. Shekar, B. Singaravel, Experimental analysis of canola oil as dielectric fluid in electric discharge machining of AISI D2 steel. *Mater. Sci. Forum* **978**, 49–54 (2020). <https://doi.org/10.4028/www.scientific.net/MSF.978.49>
31. S. Das, S. Paul, B. Doloi, An experimental and computational study on the feasibility of bio-dielectrics for sustainable electrical discharge machining. *J. Manuf. Process* **41**, 284–296 (2019). <https://doi.org/10.1016/j.jmapro.2019.04.005>
32. S.M. Basha, H.K. Dave, H.V. Patel, Experimental investigation on the quality of electric discharge machined Ti-6Al-4V using bio-oil and biodiesel. *Mater. Today: Proc.* (2020). <https://doi.org/10.1016/j.matpr.2020.06.314>
33. M.Y. Khan, A. Mittal, Extraction, characterization and wick stove performance of *Jatropha curcas* oil. *Int. J. Eng. Res. Adv. Devel.* **3**(11), 25–33 (2017)
34. K. Pramanik, Properties and use of *Jatropha curcas* oil and diesel fuel blends in compression ignition engine. *Renew. Energy* **28**(2), 239–248 (2003)
35. M.Y. Khan, P.S. Rao, B.S. Pabla, Investigations on the feasibility of *Jatropha curcas* oil based biodiesel for sustainable dielectric fluid in EDM process. *Mater. Today: Proc.* 10th Int. Conf. Mater. Process. Charact. (2020). <https://doi.org/10.1016/j.matpr.2019.11.325>
36. B. Singaravel, K. Chandra Shekar, S.D. Prasad, G.G. Reddy, Performance analysis of vegetable oil as dielectric fluid in Electric discharge machining process of Inconel 800. *Mater. Sci. Forum* **978**, 77–83 (2020). <https://doi.org/10.4028/www.scientific.net/MSF.978.77>

37. A. Gomna, K.E. N'Tsoukpoe, N. Le Pierres, Y. Coulibaly, Review of vegetable oils behaviour at high temperature for solar plants: stability, properties and current applications. *Sol. Energ. Mater. Sol. Cells* **200**, 109956 (2019)
38. S. Anbinder, C. Meiorin, C. Macchi, M.A. Mosiewicki, M.I Aranguren, A. Somoza, Structural properties of vegetable oil thermosets: effect of cross linkers, modifiers and oxidative aging. *Eur. Polym. J.* **124**, 109470 (2020)
39. Statista. Available online: www.statista.com. Accessed on 17 July 2020
40. B.P. Mishra, B.C. Routara, Evaluation of technical feasibility and environmental impact of *Calophyllum inophyllum* (Polanga) oil based bio-dielectric fluid for green EDM. *Measurement* (2020). <https://doi.org/10.1016/j.measurement.2020.107744>
41. M. Rafiq, Y.Z. Lv, Y. Zhou, K.B. Ma, W. Wang, C.R. Li, Q. Wang, Use of vegetable oils as transformer oils—a review. *Renew. Sustain. Energ. Rev.* **52**, 308–324 (2015). <https://doi.org/10.1016/j.rser.2015.07.032>

Laboratory Investigation of Composite Made of Alumina Dispersed Aluminum Prepared by UTM Pressed Powder Metallurgy Method



M. K. Manik, Mani Bhushan Shing, and Vishal Vhagat

Abstract The present study reported that fine grain powders of $\text{Al}_2\text{O}_3/\text{Al}$ composites containing 2, 4, 6, 8 and 10 wt.% of alumina, prepared by Universal testing machine (UTM) pressed powder metallurgy method (PMM) to find out the change in micro structural as well as mechanical properties as compared to pure metal. A close ball mill is used to confirm the effect of speed and time during the mixing and milling of powders. The powder mixed with binder was then pressed under UTM and then sintered at predetermined temperature. The maximum value of observed density of mixed and milled sample was recorded as 8.23% and 6.17% respectively for a mixture containing 10 %wt. of Al_2O_3 as compared to pure aluminum. It was also observed that highest densification occurs when 10 wt. % of ceramics (Al_2O_3) present in pure aluminum. The sharp increase in hardness occurs up to 4 wt.% of Al_2O_3 mixed composite. The maximum value of hardness of the composite is increased by 50%. The Poisson ratio of aluminium composite containing 4 wt.% of ceramic was calculated as 0.33 whereas the maximum value recorded 0.53 for a composite having 10 wt.% of $\text{Al}_2\text{O}_3/\text{Al}$. The micro graphical analysis clearly shows good distribution of particles and very less agglomerations of alumina within the range of composites made of PMM. The enhancement of breaking load is recorded 50.9% for composite containing 4 wt.% $\text{Al}_2\text{O}_3/\text{Al}$ and ultimate tensile strength increase to 68.3% for composite containing 6 wt.% Al_2O_3 as compared to pure aluminium.

Keywords Composite · Powder metallurgy · Milling · Crystallite and ceramics

M. K. Manik (✉) · M. B. Shing
Department of Mechanical Engineering, LDC Institute of Technical Studies, Soraon Prayagraj
211025, India

V. Vhagat
CCET, Bhilai, Chhattisgarh 492026, India

1 Introduction

The Composite of ceramic (Al_2O_3) mixed with aluminium are an important member of the class of metal-matrix composites (MMCs) and presently these composites are being extensively used in the aerospace and automobile industries [1–7]. Due to improved mechanical properties as well as high temperature stability these materials are severely used in advanced industrial and tribological applications [1–8]. As per Manik et al. the Composite is a product made up of two or more different types of materials that are combined together to form something totally different than that of the original constituents [9]. They are combined in such a way that the resulting material or composite possesses superior properties to any of their individual constituents. Composites are widespread among natural and engineering materials, a composite made of ceramics is shown in Fig. 1. The essential components in the composite are matrix and fibre, fibre is generally loaded carrying members in composites whereas matrix protects fibres from damage and acts as envelop around the fibres. The method of production has a strong influence on the mechanical and tribological properties of these composites via its effects on the matrix grain size, porosity and distribution of reinforcing particles [10–12]. Among the different processing methods, powder metallurgy (PM) is an important one for the production of MMCs. Two important advantages of PM over other casting techniques include the uniform distribution of reinforcing particles within the matrix and less degradation due to lower processing temperatures [4, 10–18]. The basic manufacturing steps in the PM technique for producing particulate MMCs include the mixing of a matrix alloy powder with reinforcing particles, followed by compacting and sintering [3, 4, 10, 12, 13, 17–19].

In general, there are three different types of composites

1. Particles reinforced composites
2. Short fibre MMCs
3. Continuous fibre or sheet reinforced Composites

The widespread application of MMCs in different fields has boosted up in the last two decades due to the accessibility of suitable strengthening elements with an easy and economical process of formulation that may direct to upliftment of

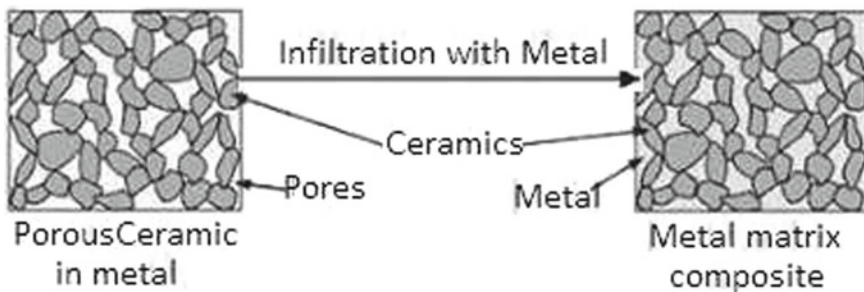


Fig. 1 Metal and ceramic formed metal-matrix composite

properties. Two different metals/alloys possess different potential at their interfacial zones (between the matrix and reinforced materials) and it acts as an essential part of MMC. The design parameters and interfacial phenomenon of matrix and reinforced particles only govern the change of mechanical, thermal and electrical properties that are of absolute importance in the composite [7]. The current advancement of Al_2O_3 reinforcements makes it possible to control physical and mechanical properties of MMCs that has directed to extensive use of Al_2O_3 composites in power electronics, aerospace, packaging and heat transfer purposes.

Latest progress in this field advocated that step-up growth of procurement of MMC economically appreciated and suggested for bright future for these types of materials. Augmented demand of MMCs have noticeably been viewed from the last decade due to their improved mechanical properties such as rupture modulus, strength; wear resistance, thermal resistance, fatigue resistance and other performance compared to the unreinforced matrix alloys. The reinforcements are added externally or formed internally by different reactions. The properties of MMCs mainly depend on the properties of matrix material, reinforcements and the matrix-reinforcement interface [8]. The shape and size of matrix as well as reinforced particles, their orientation within composite play very crucial functions in the physical properties of composite.

The cheap and available light metal is the prime source of metal-matrix composites (MMCs) used in present day. The most essential factors are the compatibility between the materials used in composites. The materials will possess compatibility when there is no undesirable chemical reaction amongst the materials that may be judged during the process of preparation or after the formation of composite. The creation of dissimilar inters metallic compounds may lead to a redundant and undesirable effect in transferring load to the matrix to the reinforced particles. As per the past literature, the reaction products may act as sites for nucleation of cracks [10]. The enhanced mechanical property of MMCs generated due to the presence of superior quality of reinforced particles may lead to increase modulus of elasticity, strength and fatigue behaviour. Generally, the ductility and fracture toughness of MMCs are inferior due to the hard and tougher reinforced element within the matrix. These qualities are very important for any load-bearing structural principle. As a result, the matrix alloys should possess higher ductility and fracture toughness to ascertain the desirable properties of MMC in different applications [10].

The author took an immense interest to prepare a composite of alumina dispersed aluminium prepared by the application of powder metallurgy technique where plastic deformation is done in green sample under UTM pressing. Several studies have been reported that fine grain (FG) materials can be used as super high strength materials, intelligent and superplastic materials for various applications. The significant findings in this paper are to show the effect of defined speed and time during mixing and milling of fine grain materials before sintering process and change in micro structural as well as mechanical behaviour on pressing and thermal diffusion after sintering. As we know the effect of impurities in the powder plays an important role in the sintering hence very high purity aluminium powder were used in this experiment.

2 Experimental Setup and Process of Preparation of Material

For the requirement of experimental investigation, initially pure aluminium in the form of small bar was collected from the chemical supplier of laboratory and the properties of pure aluminium was found out in our material laboratory by melting the supplied metal in an open furnace and pouring it into the mould cavity that was prepared with the help of wooden pattern and green sand in the casting laboratory of MNNIT Allahabad. The composition of supplied material was specified by the laboratory as Table 1.

Material is melting in furnace, preparation of moulding sand, preparation of wooden pattern and details procedure of casting is shown in Fig. 2a to h. As soon as casting of pure aluminium is prepared, then samples for a different test has been cut from the casting block as shown in Fig. 2h.

All the samples were prepared as per standard procedure and the same was tested under different testing equipment after checking their accuracy. The error of the testing equipment was adjusted for each and every case by adding (+) or subtracting (–) errors if recorded with any machine.

Table 1 Sample of aluminium is supplied by bonafide chemicals, Kanpur

Components	Fe	Si	Mn	Mg	Al wt.%
Pure Al %	0.062	0.041	0.002	0.002	99.893

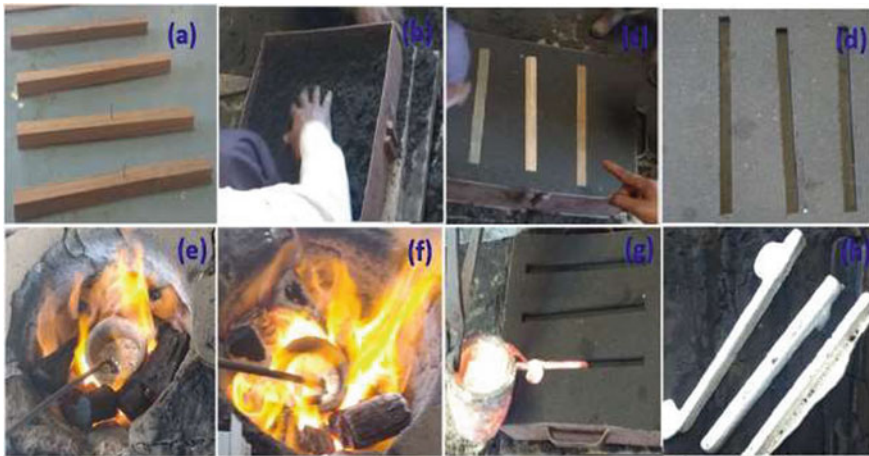


Fig. 2 a wooden patterns used for open casting. b Preparation of green sand for casting. c Patterns were placed to produce mould cavity, d mould cavity was ready for pouring liquid metal, e and, f aluminium was melted in open furnace, g liquid metal was poured into the cavity, and h casting of aluminium was ready for different samples for test

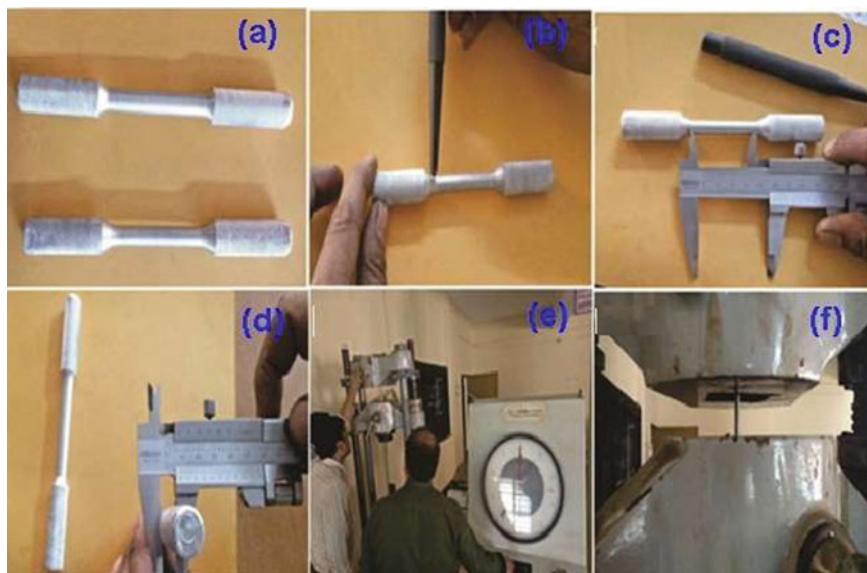


Fig. 3 a Samples were prepared for UTM test. b Punching was done to measure gauge length c and d Measurement of gauge length and diameter with Vernier caliper. e Setting of samples in UTM and process of testing is done. g Final position sample at the end of test

To find out the various test results of aluminium that was purchased for laboratory is tabulated in the datasheet for the purpose of comparison with different proportionate mixed composite of aluminium to alumina. Here a single test procedure of tensile test is shown in Fig. 3a to h. Similarly, all the samples were tested and the result of pure aluminium of various tests is tabulated in excel sheet for comparison. The same sample was then transformed into powder form by chipping and ball milling methods for further application in composites.

2.1 Method of Mixing of Samples

Alumina (Al_2O_3) powder of 2, 4, 6, 8 and 10 wt.% respectively added separately every time with pure aluminium metal powder and mixed in planetary ball mill with the agate jar and agate balls having ball to powder weight ratio (BPR) as 5:1 and allowed to rotate ball mill with the speed of 100 rpm for 2 hrs to confirm regular distribution of alumina particles throughout the aluminium matrix. Mixing speed and time was maintained constant for every mixture for making proper comparison. Toluene was used as solvent to minimize frictional heat generation for the process; the balls for milling and charging were totally submerged in toluene throughout the process (Table 2).

Table 2 Mixing parameter

Mixing	Parameter
Planetary ball mill (retsch PM 100)	Milling media-toluene Ball to powder ratio 5:1
Milling jars-agate jars	Mixing speed 100 rpm
Milling balls-agate balls	Mixing time 2 h Powder mixture weight 10 gm

Table 3 Sample code and composition for mixing

S. no.	Sample code	Sample composition
1	MCC2	98 wt% Al + 2 wt% Al ₂ O ₃
2	MCC4	96 wt% Al + 4 wt% Al ₂ O ₃
3	MCC6	94 wt% Al + 6 wt% Al ₂ O ₃
4	MCC8	92 wt% Al + 8 wt% Al ₂ O ₃
5	MCC10	90 wt% Al + 10 wt% Al ₂ O ₃

Five dissimilar mixing proportions were chosen and tabulated in Table 3. Finally, all the samples were coded as Metal Ceramic Composite (MCC) with their ceramic percentage as suffix, as for example two percent ceramics in the mixture (MCC2) and so on (Fig. 4).

2.2 Method of Milling of Samples

Different proportionate of alumina is added into aluminium metal mixed and milled in a planetary ball mill. Retsch PM 100 ball mill which is a convenient benchtop model with one grinding station is used in this experiment. This is a very high energy ball mill of maximum operating efficiency. The distinct combination of high friction with specified impact results in exceptionally fine elements within the shortest possible time. The solvent toluene was performing as process control agent in milling and its level was kept in such a way so that balls and charges could submerge totally. The detailed structural and working parameter of planetary mill and its components are described in Table 4.

2.3 Compaction of Sample Materials

Thoroughly alumina mixed aluminium samples were then collected for cold compactions under Universal Testing Machine (UTM) as shown in Fig. 5 and the sample was placed for a specific time under pre-defined load in material testing laboratory at MNNIT, Allahabad for preparing green mould for onward groundwork of



Fig. 4 Initially all the materials required for experiment were made ready in the material testing laboratory. **a** Retsch PM 100 ball mill used for mixing as well as milling. **b** Hard stainless steel jar used to hold hard steel ball that helps/milled the material under processes. **c** Hard stainless steel ball that was used with Jar, **d** ceramics powder, i.e. Al_2O_3 **e** Aluminium powder used here as base material for composite. **f** Liquid toluene was used as a solvent and stearic acid as lubricant used in the material preparation method

Table 4 Milling parameter

Milling	Parameter
Planetary ball mill (Retsch PM 100)	Milling jars-hard stainless-steel jar
Milling Balls-hard stainless steel	Milling media-toluene
Ball to powder ratio 10:1	Milling Speed 300 rpm
Milling time-10 h	Powder mixture weight 10 gm

Powder metallurgy method. Table 5 shows the detail of compaction parameters used in experiment.

Starch solution is used as binder for giving sufficient strength to green mould for handling before sintering. Stearic acid is used as lubricant to minimize die wall-particle as well as inter particles friction in the processes of compaction.



Fig. 5 Die and plunger used for compaction

Table 5 UTM pressing parameter

Parameter	Detail
Die size	12 mm Pressing force
Up to 50 kN pressing time	3 min
Binder	PVA(4 wt.% of powder weight)
Lubricant	Stearic acid

2.4 Sintering of Samples

The compacted pellets of composites were further placed inside in a horizontal tubular argon atmosphere furnace where temperature was constantly monitored at 610 °C for densification and heating rate of was constantly monitored at 10 °C/min throughout the heating period and the holding time for the samples was predetermined for 2 hrs in all cases maintaining similarity for all samples.

Finally, cooling of furnace was done at room temperature and the samples were taken away for next process. The size of the pellets was determined as 12 mm diameter and 4–5 mm thickness so that it will be easy to prepare different test samples for carrying out necessary tests after sintering. A hat was shown in Fig. 6. The detailed procedure of formulation of composite is shown in flow chart in automatic constant heating high temperature tubular furnace was used in IIT Roorkee for sintering process (Fig. 7).



Fig. 6 High temperature tubular furnace and its different subassemblies kept in material testing laboratory in IIT, Roorkee

3 Test Result and Discussion

3.1 Density Measurement

The calculation of theoretical density was determined by means of standard formula of mixture.

$$\frac{1}{\rho_c} = \frac{W_f}{\rho_f} + \frac{W_m}{\rho_m} \tag{1}$$

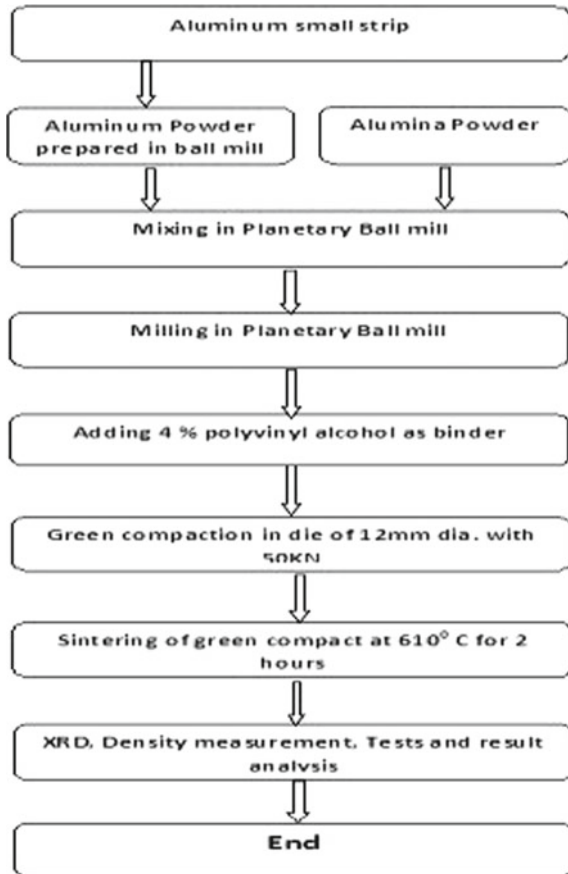
where ρ_f , ρ_m , ρ_c are density of reinforcement fibres, matrix and composite respectively and W_f , W_m are weight fraction of reinforced fibres and matrix respectively. Experimental density of sample was calculated from

$$\rho = \frac{m}{V} \tag{2}$$

where, V = Volume of samples and m = mass of sample after sintering.

Fabricated composites were reinforced with fine grains of Al_2O_3 particles in varying wt.% with pure aluminium. The mechanical properties of pure aluminium were examined in material testing laboratory before reinforcing it and the details are specified in Table 1. The different weight portions of Al_2O_3 in the mix were chosen as: 2, 4, 6, 8 and 10 wt.% respectively. Composites of diverse specifications were produced one by one through UTM compressed powder metallurgy technique.

Fig. 7 Flow chart of the complete procedure of experiment



To find out the porosity content, measurement of density was calculated in both pure and composites reinforced with all different wt.% of fine grains of Al_2O_3 particles as per Formula (1). The result of the mixed samples is tabulated in Table 2 taking into account as $\rho_{\text{Al}} = 2.77$ and ρ of $\text{Al}_2\text{O}_3 = 3.67$ respectively.

The investigated outcome of theoretical and experimental density of mixed and milled samples are tabulated in Table 6 where mixed, milled metal and ceramics powder for composites are abbreviated for 2, 4, 6, 8 and 10 are as (MCC2 to MCC10) respectively. Plot of density versus wt.% of reinforced Al_2O_3 mixed and milled samples are revealed in Fig. 8a and b. The result demonstrated that density of mixed samples increases proportionally with increased weight percentage of reinforced Al_2O_3 because the mass of single Al_2O_3 ($m = 112$) molecules is almost 3.77 times heavier than the mass of one atom of pure aluminium ($\text{Al} = 37$). In the curve, it is clearly confirmed that the density of the mixed, as well as milled sample, sharply increases up to 4 wt.% of Al_2O_3 and thereafter the slope flattens up to 10 wt.% Al_2O_3 . Sharp increase of density may be the cause of interstitial occupying of mixture

Table 6 Density of mixed and milled samples and their densifications

S. no.	Sample code	Theoretical density (g/cm ³)	Experimental density of mixed samples (g/cm ³)	Experimental density of milled samples (g/cm ³)	% Densification of mixed sample	% Densification of milled sample
1	MCC2	2.79	2.51	2.53	92.60	89.96
2	MCC4	2.81	2.55	2.59	92.20	90.75
3	MCC6	2.83	2.57	2.57	91.93	89.75
4	MCC8	2.84	2.58	2.61	92.34	90.14
5	MCC10	2.85	2.59	2.63	93.26	90.75

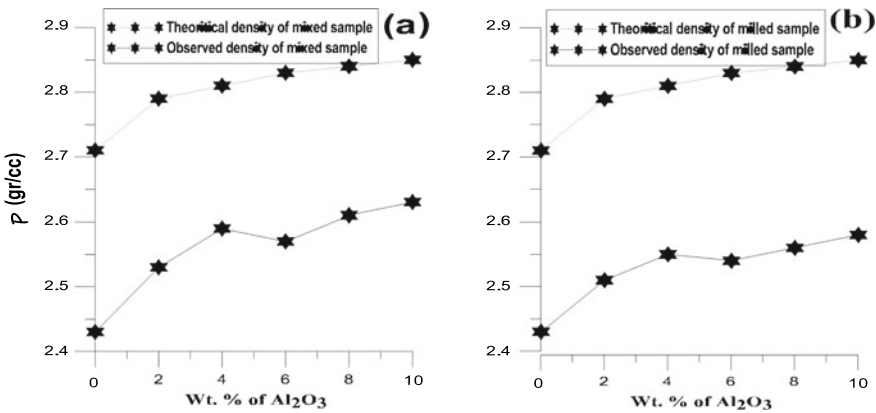


Fig. 8 a Density variation of mixed and b milled samples

molecule within the metal lattice and when excess (> 4%) are added then it occupies the place in interlayers spacing.

The plot clearly shows that the theoretical density is comparatively higher than that of observed value because in the process of physical mixing the atmospheric air and gases may be trapped and entrained within the mould that might cause of lowering density than expected value. The observed value of density of mixed and milled sample increases by 8.23% and 6.17% respectively for wt.% of 10 Al₂O₃/Al composite as compared to pure aluminium. The basis of interfacial bonding between the two phases may be due to physical and chemical interaction, interface hooking between the surfaces, interfacial friction stresses, thermal stresses between the face boundaries and finally due to adhesion that plays very vital role in strengthening the interfacial attachment that may cause higher densification, lower expansion coefficient and better mechanical properties. It is also viewed that the mixing sample possesses maximum densification closely 93.26 For Mixture Having 10 Wt.% of Al₂O₃ Whereas Milled Sample Possesses 90.75 Densifications for the Same Composition. A Similar Result Has Been Notified in the Literature [20, 21].

3.2 Hardness Measurement

Micro hardness testing was performed on the surface of polished samples using a UHL Vickers micro hardness tester kept in material testing Laboratory of MNNIT Allahabad. The indents were taken at room temperature using 100 gf load and 15 s of dwell time. A minimum of 20 indents was taken to find average and standard deviation for each value. The diagonal lengths of the square indentations were measured by the attached microscope. The Vickers hardness (H_v) was determined from the following equation: $H_v = 1.854 \frac{P}{d^2}$ and $d = \frac{d_1 + d_2}{2}$; where d , d_1 and d_2 are projected and two diagonals diameters of indenter respectively and P is the load acted on indenter. Figure 9 shows the variation of the average VHN number of aluminium reinforced with 2, 4, 6, 8, 10 wt.% of Al_2O_3/Al respectively. The diagram visibly expresses the average hardness value for samples MCC2, MCC4, MCC6, MCC8 and MCC10 with pure sample having Zero (0%) of ceramic powder.

The sharp increase in hardness up to 4 wt.% may be the cause of occupying of fine grain-particles of Al_2O_3 within the interstitial gap of aluminium matrix and partially due to grain refinement with particle strengthening effects. The value of hardness of composite increases more than 50% as compared to hardness of pure aluminium with same temperature. A similar observation has been reported in the literature [20, 21]. Generally, for a metal, the density is proportional to its hardness, so this result possesses good agreement to the metallic properties.

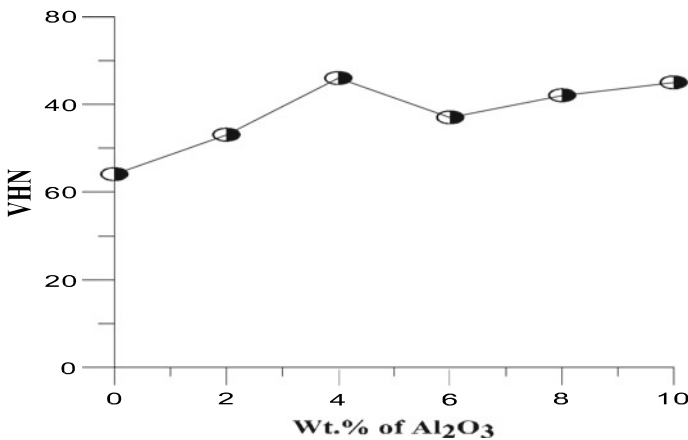


Fig. 9 Variation of micro hardness at different wt.% Al_2O_3 mixed aluminium

3.3 Result and Analysis Based on UTM Test

The accuracy of the equipment was tested by taking numbers of readings (12–15 readings) of similar samples as per standard operating conditions. The detailed shape, specification of samples of pure aluminium and its result are given in Table 7 and the same for composites are recorded in Table 8.

Details of prepared samples are marked on the base of their Al_2O_3 percentage and testing in UTM also is shown in Fig. 10a, b and c. It was observed that the stress strain relationship for all the samples follows a linear relationship from the beginning to the point of fracture. The deviation of linearity was observed in testing graph just at the point of crack on the specimen. Average of the three results was taken for comparison in all cases. The result demonstrates that Poisson ratio, Breaking load and UTS for pure samples are 0.23, 5.77 and 91.91 respectively.

Result illustrated that the elongation in composite is temporarily restricted when alumina percentage is close to 4%. It is also observed that breaking strength and ultimate tensile strength (UTS) are continuously increasing with the increase of ceramic percentage. Fig. 11a confirmed that the lowest value of Poisson ratio is recorded as 0.33 for the composite containing 4 wt.% of ceramics and the highest value is observed 0.53 for 10 wt.% of ceramic in composite. The percentage increase of Poisson ratio for composites MCC2, MCC4 ... to MCC10 is calculated as 43, 43, 91, 109 and 131 in comparison to pure metal respectively. The value of Poisson ratio remains constant within the range of 2–4% $\text{Al}_2\text{O}_3/\text{Al}$ composite indicating the higher value of hardness for a specific composition.

Figure 11b illustrates that the breaking load continuously increases with the higher value of Al_2O_3 present in the composite. Breaking load sharply increases from 5.2 to 7.4 kN with the increase of Al_2O_3 percentage in the composite up to 4 wt.% and the highest value is recorded as 8.3 kN for 10 wt.% of Al_2O_3 in composites. The peak value of breaking load for composite is calculated as 50.9% higher than base metal.

Plot of ultimate tensile strength (UTS) versus wt.% of Al_2O_3 in composite in Fig. 11c shows a very smooth curve from 92.1 to 155 MPa up to 4 wt.% of $\text{Al}_2\text{O}_3/\text{Al}$ composite and thereafter it looks like an equilibrium state with higher percentage of Al_2O_3 in the composite. The enhancement in the result may be the cause of combining effect of grain boundary refinement in mixing, strong adhesion due to impact pressure and finally thermal stress generated at the grain boundary by the cause of the huge difference of thermal expansion coefficient between aluminium and alumina in the composite. A similar effect is also viewed in the literature [22, 23], The best result comes out when percentage of Al_2O_3 is 6 wt.% in the composite. Composite is recorded as 68.3% higher breaking loads than the pure Aluminium.

Table 7 Details of sample prepared from pure aluminium and its results

Sl. No.	Job name	Testing/process	Total length (mm)	Grip dia. (mm)	Initial dia. (mm)	After exp. dia. (mm)	Initial gauge length (mm)	After exp. gauge length (mm)	% Decrease dia.	% Increase length
1	1	UTM	145	15.2	10.18	10	51	55	1.76	7.84
2	2		145	15.2	10.14	9.91	48	51.4	1.75	7.083
3	3		146	15.2	10.15	9.97	49	51.8	1.75	7.09

Table 8 UTM test result of composites

Job name	Total length (mm)	Grip dia. (mm)	Initial dia. (mm)	After exp dia. (mm)	Initial gauge length (mm)	After exp gauge length (mm)	% Decrease dia.	% Increase length
MCC2	145	15.20	10.20	9.94	51.00	53.70	2.55	5.29
MCC4	145	15.20	10.10	9.91	49.00	50.90	1.88	3.88
MCC6	146	15.20	10.20	9.97	50.00	52.30	2.22	4.60
MCC8	146	15.20	10.10	9.88	51.00	53.30	2.18	4.51
MCC10	145	15.20	10.20	9.99	49.00	51.10	2.08	4.29



Fig. 10 a Five different test samples used for tensile test, b initial setting of sample in UTM has been done and c the final elongation of sample

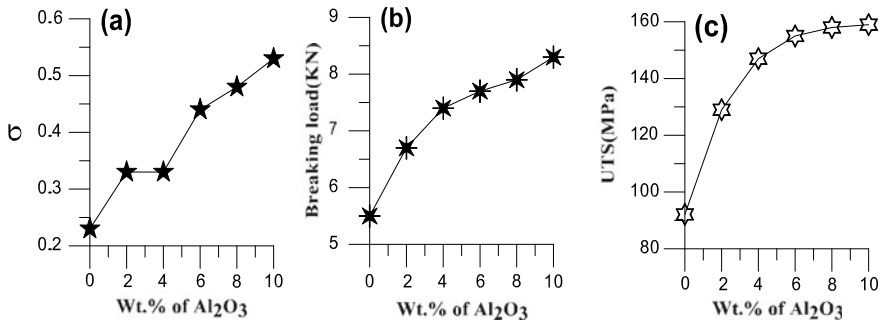


Fig. 11 a Plot of poisson ratio (σ) with varying wt.% of Al₂O₃/Al, b Breaking loads versus wt.% of Al₂O₃/Al c the graph of UTS versus wt.% of Al₂O₃/Al

3.4 X-ray Diffraction (XRD) Analysis and Characterization of Samples

XRD is based on constructive interference of monochromatic axis of crystalline samples. As we know, the pattern of XRD diffraction is the exact fingerprint of atomic arrangement pattern in crystal lattice. In XRD diffraction method X-ray is

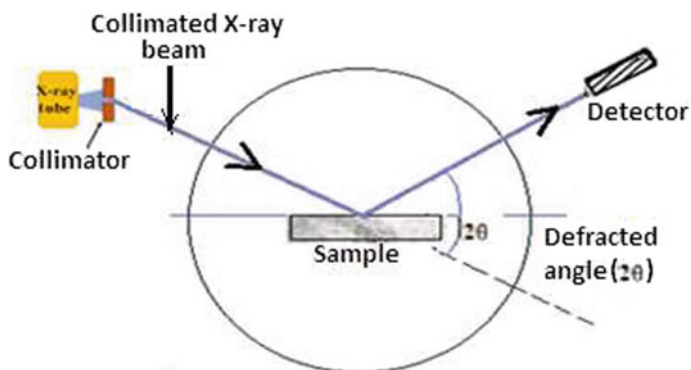


Fig. 12 That how collimated X-ray beam from X-ray tube is deflected by the planes of sample

produced by cathode ray tube, filter tube to construct monochromatic emission. This radiation is collimated as shown in Fig. 12. Electromagnetic radiation is only diffracted by the atomic planes when half of its wavelength is less than equal to the atomic distance d . When the ray interacts with the sample, it produces constructive interference when condition satisfied as per Bragg's law: $n\lambda = 2d \sin \theta$ where λ = wavelength of X-ray, d = distance of lattice plane and 2θ = diffraction angle of ray emitted from X-ray tube,

This law relates with the diffraction angle θ and wavelength of diffracted ray with the lattice plane that is marked as d here.

The deflection of X-ray occurred due to the presence of electrons in the site. A huge number of deflections mentioned the cause of availability of large number of electrons in a particular spot that indicates large many atoms accessibility in that area. Peak intensities of the deflection are confirmed by the position and the number of atoms within a unit cell and the peak intensities are produced due to superposition of all the constructive and destructive interferences based on the position of atoms. The continuous deflection of X-ray in the particular site informed a closed array of atoms in that plane and produce high intensity/peak of X-ray deflection. Therefore, higher intensity of deflection signifies strong orientation of crystalline structure and crystal size and lattice strain support the width of peak of XRD. To read the grain size or Crystallite size from the XRD, another equation, i.e. $d = 0.9 \lambda / \beta \cos \theta$ **Scherer's formula**, where λ = wavelength of X-ray, β = Full width at half maxima to be measured (FWHM), d = Crystallite size and θ = Diffracted Bragg's angle ($2\theta/2$).

Phase analysis was done by XRD technique using Rigaku Smart lab diffractometer with Cu- $K\alpha$ radiation of wavelength ($\lambda = 1.5406 \text{ \AA}$), operating at an accelerating potential of 44 kV and 40 mA current. Crystallite size and lattice parameters were also calculated along with phase identification.

The intensity of all the diffracted beams against 2θ was recorded for all the samples for angle 2θ ranging from 10–90° at a Goniometric speed of 5°/min with 0.010 step



Fig. 13 a The photograph of X-Ray Diffractometer (XRD) and b all internal components of X-ray diffractometer

size and holding time 0.2 s/step. Analytical X' Pert high score software using PAN-ICSD were used for identifying peaks of different phases present in the synthesized samples. The dimensions of regular crystallite of the powders were calculated by X-ray line broadening procedure employing **Scherer's formulae**. The photograph of XRD equipment used in the experiment is shown in Fig. 13a and b.

The data in Table 9 clearly explained that for defined FWHM and for the diffracted angle of 38.4° , the estimated crystallite size for all five different samples (Fig. 14).

Table 9 Crystallite Size of mixed powder

S. no.	Sample	Position (2θ)	FWHM	Crystallite size(\AA)
1	MCC2	38.387	0.268	339.4201
2	MCC4	38.424	0.264	347.7815
3	MCC6	38.48	0.256	364.5862
4	MCC8	38.496	0.241	391.8318
5	MCC10	38.385	0.2545	360.4869

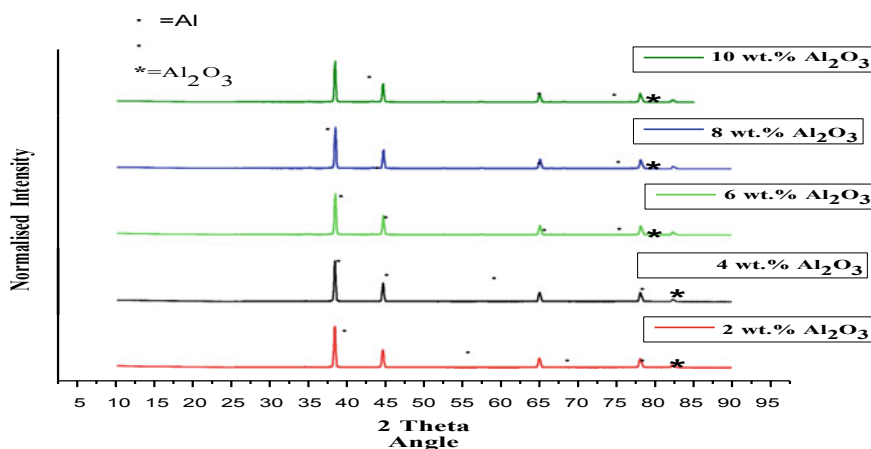


Fig. 14 Comparison of XRD image of mixed powder at different wt.% of Al_2O_3

As FWHM positions were lightly changing for different compositions, the crystallite size also changed. It was also evidently clear that gradual lower value of FWHM creates larger crystallite sizes of composites. Maximum size of crystallite size was viewed as 391.83Å for mixture containing 8 wt.% of Al₂O₃ in aluminium and the size crystallite changes within the range of 15.44% in the mixture (Table 10).

It was also clearly visible that crystallite size changes for different compositions of Al₂O₃/Al in the milling sample. The lower value of FWHM indicates larger crystallite sizes of composites. Size of crystallite varies from minimum to maximum is recorded as 35.3% in milling mixture containing 2–10 wt.% of Al₂O₃/Al (Fig. 15).

Table 10 Crystallite size of milled powder

S. no.	Sample	Position (2θ)	FWHM	Crystallite size (Å)
1	MCC2	38.419	0.268	316.7628
2	MCC4	38.388	0.332	254.2476
3	MCC6	38.415	0.318	331.1415
4	MCC8	38.559	0.286	305.6197
5	MCC10	38.668	0.261	343.997

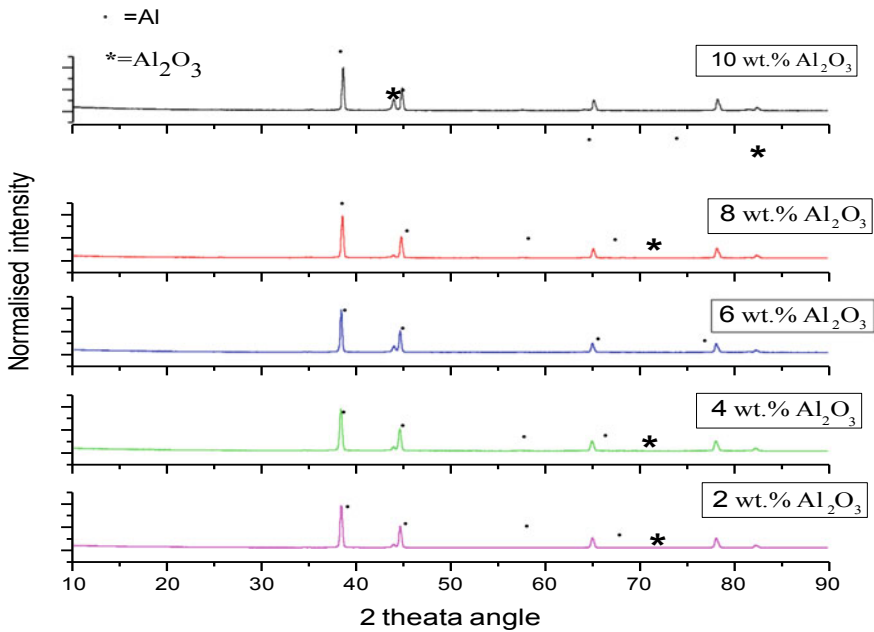


Fig. 15 Comparison of XRD image of milled powder at different wt.% of Al₂O₃

4 Conclusion and Future Scope of Work

The present laboratory experimental research brought out the following conclusions based on micro fine $\text{Al}_2\text{O}_3/\text{Al}$ composites fabricated by the method UTM pressed powder metallurgy techniques:

- (1) The maximum value of observed density of mixed and milled sample was recorded as 8.23% and 6.17% higher respectively for composite containing 10 wt.% of Al_2O_3 as compared to pure aluminium
- (2) The sharp increase in hardness up to 4 wt.% may be the cause of occupying of nano and micro-particles within the interstitial gap of aluminium matrix and partially due to grain refinement and particle strengthening effects. The value of hardness of composite increases more than 50% as compared to hardness of pure aluminium with the same temperature.
- (3) The Poisson ratio of aluminium composite containing 4 wt.% of ceramic was calculated as 0.33 whereas the maximum value was recorded 0.53 for composite having 10 wt.% of $\text{Al}_2\text{O}_3/\text{Al}$.
- (4) Result illustrated that the elongation in composite is temporarily restricted when alumina percentage is close to 4%. It was also observed that the optimum tensile strength and fracture strength were continuous functions of percentage of ceramic.
- (5) Breaking load sharply increases from 5.2 to 7.4 kN with enhancement of Al_2O_3 percentage in the composite up to 4 wt.% and the highest value is recorded as 8.3 kN for 10 wt.% of Al_2O_3 in composites. The peak value of breaking load for composite is calculated as 50.9% more than the base metal.
- (6) Ultimate tensile strength (UTS) shows a very smooth curve from 92.1 to 155 MPa up to 4 wt.% of $\text{Al}_2\text{O}_3/\text{Al}$ composite and thereafter it pursues an equilibrium status with higher percentage of Al_2O_3 in the mixture. The best result appeared at 6 wt.% of ceramics composite which is approximately 68.3% higher than the breaking strength of pure aluminium.
- (7) The micro graphical analysis vividly shows good distribution of constituents and very less agglomerations of Al_2O_3 within the composites made by powder metallurgy method.
- (8) In the XRD comparison of mixed and milled powder, as FWHM positions were slightly dropping for different compositions, the crystallite sizes were increased. It was also vivid that the crystallite size of milled powder increased to 15.4% as Al_2O_3 powder in the mixture of $\text{Al}_2\text{O}_3/\text{Al}$ increased from 2 to 8% respectively.
- (9) Size of crystallite varies in milling is recorded as 35.3% and 15.44% in mixing sample containing 2–10 wt.% of $\text{Al}_2\text{O}_3/\text{Al}$.
 - I. Study has been conducted within the specified range of Al_2O_3 in the composite but that can be extended some higher/lower percentage also.

- II. Mixing Al_2O_3 particles could be used within the smaller range like 20–40 nm to see the effect of nanoparticles in the lower dimension in the composite.
- III. Thermal and electrical properties could be compared with pure aluminium, etc.
- IV. Other metal and metallic oxides could also be added to detect mechanical and thermal properties of poly reinforced composites of aluminium.

References

1. M. Hoseini, M. Meratian, Fabrication of in situ aluminium–alumina composite with glass powder. *J. Alloy. Compd.* **471**, 378–382 (2009)
2. O. Yilmaz, S. Buytoz, Abrasive wear of Al/ Al_2O_3 -reinforced aluminium-based MMCs. *Compos. Sci. Technol.* **61**, 2381–2392 (2001)
3. A.M. Al-Qutub, I.M. Allam, T.W. Qureshi, Effect of sub-micron Al_2O_3 concentration on dry wear properties of 6061 aluminium based composite. *J. Mater. Process. Technol.* **172**, 327–331 (2006)
4. J. Ye, J. He, J.M. Schoenung, Cryomilling for the fabrication of a particulate B_4C reinforced Al nano composite: part I. Effects of process conditions on structure. *Metallurgical Mater. Trans. A. Phys. Metall. Mater. Sci.* **37**, 3099–3109 (2006)
5. K. Kawabata, E. Sato, K. Kuribayashi, Creep deformation behaviour of spherical Al_2O_3 particle reinforced Al–Mg matrix composites at high temperatures. *Acta Mater.* **50**, 3465–3474 (2002)
6. L. Yao-hui, D. Jun, Y. Si-rong, W. Wei, High temperature friction and wear behaviour of Al_2O_3 and/or carbon short fibre reinforced Al–12Si alloy composites. *Wear* **256**, 275–285 (2004)
7. E. Del-rio, J.M. Nash, J.C. Williams, M.C. Breslin, G.S. Daehn, Co-continuous composites for high-temperature applications. *Mater. Sci. Eng. A* **463**, 115–121 (2007)
8. S. Mahdavi, F. Akhlaghi, Effect of SiC content on the processing, compaction behavior, and properties of Al6061/SiC/Gr hybrid composites. *J. Mater. Sci.* **46**, 1502–1511 (2011)
9. M.K. Manik et al., Mechanical properties of epoxy resin matrix composites reinforced with jute fiber, coconut coir and human hair. *Int. J. Eng. Adv. Technol. (IJEAT)* **9**(1), ISSN: 2249–8958 (2019)
10. F. Akhlaghi, S.A. Pelaseyyed, Characterization of aluminium/graphite particulate composites synthesized using a novel method termed in-situ powder metallurgy. *Mater. Sci. Eng. A* **385**, 258–266 (2004)
11. F. Akhlaghi, P. Delshad-Khatibi, Effect of silicon content on size distribution and morphology of Al–Si powder particles produced by solid assisted melt disintegration (SAMD) method. *Powder Metall.* **54**(2), 153–159 (2011)
12. B.S.B. Reddy, K. Das, S. Das, A review on the synthesis of in situ aluminium-based composites by thermal, mechanical and mechanical–thermal activation of chemical reactions. *J. Mater. Sci.* **42**, 9366–9378 (2007)
13. J.B. Fogagnolo, F. Velasco, M.H. Robert, J.M. Torralba, Effect of mechanical alloying on the morphology, microstructure and properties of aluminium matrix composite powders. *Mater. Sci. Eng. A* **342**, 131–143 (2003)
14. U.T.S. Pillai, B.C. Pai, K.G. Satyanarayana, A.D. Damodaran, Fracture behaviour of pressure die-cast aluminium–graphite composites. *J. Mater. Sci.* **30**, 1455–1461 (1995)
15. R. Asthana, S. Das, T.K. Dan, P.K. Rohatgi, Solidification of aluminium–silicon alloy in the presence of graphite particles. *J. Mater. Sci. Lett.* **5**, 1083–1086 (1986)
16. K.S. Dunnett, R.M. Mueller, D.P. Bishop, Development of Al–Ni–Mg–(Cu) aluminium P/M alloys. *J. Mater. Process. Technol.* **198**, 31–40 (2008)

17. C.P. Chen, C.Y.A. Tsao, Response of aluminium/graphite composite to deformation in the semi-solid state. *J. Mater. Sci.* **31**, 5027–5031 (1996)
18. J.F. Lin, M.G. Shih, Y.W. Chen, The tribological performance of 6061 aluminium alloy/graphite composite materials in oil lubrications with EP additives. *Wear* **198**, 58–70 (1996)
19. I.A. MacAskill, R.L. Hexemer Jr., I.W. Donaldson, D.P. Bishop, Effects of magnesium, tin and nitrogen on the sintering response of aluminium powder. *J. Mater. Process. Technol.* **210**, 2252–2260 (2010)
20. G. Bajpai et al., Development of Al-nano composites through powder metallurgy process using a newly designed cold isostatic compaction chamber. *J. Mater. Today: Proc.* **2**, 2737–2746 (2015)
21. S.A. Sajjadi et al., Fabrication of A356 composite reinforced with micro and nano Al₂O₃ particles by a developed compocasting method and study of its properties. *J. Alloy. Compd.* **511**, 226–231 (2012)
22. X.S. Zeng, G.H. Zhou, Q. Xu, Y.J. Xiong, C. Luo, J. Wu, A new technique for dispersion of carbon nanotube in a metal melt. *Mater. Sci. Eng. A* **527**, 5335–5340 (2010)
23. X.L. Zhong, W.L.E. Wong, M. Gupta, Enhancing strength and ductility of magnesium by integrating it with aluminium nanoparticles. *Acta Mater.* **55**, 6338–6344 (2007)
24. F. Akhlaghi, H. Esfandiari, Solid-assisted melt disintegration (SAMD), a novel technique for metal powder production. *Mater. Sci. Eng. A* **452–453**, 70–77 (2007)

Numerical Investigation on Can-Combustor's Performance for Different Alternative Fuels Using CFD



P. Shankara Narayanan, Padma Ganesan, R. Arul Prakash, R. Vijayanandh,
and M. Ramesh

Abstract The rapid growth of industrialization and the increase in the population of the world leads to a sharp increase in the demand for conventional energy sources. The usage of fossil fuels leads to environmental degradation due to extreme pollutant emissions. Fossil fuel resources are getting depleted at a very fast rate so that importance has to be given towards the usage of alternate fuels. Methanol and various other alcohols can behave as suitable alternate fuels. The jet engine is the best propulsive system for all kinds of aircraft for different altitudes. In which combustor plays a vital role in energy production with a low occupying area, But the problem associated with the gas turbine combustion system is unable to execute complete combustion. The main objective of this present research work is to do the numerical study on Can combustor performance using different alternative fuel blends with Jet-A fuel and to obtain the optimized blend which will enhance the performance with low emission. The comparative analysis of can combustor for different alternative fuels is done by using advanced CFD simulations. The conceptual design and discretization processes are executed with the help of ICEM CFD 16.2. ANSYS Fluent 16.2 is used for comparative computational analysis.

Keywords Bio-fuels · CFD · Combustor · Ethanol · Optimization · Jet-A

1 Introduction

The predominant motto of this work is to pick suitable fuel for Gas Turbine Engine Combustion Chamber, in which computational thermal investigations are used as methodology. The comparative computational thermal investigations are carried out for various fuels such as Jet-A-1, Ethanol, and Methanol, etc., and thereby Ethanol performed better than other fuels. Generally, combustion is as old as civilization.

P. Shankara Narayanan · P. Ganesan · R. Arul Prakash (✉) · R. Vijayanandh · M. Ramesh
Department of Aeronautical Engineering, Kumaraguru College of Technology, Coimbatore, Tamil
Nadu 641049, India
e-mail: arulprakash.aeu@kct.ac.in

© The Author(s), under exclusive license to Springer Nature Singapore Pte Ltd. 2022
M. L. Kolhe et al. (eds.), *Smart Technologies for Energy, Environment and Sustainable
Development, Vol 1*, Springer Proceedings in Energy,
https://doi.org/10.1007/978-981-16-6875-3_62

783

Fire is one of the greatest major discoveries of man. The fire was established artificially for the first time around 30,000 years back. It is believed that Indians were first to recognize the efficacy of the fire even in the ancient Vedic era as it is described profusely in Vedas. Most of the modern technological development has emanated from the discovery of fire. Modern civilization is built upon the combustion of fuels to produce both heat and electrical power. The awareness of combustion is very important today due to the stringent emission standards and scarcity of fossil fuels. In general, aircraft are entirely powered by on-board fuel burning, combustion is defined as chemical process in which fuel is burnt in the presence of an oxidizer producing heat and light. The combustion chamber must also be capable of maintaining stable and efficient combustion over a wide range of operating conditions. Efficient combustion has played a vital role in engines because of rapid rise in commercial aircraft traffic and the consequent increase in environmental pollution. The challenges in designing high-performance combustion systems have changed significantly over the years towards a more sophisticated process. The main objective of this present research paper is to do the numerical investigation on Can combustor using methanol as a fuel blend with jet aviation fuel. The main object of combustion modeling is to simulate certain combustion processes and to help in interpreting and understanding observed combustion phenomena. It will substitute for difficult or expensive experiments combustion modeling is to determine the effect of individual parameters in combustion processes by conducting parametric studies [1–6].

2 Literature Survey

Pathan had done the three-dimensional numerical investigation of the combustion of methane-air mixture in gas turbine Can combustor by using CFD with CFX solver. Numerical investigation on Can-type combustion chamber showed the following findings: 60° swirler geometry was giving less NO emission as the temperature at the exit of the combustion chamber is less as compared to 30° and 45° swirler angle geometry. Pradhan et al. had done the CFD Analysis on can-type combustor and variation of air injection angle under typical engine conditions, the computational prediction of combustion has been a challenging task due to complexity involved in the flow parameters. A combustion analysis was made with a RANS code and $k-\varepsilon$ based turbulent model. The CFD based predictions of the combustion process can-type combustor and the performance had been evaluated for the optimal design of the Producer gas burner. Prasanna Kumar et al. had done the numerical investigation on various combustion chambers, in which methane was used as fuel and with initial atmospheric conditions also the theoretical flame temperature produced by the flame with a fast combustion reaction was 1950 K. The predicted maximum flame temperature was 1850 K of the combustion products compared well with the theoretical adiabatic flame temperature. Gaurav had done a numerical simulation on tubular combustion chamber through kerosene-methanol blend. The result showed that a good agreement with the experimental results. Further numerical analysis was

carried out to study the effect of methanol on emissions and combustor centerline temperature with blends. Results revealed a reduction in emissions like CO, CO₂, and NO_x. Temperature distribution and flame length were affected by the use of methanol blend. Mohamed Noureldin had done an experimental investigation of performance and exhaust emissions of a gas turbine engine fuelled with waste cooking oil. From the experimental results, it was found that the static thrust of the engine was reduced when the engine operated with blends of waste cooking oil compared to that of 100% Jet A-1. Also, the engine rotational speed was reduced while operating the engine with waste cooking oil biodiesel blends. The TSFC for biofuel blends was higher when compared to Jet A-1 fuel. On the other hand, the values of CO and NO_x concentrations for biodiesel blends were lower compared to that of Jet A-1. Valentina Fortunato had done the investigations on various chambers, in which the performances of the combustion chamber were discussed using methane and biogas combustion. The combustor performed very well in terms of emissions, especially CO and NO_x, for various air inlet temperatures and air-to-fuel ratios, proving the benefits of MILD combustion. The combustion chamber proved to be fuel-flexible since both ignition and stable combustion could be achieved by burning biogas. The model performed quite well both for methane and biogas. For the biogas, the most appropriate kinetic mechanism to properly model the behavior of the chamber was selected. Zhang had done combustion and stability characteristics of ultra-compact combustor using cavity for gas turbines. In this work, the combustion, emission, and stability characteristics of seven combustors were experimentally studied in detail using a gas component analyzer, particle image velocimetry, a dynamic pressure system, with the help of a data acquisition system. The fuel adaptability of the combustor was analyzed numerically. Under typical experimental conditions, the combustion efficiencies were higher than 94% and the emission indexes of unburned hydrocarbon and nitrogen oxide were in the range of 3–7 and 0.5–1.5 g/(kg fuel), respectively.

3 Methodology Used—CFD

The computational based approach for real time problems has been provided less efficiency in reliable output due to work station based working nature. Thus the quality grid generation, standard initial and boundary conditions have the power to provide robustness in the numerical output. Before the approaching numerical simulation, the problem formulation is very important to get a clear view of the computational processor and therefore the attainment of reliable output also may chance to increase in huge level. Computationally, the following phases and its contributing parameters have been supported a lot in the CFD problem formulation: computational model, grid construction, boundary conditions, definition of analysis and its solver, and governing equations used [7, 8].

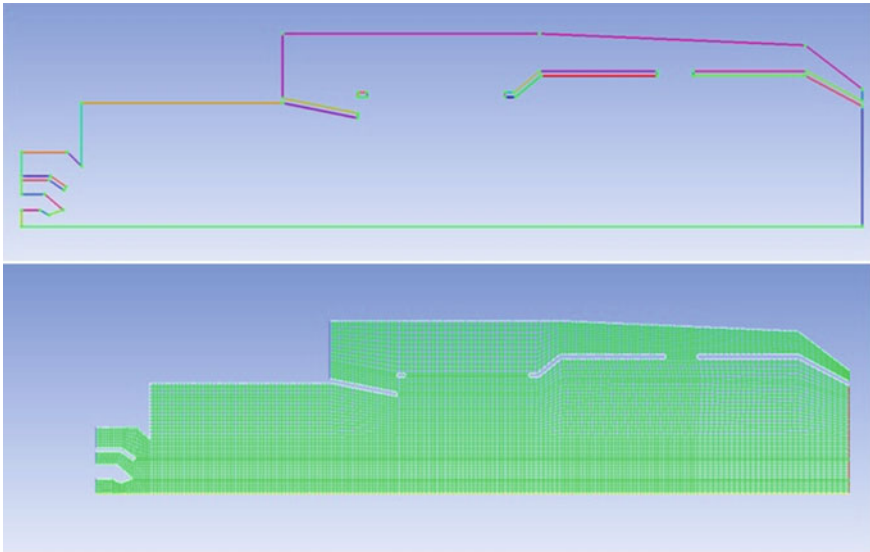


Fig. 1 Combined view of mesh

3.1 Modeling

The computational model is the platform of this work, which is clearly revealed in Fig. 1. This article is intended to analyze the comparative investigation of performance study on can combustor, which finalized the authors to concentrate on various alternative fuels and its mixture instead of can combustor design. Therefore in this work used the dimensions of the can combustor from the literature survey [9].

3.2 Meshing

Because of the comprehensive study, the two-dimensional based can combustor is shortlisted as a platform of this work. Also, the can combustor's design nature is axisymmetric, which furthermore fitted to adopt the two-dimensional based investigations. The 2D structural mesh has been created in this can combustor with the support of ANSYS ICEM 16.2, in which the average mesh quality is obtained as 0.895 and the aspect ratio is obtained 1.1025. In which, the extra fine facilities are concentrated on the inlets and outlet regions, which is clearly shown in Fig. 2.

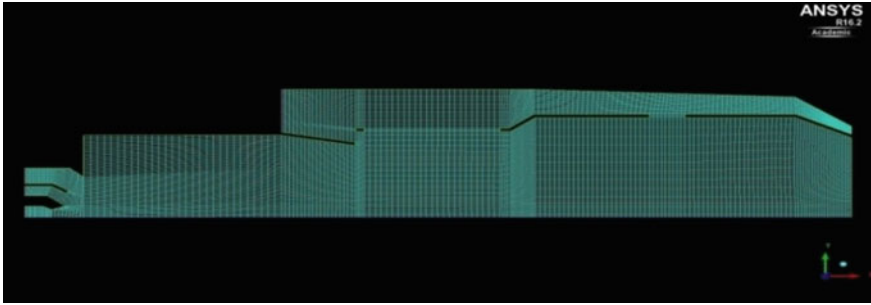


Fig. 2 Mesh case—typical view

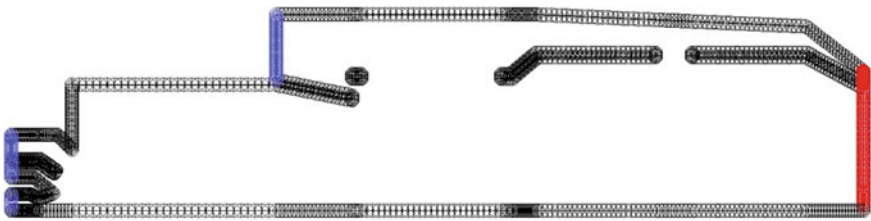


Fig. 3 Meshed model of combustor

3.3 *Boundary Conditions*

The integrated boundary conditional view of a can combustor is shown in Fig. 3, wherein the pressure outlet is mentioned in the red color, the air inlet is denoted in the blue colors at top location, the walls are represented in the block colors and the fuel inlets are shown in the blue color at bottom location of the can combustor. Also, the axisymmetric representation is very important so it's also represented in the black color at bottom of this construction. The air from the inlet enters the combustion chamber at a velocity of 0.5 m/s. Fuel from the fuel inlet enters the chamber at a velocity of 80 m/s. The outlet of the combustor is a pressure outlet. The walls of the combustor have a uniform temperature distribution. Also, the top walls are given with no slip conditions and the axisymmetric condition is given at the bottom region.

3.4 *Description of Analysis*

The species mixture based transient analysis is very toughest one so double-precision is chosen to enhance the performance of the solver. The pressure based solver is selected with inclusion of incompressible density based equations. Since the analysis is done on two-dimensional, the axisymmetric is selected under general category. The

energy equations are enabled in order to get the thermal energy variations on each and every node. To predict the presence of turbulence, the k -epsilon turbulence model is applied. The fuel and air are not mixed in prior so non-premixed combustion is carried out, where boundary species (Jet-A, Ethanol) are selected. The appropriate quantities of Jet-A and ethane are mixed and finally, a pdf table has been calculated. In addition to that other relevant fuels are added the same way. In the specification method, the turbulence intensity and hydraulic diameter are specified based on the design of can combustor. In solution methods coupled scheme is preferred, which can able to solve non-linear problems like combustors. To initialize the solution a hybrid initialization is chosen and the time step method is selected as an automatic.

3.5 Governing Equations Used in CFD

The three fundamental governing equations are included, in which the equations are filtered based on the axisymmetric nature. The continuity, r -momentum, z -momentum, and energy equation are listed in Eqs. 1, 2 3, and 4 respectively [10–17].

$$\frac{1}{r} \frac{\partial v_r}{\partial r} + \frac{\partial v_z}{\partial z} = 0. \quad (1)$$

$$\rho \left(V_r \frac{\partial v_r}{\partial r} + v_z \frac{\partial v_r}{\partial z} \right) = -\frac{\partial p}{\partial r} + \mu \left(\frac{1}{r} \frac{\partial}{\partial r} \left(r \frac{\partial v_r}{\partial r} \right) + \frac{\partial^2 v_r}{\partial z^2} - \frac{v_r}{r^2} \right). \quad (2)$$

$$\rho \left(V_r \frac{\partial v_z}{\partial r} + v_z \frac{\partial v_z}{\partial z} \right) = -\frac{\partial p}{\partial z} + \mu \left(\frac{1}{r} \frac{\partial}{\partial r} \left(r \frac{\partial v_z}{\partial r} \right) + \frac{\partial^2 v_z}{\partial z^2} \right) \quad (3)$$

$$\rho C_p \left(V_r \frac{\partial T}{\partial r} + v_z \frac{\partial T}{\partial z} \right) = k \left(\frac{1}{r} \frac{\partial}{\partial r} \left(r \frac{\partial T}{\partial r} \right) + \frac{\partial^2 T}{\partial z^2} \right) + \mu \varphi \quad (4)$$

4 Numerical Results and Discussion

4.1 Numerical Simulation of Primary Fuels

The computational simulations inside the can combustor have been carried out with the help of aforesaid boundary conditions. In which, four major fuels are implemented in this first optimizational computation, that are Jet-A fuel, CH₄ fuel, Ethanol fuel, and C₂H₂ fuel. Figures 4, 5, 6 and 7 are revealed the thermal distribution over the can combustor of aforesaid fuels. Based on the high thermal generations, the best fuels are finalized, which are: C₂H₂-Acetylene, Ethanol, and Jet-A. Further, the thermal

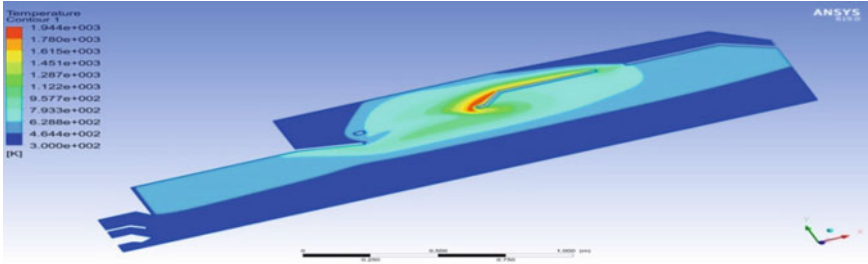


Fig. 4 Thermal variations of full jet-A fuel

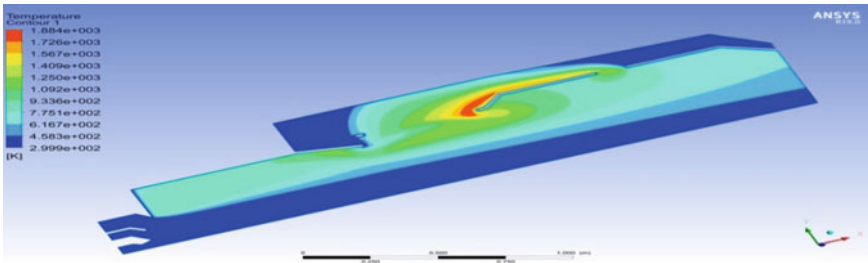


Fig. 5 Thermal variations of full CH₄ fuel

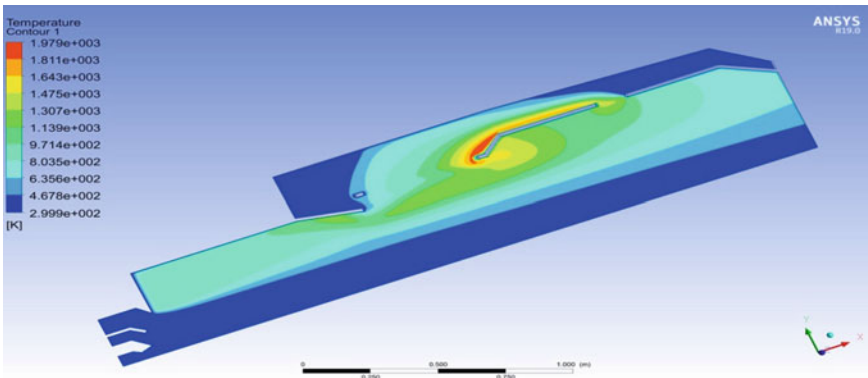


Fig. 6 Thermal variations of full ethanol fuel

analysis is expanded to a combination of the best two fuels, which are Jet-A and Ethanol. The complete discussions are explained in the upcoming sections.

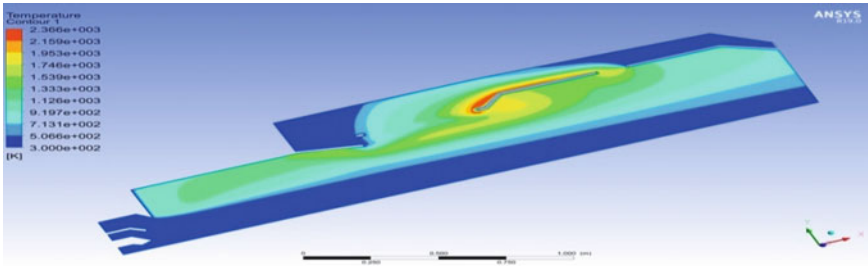


Fig. 7 Thermal variations of full C₂H₂-acetylene

4.2 Numerical Results of Jet a + Ethanol

The numerical simulations have been carried out with the full support of above-mentioned boundary conditions and thereby the targeted outputs of thermal distributions are computed by using CFD tool, i.e., ANSYS Fluent 16.2. The various results are revealed in Figs. 8, 9, 10, 11, 12, 13, 14, 15, 16, 17, 18 and 19, and the comprehensive data are shown in Fig. 20.

From Fig. 16, it has been clearly understood that the addition of Ethanol in the Jet-A fuel is drastically increasing the thermal performance of the can combustor. In which, the range of 60–90% of Ethanol has increased the thermal performance in an acceptable manner. Apart from that, 100% Ethanol based combustion is performed better than Jet-A fuel.

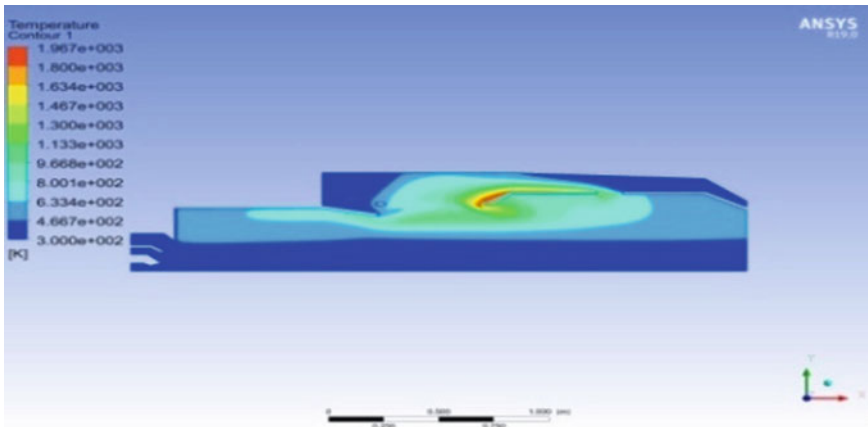


Fig. 8 Thermal variation of jet-A-85-ethanol-15

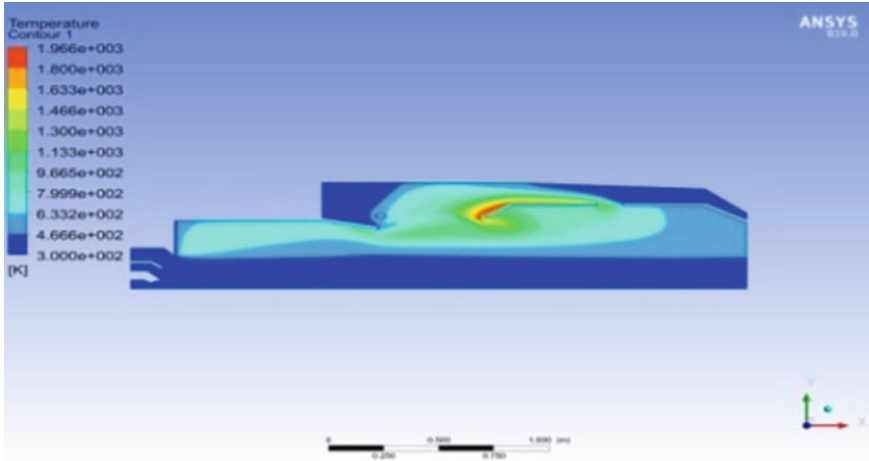


Fig. 9 Thermal variation of jet-A-80-ethanol-20

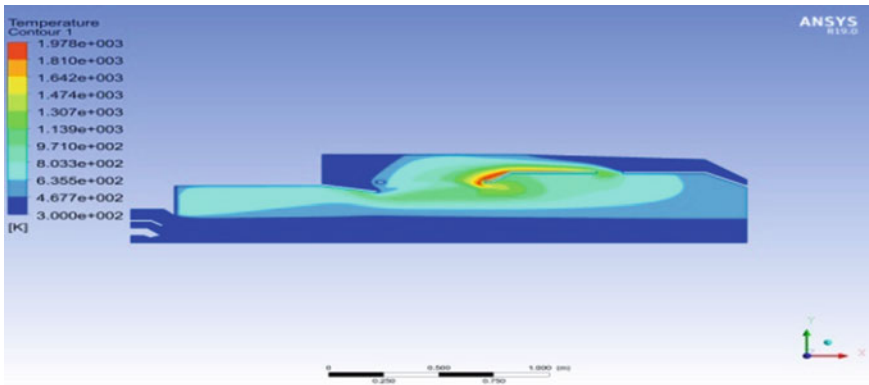


Fig. 10 Thermal variation of jet-A-70-ethanol-30

5 Conclusions

Numerical investigation on the performance of Can-type combustor using a mixture of Jet A and Ethanol as fuel was performed for the different combinations of Ethanol blend with Jet A fuel for 5–95% on a volume basis. The results show that the peak temperature inside the can combustion keeps on increasing from 5% of methanol to 85%. This result in peak temperature directly reflects on the enthalpy of combustion. From the above results, it has been concluded that the combination of 15% of Jet-A with 85% Ethanol has generated a peak temperature of 2000 K. It is also observed that there will be a drop in peak temperature while increasing the blend percentage from 90 to 95. From the above analysis result, it has been concluded that the performance

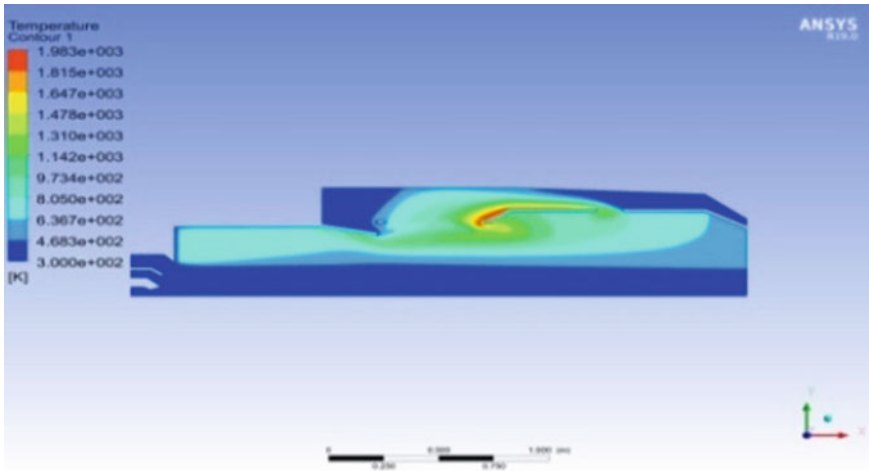


Fig. 11 Thermal variation of jet-A-75-ethanol-25

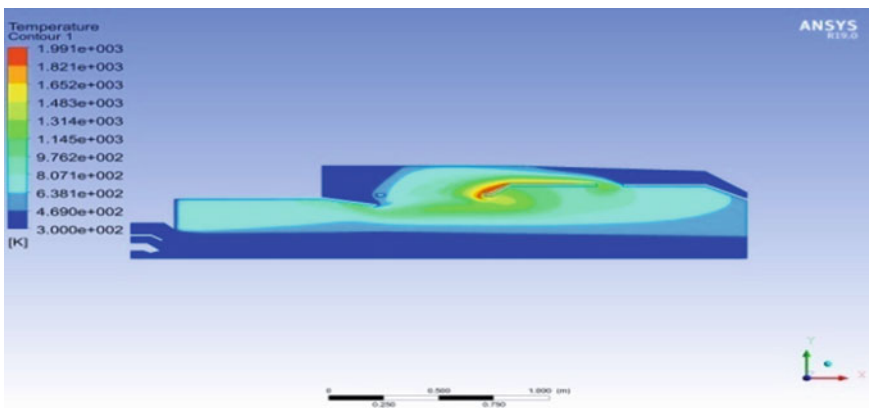


Fig. 12 Thermal variation of jet-A-45-ethanol-55

of the can combustor has been improved while using Ethanol and blend with Jet-A fuel to a certain percentage without any modification in the combustion chamber. It has been already proved that Ethanol is a clean fuel that produces no pollution in our environment.

Automotive vehicles using a blend of gasoline and Ethanol are releasing fewer emissions than they run only on gasoline, which means Ethanol will improve fossil fuels like gasoline by making them more potent and less harmful for the environment. The energy released while burning Ethanol is green and is not black like the energy produced by gasoline and diesel fuel. Mixing Ethanol with gasoline will generally improve the fuel by making it more powerful and less harmful to the environment.

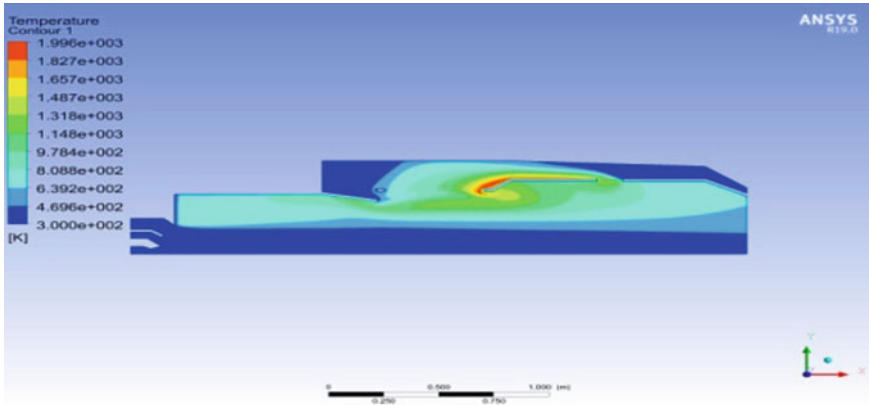


Fig. 13 Thermal variation of jet-A-35-ethanol-65

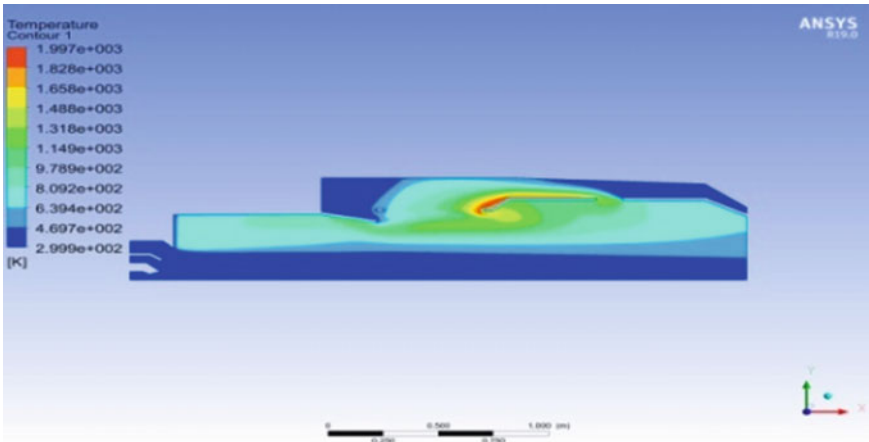


Fig. 14 Thermal variation of jet-A-30-ethanol-70

Mostly Ethanol will produce complete combustion inside the engine and will produce high heat energy, CO_2 , and water. Burning gasoline and diesel fuel will always release carbon dioxide (CO_2), and also carbon monoxide (CO), nitrogen oxides (NO_x), sulfur dioxide (SO_2), which means are way more harmful to the environment. A fuel that contains a mix of Ethanol and gasoline will ignite faster than gasoline, which will put less strain on the engine, and also it will reduce fuel consumption. Also in other aspects like the price of Ethanol will be low when compared with Jet-A fuel, so that we can suggest in the future we can use Ethanol as a complete alternative fuel for Jet-A fuel with a small modification in the combustor.

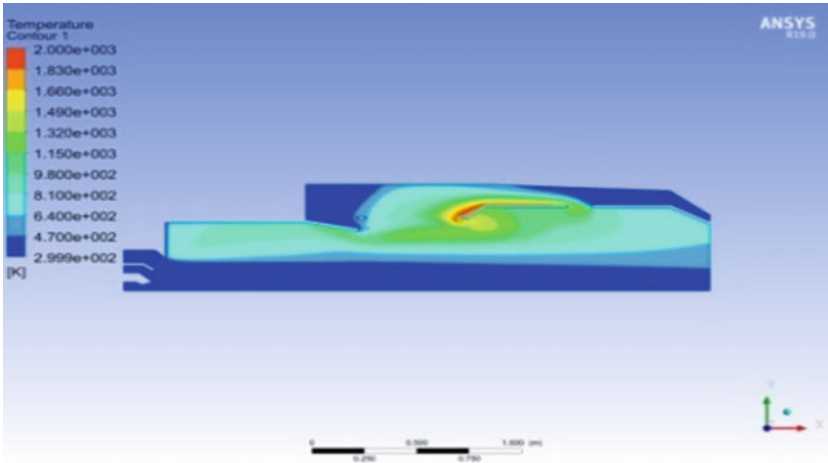


Fig. 15 Thermal variation of jet-A-25-ethanol-75

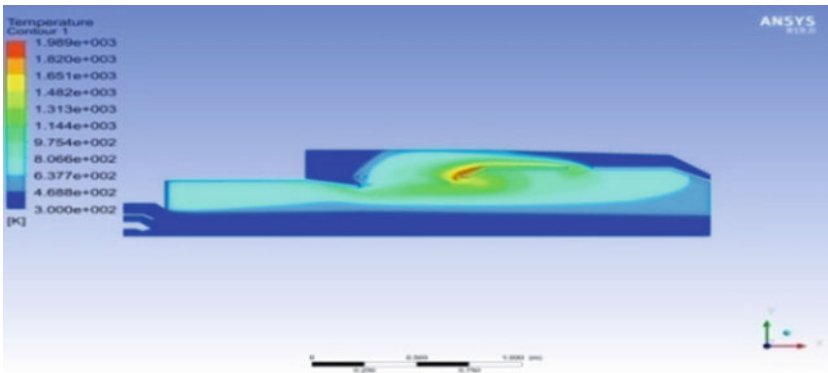


Fig. 16 Thermal variation of jet-A-20-ethanol-80

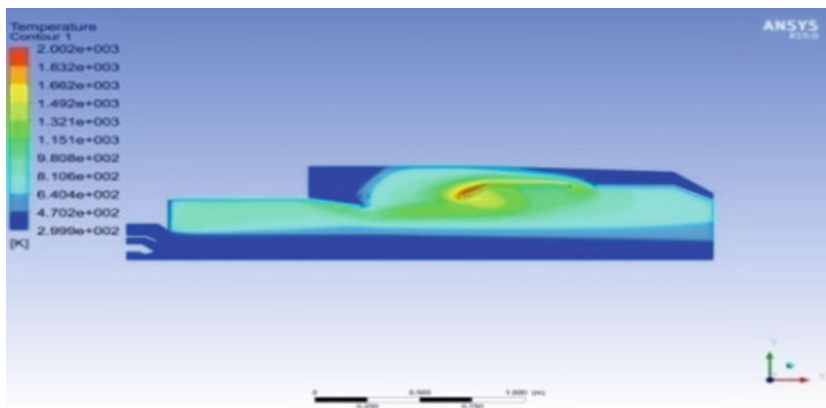


Fig. 17 Thermal variation of jet-A-15-ethanol-85

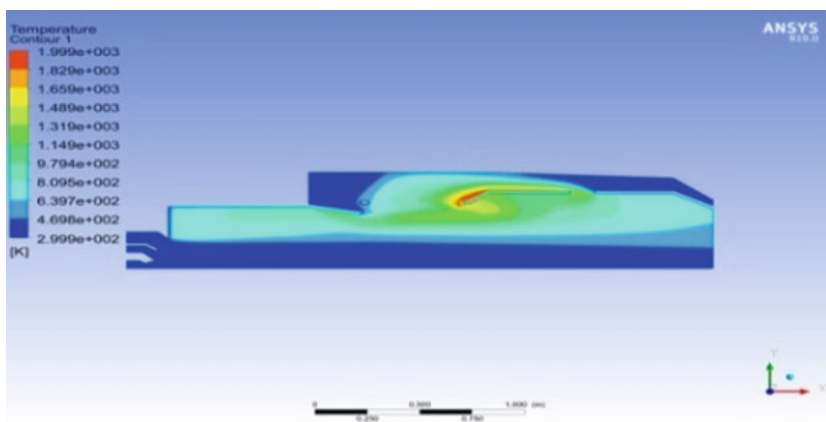


Fig. 18 Thermal variation of jet-A-10-ethanol-90

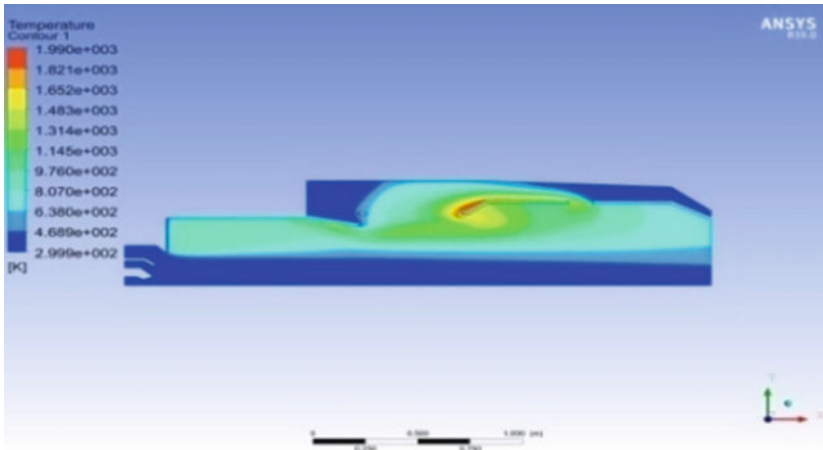


Fig. 19 Thermal variation of jet-A-05-ethanol-95

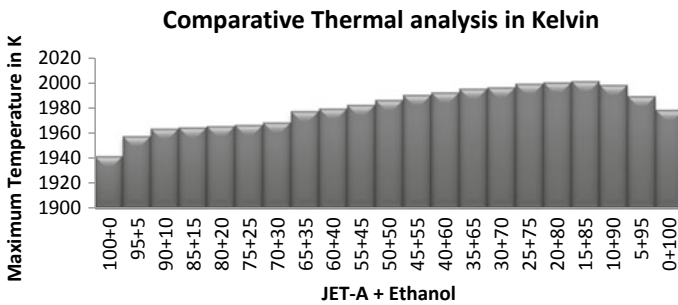


Fig. 20 Comparative thermal analysis on can combustor

References

1. R. Vijayanandh et al., Energy harvesting from a gas turbine engines exhaust heat using quantum well thermoelectric materials generator (QWTEG). *Mater. Today: Proc.* **4**(8), 8378–8386 (2017). <https://doi.org/10.1016/j.matpr.2017.07.181>
2. K. Naveenkumar, R. Vijayanandh, M. Ramesh, Design optimization of nozzle and second throat diffuser system for high altitude test using CFD. *J. Phys.: Conf. Ser.* **1355**, 012012 (2019)
3. B. Sonaimuthu, P. Panchalingam, V. Raja, Comparative analysis of propulsive system in multi-rotor unmanned aerial vehicle, in *Proceedings of the ASME 2019 Gas Turbine India Conference—GTINDIA2019*, vol. 2 (Chennai, Tamil Nadu, India, 2019) <https://doi.org/10.1115/GTIINDIA2019-2429>
4. R. Vijayanandh, K. Venkatesan, M. Senthil Kumar, G. Raj Kumar, P. Jagadeeshwaran, R. Raj Kumar, Comparative fatigue life estimations of Marine propeller by using FSI. *IOP—J. Phys.: Conf. Ser.* **1473**(012018), 1–8 (2020). <https://doi.org/10.1088/1742-6596/1473/1/012018>
5. R. Arul Prakash et al., Experimental investigation of diesel engine for various compression ratios' using calophyllum as a blend with diesel. *Nano Hybrids Compos.* **17**, 256–262 (2017) ISSN 2297–3370. <https://doi.org/10.4028/www.scientific.net/NHC.17.256>

6. R. Vijayanandh et al., Theoretical and numerical analyses on propulsive efficiency of unmanned aquatic vehicle's propeller. *IOP J. Phys.: Conf. Ser.* **1504**(012004), 1–10 (2020). <https://doi.org/10.1088/1742-6596/1504/1/012004>
7. R. Arul Prakash, S. Harish, R. Vijayanandh, M. Senthil Kumar, Performance and emission characteristics investigation of oxygen enrichment in diesel engines. *Int. J. Veh. Struct. Syst.* **10**(1) (2018) ISSN 0975–3540. <https://doi.org/10.4273/ijvss.10.1.08>
8. R. Arul Prakash, S. Harish, M. Senthil Kumar, R. Vijayanandh, K. Sundararaj, G. Raj Kumar, Experimental investigation of oxygen enrichment in a supercharged diesel engine. *Ecol. Environ. Conserv.* **24**(2018), 5–9 (2018) ISSN 0971–765X
9. C. Ghenai, Combustion of syngas fuel in gas turbine can combustor. *Adv. Mech. Eng.* Article ID 342357, 13 (2010) . <https://doi.org/10.1155/2010/342357>
10. K. Naveenkumar, R. Vijayanandh, G. Prasad, R. Naveen Kumar, The design and fatigue analysis of gas turbine annular combustor flame tube. *Int. J. Mech. Prod. Eng. Res. Dev.* **8**(7), 313–329 (2018) ISSN: 2249–6890
11. R. Murugesan, V. Raja, Acoustic investigation on unmanned aerial vehicles rotor using CFD-MRF approach, in *Proceedings of the ASME 2019, Gas Turbine India Conference—GTINDIA 2019*, vol. 2 (Chennai, Tamil Nadu, India, 2019), p. 7 GTINDIA 2019–2430, ISBN: 978–0–7918–8353–2, V002T08A005. <https://doi.org/10.1115/GTINDIA2019-2430>
12. E. Indhumathi, S. Pradesh, R. Vijayanandh, M. Senthil Kumar, R. Naveen Kumar, G. Raj Kumar, Comparative computational thermal analysis of gas turbine engine turbine-blade coated with and without lanthanum Zirconate. *Int. J. Mech. Prod. Eng. Res. Dev.* **8**(7), 1079–1088 (2018) ISSN(E): 2249–8001
13. M. Senthil Kumar, R. Vijayanandh, R. Srinivas, D. Arun Karthik, M. Tamil Mani, Acoustic analysis and comparison of chevron nozzle using numerical simulation *Int. J. Mech. Prod. Eng. Res. Dev.* **8**(7), 1089–1103 (2018)
14. R. Arul Prakash, R. Sarath Kumar, R. Vijayanandh, D.V. Praveen, K. Raja Sekar, C. Ananda Krishnan, Design optimization of convergent—divergent nozzle using computational fluid dynamics approach. *Int. J. Mech. Prod. Eng. Res. Dev.* **9**(1), 220–232 (2019) ISSN(E): 2249–8001
15. F.H. Pathan, N.K. Patel, M.V. Tadv, Numerical investigation of the combustion of methane air mixture in gas turbine can-type combustion chamber. *Int. J. Sci. Eng. Res.* **3**(3), 1–7 (2012) ISSN 2229–5518
16. N.L. Pradhani et al., CFD analysis on can-type combustor and variation of air injection angle under typical engine condition. *J. Aeronaut. Aerosp. Eng.* **5**(2), 1–5 (2016). <https://doi.org/10.4172/2168-9792.1000170>
17. G.B. More, S.K. Bhele, Numerical simulation of tubular combustion chamber using kerosene-methanol blend. *Int. J. Sci. Eng. Res.* **8**(4), 25–30 (2017) ISSN 2229–5518

Modal Analysis of Special Type of Flexure Bearing for Space Application



Suraj Bhojar, Virendra Bhojwani, Ganesh Khutwad, Gaurav Sawant, Jay Lad, and Stephen Sebastian

Abstract Flexure bearing is a significant component used in cryocoolers for space application. The cryocooler compressors are mainly used in a space application and require infinite fatigue life. The flexure resists the rubbing of the piston in the radial direction and gives acts as a spring in the direction of piston motion. This paper represents the modal analysis of flexure bearing with the dedicated fatigue life test setup designed to validate the life of bearing. The developed flexure bearing has completed the 10^8 cycles without failure. Infinite life of the flexure spring is one requirement, and other requirement is resonance operation, which ensures low power requirement. At resonance compressor requires minimum power input, as the increased vibration of the piston in axial direction leads to compression.

Keywords Flexure bearing · Cryocooler compressor · Modal analysis · Infinite fatigue life · SN curve

1 Introduction

1.1 Modal Analysis

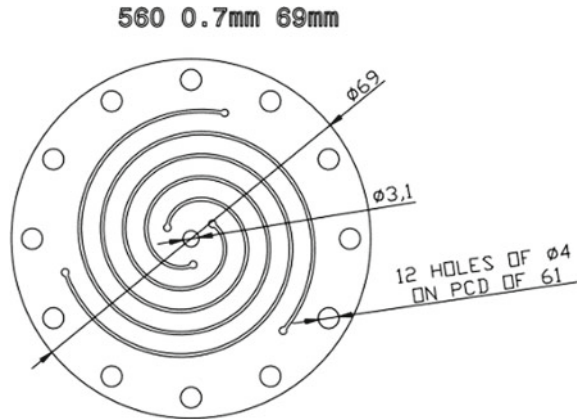
In order to discern the complex features of the engineering structure, modal analysis estimates the natural frequency of the moving object. In case of the linear compressor in cryocoolers, it predicts and helps in fine tuning of the natural frequency which should match with the prescribed operating frequency. With wide amplitude of their plangency frequency, the structure has to vibrate [1–7]. The modal analysis has been derived from the two methods:

- (1) Theoretical modal analysis is based on the description of the physical characteristics of a system in order to determine the modal model taking into account mass, damping of stiffness.

S. Bhojar (✉) · V. Bhojwani · G. Khutwad · G. Sawant · J. Lad · S. Sebastian
Department of Mechanical Engineering, MIT-ADT University, Pune 412201, India
e-mail: Suraj.bhojar@mituniversity.edu.in

© The Author(s), under exclusive license to Springer Nature Singapore Pte Ltd. 2022
M. L. Kolhe et al. (eds.), *Smart Technologies for Energy, Environment and Sustainable Development, Vol 1*, Springer Proceedings in Energy,
https://doi.org/10.1007/978-981-16-6875-3_63

Fig. 1 Flexure bearing geometrical configuration



Natural frequency formula

$$f_n = \frac{1}{2\pi} \sqrt{\frac{K_e}{m_e}}$$

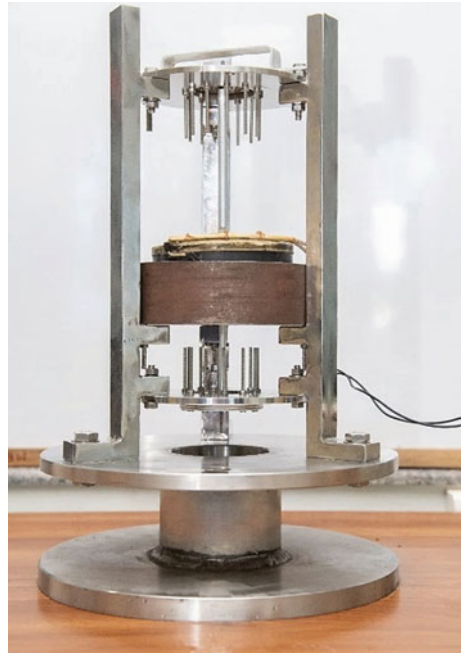
- (2) The modal model from calculated FRF (Frequency Response Function) is derived from experimental modal analysis based on the fact that the vibration response of a linear time-invariant dynamic system can be improved. The natural modes of vibration, as their linear combination, are called as series of simple harmonic motion. The analysis is carried out with the FEA package; to evaluate dynamic behavior of any structure because of certain structural properties such as damping and non-linearity. The flexure bearing used in the fatigue life test setup [8] shown in Fig. 1 is an eccentric type of flexure bearing. There are three types of the flexure bearing: (a) concentric (b) eccentric (c) triangular. The flexure bearing used for current analysis is having a diameter of 69 mm, spiral angle of 560° stacks with help of aluminum spacer as shown in Fig. 1.

The following setup was developed first to check the fatigue life of the developed flexure spring to complete 10^8 cycles. The optimized fatigue life configuration was further analyzed for modal analysis. Figure 2 shows fatigue life test setup for flexure springs.

2 Methodology

The present study follows the methodology of the modal analysis of flexure bearing buy using the FEA. In which, the process divided into four important steps:

Fig. 2 Actual fatigue life setup at vibrations lab



The modal analysis of flexure bearing is to estimate different modes of natural frequency. This process uses simple hammer test using FFT for getting fixed response.

2.1 Pre-processing

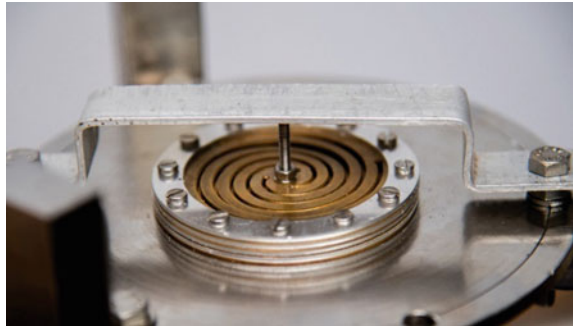
Modal analysis was carried out by the finite element analysis approach for the flexure bearing. Pre-processing for linear flexure under investigation is an integral step in the present study. Table 1 represents the preprocessor data used as input to the analysis,

2.2 Design Considerations

The design of flexure bearing was carried out by examining the criteria of infinite fatigue life, as the effect of the flexure bearing thickness on structure distribution hence of natural integrity. The fatigue life test is used to test the infinite life of

Table 1 The preprocessor data inputs

Sl. No.	Parameters	Value/type
1	Element type	Spiral
2	Thickness	0.3, 0.7, 1 mm
3	Material	Beryllium copper
4	Young's modulus MPa	130×10^3
5	Poisson's ratio	0.3
6	Density	8.25 g/cm ³

Fig. 3 Flexure assembly with stacking spaced by aluminum spacers

flexure bearing, in which the setup used to predict the number of the cycle can be subjected under the loading scheme. The setup having coil former, aluminum spacer, stainless still legs, base plate, mounting plate, magnet, shaft as shown in Fig. 3.

2.3 Boundary Conditions

The nodes on the outer periphery usefully constrained by placing fixed support. The nodes represent the point in which one thing joints another. All part of the test setup having fixed support except the flexure bearing, coil former, shaft [8] as shown in Fig. 2. The boundary conditions are imposed for flexures spiral angle 560°. The movements of flexure in the axial direction because of the inner nodes of the flexure are constrained.

The periphery of flexure spring having 12 holes which were fixed for all degrees of freedom and force was applied at the center of flexure spring.

For the analysis, there are three types of geometry are observed with thicknesses viz.0.3, 0.7, 1 mm as shown in Fig. 4.

Table 2 shows the part list that the fatigue life test setup was assigned for the modal analysis.

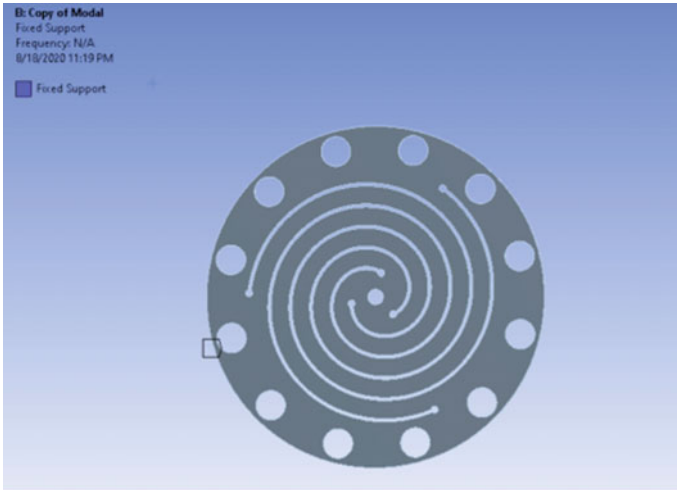


Fig. 4. 2-D CAD model of flexure

Table 2 Part list of the FL setup

Particulars	Material
Leg	SS304
Dead weight	SS304
Base plate	SS304
Mounting plate	SS304
Flexure mounting plate	SS304
Pole piece	Soft iron
Casing	SS304
Shafts	SS304
Spacer	Aluminum

2.4 Finite Element Analysis

The calculation of the natural frequency for axial loading condition was carried out using the solver in FEA package [9, 10]. Figure 5 shows the results in terms of natural frequency estimated and taken from FEA package generated for 0.3 mm flexure thickness and different number of springs stacked (Table 3).

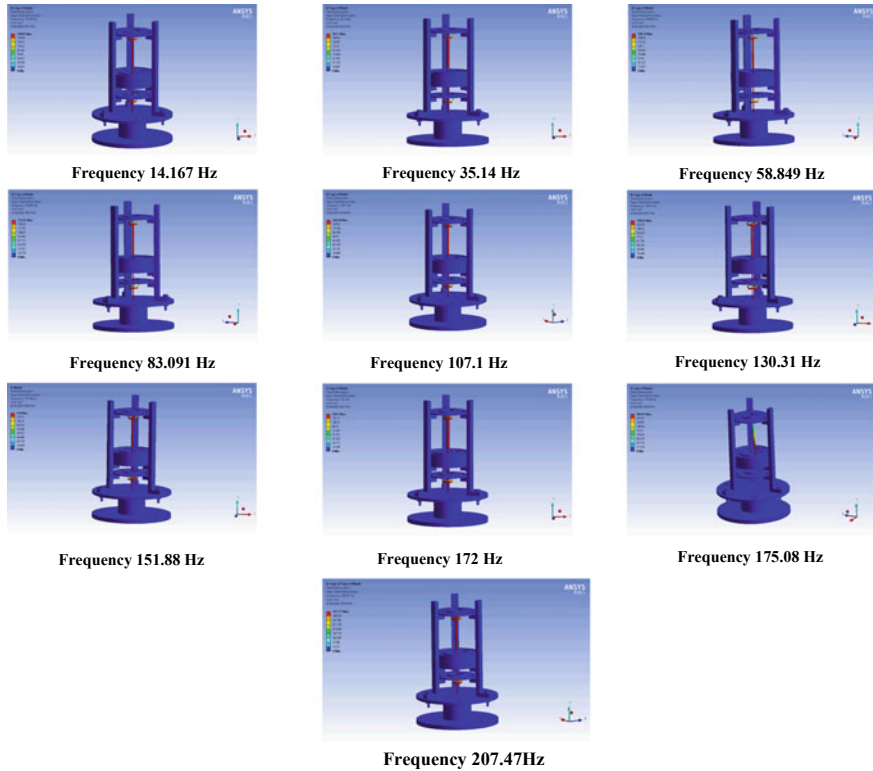


Fig. 5 Results in terms of natural frequency estimated and taken from FEA package generated for 0.3 mm flexure thickness and different number of springs stacked

Table 3 Results for 0.3 mm thick flexure bearing

No. of flexures	Frequency (Hz)	No. of flexures	Frequency (Hz)
1	14.16	6	130.1
2	35.14	7	151.88
3	58.84	8	172
4	83.09	9	175.08
5	107.1	10	207.47

2.4.1 Experimentation with Flexure Bearing of 0.3 mm Thickness

2.4.2 Result Table and Graph for 0.3 mm

For 0.3 mm thick flexure bearing, the result shows that the natural frequency is increasing with number of flexures stacked. The maximum frequency obtained for 20 no. of flexure is 207.4 Hz (Fig. 6).

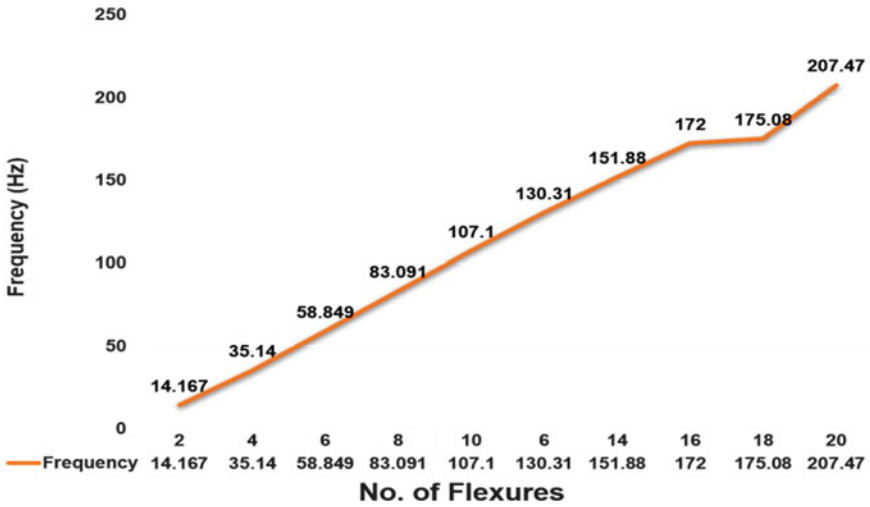


Fig. 6 Graph showing results for 0.3 mm thick flexure bearing

2.4.3 Experimentation with Flexure Bearing of 0.7 mm Thickness

Figure 7 shows variation of natural frequency for 0.7 mm thick flexure for different number of flexures stacked together (Table 4).

2.4.4 Result Table and Graph for 0.7 mm

From the table and graph of 0.7 mm thickness, and after comparing the different values of natural frequency versus number of flexures stacked; it was observed that the maximum frequency obtained for 20 flexures is 320.7 Hz (Fig. 8).

2.4.5 Experimentation with Flexure Bearing of 1 mm Thickness

Figure 9 and Table 5 show variation of natural frequency for 1 mm thick flexure for different number of flexures stacked together.

2.4.6 Result Table and Graph for 1 mm

From the table and graph of 1 mm thickness flexure, it is clear that due to damping characteristic of spring, frequency increases up to 345.7 Hz for 20 no. of flexure in the system (Fig. 10).

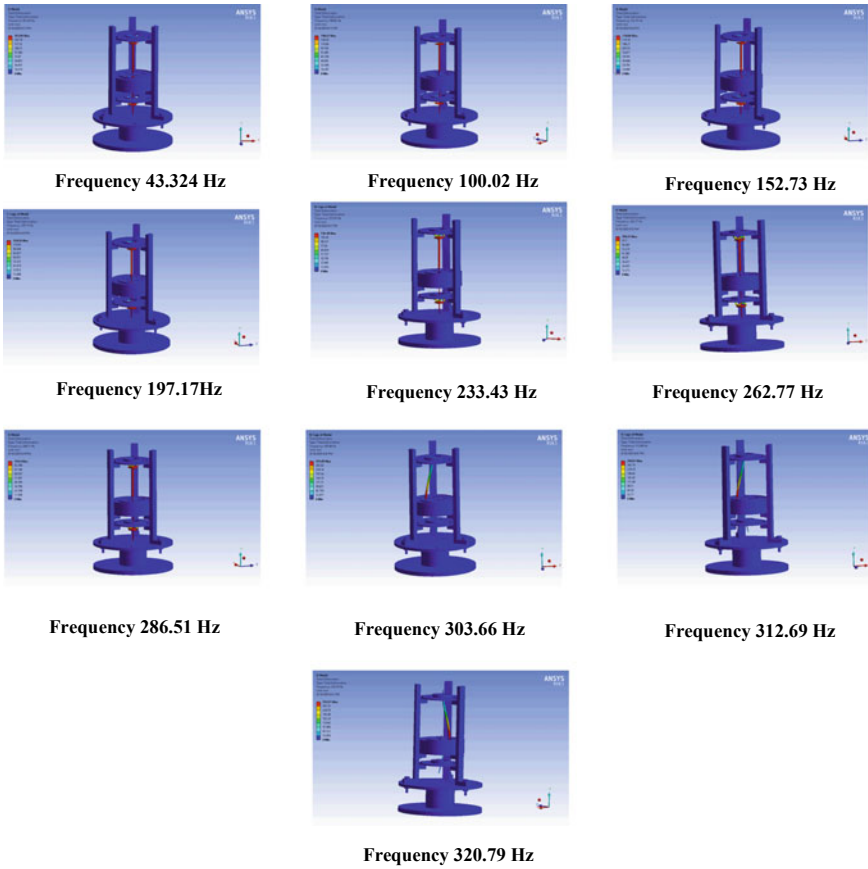


Fig. 7 Variation of natural frequency for 0.7 mm thick flexure for different number of flexures stacked together

Table 4 Results for 0.7 mm thick flexure bearing

No. of flexures	Frequency (Hz)	No. of flexures	Frequency (Hz)
1	43.324	6	262.77
2	100.02	7	286.51
3	152.73	8	303.66
4	197.17	9	312.69
5	233.43	10	320.79

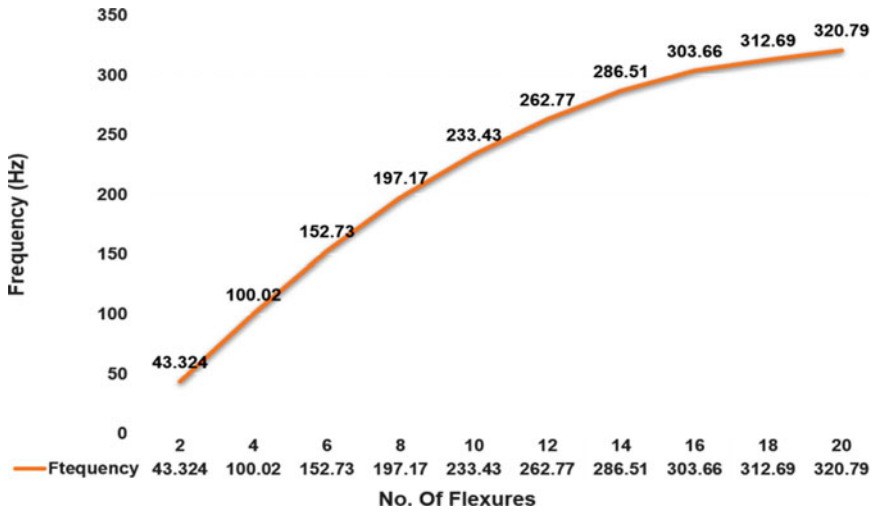


Fig. 8 Graph for 0.7 mm thick flexure bearing

3 Conclusion

This research work highlighted parametric study and modal analysis of flexure bearing designed especially for the space application in which the different thickness parameter of flexure was observed and compared with each other to fulfill the design criteria of high fatigue life and maximum stiffness. From this, the natural frequency was calculated by finite element analysis approach and it was plotted on a graph to observe that when the frequency increases the deformation also increases with an increase in stiffness but it will be for a certain limit and it will go on decreasing.

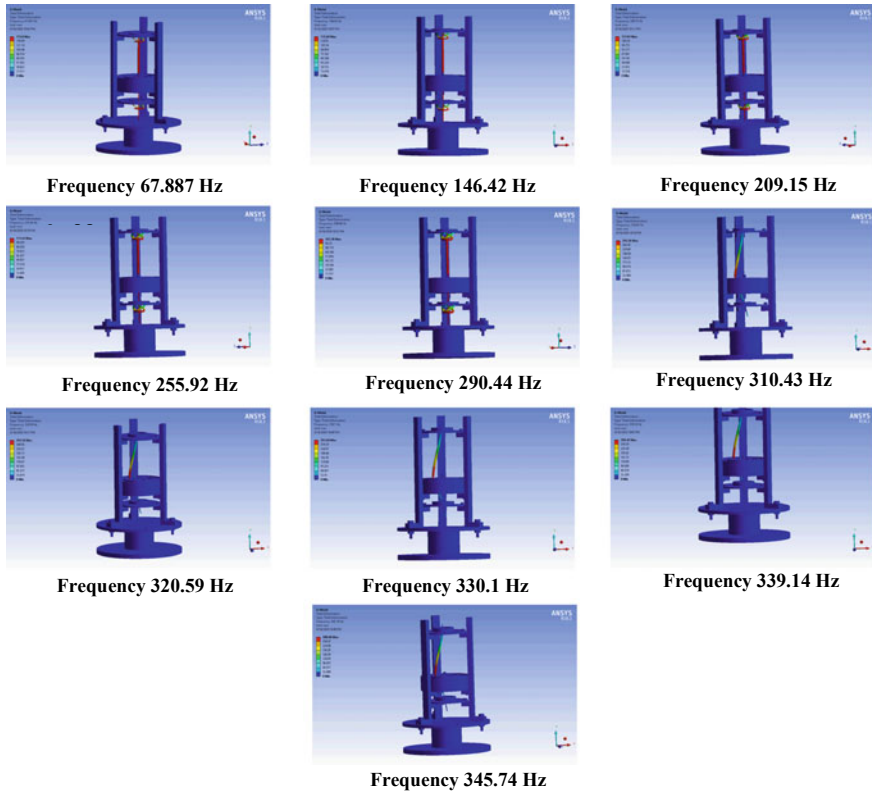


Fig. 9 Variation of natural frequency for 1 mm thick flexure for different number of flexures stacked together

Table 5 Results for 1 mm thick flexure bearing

No. of flexures	Frequency (Hz)	No. of flexures	Frequency (Hz)
1	67.88	6	310.43
2	146.42	7	320.59
3	209.15	8	330.1
4	255.92	9	339.14
5	290.44	10	345.74

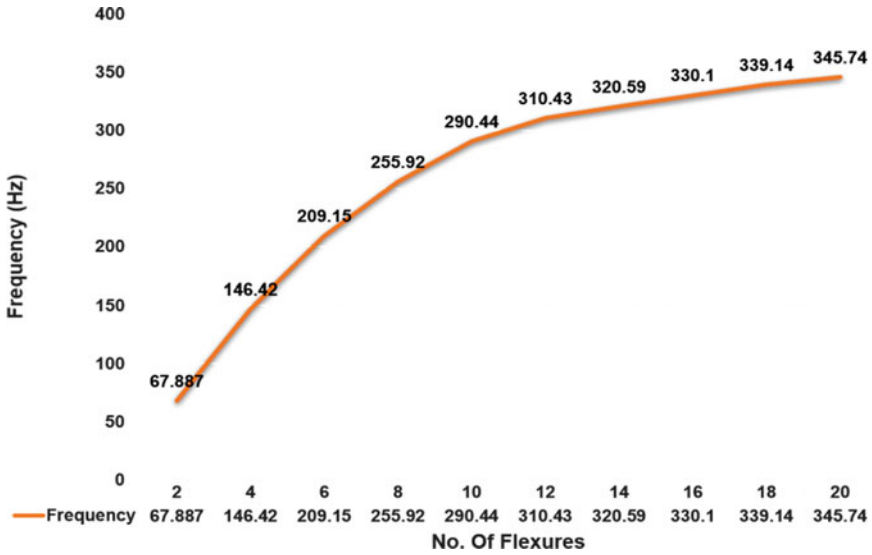


Fig. 10 Graph for 1 mm thick flexure bearing

References

1. A. Jomde, A. Anderson, V. Bhojwani, F. Kharadi, S. Deshmukh, Parametric analysis of flexure bearing for linear compressor. *Mater. Today: Proc.* **4**, 2478–2486 (2017)
2. P.S. Rao, R. Venkatesh, Modal and harmonic analysis of leaf spring using composite materials. *Int. J. Novel Res. Electr. Mech. Eng.* **2**, 67–75 (2015)
3. Z.S. Al-Otaibi, A.G. Jack, Spiral flexure springs in single-phase linear-resonant motors, in *Proceeding of 42nd International Universities Power Engineering Conference (UPEC2007)*, pp. 184–187 (2007)
4. T.E. Wong, R.B. Pan, A.L. Johnson, Novel linear flexure bearing, in *Proceeding 7th International CryoConference*, pp. 675–698 (1992)
5. T.E. Wong, R.B. Pan, H.D. Marten, C. Sve, L. Galvan, T.S. Wall, Spiral flexural bearing, in *Proceeding 8th CryoConference*, pp. 305–311 (1995)
6. I. Rajendran, S. Vijayarangan, Static and modal analysis of a leaf spring assembly using contact nonlinear 3D finite element approach (Society of Automotive Engineers, 2001), 28-0051
7. H. Jimin, F. Zhi-Fang, *Modal Analysis*, 1st edn. (Butterworth-Heinemann, Oxford, 2001)
8. S. Bhoyar, V. Bhojwani, S. Sanap, Parametric design and comparative analysis of a special purpose flexure spring. *E3S Web Conf.* **170**, 02013 (2020). <https://doi.org/10.1051/e3sconf/202017002013>
9. C.J. Simcock, Investigation of materials for long life, high reliability flexure bearing spring for Stirling cryocooler applications, in *Cryocoolers*, vol. 14, pp. 335–343 (2007)
10. A.S. Gaunekar, T. Goddenhenrich, C. Heiden, Finite element analysis and testing of flexure bearing elements, in *Cryogenics*, vol. 36, pp. 359–364 (1996)

Numerical Simulation of a Finned-Surface Prismatic Lithium-Ion Battery Thermal Management System



Pranjali Tete , Puneet Kedar , Mahendra Gupta , and Sandeep Joshi 

Abstract In today's world, transportation has become a major problem for environmental pollution as a greater amount of CO₂ has been released from conventional internal engine vehicles. An electric vehicle (EV) is the best alternative to conventional vehicles to reduce emissions and keep the environment green. Lithium-ion batteries owing to its advantages of high energy and power density are the most suitable cells for electric and hybrid electric vehicles (HEVs). Still, the performance of EVs suffered from low efficiency due to the internal heat generation of batteries. The performance of Li-ion batteries is highly sensitive to temperature; hence, a battery thermal management system (BTMS) is essential for battery packs of EVs and HEVs. In this article, a numerical study has been conducted on a single prismatic lithium-ion battery cell. Fins are mounted on the surface of the battery which helps to reduce the maximum temperature rise of the cell by increasing the heat transfer area. The location and positioning of fins on the battery surface define the novelty of the current work, and the simulation results showed that there is a large temperature drop of 13.278 °C with the proposed design of BTMS compared to the natural convection cooling.

Keywords Thermal management systems · Battery cooling techniques · Electric vehicles · Li-ion batteries

1 Introduction

Electric vehicles and hybrid electric vehicles are the best replacements for conventional internal combustion engines reducing emissions of highly toxic greenhouse gases. Lithium-ion batteries are the powerhouse of energy sources supplied to drive EVs and HEVs. The performance, life, and safety of Li-ion batteries (LIBs) are dependent on temperature, and a great amount of heat is generated inside the batteries as the temperature rises [1]. The internal heat generation occurs due to ohmic heating,

P. Tete (✉) · P. Kedar · M. Gupta · S. Joshi
Department of Mechanical Engineering, Shri Ramdeobaba College of Engineering and Management, Nagpur 440013, India

© The Author(s), under exclusive license to Springer Nature Singapore Pte Ltd. 2022
M. L. Kolhe et al. (eds.), *Smart Technologies for Energy, Environment and Sustainable Development, Vol 1*, Springer Proceedings in Energy,
https://doi.org/10.1007/978-981-16-6875-3_64

Joule heating, and entropy heating [1–4] leading to the inevitable rise in temperature of the battery cell or an entire battery pack which happens at the high current rate and fast charge–discharge rate. Chemical reactions and materials used in the batteries are also contributors to the temperature effects of the batteries which lead to power loss and capacity fading [5]. Therefore, a battery thermal management system is an effective solution to get an efficient cooling of batteries and packs. The desired temperature range for LIBs is 15–35 °C [6] or 20–40 °C [7–9], and the maximum temperature difference between two adjacent cells and modules should be less than 5 °C [8, 9]. It is a critical task to develop an efficient battery thermal management system to maintain the battery temperature within a specified range to prevent the degradation of batteries and its performance.

Considerable research studies have been found in the literature to develop an advanced BTMS such as air cooling [10–17], liquid cooling [18–21], phase change material (PCM) cooling [22–26], and hybrid cooling systems [27–30].

The conventional cooling techniques such as air cooling and liquid cooling are the most used commercial techniques of battery thermal management having their advantages and disadvantages. PCM cooling is the passive cooling technique, and a lot of studies are conducted on it recently and are still in progress. Hybrid or integrated thermal management systems are the combinations of active and passive cooling systems or more than one cooling system.

2 Modeling and Simulation

In the present simulation, a prismatic lithium-ion battery of dimension 173 mm by 168 mm by 39 mm (height × width × depth) of 55 Ah is used [31]. An aluminum sheet is attached to both the surfaces of the battery cell with several fins mounted on it. The fins are arranged in a staggered arrangement on both sides to avoid the fins collision if attached in a battery pack. The diameter of the fin is 10 mm, and it has length of 10 mm extruded in Z-direction. The vertical and horizontal distance between the two fins is 50 mm and 30 mm, respectively. Two copper tabs of dimension 20 mm diameter are attached on the top surface as anode and cathode to make the connections in series and parallel. The battery specifications and thermo-physical properties of the materials used are given in Table 1. A complete analysis of the selected battery cell is carried out in ANSYS WORKBENCH 19.2 with FLUENT 19.0 as a solver.

A geometric model is developed in ANSYS WORKBENCH 19.2 with the assumption such as radiation effect is neglected and natural convections with a convective heat transfer coefficient of 5 W/m² K is considered at the finned-surfaces of the battery. And a computational fluid dynamics (CFD) simulation of the model is performed in FLUENT 19.2. New materials have been created for battery as cell materials, aluminum, and copper and are shown in Table 1.

Table 1 Battery specifications and material properties [31]

Property	Unit	Li-ion cell	Cell material	Aluminum	Copper	Air (fluid)
Dimension	mm	168 mm (x: width) by 39 mm (y: depth) by 173 mm (z: height)	–	–	–	–
Density	kg/m ³	1700	1700	2700	8978	1.225
Heat capacity	J/kg K	830	813	900	381	1006.43
Thermal conductivity	W/m K	34	34	238	387.6	0.0242
Nominal capacity	Ah	55	–	–	–	–

Two different simulations have been carried out in this study; one without fins and the other with fin cooling. The geometrical models are as shown in Figs. 1 and 2.

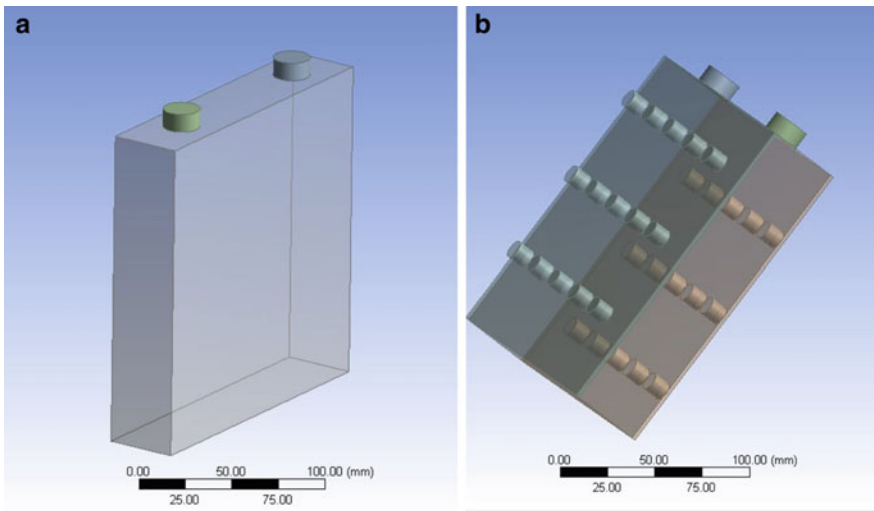


Fig. 1 Geometrical model of a prismatic Li-ion battery cell **a** without fins and **b** with fins

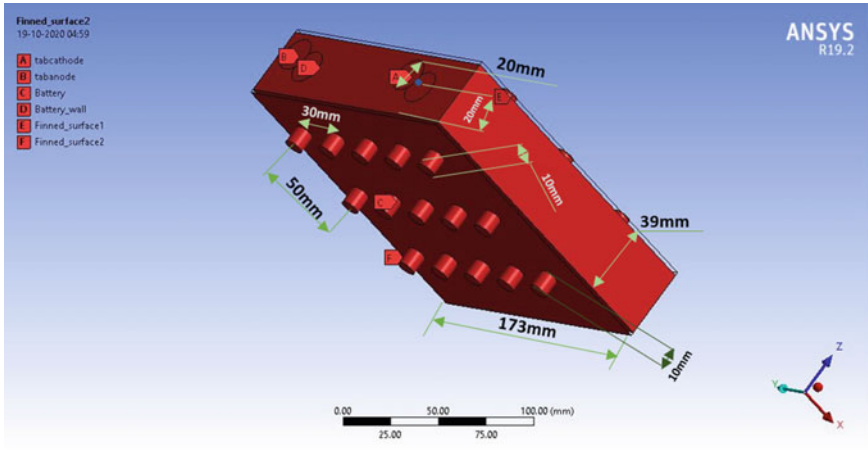


Fig. 2 Geometrical specifications of a finned-prismatic Li-ion battery

3 Mesh Independence Study

Mesh generation and the mesh statistics for the given study is as shown in Fig. 3 and Table 2, respectively. A program-controlled mechanical mesh has been generated for both the geometric models of without and with fin application.

The number of nodes and elements generated are as shown in Table 2.

Table 3 represents the boundary conditions and solver settings used in the present work for parametric studies.

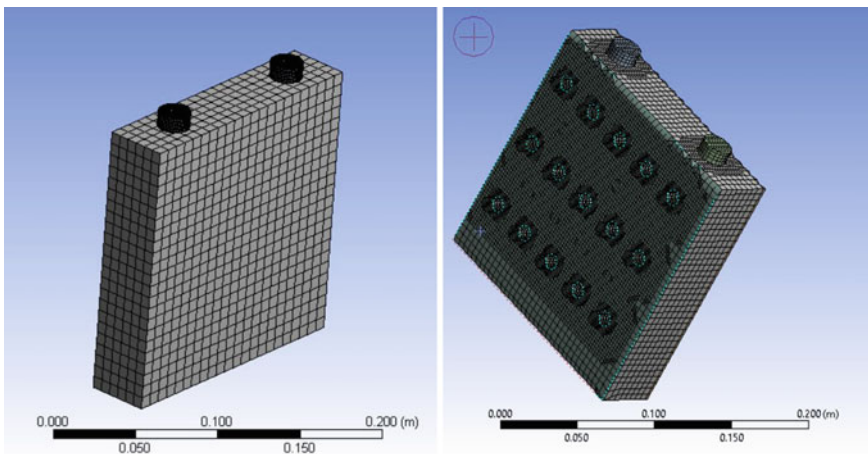


Fig. 3 Mesh generation a without fins and, b with fins

Table 2 Mesh statistics

Geometric model	Number of nodes	Number of elements
Without fins	56,458	12,287
With fins	132,337	96,315

Table 3 Boundary conditions

#	Parameter	Value
1	Viscous model	Laminar
2	Solver	Density based (relative) and transient state
3	Inlet temperature (K)	288.16
4	Convective heat transfer coefficient (W/m ² K)	5 (At the battery surfaces)
5	Source term for battery (discharge rate)	1C (Battery module is enabled)

4 Results and Discussions

To obtain the results of the proposed BTMS design, a battery module is enabled in the simulation setup in which the given battery is discharged at a 1 C rate providing the heat flux of 89.7 W/m² at the battery surface. The outer surface of the battery is exposed to natural convection with a convective heat transfer coefficient of 5 W/m² K. The initial temperature of the battery is considered as 300 K (25.85 °C) and the simulation has been run for 3600 s at 1 C rate. The simulation results indicate that the maximum temperature of the battery without fin cooling has been reached to 42.981 °C as shown in Fig. 4. On the contrary, with the applications of fins on the battery

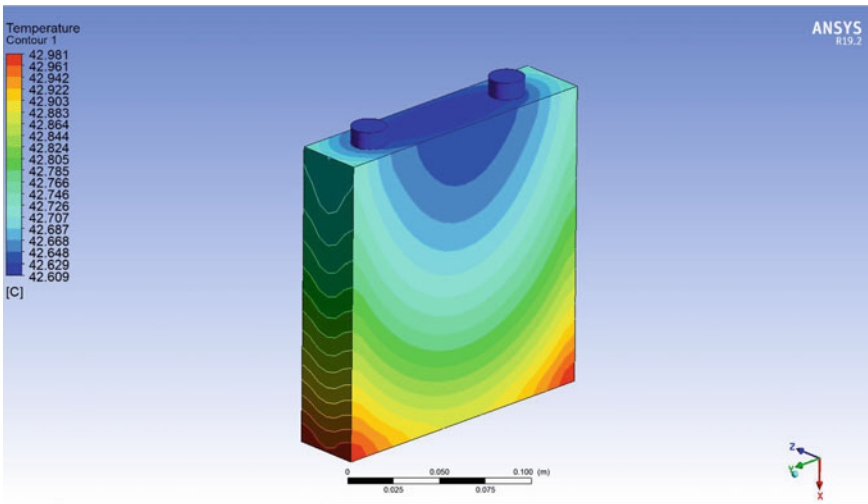


Fig. 4 Temperature contour of the battery cooling without fins

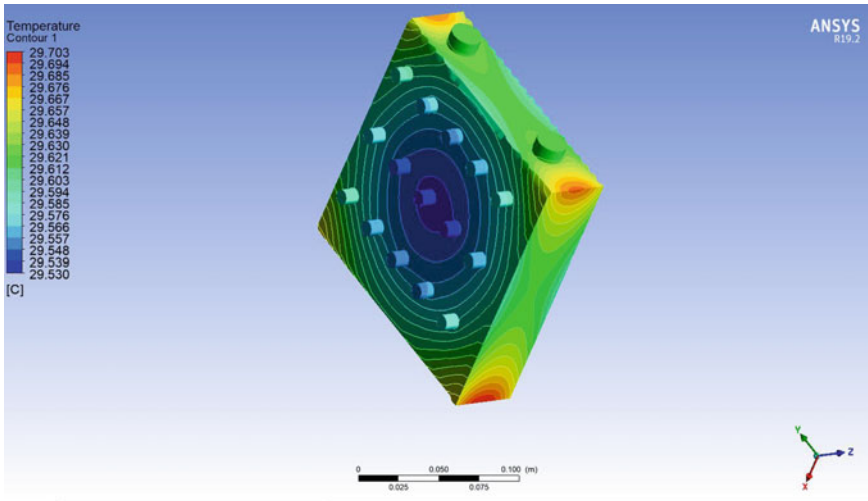


Fig. 5 Temperature contour of the battery cooling with fins

surface, the maximum temperature has been reduced to 29.703 °C. The temperature contour of the finned-battery cell is shown in Fig. 5, which indicates the temperature zones with different color contours. It is obvious from the results that the application of fins to the battery surface is an effective way to decrease the maximum temperature rise as the heat transfer area has been increased.

Further, the simulation is done in six steps of 600, 1200, 1800, 2400, 3000, and 3600 s for a better understanding of results and performance of the fins for cooling. The battery module is used for the inputs that are required for the battery operation. The battery is set for the constant 1 C discharge rate. At 600 s, the maximum temperature achieved in the battery is 27.637 °C and the minimum temperature is 27.473 °C. Again, the battery is operated at the same discharge for 1200 s, and it is found that the maximum temperature obtained is 28.202 and 28.036 °C as the minimum temperature. In both cases, temperature difference (higher limit–lower limit) is negligible so the uniformity of the battery at different surfaces is confirmed. Now, the battery is again discharged at a 1 C discharge rate for 1800s, 2400 s, 3000 s, and 3600 s and the maximum temperatures recorded are 28.679 °C, 29.080 °C, 29.418 °C, 29.703 °C, respectively, and the minimum temperatures recorded are 28.511 °C, 28.910 °C, 29.247 °C, 29.530 °C, respectively. The temperature uniformity is also confirmed through the above results. The temperature contours of the above-obtained results at different time-steps are as shown in Fig. 6.

All the temperature contours represent the thermal management of the single prismatic battery is effective while using fins at the battery surface. Figure 7 depicts the maximum temperature of a finned-battery thermal management system at different time-steps.

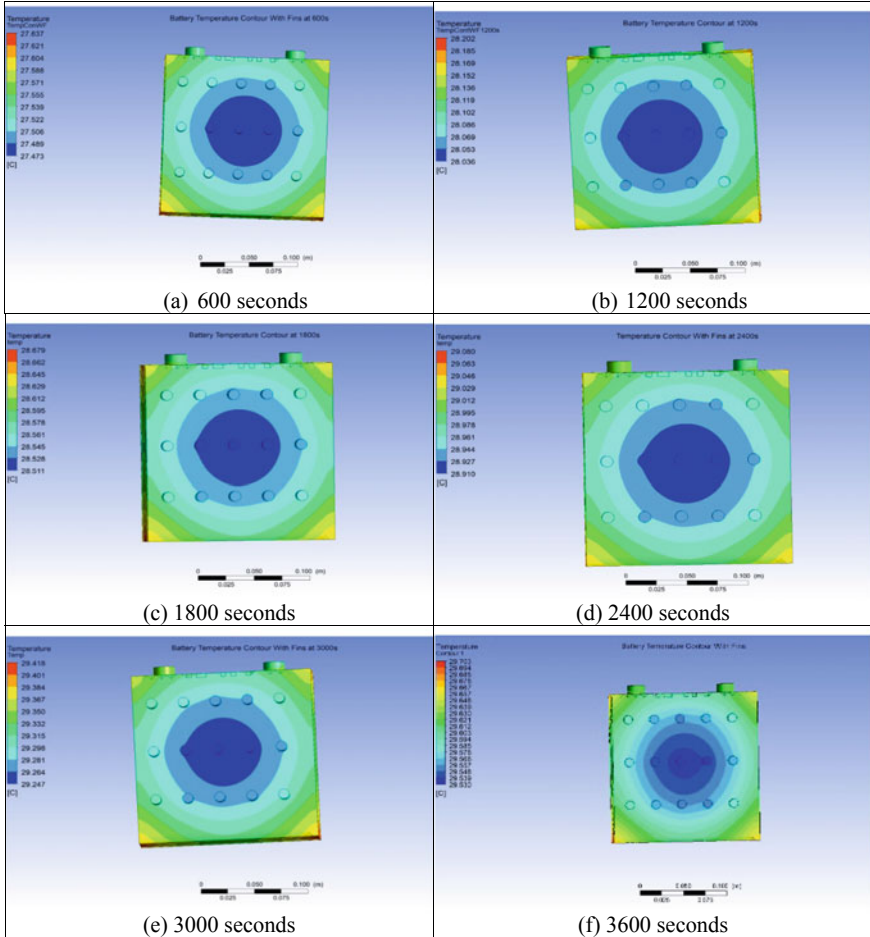


Fig. 6 Temperature contours at different time-steps of **a** 600 s **b** 1200 s **c** 1800 s **d** 2400 s **e** 3000 s and **f** 3600 s

5 Conclusion

Fins are the most inexpensive and feasible cooling solution for the thermal management of Li-ion batteries used in various applications especially in electric vehicles as large battery packs are stacked together in it. An effective cooling has been achieved by the applications of aluminum fins on both the surfaces of the prismatic battery. The maximum temperature obtained with and without fins is 29.703 °C and 42.981 °C, respectively, with a temperature drop of 13.278 °C at a discharge rate of 1 C. The maximum temperature difference of 0.173 °C is obtained in the fin-cooled battery cell which confirms the temperature uniformity inside the cell. The proposed BTMS can be numerically and experimentally investigated at different discharge rates of 2 C, 3

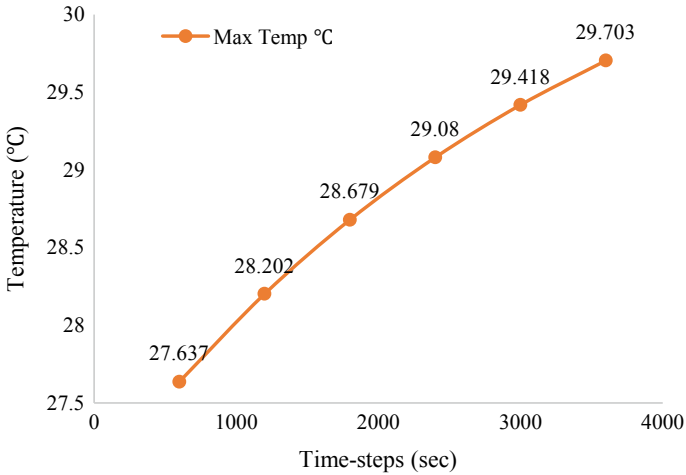


Fig. 7 Maximum temperature at different time-steps for finned-prismatic Li-ion battery

C, 4 C, and so on. Further investigations can be carried out for different fin materials and by varying the dimensions and arrangement of fins. This study provides a base for an efficient BTMS using fins for a single Li-ion battery cell; similarly, an entire battery pack can also be tested at different discharge rates and operating conditions which may result in better heat dissipation.

References

1. J. Kim, J. Oh, H. Lee, Review on battery thermal management system for electric vehicles. *Appl. Therm. Eng.* **149**, 192–212 (2019). <https://doi.org/10.1016/j.applthermaleng.2018.12.020>
2. W. Wu, S. Wang, W. Wu, K. Chen, S. Hong, Y. Lai, A critical review of battery thermal performance and liquid based battery thermal management. *Energy Convers. Manag.* **182**, 262–281 (2019). <https://doi.org/10.1016/j.enconman.2018.12.051>
3. C. Lin, S. Xu, G. Chang, J. Liu, Experiment and simulation of a LiFePO₄ battery pack with a passive thermal management system using composite phase change material and graphite sheets. *J. Power Sources* **275**, 742–749 (2015). <https://doi.org/10.1016/j.jpowsour.2014.11.068>
4. R. Mahamud, C. Park, Reciprocating air flow for Li-ion battery thermal management to improve temperature uniformity. *J. Power Sources* **196**, 5685–5696 (2011). <https://doi.org/10.1016/j.jpowsour.2011.02.076>
5. S. Ma, M. Jiang, P. Tao, C. Song, J. Wu, J. Wang, T. Deng, W. Shang, Temperature effect and thermal impact in lithium-ion batteries: a review. *Prog. Nat. Sci. Mater. Int.* **28**, 653–666 (2018). <https://doi.org/10.1016/j.pnsc.2018.11.002>
6. A.A. Pesaran, M. Keyser, G. Kim, S. Santhanagopalan, K. Smith, Tools for designing thermal management of batteries in electric drive vehicles battery temperature in xEVs. *Adv. Automot. Batter Conf.* (2013). <https://doi.org/10.2172/1064502>
7. C. Zhao, A.C.M. Sousa, F. Jiang, Minimization of thermal non-uniformity in lithium-ion battery pack cooled by channeled liquid flow. *Int. J. Heat Mass Transf.* **129**, 660–670 (2019). <https://doi.org/10.1016/j.ijheatmasstransfer.2018.10.017>

8. Z. Rao, Thermal performance of battery thermal management system using composite matrix coupled with mini-channel 1–10 (2019). <https://doi.org/10.1002/est2.59>
9. A. Greco, X. Jiang, D. Cao, An investigation of lithium-ion battery thermal management using paraffin/porous-graphite-matrix composite. *J. Power Sources* **278**, 50–68 (2015). <https://doi.org/10.1016/j.jpowsour.2014.12.027>
10. M.R. Giuliano, A.K. Prasad, S.G. Advani, Experimental study of an air-cooled thermal management system for high capacity lithium-titanate batteries. *J. Power Sources* **216**, 345–352 (2012). <https://doi.org/10.1016/j.jpowsour.2012.05.074>
11. L. Fan, J.M. Khodadadi, A.A. Pesaran, A parametric study on thermal management of an air-cooled lithium-ion battery module for plug-in hybrid electric vehicles. *J. Power Sources* **238**, 301–312 (2013). <https://doi.org/10.1016/j.jpowsour.2013.03.050>
12. H. Park, A design of air flow configuration for cooling lithium ion battery in hybrid electric vehicles. *J. Power Sources* **239**, 30–36 (2013). <https://doi.org/10.1016/j.jpowsour.2013.03.102>
13. Y. Kitagawa, K. Kato, M. Fukui, Analysis and experimentation for effective cooling of Li-ion batteries. *Procedia Technol.* **18**, 63–67 (2014). <https://doi.org/10.1016/j.protcy.2014.11.014>
14. Z. Lu, X.Z. Meng, L.C. Wei, W.Y. Hu, L.Y. Zhang, L.W. Jin, Thermal management of densely-packed EV battery with forced air cooling strategies. *Energy Procedia* **88**, 682–688 (2016). <https://doi.org/10.1016/j.egypro.2016.06.098>
15. L.H. Saw, Y. Ye, A.A.O. Tay, W.T. Chong, S.H. Kuan, M.C. Yew, Computational fluid dynamic and thermal analysis of Lithium-ion battery pack with air cooling. *Appl. Energy* **177**, 783–792 (2016). <https://doi.org/10.1016/j.apenergy.2016.05.122>
16. K. Chen, S. Wang, M. Song, L. Chen, Structure optimization of parallel air-cooled battery thermal management system. *Int. J. Heat Mass Transf.* **111**, 943–952 (2017). <https://doi.org/10.1016/j.ijheatmasstransfer.2017.04.026>
17. K. Chen, Y. Chen, Y. She, M. Song, S. Wang, L. Chen, Construction of effective symmetrical air-cooled system for battery thermal management. *Appl. Therm. Eng.* **166**, 114679 (2020). <https://doi.org/10.1016/j.applthermaleng.2019.114679>
18. Y. Huo, Z. Rao, X. Liu, J. Zhao, Investigation of power battery thermal management by using mini-channel cold plate. *Energy Convers. Manag.* **89**, 387–395 (2015). <https://doi.org/10.1016/j.enconman.2014.10.015>
19. W. Tong, K. Somasundaram, E. Birgersson, A.S. Mujumdar, C. Yap, Numerical investigation of water cooling for a lithium-ion bipolar battery pack. *Int. J. Therm. Sci.* **94**, 259–269 (2015). <https://doi.org/10.1016/j.ijthermalsci.2015.03.005>
20. S. Basu, K.S. Hariharan, S.M. Kolake, T. Song, D.K. Sohn, T. Yeo, Coupled electrochemical thermal modelling of a novel Li-ion battery pack thermal management system. *Appl. Energy* **181**, 1–13 (2016). <https://doi.org/10.1016/j.apenergy.2016.08.049>
21. S. Panchal, I. Dincer, M. Agelin-Chaab, R. Fraser, M. Fowler, Experimental and theoretical investigations of heat generation rates for a water cooled LiFePO₄ battery. *Int. J. Heat Mass Transf.* **101**, 1093–1102 (2016). <https://doi.org/10.1016/j.ijheatmasstransfer.2016.05.126>
22. U.N. Temel, Passive thermal management of a simulated battery pack at different climate conditions. *Appl. Therm. Eng.* **158**, 113796 (2019). <https://doi.org/10.1016/j.applthermaleng.2019.113796>
23. S. Park, D.S. Jang, D.C. Lee, S.H. Hong, Y. Kim, Simulation on cooling performance characteristics of a refrigerant-cooled active thermal management system for lithium ion batteries. *Int. J. Heat Mass Transf.* **135**, 131–141 (2019). <https://doi.org/10.1016/j.ijheatmasstransfer.2019.01.109>
24. F. Bai, M. Chen, W. Song, Q. Yu, Y. Li, Z. Feng, Y. Ding, Investigation of thermal management for lithium-ion pouch battery module based on phase change slurry and mini channel cooling plate. *Energy* **167**, 561–574 (2019). <https://doi.org/10.1016/j.energy.2018.10.137>
25. A. Verma, S. Shashidhara, D. Rakshit, A comparative study on battery thermal management using phase change material (PCM) (Elsevier Ltd., 2019)
26. X. Luo, Q. Guo, X. Li, Z. Tao, S. Lei, J. Liu, L. Kang, D. Zheng, Z. Liu, Experimental investigation on a novel phase change material composites coupled with graphite film used for thermal management of lithium-ion batteries. *Renew. Energy* **145**, 2046–2055 (2020). <https://doi.org/10.1016/j.renene.2019.07.112>

27. S. Arora, K. Tammi, A hybrid thermal management system with negative parasitic losses for electric vehicle battery packs. *ASME Int. Mech. Eng. Congr. Expo. Proc.* **6A-144113**, 1–6 (2018). <https://doi.org/10.1115/IMECE2018-86111>
28. S. Arora, A. Kapoor, W. Shen, A novel thermal management system for improving discharge/charge performance of Li-ion battery packs under abuse. *J. Power Sources* **378**, 759–775 (2018). <https://doi.org/10.1016/j.jpowsour.2017.12.030>
29. H. Zhang, X. Wu, Q. Wu, S. Xu, Experimental investigation of thermal performance of large-sized battery module using hybrid PCM and bottom liquid cooling configuration. *Appl. Therm. Eng.* **159**, 113968 (2019). <https://doi.org/10.1016/j.applthermaleng.2019.113968>
30. K.S. Kshetrimayum, Y.G. Yoon, H.R. Gye, C.J. Lee, Preventing heat propagation and thermal runaway in electric vehicle battery modules using integrated PCM and micro-channel plate cooling system. *Appl. Therm. Eng.* **159**, 113797 (2019). <https://doi.org/10.1016/j.applthermaleng.2019.113797>
31. C. Lan, J. Xu, Y. Qiao, Y. Ma, Thermal management for high power lithium-ion battery by minichannel aluminum tubes. *Appl. Therm. Eng.* **101**, 284–292 (2016). <https://doi.org/10.1016/j.applthermaleng.2016.02.070>

A Review on Performance and Evaluation of Modified Regenerator's Material in Stirling-Type Pulse Tube CryoCooler



Raj A. Aasole, Kaustub Ambarwele, Harshad Vaidya, Shubham Joshi, and Ashish Raut

Abstract This paper presents a comparison and solution of the regenerator's material of stirling-type pulse tube cryocooler. Here, a method of precisely controlling temperatures using different materials for regenerator in stirling-type pulse tube cryocooler (SPTC) has been studied and compared to a conventional cryosystem. The main aim is to focus on the cooling performance and to suggest best the optimal filling proportion for regenerator of SPTC. The main contribution of this work lies in the comparative study of different regenerator's material for SPTC. The study shows that the system uses meshes of stainless steel along with Pb for the first stage regenerator and HoCu₂, Er₃Ni, Pb, and SS meshes in the volume percentage ratio 27:27:27:19 for the second stage regenerator give a good specific heat. This study shall help the policymakers to choose the best criteria, while formulating a newer edition of SPTC.

Keywords Regenerator · SPTC · Regenerator's material · Cryocooler

1 Introduction

The stirling-type pulse tube cryocooler (SPTC) driven by the linear compressor provides high cooling performance and a feasible solution to the lifetime problem. As SPTC doesn't have any moving component at the cold head, it has the inherent merits of high reliability and long life at the cold end. Over the past years, stirling-type pulse tube cryocoolers (SPTCs) have been widely used in space and military applications with their inherent merits, such as high reliability, low cost, and low-mechanical vibration. The stirling-type two-stage PTCs are being investigated extensively during the last few years. A few years before, the temperature below the critical point of helium is achieved, using HoCu₂ powder as regenerator material in SPTC. The SPTC's is now recognized as a significant innovation in the regenerative cooling technology. The elimination of any moving component at the cold end brings to it

R. A. Aasole (✉) · K. Ambarwele · H. Vaidya · S. Joshi · A. Raut
G. H. Raisoni College of Engineering, Nagpur, India
e-mail: aasole_raj.me@ghrce.raisoni.net

© The Author(s), under exclusive license to Springer Nature Singapore Pte Ltd. 2022
M. L. Kolhe et al. (eds.), *Smart Technologies for Energy, Environment and Sustainable Development, Vol 1*, Springer Proceedings in Energy,
https://doi.org/10.1007/978-981-16-6875-3_65

several outstanding merits such as simple to fabricate, reliable in operating, and free of wear in the cold finger. In general, the efficiency of the STPTC under 20 K is extremely low which is mainly restricted by the efficiency of the regenerator. Rare earth compounds such as Er_3Ni , HoCu_2 , which contribute to increasing in specific heats at temperatures around 10 K are used, to match the specific heat of helium gas at these temperatures. The temperatures at the different stages have been observed with the change in mass flow rates.

The understanding of the fundamental cooling mechanisms in PTCs has been attempted by several authors by using different models has been discussed below. This paper also discusses the different regenerator's material used in various research with their end result.

2 Regenerator's Material Comparison

The performance of a regenerator is mainly determined by the heat capacity of the matrix, the heat transfer between matrix and fluid, the conductive heat loss from hot to cold ends, and the pressure drop of the flow through the porous media. The fourth-order Runge-Kutta methods have been used to discrete the analytical solutions and solve the continuous variables along the length. Based on the developed model, the regenerator of the SPTC with neither double-inlet nor multi-bypass phase-shifting has been optimized. To improve the performance of the SPTC, the different filling proportions of mixed matrices which are made of stainless steel screens are studied and compared, and then, the optimal proportion is suggested. The thermal conduction for the solid is larger than that for gas. When the segment of the 400-mesh SS screen is replaced by that of the 500-mesh SS screen, the porosity of this segment decreases, and thus, the overall thermal conductivity increases. Therefore, the conduction entropy generation increases. The experimental results indicate that the developed two-dimensional model is much more accurate than the one-dimensional one. Based on the developed model, the regenerator with mixed matrices for optimizing the SPTC is established, in which the different filling proportions of mixed matrices made of stainless steel screens are studied and compared, and then the optimal filling proportion with the combination of 400-mesh, 500-mesh, and 635-mesh SS screens is suggested [1].

The investigation of a 1.22 kg coaxial miniature pulse tube cryocooler (MPTC) demonstrates that using a higher mesh number and thinner wire diameter of stainless steel screen (SSS) can promote the coefficient of performance (COP) when using the miniature pulse tube cryocooler operating at 120 Hz. In this study, the 604 mesh SSS with 17 μm diameter of mesh wire is used as regenerator's material. Reducing the losses of the regenerator, as the core component of the cryocooler, is the key to the high-efficiency MPTC. Minimizing the average magnitude of mass flow through the regenerator is a way to decrease the losses due to the fact that pressure losses and heat transfer losses are proportional to the magnitude of mass flow. Therefore, the mass flow should be in phase with pressure in the middle of the regenerator. With

the increasing frequency, the phase angle should be guaranteed as constant. Several different equivalent diameters and lengths of the regenerator are studied and analyzed in Fig. 1, where the designed equivalent diameter is set as 7.5 mm, 8.5 mm, 9.5 mm, 10.5 mm, 11.5 mm, and 12.5 mm, respectively, and the length varies from 26 to 58 mm. It's obvious that the regenerator length and cross section area will significantly affect the COP. The SSS with a mesh number of 635 is used as the regenerator matrix. The length varies from 26 to 58 mm. The regenerator length and cross section area will significantly affect the COP (see Fig. 1). The result also shows an up-to-down COP trend of each designed equivalent diameter with increasing regenerator lengths shown is observed. The cooling power of 1 and 2 W at 80 K can be reached with input electric power of 34 and 55 W, which have a relative Carnot efficiency of 7.83 and 9.68%. The cooling power at the same temperature increases in an approximately linear relation with the input electric power. A good agreement is reached between the simulated results and experimental results displayed. When the cooling power is 1 W at 80 K, the tested input PV power is 28 and 41 W by using the 604 and 635 meshes SSS, respectively [2].

The pulse tube refrigerator has cryogenic regenerator material it is a stirling-type single-stage refrigerator used at liquid hydrogen temperature. Below 40 K, Pb, Er₃Ni, HoCu₂ have an advantage over SS in higher specific heat capacity, and hence, they are dominant in this temperature range. The filling rate of sphere materials in the regenerator is about 0.65, while that of wire-mesh materials is 0.37. The high filling rate may lead to a perhaps large flow resistance, so it is important to maintain it at a minimum, which will not harm the performance of the system. The Er₃Ni of two sizes and 500-mesh SS under steady flow conditions have been used. The flow rate of 0.055–0.07 mm (180–350 mesh) Er₃Ni is the lowest at a constant Delta P among the three tested materials, while the other two shares almost the same value with the

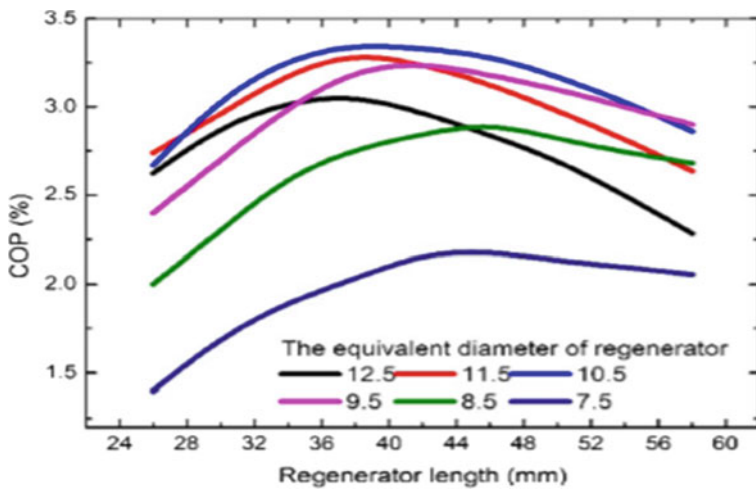


Fig. 1 Simulation on COP versus regenerator length with various equivalent diameters [2]

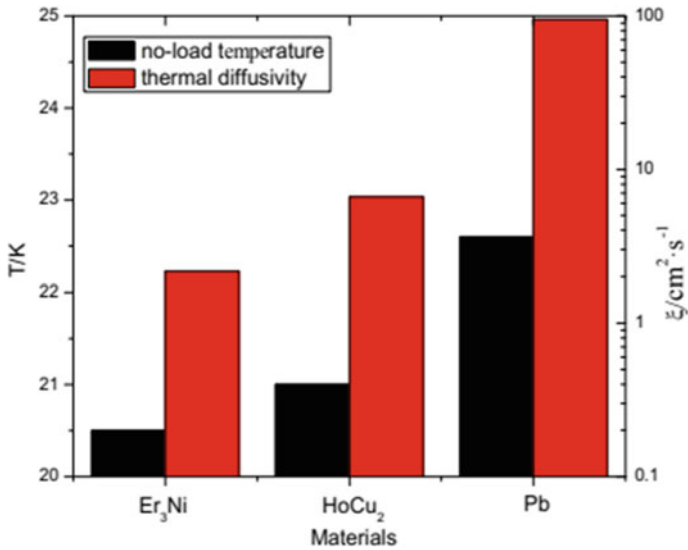


Fig. 2 No-load temperature and thermal diffusivity corresponding to different materials [3]

same regenerator filling length. Thus, from the steady flow resistance measurement, it is observed that 180–350 mesh Er₃Ni is of larger flow resistance than SS wire-mesh (see Fig. 2). The flow resistance of sphere materials is declared to be greater than that of wire-mesh by comparing and measuring both on steady flow condition directly and oscillating flow condition indirectly. After comparing different sphere regenerator materials and illustrating the principle, the most effective material has been chosen. Er₃Ni, with a large ratio of C_p to ξ , is proved to be the most promising material to replace stainless steel wire-mesh to improve the refrigerator performance [3].

The CFD modeling and experimental verification of a single-stage inertance tube coaxial stirling-type pulse tube cryocooler have been carried out. The simulation of the heat transfer processes and the flow characteristics by developing a two-dimensional axis-symmetric CFD model for the regenerator, and the whole SPTC was done. The thermal non-equilibrium mode had employed to achieve the relatively accurate simulations, and both the entropy generations inside the regenerator and the cooling performance of the SPTC with different combinations of the meshes have been calculated and compared. It is observed that the best performance occurs in Case 2 with the constant 500-mesh SS, which can provide 0.86 W of cooling at 35 K with an input PV power of 174.8 W. The temporal variations of the dynamic pressure and the mass flow rate at the outlet of the regenerator, both the phase and amplitude of the dynamic pressure at the inlet are fixed. It is observed that due to the larger flow resistance with the increasing SS mesh, the amplitudes of both the pressure and the mass flow rate at the outlet decrease, meanwhile there is a slight increase for the phase shift of the pressure wave from warm to the cold

end. The gas temperature drops sharply from about 70% of the length, resulting in a significant increase in the helium density, while the fluid velocity decreases gradually along with the whole regenerator. A mixed matrix is designed in which the first and the third segments are replaced by 400-mesh and 635-mesh ones, respectively. The modeling of cryocooler also states that the combination of the given different mesh segments can be optimized to achieve the highest cooling efficiency. Then, the verification experiments are conducted in which the satisfactory agreements about the changing tendencies between simulated and experimental results are detected. The cooler performance characteristics with various constant stainless steel mesh regenerator matrices are simulated and compared first, and the results show that both the largest cooling capacity and the highest exergy ratio through the regenerator can be achieved for the constant 500-mesh matrix [4].

Theoretical analyses and experimental verification for a three-stage stirling-type pulse tube cryocooler (SPTC) are conducted. Cryogenic phase-shifting mechanism and mixed regenerator matrices are employed to improve the performance at the third stage, and result is showing positive response. The cryogenic phase-shifting approach refers to the third-stage inertance tube and reservoir placed at cryogenic temperatures rather than in the ambient environment. Third-stage regenerators have a larger temperature gradient making the successful implementation of rare-earth mixed matrices with the high-heat specific capacity at 10 K and below including Er_{0.6}Pr_{0.4}, Er₃Ni and HoCu₂. An improved ECA model for the third stage is built, and the fourth-order Runge-Kutta method employed to solve equations. Several important factors are considered including the real gas effect of helium, the thermal properties of the matrices, and the pressure drop and the heat transfer of the regenerator. The mixed regenerator matrices involving the conventional stainless steel meshes and several rare-earth materials such as Er₃Ni, HoCu₂, and Er_{0.6}Pr_{0.4} are studied and optimized theoretically. The quantitative explanations for the difference in the heat capacity of the matrices are done by the entropy analysis. The results suggest that below 12 K the cooling performance using the mixed regenerator matrices with the optimal combination is better than that with each single matrix-2018 (see Fig. 3) [5].

A review on novel gas-coupled stirling-type pulse tube cryocooler (SPTC) has been observed. This SPTC also has a colder-stage at the cold head of the pre-cooling stage, which features an extremely compact structure shown in Fig. 4. The material used at cold side regenerator and diameter has a significant effect, while its inertance tube size has a weak effect on mass flow distribution. The sphere-type colder-stage regenerator has a different available energy loss mechanism shown below. The mesh-type regenerator of the pre-cooling stage is also considered. The dependence of mass flow distribution on the most frequently adjusted parameters during the experiment optimization, such as the diameters of regenerator material and the inertance tube size has been focused. The stainless steel (SS #635) is used as regenerator material and Er₃Ni powder is used for Pre-Regenerator #250 for PTC1 and for PTC2. A novel gas-coupled SPTC configuration is different from the commonly used structure. A negligible phase interaction is found between the two gas-coupled stages, which means the phase of each stage can be optimized individually to realize a modular design. The colder-stage regenerator material diameter has a negligible effect on its

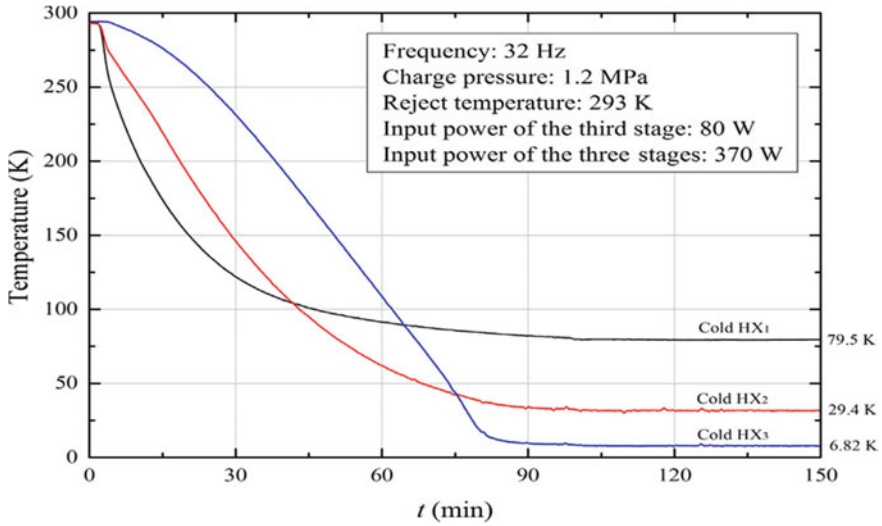


Fig. 3 Cool-down curves for the three stages, respectively [5]

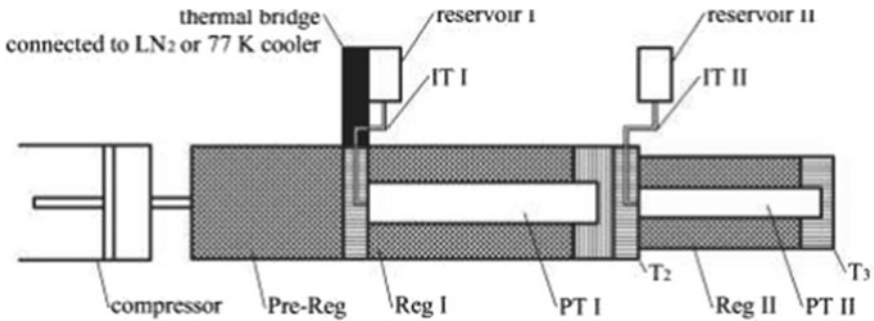
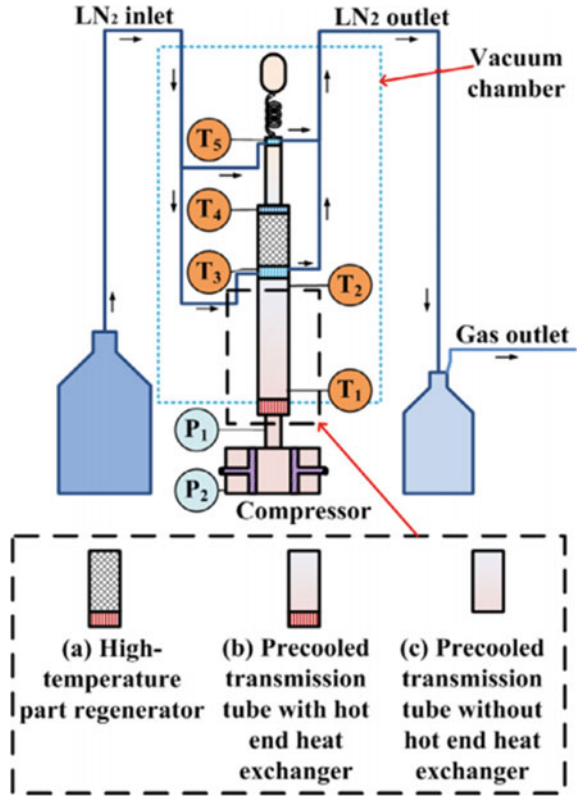


Fig. 4 Schematic of the gas-coupled SPTC [6]

inertance tube size and the colder-stage has a weak effect on mass flow distribution. The sphere-type cold-stage regenerator operating at 4–20 K has a different available energy loss mechanism with the mesh-type regenerator of the pre-cooling stage, and the mixed sphere diameter regenerator will not help to achieve a better cooling performance than the constant diameter regenerator. Cooling power of 12.4 mW/6 K has been achieved with an input power of 270 W and a pre-cooling power of 12.43 W/77 K, which shows that the novel compact gas-coupled configuration has the potential to achieve a similar or even better cooling performance with the general gas-coupled structure (see Fig. 4) [6].

Theoretically, when there is a surplus cold source such as LN₂ or LNG for precooling, the high-temperature part regenerator can be replaced by an empty tube with little pV power drop, which is increasing the efficiency of the SPTC, while

Fig. 5 Schematic of experiment system [7]



recovering cold energy. In these SPTC, a precooled transmission tube instead of a high-temperature part regenerator is observed and studied (see Fig. 5). The hot end of the transmission tube was connected to the room-temperature compressor at ~ 300 K, while its cold end was linked to the low-temperature part regenerator. Figure 5 shows the schematic diagram of the experiment setup and the structure, operating parameters, and Specifications of the SPTC model are shown in Table 1. Liquid nitrogen (LN2) is used as the pre-cooling power source for its economy. LN2 is supplied from a tank, delivered to the pre-cooling heat exchanger and the pulse tube hot end heat exchanger through LN2 pipes, and collected in another tank. An in-line SPTC with a precooled transmission tube was built for the experimental investigation. CFIC 2S175 linear compressor was used to drive the SPTC. Liquid nitrogen (LN2) is used as the pre-cooling power source for its economy. LN2 is supplied from a tank, delivered to the pre-cooling heat exchanger and the pulse tube hot end heat exchanger through LN2 pipes, and collected in another tank. Five rhodium iron resistance thermometers with an accuracy of 0.1 K (10–300 K) are used to measure the temperatures at the wall of the precooled transmission tube near the hot end (T_1), the wall of the precooled transmission tube near the cold end (T_2), the pre-cooling heat exchanger (T_3), the cold heat exchanger (T_4) and the pulse tube hot end heat

Table 1 Structure and operating parameters of the SPTC models

Parameters	Values
Length and diameter of high-temperature part regenerator/precooled transmission tube (mm)	60;28
Length and diameter of low-temperature part regenerator (mm)	52;28
Regenerator material	High-temperature part: SS400# Low-temperature part: SS635#; SS500#
Length and diameter of pulse tube (mm)	63;16
Length and diameter of inertance tube	3 mm * 1.1 m * +5 mm * 2.6 m
Volume of gas reservoir (cc)	720
Hot end heat exchanger	Slit type: 300 K
Precooling heat exchanger	Slit type: 80 K
Cold end heat exchanger	Slit type: 22 K
Pulse tube hot end heat exchanger	Slit type: 80 K
Frequency (Hz)	23
Charge pressure (MPa)	0.75

exchanger (T5). Two pressure sensors are arranged at the outlet of the compressor (P1). It largely reduces the required input pV power for the cryocooler system. It has prospects in the application where the output power of the linear compressor is limited and a surplus cold source such as LN2 or LNG is available. By using this SPTC, 70% input pV power can be saved, but the cost is that the pre-cooling power at ~80 K will be increased a lot. A no-load refrigeration temperature of 17.7 K is obtained in this SPTC with the precooled transmission tube, the cooling capacity is 1.74 W at 25.0 K, the input pV power is 52.9 W, and the calculated pre-cooling power is 36.0 W. The total efficiency at 25.0 K, considering the cost of LN2, is about 0.67% [7].

3 Conclusion

In this work, several configurations of multistage pulse tube cryocoolers have been studied, different dimensions and materials of regenerator have been observed and compared. Both theoretical and experiments show that the SPTC can work well and has a similar cooling performance to the original SPTC when using the precooled transmission tube instead of the high-temperature part regenerator. Theoretical analysis shows that when the volume of the precooled transmission tube is well designed, the hot end heat exchanger performs a small amount of heat exchange and can be removed theoretically. However, experimental results show that the hot end heat exchanger is necessary for the SPTC with the precooled transmission tube to get quick stabilization on the cooling temperature. The study shows that the system uses

meshes of stainless steel along with Pb for the first stage regenerator and HoCu_2 , Er_3Ni , Pb, and SS meshes in the volume percentage ratio 27:27:27:19 for the second stage regenerator give a good specific heat and below 12 K, using of materials like $\text{Er}_0.6\text{Pr}_0.4$, Er_3Ni and HoCu_2 gives the best high-heat specific capacity.

References

1. D. Bao, J. Tan, L. Zhang, Z. Gao, Y. Zhao, H. Dang, A two-dimensional model of regenerator with mixed matrices and experimental verifications for improving the single-stage stirling-type pulse tube cryocooler. *Cryogenics* **78**
2. H. Yu, Y. Wu, L. Ding, Z. Jiang, S. Liu, An efficient miniature 120 Hz pulse tube cryocooler using high porosity regenerator material. *Cryogenics* **88**, 22–28 (2017)
3. Q. Zhou, L. Chen, C. Pan, Y. Zhou, J. Wang, Experimental investigation on regenerator materials of stirling-type pulse-tube refrigerator working at 20 K. *Phys. Procedia* **67**, 530–535 (2015)
4. H. Dang, Y. Zhao, CFD modeling and experimental verification of a single-stage coaxial stirling-type pulse tube cryocooler without either double-inlet or multi-bypass operating at 30–35 K using mixed stainless steel mesh regenerator matrices. *Cryogenics* **78**, 40–50 (2016)
5. H. Dang, D. Bao, T. Zhang, J. Tan, R. Zhao, J. Li, N. Li, Y. Zhao, B. Zhao, Theoretical and experimental investigations on the three-stage stirling-type pulse tube cryocooler using cryogenic phase-shifting approach and mixed regenerator matrices. *Cryogenics* **93**, 7–16 (2018)
6. C. Liubiao, W. Xianlin, L. Xuming, P. Changzhao, Z. Yuan, W. Junjie, Numerical and experimental study on the characteristics of 4 K gas-coupled stirling-type pulse tube cryocooler. *Cryogenics* (2018)
7. C. Huang, X. Zhi, R. Cao, K. Liang, L. Qiu, X. Xi, A Stirling type pulse tube cryocooler working at liquid hydrogen temperatures with a precooled transmission tube. *Int. J. Refrig.* **111** (2020)

Real-Time Problem of Knob Assembly in Automobile Manufacturing Industries



Prabinkumar R. Jachak, Abhay Khalatkar, and Nilesh M. Narkhede

Abstract In automobile manufacturing industries, various amount of operations take place simultaneously to achieve the allotted target. In a limited span of time, tremendous amount of parts are being manufactured and assembled every day in the industry. Therefore, sometimes worker/operator/labor get confused between identical parts during assemble operations of automobile. This problem leads company to losses, and hence, it should be eliminated. Problem occurring in knob assembly is one of them, and thus in this paper, we have discussed and explained the solution given to the real-time problem of knob assembly in tractor manufacturing industry.

Keywords Real-time problem · Automobile industry · Knob assembly · Gear knob · Range shifter knob · Tractor manufacturing industry

1 Introduction

Manufacturing industries have target to produce quantity of product by the end of the day, and as automobile has many parts to be assemble on it, labors/workers/operators have very less time to think which part is to be assemble on what automobile during its assembly operation. Company face losses if worker/labour get confused between identical parts which they must assemble on respective automobile during its assembly operation. These losses will not only affect the production time but also quality, cost, and other aspect related to production. An average cost of one automobile is up to 10 lac (INR); thus, company can face loss in crore due to this problem. Figure 1 shows the list of companies which have manufactured the number of automobiles in the year 2019–20 [1]. Creation of confusion between identical knobs among operator/worker/labors during its assembly is one of the problems in automobile manufacturing industry. To eliminate this issue, industry hires only skilled

P. R. Jachak (✉) · A. Khalatkar
G. H. Raison College of Engineering, Nagpur, India

N. M. Narkhede
Mahindra and Mahindra Limited, Nagpur, India

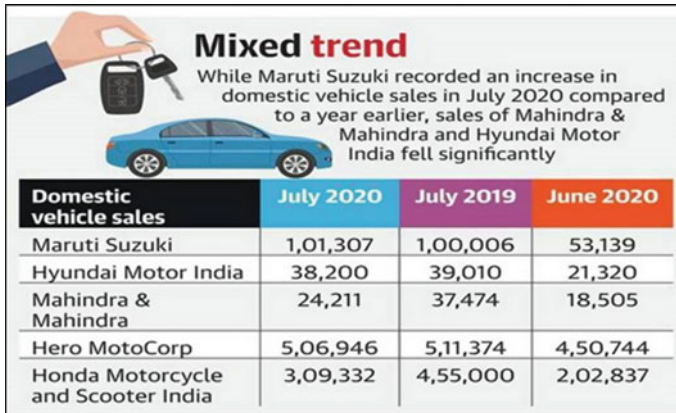


Fig. 1 Domestic vehicle sales in 2019–20

persons so that they do not have errors. But what if we still found human error during the assembly process? Therefore, to eliminate these types of problems and errors some automation is required in the process [2]. Which could not only reduce human errors but also could ease the respective assembly process. Therefore, we have come up with the idea of implementing poka-yoke [3] for knob assembly operations at automobile manufacturing industry.

2 Problem Identification

Main knobs which assembles on tractor are as follows:

1. Gear shifter knob.
2. Range shifter knob.
3. Power take off (PTO) knob.
4. Hand accelerator knob.

Nowadays, various types of knobs which are used in automobiles are available in market. Some knobs have same shift pattern embossing on them with different structure, dimensions, etc., and some have same physical appearance with different shift pattern embossing on them [4]. The arrangements of gears in gearbox for some automobile are different. Therefore, shifting pattern of those gears and embossing on their gear knobs are also different as compared to another automobile. And, if different shift pattern gets assembled on different tractors, then it could not only damage the transmission of automobile but also can cause dead of operator. During assembly of automobile, workers have to assemble many parts simultaneously as they have target to achieve by the end of the day. Thus, they have very less time to think where to assemble which part. During assembly of knobs, sometimes operator/worker/labor gets confuse between the identical knobs and knob get assembled

on different automobile which not only causes failure of automobile due to failure of engine, etc., but also loss in production, loss in quality, etc. Although there is various process for doing remanufacturing of parts of automobile like engine using IOT [5], but it not only consumes time but also cost which is not acceptable. Example of knobs having same structure, dimensions but different shift pattern embossing are as follows.

3 Proposed Solution

Although they look similar but the shifting pattern on them is different as shown in Figs. 2 and 3. Thus, it creates problem if they get assembled on wrong automobiles. To eliminate these problems, we have come up with the idea of making a machine which will not only segregate the knobs but also will distribute the respective knobs to the worker/operator for assembly so that there will be no confusion in between the identical knobs. This will not only save time but also will ease the process of knob assembly in the industry. As of now, assembly process in automobile industry are as follows:

- a. Store member loads the parts of automobile like knobs, washers, nuts, bolts, hose clip, hinge pin, cluster plug, clamps, etc., in their respective compartments present at kitting area.
- b. Then, according to line order, labor fills the LH and RH components which are to be assemble on respective automobile in its respective trolley manually.



Fig. 2 Gear knobs having same dimensions with different embossing



Fig. 3 Range shifter knobs having same dimensions with different embossing

- c. Another labor brings those trolleys to assembly line where workers assemble the respective components on automobile.

Since all these process are manual, there are chances of errors which could not only affect the production time but also quality, cost, and other aspect related to company. Chances of getting error if store member loads different knob in different compartment or labor filled wrong knob in the trolley while filling LH and RH Components of automobile, etc. Thus, to avoid all these things, we have planned to implement poka-yoke on field by making an automatic machine which will dispense the correct knob according to respective automobile.

We have distributed our mechanism into respective stages as shown in Fig. 4. All units have its own specific operation to achieve the desire output of knob.

- a. **Barcode scanning unit:** Every transmission skid which comes for assembly operation in assembly line is come up with its own traveler card. That traveler card has its unique barcode of automobile number, transmission number, and engine number. Therefore, we will scan that barcode using barcode scanner and that scanner will send the respective signal to PLC unit.
- b. **Programmable logic controller unit:** We will upload all the necessary information into PLC unit with respect their automobile's number so that when we scan the barcode of automobile's number PLC unit will configure the data and give the respective signal to dispensary unit.
- c. **Dispensary unit:** We will load one type of knob in one machine and will make compartments to store such various machines having their respective knobs.

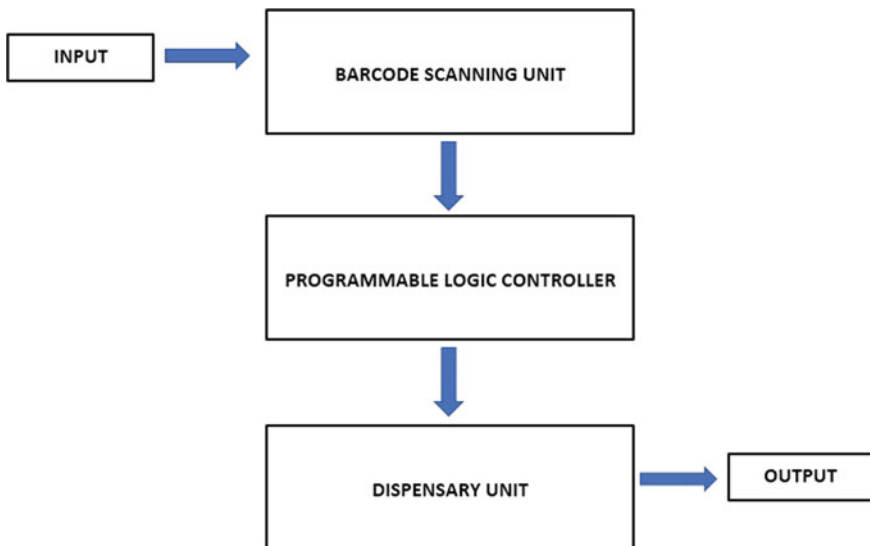


Fig. 4 Conceptual block diagram of machine

Therefore, after scanning the barcode, PLC will only send signal to its respective machine which will dispense the respective knob. And, then operator will assemble that knob on its transmission skid.

This mechanism will not only save time but also ease the process of knob assembly.

4 Conclusion

Through this paper, we aimed to explain the dispense mechanism which we will design and fabricate for knobs to eliminate its identical problem for all automobile manufacturing industries. Grzybowska et al. proclaimed that a small improvement in a vending operation directly leads to thousand dollar gained revenue [6]. We can use this mechanism in every automobile manufacturing industry to eliminate the knob mismatching problem. This mechanism will not only help to segregate the different knobs with respect to automobile but also will ease the assembly process, consume less time for assembly, etc. Thus, it will also allow the company to achieve good quality product with less production losses due to knob mismatching problem.

References

1. *July Sales Hint at Auto Sector Revival* (2020, August 1). <https://Www.Thehindu.Com/>
2. *Error Handling Within Highly Automated Automotive Industry: Current Practice and Research Needs* (2016). <https://doi.org/10.1109/ETFA.2016.7733628>
3. Wikipedia Contributors, *Poka-Yoke* (Wikipedia, 2020, October 19). <https://en.wikipedia.org/wiki/Poka-yoke>
4. A. Garg, A. Garg, *Types of Automatic Gear Shift Levers You Should Know About* (Autoportal.Com, 2017, February 14). <https://autoportal.com/articles/types-of-automatic-gear-shift-levers-you-should-know-about-10168.html>
5. https://www.researchgate.net/publication/323397399_The_'Internet_of_Things'_enabled_real-time_scheduling_for_remanufacturing_of_automobile_engines
6. H. Grzybowska, B. Kerferd, C. Gretton, S. Travis Waller, A simulation-optimisation genetic algorithm approach to product allocation in vending machine systems. *Expert Syst. Appl.* **145**, 113110 (2020). <https://doi.org/10.1016/j.eswa.2019.113110>

Effect of Various Parameters on Aerodynamic Performance of Savonius VAWT: A Review



Shivaji Suryabhan Aher and Netra Pal Singh

Abstract Wind is the cheapest alternative energy resource which can be utilized for generation of electricity. Although the vertical axis wind turbine (VAWT) was the first ever wind turbine used for generation of electricity, researchers of the modern days have lost interest in it due to the limitations offered by VAWT (Bhutta et al. in *Renew Sustain Energy Rev* 16:1926–1939, 2012) [1]. VAWT is beneficial for small-scale power generation such as in rural areas because their performance is not dependent on wind direction (Tian et al. in *Renew Energy* 117:287–299, 2018) [2]. In 1920s, Savonius-type wind turbine was reported to produce a maximum efficiency of 31% since then researchers have made a number of attempts to improve the aerodynamic performance of Savonius rotor in order to make them an attractive source of power generation (Roy and Saha in *Appl Energy* 137:117–125, 2015) [3]. Improvement in the design of wind turbine can help manufactures to reduce the cost of electricity generation with the help of wind energy (El-Askary et al. in *J Wind Eng Ind Aerod* 139, 2015) [4]. The aim of this literature is to review the work undertaken by earlier researchers and utilize this knowledge to improve the efficiency of Savonius rotor in future works to be attempted.

Keywords Savonius rotor · VAWT · HAWT · Fins · Dimples · Curtains

1 Introduction

Numerous such studies have been undertaken by researchers in the recent years to improve the performance and efficiency of wind turbines by optimizing the design in order to improve the lift–drag ratio [5]. Techniques such as curtaining the rotor, using obstacle in front of the returning blade, varying number of blades, changing shape of blade, and changing bucket overlap ratio can be found in a number of literatures to improve performance of Savonius turbines [6]. Savonius rotor is a vertical axis wind turbine patented by S.J. Savonius in 1920s which is simple in construction and

S. S. Aher (✉) · N. P. Singh

Research Scholar, Department of Mechanical Engineering, Oriental University, Indore, MP, India

can operate with wind flow from any direction. The basic principle of operation lies on the drag and lift force exerted by the winds on the buckets (blades) which cause the turbine to rotate [7]. Despite number of advantages, the Savonius vertical axis wind turbines have been rarely used for generation of wind energy due to their low aerodynamic performance [8]. Nakajima et al. [9] used Savonius rotor to generate hydroelectricity. The researchers were aware about the limitations of the Savonius rotor, so they modified the double-stage Savonius rotor by creating a phase difference between the buckets. A 90° phase difference helped to achieve a power coefficient improvement by 10%.

Use of dimples to reduce the drag force has been applied in numerous fields of engineering. Zhang et al. [10] investigated drag reduction in marine vessels due to use of air filled dimples, and Livya et al. [11] studied the aerodynamic performance of aircraft wings by employing dimples of different shape. Dimples are found to enhance the stall angle and increase the lift–drag coefficient [12]. The conclusive discussion shows that dimples have the ability to delay the flow separation point, thereby improving efficiency. Hence, dimples can be used as an effective method to improve aerodynamic performance of wind turbines.

In some of the literatures, researchers have even made use of fins to improve efficiency of Savonius vertical axis wind turbines. The efficiency of Savonius VAWT can be expressed in terms of C_p , C_T and TSR [13]. The aim of this research is to investigate the literatures of earlier researchers.

2 Effect of Dimple and Fins on the Aerodynamic Performance of Savonius Rotor

Gedyon et al. [14] studied the aerodynamic performance of HAWT blades with inward and outward dimples. The researchers tested a baseline blade against six other specimens with dimples: 10 cm, 5 cm inward dimple on suction side (02 specimens); 10 cm, 5 cm outward dimple on suction side (02 specimens); 10 cm inward dimple on suction and pressure side (01 specimen), and 10 cm outward dimple on suction and pressure side (01 specimen). The aerodynamic performance of the blade was studied for different wind speeds, namely 3, 10, and 22 m/s with different angles of attack. The HAWT blades with inward dimples (all specimens) showed a better aerodynamic performance compared to the baseline blade and blades with outward dimples. Results show that blades with outward dimples increase additional drag force on the blades.

Hamed et al. [5] examined the changes in aerodynamic performance of an air foil HAWT by forming spherical-shaped dimples on the suction side of the blade. In three different rows, 150 dimples were formed on the blade, and the pitch distance between them was maintained at 200 mm. The performance of the blade was tested at six different values of pitch angle and wind speeds between 14 and 16 m/s. Results showed that dimples could help to improve the drag–lift ratio of the turbine, and it

also influenced the power generation and torque characteristics which increased by nearly 16%.

Arun k et al. [15] simulated the performance of a baseline blade with and without dimples using the Ansys software. At room temperature, wind speed 12–20 m/s was used to study the performance of baseline blade. The pressure contour view showed that the pressure developed at the bottom was higher than at the top. Using the cross-sectional view, the researchers were able to identify the point where the pressure was maximum. The point of maximum pressure creates a drag for rotation. Hence, for the second model, researchers created dimples only in those portions of the blade which showed high pressure. Results reveal that addition of dimples to the blade improved its performance by 14.7%.

Tay et al. [16] investigated the effect of dimple shape on the drag coefficient. The circular dimple was modified to obtain a teardrop shape by modifying the half portion of the circular dimple. The researchers investigated the performance of teardrop dimple by first pointing the sharp tip of the teardrop to upstream wind flow and in the second case to downstream wind flow. The experiment was carried out for Reynold's number ranging from 5000 to 50,000, and it was observed that with tip pointing downstream the drag coefficient decreased by 5% whereas, for tip pointing upstream, the drag coefficient reduced by 6%. The researchers concluded that drag coefficient could be further reduced by focusing on the upstream and downstream wall slopes.

Ridwan et al. [17] used the SOLIDWORKS simulation tool to study the effects of fins on the drag coefficient and drag force. The researchers modeled a 4-blade U-type Savonius rotor with 0, 1, and 2 fins. The models were subjected to wind speeds of 5 m/s and 7 m/s, respectively. Simulation results show that for both values of wind speed the model with two fins showed the highest drag coefficient and drag force. Two fins on the blade also produced the highest pressure and velocity distribution.

Pamungkas et al. [18] studied the effects of adding fins to the 'S'-shaped Savonius wind turbine. Performance of five different Savonius turbines were compared against each other. Savonius wind turbines with 0, 1, 2, 3, and 4 fins were constructed and connected to a generator. At 4.5 m/s of wind speed, the Savonius rotor turbine with 1 fin showed the highest performance and produced an electrical power of 13.4 W which was 22.71% higher than the Savonius turbine with 0 fins. The performance of Savonius turbine with four fins was the lowest; it generated an electrical power of 10.8 W which was 1.09% lower than the plain Savonius wind turbine (Table 1).

3 Effect of Number of Blades

Wenhenubun et al. [19] performed a study to compare the performance of 2-, 3-, and 4-blade Savonius wind turbine based on tip speed ratio, torque, and power coefficient. Ansys software was used to simulate the pressure distribution of wind turbines. Results show that the performance of 3-blade Savonius wind turbine was better than the other two models in terms of tip speed ratio (0.555) and power coefficient for

Table 1 Summary of research on the effect of dimple and fins

Title	Journal	Summary	Author
Effects of dimples on aerodynamic performance of horizontal axis wind turbine blades	International Research Journal of Engineering and Technology	Inward dimples have better performance than outward dimples	Gedyon et al. [14]
Aerodynamic performance enhancement of horizontal axis wind turbines by dimples on blades: numerical investigation	Energy	Results showed that dimples could help to improve the drag–lift ratio of the turbine, and it also influenced the power generation and torque characteristics which increased by nearly 16%	Hamed et al. [5]
Analyzing the effect of dimples on wind turbine efficiency using CFD	International Journal of Applied Engineering Research	Addition of dimples improved the performance of Savonius turbine by 14.7%	Arun et al. [15]
Drag reduction with teardrop-shaped dimples	Flow Control Conference, Atlanta, Georgia	Drag coefficient can be decreased by optimizing the upstream and downstream wall slopes of a teardrop-shaped dimple	Tay et al. [16]
Performance of vertical axis Savonius wind turbines related to the fin number on the blade	Materials Science and Engineering	Pressure and velocity distribution increases with an increase in the number of fins on the blade	Ridwan et al. [17]
Performance of ‘S’-type Savonius wind turbine with variation of fin addition on blade	Materials Science and Engineering	Power generation of a Savonius turbine improves by 22.71% due to addition of single fin	Pamungkas et al. [18]

wind speed of 7 m/s. In terms of torque, the 4-blade wind turbine produced the highest torque compared to other wind turbine rotors. Simulation result reveals that pressure distribution on the concave blades was greater than the convex blades.

Ali [20] compared the performance of a 2- and 3-blade Savonius wind turbine in a wind tunnel at low wind speed. The wind speed was gradually increased from 0 to 6 m/s, and the cut-in wind speed was initially noted. It was found that the cut-in wind speed for the arrangement was 2.5 m/s in case of 3-blade Savonius model, while it

Table 2 Summary of research on the effect of number of blades

Title	Journal	Summary	Author
An experimental study on the performance of Savonius wind turbines related with the number of blades	Energy Procedia	3-blade simulation model showed better tip speed ratio, whereas 4-blade model produced the highest torque coefficient	Wenehenubun et al. [19]
Experimental comparison study for Savonius wind turbine of two and three blades at low wind speed	International Journal of Modern Engineering Research	Higher number of blades increase drag coefficient and reverse torque on the turbine	Ali et al. [20]
An experimental study on improvement of Savonius rotor performance	Alexandria Engineering Journal	A two-stage rotor with end plates has better performance than 3- and 4-blade rotor with bucket overlap	Mahmoud et al. [21]

was slightly less in case of 2-blade model. The 2-blade model achieved an rpm of 550 with wind speed of 6 m/s which was better than the 3-blade model. The plot of variation in static torque coefficient with angle of rotation shows that at 5.3 m/s wind speed 2-blade model achieved a static torque coefficient of 0.83 and a power coefficient of 0.21 at tip speed ratio of 0.8 which was better than a 3-blade model. Results reveal that higher number of blades increase the drag coefficient and increase the reverse torque due to which performance of 3-blade model was lower than the 2-blade model.

Mahmoud et al. [21] performed a study to evaluate the performance of Savonius rotor with different arrangements. The researchers designed the Savonius rotor with 2, 3, and 4 blades in single- and two-stage arrangement with and without the end plate, using different aspect (0.5, 1, 2, 4, and 5) and overlap (0–0.35) ratio. Results show that higher performance efficiency was achieved with a two-stage rotor arrangement consisting of two blades with end plate and no overlap ratio. The power coefficient increased with an increase in the aspect ratio (Table 2).

4 Effect of Flow Rate Augmentation Device

Wong et al. [22] performed a literature survey on various flow augmentation devices that can be used to improve efficiency of VAWT. The researchers have described number of flow augmentation devices in this literature including the guided vanes, diffusers, plates, shrouds, and deflectors. The use of these devices can help to converge the wind flow from a larger area into a smaller area which can increase

the starting torque on the VAWT and increase its efficiency. Though the augmentation devices increase the positive torque, they are also helpful in reducing the negative torque in case of drag-type VAWT.

Tratuferi et al. [23] modified the design of Savonius rotor by using the airfoil shaped blades and a self-orienting conveyer–deflector curtain system. The researchers found that the new curtaining system helped to reduce the drag force on the returning blade and the use of airfoil-shaped blade produced a high output power. Though these modifications helped to increase output power, researchers found that it also made the rotor geometry complex.

Mohamed et al. [24] optimized the blade shape of a Savonius rotor by partially placing an obstacle in front of the returning blade and compared the performance of the simulated model to a standard Savonius rotor. The researchers made use of Ansys-Fluent industrial simulator for the experiment. Evolutionary algorithm was used to optimize the blade shape (skeleton line), and the geometrical configuration was evaluated using CFD simulation. The researchers found that the optimized blade shape, in which the returning blade is partially covered by an obstacle, leads to a power coefficient improvement by 38.9% at $\lambda = 0.7$. The optimized blade also showed a self-starting capability at any angle of wind flow. The researchers concluded that such an optimization of Savonius turbines can improve its performance by 30% over the entire range of λ .

Altan et al. ([25]) carried out a study to improve the efficiency of Savonius rotor by using the curtain arrangement. Wind deflecting plates (curtains C1, C2, C3) of different lengths were designed and placed in front of the rotor at different curtain angles (α , β) without changing the rotor design. Results reveal that curtain C1 at $\alpha = 45^\circ$ and $\beta = 15^\circ$ produced a better power coefficient. The power coefficient of Savonius rotor due to C1 improved by 38%, whereas for C2, C3, it was 16% more than the Savonius rotor without curtains (Table 3).

5 Effect of Change in Rotor Design

Tian et al. [2] experimentally investigated the effect of rotor blade geometry on the coefficient of power. The dimensionless heights of the concave and convex sides of the rotor blade were modified, and the performance was compared with a traditional Savonius rotor in terms of coefficient of power. Results show that the modification in blade geometry helped to improve the coefficient of power by nearly 4%.

Roy et al. [3] carried out a series of experiment to compare the performance of a conventional semicircular blade with a semi-elliptical, Benesh-type, and a modified Bach-type blade. The dimensions of the modified Bach-type blade were modified a number of times to perform a series of experiments and achieve an improvement in the aerodynamic performance of the wind turbine. The turbine with modified Bach-type blade was tested in a low-speed wind tunnel and helped to achieve an improvement in power coefficient by nearly 34%.

Table 3 Summary of research on the effect of flow rate augmentation device

Title	Journal	Summary	Author
Performance enhancements on vertical axis wind turbines using flow augmentation systems: a review	Renewable and Sustainable Energy Review	Use of flow rate augmentation devices can help to increase positive torque on the VAWT, thereby improving its efficiency	Wong et al. [22]
Enhancement of Savonius wind rotor aerodynamic performance: a computational study of new blade shapes and curtaining systems	Energy	Use of air foil-shaped blade and new curtaining arrangement improved output power but results in a complex rotor geometry	Tratuferi et al. [23]
Optimal blade shape of a modified Savonius turbine using an obstacle shielding the returning blade	Energy Conversion and Management	Returning blade partially covered by an obstacle leads to a power coefficient improvement by 38.9% at $\lambda = 0.7$	Mohamed et al. [24]
An experimental study on improvement of a Savonius rotor performance with curtaining	Experimental Thermal and Fluid Science	Power coefficient improved by 38% due to addition of curtain	Altan et al. [25]

Damak et al. [26] investigated the performance of a helical Savonius rotor designed by retaining the semicircular cross section of the blades from bottom to the top. With respect to the bottom, the top portion of the blade was twisted by 180°. The performance of the rotor was tested in a low-speed wind tunnel. Results reveal that the modified geometry had better performance than the conventional-type Savonius rotor. However, the modified design was sensitive to Reynold's number.

Kacprzak et al. [27] investigated the performance of three rotor geometries using the Ansys simulation software. The researchers compared aerodynamic performance of Bach-type Savonius rotor and the elliptical rotor found in some of the literatures with conventional Savonius rotor. Simulation results show that Bach-type Savonius rotor has a better aerodynamic performance than the conventional- and elliptical-type rotor in terms of power coefficient as it reduces the impact of negative torque on the returning blade to a greater extent (Table 4).

Table 4 Summary of research on the effect of change in rotor design

Title	Journal	Summary	Author
Shape optimization of a Savonius wind rotor with different convex and concave sides	Renewable Energy	Modification in concave and convex side geometry of the traditional rotor blade improved its coefficient of power by 4%	Tian et al. [2]
Wind tunnel experiments of a newly developed two-bladed Savonius-style wind turbine	Applied Energy	Turbine with modified Bach-type blade helped to achieve improvement in power coefficient by nearly 34%	Roy et al. [3]
Experimental investigation of helical Savonius rotor with a twist of 180	Renewable Energy	Helical-type Savonius rotor is better in performance than conventional Savonius rotor. Sensitive to Reynold's number	Damak et al. [26]
Numerical investigation of conventional and modified Savonius wind turbines	Renewable Energy	Simulation results show that Bach-type Savonius rotor has a better aerodynamic performance than the conventional- and elliptical-type rotor in terms of power coefficient	Kacprzak et al. [27]

6 Effect of Bucket Overlap Ratio

Jaoa et al. [28] studied the effect of bucket overlap ratio on the aerodynamic performance of Savonius rotor. The researchers used star-CCM⁺ software to compute the pressure and velocity field of the flow and the forces acting on the bucket. The researchers found that due to overlap a gap is created between the advancing and returning buckets due to which air creates a pressure on the concave side of the returning bucket, thereby improving the power coefficient to certain extent of overlap. The highest power coefficient achieved was 31.61% with a 15% bucket overlap ratio.

Gupta et al. [29] performed a comparative study to examine the aerodynamic performance of three-bucket Savonius rotor with a combined three-blade Savonius–Darrieus rotor (two-stage arrangement) with different overlap ratios. The researchers examined the performance of the two rotors at 0, 16.2, and 20% overlap ratio. In case of 3-blade Savonius rotor, they found that the power and torque coefficient increased with an increase in the overlap. For the combined rotor, the results were different. Power coefficient decreased with an increase in the overlap. Highest power coefficient efficiency of 51% was observed in case of combined rotor with no overlap which was even highest than the Savonius rotor (Table 5).

Table 5 Summary of research on the effect of bucket overlap ratio

Title	Journal	Summary	Author
Discussion on the verification of the overlap ratio influence on performance coefficients of a Savonius wind rotor using computational fluid dynamics	Renewable Energy	15% bucket overlap ratio produced the highest power coefficient of 31.61%	Joao et al. [28]
Comparative study of a three-bucket Savonius rotor with a combined three-bucket Savonius–three-bladed Darrieus rotor	Renewable Energy	A combined two-stage Savonius–Darrieus rotor has better performance than a standard Savonius rotor with different bucket overlap ratios	Gupta et al. [29]

7 Conclusion

Through the literatures reviewed, it was found that though Savonius-type wind turbines are simple in construction and cost they suffer from the drawback of low output power. Numerous methods to improve aerodynamic performance of Savonius wind turbine can be found in a number of literatures where researchers have made use of curtain and fin arrangement to successfully improve the power efficiency of Savonius rotor to some extent. From these findings, it can be briefly concluded that while curtaining arrangement helps to reduce the effect of negative torque acting on the rotor bucket, addition of fins yields a self-starting ability in the rotor at low wind speed.

Through numerical investigations, it has been shown that dimples are effective in reducing the drag force acting on the blade surface. Gedyon et al. [14] experimentally proved that blades with inward dimples can produce better efficiency compared to blades with outward dimples. It was also shown that the aerodynamic performance of a blade is affected by the number and position of the dimples. While circular-shaped inward dimples appear in a number of research papers, Tay et al. [16] presented the idea of a tear-shaped dimple to effectively reduce the drag force acting on the blade surface. In other works presented by some researchers, it was reported that change in rotor geometry and bucket overlap ratio can also influence the performance of Savonius rotor to a certain extent. With the knowledge acquired through these findings, we aim to improve the aerodynamic performance of a Savonius VAWT by keeping in mind the pros and cons of including the dimple and fin arrangement in the rotor blade geometry in our future work.

References

1. M.M.A. Bhutta, N. Hayat, A.U. Farooq, Z. Ali, S.R. Jamil, Z. Hussain, Vertical axis wind turbine a review of various configurations and design techniques. *Renew. Sustain. Energy Rev.* **16**(4), 1926–1939 (2012)
2. W. Tian, Z. Mao, B. Zhang, Y. Li, Shape optimization of a Savonius wind rotor with different convex and concave sides. *Renew. Energy* **117**, 287–299 (2018)
3. S. Roy, U.K. Saha, Wind tunnel experiments of a newly developed two-bladed Savonius-style wind turbine. *Appl. Energy* **137**, 117–125 (2015)
4. W. El-Askary, M. Nasef, A. Abdel-Hamid, H. Gad, Harvesting wind energy for improving performance of Savonius rotor. *J. Wind Eng. Ind. Aerod.* **139** (2015)
5. S. Hamed, A. Pooria, S. Ali, Aerodynamic performance enhancement of horizontal axis wind turbines by dimples on blades: numerical investigation. *Energy* **195**, 117056 (2020)
6. K. Emeel, T. Dominique, Optimal shape of thick blades for a hydraulic Savonius turbine. *Renew. Energy* **134**, 629–638 (2019)
7. J. Vicente, H. Antonio, A. Prisco, A review on the performance of Savonius wind turbines. *Renew. Sustain. Energy Rev.* **16**, 3054–3064 (2012)
8. B.D. Altan, M. Atilgan, An experimental and numerical study on the improvement of the performance of Savonius wind rotor. *Energy Convers. Manag.* **49**, 3425–3432 (2008)
9. M. Nakajima, S. Iio, T. Ikeda, Performance of double-step Savonius rotor for environmentally friendly hydraulic turbine. *J. Fluid Sci. Technol.* **3**, 410–419 (2008)
10. G.Q. Zhang, J. Schlüter, X. Hu, Parametric investigation of drag reduction for marine vessels using air-filled dimpled surfaces. *Ships and Offshore Structures* (2017)
11. E. Livya, G. Anitha, P. Valli, Aerodynamic analysis of dimple effect over aircraft wing. *Int. J. Mech. Aerosp. Ind. Mechatron. Eng.* **9**(2), 350–353 (2015)
12. D. Raja Joesph, P. Booma Devi, M. Gopalsamy, Investigation on effect of square dimples on NACA0012 airfoil with various Reynolds number. *Int. J. Ambient Energy* (2018)
13. M. Zemamou, M. Aggour, A. Toumi, Review of savonius wind turbine design and performance. *Energy Procedia* **141**, 383–388 (2017)
14. F. Gedyon, B. Addisu, V. Chandraprabu, P. Mohanram, Effects of dimples on aerodynamic performance of horizontal axis wind turbine blades. *Int. Res. J. Eng. Technol.* **07**(01), 525–539 (2020)
15. K.K. Arun, V.R. Navaneeth, S. Sam Vimal Kumar, R. Ajay, Analyzing the effect of dimples on wind turbine efficiency using CFD. *Int. J. Appl. Eng. Res.* **13**(6), 4484–4489 (2018)
16. C.M.J. Tay, T.T. Lim, *Drag Reduction with Teardrop-Shaped Dimples* (Flow Control Conference, Atlanta, Georgia, 2018)
17. R. Ridwan, I. Setyawan, Setiyono, Performance of vertical axis Savonius wind turbines related to the fin number on the blade. *Int. Conf. Des. Energy Mater. Manuf. Mater. Sci. Eng.* **539** (2019)
18. S.F. Pamungkas, D.S. Wijayanto, H. Saputro, I. Widiastuti, Performance ‘S’ type Savonius wind turbine with variation of fin addition on blade, in *The 2nd Annual Applied Science and Engineering Conference, Materials Science and Engineering*, vol 288 (2018)
19. F. Wenehenubun, A. Saputra, H. Sutanto, An experimental study on the performance of Savonius wind turbines related with the number of blades. *Energy Procedia* **68**, 297–304 (2015)
20. M.H. Ali, Experimental comparison study for Savonius wind turbine of two and three blades at low wind speed. *Int. J. Mod. Eng. Res.* **3**(5), 2978–2986 (2013)
21. N.H. Mahmoud, A.A. El-Haroun, E. Wahba, M.H. Nasef, An experimental study on improvement of Savonius rotor performance. *Alexandria Eng. J.* **51**, 19–25 (2012)
22. K.H. Wong, W.T. Chong, N.L. Sukiman, S.C. Poh, Y.C. Shiah, C.T. Wang, Performance enhancements on vertical axis wind turbines using flow augmentation systems: a review. *Renew. Sustain. Energy Rev.* **73**, 904–921 (2017)
23. M. Tartuferi, V. D’Alessandro, S. Montelpare, R. Ricci, Enhancement of Savonius wind rotor aerodynamic performance: a computational study of new blade shapes and curtain systems. *Energy* **79**, 371–384 (2015)

24. M.H. Mohamed, G. Janiga, E. Pap, D. Thevenin, Optimal blade shape of a modified Savonius turbine using an obstacle shielding the returning blade. *Energy Convers. Manag.* **52**, 236–242 (2011)
25. B.D. Altan, M. Atlgan, A. Ozdamar, An experimental study on improvement of a Savonius rotor performance with curtaining. *Exp. Therm. Fluid Sci.* **32**, 1673–1678 (2008)
26. A. Damak, Z. Driss, M.S. Abid, Experimental investigation of helical Savonius rotor with a twist of 180. *Renew. Energy* **52**, 136–142 (2013)
27. K. Kacprzak, G. Liskiewicz, K. Sobczak, Numerical investigation of conventional and modified Savonius wind turbines. *Renew. Energy* **60**, 578–585 (2013)
28. V.A. Joao, G.A. da Silva Júnior, A.P. Petry, Discussion on the verification of the overlap ratio influence on performance coefficients of a Savonius wind rotor using computational fluid dynamics. *Renew. Energy* **38**, 141–149 (2012)
29. R. Gupta, A. Biswas, K.K. Sharma, Comparative study of a three-bucket Savonius rotor with a combined three-bucket Savonius—three-bladed Darrieus rotor. *Renew. Energy* **33**, 1974–1981 (2008)

Finite Time Thermodynamic Investigation of a Solar-Boosted Irreversible OTEC



Aravind Ramachandran , U. B. Arun Shal ,
and Siddharth Ramachandran 

Abstract Ever-increasing population and its resultant stress on the energy sector are pushing us toward more cleaner and sustainable energy solutions. Ocean thermal energy conversion (OTEC) is one such clean energy technology, which has almost no emission and higher reliability. It utilizes the temperature gradient occurring in oceans due to the incident solar radiation to produce electricity. The efficiency and power output of OTEC systems can be increased with the addition of solar collectors for preheating the sea water. In order to design a practical solar-boosted OTEC system, it is imperative to understand the irreversibilities occurring in the heat exchangers of the systems. The limits of such irreversibilities are quantified using the well-established approach of the finite time thermodynamics. It was found out that for a simple OTEC system and a solar-boosted OTEC system, the limits for internal irreversibilities are in a range of 1.01–1.05 and 1.01–1.115, respectively.

Keywords OTEC · Finite time thermodynamics · Energy conversion

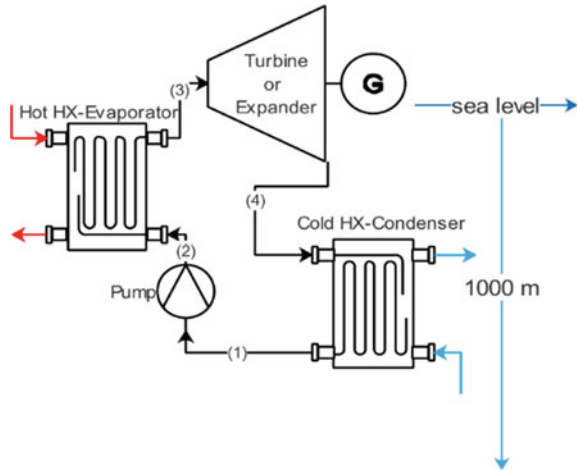
1 Introduction

Oceans cover almost 70% of the total surface area of the earth and absorb a large amount of incident solar radiation. Due to this absorption of solar thermal energy, there exists a temperature gradient between the surface and deep seawater mostly in the areas between the two tropics. The resultant temperature gradients are used as the temperature source and sink to run an organic Rankine cycle (ORC) which in turn produces electricity [1]. During daytime ocean surfaces get heated up by this insolation, whereas the temperatures at depths of oceans are assumed to remain constant irrespective of amount of the solar energy received at the surface (see Fig. 1). The

A. Ramachandran (✉) · U. B. Arun Shal
Government Engineering College, Kozhikode, Kerala, India

S. Ramachandran
Indian Institute of Information Technology, Design and Manufacturing, Kanchipuram, Chennai,
Tamil Nadu, India

Fig. 1 Simple OTEC system



ocean thermal energy conversion (OTEC) systems utilize this temperature difference formed between the surface and depths of oceans to produce electricity [2]. A typical OTEC power plant is able to provide a stable load mainly due to very low variation of temperature over time and has thermal efficiency in the range of 3–5% [3]. The major applications include power supply for seawater desalination units and cold storage units of fisheries industry [4]. Since the 1980s, considerable research efforts have been made into two directions to improve the performance of the OTEC system. The first research direction has been targeted to the thermodynamic optimization of Rankine-based cycles for higher efficiencies [3, 5, 6]. Even in tropical areas, the temperature gradient available is in the range of 20–25 K, where a typical OTEC power plant can get a nominal efficiency [1]. Thus, a large mass flow rates of the sea water and surface area of heat exchangers are required to generate power output in MW range. Plate heat exchangers are normally employed at the condenser and evaporator of the OTEC system [1]. Min-Hsiung et al. [7] investigated the optimal working temperatures of the OTEC system and observed that the cold seawater temperature has a major effect on influencing the optimal condensing temperature better than the optimal evaporating temperature in an ORC.

Uhera et al. [1] investigated the working conditions of a shell- and plate-type heat exchanger and concluded that, it can be used in conditions where the working fluid is seawater due to its non-corrosive characteristics. Further, Aungier et al. [8] observed that for lower vapor-specific volume-induced working fluid, a radial flow turbine will give the optimum results in terms of power production as well as it has non-corrosive characteristics. Yamada et al. [5] numerically investigated the feasibility of incorporating solar energy to superheat the seawater in OTEC, demonstrating that the net efficiency can increase with solar superheating (see Fig. 2). It was observed from various literatures that, a hybrid system which involves the integration of the present simple OTEC system with additional concentric solar collectors can improve the efficiency of the system by above-mentioned method increasing the temperature

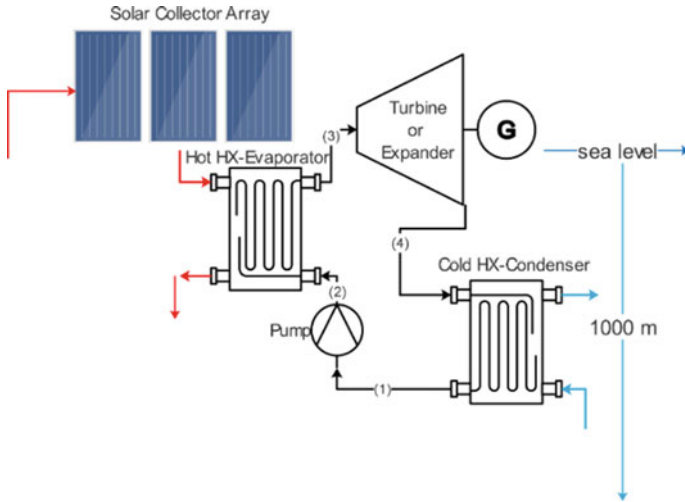


Fig. 2 Solar-boasted OTEC system

gradient formed between the condenser and evaporative heat exchanger (3 to 4%) [9]. Winston et al. [10], for the purpose of integration of solar thermal energy into the existing OTEC cycle, there exists a need to find the optimal solar collector. Since the solar collector for the OTEC system does not need a high concentration of solar irradiation, a compound parabolic concentrator (CPC) type solar collector is chosen as the solar thermal superheater in this study.

Even though previous literatures investigated the possibility of these systems, its components are not yet optimized for maximum power conditions. For this, the well-known approach of finite time thermodynamics was adapted in this investigation [11]. Finite time thermodynamic (FTT) analysis, a new disciple of modern thermodynamics, takes into account endo-reversible nature of cyclic devices by considering heat transfer losses as cyclic irreversibility and optimizes the design parameters with respect to maximum power output [12, 13]. Finite time thermodynamics is utilized, when there is a need to limit that extra expenditure which occurs during energy and entropy production [4, 14, 15]. Based on the above observations, following inferences as objectives are diluted in the present manuscript as,

- To investigate the performance of ocean thermal energy conversion (OTEC) systems enhanced with solar thermal collectors.
- To develop a simple and accurate thermal model to predict the performance of OTEC at preliminary design stages.
- To quantify the effect of internal irreversibility for both OTEC and solar-boasted OTEC for the first time in literature using novel FTT approach.

2 Finite Time Thermodynamic Model of Solar-Boosted OTEC

In order to consider the external irreversibilities, the real-time heat transfer processes happening on finite time as well as finite capacity has to be considered [12, 16]. The amount of heat lost from the sea water is absorbed by the working fluid of the OTEC through an evaporative heat exchanger. This process is assumed to be happening in finite time and finite heat capacity in order to bring the real-time scenario into the picture (see Fig. 3). An energy balance of this process is carried out using first law of thermodynamics and is given below as [11],

$$q_E = Q_E/t_E = U_E A_E (\theta_{LM-E}) = \dot{m}_E C_E (T_{wi} - T_w) \tag{1}$$

where the temperature profile of the evaporative heat exchanger is assumed to be linear and corresponding logarithmic mean temperature difference has been taken as,

$$(\theta_{LM-E}) = \frac{[(T_{wi} - T_w) - (T_{wo} - T_w)]}{\ln \frac{(T_{wi}-T_w)}{(T_{wo}-T_w)}} \tag{2}$$

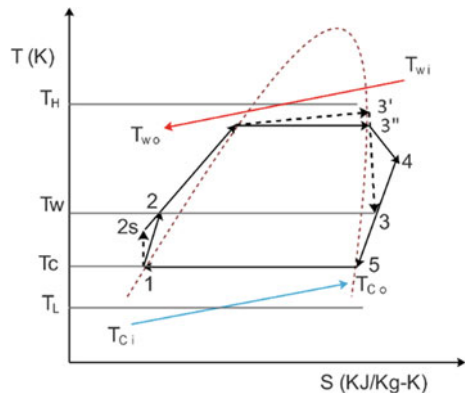
Similarly, the heat transfer process in the condenser is given in Eqs. (3) and (4).

$$q_C = Q_C/t_C = U_C A_C (\theta_{LM-C}) = \dot{m}_C C_C (T_{ci} - T_{co}) \tag{3}$$

$$(\theta_{LM-C}) = \frac{[(T_1 - T_{ci}) - (T_1 - T_{co})]}{\ln \frac{(T_1-T_{ci})}{(T_1-T_{co})}} \tag{4}$$

The total time of the cyclic process is assumed to be the sum of individual processes happening in the thermodynamic Rankine cycle and further the time for isentropic

Fig. 3 T-S diagram



expansion and isentropic compression processes are considered negligible.

$$t_{cy} = t_E + t_C + t_{12} + t_{34} \tag{5}$$

$$t_{cy} = t_E + t_C \tag{6}$$

Equations (1) and (3) are substituted in Eq. (5) to realize total cyclic time in terms of heat addition and rejection.

$$t_{cy} = \frac{Q_E}{\dot{m}_E c_{pE} (T_{wi} - T_{wo})} + \frac{Q_C}{\dot{m}_C c_{pC} (T_{ci} - T_{co})} \tag{7}$$

where the warm seawater outlet temperature and cold seawater outlet temperature are given as Eqs. (8) and (9), respectively, as,

$$T_{wo} = T_w + (T_{wi} - T_w) e^{\left[\frac{-U_E A_E}{\dot{m}_E c_{pE}} \right]} \tag{8}$$

$$T_{co} = T_l + (T_l - T_{ci}) e^{\left[\frac{-U_C A_C}{\dot{m}_C c_{pC}} \right]} \tag{9}$$

Equations (8) and (9) are substituted in Eq. (7) and modified as,

$$t_{cy} = \frac{Q_E}{\alpha (T_{wi} - T_w)} + \frac{Q_C}{\beta (T_l - T_{ci})} \tag{10}$$

where α and β are the product of overall heat transfer coefficient and surface area of the heat exchangers at warm, cold side and are given by Eqs. (11) and (12),

$$\alpha = \dot{m}_C c_{pC} \left(1 - e^{\left[\frac{-U_E A_E}{\dot{m}_E c_{pE}} \right]} \right) \tag{11}$$

$$\beta = \dot{m}_C c_{pC} \left(1 - e^{\left[\frac{-U_C A_C}{\dot{m}_C c_{pC}} \right]} \right) \tag{12}$$

Further it is assumed that the performance of evaporator and condenser is same; hence, the time taken for the heat transfer is also same.

$$t_E = t_C \tag{13}$$

By combining the first and second law of thermodynamic, the heat addition from the arm seawater and heat rejected to the cold seawater is given as Eqs. (16) and (17).

$$W = Q_E - Q_C \tag{14}$$

$$\frac{Q_E}{T_w} = \frac{Q_C}{T_1} \tag{15}$$

$$Q_E = \frac{w * T_w}{T_w - T_1} \tag{16}$$

$$Q_C = \frac{w * T_1}{T_w - T_1} \tag{17}$$

The power output from the thermodynamic OTEC cycle is given as the ratio of work done to the cyclic process time [12],

$$P = \frac{W}{T_{cy}} = \alpha(T_{wi} - T_w) \left[\frac{T_w(\alpha + \beta) - \alpha T_{wi} - \beta T_{ci}}{(\alpha + \beta)T_{wi} - \alpha T_{wi}} \right] \tag{18}$$

In order to maximize the power output, Eq. (18) is differentiated with respect to the mean temperature of heat addition ($\frac{dP}{dT_w} = 0$) to get the optimal conditions. The optimal mean temperature of heat addition and rejection is found to be,

$$T_w = \gamma\sqrt{T_{wi}} \quad \text{and} \quad T_1 = \gamma\sqrt{T_{ci}} \tag{19}$$

where $\gamma = \left[\frac{\alpha\sqrt{T_w} + \beta\sqrt{T_{ci}}}{(\alpha + \beta)} \right]$.

Equation (19) is substituted in Eq. (18) in order to get the maximum power output, and its corresponding thermal efficiency is given as,

$$P_{max} = \frac{\alpha\beta(\sqrt{T_{wi}} - \sqrt{T_{ci}})^2}{(\alpha + \beta)} \tag{20}$$

$$\eta = 1 - \sqrt{\frac{T_{ci}}{T_{wi}}} \tag{21}$$

Further, it is vital to consider and quantify internal irreversibilities (ΔS_{IR}) of the thermodynamic Rankine cycle to predict the performance of OTEC in real time [8]. So in accordance with Eq. (15), the second law of thermodynamics is expressed as,

$$\int \frac{dQ}{T} = \frac{Q_E}{T} - \frac{Q_C}{T} \leq 0 \tag{22}$$

$$\frac{Q_c}{T_1} / \frac{Q_E}{T_w} = \frac{(S_4 - S_1)}{(S_3 - S_2)} = \Delta S_{IR} \tag{23}$$

$$\Delta S_{IR} \frac{Q_E}{T_w} = \frac{Q_C}{T_1} \tag{24}$$

The internal irreversibility parameters can be generalized as the ratio of entropy generation at heat rejection process to heat addition process. Thus, the maximum power output and the corresponding thermal efficiency from Eqs. (20) and (21) can be modified as [15],

$$P_{\max} = \frac{\alpha\beta(\sqrt{T_{wi}} - \sqrt{\Delta S_{IR} T_{ci}})^2}{(\alpha + \beta)} \tag{25}$$

$$\eta = 1 - \sqrt{\frac{\Delta S_{IR} T_{ci}}{T_{wi}}} \tag{26}$$

Equations (25) and (26) are solved simultaneously with respect to operating parameters such as mass flow rate, convective heat transfers coefficient, inlet temperature of warm and cold seawater, surface area of the evaporator and condenser heat exchangers.

In addition, internal irreversibilities are quantified and incorporated to realize its effect on maximum power output and corresponding thermal efficiency.

3 Results and Discussion

In order to investigate the performance of an irreversible OTEC, the external and internal irreversibilities must be accounted. Apart from the external irreversibility causing parameters, the effect of frictional losses, entropy generation inside the turbine and pump, working fluid imbalances are accounted as a single parameter, i.e., internal irreversibility parameter and investigated.

Initial values to be assumed are taken from previous study and is given in Table 1. These parameters and FTT model equations are coded into the Engineering equation solver (EES), and the results were compiled.

Table 1 Parameters and initial values taken for investigation [5]

Sl. No.	Parameters	Values
1	Overall heat transfer coefficient of evaporator	4 kW/m ² K
2	Overall heat transfer coefficient of condenser	3.5 kW/m ² K
3	Area of evaporator	232 m ²
4	Area of condenser	390 m ²
5	Specific heat of water (warm and cold)	4.025 kJ/kg K
6	Mass flowrate of seawater	260 kg/s
7	Inlet temperature of warm seawater	298.7 K
8	Inlet temperature of cold seawater	277.4 K

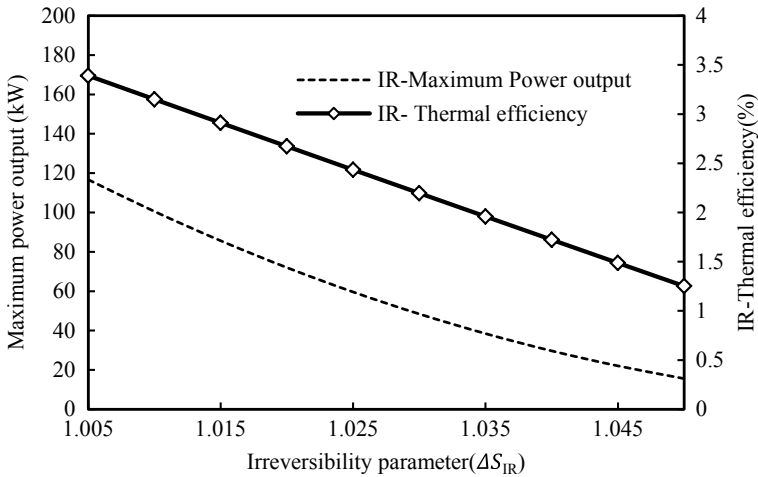


Fig. 4 Variation in maximum power output and corresponding thermal efficiency with internal irreversibility parameter for a simple OTEC system

For a simple OTEC system, it is observed that the limits of this internal irreversibility parameter is between 1 and 1.05 for the operation conditions assumed for this investigation; i.e., when this parameter is unity then the thermodynamic cycle must be internally reversible. From Fig. 4, it is clear that the increase in internal irreversibility parameter decreases the maximum power output exponentially and corresponding thermal efficiency linearly.

The efficiency of a simple ORC can be increased by increasing the temperature gradient between the sink. Keeping this in mind researchers have found out that on addition of solar collectors to preheat the warm seawater, the temperature at the inlet of the evaporative heat exchanger can be increased by about 7% [17]. This temperature increase results in the increase of maximum power output by 5 times (up to 500 kW) due to additional heating of solar collectors. Since the external irreversibilities are considered it is imperative to investigate the importance of temperature degradation in the source and sink of any thermodynamic cycles. In Fig. 5, the warm seawater inlet temperature has been varied from 294 to 320 K in order to investigate its effect on performance of solar-boosted OTEC system.

As in the case of solar-boosted irreversible OTEC, the external and internal irreversibilities must be accounted. It is observed that the limits of this internal irreversibility parameter are between 1 and 1.115 for the operation conditions assumed for this investigation. (Note that the average temperature of heat addition in this case is taken as 320 K [17], as in the case for solar preheating of warm seawater.)

From Fig. 6, it is clear that the increase in internal irreversibility parameter decreases the maximum power output exponentially and corresponding thermal efficiency linearly. Irreversibilities of the system can be reduced by heat addition at higher temperature and heat rejection at lowest possible temperature. Generally, this is

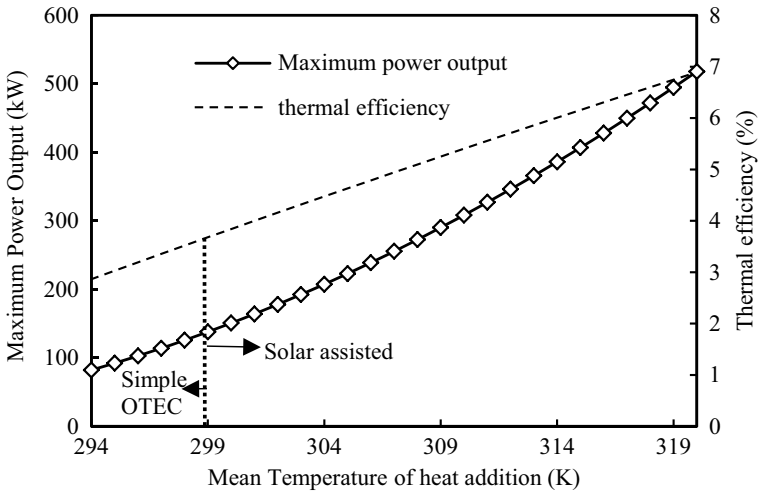


Fig. 5 Variation in maximum power output and thermal efficiency for solar-assisted OTEC system

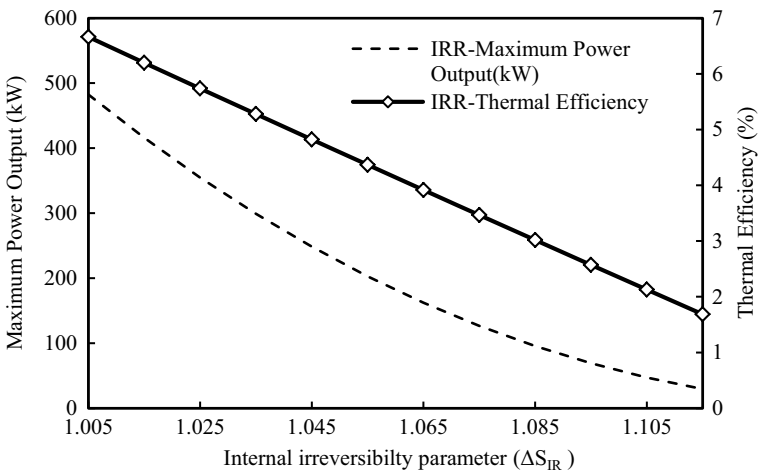


Fig. 6 Variation in maximum power output and corresponding thermal efficiency with internal irreversibility parameter for a solar-boostered OTEC system

achieved by operating the sink at lower pressure and the source at higher pressure. Enhancement of effectiveness of the condenser and evaporator can also reduce the irreversibilities, but it comes at the cost of increased pressure drop, pumping power, and capital cost.

Frictional losses in the pipes, irreversible expansion and compression of the working fluid at the turbine and pumps are another major source of entropy generation in the cycle [18–20]. Expansion of the working fluid in the turbine and its

resultant losses can be subdued to an extent by superheating the working fluid at higher pressure. However, it comes with increased irreversibilities at the evaporator side heat exchanger. Thus, it becomes clear that design and enhancement of heat exchangers is vital to improve the performance of such systems.

4 Conclusion

An irreversible thermodynamic OTEC cycle is modeled and optimized using finite time thermodynamic approach. Both external and internal irreversibilities are quantified and its effect on performance of the OTEC system is investigated and it was found that,

1. The limits of internal irreversibility parameter are 1–1.05 for a simple OTEC system.
2. The limits of internal irreversibility parameter are 1–1.115 for a solar-boosted OTEC system.

It can be noted that for a given value of internal irreversibility (e.g., 1.03), the thermal efficiency and maximum power output for a solar-boosted OTEC system will be always higher than a simple OTEC system. Further the study can be used as a base for multiobjective optimization using maximum power output and corresponding thermal efficiency as objective functions.

References

1. H. Uehara et al., Shell-and plate type heat exchangers for OTEC plants. *J. Solar Energy Engineering*, Elsevier Ltd, **106**(3), 286–290 (1984); **34**(7), 1752–1758
2. S. Rao et al., *Energy Technology Nonconventional, Renewable and Conventional* (Khanna Publication, 2014)
3. H. Uehara, Y. Ikegami, Optimization of a closed-cycle OTEC system. *J. Solar Energy Eng.* **112**, 247–256 (1990)
4. B. Andresen, Current trends in finite-time thermodynamics. *Angewandte Chemie Int. Edition-Wiley* **50**(12) (2011)
5. N. Yamada, A. Hoshi, Y. Ikegami, Performance simulation of solar-boosted ocean thermal energy conversion plant. *Renew. Energy* (2009)
6. F. Sun et al., Optimization design and exergy analysis of organic Rankine cycle in ocean thermal energy conversion. *Appl. Ocean Res.* Elsevier Ltd **35**, 38–46 (2012)
7. Y. Min-Hsiung, Y. Rong-Hua, Analysis of optimization in an OTEC plant using organic Rankine cycle. *Renew. Energy* **68**, 25–34 (2014)
8. R.H. Aungier, Turbine aerodynamics: axial-flow and radial-flow turbine design and analysis. ASME Press 236–240 (2006)
9. N. Khan, A. Kalair, N. Abas, A. Haider, Review of ocean tidal, wave and thermal energy technologies. *Renew. Sustain. Energy Rev.* **72**, 590–604 (2017)
10. R. Winston, Principles of solar concentrators of a novel design. *Sol. Energy* **16**, 89–95 (1974)
11. F.L. Curzon, B. Ahlborn, Efficiency of a Carnot engine at maximum power output. *Am. J. Phys.* **0002-9505**(43), 22–24 (1975)

12. S.C. Kaushik, S.K. Tyagi, P. Kumar, Finite time thermodynamics of power and refrigeration cycles, in *Finite Time Thermodynamics of Power and Refrigeration Cycles* (Springer International Publishing, 2017)
13. S. Ramachandran, N. Kumar, M.V. Timmaraju, Thermodynamic analysis of solar low-temperature differential stirling engine considering imperfect regeneration and thermal losses. *ASME. J. Sol. Energy Eng.* **142**(5), 051012 (2020)
14. D. Ahmet, S.S. Oguz et al., Optimization of thermal systems based on finite-time thermodynamics and thermoconomics. *Prog. Energy Combust. Sci.* **30**(2), 175–217 (2004)
15. A. McMahan, S.A. Klein, D.T. Reindl, A finite-time thermodynamic framework for optimizing solar-thermal power plants. *J. Sol. Energy Eng.* **129**(4), 355–362 (2007)
16. T. Yasunaga, Y. Ikegami, Finite-time thermodynamic model for evaluating heat engines in OTEC. *Entropy* **211**, 22 (2020)
17. H. Aydin et al., Off-design performance analysis of a closed-cycle ocean thermal energy conversion system with solar thermal preheating and superheating. *Renew. Energy (Elsevier Ltd.)* **72**, 154–163 (2014)
18. H.V. James, T.R. Lynn, L. Louis, An assessment of Florida's ocean thermal energy conversion (OTEC) resource. *Renew. Sustain. Energy Rev.* **75** (2017)
19. C. Lingen, W. Chih, S. Fengrui, Finite time thermodynamic optimization or entropy generation minimization of energy systems. *J. Non-Equilib. Thermodyn.* **24**(4) (1999)
20. A. Durmayaz et al., Optimization of thermal systems based on finite-time thermodynamics and thermoconomics. *Prog. Energy Combust. Sci.* **30**(2), 175–217 (2004)

Process Parameter Optimization of Fused Deposition Modeling Using Taguchi's Design of Experiment



Pankaj B. Ranade, Shivam H. Dandgavhal, Apurva K. Dhokane, and Apoorva R. Kale

Abstract Fused Deposition Modeling (FDM) is an Additive Manufacturing (AM) technique that constructs objects layer upon layer and is a state of art evolving technology with the ability to produce intricate 3D geometries and parts, with huge potential to make production system flexible in terms of product variety and quantity. Building 3D printed consumer end functional product with FDM is challenging because of variation in multiple process parameters that affects the product quality. This paper presents empirical research on minimizing process input parameter variation to find the optimal setting and get the best quality surface roughness (Ra) value of 3D printed parts. Full factorial design of experiment is a challenging method to investigate influence of multiple process input parameters on objective parameters, which may/may not behave linearly and a large set of trials will be required. Taguchi's Design of Experiment (DOE) method of orthogonal arrays is used in this paper to achieve parametric optimization in minimum number of trials. A brief literature review and multiple pilot experimentations were performed to identify the influential input process parameters and their discrete quantitative levels affecting the objective parameter (Ra value) which were namely Layer Height, Print Speed, Nozzle Temperature and Loop Count (Shell Thickness). Product samples were 3D printed using PLA material and corresponding surface roughness data for each trial was recorded. Signal to Noise ratio analysis was performed and main effect plots were analyzed to discover the combination of optimal process parameters for maximizing product quality, which stated that Layer Height affected the most followed by Nozzle Temperature, Loop Count and Print Speed. Regression Analysis was performed to predict the surface roughness obtainable by conducting trial using optimal parameters and confirmation trial was run to validate the results.

Keywords 3D printing · FDM · Optimization · Taguchi · Design of experiment · Regression analysis · ANOVA

P. B. Ranade (✉) · S. H. Dandgavhal · A. K. Dhokane · A. R. Kale
Department of Mechanical Engineering, KKWIEER, Nashik, Maharashtra, India

© The Author(s), under exclusive license to Springer Nature Singapore Pte Ltd. 2022
M. L. Kolhe et al. (eds.), *Smart Technologies for Energy, Environment and Sustainable Development, Vol 1*, Springer Proceedings in Energy,
https://doi.org/10.1007/978-981-16-6875-3_69

861

1 Introduction

Fused Deposition Modeling is a 3D printing (Additive Manufacturing) technique that allows production of intricate geometric objects by layer upon layer accumulation of material filament. In this process, filament material is heated up to melting temperature and deposited by nozzle layer by layer on the platform bed. The nozzle/extrusion head and platform/bed is numerically controlled and can be translated in lateral and longitudinal directions respectively. The part is built from bottom to top layer by layer at a time as the extruder head follows the path generated by slicing software. Inferior Surface Finish, Poor mechanical properties, need for post processing and slow printing speeds are the major challenges faced constraining the use of AM techniques for mass production. Flexibility in production of product variety and quantity is feasible with use of additive manufacturing techniques over the conventional subtractive manufacturing techniques. Due to large competition in global markets and changing market dynamics, it's the need of time to provide customized and personalized products, induction of new business models, reduced lead times and induce flexibility in production systems by fabrication intricate parts in medium to small sized batches [1, 2]. Need of Molds, Dies and new tooling is eliminated whenever design changes are made and highly customized products can be delivered due to small cycle time in product design stage. Building part in single operation, Minimum raw material wastage, No/minimum tooling requirement and setup change has made AM more desirable.

1.1 Background

3D printing is the need of time in Industry 4.0 and a major component of flexible manufacturing systems. Fused Deposition Modeling (FDM), Stereo Lithography Apparatus (SLA), Selective Laser Sintering (SLS) and Laminated Object Manufacturing (LOM) are the types of 3D Printing processes. FDM has become a hot research topic owing to its ability to produce complex 3D geometries, ease of use, no tooling, use of low melting point polymers, non-laser application, low cost and maintenance. Automobile, aerospace, prosthetics, biomedical, drug delivery, smart home equipment's, interior decoration and gifts are the wide applications of FDM. In 2014, first FDM 3D printer was sent to space by NASA and US National Aeronautics to print the spanner for repair and maintenance space stations [3] In addition this NASA has also planned to send the second 3D Printer to space for recycling 10,000 plastic bags [4].

1.2 Filament Materials

FDM facilitates printing of wide range of materials namely Polylactic Acid (PLA), Acrylonitrile Butadiene Styrene (ABS), Carbon Fibre, Polyethylene terephthalate glycol (PETG), High Impact Polystyrene (HIPS), Bio filaments and Nylon. PLA and ABS are the most widely used printing materials owing to its good mechanical properties. 3D Printing material is the key factor limiting the development of this booming technology. Extensive research is being conducted on interface bonding properties, material mechanical properties, PLA modification by improving crystallinity of molecular chains and cross linking state. Compound Modification of PLA can facilitate the improvement in heat stability, biocompatibility, antistatic property, electrical conductivity, temperature-controlled heating property and electromagnetic shielding for expanding the application range of 3D Printed FDM parts.

1.3 Applications of Fused Deposition Modeling

3D Printing has diverse applications ranging from simple household applications, interior and fashion designing to intricate parts in prosthetics, aerospace engineering, robotics, automobile, etc. Fused Deposition Modeling was used to manufacture Aurora jet aircraft [5]. Rapid Prototyping to visualize the cosmetic model of product is a major application of 3D printing. Considerable growth in field of composites has developed the necessity to make fibre reinforced composite filament material for fabricating industrial products [6]. Customized inductive coil for MRI applications, composite dielectric polymer material, energy storage conductive filaments, hollow resonators, sinusoidal valve and corrugations and other 3D printed micro-electronics are characteristic electrical applications of FDM process. Printing Scaffolds, Scalpel, surgical equipment's, biomedical prosthetics, dentistry and edentulous jaws, orthopaedic applications, tissue synthesis/fabrication using bio filaments are the characteristic biomedical applications of FDM process.

1.4 Process Parameters

Process parameters are the controllable and monitored value of a particular process that may directly or indirectly affect the objective of that process. Process Parameters in an FDM process can be controlled during the slicing of 3D model in a slicer software during preparation of GCode.

- **Surface Roughness:** The micro-irregularities on the surface caused by various machining and non-machining operations. It is the deviation of the profile surface from the mean. It is expressed in microns and generally, smooth surface roughness

is desired to minimize friction and facilitate efficient working. It is most commonly considered as an objective output parameter.

- **Layer Height:** It is the vertical thickness of a single layer deposited in an FDM process.
- **Extruder/Nozzle Temperature:** It is the temperature of extruder head where the material filament gets heated up to the melting point.
- **Print Speed:** It is the movement speed of the extruder head while depositing material in lateral directions (mm/sec).
- **Loop Count/Shell Thickness:** Loop Count is the number of exterior shells in a 3D printed object. By changing loop count we are increasing shell thickness of the 3D printed object. A general relation between loop count and shell thickness is $\text{Shellthickness} = \text{Loopcount} \times \text{Nozzlewidth}$.

Poor surface roughness due to subsequent deposition of material is a major drawback of FDM process. In this paper, Taguchi's Design of Experiment and Signal to Noise Ratio analysis has been performed to minimize the Ra value and obtain smooth surface finish by optimizing the input process parameters identified from the literature review and pilot experimentation. PLA material has been used to print the 3d models and trials due to its widespread use and applications. Regression analysis is performed to predict the optimal surface roughness from obtained set of optimal input parameters. Experimental Validation is done by running a confirmation trial.

The structure of the paper is ordered as follows: State of the art literature on optimization of additive manufacturing process has been reviewed and analyzed in Sect. 2. This analysis enabled us to identify and define the problem. Section 3 incorporates the experimental analysis and validation of optimized objective parameters. Results have been discussed in brief in Sect. 4 and concluded in Sect. 5. Finally, the future scope has been remarked in Sect. 6.

2 Literature Review

Several attempts have been made in the literature to investigate the influence of process parameters on the mechanical properties, dimensional accuracy and surface roughness of FDM parts. In FDM 3D printer, the process initiates with designing CAD model and its conversion into Standard Tessellation Language (.STL) file format. This .STL file is then inserted into the slicer software where the FDM parameters like infill density, layer height, etc. can be varied and support structures can be generated as per the requirement. Slice software slices the CAD model into 2D cross section slices as per the input layer height and generates G Code for coordinated movement of extruder nozzle in X - Y direction and platform bed in Z direction. Filament material like PLA and ABS is most commonly used and is melted in extruder head which is deposited on the bed as the extruder moves.

Ahmad et al. [8] optimized the cross print pattern, Y axis orientation, support angle and sidewalk offset to minimize the surface roughness of FDM 3D printed

parts using Taguchi's L9 orthogonal array. 3D thermomechanical simulation model was developed by El Moumen et al. [9] capable of computing stresses caused by the temperature gradient in additive manufacturing for investigating defects of ASTM D638 composite polymer. High stress concentration was observed between two layers as a result of rapid fluctuation in temperatures which may cause delamination among the layers of printed parts. Liu et al. [10] reviewed the current state of art ongoing research on mechanical properties, interface bonding, shape precision and functional expansion of applications based on FDM based 3D printing. Importance of aesthetically appealing, low cost and functional 3D printed products has been expressed by Samykano et al. [11]. Raster Angle, Layer Height and Infill Density parameters were considered in this study to achieve good mechanical properties of 3D printed ABS products. An attempt to gain experimental insights on development of large scale prototype of 3D printer was made by Shah et al. [12]. Warping of thermoplastic material due to temperature gradient gave rise to necessity of precise environmental control and efficient melting of material in nozzle during printing operation was found challenging. Kadkhoda-Ahmadi et al. [13] proposed multi-criteria evaluation system based on Analytical Hierarchy Process to investigate manufacturability, resources and process selection issues of additive manufacturing.

Comparative analysis of Multi Objective Optimization using Ratio Analysis (MOORA) and the Technique for Order of Preference by Similarity to Ideal Solution (TOPSIS) method was done by Vinodh and Shinde [14] for optimization of FDM printed parts by optimizing build pattern, fill pattern and layer thickness to achieve optimal surface roughness and building time. Fuzzy Taguchi Analysis and Artificial Neural Network predictive models were utilized by Padhi et al. [15] to investigate the effect of raster angle, air gap, layer height and raster width on optimizing and predicting the optimal dimensional accuracy of ABS products printed by FDM technique. Aerospace industrial case study was explored by Uz Zaman et al. [16] to investigate the impact of infill density, layer height, infill pattern and shell thickness on the compressive strength of FDM printed parts using the ANOVA and S/N ratio analysis. Number of contour loops/shell thickness and print speed was the most important influential parameter affecting the material consumption, dimensional accuracy and manufacturing time of FDM products in the study conducted by Barkoczy et al. [17] using the design of experiments. Artificial neural network (ANN), Response surface methodology coupled with genetic algorithm (RSM-GA) and artificial neural network coupled with genetic algorithm (ANN-GA) were used by Deswal et al. [18] to optimize the dimensional precision of FDM parts by considering build orientation, number of contours, infill density and layer thickness. Mathematical model presenting the correlation between process parameters and dimensional preciseness was developed and ANN-GA was found to be the most effective method for optimization. Influence of layer thickness, orientation and chemical post processing on dimensional accuracy of ABS FDM parts was studied by Khan and Dash [19]. Shrinkage in dimension was observed after acetone chemical post processing with an increase in surface quality and the use of ethylene solvents were proposed for better results. Taguchi's Design of Experiment was used by Mahmood et al. [20] to optimize the geometric features and dimensional accuracy by considering

13 input process parameters. Increase in deviation from nominal size was observed as the geometric size was increased. Five parameters namely deposition orientation, raster width, layer thickness, raster gap and deposition style with three levels each were considered by Liu et al. [21] to study impact strength, flexural strength and tensile strength of FDM parts by using orthogonal arrays and grey relational analysis. Camargo et al. [22] used central composite design (CCD) to articulate that increase in infill density and layer height will increase tensile strength and flexural strength of PLA-graphene FDM printed parts, whereas the impact energy will decrease with an increase in infill density. Lyu and Manoochehri [23] investigated the reliability of FDM system by studying the degradation of machine components and process parameter deviation. Minimization of cumulative failures and life cycle expenditure was considered as objective parameters in this study and preventive maintenance was suggested. Q-optimal response surface methodology was used by Mohamed et al. [24] to articulate that layer thickness, build orientation, air gap and number of contours/shell thickness were influential on the build time, flexural modulus and material consumption, whereas the road width and raster angle made a minor impact on material consumption and build time. Mathematical model was developed to forecast the material consumption and build time in FDM and ANOVA was utilized to check significance and sufficiency of these models. Design of Experiment method was used by Griffiths et al. [25] to investigate the effects of infill percentage and number of shells/shell thickness on tensile properties and efficiency output in terms of scrap weight minimization. Comparative analysis of two FDM printers in terms of dimensional accuracy output by optimizing the process parameters using factorial design of experiment was undertaken by Galantucci et al. [26]. Gray Taguchi Method and ANN were used by Sood et al. [27] to optimize and predict the dimensional accuracy of ABS FDM printed parts respectively by considering interactions between air gap, layer thickness, raster angle, part orientation and raster width. Shrinkage in dimensions was observed along the length and width, however, thickness was observed to be more than actual dimension. Rao et al. [28] utilized full factorial design for optimizing tensile strength of Carbon fibre PLA by considering printing temperature, infill pattern and layer thickness parameters with three levels each. Data were analyzed by ANOVA and results stated that layer thickness has a significant effect on tensile strength followed by extrusion temperature and infill pattern. Tensile strength and dimensional accuracy of ASTM D638 parts were investigated by Alafaghania et al. [29] and finite element model was proposed for AM. It was remarked that dimensional accuracy is more affected by building direction, layer height and extrusion temperature and less affected by printing speed, infill percentage and infill pattern. High nozzle temperature with large layer height is desired in conjunction with proper building direction for good mechanical properties. Future scope was proposed on studying the effects of cooling rates and environmental conditions on printing process. Taguchis L9 Orthogonal array was selected by Vishwas and Basavaraj [30] to optimize the model orientation, shell thickness and layer height to achieve optimal ultimate tensile strength and dimensional accuracy of ABS parts. ANOVA was performed to get relative percentage contribution of each process parameter. Better bonding strength and axial loading properties were

achieved with thinner layer height. Changes in orientation angle made a significant impact on bonding strength and dimensional accuracy of ABS and Nylon products [31]. High Nozzle temperature, a triangular infill pattern, optimal layer height and high infill density were required to achieve high tensile strength, whereas small layer thickness, low nozzle temperature, hexagonal infill pattern and lower infill density were required to achieve good dimensional accuracy in a study done by Alafaghani and Qattawi [32] by using Taguchi's DOE. Dimensional accuracy and geometric characteristics were optimized by Mahmood et al. [33] by using Taguchi Design of experiment and an increase in deviations with an increase in dimensions and geometric characteristic size was observed. Deviations from nominal size of recessed aspects (holes) were larger and undersized whereas the deviations for extruded aspects (bosses) were small and oversized. Excess dimension along the thickness was observed; whereas shrinkage was observed along the width, length and diameter of part in a dimensional accuracy optimization study taken by Sood et al. [34] using the grey Taguchi L27 orthogonal array tabulated using layer thickness, raster angle, raster width, air gap and build orientation parameters. Hsu and Lai [35] investigated optimal parameter settings for NCKU-1 powder and ZP 100 to achieve better dimensional accuracy using Taguchi and ANOVA analysis. Layer Height, shell and core, location of green parts and binder setting saturation value were the parameters considered in the study. Srivastava and Rathee [36] considered four FDM parameters namely raster width, slice height, air gap and contour width/shell thickness with three levels each to investigate the model material volume using Taguchi analysis. It was reported that air gap had a maximum impact over model material volume followed by contour width and slice height. Comparative analysis of response surface method and Taguchi DOE was done by Tontowi et al. [37] to optimize the tensile strength and dimensional accuracy of PLA printed parts. Layer height, raster angle and temperature were the three input parameters considered and better optimal results were observed in case of RSM over the conventional Taguchi analysis. Experimental Design Methods were used by Santana et al. [38] to investigate the influence of slicing software, infill density, layer height, infill speed, perimeter speeds, first layer height, nozzle temperature and multiplier over the dimensional accuracy of PLA printed products. High influence of slicing software and its strategic G Code over the quality of printed products was reported in this paper. Huynh et al. [39] utilized fuzzy Taguchi approach over conventional Taguchi method to improve the dimensional accuracy of PLA products by optimizing layer height, print speed, build style and infill density of FDM process. Alsofi and Elsayed [40] investigated the impact of change in measuring direction of surface roughness. Surface roughness was measured at 0°, 45° and 90° angles with respect to build orientation. Moderate to high variation from mean was observed in roughness values for 45° and 90° measuring angle, however, roughness values were found to be too small and vulnerable at 0° measurement angles.

2.1 Inferences from Literature Review

State of art latest literature was reviewed in Sect. 2 and following inference has been drawn on the same. It was observed that a significant amount of research has been done on optimizing the process parameter of a single material. From Fig. 1, it has been observed that ABS and PLA filament material has been the choice of researchers due to its wide usage, chemical properties, mechanical properties and wide range of applications.

Taguchi’s Method of Optimization has been the most preferable method for researchers for optimizing the process parameters of fused deposition modelling followed by response surface methodology, Full Factorial DOE and Q-optimal method. Unlike Full Factorial DOE, Taguchi’s DOE method of using special orthogonal arrays enables the researchers to get the optimal results in a minimum number of trials. Artificial Neural Network, Genetic Algorithm and Regression Analysis have been used in most cases to predict the outcomes of response parameter. ANOVA remains the most preferred choice of researchers to investigate the contribution percentage of each individual input parameter under consideration.

Gray relational analysis methodology has been used by researchers to achieve multi objective parametric optimization. As shown in Fig. 2, High importance has been given by the researchers to optimizing the dimensional accuracy of FDM parts followed the ultimate tensile strength as objective parameter. However, very little research has been performed on optimizing the surface roughness and aesthetics quality of FDM printed parts.

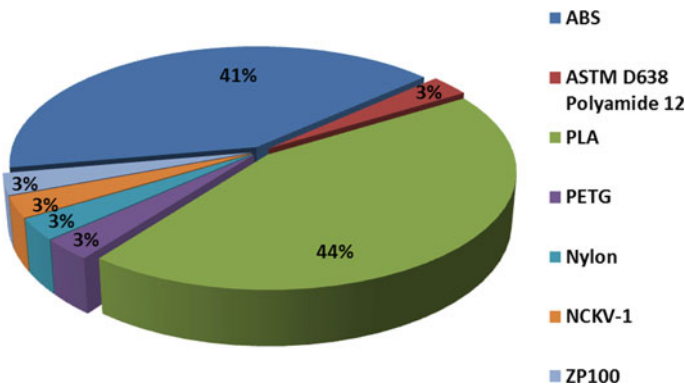


Fig. 1 Percentage comparison of frequency of material used

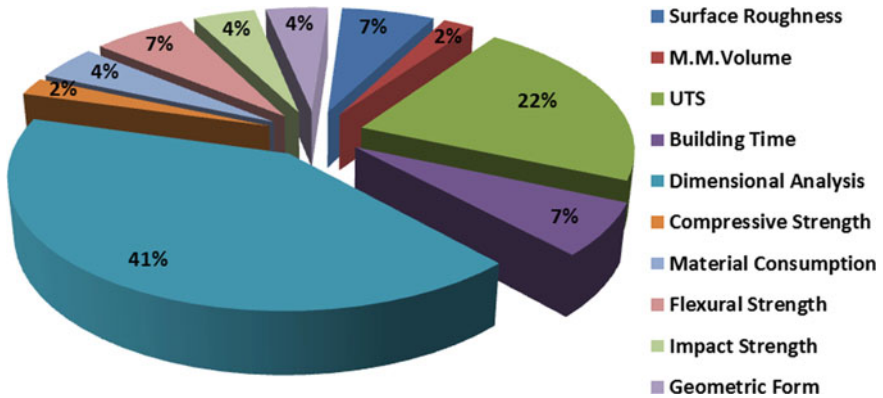


Fig. 2 Percentage comparison of frequency of objective parameters focused by researchers

3 Research Methodology and Experimental Details.

Taguchi’s Design of Experiment methodology [41] has been followed in this study to optimize the process parameters of FDM and get minimum possible value of surface roughness. Main objective of this method was to make the system design robust by nullifying the losses that occurred due to variation in environmental, manufacturing, cumulative and other miscellaneous parameters. Figure 3 depicts the methodology followed in this paper in brief.

1. Conduct	• Literature Review of SCI Journals is carried out
2. Gray Areas	• Grey Areas and Objective is identified
3. Application	• Fused Deposition Modelling 3D Printing
4. Material	• Polylactic Acid
5. Select	• Input and Response Parameters
6. DOE	• L9 Orthogonal Array
7. Taguchi Analysis	• Taguchi Analysis to Find Optimal Ra Value
8. Validation	• Experimental Validation is done

Fig. 3 Research workflow

3.1 Design of Experiment

Desired designed product quality can be achieved by the three step design procedure suggested by Taguchi.

- **System Design.** This stage is a synthesis and conceptualization of a process or product where, the innovation, theories and information in technological domain are used to find the correct combination of parts, design factors, material and processes to satisfy the operative specifications of the product.
- **Parameter Design.** Optimal process parameters are found using Taguchi's DOE for getting good operational performance & make the system process robust against noise or uncontrollable parameters.
- **Tolerance Design.** This stage allows us to improve the product quality by imparting tightened tolerances in different conditions without altering the material of part.

3.2 Orthogonal Array

Investigating the process parameters by minimal number of experiments has been made possible by the use of Taguchi's design of experiment. Orthogonal arrays like L_{27} , L_{18} , L_{16} , L_{12} , L_9 , L_8 and L_4 has been implemented in Taguchi's method to test the influence of varying control process parameters. Experimental trials with their corresponding process parameters are organized in rows while the control variables with their respective levels have been specified in columns. Orthogonal Array is selected with the use of the following formula:-

$$N_{\text{Taguchi}} = 1 + NV \times (L - 1)$$

where,

N_{Taguchi}	Number of trials to be run,
NV	Number of parameters under consideration,
L	Number of levels corresponding to control variable (eg. Low, Medium, High).

3.3 Stepwise Taguchi Procedure

Product and process quality can be improved by Taguchi's approach of orthogonal arrays for statistical design of experiment methodology.

Define objective output control parameters for the optimization process. Final output desired parameter to be improved is finalized. Standard examples of such are

material removal rate (MRR), cost, weight, surface roughness (Ra), hole diameter and electromagnetic radiation, etc.

Identify uncontrollable test conditions, parameters and noise factors. Factors such as part degradation and environmental conditions, which are uncontrollable are treated as noise variables and may create foul effects on product/process quality and functional performance.

Identify the influential input control process parameter. Input variable control variable with significant effect on objective parameter must be identified with their respective levels in discrete steps.

Design the matrix experiment and data analysis procedure. This stage includes an appropriate selection of orthogonal array as per the application and matrix experimentation with properly defined data analysis technique.

Conducting Matrix Experimentation. Trials should be conducted as per the tabulated matrix of experiments and corresponding value of response parameter should be noted for each trial. Trial may consist of running a mathematical model, simulation models, hardware experiments or computer algorithm.

Analyze the data and find the optimal level. Signal to Noise Ratio (SNR) and Mean Standard Deviation (MSD) is calculated at this stage to obtain the optimal input process parameters achieving for desired objective.

Predicting objective parameters at optimal levels. Objective parameters should be forecasted with an obtained set of optimal process parameters for sake of experimental validation by running an experimental check.

3.4 Experimental Setup

Jak Machinery JM1200 Fused Deposition Modeling type of 3D Printer (Fig. 4.) has been selected to conduct the experimentation. Mitutoyo SJ 210 Surface Roughness Tester is used to measure the surface roughness of the printed parts. Table 1 provides detailed setup specifications of the JM1200 machine.

3.5 Material Selection

In Sect. 2, brief literature review has been conducted and wide spread application of Poly(lactic acid) (PLA) has been identified. In this study, PLA material has been selected due to its low melting point, mechanical properties and wide applications.



Fig. 4 Jak Machinery JM1200 FDM type 3D printer and Mitutoyo SJ 210 surface roughness tester respectively

Table 1 Technical specification of Jak Machinery JM1200 FDM printer

S. No.	Parameter	Specification	S. No.	Parameter	Specification
1	Printing volume	1100 × 600 × 700	7	Power consumption	1000 W
2	Motion speed	250 mm/s	8	Motor resolution	0.0125 mm
3	Printing speed	90 mm/s	9	Nozzle diameter	0.8 mm
4	Vertical layer resolution	0.05 mm	10	Max nozzle temperature	260 °C
5	Extruder type	Direct drive	11	Machine weight	50 kg
6	Max bed temperature	80 °C	12	Input power	220 V AC

3.6 Identification of Process Parameters and Corresponding Levels

Developed CAD model in .STL format was inserted in Craftware slicing software where the functional specifications and control factors were identified. Working parameters influencing the surface roughness (Ra value) of FDM part were identified. Selection of parameters affecting surface roughness was done with the help of a literature review carried out in Sect. 2 and by running individual pilot experimentations. During pilot experimentations, it was observed that significant improvement in surface roughness was observed when the number of loop counts

Table 2 Control factors were kept constant during experimentation

S. No.	Control factors	Values	S. No.	Control factor	Value
1	Nozzle/extruder width	0.8 mm	4	Infill density	25%
2	Filament diameter	1.75 mm	5	Bed temperature	60 °C
3	Infill pattern type	Square	6	First layer height	0.4 mm

Table 3 Variable input process parameters with respective levels

S. No.	Parameters	Levels		
		Low	Medium	High
1	Print speed in mm/s	20	40	60
2	Extruder temp in °C	210	220	230
3	Layer height in mm	0.2	0.3	0.4
4	Contour loop	2	4	6

(Shellthickness = Loopcount × nozzlewidth) is increased. Selection of Levels (Low, Medium, High) corresponding to each input process parameter was done with help of material properties catalogue and considering the technical specifications of machine as given in Table 1. Control factors kept constant during the experimentation are given in Table 2, whereas the variable input process parameters with their respective levels are tabulated in Table 3.

3.7 Selection of Orthogonal Array

Minimum number of experiment to be conducted in an orthogonal array is given by $N_{Taguchi} = 1 + NV \times (L - 1)$ where, $N_{Taguchi}$ = Number of experiments to be conducted, NV = Number of variables L = Number of levels. Four FDM parameters are considered as input process parameters namely, printing speed, extruder temperature, layer height, number of contour loops and each parameter has three levels—namely low, medium and high respectively.

- (1) Number of control factors = 4
- (2) Number of levels for each control factor = 3
- (3) Number of experiments to be conducted = $1 + 4(3 - 1) = 9$.

As per the calculations, minimum of nine experiments are to be conducted and $L_9 (3^4)$ orthogonal array is selected which is tabulated in Table 4.

Table 4 DOE L9 orthogonal array

Trial No.	Input parameters			
	Print speed in mm/s	Extruder temp in °C	Layer height in mm	Contour loop count
1	20	210	0.2	2
2	20	220	0.3	4
3	20	230	0.4	6
4	40	210	0.3	6
5	40	220	0.4	2
6	40	230	0.2	4
7	60	210	0.4	4
8	60	220	0.2	6
9	60	230	0.3	2

4 Results and Discussion

A Cube of Dimension 50 mm × 40 mm × 40 mm has been selected for printing purposes and nine trials (Table 4) as per the orthogonal array have been performed (Fig. 5).

4.1 Experimental Data Collection

As per the proposed workflow and DOE experiments are conducted using PLA material. Surface roughness (Ra) values are measured perpendicular [40] to the printing direction using the Mitutoyo SJ 210 surface roughness tester at three different points on the printed part and collected data are tabulated in Table 5. Corresponding mean standard deviation as per the data is calculated.

Fig. 5 Nine trials conducted as per the orthogonal array



Table 5 Experimental readings of Ra for PLA

Trial No.	Input parameters			Loop count	Response parameter			Mean Ra (μm)	MSD	SNR
	Print speed (mm/s)	Nozzle temp ($^{\circ}\text{C}$)	Layer height (mm)		Ra 1 (μm)	Ra 2 (μm)	Ra 3 (μm)			
1	20	210	0.2	2	27.128	23.162	27.317	25.87	672.88	- 28.28
2	20	220	0.3	4	27.726	30.818	28.843	29.13	850.13	- 29.29
3	20	230	0.4	6	44.805	37.103	36.791	39.57	1579.23	- 31.98
4	40	210	0.3	6	25.938	26.878	26.254	26.36	694.83	- 28.42
5	40	220	0.4	2	34.098	34.606	35.015	34.57	1195.43	- 30.78
6	40	230	0.2	4	48.042	43.713	42.952	44.90	2021.24	- 33.06
7	60	210	0.4	4	26.475	26.244	27.005	26.57	706.31	- 28.49
8	60	220	0.2	6	40.013	39.939	36.370	38.77	1506.31	- 31.78
9	60	230	0.3	2	24.980	25.030	25.260	25.09	629.52	- 27.99

4.2 Signal to Noise Ratio (SNR)

The term “signal” signifies the desirable effect of output characteristic and the term “noise” signifies unwanted effect or disturbance which influences the output characteristic. The signal to noise ratio is given by S/N ratio, $\eta = -10 \log (\text{MSD})$. High SNR signifies high signal and weak noise making the process robust. Lower the better SNR, Higher the better SNR and nominal the better SNR are three types of SNR ratios. To obtain a minimum surface roughness value, the lower-the-better SNR ratio must be considered. The mean square deviation (M.S.D.) for the smaller—the-better quality characteristic is expressed as

$$\text{MSD} = \frac{1}{n} \sum_{i=1}^n y_i^2$$

where,

- n number of repetitions or observations and
- y_i the observed data.

4.3 Optimal Process Parameters

Main effect plot for the mean Ra value (Fig. 6) has been charted to study the influence of individual parameters on surface roughness. Main effect plot for Signal to Noise

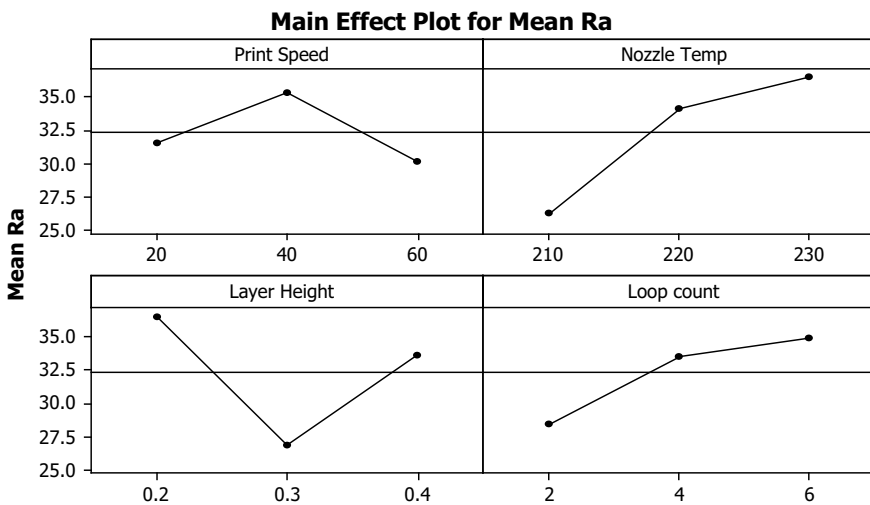


Fig. 6 Main effect plot of mean Ra

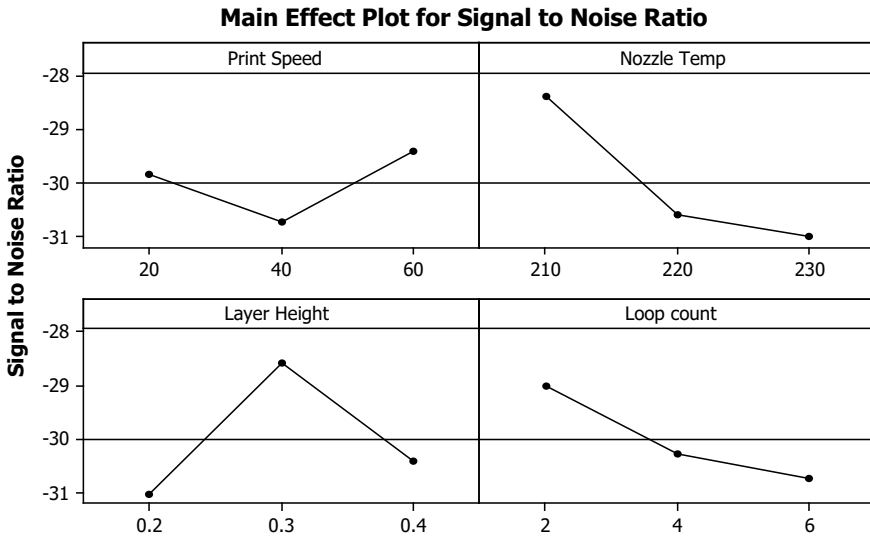


Fig. 7 Main effect plot of signal to noise ratio

ratio (Fig. 7) has been plotted for individual parameters. Optimal Levels to get best surface finish have been determined from these main effect plots.

- The optimization levels obtained are Print Speed of 60 mm/s, Nozzle Temp of 210 °C, Layer Height of 0.3 mm and Loop Count of 2.
- Higher Print speed gives better results in terms of surface finish but precise control is required. 210 °C is found to be best suited for the PLA material. Whereas, very extreme high temperatures may result in seizing of nozzle and result in poor surface finish.
- Moderate layer height will be most preferable to get better surface finish. Small Layer Height tends to be easily affected due to temperature and environmental effects. Precise control of small layers is very difficult and requires precise control of temperature and slow print speed to get good adhesion between layers. Smaller Layer height also adversely increases the total printing time.
- Smaller loop count means smaller shell thickness gives a better surface roughness finish.

4.4 Regression Analysis

Regression analysis is conducted to forecast the surface roughness obtainable from the optimal process parameters. Figure 8 portrays normal probability plot of residuals for mean Ra. Best fit is obtained in form of a straight line for regression analysis.

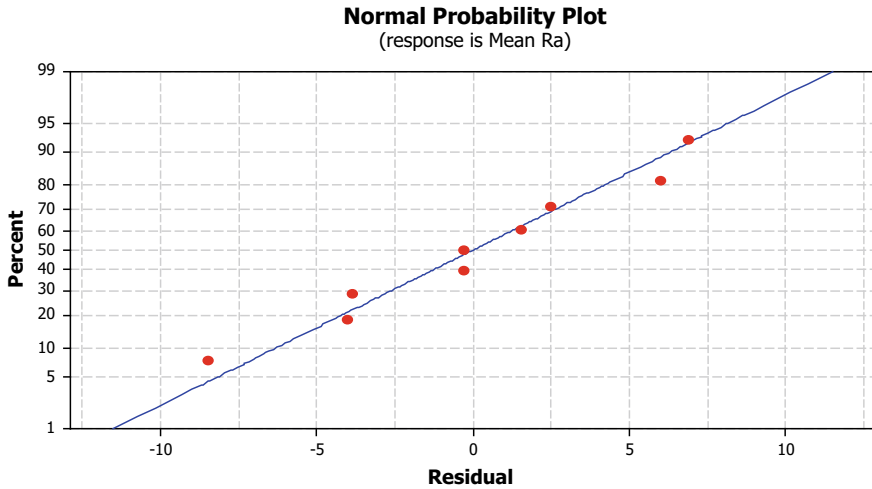


Fig. 8 Normal probability plot of residuals for mean Ra

Regression Equation obtained to forecast the mean Ra for given set of parameters is given as

$$\begin{aligned} \text{Mean Ra} = & - 81.063 - 0.0343806(\text{Print Speed}) \\ & + 0.512639(\text{Nozzle Temperature}) \\ & - 14.7189(\text{Layer Height}) + 1.59708(\text{Loop Count}) \end{aligned}$$

Inputting the obtained set of optimal parameters which is Print Speed of 60 mm/s, Nozzle Temp of 210 °C, Layer Height of 0.3 mm and Loop Count of 2 in the regression equation, we get Mean Ra forecast as 23.30 μm.

4.5 Experimental Validation

A validation check experiment is run printing the job with Print Speed of 60 mm/s, Nozzle Temp of 210 °C, Layer Height of 0.3 mm and Loop Count of 2 and keeping all the other parameters constant with same job dimensions. Ra value of 24.02 μm is obtained in the validation experiment. Error of only 3.09% is incurred in forecast value and actual value. Thus, Regression analysis is proved to be the best way to forecast the surface roughness of 3D printed products.

5 Conclusion

Taguchi's Design of Experiment has proven to be the best way for optimizing the process parameters of Fused Deposition Modeling. High printing speed with precisely control movement, Low melting temperature, Moderate layer height and thin shell thickness or less number of loop counts are required to get the best surface finish of 3D printed parts. Regression Analysis has proven to be a powerful method to forecast the surface roughness of FDM printed parts.

References

1. B. Ahuja, M. Karg, M. Schmidt, Additive manufacturing in production: challenges and opportunities, in *Laser 3D Manufacturing II*, vol. 9353 (International Society for Optics and Photonics, Mar 2015), p. 935304
2. D.E. Whitney, Manufacturing by design. *Harvard Bus. Rev.* **66**(4), 83–91 (1988)
3. M. Wall, Space station's 3d printer makes wrench from "beamed up" design (Online). Available at <https://www.space.com/28095-3d-printer-space-station-ratchet-wrench.html>. Accessed 16/02/20
4. J. Anderson, Full circle: NASA to demonstrate refabricator to recycle, reuse, repeat (Online). Available at https://www.nasa.gov/mission_pages/centers/marshall/images/refabricator.html. Accessed on 16th Feb 2020
5. Aurora Flight Sciences 3D Printing Case Study [Online Document]. Available at <https://www.stratasys.com/resources/search/case-studies/aurora>. Accessed on 16th Feb 2020
6. R. Anandkumar, S.R. Babu, FDM filaments with unique segmentation since evolution: a critical review. *Progr. Addit. Manuf.* 1–9 (2018)
7. M. Srivastava, S. Rathee, Optimization of FDM process parameters by Taguchi method for imparting customized properties to components. *Virtual Phys. Prototyping* **13**, 203–210 (2018). <https://doi.org/10.1080/17452759.2018.1440722>
8. M.N. Ahmad, M.H. Ab Rahman, N.A. Maidin, M.H. Osman, M.K. Wahid, H.M.S. Firdaus, N.A.A. Aziz, Optimization on surface roughness of fused deposition modelling (FDM) 3D printed parts using Taguchi approach, in *Symposium on Intelligent Manufacturing and Mechatronics* (Springer, Singapore, July, 2019), pp. 230–243
9. A. El Moumen, M. Tarfaoui, K. Lafdi, Modelling of the temperature and residual stress fields during 3D printing of polymer composites. *Int. J. Adv. Manuf. Technol.* 1–16 (2019)
10. Z. Liu, Y. Wang, B. Wu, C. Cui, Y. Guo, C. Yan, A critical review of fused deposition modeling 3D printing technology in manufacturing polylactic acid parts. *Int. J. Adv. Manuf. Technol.* **102**(9–12), 2877–2889 (2019)
11. M. Samykano, S.K. Selvamani, K. Kadrigama, W.K. Ngui, G. Kanagaraj, K. Sudhakar, Mechanical property of FDM printed ABS: influence of printing parameters. *Int. J. Adv. Manuf. Technol.* **102**(9–12), 2779–2796 (2019)
12. J. Shah, B. Snider, T. Clarke, S. Kozutsky, M. Lacki, A. Hosseini, A. Large-scale 3D printers for additive manufacturing: design considerations and challenges. *Int. J. Adv. Manuf. Technol.* 1–15 (2019)
13. S. Kadhoda-Ahmadi, A. Hassan, E. Asadollahi-Yazdi, Process and resource selection methodology in design for additive manufacturing. *Int. J. Adv. Manuf. Technol.* 1–17 (2019)
14. S. Vinodh, P. Shinde, Parametric optimization of 3D printing process using MCDM method, in *Precision Product-Process Design and Optimization* (Springer, Singapore, 2018), pp. 141–159
15. S.K. Padhi, R.K. Sahu, S.S. Mahapatra, H.C. Das, A.K. Sood, B. Patro, A.K. Mondal, Optimization of fused deposition modeling process parameters using a fuzzy inference system coupled with Taguchi philosophy. *Adv. Manuf.* **5**(3), 231–242 (2017)

16. U.K. Uz Zaman, E. Boesch, A. Siadat, M. Rivette, A.A. Baqai, Impact of fused deposition modeling (FDM) process parameters on strength of built parts using Taguchi's design of experiments. *Int. J. Adv. Manuf. Technol.* **101**(5–8), 1215–1226 (2019)
17. L.F.C. Durão, R. Barkoczy, E. Zancul, L.L. Ho, R. Bonnard, Optimizing additive manufacturing parameters for the fused deposition modeling technology using a design of experiments. *Progr. Addit. Manuf.* 1–23 (2019)
18. S. Deswal, R. Narang, D. Chhabra, Modeling and parametric optimization of FDM 3D printing process using hybrid techniques for enhancing dimensional preciseness. *Int. J. Interactive Des. Manuf. (IJIDeM)*, 1–18 (2019)
19. M.S. Khan, J.P. Dash, Enhancing surface finish of fused deposition modeling parts, in *3D Printing and Additive Manufacturing Technologies* (Springer, Singapore, 2019), pp. 45–57
20. S. Mahmood, A.J. Qureshi, D. Talamona, Taguchi based process optimization for dimension and tolerance control for fused deposition modeling. *Addit. Manuf.* **21**, 183–190 (2018)
21. X. Liu, M. Zhang, S. Li, L. Si, J. Peng, Y. Hu, Mechanical property parametric appraisal of fused deposition modeling parts based on the gray Taguchi method. *Int. J. Adv. Manuf. Technol.* **89**(5–8), 2387–2397 (2017)
22. J.C. Camargo, Á.R. Machado, E.C. Almeida, E.F.M.S. Silva, Mechanical properties of PLA-graphene filament for FDM 3D printing. *Int. J. Adv. Manuf. Technol.* **103**(5–8), 2423–2443 (2019)
23. J. Lyu, S. Manoochchri, Multi-objective optimization based on machine reliability and process-dependent product quality for FDM system. *Int. J. Adv. Manuf. Technol.* **102**(5–8), 2511–2520 (2019)
24. O.A. Mohamed, S.H. Masood, J.L. Bhowmik, Mathematical modeling and FDM process parameters optimization using response surface methodology based on Q-optimal design. *Appl. Math. Modell.* **40**(23–24), 10052–10073 (2016)
25. C.A. Griffiths, J. Howarth, G.D.A. Rowbotham, A. Rees, Effect of build parameters on processing efficiency and material performance in fused deposition modelling. *Proc. CIRP* **49** (2016)
26. L.M. Galantucci, I. Bodi, J. Kacani, F. Lavecchia, Analysis of dimensional performance for a 3D open-source printer based on fused deposition modeling technique. *Proc. CIRP* **28**, 82–87 (2015)
27. A.K. Sood, R.K. Ohdar, S.S. Mahapatra, Improving dimensional accuracy of fused deposition modelling processed part using grey Taguchi method. *Mater. Des.* **30**(10), 4243–4252 (2009)
28. V.D.P. Rao, P. Rajiv, V.N. Geethika, Effect of fused deposition modelling (FDM) process parameters on tensile strength of carbon fibre PLA. *Mater. Today Proc.* (2019)
29. A. Qattawi, B. Alrawi, A. Guzman, Experimental optimization of fused deposition modelling processing parameters: a design-for-manufacturing approach. *Proc. Manuf.* **10**, 791–803 (2017)
30. M. Vishwas, C.K. Basavaraj, Studies on optimizing process parameters of fused deposition modelling technology for ABS. *Mater. Today Proc.* **4**(10), 10994–11003 (2017)
31. M. Vishwas, C.K. Basavaraj, M. Vinyas, Experimental investigation using taguchi method to optimize process parameters of fused deposition modeling for ABS and nylon materials. *Mater. Today Proc.* **5**(2), 7106–7114 (2018)
32. A. Qattawi, Investigating the effect of fused deposition modeling processing parameters using Taguchi design of experiment method. *J. Manuf. Process.* **36**, 164–174 (2018)
33. S. Mahmood, A.J. Qureshi, D. Talamona, Taguchi based process optimization for dimension and tolerance control for fused deposition modelling. *Addit. Manuf.* **21**, 183–190 (2018)
34. A.K. Sood, R.K. Ohdar, S.S. Mahapatra, Parametric appraisal of fused deposition modelling process using the grey Taguchi method. *Proc. Inst. Mech. Eng. Part B J. Eng. Manuf.* **224**(1), 135–145 (2010)
35. T.J. Hsu, W.H. Lai, Manufacturing parts optimization in the three-dimensional printing process by the Taguchi method. *J. Chinese Inst Eng* **33**(1), 121–130 (2010)
36. M. Srivastava, S. Rathee, Optimisation of FDM process parameters by Taguchi method for imparting customised properties to components. *Virtual Phys. Prototyping* **13**(3), 203–210 (2018)

37. A.E. Tontowi, L. Ramdani, R.V. Erdizon, D.K. Baroroh, Optimization of 3D-printer process parameters for improving quality of polylactic acid printed part. *Int. J. Eng. Technol. (IJET)* **9**(2), 589–600 (2017)
38. L. Santana, J.L. Alves, A.D.C.S. Netto, A study of parametric calibration for low cost 3D printing: seeking improvement in dimensional quality. *Mater. Des.* **135**, 159–172 (2017)
39. H.N. Huynh, A.T. Nguyen, N.L. Ha, T.T.H. Thai, Application of fuzzy Taguchi method to improve the dimensional accuracy of Fused Deposition Modeling processed product, in *2017 International Conference on System Science and Engineering (ICSSE)* (IEEE, 2017), pp. 107–112
40. M.S. Alsoufi, A.E. Elsayed, How surface roughness performance of printed parts manufactured by desktop FDM 3D printer with PLA+ is influenced by measuring direction. *Am. J. Mech. Eng* **5**(5), 211–222 (2017)
41. G. Taguchi, Introduction to quality engineering: designing quality into products and processes (No. 658.562 T3) (1986)

Optimization of Process Parameters to Analyze Wear Behavior of an Uncoated Tool on AL-MMC



Seema V. Yerigeri and Shantisagar K. Biradar

Abstract Extensive use of aluminum metal matrix (Al-MMC) composites in today's world has led to the development of high-quality alloys. MMCs have an inimitable characteristic to syndicate different characteristics of the materials that make up the composition. Al-MMCs lend themselves for use in applications where high temperatures need to be withstood. The present study attempts to investigate the stimulus of an applied load, sliding velocity, and percentage composition of reinforcement (composite) on the wear rate of various aluminum (Al) alloys reinforced with 0, 3, 6% by wt. of ZrB_2 which was fabricated using the stir casting technique. Optimization of the wear of Al-MMC developed by the stir casting method utilizing Taguchi's signal to noise (S/N) analysis is examined to analyze its effect on uncoated tool wear. An L9 orthogonal array is selected for performing various dry wear tests. Parameters that are input like load, sliding distance, sliding speed, and reinforcement percentages are optimized, taking into account a minimum wear rate. Then, the best values obtained are made use of to conduct experimentation to confirm the hypotheses. The technique known as analysis of variance (ANOVA) is used to estimate the consequence of the wear parameters. From this, it is observed that the tribological properties such as wear rate are improved. Outcomes revealed that the composite affects the sliding velocity, the load, and the wear rate to the greatest extent.

Keywords Al-MMC · ANOVA · Orthogonal array · Taguchi technique · Stir casting · Wear behavior

S. V. Yerigeri (✉)

Department Mechanical Engineering, M.B.E. Society's College of Engineering, Ambajogai, Beed, India

e-mail: seemayerigeri1877@gmail.com

Department of Mechanical Engineering, G. S. Mandal's, Maharashtra Institute of Technology, Aurangabad, India

S. K. Biradar

M.S.S. College of Engineering and Technology, Nagewadi, Aurangabad—Jalna Road, Jalna, India

1 Introduction

Current technology necessitates use aluminum, which is light weight, has longer wear life, and is highly cost effective. This extensive use has led to the advancement of innovative materials with exceptional characteristics such as high stiffness and high specific strength including higher resistance to wear. Cost performance relationship, fatigue strength, thermal shocks, and wear behavior have resulted in composites being highly prevalent in several industries. In the locomotive industry, Al-MMC is used to manufacture fiber-reinforced pistons, Al crank shafts that have strengthened cylinder surface, as well as brake drums [1]. The manufacture of MMC by varying methods (e.g., casting) was deliberated to manufacture parts that were entirely flawless to meet customer's requirements [2]. The wear behavior of materials that are composite has been studied by researchers for a very long time as there was always room for improvement. This was done using a variety of methods through which the wear behavior could be analyzed. Alloys made from Al are the metals utilized very extensively because their density is very low, their ductility is high, and these metals are very economical. Al alloy composites are very much in demand, but they possess a low wear resistance, making it necessary to reinforce these alloys using a tougher material [3, 4]. It is this necessity that has led to the study of wear analysis of Al-MMC. Serdar and Soner [5] investigated the relation between the sliding wear and thermal behavior of Al6061/Al-MMC and noticed that a rise in alumina volume percentage reduced both, the thermal conductivity and the coefficient of friction (COF). During the study, it was seen that the wear resistance was good as compared to unreinforced matrix alloy [6, 7]. A comparison has been made between the wear behavior of Al-MMC sliding against automobile friction material and conventional material (e.g., gray cast iron) [8]. When sliding with an MMC disc, the wear of the lining material was noticed to be higher due to silicon carbide (SiC) plowing the lining material [9]. As per literature, it is observed that the method developed by Taguchi is widely used in the field of wear studies [10]. Experimentation conducted on the basis of the Taguchi method exhibited that the addition of SiC and graphite increases the wear resistance significantly. Moreover, numerous studies have been performed on simultaneous optimizations using fuzzy logic [11]. Case studies using the Taguchi method on optimization of EDM process parameters have been deliberated [12]. From literature survey, it is seen that MMC is currently the leading innovative material with a rigid and abrasive nature causing the tools used for machining it to wear out rapidly and weakening surface roughness during the working process [13]. Machining of MMCs were first investigated and testified in 1985 with the performance of different tool materials on Al-MMC (reinforced with SiC particles) being assessed [14]. MMCs are considered more difficult materials for machining due to their hard abrasiveness and ceramic reinforcements [15], whereas Singh et al. [16] investigated experimentally the turning of Al/SiC/Gr MMC component and detected increasing roughness in the surface when the feed rate as well as the depth of the cut rose. According to Tomac et al. [17], ceramics tools did not measure up compared to the carbides when machining at lower speeds

for cutting and feed rates that were high. A few researchers observed how various coatings affected the functioning of carbide cutting tools while machining MMC and came up with a proposal stating that coatings that were less hard than that of the reinforced alloy resulted in no improvement in the performance of tools [18, 19].

As per the literature review, it is seen that to improve the wear resistance during the sliding process in various applications Al-MMC is an appropriate substitute for other metals (e.g., cast iron). Hence, in this work, a 0%, 3%, and 6% by wt. of ZrB_2 has been added to the matrix of Al alloy as a nano-ingredient using a liquid metallurgy technique. The Taguchi procedure along with ANOVA has been used for the dry sliding wear experiment. The impact of various parameters on the wear rate has been analyzed.

2 Taguchi Procedure

Design of experiments (DOE) is made use of to assess how the multiple input parameters are impacted on a given output. DOE along with the technique developed by Taguchi is used to discover the ideal combination of parameters for a specific set of responses [20]. It delivers an optimized perspective to advance the functioning, effectiveness, and expense. This technique is utilized in the estimation of orthogonal arrays. The differences are recognized making use of a S/N ratio. An effect of noise is given by this S/N ratio on several properties. ANOVA was made use of to regulate the percentage of the impact of various parameters on the response [21]. It was a quantifiable calculation to regulate the involvement of each and every parameter on the response.

3 Experimentation

Figure 1 depicts a dry test that was conducted on a pin-on-disk machine. Samples with a length of 30 mm and a diameter of 10 mm were brought into use. The machining and polishing of the specimens were undertaken based on ASTM standards. The pin specimen was manufactured such that both ends of the pin were flat. As per the ASTM standards, the smooth, flat ends of the pin specimen were placed such that they were in contact with a disc. The experiments were planned to hold the pin against an EN32 rotating disk with additional weights in the weight pan. A 100 mm track diameter was set and kept constant for all tests. Experiments were conducted by changing the values of the sliding velocity and applied load for three levels. This is depicted in Table 1. These experiments were performed at room temperature. Nine samples were examined in this test. The weight loss experienced by the samples before and after wear was calculated by an electronic weighing machine. Weight forfeiture was experienced due to friction existing between the disk and the samples.

Fig. 1 Pin-on-disk apparatus

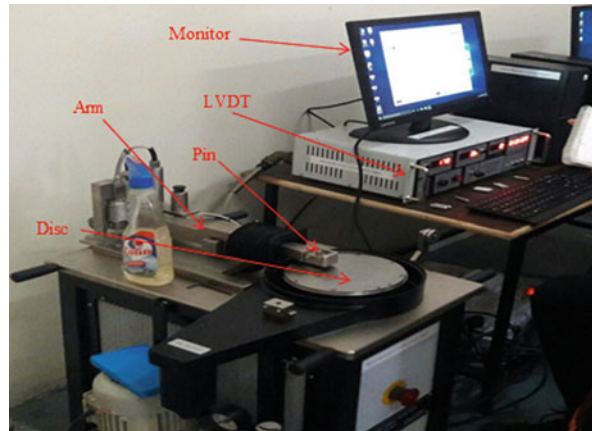


Table 1 Parameter inputs for the pin-on-disk wear test

Parameters (I/P)	Ranges
Composition (%)	0, 3 and 6
Load (N)	30, 40 and 50
Velocity (m/s)	140, 150 and 160

The composite (%), load (N), and velocity (m/s) were taken as parameters that were inputs.

3.1 Optimization Techniques

The Taguchi method along with the ANOVA procedure were utilized as the optimization technique. The Taguchi method was utilized in the design of the input parameters as exhibited in Table 2. The S/N ratio is normally examined based on the following settings: ‘smaller is better,’ ‘nominal is better,’ and ‘larger is better.’ For the purpose of this work, the ‘smaller is better’ setting has been chosen for the minimal wear rate.

4 Results and Discussion

4.1 Taguchi Optimization Technique

A Taguchi orthogonal L9 (3^4) array was used in the experimental design with a total of nine experiments as shown in Table 2. Al 6061, Al 6063, and Al 7075 were mixed

Table 2 L9 orthogonal array

S. No.	Composition (%)	Load (N)	Velocity (m/s)
1	0	30	140
2	0	40	150
3	0	50	160
4	3	30	150
5	3	40	160
6	3	50	140
7	6	30	160
8	6	40	140
9	6	50	150

with ZrB₂ for better results. Three considerations such as velocity, composite weight percentage, and load were chosen for analysis. Nine iterations of the experiments were calculated collectively under the iterated form – $10 \times \text{Log } 10 (\text{sum } (Y^2)/n)$. Based on the various tests, the wear rate was noted. After numerous iterations, the minimal wear was noted as 0.001815 mm³/m which was a result of 6% weight percentage Al 6063 and was measured at 30 N load on the pin-on-disk apparatus and 160 m/s velocity of the disc. The results that are optimized are as shown in Table 3. They show the input as well as the output of the nine trial runs.

The parameters responsible for the wear process were analyzed in MINITAB. S/N ratios were obtained using ANOVA. Table 4 depicts the repetitive value of the S/N, and Table 5 shows the repetitive values of the data mean.

Graphical presentations for means and S/N ratio are depicted in detail as shown in Figures 2 and 3. An analysis of two graphs has been conducted by maintaining the wear rate on the Y axis.

Table 3 Optimized result

S. No.	Composition (%)	Load (N)	Velocity (m/s)	Wear rate (mm ³ /m)
1	0	30	140	0.005610
2	0	40	150	0.005610
3	0	50	160	0.008130
4	3	30	150	0.006408
5	3	40	160	0.003307
6	3	50	140	0.002506
7	6	30	160	0.001815
8	6	40	140	0.002485
9	6	50	150	0.001906

Table 4 Response for S/N ratio

Level	Composite	Load	Velocity
1	43.95	47.90	49.71
2	48.50	48.91	47.76
3	53.77	49.41	48.74
Delta	9.82	1.50	1.95
Rank	1	3	2

Table 5 Response for means

Level	Composites	Load	Velocity
1	0.006450	0.004611	0.003534
2	0.004074	0.003801	0.004641
3	0.002069	0.004181	0.004417
Delta	0.004381	0.000810	0.001108
Rank	1	3	2

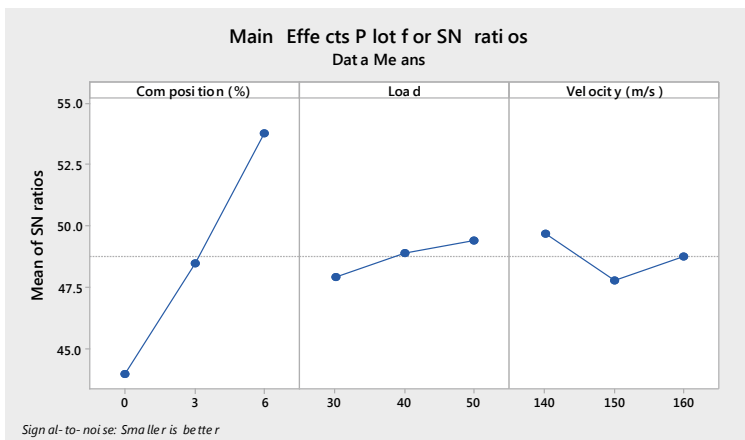


Fig. 2 Plot for the main effect of S/N ratios

4.2 Analysis of Variance Technique

The ANOVA technique is a statistical technique. It analyzes the variances between the group mean and their associated procedure. Table 6 presents the percentage of inheritance of all individual parameters. A model summary for the transformed response is presented in Table 7. In this experiment, the factors are composition, load, and velocity, and the response is S/R. The result obtained by ANOVA is depicted in Table 6. In percentage contribution, it shows that the percentage composition has the

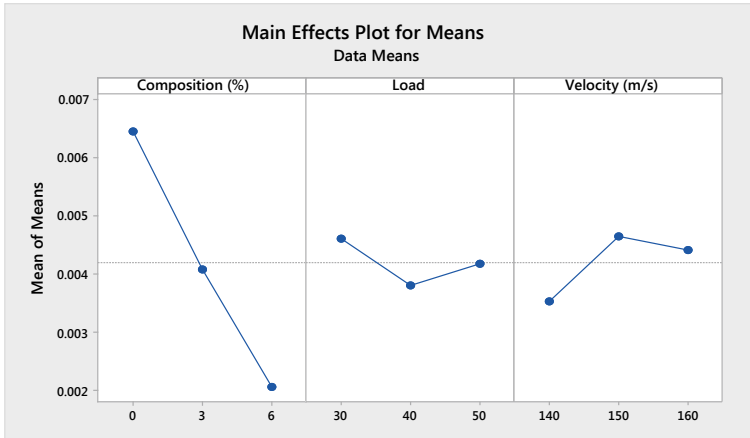


Fig. 3 Plot for the main effect of means

Table 6 ANOVA-transformed response

Source	DF	Adj SS	Adj MS	f-value	p-value
Composition (%)	2	137.893	68.947	4.38	0.186
Load (N)	2	3.771	1.886	0.12	0.893
Velocity (m/s)	2	3.760	1.880	0.12	0.893
Error	2	31.456	15.728		
Total	8	176.881			

Table 7 Model summary-transformed response

S	R ² (%)	R ² (adj) (%)	R ² (pred) (%)
3.96586	82.22	28.86	0.00

highest contribution of the S/N ratio, whereas the load and sliding velocity have the lowest influence and contribute equally.

5 Conclusions

The objective of this work was to examine and verify the impact of applied load, sliding velocity, and composition of the reinforcement (composite) in percentage on the wear rate of various Al alloys reinforced with 0, 3, and 6% by wt. of ZrB₂ for an uncoated tool insert. The objective is achieved with the help of statistical analysis initially followed by experimental work. The following conclusions are arrived at based on statistical analysis and experimental investigations.

- Reinforcing Al with ZrB₂ nano-ingredients shows an appreciable increase in its mechanical and tribological properties (wear resistance).
- Tool wear increased for 6% by wt. of ZrB₂ as compared to others.
- For the minimum wear of material and maximum wear of tool insert, the input parameters such as load, sliding speed, sliding distance, and reinforcement percentages are optimized.

References

1. H.B. Bhaskarand, A. Sharief, Dry sliding wear behaviour of aluminium/Be₃Al₂(SiO₃)₆ composite using Taguchi method. *J. Minerals Mater. Characterization Eng.* **11**(7), 679–684 (2012)
2. W. Kaczmar, K. Pietrzak, W. Wlosinski, The production and application of metal matrix composites materials. *J. Mater. Process. Technol.* **106**(1–3), 58–67 (2000)
3. R. Siriyala, G.K. Alluru, R. Murthy, R. Penmetsa, M. Duraiselvam, Applications of grey Taguchi method for optimization of dry sliding wear properties of aluminium MMCs. *Front. Mech. Eng.* **7**(3), 279–287 (2012)
4. M.O. Shabani, A. Mazahery, Development of an extrusion process to ameliorate the tribological properties of heat-treated Al Mg Si (Cu) system alloys matrix composites in consolidated state. *Tribol. Industry.* **34**(3), 166–173 (2012)
5. O.Y. Serdar, S. Buytoz, Relationship between thermal and sliding wear behaviour of Al6061/Al₂O₃ metal matrix composite. *J. Mater. Sci.* **42**(12), 4485–4493 (2007)
6. S.C. Sharma, The sliding wear behaviour of Al6061-garnate particulate composite. *Wear* **249**(12), 1036–1045 (2001)
7. R.L. Deuis, C. Subramanian, J.M. Yellup, Dry sliding wear of aluminium composites—a review. *Compos. Sci. Technol.* **57**, 415–435 (1997)
8. M. Demirel, M. Mouratoglu, Influence of load and temperature on the dry sliding wear behaviour of aluminium-Ni₃Al composites. *Indian J. Eng. Mater. Sci.* **18**(4), 268–282 (2011)
9. N. Natarajan, S. Vijayarangan, I. Rajendran, Wear behaviour of A356/25SiCp aluminium matrix composites sliding against automobile friction material. *Wear* **261**(7–8), 812–822 (2006)
10. S. Basavarajappa, K.V. Arun, J. Paulo Davim, Effect of filler materials on dry sliding wear behaviour of polymer matrix composite-Taguchi approach. *J. Min. Mater. Characterization Eng.* **8**(5), 379–391 (2009)
11. Y.N. Puri, N.V. Deshpandae, Simultaneous optimisation of multiple quality characteristics using fuzzy logic and Taguchi technique, in *Proceedings of the fifth Asia pacific Industrial Engineering and Management Conference* (2004)
12. P.R. Apte, Optimization of EDM using Taguchi technique, in *Methods Workshop Using UNIMAP* (2012)
13. A. Dolata-Grosz, J. Wiczorek, Tribological properties of composite working under dry technically friction condition. *J. Achievements Mater. Manuf. Eng.* **18**(1–2), 83–86 (2006)
14. N.M. Rajneesh, S. Kanakuppi, Dry sliding wear behaviour of Sic particles reinforced Zn-Aluminium (ZA43) alloy metal matrix composite. *J. Min. Mater. Characterization Eng.* **10**(5), 419–425 (2011)
15. J.P. Davin, *Machining of Metal Matrix Composites* (Springer-Verlag London limited, 2012)
16. G. Singh, M. Pal Singh, G. Singh, Optimization of the machining parameters for surface roughness during turning of Al/SiC/Gr Hybrid MMC. *Int. J. Eng. Res. Technol.* **2**(11), 1613–1617 (2013)
17. N. Tomac, K. Tannessen, F.O. Rasch, Machinability of particulate aluminium matrix composites. *CIRP Ann. Manuf. Technol.* **41**(1), 55–58 (1992)

18. C. Lane, The effect of different reinforcements on PCD tool life for aluminium composites, in *Proceedings of the Machining of Composite Materials Symposium* (ASM Material Week, Chicago, 1992), pp. 17–27
19. K. Weinert, W.A. König, Consideration of tool wear mechanism when machining metal matrix composites (MMC). *CIRP Ann. Manuf. Technol.* **42**(1), 95–98 (1993)
20. A. Pramanik, J.A. Arsecularatne, L.C. Zhang, Machining of particulate-reinforced metal matrix composites, in *School of Aerospace, Mechanical and Mechatronics Engineering* (The University of Sydney, Sydney, NSW 2006, Australia, 2006)
21. M. Kathirvel, S. Pusushothaman, Applications of ANOVA in validating hybrid metal matrix composite machinability data. *ARPN J. Eng. Appl. Sci.* **6**(10), 8–18 (2011)

Estimation of Natural Frequencies of Gear Meshing System Using Modal Analysis



Rahul A. Jibhakate, Prafull S. Thakare, Chetan J. Choudhari,
and Piyush Patil

Abstract In high-speed applications like synchromesh gear mesh system, vibration is inevitable due to torsional motion. If designer knows the natural frequency of gear mesh, then it can be compared with operating frequency, which ultimately gives the behavior of gear mesh system at resonance frequency. This paper presents estimation of natural frequency of synchronized gear meshing system to avoid resonance condition. The implicit FE solver, a tool of finite element analysis, is used to determine the natural frequency. In further to validate these results, Holzer method is also used. After comparing both results, it has been concluded that FEM is very reliable and fast method to find natural frequency of complex structure.

Keywords Natural frequency · Holzer method · FEM · Gear meshing system

1 Introduction

A synchromesh gearbox is usually manually operated transmission in which a change of gears takes place between gears that are already revolving at the same speed. Due to continuous revolution of gear and shaft, vibration takes place in gearbox. By simulating and predicting the vibration of a gearbox, designers can gain insight early in the design process. The measurement of vibration in gear meshing is strenuous, unfeasible and exorbitant. Numerical and analytical methods have been used to determine vibration in gear. In order to find out vibration, it is important to know

R. A. Jibhakate
G.H.Raisoni College of Engineering, Nagpur, India

P. S. Thakare (✉)
MSS College of Engineering and Technology, Jalna, India

C. J. Choudhari
Julelal Institute of Technology, Nagpur, India

P. Patil
Suryodaya College Raisoni College of Engineering, Nagpur, India

natural frequency of gearbox. Knowing natural frequency helps to understand resonance condition of gearbox [1, 2]. Therefore, finite element method is a very reliable technique to find out natural frequencies of gearbox using Ansys solver [3]. The natural frequency and mode shapes of a gear meshing are determined by iteration method as devised by Holzer. It is applicable to forced, free, damped, undamped and semi-definite systems. The analytical iterative Holzer method is reliable to determine natural frequencies for gear meshing [4, 5].

In this paper, different mode shapes and natural frequencies are evaluated through computer Modal analyses. Detailed finite element (FE) model is created for synchromesh gear meshing and used for the finite element analyses of computer tool Ansys. The natural frequency is obtained by the Holzer method compared with the results for the numerical analysis in Ansys.

2 Problem Statement

Natural frequencies are generated by impacts of the internal parts of a rolling-element bearing of shaft mounting of gear meshing. A vibrating object may have one or multiple natural frequencies. Simple harmonic oscillators can be used to model the natural frequency of an object [6]. Natural frequency, also known as eigenfrequency, is the frequency at which a system tends to oscillate in the absence of any driving or damping force. Natural frequency is having importance because if dynamic forces in the system match natural frequency then it will cause resonance, and at resonance even small force will cause large amplitudes.

For research purpose, approximate dimension of spline shaft and counter shaft of tractor synchromesh gearbox meshing system is taken as mentioned in Table 1. Detailed model is developed on modeling package NX as shown in Fig. 1. The gears are made of the alloy steel with the material properties of density = 7872 kg/m³, Young’s modulus $E = 207$ GPA, Poisson’s ratio = 0.3, yield stress = 200 MPa and maximum speed during operation 2300 rpm (Tables 2, 3, 4 and 5).

Table 1 Specifications of meshing gear system

Gear No.	Upper shaft (spline shaft)			Lower shaft (counter shaft)		
	No. of teeth (T)	Width (W, mm)	P.C.D. (D, mm)	No. of teeth (T)	Width (W, mm)	P.C.D. (D, mm)
G-1	59	24.2	190.5	21	27.6	76.10
G-2	49	20.5	167.83	25	45.5	100.87
G-3	38	19	146.05	31	21	122.64
G-4	31	16.7	122.7	39	16.3	146

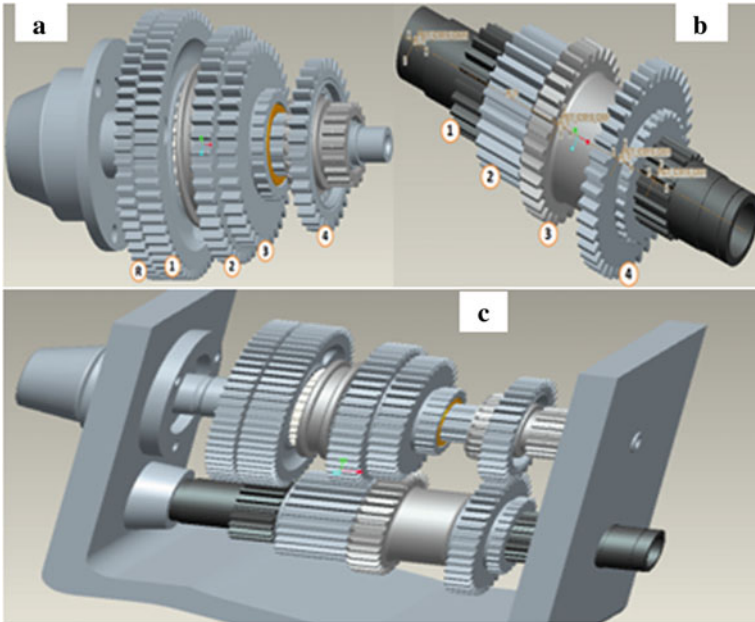


Fig. 1 Pictorial view of gear meshing system showing **a** upper shaft, **b** lower shaft and **c** gear mounting

Table 2 Mass moment of inertia

Gear No.	Upper shaft (spline shaft)	Lower shaft (counter shaft)
	Mass moment of inertia (I , kg mm ²)	Mass moment of inertia (I , kg mm ²)
G-1	23,397	183.04
G-2	10,421	1547.7
G-3	5798.9	3513.6
G-4	2654.5	5548.5

Table 3 Equivalent mass moment of inertia (kg mm²)

Gear pair	1st gear ratio (2.81)	2nd gear ratio (1.76)	3rd gear ratio (1.23)	4th gear ratio (0.795)
1st gear pair	184,929.14	23,580.17	23,580.17	23,580.17
2nd gear pair	11,968.8	33,828.09	11,968.8	11,968.8
3rd gear pair	9312.59	9312.59	12,236.8	9312.59
4th gear pair	8202.9	8202.9	8202.9	7226.14

Table 4 Equivalent length (mm)

Section of shaft	1st gear ratio (2.81)	2nd gear ratio (1.76)	3rd gear ratio (1.23)	4th gear ratio (0.795)
Le1 (mm)	1049.07	411.54	201.04	83.97
Le2 (mm)	970.39	380.68	185.92	77.67
Le3 (mm)	1311.34	514.43	251.25	104.97

Table 5 Torsional spring constant of shaft (N mm/rad)

Section of shaft	1st gear ratio (2.81)	2nd gear ratio (1.76)	3rd gear ratio (1.23)	4th gear ratio (0.795)
Kt1	54,780,153.4	139,640,231.2	285,907,677.1	684,387,614.1
Kt2	59,221,792.55	150,962,145.1	309,089,355.1	739,878,335.2
Kt3	43,824,125.22	111,712,201.2	22,872,696.1	547,509,700.1

3 Estimation of Natural Frequencies of Equivalent System by Holzer Method

Holzer's method is a tabular method which is used for the analysis of multi-DoF system. It is useful for the analysis of free and forced vibrations and also for the system with or without damping. It is a trial and error method and can be used to find the higher modes independent of fundamental mode. In addition to natural frequencies, amplitude ratios of masses and the node points can also be established using this method [4].

3.1 Concept of Equivalent System for Holzer Method

In a complicated system, the various parts operate at different speeds and have different elastic properties and weights. In such a system, all parts are reduced to an equivalent rotating system. The weight and elastic members are varied to give an equivalent energy system. In this equivalent system, all elastic members are reduced to an equivalent shaft of unit diameter and of such a length as to give an equivalent energy storage capacity at the speed of the equivalent mass. The inertia mass is reduced to give an equivalent energy storage capacity at the speed of the equivalent inertia disk. In cases of members having a variable inertia effect, the equivalent inertia disk is chosen to give the average effect over a cycle of the variable inertia [7].

3.2 Equivalent Weight and Inertia System

The general principle used in reducing these various mass systems to an equivalent simple rotating system is to make the conversion on the basis of equivalent kinetic energy storage capacity [7]. Using analytical relation, mass moment of inertia (I), equivalent mass moment of inertia (I_e), equivalent length (L_e) and torsional spring constant of shaft (K_t) are calculated as follows.

3.3 Procedure of Holzer Method

In the calculation of natural frequency, Holzer method is the most widely used, and this method is common due to its simplicity in calculations and understanding. The first step of the procedure as usual is to find out M.I. of rotating parts and reduce the system to a simpler form containing disks. It is always easier to reduce the installation to concentrated mass equivalent system. Then, trials are started with a certain guessed value of natural frequency. The guess may be made on the basis of previous experience of some comparable installation or by computation of a simple three-mass system to which all the assemblies can be reduced easily.

Assumption: Three disks and two shaft systems.

$$K_{t1} = K_{t2} = 1 \text{ N cm}^2/\text{s}$$

$$I_1 = I_2 = I_3 = 1 \text{ kg cm}^2$$

$$\omega = 1.7, \text{ so } \omega^2 = 2.89$$

S. No.	I	R	ω^2	$I r \omega^2$	$\Sigma I r \omega^2$	K_t	$\Sigma I r \omega^2 / K_t$
1	1	1	2.89	2.89	2.89	1	2.89
2	1	- 1.89	2.89	- 5.46	- 2.57	1	- 2.57
3	1	0.68	2.89	1.971	- 0.06	-	-

where

- I Moment of inertia (kg cm^2).
- ω Natural frequency (rad/s).
- r Maximum relative angle between the masses (rad).
- $I r \omega^2$ Torque applied on shaft ($\text{kg cm}^2/\text{s}$).
- K_t Torsional spring constant for shaft ($\text{N cm}^2/\text{s}$).
- $\Sigma I r \omega^2 / K_t$ Relative angle between the masses of disk [8].
- $\Sigma I r \omega^2$ - 0.06 = Zero.

Table 6 Natural frequencies using FE model

Mode	Inertia force (Rad/s)	Natural frequency (Hz)
1	37.1144	5.892
2	87.64	15.43
3	131.433	24.867
4	77.970	12.64
5	112.571	19.87
6	198.870	36.43
7	109.96	18.96
8	205.4	34.352
9	177.297	27.89

So answer is $\omega = 1.7$ rad/s.

4 Finite Element Modeling of Gear Meshing System

The finite element analysis (FEA) is the simulation of gearbox using the numerical technique. It reduces the number of physical prototypes and experiments and optimizes components in their design phase to develop better products, faster while saving on expenses. Modal analysis and linear static analysis are two common methods in FEA. Modal analysis is used to calculate the natural frequencies of gearbox to know which frequencies can be destructive and dangerous for it. Using modal analysis, we come to conclusion of “resonance frequencies” of gearbox.

As mentioned earlier, we have dimension of synchromesh gear meshing. As per the dimension, gearbox model is developed as shown in Fig. 1. Now, the implicit FE solver Ansys is used to generate the geometric solid models. The natural frequencies are calculated using modal analysis and harmonic response solver at different inertia forces. The FEA results are listed in Table 6, and Fig. 2 plots deformed configuration of such FE models.

5 Results and Discussion

In the aforementioned sections, estimating natural frequency of gear meshing system for different gear ratios using Holzer method and FEM simulation is discussed. This paper mainly reported the potentiality of numerical method using FE simulation, and therefore, Holzer method is not discussed in detail. Modal analysis and harmonic response are performed, and results are shown in Table 6. In this section, results of natural frequencies estimated using FE simulation are compared with Holzer method, and percentage variation is evaluated using Eq. (1) [10]. Percentage variation of the

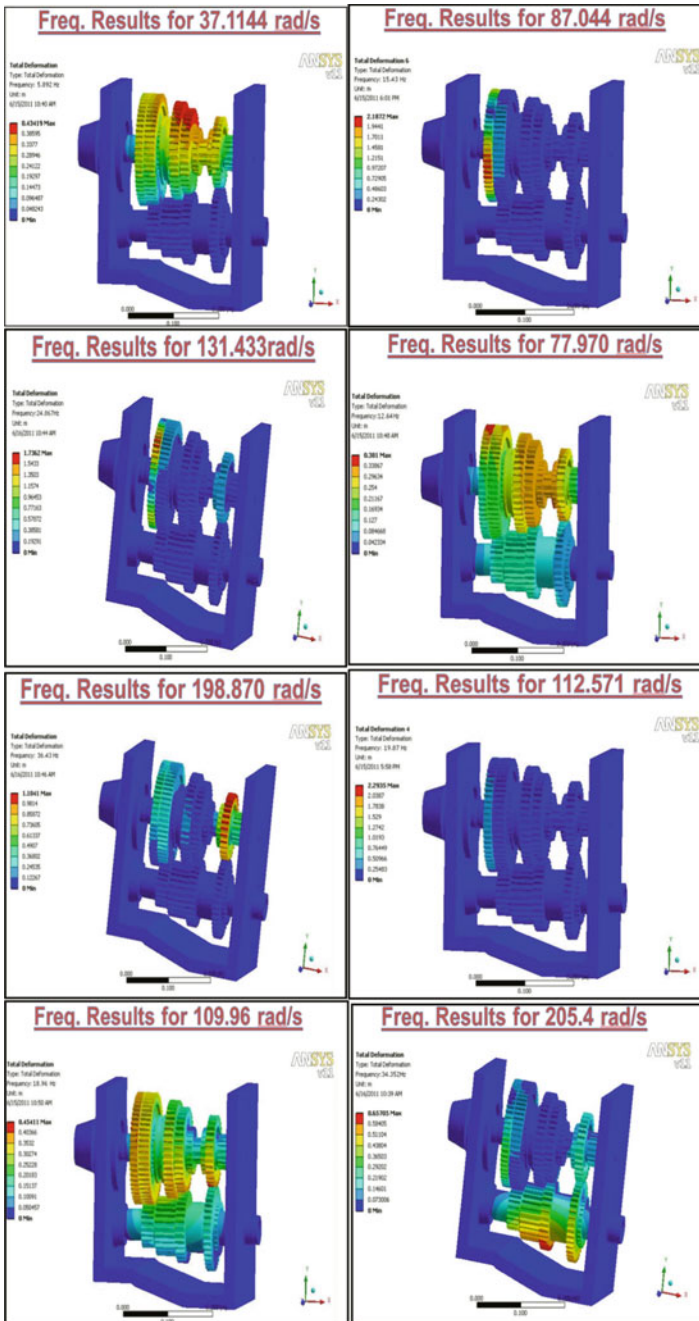


Fig. 2 Modal analysis and harmonic response

FE results compared to Holzer method shows the closeness of these methods [10].

$$\text{Percentage Variation} = \frac{\text{Analytical results} - \text{Numerical results}}{\text{Analytical results}} \times 100 \quad (1)$$

Table 7 illustrates the results using both methods and respective percentage variation. As seen from Table 7, minimum and maximum percentage variation is 1.91% and 10.02%, respectively, and proves the potentiality and applicability of numerical method using FE model. Figures 3 and 4 show comparison of estimated results of natural frequency of gear meshing system with afore-stated specifications. Trend of results is similar for both methods, represented by Fig. 4.

Table 7 Comparison of results and estimating percentage variations

Gear ratio	Natural frequency	Holzer method	FEM	Percentage variation
I gear ratio	ω_1	6.2069	5.892	5.07
	ω_2	14.253	15.43	8.26
	ω_3	22.9182	24.864	8.49
II gear ratio	ω_1	12.4031	12.64	1.91
	ω_2	18.2162	19.89	9.19
	ω_3	33.1123	36.43	10.02
III gear ratio	ω_1	29.7504	32.6904	9.88
	ω_2	31.26	34.352	9.89
IV gear ratio	ω_1	29.2176	27.89	4.54

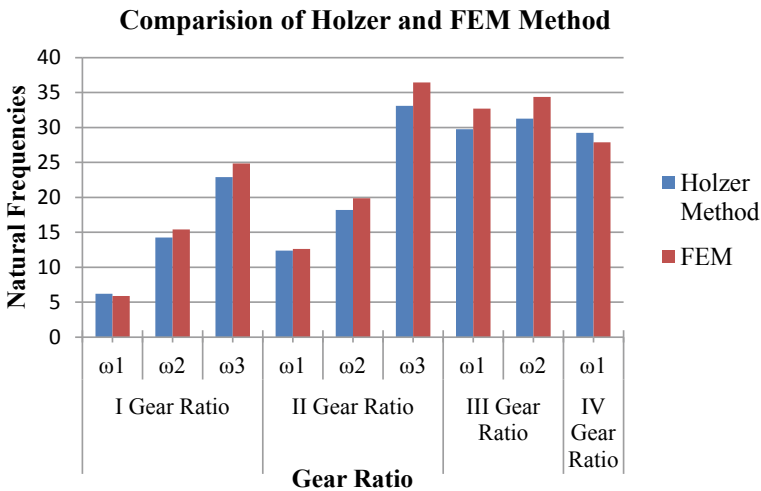


Fig. 3 Bar graph showing results of Holzer method and FE model

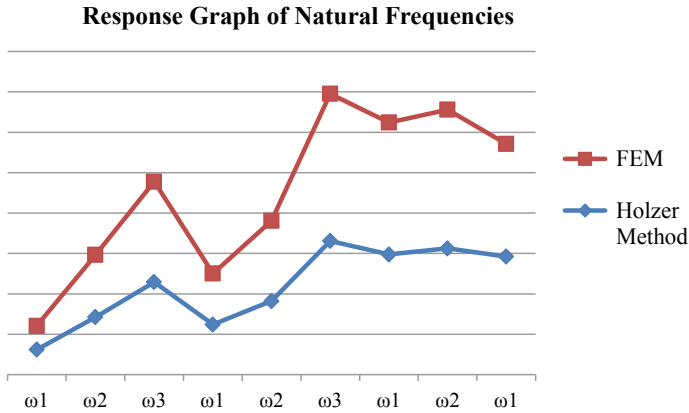


Fig. 4 Trend of results for Holzer method and FE model

6 Conclusion

In this paper, vibration analysis of synchronized gear meshing system was performed using Holzer method and FE simulation. Modal analysis was used to estimate natural frequencies of the specified gear meshing system for different gear ratios. The implicit FE solver Ansys was used to generate the geometric solid models. Results obtained from FE solver were then compared with Holzer method. Percentage variation was evaluated to check the goodness of these methods. It is seen from the analysis that maximum percentage variation is approximately less than 10%, showing the correctness of FE methodology. From the analysis, it can be revealed that FE simulation using implicit FE solver can be effectively useful for the given application.

The author is expected to perform experimentation on the synchronized gearbox using FFT analyzer.

References

1. M. Sofian, et al., A study of vibration analysis for gearbox casing using finite element analysis (2009)
2. J. Quiroga, et al., Torsional natural frequencies by Holzer method. J. Phys. Conf. Ser. **1160**(1) (2019)
3. M.P. Vinod, K. Vijay Kumar, A. Venkatram Reddy, Pressure die casting tool design for side engine cover of gear box casing
4. V. Kushwaha, Analysis of torsional vibration characteristics for multi-rotor and gear-branched systems using finite element method. Dissertation (2012)
5. J.P. Denhartog, J.P. Li, Forced torsional vibrations with damping-an extension of Holzer method. J. Appl. Mech. Trans. ASME **13**(4), A276–A280 (1946)
6. R.K. Mobley, Vibration monitoring and analysis, in *Plant Engineer's Handbook* (Butterworth-Heinemann, 2001), pp. 757–811

7. C.R. Freberg, E.N. Kemler, *Element of Mechanical Vibration Equivalent Systems* (John Wiley & Sons Chapman & Hall Limited New York, London), Chap. VI, pp. 109–117
8. P.H.K. Nafees, G.D. Mehta, J.P. Modak, An approximate estimation of natural frequencies of equivalent system of four wheeler drive. **2(III)**, 271–289. ISSN 0975-7074
9. Y. Liu, *Lecture note on Finite Element Method* (CAE Reserch Laboratory, Mechanical Engineering Department, University of Cincinati USA)
10. P.S. Thakare, S.M. Salodkar, C.C. Handa, Development of mathematical model for top roller displacement of three-roller bending machine using dimensional analysis, in *Proceedings of International Conference on Intelligent Manufacturing and Automation* (Springer, Singapore, 2019)

An Arrangement and Robust Design of Automated Grass Cutter Gadget Using Computer-Aided Design



Kanchan D. Ganvir and Akshay D. Anjekar

Abstract The paper centers on the plan of robust design of automated grass shaper, and the gadget is a grass cutting automated vehicle operated by controller which keeps away from obstacles and deterrents and cuts the grass with no need of human involvement. As innovation is progressing, numerous gadgets are getting changed and robotized, and grass shaper is one of them. In present age, this sort of machines is getting exceptionally mainstream. The aim behind the paper is to make the grass shaper which is worked by an elective source which decreases labor. A self-moved grass shaper is adjusted to be constrained by a distantly situated administrator. A recipient mounted on the grass shaper controls servomotors, which thus work miniature switches and transfers amassed there with to specifically empower a majority of reversible electric engines which are coupled precisely with the guiding wheel, footing haggles transmission between the last mentioned and the principle driving shaft. A controller grass shaper has two refinements incorporate the controller of the choke change of the air conditioner engines with gear boxes for forward/invert/turning speed control, a gyro for quick straight line cuts, a cerebrum including microchips, an another engine to cut the grass. All substantial parts, for example, batteries, engines ought to be designed for ideal adjusted in the entirety of its extents. It is a quick, safe, energy-productive, and easy-to-control grass shaper that does not bargain speed or capacity to cut the yard. Hence, an attempt has been made to design a grass cutter shaper which can be operated by remote controlled by hydrogen fuel cell.

Keywords High speed DC motors · Pump · Blades · Sprinkler · Water tank · RF module

1 Introduction

As innovation is progressing, numerous gadgets are getting changed and robotized, and grass shaper is one of them. In present age, this sort of machines is getting

K. D. Ganvir (✉) · A. D. Anjekar

Department of Mechanical Engineering, Priyadarshini Bhagwati College of Engineering, Nagpur, Maharashtra 440009, India

© The Author(s), under exclusive license to Springer Nature Singapore Pte Ltd. 2022
M. L. Kolhe et al. (eds.), *Smart Technologies for Energy, Environment and Sustainable Development, Vol 1*, Springer Proceedings in Energy,
https://doi.org/10.1007/978-981-16-6875-3_72

903

exceptionally mainstream. Contamination is artificial, which we observe in our everyday life. In past model of grass shaper, IC motor was the fundamental main player; on other hand, the ecological factor began influencing due to the discharge because of IC motors. Thus, in light of such effect, contamination level is ascending to its most significant level from most recent couple of many years. Advanced mechanics is one of the strategies for creating PC programs. It decreases season of improvement and costs. In particular, advanced mechanics iteratively changes a populace of PC programs into another age of projects by applying analogs of normally happening hereditary activities. The objective is that the cutting edge projects should each time get better outcomes at tackling given issue than the past age and that is the reason the determination of appropriate people for hereditary tasks is so significant. This is given by wellness capacity and choice strategies. The general objective is to advance an effective control program for programmed grass shaper by methods for hereditary programming. The fundamental work is the way hereditary programming can be applied to a basic issue. The issue is to find strategy which can control grass shaper with arbitrarily orchestrated snags and to cut biggest region without repetitive moves. The point is the means by which determination of appropriate people for production of cutting edge is finished by plan programmed grass shaper.

2 Identification of Problem

The previous category of grass cutting is physically operated by the utilization of hard gadget like scissor, this work leads to layman's laborious work and involved into more human efforts, and additional time was also required for achieving the outcome of the work [1]. Similarly also unevenness of the grass heights and in consistency. Likewise usage of motor-operated mechanisms created noise pollution. Additionally, emission of contaminated gases, i.e., air pollution would also be created if fuel-operated motor grass cutter was used. Now, all these drawbacks resulted an attempt toward the innovation for grass cutter and shaper which would definitely reduce all the above problems mentioned.

3 Engineering Approach

The research is planned to execute a well-defined programmed grass mover and shaper which is ought to work with the help of RF module and maintain a strategic distance from the downsides of old yard mover. The reason for existing is to maintain a strategic distance from energy emergency in India and diminish the human endeavors, working expense, and support cost. Additionally, it keeps the climate perfect and sound. It is utilized for cutting various sorts of grasses for different applications. The RF module (collector and transmitter) is utilized in the model.

Components

- RF module (transmitter and receiver) remote
- High-speed DC motors
- Controller
- Sprinkle.

3.1 RF Module (Transmitter and Receiver) Remote

The principle part of the RF-based home automation is the RF module. A RF module is a little electronic circuit which is utilized to send or get information wirelessly. RF modules are frequently utilized in purchaser applications where you have to distantly control a few machines or apparatuses without connecting with them. A portion of the basic applications are remote alert frameworks, carport entryway openers, modern controllers, remote home computerization frameworks, and keen sensor applications. RF modules do not need view activity. Thus, they are frequently utilized rather than infrared controllers. Contingent on the sort of utilization, the RF module is picked. For instance, in the event of short-range wireless control applications, we can use ASK-modulated RF module of frequency 315 or 433 MHz. RF module generally comprises an RF transmitter and an RF receiver. RF transmitter is used to transmit the data, while the RF receiver is used to receive the data (Figs. 1 and 2).

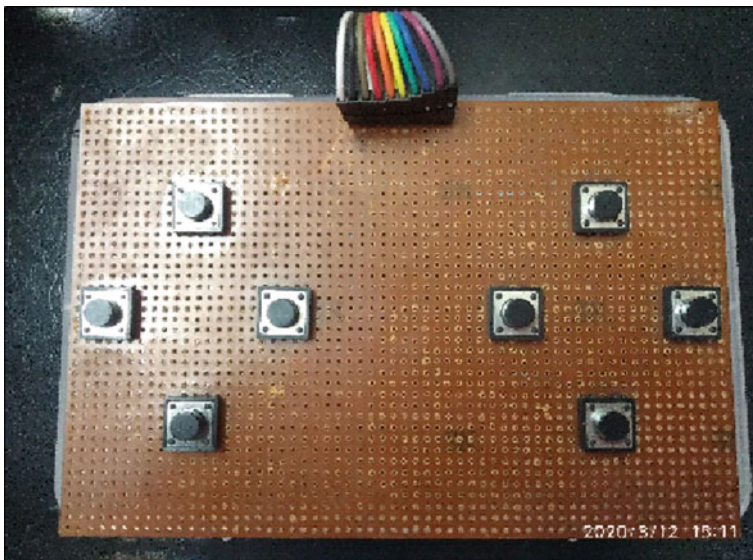


Fig. 1 RF module

Fig. 2 Transmitter and receiver

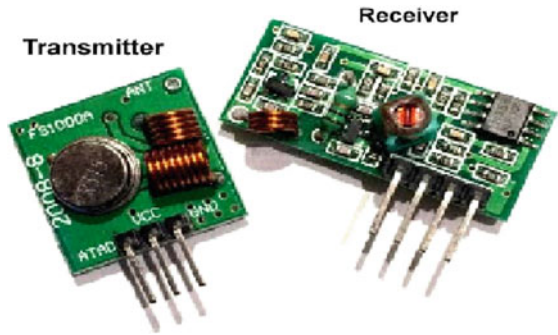


Fig. 3 DC motor



3.2 DC Motor

DC stands for “direct current,” and they were the first type of motors that were commonly used because they could be powered from a preexisting power distribution system. The speed in a DC motor can be adjusted through the intensity of its current [2]. The current is carried through an armature or stator. The armature contains the coiled (star formation for a stator) copper or aluminum wiring (commonly referred to as “windings”), and they both provide points for the wire to connect to the rest of the motor so that the electricity can continue to flow properly (Fig. 3).

3.3 Controller

A controller is a comparative device that receives an input signal from a measured process variable, compares this value with that of a predetermined control point value (set point), and determines the appropriate amount of output signal required by the final control element to provide corrective action within a control loop. An electronic controller uses electrical signals and digital algorithms to perform its receptive, comparative, and corrective functions [3]. An electronic controller is best suited for applications where large load changes are encountered and/or fast response



Fig. 4 Sprinkle

changes are required. Electronic controllers have full auto tuning and PID capabilities and offer a host of available options, including user-selectable inputs and ranges, outputs, setback functions, and alarms. An economical “on/off” only style is also available for simple control applications.

3.4 Sprinkler

The sprinkler heads work on a pressure system that when the water goes through the pipe, it pushes them up above the ground. When the water pressure stops, they retract back down to ground level (Fig. 4).

4 Engineering Computer-Aided Design for the Proposed Model

With the help of CAD, the proposed diagram done in previous work is drawn with proper designed material and specification (Figs. 5, 6, 7 and 8).

Fig. 5 CAD model of grass shaper

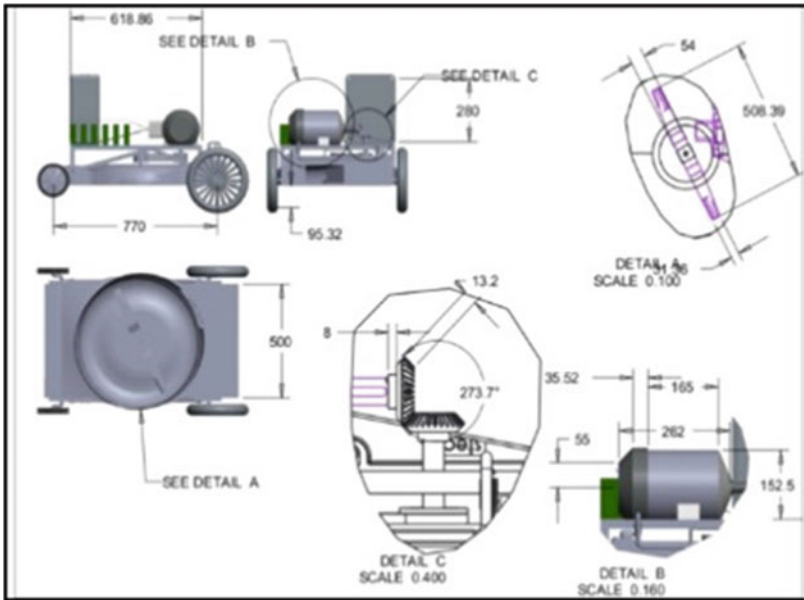
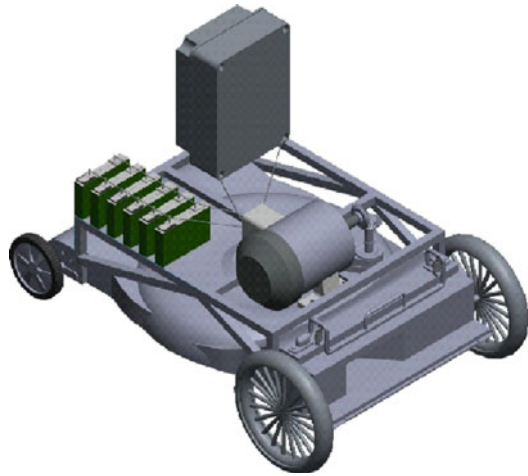


Fig. 6 Assembly of CAD model

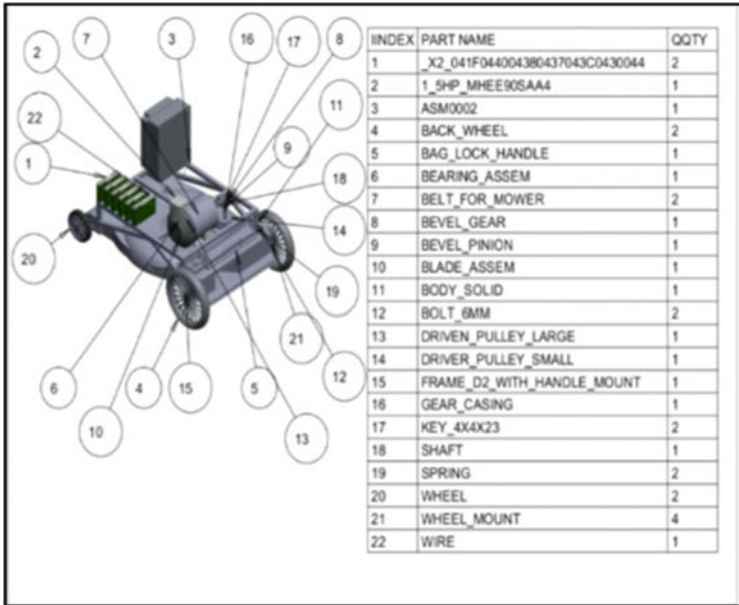


Fig. 7 Different parts of grass shaper showing the assembly

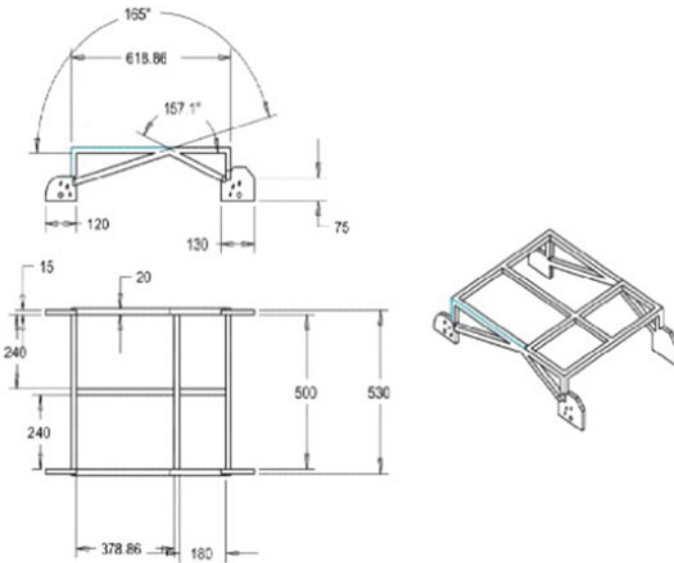
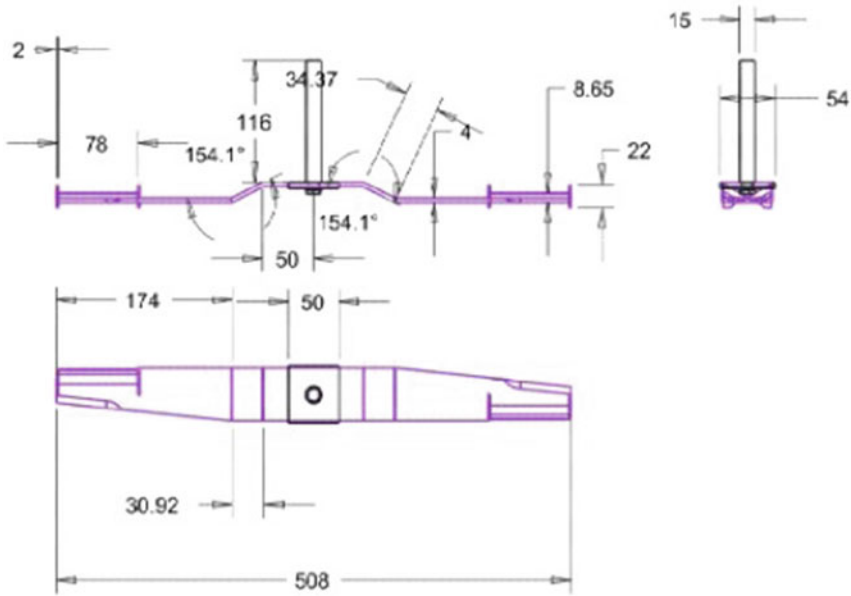


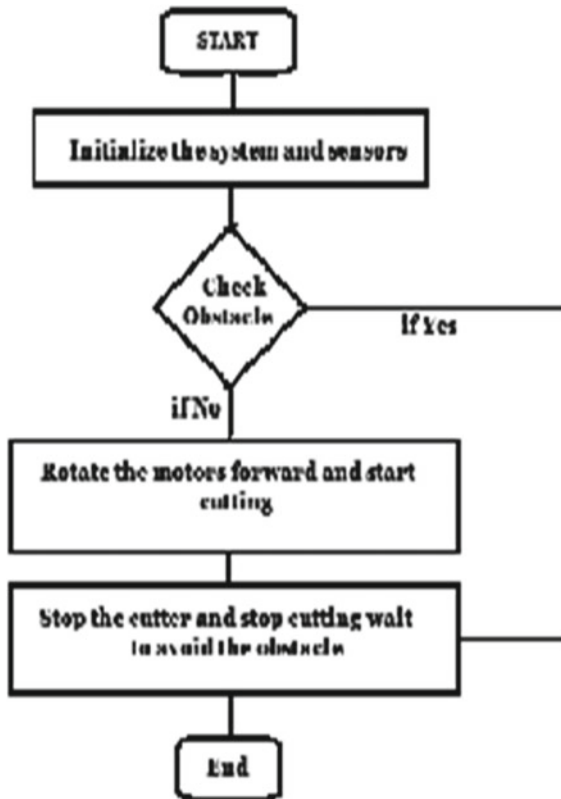
Fig. 8 Drafting view of the assembly



5 Research Methodology

The project concentrates basically on designing a suitable and easy-to-use operating system. To maintain simplicity and economy in the design, the locally fabricated unit has been used. The hybrid machine is fabricated using PVC pipes so as to make the vehicle lightweight, robust, and non-corrosive [4]. Automatic grass cutter is a control device used to cut the grass at variable heights using rechargeable batteries. Two batteries are used with two vehicle motors for forward movement of the cutter as well as for steering and a high-speed high torque DC motor for cutter. The chassis is powered by DC-gearred motor which is also supplied from same power source. The chassis is remotely operated using RF module (transmitter and receiver). For forward, reverse movement the motor are supplied at the same time by module and for left/right operation any one motor is to the power source. The motor is connected to the batteries through charge controller. Between these, a two motor driver is provided. It starts and stops the working of the motor. From this motor, the power transmits to the mechanism, this makes the blade to rotate with high speed, and this makes to cut the grass as well as mopping operation [5]. The blade will get kinetic energy while increasing the rpm. The edges are very smooth and accurate. Also, grass cutting machines are much easier to be used in garden, lawn, and grass fields. In order to enhance the beauty of lawns and playgrounds, an arrangement is also provided to cut the grass in required length. For fan operation, the movable arm is tilted to 90

vertical, and by replacing the detachable cutting blade with fan propeller, we can use the same project for fan operation.



6 Working of Grass Cutter

Coming to the working of grass cutter, it has sprinkler mounted on the top of the model in the particular arrangement such that it sprays water at the lawn by moving around. The electric energy is stored in the battery i.e., fuel cell. The motor is connected to the battery through connecting wires. The model can operate through RF module by the remote controller at a long range. The cutting blades tap the power from DC motor which in turn actuates the blades, and hence, rotating blades cut the grass. Also, it can give proper shape to grass as per the requirement.

7 Discussion and Conclusion

Automatic grass cutter is a device specifically operated by remote, and the best part of the cutter is that it is operated by fuel cell. The energy generated to be converted in fuel cell is done experimentally and successfully completed. Also, the scope of the project is that it can be further used for further modifications. The salient feature of grass cutter is that it occupies less space as it is compact in size, and additionally, it is light in weight. An automatic grass cutter is a modern-day tool which erases much of human efforts of its users by saving the time, is easy to use in any weather conditions, and provides an interface which is easy to use [6]. The project has opened doors for variant like automatic multiple grass cutter or super modified cutter which can bring revolution in agriculture field. As price of fuel is rising, world is moving toward renewable energy. Mostly remote operated that too by fuel cell batteries is big innovation. Grass cutter is used to keep the lawn clean and uniform in gardens, schools, and playgrounds.

References

1. E. Naresh, B. Babu, G. Rahul, Grass cutting machiner. *Int. J. Mag. Eng. Technol. Manage. Res.* **3**, 2348–4845 (2016)
2. P.P. Ulhe, M.D. Inwate, F.D. Wankhede, K.S. Dhakle, Modification of solar grass cutting machine. *Int. J. Innov. Res. Sci. Technol.* **2**, 2349–6010 (2016)
3. V. Jain, S. Patil, P. Bagane, S.S. Patil, Solar based wireless grass cutter. *Int. J. Sci. Technol. Eng.* **2**, 2349–784X (2016)
4. S. Mohyuddin, K.D. Digesh, T.K. Vivek, F. Nazeya Khanam, H.V. Vidyashree, Automatic grass cutter. *Int. J. Sci. Technol. Eng.* **2**, 2349–784X (2016)
5. D. Satwik, N. Ramalingeswara Rao, S. Reddy, Design and fabrication of lever operated solar lawn mower
6. O.A Tanimola, P.D Diabana, Y.O. Bankole, Design and development of a solar powered lawn mower. *Int. J. Sci. Eng. Res.* **5** (2014)
7. S. Sujendran, P. Vanitha, Smart lawn mower for grass trimming. *Int. J. Sci. Res.* **3**, 2319–7064 (2014)
8. A.G. Khan, A.-H. Qurishi, Commercial grass cutting cum collecting machine. **10**(1) (2013)
9. Mower History, *The Old Lawnmower Club Collection, Preservation and Display of Old Lawn Mowers*. N.p., n.d. Web. 29 Feb 2012
10. A. Dipin, T.K. Chandrashekhar, Solar powered vision based robotic lawn mower. *Int. J. Eng. Res. Rev.* **2**, 53–56 (2014)
11. S. Diggs, *Corded Versus Cordless Electric Lawn Mowers*. ehow. N.p., n.d. Web. 29 Feb 2012

Performance Evaluation of Adhesive Bonded Tools Using Design of Experiments



Shrikant Jachak, Ashvin Amale, and Sachin Mahakalkar

Abstract Metal cutting is a significant operation in industries of developed countries and is developed to its maximum extent. Still, an alternate cutting tool material in the turning operations is gaining popularity against conventional tool materials over the past few years. This paper reports performance investigation of the adhesive bonded cutting tools as compared to the conventional brazed tools. The comparison was carried out by using factorial experimentation. A statistical mathematical model of the process is obtained by using factorial experimentation, regression analysis and movement along the gradient. Response surface methodology and steepest ascent method is used for finding the performance of the adhesive bonded tools as against the brazed tools. This experimentation indicates that all the major constraints of measuring cutting tool performance, namely tool life, cutting forces and surface roughness of machined parts, are improved as compared to the conventional brazed tools. The present work has indicated that adhesive bonded tools has an edge over brazing tools and hence may be used with distinct advantages in the field of metal cutting.

Keywords Adhesive bonded tool · Factorial experimentation · Regression analysis · Steepest ascent method · Cutting force · Surface roughness · Tool life

1 Introduction

The development of carbide-tipped tools has revolutionized metal cutting field. In the field of metal cutting, most of the operations are being performed by tools having inserts fitted on pre-machined M.S. shank seat by brazing, welding or mechanical

Present Address:

S. Jachak (✉) · A. Amale
Department of Mechanical Engineering, Yeshwantrao Chavan College of Engineering, Nagpur,
Maharashtra 441110, India

S. Mahakalkar
Department of Mechanical Engineering, Rajiv Gandhi College of Engineering and Research,
Nagpur, Maharashtra 441110, India

clamping. Microfissures resulting from high temperature of brazing operation and inadequate contact stiffness in mechanical clamping adversely affect tool life, cutting forces, surface roughness of machined components and is subjected to more vibrations of tools [1]. The desire to achieve maximization of tool life for inserts in the most economic and effective manner, reducing the cutting forces and imparting better surface finish to the machined components, has led the use of adhesive bonding as a possible alternative to conventional processes of brazing and mechanical clamping [1, 2]. Apart from achieving tool economy by way of reduced insert rejections, adhesive bonding has also the advantage of requiring lower temperatures during assembly, less skilled labors and improved damping capacity [2, 3]. The principal objective of this paper is to search whether Anabond 220 bonding tool can be used as a possible substitute to the conventional processes of assembling inserts with shanks and compare the performance of adhesive bonded tool and brazed tool in the turning operation. Cutting forces acting on the tools, tool life and the surface roughness of the machined parts are the parameters considered in this experimentation work to observe the performance of the Anabond 220 and conventional brazed tools [4]. While observing the performance, the factors which affect the performance of the tools such as the cutting speed, feed, depth of cut, coolant flow rate and tool geometry are kept same for both the adhesive bonded tools and conventional brazed tools [5, 6]. The adhesive bonded tools are manufactured by fixing the carbide inserts on the pre-machined shanks with the help of Anabond 220 epoxy. Brazed tools of similar geometry and having same carbide inserts are manufactured. The experiment is planned by using full factorial experimentation. Experimentation is carried out and cutting forces acting on these tools, surface roughness of the machined components and tool lives are measured [6, 7]. Response surface methodology is used for finding the optimal conditions. ANOVA is performed in order to statistically analyze the results. The adequacy of the model is checked and process optimization is done using response surface methodology [8].

2 Research Approach and Experimental Procedure

The main aim of the study is assessment of the cutting forces acting on the tool, tool life and surface finish produced during turning operation keeping the similar cutting conditions for both conventional brazed tool and Anabond 220 tools. Turning tests are performed on a high-rigidity HMT TL 20 lathe. Work pieces of an unalloyed medium carbon steel EN8 HB 230 is used. They are 250 mm long with an external diameter of 50 mm. The cutting tool material is Sandvik TNMG 16 04 04 MF. The inserts conformed to the ISO code: (a) conventional SNGN 120408 T01020. According to the data provided by the manufacturer, the insert used for bonded and brazed tools has the specifications: (i) Inscribed circle (IC) = 9,525 mm, (ii) Insert thickness = 3 mm, (iii) Nose radius = 1.6 mm, (iv) Cutting edge condition = negative land, (v) Insert shape = equilateral triangle of side 14 mm [7].

Table 1 Specifications of machining parameters

Factors	Basic level	Upper level	Lower level
Cutting speed (m/min)	89	112	66
Feed rate (mm/rev)	0.09	0.13	0.05
Depth of cut (mm)	1.0	0.5	1.5
Coolant flow rate (mL/s)	34	48	20

A one work piece dynamometer is designed and manufactured for the measurement of cutting forces. The surface roughness of the machined component is measured by Mitutoyo make SJ-201 surface roughness tester. AC variac transformer is used for varying the flow of the coolant pump. The turning process parameters that may affect the machining characteristics of the machined parts have been decided on the basis of the literature survey and the strength of the Anabond 220. Result of the pilot experiments are also utilized for deciding the levels of parameters for the feed rate, cutting speed, depth of cut and coolant flow rate. The cutting conditions used during machining operations are shown in Table 1.

3 Design of Experiments

Design of experiments are considered to be a very useful tool for generating clear and accurate data in an orderly manner. In this phase of experimentation, a design of experimentation technique, viz., response surface method is used for understanding the influence of four process factors, i.e., cutting speed, feed rate, depth of cut and coolant flow rate on the response functions such as the cutting forces exerted on the tool, surface roughness of the machined component and the tool lives of the Anabond 220 tools and the brazed tools. A two-level four-factor full experimentation is performed [8–10].

3.1 Response Surface Methodology

Box and Wilson have proposed response surface methodology for the optimization of experiments. An empirical relationship between various process parameters and response with the various desired criteria and searching the significance of these process parameters on the coupled response is given by response surface methodology [11]. It is a sequential experimentation strategy for model building and its optimization. By using the design of experiments and applying regression analysis, the modeling of the desired response to several independent input variables could be

gained. Response surface methodology gives the relationship between the desired output and independent input parameters and can be represented as [12, 13].

$$y = f(x_1, x_2, x_3, \dots x_n) \pm er \tag{1}$$

where y is the desired response, f is the response function, er is fitting error and $X_1, X_2, X_3 \dots X_n$ are independent input parameters. In this research, the approximation of f will be proposed using the fitted second-order polynomial regression model called the quadratic model.

4 Planning of Experimentation

Turning of medium carbon steel EN8 HB 230 is carried out by tungsten carbide inserts fitted on shank by means of brazing and Anabond 220 adhesive on a sturdy HMT TL-20 lathe machine as per the plan of experiments [14, 15]. Values of responses, viz., cutting forces exerted on Anabond tools and brazed tools, surface roughness of machined components and tool lives of Anabond tools and brazed tools are measured [16]. The measured values of the responses are shown in Tables 2 and 3.

Table 2 Experimental observations for adhesive bonded tools

Trial No.	Cutting speed (m/min)	Feed (mm/rev)	Depth of Cut (mm)	Coolant flow rate (mL/s)	Cutting force (N)	Surface roughness (µm)	Tool life (min)
1	66	0.05	0.5	20	92.66	14.6	70.4
2	112	0.05	0.5	20	102.61	9.0	39.1
3	66	0.15	0.5	20	163.92	15.9	20.6
4	112	0.15	0.5	20	226.91	12.5	12.8
5	66	0.05	1.5	20	201.20	15.0	60.9
6	112	0.05	1.5	20	308.76	7.5	31.8
7	66	0.15	1.5	20	516.64	21.0	17.9
8	112	0.15	1.5	20	568.19	18.0	10.3
9	66	0.05	0.5	48	87.21	14.5	71.4
10	112	0.05	0.5	48	92.45	8.0	39.4
11	66	0.15	0.5	48	160.49	16.0	21.2
12	112	0.15	0.5	48	216.70	12.0	13.1
13	66	0.05	1.5	48	196.69	14.5	61.9
14	112	0.05	1.5	48	257.75	7.5	32.3
15	66	0.15	1.5	48	490.59	20.75	18.2
16	112	0.15	1.5	48	515.90	16.5	10.7

Table 3 Experimental observations for brazed tools

Trial No.	Cutting speed (m/min)	Feed (mm/rev)	Depth of cut (mm)	Coolant flow rate (mL/sec)	Cutting force (N)	Surface roughness (μm)	Tool life (min)
1	66	0.05	0.5	20	98.06	15.1	65.45
2	112	0.05	0.5	20	103.21	10.1	36.4
3	66	0.15	0.5	20	175.50	17.0	19.7
4	112	0.15	0.5	20	247.80	14.0	12.0
5	66	0.05	1.5	20	206.50	16.5	51.4
6	112	0.05	1.5	20	320.10	7.7	29.1
7	66	0.15	1.5	20	567.90	21.3	16.1
8	112	0.15	1.5	20	619.50	18.3	9.35
9	66	0.05	0.5	48	87.70	16.6	67.8
10	112	0.05	0.5	48	98.1	9.0	36.9
11	66	0.15	0.5	48	165.20	16.1	20.8
12	112	0.15	0.5	48	232.30	12.6	12.6
13	66	0.05	1.5	48	201.30	15.0	52.9
14	112	0.05	1.5	48	273.60	7.8	30.4
15	66	0.15	1.5	48	516.25	20.5	17.7
16	112	0.15	1.5	48	577.71	16.8	10.3

5 Results

Experimental results during turning of medium carbon steel EN8 by using Anabond tools and brazed tools have been analyzed. In order to statistically analyze the results, ANOVA is performed for the cutting forces exerted on tools, surface roughness of the machined components and tool lives of the Anabond 220 tools and conventional brazed tools.

5.1 Comparative Cutting Forces for Bonded and Brazed Tools

The cutting force exerted on the adhesive bonded tools and brazed tools for the optimum cutting conditions are as shown in Table 4.

The regression equations for the response characteristics as a function for the input factors considered in this experiment are given below.

1. Relationship between cutting force and the various factors for adhesive bonded tools are:

Table 4 Optimum cutting conditions for cutting force

Type of tool	Cutting speed (m/min)	Feed (mm/rev)	Depth of cut (mm)	Coolant flow rate (mL/s)	Cutting force (N)
Anabond tools	83	0.105	1.21	33.5	563
Brazed tools	83	0.105	1.21	33.5	602

$$\text{Cutting Force} = 26.75 + 2.4203 x_1 + 9.6653 x_2 + 12.1867 x_3 - 1.0390 x_4 + 0.0966 x_1 x_2 + 0.7153 x_1 x_3 - 0.5353 x_1 x_4 + 4.6678 x_2 x_3 - 0.1341 x_2 x_4 - 0.6916 x_3 x_4 - 1.2722 x_1 x_2 x_3 + 0.0972 x_1 x_2 x_4.$$

2. Relationship between cutting force and various factors for brazed tools are:

$$\text{Cutting Force} = 28.61 + 2.8919 x_1 + 10.9175 x_2 + 13.22 x_3 - 1.1875 x_4 + 0.325 x_1 x_2 + 0.9175 x_1 x_3 - 0.2 x_1 x_4 + 5.3906 x_2 x_3 - 0.3319 x_2 x_4 - 0.6619 x_3 x_4 - 1.2531 x_1 x_2 x_3 + 0.2594 x_1 x_2 x_4 - 0.2006 x_1 x_3 x_4 - 0.2 x_2 x_3 x_4 + 0.3925 x_1 x_2 x_3 x_4.$$

In this analysis, it has been found that the regression co-efficient for all the factors for brazed tools are comparatively larger than that of bonded tools. This indicates that with increase in the value of cutting speed, feed rate and depth of the value of cutting force increase. Increasing the value of coolant flow rate, the cutting force diminishes. In this investigation, cutting forces acting on the adhesive bonded tools are found out to be less as compared to the conventional brazed tool.

5.2 Comparative Surface Roughness for Bonded and Brazed Tools

The surface roughness values for adhesive bonded tools and brazed tools for the optimum cutting conditions are as shown in Table 5.

The regression equations for the response characteristics as a function for the input factors considered in this experiment are given below.

1. Relationship between surface roughness and the various factors for adhesive bonded tools:

Table 5 Optimum cutting conditions for surface roughness

Type of tool	Cutting speed (m/min)	Feed (mm/rev)	Depth of cut (mm)	Coolant flow rate (mL/s)	Surface roughness (µm)
Anabond tools	54	0.129	1.186	32.5	20.31
Brazed tools	54	0.129	1.186	32.5	21.21

$$\text{Surface Roughness} = 13.84 - 2.4406 x_1 + 2.5969 x_2 + 1.1406 x_3 - 0.2781 x_4 + 0.7469 x_1x_2 - 0.1094 x_1x_3 - 0.0656 x_1x_4 + 1.2031 x_2x_3 - 0.1281 x_2x_4 - 0.1094 x_3x_4 - 0.2656 x_1x_2x_3 - 0.0281 x_1x_2x_4 + 0.1406 x_1x_3x_4 - 0.1969 x_2x_3x_4 - 0.0844 x_1x_2x_3x_4.$$

2. Relationship between surface roughness and the various factors for brazed tools:

$$\text{Surface Roughness} = 14.5125 - 2.475 x_1 + 2.55 x_2 + 0.975 x_3 - 0.4875 x_4 + 0.8375 x_1x_2 - 0.3625 x_1x_3 + 1.1875 x_2x_3 - 0.1 x_2x_4 + 0.025 x_3x_4 + 0.325 x_1x_2x_3 - 0.1375 x_1x_2x_4 + 0.1125 x_1x_3x_4 - 0.125 x_2x_3x_4 - 0.15 x_1x_2x_3x_4.$$

In this analysis, it has been found that the regression co-efficient for all the factors for brazed tools are comparatively larger than that of bonded tools. In the optimal conditions, it is found that the surface finish value of the brazed tool is larger than that acting on bonded tools.

5.3 Comparative Tool Lives for Bonded and Brazed Tools

The tool lives values for adhesive bonded tools and brazed tools for the optimum cutting conditions are as shown in Table 6.

The regression equations for the response characteristics as a function for the input factors considered in this experiment are given below.

1. Relationship between tool life and the various factors for adhesive bonded tools:

$$\text{Tool Life} = 33.25 - 9.5625 x_1 - 17.65 x_2 - 2.75 x_3 + 0.275 x_4 + 5.6875 x_1x_2 + 0.3375 x_1x_3 - 0.0875 x_1x_4 + 1.425 x_2x_3 - 0.075 x_2x_4 - 0.2375 x_1x_2x_3 + 0.0625 x_1x_2x_4 + 0.0375 x_1x_3x_4 - 0.025 x_2x_3x_4 - 0.0125 x_1x_2x_3x_4.$$

2. Relationship between tool life and the various factors for brazed tools:

$$\text{Tool Life} = 30.6188 - 8.3625 x_1 - 15.675 x_2 - 3.4 x_3 + 0.6813x_4 + 4.7312 x_1x_2 + 1.0563 x_1x_3 - 0.1375 x_1x_3 + 1.9438 x_2x_3 - 0.025 x_2x_4 + 0.05 x_3x_4 - 0.8375 x_1x_2x_3 + 0.1188 x_1x_2x_4 + 0.0938 x_1x_3x_4 - 0.0563x_2x_3x_4 - 0.1125 x_1x_2x_3x_4.$$

It has been found that the regression co-efficient for all the factors for brazed tools are comparatively larger than that of bonded tools. Here, negative sign indicates the decrease in tool life. In the optimal conditions, it is found that the tool life for the

Table 6 Optimum cutting conditions for tool lives

Type of tool	Cutting speed (m/min)	Feed (mm/rev)	Depth of cut (mm)	Coolant flow rate (mL/s)	Tool life (min)
Anabond tools	71	0.06	0.94	36.5	52.25
Brazed tools	71	0.06	0.94	36.5	46.86

brazed tool is less than the bonded tools. In this experimentation, it has been found that the cutting forces acting on the adhesive bonded tools are reduced by 6.5% as compared to that on the conventional brazed tools. 4.25% improved surface finish is obtained with adhesive bonded tools than the brazed tools, and 11.5% increased tool life is observed for adhesive bonded tools as compared to brazed tools.

6 Conclusions

The aim of research was to check the feasibility of adhesive bonding as a possible substitute to the traditional process of assembling inserts with shanks by comparing the performance of adhesive bonded tools and brazed tools in the turning operation. Following logical conclusions are drawn while assessing the performance of the adhesive bonded in relation to brazed tool in the turning operation:

- Most of the adhesives are inherently less rigid than metals and damp vibrations. Due to damping provided by the adhesives, the cutting forces exerted on the adhesive bonded tools are less as compared to the conventional brazed tools.
- Surface finish is largely dependent on the cutting edge, its sharpness. But in case of brazing, due to high brazing temperature, microfissures are formed over the entire surface of the carbide inserts, which are mainly responsible for poor surface finish. Whereas, bonding involves very less curing temperature and does not form such microfissures. Hence, adhesive bonded tools fractured less as compared to brazed tools. As a result, improved surface finish is obtained with adhesive bonded tools than the brazed tools.
- Anabond 220 adhesive has good damping properties, and their use for cutting tool fabrication would result in an improvement in the damping parameters of the adhesive bonded tools and consequently decrease any wear which results from tool vibration; hence, increased tool life is observed for adhesive bonded tools as compared to brazed tools. To summarize, this research has provided deeper insights while comparing the performance of the above-mentioned tools, and it was found that the adhesive bonded tools has an edge over brazed tools and hence, may be used with distinct advantages in the field of metal cutting.

Scope of Future Work

The present work has indicated that adhesive bonding may be employed with distinct advantages over brazing in the field of tool manufacturing. However, there is a lot of scope for furthering knowledge and expertise in this field, which is summed up below:

- A suitable adhesive needs to be investigated and subsequent emergence of the most suitable one can be considered for adhesive bonded tools manufacturing. Literature reveals that adhesive bonded tools have shown better performance in

milling operations; hence applications of bonding to multipoint tools such as drilling, reaming needs to be studied and explored.

- A hybrid tool, i.e., a combination of mechanically clamped tools and adhesive bonded tools, may perform even better than the conventional tools.

References

1. S. Darwish, S. Davies, Adhesive bonding of metal cutting tools. *Int. J. Mach. Tools Manuf.* **29**, 141–152 (1989)
2. A.M. Al-Samhan, Thermal-stresses in carbide-tip bonded face milling cutters. *J. King Saud. Univ. Eng. Sci.* 85–94 (2012)
3. M.A. Younis, Mechanical and thermal stresses in clamped, brazed, and bonded carbide tools. *J. Eng. Indust.* **144**, 377–385 (1992)
4. U. Alpher, Turning performance of bonded cutting tools with nanographene or multi-walled carbon nanotube particle-reinforced epoxy-based nanocomposite adhesives. An article, Springer professionals (2019)
5. W. Grzesik, T. Wanat, Surface finish generated in hard turning of quenched alloy steel parts using conventional and wiper ceramic inserts. *Int. J. Mach. Tools Manuf.* **46**(15) (2006)
6. M. Movahhedy, M.S. Gadala, Y. Altintas, Simulation of orthogonal metal cutting process using an arbitrary Lagrangian-Eulerian finite-element method. *J. Mater. Process. Technol.* **103**, 267–275 (2000)
7. J.A. Arsecularatne, P. Matthew, Calculation of optimum cutting conditions for turning operations using a machining theory. *Int. J. Mach. Tools Manuf.* **40**, 1709–1733 (2000)
8. C.J. Rao, D. Nageshwara Rao, P. Srihari, Influence of cutting parameters on cutting force and surface finish in turning operation. *Proc. Eng.* **64**, 1405–1415 (2013)
9. M. Nasser, B. Jawad, Design of experiments as effective design tools. *Int. Mech. Eng. Congr. Expos.* **4**, 441–448 (2008)
10. A. Esposito, P. Fabio, F. Postiglione, M. Guida, C. Pianese, A. Pohjoranta, Experimental test plan and data analysis based on the design of experiment methodology, in *International Conference on Fuel Cell Science, Engineering and Technology Collocated with the ASME*, pp. 293–302 (2012)
11. S.R. Das, R.P. Nayak, D. Dhupal, Optimization of cutting parameters on tool wear and work-piece surface temperature In turning of AISI D2 steel. *Int. J. Lean Think.* **3**, 141–153 (2012)
12. M.N. Islam, B. Boswell, An investigation of surface finish in dry turning, vol. 1, in *Proceedings of the World Congress on Engineering* (2011)
13. A.D. Crocombe, D.A. Bigwood, G. Richardson, Analyzing structural adhesive joints for failure. *Int. J. Adhesion Adhesives* **10**(3), 167–178 (1990)
14. X. Wu, The Effect of adhesive curing condition on bonding strength in auto body assembly. *J. Manuf. Sci. Eng.* 411–19 (2005)
15. P. Glass, H. Chung, C. Lee, E. Tworzoski, N.R. Washburn, M. Sitti, Biologically-inspired patterned and coated adhesives for medical devices. *J. Med. Dev.* **3** (2009)
16. J. Zuo, L. Youxi, H. Ming, An investigation of the adhesive effect on the flank wear properties of a wc/co-based tialn-coated tool for milling a be/cu alloy metals (2019)

Analyzing the Mutual Interaction Among the Barriers of Additive Manufacturing: An Interpretive Structural Modelling Approach



Reetika Pandey and Ubaid Ahmad Khan

Abstract Additive Manufacturing (AM) technologies have seen substantial growth in the past few decades. By democratizing design and manufacturing Additive Manufacturing also inspired the maker movement, even though AM in itself is theoretically adequate, practically various delicate barriers intercept the AM implementation. Therefore, this paper tries to find those AM barriers and understand interplay between barriers. These AM barriers were identified and validated by expert opinion and by a detailed literature review. For determining the mutual influences between the barriers the Interpretive Structural Modelling (ISM) is used for finding the cross-effect amidst AM barriers. ISM ascertains the level of barriers and categorises AM barriers according to dependence and driving power.

Keywords Additive manufacturing · Additive manufacturing barriers · Interpretive structural modelling

1 Introduction

Embarkation of AM has received worldwide consideration, with renewed interest; This AM technology is constantly being re-defined, revised, also adapted to a vast range of applications namely medicine, automobile, aerospace engineering, food supply chain, biological systems. The history of AM shows that the beginning of AM comes from Photographic sculpture and topography (in the 1860s) (in the 1890s) [1]. AM process commences with the three dimensional solid prototypes, which is preliminary scanned or pre-modelled as a digital CAD file, after that shredded among the numbers of flakes (based on resolution) through the preparation software. Every flake is generated through a selective material deposition to create a printed primitive. When AM is combined with other technology it has considerable future potential. Four main trends-vat photo polymerization, powder bed fusion, material extrusion and binder jetting is the root of recent AM technologies [2, 3].

R. Pandey · U. A. Khan (✉)

Department of Mechanical Engineering, Shambhunath Institute of Engineering & Technology, Prayagraj, U.P., India

The objective of the research is to find the main AM barriers that become a hurdle in the application of AM in manufacturing industries. In this research paper, 16 AM barriers have been identified. ISM methodology is employed to generate the sequence of the pre-discerned AM barriers. AM barriers at the root of the sequence are called driver barriers as well as at the top of the sequence are known as dependent barriers. This research paper is split into six sections with an introduction in the first section, the second with regard to the literature, the third with regard to the ISM approach, the fourth with regard to the ISM model, the fifth with regard to the categorization of AM obstacles and the sixth with regard to the conclusion and possible facets of this research paper.

2 Literature Review

The growth of AM has not been less than extraordinary over the past few decades [4]. The AM method creates physical objects line-by-line, part-by-part, layer-by-layer or surface-by-surface from digital information [5, 6].

For infrequently demanded manufacturing goods AM can create a market [7]. Very few researchers concluded on Additive Manufacturing barriers and their effectiveness with the help of ISM. By increasing, workpiece mass AM processes are characterized. They constitute one of the three main categories of the manufacturing techniques, together by a formative procedure in which the ambient part of the piece is preserved and subtractive processes in which the mass of the workpiece is reduced [8]. In Table 1, there are 16 AM hurdles that are selected from separate literature reviews and discussed with industry experts.

3 ISM Methodology

ISM methodology is a procedure that transforms indistinct and badly lucid mental samplers of a method in form of an apparent and demonstrated sampler. In 1974 First J. Warfield introduced ISM [12]. The ISM deals with the interpretation of the object via graph theory with contractual connection among the elements. For the development of ISM model, we use variables in limited numbers. If the variable number in the problem increases, then it increases the complexity of ISM.

3.1 Structural Self Interaction Matrix (SSIM)

For build relationships between barriers, we discussed with academics, industry specialists and a group of engineers. The contextual relationship of the type of “influences” or “leads” should be chosen for the factor analysis [13]. This suggests that

Table 1 Additive manufacturing barriers (AMBs)

AM barriers No.	AM barriers	[1]	[4]	[9]	[10]	[11]
1	Software complexity		✓	✓		✓
2	Lack of expert designers			✓		
3	Cost incurred in AM implementation			✓	✓	
4	Poor surface finish	✓	✓	✓		
5	Limited object size			✓		
6	Low production rate					✓
7	Part to part variation		✓			
8	Unavailability of industry wide slandered	✓				✓
9	Lack of skilled operators				✓	
10	Changing designer’s traditional attitude				✓	
11	Fear of stealing design inventory		✓			
12	Manual post processing	✓	✓			
13	Disjointed AM ecosystem			✓		
14	Lack of digital infrastructure			✓		
15	Production technology limitations				✓	
16	Lack of understanding and expertise					✓

one variable affects another. The qualitative alliance among the deciding factors is defined on this basis [14]. Following four symbols denotes the alliance among the additive manufacturing barriers. The notations “*i*” along with “*j*” is used to perceive the alliance among two AMB’s.

‘V’ is used when AMB *i* lead to or influences AM barrier *j* (from *i* to *j*).

‘A’ is used when AMB *i* lead to or influences by AM barriers *j* (from *j* to *i*).

‘X’ is used when AMB *i* along with *j* leads to or influences mutually (from *i* to *j* and *j* to *i*).

‘O’ is used when AM barrier *i* and *j* do not lead to or influences each other (*i* and *j* are unrelated) (Table 2).

3.2 Initial Reachability Matrix

Our next step in the ISM method is to transform SSIM into an initial reachability matrix. For converting SSIM the emblems V, X, A and O are substituting by one along with zero in initial reachability matrix (Table 3).

Table 3 Initial reachability matrix

AMB	1	2	3	4	5	6	7	8	9	10	11	12	13	14	15	16
Additive manufacturing barriers (AMBs)	1	1	1	1	1	1	1	1	1	1	1	1	1	1	1	1
Software complexity	1	1	1	1	1	1	1	1	1	1	1	1	1	1	1	1
Lack of expert designers	1	1	1	1	1	1	1	1	1	1	1	1	1	1	1	1
Cost Incurred in AM implementation	0	0	1	0	1	0	0	1	0	1	1	0	1	1	0	1
Poor surface finish	0	0	1	1	0	1	0	0	0	0	0	0	0	0	0	0
Limited object size	0	0	0	0	1	0	0	0	0	0	0	0	0	0	0	0
Low production rate	0	0	1	1	1	1	0	0	0	0	0	0	0	0	0	0
Part to part variation	0	0	0	1	1	1	1	0	1	0	0	1	0	0	0	0
Unavailability of industry wide standards	0	0	0	0	0	0	0	1	0	1	0	0	1	0	0	1
Lack of skilled operators	0	0	0	1	1	1	0	0	1	1	0	1	1	1	0	1
Changing designer's traditional attitude	0	0	0	0	1	0	0	0	0	1	0	0	0	0	0	0
Fear of stealing digital inventory	0	0	0	0	1	0	0	0	0	0	1	0	0	0	0	0
Manual post processing	0	0	1	1	0	1	0	0	0	0	0	1	0	0	0	0
Disjointed A.M. ecosystem	0	0	0	0	1	0	0	0	0	1	0	0	1	0	0	0
Lack of digital infrastructure	0	0	0	0	1	0	0	1	0	1	1	0	1	1	0	1
Production technology limitations	0	0	1	1	1	1	0	0	0	0	0	1	0	0	1	0
Lack of understanding and expertise in A.M.	0	0	0	0	1	0	0	1	0	1	1	0	1	0	0	1

(i, j) entry in SSIM	In reachability matrix	
	(i, j) entry	(j, i) entry
V	1	0
A	0	1
X	1	1
O	0	0

3.3 Final Reachability Matrix

The final reachability matrix was established after the imposition of the transitivity relationship for 1^* (Table 4).

3.4 Partition of Reachability Matrix

Hierarchy among the factors (barriers) established by the final reachability matrix in the level partition process [15]. Every factor's, antecedent sets and reachability sets are derived. A cluster of positive relationships 1 s and 1^* in column (antecedent) and row (reachability), derived to develop a category of partition. The intersection set would be segregated from consideration and held at the first level of the hierarchy, similar to the reachability set. Up until the last stage of the AM barriers, this step will be repeated. For the final reachability matrix, the degree recognition of these AM obstacles was achieved in 11 iterations (Table 5).

3.5 Development of the ISM Model

Eleven total strata establish for 16 AM barriers. Looking at these 11 levels, the ISM model includes transitive link acquired. The number of indirect and direct connections in the final reachability matrix depends on the relationships allocated by '1' and '1*', which can be indicated by a large number of arrows. On the top of the model, the top level AM barriers are mounted, while the ISM model is built and the second level AM barriers are positioned in the second position, etc. The bottom level is located at the lowest spot (Fig. 1).

Table 4 Final reachability matrix

AMB	1	2	3	4	5	6	7	8	9	10	11	12	13	14	15	16	D.P.
Additive manufacturing barriers (AMBs)	1	1	1	1	1	1	1	1	1	1	1	1	1	1	1	1	16
Software complexity	1	1	1	1	1	1	1	1	1	1	1	1	1	1	1	1	16
Lack of expert designers	1	1	1	1	1	1	1	1	1	1	1	1	1	1	1	1	16
Cost Incurred in AM implementation	0	0	1	0	1	0	0	1	0	1	1	0	1	1	0	1	8
Poor surface finish	0	0	1	1	1*	1	0	1*	0	1*	1*	0	1*	0	0	1*	9
Limited object size	0	0	0	0	1	0	0	0	0	0	0	0	0	0	0	0	1
Low production rate	0	0	1	1	1	1	0	1*	0	1*	1*	0	1*	0	0	1*	9
Part to part variation	0	0	1*	1	1	1	1	0	1	0	0	1	0	0	0	0	7
Unavailability of industry wide standards	0	0	0	0	1*	0	0	1	0	1	1*	0	1	0	0	1	6
Lack of skilled operators	0	0	1*	1	1	1	0	1*	1	1	1*	1	1	1	0	1	12
Changing designer's traditional attitude	0	0	0	0	1	0	0	0	0	1	0	0	0	0	0	0	2
Fear of stealing digital inventory	0	0	0	0	1	0	0	0	0	0	1	0	0	0	0	0	2
Manual post processing	0	0	1	1	1*	1	0	1*	0	1*	1*	1	1*	0	0	1*	10
Disjointed A.M. ecosystem	0	0	0	0	1	0	0	0	0	1	0	0	1	0	0	0	3
Lack of digital infrastructure	0	0	0	0	1	0	0	1	0	1	1	0	1	1	0	1	7
Production technology limitations	0	0	1	1	1	1	0	1*	1*	1*	1*	1	1*	0	1	1*	12
Lack of understanding and expertise in A.M.	0	0	0	0	1	0	0	1	0	1	1	0	1	0	0	1	6
Dp.P	2	2	9	8	16	8	3	11	5	13	12	6	12	5	3	11	

Table 5 Partition of reachability matrix

Barrier No.	Reachability set	Antecedent set	Intersection set	Level
1	1, 2	1, 2	1, 2	XI
2	1, 2	1, 2	1, 2	XI
3	3	1, 2, 3, 4, 6, 7, 9, 12, 15	3	VI
4	4, 6	1, 2, 4, 6, 7, 9, 12, 14, 15	4, 6	VII
5	5	1, 2, 3, 4, 5, 6, 7, 8, 9, 10, 11, 12, 13, 14, 15, 16	5	I
6	4, 6	1, 2, 4, 6, 7, 9, 12, 15	4, 6	VII
7	7	1, 2, 7	7	X
8	8, 16	1, 2, 3, 4, 6, 8, 9, 12, 14, 15, 16	8, 16	IV
9	9	1, 2, 7, 9, 14, 15	9, 14	IX
10	10	1, 2, 3, 4, 6, 8, 9, 10, 12, 13, 14, 15, 16	10	II
11	11	1, 2, 3, 4, 6, 8, 9, 11, 12, 14, 15, 16	11	II
12	12	1, 2, 7, 9, 12, 15	12	VIII
13	13	1, 2, 3, 4, 6, 8, 9, 12, 13, 14, 15, 16	13	III
14	14	1, 2, 3, 9, 14	14	V
15	15	1, 2, 15	15	X
16	8, 16	1, 2, 3, 4, 6, 8, 9, 12, 14, 15, 16	8, 16	IV

3.6 MICMAC Analysis

The principle of MICMAC is rooted in characteristics of matrices Multiplication [16]. This analyzes driving and dependence power of Additive manufacturing barriers. This identifies the key additive manufacturing barriers that classify the barriers in various clusters autonomous, linkage, dependent and driver additive manufacturing barriers.

Autonomous AMB Cluster-I—The autonomous AMB’s have low driving power with weak dependency power. They didn’t have too much control over the system. Barriers 7 and 14 are an autonomous barrier.

Dependent AMB Cluster-II—The dependent Barriers have low driving power with high dependency power. Dependent barriers are situated on top of the model. Therefore they are recognized as a vital barrier. In this study barriers number 3, 8, 16, 13, 11, 10 and 5 are dependent AMB’s.

Linkages AMB Cluster-III—The linkages AMB have high driving with high dependency power. They also affect the well-turned Additive Manufacturing execution. In this study linkage barriers are nil.

Independent or Driver AMB Cluster-IV—The independent AMB are having high driving power with low dependency power. Because of that, the manager should focus on these barriers to eliminate these independent AMBs for the successful

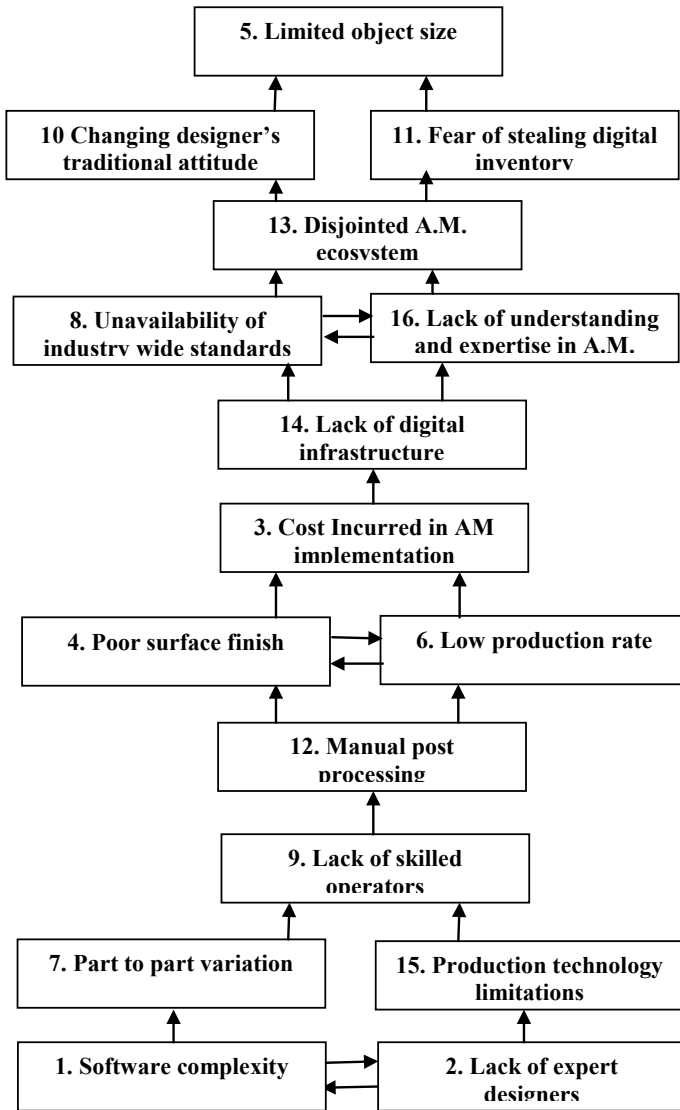


Fig. 1 ISM model of AM barriers

implementation of Additive Manufacturing. In this study barriers number 1, 2, 15, 9, 12, 4 and 6 are driving barriers (Fig. 2).

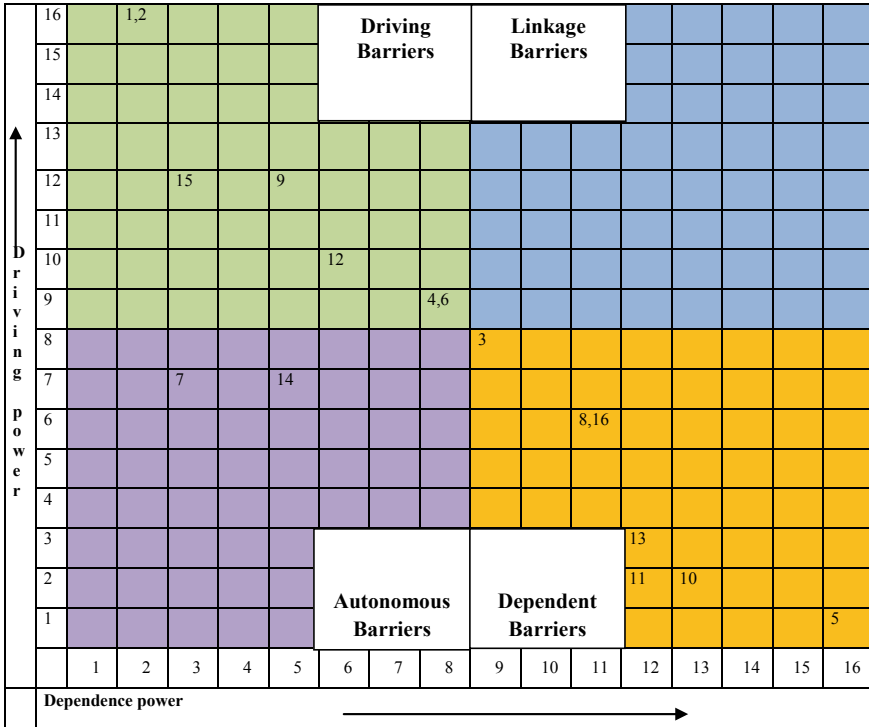


Fig. 2 MICMAC analysis

4 Conclusion

In this research, we have identified those AM barriers which become a hurdle in the way of additive manufacturing by the use of ISM methodology. Based on the survey and opinion of an expert, barrier’s framework evolved. We create a hierarchy of AM barriers that are depending upon driving and dependence power. The software complexity and lack of expert designer has highest driving power, in this research paper. Part to part variation and production technology limitation is the second highest driving power, as soon as possible the industry should remove these AM barriers to the smooth implementation of additive manufacturing.

References

1. M. Shukla, I. Todorov, D. Kapletia, Application of additive manufacturing for mass customisation: understanding the interaction of critical barriers. *Prod. Plann. Control* **29**(10), 814–825 (2018). <https://doi.org/10.1080/09537287.2018.1474395>

2. W.A. Gao, Y.A. Zhang, D.A. Ramanujan, The status, challenges, and future of additive manufacturing in engineering. *Comput. Aided Des.* **69**, 65–89 (2015). <https://doi.org/10.1016/j.cad.2015.04.001>
3. I. Gibson, Additive manufacturing technologies: rapid prototyping to direct digital manufacturing. *Assembly Autom.* **32**(2) (2010). Isbn: 978-1-4419-1119-3. <https://doi.org/10.1108/aa.2012.03332baa.010>
4. A. Sasson, J.C. Johnson, The 3D printing order: variability, supercenters and supply chain reconfigurations. *Int. J. Phys. Distrib. Logist. Manage.* **46**(1), 82–94 (2016). <https://doi.org/10.1108/ijpdlm-10-2015-0257>
5. M.K.A. Thompson, G.B. Moron, T.C. Vaneker, Design for additive manufacturing: trends, opportunity, considerations and constraints. *Manuf. Technol.* **65**(2), 737–760 (2016). <https://doi.org/10.1016/j.ciro.2016.05.004>
6. G. Dwivedi, S.K. Shrivastava, R.K. Shrivastava, Analysis of barriers to implement additive manufacturing technology in the Indian automotive sector. **47**(10), 972–991 (2017). <https://doi.org/10.1108/IJPDLM-07-2017-0222>
7. I. Gibson, The changing face of additive manufacturing. *J. Manuf. Technol. Manage.* **28**(1), 10–17 (2017). <https://doi.org/10.1108/JMTM-12-2016-0182>
8. D.L. Bourell, D.W. Rosen, M.C. Leu, The roadmap for additive manufacturing and its impact. *3D Print. Addit. Manuf.* **1**(1), 6–9 (2014). <https://doi.org/10.1089/3dp.2013.0002>
9. T. Raj, R. Attri, V. Jain, Modelling the factor affecting flexibility in FMS. *Int. J. Indust. Syst. Eng.* **11**(4), 350–374 (2012)
10. J.P. Kruth, Material increase manufacturing by rapid prototyping techniques. *CIRP Ann. Manuf. Technol.* **40**(2), 603–614 (1991)
11. P. Nigam, Interpretive structural modelling (ISM) of the barriers to green supply chain management in Indian companies. *Int. J. Bus. Perform. Supply Chain Modell.* **6**(2), 183 (2014). <https://doi.org/10.1504/ijbpscm.2014.062466>
12. S. Sushil, Interpreting the interpretive structural model. *Glob. J. Flex. Syst. Manage.* **13**(2), 87–106 (2012)
13. R. Attri, N. Dev, V. Sharma, Interpretive structural modelling (ISM) approach: an overview. *Res. J. Manage. Sci.* ISSN 2319–1171 (2013)
14. D. Tiwari, K.K. Shukla, U.A. Khan, in *Advances in Intelligent Manufacturing*. To find the effectiveness of barriers in reverse logistics by using ISM (2020), pp. 81–91
15. F.R. Janes, Interpretive structural modelling: a methodology for structuring complex issues. *Trans. Inst. Meas. Contr.* **10**(3), 145–154 (1988)
16. K. Mathiyazhagan, K. Govindan, A. NoorulHaq, Y. Geng, An ISM approach for the barrier analysis in implementing green supply chain management. *J. Cleaner Prod.* **47**, 283–297 (2013)

Addressing the Agile Manufacturing Drivers Using Interpretive Structural Modeling



Rohit Sharma and Ubaid Ahmad Khan

Abstract While manufacturing is very important in all aspects of today's world, traditional manufacturing itself is not the perfect process to deal with the dynamic and continuous change of demand from customers. Responding quickly to their needs without compromising on quality and cost has been a challenging task in today's cut-throat global market competition, driven by products and services tailored to consumers. Agile manufacturing methods have recently emerged as a new, faster and more efficient way to improve the manufacturing process compared to traditional manufacturing. With this, many drivers are organized and integrated into manufacturing in order to balance the customer satisfaction and profit yields and use this market change as an opportunity to make dominance over its competitors. Finally, the results obtained help industry managers to focus mainly on drivers who have improved agile performance better than on other things. In this project, we find a lot of assisting drivers for agile manufacturing, but only 16 of them are used for analysis. Interpretive structure modeling is used to identify relationships between these drivers. From these 16 selected drivers, some are significant. Top management support, training and education and IT integration and database management are important.

Keywords Agile manufacturing · Agile manufacturing drivers (AMDs) · Interpretive structural modeling (ISM)

1 Introduction

Agile manufacturing is identified as the capacity to succeed in a competitive environment of uninterrupted and uncertain adjustment by responding promptly and effectively to qualifying markets, powered by products and services designed by customer [1]. Henceforth, in this era of consistent and complex improvements occurring through

R. Sharma · U. A. Khan (✉)

Department of Mechanical Engineering, Shambhunath Institute of Engineering and Technology, Prayagraj, U.P., India

customer section, we may conclude that agile development allows the association to flourish [2].

It is the advancement of manufacturing process for customer needs. The best potential is offered by agility for business development. In current scenario, the customer demands are persistently changing, and furthermore, there is bunches of expansion in sophisticated demands by customer. Goldman in 1995 has delineated four significant percepts of agile manufacturing. Agile manufacturing helps in enriching the customer, enhance the competitiveness, mastering the change and inconstancy, leveraging individual as well as data [3]. Agile manufacturing deals with the premise of a combination of techniques as well as different manufacturing techniques. The intention of applying these methods and methodologies is to get adaptable. This worldview of adaptability and reacting promptly to the changing demands is currently turning into a very significant technique for endurance in violent and unpredictable business sectors.

The researcher published an article entitled '21st-century world-class manufacturing' at Lacoca Institute, USA. The researcher found that the market is continuously changing due to the dynamic change in preference and demand of customers [4].

Full-grown endeavors are aware of the need of adaptability and nimbleness of their assembly lines. Chiefs perceive the significance of re-configurability in manufacturing and assembly systems together relying upon the monetary setting and market. Conventional manufacturing practices are unable to cope up with these changes. So, they decide to develop a new manufacturing model known as agile manufacturing system. Intense competition in the market makes the organization focus on customer demands. As importance is given to customer demand, they feel that the organization is working to satisfy their demand and it generates goodwill of customers toward the organization. Agile manufacturing takes competition as an opportunity to capture the market. Hence, we can say that agile manufacturing provides an exponent to compete in the market. In the Indian technological sector, it is an opinion that we can achieve a feasible and economic response to counter any unforeseen change through agile manufacturing. Agile manufacturing support quick dispatch of unplanned product required to fulfill urgent customer requirement [5]. Agile manufacturing becomes a necessity in this era of unpredictable market and only those organisation can excel in this era which have an exponent to alteration in their organization.

2 Literature Review

The agile manufacturing system contributes an organization to respond promptly and effectively conforming to the customer demand using various technologies such as information technology and customization of the goods and services. Agile manufacturing and the idea of agility mean expertness of a product and service maker to flourish in the race of constant and unforeseen shifts [6]. The manufacturing sector has experienced a fast change over the previous century from the large-scale industry of Henry Ford to Lean manufacturing, based on Toyota Production System. There

have been various thoughts between these two poles such as cellular manufacturing and continuous improvement, total quality management and flexible manufacturing system [7].

The basic elements of each of these have been to increase the product caliber and reduce the cost by eliminating the waste. To reach out quick response, one must have to take over agile manufacturing. It is agile manufacturing which delivers reconfigurable functional layout to face any irregular and unexpected demand from the sides of customer. Agile manufacturing not only delivers agility but also swiftness in performing some process. For implementing the agile manufacturing, organization should have to enroll only skilled and trained personnel. Right person with appropriate skill should be placed at right place. Seminar should be organized regularly in order to train and educate knowledgeable workers and employee that help in the productive execution of agile manufacturing. The basic factors which are driving force for implementing the agile manufacturing are globalization, intense competition, information technology, growth in technology and innovation and increasing customer expectations. Virtual integration between inter-organization and intra-organization helps the organization to achieve the required needs and methodology for their under progress projects.

In our study, we have taken versatile drivers from various literatures and expert opinion, but we have taken only few of them. Table 1 shows the identified AMDs from the four research papers. In this study, we have discussed sixteen drivers to

Table 1 Identifying agile manufacturing drivers (AMDs)

S. no.	AMDs	[8]	[9]	[10]	[11]
1	Responsive supply chain			✓	
2	Top management support	✓		✓	
3	Training and education			✓	
4	Customer response adoption				✓
5	Concurrent engineering		✓	✓	
6	Re-configurable layout		✓		
7	Appropriate hardware			✓	
8	Rapid prototyping		✓		
9	Organizational culture	✓			
10	Customer involvement	✓			
11	Knowledgeable workers			✓	
12	Employee involvement				✓
13	Proper database management			✓	
14	Automation				✓
15	Virtual enterprise		✓	✓	
16	IT integrations			✓	✓

agile manufacturing. On these sixteen drivers, we implement interpretive structural modeling (ISM) to find the interrelation between them.

3 ISM Methodology

ISM stands for interpretive structural modeling. It is formulated by J. Warfield. Its motivation is to dissect the progression of perplexing financial frameworks in the year 1974. ISM methodology assists to entail grid and focus on the participation of bond within member of a system [12].

It is a modeling method as the particular bonds or links and global structure are depicted in a model. It is much interpretive as the judgment of the gathering chooses whether and how the parameters are interrelated. Based on relationship, it is structural, and an overall expression are mined from the complex set of parameters [13]. Below are the steps for ISM methodology.

1. Parameters affecting the agile manufacturing system are listed; parameters may be intention, action, individual, barriers, enablers, etc.
2. From the variable outlined in our study, a contextual relation is accomplished among drivers concerning which set of driver would be analyzed.
3. For AMDs who manage pair-wise relationship between drivers, a structural self-interaction matrix (SSIM) is developed.
4. An initial reachability matrix is fabricated from SSIM. After this, matrix is verified for transitivity, and final reachability matrix is procured.
5. Several levels are segmented from the reachability matrix.
6. A graph is framed from the reachability matrix.
7. Obtained graph is altered to model by supplanting nodes with the statement.
8. Then, model is reassessed to check for design incoherency and essential adaptation.

3.1 Structural Self-Interaction (SSIM) Matrix

SSIM is fabricated as shown in the table. Acronyms *V*, *A*, *X*, *O* are used to indicate steering of the dependence among agile manufacturing drivers for the fabrication of SSIM.

The acronym 'V' is used to describe the dependence between the AMDs when AMDs '*i*' influence the AMDs '*j*'. As 'V' is open from one face upside and closes from another face, it forms a clockwise loop which depicts variable '*i*' support variable '*j*'.

The acronym 'A' is used to describe the dependence between the AMDs when AMDs '*j*' influence the AMDs '*i*'. As 'A' is open from one face down side and close from another face hence form a clockwise loop which depicts variable '*j*' support variable '*i*'.

Table 2 SSIM

AMDs	16	15	14	13	12	11	10	9	8	7	6	5	4	3	2	1
1	A	A	A	A	A	A	A	A	A	A	A	A	A	A	A	X
2	V	V	V	V	V	V	V	V	V	V	V	V	V	V	V	X
3	V	O	V	V	V	V	V	O	V	V	V	V	V	V	X	
4	A	V	O	A	A	A	X	A	V	V	O	V	X			
5	A	X	X	A	A	A	A	A	V	O	A	X				
6	O	O	V	A	A	A	O	O	V	O	X					
7	O	O	V	O	A	A	A	O	V	X						
8	A	A	A	A	A	A	A	O	X							
9	V	V	O	V	A	A	V	X								
10	O	V	O	O	A	A	X									
11	V	V	O	O	X	X										
12	O	V	V	O	X											
13	X	V	V	X												
14	A	X	X													
15	A	X														
16	X															

The acronym ‘X’ is used to describe the dependence between the AMDs when both AMDs influence each other. As X is open from both faces, both AMDs influence each other.

The acronym ‘O’ is used to describe the dependence between the AMDs when both AMDs do not influence each other. As O is closed from both face, both AMDs do not influence each other (Table 2).

3.2 Development of Initial Reachability Matrix

By using the information from the SSIM matrix, initial reachability matrix is formulated in the form binary number form. In this step, we replaced the term V, A, X, O by 0 and 1.

- The (i, j) cell is given the acronym [V] in SSIM, the value of the (i, j) cell is changed to 1, and the value of the (j, i) cell value is changed to 0. If the (i, j) cell gives the acronym [A] in SSIM, (i, j) cell value is changed to 0, and the (j, i) cell value is changed to 1.
- If the (i, j) cell is given the acronym [O] in SSIM, (i, j) cell value is changed to 0, and the (j, i) cell value is changed to 0. If the (i, j) cell gives the acronym [X] in SSIM, (i, j) cell value is changed to 1, and the (j, i) cell value is changed to 1.

Table 3 Final reachability matrix

AMD	1	2	3	4	5	6	7	8	9	10	11	12	13	14	15	16	D.P
1	1	0	0	0	0	0	0	0	0	0	0	0	0	0	0	0	1
2	1	1	1	1	1	1	1	1	1	1	1	1	1	1	1	1	16
3	1	0	1	1	1	1	1	1	1*	1	1	1	1	1	1*	1	15
4	1	0	0	1	1	1*	1	1	0	1	0	0	0	1*	1	0	9
5	1	0	0	0	1	0	0	1	0	0	0	0	0	1	1	0	6
6	1	0	0	0	1	1	0	1	0	0	0	0	0	1	1*	0	6
7	1	0	0	0	1*	0	1	1	0	0	0	0	0	1	1*	0	6
8	1	0	0	0	0	0	0	1	0	0	0	0	0	0	0	0	2
9	1	0	0	1	1	1*	1*	1*	1	1	0	0	1	1*	1	1	12
10	1	0	0	1	1	1*	1	1	0	1	0	0	0	1*	1	0	9
11	1	0	0	1	1	1	1	1	1	1	1	1	1*	1*	1	1	14
12	1	0	0	1	1	1	1	1	1	1	1	1	1*	1	1	1*	14
13	1	0	0	1	1	1	1*	1	0	1*	0	0	1	1	1	1	11
14	1	0	0	0	1	0	0	1	0	0	0	0	0	1	1	0	6
15	1	0	0	0	1	0	0	1	0	0	0	0	0	1	1	0	6
16	1	0	0	1*	1	1*	0	1	0	0	0	0	1	1	1	1	9
D.P.P	16	1	2	9	14	13	9	15	5	8	4	4	7	14	14	7	142

3.3 Development of Final Reachability Matrix

After acquiring initial reachability matrix, we have to stub out transitivity to get the final reachability matrix (Table 3).

3.4 Partitioning of Reachability Matrix

By using final reachability, we get reachability set and antecedent set to partition level (Table 4).

3.5 Development of ISM Model

For sixteen AMDs, all ten levels were found. From these outcomes ISM model has been generated (Fig. 1).

By examining this model, we can summarize that which agile manufacturing driver has more importance compared to other, in this model beside the AMDs, level and rank are also modeled. The level explains that the driver at higher level has more

Table 4 Level partitioning

AMD	Reachability set	Antecedent set	Intersection set	Level
1	1	1, 2, 3, 4, 5, 6, 7, 8, 9, 10, 11, 12, 13, 14, 15, 16	1	I
2	2	2	2	X
3	3	2, 3	3	IX
4	4, 10	2, 3, 4, 9, 10, 11, 12, 13, 16	4, 10	V
5	5, 14, 15	2, 3, 4, 5, 6, 7, 9, 10, 11, 12, 13, 14, 15, 16	5, 14, 15	III
6	6	2, 3, 4, 6, 9, 10, 11, 12, 13, 16	6	IV
7	7	2, 3, 4, 7, 9, 10, 11, 12, 13, 16	7	IV
8	8	2, 3, 4, 5, 6, 7, 8, 9, 10, 11, 12, 13, 14, 15, 16	8	II
9	9	2, 3, 9, 11, 12	9	VII
10	4, 10	2, 3, 4, 9, 10, 11, 12, 13, 16	4, 10	V
11	11, 12	2, 3, 11, 12	11, 12	VIII
12	11, 12	2, 3, 11, 12	11, 12	VIII
13	13, 16	2, 3, 9, 11, 12, 13, 16	13, 16	VI
14	5, 14, 15	2, 3, 4, 5, 6, 7, 9, 10, 11, 12, 13, 14, 15, 16	5, 14, 15	III
15	5, 14, 15	2, 3, 4, 5, 7, 9, 10, 11, 12, 13, 14, 15, 16	5, 14, 15	III
16	13, 16	2, 3, 9, 11, 12, 13, 16	13, 16	VI

importance than the lower level driver, rank order is inversely proportional to level order, and here, the highest rank AMDs are the lowest level AMDs. As in our Fig. 1, rank 1 has the same AMDs which is at level X, and rank 10 has the same AMDs which is at level I, so they show vice versa relationship as we see this by arrow representation.

3.6 MICMAC Analysis

The main objective of MICMAC is to find out the driving power and dependence power of each factor. MICMAC is based on the principle of multiplication properties. Using their driving power and dependence power of agile drivers, they are assigned among four groups, namely driving AMDs, linkage AMDs, autonomous AMDs and dependent AMDs (Fig. 2).

4 Conclusion and Discussion

In this report, an effort has been made to examine and key out the agile manufacturing drivers (AMDs) and correlation among them. To balance the requisite of

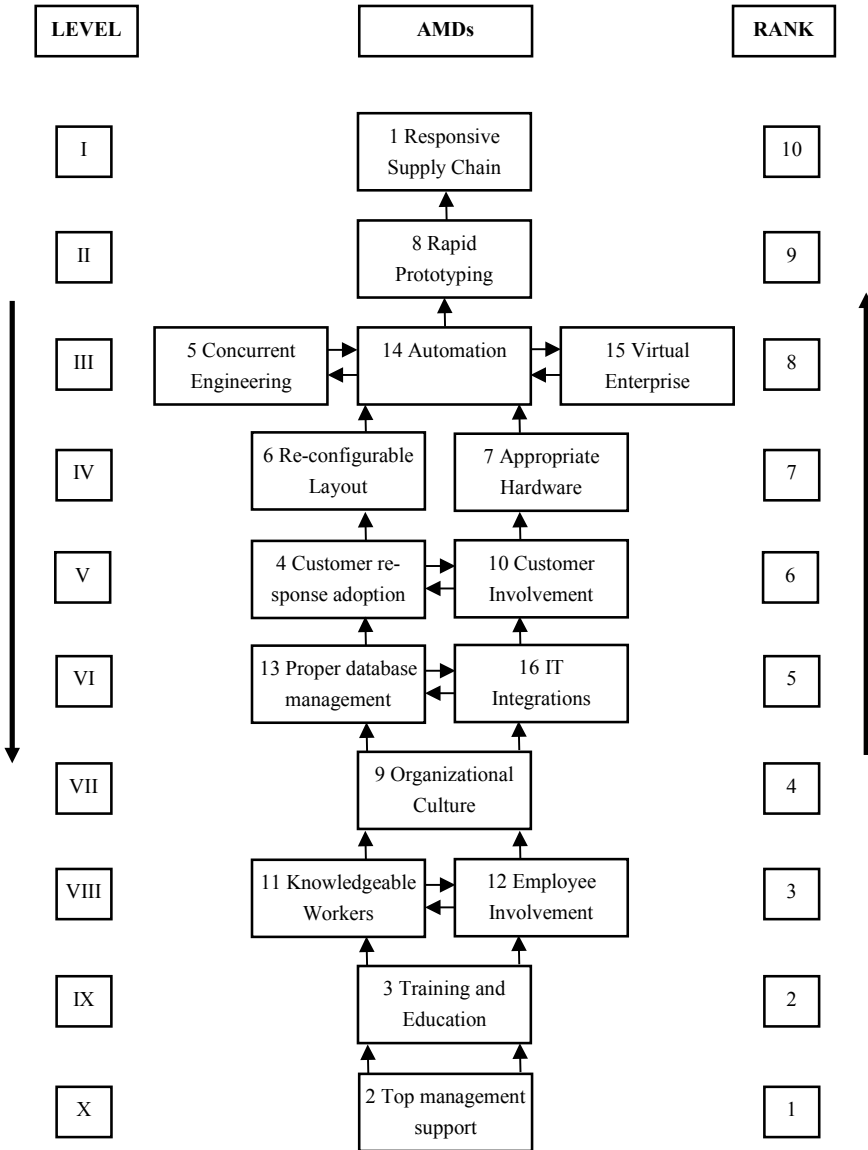


Fig. 1 ISM model of AMDs

customers through quality and support without compromise in economic profit, every organization is in the urge to go across agile manufacturing.

Result of the study shows that AMD Top management support, Training and Education, Knowledgeable workers are the top three suggested significant AMDs for the implementation of agile manufacturing system as they have high driving power

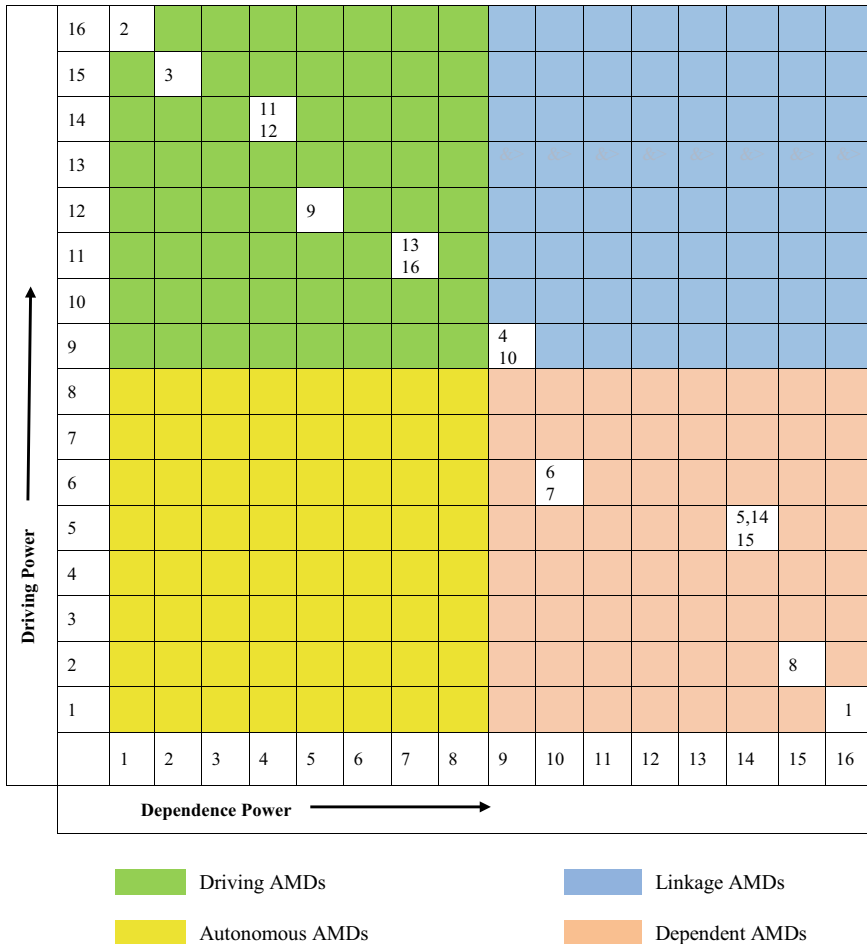


Fig. 2 Classification of AMBs

and they reserve top position in progression of ISM model. For effective execution of agile manufacturing first, we need to implement these AMDs which occupy the top position in the model. It is necessary to develop an environment to implement these AMDs. The result obtained from this study is that this can serve more beneficiaries by delivering assistance to the industrial managers to particularly focus on the influential factor. Agile manufacturing aids the organization to cope with dynamic change in demand, so industries should conduct the seminar and meets to make their employee familiar, have training and education to agile manufacturing. Agile manufacturing can play a significant role in making an organization capable of reacting promptly, efficiently and effectively to manage uninterrupted and unpredictable changes in demand.

References

1. H. Cho, M. Jung, M. Kim, Enabling technologies of agile manufacturing and its related activities in Korea. *Comput. Ind. Eng.* **30**, 323–334 (1996)
2. A. Haider, U. Khan, Finding the percentage effectiveness of agile manufacturing barriers: an AHP approach. *Lecture Notes in Mechanical Engineering* (2020), pp. 133–145
3. L. Goldman, R. Nagel, K. Preiss, *Agile competitors and virtual organizations—strategies for enriching the customer* (1995)
4. R.N. Nagel, Iacocca Institute, *21st Century Manufacturing Enterprise Strategy* (Lehigh University, Bethlehem, PA, 1991)
5. D.A. Elkins, N. Huang, J.M. Alden, Agile manufacturing systems in the automotive industry. *Int. J. Prod. Econ.* **91**, 201–204 (2004)
6. M. Asif Hasan, R. Shankar, J. Sarkis, A study of barriers to agile manufacturing'. *Int. J. Agile Syst. Manage.* **2**, 1–22 (2007)
7. S. Timms, T. Ogle, M. Jackson, Chris Cooper BAE system Agile Manufacturing Processes ICAS 2000 congress (2000)
8. A. Aldahmash, A. Gravell, Y. Howard, Using factor analysis to study the critical success factors of agile software development. *J. Softw.* **12**(12), 957–963 (2017)
9. D. Kumar, S.P. Agarwal, A.K. Mishra, S.K. Singh, An ISM approach to analysis of enablers of agile manufacturing. *J. Mater. Sci. Mech. Eng.* (2015)
10. M. Hasan, R. Shankar, J. Sarkis, A. Suhail, S. Asif, A study of enablers of agile manufacturing. *Int. J. Ind. Syst. Eng.* **4**(4), 407 (2009)
11. C. Ajay Guru Dev, V. Senthil Kumar, Analysis on critical success factors for agile manufacturing evaluation in original equipment manufacturing industry—an AHP approach. *Chin. J. Mech. Eng.* **29**(5), 880–888 (2016)
12. A. Sage, *Interpretive Structural Modeling: Methodology for Large-Scale Systems* (McGraw-Hill, New York, 1977)
13. A. Dwivedi, S. Tandon, U. Khan, Analysis of most effective critical success factors that help industry to implement green supply chain management. *Int. J. Emerg. Technol. Adv. Eng.* **6**(5) (2016)

Minimization of Surface Roughness of WEDM'ed H13 Tool Steel Using Taguchi Method



Lakhan Rathod, Bonde Assefa, Duba Chena Dero, and Ramesh Rudrapati

Abstract Wire electric discharge machining (WEDM) is an advanced metal cutting technique that extensively creates complex features on advanced parts. In WEDM, the optimum processing conditions selection has an important role to manufacture quality of equipment. It is very difficult to select the proper operating variables for producing fine surface finish on parts due to numerous variables associated with WEDM while analysis. The present study is used Taguchi technique for optimization of processing variables in WEDM of H13 high-speed steel. The experiments run has been carried out by L_{16} orthogonal array (OA) of Taguchi method (TM). Significances of machining conditions on surface roughness are studied by S/N ratio and graphical main effect plots. The research work is carried out to optimization of input parameters by Taguchi method for minimization of surface roughness. Confirmatory test has been conducted to inshore the predicted parameter set for WEDM process.

Keywords WEDM · Surface roughness · H13 tool steel · Taguchi method

1 Introduction

An important basis of engineering industry is machining and it is involved in the production of nearly most of the parts of modern civilization. Metal cutting processes are classified into two types such as traditional metal removal methods and non-traditional techniques [1]. Traditional machining methodologies are used to machine traditional components and these techniques are not economical to process advanced materials like high hard alloys/composites. Non-conventional machining processes are specially designed and developed to cut difficult to machine materials

L. Rathod (✉)

Department of Mechanical Engineering, JSPM's BSIOTR, Wagholi, Pune, India

B. Assefa · R. Rudrapati

Department Industrial Engineering, Bule Hora University, Bule Hora, Ethiopia

D. C. Dero

College of Engineering and Technology, Bule Hora University, Bule Hora, Ethiopia

by conventional metal cutting processes [2]. Non-traditional processes are classified into various types based on energy utilized for machining operations. Thermal energy-based technique like electric discharge machining (EDM), is important manufacturing process among others. Wire electric discharge machining (WEDM) is advanced machining technology of EDM which used for cutting an intricate and complicated shape from high hardness material [3]. In modern industries, very often, need to produce high strength, hardness, toughness and good wear and tear resistance and high temperature resistant alloys like titanium, Inconel, ceramics, zirconium, stainless steel, etc., for use in automobile, aerospace, medical, defence, tool and die manufacturing industries. Machining advanced materials by using conventional processes is difficult and sometimes impossible. Thus, non-conventional methodologies are employed instead of traditional metal cutting methods for machine extremely high strength, hard/and brittle work parts.

An EDM process, called travel Wire EDM (TWEDM) or WEDM, has been developed. A wire is used as a cathode in WEDM instead of a firm tool [4]. The wire is passed axially around the work-piece, while the work-piece is fed to various forms in the X and Y directions. The device can be machined with guided and complicated 3D shapes [5]. WEDM is a non-traditional way of the machining method as mentioned earlier and it is a modified version of EDM [6]. Wire is used as an electrode or cutting tool in WEDM. Wire is regularly passed from a bundle and is shown by bottom and top nozzle in WEDM [7]. The quality levels achieved in WEDM highly depend on systematic selection of operating conditions [8]. Surface finish is one of the quality measures used to describe the efficiency of machining [9]. As WEDM is a newly developed advanced technique, various aspects related to enhancement of production procedures need to be explored. Taguchi methodology is found to be an intelligent technique that may be advantageous for control and monitor WEDM for achieving better machining economics [10]. Literature survey is studied in the research to review the published articles based on WEDM, Taguchi methods (TM) and applications of TM for predicting machining responses in various manufacturing techniques.

Vellingiri et al. [11] had been analyzed and explored the effects of operating conditions on quality of WEDM'ed part with the utilization of Taguchi method (TM) while machining of LM13 alloy and LM13/SiC composites. Chatterjee et al. [12] were experimented and predicted the surface roughness in cylindrical grinding by TM. Lodhi et al. [13] had optimized the WEDM operating combinations for minimizing surface roughness of EN41B steel by TM and analysis of variance. Kumar and Agarwal [14] had processed the D3 steel by Taguchi method in WEDM and response, wire offset is predicted. Sharma et al. [15] had been predicted WEDM measures by controlling operating conditions with the use of TM. Rudrapati et al. [16] presented the applications of TM to study and predict the quality measures in through transmission laser welding of acrylics. Kumar [17] had visualized the significances of WEDM operating conditions on surface roughness by ANOVA. They predicted response measures by TM. Manikandan et al. [8] were also predicted WEDM operating setting by TM for achieving good surface qualities on parts.

In the present research investigation, influences of operating conditions on surface roughness (SR) of WEDM'ed H13 tool steel have been studied and predicted by Taguchi method and ANOVA. Experiments have been planned by L_{16} orthogonal array. Impact of processing conditions on SR is visualized by main effects graphs. Finally, SR is minimized by controlling WEDM process using applications of Taguchi method.

2 Material and Methodology

Advanced materials like H13 tool steel are utilized for high end appliances due to its excellent properties like high hardness, heat tolerance, good strength, strong thermal conductivity and hot cracking insensitivity and these qualities make it ideal not only for hot die but for plastic moulds as well. There are many applications for the manufacture of hot spots, twists, spoils and forges, hot extrusion dies for aluminium pins, ejector pins, aluminium, tin and plumb die casting inserts and boxes. H13 High-speed steel is flexible hot work steel made of chromium molybdenum used extensively in hot work and cold tooling. The hot hardness (hot strength) of H13 resists thermal fatigue cracking that occurs as a consequence of cyclic heating and cooling cycles in hot job tooling applications. chemical composition of WEDM is C-0.32–0.45%, Cr 4.75–5.50%, Mo 1.10–1.75%, V 0.80–1.20%, Si 0.80–1.25, Mn 0.25–0.50%, S 0.3 max, P 0.30 max, Fe balanced.

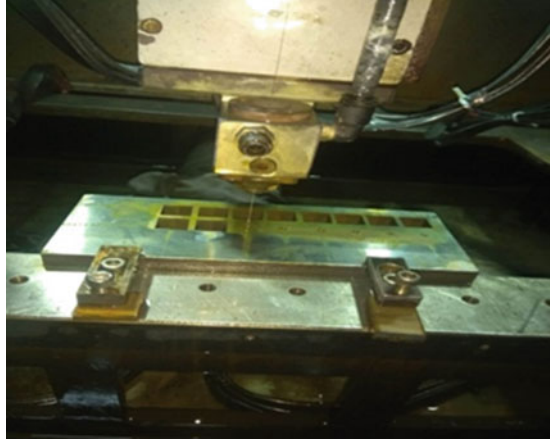
2.1 Experimental Setup

The work-piece should be clamped in the WEDM machine for pocketing action on the work-piece after drilling, as seen in Fig. 1. In WEDM, brass is normally fed into the work-piece by a thin single-strand metal thread. Between the upper and lower guides, the wire that is continuously fed from a spool is held. In the X – Y axis, the guides move and often the upper guide will also move independently, creating transitional forms (circle at the top of the bottom square). This offers the opportunity to configure the Wire EDM to cut very complex types.

2.2 Methodology

The theory of Taguchi is an important method for planning tests and evaluating the mechanism of development and enhancing the efficiency of the system. The definition of the orthogonal collection of Taguchi process experiments allows to evaluate variables with a minimum number of experiments that most influence product consistency, saving time and energy. It utilizes the ratio of statistical S/N ratio to calculate

Fig. 1 Pocketing operation on work-piece



process efficiency [18]. Three distinct objective functions are used in the Taguchi system S/N ratio: larger-the-best, smaller the better and nominal-the best to evaluate the response component. The best criterion is given in Eq. 1 smaller better.

$$\text{Smaller the better: } S/N = -10 \log 1/n \left(\sum y^2 \right) \tag{1}$$

3 Experimental Procedure

Utilizing L_{16} OA Taguchi techniques, the experimental runs were performed on WEDM with four variables, four levels each. In Table 1, the selected input variables and their levels were given. Table 2 displays L_{16} orthogonal array structures for the conduct of experiments. As per the parametric combinations shown in Table 2, experimental runs of H13 high-speed steel were carried out on WEDM. The subsequent response, SR (Ra) is displayed in Table 2.

Table 1 Input control parameters and their levels

Parameters	Units	Level-1	Level-2	Level-3	Level-4
Voltage gap (A)	Volts	17	18	19	20
Wire feed (B)	mm/min	3	4	5	6
Pulse on time (C)	μ s	118	121	122	123
Pulse off time (D)	μ s	55	54	51	50

Table 2 L_{16} orthogonal array of Taguchi method for Ra

Sr. No	Input parameters				Output response
	A	B	C	D	Ra
1	17	3	118	55	2.652
2	17	4	121	54	2.640
3	17	5	122	53	2.690
4	17	6	123	50	3.220
5	18	3	121	53	2.576
6	18	4	118	50	2.399
7	18	5	123	55	2.771
8	18	6	122	54	2.474
9	19	3	122	50	2.639
10	19	4	123	53	2.772
11	19	5	118	54	2.343
12	19	6	121	55	2.611
13	20	3	123	54	2.838
14	20	4	122	55	2.579
15	20	5	121	50	2.929
16	20	6	118	53	2.629

4 Results and Analysis

Present work is designed to examine the importance of WEDM process variables on surface roughness (Ra) of H13 steel material, as mentioned earlier. The experimental data of SR given in Table 2 has been utilized to analyses and optimize the WEDM operation to minimize the Ra of H13 tool steel material with the use of statistical analysis of S/N ratio and TM.

4.1 Analysis of Signal-To-Noise (S/N) Ratio for Surface Roughness (Ra)

Analysis of S/N ratio from MINITAB 16.2 software is applied on the experimental ANOVA test is performed on the experimental data of Ra of WEDM'ed H13 tool steel to test the significance of process variables on output responses. ANOVA test results of Ra is given in Table 3. If P value is smaller than 0.05 then the correlating parameter(s) have a considerable effect on respective response variable at 95% confidence level, i.e. 5% significance level.

Voltage gap (VG) (A), Ton (C) have significant effect on Ra of WEDM'ed H13 steel which has been found from Table 3 because their P values are less than 0.05. Toff

Table 3 ANOVA for surface roughness (Ra) of WEDM of H13 steel

Source	DF	Seq SS	Adj SS	Adj MS	F	P
A	3	1.7138	1.7138	0.57125	15.39	0.025
B	3	0.351	0.351	0.11699	3.15	0.186
C	3	3.4934	3.4934	1.16446	31.37	0.009
D	3	0.9652	0.9652	0.32175	8.67	0.055
Residual error	3	0.1114	0.1114	0.03712	–	–
Total	15	6.6347	S = 0.1927; R-Sq = 98.3%; R-Sq(adj) = 91.6%			

Table 4 Response table for signal-to-noise ratio for Ra (smaller is better)

Level	A	B	C	D
1	–8.914	–8.545	–7.967	–8.88
2	–8.136	–8.279	–8.58	–8.517
3	–8.254	–8.545	–8.28	–8.189
4	–8.754	–8.69	–9.231	–8.473
Delta	0.778	0.41	1.265	0.691
Rank	2	4	1	3

(D) has a considerable effect on Ra as its *P* value is close to 0.05. Input parameters, WF (B) does not have any impact on Ra because its *P* value is more than 0.05, as observed in Table 3. It is stated from Table 3 that VG (A) and Ton (C) are influential parameters for Ra as compared to the other two parameters namely Toff (D) and WF (B).

It is confirmed from the statistical values of *R* square and adjusted *R*-square values as given in Table 3 that experimental data obtained from the experimental tests as shown in Table 2 contains good correlation between the experimental design matrix and obtained performance characteristics.

Response tables for S/N ratio of Ra of WEDM of H13 steel are made and given in Table 4. Based delta value obtained from S/N ratio test, ranking is allocated to all the processing conditions selected in present work. As per delta rankings, parameters which have the highest influence on corresponding performance characteristic has determined[19]. From the results as given in Table 4, it has been noted that Ton (C) is the most influential parameter because its delta rank is one and next is voltage gap (A), Toff (D) and WF (B).

4.2 Main Effect Plots for Ra of WEDM’ed H13 Steel

Main effects plots are drawn based on the S/N ratio of output responses: Ra for WEDM’ed H13 steel material using MINITAB 16.1 software and shown in Fig. 2.

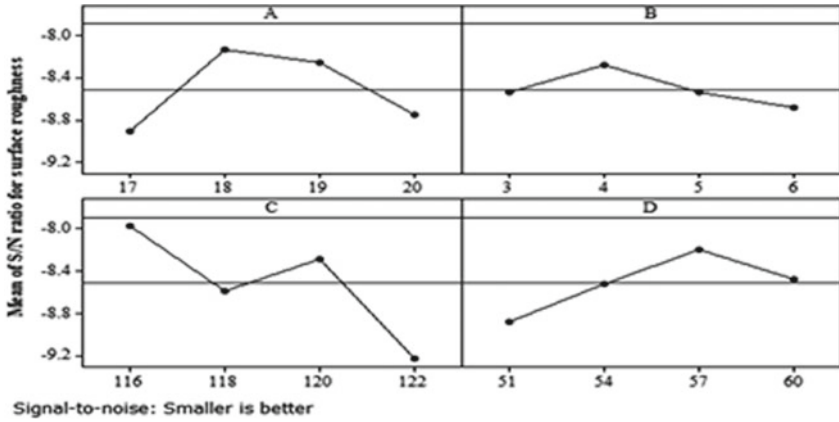


Fig. 2 Main effect plots for Ra of WEDM'ed H13 steel

As mentioned earlier that main effect plots are useful to determine the significances of input parameters on output variables [20].

From the main result plots of Ra as given in Fig. 2, it has been noted that Ra value is increasing with increase of voltage gap (A) from level I to level II and then decreasing up to level IV. It is observed from Fig. 2 that Ra value is increasing with increase of WF (B) from level I to level II and then decreasing until to reach level IV. With an increase of Ton (C) from level I to level II, surface roughness is decreasing and then increasing from level II to level III again it is decreasing from level III to level IV. Surface roughness is increasing with an increase of pulse Toff (D) from level I to level III and then decreasing till reach level IV, as observed from Fig. 2. It is observed from Fig. 2 that that selected process parametric combinations such as VG (A), WF (B), Ton (C) and Toff (D) significantly influence Ra.

Optimal WEDM operating conditions may also be identified from main effects graph [16] as shown in Fig. 2 at highest value of S/N ratio of each factor. From Fig. 2, it is identified that level II of voltage gap (A) and wire feed (B) and level I of pulse on time (C) and level III of pulse off time (D) is optimal for predicting better surface finish value.

Confirmatory experiment To verify the above optimized condition, a confirmatory test has been performed. The results of confirmatory test have good agreement with the initial experimental runs those results confirm the predicted parametric condition by Taguchi methodology.

5 Conclusions

In this research, an experimental investigation has been performed to analyze and optimize the machining characteristics in WEDM process of H13 steel to minimize the Ra the following results are drawn:

- Analysis of S/N ratio conducted to determine the factor effects on Ra
- From the analysis of S/N ratio, It is identified that voltage gap and Ton (C) are influential parameters for SR (Ra)
- Main effect graph reveals that WEDM operating conditions highly influential for SR of H13 high-speed steel
- Optimum WEDM processing condition is obtained by Taguchi method is: voltage gap = 18 V; wire feed = 4 mm/min; pulse on time = 118 μ s; and pulse off time = 51 μ s
- Confirmatory test validates the predicted parametric setting for optimizing SR

References

1. H.A. Youssef, *Machining of Stainless Steels and Super Alloys* (2015)
2. A. Gupta, H. Kumar, L. Nagdeve, P.K. Arora, EDM parametric study of composite materials : a review 7(4) (2020)
3. R. Rudrapati, *Machining of Stainless Steels and Alloys Using Non-Traditional Machining Processes. Stainless Steels and Alloys 2* (Intech Open, 2019), pp. 15–29
4. K. Ishfaq, Optimization of WEDM for precise machining of novel developed Al6061-7.5% SiC squeeze-casted composite. *Int. J. Adv. Manuf. Technol.* **111**(7–8), 2031–2049 (2020)
5. L. Rathod, N. Poonawala, R. Rudrapati, Multi response optimization in WEDM of H13 steel using hybrid optimization approach. *IOP Conf. Ser.: Mater. Sci. Eng.* **814**(1), 012015 (2020)
6. A. Pramanick, S. Mandal, P.P. Dey, P.K. Das, Comparative analysis for the prediction of WEDM responses for machining spark plasma sintered boron carbide ceramic sample by RSM and ANFIS. *Mater. Today: Proc.* (2020)
7. R. Rudrapati, L. Rathod, Effects of wire-EDM machining variables on surface roughness of D2 steel material. *Mater. Sci. Forum* **969**, 656–661 (2019)
8. N. Manikandan, J.S. Binoj, P. Thejasree, P. Sasikala, P. Anusha, Application of Taguchi method on wire electrical discharge machining of Inconel 625. *Mater. Today: Proc.* (2020)
9. R. Rudrapati, A. Bandyopadhyay, P.K. Pal, Investigation on surface roughness in cylindrical grinding, in *AIP Conference Proceedings* (2010), p. 1315
10. M.M. Fakkir, K. Lenin, Optimization of wire EDM process parameters using Taguchi technique. *Mater. Today: Proc.* **21**, 527–530 (2020)
11. S. Vellingiri, R. Soundararajan, N. Mohankumar, K. Nithyananthakumar, K. Muthuselvam, Exploration on WEDM process parameters effect on LM13 alloy and LM13/SiC composites using Taguchi method. *Mater. Today: Proc.* (2020)
12. S. Chatterjee, R. Rudrapati, P.P. Kumar, G. Nandi, Experiments, analysis and parametric optimization of cylindrical traverse cut grinding of aluminium bronze. *Mater. Today: Proc.* **5**(2), 5272–5280 (2018)
13. B.K. Lodhi, S. Agarwal, S. Ahamad, Optimization of WEDM parameters on surface roughness of EN41B steel. *Mater. Today: Proc.* **25**, 816–820 (2019)
14. L.B. Kumar, S. Agarwal, Optimization of wire off set in WEDM process by Taguchi method. *Mater. Today: Proc.* **22**, 2366–2371 (2019)
15. S. Sharma, V.U. Kumar, A. Bansal, Parametric optimization in wire EDM of D2 tool steel using Taguchi method. *Mater. Today: Proc.* (2020)
16. R. Rudrapati, N. Kumar, P.K. Pal, Application of Taguchi method for parametric optimization of through transmission laser welding of acrylic plastics, in *AIP Conference Proceedings*, vol. 2057, p. 020013 (2019)

17. A. Kumar, Modelling and optimizing process parameters of AISI D2 tool steel for WEDM automation modelling and optimizing process parameters of AISI D2 tool steel for WEDM automation. In ICRDMSA 2020. IOP Conf. Ser.: Mater. Sci. Eng. **988**, 012065 (2020)
18. N. Ghosh, P.P. Kumar, G. Nandi, R. Rudrapati, Parametric optimization of gas metal arc welding process by PCA based Taguchi method on austenitic stainless steel AISI 316L. Mater. Today: Proc. **5**(1) (2018)
19. R. Rudrapati, A. Bandyopadhyay, P.K. Pal, Parametric optimization of cylindrical grinding process through hybrid Taguchi method and RSM approach using genetic algorithm. Iran. J. Mech. Eng. Trans. ISME **19**(1), 34–62 (2018)
20. P.K. Pal, A. Bandyopadhyay, R. Rudrapati, Effects of process parameters on surface finish in cylindrical grinding **264–265** (2011)

Brief Overview on Study of Various Parameters Affecting the Productivity of Cotton Yarn



Kedar M. Kulkarni  and Anil R. Sahu 

Abstract This paper aims to study the various yarn parameters affecting quality. The collective information of various fault detection techniques should be verified according to customer requirements at every stage. The quantity and quality of yarn should be monitored with the same importance. Various techniques of yarn are elaborated in the paper. The learning of various parameters affecting yarn productivity is an essential part of cotton yarn making process. The produced yarn should be maintained with good quality and should satisfy customer requirements. The various parameters such as fibre length, fibre fineness, fibre maturity, linear density, tensile properties, yarn hairiness, moisture, twist while spinning, and evenness are some of the properties that need to be studied. The tests should be conducted to fulfil the technologies that are developed to test each parameter of yarn such as the artificial neural network model and modelling and simulation in the appropriate software. The good quality results were found by simulation and modelling, and the proposed model should undergo the testing process. The comparison between rotor, compact, and ring spinning process should be carried out to obtain the best process out of the three which leads to giving the best quality yarn. The cotton farmers producing various types of cotton need to be improved. The quality of cotton production is affected by irregular atmospheric conditions. In this paper, the studies of various parameters affecting the production of yarn were investigated from literature.

Keywords Cotton crop · Optimization of yarn making process · Quality of yarn · Yarn hairiness · Yarn productivity

1 Introduction

The main objective of the paper is to study the various yarn parameters affecting the quality and to give collective information of various fault detection techniques of yarn. The study of various parameters affecting the quality of cotton yarn should be

K. M. Kulkarni (✉) · A. R. Sahu
Department of Mechanical Engineering, G H Raisoni College of Engineering and Management,
Pune, Wagholi 412207, India

© The Author(s), under exclusive license to Springer Nature Singapore Pte Ltd. 2022
M. L. Kolhe et al. (eds.), *Smart Technologies for Energy, Environment and Sustainable Development, Vol 1*, Springer Proceedings in Energy,
https://doi.org/10.1007/978-981-16-6875-3_77

955

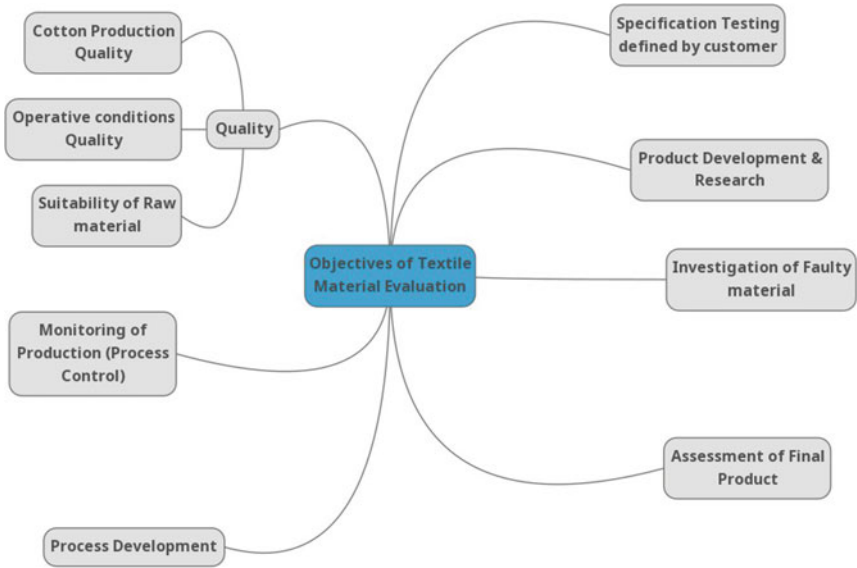


Fig. 1 Mind map for objectives of textile material evaluation

followed by various objectives defined for textile material evaluation. Figure 1 gives the mind map for the objectives. The detailed objectives are discussed in Fig. 1 and are discussed below:

1.1 Quality

The quality is considered for evaluation of any textile materials by using three parameters:

Cotton production About 60% of the total cotton produced is used in India for various textile industries. But the quality of staple fibres is not remarkable for further processing. This condition is raised due to atmospheric conditions and some factors (particularly in India). The irregular rainfall, instability in market, and poor delivery chain of cotton are the main factors affecting yarn production. This leads to cause more suicide cases to farmers. The textile engineers and farmers need to restructure the process of cotton production by considering further needs.

Operative conditions There is a need to inspect that the raw material is suitable for a particular operation with the atmospheric condition. There is a need for inspecting the cotton crop current condition before producing yarn. The room of yarn production is having moisture, then, it should be tested by using the dry bulb and wet bulb temperature technologies, and accordingly, the temperature should be maintained. If the moisture is more, then it will reduce productivity and quality.

Suitability of raw material The raw cotton used for the production of yarn should be checked for its suitability. The cotton should be selected in such a way that the customer should get the yarn having desired characteristics.

1.2 Monitoring of Production (Process Control)

The monitoring is required at every stage of the yarn production process. Lean manufacturing should be implemented to reduce the waste in textile industries. 'Doing the right things on a prior basis' is the main lesson of the textile industry. The optimization of small batch production and improvement in factory layouts are the need for increasing the productivity of the yarn. The wastage of raw material from the blow room to finished yarn packaged into cones should be less [1].

1.3 Process Development

The process should be developed in such a way that the controlled setting of the speed of various components of the speed frame machine is obtained. The short fibres and long fibres should be separated whenever needed. Percentage reduction in fibre length should be checked [1].

1.4 Assessment of Final Product

The fibre properties, carding, drawing and roving sliver properties, imperfections, breaking strength, unevenness, elongation and hairiness parameters should be tested as per the requirement of the final product [2].

1.5 Investigate Faulty Material

Fibre costs more than 50% of cotton production cost [2]. Therefore, the faulty raw material should not be taken into account for yarn production. Similarly, the produced faulty yarn should be recycled after assessment of the final product.

1.6 Product Development and Research

The product development and research should be done in the textile area by using Industry 4.0, machine learning, artificial intelligence, and Internet of things [3]. The neural network should be prepared to detect the fault/defects in the yarn.

1.7 Specification Testing

The specifications such as uniformity, strength, and hairiness should satisfy the specifications given by the customer. The innovative testing techniques should be implemented by taking inputs from the latest research and development.

2 Factors Affecting Yarn Productivity

The extensive review and documentation of the existing work relevant to the parameters affecting the yarn productivity are presented. An ideas of all the studies have clarified in this section.

2.1 Study of Fibre Parameters

Yarn strength is calculated based on length, strength, and fineness. The yarn can be tested physically to study the strength, but there is no need to study the yarn strength physically for each inspection. For example [4], yarn strength is affected by both roving and spinning processes. They have told that the artificial neural network can be used to test the yarn strength without a physical inspection of it. They have created a database based on five input parameters, based on these, they have got 98 results, and then, the results are compared with 50 new tests by using multiple regressions. The model is giving desired output in less than 1 s. Unskilled user can decide for best process parameters from the five parameters selected by the author. Charles Busch land street [5] had studied the experiment of spinning tension and its relation to fibre properties and its end breakage. In the ancient spinning mill, twist insertion is used in the last step of making the fibrous yarn by reducing the weight per unit length of a material to continuous strand. The synthetic aprons and precision rollers were used to obtain the desired aim of reducing weight per unit length. The twisting operation is done around one axis. The researcher has studied to measure the spinning tension for a wide range. The development of end breakage of yarn had done for using it in the laboratories. Fineness, tenacity, and fibre length are tested to test for end breakage. Two tension metres were designed and developed for the measurement of

end breakage. The maximum spindle speed affects badly on fibre length. It is not affecting the tenacity and fineness. The portable tension metre should be installed to measure the spinning tension.

Yarn may be twisted or single. But yarn is twisted in the case where a bundle of singles is to fold and followed by a twist. Yarn is having the circular form structure. The structure needs to be studied for checking the parameters such as Length, transverse dimensions, tensile properties, colour. Impurities, fibre blend, periodic unevenness and optimization. Stjepanovic [6] have studied these properties and sorted out some important parameter need to be studied such as the diameter, linear density, yarn strength, elasticity of the yarn, overall or general evenness, and irregularity of the yarn. The properties available must be known in detail. The single and bundle test methods should be carried out. The blends should be used to get the yarn with minimum cost. Optimization of various machine parameters should be carried out for the process from Blow room to spun yarn. The spinning systems are having various methods for the production of the yarn. Islam [7] has studied the three types of spinning processes—ring, rotor, and compact spinning system. This study was done by comparing the parameters such as percentage deviation, coefficient of mass variation, strength, imperfection, elongation, and hairiness. The highest strength of the yarn and elongation is observed in the compact spinning process. Rotor spun yarn is having less irregularity than that of ring spun. The generally preferred order of spinning process to be used is

1. Compact spinning system
2. Rotor spinning system
3. Ring spinning system.

But the choice of spinning system depends on the requirement of the customer. The parameters such as yarn length, fineness, elongation, strength, short fibre, deviation, and twist per inch (TPI) contents play an important role in yarn quality evaluation as defined by Patil et al. Lower strength and lower elongation in the fibre are mainly due to less number of fibres in the bundle. The quality of the yarn is depending upon raw material and damaged material. Thick place and thin places should be identified with diameter consideration and number of fibres present at every point in the produced yarn. But the study was based on the effect of twist on yarn. It shows that twist per inch increases the strength of the yarn decreases. Hapra et al. [8] have optimized the yarn quality by making cotton mixture design. The customer requirement should be fulfilled without failure of yarn production. So, they have mixed the cotton bales of various lots and made two mixtures. Fibres length, uniformity index, micronaire, fibres tenacity, elongation, trash, and colour are the parameters studied for both cases. Uster Evenness tester is used to test the evenness in fibre. The parameter requirement should be defined clearly to produce a cotton mixture. The cotton mixture can be made by considering the output parameters satisfying the customer requirements.

Micronaire, maturity index, length (mm), uniformity, short fibre index, strength (g/tex), elongation (%), moisture content (%), reflectance (Rd), yellowness (+b), and trash Area (%) are the parameters considered by [2]. The effect of cotton fibre characteristics on the mentioned yarn properties is investigated. The research proved

that the various properties are affected by various cotton parameters. The linear regression model has to be prepared for the study of yarn properties, and further manufacturing should be done by taking results from regression. Mahmood [1] has suggested the smart lean in ring spinning. The textile industries are lagging in the leanness to sustain in the intense competition. Simulation of the future state of the yarn production should be carried out to get a clear idea. This process will reduce the wastage of material. The lean manufacturing (LM) tool should be used to carry out good quality and large quantity production with the smart process.

Table 1 shows various parameters considered by various researchers in the textile industry. Length, strength, fineness, and tenacity are the parameters which have studied more as compared to other parameters.

2.2 Various Techniques to Study Yarn Properties

Fault diagnosis in the yarn is essential to study and redevelop the process of yarn production. Amin [10] has presented a fault diagnosis by using spectrogram. Wavelength calculations are done for every stage of the spinning process from blow room to the spinning process to obtain spun yarn. The wavelength study and use of genetic algorithm carried a more accurate result than ancient methods. This technology needs to be developed further. The machine learning should be applied for yarn finish operations proposed by Seckin [3]. The regression and correlation can be done easily to extract the quality of parameters. The faulty parameters can be easily identified and can be redeveloped.

The various researches made by research techniques are mentioned in Table 2. Liu et al. [11] have studied and developed the defect detection in fabrics by using neural networks. The study was based to overcome the drawbacks of traditional network. The proposed network is a special network which can detect various layers of fabrics and detects the fault. The cotton mixture can be prepared during carding process for curing of carded cotton. The epoxy resin with curing agent can be mixed with carded web of cotton to get desired quality of thermoplastic web of cotton proposed by Kamble and Behera [12]. The productivity of the yarn should be increased by reducing its breakage rates in spinning. The yarn breakage detection and increased yarn strength should be carried out accordingly.

3 Conclusion

The length, strength, tenacity, and fineness are the major parameters to be studied to obtain good quality yarn. Other parameters such as evenness and elongation are the effect of the four major parameters. Artificial intelligence, neural networks, and Industry 4.0 need to be studied and implemented for the field of textile industry. Lean manufacturing tools, blending of cotton, and processing of waste cotton are the

Table 1 Yarn parameter identified through literature review

S. No.	Parameters studied	References
1	Length	[2, 4–6, 8]
2	Strength	[2, 6, 7, 9]
3	Fineness	[5, 9]
4	Tenacity	[5, 6, 8]
5	Twist per inch (TPI)	[5]
6	Transverse dimensions	[6]
7	Colour	[2, 6, 8]
8	Impurities	[6]
9	Fibre blend	[6]
10	Evenness	[6, 8]
11	Optimization	[6]
12	Diameter	[6]
13	Linear density	[6]
14	The elasticity of the yarn	[6]
15	Irregularity	[6]
16	CV (coefficient of mass variation)	[7]
17	Imperfection	[7]
18	Elongation	[2, 7, 8]
19	Hairiness	[7]
20	Short fibre	[2]
21	Deviation	–
22	Uniformity index,	[2, 8]
23	Micronaire	[2, 8]
24	Trash	[2, 8]
25	Maturity index	[2]
26	Moisture content	[2]
27	Reflectance	[2]
28	Lean manufacturing	[1]

techniques to be used effectively in the textile industries. The yarn produced from waste material gives better quality. The combination of various cotton bales and mixture of carded cotton with particular chemicals will increase the productivity of the yarn. The specific requirement of the customer can be satisfied with produced yarn and raw material. The atmospheric conditions are also affecting the yarn production. The surrounding moisture and temperature of the room should be maintained as

Table 2 Techniques developed for fault detection and increase in strength of yarn through literature review

S. no.	Techniques studied/developed	References
<i>Fault detection techniques:</i>		
1	Signal acquisition system and physical–mathematical equations	[13]
2	Machine learning	[10]
3	Neural networks	[11]
4	Using spectrogram	[10]
<i>Techniques to improve yarn strength and properties:</i>		
5	Textile wastage recovery by composite reinforced with cotton fibres	[12]
6	Failure patterns of various yarn and require classic knowledge to study, compare	[14]
7	Traditional technique: Use of trashed cotton to improve quality by model D Opener spinning system	[15]
8	Aware, cost-effective, efficient, flexible machine development with raw cotton and wastage cotton use	[16]
9	Image recognized soft robots for textile usage	[17]
10	Visual and tactile sense to obtain summer shirt fabric	[18]

per requirement. Selection of raw cotton, ease of availability of cotton from nearby farmers, and irregular rainfall also affect the yarn quality.

Future Scope

Growth of textile industries and their effect on the environment should be studied. Only 60% cotton is used in the industry of textile in India from Indian cotton crops production. The high quality with less trouble in maintenance and cost is the present requirement to increase the textile application. This will improve the education in the rural areas. This will increase the employment rate also. As a result, this scenario will increase the productivity with good quality of yarn in textile industries.

References

1. A. Mahmood, Smart lean in ring spinning—a case study to improve performance of yarn manufacturing process. *J. Text. Inst.* **5000** (2020). <https://doi.org/10.1080/00405000.2020.1724461>
2. E. Oner, S. Topcuoglu, O. Kutlu, The effect of cotton fibre characteristic on yarn properties. *IOP Conf. Ser. Mater. Sci. Eng.* **459**(1) (2018). <https://doi.org/10.1088/1757-899X/459/1/012057>
3. M. Seçkin, A.Ç. Seçkin, A. Coşkun, Production fault simulation and forecasting from time series data with machine learning in glove textile industry. *J. Eng. Fibers Fabr.* **14** (2019). <https://doi.org/10.1177/1558925019883462>
4. R. Furferi, M. Gelli, Yarn strength prediction: a practical model based on artificial neural networks. *Adv. Mech. Eng.* **2010**, 2010 (2010). <https://doi.org/10.1155/2010/640103>

5. C.B. Landstreet, An experimental study of spinning tension and its relation to fiber properties and end breakage (1963)
6. Z. Stjepanovi, Ensuring yarns for high quality weaving by effective (2015)
7. Z. Islam, Comparing quality parameters of yarn produced by ring, rotor, and compact spinning system. *Eur. Sci. J. ESJ* **15**(3), 461–477 (2019). <https://doi.org/10.19044/esj.2019.v15n3p461>
8. R. Harpa, A. Curteza, I. Cristian, C. Piroi, Optimizing the yarn quality by means of cotton mixture design. ITC DC B, in *Proceeding 4th International Textile Clothing Design Conference—Magic World Text*, pp. 763–768 (2008)
9. R. Furferi, M. Gelli, Yarn strength prediction: a practical model based on artificial neural networks. *Adv. Mech. Eng.* **2010** (2010). <https://doi.org/10.1155/2010/640103>
10. A.E. Amin, A.S. El-Gehehi, I.A. El-Hawary, R.A. El-Beali, Detecting the fault from spectrograms by using genetic algorithm techniques. *AUTEX Res. J.* **7**, 80–88 (2007)
11. Z. Liu, C. Zhang, C. Li, S. Ding, Y. Dong, Y. Huang, Fabric defect recognition using optimized neural networks. *J. Eng. Fibers Fabr.* **14**(41) (2019). <https://doi.org/10.1177/1558925019897396>
12. Z. Kamble, B.K. Behera, Mechanical properties and water absorption characteristics of composites reinforced with cotton fibres recovered from textile waste. *J. Eng. Fibers Fabr.* **15**, 1–7 (2020). <https://doi.org/10.1177/1558925020901530>
13. P. Cui, Y. Zhang, Y. Xue, A novel method of analyzing spinning tensions for yarn breakage detection in ring frame. *J. Eng. Fibers Fabr.* **15** (2020). <https://doi.org/10.1177/1558925020902979>
14. R.A. Angelova, Failure of yarns in different textile applications. (Elsevier LTD., 2020)
15. K. Aoki, A. Aoki, T. Iwai, Some mill test results by model D opener for trashed machine picked cotton. *J. Text. Mach. Soc. Jpn.* **4**(1), 56–58 (1958)
16. W. Oxenham, Innovations in spun yarn technologies—present and future. *Indian J. Fibre Text. Res.* **31**(1), 116–124 (2006)
17. W. Pyka et al., On the use of textile materials in robotics. *J. Eng. Fiber Fabr.* **15** (2020). <https://doi.org/10.1177/1558925020910725>
18. Y. Zhao et al., A study on customer's preference toward summer-shirt fabric. *J. Eng. Fibers Fabr.* **15**(2) (2020). <https://doi.org/10.1177/1558925020902975>

Experimental Investigation of Hybrid Nanofluids Characteristics in Ti6Al4V Drilling Using Minimum Quantity Lubrication Technique



P. A. Dalke, B. N. Tripathi, and G. P. Deshmukh

Abstract Lean manufacturing is the concept that is driving the industry to cut losses and maximize profits which have big effect on the manufacturing industry where tool life and quality of operation are of utmost importance. Tool life as well as quality of operation can control by controlling various parameters among which lubrication is an important one. Drilling of titanium-based alloys such as Ti6Al4V has a challenge of rapid wear of drilling tool which reduces tool life and also the quality of the drill. Proper lubrication, if used, can reduce wear of the tool. There are many nanoparticles used in lubrication which reduces heat production and friction between tool and work-piece. Using the minimum quantity lubrication process and using nanoparticles such as Al_2O_3 and MWCNT in cryogenic conditions, it can enhance tool life and also result in the high-quality drill. In this paper, we have analyzed effects of MQL + cryogenic with nanoparticle lubrication and wet lubrication method on the effects of the drilling operation.

Keywords Nanoparticles · Lubrication · Drilling · MQC · Ti6Al4V

1 Introduction

Nanofluid is an engineered colloidal suspension nanometer-sized particles base fluids. The nanoparticles used in Nanofluids are typically made of metal, oxide, carbide, otherwise carbon nanotube, etc. Mutual base fluids include water, oil, ethylene, and oil. Nanofluid has improved thermophysical properties as compared to other base fluids. This project aims at improving the cooling efficiency by using organic oil and hybrid nanoparticles as a coolant for machining operation [1].

P. A. Dalke (✉) · B. N. Tripathi

Department of Mechanical Engineering, Chhatrapati Shivaji Maharaj University, Panvel Navi Mumbai, India

G. P. Deshmukh

Department of Mechanical Engineering, A C Patil College of Engineering, Navi Mumbai, India

Several properties of titanium and its alloys such as great strength to weight ratio high oxidization resistivity, higher value of yield stress as well as wear resistance, and high toughness make it eligible for functional and lightweight applications. Relative study among titanium 6-aluminum 4-vanadium alloy, big strength steels like 34CrMo4, big strength aluminum alloys just like AlZnMg_A17075, and high strength magnesium alloy has been presented in terms of their properties and applications. Ti-6Al-4V is advantageous for designing of higher strength or fatigue strength structural components. Besides the superior properties of titanium alloy, few inherent characteristics such as very high chemical reactivity and low thermal conductivity lead to the poor machinability as well as result in premature tool failure and reduced tool life. Furthermore, the generated high cutting temperature, mechanical pressure, dynamic load, then tendency to adhesion, and forming a built-up edge are other main subjects associated with machining of titanium alloys included. In opinions of their potential market, lot of the largest corporation (for examples BMW, Bentley, etc.) now day dissimilar studies to grow appropriate process for machining Ti to reduce the machining price achieved outstanding surface quality, sensible production rates by considering the rare characteristics of titanium alloys as well as developing novel sustainable energy systems. Main issues that affect machinability of Ti alloy are cutting parameters, mechanical property of the materials, pattern, and property of cutting tools cooling policy. Utmost importance of cutting parameters is cutting speed besides feed rate. A rise in cutting speed accelerates tool wear also thereby tool failure. As feed rate has a large effect on surfaces crudeness decline feed rate progresses, the induced surface quality. Furthermore, mechanical property such as low thermal conductivity and high chemical reactivity can be negatively impacts on the machinability. The unsuitable applications of cutting fluids may outcome several difficulties. So, various studies have already been published in the exposed literatures to present progressive cutting fluids techniques to enhance the cutting fluid efficiency particular when machining gets hard to cut material. These materials have greater characteristics likely big strength to weight ratio, oxidization resistances, and temperature resistance that make it material of choice in various industry automotives, etc. Despites their required feature, wide applications of this material have compromised due to the several problems that rise as their machining [2].

Thus, it can reduce heat generation in drilling operations process by actual lubrication. Hence, that hybrid nanofluid produced with such dual nanoparticles had the potential to dissipate heat addition efficiently than ordinary metal working fluid as well as many other nanofluids. By combination multiwall carbon nanotube and Al₂O₃ nanoparticle and generation of hybrid MWCTNs/Al₂O₃, effective lubrication and cooling are anticipated [3].

Not much literature is available on MQL, and thus, further research is necessary with experimentation to determine the dynamics during operation. MQL + cryogenic is also called hybrid machining which is ecofriendly as compared to other techniques. The work-piece surface and subsurface are greatly improved under MQL. Further, research needs to be carried out on-chip morphology under various conditions.

2 Problem Definition

The manufacturing plants are continuously looking the problem of friction between tool-chip interfaces result in reducing in a cutting force, cause tool wear, produce vibration, and also increase tool temperature. Due to the wearing of tool, the surface finishing of the work-piece where the operation is being done and is damaged which needs additional operation hence increasing the time, cost, and needs of tools. Ti6AL4V is extensively used in aeronautics and biomedical applications, and it is important to achieve a good quality of surface finish during operation which needs proper lubrication. Due to bad lubricant, amount of the machine power is directly converted to vibratory control during the machining operations. Therefore, unremitting beat has encountered in many machining operations. Due to bad lubrication, very often a terrible breakdown occurs in machinery result will cause major peripheral damage to the machine, greatly increasing the cost of the repair. At present, for convention lubrication, waste handling is difficult as it's in large quantity. Hence, there is a need for MQL system with nanoparticles to reduce the wastage and maximize the profit [4].

3 Objective of Investigation

The objective of this investigation is to analyze the effects of MQL + cryogenic with nanoparticle lubrication in comparison of wet lubrication for drilling operation on Ti6AL4V metal bar with various hole diameters.

4 Conditions for Experiment

Performing simulation on the effects of various lubrications while performing drilling operation, two separate models for MQL + cryogenic and wet lubrication were prepared and simulated with boundary condition as mentioned in Table 1 for modeling setup below.

5 Results and Discussion

1. MQL + cryogenic lubrication ideal conditions coolant analysis

(i) Temperature

The temperature difference obtained on the plate is around max 292 K in the midsections whereas, near the wall, the temperature difference is approx. 290 K. The fluid temperature, as shown in the chart, is varying for

Table 1 Modeling setup

Fluent parameters/boundary conditions	MQL + cryogenic	Wet
Model setup	Energy equation viscous- $K-\epsilon$ 2 equation model	Energy equation viscous- $K-\epsilon$ 2 equation model
Materials-coolant	Alumina mist room temperature	Engine oil room temperature
Rectangular enclosure is given	Yes	Yes
Inlet condition-velocity inlet	20 m/s	20 m/s
Outlet condition-pressure outlet-static pressure	0 Pa	0 Pa
Temperature inside enclosure	Cryogenic—approx. 196 °C—LN2	Room temperature—approx. 20 °C

a small hole and is of average magnitude ~ 282 K. The fluid temperature in the middle and large holes does not show much effect due to the difference in the areas as compared to a small hole, therefore, the magnitude is almost constant, i.e., 283.10 K (Figs. 1 and 2).

(ii) Pressure

The fluid pressure for the small hole increases with the decrease in the area, as seen from the chart/simulated figure. The magnitude is approx. 14,000 Pa. The fluid pressure on the plate for the middle and large hole decreases with an increase in area, therefore, the magnitude is approx. varying between 6000 Pa to 12,000 Pa (Figs. 3 and 4).

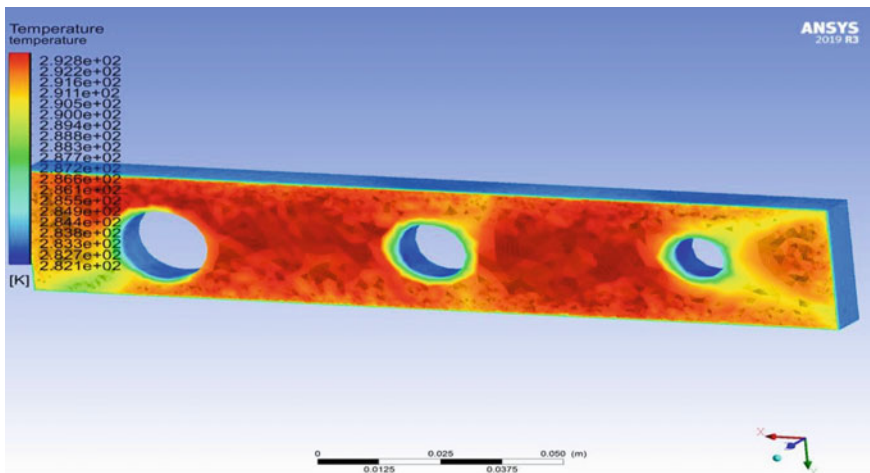


Fig. 1 Temperature distribution for drilling with MQL + cryogenic lubrication

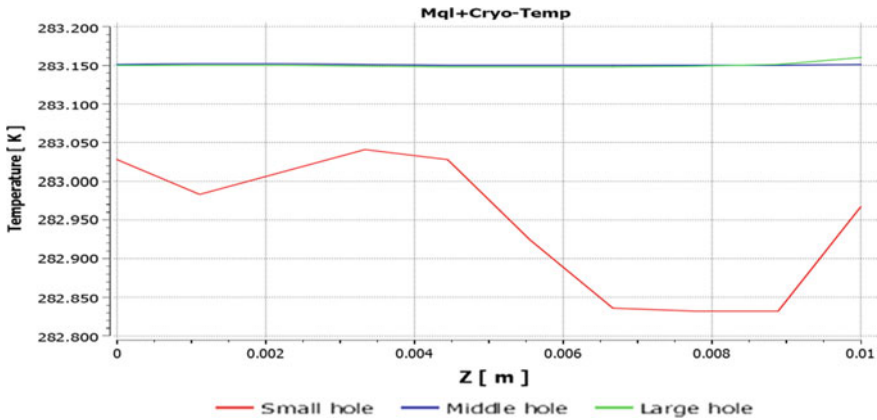


Fig. 2 Temperature vs time graph for drilling with MQL + cryogenic lubrication

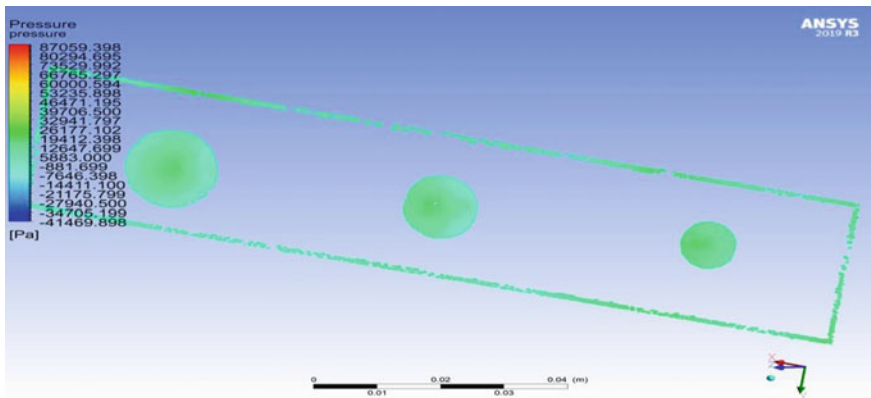


Fig. 3 Pressure distribution for drilling with MQL + cryogenic lubrication

(iii) Velocity

The velocity is low at the boundary conditions due to skin friction; therefore, the magnitude of velocity at boundary surfaces for the small hole is ~40 m/s and the magnitude for the same for middle and large holes is ~70 m/s. The velocity of the fluid flow in the laminar area (i.e., in the middle sections of each hole are comparatively more than the fluid flow at boundaries.) is of the magnitude that is approx. more than 160 m/s (Figs. 5, 6 and 7).

2. Wet Lubrication Ideal Condition Coolant Analysis

(i) Temperature

The temperature difference obtained on the plate is around max ~300 K in the midsections whereas, near the wall, the temperature difference is

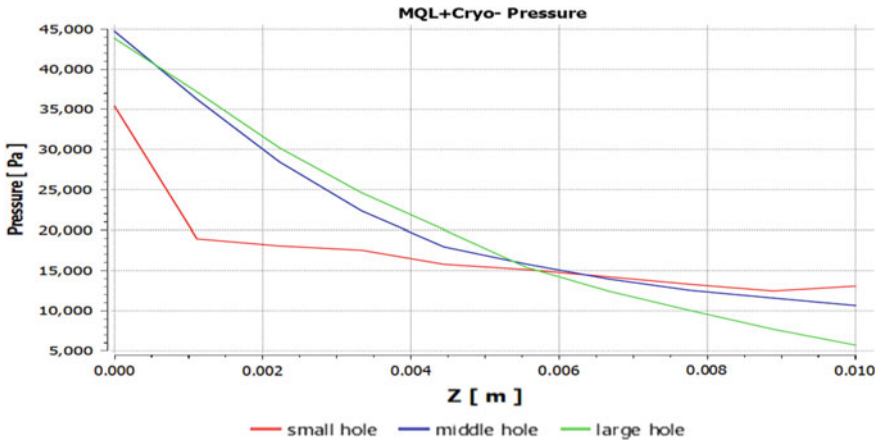


Fig. 4 Pressure vs time graph for drilling with MQL + cryogenic lubrication

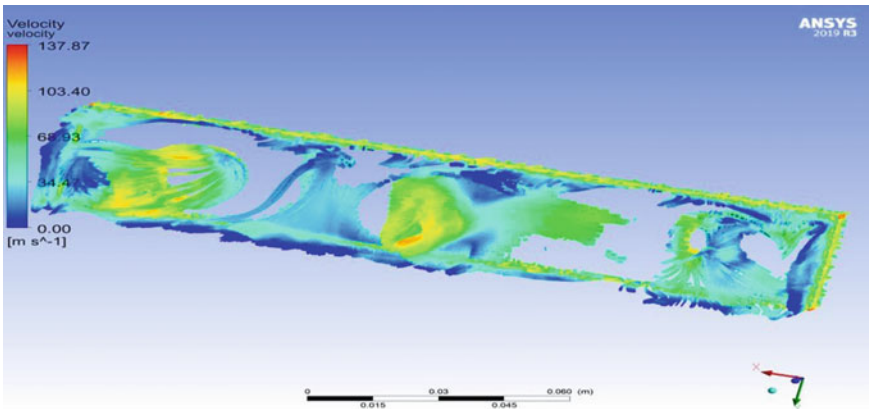


Fig. 5 Velocity distribution for drilling with MQL + cryogenic lubrication

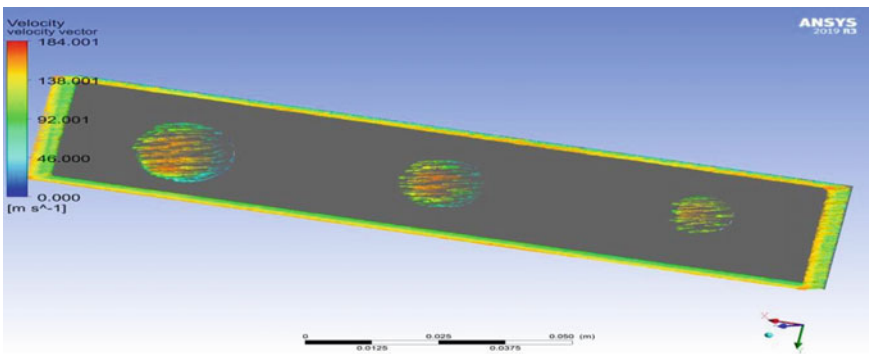


Fig. 6 Velocity vector distribution for drilling with MQL + cryogenic lubrication

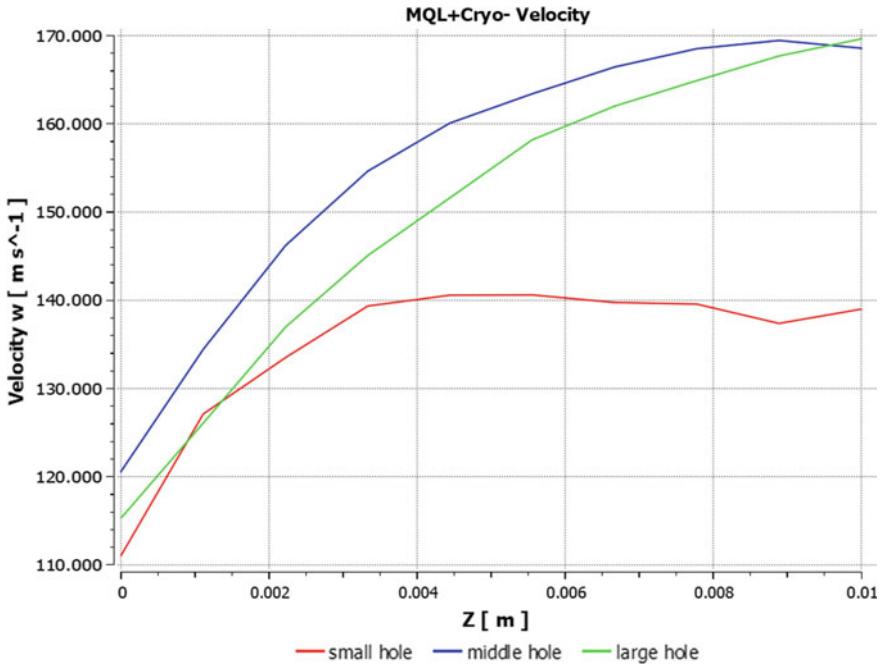


Fig. 7 Velocity versus time graph for drilling with MQL + cryogenic lubrication

approx. 297 K. The fluid temperature as shown in the chart for a small hole and is of average magnitude ~296 K. The fluid temperature in the middle and large holes does not show much effect due to the difference in the areas as compared to a small hole, therefore, the magnitude is almost constant, i.e., 295 K. The change in the magnitude is negligible. The temperature difference is not much because the atmospheric and coolant temperature is almost the same (Figs. 8 and 9).

(ii) Pressure

The fluid pressure for the small hole increases with the decrease in the area, as seen from the chart/simulated figure. The magnitude is approx. 6–7 MPa. The fluid pressure on the plate for the middle and large hole decreases with an increase in area, therefore, the magnitude is approx. varying between 0.7 MPa to 3 MPa. The appropriate relation would be to compare with temperature as pressure is directly proportional to temperature (Figs. 10 and 11).

(iii) Velocity

The velocity is low at the boundary conditions due to skin friction; therefore, the magnitude of velocity at boundary surfaces for a small hole is ~40 m/s and the magnitude for the same for middle and large holes is

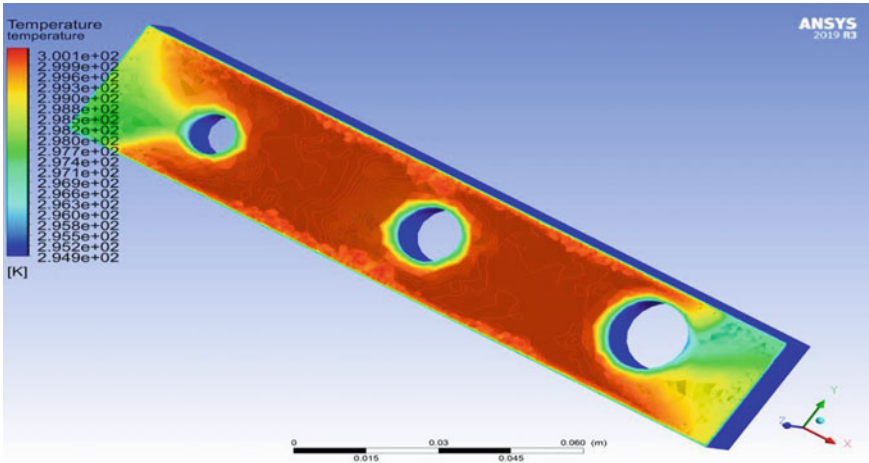


Fig. 8 Temperature distribution for drilling with wet lubrication

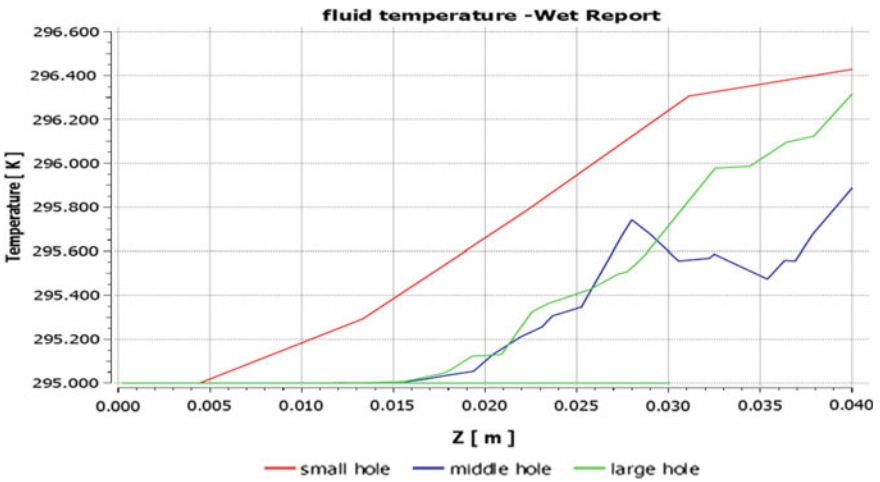


Fig. 9 Temperature versus time graph for drilling with wet lubrication

~90 m/s. The velocity of the fluid flow in the laminar area (i.e., in the middle sections of each hole are comparatively more than the fluid flow at boundaries.) is of the magnitude that is approx. 170 m/s for a small hole and 200 m/s for middle and large holes (Figs. 12, 13 and 14).

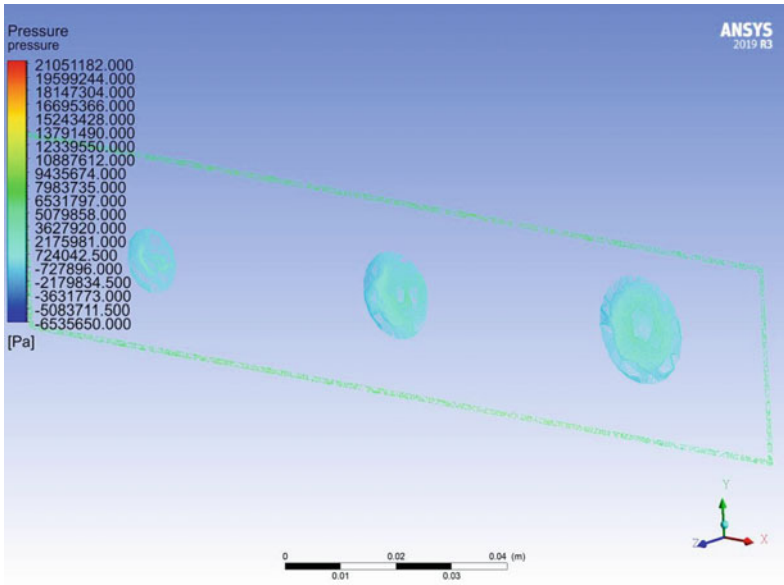


Fig. 10 Pressure distribution for drilling with wet lubrication

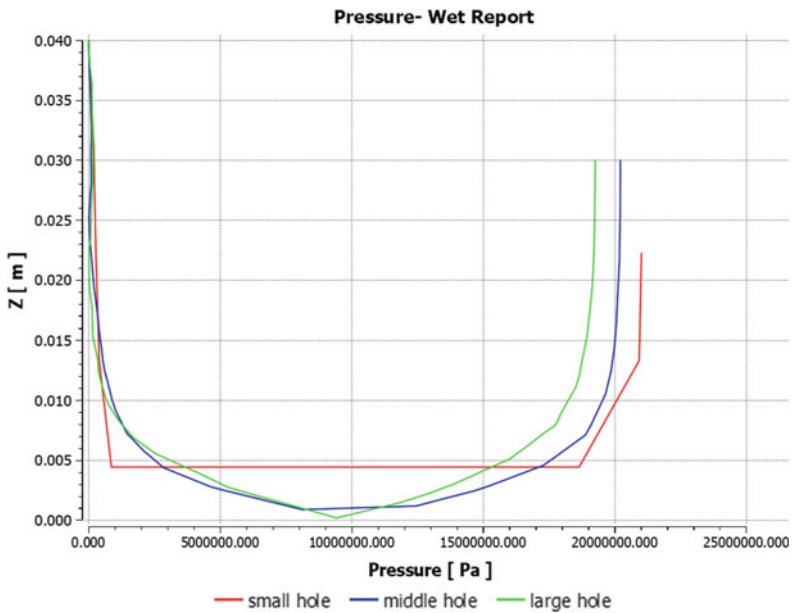


Fig. 11 Pressure versus time graph for drilling with wet lubrication

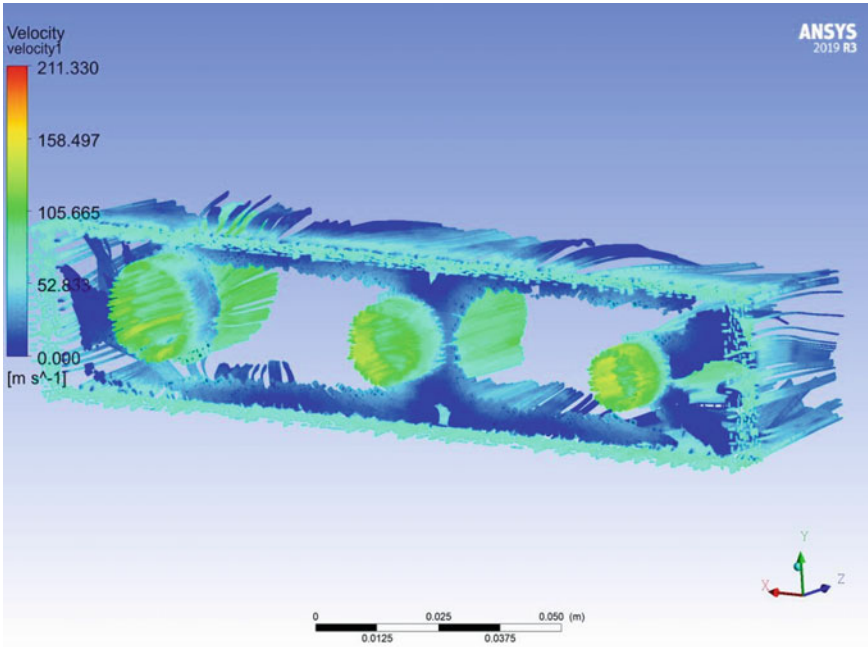


Fig. 12 Velocity distribution for drilling with wet lubrication

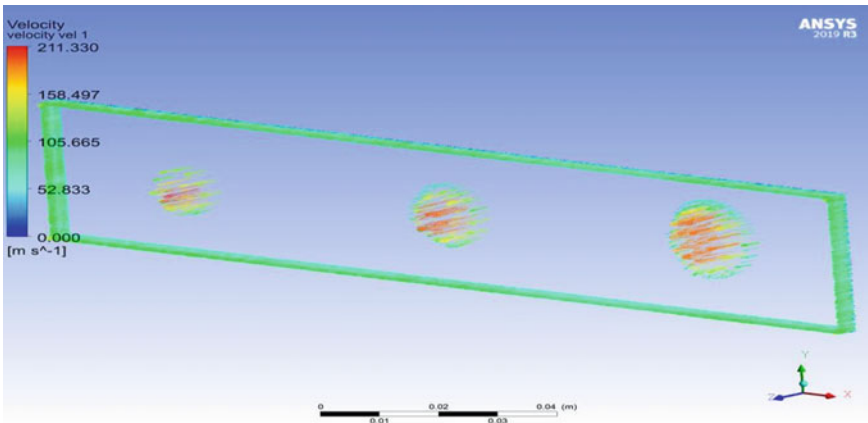


Fig. 13 Velocity vector distribution for drilling with wet lubrication

6 Conclusion

As seen from the results above, the MQL + cryogenic technique is found to be more efficient than the wet technique. The cryogenic conditions maintained at certain

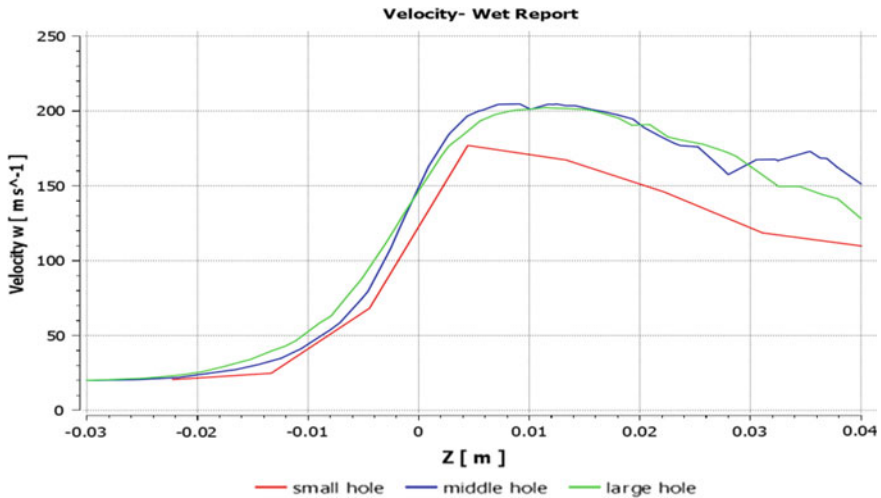


Fig. 14 Velocity versus time graph for drilling with wet lubrication

temperatures and pressure can yield far better postoperative results on the plate than the wet technique. During the MQL + cryogenic machining operations on the plate, temperature variation is very low, whereas, pressure gradient found to be in the range of 6–12 KPa. With the use of high feed and cutting rates in such environment, we can increase the tool life with tools having carbide coating and lowering the residual stresses in the plate. Among those two techniques, temperature fluctuations found to be less in MQL technique as compared to wet technique. While drilling titanium alloy under MQL, certain parameters are needed to be taken into consideration viz., internal/external MQL operating condition, coolant-nanoparticles type usage, number of nozzles, coolant velocity, etc. These factors play a critical role in determining the temperature of the plate in operation. According to the recent surveys, internal MQL + cryogenic condition is better than the traditional methods of machining.

References

1. CHR. Vikram Kumar, B. Ramamoorthy, Performance of coated tools during hard turning under minimum fluid application. *J. Mater. Process. Technol.* **185**, 210–216 (2007)
2. M.Y. Noordin, V.C Venkatesh, S. Sharif, Dry turning of tempered martensitic stainless tool steel using coated cermet and coated carbide tools. *J. Mater. Process. Technol.* **185**, 83–90 (2007)
3. Y.S. Liao, H.M. Lin, Mechanism of minimum quantity lubrication in high-speed milling of hardened steel. *Int. J. Mach. Tools Manuf.* **47**, 1660–1666 (2007)
4. S.Y. Liang, R. Autret, Minimum quantity lubrication in finish hard turning. To appear in *HNICEM '03* (2003)

Simple Automatic Temperature Controller for Chemical Batch Reactor



Gogullan Amirthakulasingam , Rohan Edirisooriya Patabendige ,
Sumith Baduge, and Buddhika Annasiwaththa

Abstract Converting waste plastics into hydrocarbon fuel facilitate waste management and reduce the negative environmental impact of the waste plastics. To do this, a cost-effective and an efficient controller is required to maintain the temperature of reactor in desired range to improve the yield and quality of the liquid and gaseous products derived in the waste plastics to fuel conversion process. Existing controllers are not performed well in above process since this reactor system is a “classic slow control system” which has time delays and many nonlinearities with the time-variant characteristics. Therefore, a suitable proportional only controller which generates a digital variable frequency pulse signal which have unequal ON time and OFF time to maintain the temperature of reactor in an acceptable range was developed in this study. The delay in the system is reasonably managed by the controller while “the settling time of temperature of the reactor within acceptable range” was marginally high due to the sensitivity for the initial set points. Further, overall mass could be measured continuously to calculate the mass outflow rate to identify the rate of reaction. A PID controller could be used to reduce the settling time of the temperature of the reactor within an acceptable range.

Keywords Temperature controller · Time-variant system · Waste plastics derived fuel · Batch reactor · Microcontroller

G. Amirthakulasingam · R. E. Patabendige · S. Baduge · B. Annasiwaththa (✉)
Department of Mechanical and Manufacturing Engineering, Faculty of Engineering,
University of Ruhuna, Galle, Sri Lanka
e-mail: annasi@mme.ruh.ac.lk

R. E. Patabendige
e-mail: rohanep@mme.ruh.ac.lk

S. Baduge
e-mail: sumithb@mme.ruh.ac.lk

1 Introduction

Considering the continuing depletion of fossil fuel reserves and the escalation of environmental problems, significant attention is being paid to new alternatives that will secure future energy supplies while minimizing environmental problems. Therefore, the waste plastics are used as raw materials and depolymerized to generate alternative fuel. This could contribute to save fossil fuel reserves and help to ease increasing environmental problems. The production of this type of alternative fuel facilitates waste management and to reduce the negative environmental impact of waste plastics. A thermally insulated batch reactor equipped with heating coils is required to carry out the process of converting waste plastics into hydrocarbon fuel.

In literature, batch reactors play a key role in chemical, biotechnical, and pharmaceutical industries [1]. Unknown disturbances, nonlinearity, model mismatch, large time delay, time-varying parameters are some of the major complex characteristics of batch reactors. These parameters introduce challenges to optimum control of batch reactors to achieve optimum product yield and quality [2–4]. Many efforts have been made to obtain more effective solutions on batch reactor temperature control. A simple practical technique that has been used in industry for decades where the set point of a temperature (or pressure) controller is ramped up at a predetermined rate; however, if the demand for coolant increases too much, the ramp is stopped until the demand for control effort drops down to a normal level is discussed in [5]. Arduino combined with MATLAB is used to control the temperature of a small volume thermal chamber in-between + 450 °C and –70 °C by using a *K*-type thermocouple to measure the reactor temperature, heater coils for heating, and liquid nitrogen for cooling [6]. An automated cryostat temperature control system for low-temperature galvanomagnetic measurements has been discussed by Sus and Hunkalo [7] with change of the pulse duration at a constant pulse frequency in the circuit control. In study of Beerelli et al. [8], a GUI-based control interface was designed using LabVIEW graphical programming software with 8051 microcontroller and developed a reactor with automated temperature control. The model predictive control (MPC) scheme is applied to batch polymerization reactor for polystyrene production with single input and output, highly dynamic behavior, and multivariable interaction. The MPC controller can provide reliable control performance for previously known system [9]. The batch reactor temperature can be controlled stably and robustly by using a dynamic matrix control (DMC) strategy to optimize and adjust PID controller parameters adaptively according to the working condition [10]. In “Temperature control of a batch polymerization reactor”, a laboratory-scale experiment was shown that DMC and internal model control (IMC) can control temperature well in a polymerization reactor, and the implementation of a DMC controller at the industrial scale for temperature control of batch polymerization reactors is recommended [11].

Reasonable search has been done to identify a literature that had tackled denoted problem in the past, yet authors were unable to locate one as a result it has been concluded that there are no similar studies that have been carried out or documented. Therefore, a simple cost-effective method that utilizes a microcontroller unit (MCU) to control the temperature of a thermally insulated small-scale chemical batch reactor is discussed.

2 Materials and Method

2.1 The Experimental Setup

The schematic diagram of the experimental setup is presented in Fig. 1. Initially, the waste plastic is loaded to the batch chemical reactor and reactor lid is closed. Then the reactor discharge valve is closed, and air inside the reactor is extracted by utilizing a vacuum pump. Subsequently, the heaters are switched ON and temperature of the reactor can increase until a predetermined value maintaining closed and inert environment. The reactor discharge valve is opened when the temperature reached the predetermined value where thermal cracking of waste plastic is taken place. Generated hydrocarbon gasses inside the reactor can pass through the condenser where condensation of gasses takes place at room temperature and atmospheric pressure under water cooling. Temperature of the reactor should be controlled precisely to maintain product yield and quality at the expected level.

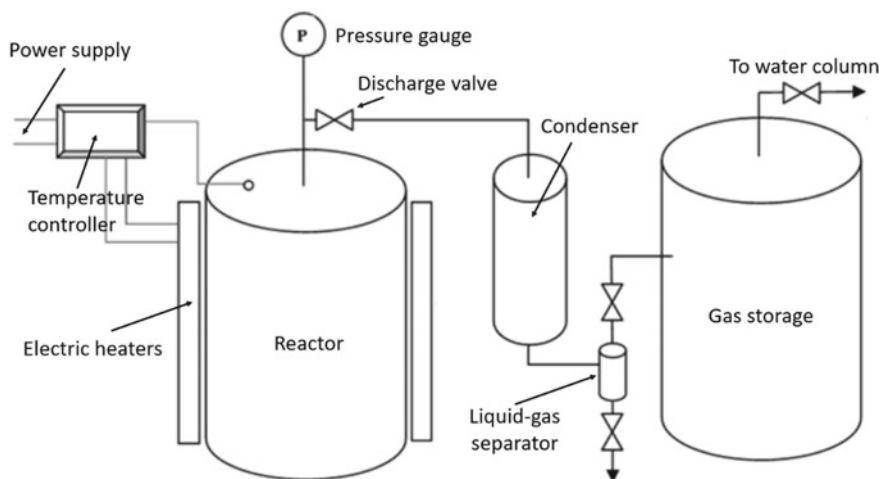


Fig. 1 Schematic diagram of the plant

2.2 The Design of Controller

Figure 2 shows the block diagram of the controller which was developed for above reactor. A cold junction *K*-type thermocouple digitizer module based on MAX6675 with *K*-type thermocouple is used to measure the temperature of the reactor. Three 2.5 kW band heaters were used to supply heat required for the reactor; no cooling coils were equipped with the reactor to cool it whenever required in temperature controlling; hence, entire controlling should be done by the heater. A relay module was used to switch the heaters ON and OFF. A PC-based data acquisition system was used to record the data of the experiment.

2.3 The Working Pattern of Controller

The primary aim of this study is to control batch reactor temperature. Let the set temperature of the batch reactor be θ °C, and the acceptable temperature tolerance of reactor is $\pm \Delta\theta$ °C.

Phase I

Initially, an array of heating coils is utilized to heat the batch reactor from atmospheric temperature to θ °C. But the upper limit of the temperature range ($\theta + \Delta\theta$ °C) is exceeded by the temperature of the reactor as the system has a large delay in the temperature measurement. The temperature measurement delay depends on many parameters, and state of the reactor and a reliable model to predict the temperature in the real plant was not found yet. A new temperature setpoint Q is assumed to exist lower than θ °C to eliminate this first peak overshoot of the reactor temperature as presented in Fig. 3.

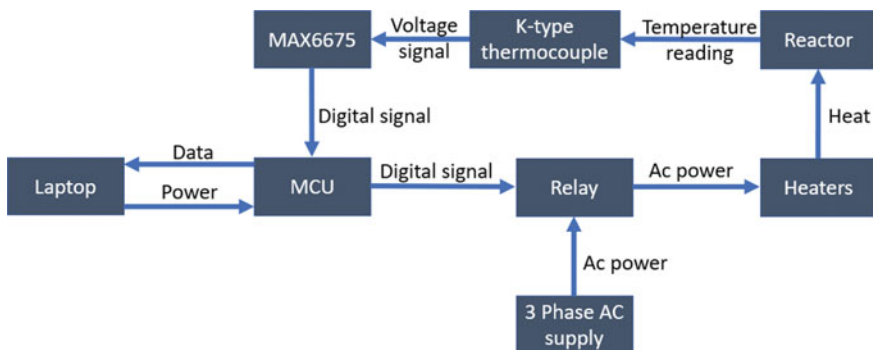


Fig. 2 Schematic diagram of the developed reactor controller

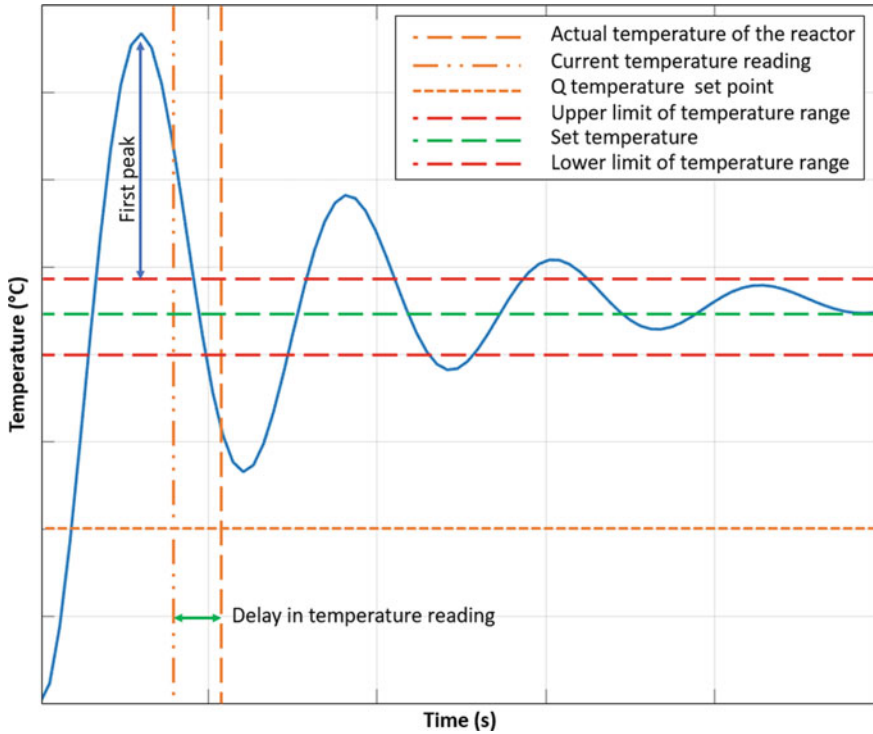


Fig. 3 Working pattern of the controller during initial stage

Phase II

Thereafter, when the temperature value Q is traversed by the temperature of the reactor, a digital variable frequency pulse signal as shown in Fig. 4, which have unequal ON time (t_{ON}) and OFF time (t_{OFF}) will be generated by the controller to control the heating coils. When the temperature is higher than Q , the heaters are turned OFF and the reactor is cooled down via heat convection to the environment and gas emitted by exhaust line. Heating and cooling rates vary depending on environmental conditions and change of mass of plastic in the reactor, and therefore, heater ON time (t_{ON}) and heater OFF time (t_{OFF}) could not be the same.



Fig. 4 Digital variable frequency pulse signal

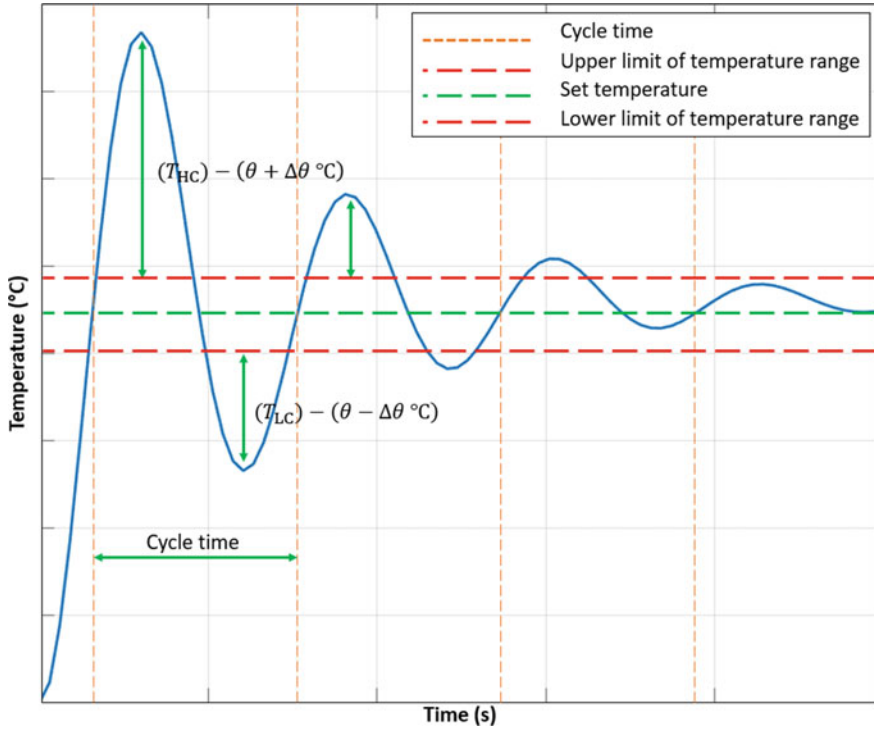


Fig. 5 Working pattern of the controller

The highest temperature of the reactor (T_{HC}) and the lowest temperature of the reactor (T_{LC}) during a cycle are calculated by the controller, and a proportional only controller (P_1, P_2) is used to adjust t_{ON} and t_{OFF} according to the difference between T_{HC} and $(\theta + \Delta\theta \text{ } ^\circ\text{C})$ and the difference between T_{LC} and $(\theta - \Delta\theta \text{ } ^\circ\text{C})$, respectively, to maintain the temperature of the reactor in the acceptable range as explained in Fig. 5.

Pseudocode

```

Begin
Input  $Q, \Delta\theta, P_1, P_2, t_{ON}, t_{OFF}$ 
While (1)
  Input  $\theta$ 
  If ( $\theta < Q$ )
    Heaters ON
  Else
    Find  $T_{HC}$ 
    If ( $(T_{HC} - (\theta + \Delta\theta)) > 0$ )
       $t_{ON} = t_{ON}(1 - P_1(T_{HC} - (\theta + \Delta\theta)))$ 
    End if
    Find  $T_{LC}$ 
    If ( $((\theta - \Delta\theta) - T_{LC}) > 0$ )
       $t_{OFF} = t_{OFF}(1 - P_2((\theta - \Delta\theta) - T_{LC}))$ 
    End if
  End if
  Generate variable frequency pulse signal
End while
End

```

3 Results and Discussions

- The set temperature (θ) was 425 °C.
- The acceptable range of temperature difference ($\pm\Delta\theta$ °C) was ± 3 °C.
- The temperature setpoint Q was 415 °C.
- Initial heater ON time (t_{ON}) was 50 s.
- Initial heater OFF time (t_{OFF}) was 100 s.

As shown in Fig. 6, the total time of the experiment was 8100 s. Heaters were continuously ON until the temperature setpoint Q is reached at 2410 s. The temperature of the reactor settles down to the required range within 680 s from 2410 s. From 3090 to 8100 s, the temperature of the reactor was maintained within the acceptable range using the developed controller.

During phase I, the heaters was ON consistently. Up to 500 s, the K -type thermocouple reading of the batch reactor temperature was close to room temperature. A reasonable change in the reactor temperature as observed after that is shown in Fig. 7.

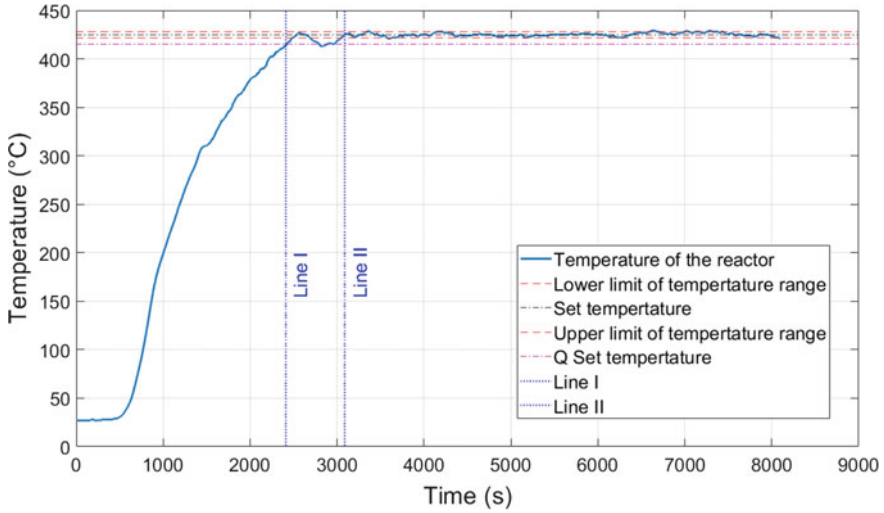


Fig. 6 Temperature of the reactor during the experiment

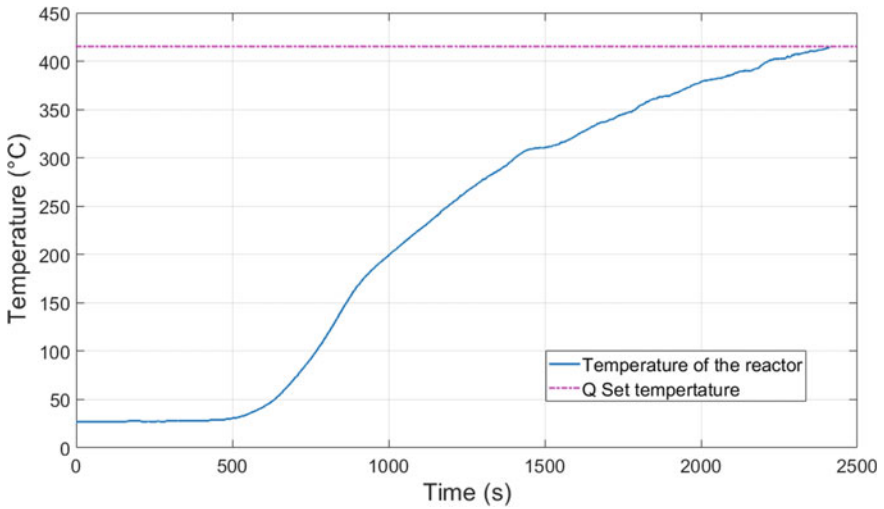


Fig. 7 Temperature of the reactor during phase I

A magnified portion of between Line I and Line II of Fig. 6 is shown in Fig. 8 which illustrates initial 680 s of phase II that were taken by the controller to settle the temperature of the reactor within the acceptable range.

As presented in Fig. 9, the temperature of the reactor was maintained within the acceptable range from 3090 to 8100 s with some minor exclusions which suggest that the controller is generally sufficient, however could be improved further.

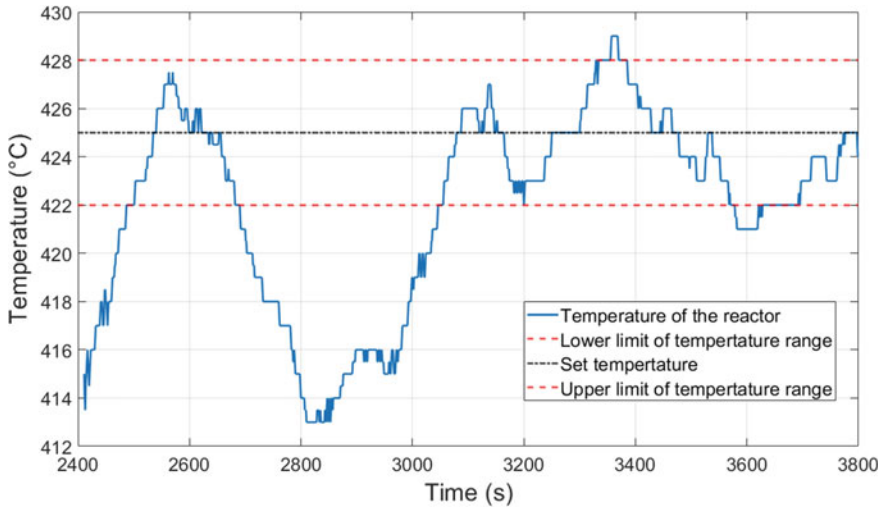


Fig. 8 Temperature of reactor until stabilizing the controller

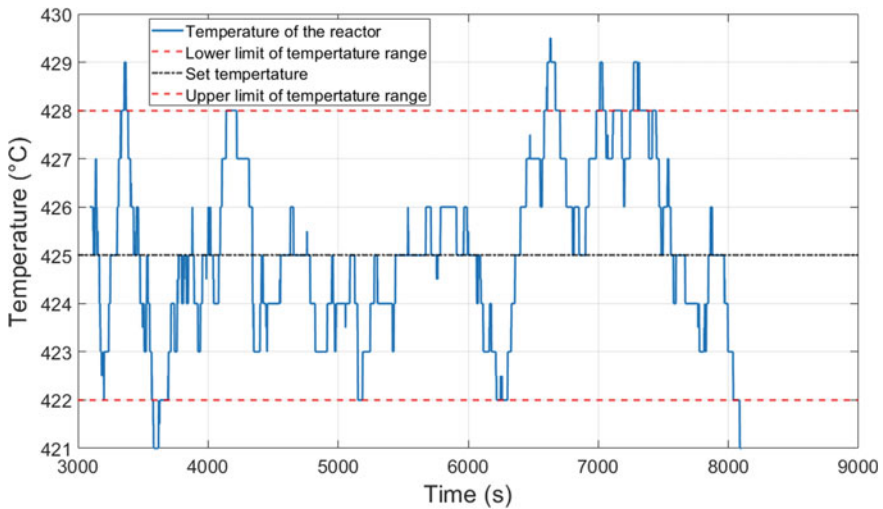


Fig. 9 Temperature of reactor after stabilizing the controller

4 Conclusion

Each batch of waste plastics has a different composition, and therefore, each experiment has a unique system model. There was no clear steady state identified for the reactor during the experiments as it was time-variant. The rate of reaction was not at the same rate, and it was observed that the outflow of the reactor has a variable gas

flow rate. Furthermore, the outflow of gasses reduces the mass of the waste plastic raw material and hence the system. The delay in temperature reading is also time-variant because the amount of molten plastic inside the reactor is time-variant. The composition of the generated hydrocarbon gases is depended on the temperature of the reactor. The delay in the temperature reading varies with the composition of the generated hydrocarbon gases and proportion of the raw material. The reactor system is a “classic slow control system” with many nonlinearities mentioned earlier. The cooling rate depends on environmental conditions including temperature and humidity as well as the state of the reactor.

The controller was sensitive for the initial value of Q , t_{ON} , and t_{OFF} which determines the settling time of the temperature of the reactor within the acceptable range. The introduced temperature set point Q was concluded to be acceptable because the first peak temperature overshoot was within the required temperature range. The first downward peak of the temperature was high due to the initial value of t_{OFF} , which could be further improved by better tuning the control system.

A PID controller could be used to reduce the settling time of the temperature of the reactor within an acceptable range. Overall mass could be measured continuously to calculate the mass outflow rate to identify the rate of reaction. The quality of the product must be evaluated to conclude whether a more advanced control law requiring a nonlinear model of the reactor is required.

References

1. X. Hua, S. Rohani, A. Jutan, Cascade closed-loop optimization and control of batch reactors. *Chem. Eng. Sci.* (2004). <https://doi.org/10.1016/j.ces.2004.04.002>
2. D. Bonvin, Optimal operation of batch reactors—a personal view. *J. Process Control* (1998). [https://doi.org/10.1016/S0959-1524\(98\)00010-9](https://doi.org/10.1016/S0959-1524(98)00010-9)
3. P.T. Benavides, U. Diwekar, Optimal control of biodiesel production in a batch reactor: part I: deterministic control. *Fuel* **94**, 211–217 (2012). <https://doi.org/10.1016/j.fuel.2011.08.035>
4. N. Aziz, I.M. Mujtaba, Optimal operation policies in batch reactors. *Chem. Eng. J.* (2002). [https://doi.org/10.1016/S1385-8947\(01\)00169-3](https://doi.org/10.1016/S1385-8947(01)00169-3)
5. W.L. Luyben, Temperature setpoint-ramp control structure for batch reactors. *Chem. Eng. Sci.* **208**, 115124 (2019). <https://doi.org/10.1016/j.ces.2019.07.042>
6. A. Bayram, Temperature control of a small volume—thermal system in heating and cooling processes with Arduino. *Bitlis Eren Üniversitesi Fen Bilim. Derg.* **8**(4), 1373–1383 (2019). <https://doi.org/10.17798/bitlisfen.531285>
7. B. Sus, A. Hunkalo, ARDUINO based automated temperature controller system for cryostat. *Meas. Equip. Metrol.* **78**, 61–64 (2017). <https://doi.org/10.23939/istcm2017.78.061>
8. A. Beerelli, P.C. Dheeraj, S. Arunkumar, M. Venkatesan, Automated temperature control in batch reactor using LabVIEW, in *2014 IEEE International Conference on Computational Intelligence and Computing Research* (IEEE ICCIC 2014), pp. 449–488 (2015). <https://doi.org/10.1109/ICCIC.2014.7238355>
9. N. Ghasem, Application of model predictive control to batch polymerization reactor. *Univ. Sci.* **11**(1), 49–58 (2006)
10. J. Xiao, C. Shao, L. Zhu, T. Song, Batch reactor temperature control based on DMC-optimization PID, in *2015 IEEE International Conference on Cyber Technology in Automation,*

Control, and Intelligent System (IEEE-CYBER 2015), pp. 371–376 (2015). <https://doi.org/10.1109/CYBER.2015.7287965>

11. S. Yüce, A. Hasaltun, S. Erdoğan, M. Albaz, Temperature control of a batch polymerization reactor. *Chem. Eng. Res. Des.* **77**(5), 413–420 (1999). <https://doi.org/10.1205/026387699526395>